REPORT
VOLUME V

COLUMBIA
ACCIDENT INVESTIGATION BOARD

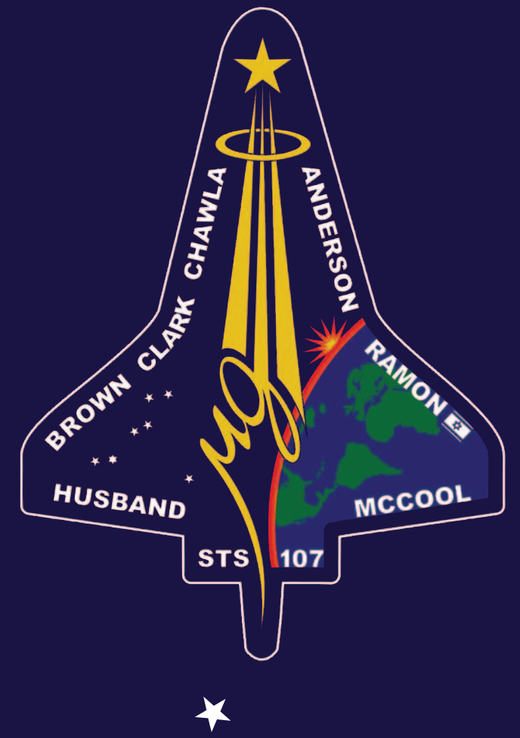

COLUMBIA ACCIDENT INVESTIGATION BOARD

OCTOBER
2003

REPORT VOLUME V
APPENDIX G.13
OCTOBER 2003

COLUMBIA

ACCIDENT INVESTIGATION BOARD

Note: Volumes II – VI contain a number of conclusions and recommendations, several of which were adopted by the Board in Volume I. The other conclusions and recommendations drawn in Volumes II – VI do not necessarily reflect the opinion of the Board, but are included for the record. When there is conflict, Volume I takes precedence.

REPORT VOLUME V
APPENDIX G.13
OCTOBER 2003

On the Front Cover

This was the crew patch for STS-107. The central element of the patch was the microgravity symbol, µg, flowing into the rays of the Astronaut symbol. The orbital inclination was portrayed by the 39-degree angle of the Earth's horizon to the Astronaut symbol. The sunrise was representative of the numerous science experiments that were the dawn of a new era for continued microgravity research on the International Space Station and beyond. The breadth of science conducted on this mission had widespread benefits to life on Earth and the continued exploration of space, illustrated by the Earth and stars. The constellation Columba (the dove) was chosen to symbolize peace on Earth and the Space Shuttle Columbia. In addition, the seven stars represent the STS-107 crew members, as well as honoring the original Mercury 7 astronauts who paved the way to make research in space possible. The Israeli flag represented the first person from that country to fly on the Space Shuttle.

On the Back Cover

This emblem memorializes the three U.S. human space flight accidents – Apollo 1, Challenger, and Columbia. The words across the top translate to: "To The Stars, Despite Adversity – Always Explore"

The Board would like to acknowledge the hard work and effort of the following individuals in the production of Volumes II – VI.

Maj. Gen. John L. Barry	Executive Director to the Chairman
Dennis R. Jenkins	Investigator and Liaison to the Board
Lt. Col. Donald J. White	Technical Editor
Lt. Col. Patrick A. Goodman	Technical Editor
Joshua M. Limbaugh	Layout Artist
Joseph A. Reid	Graphic Designer
Christine F. Cole	Administrative Assistant
Jana T. Schultz	Administrative Assistant
Lester A. Reingold	Lead Editor
Christopher M. Kirchhoff	Editor
Ariel H. Simon	Assistant Editor
Jennifer L. Bukvics	Lead Project Manager
Donna J. Fudge	Senior Paralegal, Group II Coordinator
Susan M. Plott	Project Supervisor, Group III Coordinator
Ellen M. Tanner	Project Supervisor
Matthew J. Martin	Government Relations Consultant
Frances C. Fisher	ANSER Liaison

Limited First Printing, October 2003, by the
Columbia Accident Investigation Board

Subsequent Printing and Distribution by the
National Aeronautics and Space Administration
and the
Government Printing Office
Washington, D.C.

VOLUME I

VOLUME II

CAIB TECHNICAL DOCUMENTS CITED IN THE REPORT

Reader's Guide to Volume V

Volume V of the Report contains appendices that were not cited in Volume I. These consist of documents produced by NASA and other organizations, which were provided to the Columbia Accident Investigation Board in support of its inquiry into the February 1, 2003 destruction of the Space Shuttle *Columbia*. The documents are compiled in this volume in the interest of establishing a complete record, but they do not necessarily represent the views of the Board. Volume I contains the Board's findings, analysis, and recommendations. The documents in Volume V are also contained in their original color format on the DVD disc in the back of Volume II.

THIS PAGE INTENTIONALLY LEFT BLANK

Volume V
Appendix G.13

Aero/Aerothermal/Thermal/Structures Team Final Report, Aug 6, 2003

This Appendix contains NSTS-37398 Aero/Aerothermal/Thermal/Structures Team Final Report in Support of the *Columbia* Accident Investigation, 6 August 2003.

THIS PAGE INTENTIONALLY LEFT BLANK

NSTS-37398

Aero/Aerothermal/Thermal/Structures Team Final Report

in support of the *Columbia* Accident Investigation

August 6, 2003

Submitted by

Original signature obtained
Pam Madera, USA
Team Lead

Original signature obtained
Steve Labbe, NASA JSC
Aerodynamics

Original signature obtained
Joe Caram, NASA JSC
Aerothermodynamics

Original signature obtained
Chris Madden, NASA JSC
Thermal

Original signature obtained
Mike Dunham, Boeing
Stress, Loads and Dynamics

Contributing Authors - Aerodynamics

Karen Bibb, NASA Langley Research Center
Greg Brauckmann, NASA Langley Research Center
Olman Carvajal, Boeing-Houston
Kevin Dries, NASA Johnson Space Center
Randy Lillard, NASA Johnson Space Center
Ramadas K. Prabhu, LESC-Hampton
Karuna Rajagopal, Boeing-Huntington Beach
James Reuther, NASA Ames Research Center
William I. Scallion, NASA Langley Research Center
Jeff Stone, Boeing-Huntington Beach

Contributing Authors – Aerothermodynamics

Steve Alter, NASA Langley Research Center
Steve Barson, Boeing Rocketdyne Propulsion and Power
Maria Bobskill, Ph. D. , NASA Langley Research Center
Stan Bouslog, Lockheed Martin
Katie Boyles, NASA Johnson Space Center
Kevin Bowcut, Ph. D., Boeing Huntington Beach
Charles Campbell, NASA Johnson Space Center
Steve Fitzgerald, NASA Johnson Space Center
Michail Gallis, Ph. D., Sandia National Laboratories
Peter Gnoffo, Ph. D. , NASA Langley Research Center
Scott Halloran, Boeing Rocketdyne Propulsion and Power
Tom Horvath, NASA Langley Research Center
Randy Lillard, NASA Johnson Space Center
Joe Olejniczak Ph. D., NASA Ames Research Center

Tom Paul, Lockheed Martin
Jeff Payne, Sandia National Laboratories
Don Picetti, Boeing Huntington Beach
Karuna Rajagopal, Ph. D., Boeing Huntington Beach
James Reuther, Ph. D, NASA Ames Research Center
Joe Ruf, NASA Marshall Space Flight Center
Greg Schunk, NASA Marshall Space Flight Center
John Sharp, NASA Marshall Space Flight Center
Joel Stolzfus, NASA Johnson Space Center White Sands Test Facility
Ricky Thompson, NASA Langley Research Center
K. C. Wang, Boeing Houston
Vince Zoby, NASA Langley Research Center

Contributing Authors - Thermal

Donald Curry, NASA Johnson Space Center
Steven Del Papa, NASA Johnson Space Center
Ronald Lewis, NASA Johnson Space Center
Dan Newswander, NASA Johnson Space Center
Don Picetti, Boeing Huntington Beach
Alvaro Rodriguez, NASA Johnson Space Center

Contributing Authors – Stress

Jason Adair, BNA-Houston
Charles Park, BNA- Huntington Beach
Paul Parker, BNA-Houston
Shawn Sorenson, BNA-Houston

Table of Contents

Executive Summary

The Aerodynamic/Aerothermodynamic/Thermal/Structures (AATS) Team was formed by the Orbiter Vehicle Engineering Working Group (OVEWG) to assist in the STS-107 Columbia Accident Investigation. The primary objective of this team was to provide an analytical basis for a most probable damage scenario for the STS-107 entry. This team was not chartered with the task of defining how the initial damage was incurred.

The approach used by the AATS Team was to postulate the approximate location and extent of damage experienced by Columbia during entry. The team would then formulate analyses or tests that would emulate the vehicle aerodynamic, thermal, or structural responses to the postulated hardware damage. The results of the analyses or tests were compared to anomalous MADS and OI measured data or off-nominal aerodynamic increments associated with the STS-107 entry to determine if the postulated damage condition was feasible. Results were then integrated to ensure that the postulated damage condition could be supported across the technical disciplines. Where appropriate to ensure consistency, corresponding analysis of damage conditions were completed for the ascent phase of flight. Finally, postulated damage conditions were evaluated to ensure that they would not conflict with the condition of recovered hardware or other flight data.

The AATS Team efforts were primarily focused on postulated damage conditions starting at entry interface (EI) and extending to approximately 615 seconds from EI. Evaluations of off-nominal indications during this time frame were expected to provide the best insight into identifying the initial damage condition. An evaluation of damage conditions consistent with aerodynamic increments just prior to loss of signal (LOS) was conducted for completeness.

The culmination of multiple analyses substantiates a most probable entry damage scenario that begins with damage to the wing leading edge reinforced carbon-carbon (RCC) prior to EI. Analyses indicate that the initial damage was consistent with a breach in the lower portion of RCC panel 8. The breach can be described as an aperture with an area equivalent to that of a six to ten inch diameter hole. From the beginning of the entry profile, hot gas was ingested into the wing leading edge cavity behind the RCC panels. The flow of hot gas into the cavity was disturbed by complex internal geometry increasing both the local pressure in the cavity and the heating of local surfaces. The increase in RCC cavity pressure and internal flow patterns increased flow out of the vents located at the top of the cavity. By approximately EI+340 seconds from EI, the vent paths were increased slightly due to thermal degradation. Flow out of the upper vents resulted in a disturbance of flow on the leeside of the vehicle, thereby displacing the strake and canopy vortices and temporarily reducing heating to the left sidewall and left Orbital Maneuver System (OMS) pod. Heating of local surfaces inside the RCC cavity eventually resulted in burn through of the wing leading edge spar by approximately EI plus 487 seconds. The transverse momentum of the flow of hot gas entering the RCC cavity was redirected as the flow impinges on RCC ribs and spanner beam hardware and insulation. As a result, the plume entering the intermediate wing was directed normal from the spar toward the main landing gear compartment wall. The impingement of the plume in this region resulted in burning of the four OI/MADS wire bundles, burn through of the main landing gear compartment wall, and burn through of the upper wing skin. Burn through of the main landing gear compartment wall resulted in an abnormal temperature rise of main landing gear components in the wheel well due to convective heating. Increased outer mold line heating of the left sidewall and OMS pod can be explained by redirection of the wing leading edge windward flow to the leeside through either a severely damaged and/or missing upper RCC carrier panel(s), severely damaged or missing full RCC panel (e.g. panel 9), or damaged upper wing just aft of the wing leading edge. These damage conditions are also consistent with anomalous aerodynamic increments between EI+500 to EI+600 seconds. Damage in the left wing cavity continued to progress until loss of signal. This damage resulted in a significant depression being formed on the lower surface of the left wing due to burn though of intermediate wing truss tubes and compromised structural strength associated with heating internal to the wing. The depression in the lower wing resulted in external flow patterns that effectively increased the lift and drag on the left wing resulting in the positive rolling moment and negative yawing moment just prior to loss of signal. This report details the tests and analyses results that lend credence to this damage progression as a plausible explanation of Columbia's final moments of flight.

1 INTRODUCTION

The AATS Team was formed by the Orbiter Vehicle Engineering Working Group (OVEWG) to aid the NASA community in the investigation of the STS-107 accident. The team was formed with members from various organizations and technical disciplines throughout the NASA and contractor communities. The team was organized with sub-team leads for each significant technical area as shown in Figure 1.1. A short biography of team leads and a list of team members can be found in Appendix B of this report.

This report summarizes the analyses performed by the AATS Team to support scenario development and to address actions levied and/or requests made by the Columbia Accident Investigation Board, OVEWG, and other teams supporting the investigation.

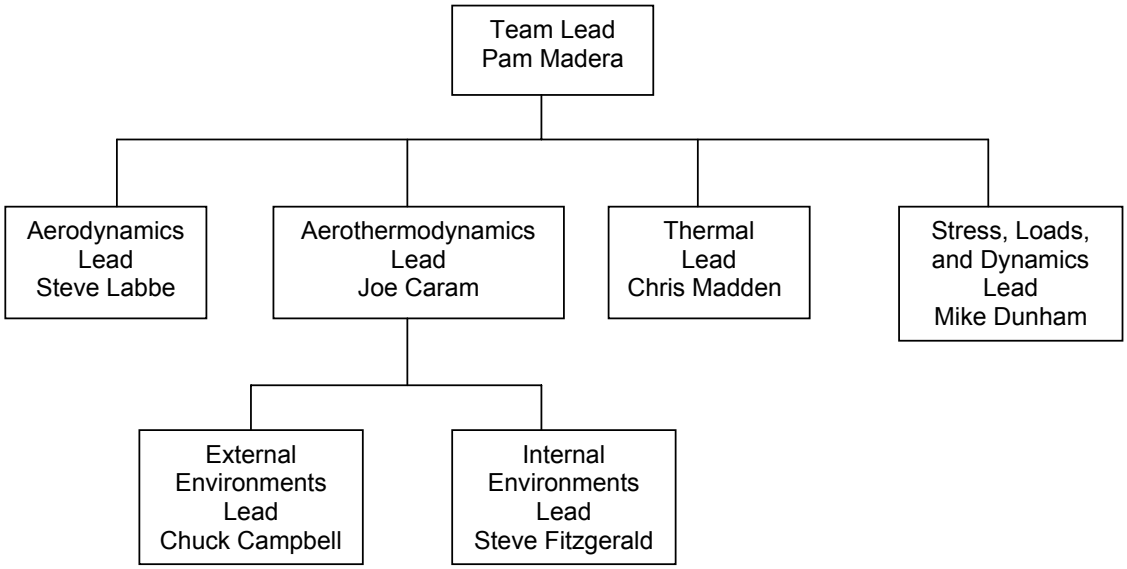

Figure 1-1 Team Organization

2 PURPOSE & SCOPE

This report documents the analyses performed by the AATS Team that provided substantiation for a most probable damage scenario for the Columbia accident. Damage conditions were analyzed to a level of fidelity that would provide the NASA OVEWG, NAIT, and CAIB sufficient insight to ensure that the appropriate corrective action steps would be taken prior to return to flight. In some cases, engineering level analysis was sufficient to understand the off-nominal conditions. This team was not chartered with the task of defining how the initial damage was incurred.

The AATS Team efforts were primarily focused on postulated damage conditions starting at entry interface (EI) and extending to approximately 615 seconds from EI. Evaluations of off-nominal indications during this time frame were expected to provide the best insight to identify the initial damage condition.

An evaluation of damage conditions consistent with aerodynamic increments just prior to loss of signal (LOS) was conducted for completeness.
It should be noted that analyses and tests conducted for the investigation were performed on representative geometries. The fact that these geometries were chosen for investigation purposes should not be misconstrued as exactly reproducing the damaged configuration encountered in flight. These

representative damage configurations, however, do provide insight into the nature and level of damage necessary to result in the loss of Columbia and her STS-107 crew.

3 METHODOLOGY

The completion of the scope of this team's charter required a significant amount of analyses to be completed in a short amount of time. To accomplish the largest amount of work in the shortest amount of time, many analysis efforts were performed parametrically in parallel with comparisons and integration completed at various points throughout the investigation. Some tasks were performed in sequence out of necessity. For example, most of the final thermal analyses could not be completed until internal aerothermodyanmic environments were developed. Wherever possible, independent and/or redundant processes and tools were used to help ensure the validity of the analysis results and subsequent conclusions.

Overall, the approach used by the AATS Team was to postulate the approximate location and extent of damage experienced by Columbia during entry. The team would then formulate analyses or tests that would emulate the aerodynamic, thermal, and structural responses of the postulated hardware damage. The results of the analysis or test were compared to anomalous MADS and OI measured data and off-nominal aerodynamic increments associated with the STS-107 entry to determine if the postulated damage condition was feasible. Results were then integrated to ensure that the postulated damage condition could be supported by each technical discipline. Progression of damage was reviewed to make sure it made logical sense. Where appropriate, corresponding analysis of damage conditions were completed for the ascent phase of flight. Finally, postulated damage conditions were evaluated to ensure that they would not conflict with the condition of recovered hardware or other flight data.

Completion of these steps required the identification of key off nominal data that required the postulation of damage conditions. Figure 3-1provides a high level summary of key data measurements and events that were identified to be evaluated.

GMT Time mm:ss	Time after EI sec	Key Data Measurements and Events
48:39	270	RCC panel 9 spar strain gauge shows off nominal response
48:59	290	Clevis fitting 9/10 sees first indication of temperature increase
49:49	340	OMS pod temperature experiences reduced heating
51:14	425	Panel 9 spar temperature starts off-nominal rise
52:16	487	First MADS measurement begins to fail behind wing spar
52:17	488	First temperature rise in wheel well (LMG brake line bit flip)
52:17	488	Xo 1040 spar strain gauge shows off-nominal response
52:19	490	Unusual response in chin panel outboard clevis temperature
52:30	501	Unusual water dump and vacuum vent nozzle temperature response
52:44	515	Start of delta yaw
52:50	521	Start of delta roll
54:09	600	Debris 5 (Flash "0")
54:10	601	Start of significant temperature rise in wheel well (LMG brake line b)
54:11	602	Reversal of delta roll trend
54:20	611	Start of Slow Aileron Trim Change
54:22	613	Mid Fuse and sidewall temperature rise
54:33	624	Flash 1

Figure 3-1 Key Data Measurements and Events

Several of the events occurred in nearly coincident time frames as shown in Figure 3-2. These corresponding events were reviewed to identify areas of commonality and to ensure consistency in damage progression.

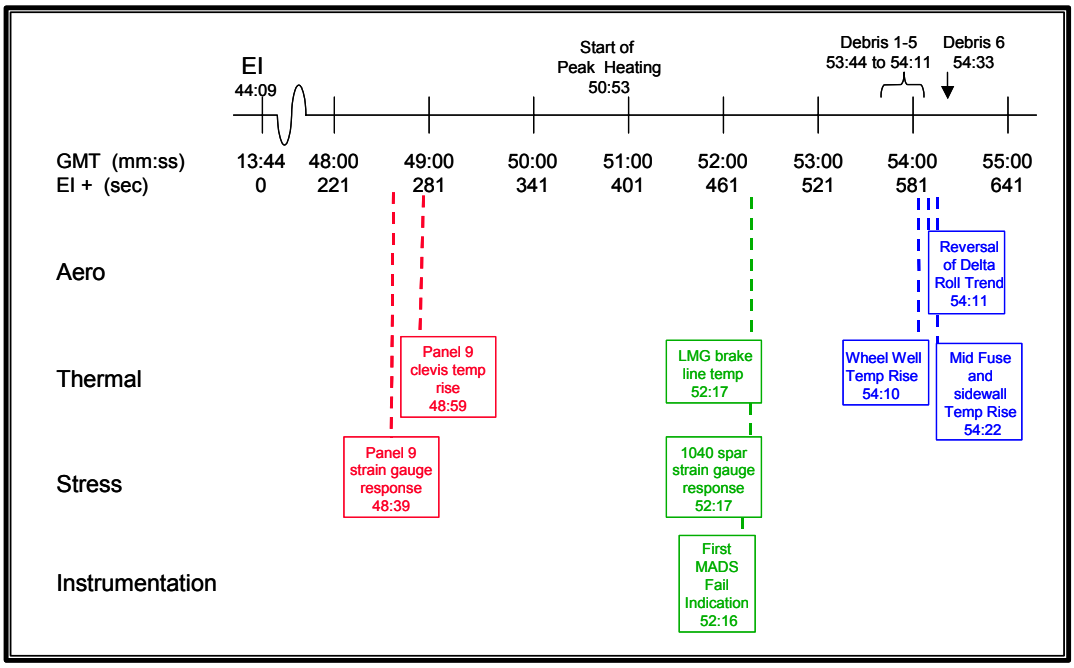

Figure 3-2 Corresponding Events

The AATS Team worked closely with the Scenario team. Analyses were used to formulate a most probable scenario of initial damage and damage progression within the scope of the team's charter. Coordination with the Scenario Team and the Technical Integration Team helped ensure that AATS analysis activities did not conflict with other investigation data/findings.

4 AERODYNAMICS

4.1 Introduction

4.1.1 Team Objectives

The STS-107 entry flight aerodynamic reconstruction effort had two primary objectives. The first was to define the aerodynamic forces and moments experienced by Columbia during atmospheric flight from entry interface (EI) up to the point of loss of signal (LOS) + 5 sec (the last reliable data set point). These extracted forces and moments were then compared to predictions obtained from the orbiter operational aerodynamic data base (OADB) with the resulting differences attributed to the effects of vehicle damage. This served as the basis for the second objective which focused on reproducing the observed off nominal force and moment aerodynamics through wind tunnel (WT) test and/or computational fluid dynamics (CFD) analysis of postulated damaged orbiter configurations. Developing a match between the extracted off nominal aerodynamics and the damage assessment test and analysis results was then used as one basis to substantiate or refute plausible damage scenarios. The ultimate goal was to correlate these results with a vehicle damage scenario that progressed from an initial stage at EI to a considerably more aerodynamically significant damaged configuration just prior to LOS, while maintaining consistency with results from the aerodynamic heating and other analyses. In the end, this leads to a damaged configuration that produced the overwhelming off nominal asymmetric aerodynamic moments resulting in Columbia's loss of control and vehicle breakup.

4.1.2 Nominal Orbiter Aerodynamic Entry Flight Overview

The Orbiter entry is initiated by the firing of the Orbiter Maneuvering System (OMS) jets, slowing the Orbiter and allowing the vehicle to descend to the atmospheric EI, nominally at an altitude of 400,000 feet. During the initial entry phase, which extends to a dynamic pressure of 20 psf. (approx. 250,000 ft), vehicle lateral/directional control and trim is provided by a combination of RCS jet firings, aileron deflections, and sideslip angle. This hypersonic entry flight phase, continuing down through a Mach number of less than five, is accomplished at a high angle of attack during which the blanketing effect of the wing and fuselage essentially precludes any use of the rudder for yaw control. With the rudder not activated until Mach 5, prior to this point in the entry the lateral axis is trimmed solely by aileron deflection with a resulting sideslip angle to balance the roll and yaw moments, augmented by occasional RCS yaw ret firings. Range control is achieved through a series of banking maneuvers while following a predetermined angle of attack schedule. STS-107 trajectory parameters from EI to LOS (approximately Mach 18 near 200,000 ft) are included in Figure 4.1-1 to Figure 4.1-3. Note that for the extent of the STS-107 entry, Columbia was in a high Mach Number, low dynamic pressure flight condition near the 40 deg nominal entry angle-of-attack.

Typically, a terminal phase would then begin as angle of attack is reduced below 18 degrees. As the vehicle continues its descent, air data probes are then extended (at approximately Mach 5) to provide air data relative to the Orbiter. Subsonic flight is attained at an altitude of approximately 40,000 ft. Range control during subsonic flight is obtained by angle of attack modulation with velocity control maintained by the rudder speed-brake. The approach and landing interface occurs at 10,000 ft and a pre-flare is initiated at the appropriate altitude, followed by a deceleration float and touchdown.

Aerodynamic coordinate systems, reference lengths and areas, etc. are included in Aerodynamic Appendices, Section 4.7.1

4.1.3 Chronology of Investigation – Test & Analysis

The STS-107 aerodynamic investigation began with a focus on the orbiter lower wing, primarily in the region of the main landing gear (MLG) door. This was based on the preliminary ascent foam debris impact assessment and operational instrumentation (OI) indications of off-nominal temperature and pressure sensor data in the left wing, particularly in the MLG wheel well. Testing was initiated in the Langley Research Center (LaRC) 20-Inch Mach 6 Air Tunnel, concentrating on lower surface tile damage scenarios, boundary layer transition effects and potential MLG door and/or wheel well cavity exposure.

Further analysis of the ascent debris trajectory suggested that foam may have impacted the WLE. Additionally, preliminary forensics of recovered Columbia hardware suggested WLE damage as an increasingly likely scenario. An LaRC inviscid (FELISA) CFD analysis of a damaged WLE reinforced carbon-carbon (RCC) panel, corroborated by preliminary LaRC WT test results, indicated side fuselage heating augmentation consistent with the OI data. Thus, the aerodynamic investigation priority was shifted to a WLE damage assessment with a concentrated effort to understand the aerodynamic and aerothermodynamic effects of damaged or missing WLE RCC panels. This combined aerodynamic/aerothermal approach was a fundamental part of the investigation process. The evaluations included WT testing in the LaRC Mach 6 air and carbon tetra-fluoride (CF4) hypersonic facilities complemented with CFD analysis by various groups from across the agency. These results were focused even further by the recovery of the Orbiter Experiments (OEX) recorder and associated pressure, temperature and strain data as well as continuing forensic analysis of Columbia's recovered WLE components.

Subsequently the Technical Integration Team conducted a failure analysis technical interchange meeting (TIM) where, based on all the latest investigation information a decision was approved by the Orbiter Vehicle Engineering Working Group (OVEWG) board to concentrate on WLE RCC Panel 5-9 damage as the primary working scenario. Test and analysis of missing partial WLE RCC panels was initiated based on the recovery of portions of each of Columbia's left hand side WLE panels. These results extended the data set for missing full RCC panels to a range of WLE damage configurations. Additionally, leeside flow field effects became a focus of the investigation based on off-nominal readings from the mid fuselage and OMS pod surface thermocouples as well as the unique damage patterns on the left hand side OMS pod and vertical tail. The source of these leeside flow disturbances was evaluated by addressing increased venting as well as the development of various holes through the wing.

As a final investigation thrust, the potential for orbiter lower surface wing deformation was evaluated. This ultimately provided the best match as the source of the changing trends in the aerodynamic moments. Finally, the results of the test and analysis were combined into a potential damage progression path that can reproduce the extracted off-nominal aerodynamics from EI to just prior to LOS.

4.1.4 Approach / Processes – Methodology to Achieve Objectives

The STS-107 Aerodynamic Reconstruction process is illustrated by the flow chart depicted in Figure 4.1-4. The process consisted of two primary phases: Step 1) an Aerodynamic Extraction which then served as the basis for Step 2) Aerodynamic Damage Assessment.

4.1.4.1 Aerodynamic Extraction

Aerodynamic (aero) increments were extracted from flight data to establish the off-nominal aero moments due to damage using an iterative approach. Evaluation tools were developed to extract the un-modeled yawing, rolling and pitching moment increments as well as the normal, axial and side force increments using a three-step process. First, flight parameters including Mach number, angle–of-attack and sideslip, and control surface settings, were used to extract a predicted set of nominal forces and moments using the Orbiter OADB. Second, flight measured acceleration and rate data, estimated orbiter mass properties and estimated atmospheric data were used to extract flight aerodynamic forces and moments based on the standard aircraft equations of motion. Then, the difference between the two sets of data (flight extracted minus nominal Orbiter OADB) produced the un-modeled (off-nominal) delta aerodynamic forces and moments experienced in flight. Figure 4.1-5 provides an outline of this process.

These force and moment increments were then provided to the GN&C flight trajectory simulation for evaluation. Simulations of the STS-107 entry trajectory were performed with and without the off-nominal delta aerodynamic increments and provided trajectory data and flight control system responses. A comparison of the STS-107 flight sensor data against the simulated trajectory predictions with the off-nominal aero increments was used to assess the adequacy of the increments. While the technique employed essentially forces a match between flight and simulation, the distribution of the off-nominal flight response between aerodynamics, atmospheric conditions, model uncertainty, etc. was critical to establishing the final aero increment magnitudes to be attributed solely to damage. After multiple iterations of this process, a good match was produced by taking into account all of these aspects of the flight

reconstruction. The resulting aero increments were considered defined and ready to serve as a measure for the damage assessment evaluation.

4.1.4.2 Damage Assessment

Assessing the change in aerodynamics due to damage required a definition of modified configurations such as those shown in Figure 4.1-6 & Figure 4.1-7, for test and analysis, consistent with a postulated damage scenario. As previously mentioned in the chronology of the investigation, the range and specifics of the postulated damage varied as the investigation matured. For example, WLE damage was initially modeled by removal of entire RCC panels. As new data and findings emerged, the postulated damage configurations were modified (e.g. the follow on test of missing partial WLE RCC panels) to be more consistent with the latest available information and the rapid pace of the investigation. It should be noted that evaluation of the damaged configurations was approached as an integrated aerodynamic and aerothermodynamic effort. This combined aerodynamic/aerothermal approach was a fundamental part of the process throughout the investigation. The test and analysis results were balanced against both of these aspects in judging their merits in supporting any particular damage scenario. The aerothermal results are detailed in Section 5.2.

Also essential to the assessment were reliable hypersonic test facilities and analysis capabilities. All of the wind tunnel tests conducted in support of this investigation were completed in either of two LaRC hypersonic wind tunnel test facilities, the 20-Inch Mach 6 Air Tunnel or the 20-Inch Mach 6 CF4 Tunnel. The vast majority of the testing was ultimately conducted in the CF4 facility because of the established capability of this facility to reproduce high Mach number (13-18) orbiter aerodynamic characteristics by accurately simulating the relevant flow field gas dynamics (see Sections 4.3.1 and 5.2.3.1 for more details). Complementing the WT testing was the application of various CFD analysis codes. These ranged from basic Newtonian estimation routines (SNEWT-JSC & CBAERO-ARC) to inviscid Euler calculations (CART3D-JSC & FELISA-LaRC) as well as several high-fidelity viscous Navier-Stokes simulations (Overflow-JSC, LAURA-LaRC, GASP-ARC & USA-Boeing). CFD analyses results were provided for both wind tunnel and flight conditions (including high temperature gas chemistry effects). The CFD analysis tools were employed in various ways to support damage assessment and evaluation. First, Newtonian and inviscid methods were used as a rapid screening tool for postulated damage scenarios. The CFD flow fields generated for the various damaged configurations were reviewed to gain a more complete understanding of the resulting aerodynamic deltas. Additionally, the CFD analysis was used to evaluate Mach number and angle-of-attack sensitivities as well as WT-to-flight extrapolation. Finally, CFD analysis was employed heavily to interrogate the contribution of leeside flow interactions and any resulting contribution to the delta aerodynamic patterns. These test and analysis capabilities and results are covered in detail in Section 4.3.

For each damage scenario, wind tunnel test models and CFD analysis grids were modified to represent a damaged configuration. The method to establish the change in aerodynamics utilized a baseline run for comparison. First, the nominal or clean configuration aerodynamic baseline was established for each wind tunnel run or CFD analysis. Then the model/grid geometry was modified to represent the damaged configuration under consideration. The test or analysis was repeated with this modified model and the delta aerodynamic force (normal, axial & side) and moments (roll, pitch & yaw) were determined as the difference (Delta = damaged – baseline). These assessment results were collected for the varied set of damaged configurations being considered, including lower surface wing gouges, raised MLG door forward edge, MLG door removed / open wheel well cavity, MLG and door deployed, missing WLE RCC panels (2-12 individually and in combination), partial RCC panels missing (lower half to apex), T-Seal slot, holes through wing with upper and/or lower carrier panel missing, wing deformation including lower surface depressions, as well as vertical tail and leeside interaction – see WT Test matrix (Aerodynamic Appendices, Section 4.7.3) and CFD Analysis case matrix (Table 4.3-6).

All the test and analysis results were then used in developing a match between the extracted off nominal aerodynamics and the damage assessment delta aerodynamics as well as the external aerodynamic heating patterns. The ultimate goal was to correlate these results with vehicle damage consistent with the final working scenario that progressed from an initial damage stage at EI to a considerably more aerodynamically significant damaged configuration just prior to LOS.

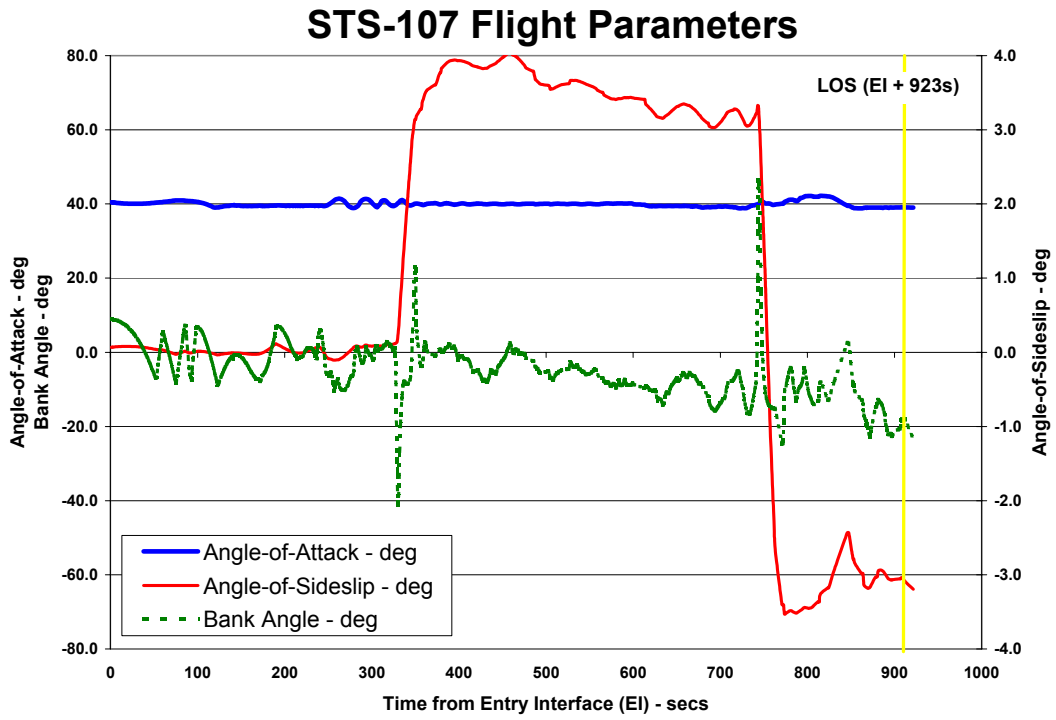

Figure 4.1-1 STS-107 Angle-of-Attack, Sideslip & Bank

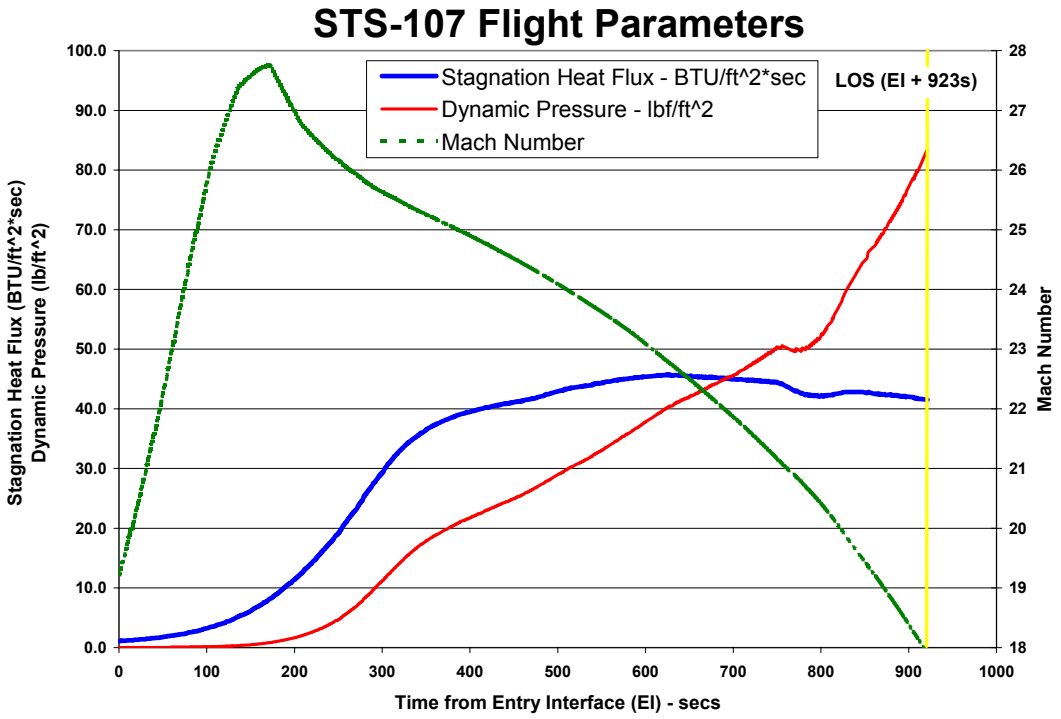

Figure 4.1-2 Mach No., Dynamic Pressure & Stagnation Heat Flux

8

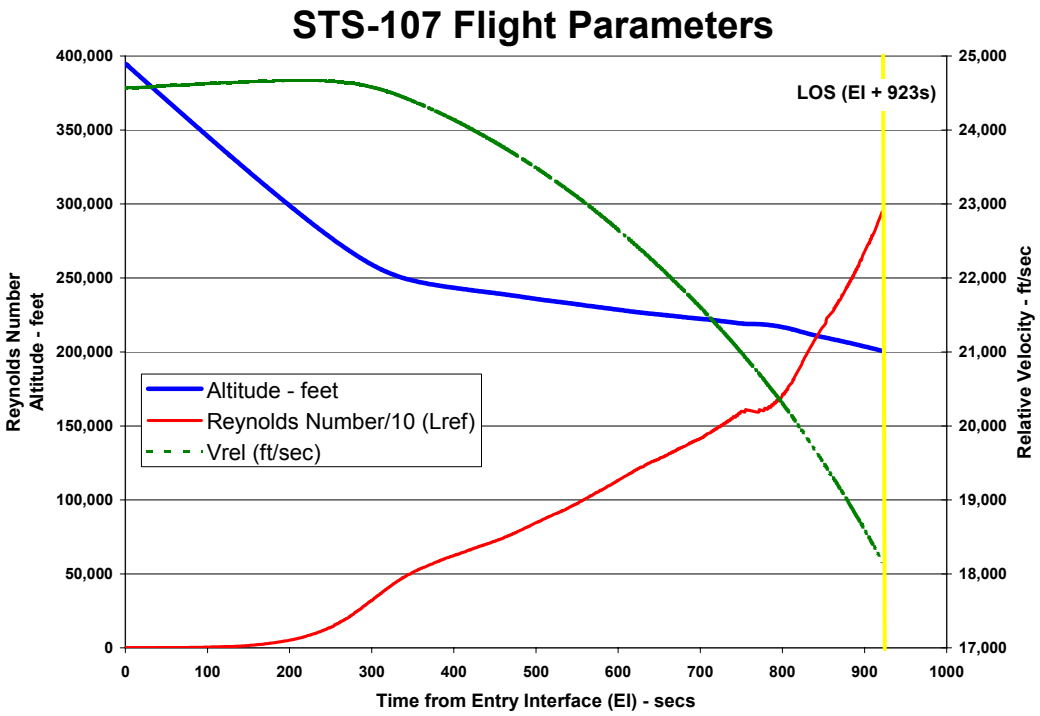

Figure 4.1-3 Altitude, Velocity & Reynolds No.

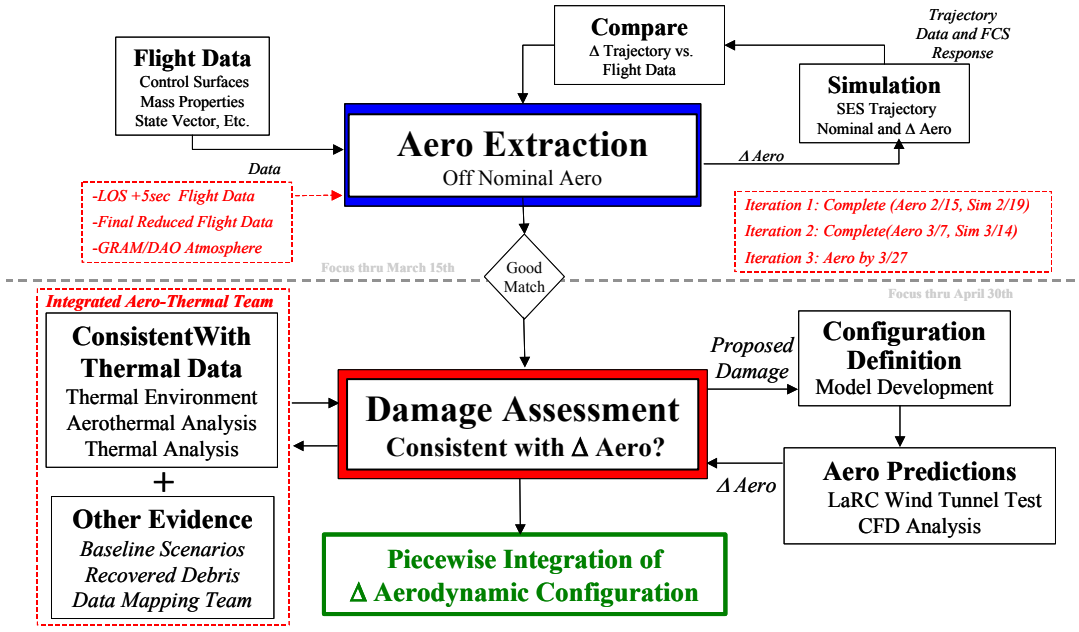

Figure 4.1-4 Aerodynamic Reconstruction Process

1) Orbiter aerodynamic database defines nominal aerodynamics

Input Flight Data:
Control Surfaces (δa, δe, δr, δbf) & RCS Jets
Air Data (Mach, Alpha, Beta, Qbar, Vinf)
Angular Rates (P,Q,R)
Mass Properties

Orbiter Aero Data Book Table Lookup

Nominal Aerodynamic F&M Coefficients:
C_N – Normal C_Y – Side
C_A – Axial C_l – Roll
C_m – Pitch C_n – Yaw

2) Aerodynamic coefficients extracted from flight data

Input Flight Data:
Accelerations (Ax, Ay, Az)
Angular Rates (P,Q,R)
Atmosphere (winds, Qbar)
Mass Properties

Aircraft Equations of Motion

Flight Aerodynamic F&M Coefficients:
C_N – Normal C_Y – Side
C_A – Axial C_l – Roll
C_m – Pitch C_n – Yaw

3) Flight extracted - Nominal Database = Unmodeled (delta aero) F&Ms

$$\Delta Cn_{Reconstructed} = Cn_{Flight\ Extracted} - Cn_{Aero\ Database}$$

Figure 4.1-5 Aerodynamic Extraction Methodology

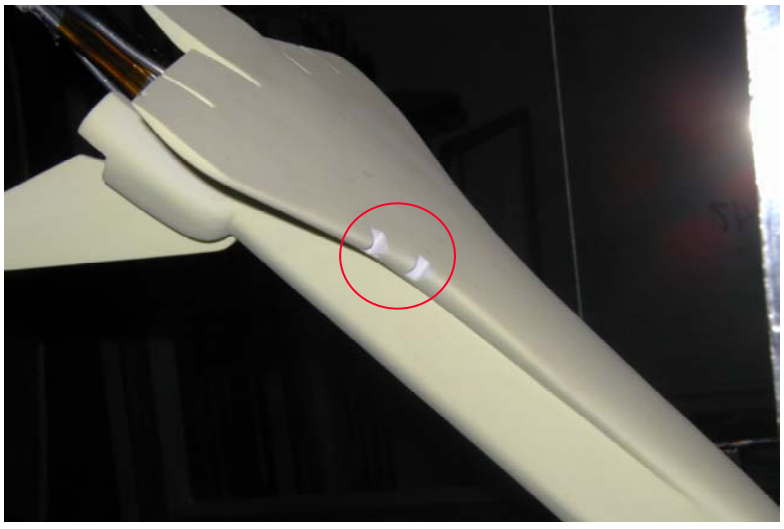

Figure 4.1-6 WT Model with WLE RCC panels (6 & 9) removed

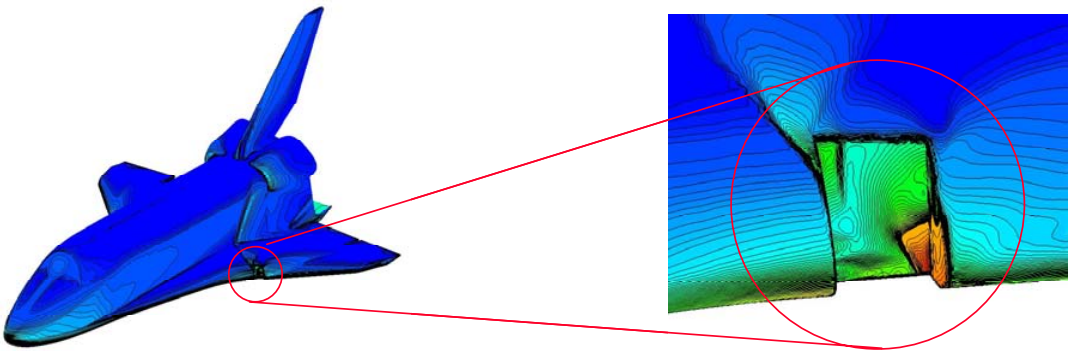

Figure 4.1-7 FELISA Grid with WLE RCC panel 9 removed

4.2 Aerodynamic Extraction

Aerodynamic (aero) increments were extracted from flight data to establish the off-nominal aero moments due to damage using an iterative approach. This section addresses the details of the atmospheric model, high altitude winds and the aerodynamic extraction process and results.

4.2.1 Atmospheric Model

An accurate simulation of the STS-107 entry depended in part on a reliable model of the environment through which the vehicle flew. By using the flight data from EI-5 to LOS and the wind information provided by experts from the Data Assimilation Office (DAO) and the Marshall Space Flight Center (MSFC), atmospheric parameters such as density, temperature, and pressure at a set of altitude reference points were derived with a process slightly modified from that used previously for post-flight analysis. Results compared favorably with the independent assessment of corresponding parameters from DAO/MSFC and contributed greatly to the fidelity of the resulting match between the integrated simulation output and the down listed flight data.

The original atmospheric reconstruction process used as its inputs a pre-defined set of 22 down listed measurements from the Orbiter Data Reduction Complex (ODRC), including such information as vehicle position and orientation, rates and accelerations, and control surface deflections, over the time period for which the atmospheric data was to be derived. This information along with data from the Orbiter OADB was used in an iterative process to generate an estimate of the atmospheric density, pressure, and temperature of the environment. This technique was then revised to make use of higher fidelity data compiled as a part of this investigation, as well as data that was not available when the code was originally developed.

Wind data from DAO/MSFC, for example, was incorporated into the determination of the values for angle of attack, sideslip, and true airspeed. As shown in Figure 4.2-1, the angle of attack (α) and sideslip (β), are defined by the angles the body-fixed frame must be rotated around the - Y_b and Z_b axes, respectively, to align the X_b axis along the velocity vector. At high altitudes where there is no sensed air data available, a navigation-based angle of attack and sideslip are determined on-board relative to the Earth-fixed velocity provided by the inertial measurement unit (IMU). However, when the vehicle is flying through an atmosphere that is moving relative to the ground, the velocity of the vehicle relative to the Earth differs from that relative to the air. Thus, the true air speed (TAS) is comprised by the difference in the Earth-fixed velocity and the wind velocity, and it is this vector into which the body axis must be rotated to determine the environment angle of attack and sideslip.

Since the process resulted in rather noisy output at very high altitudes and there was no flight data available below 200,000 ft, the Global Reference Atmosphere Model (GRAM) data was used in those regions for the final data file delivery. In the lower altitude region, the GRAM data was used up to 190,000 ft, and a spline fit was used to smoothly connect the GRAM and reconstructed data in the intervening

10,000 ft region. At very high altitudes, the extremely low densities were not reliably reconstructed by the process, and the resulting temperature and pressure profiles were quite noisy. The GRAM data was identified as a reasonable approximation to this noisy data, and was substituted for reconstructed atmospheric data above 320,000 ft. Thus a smooth and continuous set of data representing the entire atmosphere was created for use in subsequent simulations. The final set of density, pressure, and temperature profiles appear as illustrated in Figure 4.2-2.

4.2.2 GSFC/DAO Upper Atmospheric Wind Model

In the course of the investigation, it became apparent that a more complete understanding of the atmosphere and in particular a more precise estimation of the high altitude winds and density encountered during entry was critical to the reconstruction of the flight and the associated aerodynamic increments. Since a direct and independent measurement of the density and winds is not available from the onboard data system an effort was initiated to use meteorological resources to generate an atmosphere along the orbiter trajectory for the time of entry.

Generation of a meteorologically derived atmosphere had not been done since very early in the space shuttle program and therefore there was a development effort involving many resources in the meteorological community. The DAO at the Goddard Space Flight Center (GSFC) was the principal organization tasked to provide the atmosphere. The DAO uses space and ground based resources on a regular basis to assimilate measured data for atmospheric research. In order to better support the requirement for high altitude (> 200,000 ft) meteorological data, the DAO additionally assimilated data from the Sounding of the Atmosphere using Broadband Emission Radiometry (SABER) instrument on the Thermosphere Ionosphere Mesosphere Energetics and Dynamics (TIMED) satellite. Through the assimilation process and several iterations, the DAO was eventually able to generate atmosphere data up to an altitude of approximately 250,000 ft., Figure 4.2-3to Figure 4.2-5.

The DAO atmosphere was then faired with the GRAM February atmosphere by the MSFC. Details of the DAO assimilation and fairing methodology can be found in the STS-107 Natural Environments Document (Aerodynamic Reference 4.6 2).

4.2.3 Aerodynamic Increment Extraction Results

Three aerodynamic predictor tools were modified or developed to extract the STS-107 aerodynamic increments. These tools provided a source for rapid comparison between Orbiter OADB aero and flight predicted aero derived from the observed motion of the vehicle. Two existing tools had been developed as part of the experimental X-38 and X-40 flight test programs. Application of these tools to STS-107 was validated by processing flight data and simulator results from two previous Columbia flights (STS-109 & STS-73). A third tool was developed for the analysis using existing Orbiter OADB look-up routines to provide further substantiation. Also, hand calculations completed the analysis and served as a verification of results. Finally, an independent evaluation focused on the time frame from EI to EI+ 600 sec also confirmed these results.

As input flight data was analyzed and refined by the Integrated Entry Environment (IEE) team and as new atmospheric data became available, the aerodynamic increment model went through four revisions to improve accuracy by accounting for all relevant aspects of the flight reconstruction. Wind correction adjustments made to angle-of-attack and sideslip using the final DAO atmosphere greatly influenced the aerodynamic increment results in the fourth and final revision (Figure 4.2-6 thru Figure 4.2-10) (reducing the magnitude of the rolling and yawing moments by approximately 50%). Various uncertainties were also assessed to characterize the relative magnitude of the off-nominal aero forces and moments against other potential asymmetric aerodynamic contributions. These design level asymmetries are also depicted in the figures (note labels). The aerodynamic increment model reference table (Figure 4.2-14) was provided to the GN&C community for inclusion in flight simulations.

Evaluation of the resulting increments indicates that off-nominal aerodynamics were not apparent during the early portion of the STS-107 flight. The first clear indication of off-nominal yawing and rolling moments does not occur until EI + 515 and EI + 521 seconds, respectively. A corresponding small deviation in side

force can also be correlated to this time. The delta pitching moment is first observed in an off-nominal trend much later in the flight, around EI + 836 sec. Further review of data shows that substantial deviation in all three moments does not begin until around EI + 850 sec, which then continues through LOS. For clarity, an expanded section showing the substantial deviation in all three moments late in flight are provided in Figure 4.2-11 through Figure 4.2-13.

As discussed in the derived atmosphere model section, at high altitudes where there is no sensed air data available, the extraction technique must utilize the orbiter on board (normal) acceleration as an input to estimate the atmospheric density profile. As applied, this produces a normal force increment of zero. While necessary to accurately define the density, the zero normal force increment result is not considered accurate. Accounting for limitations presented by the data available, extracting accurate side and axial force increments were considered higher priority and the normal force extraction was thus sacrificed in the process.

Furthermore, it should be noted that the extracted force increments due to damage are a very small percentage (1-2%) of the expected total forces. This is consistent with the small off-nominal moments seen for the majority of the entry flight time. Considering the accuracy of the data available to extract these force increments, it was determined that the forces would not be considered a good measures of the damage induced aerodynamics. Therefore, the damage assessment did not attempt to match the aerodynamic force increments.

On the other hand, the extracted moments provide direct indication of off-nominal asymmetric aerodynamics. In flight the orbiter flight control system is continuously maintaining a trimmed (or zero moment) condition. Any small (non-zero) offset from this trimmed flight condition will manifest itself in the derived off-nominal moment increments. These delta aerodynamic moment increments are thus clear indicators of off-nominal aero and were the primary focus of the damage assessment efforts.

4.2.4 Correlation to Working Scenario

A thorough review of the final increments indicates that initially the damage to Columbia's left wing was too small to produce significant aero effects. The extracted moments early in entry (prior to EI + 500 sec) tend to correlate well with past OV-102 flight results from STS-109 and STS-73 (Figure 4.2-15 to Figure 4.2-17). Combined with the level of uncertainties accounted for in this flight regime, the near zero increments are consistent with no significant damage. As the flight progresses, a clear break in the previous flight trends becomes obvious in the rolling and yawing moment increments at a point after EI + 500 sec. The pitching moment increment, however trends well with previous flights (particularly STS-73) until even later in entry and can only be considered truly off-nominal sometime after EI + 800 sec.

To aid in the reconstruction effort and present correlation between vehicle reaction, debris sightings and onboard measurements, the increments were presented with these events labeled (Figure 4.4-20 to Figure 4.4-23). The correlation with this other available data provides the basis for defining the initial indication of off-nominal aerodynamics around EI+515 sec. While relatively small, the initial rolling and yawing moment increments are both negative. In this flight regime the only possible source of aerodynamic asymmetries are either due to a Yc.g. offset (i.e. other than on the centerline), a very small bent airframe term or the high altitude winds. Asymmetric boundary layer transition (ABLT) has been seen on a number of orbiter entry flights, but never this early in the entry profile, (in fact never prior to the end of STS-107 flight near Mach 18). Additionally, this (-roll/-yaw) pattern is inconsistent with previous asymmetric boundary layer transition observations which have always produced a +roll and -yaw for a left side ABLT. Since winds and c.g. offset have been accounted for and ABLT ruled out, the damage to Columbia's left wing is the only remaining source of the off-nominal aerodynamics.

A distinct change in the aerodynamic increment trend occurs at EI + 602 sec corresponding precisely with Debris Event No. 5 as well as the onset of the slow but steady aileron trim change response by Columbia's flight control system. At this point in flight, the rolling moment increment trend changes from increasing negative to increasing positive. It is postulated that this corresponds to an abrupt configuration change as the left wing damage progressed (this will be elaborated on in Section 4.5). After this point, both rolling (+) and yawing moment (-) trends increase in what is essentially a linear fashion until EI + 836 sec. It should be noted that up to this point in flight the aerodynamic increments are still relatively small (less that than

the worst case asymmetric aerodynamic design levels). The orbiter flight control system has continued to easily account for this slight change in the vehicles aerodynamics and trimmed flight is maintained. At EI + 766 sec, the Orbiter completes the initial roll reversal with no apparent impact from the damaged left wing. However, around EI + 836 sec the aileron trim begins a sharp increase and the rate of rolling and yawing moment increment growth abruptly increases. These extracted moments eventually exceed asymmetric aerodynamic design levels as defined by the Orbiter OADB ABLT after EI + 877 sec.

Between EI + 920 and 928 sec (LOS + 5 sec) the off-nominal rolling and yawing moments dramatically increase in magnitude to levels exceeding 6 times the asymmetric aerodynamic design levels. Flight control responds by maximizing the aileron trim rate and eventually fires all 4 RCS yaw jets continuously to maintain trimmed flight. This rapid increase in the off nominal moments near the end of flight effectively saturates Columbia's flight control system trim capability and eventually led to loss of control and vehicle breakup. For further explanation of the vehicle response to the off nominal aerodynamics encountered see the STS-107 Integrated Entry Environment Team Final Report, Aerodynamic Reference 3.

Based on these observations, the final aero increments indicate that initial damage did not produce significant changes in the nominal aerodynamic properties of the vehicle early in flight (prior to EI + 515 sec). Therefore, the aerodynamic extraction cannot be used to conclude damage to Columbia's wing existed at EI. These increments should primarily be used for flight reconstruction and as a screening mechanism for wind tunnel and CFD damage progression assessments in correlation with the aerothermodynamic evaluations and the other available data.

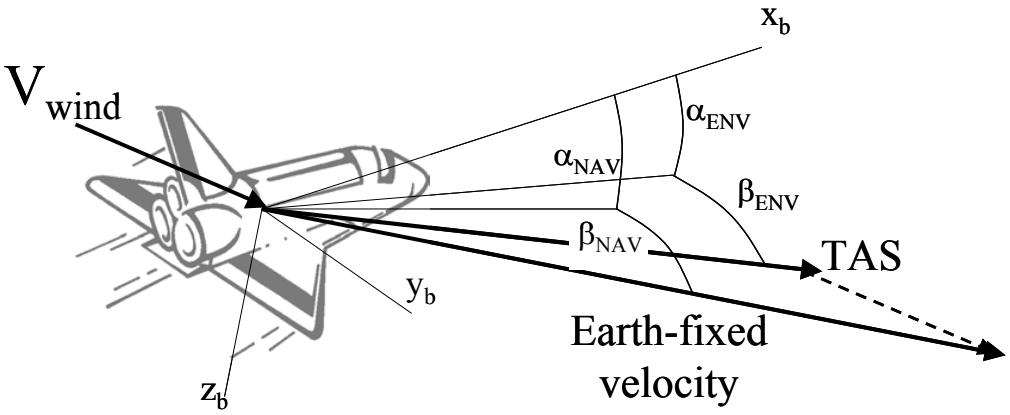

Figure 4.2-1 Determination of Angle-of-Attack & Sideslip

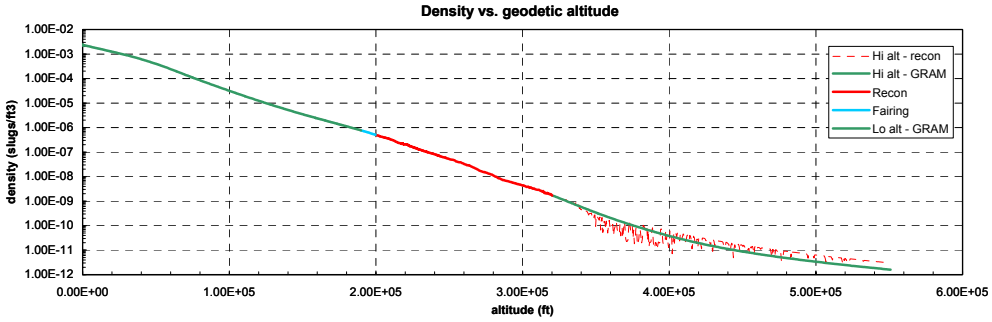

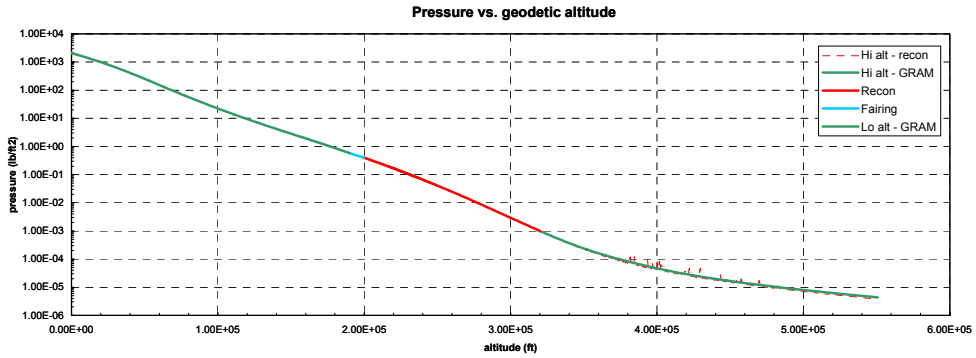

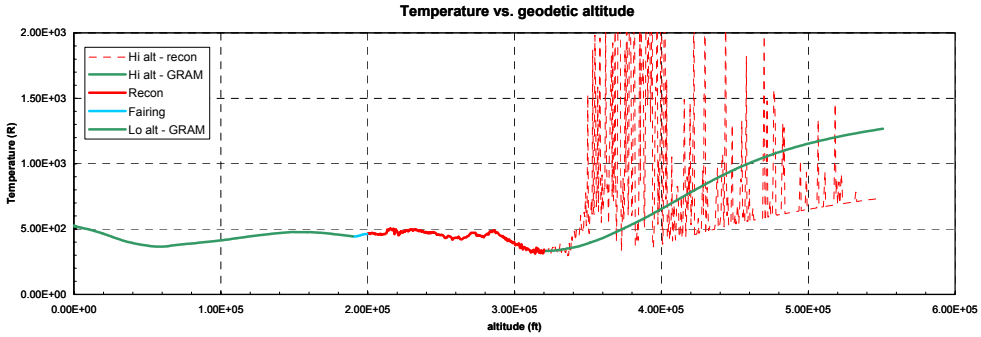

Figure 4.2-2 Reconstructed Atmospheric Density, Pressure & Temperature

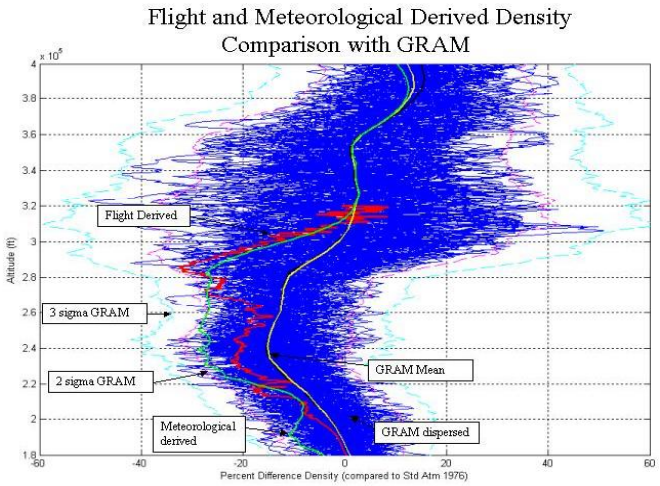

Figure 4.2-3 Flight & Meteorological Derived Density

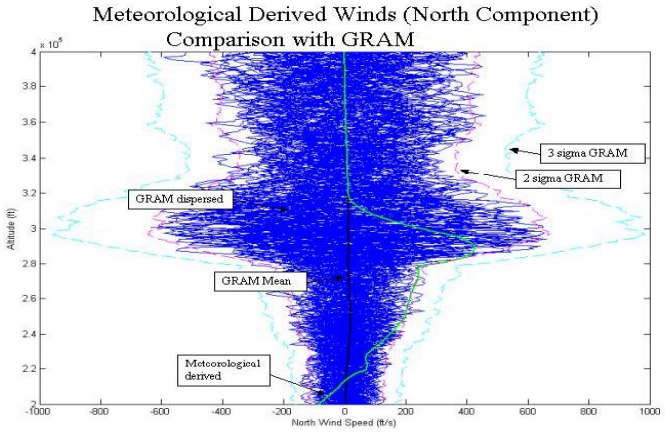

Figure 4.2-4 Meteorological Derived Winds (North Component)

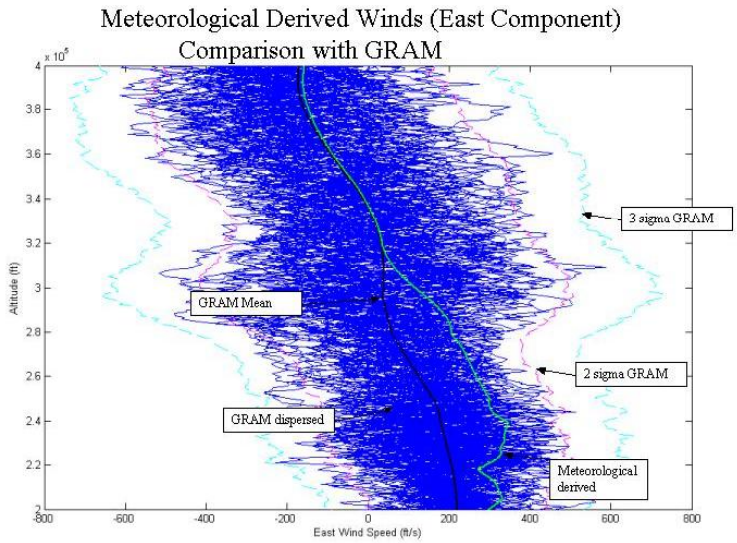

Figure 4.2-5 Meteorological Derived Winds (East Comp.)

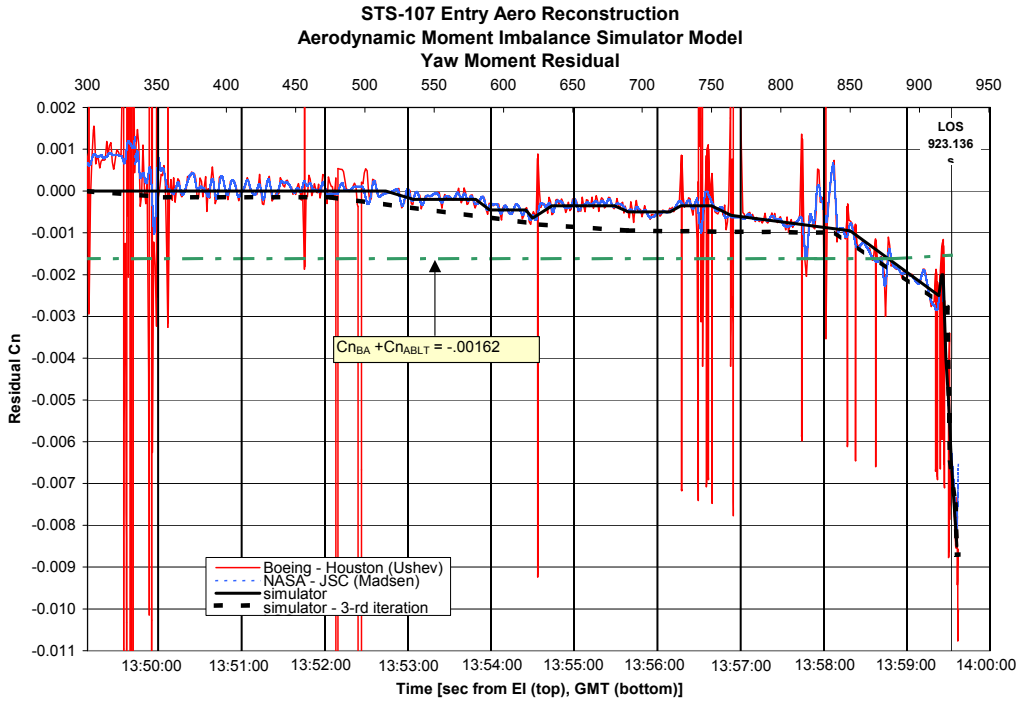

Figure 4.2-6 Delta Yawing Moment Coefficient

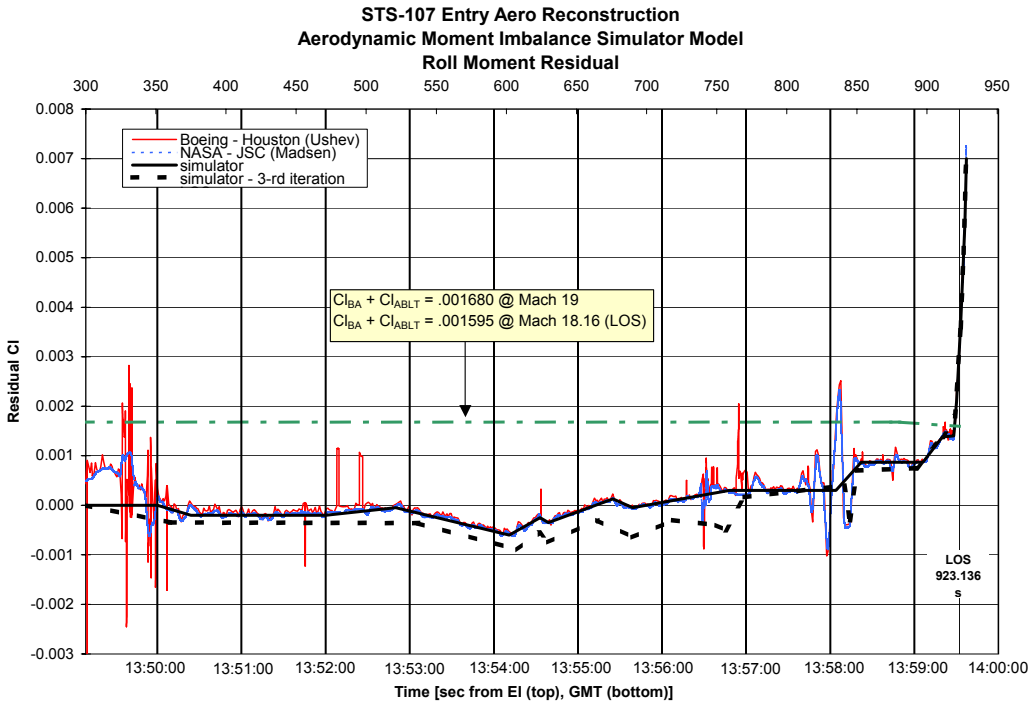

Figure 4.2-7 Delta Rolling Moment Coefficient

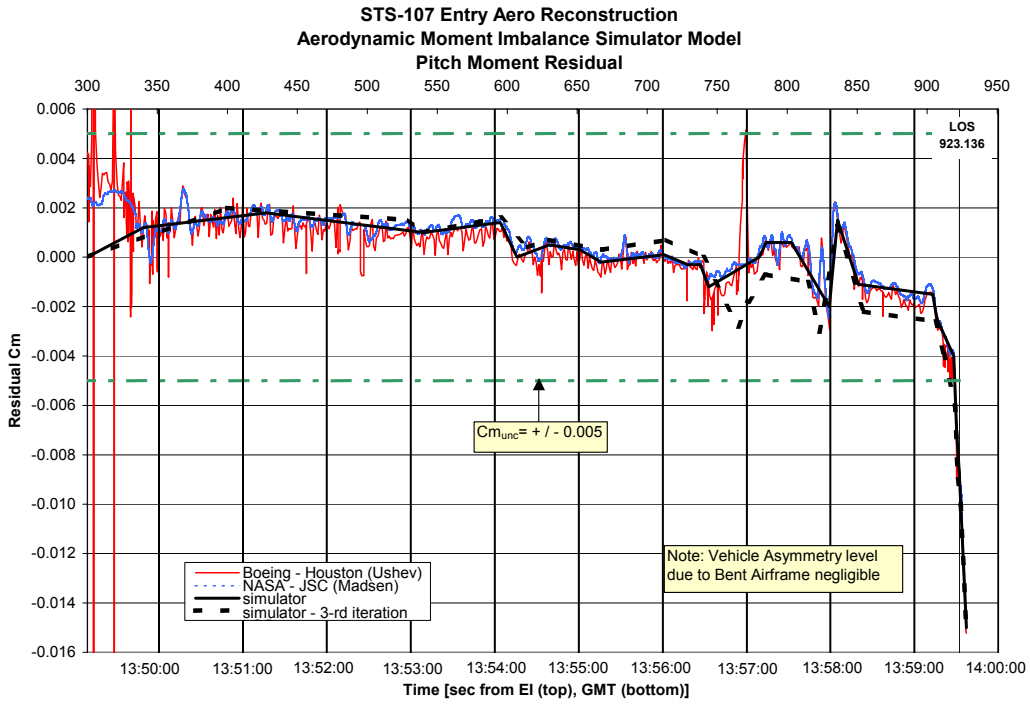

Figure 4.2-8 Delta Pitching Moment Coefficient

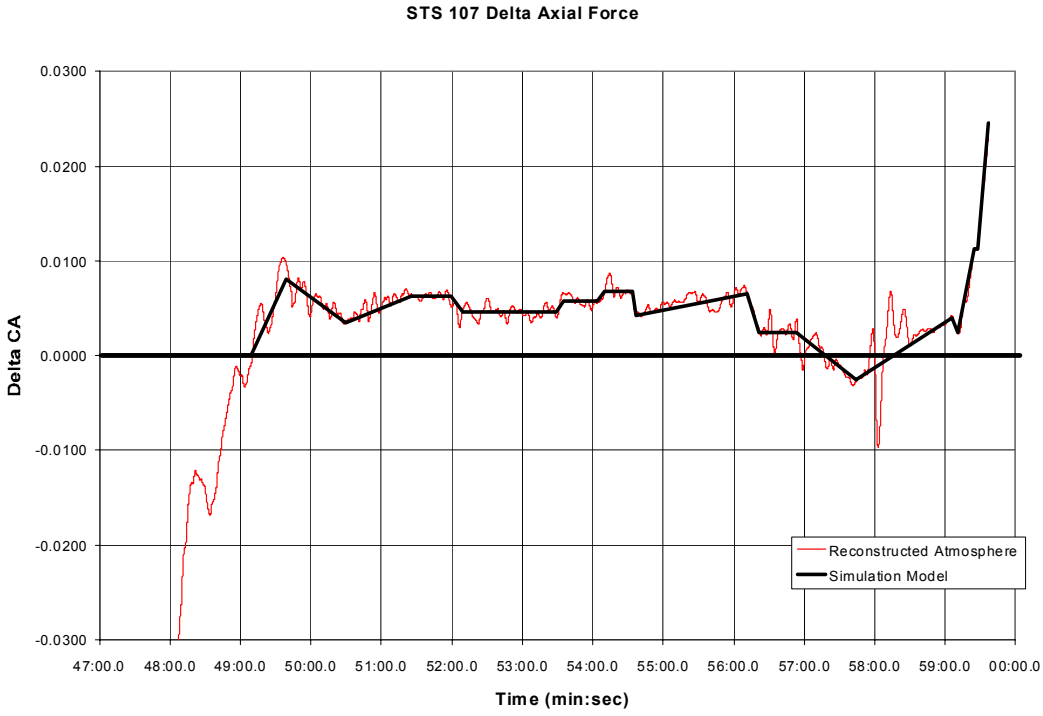

Figure 4.2-9 Delta Axial Force Coefficient

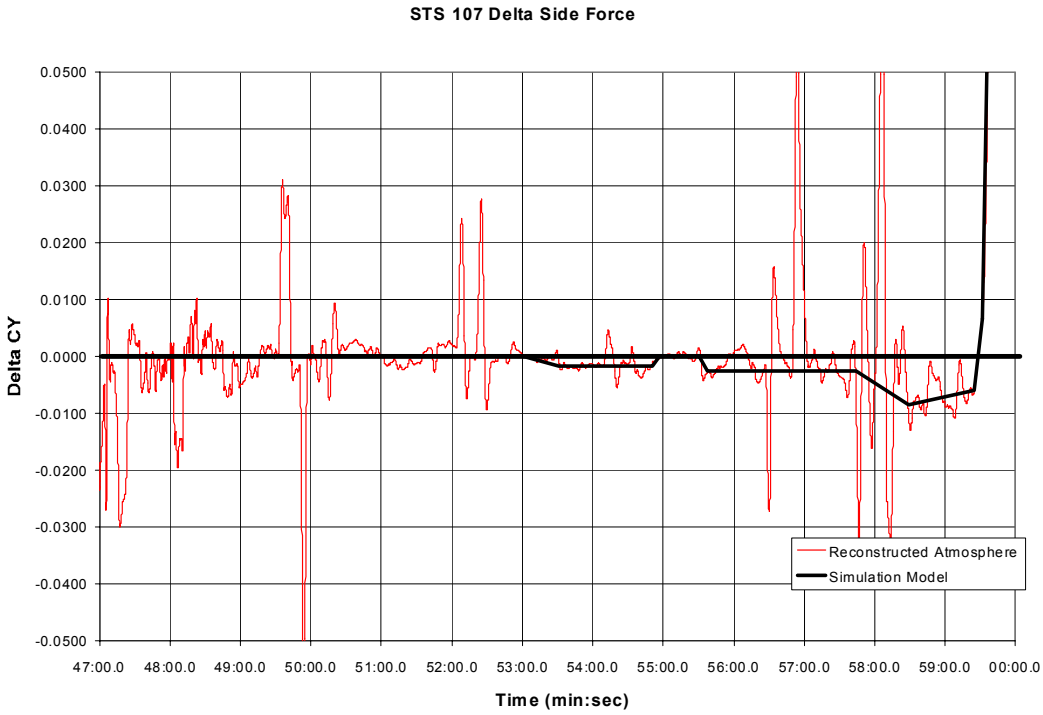

Figure 4.2-10 Delta Side Force Coefficient

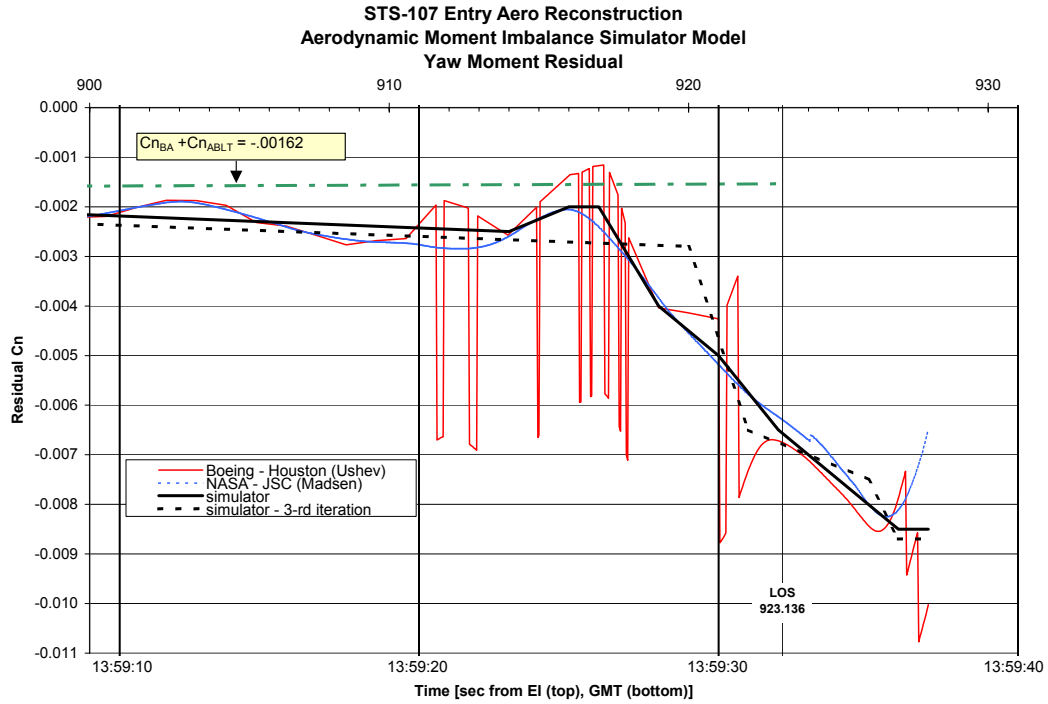

Figure 4.2-11 Delta Yawing Moment Coefficient (just prior to LOS)

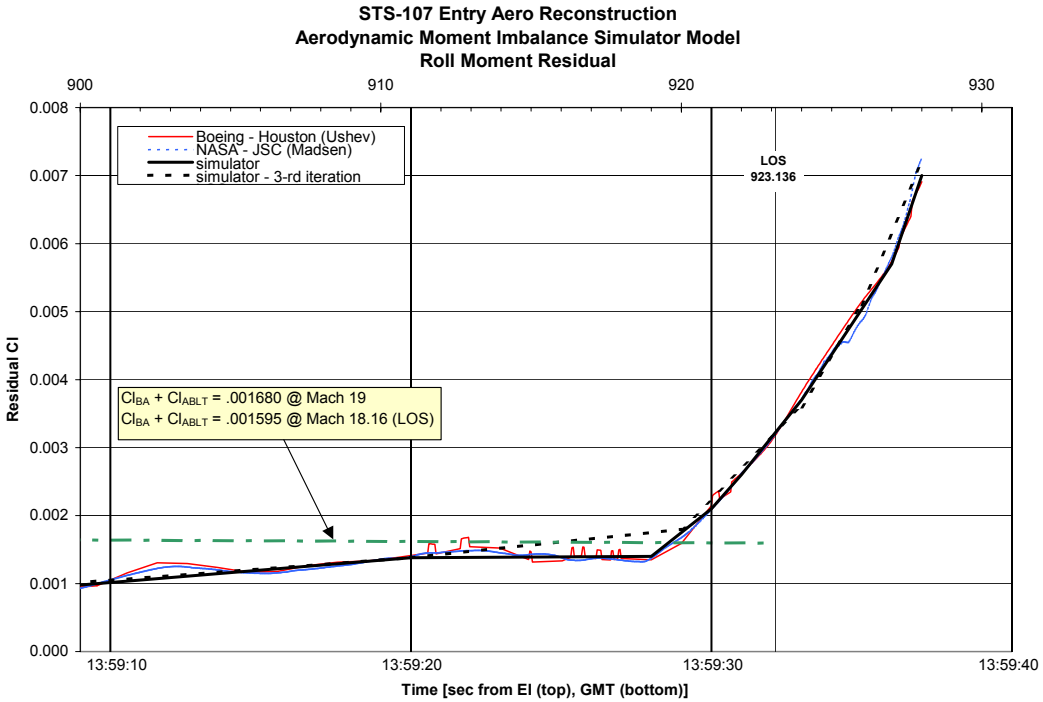

Figure 4.2-12 Delta Rolling Moment Coefficient (just prior to LOS)

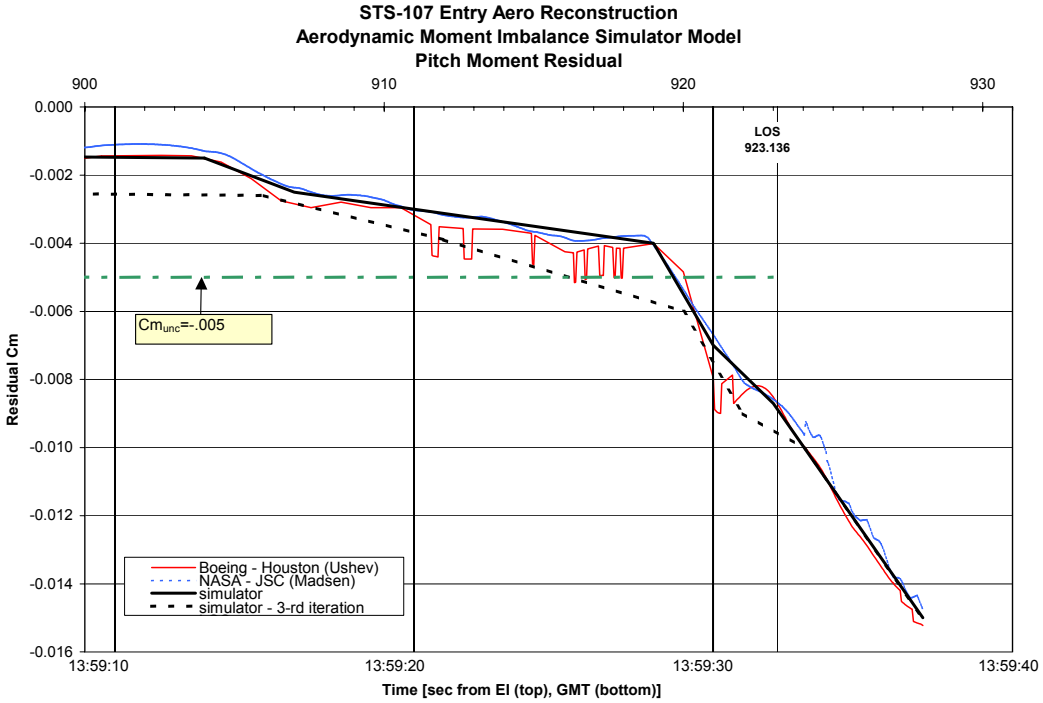

Figure 4.2-13 Delta Pitching Moment Coefficient (just prior to LOS)

STS-107 Simulator Moment Imbalance Model – Reference Table

(time is seconds from EI)

Pitch Moment (Cm) Imbalance

Time	Cm
0	0.00000
300	0.00000
340	0.00120
428	0.00180
540	0.00100
595	0.00140
607	0.00000
630	0.00050
652	0.00030
667	-0.00020
712	0.00010
729	-0.00030
738	-0.00030
744	-0.00120
780	0.00000
785	0.00060
803	0.00060
830	-0.00200
836	0.00150
851	-0.00110
904	-0.00150
907	-0.00250
919	-0.00400
921	-0.00700
923	-0.00870
928	-0.01500

Yaw Moment (Cn) Imbalance

Time	Cn
0	0.00000
300	0.00000
356	0.00000
515	0.00000
535	-0.00020
580	-0.00020
590	-0.00045
616	-0.00045
621	-0.00065
635	-0.00035
680	-0.00035
690	-0.00050
720	-0.00050
728	-0.00035
750	-0.00035
764	-0.00058
850	-0.00095
914	-0.00250
916	-0.00200
917	-0.00200
919	-0.00400
921	-0.00500
923	-0.00650
927	-0.00850
928	-0.00850

Roll Moment (Cl) Imbalance

Time	Cl
0	0.00000
351	0.00000
375	-0.00020
471	-0.00020
521	-0.00005
602	-0.00060
624	-0.00025
630	-0.00035
676	0.00013
690	-0.00005
759	0.00030
835	0.00030
853	0.00087
897	0.00087
911	0.00138
919	0.00140
921	0.00210
922	0.00260
924	0.00370
927	0.00570
928	0.00700

Axial Force (CA) Imbalance

Time	CA
0	0.00000
360	0.00000
368	0.00100
440	0.00100
445	0.00050
495	0.00050
510	0.00120
597	0.00300
606	0.00490
632	0.00200
742	0.00200
764	0.00400
769	0.00250
892	0.00480
897	0.00580
902	0.00450
916	0.01250
919	0.01250
928	0.02450

Side Force (CY) Imbalance

Time	CY
0	0.00000
349	0.00000
354	-0.00070
695	-0.00160
719	-0.00190
730	-0.00050
740	-0.00050
745	-0.00120
860	-0.00120
862	0.00000
875	0.00000
880	-0.00200
895	0.00000
924	-0.00400
928	-0.02222

Figure 4.2-14 STS-107 Delta Aero Increment Model

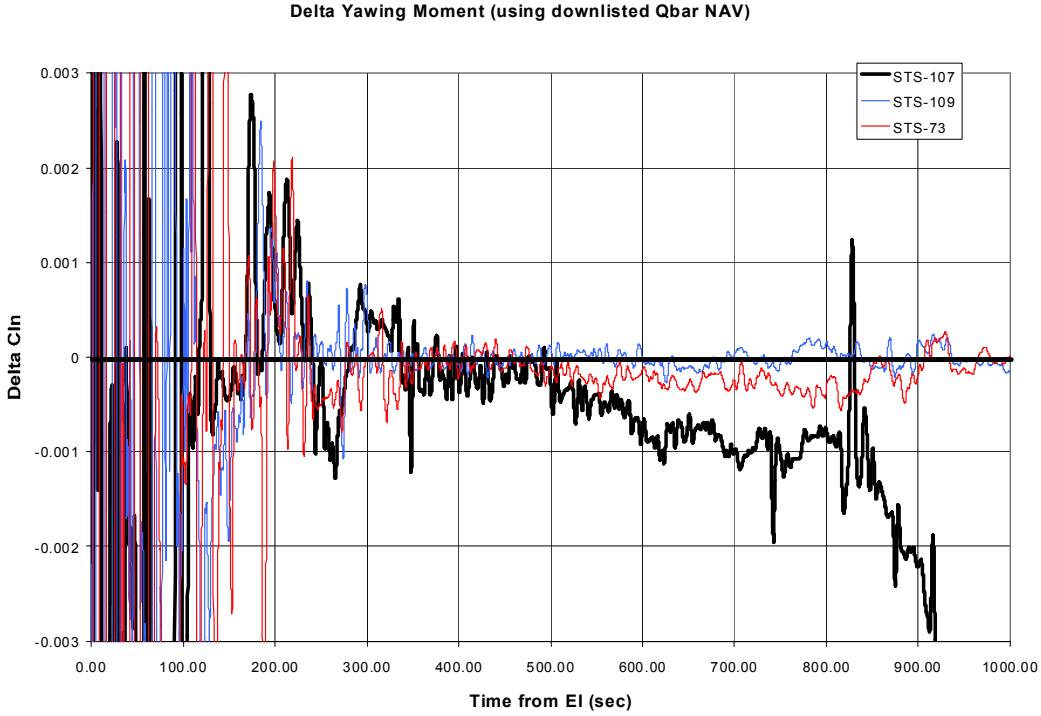

Figure 4.2-15 Delta Yawing Moment (STS-107, 109 & 73)

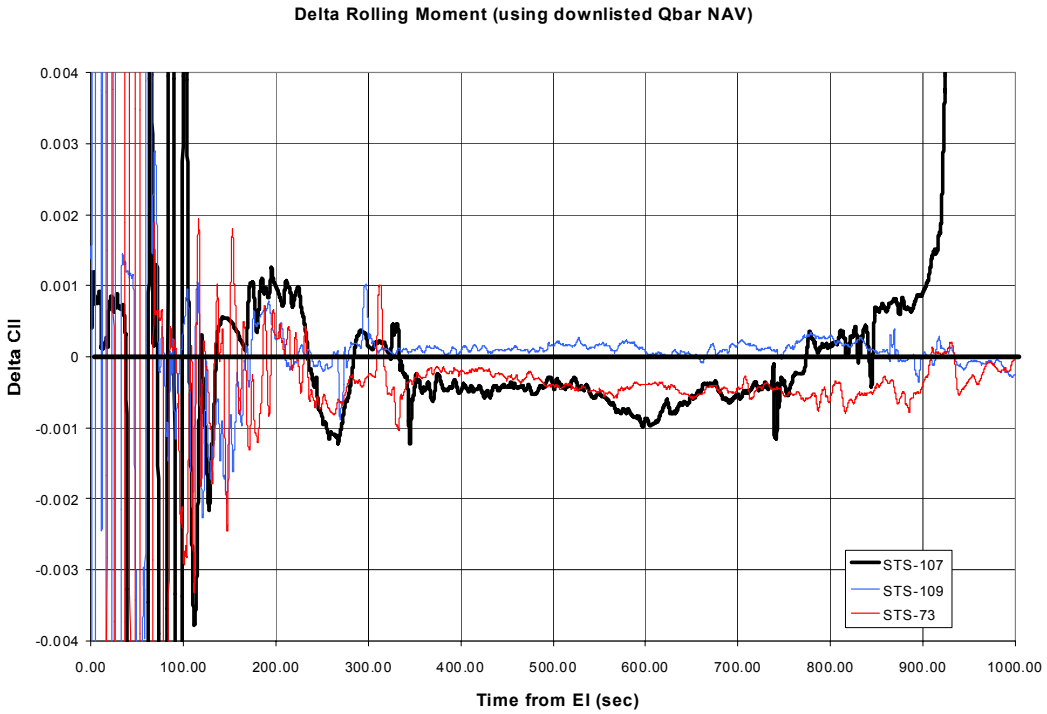

Figure 4.2-16 Delta Rolling Moment (STS-107, 109 & 73)

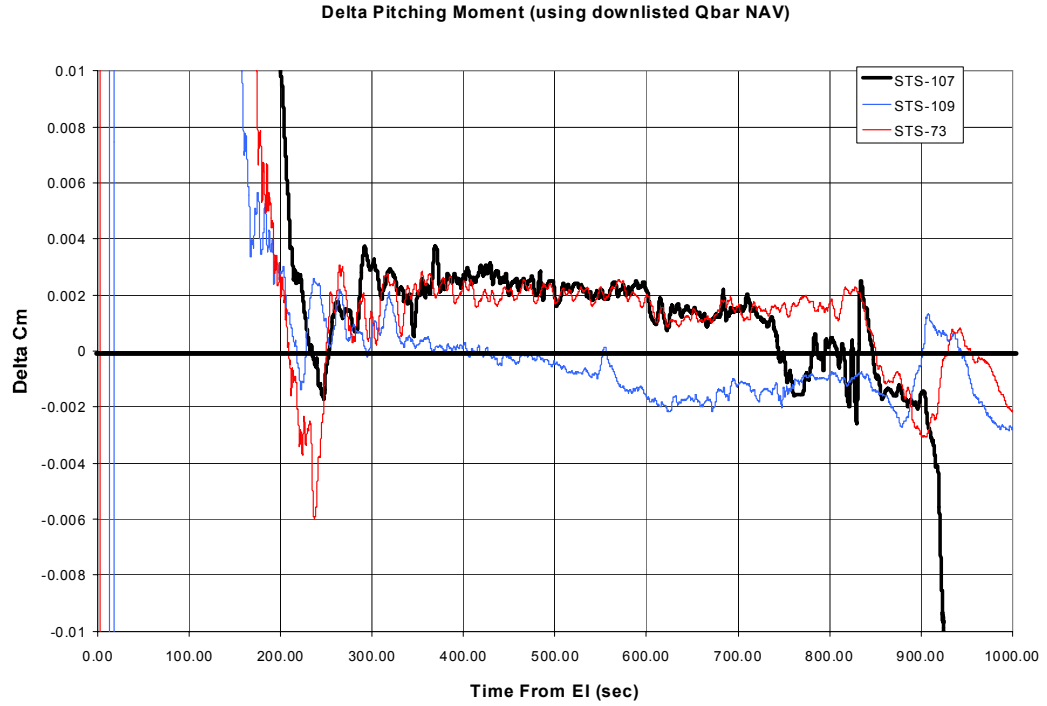

Figure 4.2-17 Delta Pitching Moment (STS-107, 109 & 73)

4.3 Damage Assessment Aero

4.3.1 Wind Tunnel Testing

Aerodynamic tests in support of the Columbia accident investigation were conducted in two hypersonic wind tunnels at the NASA Langley Research Center. The primary purpose of these tests was to measure the forces and moments generated by a variety of outer mold line alterations (damage scenarios). Simultaneously acquired global heat transfer mappings were obtained for a majority of the configurations tested. Schlieren photography visualizing the shock structures in the flow was utilized when possible. The damage scenarios evaluated included asymmetric boundary layer transition, gouges in the windward surface acreage thermal protection system tiles, wing leading edge damage (partially and fully missing RCC panels), holes through the wing from the windward surface to the leeside, deformation of the wing windward surface, and main landing gear door and/or gear deployment. The aerodynamic data were compared to the magnitudes and directions observed in flight, and the heating images were evaluated in terms of the location of the generated disturbances and how these disturbance might relate to the response of discreet gages on the Columbia Orbiter vehicle during entry.

4.3.1.1 Wind Tunnel Facilities

The two facilities used in this investigation were the 20-Inch Mach 6 Air Tunnel and the 20-Inch Mach 6 CF4 Tunnel. These facilities are conventional (as compared to impulse), low-enthalpy, blow-down type hypersonic tunnels. The Mach 6 air tunnel uses heated, dried, and filtered air as the test gas. Typical operating conditions for the tunnel are: stagnation pressures from 30 to 500 psia; stagnation temperatures from 760 to 1000 °R, free stream Mach number from 5.8 to 6.1; free stream unit Reynolds numbers from 0.5 to 8 million per foot; a free stream and post-normal shock ratio of specific heats (gamma) of 1.4; and a normal shock density ratio of 5.3. The facility has a two-dimensional contoured nozzle leading to a closed, solid-wall test section with dimensions of 20.5 by 20 inches. The test core varies from 12 to 14 inches depending on the operating condition. Nominal run time is approximately 60 to 120 seconds, although longer runs times are possible.

The CF4 Tunnel uses heated, dried, and filtered carbon tetrafluoride (Freon 14; molecular weight of 88 which is three times heavier than air) as the test gas. Typical operating conditions for the tunnel are: stagnation pressures from 85 to 2000 psia; stagnation temperatures up to 1300 °R, free stream Mach number from 5.9 to 6.0; free stream unit Reynolds numbers from 0.02 to 0.55 million per foot; a free stream gamma of 1.21 and a post-normal shock gamma of 1.10; and a normal shock density ratio of 11.7. The facility has a contoured axisymmetric nozzle with a nozzle exit diameter of 20 inches, leading to an open-jet test section. The test core varies from 12 to 14 inches depending on the operating condition. Nominal run time is approximately 20 seconds.

The test conditions in the two facilities for the tests performed for this investigation are summarized below. The majority of the runs in the Mach 6 air tunnel were made at a length Reynolds number of 2.4 million (based on a reference body length of 1290.3 inches full scale), which corresponds roughly to flight at Mach 19 and 207,00 feet, near loss of signal. The majority of the runs in the CF4 tunnel were made at a length Reynolds number of 0.36 million (based on a reference body length of 1290.3 inches full scale), which corresponds roughly to flight at Mach 25 and 256,00 feet.

Nominal Flow Conditions in NASA LaRC Aerothermodynamics Laboratory

Facility	M_∞	q_∞ (psi)	$P_{t,1}$ (psi)	$T_{t,1}$ (°R)	ρ_2/ρ_∞	Re_∞/ft ($x10^6$)
20-Inch Mach 6 Air	5.90	1.04	60	890	5.2	1.0
	5.94	2.10	125	910	5.3	2.1
	5.96	3.05	180	910	5.3	3.0
20-Inch Mach 6 CF4	5.94	0.65	750	1180	11.7	0.27
	5.94	1.27	1330	1210	11.7	0.45

4.3.1.2 Applicability of Wind Tunnels to STS-107 Flight Conditions

The loss of STS-107 occurred during entry at high Mach number and enthalpy levels, and relatively low Reynolds numbers. At these flight conditions high-temperature effects (i.e. flow chemistry) are significant due to the dissociation-recombination and ionization of the gas as it passes through the vehicle bow and wing shocks. These high-temperature effects increase the shock density ratio and lower the specific heat ratio (gamma) of the gas within the shock layer, causing shocks to lie closer to the vehicle surface and altering their interaction locations; these high-temperature effects cause the gas to expand to lower pressures than would occur for a non-reacting gas. The CF4 tunnel provides a simulation of these high-temperature effects via its low value of gamma, which is near the value in the Orbiter windward flow field at hypervelocity flight conditions. For example, lower pressure levels than expected on the rear windward portion of the Shuttle were identified as the root cause of the so-called Orbiter pitch-up anomaly that occurred during the first flight of Columbia, STS-1, wherein the Orbiter experienced a nose-up pitch increment relative to pre-flight predictions. The CF4 tunnel has been used to successfully demonstrate the magnitude and direction of this pitch-up increment. While the ability of the CF4 tunnel to accurately simulate the leeside flow has not been validated to the extent of the windward flow, the damage scenarios investigated have their initiation on the wing leading edge and the windward surface, and thus the CF4 tunnel is expected to provide credible simulation of their effects.

The Mach 6 air tunnel uses a perfect gas, but all the flow physics phenomena such as flow separation-reattachment, boundary layer transition, and shock-shock interactions, will be present. The high-temperature effects may alter the level and location of these phenomena, but should not add or delete from them. Thus the Mach 6 air tunnel may be used as a preliminary or screening facility, with the CF4 tunnel used to refine the results. A more detailed discussion of the use of these facilities and their relation to the flight environment can be found in section 5.2.3.1.

4.3.1.3 Wind Tunnel Models

Two types of force-and-moment models were used in this investigation, one made from stainless steel and several from cast silica ceramic. The steel model was an existing 0.0075-scale model that was modified to allow testing of gear and door deployment. A wheel well with a maximum depth of 0.35 inches was machined into the wing, a door was fabricated with a tab to allow installation on the model, and a simplified gear was constructed consisting of a single rod ending in a wheel assembly. The ceramic models were built from a mold that used the steel model as a pattern. Individual models were slip cast, and then a steel sleeve was bonded to the inside to accept the strain-gage force balance. The ceramic models then had the locations of the RCC and carrier panels marked using a coordinate measurement system by the LaRC surface verification laboratory. Individual missing panels were removed using the location marks as a guide. Several photographs of the models with the different damage scenarios are shown in Figure 4.3-1. All models had 0° control surface deflections of the elevons and body flap. The gap between the inboard and outboard elevons was present for the ceramic models, but was filled in for the steel model.

4.3.1.4 Test Techniques

Force and moment measurements were obtained using a six-component water-cooled balance. The balance was selected to maximize accuracy of the lateral-directional data. One balance was used for the steel model and another for the lighter-weight ceramic models. Usual corrections for balance interactions, weight tares, and sting bending were made. A baseline (no damage, 0° control surface deflections) set of aerodynamic coefficients was established for each model over an angle-of-attack range from 38° to 42°. This baseline was then subtracted from subsequent runs of the different damage scenarios to provide the residual aerodynamic increments.

The global heat-transfer mappings obtained in the Mach 6 air tunnel were obtained using an infrared (IR) imaging system with an un-cooled micro-bolometer-based focal plane array detector. The measured infrared radiation was converted to surface temperatures using the emittance of the target, which for the phosphor-coated fused silica model was determined to be 0.906. The global heat-transfer mappings obtained in the CF4 tunnel were generated with the two-color relative-intensity phosphor thermography

technique. IR techniques are not applicable to the CF4 tunnel as the freon gas absorbs the infrared radiation. The ceramic models were coated with phosphors that fluoresce in two regions of the visible spectrum when illuminated with ultraviolet light. The fluorescence intensity is dependent upon the amount of incident ultraviolet light and the local surface temperature of the phosphors. A temperature calibration of the system conducted prior to the study provides tables used to convert the ratio of green and red intensity images to global temperature mappings. For both the infrared and phosphor techniques, the global heat-transfer images are computed assuming one-dimensional semi-infinite heat conduction. The advantage of these techniques is their non-intrusive and global resolution of the quantitative heat-transfer data. These thermography techniques were used to identify the heating footprints associated with complex, three-dimensional flow phenomena such as boundary layer transition locations, flow separation and reattachment locations, etc. that would be extremely difficult to resolve using discrete measurement techniques.

4.3.1.5 Results from 20-Inch Mach 6 Air Tunnel

4.3.1.5.1 Raised boundary layer trips and gouge

At the beginning of the investigation the primary area of interest was early asymmetric boundary layer transition (ABLT), and in damage to the acreage tiles on the windward surface. Damage scenarios tested in the Mach 6 tunnel therefore included a single boundary layer trip at RCC panel 6 (0.6 inch high full scale), a gouge in the center of the main landing gear door (approximately 7 by 32 by 4 (WxLxD) inches, full scale), a raised main landing gear door (raised 0.9 inch full scale), and 7 trips (0.6 inch high full scale) arrayed span-wise across the leading edge of the door (to further simulate a raised door panel). In addition a “full” asymmetric transition configuration was tested which had 10 trips along the wing leading edge as well as 2 trips well forward near where surface protuberances were observed to cause early transition during flight of STS-28 (x/l =0.26). The extent of the turbulent flow generated by these disturbances is shown in Figure 4.3-2. The turbulent wedge from the single trip at RCC panel 6 is swept outboard and affects only the outermost portion of the left wing, as compared to the trips along the forward edge of the main landing gear door, which affect the flow more inboard. These individual trips were more effective than the raised door (not shown) as the door acted more like a two-dimensional trip or step, which is not as effective in promoting turbulent flow. The gouge did not produce turbulent flow, although a small increase in heating was generated. The “full” asymmetric transition case is seen to provide turbulent flow over the aft 2/3 of the left side of the model windward surface. The aerodynamic increments generated by these OML changes are shown in Figure 4.3-3(rolling moment) and Figure 4.3-4 (yawing moment). The gouge in the door and the raised door had minimal effect on the model aerodynamics. The single trip at RCC panel 6 and the 7 trips at the door leading edge had similar effects to each other, causing a positive rolling moment (right wing down) and a small negative yawing moment (nose left). All increments were less than the “full” ABLT condition.

4.3.1.5.2 Main Landing Gear/Door Deployment

Possible deployment of the main landing gear was examined by testing various combinations of the gear, door, and an open wheel well. In general the results were similar to those determined in the CF4 tunnel and will be discussed in the next section.

4.3.1.6 Results from 20-Inch CF4 Tunnel

4.3.1.6.1 Main Landing Gear/Door Deployment

Deployment of the main landing gear and door was tested in the CF4 tunnel, as well as the Mach 6 air tunnel. Although not a leading initial damage scenario, this scenario was examined due to the large aerodynamic moments observed towards the end of flight, which to this point had not been observed in any of the tunnel tests. An open wheel well (no door), door alone, gear alone, and door and gear deployed were tested. Filler plates were used to create three different depths of the open wheel well in order to simulate the presence of the gear (it was thought that the presence of the gear would tend to fill in the cavity, making the wheel well effectively shallower). A sketch of these configurations is shown in Figure 4.3-5. The aerodynamic results in terms of delta rolling, yawing, and pitching moments for these configurations are shown in Figure 4.3-6. Large rolling and yawing moments were generated for the door

and/or gear combinations (lines D and E) consistent with flight, but pitching moments were in the opposite direction than those inferred from flight measurements. However, for the open wheel well configurations (lines A and B), as the cavity was made shallower, all three moments increased, and in the same direction as flight. This trend is consistent with “open” and “closed” type cavity flows. For the deeper cavity, some flow re-circulates within the cavity, but the main flow essentially passes over the cavity; as the depth is decreased, the flow impinges on and attaches to the cavity floor, a shock is formed as the flow reaches the aft wall, and the pressure on the cavity floor is significantly increased. This increased pressure generates the rolling, yawing, and pitching moments observed.

4.3.1.6.2 Missing Full RCC Panels

As the investigation progressed it was known that two temperature instruments on the left side of the fuselage (V34T1106A, V09T1724A) had experienced large increases in heating rates. Investigators at Langley had modified the wing leading edge with a “notch”, both experimentally and computationally, and side fuselage disturbances near these gages were produced by both techniques. Given this knowledge, an extensive survey of wing leading edge damage in terms of missing RCC panels was undertaken. Five ceramic models were fabricated with one or more missing RCC panels. The missing panel area was filled and a baseline data set was again generated. The filled area was then removed and incremental aerodynamic data obtained. Simultaneous heat transfer images were obtained, but their discussion is left to section 5.2.3.4, where results from dedicated heat transfer models are presented. The aerodynamic results for single missing panels as a function of panel location are shown in Figure 4.3-7 through Figure 4.3-9. The solid line represents a least-square linear fit to all the single-panel-missing data. The results show a nearly constant negative value of delta roll for a given missing panel location (Figure 4.3-7). This left-wing-down roll is believed to be due to loss of lift on the left wing due to the loss of area. Delta yawing moment (Figure 4.3-8) exhibited a relatively strong dependence on missing panel location, with a more nose-left yawing moment generated for the more outboard locations. The solid forward facing rear wall and side walls of the notch generate a shock system causing a local high-pressure area, and combined with the larger moment arm for more outboard locations, leads to the observed trend. Delta pitching moment (Figure 4.3-9) showed a dependence on missing panel location also, as nose-down pitch increased for more outboard panel locations. Multiple missing RCC panels were also tested; for instance, one series of tests started with panel 6 out, then 5 and 6, then 5 through 7. A sample of these results is given in Figure 4.3-10 through Figure 4.3-12, where delta roll, yaw, and pitch are plotted as a constant against time from entry interface. The dominant trend is that the delta roll, delta yaw, and delta pitch increments all become progressively more negative (left wing down, nose left, nose down) as the number of missing panels is increased. Superposition of single missing RCC panels was somewhat successful in predicting two-panel out increments, but less so for three or more panels missing.

A brief series of tests examined Reynolds number effects. Missing RCC panel 9, and missing RCC panels 6 and 9 together, were tested at two Reynolds numbers, 0.27 and 0.46 per foot. No significant Reynolds number effect was observed for this factor of two variation in Reynolds number.

4.3.1.6.3 Missing Partial RCC Panels

As more of the debris was recovered and analyzed, a scenario emerged that a partially damaged RCC panel or panels may more appropriately model the actual damage, as opposed to a full panel missing. Thus a series of tests was undertaken to look at the effect of missing lower RCC panels. The wing leading edge was modified by removing the lower portion of the panel from the wing apex to the start of the lower carrier panel. The aerodynamic results for individually removed lower panels 4 through 9 are shown in Figure 4.3-13 through Figure 4.3-15. The solid line again represents a least-square linear fit to the data. For comparison, the linear fit to the full panel out data presented in the previous section is shown by the dashed line. Overall, the magnitudes of the rolling, yawing, and pitching moment increments for missing partial panels were smaller than those for a full missing panel. The rolling moment increment was slightly more positive (right wing down) for a more outboard missing panel location. This trend is believed due to the locally increased pressure acting on the underside of the RCC panel cutout, and thus as the moment arm increases with increasing outboard location, the roll becomes more positive. The yawing moment was nearly constant for any particular missing panel location, which was different than for the full panel out data where a strong dependence on panel location was observed. The pitching moment was again more nose-down for more outboard panel locations.

A recurring question was what wing leading edge or windward surface damage scenario would provide aerodynamic characteristics observed in flight and simultaneously generate leeside disturbances (side fuselage heating) also observed in flight. This had been shown to be possible for a full missing panel. Phosphor thermography images taken for the series of missing lower RCC panels (Figure 4.3-16) show that for panel 4, and to a lesser extent panel 5, a disturbance is generated that moves to the leeside of the model. This disturbance is not observed for missing partial panels 6 or 9. The relative location of the partially missing panel to the local attachment line largely determines if the disturbance is swept to the leeside.

4.3.1.6.4 Holes and Slots through the Wing

Another mechanism examined for flow reaching the leeside was through holes or slots in the upper surface. For one series of tests, small holes (0.030-inch diameter model scale, 4 inch diameter full scale) were drilled through the wing, from windward surface to the leeside, at the carrier panel locations behind RCC panels 6, 9, and 12 (separate runs). No effect of these holes through the wing was seen in either the aerodynamic increments or the side fuselage images. For another series of tests, a 0.030-inch hole was drilled from the windward surface (center, aft end of the partially missing panel 8) to the leeside side through upper carrier panel 8. Afterwards this hole was widened to a 0.030-inch slot, in effect removing most of the upper carrier panel. Phosphor thermography images of the fuselage side are shown in Figure 4.3-17. A slight effect on heating to the OMS pod can be seen for the single hole. The slot creates a larger disturbance in the leeside flow field, resulting in increased heating on the side of the fuselage and the OMS pod, similar to that observed for a full missing panel, though the heating rate is lower. The aerodynamic increments in rolling and pitching moments associated with the hole and slot are very small, but there is a measurable increase in the nose-left yawing moment increment when the hole is widened to a slot, as shown in Figure 4.3-18.

4.3.1.6.5 Effect of Vertical Tail

Another aspect that was investigated was whether flow to the leeside was impinging on or in some way affecting the flow on the vertical tail. A piece of the vertical tail had been found that showed damage to the left side, but not the right. In addition, the tail was seen as a possible contributor to the large roll and yaw increments seen late in flight, and especially for the change in rolling moment behavior after EI + 600 sec. A model was tested with the tail on and off, with and without panel 9 missing. As observed from the table in Figure 4.3-19 for missing RCC panel 9, the increments with and without the vertical tail are very close in value, leading to the conclusion that the tail was not affected nor a contributor to the moments in question.

4.3.1.6.6 Windward Surface Depression

A final series of aerodynamic tests were performed to determine if a damage scenario related to deformation of the left wing would cause the change in direction of the rolling moment seen to occur 602 seconds after entry interface. Influenced by the results from the open wheel well, a shallow depression was created in the left wing windward surface to simulate what might occur as the wing internal structure was degraded and the lower skin was pressed inward by the greater external surface pressure. A single groove was milled into the lower surface of the model, starting just behind RCC panel 8. The length of this groove was varied in three increments with the longest groove extending slightly past the aft end of the wheel well. This groove was then widened to simulate progressive damage. Measured aerodynamic moments show (Figure 4.3-20 through Figure 4.3-22) that a minimum length of the groove is needed to provide a measurable increase in rolling moment, similar to the critical depth of the open wheel well. The required aspect ratio (L/h) of the groove is greater than for the open wheel well; this effect may be related to the angle of the local streamlines, in that they will cross the groove as opposed to running parallel to it, thus in effect shortening the groove and reducing the aspect ratio. However, the depression does indeed cause a positive (right wing down) rolling moment as observed in flight, and the magnitude of the rolling moment increases as the width of the depression is increased. Furthermore, the yawing moment and pitching moment generated by the depression are similar in magnitude and in the same direction as observed for flight.

4.3.1.7 Observations:

4.3.1.7.1 Asymmetric Boundary Layer Transition

The preliminary work done in the Mach 6 air tunnel focused primarily on ABLT. For the damage scenarios examined, the rolling and yawing moments generated were consistent in terms of direction with the Shuttle ABLT model, which is a positive rolling moment (right wing down) combined with a negative (nose left) yawing moment. These results are inconsistent with the extracted STS-107 flight data for the early portion of the flight, which have a left-wing down rolling moment combined with a nose-left yawing moment, indicating that asymmetric transition was not an initiating cause of the accident. Boundary layer transition may have been a contributor later in the flight, when the rolling moment trend became positive.

4.3.1.7.2 Progressive Damage Scenario

As a final summation to the aerodynamic work, a progressive build-up of individual damage scenarios was developed and compared to the flight moment increments. The results are shown in figures Figure 4.3-23 through Figure 4.3-25. The time from entry interface is subjective, as are the damage scenarios themselves. Nonetheless, a plausible scenario can be developed, which has the same trends as the flight data, although an exact correlation of flight magnitudes and time is not achieved. The initial damage is loss of the lower portion of RCC panel 8. The magnitudes of the moment increments are small, as they were for the first 500 seconds of flight. This initial damage is followed by the addition of the slot through the upper portion of carrier panel 8, and then the complete removal of panel 9 at 615 seconds from entry interface (EI). It was at this time (615 seconds) that significant heating to the side fuselage was seen, and both the slot in carrier panel 8 and the complete removal of panel 9 allow flow to impinge on the leeside of the vehicle. The reversal in direction of the rolling moment is attributed to the windward surface depression, with the magnitude increasing as the size of the depression is increased (as more of the internal wing structure is degraded). The yawing and pitching moments continue their increasing negative trend as the depression is enlarged.

Figure 4.3-1 Wind Tunnel Test Model Configurations

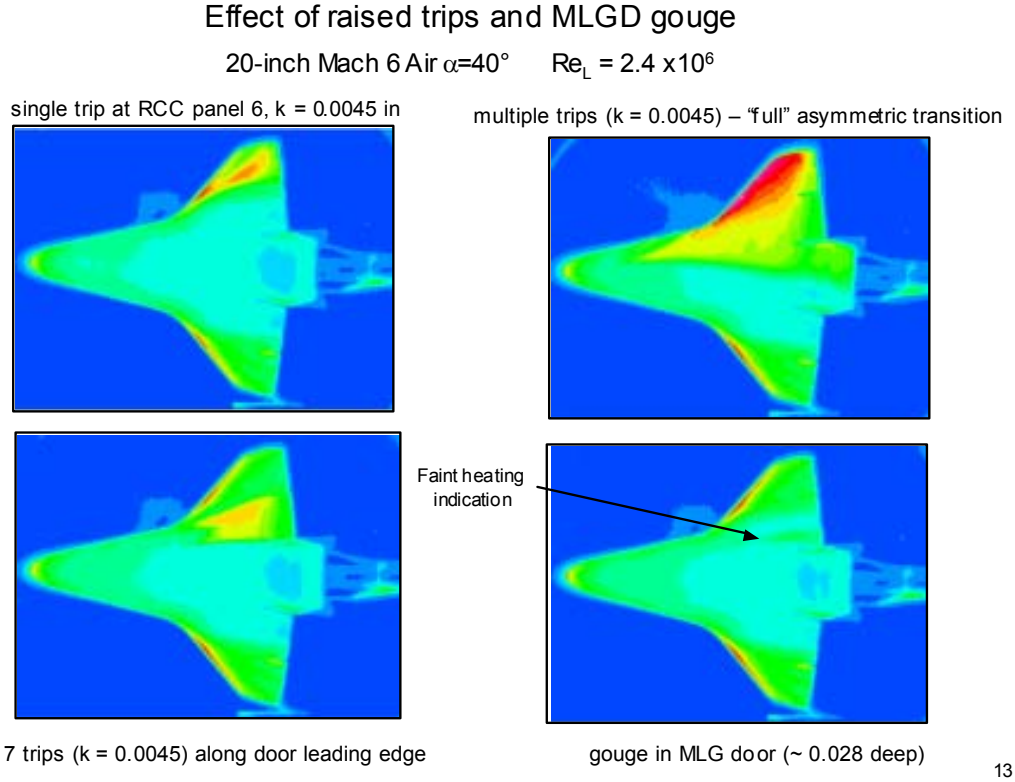

Figure 4.3-2 Infra-red Thermography Images Showing Extent of BL Transition

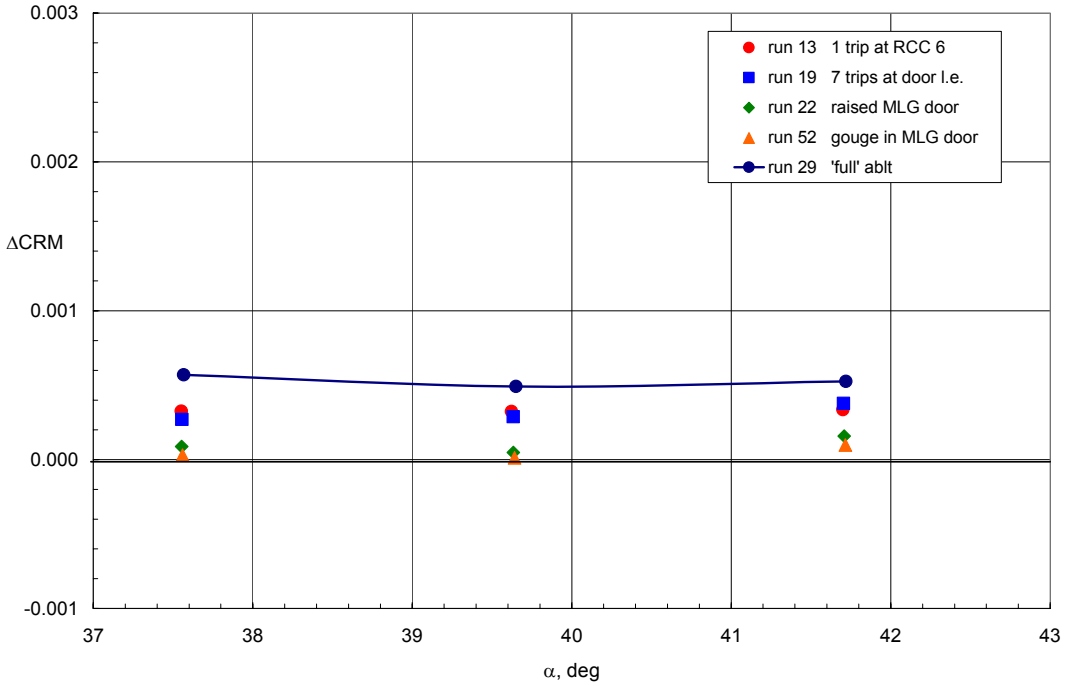

Figure 4.3-3 Boundary Layer Transition Aerodynamic Increments (Delta Roll)

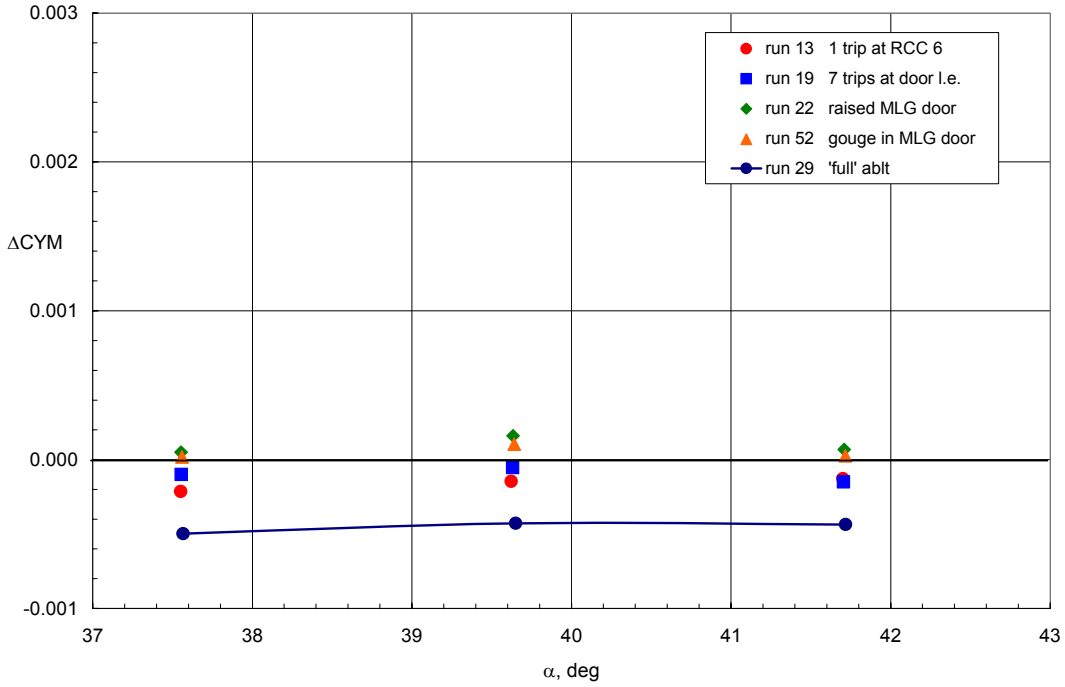

Figure 4.3-4 Boundary Layer Transition Aerodynamic Increments (Delta Yaw)

Test Configurations – Steel Model

Large OML Changes

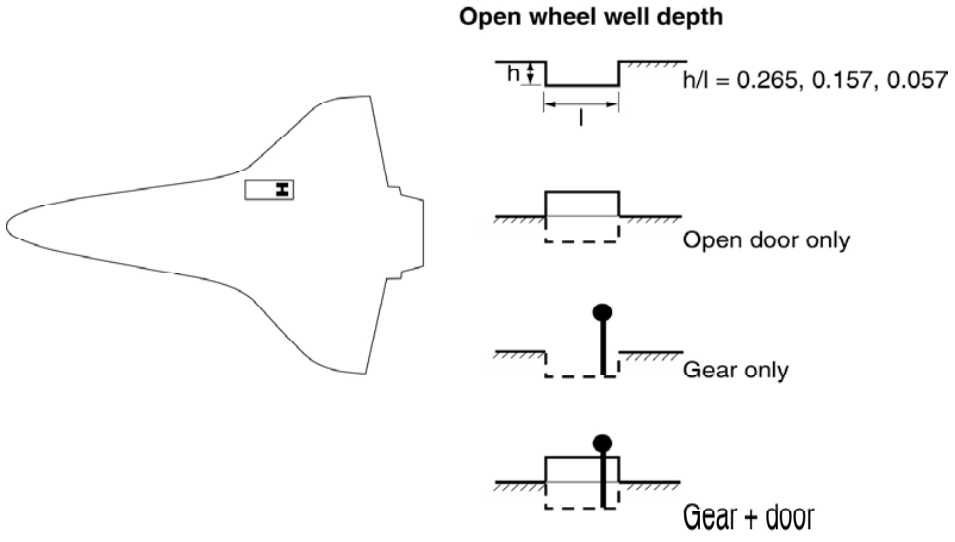

Figure 4.3-5 Stainless Steel Model Configurations Tested

MLG Door / Gear Scenarios in 20-Inch CF4 Tunnel

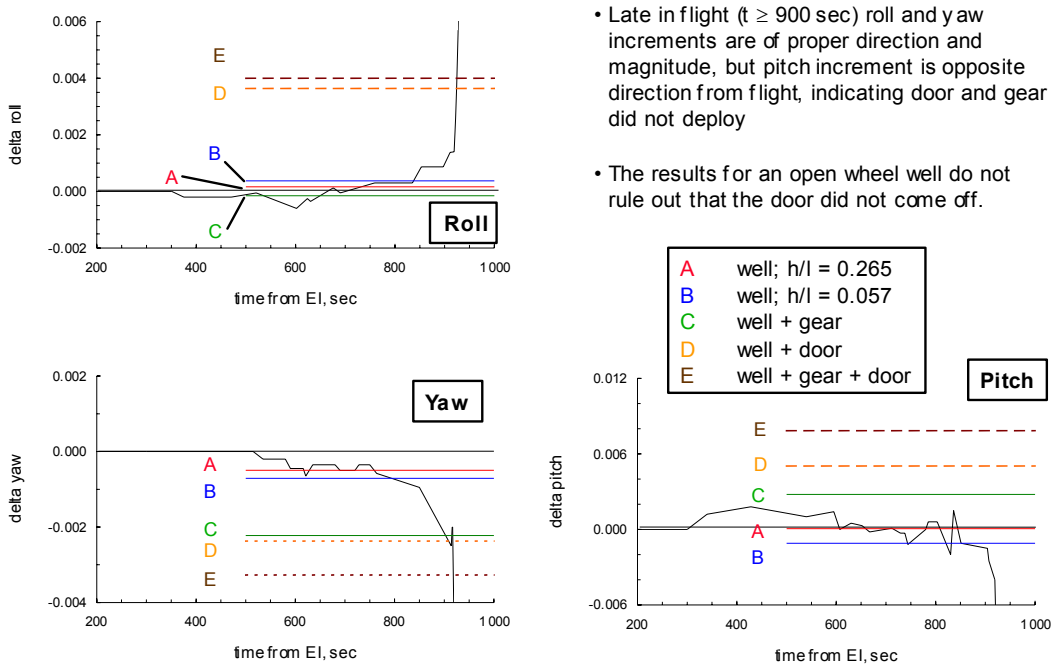

- Late in flight (t ≥ 900 sec) roll and yaw increments are of proper direction and magnitude, but pitch increment is opposite direction from flight, indicating door and gear did not deploy
- The results for an open wheel well do not rule out that the door did not come off.

Figure 4.3-6 Aerodynamic Increments (Roll, Pitch, Yaw) for MLG Door Scenarios

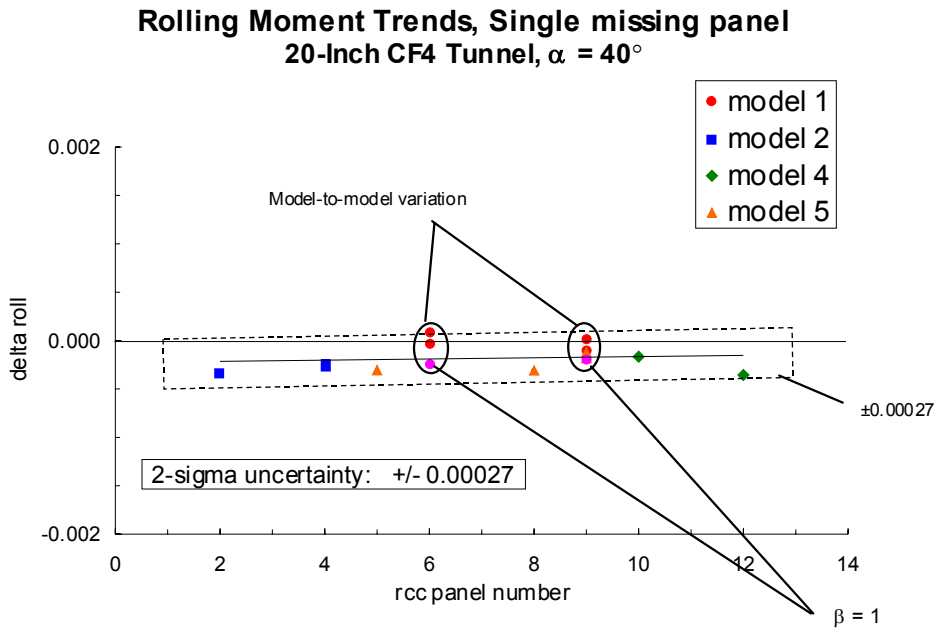

• Roll increment is relatively constant for a given missing panel

Figure 4.3-7 Aerodynamic Increment (delta Roll) – Missing Full RCC Panel by Location

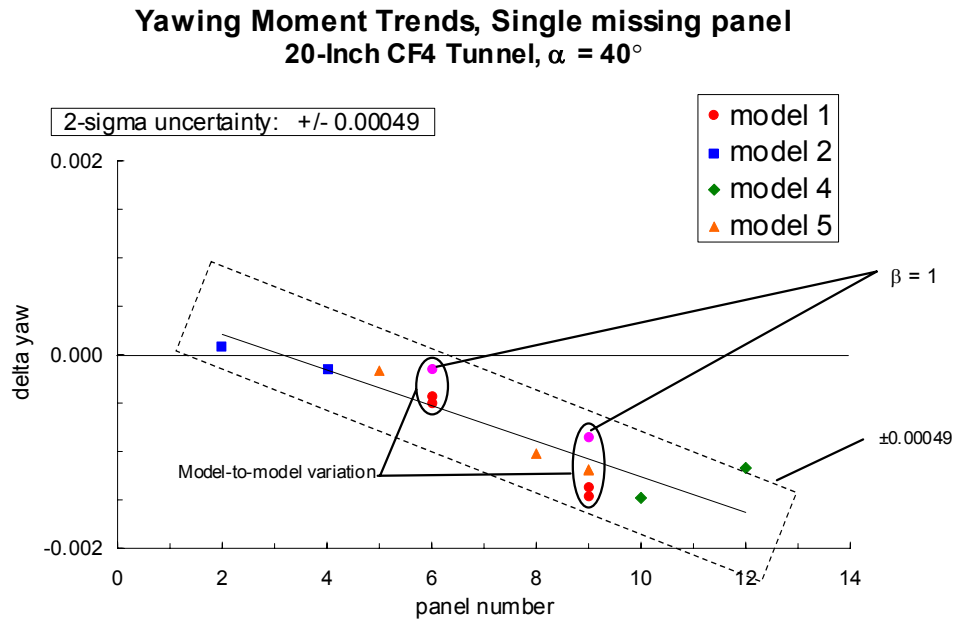

• Yaw increment is highly dependent on panel outboard location

Figure 4.3-8 Aerodynamic Increment (delta Yaw) – Missing Full RCC Panel by Location

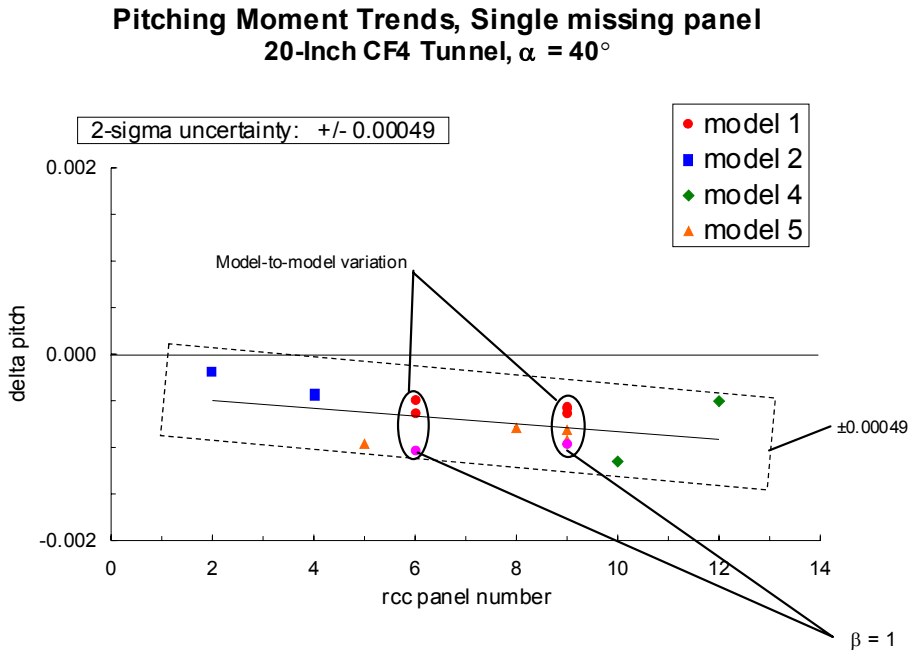

• Pitch increment is moderately dependent on panel location

Figure 4.3-9 Aerodynamic Increment (delta Pitch) – Missing Full RCC Panel by Location

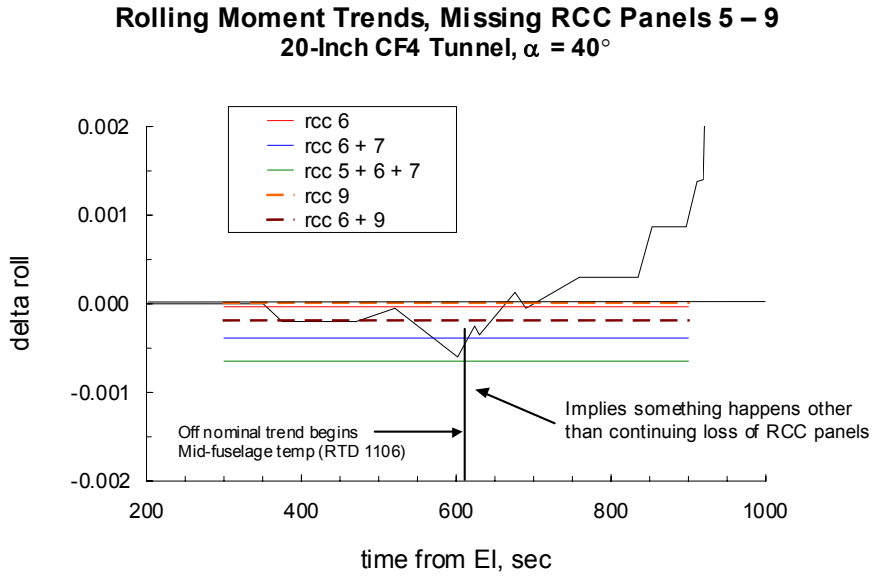

• Roll increment increases with increasing number of panels missing
• Two adjacent panels have larger increment than two separated panels
• Roll trend reverses at 615 sec; opposite effect from losing more leading edge panels

Figure 4.3-10 Rolling Moment Increment Trends - Missing RCC Panels 5-9

Yawing Moment Trends, Missing RCC Panels 5 – 9
20-Inch CF4 Tunnel, α = 40°

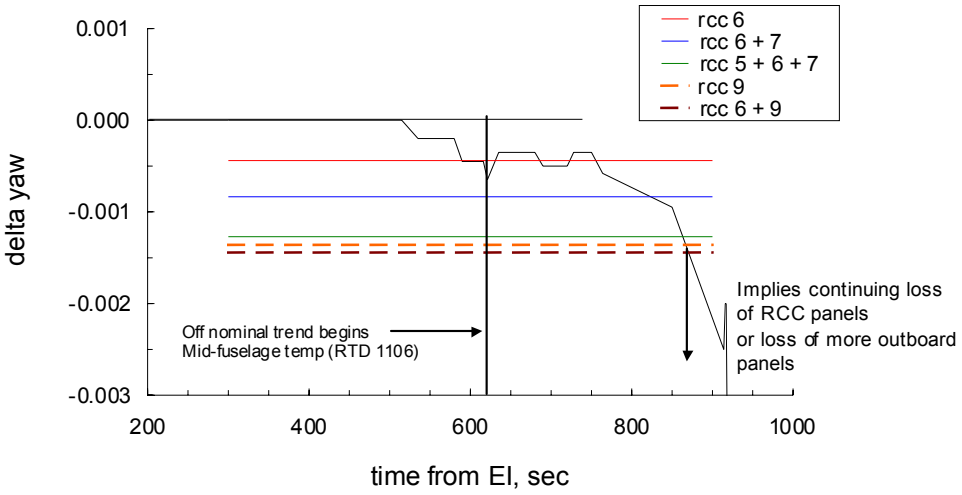

- Yaw increment increases for more outboard panels
- Yaw increment increases with increasing number of panels missing

Figure 4.3-11 Yawing Moment Increment Trends - Missing RCC Panels 5-9

Pitching Moment Trends, Missing RCC Panels 5 – 9
20-Inch CF4 Tunnel, α = 40°

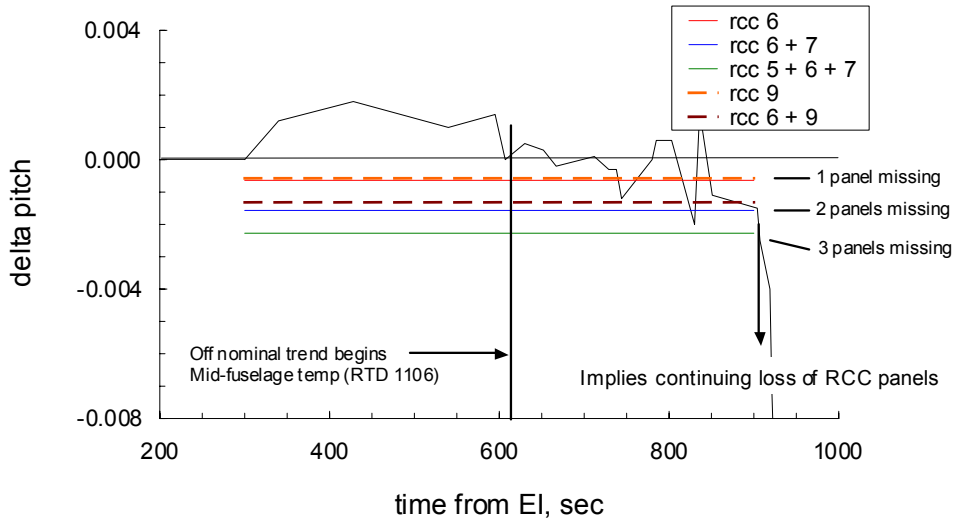

- Pitch increment nearly independent of panel outboard position
- Pitch increment increases nose-down with increasing number of panels missing

Figure 4.3-12 Pitching Moment Increment Trends - Missing RCC Panels 5-9

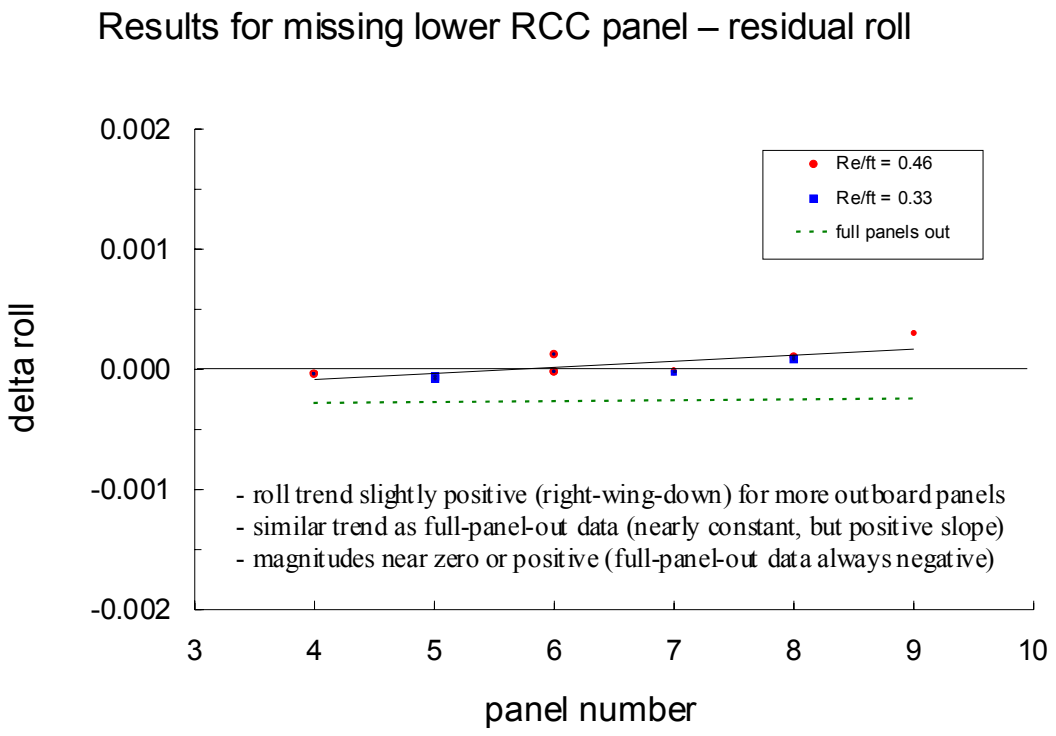

Figure 4.3-13 Aerodynamic Increment (delta Roll) – Missing Partial RCC Panel by Location

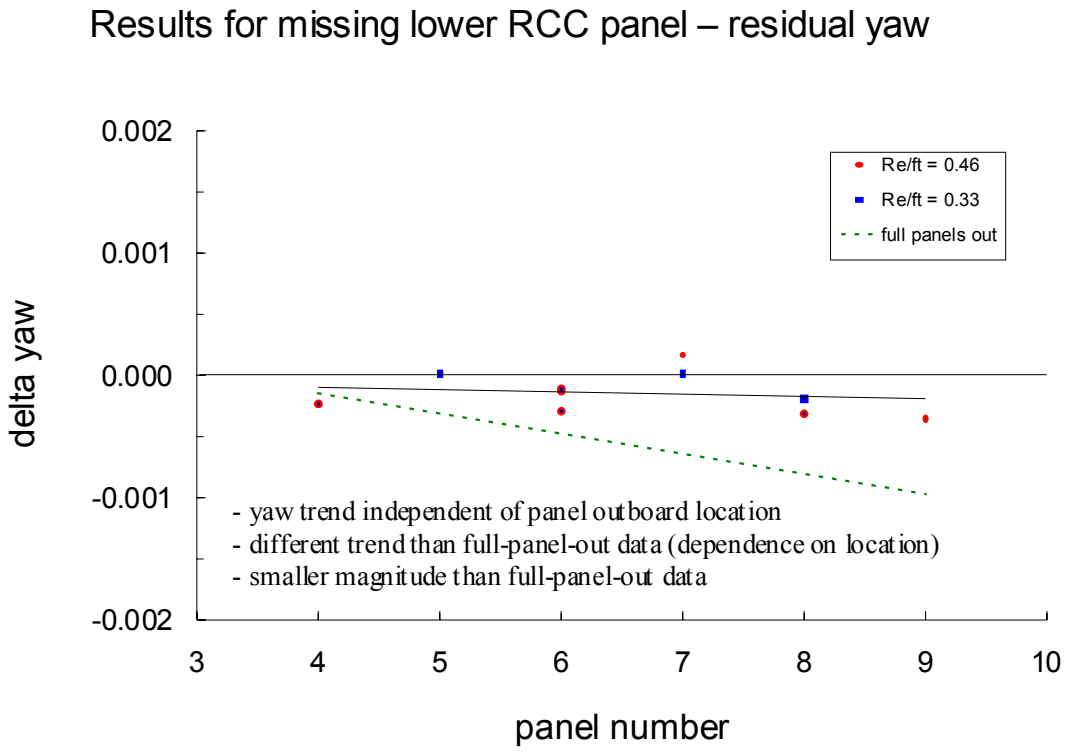

Figure 4.3-14 Aerodynamic Increment (delta Yaw) – Missing Partial RCC Panel by Location

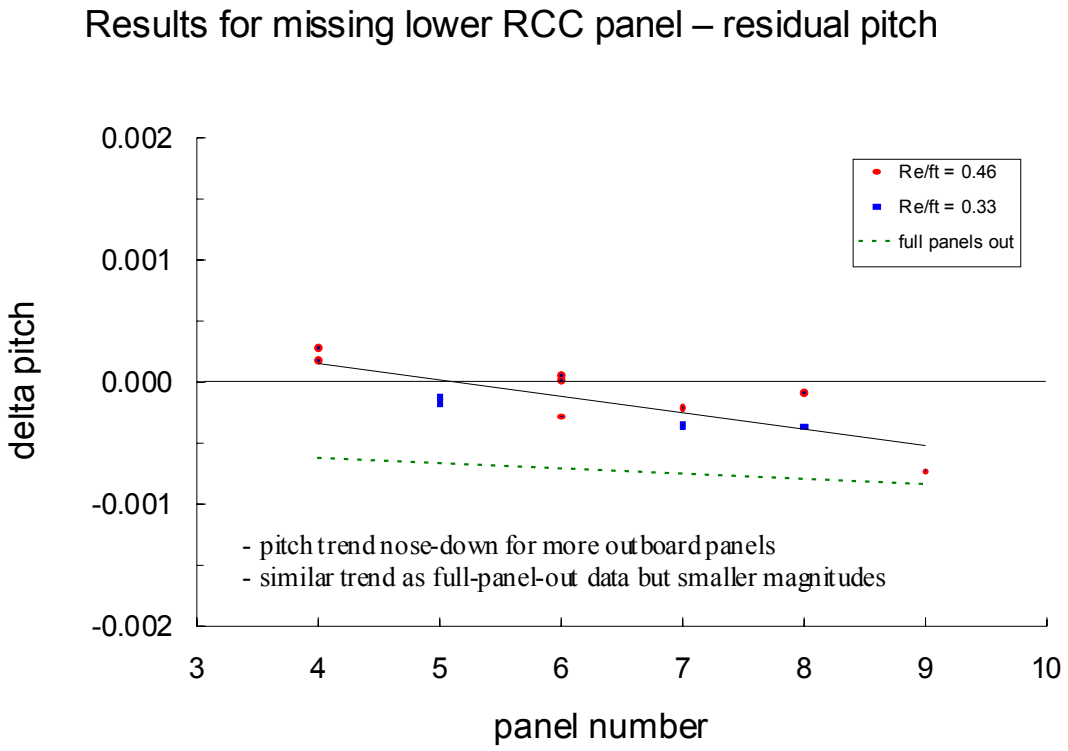

Figure 4.3-15 Aerodynamic Increment (delta Pitch) – Missing Partial RCC Panel by Location

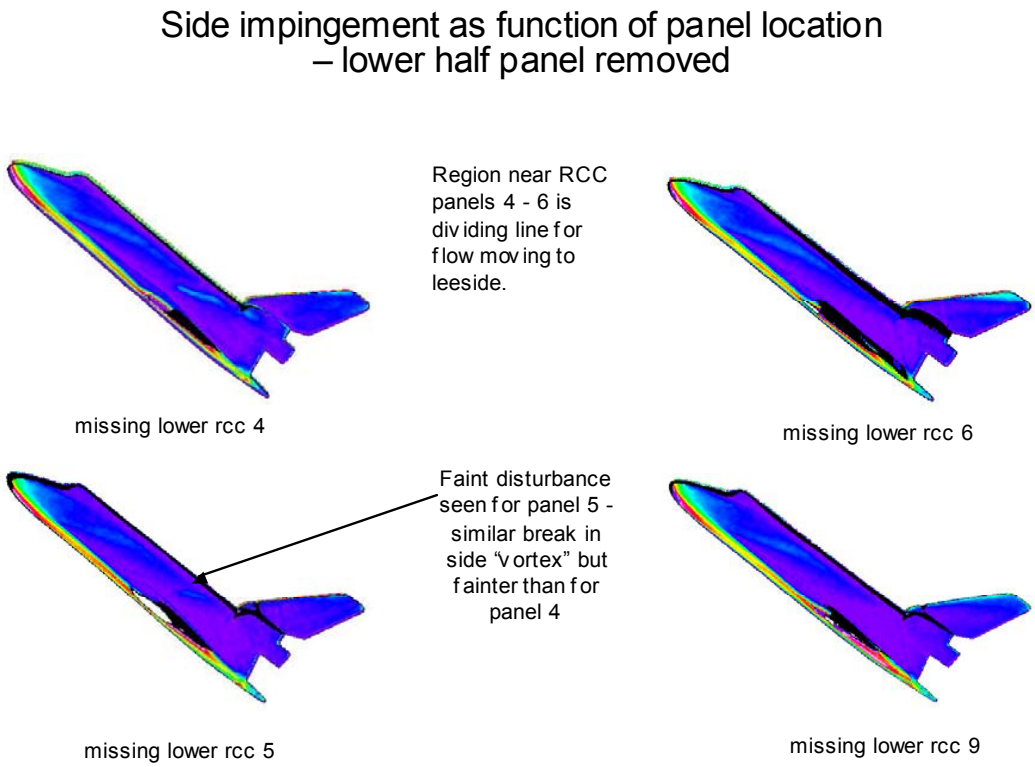

Figure 4.3-16 Side Fuselage Heating Augmentation – Missing Partial RCC Panel

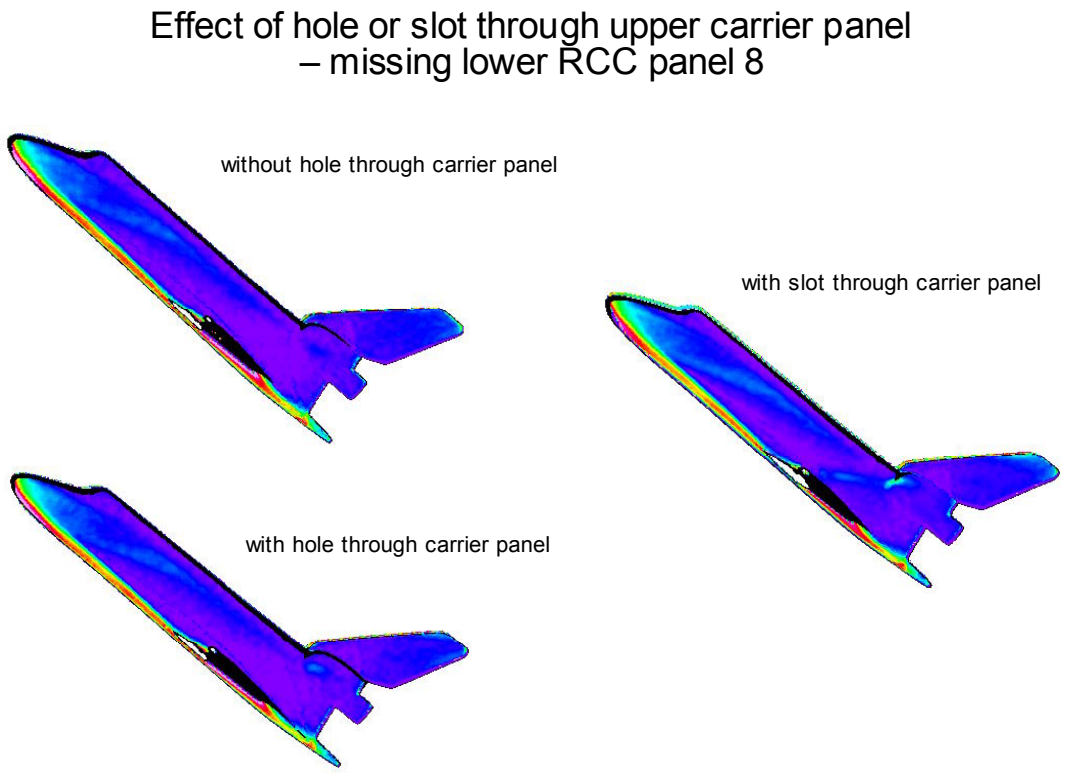

Figure 4.3-17 Side Fuselage Heating Augmentation – Missing Partial RCC Panel + Hole/Slot

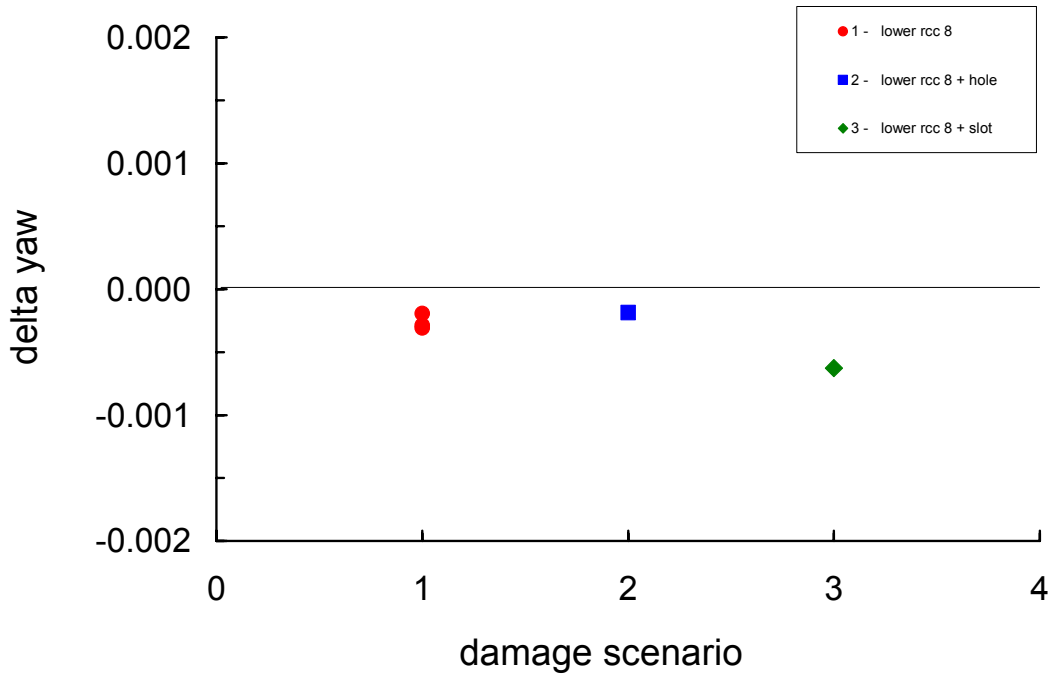

Figure 4.3-18 Aerodynamic Increment (delta Yaw) – Missing Partial RCC Panel + Hole/Slot

37

Vertical Tail on / off, missing Panel 9

Run	Tail	Alpha	Re/ft	ΔCrm	ΔCym	ΔCm	ΔCY	Model
30	on	40.2	0.45	-0.00006	-0.00115	-0.00105	0.00013	A
44	on	40.5	0.46	0.00007	-0.00131	-0.00128	-0.00037	5
45	on	40.5	0.45	0.00008	-0.00132	-0.00128	0.00022	5
63	off	40.5	0.46	-0.00007	-0.00122	-0.00125	-0.00006	5
64	off	40.5	0.44	-0.00013	-0.00122	-0.00117	0.00006	5
Avg	on	40.4	0.45	0.00003	-0.00126	-0.00120	-0.00001	
Avg	off	40.5	0.45	-0.00010	-0.00122	-0.00121	0.00000	
Delta		-0.1	0.00	0.00013	-0.00004	0.00001	-0.00001	

Effect of vertical tail is negligible, for missing RCC panel 9

Figure 4.3-19 Aerodynamic Increments -- Missing Full RCC Panel 9 with & w/o Vertical Tail

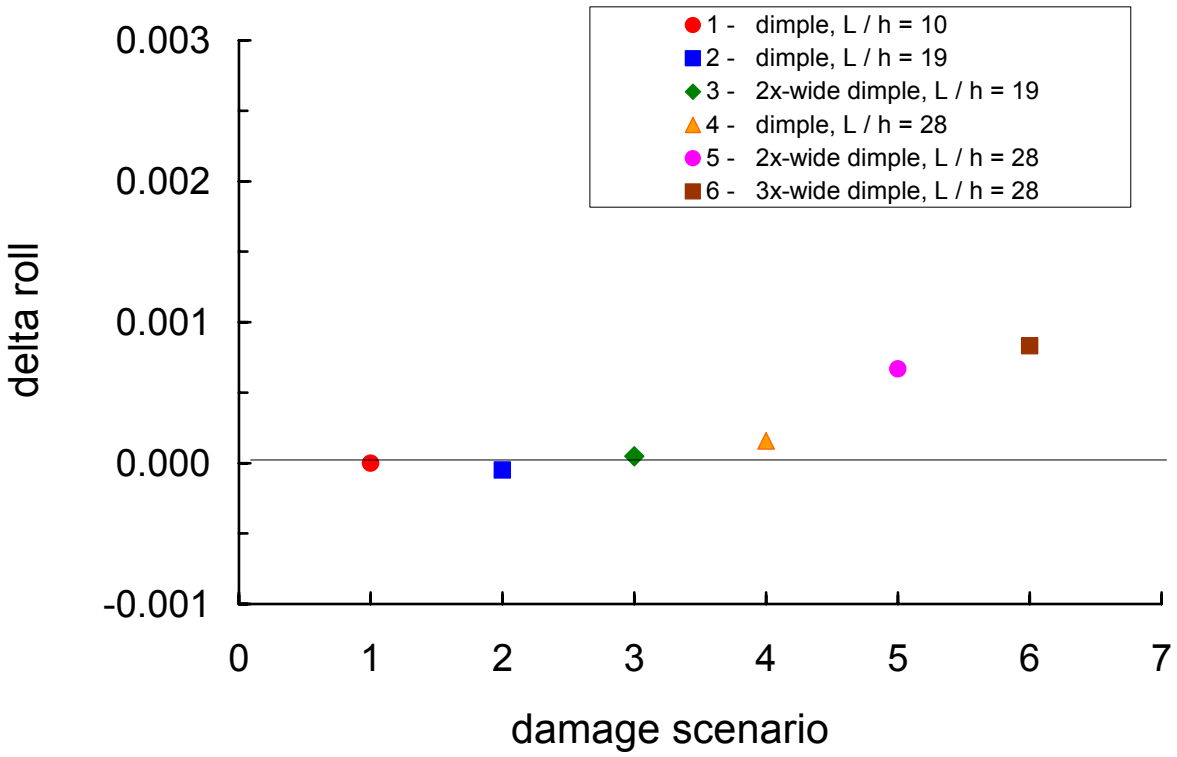

Figure 4.3-20 Aerodynamic Increment (delta Roll) – Lower Wing Surface Deformation / Dimple

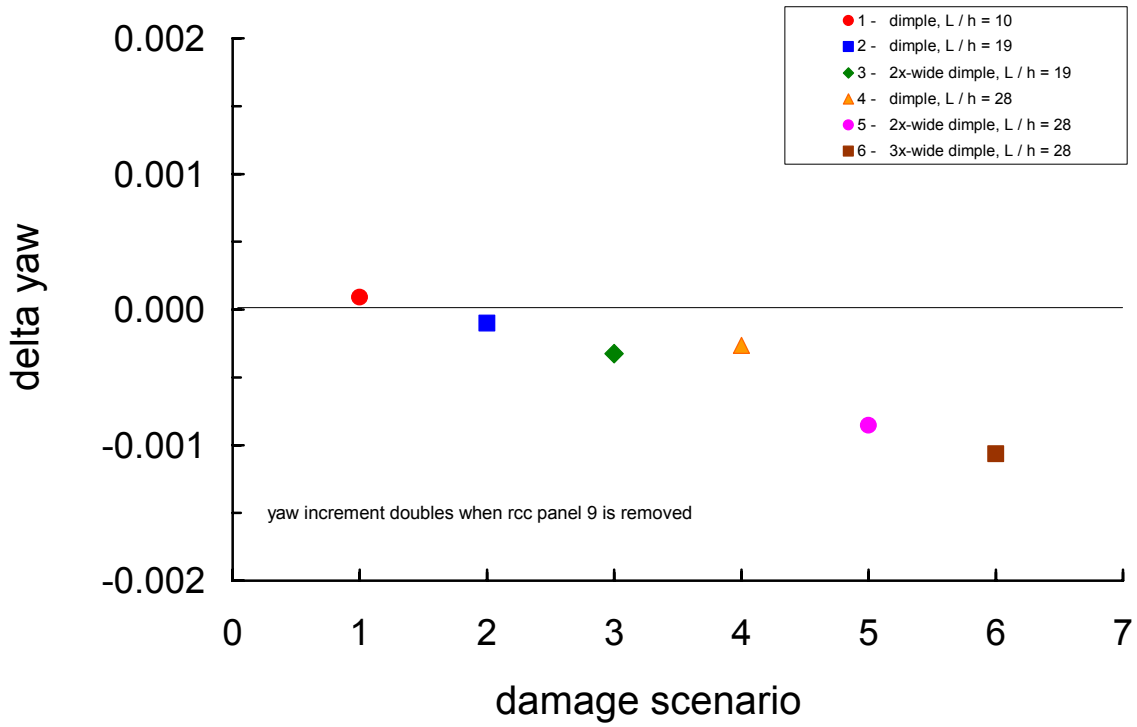

Figure 4.3-21 Aerodynamic Increment (delta Yaw) – Lower Wing Surface Deformation / Dimple

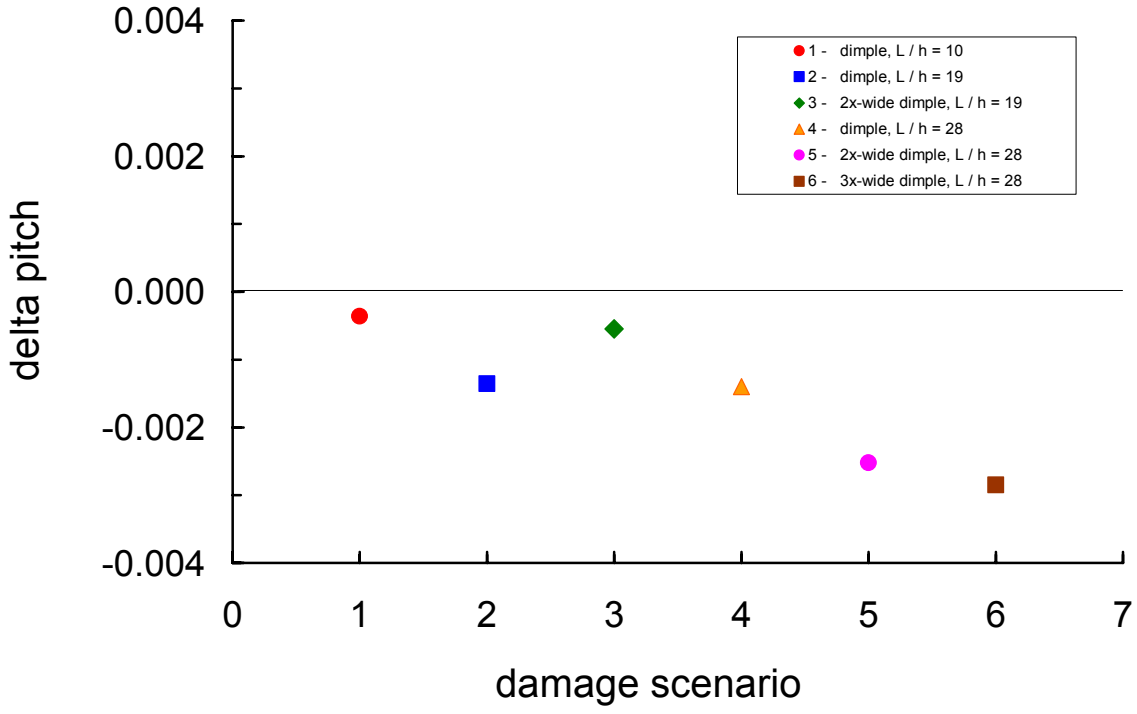

Figure 4.3-22 Aerodynamic Increment (delta Pitch) – Lower Wing Surface Deformation / Dimple

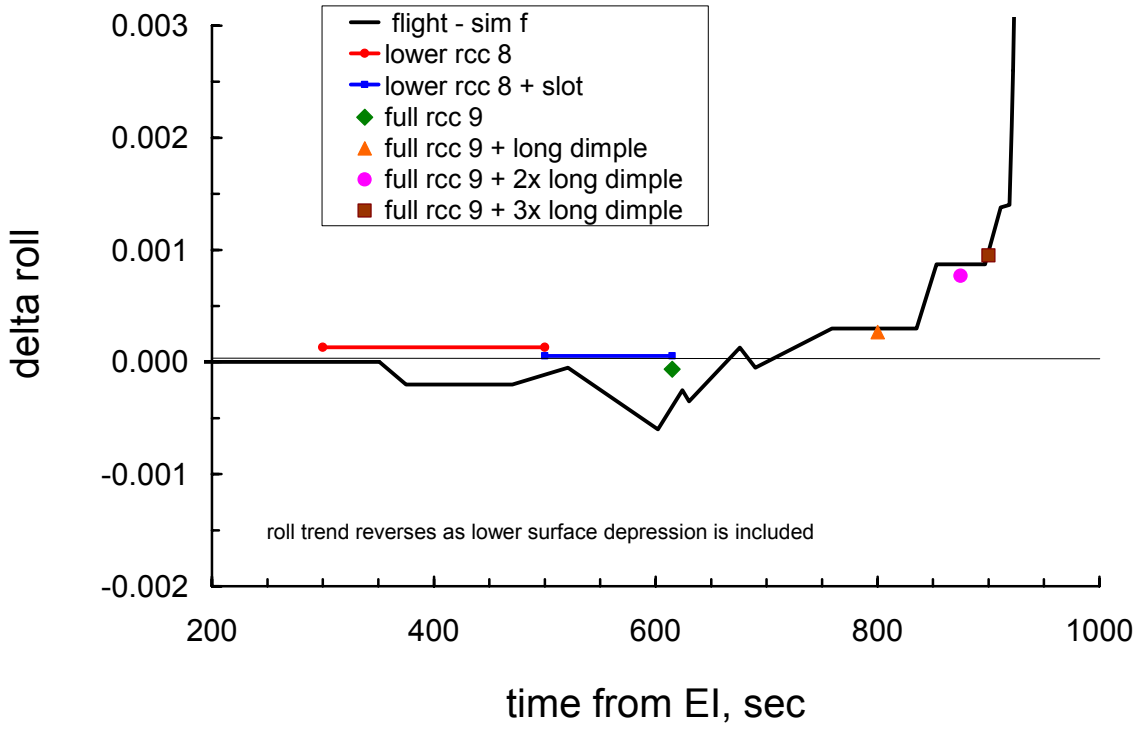

Figure 4.3-23 Aerodynamic Increment (delta Roll) – Damage Progression

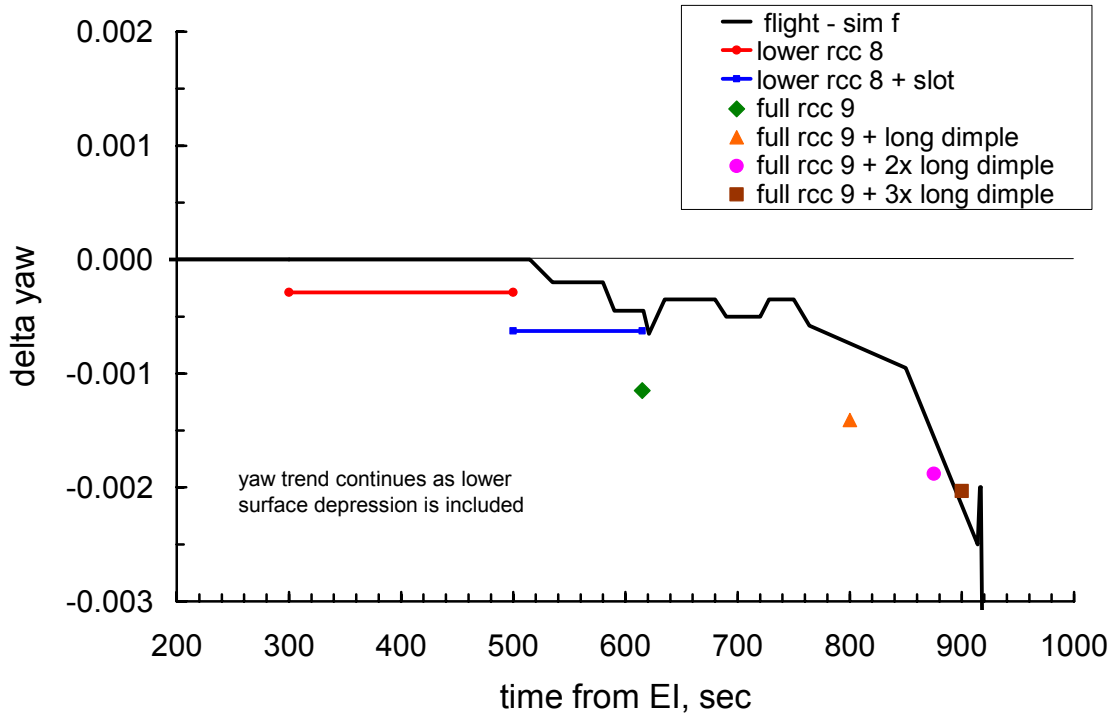

Figure 4.3-24 Aerodynamic Increment (delta Yaw) – Damage Progression

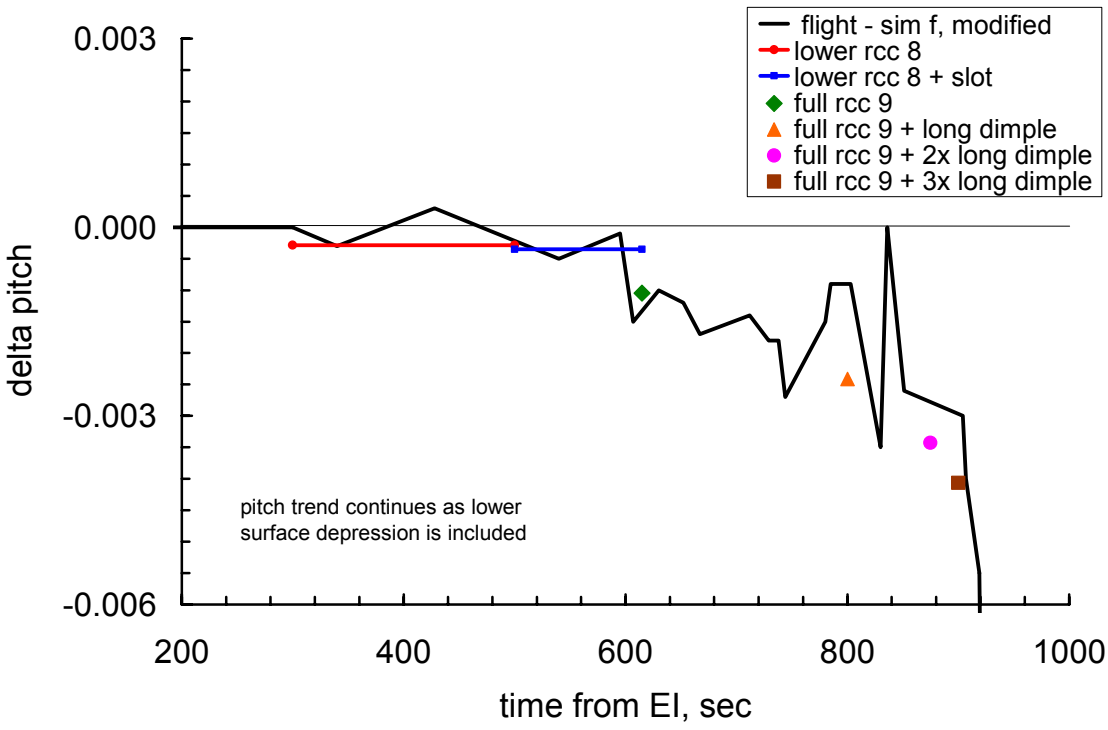

Figure 4.3-25 Aerodynamic Increment (delta Pitch) – Damage Progression

4.3.2 Damage Assessment Using Computational Fluid Dynamics

Computational tools were used to complement the wind tunnel testing of Columbia damage scenarios. The ability to simulate flight and wind tunnel conditions provided a bridge between the extensive wind tunnel test program and the STS-107 flight. The flow solutions provided a detailed view of the flow field characteristics and the contribution of orbiter components (vertical tail, wing, etc.) to aerodynamic forces and moments. In some cases, rapid, inviscid, unstructured CFD methods were able to guide the wind tunnel efforts. The inviscid methods are limited by the inability to accurately simulate viscous dominated flows such as occur in the highly separated flow region on the leeward side of the orbiter, but still proved very useful in a screening capacity. The structured mesh viscous methods are limited by the time it takes to develop a mesh for a complex geometry and in solution time. Having a limited number of the more accurate viscous solutions available provided a valuable check on the lower fidelity inviscid methods and served as an additional bridge between wind tunnel and flight conditions.

The sections below present the background for and data from computations that contributed to the understanding of the final damage scenario. Additional work performed by the analysts to verify assumptions of the computations, and on early analysis that led to the final working scenario is presented in the Aerodynamic Section Appendices.

4.3.2.1 CFD Analysis Introduction / Application Description

Several computational tools of varying levels of fidelity were used to predict aerodynamic forces and moments in support of the investigation. The inviscid methods provided a rapid meshing capability and a highly parallelized solution algorithm that allowed them to be used to screen a large number of damage scenarios over the course of the investigation. Development of the computational meshes for the viscous solver took much longer (weeks instead of a day), and the flow solutions were more computationally intensive (days/weeks instead of hours); thus the viscous solvers were used primarily as a check on the more abundant (from an aerodynamic perspective) inviscid work. The application of the various flow solvers utilized is briefly described and summarized in Table 4.3-1. Each is described in more detail in Aerodynamic Appendices Section 4.7.8.

The inviscid, unstructured mesh tool FELISA was the computational 'workhorse' of the aerodynamic investigation. It provides the capability to turn around complex geometries (mesh + solution) in under 2 days. Additionally its unique (among inviscid solvers) capability to model the flight environment with equilibrium air chemistry as well as the perfect gas environment of the Mach 6 air facility and the environment of the CF_4 tunnel provided ground test to flight condition trending. The inviscid, Cartesian mesh code CART3D was used to provide a set of rapid solutions at the Mach 6 air wind tunnel conditions. The viscous overset mesh solver OVERFLOW provided several Mach 6 laminar air solutions and was used to specifically address leeside flow interactions including the effects of the SILTS pod on the vertical tail. The viscous solvers GASP, USA and LAURA provided a set of solutions for the undamaged orbiter at hypervelocity flight conditions with full non-equilibrium chemistry, matched against a several solutions corresponding to wing leading edge damage scenarios, and a few coupled external/internal solutions.

4.3.2.2 STS-107 CFD Analysis Case Definition

Several sets of flow conditions were used in the analysis process. In the initial phase of the investigation, flow conditions and corresponding solutions for the STS-2 trajectory that have been widely reported in the open literature, and are listed in Table 4.3-2, were used as investigators geared up to support the investigation. Once the flight data from STS-107 became available, a joint effort undertaken by the aerodynamic and the aerothermodynamic teams, established a common set of flight conditions for use in all computational analyses. Table 4.3-4 lists the CFD points that were chosen along the STS-107 trajectory. Together, the 10 points span the range of STS-107 atmospheric flight conditions from entry interface (EI) to loss of signal (LOS). Points labeled condition AA and condition A were chosen for DSMC analysis at rarefied gas dynamic conditions, while the points, B and 1 - 6 were chosen for continuum flow (Navier-Stokes and Euler) methods. The conditions labeled 1-6 were chosen along the trajectory to correspond to key events that were noted in the initial evaluation of the OI data, and are described in Table 4.3-4. The CFD points were established well before the OEX data recorder was recovered and the MADS data became available. A final point, condition VN, was added near the end of the investigation to capture

the point at which the vacuum vent and water supply nozzle thermocouples indicate a brief off-nominal increase in temperature rise rate.

The challenge associated with the selection of the points was the lack of detailed atmospheric information during STS-107 entry flight combined with the need to quickly establish common CFD conditions to support the rapid pace of the investigation. In order to establish the complete set of conditions for these data points, several sources of information were combined. The most crucial data came from the GPS tracking that accompanied the OI telemetry data set. The GPS data provided the most accurate information on position (altitude, longitude, latitude) and relative velocity (speed, flight path angle, azimuth angle). The aerodynamic/ aerothermodynamic teams next assessed the OI data, which provided inertial navigation data information. While these data sets were less accurate in providing velocity and position compared to the GPS data, they did provide reasonably accurate information on vehicle attitude (alpha, beta and bank) as well as the actual control surface deflections (body flap, inboard and outboard elevons). To complete the needed data set, the February GRAM atmosphere model was utilized. An important note regarding the GPS velocity and OI derived vehicle attitude information is that neither accounts for the presence of any winds. When the CFD points were defined, the DAO/MSFC atmospheric reconstruction had not yet been developed. Furthermore, no attempt was made to re-compute the atmospherically derived parameters or account for the effect of wind on vehicle velocity and attitude parameters. By the time the DAO/MSFC atmospheric model became available, the computationally expensive CFD calculations were well under way. It is important to note that the delta aerodynamic analyses show little sensitivity to Mach number and angle of attack. Table 4.3-3 gives an accounting of how all the parameters were calculated. Figure 4.3-26 through Figure 4.3-29 depict various key trajectory parameters and labels the chosen CFD analysis conditions.

Additionally, CFD cases were run at wind tunnel conditions for both the Langley Mach 6 air and CF_4 facilities. The wind tunnel flow conditions used for the various flow solvers are shown in Table 4.3-5.

4.3.2.3 Configuration Summary and Analysis

All of the baseline and damaged configurations that were analyzed and the flow solver(s) and conditions used for analysis are summarized in Table 4.3-6. The scenarios are grouped by type/progression of damage, with baseline geometries listed first. The damaged configurations are grouped into three categories. The first group is for single and multiple missing RCC panels (full or partial), and includes the initial panel 6 damage simulation. The second grouping is a series of cases for progressive damage, increasing in severity, in the region of RCC panel 9. The third group of computations was for windward surface deformations, including an open wheel well and windward surface depressions/dimples (these simulate possible structural deformation of the wing skin due to the internal heating damage to the intermediate wing structure). The following subsections discuss the geometries, flow conditions, and analysis tools and present flow field images as well as the delta aerodynamic moment increments. The delta aerodynamic forces are not discussed here, as the extraction of these quantities from the flight data was considered unreliable.

4.3.2.3.1 Baseline Geometry and Analysis

While it would have been ideal for every computational and wind tunnel model to be generated from the same solid CAD model, time constraints and the availability of existing models already tailored to each particular application led to the decision to ‘go with what we have’ and to assess the impact of this decision when a common geometry became available. An 1997 CAD geometry was the basis for all of the computational meshes that existed prior to the Columbia accident. The 2003 CAD geometry was made available to all of the investigators shortly after the accident, and served as the geometry for the common baseline mesh (detailed in Aerothermodynamics Section 5.2.4.2) used for all of the structured mesh viscous computations. Table 4.3-7 lists the geometries that various computational meshes were generated from, and their relationship to the two ‘official’ CAD definitions. An effort was made to ensure that all investigators were modeling the damage consistently. The common geometries that were used to model the damaged orbiter are listed in Table 4.3-8.

An important assumption was made in all of the analysis, both wind tunnel and computational. Even if the model did not exactly capture the absolute aerodynamics of the orbiter at flight conditions, the delta

aerodynamic coefficients (calculated as *delta* = *damaged* – *baseline*) yield a reasonable approximation (when the damaged and baseline models are as close as possible with the exception of the damage area). For the computations great care was taken to have comparable mesh spacing in areas not affected by the damage. This eliminated any potential for deltas due to mesh differences corrupting the results.

Several geometric modeling simplifications were made for the various computations on an individual code and scenario basis. Early in the investigation, many computations were made excluding the vertical tail. The vertical tail is typically not important for hypersonic aerodynamics at high angle of attack conditions, and it's presence in a simulation adds a significant number of mesh points while hindering solution convergence. As it became apparent via Columbia's recovered debris forensics that there was significant off-nominal flow to the OMS pod and vertical tail, the tail was added into most computational models. Additionally, except for one set of OVERFLOW calculations, none of the computational models included the SILTS pod located on the tip of Columbia's vertical tail. For most cases, only half-body (i.e., 180°) simulations were computed, assuming no flow across the centerline of the vehicle. This modeling decision is the norm for CFD simulations as it facilitates more rapid simulations. While the assumption of no flow across the centerline was not strictly valid for the simulations where the leeside flow of the vehicle was interacting with flow through WLE damage, both FELISA and OVERFLOW results indicated that this assumption had little effect on predicted aerodynamic forces and moments (See Aerodynamic Appendices, section 4.7.5 for details of the OVERFLOW evaluation.) Also, the base of the orbiter was not modeled, another typical simplification for hypersonic simulations when the primary interest is heating or aerodynamic screening. The complex separated base flow typically requires a large mesh, and further slows convergence. It was apparent early in the investigation that damage was centered near the WLE or the wheel well, and that any effect to the base flow was likely insignificant. For many of the viscous simulations, the body flap was not included and neither were the gaps between the inboard and outboard elevons and the fuselage. Since the investigation was primarily concerned with the delta aerodynamics, no attempt was made to model the body flap and elevons at STS-107 flight deflections; all control surfaces were set at the zero degrees or trail position. Unless otherwise noted, all computations presented here assume a half-body, and do not compute the base flow. Additionally, a notation is made when the tail or body flap is not present in the computation.

Flow solutions on the baseline (undamaged) geometry were used by the Aerodynamics Team to compute the differences in aerodynamic forces and moments between the baseline and the damaged configurations, and for flow field comparisons. The External Aerothermodynamics Team also made extensive use of the baseline solutions to determine environments for engineering heating methods. To understand how well the inviscid and viscous computational methodologies reproduced the Orbiter OADB, a comparison was made between the OADB data and CFD results. Solutions computed on the baseline geometry as well as a missing panel 6 geometry with FELISA, and on the baseline geometry (without the body flap) with LAURA were utilized for this evaluation

The total normal and axial forces, and pitching moments for the solutions at CFD conditions 1 through 6 are plotted against time from EI of the STS-107 trajectory in Figure 4.3-30 (Note: side force, rolling and yawing moments are all zero for the symmetric baseline). The force and moments for the FELISA solutions are computed with and without the body flap, to serve as a bridge between the Orbiter OADB data and the LAURA computations. For pitching moment, the FELISA data is in better agreement with both the Orbiter OADB data and LAURA computations later in the flight, suggesting that the inviscid equilibrium chemistry model is not as appropriate for the higher Mach number range (M > 21). The trend in the LAURA predictions against FELISA without the body flap is similar to the trend of the Orbiter OADB data against the full FELISA solution, suggesting that the LAURA data is in good agreement with the flight database. The FELISA missing panel 6 result is also included in Figure 4.3-30 to illustrate how relatively small the delta aerodynamics due to damage are with respect to the absolute aerodynamics. A detailed discussion of this topic is included in the Aerodynamic Appendices Section 4.7.4.2.

4.3.2.3.2 Full RCC Panel missing

A damage scenario considered early in the investigation was that an entire RCC panel or perhaps several panels had been lost. This scenario was reinforced by an early FELISA computation (and subsequent wind tunnel testing) that showed windward flow passing through a notch in the WLE created by a simulated missing RCC panel. The notch was modeled with solid side surfaces and the open channel

behind the RCC panels was not represented. The flow was compressed as it passed through the notch, sending a jet over the leeward surface of the wing where it impinged on the side of the fuselage. This was this first evidence of a source for the augmented heating recorded by Columbia's fuselage and OMS pod surface temperature measurements. Consequently, a large portion of the computational effort in the investigation was spent looking at missing RCC panel configurations to gain an understanding of the effect of location and size of WLE damage on the aerodynamics and aerodynamic heating characteristics of the vehicle. The bulk of the computations were performed utilizing FELISA at both CF4 tunnel and flight conditions to establish a link between the wind tunnel results and the STS-107 flight data. A limited number of CART3D and OVERFLOW solutions were exercised at Mach 6 air and at flight Mach numbers with perfect gas (see Aerodynamic Appendices sections 4.7.5 (OVERFLOW) and 4.7.6 (CART3D) for more details), to provide additional insight into the trends shown with the wind tunnel and with FELISA. Additionally fully reacting Navier-Stokes calculations, primarily in support of the aerothermodynamic evaluation, were completed using LAURA, GASP and USA codes for several specific WLE damage cases. (see Aerodynamic Appendices Section 4.7.7 (USA) and Aerothermodynamics Section 5.2.4.5 (LAURA & GASP) for more details). Even though the debris recovery and subsequent analysis led to a more complex picture of the damage progression, the insight into the delta aerodynamics and the corresponding flow field characteristics gained by systematically looking at missing RCC damage proved invaluable to the investigation.

Numerous codes and both wind tunnels were utilized to study the effect of missing panel 6. While this damage was later ruled out for the STS-107 flight by recovered debris and while it had a very small impact on the aerodynamics, it offers an opportunity to explore the flow physics that are associated with wing leading edge damage. The initial panel 6 missing configuration was defined in the days after the accident without the benefit of a CAD definition, and, as shown in Figure 4.3-31, does not encompass the full RCC panel. This geometry roughly corresponds to the panel 6 'notch' geometry that was also evaluated in the wind tunnel.

Streamlines for both the baseline (blue) and missing RCC panel 6 (red) configurations are shown in Figure 4.3-32, for a FELISA computation at an STS-2, Mach 24 condition. With the orbiter at a 40° angle-of-attack, there is a strong expansion around the WLE, and the leeside flow field pressure and density are very low. When a section of material (such as an RCC panel) is removed from the orbiter WLE, the resulting gap has the effect of channeling the higher energy flow from the windward to the leeside, forming a jet-like flow structure. This 'jet' of high enthalpy flow carries substantially higher momentum than the surrounding leeside flow, and therefore is not significantly influenced by it. Pressure contours shown in Figure 4.3-33 (STS-107 Mach 24.2 condition) show the footprint of a shock on the leeside surface, and flow impingement on the side fuselage. This impingement would have the effect of increasing the heating rate on the side fuselage, a trend that was identified by the OI flight data early in the investigation. The effect of the missing panel on the windward surface is localized. The windward view of streamlines in Figure 4.3-32 show that the flow pattern is not affected just inboard of the missing panel, and the Cp (pressure coefficient) contours in Figure 4.3-33 indicate that the pressure distribution on the windward acreage of the damaged wing is essentially unchanged by the damage.

The full list of missing RCC panel cases analyzed computationally is given in Table 4.3-10, with the configuration details (tail/no tail, etc) and the flow conditions for each computation. Figure 4.3-34(a-e) shows the missing panel configurations as run with FELISA, except for the cases with all panels 1-7 removed. The surface pressure (C_p) contours on the side fuselage are shown in Figure 4.3-35 for each configuration at the STS-107 CFD condition 2 (Mach 24.2, α=40°). The disturbance on the fuselage moved further down the body and produced a higher C_p as the location of the missing RCC panel moved outboard (Figure 4.3-35a). For multiple missing panels, the trends are not as clear. There is a significant increase (> 2x) in the peak pressure on the side fuselage for missing panels 6+7 as compared to 6 only (Figure 4.3-35b). Removing more panels (5+6+7 or 1-7) spreads the region of influence, and the peak pressure drops. Figure 4.3-36 shows the leeside view for missing panels 6, 6+7, and 9. The influence of the size and orientation of the missing panel(s) is evident in the footprint of the expansion out of the channel and the shock due to the resulting 'jet' directed towards the fuselage. The missing panel 9 and missing panels 6+7 results show significantly stronger interaction on the wing leeside than the panel 6 removed case. For missing panels 6+7, the disturbance actually expands upstream of the damage area, indicating the strength of the jet relative to the leeside flow.

All computational methodologies consistently produced negative delta yawing (ΔCn) and pitching moments (ΔCm), and near zero to negative delta rolling moments (ΔCl) for a full missing RCC panel. Magnitudes of the predicted aerodynamic moments varied with the geometry, and to a lesser degree with flow condition (Mach 6 air, CF4, flight). The trends observed are very similar to those measured in the wind tunnel.

The delta aerodynamic moments computed with FELISA for several panel out configurations at flight (CFD condition 2, Mach 24.2) and CF4 are compared to the CF4 wind tunnel results in Figure 4.3-37. The x-axis of the plot is simply the configuration (labeled individually). The lines connecting the points for each configuration are included only to illustrate the trends; there is no expectation that interim damages can be predicted. Overall, the trend agreement between the computations and the wind tunnel is excellent. As additional RCC panels are removed, the moment increments become more negative. Delta pitching and rolling moments are relatively constant as the missing panel location moves outboard, while the yawing moment increment shows a more negative trend as the missing panel moves outboard. A single FELISA solution at flight (CFD condition 2, Mach 24.2) was computed for the full missing RCC panel 6 (RCC + carrier panel) to compare to the initial, or notched panel 6 results. Removing more material at the same location has a noticeable impact on the pitch and roll increments, but little effect on the yawing moment increment.

While the trends shown by the FELISA computations are consistent with the CF4 wind tunnel results, there is definite variation in magnitudes. Comparing the computed CF4 data to the WT measured values, FELISA over-predicts the roll, under-predicts the pitch increment, with close agreement for the yawing increment. When comparing flight condition to CF4 predictions, the flight computations produce consistently lower (larger value, more negative) pitch and yaw increments, while predicting higher (smaller value, more positive) rolling moment increments. While these differences appear large on the scales plotted in Figure 4.3-37, the magnitude of all of the delta moments for the missing panel configurations are represent very small aerodynamic values. The level of correlation between the flight and CF4 computations and the wind tunnel data shown in Figure 4.3-37 strongly suggest that the trends shown in the wind tunnel results are valid for STS-107 flight conditions.

The delta aerodynamic moments from missing panel computations using OVERFLOW, CART3D, LAURA, GASP, are shown in Figure 4.3-38, with the data in Figure 4.3-37 repeated. There is some variation in the geometries for the missing panel 6 and missing panel 9 cases, making exact comparisons impracticable. The CART3D computations did not include a vertical tail, the viscous GASP and LAURA computations terminated the grid systems at the body flap, and both GASP and OVERFLOW results were completed with and without the vertical tail (OVERFLOW with the SILTS pod – Aerodynamic Appendices section 4.7.5). Despite this range of geometry, the agreement for missing panel 6 is reasonable, with near zero increments. There is more of a spread for the missing panel 9 computations with larger increments indicated. Only CART3D and FELISA were used for the multiple missing panels. The CART3D Mach 6 computations indicate the same trends as FELISA and the wind tunnel, but with less variation for the multiple missing panels. For wing leading edge damage the results from all the various tools all indicate relatively small, negative moment increments with similar trends as the damage varies. While the variation suggest the exact magnitudes are uncertain, the body of data suggests the trends are legitimate and can be used to understand how this type of damage of relates to the STS-107 reconstruction.

With computational simulations, the contributions to the vehicle aerodynamics of each vehicle component (vertical tail, wing, etc.) can be isolated. Figure 4.3-39 shows the definition of the vertical tail, wing, OMS pod, and fuselage regions of the orbiter for which component contributions of the delta aerodynamics were calculated. Figure 4.3-40 shows the contributions of each of these regions to the total delta aerodynamic moments for missing panel configurations at flight conditions (CFD condition 2, Mach 24.2). Also shown are the total aerodynamic moments for the CF4 tunnel results. As in Figure 4.3-37, the missing panel configuration is plotted along the x-axis,. Each component is color coded according to the colors in Figure 4.3-39, and labeled on the plot, with the solid symbols representing flight computations. Figure 4.3-41 repeats the format of Figure 4.3-40, with hollow symbols for predictions at CF4 WT conditions.

Figure 4.3-40(a) and Figure 4.3-41(a) clearly show that the pressure loads to the wing dominate the delta pitching moment for both flight and CF4 conditions. For the multiple missing panel cases (6+7, 5+6+7) at flight conditions, Figure 4.3-40(b) and (c) show that the delta rolling and yawing moments are also dominated by the wing. For the single missing panels, however, the influences of the vertical tail and wing

balance each other in roll, essentially yielding a zero total increment. The vertical tail, the fuselage and the wing all produce negative increments for yawing moment, thereby providing a relatively large, negative delta yawing moment. The vertical tail contributions are more pronounced in flight for missing panel 9 than for missing panel 6. The CF4 (Figure 4.3-40) conditions show more influence of the vertical tail on the delta rolling and yawing moments for all configurations, with only missing panel 9 giving a positive contribution to the total delta rolling moment. Overall the component breakdown results indicate that there is not a large enough delta rolling moment contribution from the vertical tail to cause a substantial positive (right wing down) total delta rolling moment as seen late in flight.

Several of the missing panel configurations were run at multiple flight conditions to establish trends in the delta aerodynamics due to variations in the flight conditions. Figure 4.3-42 shows the computed delta aerodynamic moments and the extracted flight increments plotted against time from EI. The angle of attack varies between 38° and 42° (See Table 4.3-4for the flow conditions at each point). The CF4 computational and wind tunnel results are also shown to the right of the trajectory data. The delta pitching moment shows little variation, for each missing panel configuration, over the trajectory. The delta rolling moment shows somewhat of a negative trend toward the end of the trajectory, but the variation is small. Only the delta yawing moment shows a definite (more positive, smaller value) trend across the trajectory. A more systematic study where angle of attack and flow condition were varied independently confirmed that only the delta yawing moment was strongly influenced by the Mach number; these results are contained in Aerodynamic Appendices Section 4.7.4.4..

Overall, the computational results (both for flight and CF4 conditions) for missing panel damage scenarios were consistent with the wind tunnel results. The flow field analysis from these computations clearly indicates that when the windward flow is diverted by WLE damage, the flow field on the leeside of the vehicle is disturbed in a way that is consistent with the increased heating patterns observed during the STS-107 flight. The aerodynamic test and analysis results demonstrate that as more material is removed from the WLE all of the delta moments trend to more negative values. This is counter to the trend toward a more positive rolling moment seen later (after EI + 600 sec) in the STS-107 flight. These two observations taken together suggest the initial STS-107 aerodynamic increments are consistent with WLE damage. However, an additional damage progression scenario, other than simply continuing loss of RCC panel(s), is required to explain the aerodynamic trends later in flight.

4.3.2.3.3 Progressive Damage in Region of RCC Panel 9

As the investigation progressed, the primary damage location was focused towards RCC panels 8-9. The recovered WLE hardware also suggested that, at least initially, the damage was not as extensive as a full missing RCC panel. The second grouping of damaged configurations is a series of damaged configurations, increasing in severity, in the region of RCC panel 9. The damage scenarios and complete set of flow conditions for FELISA cases are shown in Table 4.3-11. Representative cross-sections of the wing in the region of panel 9 are shown for each damage scenario in Figure 4.3-43. For ease of discussion, these damages will be referred to as (a) – (g), as ordered in Figure 4.3-43. Damages (a) – (d) are partial damages to RCC panel 9, and (e) – (g) correspond toe full RCC panel 9 missing configurations. Damage (a) is the lower half of RCC panel 9 missing, with solid walls, and is the same configuration as tested in the CF4 wind tunnel. Damage (b) is a 1.0 inch slot from windward to leeside, at the front edge of the upper and lower carrier panels. Damage (c) is the lower half panel 9 with an internal cavity 'carved' out, and the upper carrier panel removed to create a flow path from windward to leeside. This geometry is repeated in damage (d), with an additional 810 in^2 of leeside material removed aft and inboard of the upper carrier panel, for a total leeside exit area of ~1000 in^2. The full panel missing geometries include an RCC panel 9 missing, damage (e) and the full RCC and both (upper and lower) carrier panels missing damage (f), (this data is repeated from the section on missing full RCC panels). Damage (g) has the same damage as in (d), but with the full RCC panel removed. Both damages (d) and (g) were created in an effort to direct as much mass flow as possible towards the OMS pod and vertical tail, to establish if it was possible to generate the positive delta rolling moment observed in flight by directing flow from the windward to leeside through a hole in the upper wing surface aft of the leading edge. Additional evaluation of progressive wing damage using CART3D is discussed in Aerodynamic Appendices Section 4.7.6.

The leeside flow fields for several of these damages at flight conditions (CFD condition 4, M=20.2) are shown in Figure 4.3-44. The flow patterns on the leeside wing and the side fuselage appear very similar,

despite the fact that the flow is coming through very different size damage geometries. The strength of the impingement (maximum Cp) on the side fuselage increases as the size of the hole increases beyond the upper carrier panel area, but is relatively constant for cases (d) – (g). The similarities in the flow patterns and pressure levels suggest that it is very difficult to isolate the damage size and location from correlations with the side fuselage MADS data. A wide range of damage scenarios, that enable windward to leeward flow, appear equally valid.

The delta aerodynamic moments for FELISA cases with progressive damage in the RCC panel 9 region, at flight (CFD condition 4, M=20.2) and CF4 conditions, are shown in Figure 4.3-45. The half panel 9 geometry (a) gives a very small increment in rolling (positive) and yawing (negative) moments, as no windward flow is diverted to the leeside. The delta aerodynamics for the one inch wide slot at RCC panel 9 are essentially zero. Establishing a larger flow path by removing the whole upper carrier panel 9 (c) continues the small positive increment to the rolling moment, and significantly shifts the yawing moment to a more negative value. When the size of the hole on the leeside is increased (d) from 188 in^2 (size of the upper carrier panel) to 998 in^2, there is little change in the delta rolling moment, and a small increase in the delta yawing moment. For the full panel out cases, the delta rolling moment becomes more negative as more WLE material is removed, from (e) to (f), while the delta yaw stays constant. When the additional leeside material is removed in (g), the delta yawing moment becomes less negative, and the delta rolling moment remains unchanged.

The component breakdown of the contributions to the delta aerodynamic moments is shown in Figure 4.3-46 and Figure 4.3-47 (See Figure 4.3-39 for the component definition). For delta rolling moment, the vertical tail gives a consistently positive contribution, which is offset to some degree by the wing. The half panel cases ((c) and (d), primarily) result in a small contribution from the wing, and thus a positive rolling moment. The full panel cases ((e) – (g)) have more contribution from the wing, resulting in a slightly negative rolling moment. The delta yawing moment is consistently negative, with fuselage and tail contributing more for the flight cases than the CF4. This analysis of component contributions to the total delta aerodynamics further underscores the observation that a large positive roll does not come from the flow over the vertical tail.

The leeside flow fields suggest that any of the damage progression configurations enabling flow to the leeside ((c) – (g)) can produce a significant disturbance on the side fuselage and OMS pod. The aerodynamic data, however, indicate that the damage that produces the more positive delta rolling moment (albeit near zero) is one with only partial damage to the RCC panel with flow to the leeside through an area behind the RCC, rather than a complete RCC panel missing. This set of damage scenarios did not produce a large positive rolling moment increment as observed late flight (EI + 800 sec). Indeed, it is clear that progressively damaging a particular RCC panel does not produce the steadily increasing trend in rolling moment increment seen in flight. This suggests that there must be another type of damage in addition to the WLE damage scenarios examined.

4.3.2.3.4 Windward Surface Deformation (Depressions and WLE Deformation)

One of the clearest trends in the reconstructed flight data was a change in the trend of the delta rolling moment that occurred around 600 seconds after EI. This change in rolling moment trend, and particularly the relatively large positive rolling moment late in flight (> EI + 800 sec), was not explained by any of the full or partial RCC panel damage configurations. Early wind tunnel tests with shallow wheel well cavities exposed had indicated that windward surface cavities could produce the positive roll and negative yaw observed late in flight.
A third group of computations conducted to investigate windward surface depressions/dimples in an attempt to model the structural deformation of the wing due to the heating damage to the intermediate wing internal structure. The depressions are assumed to result from the wing skin “dimpling” due to failure of the ribs and delamination of the wing honeycomb skin panels. Figure 4.3-48(a) shows an intermediate length (L=98”) depression that extends to the end of the wheel well, and has a depth that is approximately half (d=2.8”) of the depth modeled in the wind tunnel. Figure 4.3-48(b) shows the damage configuration that corresponds to full length, “single wide” (1w) depression with RCC panel 9 removed that was also tested in the CF4 tunnel. The depression created in the ceramic wind tunnel model was milled such that the interior corners were rounded, as opposed to sharp edges in the FELISA model. Aerodynamic

increments for the intermediate length dimple at 2 depths and a full length depression with and without RCC panel 9 removed were computed with FELISA for flight and CF4 conditions. The structural analysis group at JSC performed a FEM simulation of the global deformation of the wing, assuming failure and degraded strength of the structure in the intermediate wing box area. Additional engineering calculations were made on the damaged structure to simulate the localize deformation of the wing skin. Figure 4.3-48(c) shows the resulting geometry, as modeled with FELISA. The structural analysis efforts to understand the wing deformation late in flight are covered in Section 7.5. An additional geometry, which was an attempt to deform the WLE by rotating several of the RCC panels, around RCC panel 9, is included in this group. Figure 4.3-49 shows the deformed geometry overlay on the original. In the region of RCC panel 9, the WLE is rotated up. The amount of rotation tapers off away from RCC panel 9. Table 4.3-12 summarizes the damaged geometries and flow conditions that were run with FELISA for the windward surface deformation cases.

Windward surface pressure contours and surface streamlines are shown in Figure 4.3-50 for CF4 conditions and in Figure 4.3-51 for flight (CFD Condition 4, M=20.2) conditions, for several of the windward surface damage configurations. The depression configurations that simulate the 'single wide' wind tunnel geometries show a very strong compression along the aft face of the damaged area. The shorter length depression shows the same flow pattern in the expansion area at the front of the depression as the longer length. Thus, the longer depression has more area that is at a higher pressure than the baseline. Additionally, the shallower depression shows a smaller and weaker compression at the aft face of the depression. The character of the flow patterns for the damage resulting from the structural analysis is quite different than for the 'single wide' geometries. Since there are no sharp slope changes, a gentle expansion then recompression of the flow occurs within the dimpled area, and therefore a smoother and smaller variation in the surface pressure. This results in smaller delta aerodynamic moments than for the wind tunnel cases configurations.

The delta aerodynamics for the windward damage cases and corresponding CF4 tunnel data are shown in Figure 4.3-52. The WLE deformation case showed zero delta rolling and pitching moments, and a relatively small increment in yawing moment. The zero increment in rolling moment is due to canceling contributions of an increase in normal force (giving positive rolling moment) and a positive side force (which gives a negative rolling moment). It is possible that a WLE deformation that rotates more RCC panels at a smaller angle so less side force is produced would show a positive delta rolling moment. The agreement between the computations and wind tunnel for the single wide depressions is comparable for the delta yawing and pitching moments, but is not as good quantitatively for rolling moment as has been shown for other damaged configurations evaluated (See Figure 4.3-37 and Figure 4.3-45). The computations show the largest positive rolling moment for any of the damage configurations assessed, and is positive for all of the depressions considered. The wind tunnel only showed positive delta rolling moment for the longer depressions. This discrepancy is likely due to a combination of geometry differences (particularly the contoured back wall of the depression for the wind tunnel model) and a strong viscous component to this cavity-like flow. The damage from the structural analysis dimple configuration shows a smaller, though still positive rolling moment increment, and very small pitch and yawing moment increments. This is expected, in part because the strong compression at the back of the single width depression will produce larger delta moments when compared to the more gentle sloping of the structural analysis depression.

In addition to showing computed and measured delta aerodynamics, Figure 4.3-52 also shows an estimate, using simple superposition, of the delta aerodynamics for the cases where the windward surface damage was combined with a missing RCC panel. The superposition values compare well with the computed values for the longer, single width depression combined with missing RCC panel 9, and indicate that the postulated structural damage would produce the positive roll and negative yaw that was seen in flight.

Overall, the delta aerodynamics computed with FELISA for windward surface damage configurations corroborate the trends produced in the wind tunnel. The data trends support the hypothesis of progressive internal structural damage occurring late in the flight that produces a gradual windward surface deformation. This gradual deformation produces the steady increase in rolling moment and yawing moment increments seen late in flight.

Tables

Computational Tools Used in STS-107 Investigation - Aerodynamic Analysis					
Code / Tool	**Physics Model**	**Mesh type**	**Available Gas Models**	**Mach number range**	**Analysts**
FELISA	Inviscid	unstructured	perfect gas air, CF4 gas, equilibrium air	restricted by continuum flow boundaries	LaRC (Bibb, Prabhu)
CART3D	Inviscid	cartesian unstructured	perfect gas air	<10 (applied @ Mach 6)	JSC (Dries, Greathouse)
OVERFLOW	Viscous	structured, overset	perfect gas air	<18 (applied @ Mach 6)	JSC (Lillard)
LAURA	Viscous	structured	perfect gas, equilibrium, non-equilibrium, CF4	restricted by continuum flow boundaries	LaRC (Gnoffo, Bobskill, Thompson)
GASP	Viscous	structured	perfect gas, equilibrium, non-equilibrium	restricted by continuum flow boundaries	ARC (Reuther, Jones)
USA	Viscous	structured	perfect gas, equilibrium, non-equilibrium	restricted by continuum flow boundaries	Boeing-HB (Rajagopal)

Table 4.3-1 CFD Flow Solvers used in Aerodynamic Analysis for STS-107 Investigation

OEX / STS-2 Conditions							
Case	Mach	Angle-of-Attack (Alpha) deg	Angle-of-Sideslip (Beta) deg	Velocity ft/sec	Density slug/ft^3	Temperature °R	Reynolds Number / ft
STS-2a	18.07	40˚	0º	18429.4	3.1673E-07	433.1	9070
STS-2b	24.3	40˚	0º	22704.5	1.1200E-07	363.6	17950

Table 4.3-2 STS-2 Conditions Utilized in Initial Phase of Investigation

Parameter	Derivation	Comment
altitude	GPS data	
longitude	GPS data	
latitude	GPS data	
Velocity	GPS data	should be wind corrected to get true airspeed
flight path angle	GPS data	should be wind corrected
azmithul angle	GPS data	should be wind corrected
density	GPS altitude + GRAM February model	should be updated with DOA/MSFC atmosphere
temperature	GPS altitude + GRAM February model	should be updated with DOA/MSFC atmosphere
dynamic pressure	GPS velocity + density	should be updated with DOA/MSFC atmosphere
viscosity	Sutherland Law + Temperature	should be updated with DOA/MSFC atmosphere
Mach number	GPS velocity + Temperature	should be updated with DOA/MSFC atmosphere
Reynolds number	GPS velocity + Temperature	should be updated with DOA/MSFC atmosphere
Stagnation radiative equilibrium Heat Flux	Fey-Ridell + GPS data + GRAM data	should be updated with DOA/MSFC atmosphere
Stagnation radiative equilibrium Temperature	Fey-Ridell + GPS data + GRAM data	should be updated with DOA/MSFC atmosphere
Alpha	OI inertial navigation data	should be wind corrected
Beta	OI inertial navigation data	should be wind corrected
Bank	OI inertial navigation data	should be wind corrected
Body Flap	OI data	
Left Inboard Elevon	OI data	
Left Outboard Elevon	OI data	
Right Inboard Elevon	OI data	
Right Outboard Elevon	OI data	

Table 4.3-3 Parameter Calculation Method for STS-107 Investigation Conditions

Point Name	Comments	GMT (mm:ss.ss)	Time past e.i. (sec)	Altitude (ft)	VREL (ft/sec)	Mach Num.	Reynolds # per foot (Re/ft)	Alpha (deg)	Beta (deg)
Condition AA	350,000 ft DSMC point	45:40.0	91.04	350,274	24,622	25.10	26	40.78	-0.29
Condition A	300,000 ft DSMC vs NS comparison point	47:26.6	197.60	300,004	24,666	27.04	456	39.55	0.30
Condition B	Early Entry Navier-Stokes solution point	49:00.7	291.68	261,730	24,603	25.70	2,679	41.35	-0.07
Condition 1	Start Peak Heat	50:53.0	404.00	243,048	24,116	24.87	5,872	40.17	-0.06
Condition 2	First Off Nominal Event	52:20.4	491.36	236,527	23,554	24.17	7,644	39.99	-0.25
Condition VN	Off nominal vent nozzle temp. rise rate	52:45.3	516.32	234,623	23,368	23.94	8,274	40.04	-0.50
Condition 3	Mid Fuselage Bond Line Temperatures @ x=1215 and 1410 start off nominal trend	54:24.2	615.20	227,423	22,505	22.91	10,997	39.59	-0.47
Condition 4	Start of elevon roll trim corrections	57:35.2	806.24	216,064	20,210	20.30	16,244	42.01	-0.69
Condition 5	Near start of sharp aileron trim	58:23.2	854.24	209,368	19,428	19.35	20,729	38.87	-0.52
Condition 6	Last Good GPS point	59:30.4	921.44	200,767	18,164	17.88	27,409	39.02	-1.16

Point Name	Comments	GMT (mm:ss.ss)	Time past e.i. (sec)	Density (slugs/ft^3)	Temp (deg R)	Dynamic Pressure (lbf/ft^2)	Viscosity (slugs/(ft*sec))	Stag. heat flux (BTU/ft^2*sec)	Stag. rad. eq. Temp. (deg R)
Condition AA	350,000 ft DSMC point	45:40.0	91.04	3.345E-10	400.4	0.1014	3.169E-07	2.820	1,627
Condition A	300,000 ft DSMC vs NS comparison point	47:26.6	197.60	5.181E-09	346.2	1.5762	2.802E-07	11.102	2,289
Condition B	Early Entry Navier-Stokes solution point	49:00.7	291.68	3.314E-08	381.5	10.0292	3.043E-07	27.844	2,881
Condition 1	Start Peak Heat	50:53.0	404.00	7.568E-08	391.2	22.0077	3.108E-07	39.651	3,147
Condition 2	First Off Nominal Event	52:20.4	491.36	1.017E-07	395.2	28.2189	3.135E-07	42.559	3,203
Condition VN	Off nominal vent nozzle temp. rise rate	52:45.3	516.32	1.113E-07	396.4	30.3782	3.142E-07	43.528	3,221
Condition 3	Mid Fuselage Bond Line Temperatures @ x=1215 and 1410 start off nominal trend	54:24.2	615.20	1.552E-07	401.4	39.2967	3.176E-07	45.643	3,258
Condition 4	Start of elevon roll trim corrections	57:35.2	806.24	2.610E-07	412.5	53.3117	3.248E-07	42.119	3,195
Condition 5	Near start of sharp aileron trim	58:23.2	854.24	3.515E-07	419.6	66.3299	3.294E-07	42.824	3,208
Condition 6	Last Good GPS point	59:30.4	921.44	5.064E-07	429.3	83.5424	3.356E-07	41.502	3,182

Point Name	Comments	GMT (mm:ss.ss)	Time past e.i. (sec)	Bank (deg)	Body Flap (deg)	Lf. Inbd. El. (deg)	Lf. Outbrd. Elv. (deg)	Rt. Inbrd. Elv. (deg)	Rt. Outbrd. Elv. (deg)
Condition AA	350,000 ft DSMC point	45:40.0	91.04	-0.19	-4.32	1.97	1.88	1.97	1.96
Condition A	300,000 ft DSMC vs NS comparison point	47:26.6	197.60	1.36	-4.28	1.97	1.91	1.97	1.96
Condition B	Early Entry Navier-Stokes solution point	49:00.7	291.68	1.79	-4.46	-1.03	-1.06	-1.27	-1.25
Condition 1	Start Peak Heat	50:53.0	404.00	78.55	1.18	-2.30	-2.32	-3.54	-3.55
Condition 2	First Off Nominal Event	52:20.4	491.36	72.77	1.19	-2.71	-2.67	-3.53	-3.51
Condition VN	Off nominal vent nozzle temp. rise rate	52:45.3	516.32	72.05	1.19	-2.74	-2.74	-3.50	-3.45
Condition 3	Mid Fuselage Bond Line Temperatures @ x=1215 and 1410 start off nominal trend	54:24.2	615.20	66.75	1.23	-2.17	-2.21	-3.18	-3.19
Condition 4	Start of elevon roll trim corrections	57:35.2	806.24	-68.57	-1.81	-4.58	-4.58	-3.51	-3.50
Condition 5	Near start of sharp aileron trim	58:23.2	854.24	-56.75	-0.26	-3.27	-3.14	-1.37	-1.38
Condition 6	Last Good GPS point	59:30.4	921.44	-63.85	0.09	-6.07	-6.03	-1.63	-1.64

Table 4.3-4 STS-107 Investigation CFD Case Flight Conditions

Mach 6 Air Conditions (LaRC Tunnel)							
Case	Mach	alpha,	beta,de	velocity, ft/sec	density, slug/ft^	T, °R	Reynolds Number / ft
LAURA Wind Tunnel	5.94	40°	0º	3092.9	6.3517E-05	113.0	2.08 Million/ft
OVERFLOW Wind Tunnel	5.96	40°	0º	3096.0	2.5556E-05	112.3	2.98 Million/ft
Perfect Gas, FELISA,CART3D	6	40°	0º	---	---	---	---

Mach 6 CF4 Conditions (LaRC Tunnel)							
Case	Mach	alpha,	beta,de	velocity, ft/sec	density, slug/ft^	T, °R	Reynolds Number / ft
LAURA, low Re	5.894	40°	0º	2917.5	1.4805E-05	357.7	0.17 Million/ft
LAURA, high Re	5.902	40°	0º	2934.1	4.7026E-05	361.2	0.55 Million/ft
LAURA, final	5.913	40°	0º	2910.9	3.8915E-05	353.0	0.46 Million/ft
FELISA	5.85	40°	0º	2994.0	2.9393E-05	387.4	---

Table 4.3-5: Wind Tunnel Conditions Utilized in STS-107 Investigation

Scenario		Flow Solver	Mach 6	CF4	Flight
WLE Damage - Full / Partial Missing RCC					
Panel 6 removed	includes LaRC initial panel 6, RCC 6, and RCC+carrier panel 6	**FELISA**	**X**	**X**	**X**
		CART3D	**X**		
		OVERFLOW	**X**		
		LAURA			**X**
		GASP			**X**
		USA			**X**
Panels 6-7 removed	includes RCC 6+7, and RCC+carrier panel 6+7	**FELISA**		**X**	**X**
		CART3D	**X**		
Panels 5-7 removed	includes RCC 5+6+7, and RCC+carrier panel 5+6+7	**FELISA**		**X**	**X**
		CART3D	**X**		
Panel 9 removed	includes RCC 9, and RCC+carrier panel 9, LAURA/GASP also with open RCC channel	**FELISA**		**X**	**X**
		CART3D	**X**		
		OVERFLOW	**X**		
		GASP			**X**
		LAURA			**X**
Panels 1-7 removed		**FELISA**		**X**	**X**
		CART3D	**X**		
Half Panels Removed	CART3D (7, 8, 9), FELISA (9), GASP (6, 9)	**FELISA**		**X**	
		GASP			**X**
		CART3D	**X**		
Missing T-Seal 9		**CART3D**	**X**		
Progressive Damage near RCC Panel 9					
Half Panel 9	solid walls	**FELISA**		**X**	
		CART3D	**X**		
		GASP			**X**
Half Panel 9 with RCC cavity, upper carrier panel missing	GASP has vented walls, no upper cavity	**FELISA**		**X**	**X**
		GASP			**X**
Half Panel 9 with cavity, upper carrier panel missing, additional leeside material removed		**FELISA**		**X**	**X**
RCC Panel 9 removed		**FELISA**		**X**	**X**
RCC + carrier panels at 9 removed		**FELISA**		**X**	**X**
RCC 9, upper carrier 9, and additional leeside material removed		**FELISA**		**X**	**X**
Lower Carrier Panel 8 w/large upper wing hole		**CART3D**	**X**		
Half 8 (w/Full Panel 9 removed or small upper wing hole or large upper wing hole)		**CART3D**	**X**		
Windward Surface Damage					
WLE deformation	GEOLAB modification	**FELISA**		**X**	
B. Scallion dimple (depression created between the 163 and 192 ribs)	2 lengths, 2 depths, with and without RCC 9 removed	**FELISA**		**X**	**X**
Depression from structural analysis	Depth = 5.09"	**FELISA**		**X**	**X**

Table 4.3-6 Master Configuration Matrix for STS-107 Aerodynamic Analysis

Geometry Model / Mesh	Original Geometry Source	Comments
LaRC legacy structured mesh	1997 CAD defiinition	
gridTool model		All FELISA meshes were built from a gridTool watertight surface model, which was built from the LaRC legacy structured mesh.
FELISA unstructured surface mesh		CART3D meshes were built using the FELISA baseline mesh for the surface geometry
ARC legacy structured mesh		
Boeing legacy structured mesh		
Common Baseline Grid	2003 CAD definition	.igs and .stp exported geometry (R. Gomez-JSC)

Table 4.3-7 Geometry Pedigree for Baseline Geometries

Auxilliary Geometry for Damage Analysis	Short Name	Source	Comments
SILTS Pod	SILTS Pod	JSC Engineering	Simplified representation estimatedfrom SILTS Pod drawings
LaRC initial panel 6	LaRC initial panel 6	OEX Aerothermodynamics Symposium, NASA CP 3248, Part2, page 759	Estimated RCC panel 6 location from drawing in report -- *referred to as initial panel 6 definition or panel 6 "notch"*
Initial RCC Panel Definition	Greathouse RCC	Orbiter Drawings	RCC panel corner points were digitized from orbiter drawings. Leading edge was cut into individual pieces to approximate RCC panels 1-22
Dries/GEOLAB RCC and Carrier Panel Definition	Dries/GEOLAB	Drawing 221-50000 Rev. A, General Arrangement; Drawing MD-V70-10-002, Wing Reference System Diagram; LESS/RCC Recovery and Reconstruction Data	Panel locations provided by JSC/K. Dries and integrated into CAD definition by LaRC/GEOLAB

Table 4.3-8 Damage Geometry Pedigree

Scenario	Configuration Details	geometry pedigree	Flow Solver	STS-2	STS-107						CF4 Air Tunnel	Mach 6 Air Tunnel
					1	2	3	4	5	6		
Baseline, half body	with vertical tail, bodyflap	1997	FELISA	a, b	X	X	X	X	X	X	X	X
		1997	CART3D									X
		1997	USA									
	full body with vertical tail, bodyflap	1997	FELISA								β=-1°, +1°	
	vertical tail with SILTS pod	2003	OVERFLOW									X
	without bodyflap	1997	LAURA	a, b	X	X	X			X		
		2003	LAURA	a, b	X	X	X			X	X	X
		2003	GASP	a, b	X	X	X			X	X	X
	without vertical tail	1997	FELISA			X						
		1997	CART3D									X
		2003	OVERFLOW									X
	without vertical tail, bodyflap	1997	GASP									

Table 4.3-9 Baseline Orbiter Cases

Scenario	Configuration Details	geometry pedigree	Flow Solver	STS-2	STS-107						CF4 Air Tunnel	Mach 6 Air Tunnel
					1	2	3	4	5	6		
Full missing RCC panels												
Panel 6 removed	LaRC panel 6, vertical tail, bodyflap	1997	**FELISA**	**a, b**	**X**	**X**	**X**	**X**	**X**	**X**	**X**	**X**
	LaRC panel 6, no vertical tail	1997	**CART3D**									**X**
	LaRC panel 6, no vertical tail	2003	**OVERFLOW**									**X**
	LaRC panel 6. without bodyflap	1997	**LAURA**		**X**							
	RCC only, without bodyflap	2003	**GASP**		**X**							
	RCC + carrier panel 6, vertical tail, bodyflap	1997	**FELISA**			**X**						
	??	1997	**USA**						**X???**			
panels 6-7 removed	RCC + carrier panel, vertical tail, bodyflap	1997	**FELISA**		**X**	**X**	**X**	**α = 38°, 40°, 42°**	**X**	**X**	**X, α = 40°**	
	RCC only, no vertical tail	1997	**CART3D**									**X**
panels 5-7 removed	RCC + carrier panel, vertical tail, bodyflap	1997	**FELISA**			**X**					**X**	
	RCC only, no vertical tail	1997	**CART3D**									**X**
panel 9 removed	RCC + carrier panel, vertical tail, bodyflap	1997	**FELISA**		**X**	**X**	**X**	**X**			**X**	
	RCC only, no vertical tail	1997	**CART3D**									**X**
	RCC only, vertical tail, bodyflap	1997	**FELISA**		**X**	**X**		**X**			**X**	
	RCC + carrier panel, vertical tail, bodyflap, full (360°)	1997	**FELISA**								**β=-1°, 0°, +1°**	
	RCC only, with vertical tail and SILTS pod, full (360°)	2003	**OVERFLOW**									**X**
	RCC only, without vertical tail	2003	**OVERFLOW**									**X**
	RCC only, without tail, without bodyflap	2003	**GASP**		**X**							
	RCC only, without tail, without bodyflap. **Vented RCC channel**	2003	**GASP**		**X**							
	RCC only, vented RCC channel	2003	**LAURA**		**X**							
panels 1-7 removed	RCC only, no vertical tail	1997	**FELISA**			**X**					**X**	
			CART3D									**X**

Table 4.3-10 Missing RCC cases, FELISA

Scenario	Configuration Details	geometry pedigree	Flow Solver	STS-2	STS-107 1	STS-107 2	STS-107 3	STS-107 4	STS-107 5	STS-107 6	CF4 Air Tunnel	Mach 6 Air Tunnel
Progressive Damage near RCC Panel 9												
half panel 9	solid walls, with vertical tail, bodyflap	1997	**FELISA**								X	
		1997	**CART3D**									X
	solid walls, without vertical tail, no bodyflap	2003	**GASP**		X							
	vented RCC channel, without vertical tail, no bodyflap	2003	**GASP**		X							
slot behind RCC panel 9	width ~ .5"	1997	**FELISA**								X	
	width ~ 1"	1997	**FELISA**								X	
half panel 9 with RCC cavity, upper carrier panel missing		1997	**FELISA**					X			X	
	vented RCC channel, without vertical tail, no bodyflap	2003	**GASP**		X							
half panel 9 with cavity, upper carrier panel missing, additional leeside material removed		1997	**FELISA**					X			X	
RCC 9 removed	RCC 9 only	1997	**FELISA**		X	X		X			X	
RCC + carrier panels at 9 removed		1997	**FELISA**			X	X	X			X	
RCC 9, upper carrier 9, and additional leeside material removed		1997	**FELISA**			X		X			X	

Table 4.3-11 Progressive Damage at RCC Panel 9, FELISA Cases

Scenario	Configuration Details	geometry pedigree	Flow Solver	STS-2	STS-107 1	STS-107 2	STS-107 3	STS-107 4	STS-107 5	STS-107 6	CF4 Air Tunnel	Mach 6 Air Tunnel
Windward Surface Damage												
wheel well cavity open	d = 6", 15", 30"		**FELISA**								X	
WLE deformation	GEOLAB modification		**FELISA**								X	
scallion dimple (depression created between the 163 and 192 ribs)	L=98", d=2.8"	1997	**FELISA**								X	
	L=98", d=5.4"	1997	**FELISA**								X	
	L=150", d=5.3"	1997	**FELISA**			X	X	X			X	
	L=150", d=5.3", RCC 9 removed	1997	**FELISA**			X	X	X			X	
depression from structural analysis	d = 5.09"	1997	**FELISA**			X	X	X			X	

Table 4.3-12 Windward Surface Damage, FELISA Cases

Figures

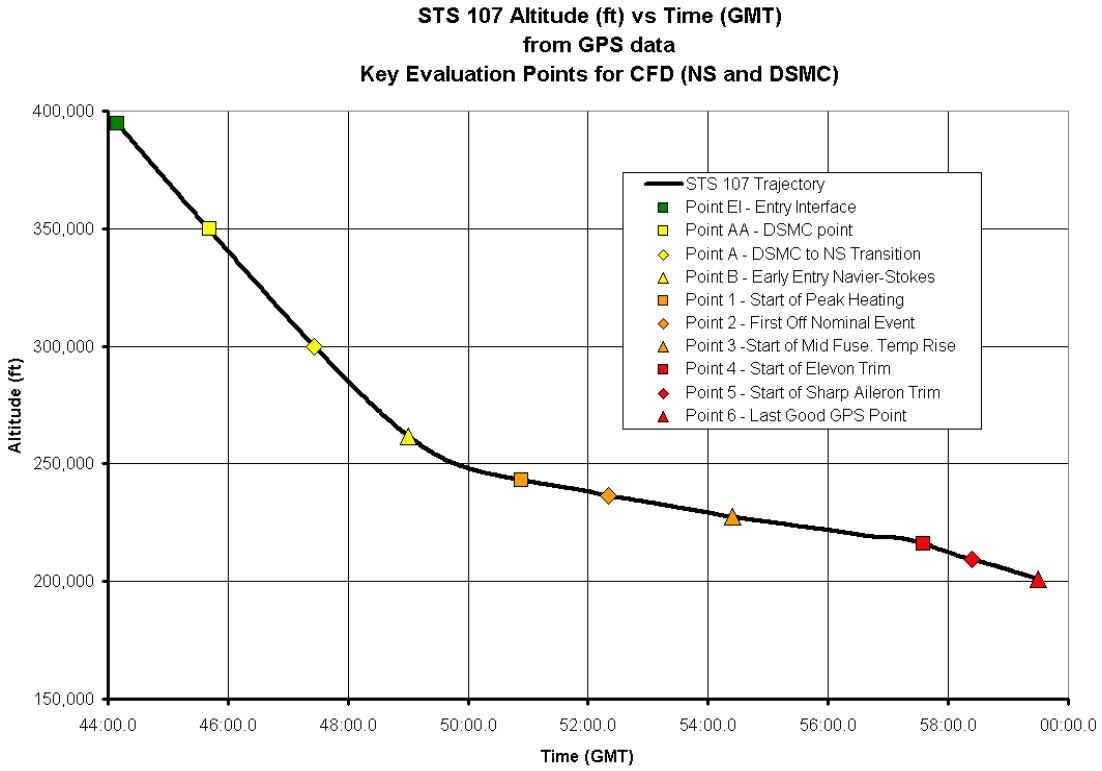

Figure 4.3-26 STS-107 Trajectory (Altitude vs. Time)

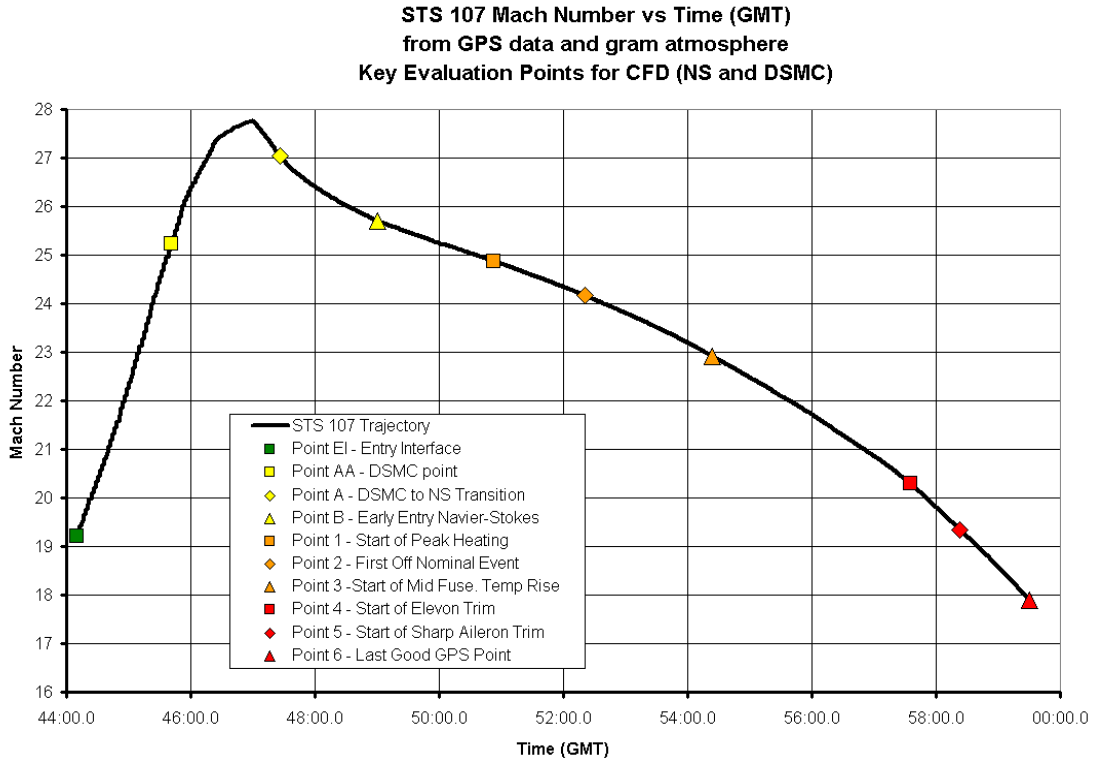

Figure 4.3-27 STS-107 Trajectory (Mach No. vs. Time)

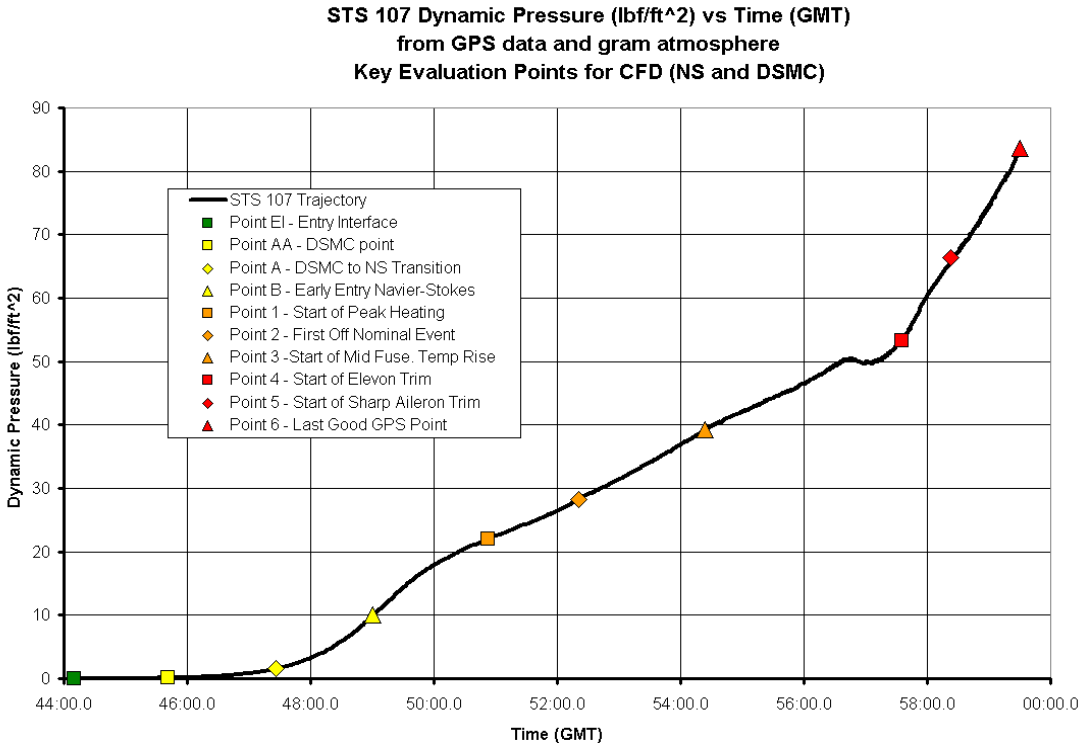

Figure 4.3-28 STS-107 Trajectory (Dynamic Pressure vs. Time)

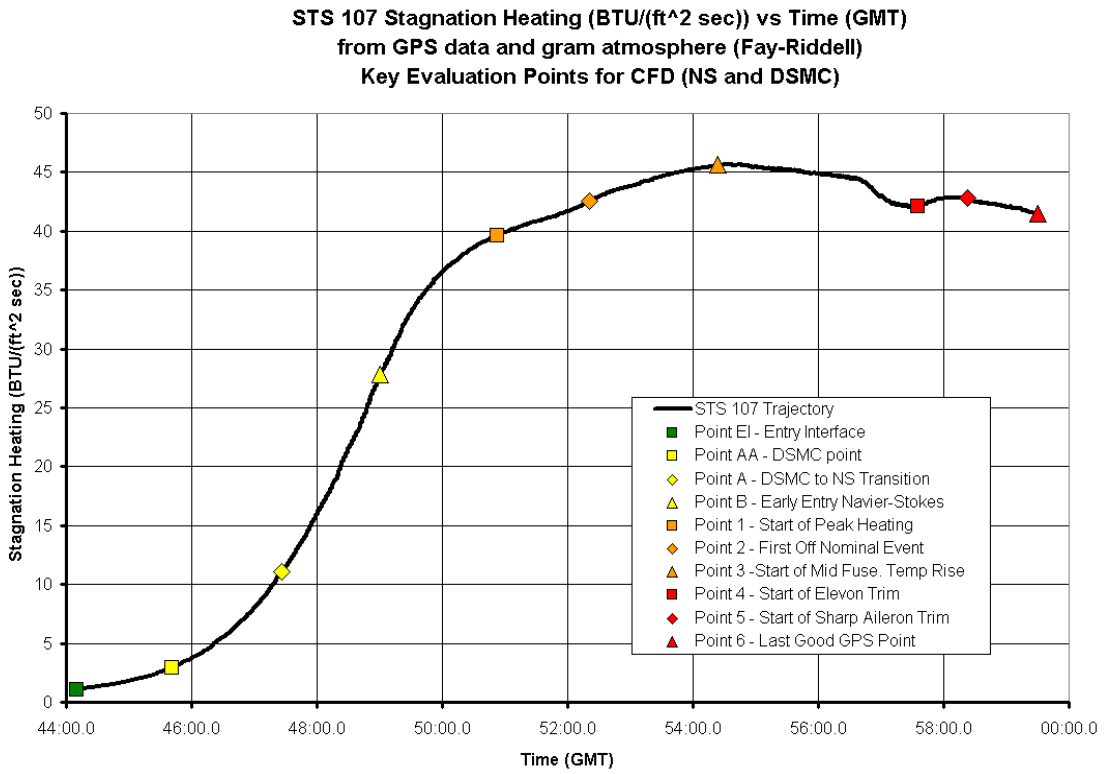

Figure 4.3-29: STS-107 Trajectory (Stagnation Point Heating vs. Time)

Comparison of Inviscid FELISA to Viscous LAURA Solutions and Flight Database

- Aerodynamic Coefficients vs. Time from Entry Interface
  - FELISA - Equilibrium Air
  - LAURA – Finite Rate Chemistry, Thermal Equilibrium
  - Angle of attack varies over flight
- LAURA geometry doesn't include bodyflap, FELISA loads reduced with and without bodyflap.
- FELISA has elevon gaps, LAURA does not.

FELISA vs. LAURA
(no bodyflap)

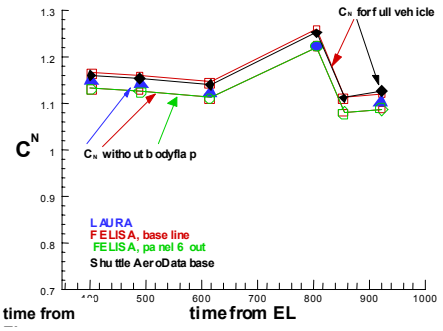

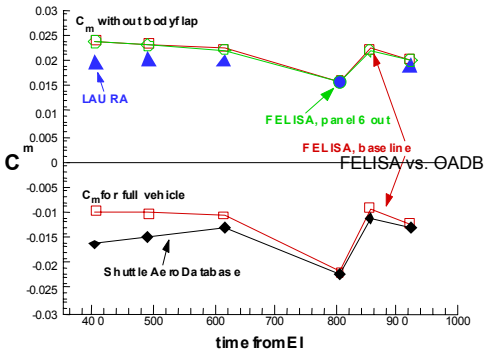

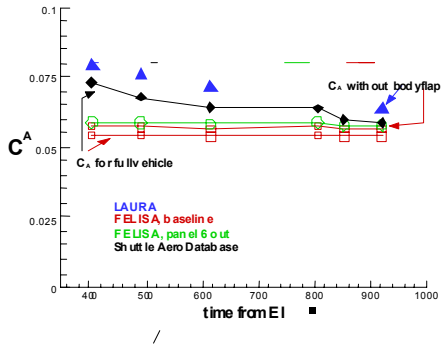

Figure 4.3-30 Baseline Aerodynamic Comparisons (Orbiter OADB vs. CFD Prediction)

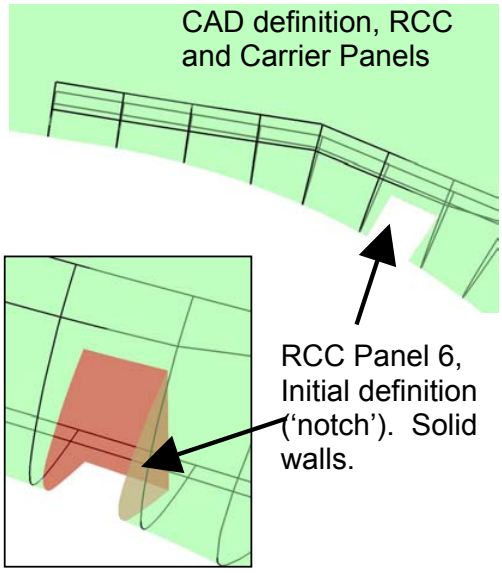

Figure 4.3-31 RCC Panel 6, Initial Definition

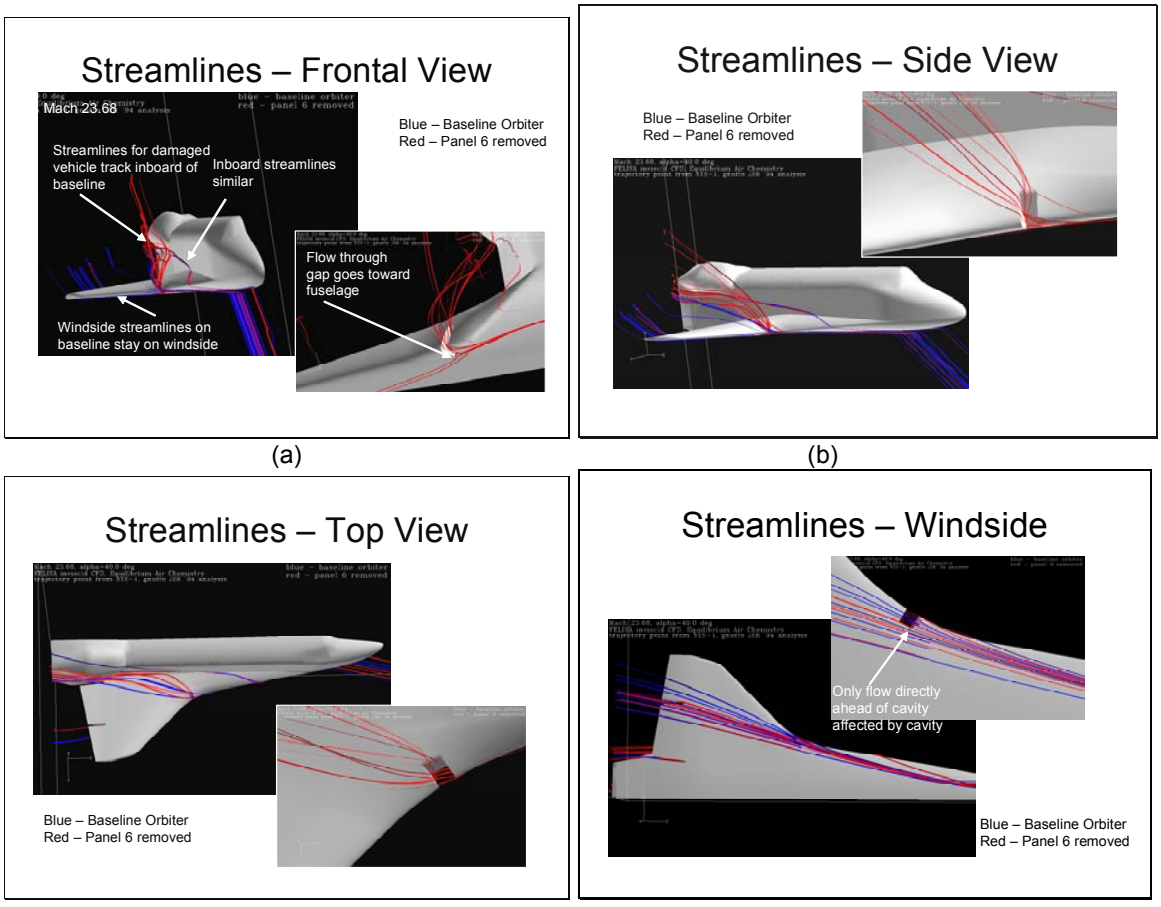

Figure 4.3-32 Nominal & Missing RCC Panel 6, Streamlines

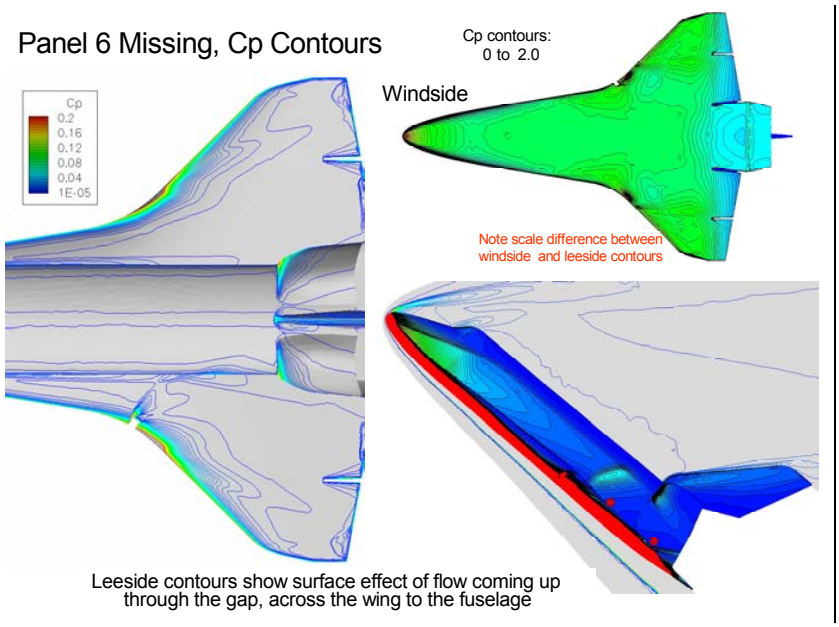

Figure 4.3-33 Panel 6 Missing – Surface Pressure Distribution

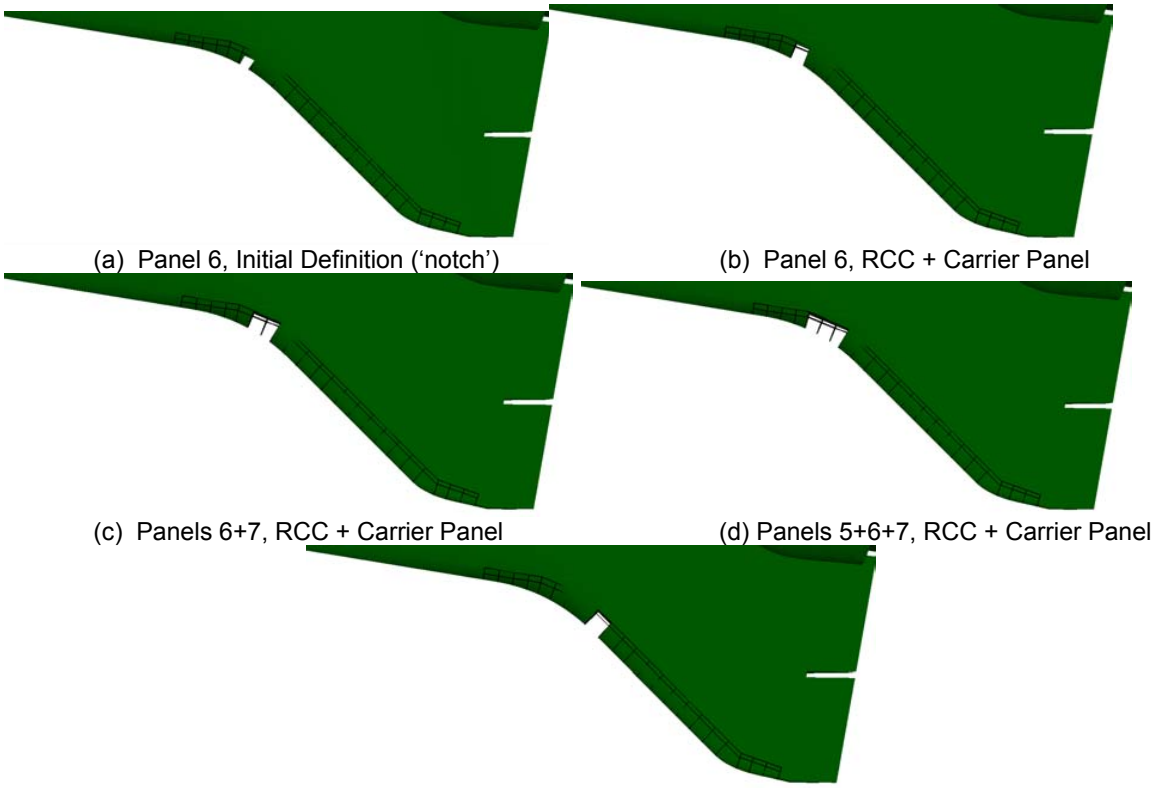

(a) Panel 6, Initial Definition ('notch')

(b) Panel 6, RCC + Carrier Panel

(c) Panels 6+7, RCC + Carrier Panel

(d) Panels 5+6+7, RCC + Carrier Panel

(e) Panel 9, RCC + Carrier Panel

Figure 4.3-34 Missing RCC Panel Geometries, FELISA

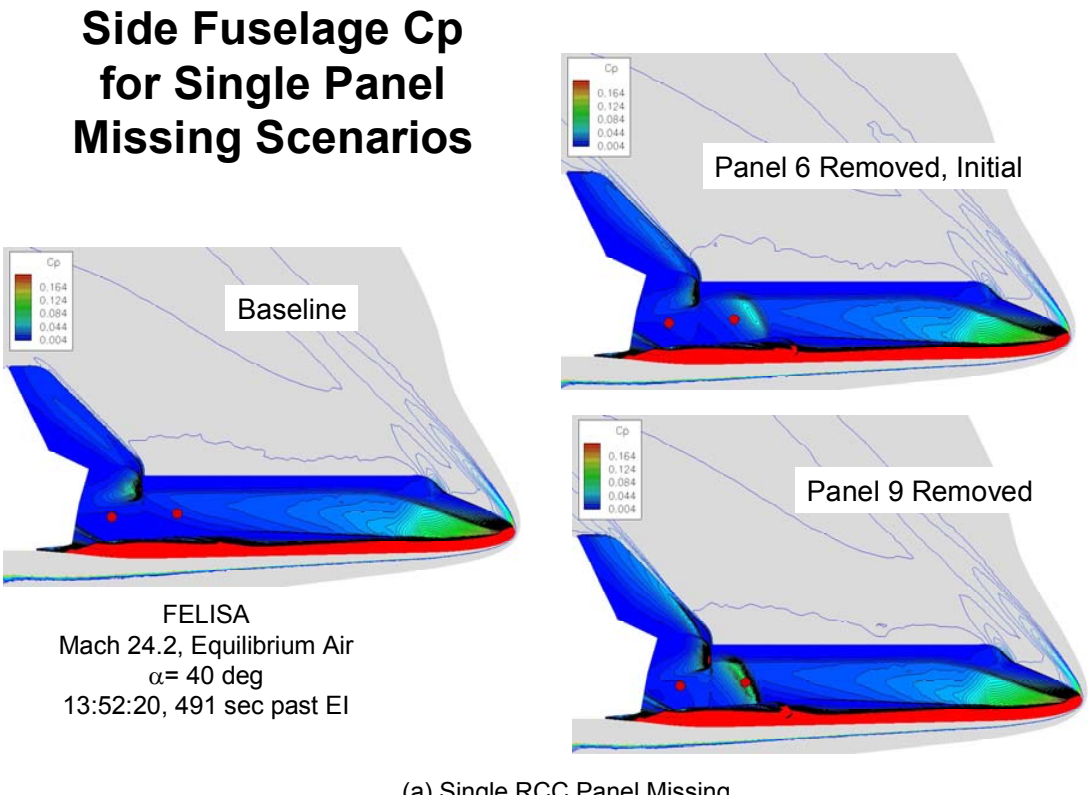

(a) Single RCC Panel Missing

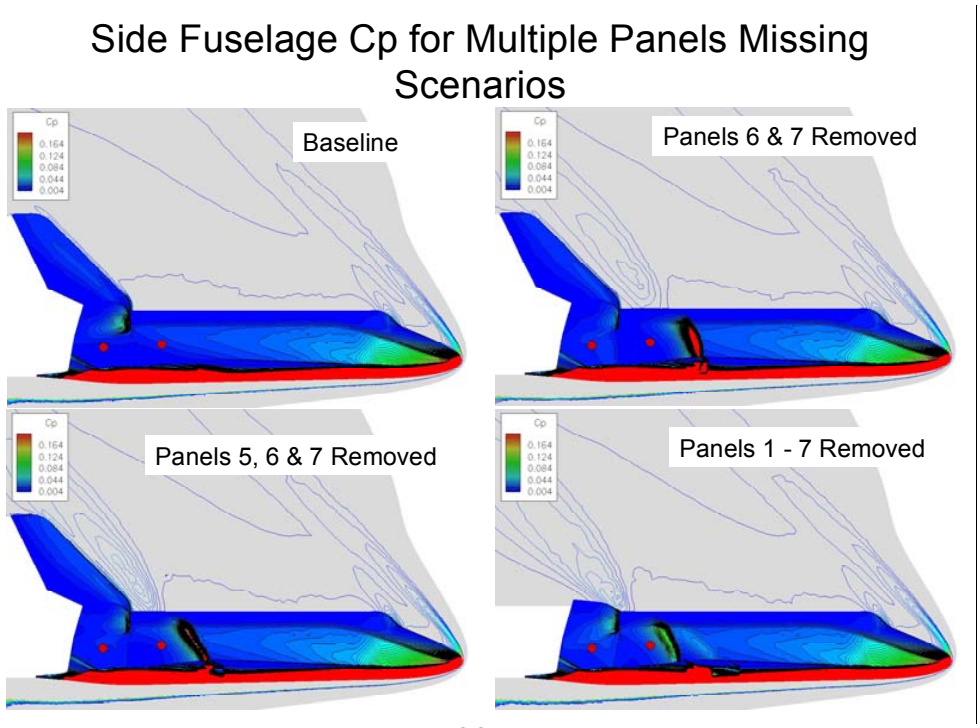

(b) Multiple RCC Panels Missing

Figure 4.3-35 Missing Panels, FELISA Cp Contours, side view

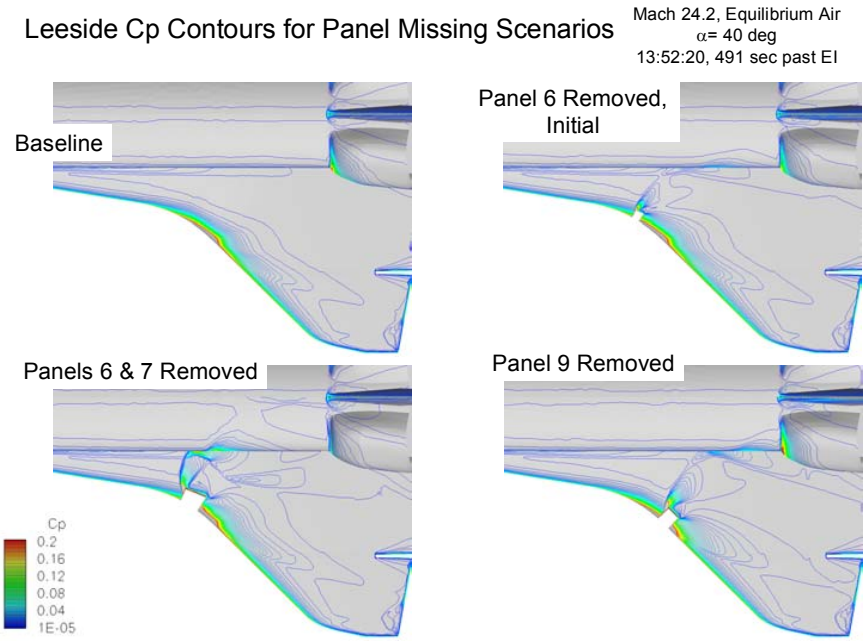

Figure 4.3-36 Missing Panels, FELISA Cp Contours, Leeside View

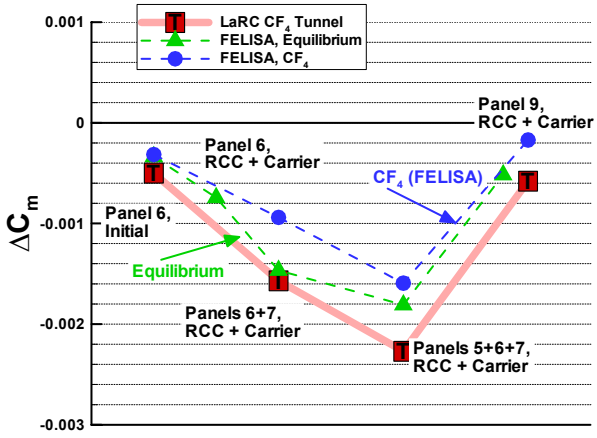

(a) Delta Pitching Moment

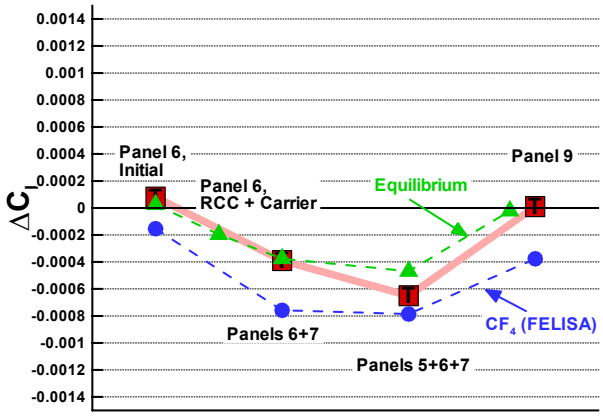

(b) Delta Rolling Moment

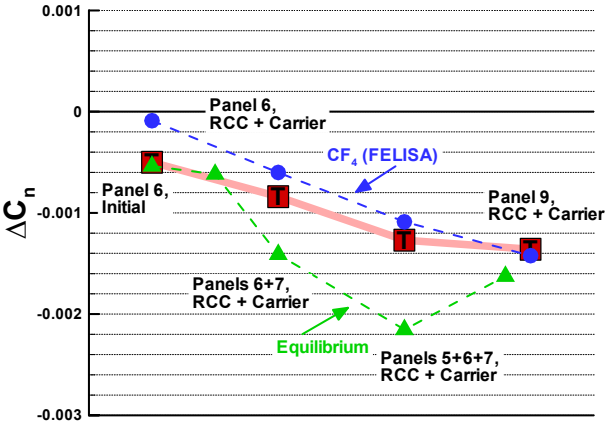

(c) Delta Yawing Moment

Figure 4.3-37 Missing Panel Delta Aero, FELISA and CF4 Tunnel

64

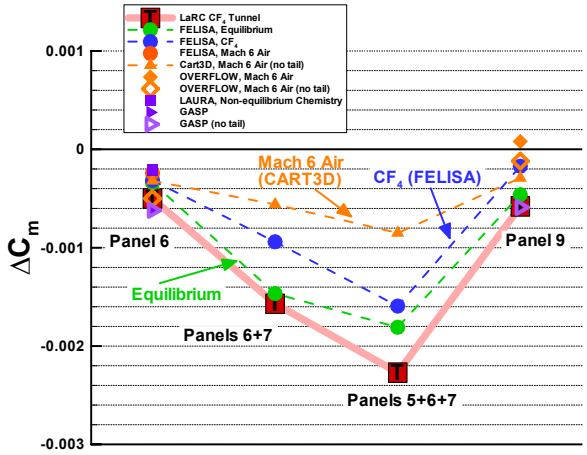

(a) Delta Pitching Moment

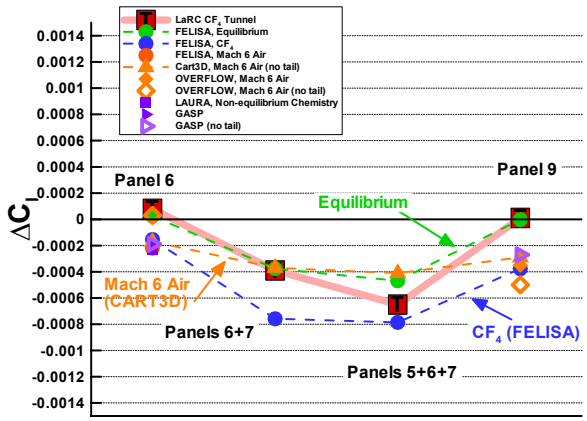

(b) Delta Rolling Moment

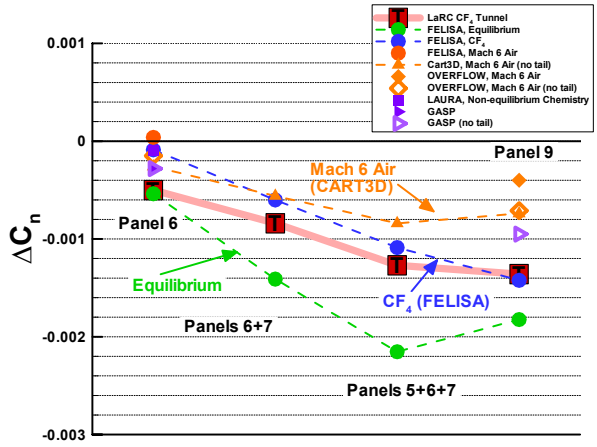

(c) Delta Yawing Moment

Figure 4.3-38 Missing Panel Delta Aero, All Computations and CF4 Tunnel

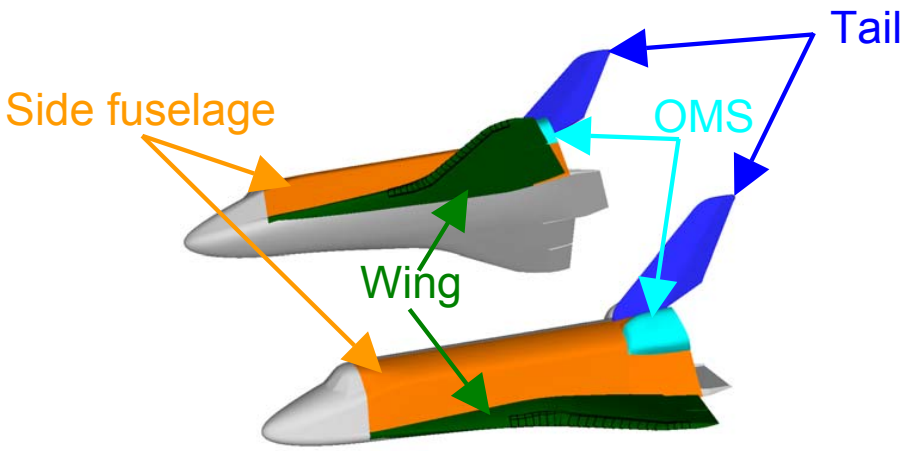

Figure 4.3-39 Orbiter Delta Aerodynamic Component Definition

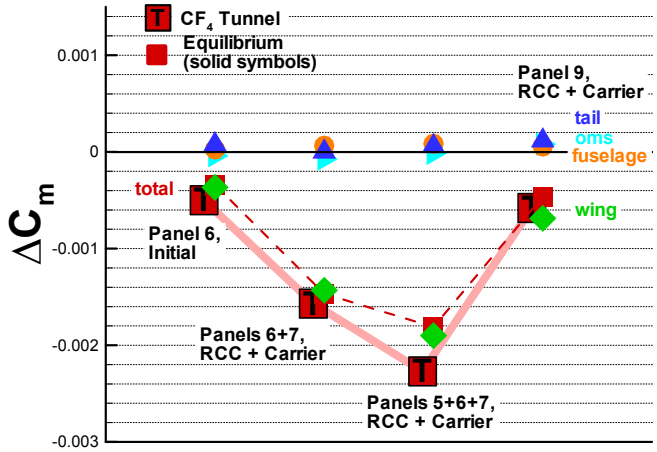

(a) Delta Pitching Moment

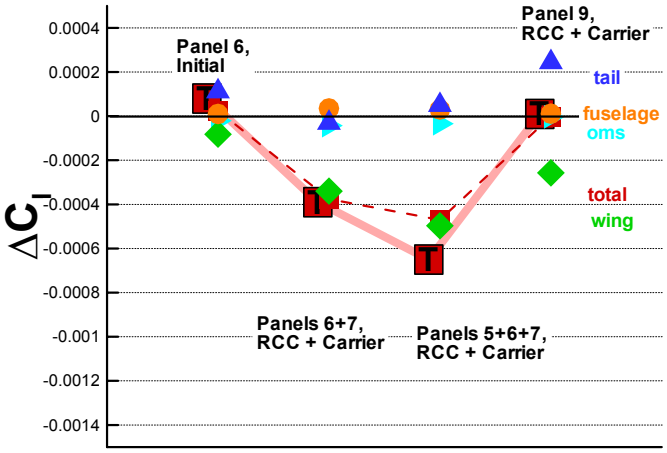

(b) Delta Rolling Moment

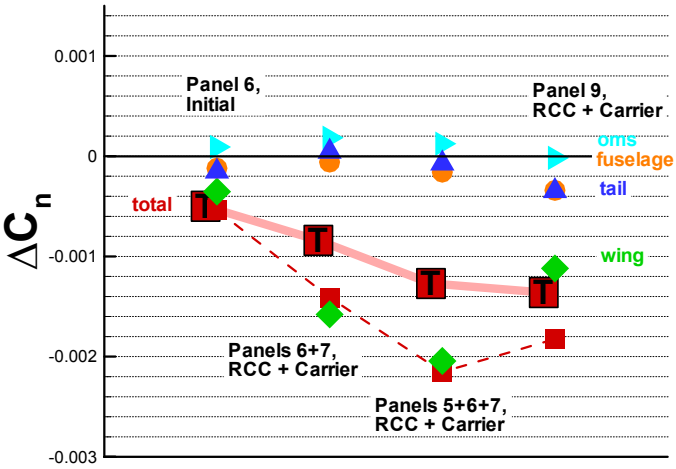

(c) Delta Yawing Moment

Figure 4.3-40 Missing Panel Delta Aero Component Breakdown(Flight Condition 2)

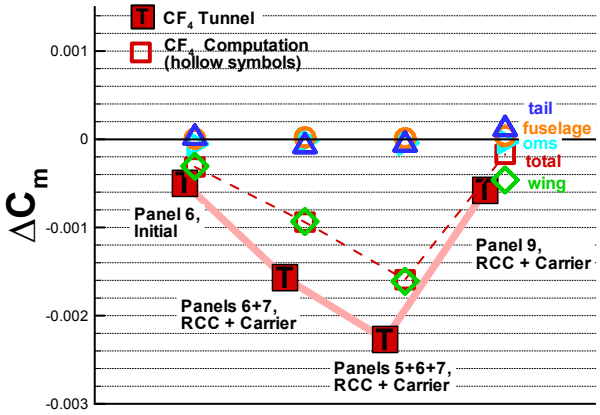

(a) Delta Pitching Moment

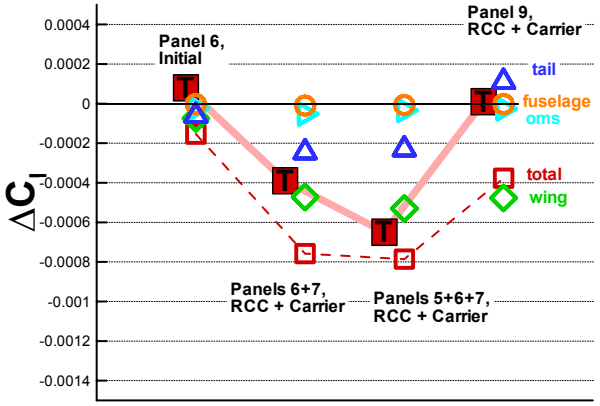

(b) Delta Rolling Moment

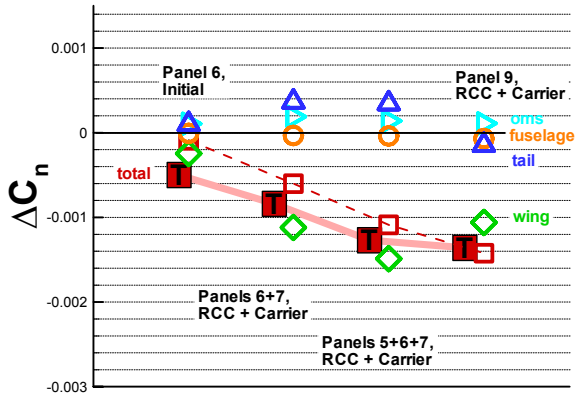

(c) Delta Yawing Moment

Figure 4.3-41 Missing Panel Delta Aero Component Breakdown (CF4 WT Condition)

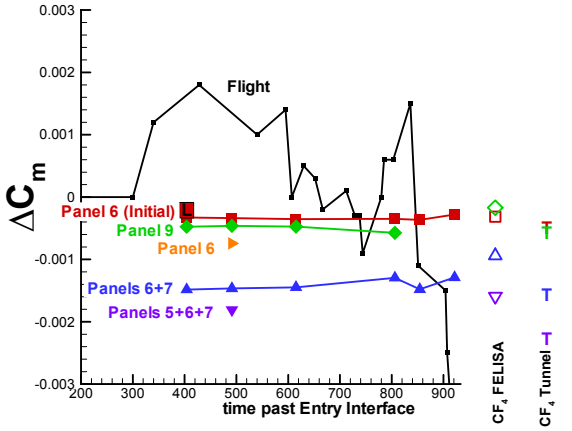

(a) Delta Pitching Moment

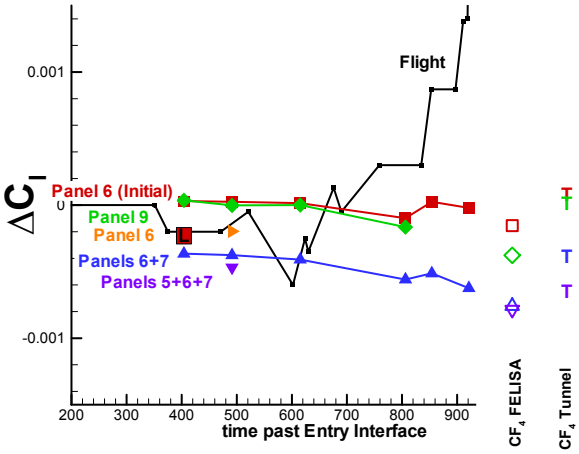

(b) Delta Rolling Moment

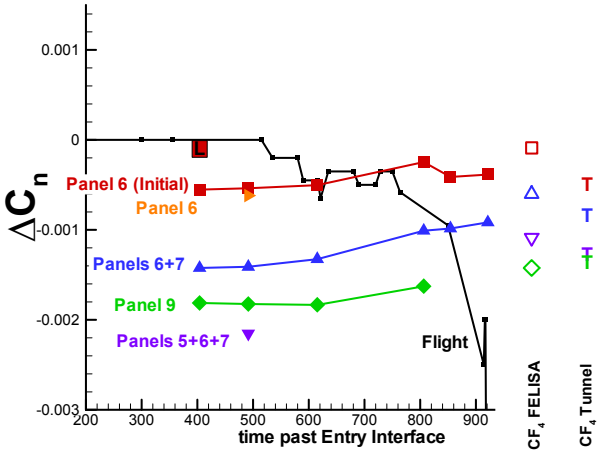

(c) Delta Yawing Moment

Figure 4.3-42 Missing Panel Delta Aero, Across Trajectory

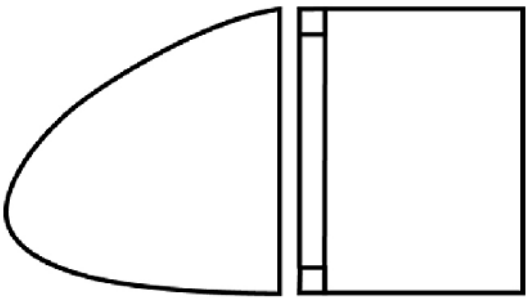

(a) Partial Panel 9 Damage, Slot

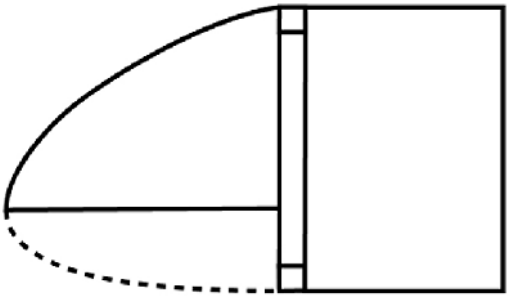

(b) Partial Panel 9 Damage, Half-Panel 9

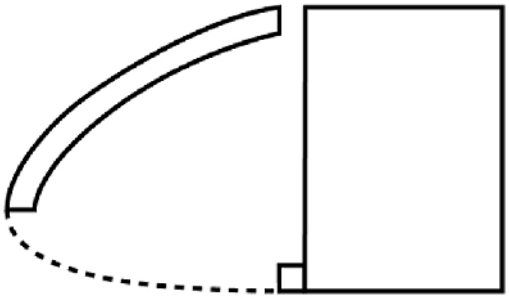

(c) Half Panel 9 with Cavity and Upper Carrier Panel 9 Removed

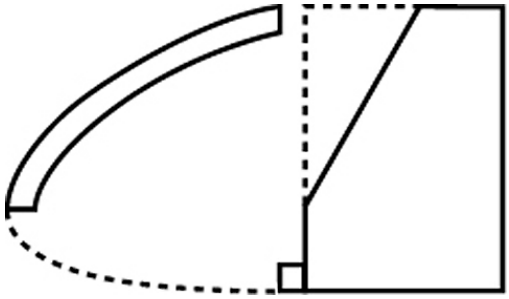

(d) Half Panel 9 with Cavity, Upper Carrier Panel 9, and Leeside Material removed

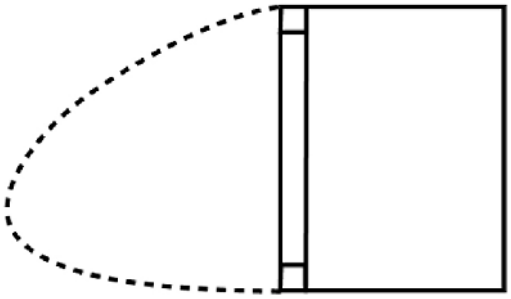

(e) RCC 9 Removed

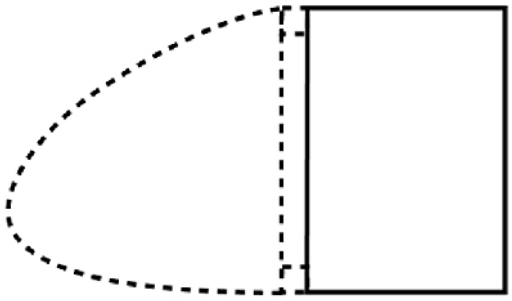

(f) Panel 9 Removed, RCC + Carrier Panel

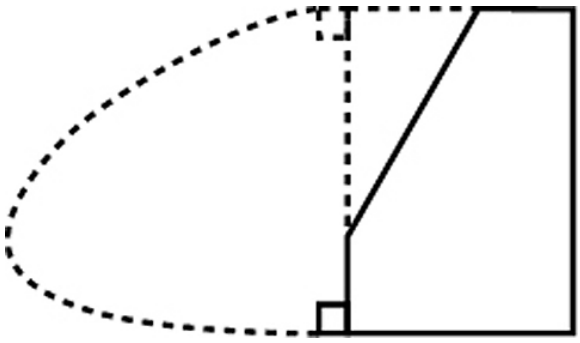

(g) RCC Panel 9, Upper Carrier Panel 9, and Leeside Material Removed

Figure 4.3-43 RCC Panel 9 Progressive Damage Configurations

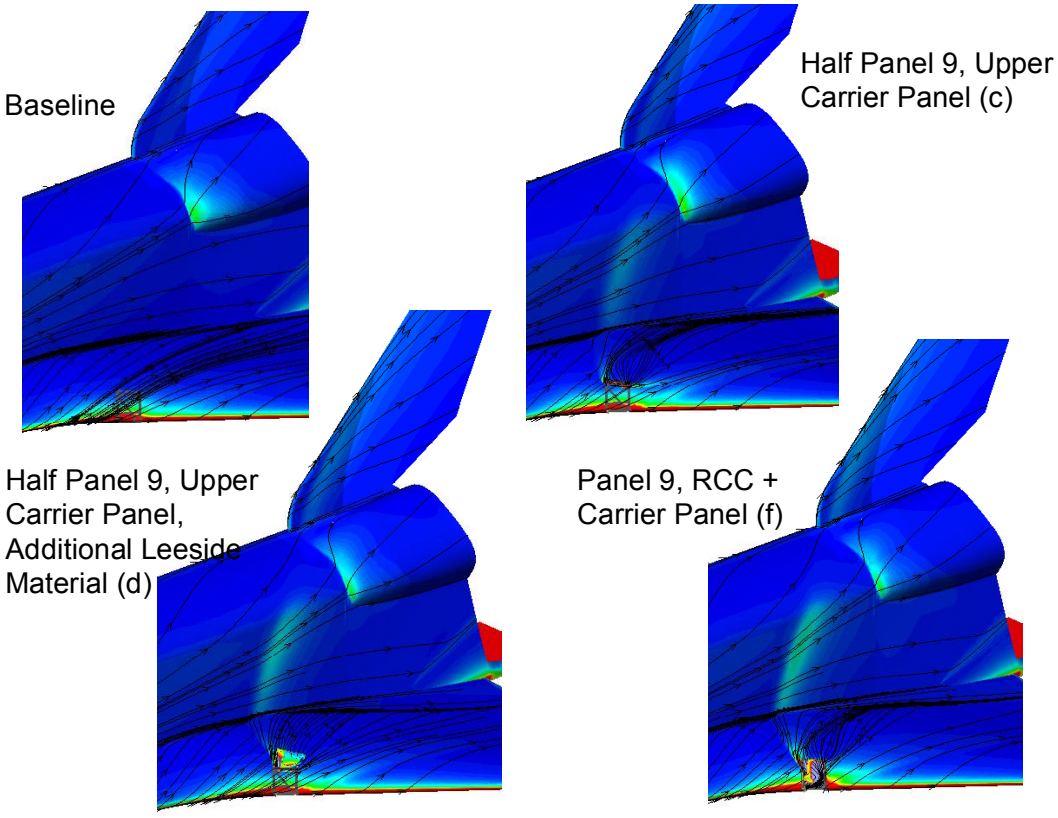

Figure 4.3-44: Leeside Flow field for Selected Panel 9 Progressive Damage Configurations

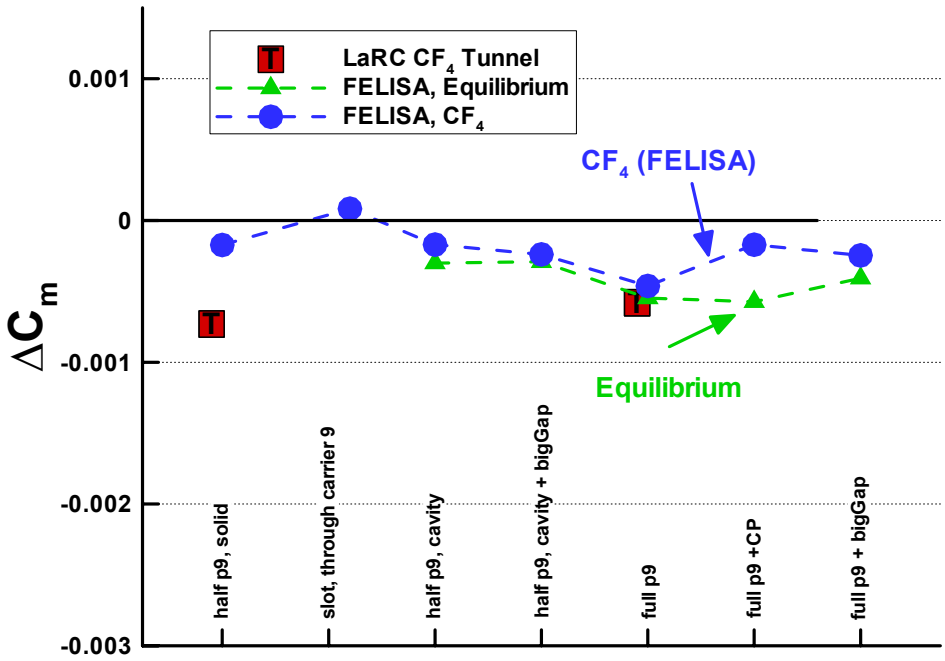

(a) Delta Pitching Moment

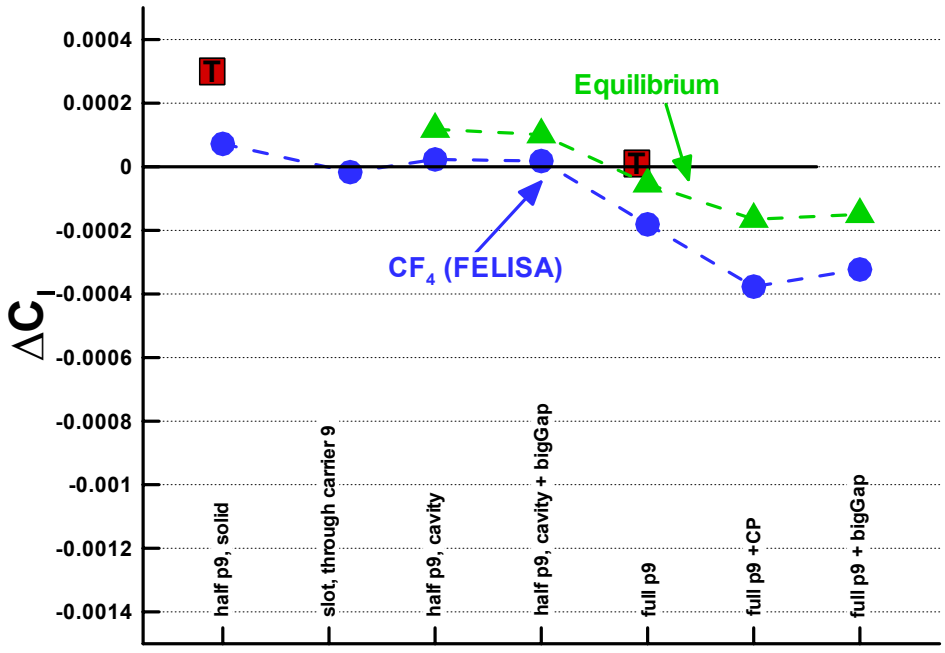

(b) Delta Rolling Moment

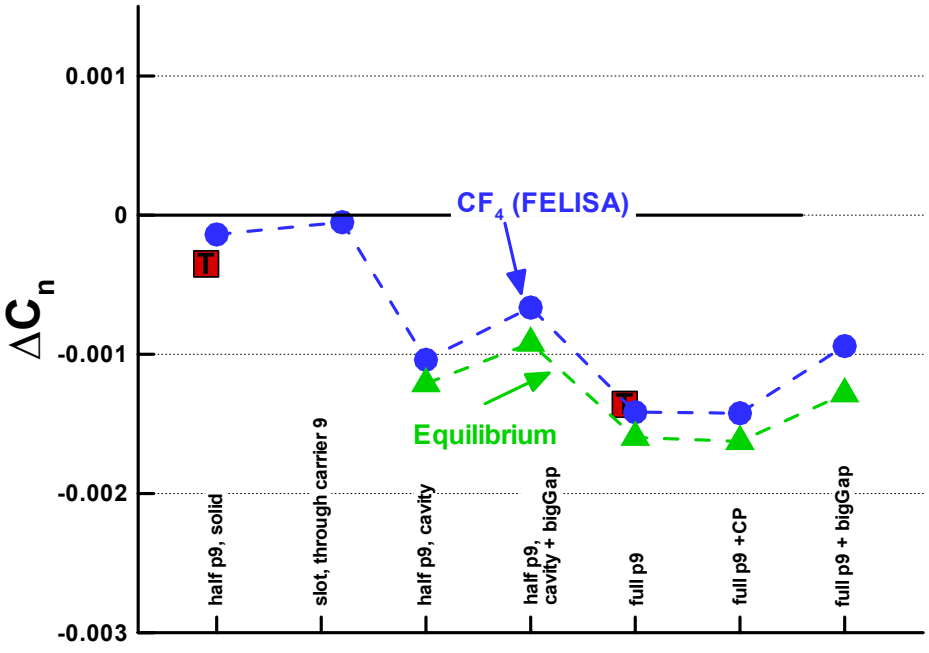

(c) Delta Yawing Moment

Figure 4.3-45 Partial Panel 9 Damage Progression, Delta Aero

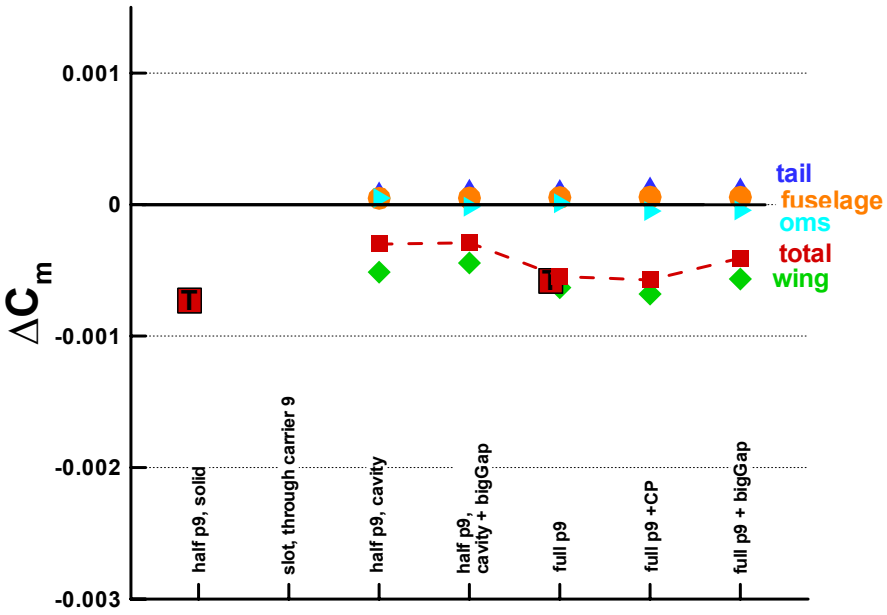

(a) Delta Pitching Moment

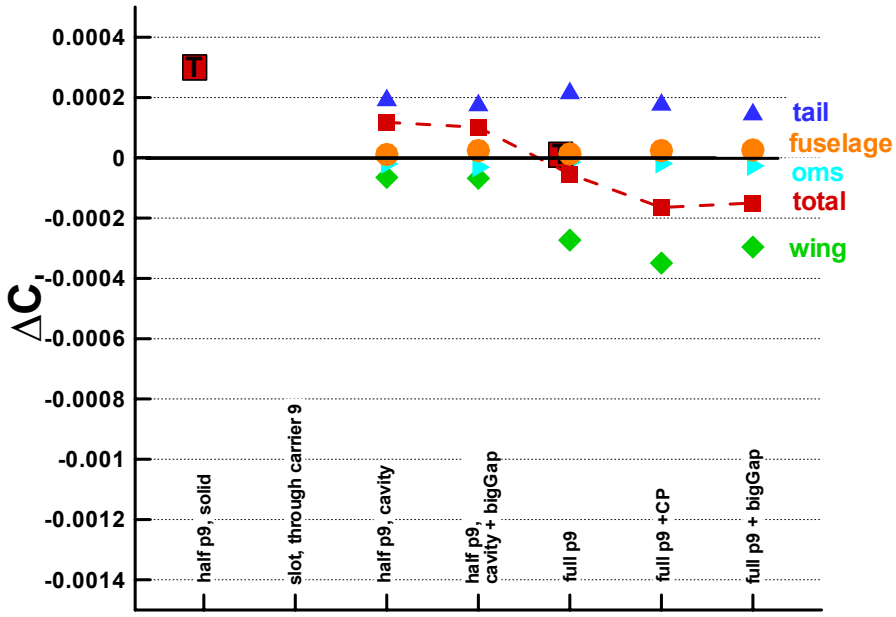

(b) Delta Rolling Moment

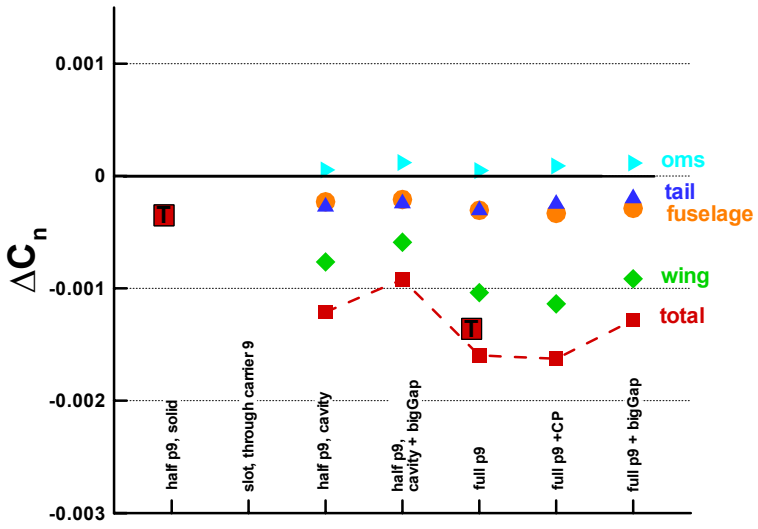

(c) Delta Yawing Moment

Figure 4.3-46 Partial Missing Panel 9 Delta Aero Component Breakdown(Flight Condition 2)

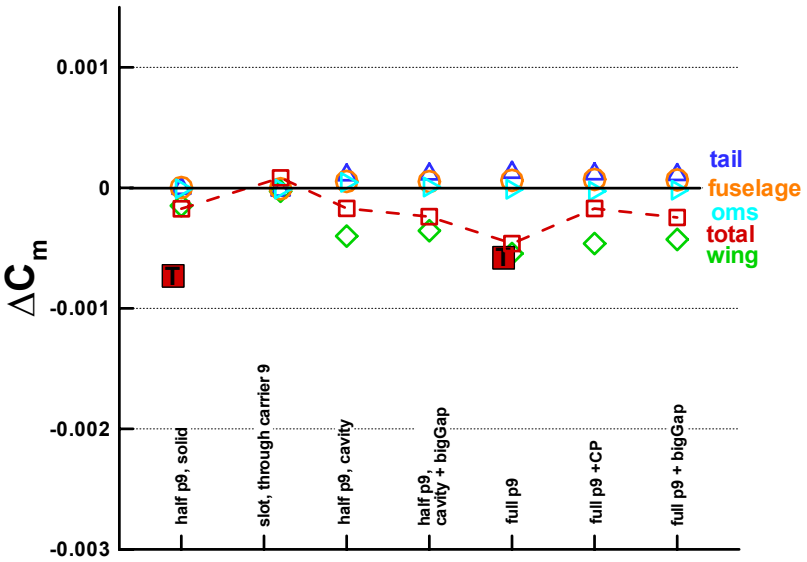

(a) Delta Pitching Moment

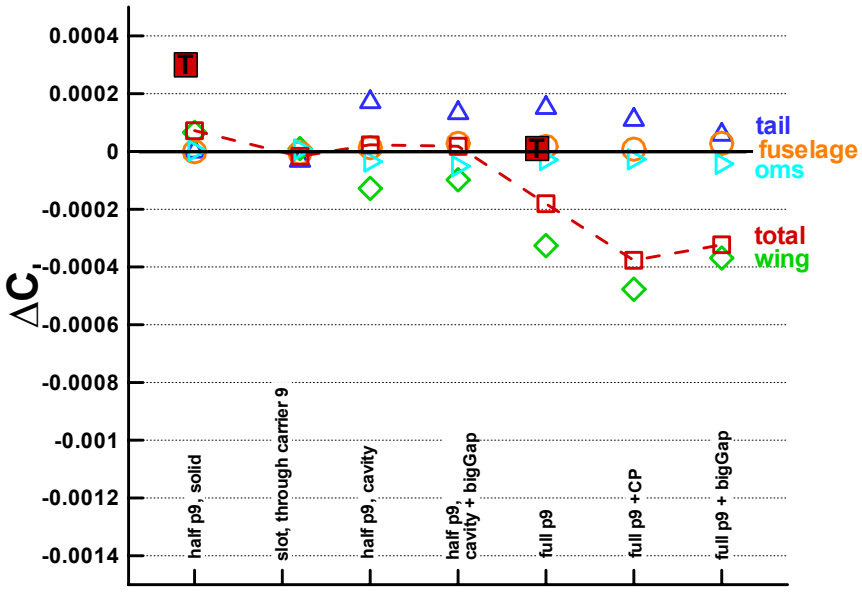

(b) Delta Rolling Moment

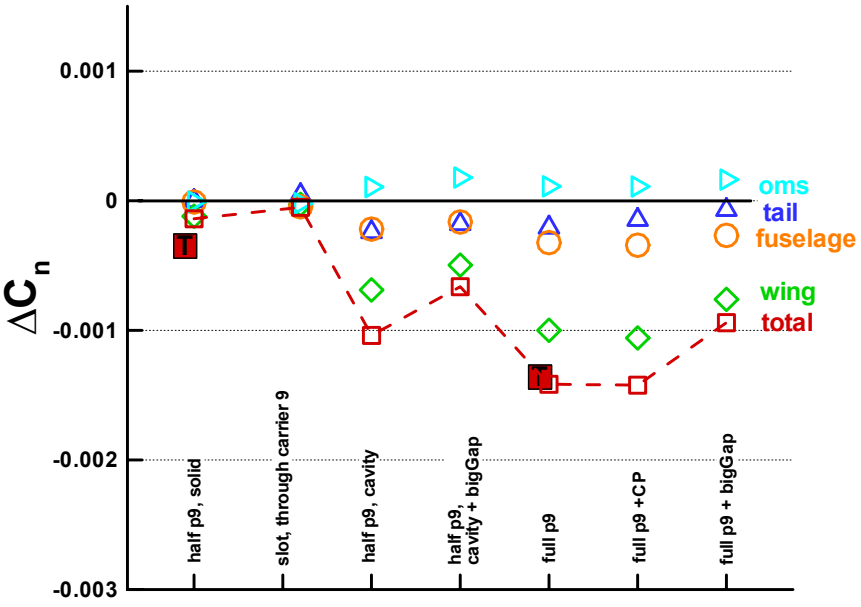

(c) Delta Yawing Moment

Figure 4.3-47 Partial Missing Panel 9 Delta Aero Component Breakdown(CF4 WT Condition)

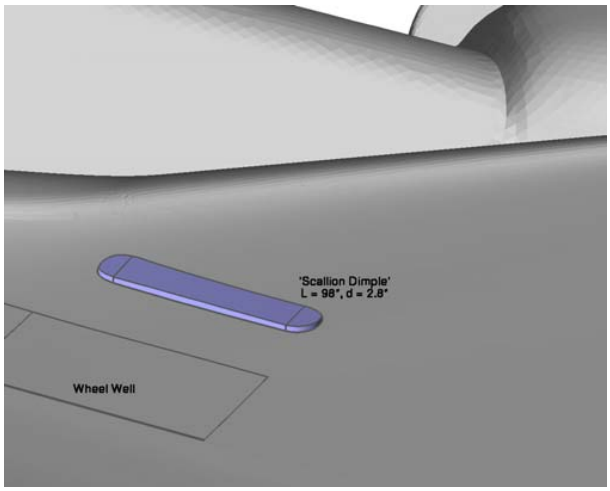

(a) Intermediate Length Windward Surface Depression

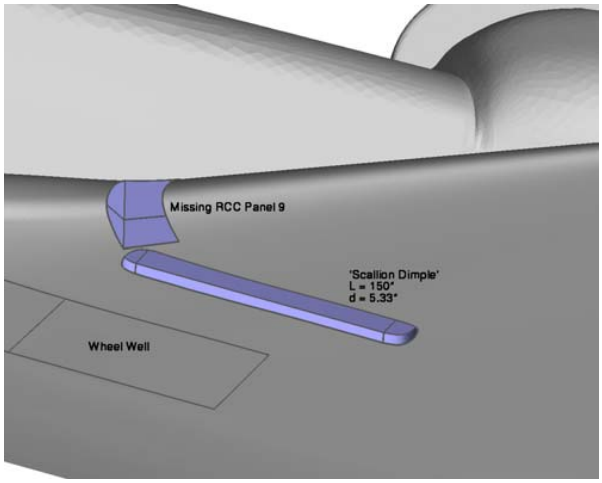

(b) Long Windward Surface Depression with RCC Panel 9 Removed

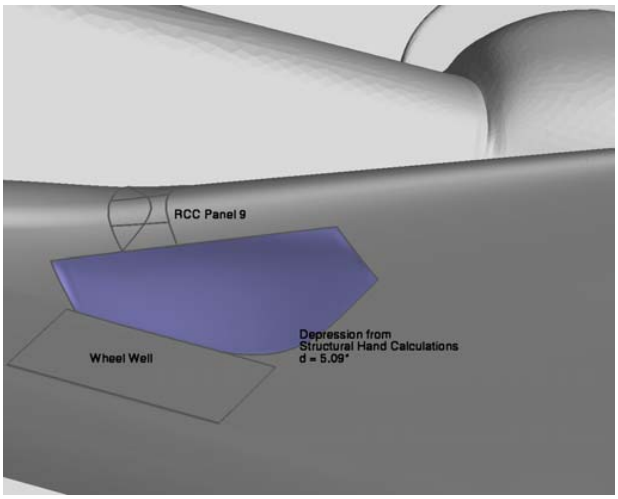

(c) Depression from Structural Calculations, d = 5.03”

Figure 4.3-48: Windward Surface Damage Configurations

Wing Leading Edge Deformation

- Geometry Assumptions:
  - spar compromised at panel 8-9
  - RCC will twist upwards and toward back
  - Deformation allowed in red and black regions
- Aero Effect:
  - Increased angle of attack in panel 7-10 region

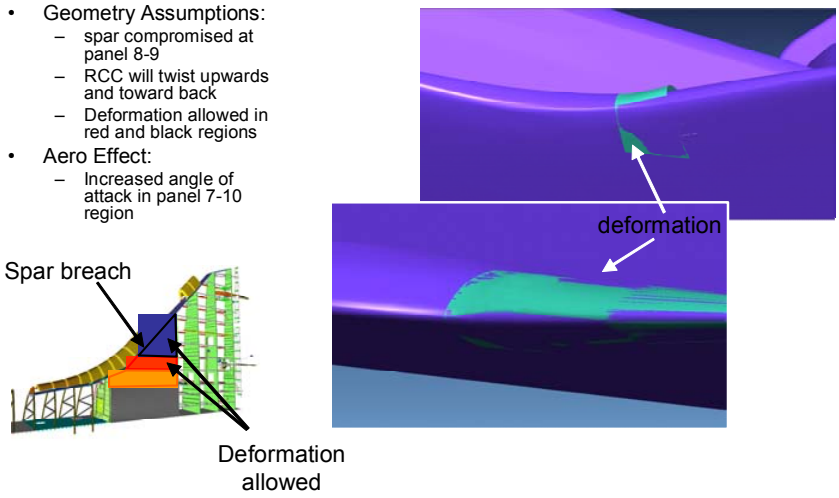

Figure 4.3-49 Geometry for Wing Leading Edge Deformation

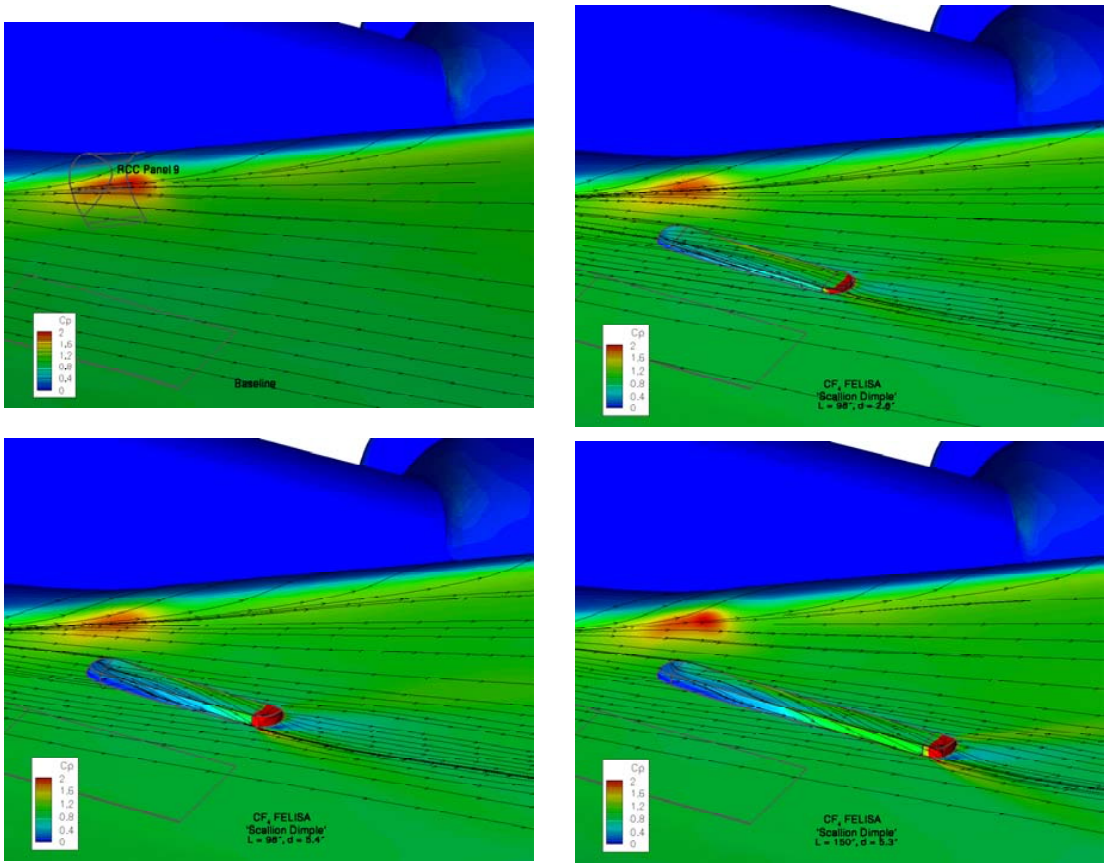

Figure 4.3-50: Pressure Contours and Streamlines - Windward Surface Depressions (CF4 WT Condition)

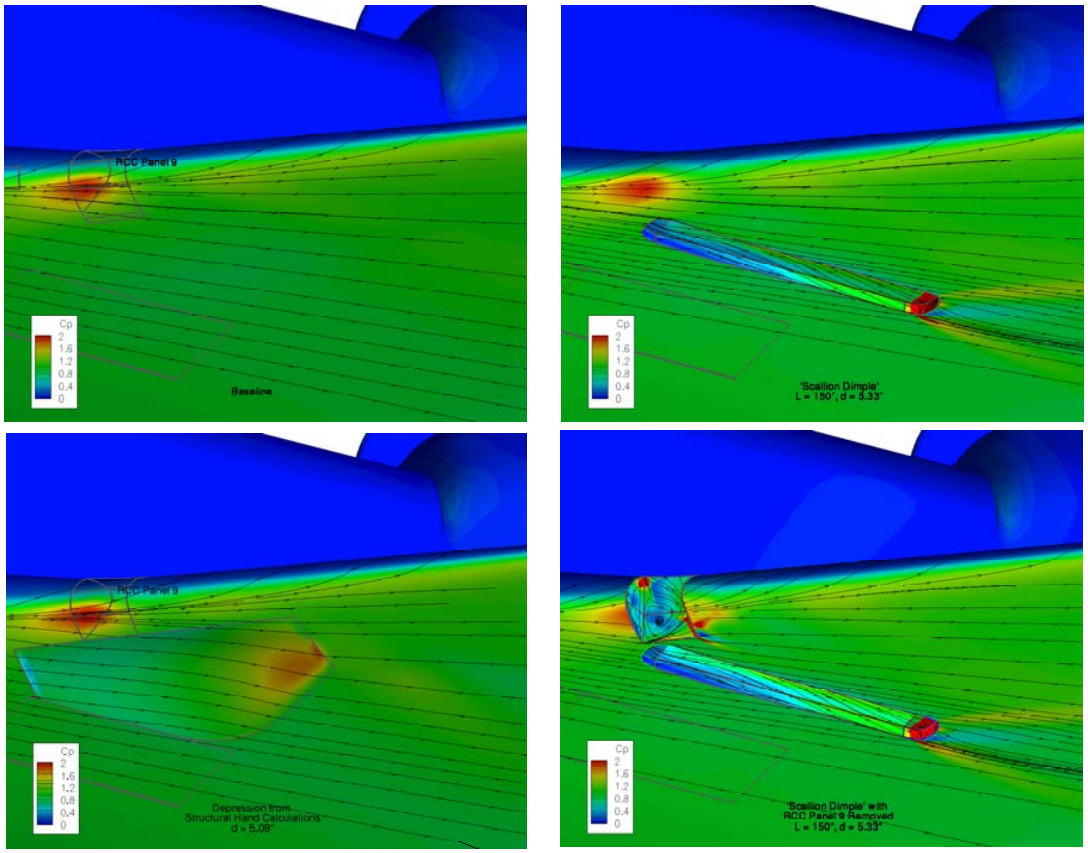

Figure 4.3-51: Pressure Contours and Streamlines - Windward Damage Configurations (Flight CFD Condition 4)

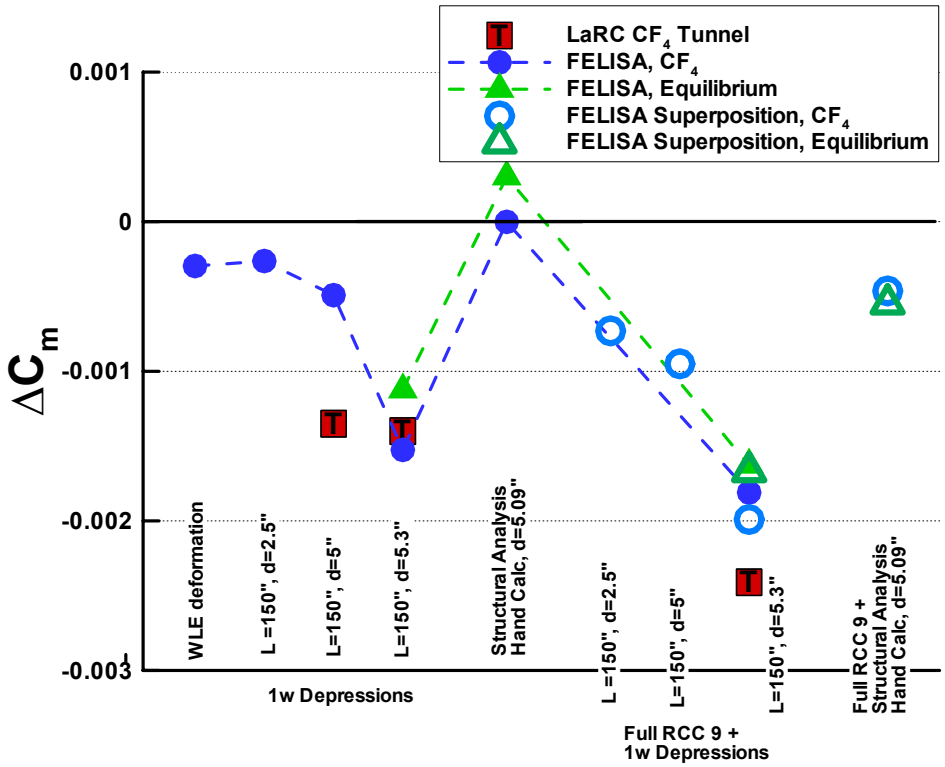

(a) Delta Pitching Moment

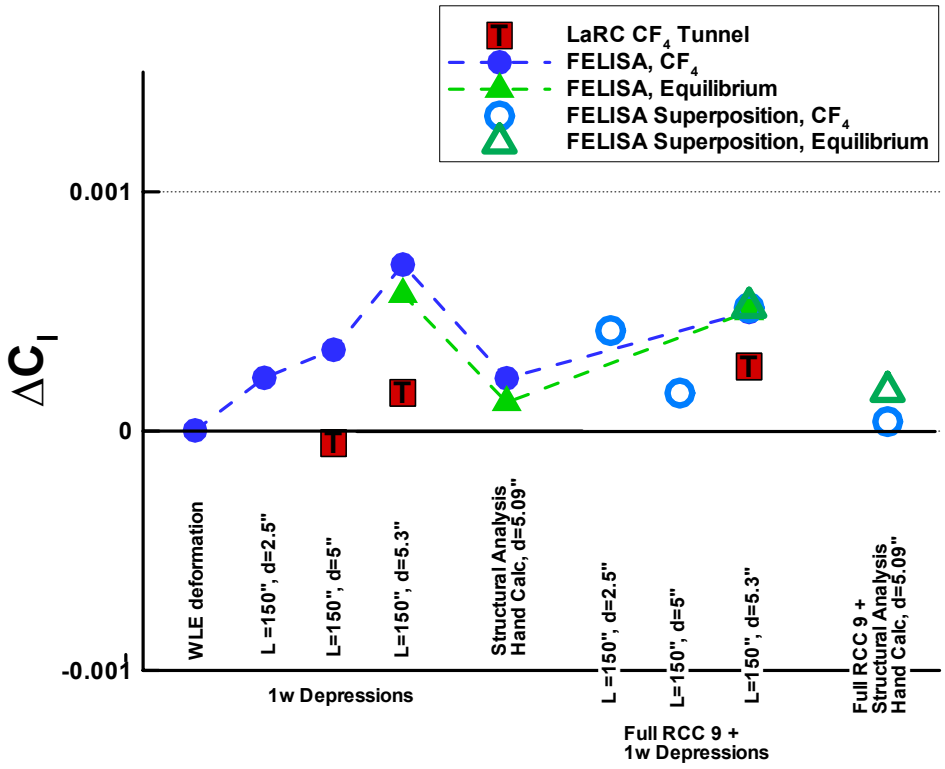

(b) Delta Rolling Moment

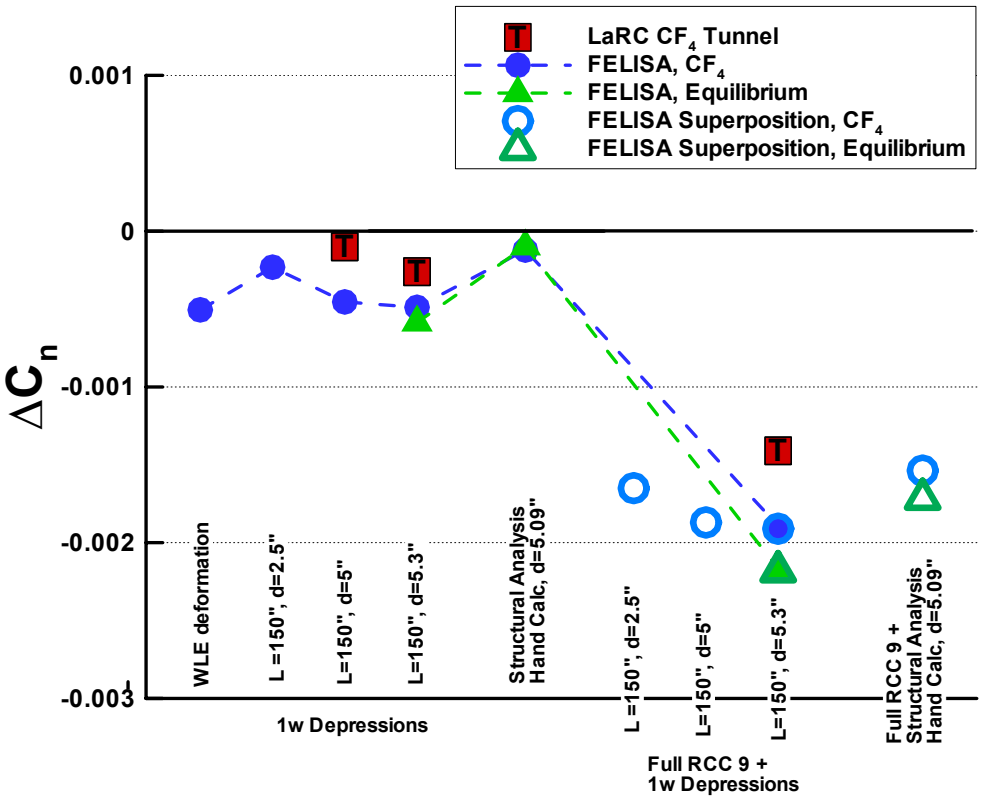

(c) Delta Yawing Moment

Figure 4.3-52 Windward Structural Damage, Delta Aerodynamic Moments

4.4 Application of Data to the Working Scenario

4.4.1 Correlation of CFD & WTT – Results by Timeline Section

The ultimate goal of the STS-107 aerodynamic reconstruction was to correlate the CFD analysis and WT test damage assessment results to the extracted flight delta aerodynamics from an initial damage stage at EI through a damage propagation that is consistent with the final working scenario. To develop a postulated damage progression the timeline was divided into four periods. Each timeline period represents a particular damaged configuration stage along the progression. The test and analysis results of a representative damaged configuration are then compared with the extracted aero increments for each timeline period. When providing a match, these comparisons lead to a postulated damage progression. Consistency with the working scenario is achieved by correlating to other available sources of data, timeline events, aerothermal, thermal, stress test and analysis results, OEX data signatures, recovered hardware forensics, etc. The resulting damage progression and data correlations are explained in this section.

4.4.1.1 Initial Timeline Section – No Observable Aerodynamic Increments

As stated in Section 4.3, off-nominal aerodynamics were not apparent during the initial portion of Columbia's STS-107 entry flight profile. This initial timeline period starts at EI (GMT 13:44:09) and extends to EI + 515 sec (GMT 13:52:44) corresponding to flight conditions which range from Mach 28 down to 24.4, with dynamic pressure increasing from 0 to 25 psf while descending through altitudes from 400,000 to 235,000 ft. The official timeline (and working scenario) identifies several major events during this period of flight (see Figure 4.4-20).

The initial portion of this time frame EI to EI + 330 sec / GMT 13:44:09 -13:49:39 suggests a breach or hole in a WLE RCC panel (5-9) existing at EI. This conclusion is supported by instrumentation near RCC Panel 9 responding to an apparent WLE internal flow thermal event. No identifiable aerodynamic increments are observed during this time frame. This is followed by a period from EI + 330 to 460 sec / GMT 13:49:39 -13:51:49 in which the initial indication of a leeside flow disturbance becomes apparent. This leeside disturbance is identified via left hand side OMS pod and fuselage surface temperature measurements indicating substantially reduced heating levels (below those seen on previous Columbia flights). Again no identifiable aerodynamic increments are observed in this time frame. Based on analysis and internal wing measurements the wing leading edge spar is breached sometime in the period covering EI + 460 to 515 sec / GMT 13:51:49 -13:52:44. This corresponds to the timeframe where all measurements along WLE Spar along with numerous others within left wing fail. Still, no identifiable aerodynamic increment is observed.

It is apparent from the data that during this initial (515 sec) atmospheric flight period the orbiters left wing is damaged to the extent that internal and external thermal events are occurring, without any clear indication of off-nominal aerodynamics. Several results from the investigation's test and analysis of probable initial damage support this observation.

An analysis, to define internal heating to the WLE spar, was completed for a circular hole in RCC panel 6 using the LaRC Navier-Stokes LAURA code. Hole sizes of 2, 4 and 6 inch diameter were analyzed at STS-107 flight condition 1 (Mach 24.7, AOA =40.2, h=243,000 ft). As shown in Figure 4.4-1, there is little if any change (even locally) to the computed external surface temperature distribution. As expected the aerodynamic normal and axial force increments extracted for this case are negligible (less than 0.3% of the total). In the wind tunnel this level of damage and its potential disruption of the flow field was evaluated by placing boundary layer trips along the wing leading edge. In Figure 4.4-2, the measured surface heating distribution shows that a relatively small area of the lower wing surface is affected for a single trip located at RCC panel 6. It should be noted that on STS-107 starting around EI + 370 sec, an external surface thermocouple, (V07T9666A) downstream of RCC panel 9 indicates a small increase in heating, similar to what this type of lower

surface heating augmentation could produce (see Aerothermodynamics Section 5.2.1.2). However, the associated aerodynamic moment increments measured for this test run are very small (essentially zero) and are listed in Table 4.4-1.

The reduced levels of heating on the fuselage and OMS Pod require some interaction of the higher energy windward flow with the relatively low energy leeside flow. While this interaction produces the change in heating during this time period, there is no associated change in aerodynamics. The source of the reduced heating has been attributed to flow exiting the WLE cavity through design vent locations along the wing upper surface at the RCC / carrier panel interface (see Aerothermodynamics Section 5.2.3.5). Several wind tunnel runs with either a single or multiple holes through (windward to leeward) the wing at these venting locations were conducted early in the investigation to identify any potential aerodynamic effects. In Figure 4.4-3, the measured surface heating distribution shows a fairly widespread disturbance over the lower wing surface due to the presence of these holes. However, the associated aerodynamic moment increments measured in these runs are also very small (essentially zero) and are listed in Table 4.4-1. (Note subsequent testing to better characterize the venting as the source of the reduced heating has been successful – however these dedicated aerothermal tests did not include simultaneous aerodynamic force and moment measurements – see Aerothermodynamics Section 5.2.3.4.). Given the suspected initial breach in the lower surface of an RCC panel, progression to a missing partial panel damaged configuration is plausible. Wind tunnel testing (section 4.3.1.6.3) and CFD analysis (section 4.3.2.3.3) results indicate little or no aerodynamic increments for this type of damage. Additionally the observed orbiter data (loss of measurements) suggests the onset of internal wing damage occurring during this time period. This is consistent with growing upper surface damage and increased venting or flow through an upper carrier panel, via the WLE breach yielding the observed aerothermodynamic response but still producing little or no aerodynamic change.

4.4.1.2 Timeline Section Two – Initial Onset of Aerodynamic Increments

The first clear indication of off-nominal aerodynamics has been identified at EI + 515 sec (GMT 13:52:44). This second timeline period extends from that point to EI + 602 sec (GMT 13:54:11) and corresponds to flight conditions ranging from Mach 24.4 down to 23.2, with dynamic pressure continuing to increase from 25 to 37 psf as Columbia descended from an altitude of 235,000 to 229,000 ft. The official timeline identifies several major events during this period of flight (see Figure 4.4-21) including a significant change in the leeside flow disturbance. The fuselage and OMS Pod measurements that were indicating reduced heating levels begin registering increased heating levels (above those seen on previous Columbia flights). Nearly all (99%) of the left wing instrumentation in the 4 major wire bundles which run along the MLG wheel well have failed by the end of this period. Additionally, the first four instances (captured by ground observers) of debris leaving the orbiter are recorded. During this time period the delta yawing and rolling moment increments show a slow steady negative growth trend. By EI + 602 sec, the off nominal delta yawing moment has increased to -0.00045 with delta rolling moment increasing to -0.0006.

Based on the WT test and CFD analysis results, WLE RCC panel damage provides the best match to the aerodynamic and aerothermodynamic events observed during this time period. Extensive test and analysis of missing full WLE RCC panels was conducted to provide a comprehensive evaluation of this particular damage scenario. As mentioned, a follow on partial missing WLE RCC panel test and analysis was conducted in order to maintain consistency with the latest recovered hardware forensics, which included significant portions of every left wing RCC panel except for panel 9. (The details are covered in Section 4.3.1.6 – WT test and Section 4.3.2.3 – CFD analysis).

In testing and analysis the clearest way to affect the leeside flow field was to provide a path for the higher energy windward flow to pass through the wing. A missing RCC panel produces this flow path. Additionally, depending on panel location, it produced augmented heating to the side of the fuselage and OMS pod, consistent with the onboard measurements. In
Figure 4.4-4 WT test aerodynamic heating measurements and

Figure 4.4-5 CFD analysis surface pressures the side fuselage effects due to the flow field interaction are clearly indicated. The aerodynamics for missing RCC panels are summarized in Figure 4.4-6 and presented along with the flight extracted aerodynamic increments for rolling and yawing moment. The shaded area represents the range of CF4 wind tunnel test data for all of the single panel testing. Several specific WT test and CFD analysis points are also included. The data shows that a missing RCC panel will produce the negative roll and yaw increments consistent with this time period (Yawing moment test data being slightly larger in magnitude than the flight data, rolling moment slightly lower). At the EI + 602 sec time point the data for a missing RCC Panel 9 is possibly the best match to the aerodynamic increments (as well as the side fuselage/OMS Pod heating augmentation pattern, see Aerothermodynamics Figure 5.2.3-16).

The recovered debris is more consistent with a partial WLE damage scenario. As mentioned previously, the WT test and CFD analysis of these configurations produced little if any rolling moment increment (actually positive for partial panels 8 & 9, see Figure 4.3-13) and a reduced (relative to a full panel) yawing moment increment (see Figure 4.3-14). Given that WLE damage most likely started as a breach in the lower half of the RCC, an expected progression would be growth to a partial panel type damage configuration. However, the side fuselage impingement is not evident from WT test results of missing partial RCC panels 6 through 9, see Figure 4.3-16. All test and analysis results show that to produce the augmented heating on the fuselage, flow through the wing (or WLE) is required. Combining a missing half panel 9 with a missing upper carrier panel did produce OMS Pod and possibly side fuselage heating augmentation without any significant aerodynamic increments. Based on these results, a partial panel damage configuration is more consistent with the initial timeline period (EI to EI + 515 sec where no clear indication of aerodynamic increments is consistent with the partial panel missing data) than with this second time period.

Another suggested damage progression involved multiple missing RCC panels. Test and analysis were conducted for this damage scenario in an attempt to match the flight extracted aerodynamics time history. Results, shown for yawing moment in Figure 4.4-7 and rolling moment in Figure 4.4-8, cover single then multiple missing panel combinations ranging over RCC panels 5 through 9. For rolling moment the continuing loss of WLE panels produces the maximum negative rolling moment observed at EI + 602 sec, while the yawing moment grows well beyond the levels observed during this time period. While this yawing moment trend is consistent with the time history beyond EI + 602 sec, the rolling moment trend is not. This implies that the damage progression must have involved something other than a continuing loss of RCC panels.

4.4.1.3 Timeline Section Three – Rolling Moment Increment Trend Reversal

At EI + 602 sec (GMT 13:54:11) the delta rolling moment trend abruptly reverses sign from increasing negative to a gradual increasing positive trend which continues for nearly all of the remainder of flight. The third timeline period focuses on this distinct event and extends to EI + 710 sec (GMT13:55:59). Flight conditions range from Mach 23.2 to 21.7, dynamic pressure from 37 to 47 psf over altitudes from 229,000 to 222,000 ft. The official timeline identifies continuing major events during this period of flight (see Figure 4.4-21). Several of these occur within approximately 10 seconds of the abrupt rolling moment trend reversal. These include observed Debris event 5 (@ EI + 602 sec), as well as the start of the slow aileron trim change, mid-fuselage bondline off-nominal temperature trends indicating increased sidewall heating levels and off scale low temperatures in the left hand elevon hydraulic system (all @ EI + 611 sec). These are followed by several observed flash events, Debris event 6 considered particularly large as well as Debris events 7 through 13 through the end of this period. During this timeline period while the delta rolling moment is gradually increasing in a positive trend, the delta yawing moment remains relatively constant. At the EI + 710 sec point, the delta rolling moment has become positive at +0.0001 and the delta yawing moment is essentially unchanged at -0.005.

The combination of a negative yawing and rolling moment increment prior to EI + 602 sec has been attributed to the increased drag and decreased lift on the left wing produced by wing leading edge

damage. The abrupt change in rolling moment trend requires an increasing wing lift condition and/or a side force increment developing on the leeside (above the c.g.). Numerous potential contributing sources were evaluated in order to develop the most probable explanation for this significant event.

The onset of ABLT was first considered as a possible explanation for the observed trend. While no orbiter entry has previously experienced boundary layer transition prior to Mach 19, given the suggested extent of damage to the wing leading edge, the possibility of an early ABLT seemed plausible. While the change in rolling moment trend is consistent with a left wing ABLT, the fact that the delta yawing moment remains constant is not. To illustrate this, Figure 4.4-9, shows the flight extracted delta rolling and yawing moment with wind tunnel predicted ABLT increments applied at EI + 602 sec. The increments were established from a wind tunnel run forcing full ABLT over the left hand side of the orbiter (full ABLT as shown in Figure 4.3-2 through Figure 4.3-4). These results clearly illustrates that early ABLT is not consistent with the yawing moment and therefore cannot be the source of the delta rolling moment trend reversal.

Another plausible explanation considered involved the potential for disturbed flow over the inboard elevon surface thereby altering the control surface effectiveness yielding the change in the rolling moment increment trend. This theory was bolstered by the recovered left hand inboard (LHIB) elevon actuator (debris item 7327) which incurred significant damage including a casing burn through suggesting the possibility of high energy flow through the wing and onto the actuator. However, the wing box primary vent is through the mid-fuselage and there is no design vent through the aft spar, (however there is some leakage). Also, the flipper door vents are intended to vent the elevon cove area only and not the wing. Therefore, no clear design flow path exists. Also the inboard elevon hinge moment data, Figure 4.4-10, shows no indication of off-nominal behavior during this time period and particularly nothing is evident at EI + 602 sec. Additionally, LHIB Elevon temperature sensors remained operational with nominal data throughout the time period. Based on the data available and these observations, there is no indication of flow exiting from aft spar and disturbing elevon flow field during this time period so as to contribute to the change in the rolling moment increment trend

From the point of wing leading edge spar breach (approx. EI + 460 sec) the internal wing cavity was ingesting the high energy air and being pressurized. In this time period, based on the MLG measurements, it is suspected that the outboard wall of the wheel well cavity is breached and allowing this cavity to pressurize. Recovered left hand MLG door and adjacent structure and TPS indicate patterns suggesting potential outflow from the wheel well at some point during the flight. It was postulated that this jet flow exiting the MLG door area could interact with the external flow field and produce the observed rolling moment increment trends.

A baseline solution for CFD Point 1 (Table 4.3-4 - Mach 24.7, AOA =40.2, h=243,000 ft) in the STS-107 accident investigation was modified to include effects of a scarfed, conical nozzle directed toward the centerline of the vehicle from the forward, inboard corner of the landing gear door. The intent of the simulation was to approximately model effects of a relatively large internal wing pressure, fueled by combusting aluminum, which deforms the corner of the landing gear door and directs a jet across the windward surface. This simulation did not include details of aluminum combustion but does consider extremes of internal conditions ($p_{internal}$ = **2** $\rho_\infty V_\infty^2$ and $T_{internal}$ = 4000 K) that are expected to provide an upper limit on this potential effect. *(An associated analysis of flow through a breach in the leading edge of Panel 6 into a vented cavity indicates internal pressures of* ***(1/8)*** $\rho_\infty V_\infty^2$ *fed by an external pressure of (1/2)* $\rho_\infty V_\infty^2$*).* The analysis includes interaction of the shock layer flow with the jet. The scarfed nozzle has a 3-inch diameter throat and a 1.3 ft^2 elliptical footprint on the windward surface. Perturbations to baseline aerodynamic coefficients are expected to scale with throat area for the specified internal conditions because the interaction disturbs only a small region (roughly double the exit area) in the vicinity of the exit plane. Aerodynamic coefficient perturbations are of order 10^{-3} to 10^{-5} of right-half-body values. These values account for both interaction and any potential thrust generated by the exiting jet. The exiting jet is substantially entrained in the windward boundary layer with relatively weak perturbations to the external flow as

shown in Figure 4.4-11. These results indicate that external flow interaction with an exiting jet is an unlikely source for the delta rolling moment trend reversal.

The recovered hardware included a portion of the left hand OMS pod and several portions of the vertical tail (VT). All showed a consistent pattern of heavy damage with Aluminum deposits on the left hand side, while the right hand side remained relatively clean. This forensic evidence combined with the increased heating indications on the left hand fuselage sidewall plus the relatively large moment arm available via the VT suggest disturbed flow on the left hand side of the vehicle as an explanation for the rolling moment increment trends. Flow through wing leading edge damage and/or a hole through the upper wing surface with a resulting leeside (Fuselage, OMS, VT) flow interaction could produce the relatively small delta pressure on the VT required to reproduce delta rolling and yawing moment trends seen during this time period.

It has already been noted that flow through the WLE via a missing RCC panel produces an interaction with the leeside flow field and that this interaction increases the heating rate on both the fuselage side and the OMS pod. As part of the investigation into this leeside interaction being correlated to the aerodynamic increment pattern, other flow paths through the wing were investigated. Debris event 5 is better characterized to be more like a flash event and is closely followed by Flash event 1 and then immediately followed by Debris event 6 (see Figure 4.4-21) which is considered by evaluation as the largest debris shed by the orbiter. Together, these have been hypothesized to be the onset of an upper wing surface breach (flashes representing venting of ingested gas/burned internal wing components) and then Debris event 6 is the release of a large section of the upper wing skin. Therefore the additional flow paths through the wing investigated included flow in through lower WLE damage and out via missing upper carrier panels or missing upper surface acreage as well as holes directly through the wing from windward to leeward side.

An extensive evaluation to characterize the leeside interaction effects was undertaken through WT test, CFD analysis and hand calculations to determine the plausibility of this contribution and evaluate the various potential sources for windward surface flow to interact with the leeward side flow. It should be noted that the leeside flow field with strake vortex along with OMS pod and VT interaction is extremely complicated, even without the added complexity of interaction due to wing damage. This complexity is illustrated in Figure 4.4-12, showing the details of the flow patterns and the local interactions over this region of the orbiter at hypersonic flight conditions.

As stated, some of Columbia's recovered hardware came from the VT. Figure 4.4-13 shows recovered Columbia hardware, VT Spar, debris item No. 52092. The difference in damage to the left and right sides is evident. Additionally the left hand side pattern suggests an aft-to-fore / base-to-tip flow direction. CFD analysis was conducted to investigate the possibility of this flow pattern and the changes to this interaction as a function of wing damage. In Figure 4.4-14 the flow patterns from inviscid calculations are shown for both a baseline and a missing RCC panel 9 case. These are compared against the direction inferred from the damage pattern. The missing panel has a small effect on the flow pattern over the VT. The patterns seen on the recovered hardware are not consistent with the CFD results. These inviscid calculations and analysis for various Panel 9 damage scenarios (including holes through the wing) are detailed in section 4.3.2.3.3. This includes a breakdown of the contributions from different orbiter components (Wing, Fuselage, Tail, OMS). In Figure 4.3-39 through Figure 4.3-41 this breakdown is detailed. These results suggest that while the VT can contribute partially to the positive delta roll trend, change to the wing flow field remains the principle contributor to the aerodynamic moment increments.

Because of the complexity and concerns that an inviscid solver may not adequately capture these leeside interactions, Navier-Stokes CFD analysis was also completed for a RCC Panel 9 missing case to further assess these interactions. In Figure 4.4-15 the change in pressure on the vertical tail is shown along with the delta aerodynamic increments. This analysis of the tail flow field and the delta pressures clearly demonstrate differences in the flow field for the Panel 9 missing case. However, the delta pressure change is very small, likewise the delta aero increment from the vertical tail is very small. For this case an order of magnitude less than the increments from the wing (see

Table 4.7-6). The details of this analysis are reported in the Aerodynamics Appendices, Section 4.7.4.

As a final check to ensure that the nature of this highly separated flow field was not being misinterpreted, several wind tunnel test runs were made with and without the VT. The details of these test runs are covered in 4.3.1.6.5 with the actual test data listed in Figure 4.3-19. The aerodynamic increments with and without the vertical tail are very close in value, supporting the conclusion that the vertical tail was not the major contributor to the delta aerodynamic increments for a missing panel 9 configuration.

One other point to put forth concerns consistency with the flight data extraction. If interaction with the vertical tail was the primary contributor to the change in delta rolling moment trends via increased pressure on the left hand side of the vertical tail, this would manifest itself in a positive (being out the right wing) side force increment. Flight data extraction of the side force increment shows a small but negative (out the left wing) side force increment (Figure 4.2-10) during this time period. This inconsistency between extracted force and moments implies the primary contributor must be a change in lift, likely produced by the wing, to yield the rolling moment increment trend.

While clear evidence of leeside flow field interaction exists for the fuselage and VT (i.e. recovered debris, temperature measurements, etc.), the reproduction of required delta pressure pattern has not materialized in either test or analysis. Leeside interaction is not the primary contributing source to the delta rolling moment trend reversal in this time period.

Lower surface damage configurations were initially centered around the MLG/wheel well area and were assessed via WT testing of the stainless steel model in the LaRC Mach 6 air facility. Various damaged configurations were evaluated including MLG and door deployed as well as three open wheel well cavities of various depths. The results of the testing produced several important observations.

The MLG and door deployed configuration produced both large positive rolling moment and large negative yawing moment increments similar to extracted aerodynamic trends seen just prior to LOS. However the configuration also produced a large positive pitching moment increment (see lines D & E in Figure 4.3-6). This wind tunnel measured pitching moment increment is not consistent with the large negative pitching moment extracted from flight just prior to LOS. Based on these results it is clear that the MLG did not deploy prematurely.

Another extension of these results was to utilize the MLG (only) down, with no door, test configuration as representative of lower wing surface damage that results in a forward facing step. Test results for this configuration produce both large -yawing and -rolling increments as shown in (Figure 4.4-16) This is not consistent with the (-yaw/+roll) flight extracted trends seen late in flight and suggest that whatever damage Columbia's left wing was enduring did not result in a lower surface forward facing step.

An open wheel well of various depths was investigated as part of this series of testing. These results provided the first indication that an open cavity on lower wing produces (+) rolling and (-) yawing moment increments, consistent with changing trend for roll moment and constant yaw moment seen after EI + 602 sec. (see
Figure 4.4-16). As can be seen in the data the shallower cavity yields larger increments (both yaw and roll).

The lower surface cavity wind tunnel results combined with forensic evidence, the extracted aerodynamic flight data patterns and wing structural design/loading suggest a lower surface deformation as the damaged configuration that best reproduces the observed change in rolling and yawing moments. The gradual aerodynamic moment increment growth is consistent with leeward debris and not loss of windward surface material. A lower surface deformation or recession could yield the necessary gradual change to windward surface by slowly growing in area and/or depth. To

assess this scenario in more detail a combined aerodynamic, internal heating and structural analysis was completed.

The orbiter intermediate wing structure was not designed to carry large loads and essentially supports the lower and upper skin and the associated distributed loads. The WLE spar, the outboard wheel well wall and the 1191 spar provide the primary strength and serve to outline the intermediate wing area (Figure 4.4-17). Structural analysis was used to define possible wing deformation considering the aerodynamic loads and potential internal wing damage. Finite element model analysis provided global wing deformation. Associated stress calculations were then used to provide localized skin deformation. The hot gas entering the intermediate wing does so as a high energy plume, therefore damage to much of the internal structure is likely to have occurred. The predicted wing deformation (global and local) was heavily influenced by the hypothesized damage which included reduced structural modulus to represent missing or severe damage to the WLE spar behind one RCC panel, reduced strength of the spar caps, missing wing truss tubes, and loss of wing skin inner face sheet. For structural analysis details see Section 7.5.

Structural and surface deflections from the analysis were provided to the aerodynamics group for assessment. The global structural deformation is relatively small. Even considering the damage, the overall delta between an undamaged wing and a damaged wing yielded a deflection change of less than 0.8 inches. The wing deflection (z-component) is shown in Figure 4.4-18. Newtonian aerodynamic analysis of this deformation produced a small -yawing and +rolling moment increments.

Similarly the local surface skin deflections as generated through stress analysis were also evaluated. These provided relatively large (maximum of 5+ inches) surface deflections Figure 4.4-19. Newtonian as well as inviscid (FELISA - Section 4.3.2.3.4 and CART3D) calculations were completed on this localized damaged configuration. These calculations also produced small -yawing and +rolling moment increments. Note that the global and local wing deformations were not combined and these cases were independently assessed. While the CFD analysis yields the correct signs (-yaw/+roll) the values are relatively low.

Wind tunnel testing of lower surface recession was completed in the LaRC CF4 tunnel. Test configurations considered a range of width and length for a 5 inch deep recession behind RCC panels 8 and 9. Three lengths were considered ranging from Xo=1146 to 1243. Single, double and triple wide recessions were tested (single being 23 inches wide). Testing was done with and without RCC panel 9 missing. These results are summarized in Section 4.3.1.6.6 and the configurations and results are shown in Figure 4.3-20 through Figure 4.3-22. These lower surface depressions do result in a positive (right wing down) rolling moment as observed in flight, and the magnitude of the rolling moment increases as the width of the depression is increased. Furthermore, the yawing moment and pitching moment generated by the depression are similar in magnitude and in the same direction as observed for flight.

The test and analysis concentrated on this timeline period in an attempt to identify the cause of the distinct pattern in the flight extracted aerodynamics. Several possible contributors to the change in rolling moment trend were identified and include leeside flow field effects, potential (very) early ABLT and flow through the wing. However, none of these serve as the primary contributor. Of all of the plausible explanations evaluated, only a lower wing surface deformation appears consistent with the data and therefore the rolling moment delta trend change is attributed to wing deformation.

4.4.1.4 Timeline Section Four – Progressive Damage Aerodynamics

The fourth timeline period covers what is essentially the remainder of flight from EI + 710 sec through EI + 918 sec (GMT13:55:59 – 13:59:27), just prior to LOS. Flight conditions range from Mach 21.7 to 17.8, dynamic pressure from 47 to 83 psf over altitudes from 222,000 down to 200,000 ft. The official timeline identifies continuing major events during this period of flight (see Figure 4.4-22 and Figure 4.4-23). These include debris events 14-17, loss of instrumentation within the

wheel well cavity, the sharp increase aileron trim rate, loss of upper and lower wing skin (OI) temperature measurements each suggesting a continuing degradation of the left wing. However Columbia does complete a planned roll reversal around EI + 765 sec with nominal performance indicating major vehicle and wing integrity still exists.

While the exact state of Columbia's damaged left hand wing is unknown, despite the extensive internal wing damage, the hypersonic aerodynamic asymmetries remain manageable, with the orbiter windward surface still basically intact. Based on the continuing observations of debris loss, the expected continual damage to the wing internal structure, the gradual increase in +rolling moment increment and - yawing moment increment as well as the onset of a -pitching moment increment, that the lower surface wing deformation remains the most plausible explanation for the aerodynamics observed during this time period.

The results for progressive growth in the lower wing surface deformation are summarized in section 4.3.1.6.6 (wind tunnel testing) and section 4.3.2.3.4 (CFD analysis). The wind tunnel test configurations and results are shown in Figure 4.3-20 through Figure 4.3-22. The data indicates that as the lower surface depression width increases from a single to triple wide configuration, the rolling moment (+), yawing moment (-) and pitching moment (-) increments each gradually increase in magnitude as observed in flight during this time period.

CFD analysis of the single wide lower surface depressions provided similar trends as the wind tunnel for rolling, yawing and pitching moment Figure 4.3-52. When combined (by superposition) with RCC panel 9 missing the resulting rolling moment (+), yawing moment (-) and pitching moment (-) increments each reach magnitudes consistent with those observed in flight during this period. Also included in these plots are the data for the localized lower wing skin deformation as predicted by stress analysis for a substantially damaged intermediate wing structure. While the CFD analysis yields the correct signs (-yaw/+roll) the values are relatively low for this case.

Overall, the delta aerodynamics computed and measured for windward surface damage configurations correlate well with the increments observed late in flight. The data trends support the hypothesis of progressive internal structural damage that produces a gradual windward surface deformation. This gradual deformation produces the steady increase in rolling moment and yawing moment as well as the pitching moment increments seen during this late period in flight.

4.4.2 Damage Progression Theory and Supporting Aero

Based on the damage assessment and timeline period correlations covered in Section 4.4.1, the following is a postulated damage progression theory based on the results of the aerodynamic investigation. This damage progression, approached from an aerodynamic perspective, is consistent with the working scenario and attempts to maintain consistency with other data from the investigation. References are made to figures which include a combination of aerodynamic extraction results and the major timeline events noted.

An initial WLE breach (small hole or slot) in an RCC panel exists at entry interface. By EI + 300 sec thermal events are occurring internal to the WLE cavity, however no identifiable aerodynamic increments are observed. The breach continues to grow into a larger hole and between EI + 300 to 450 sec has resulted in the loss of most of a lower RCC (7,8 or 9?) panel. The partial missing RCC panel configuration produces little if any delta aerodynamic effect, nothing observable (see Figure 4.4-20). Breach of the WLE spar follows somewhere between EI + 450 to 500 sec and internal wing pressurization and heating damage begin. Still no external aerodynamic effect is observed. As the WLE damage progresses it results in the onset of high energy windward flow passing through the WLE and interacting with the leeside flow field between EI + 500 to 600 sec (see Figure 4.4-21). The OMS pod and side fuselage surface temperature measurements indicate increased heating as a result of this interaction. This is most likely the result of loss of a considerable portion of RCC Panel 9 and/or an upper carrier panel (9,10 or 11?) and produces the first clear indication of off nominal aerodynamic increments (-yaw & -roll). Both continue to slowly increase with negative growth trends

for approximately 90 seconds. By EI + 600 sec internal wing damage has become significant. The four major OI/MADS wire bundles have burned through and the MLG wheel well wall is likely breached, much of the intermediate wing structure has been significantly damaged. Soon after, breaches through the left hand wing upper surface begin to develop as marked by a series of flash events, Debris 5 (or Flash "0") at EI +602 sec and Flash 1 (EI +624 sec) indicating a forced external venting of the gas and damaged material built up in the intermediate wing. At EI + 627 sec, Debris 6 (the largest observed debris event) most likely represents a large portion of the upper wing surface departing the orbiter. This release of the internal pressure buildup relieves the offset to the external lower surface pressure and combined with the extensive internal wing damage results in the onset of a lower wing surface deformation or dimple. Initiated at the EI + 602 sec mark, this corresponds to the Debris 5 flash event, the onset of the slow aileron trim change and the change in the delta rolling moment increment trend, which abruptly changes sign and begins positive growth. Beyond EI + 630 sec (see Figure 4.4-22), the WLE damage becomes extensive, perhaps to the point of loss of lower RCC Panel 8 and most or all of RCC Panel 9. The combination of WLE damage and lower surface wing deformation produces the slow growth in the delta rolling (+) and yawing (-) moment increments. The continuing observed debris events are postulated as primarily upper surface structure and TPS, so despite the extensive wing damage, the hypersonic aerodynamic asymmetries remain manageable, with the orbiter windward surface still basically intact. As the lower surface deformation continues to grow, between EI + 700 to 850 sec, it produces gradually larger delta rolling (+) and delta yawing (-) moment increments. Even with the developing damage to the left wing, Columbia completes a planned roll reversal with nominal performance at approximately EI + 765 sec. Shortly after this maneuver, at EI + 835 sec (see Figure 4.4-23) the aileron trim rate increases sharply in response to a corresponding sharp increase in the growth of both the rolling and yawing moment increments. The initial delta pitching (-) moment increment is now also observed. As large scale wing deformation continues to grow beyond EI + 870 sec the asymmetric aerodynamics exceed design levels. Columbia manages trimmed flight for approximately another 60 sec, eventually requiring the use of all 4 RCS aft yaw jets and maximum rate of aileron to maintain trim. However, the asymmetric yaw and roll moment growth increases drastically exceeding 6 times the design levels just prior to LOS + 5 sec. Under this extreme asymmetric condition, the flight control system can no longer maintain trimmed flight. Columbia soon departs from controlled flight leading to the loss of vehicle and crew.

The damage assessment results summarized in section 4.4.1 can be mapped to this progressive damage scenario. Since the exact damaged configuration can never truly be known, a subjective placement of the measured aerodynamic increments along the timeline of the extracted increments is reasonable. In Figure 4.4-24 through Figure 4.4-26 the rolling, yawing and pitching moment increments from the LaRC CF4 wind tunnel test results of configurations in line with the damage progression outlined above are presented. The time history trends of the yawing, rolling and pitching moment increments can be matched remarkably well. Although an exact correlation of flight magnitudes and time is not achieved, since the exact damaged configuration is unknown, a plausible damage progression scenario has been developed which has the same aerodynamic trends as the extracted flight data.

As a final comment on the damaged configuration test and analysis results, it must be pointed out again that the nature of this analysis and the conclusions to be drawn from them should be limited to a proper engineering perspective. The test and analysis conducted for the aerodynamic (and aerothermodynamic) portion of the investigation were performed on representative geometries. The representative geometries that have been assessed were chosen in a very dynamic investigation environment as engineers interpreted the latest results from wind tunnel testing, CFD analysis, flight measurement evaluation, recovered hardware forensics, etc. The fact that these geometries were chosen for investigation purposes should not be misconstrued as exactly reproducing the damaged configuration encountered in flight. These representative damaged configurations, however, do provide an insight into the nature and level of damage necessary to result in the loss of Columbia and her STS-107 crew.

TABLES

CASE	Damage Location	ΔCm	ΔCn	ΔCl
Boundary Layer Trip	RCC Panel 6	-0.00062	-0.00015	0.00032
Boundary Layer Trip	RCC Panel 6 (fwd)	-0.00019	-0.00004	0.00019
Holes Through Wing	4 holes (Mach 6)	0.00012	-0.00008	0.00017
Hole Through Wing	Carrier Panel 6 (CF4)	0.00040	0.00006	-0.00005
Hole Through Wing	Carrier Panel 9 (CF4)	0.00010	-0.00004	0.00000
Hole Through Wing	Carrier Panel 12 (CF4)	0.00014	-0.00003	-0.00004
Flight Extracted	**EI to EI + 515 sec**	**0.0000**	**0.0000**	**0.0000**

Table 4.4-1 Aerodynamic Increments – WT Results for BL Trips & Hole(s) Through Wing

	Full-vehicle baseline	Δ interaction (new-baseline)	Δ thrust	Δ net
axial	.0781751	$1.23\ 10^{-7}$	$3.07\ 10^{-7}$	$4.30\ 10^{-7}$
side	0	$3.66\ 10^{-5}$	$-8.12\ 10^{-5}$	$-4.46\ 10^{-5}$
normal	1.1322635	$-3.03\ 10^{-5}$	$4.08\ 10^{-5}$	$1.05\ 10^{-5}$
roll	0	$-2.79\ 10^{-5}$	$2.76\ 10^{-5}$	$-0.03\ 10^{-5}$
pitch	.0279899	$3.98\ 10^{-5}$	$2.67\ 10^{-6}$	$4.25\ 10^{-5}$
yaw	0	$8.50\ 10^{-6}$	$-5.53\ 10^{-6}$	$2.97\ 10^{-6}$

Table 4.4-2 Aerodynamic Increments – LAURA CFD – Jet exiting MLG door w/External Flow Interaction

FIGURES

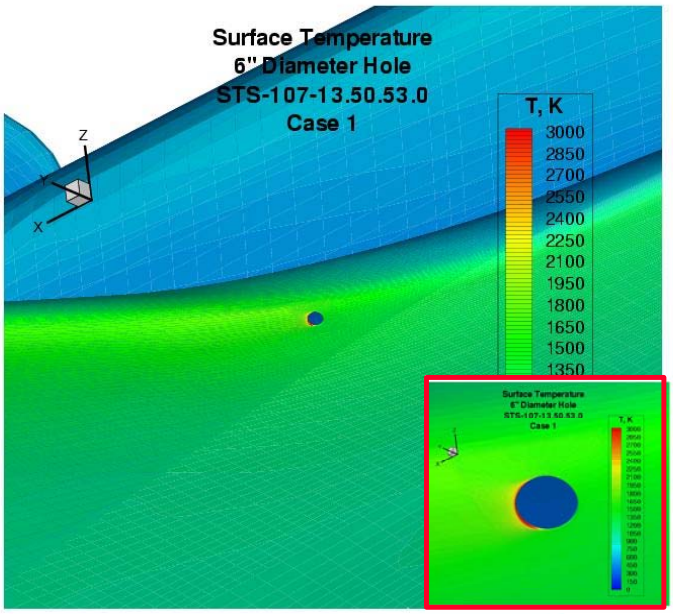

Figure 4.4-1 Surface Temperature - LAURA CFD Analysis – 6" Hole in WLE RCC Panel 6

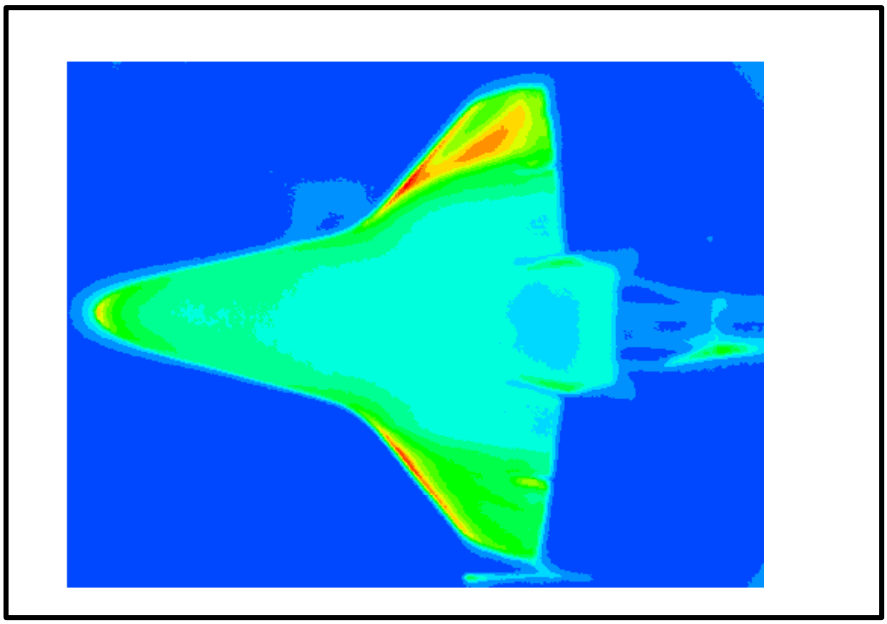

Figure 4.4-2 Infra-red Thermography Surface Heating Distribution – BL Trip at RCC Panel 6

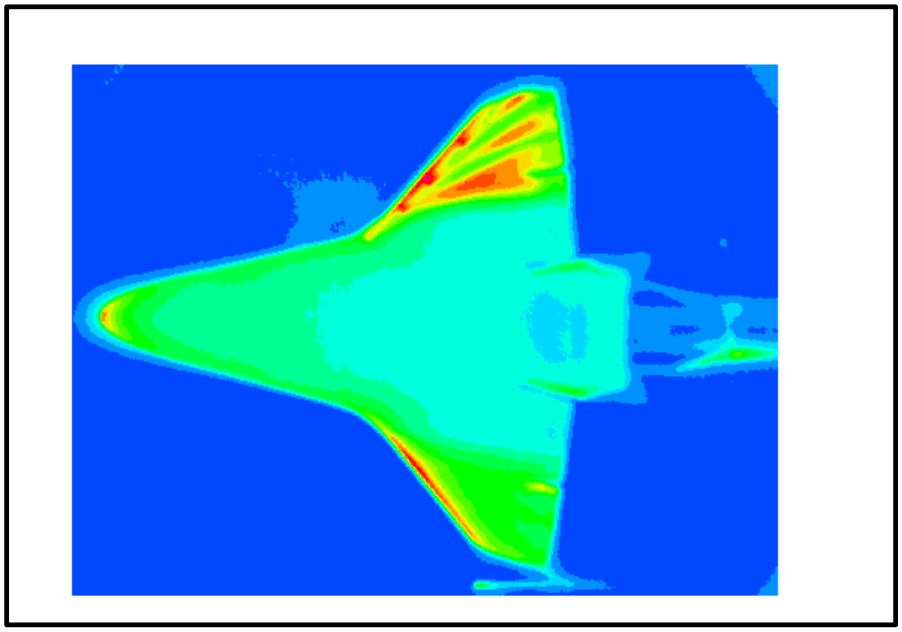

Figure 4.4-3 Infra-red Thermography Surface Heating Distribution – Holes (4) at RCC Vent Locations

Experimental Aeroheating -- 20-inch CF4 tunnel, $\alpha = 40°$

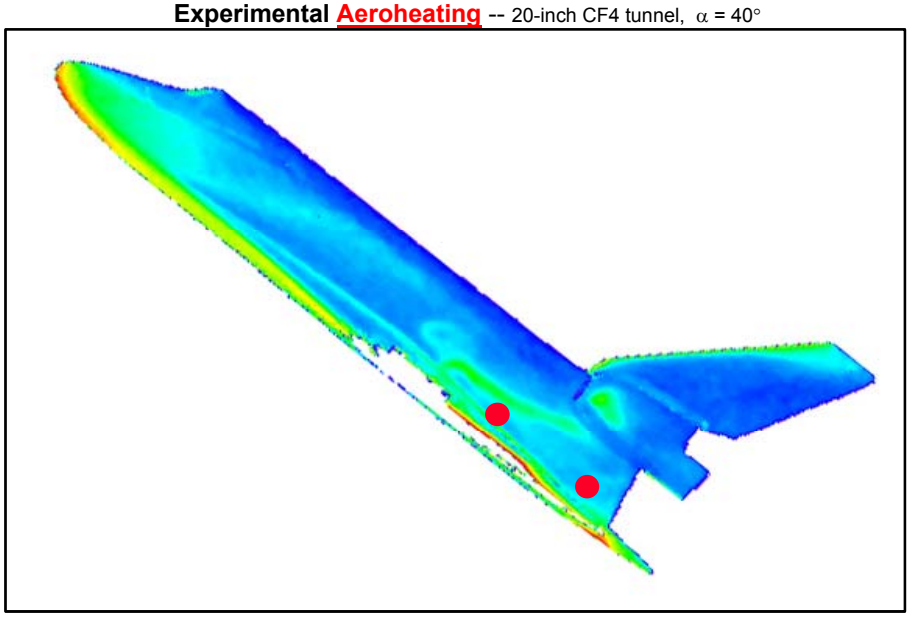

Figure 4.4-4 Phosphor Thermography WT Test Surface Heating Distribution – RCC Panel 9 Missing

FELISA Prediction of Surface Pressure

M = 24.2, Equilibrium air, $\alpha = 40°$

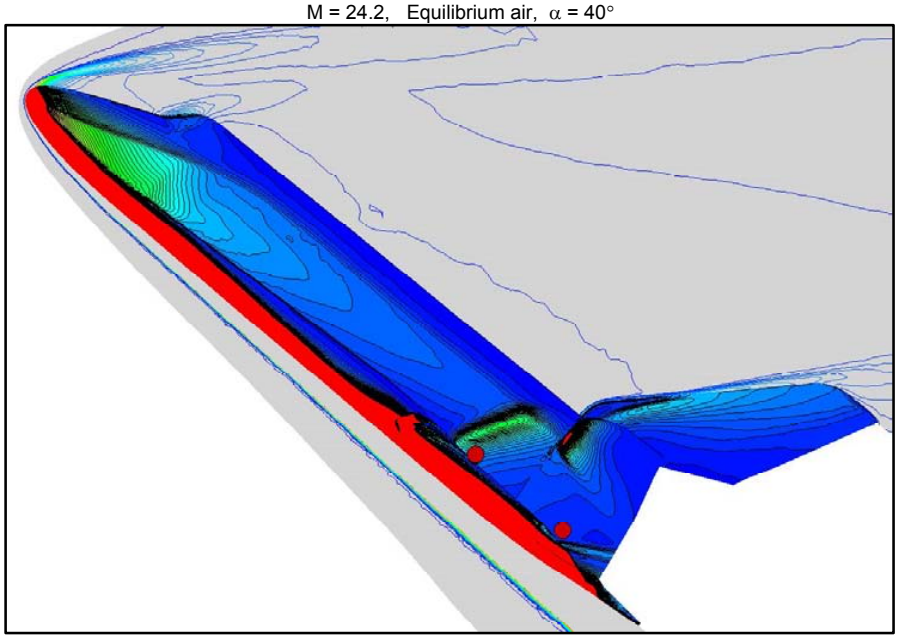

Figure 4.4-5 Surface Pressure Distribution – CFD Analysis - RCC Panel 9 Missing

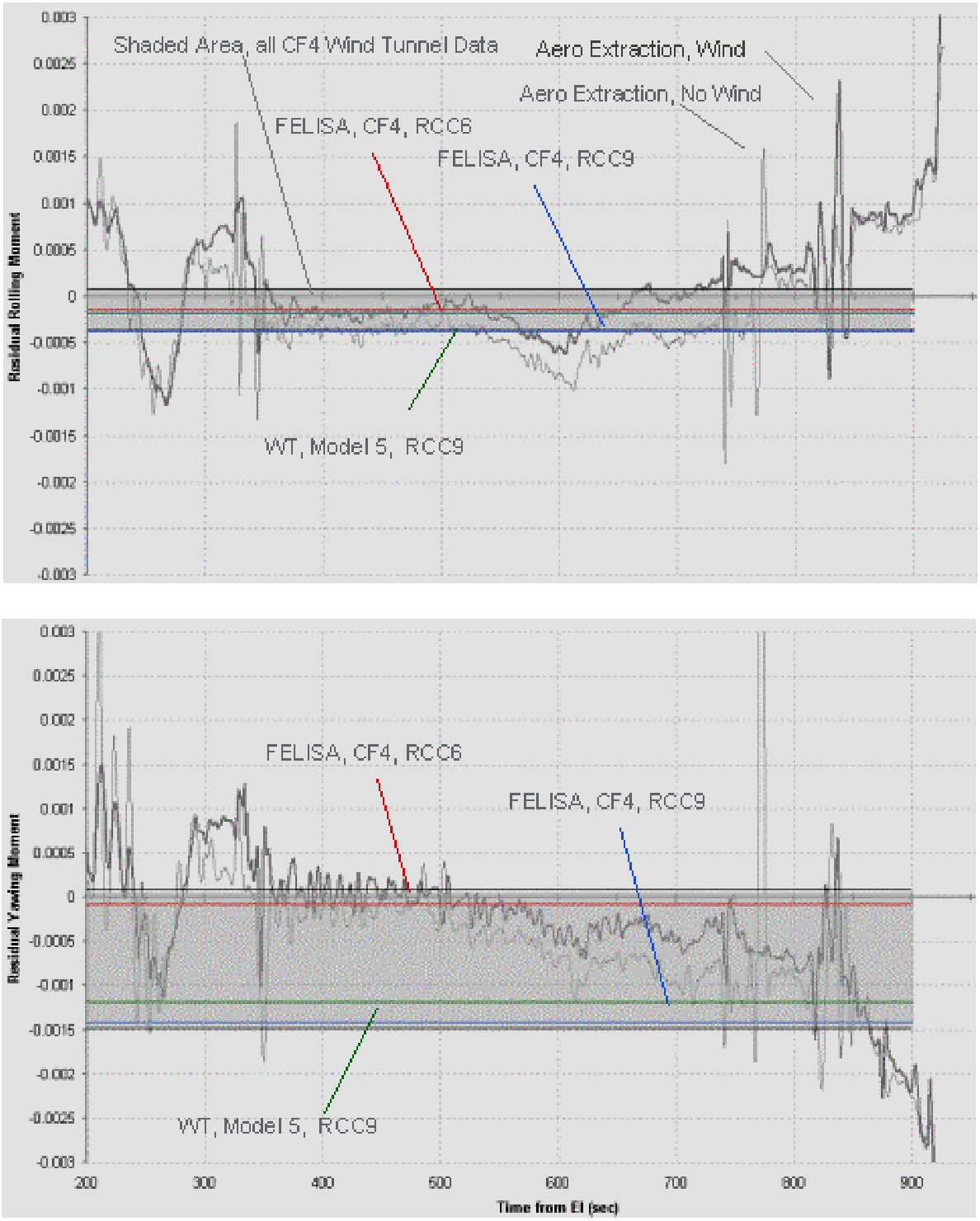

Figure 4.4-6 LaRC CF4 WT Test & FELISA (Inviscid) CFD Results – Single Panel Damage Predicted Delta Aerodynamics vs. Flight Extracted Increments

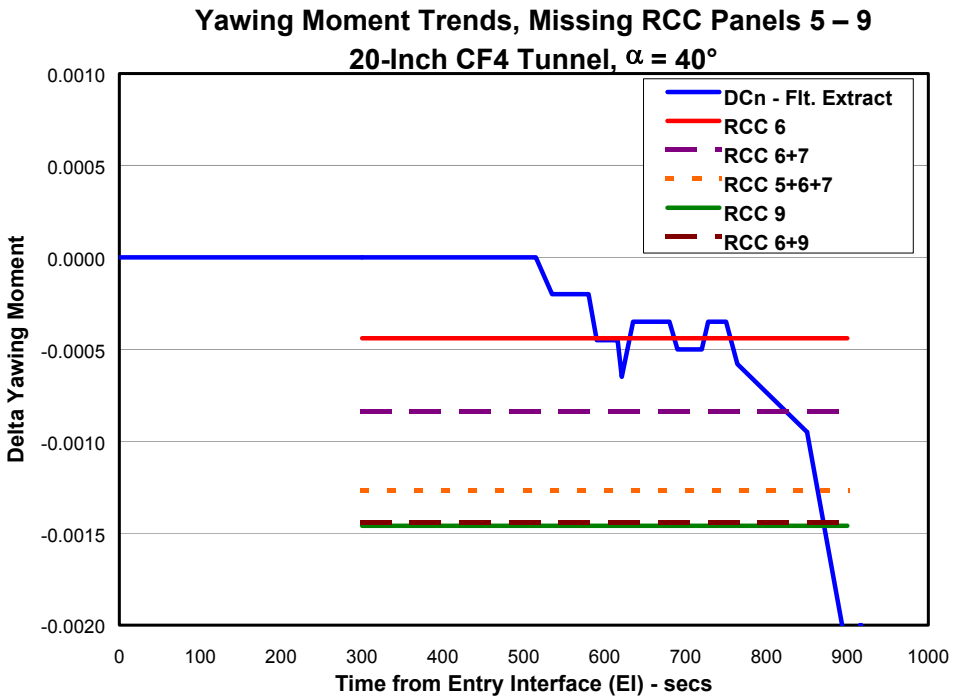

Figure 4.4-7 Aerodynamic Increment (delta Yaw) - Multiple RCC Panels Missing

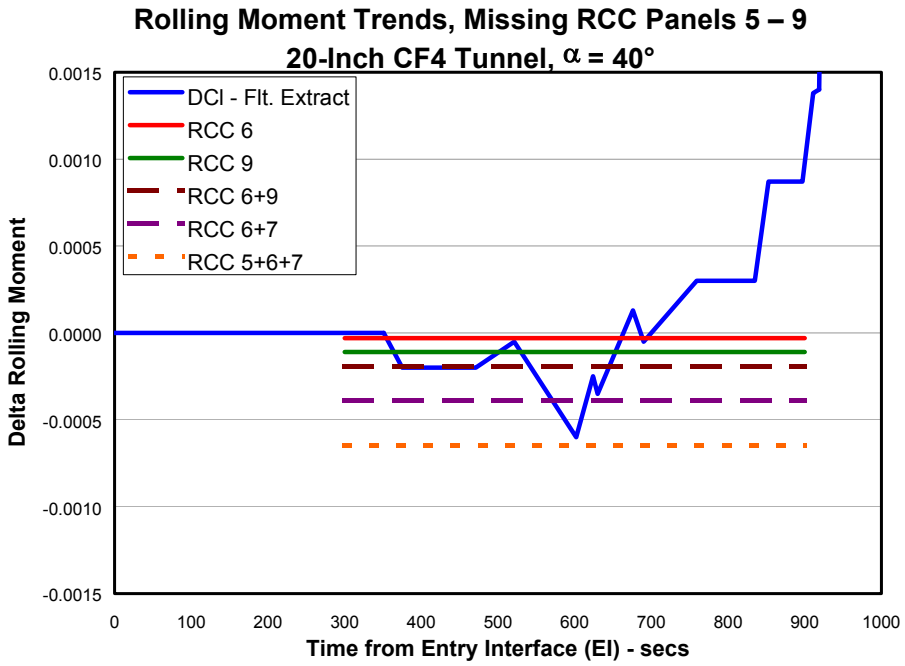

Figure 4.4-8 Aerodynamic Increment (delta Roll) - Multiple RCC Panels Missing

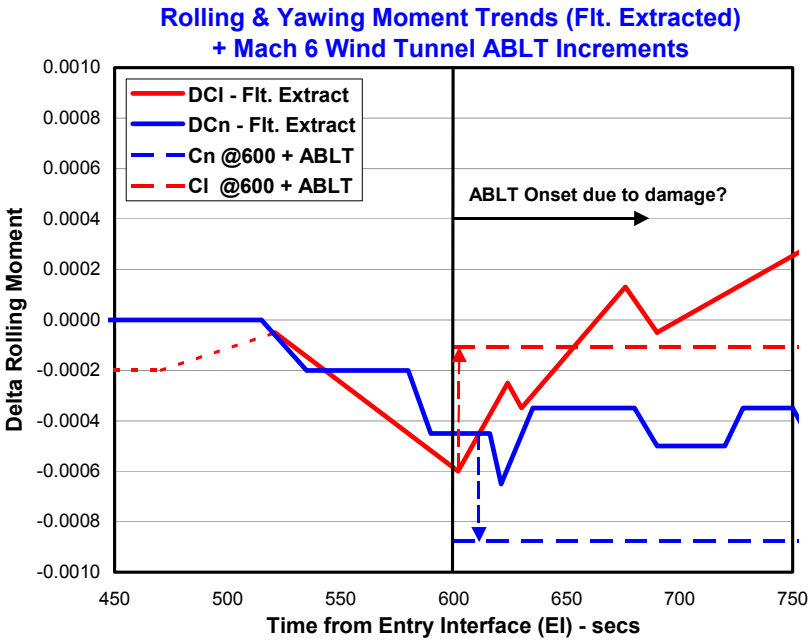

Figure 4.4-9 Delta Rolling Moment Trend Change - Early ABLT Onset?

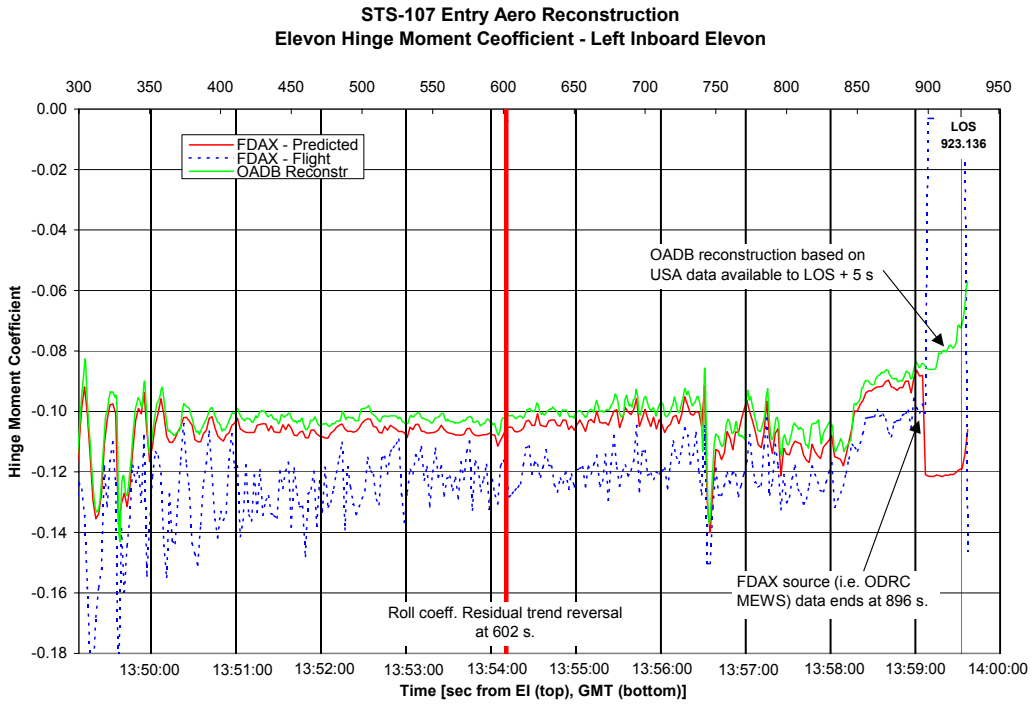

Figure 4.4-10 Delta Rolling Moment Trend Change – Disturbed flow over LHIB Elevon?

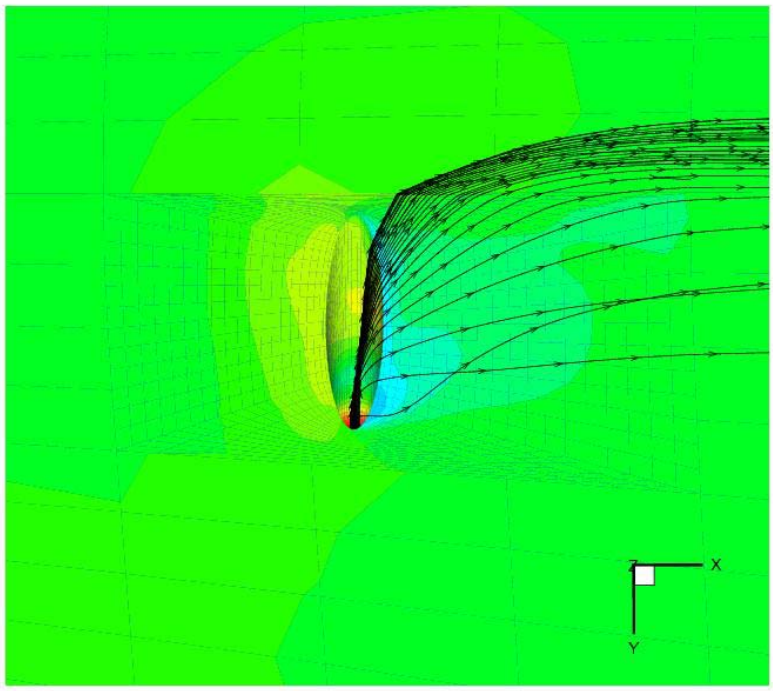

Figure 4.4-11 Delta Rolling Moment Trend Change – Flow Interaction w/Exiting Jet?

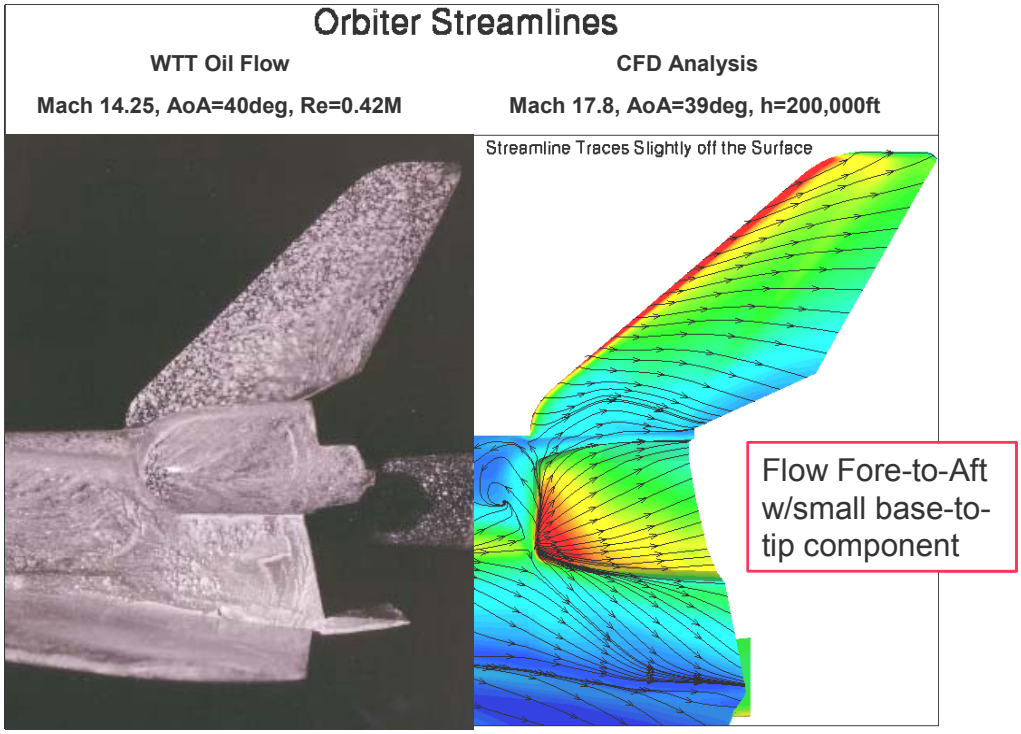

Figure 4.4-12 Orbiter Leeside (Fuselage, VT, OMS) Flow Field Visualization

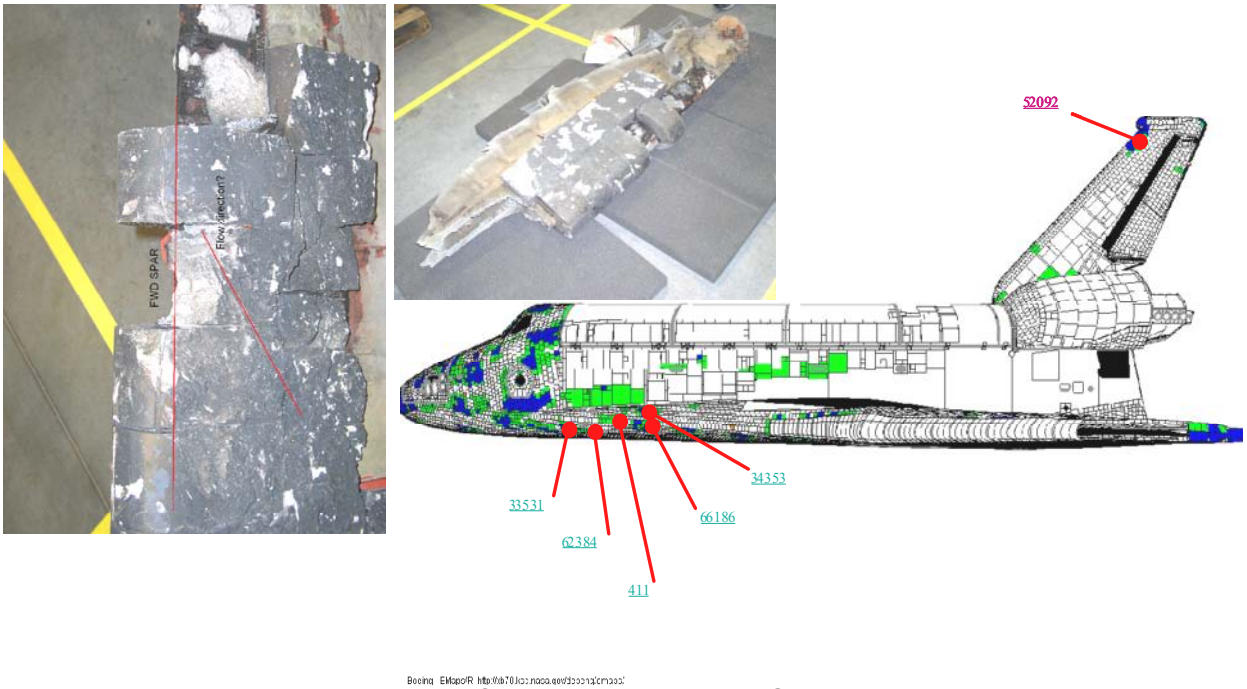

Figure 4.4-13 Recovered Columbia Hardware - VT Spar Debris Item 52092

FELISA --Inviscid Solver
Mach 24.2, Equilibrium Air, q = 28.2 psf, α= 40 deg (13:52:20, EI+491 sec)

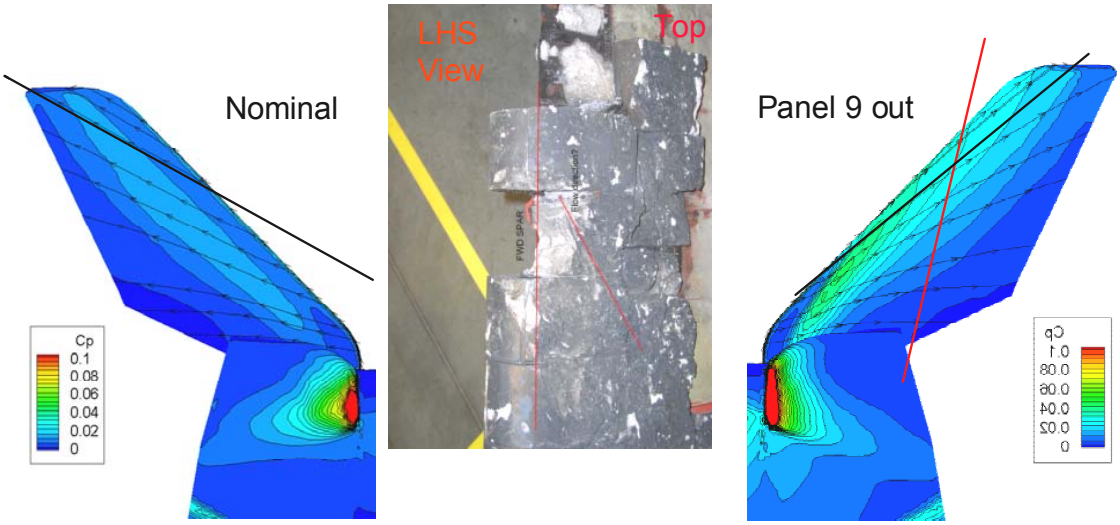

Figure 4.4-14 VT Flow Patterns - FELISA CFD Results - Baseline & w/Panel 9 Missing

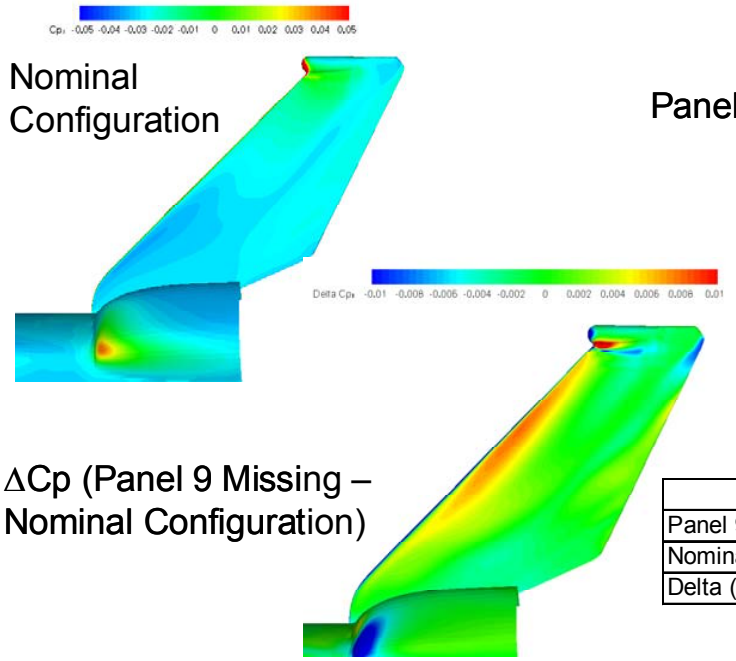

	Cl	Cm	Cn
Panel 9 (P9)	-0.00026	-0.00614	-0.00063
Nominal (clean)	0.00001	-0.00623	-0.00002
Delta (P9 - clean)	-0.00027	0.00009	-0.00061

Figure 4.4-15 Leeside Flow Interaction - Overflow CFD analysis - Delta CP on Vertical Tail

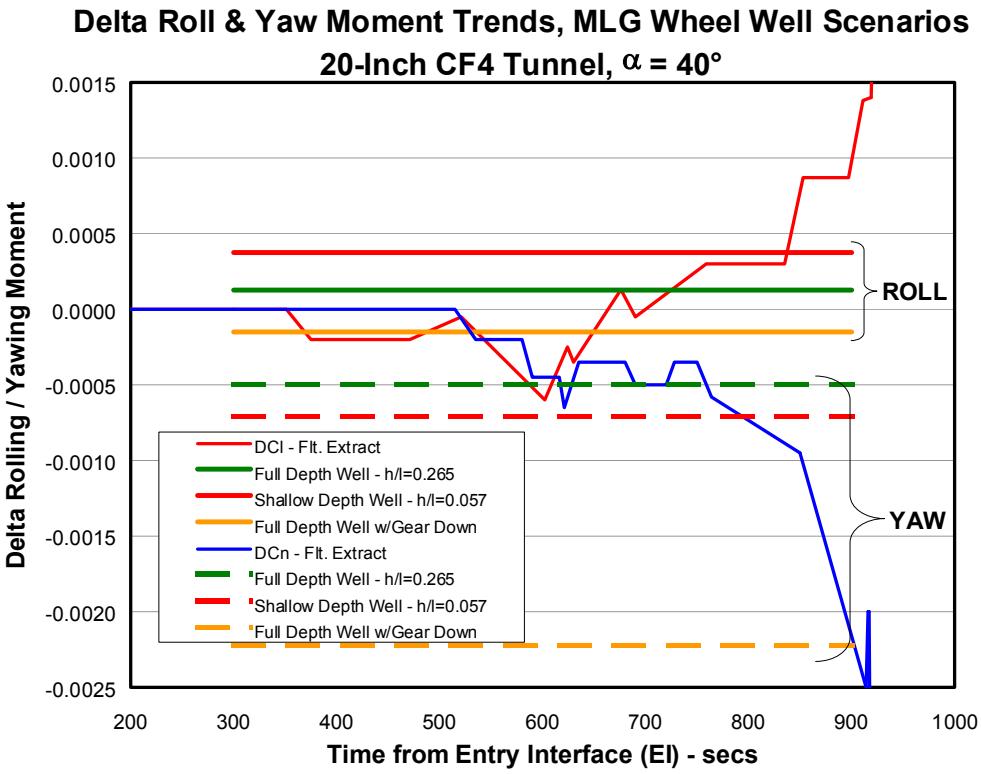

Figure 4.4-16 Delta Aero Increments - Roll & Yaw (MLG Wheel Well Scenarios)

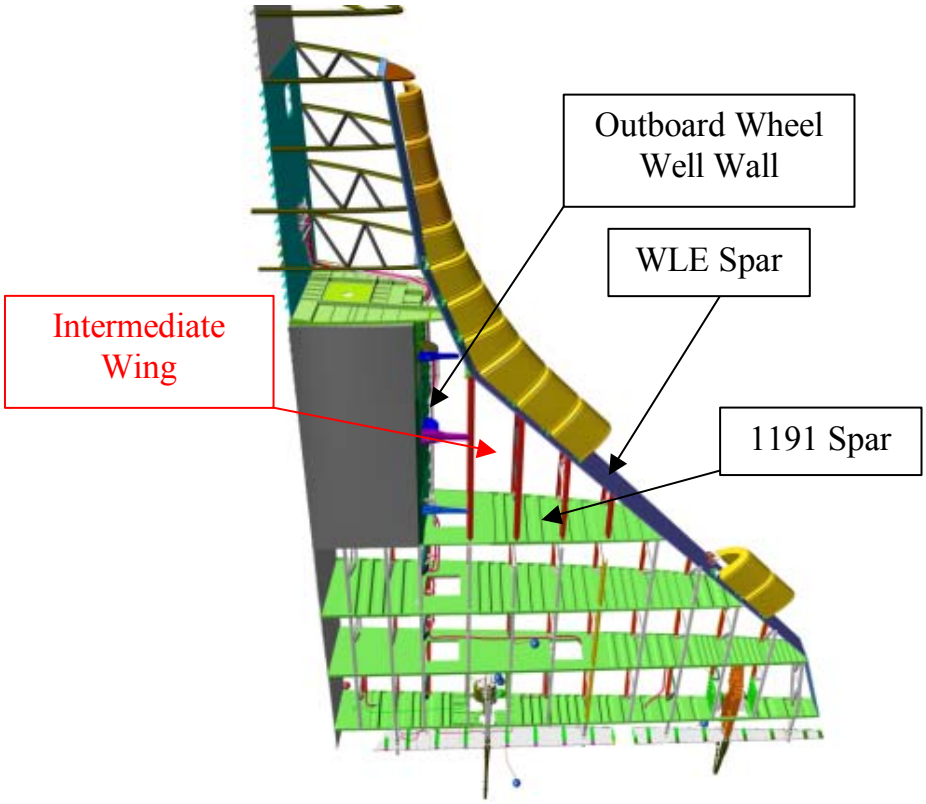

Figure 4.4-17 Orbiter Wing Structure Layout - Intermediate Wing Area

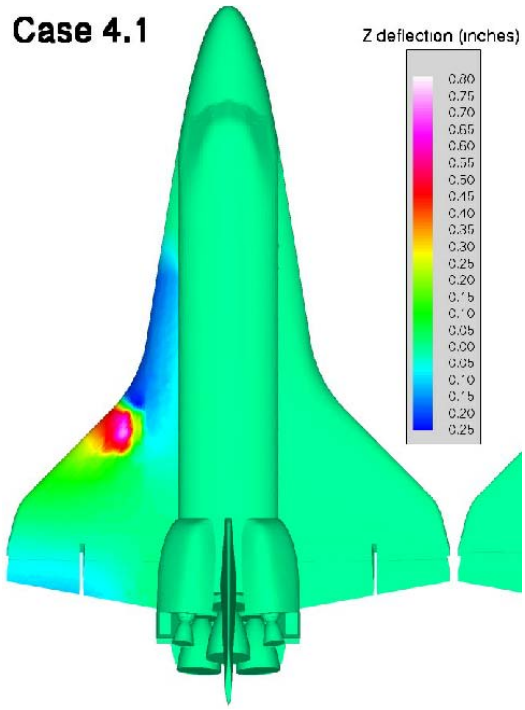

Figure 4.4-18 Orbiter Wing Structure Delta Deflection – Surface (z) Change With Damage

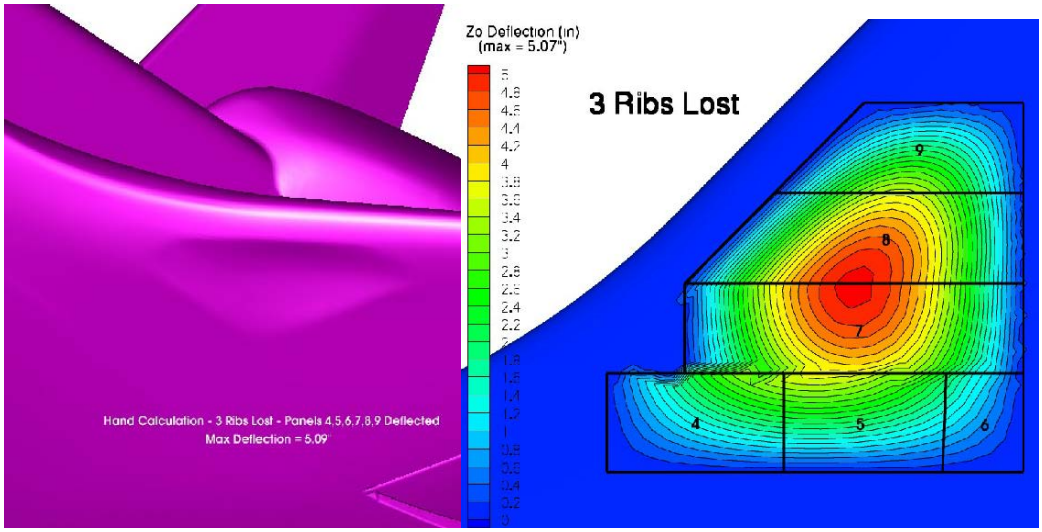

Figure 4.4-19 Orbiter Wing Surface (Skin) Deflection (z) – With Damage – 3 Ribs lost

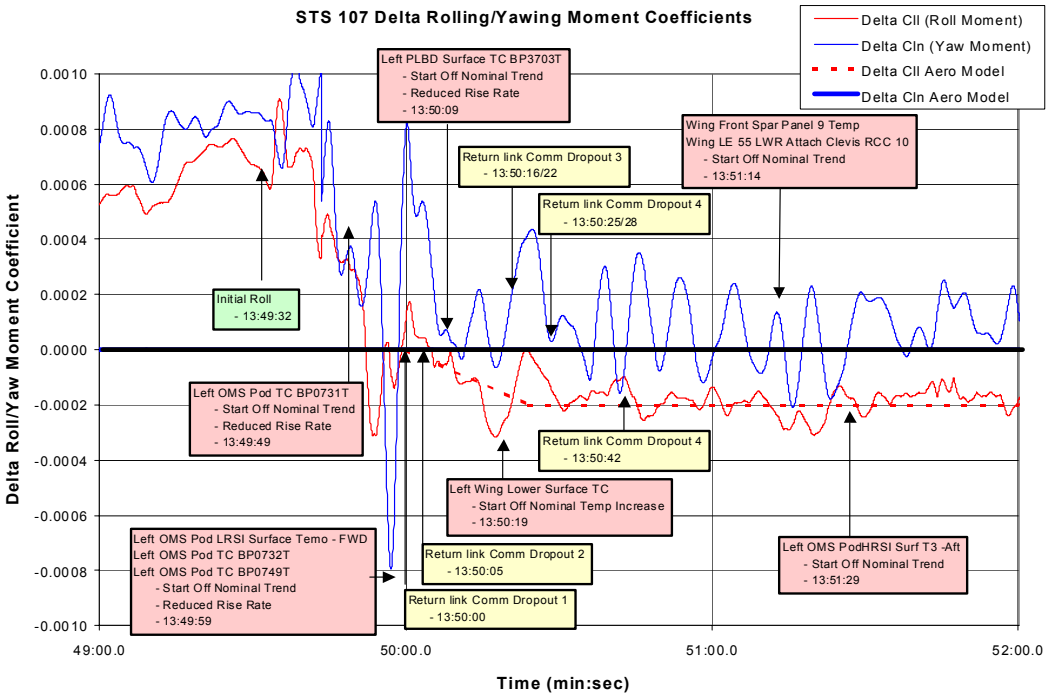

Figure 4.4-20 Aero Increments GMT 13:49:00 to 13:52:00

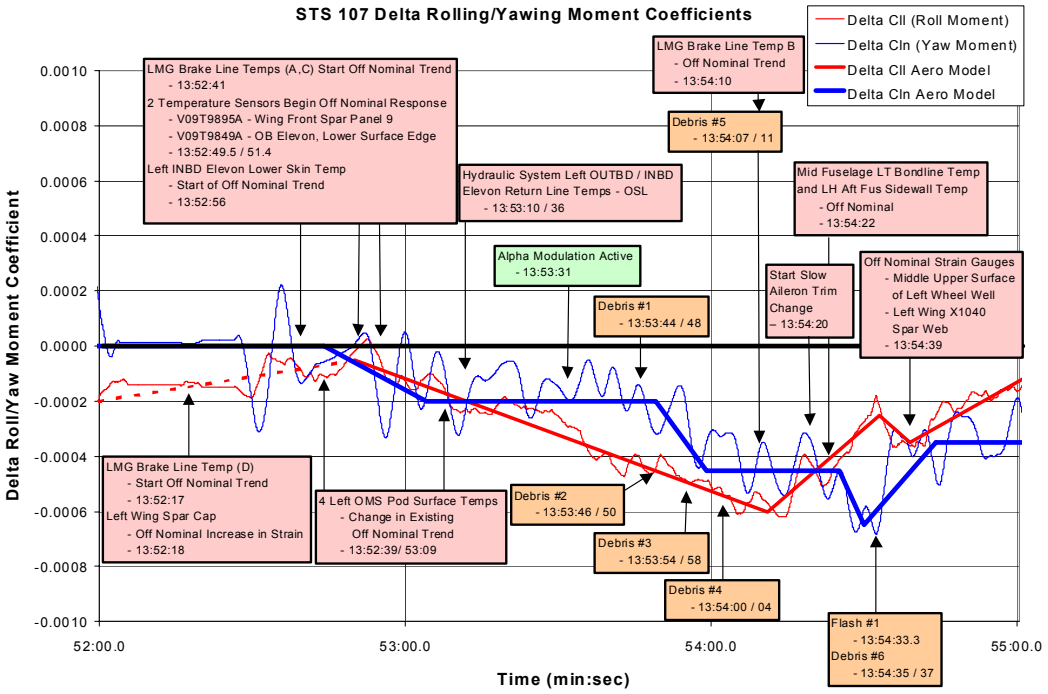

Figure 4.4-21 Aero Increments GMT 13:52:00 to 13:55:00

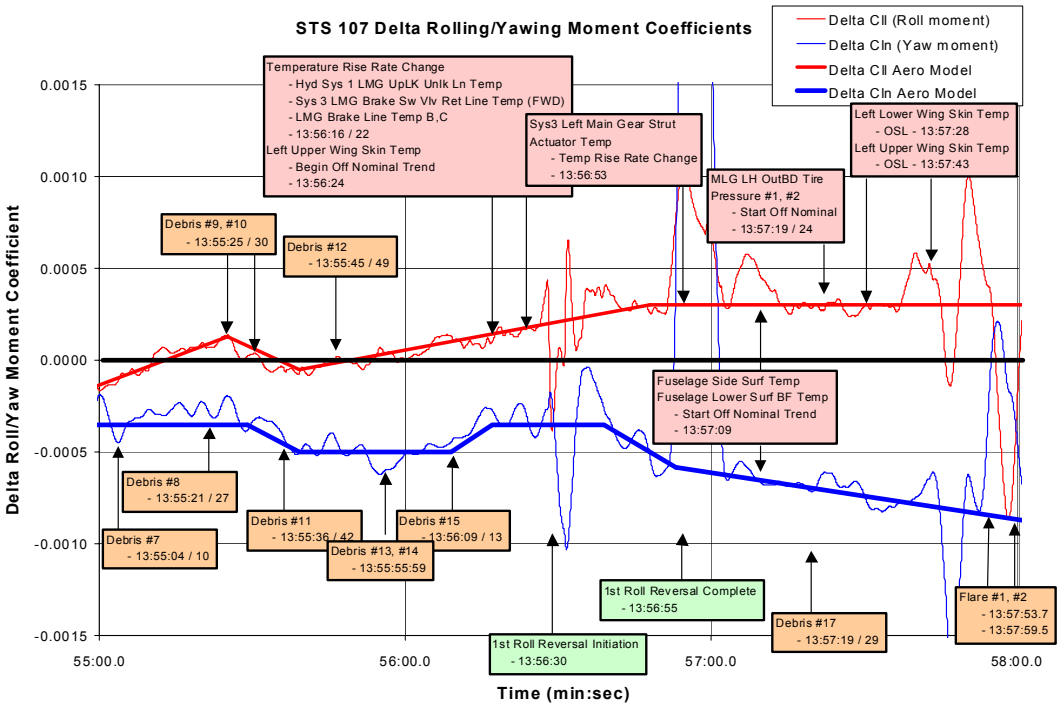

Figure 4.4-22 Aero Increments GMT 13:55:00 to 13:58:00

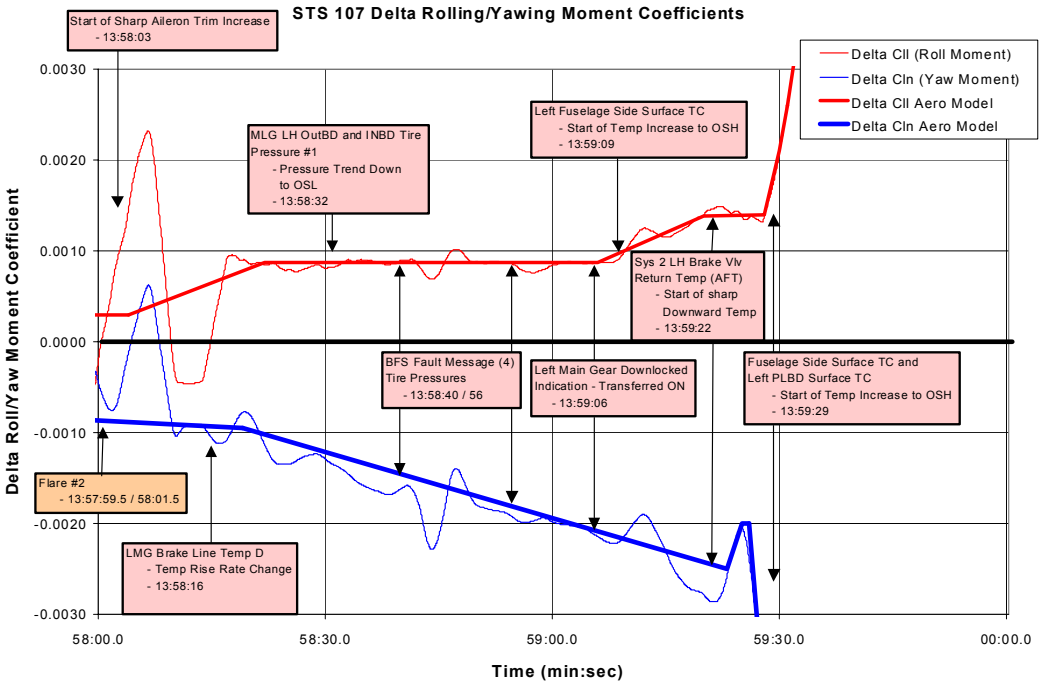

Figure 4.4-23 Aero Increments GMT 13:58:00 to 13:59:30

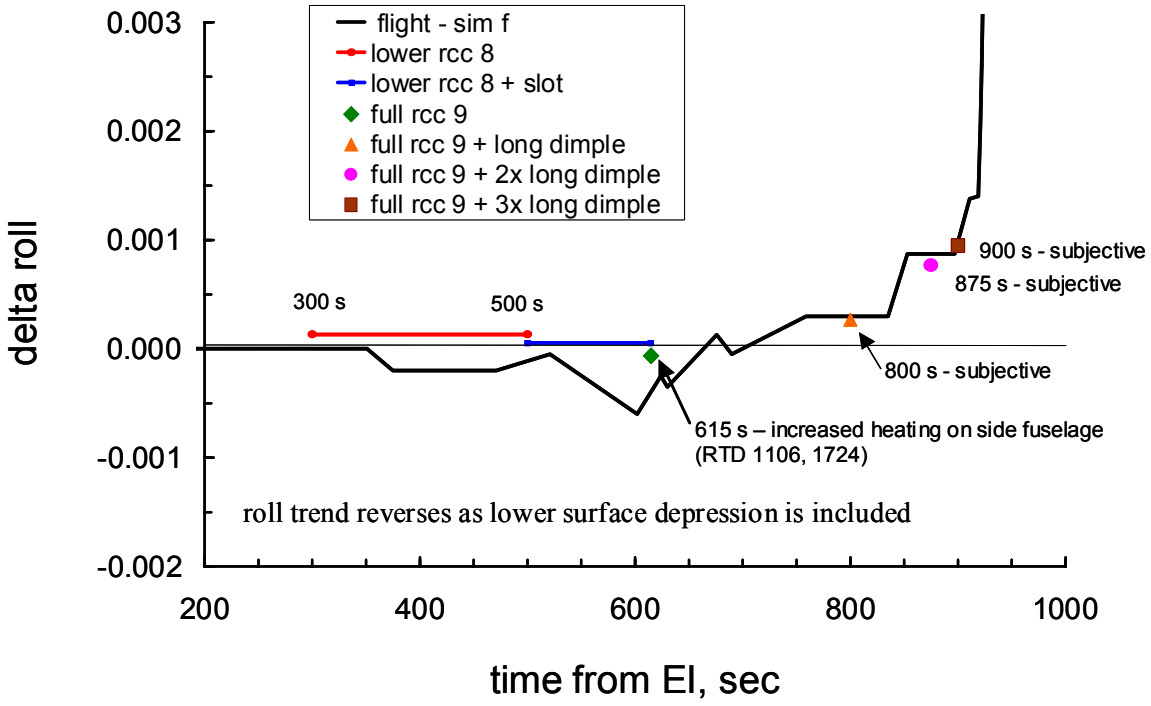

Figure 4.4-24 Aerodynamic Damage Progression Scenario – Delta Rolling Moment

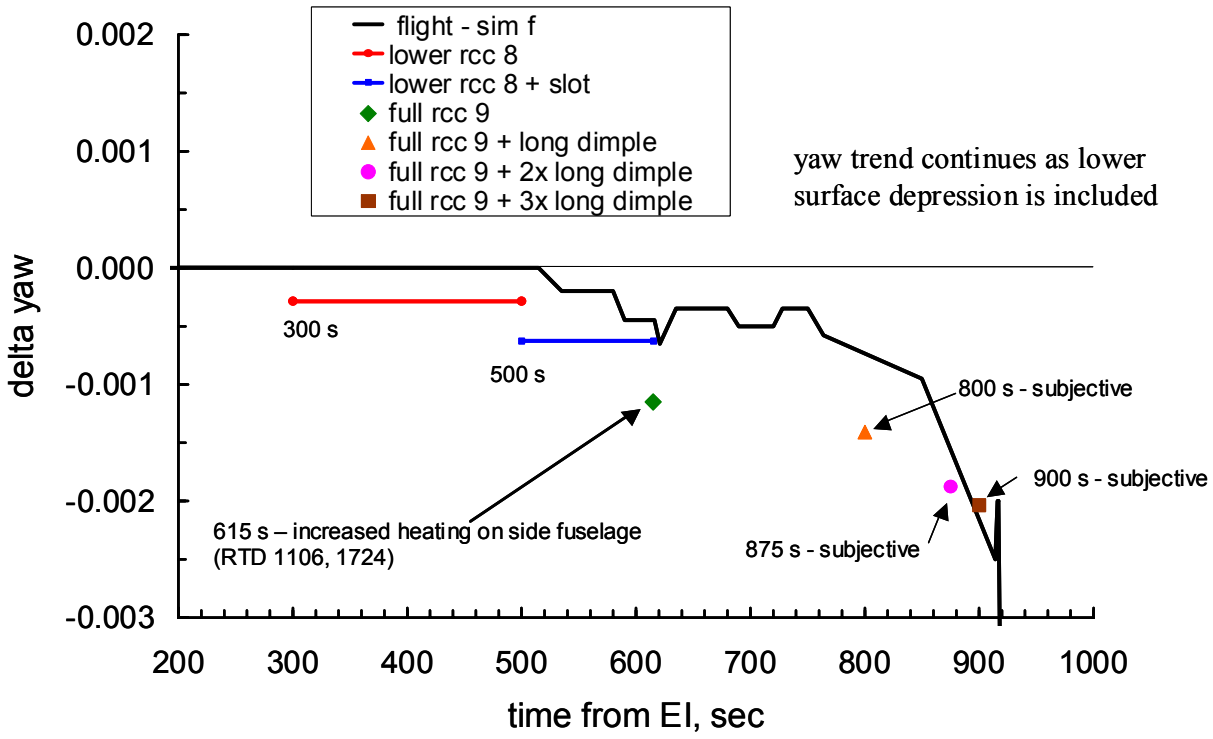

Figure 4.4-25 Aerodynamic Damage Progression Scenario – Delta Yawing Moment

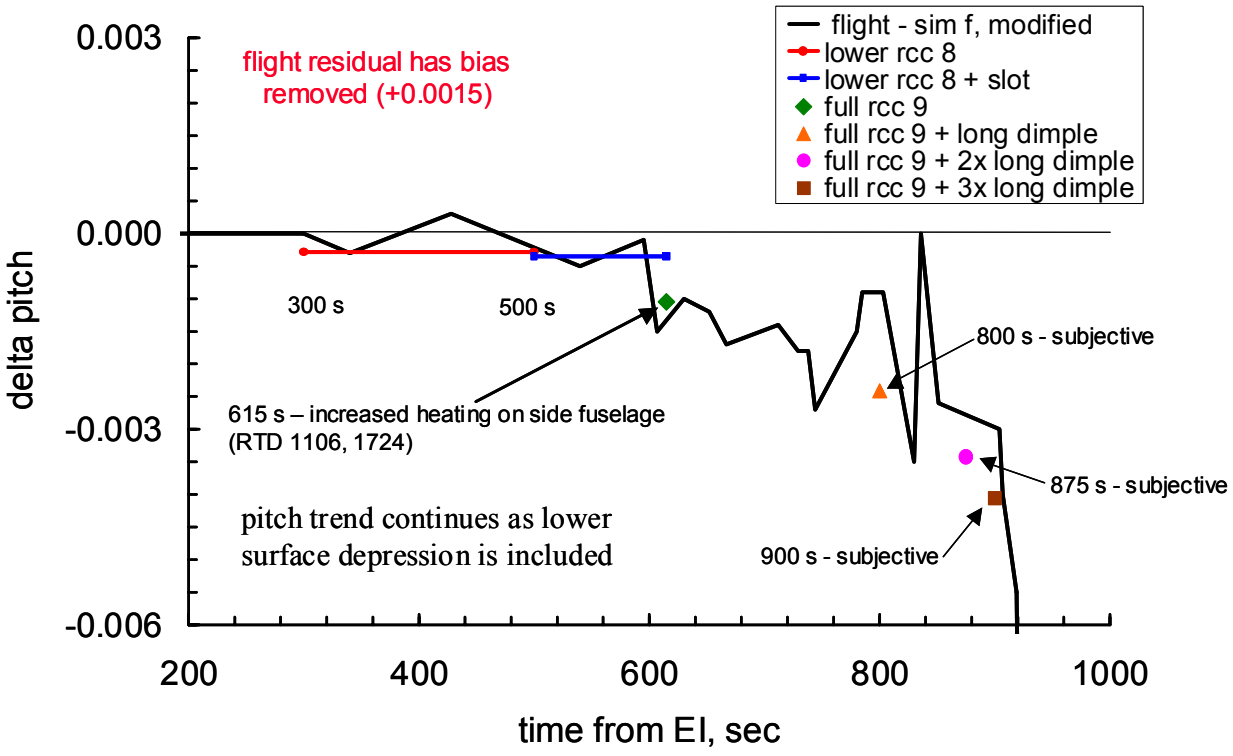

Figure 4.4-26 Aerodynamic Damage Progression Scenario – Delta Pitching Moment

4.5 Summary – conclusions & observations

1) Flight measured Orbiter rates, accelerations, trajectory parameters, control surface deflections, etc. can be used to define the off-nominal aerodynamics experienced by Columbia during STS-107 entry flight. The off-nominal aero is characterized by delta aerodynamic force and moment increments (Delta defined as Actual - Nominal).
2) High altitude winds have a pronounced effect on the magnitude of the off-nominal delta aerodynamic forces and moments, as much as 50%, but do not effect the trends vs. time.
3) Off nominal aerodynamic increments are not clearly evident until after EI + 515 sec.
4) At EI + 602 sec, the rolling moment increment trend abruptly reverses from increasing negative to increasing positive, corresponding to several other timeline events. These include the first evidence of flight control system compensation for asymmetric aero due to damage as well as debris event No. 5 (or Flash event "0").
5) The extracted moments do not exceed asymmetric aerodynamic design levels as defined by the Asymmetric Boundary Layer Transition (ABLT) model until very late in the flight timeline (after the EI + 877 sec point).
6) The flight control system manages the growing asymmetry as designed throughout the flight up to Loss of Signal (LOS).
7) The off nominal aerodynamics increase rapidly in the last 60 sec of flight producing overwhelming asymmetric moments (after EI + 920 sec) resulting in Columbia's loss of control leading to vehicle breakup.
8) Wind tunnel test and CFD analysis of proposed damaged configurations has been successful in producing aerodynamic increments consistent with a progressive damage scenario.
9) Initial delta aerodynamic yawing (-) and rolling (-) increments are not consistent with early ABLT which has always produced opposite signs for these moments.
10) Wing leading edge (RCC panel) damage produces the (-) roll and (-) yaw increments early in flight (plus the augmented heating observed on the side fuselage and OMS pod).
11) The primary source of the rolling moment trend change (@EI + 602 sec) cannot be attributed to leeside (VT, OMS, fuselage) interaction
12) Lower wing surface deformation (i.e. cavity or depression) produces the (-) yawing and (+) rolling moment increment trends seen later in the flight. These deformations are consistent with anticipated internal wing damage due to ingestion of hot gas through a Wing Leading Edge breach.
13) Increments measured for Main Landing Gear / Door deployment while matching the roll and yaw increments later in flight do not match the pitching moment. Based on this data the Main Landing Gear did not prematurely deploy.
14) Based on WT test and CFD analysis results a progressive damage scenario can be matched to the extracted aerodynamic increments that is consistent with other observed data trends, analysis and recovered hardware forensics.
15) The test and analysis conducted for the aerodynamic (and aerothermodynamic) portion of the investigation were performed on representative geometries. The fact that these geometries were chosen for investigation purposes should not be misconstrued as exactly reproducing the damaged configuration encountered in flight. These representative damaged configurations, however, do provide an insight into the nature and level of damage necessary to result in the loss of Columbia and her STS-107 crew.

4.6 References – Aerodynamics

1) Operational Aerodynamic Design Data Book, STS85-0118-1 CHG 8, August, 1996
2) STS-107 Natural Environments Report, MSFC ED44 (03-012), May 16, 2003
3) STS-107 Integrated Entry Environment (IEE) Team Final Report, NSTS-37382, May 30, 2003
4) OV-102 Investigation Vehicle Data Mapping (VDM) Team Quantitative Report, Preliminary - Rev. 6, May 02, 2003.

4.7 Appendices – Aerodynamics

4.7.1 Aerodynamic Definitions, Coordinate Systems and References

The following figures (pages from the Orbiter OADB) summarize the Orbiter aerodynamic coordinate system, aerodynamic definitions, moment reference center and the reference areas and lengths.

The aerodynamic force and moment sign convention is illustrated in Figure 3.1.5-4 which also includes the longitudinal equations for conversion from stability to body axis system.

STABILITY AXIS

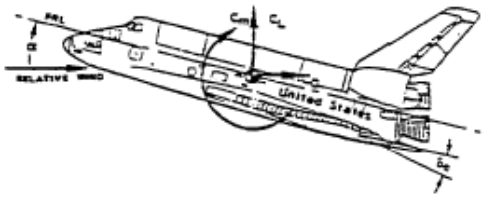

Conversion to body axis system:

$C_N = C_L \cos \alpha + C_D \sin \alpha$

$C_A = C_D \cos \alpha - C_L \sin \alpha$

BODY AXIS

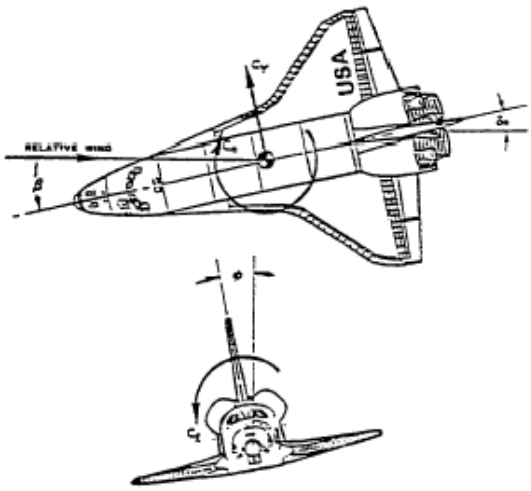

Figure 3.1.5-4
ORBITER SIGN CONVENTION

4.2.1.1 LONGITUDINAL AERODYNAMICS. The basic aerodynamic characteristics for the longitudinal degrees-of-freedom are presented as full-scale, rigid and elastic, forces and moment in both the stability and body axis systems (cf.Section 3.1.5). These forces and moments are defined for three phases or categories:

1.) ON-ORBIT (PAYLOAD BAY DOORS OPEN)

2.) ON-ORBIT (PAYLOAD BAY DOORS CLOSED)

3.) ENTRY

The total longitudinal forces and moment for the Orbiter Vehicle are defined as:

LIFT FORCE, $L_{TOTAL} = \bar{q}\, S_w C_{L_{TOTAL}} + L_{RCS}$ (lb)

NORMAL FORCE, $N_{TOTAL} = \bar{q}\, S_w C_{N_{TOTAL}} + N_{RCS}$ (lb)

DRAG FORCE, $D_{TOTAL} = \bar{q}\, S_w C_{D_{TOTAL}} + D_{RCS}$ (lb)

AXIAL FORCE, $A_{TOTAL} = \bar{q}\, S_w C_{A_{TOTAL}} + A_{RCS}$ (lb)

PITCHING MOMENT, $M_{TOTAL} = \bar{q}\, S_w \bar{c}_w C_{m_{TOTAL}} + M_{RCS}$ (ft-lb)

where, $\bar{q}$ = dynamic pressure (lb/ft^2)

S_w = Wing Reference Area (2690.00 ft^2)

$\bar{c}_w$ = Wing Mean Aerodynamic Chord (39.56 feet) (see Figure 3.1.5-2b)

RCS flow field interactions are defined as contributions to the total forces or moment rather than coefficients since the terms due to jet thrust and impingement are independent of dynamic pressure and cannot, therefore, be normalized in the conventional manner.

4.2.1.2 LATERAL-DIRECTIONAL AERODYNAMICS. The basic aerodynamic characteristics for the lateral-directional degrees-of-freedom are presented as full-scale, rigid and elastic, force and moments in the body-axis system (cf. Section 3.1.5). The lateral-directional characteristics are defined under the same three categories listed in Section 4.2.1.1.

The total lateral-directional force and moments for the Orbiter Vehicle are defined as:

SIDE FORCE, $Y_{TOTAL} = \bar{q}\, S_w C_{Y_{TOTAL}} + Y_{RCS}$ (lb)

YAWING MOMENT, $\mathcal{N}_{TOTAL} = \bar{q}\, S_w b_w C_{n_{TOTAL}} + \mathcal{N}_{RCS}$ (ft-lb)

ROLLING MOMENT, $\mathcal{L}_{TOTAL} = \bar{q}\, S_w b_w C_{\ell_{TOTAL}} + \mathcal{L}_{RCS}$ (ft-lb)

where, $\bar{q}$ = dynamic pressure (lb/ft^2)

S_w = Wing Reference Area (2690.00 ft^2)

b_w = Wing Span (78.057 ft)
(see Figure 3.1.5-2b)

RCS flow field interactions are defined as contributions to the total force or moments rather than coefficients since the terms due to jet thrust and impingement are independent of dynamic pressure and cannot, therefore, be normalized in the conventional manner.

3.1.5 ORBITER VEHICLE. The aerodynamic design of the Orbiter Vehicle configuration is the result of a selection which would achieve high cross-range aerodynamically and which would be capable of trimmed flight over a wide range of angles of attack. The double-delta wing planform, combined with a moderately low fineness ratio (approximately 5) body, minimizes interference heating effects, provides the required L/D ratio to meet cross-range requirements, and possesses an acceptable trim range over the flight Mach regime. Figure 3.1.5-1 presents a general arrangement drawing of the Orbiter Vehicle.

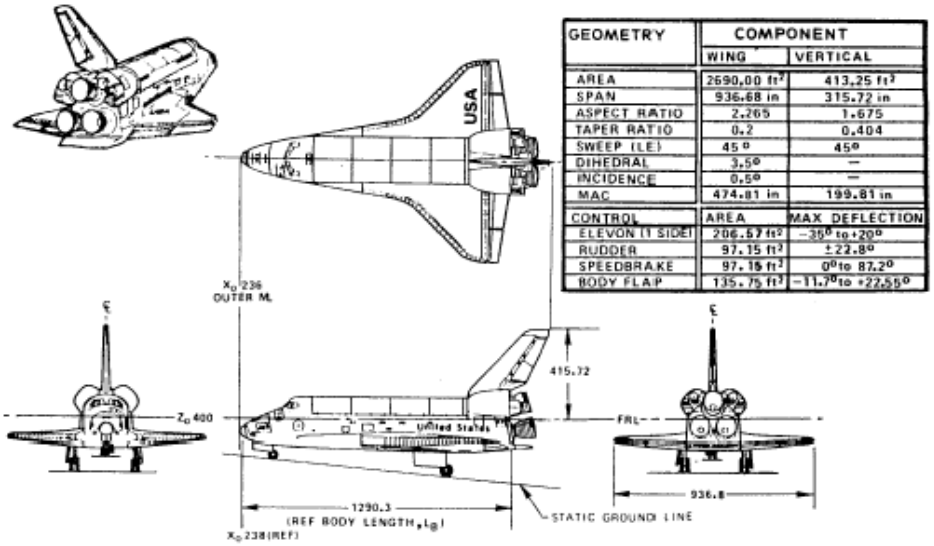

GEOMETRY	COMPONENT	
	WING	VERTICAL
AREA	2690.00 ft²	413.25 ft²
SPAN	936.68 in	315.72 in
ASPECT RATIO	2.765	1.675
TAPER RATIO	0.2	0.404
SWEEP (LE)	45°	45°
DIHEDRAL	3.5°	—
INCIDENCE	0.5°	—
MAC	474.81 in	199.81 in
CONTROL	**AREA**	**MAX DEFLECTION**
ELEVON (1 SIDE)	206.57 ft²	−35° to +20°
RUDDER	97.15 ft²	±22.8°
SPEEDBRAKE	97.15 ft²	0° to 87.2°
BODY FLAP	135.75 ft²	−11.7° to +22.55°

Figure 3.1.5-1
ORBITER GEOMETRY

Orbiter Vehicle design geometry is presented in Figure(s) 3.1.5-2 (a through f). The Orbiter Vehicle axis system for design drawing and mass properties statements is illustrated in the sketch. This axis system is defined in the Space Shuttle Master Dimensions Specification (Reference 3-7) and on Figure 3.1.5-2. All vehicle and design drawing axes systems are in accordance with NASA Phase B Technical Directives 2519 and 2519A.

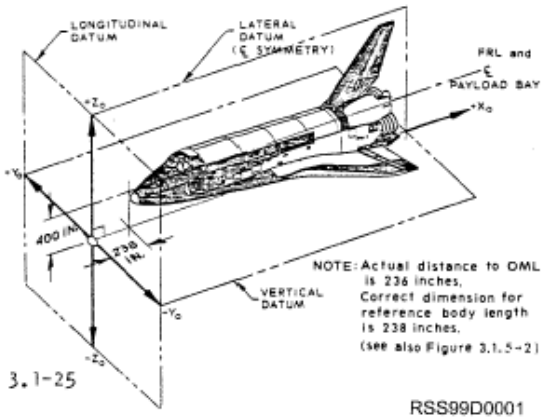

4.7.2 Surface Pressure Entry Data Evaluation

Orbiter Experiments (OEX) pressure data was installed on Columbia in support of the Ascent Wing Loads Verification Program. The pressure transducers were therefore sized (typically 0 to 16 psia) for ascent load environments and analysis of these flight results were incorporated into the Performance Enhancement Design Airloads database. These specific requirements limited the use of data for the entry phase. Entry data review was typically performed for the Mach 3.5 to 0.6 region which covers the Operational Entry Airloads Database. Since culmination of the Airloads Verification Program, the typical extent of the entry review was for instrument functionality and signature comparisons with past flights.

Analysis of the OEX recorder pressure data for STS-107 was made possible with the finding, identification and processing of the OEX data recorder. This data included 181 wing pressure measurement gages on two of the three Pulse Code Modulation (PCM) units of the recorder. PCM1 had 91 gages while PCM2 had 90 gages with no measurements recorded on PCM3. A previous instrument survey performed for STS-109 (Columbia's previous flight) had identified that only 116 gages were producing useable data. These 116 gages break down as 68 for left wing (41 upper, 27 lower) and 48 for the right wing (34 lower and 14 upper). The only active pressure gages on Columbia during STS-107 were those on the wings.

Analysis of the STS-107 OEX entry pressure data was of very limited use for aerodynamic evaluation. Even though data was recorded to EI + 970 seconds, the useful recorded pressures typically do not start until around 1420 seconds after EI near Mach 3.5, Figure 4.7-1. Since the extent of STS-107 entry was above this condition and at such high altitude, low density conditions, no useful aerodynamic data was recorded. Most pressure gages exhibited pressure "spikes" in the EI + 480-660 sec and 930-970 sec regions, with these trends identified on both wings Figure 4.7-2. OEX pressure data utilization was limited to identification of these off-nominal signatures. The first gages to exhibit this behavior and the failure patterns were provided to the Time Line Group for inclusion of OEX pressure data into the master time line in support of the working scenario.

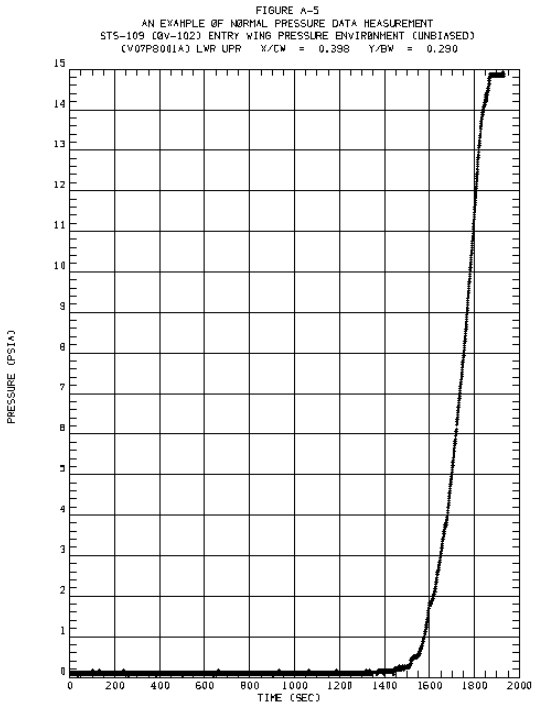

Figure 4.7-1 Typical OEX Entry Pressure Gage Signature (STS-109)

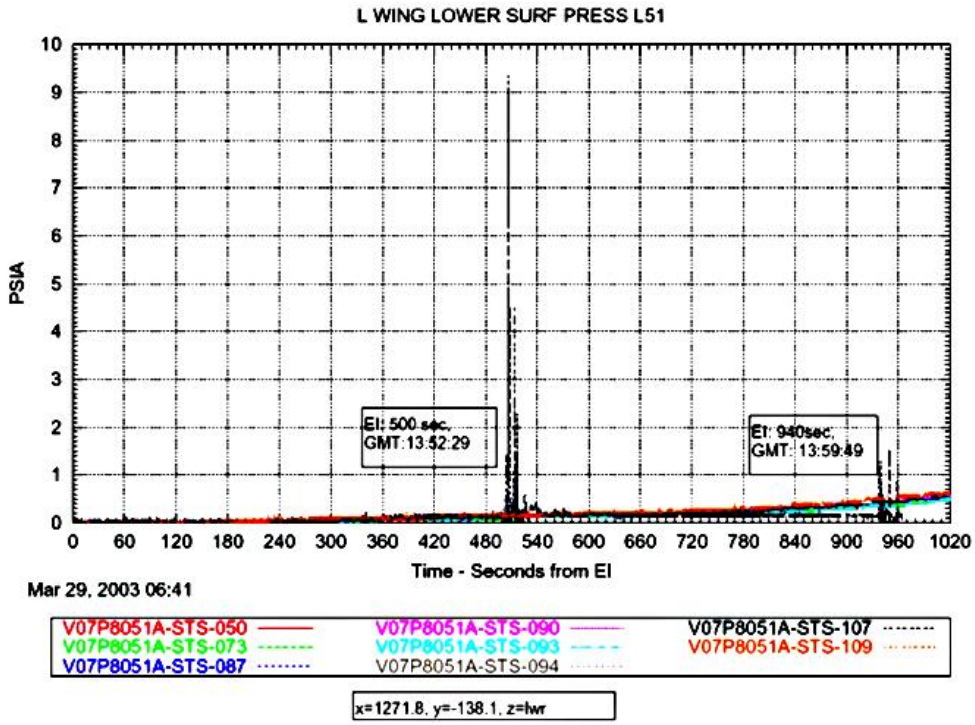

Figure 4.7-2 Typical OEX Entry Pressure Gage Signature (STS-107)

4.7.3 Wind Tunnel Test Matrix – Comprehensive Listing

Test	Run	Re/ft	Alpha	Beta	Mach	Gamma	Model	Configuration
6853	9	3.0	37.5	0.0	6.00	1.40	ceramic 1	baseline - ceramic 1; Re/ft = 3.0e6
6853	10	2.9	37.6	0.0	6.00	1.40	ceramic 1	baseline - ceramic 1, repeat; Re/ft = 3.0e6
6853	11	2.9	37.5	0.0	6.00	1.40	ceramic 1	baseline - ceramic 1, repeat; Re/ft = 3.0e6
6853	12	3.0	37.6	0.0	6.00	1.40	ceramic 1	trip at rcc panel 6 (1 trip, 0.0035 in)
6853	13	2.9	37.6	0.0	6.00	1.40	ceramic 1	trip at rcc panel 6 (1 trip, 0.0045 in)
6853	14	2.9	37.6	0.0	6.00	1.40	ceramic 1	trip at rcc panel 9 (1 trip, 0.0045 in)
6853	15	3.0	37.6	0.0	6.00	1.40	ceramic 1	trip at rcc panel 9 (1 trip, 0.0045 in)
6853	16	3.0	37.6	0.0	6.00	1.40	ceramic 1	trip at rcc panel 6 (1 trip, 0.0050 in)
6853	17	3.0	37.5	0.0	5.99	1.40	ceramic 1	trip at rcc panel 6 (1 trip, 0.0045 in)
6853	18	3.0	37.6	0.0	5.99	1.40	ceramic 1	trip at MLG door le,outboard corner (1 trip, 0.0045 in)
6853	19	3.0	37.6	0.0	5.99	1.40	ceramic 1	trips along MLG door le (7 trips, 0.0045 in)
6853	20	3.0	37.6	0.0	5.99	1.40	ceramic 1	trips along MLG door le (7 trips, 0.0045 in)
6853	21	3.0	37.6	0.0	5.99	1.40	ceramic 1	trips along MLG door le,down side (12 trips, 0.0045 in)
6853	22	3.0	37.6	0.0	5.99	1.40	ceramic 1	raised MLG door (1 "trip", 0.0065 in)
6853	23	3.0	37.5	0.0	5.98	1.40	ceramic 1	raised MLG door w/ slash (1 "trip", 0.0065 in)
6853	24	3.0	37.6	0.0	5.98	1.40	ceramic 1	trip at rcc panel 6; match test 6852 (1 trip, 0.0035 in)
6853	25	3.0	37.6	0.0	5.98	1.40	ceramic 1	trip at rcc panel 6, biased windward (1 trip, 0.0035 in)
6853	26	3.0	37.6	0.0	5.98	1.40	ceramic 1	trip at rcc panel 6, biased leeward (1 trip, 0.0035 in)
6853	27	2.9	37.5	0.0	5.98	1.40	ceramic 1	trip at rcc panel 6, biased windward (1 trip, 0.0065 in)
6853	28	3.0	37.6	0.0	5.98	1.40	ceramic 1	"full" ablt (10 trips along wing le)
6853	29	3.0	37.6	0.0	5.98	1.40	ceramic 1	"full" ablt (10 trips along wing le, 2 fwd)
6853	31	3.0	37.6	0.0	5.98	1.40	ceramic 1	baseline - ceramic 1, repeat; Re/ft = 3.0e6
6853	33	2.1	37.5	0.0	5.96	1.40	steel 1	baseline - steel 1; Re/ft = 2.0e6
6853	34	3.0	37.8	0.0	5.98	1.40	steel 1	baseline - steel 1; Re/ft = 3.0e6
6853	36	2.0	37.5	0.0	5.96	1.40	steel 1	open wheel well, L/H = 3.8, Re/ft = 2.0e6
6853	37	3.0	37.8	0.0	5.98	1.40	steel 1	open wheel well, L/H = 3.8, Re/ft = 3.0e6
6853	39	3.0	37.8	0.0	5.98	1.40	steel 1	open wheel well, L/H = 6.4, Re/ft = 3.0e6
6853	41	3.0	37.8	0.0	5.98	1.40	steel 1	open wheel well, L/H = 17.5, Re/ft = 3.0e6
6853	42	2.1	37.5	0.0	5.97	1.40	steel 1	open wheel well, L/H = 17.5, Re/ft = 2.0e6
6853	44	3.0	37.8	0.1	5.98	1.40	steel 1	open wheel well w/ door; L/H = 3.8
6853	46	3.0	37.9	0.1	5.98	1.40	steel 1	open wheel well w/ door and gear; L/H = 3.8
6853	48	3.0	37.8	0.0	5.98	1.40	steel 1	open wheel well w/ gear; L/H = 3.8
6853	49	3.0	37.8	0.0	5.98	1.40	steel 1	baseline - steel 1, repeat; Re/ft = 3.0e6
6853	51	3.0	37.6	0.0	5.98	1.40	ceramic 1	missing rcc panel 6
6853	52	3.0	37.6	0.0	5.98	1.40	ceramic 1	gouge in MLG door
6853	53	3.0	37.6	0.0	5.98	1.40	ceramic 1	holes through carrier panels 6, 9, 12, 16
6853	54	3.0	37.6	0.0	5.98	1.40	ceramic 1	baseline - ceramic 1, repeat; Re/ft = 3.0e6
6853	55	0.0	37.8	0.7	5.97	1.40	steel 1	baseline - steel 1; Re/ft = 3.0e6; beta = 0.7
6853	57	3.0	37.8	0.7	5.97	1.40	steel 1	open wheel well, L/H = 3.8; beta = 0.7
6853	58	3.0	37.8	0.7	5.98	1.40	steel 1	open wheel well w/ gear; L/H = 3.8; beta = 0.7
6853	59	3.0	37.9	0.8	5.98	1.40	steel 1	open wheel well w/ door + gear; L/H = 3.8; beta = 0.7
6853	60	3.0	37.8	0.7	5.98	1.40	steel 1	open wheel well w/ door; L/H = 3.8; beta = 0.7
6853	61	3.0	37.9	-0.8	5.98	1.40	steel 1	open wheel well w/ door + gear; L/H = 3.8; beta = -0.8
6853	62	3.0	37.8	-0.8	5.98	1.40	steel 1	open wheel well w/ door; L/H = 3.8; beta = -0.8
6853	63	3.0	37.8	-0.9	5.98	1.40	steel 1	baseline - steel 1; beta = -0.8

Table 4.7-1 Test LaRC 6853-Mach 6 Air Hypersonic Wind Tunnel Facility - STS-107 Investigation

Test	Run	Re/ft	Alpha	Beta	Mach	Gamma	Model	Configuration
144	10	0.46	38.1	0.0	5.93	1.22	steel 1	baseline - steel 1
144	11	0.46	40.2	0.0	5.90	1.21	steel 1	baseline - steel 1, repeat
144	12	0.45	42.2	0.0	5.89	1.21	steel 1	baseline - steel 1, repeat
144	13	0.44	38.2	0.0	5.95	1.22	steel 1	baseline - steel 1, repeat
144	14	0.45	40.2	0.0	5.93	1.22	steel 1	open wheel well, L/H = 3.8
144	16	0.45	42.2	0.0	5.91	1.21	steel 1	open wheel well, L/H = 17.5
144	17	0.45	38.2	0.0	5.90	1.21	steel 1	open wheel well w/ door and gear; L/H = 3.8
144	18	0.44	40.2	0.0	5.89	1.21	steel 1	open wheel well w/ door; L/H = 3.8
144	19	0.46	42.2	0.0	5.94	1.22	steel 1	open wheel well w/ gear; L/H = 3.8
144	20	0.45	38.2	0.0	5.93	1.22	steel 1	open wheel well, L/H = 6.4
144	28	0.15	40.0	0.0	6.00	1.23	steel 1	baseline - steel 1; Re/ft = 0.15
144	29	0.41	40.2	0.0	5.88	1.21	steel 1	baseline - steel 1, repeat
144	43	0.47	37.2	0.0	5.96	1.22	ceramic 1	baseline - ceramic 1
144	44	0.45	40.1	0.0	5.94	1.22	ceramic 1	baseline - ceramic 1, repeat
144	45	0.47	42.2	0.0	5.94	1.22	ceramic 1	baseline - ceramic 1, repeat
144	47	0.47	40.1	0.0	5.92	1.22	ceramic 1	missing rcc panel 9
144	48	0.45	40.1	0.0	5.90	1.21	ceramic 1	missing rcc panels 6 and 9
144	49	0.46	40.2	0.0	5.90	1.21	ceramic 1	missing rcc panel 6
144	50	0.44	40.1	0.0	5.89	1.21	ceramic 1	baseline - ceramic 1, repeat
144	51	0.47	38.0	0.0	5.94	1.22	ceramic 1	missing rcc panel 6, repeat
144	52	0.47	40.1	0.0	5.93	1.22	ceramic 1	missing rcc panels 6 and 7
144	54	0.44	37.7	0.0	5.91	1.21	ceramic 2	baseline - ceramic 2
144	55	0.47	39.8	0.0	5.95	1.22	ceramic 2	baseline - ceramic 2, repeat
144	56	0.46	41.8	0.0	5.93	1.21	ceramic 2	baseline - ceramic 2, repeat
144	58	0.48	40.0	0.0	5.96	1.22	ceramic 2	missing rcc panel 4
144	59	0.48	40.0	0.0	5.95	1.22	ceramic 2	missing rcc panels 2 and 4
144	60	0.45	40.0	0.0	5.92	1.22	ceramic 2	missing rcc panel 2
144	61	0.46	40.3	0.0	5.90	1.21	ceramic 1	missing rcc panels 5, 6, and 7
144	62	0.45	40.0	0.0	5.89	1.21	ceramic 4	baseline - ceramic 4
144	64	0.45	37.9	0.0	5.89	1.21	ceramic 4	baseline - ceramic 4, repeat
144	65	0.47	42.0	0.0	5.94	1.22	ceramic 4	baseline - ceramic 4, repeat
144	66	0.47	40.2	0.0	5.93	1.22	ceramic 4	missing rcc panel 10
144	67	0.46	40.2	0.0	5.91	1.21	ceramic 4	missing rcc panels 10 and 12
144	68	0.46	40.2	0.0	5.90	1.21	ceramic 4	missing rcc panel 12
144	69	0.46	40.3	0.0	5.90	1.21	ceramic 1	missing rcc panels 5, 6, 7, and 8
144	70	0.45	40.4	0.0	5.89	1.21	ceramic 1	baseline - ceramic 1, repeat
144	71	0.47	40.3	0.0	5.94	1.22	ceramic 1	missing rcc panel 9, repeat
144	72	0.46	40.3	0.1	5.93	1.22	ceramic 1	missing rcc panels 5, 6, 7, 8, and 9
144	73	0.46	40.2	0.0	5.91	1.21	ceramic 4	missing rcc panels 9 and 10
144	74	0.46	40.2	0.0	5.90	1.21	ceramic 4	missing rcc panels 9 and 10, repeat
144	75	0.45	40.2	0.0	5.88	1.21	ceramic 4	missing rcc panels 9, 10 and 12
144	76	0.46	39.8	0.0	5.89	1.21	ceramic 2	baseline - ceramic 2, repeat
144	77	0.47	39.8	0.0	5.94	1.22	ceramic 2	hole through carrier panel 6
144	78	0.46	40.0	0.0	5.93	1.22	ceramic 2	hole through carrier panel 9
144	79	0.46	40.0	0.0	5.91	1.21	ceramic 2	hole through carrier panel 12
144	80	0.45	37.7	0.0	5.90	1.21	ceramic 2	baseline - ceramic 2, repeat
144	81	0.45	41.9	0.0	5.89	1.21	ceramic 2	baseline - ceramic 2, repeat
144	82	0.45	38.0	0.0	5.88	1.21	ceramic 1	baseline - ceramic 1, repeat
144	83	0.47	40.1	0.0	5.94	1.22	ceramic 1	baseline - ceramic 1, repeat
144	84	0.46	40.0	0.0	5.92	1.22	ceramic 2	missing rcc panel 4, repeat
144	85	0.46	40.0	0.1	5.91	1.21	ceramic 2	missing rcc panels 2 and 4, repeat
144	86	0.45	40.2	0.1	5.90	1.21	ceramic 4	missing rcc panels 9, 10, 11 and 12
144	88	0.27	37.3	0.0	5.92	1.22	ceramic 5	baseline - ceramic model 5; Re/ft = 0.26e6
144	89	0.44	37.8	0.0	5.87	1.21	ceramic 5	baseline - ceramic model 5; Re/ft = 0.46e6
144	90	0.30	39.3	0.0	6.00	1.23	ceramic 5	baseline - ceramic model 5, repeat; Re/ft = 0.26e6
144	91	0.46	39.9	0.0	5.93	1.22	ceramic 5	baseline - ceramic model 5, repeat; Re/ft = 0.46e6
144	92	0.28	39.3	0.0	5.96	1.22	ceramic 5	baseline - ceramic model 5, repeat; Re/ft = 0.26e6
144	93	0.45	39.9	0.0	5.90	1.21	ceramic 5	baseline - ceramic model 5, repeat; Re/ft = 0.46e6
144	94	0.27	41.4	0.0	5.92	1.22	ceramic 5	baseline - ceramic model 5, repeat; Re/ft = 0.26e6
144	95	0.44	42.0	0.0	5.87	1.21	ceramic 5	baseline - ceramic model 5, repeat; Re/ft = 0.46e6
144	96	0.27	41.3	0.0	5.98	1.23	ceramic 5	baseline - ceramic model 5, repeat; Re/ft = 0.26e6
144	97	0.45	41.9	0.0	5.92	1.22	ceramic 5	baseline - ceramic model 5, repeat; Re/ft = 0.46e6
144	98	0.27	39.5	0.0	5.94	1.22	ceramic 5	missing rcc panel 9; Re/ft = 0.26e6
144	99	0.45	40.1	0.1	5.89	1.21	ceramic 5	missing rcc panel 9; Re/ft = 0.46e6
144	100	0.28	39.5	0.0	5.94	1.22	ceramic 5	missing rcc panels 6 and 9; Re/ft = 0.26e6
144	101	0.45	40.1	0.1	5.87	1.21	ceramic 5	missing rcc panels 6 and 9; Re/ft = 0.46e6
144	102	0.46	39.9	0.0	5.89	1.21	ceramic 5	baseline - ceramic model 5, repeat; Re/ft = 0.46e6
144	103	0.47	40.0	0.0	5.94	1.22	ceramic 5	missing rcc panel 8, right wing
144	104	0.46	39.9	0.0	5.92	1.22	ceramic 5	baseline - ceramic model 5, repeat; Re/ft = 0.46e6
144	105	0.46	40.1	0.0	5.90	1.21	ceramic 5	missing rcc panel 5, right wing
144	106	0.46	39.9	1.1	5.90	1.21	ceramic 5	baseline - ceramic model 5; Re/ft = 0.46e6; beta = 1

Table 4.7-2 Test LaRC 144 - CF4 Hypersonic Wind Tunnel Facility - STS-107 Investigation

Test	Run	Re/ft	Alpha	Beta	Mach	Gamma	Model	Configuration
148	13	0.45	38.2	0.0	5.91	1.21	ceramic A	baseline - ceramic A, repeat
148	14	0.47	38.1	0.0	5.95	1.22	ceramic A	single windward groove, L/H = 10.0
148	15	0.47	38.1	0.0	5.92	1.22	ceramic A	single windward groove, L/H = 18.9
148	16	0.46	38.1	0.0	5.91	1.21	ceramic A	single windward groove, L/H = 27.8
148	17	0.45	38.4	0.0	5.90	1.21	ceramic C	baseline - ceramic C
148	19	0.46	38.4	0.0	5.90	1.21	ceramic C	baseline - ceramic C
148	20	0.43	38.4	0.0	5.88	1.21	ceramic C	missing lower rcc 9
148	21	0.47	38.4	0.0	5.93	1.22	ceramic C	missing lower rcc 7
148	22	0.46	38.4	0.0	5.92	1.22	ceramic C	baseline - ceramic C, repeat
148	23	0.46	38.1	0.0	5.92	1.22	ceramic A	double windward groove, L/H = 27.8; missing rcc 9
148	24	0.46	38.1	0.0	5.91	1.21	ceramic A	double windward groove, L/H = 27.8
148	25	0.46	38.2	0.0	5.90	1.21	ceramic A	double windward groove, L/H = 18.9
148	26	0.47	38.1	0.0	5.95	1.22	ceramic A	double windward groove, L/H = 18.9, repeat
148	27	0.45	38.1	0.0	5.92	1.22	ceramic A	double windward groove, L/H = 27.8; missing rcc 9, repeat
148	28	0.47	38.2	0.0	5.92	1.22	ceramic A	double windward groove, L/H = 27.8, repeat
148	29	0.45	38.1	0.0	5.89	1.21	ceramic A	baseline - ceramic A, repeat
148	30	0.46	38.2	0.0	5.89	1.21	ceramic A	missing rcc panel 9
148	31	0.45	38.0	0.0	5.95	1.22	ceramic A	baseline - ceramic A, repeat
148	32	0.46	38.1	0.0	5.93	1.22	ceramic A	single windward groove, L/H = 27.8; missing rcc 9
148	34	0.45	38.3	0.0	5.91	1.21	ceramic B	baseline - ceramic B
148	35	0.45	38.3	0.0	5.90	1.21	ceramic B	baseline - ceramic B, repeat
148	36	0.44	38.4	0.0	5.89	1.21	ceramic B	missing lower rcc panel 4
148	37	0.47	38.3	0.0	5.95	1.22	ceramic B	missing lower rcc panel 4, repeat
148	38	0.43	38.2	0.0	5.92	1.22	ceramic B	missing lower rcc panel 6
148	39	0.44	38.2	0.0	5.90	1.21	ceramic B	missing lower rcc panel 6, repeat
148	40	0.43	38.3	0.0	5.89	1.21	ceramic B	missing lower rcc panel 8
148	41	0.44	38.3	0.0	5.89	1.21	ceramic B	missing lower rcc panel 8, repeat
148	43	0.42	38.4	0.0	5.89	1.21	ceramic 5	baseline - ceramic 5
148	44	0.46	38.4	0.0	5.94	1.22	ceramic 5	missing rcc panel 9
148	45	0.45	38.4	0.0	5.92	1.22	ceramic 5	missing rcc panel 9, repeat
148	46	0.44	38.4	0.0	5.92	1.22	ceramic 5	baseline - ceramic 5
148	47	0.34	38.0	0.0	5.94	1.22	ceramic B	missing lower rcc panel 8; Re/ft = 0.35e6
148	48	0.33	37.9	0.0	5.92	1.22	ceramic B	missing lower rcc panel 8, with through hole; Re/ft = 0.35e6
148	49	0.32	37.9	0.0	5.90	1.21	ceramic B	baseline - ceramic B; Re/ft = 0.35e6
148	50	0.20	37.5	0.0	5.97	1.23	ceramic C	baseline - ceramic C; Re/ft = 0.20e6
148	51	0.33	38.0	0.0	5.91	1.21	ceramic C	baseline - ceramic C; Re/ft = 0.35e6
148	52	0.33	38.1	0.0	5.90	1.21	ceramic C	missing lower rcc panel 5
148	53	0.32	38.1	0.0	5.88	1.21	ceramic C	missing lower rcc panel 5, repeat
148	54	0.32	38.1	0.0	5.88	1.21	ceramic C	baseline - ceramic C, repeat; Re/ft = 0.35e6
148	55	0.31	38.1	0.0	5.87	1.21	ceramic C	missing lower rcc panel 7
148	57	0.21	37.8	0.0	5.99	1.23	ceramic 2	simulated leeside venting (fence); Re/ft = 0.20
148	61	0.45	38.5	0.0	5.90	1.21	ceramic 5	baseline - ceramic 5, tail removed
148	62	0.46	38.5	0.0	5.90	1.21	ceramic 5	baseline - ceramic 5, tail removed
148	63	0.47	38.5	0.0	5.95	1.22	ceramic 5	missing rcc panel 9, tail removed
148	64	0.45	38.5	0.0	5.92	1.22	ceramic 5	missing rcc panel 9, tail removed, repeat
148	65	0.44	38.1	0.0	5.90	1.21	ceramic A	triple windward groove, L/H = 27.8
148	67	0.45	38.2	0.0	5.89	1.21	ceramic A	triple windward groove, L/H = 22.5; faired aft edge
148	68	0.47	38.0	0.0	5.95	1.22	ceramic A	triple windward groove, L/H = 27.8, missing rcc 9
148	69	0.46	38.1	0.0	5.93	1.22	ceramic A	triple windward groove, L/H = 27.8, missing rcc 9, repeat
148	70	0.45	38.2	0.0	5.91	1.21	ceramic B	missing lower rcc panel 8, with through slot
148	75	0.20	37.8	0.0	5.98	1.23	ceramic 2	simulated leeside venting (fence); Re/ft = 0.20
148	76	0.46	37.8	0.1	5.92	1.22	ceramic 2	simulated leeside venting (fence); Re/ft = 0.46
148	81	0.20	40.0	0.0	6.01	1.24	ceramic 2	simulated leeside venting (fence), missing rcc 9; Re/ft = 0.20
148	82	0.43	40.0	0.0	5.89	1.21	ceramic 2	simulated leeside venting (fence), missing rcc 9; Re/ft = 0.46
148	86	0.50	40.2	0.0	5.98	1.23	sla D	leeside vent
148	87	0.48	40.2	0.0	5.95	1.22	sla D	leeside vent w/ windward cavity
148	88	0.46	40.2	0.0	5.93	1.22	sla D	leeside vent w/ missing T-seal (8/9)
148	89	0.17	40.2	0.0	5.90	1.21	sla D	leeside vent w/ missing T-seal (8/9); Re/ft = 0.17
148	90	0.44	40.3	0.0	5.88	1.21	sla D	leeside vent (sealed) w/ windward cavity
148	91	0.47	40.3	0.0	5.95	1.22	sla D	leeside vent (sealed) w/ windward cavity, repeat
148	92	0.47	40.3	0.0	5.94	1.22	sla D	leeside vent w/ windward cavity

Table 4.7-3 Test LaRC 148 - CF4 Hypersonic Wind Tunnel Facility - STS-107 Investigation

4.7.4 FELISA Inviscid CFD - Comments and Additional Analysis

The work presented in Section 4.3.2, Damage Assessment Using Computational Fluid Dynamics, summarized the delta aerodynamics produced by numerous damage scenarios. This sections contains supporting computations that verified some of the assumptions used in the analysis and a discussion of how convergence is assessed.

4.7.4.1 Flow Solver Convergence

Two criteria are used in assessing convergence of a FELISA solution. The methodology in FELISA preserves total enthalpy, and thus the maximum and minimum total enthalpies are tracked. Since the primary utilization of FELISA is to compute aerodynamic loads, their convergence is also evaluate. Figure 4.7-3 shows the typical set of plots that are evaluated to assess convergence. Even though the residual is still dropping, the aerodynamic loads and the enthalpies have converged to a steady state. For many of the damage scenarios evaluated, the solver did not converge to a steady state solution. This is not unexpected given the types of damage (particularly the WLE damage) being evaluated. The convergence history of the loads for the baseline and the damaged configuration were co-plotted, to determine if the oscillation of the aerodynamic loads was larger than the delta aerodynamics. Figure 4.7-4 shows the aerodynamic loads convergence for a damaged (windward surface depression) and a baseline solution, where the damaged solution has reached a steady state. Figure 4.7-5 shows the same plot for a damaged solution (half panel 9 with upper carrier panel removed) that shows definite oscillations in the loads. The oscillations, however are small compared to the difference between the damaged and the baseline. The practical implication of the unsteady nature of many of the computations is that there is an bound on the delta aerodynamics, and that the idea that it is the trend of many computations that is important in the analysis of these damage scenarios.

4.7.4.2 Comparison of Absolute Aerodynamics for Flight, CF4, and Mach 6 Air

All of the delta aerodynamic analysis described in Section 4.3.2 was based on the assumption that even if the total aerodynamics did not compare exactly with the 'true' aerodynamics, the delta aerodynamics for the damaged configurations would compare well with the 'true' delta aerodynamics due to damage. Indeed, when the delta aerodynamics for wind tunnel, inviscid flight, viscous flight, and even Mach 6 perfect gas air simulations were compared, the trends gave a consistent picture. Figure 4.7-6 shows the total aerodynamics plotted against time from EI for the baseline and missing RCC panel 6+7 at flight conditions, and the baseline and missing RCC panel 6 for CF4 and Mach 6 air conditions. This figure shows that the difference between the flight, CF4, and Mach 6 air aerodynamics is much larger than the deltas between the baseline and the damaged aerodynamics for a given configuration.

4.7.4.3 Aerodynamics for Full (360°) Configurations, Baseline and Damaged

In order to assess the impact of using half body configurations for the delta aerodynamics, a set of computations was made with a full configuration, with an undamaged right side, and a missing RCC panel 9 on the left. The asymmetric aerodynamics (side force, rolling and yawing moments) are shown in Figure 4.7-7(a), and the symmetric loads (axial and normal force, and pitching moment) in Figure 4.7-7(b), plotted against sideslip. The half body aerodynamics (at β=0°) are shown, and indicate that there is little difference between the full and half-body aerodynamics.

4.7.4.4 Systematic Angle of Attack and Mach number Effect in Delta Aerodynamics

The delta aerodynamics presented in Figure 4.3-42 show the missing RCC panel aerodynamics for a range of flight conditions, which have varying Mach and angle of attack. Several computations were run to isolate the Mach number and the angle of attack effect in the delta aerodynamics, for the missing RCC panels 6+7 configuration. Figure 4.7-8 shows the delta aerodynamics plotted against Mach number (which is opposite in trend from time from EI) for an angle of attack of 40° Only the delta yawing moment showed a strong trend, decreasing with increasing Mach number. The delta

rolling and pitching moments showed a very shallow trend toward positive with increasing Mach number. Figure 4.7-9 shows the aerodynamics and delta aerodynamics plotted against angle of attack, for a constant Mach number of 20.2 (CFD condition 4). While the typical trends with angle of attack are observed in the symmetric aerodynamics (normal force in particular), the delta aerodynamics show are not affected by angle of attack,

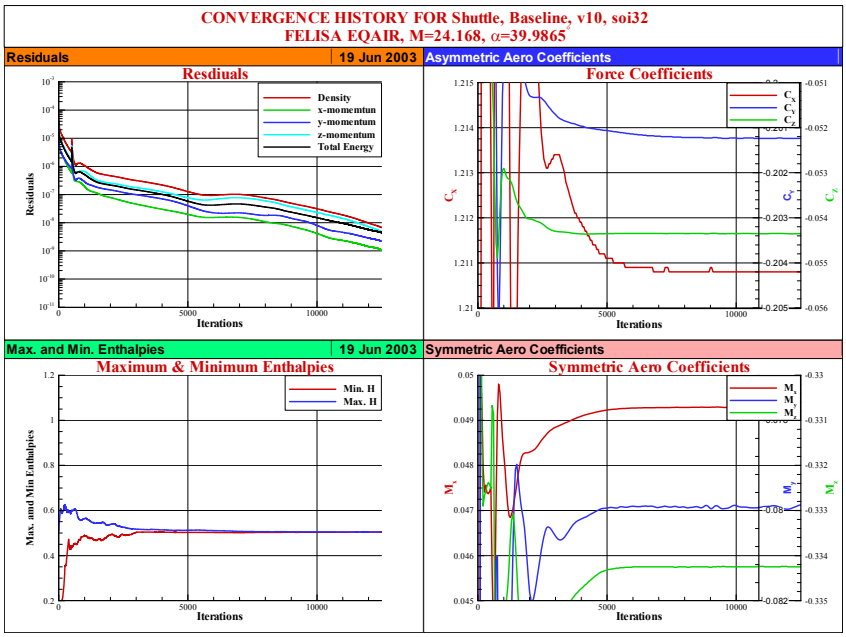

Figure 4.7-3 Typical Convergence History Plots from FELISA

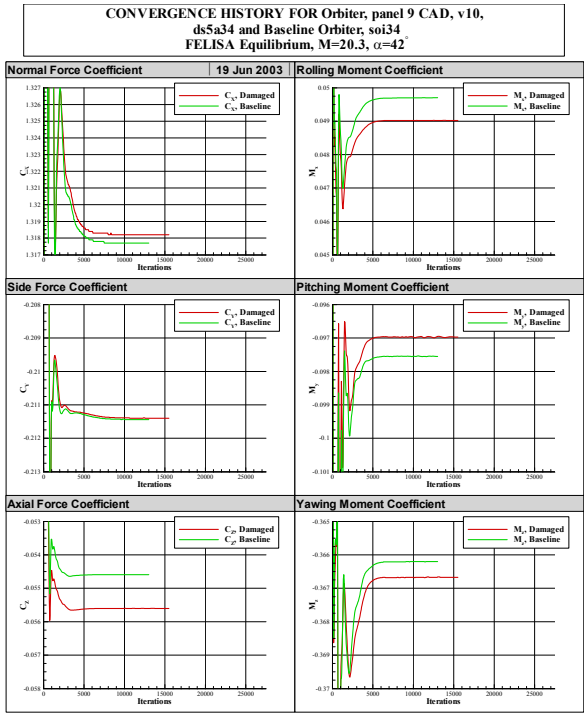

Figure 4.7-4 Aerodynamic Force and Moment Convergence for Steady Solution

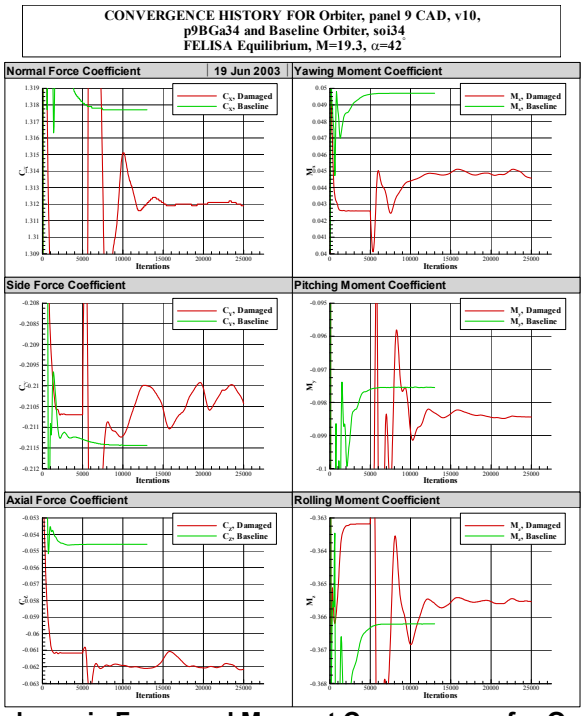

Figure 4.7-5 Aerodynamic Force and Moment Convergence for Oscillating Solution

FELISA Prediction of Aerodynamic Coefficients for Flight and Wind Tunnel Conditions, a = 40°

- At this scale, effect of missing panel small except in axial direction at
- Flight cases are for panels removed, CF_4 and Mach 6 are for panel 6 only.
- CF_4 doesn't match flight, but is closer than Mach

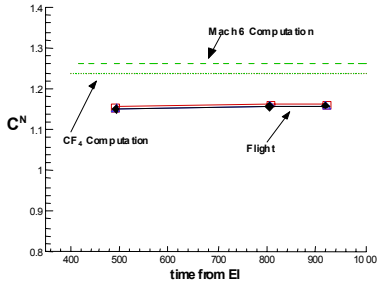

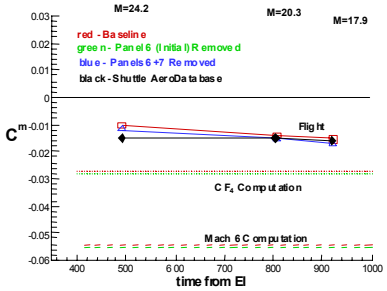

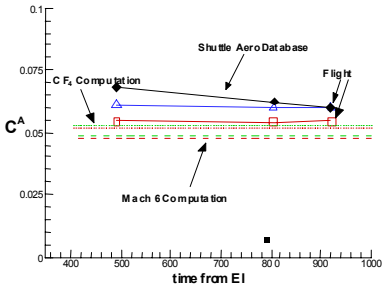

Figure 4.7-6 Comparison of Total Aerodynamics for Flight, CF4, & Mach 6 WT Conditions

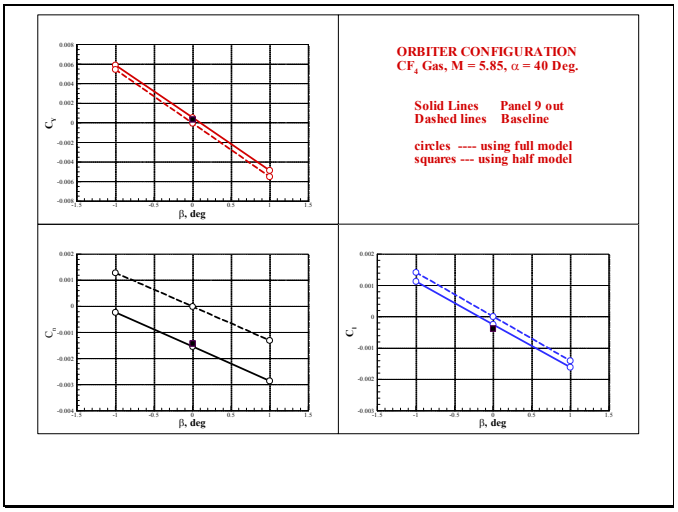

(a) Asymmetric Forces and Moments

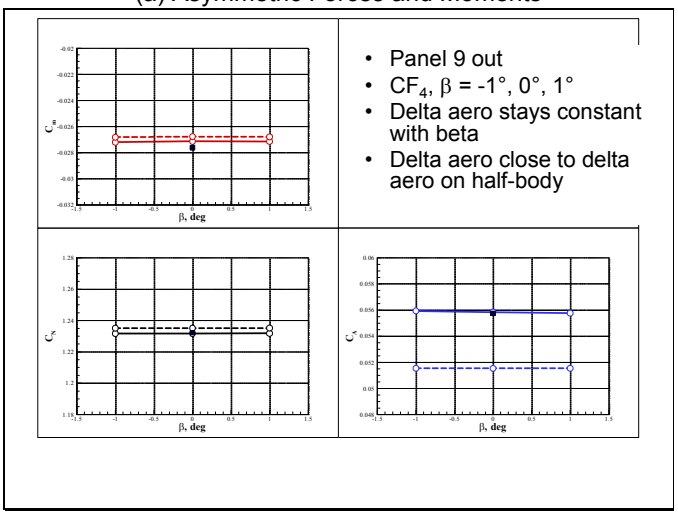

(b) Symmetric Forces and Moments

Figure 4.7-7 Forces and Moments for Baseline and Missing RCC Panel 9 for Range of Sideslip Angles

Effect of Mach Number, Hence Flow Chemistry, on Aerodynamic Coefficients and Deltas , a = 40°

- Pitch shows an increase with Mach, normal force a slight decrease
- Delta pitch flat, delta rolls shows slight increase, yaw shows significant decrease. Helps explain discrepancies between CF4 and flight computations.

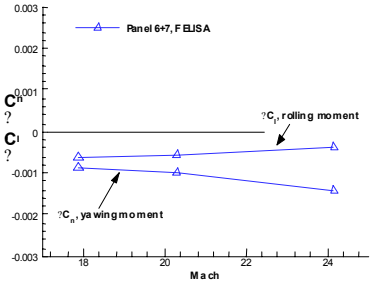

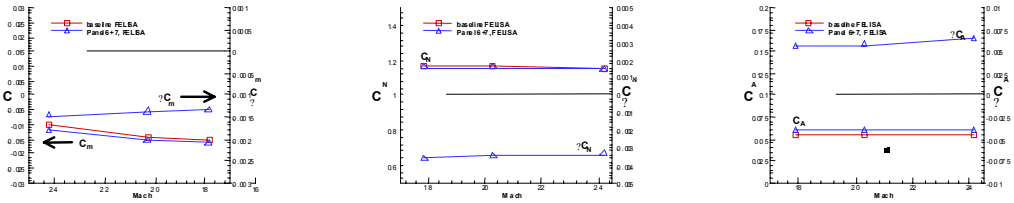

Figure 4.7-8 Effect of Mach Number on Delta Aerodynamics

Effect of Angle of Attack on Aerodynamic Coefficients and Deltas
FELISA, M = 20.3

- Forces and moments show typical trends with alpha
- Deltas have no significant trends for symmetric or asymmetric loads

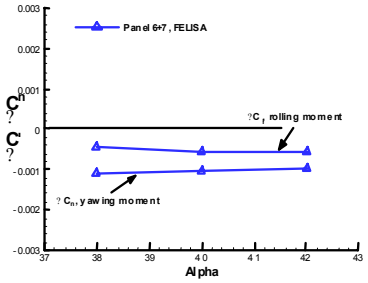

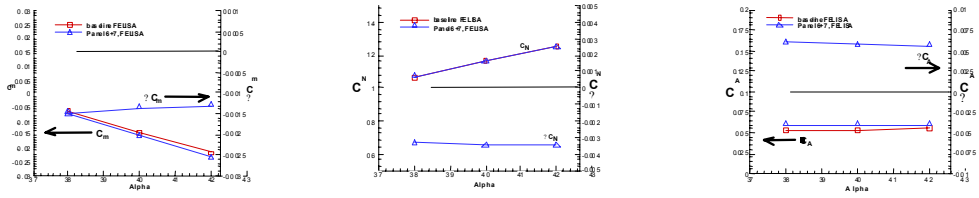

Figure 4.7-9 Effect of Angle of Attack on Delta Aerodynamics

4.7.5 OVERFLOW CFD Analysis of Leeside Flow field Interactions

4.7.5.1 Brief CFD Intro / Application Description

Missing RCC panel Navier Stokes solutions were done with the OVERFLOW code. Delta aero increments were extracted and the flow fields were analyzed for differences between missing panel solutions and the nominal configuration. Delta aero increments were obtained, including component aero from the wing, fuselage, and tail. The simulations were done to compare with the LaRC Mach 6 air tunnel. The wind tunnel model scale was 0.0075 of the full-scale orbiter corresponding to a vehicle length of approximately 9.678". The free stream conditions for the test and analysis were Mach = 5.96 at a Re / ft = 2.976 Million and Tinf = 112.27 R.

4.7.5.2 Configurations Analyzed

Three configurations were analyzed: baseline (no damage), panel 6 missing (original Karen Bibb geometry), and panel 9 missing. The grids were obtained from the External Aerothermal group's common grid for the nominal configuration (Aerothermodynamics Section 5.2.4.2). The common grid was modified to have overset boundaries in place of block zonal. The panel 6 and panel 9 grids were then created to match the resolution of the common grid in the missing panel region. The only difference between the grid systems was the addition of the missing panel grids. Figure 4.7-10 shows the surface grid for panel 9. The original grids were run for half the vehicle (without a VT). After evaluating the solutions, the flow field around the tail was desired so the symmetric grids were copied into both halves of the vehicle and combined to create the full geometry. The vertical tail, including the SILTS pod was added to the overset grid system. The missing panel grids didn't change, although only the RCC panel 9 missing configuration was computed on the vertical tail grid system.

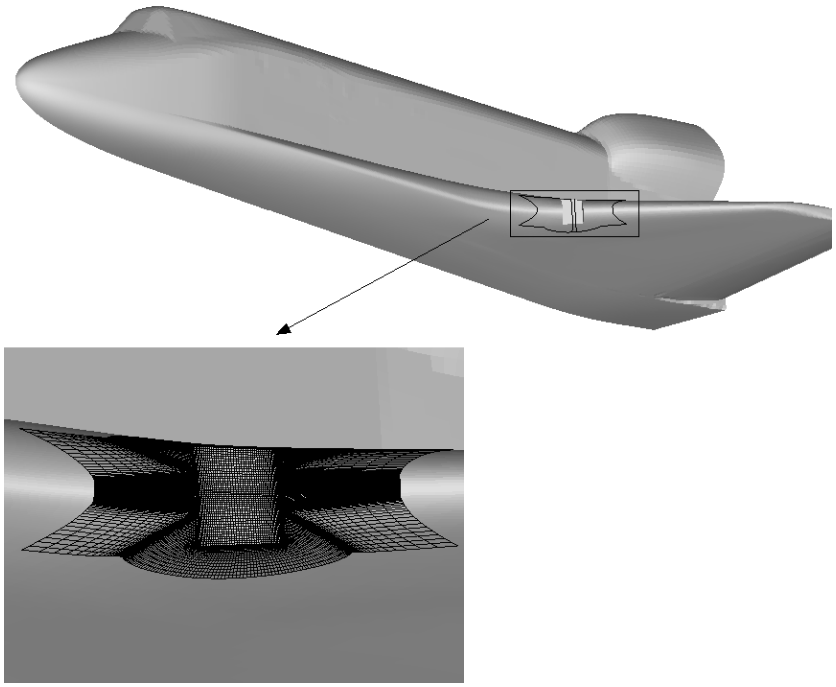

Figure 4.7-10 Surface Grid of a Missing RCC panel 9

4.7.5.3 Delta Aerodynamic Results

Table 4.7-4 shows the results for the original grid system (no VT). The delta aero increments in roll and yaw were very small for panel 6 removed.

	Cl	Cm	Cn
p6	0.09209	-0.00918	0.01287
p9	0.09156	-0.00881	0.01230
clean	0.09205	-0.00869	0.01302
Delta (p6 - clean)	0.00003	-0.00050	-0.00015
Delta (p9 - clean)	-0.00050	-0.00012	-0.00071

Table 4.7-4 Delta Aero Increments - Original grid system (no vertical tail)

The solutions done for the full grid system (baseline and the missing panel 9) with the vertical tail included gave similar delta aero as the original grid system without the tail. Table 4.7-5 shows these results.

	Cl	Cm	Cn
p9	-0.00034	-0.00615	-0.00043
clean	0.00001	-0.00623	-0.00002
Delta (p9 - clean)	-0.00035	0.00008	-0.00040

Table 4.7-5 Delta Aero Increments - Full grid system (w/vertical tail)

To better understand the source of the delta aero, the aero results were broken into the fuselage, wing, and vertical tail components. Table 4.7-6 shows these aero components. The fuselage and tail increments are very small in comparison to the wing increments. This points to the wing having the largest affect on the delta aero increments.

(p9 - clean)	ΔCl	ΔCm	ΔCn
FUSELAGE	0.000016	-0.000046	-0.000022
WING	-0.000355	0.000159	-0.000418
TAIL	-0.000010	-0.000041	0.000039
TOTAL	-0.000348	0.000084	-0.000403

Table 4.7-6 Delta Aero Increments (component breakdown) - Full grid system

4.7.5.4 Observations – Missing RCC Panels (Original Grid System)

Figure 4.7-11 shows the surface Cp for the baseline configuration. Figure 4.7-12 and Figure 4.7-13 show the surface Cp for the panels 6 and 9 removed, respectively. The black dots on the figures represent several of the flight temperature measurement gage locations.

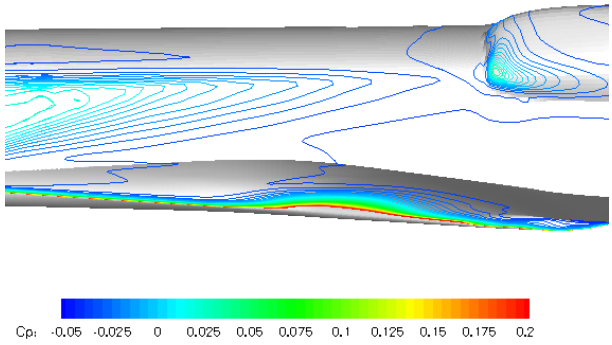

Figure 4.7-11 Surface Pressure (Cp) Baseline (no damage) Configuration.

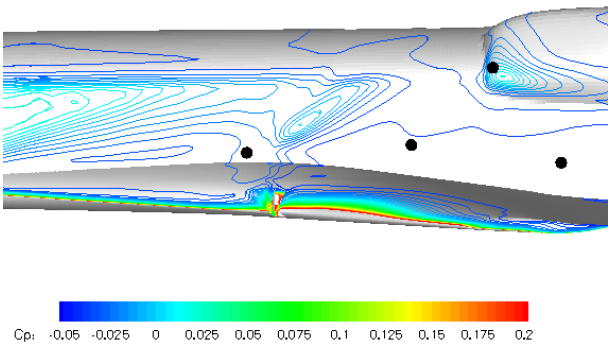

Figure 4.7-12 Surface Pressure (Cp) – Missing RCC Panel 6

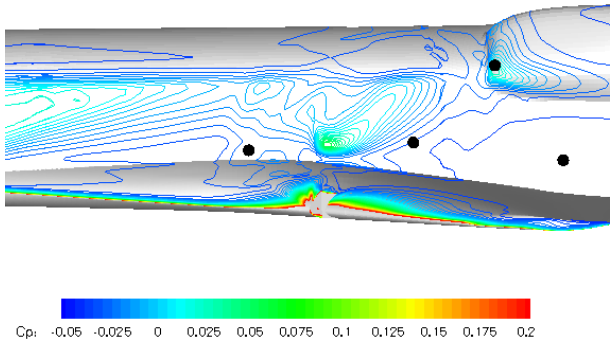

Figure 4.7-13 Surface Pressure (Cp) – Missing RCC panel 9

The interaction between the flow coming through the panel and the fuselage is very apparent for the panel 9 missing case. This impingement is much stronger with panel 9 missing than with panel 6 missing.

4.7.5.5 Observations – Missing RCC Panels (Full Grid System)

To further investigate the leeside interaction, the surface pressures on the vertical tail were analyzed to provide more information on tail pressure increments. Figure 4.7-14 shows the delta pressure coefficient (Cp panel 9 missing – nominal configuration) on the tail. It is evident from this figure the flow field on the tail is disturbed, but the maximum delta Cp values are on the order of 0.01, representing a very small change.

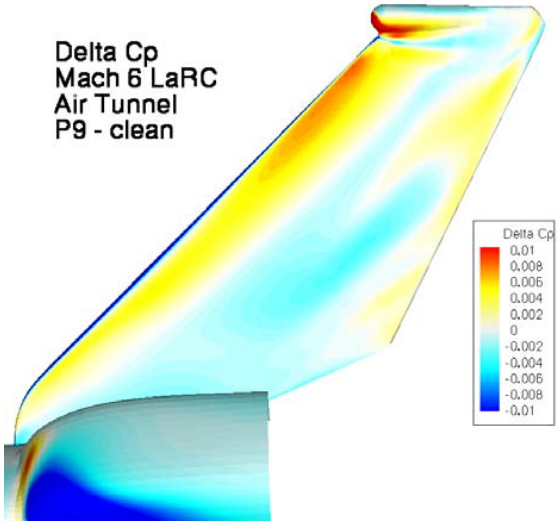

Figure 4.7-14 Delta Pressure (Cp) – Vertical Tail Surface (P9 – Baseline)

Figure 4.7-15 shows surface streamlines (k = 3 surface) for both the baseline configuration and the panel 9 missing. The largest difference between the 2 configurations is the flow on the lower part of the tail. The direction of the flow in this region changed directions.

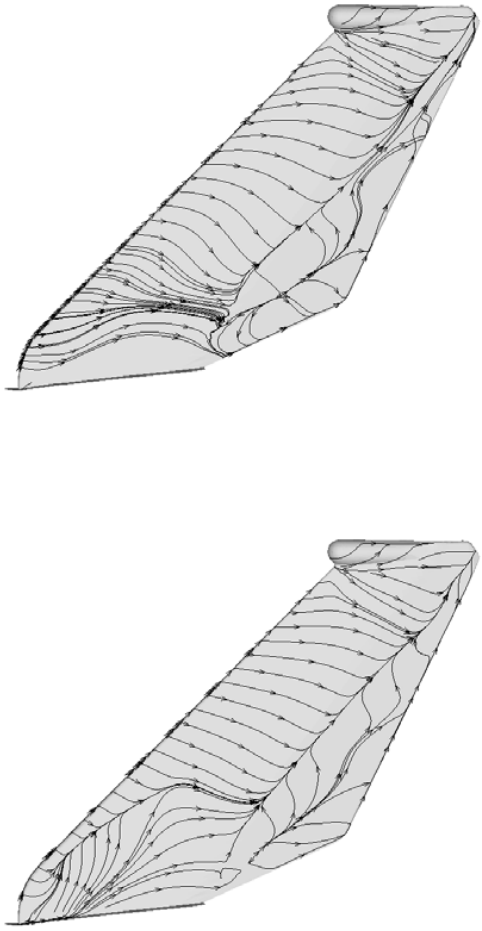

Figure 4.7-15 Surface Streamlines – Baseline and Panel 9 Configurations

The flow field on the leeside of the vehicle is directly affected by the vortex that emanates from the intersection of the wing and the fuselage (strake). Figure 4.7-16 represents this vortex by using volume ribbons. The vortex starting from the left strake never crosses the centerline of the vehicle for the baseline configuration. This is not the case for the missing panel 9 configuration. The vortex is disturbed towards the leading edge of the wing and is then pushed across the pitch plane in front of the tail. This dramatically affects the flow field on the leeside.

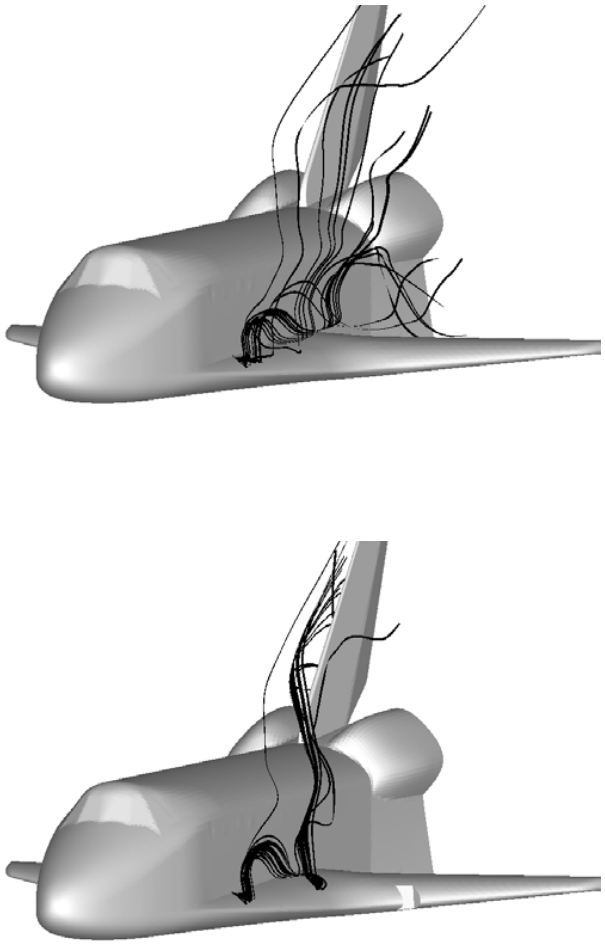

Figure 4.7-16 Volume Ribbons Emanating From the Strake - Baseline & RCC Panel 9 Missing

Based on the volume ribbon patterns, a delta pressure (Cp) plot (similar to Figure 4.7-14) was made showing the leeside of the vehicle, including the tail. Figure 4.7-17 shows this delta Cp plot. The figure shows that the flow on the port and starboard side of the tail is disturbed.

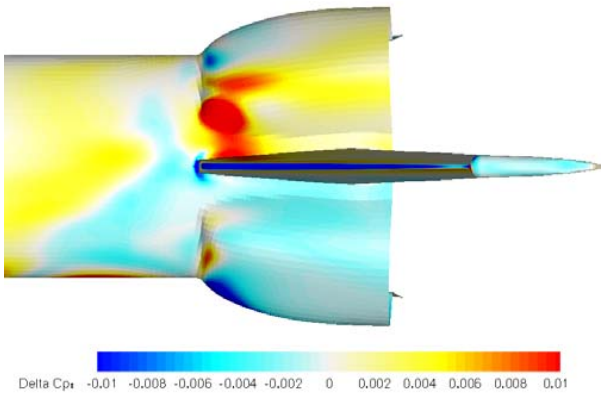

Figure 4.7-17 Delta Pressure (Cp) On the Vertical Tail Surface (P9 – Baseline).

4.7.5.6 Conclusions

The delta aerodynamic increments predicted by the OVERFLOW analysis at Mach 6 tunnel conditions are consistent with test measurements and other sources for Panel 6 or Panel 9 missing. Although the analysis of the tail flow field and the delta pressure coefficient demonstrate differences in the flow field, the delta aero increment from the tail was very small (an order of magnitude less than the increments from the wing).

4.7.6 Aerodynamic Investigation using CART3D CFD Analysis

4.7.6.1 Introduction

CART3D is a high fidelity, inviscid analysis package that uses adaptively refined Cartesian grids to discretize the volume around a defined surface geometry. It is used for conceptual and preliminary aerodynamic design and enables rapid CFD analysis on complex geometries.

4.7.6.2 STS-107 CART3D Case Definition

All the cases were completed at wind tunnel conditions of Mach 6 and 40-degrees angle of attack (corresponding to the LaRC Mach 6 air wind tunnel, Table 4.3-5).

4.7.6.3 Configurations Analyzed

In support of the STS-107 Investigation, different damage scenarios have been analyzed to try and reproduce the aerodynamics observed during Columbia's final flight. These damage scenarios were produced using two different geometries, one without a vertical tail and one including the tail. Karen Bibb, LaRC supplied the grids used to represent the baseline surface geometries. The LaRC GEOLAB defined the WLE RCC panel cutouts used to produce the different damaged configurations analyzed. Figure 4.7-18a shows the clean geometry without the vertical tail, and Figure 4.7-18b shows the clean geometry with the tail. The surface grid for the initial geometry without the vertical tail had a low resolution grid on the leeside, especially in the OMS pod region. Nominally, the resolution is appropriate because at hypersonic conditions, there are not significant aerodynamic interactions and flow features on the leeside of the vehicle. Since the initial analysis focused on WLE damage, this grid was sufficient to resolve the wing surface pressures. Once the analysis shifted to focus on the effects on the OMS pod and tail, the more refined surface grid with the vertical tail was required to ensure the leeside surface pressures were adequately resolved.

There were fourteen damage configurations analyzed using CART3D (listed in Table 4.7-7). Initial analysis focused on WLE damage. The first five configurations analyzed were for entire WLE RCC panels missing on the geometry without a vertical tail. The five configurations analyzed were: RCC 6 missing, RCC 9 missing, RCC 6 and 7 missing, RCC 5-7 missing, and RCC 1-7 missing. Figure 4.7-19 shows RCC 9 missing and an outline of RCC panels 1-7. Note that to model a missing RCC panel in this analysis, solid sidewalls in the cavity were included as a simplification over the actual geometry with an open channel between the RCC and the WLE spar. Additionally, the missing geometry accounts for removal of only the RCC panel and not the carrier panel geometry. Therefore, the back wall surface is approximately 4 to 6 inches forward of the WLE spar.

Based on debris forensics that suggested WLE damage could not include entire panels missing, partial RCC panel damage configurations were addressed. The next four cases analyzed were the lower (or windward half) of the RCC panel missing as well as a missing T-Seal. Three half-panel damage cases were computed: half of RCC 7 missing, half of RCC 8 missing, and half of RCC 9 missing. The T-Seal case was for T-Seal 9 removed, resulting in an open slot or gap between RCC panels 8 and 9. All four damaged configurations were analyzed using the geometry without the vertical tail.

Damage progression cases were analyzed next in an attempt to understand the sensitivity of the delta aerodynamics to increased levels of damage and further investigate leeside interaction effects. The final five cases were computed on the more refined (increased resolution) surface grid for the geometry with the vertical tail. The five cases were: half of RCC 7 missing, half of RCC 8 and all of RCC 9 missing, half of RCC 8 and hole #1 through the wing, lower (windward surface) carrier panel 8 and hole #2 through the wing, and half of RCC 8 and hole #2 through the wing. Hole #1 is the width of RCC 8, 20-inches long and is oriented directly behind RCC 8 funning inboard and aft. Hole #2 is 46-inches long, 28-inches wide and oriented behind RCC 9 and 10, running inboard and aft. Figure 4.7-20 thru Figure 4.7-25 show the holes and missing parts of the RCC and carrier panel.

4.7.6.4 Delta Aerodynamic Results

Table 4.7-7 lists the values of the aerodynamic coefficients for the clean configurations (with & without vertical tail) and the resulting delta values for the damaged configurations analyzed.

	Axial force (+ Aft)	Side force (+ Right)	Normal force (+ Up)	Rolling Moment (+ Right Wing down)	Pitching Moment (+ Nose Up)	Yawing Moment (+ Nose to the Right)
	Delta CA	**Delta CY**	**Delta CN**	**Delta Cl**	**Delta Cm**	**Delta Cn**
Without Vertical Tail						
Clean	**0.05100**	**0.14983**	**1.26233**	**0.18748**	**-0.06117**	**0.02718**
Panel 6	0.00115	0.00096	-0.00126	-0.00017	-0.00032	-0.00026
Panel 9	0.00202	0.00036	-0.00193	-0.00030	-0.00028	-0.00074
Panels 6-7	0.00255	0.00116	-0.00259	-0.00037	-0.00056	-0.00056
Panels 5-7	0.00336	0.00127	-0.00306	-0.00041	-0.00085	-0.00084
Panels 1-7	0.00358	0.00096	-0.00501	-0.00069	-0.00150	-0.00099
Half 7	-0.00023	0.00039	-0.00374	-0.00007	-0.00283	-0.00008
half 8	-0.00019	0.00046	-0.00394	-0.00013	-0.00263	-0.00011
Half 9	-0.00006	0.00032	-0.00371	-0.00005	-0.00281	-0.00012
T-Seal 9	-0.00024	0.00051	-0.00423	-0.00017	-0.00242	-0.00001
With Vertical Tail						
Clean	**0.05125**	**0.14347**	**1.25942**	**0.18578**	**-0.06233**	**0.03068**
Half 7	0.00021	0.00023	-0.00013	-0.00001	0.00003	-0.00010
Half 8 Full 9	0.00421	0.00159	-0.00454	-0.00067	-0.00028	-0.00156
Half 8 & Hole #1	0.00026	-0.00095	-0.00023	-0.00017	-0.00019	0.00025
Carrier Panel 8 & Hole #2	-0.00002	0.00004	-0.00036	0.00003	-0.00014	-0.00002
Half 8 & Hole #2	0.00061	0.00056	-0.00145	-0.00023	0.00037	-0.00024

Table 4.7-7 CART3D CFD Analysis - Results by Configuration - Delta Aero Coefficients

During latter portion (after EI + 700 sec) of the STS-107 entry flight, Columbia demonstrated a negative delta yaw and a positive delta roll when compared to a nominal entry trajectory. Most of the damage configurations analyzed by CART3D show a negative delta yaw and a negative delta roll, which corresponds to the earlier portion (before EI + 600 sec) of STS-107 entry. The windward half of RCC 8 missing with hole #1 in the wing configuration shows a negative delta roll and a positive delta yaw, a pattern not seen in flight. The windward carrier panel 8 missing with hole #2 in the wing configuration shows a positive delta roll and a negative delta yaw, but the deltas are relatively small.

Figure 4.7-27a shows the surface pressure in terms of pressure coefficient (Cp) on the leeward side of the shuttle for the clean configuration. Figure 4.7-27b through Figure 4.7-29 show the Cp on the leeward side for the complete RCC panel removed damaged configurations. Notice the increase in pressure on the side of fuselage near the region of augmented heating recorded by onboard instrumentation. For these Mach 6 computations on this lower grid resolution system, none of the whole RCC panel out cases affects the pressure on the OMS pod or the area around the base of the tail.

The results from the half RCC missing configurations however do show an increase in the pressure on the OMS Pod. Figure 4.7-29 shows the surface pressure distribution on the OMS Pod for the clean configuration. Figure 4.7-31 and Figure 4.7-32a show the surface pressure distribution on the OMS Pod for the half-panel missing cases, and Figure 4.7-32b is for the missing T-Seal. For half of RCC 7 and half of RCC 8, the pressure on the forward section of the OMS Pod increases. The pressure also increases for the missing T-Seal case, and there is a slight change for the half of RCC 9 missing case. Although there were no OMS pod surface pressure measurements, recovered OMS pod debris indicates significant impact damage most likely attributed from flow through the WLE damage. These cases would support the observation that the initial damage was inboard of RCC 9 as the pressure change on the OMS pod decreases as the damage moves outboard.

The five configurations with the tail were run to evaluate the pressure impact on the tail and the OMS Pod as a possible source for the change in extracted rolling moment after EI + 600 sec. Figure 4.7-33 shows the surface pressure distribution on the tail and OMS Pod for the clean configuration. Figure 4.7-33 through Figure 4.7-36 show the surface pressure distribution on the tail and OMS Pod for the five damage configurations. The half of RCC 8 and all of RCC 9 case had the largest overall impact on the Cp distribution. There was an increase on the tail, OMS Pod and the side of the fuselage. Both Hole #2 cases showed significant impact on the tail and the OMS Pod. Half of RCC 8 and hole #1 increased the pressure on the side of the fuselage. However, it decreased the pressure on the OMS pod and tail because of the orientation of the hole with respect to RCC panel 8. The results indicate only a small amount of interaction with relatively low changes in pressure over a limited area of the vertical tail and OMS pod. Based on these and other results it was concluded that the leeside flow interaction with the vertical tail and OMS pod was not the primary source for the trend change in extracted rolling moment.

4.7.6.5 Observations

The complete loss of an RCC panel matches the early off-nominal flight trends, but does not match the trends later in flight. Additionally complete RCC panel loss increases the pressure only on the side of the fuselage, consistent with other side fuselage observations, but does not impact the vertical tail region (at the computed Mach 6 condition). However, the loss of the windward half of RCC panels 7 and 8 redirects the flow onto the OMS pod and tail area, which increases the pressure in those areas. These increases are not large enough to produce the delta roll and delta yaw trends seen in flight, but are consistent with debris forensics and elevated heating rates observed on the OMS pod

One of the most influential damage configurations is a hole through the wing. The effect on the OMS pod and tail area is driven by the orientation of the hole with respect to the flow field and alignment of the fuselage. The delta aerodynamics for these cases is more consistent with early flight trends.

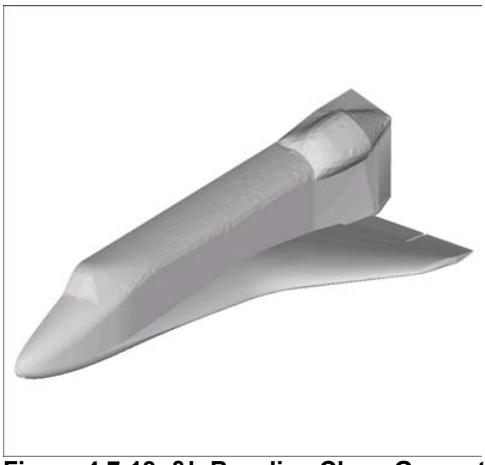

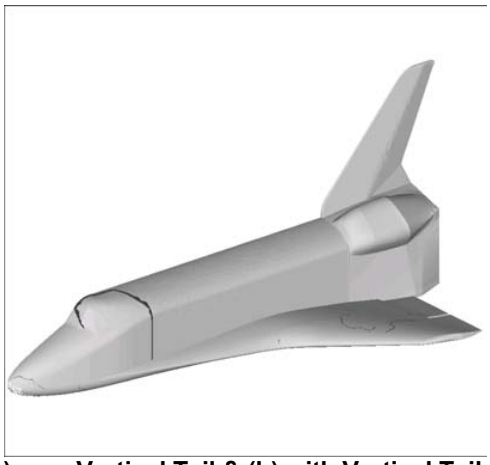

Figure 4.7-18a&b Baseline Clean Geometry (a) – no Vertical Tail & (b) with Vertical Tail

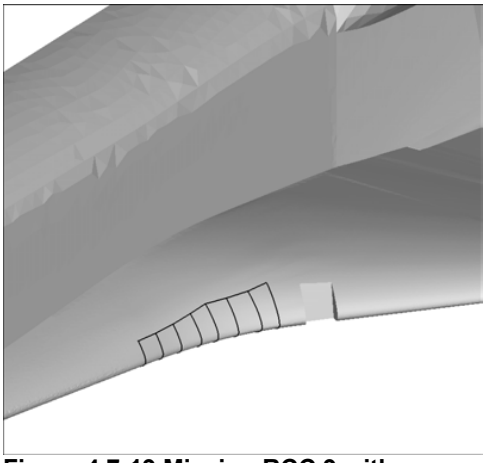

Figure 4.7-19 Missing RCC 9 with Outline of RCC 1 thru 7

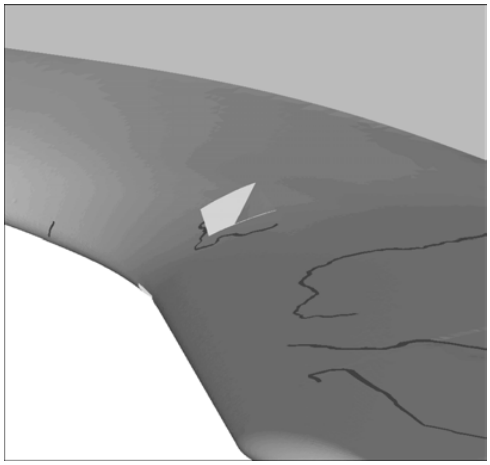

Figure 4.7-20 Windward View – Missing Lower Half of RCC 8 w/Hole #1 thru Wing

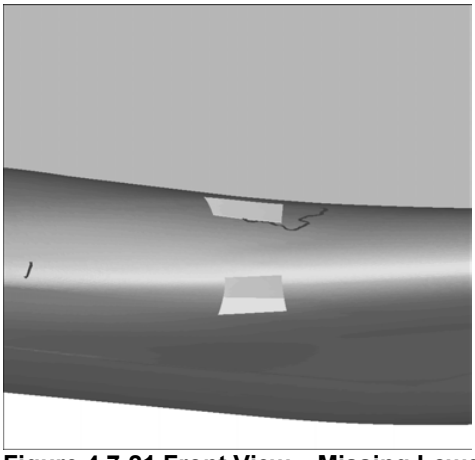

Figure 4.7-21 Front View – Missing Lower Half of RCC 8 w/Hole # 1 thru Wing

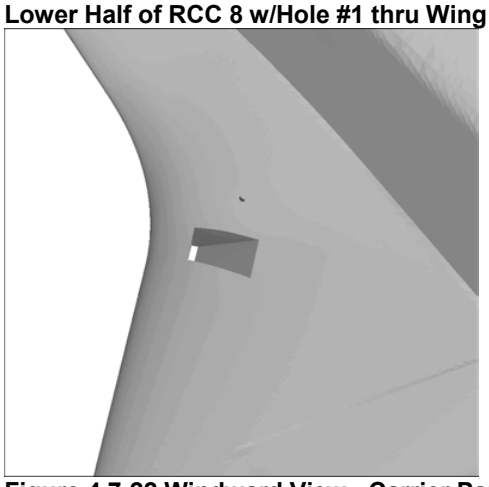

Figure 4.7-22 Windward View - Carrier Panel 8 Missing and Hole # 2 in Wing

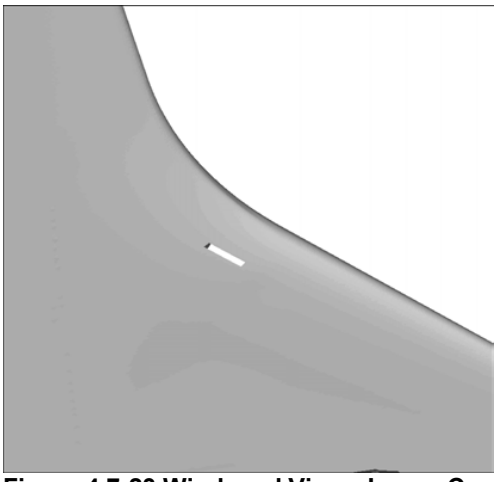

Figure 4.7-23 Windward View - Lower Carrier Panel 8 Missing and Hole #2 through Wing

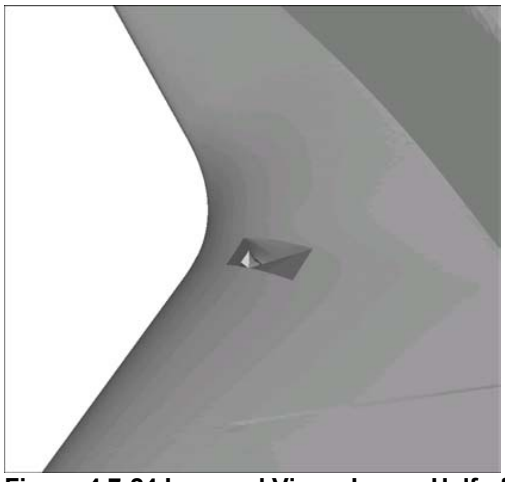

Figure 4.7-24 Leeward View - Lower Half of RCC 8 Missing and Hole # 2 through Wing

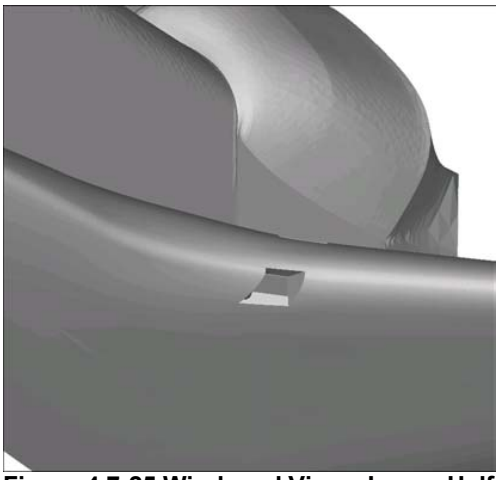

Figure 4.7-25 Windward View - Lower Half of RCC 8 Missing and Hole # 2 Through Wing

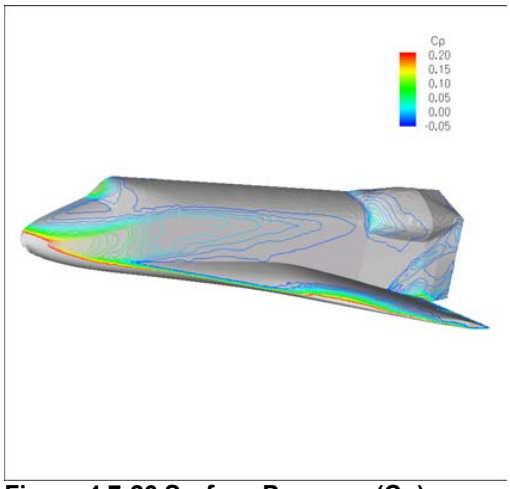

Figure 4.7-26 Surface Pressure (Cp) – Baseline Configuration

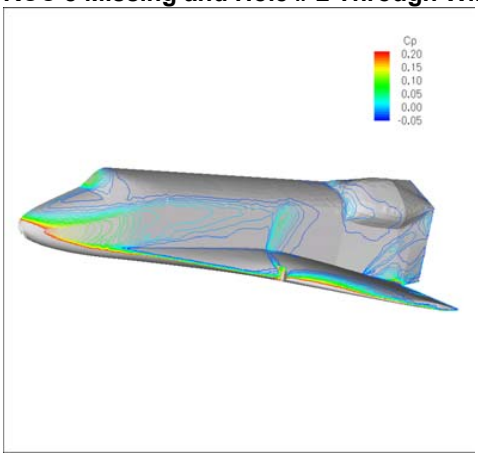

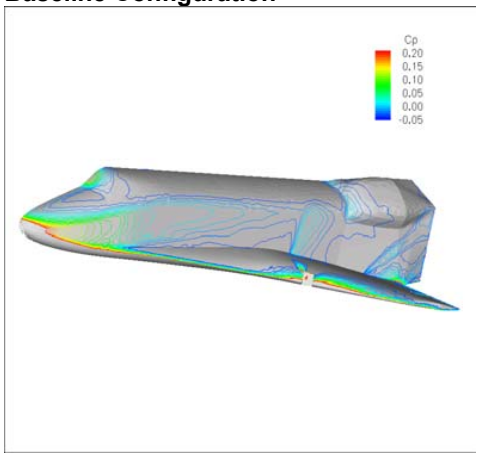

Figure 4.7-27a&b - Surface Pressure (Cp) – (a) Missing Panel 6 & (b) Missing Panel 9

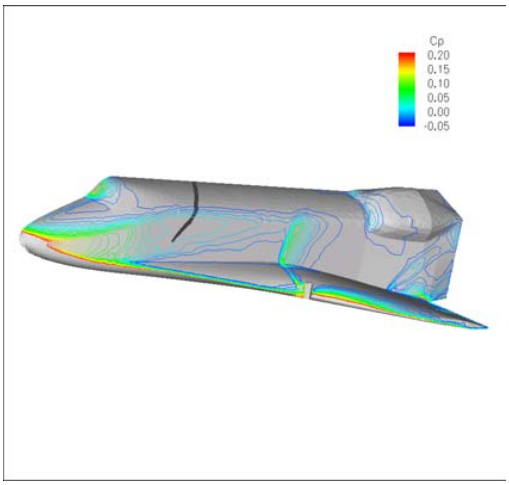

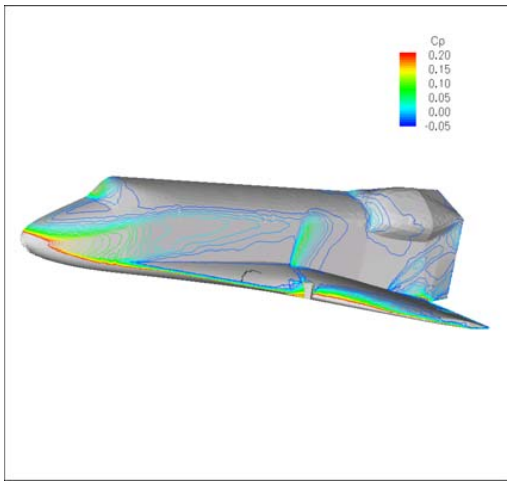

Figure 4.7-28a&b - Surface Pressure (Cp) - (a) Missing RCC Panels 6&7 & (b) Missing 5-7

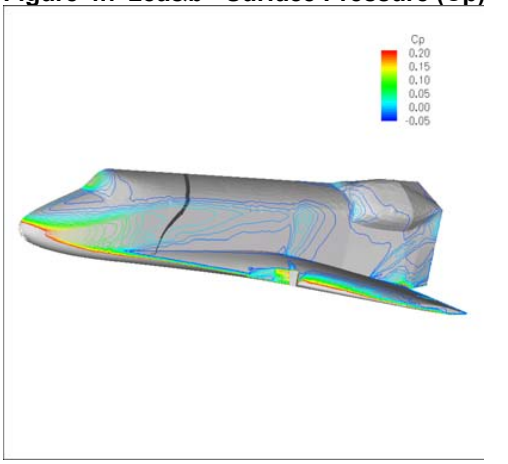

Figure 4.7-29 Surface Pressure (Cp) - Missing RCC Panels 1 through 7

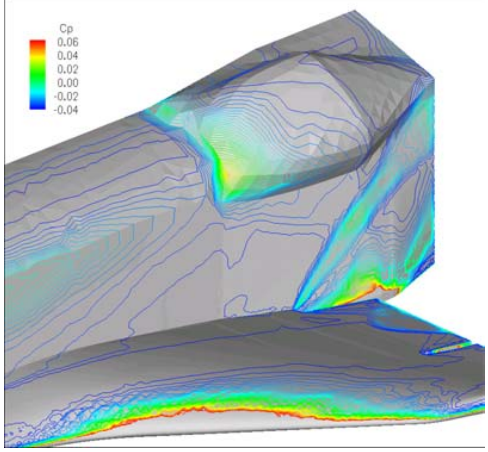

Figure 4.7-30 Surface Pressure (Cp) – Baseline Configuration (OMS Pod)

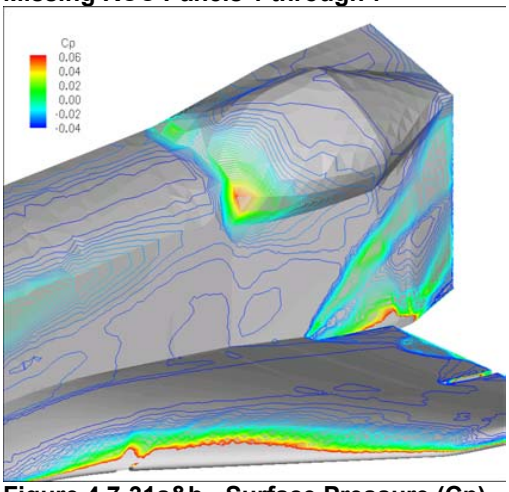

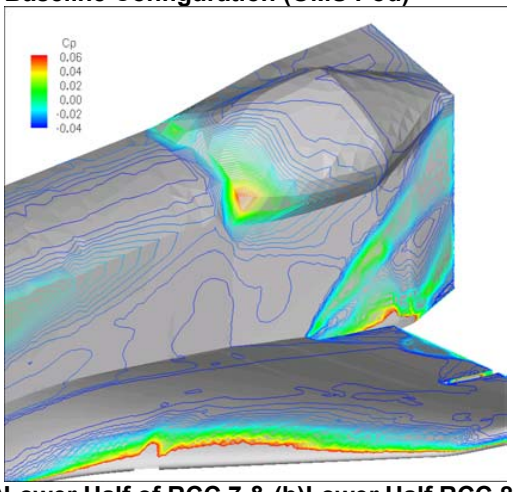

Figure 4.7-31a&b - Surface Pressure (Cp) - (a)Lower Half of RCC 7 & (b)Lower Half RCC 8

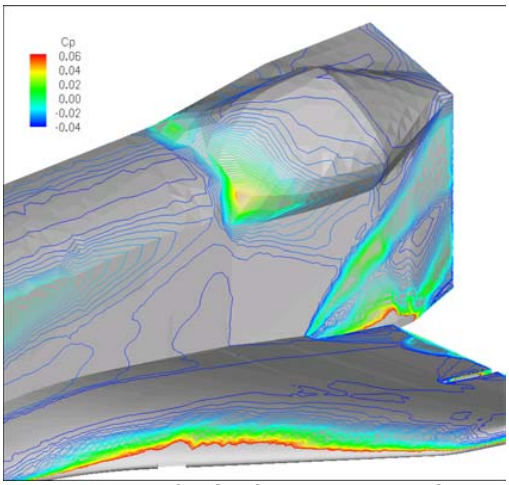

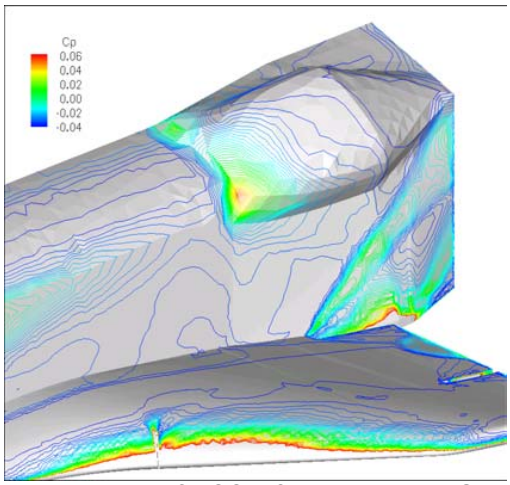

Figure 4.7-32a&b Surface Pressure (Cp) - Missing Lower Half RCC 9 & (b) Missing T-Seal 9

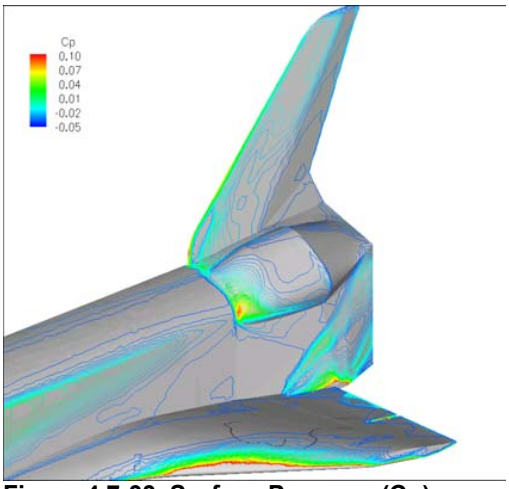

Figure 4.7-33 Surface Pressure (Cp) - Baseline Configuration (OMS & VT)

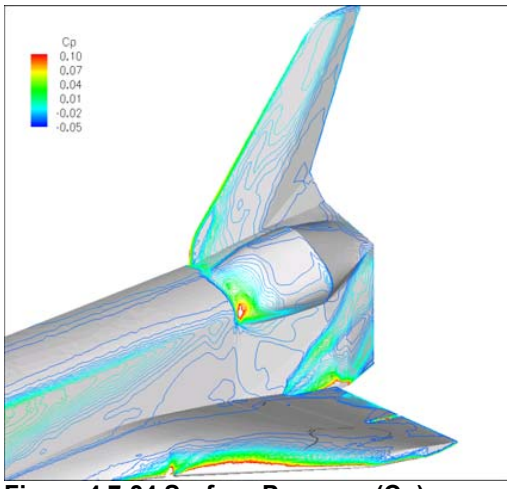

Figure 4.7-34 Surface Pressure (Cp) - Lower Half of RCC 7 Missing

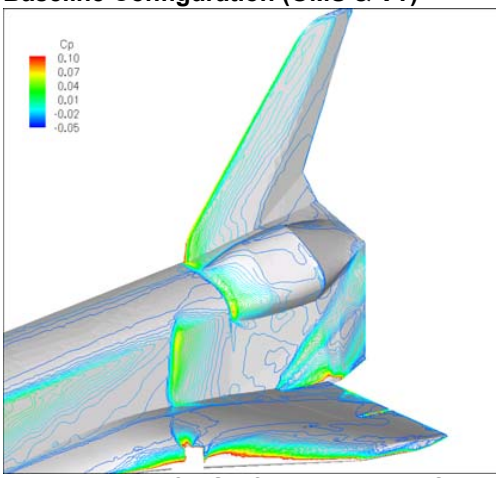

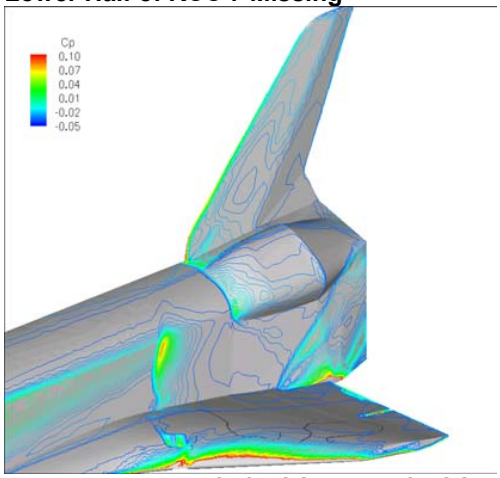

Figure 4.7-35a&b Surface Pressure (Cp) - (a) Missing Lower Half of RCC 8+ all of RCC 9 (b) Missing Lower Half of RCC 8 + Hole No. 1 through Wing

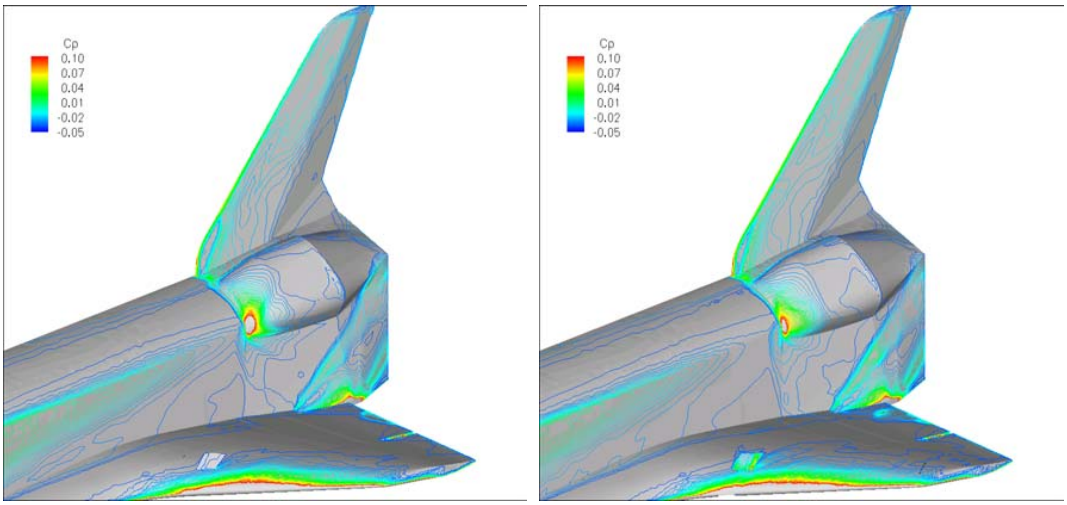

Figure 4.7-36a&b Surface Pressure (Cp) - (a) Lower Carrier Panel 8 Missing + Hole No. 2 Through Wing & (b) Lower Half of RCC 8 Missing + Hole No. 2 Through Wing

4.7.7 Aerodynamic Investigation using USA CFD Analysis

Boeing-Huntington Beach completed a CFD analysis of a damaged orbiter configuration (missing RCC Panel 6) using their USA Navier-Stokes solver at flight conditions.

4.7.7.1 USA Description

The unified solution algorithm (USA) code is a very versatile flow solver that can be used to compute numerical solutions to a large class of aerodynamic and aerothermodynamic problems by solving the Euler or Reynolds averaged Navier-Stokes (RANS) equations. The discretization is of TVD formulation using finite volume framework. Various Riemann solvers can be used with the preferred one being the modified Lax-Freidrichs scheme. A multi-zonal structural grid bookkeeping method facilitates the treatment of complex geometric topologies. A real gas approach based on a finite rate chemistry formulation can be coupled or uncoupled with the fluid dynamics to treat reacting and non-reacting gaseous species. In this work, the approximate factorization scheme using the implicit time marching option was used. The simulations were speeded up using grid-sequencing. The convergence of flow simulations were confirmed by monitoring the time history of surface results.

4.7.7.2 STS 107 CFD case definition

This analysis was done to quantify the effect on the force and moment coefficients due to the removal of the leading edge panel number 6. The cavity was modeled without any representation of the actual exposed interior components of the wing leading edge. The geometry represents the initial panel 6 definition. As detailed in Section 4.3.2.3.2 this is somewhat less than the full panel 6 geometry.

Configurations analyzed

There were two real gas CFD cases considered under this effort. The first one consisted of analysis of the intact vehicle and the second was for vehicle with RCC panel 6 missing. Flight conditions consisted of free stream Mach 18 and angle of attack of 40 degrees. Equilibrium air assumptions were utilized to handle this Mach number. A third case with perfect gas assumption was also conducted for the baseline geometry.

4.7.7.3 Delta Aerodynamic results

CASE	Geometry	Chemistry	CA	CN	CLM	CLL	CLN
OADB	OADB	-	0.06284	1.1598	-0.01667	0	0
1	Baseline	Real Gas/Equilbrium	0.06861	1.1158	-0.01297	0	0
2	"	Perfect gas	0.06439	1.201	-0.04693	0	0
3	RCC#6 Off	Real Gas/Equilbrium	0.069	1.1587	-0.0248	-0.0004	-0.0015

4.7.7.4 Observations/Conclusions

The analysis were carried out using an orbiter half model. The rolling moment and yawing moments were estimated from two half model solutions with the assumption of flow being essentially axial along the symmetry plane. The magnitude of these numbers were of the same order as the error band for the solution convergence and hence not highly reliable.

4.7.8 CFD Tools:

4.7.8.1 FELISA Inviscid Mesh Generation and Flow Solver

Computations of the present study were performed using the FELISA unstructured grid software. This software package consists of a set of computer codes for unstructured grid generation, and the simulation of three-dimensional steady inviscid flows using unstructured tetrahedral grids.

The mesh generation process starts with the definition of a geometry. The computational domain must be a watertight solid. The solid can be developed within a solid modeling CAD package (i.e., Unigraphics or Pro-Engineer), a geometry preprocessor such as GridTool, or by hand. For all of the FELISA work on the Columbia Accident Investigation, the baseline and damaged geometry models were developed within GridTool, with the starting baseline geometry as the structured grid developed at LaRC several years ago using a 1997 Orbiter CAD model. (A solid model based on the 2003 Orbiter CAD model was developed for use with FELISA, but it came available in the middle of the investigation, and the decision was made to continue using the original model.) The second step in the mesh generation process is to graphically define the spacing functions, which determine local mesh size, within either GridTool or GridEx. (GridEx is a mesh generation package under development at LaRC, and has the option of using the FELISA mesh generator). The mesh generation takes place in 2 steps. The surface is triangulated with either the FELISA-SURFACE code, or within the GridEx tool. Generation of the tetrahedral volume mesh is performed using the FELISA-3D_mesh code. Both surface and volume grids are essentially isotropic with little or no stretching. Once the baseline geometry and the mesh spacing were defined for the flight and CF4 conditions, producing a mesh for a new damage scenario only took a couple of hours of preparation work, and 4-8 hours of computer time. Mesh sizes for the damage scenario cases ranged from 2.5 to 5.5 million nodes, up to 30 million tetrahedral elements.

Two flow solvers are available with FELISA--one applicable for transonic flows, and the other for hypersonic flows. The hypersonic flow solver has options for perfect gas, equilibrium air, CF4, CO2, and several other gases (including Mars, Neptune, and Titan atmosphere) in equilibrium. This solver also has the capability of solving chemical non-equilibrium flow, and real gas (chemical and thermal non-equilibrium) flow. This software package has been used extensively for inviscid computations for X-34, X-33, X-37, Mars landers, and also for the Space Shuttle Orbiter at high angles of attack (see Ref. 1). The hypersonic flow solver with the equilibrium air and with the CF4 options was used for the present computations. The solvers are parallelized using MPI for rapid computations. For this investigation, the code was run both a local cluster of PC's with up to 24 processors, and on the NAS Origin 3000 system, 'chapman', with up to 64 processors. Wall clock time for obtaining a converged solution ranged from 8 – 24 hours, and depended on mesh size and the complexity of the damage scenario.

Post-processors such as the aerodynamic analysis routine are part of the software package. More information on FELISA software may be found in Ref. 2. A description of the hypersonic flow solver may be found in Ref. 3.

1. R. K. Prabhu: "Inviscid Flow Computations of the Shuttle Orbiter for Mach 10 and 15 and Angles of Attack 40 to 60 Degrees," NASA/CR-2001-211267, December 2001.

2. J. Peiro, J. Peraire, and K. Morgan: "FELISA System Reference Manual and User's Guide," University College Swansea Report, 1993.

3. K. L. Bibb, J. Peraire, and C. J. Riley: "Hypersonic Flow Computations on Unstructured Meshes," AIAA Paper 97-0625, January 1997.

4.7.8.2 Overflow

OVERFLOW is a structured (overset) grid, Navier-Stokes flow solver. It uses a finite-difference formulation, with flow quantities stored at the grid nodes. OVERFLOW has central- and Roe upwind-difference options, and uses a diagonalized, implicit approximate factorization scheme for the time advance. Local time stepping, multigrid and grid sequencing are used to accelerate convergence to a steady state. In this study, 2nd-order central differencing with Jameson-type 2nd/4th-order scalar dissipation is used. Thin-layer viscous terms are computed in wall-normal directions by default.

References:

D.C. Jespersen, T.H. Pulliam, and P.G. Buning, "Recent Enhancements to OVERFLOW," AIAA-97-0644, AIAA 35th Aerospace Sciences Meeting, Reno, NV, Jan. 1997.
http://science.nas.nasa.gov/~jesperse/papers/aiaa97-0644.ps.Z

P.G. Buning, D.C. Jespersen, T.H. Pulliam, G.H. Klopfer, W.M. Chan, J.P. Slotnick, S.E. Krist, and K.J. Renze, "OVERFLOW User's Manual, Version 1.8s," NASA Langley Research Center, Nov. 2000.

4.7.8.3 CART3D

CART3D is a high fidelity inviscid analysis package developed at NASA Ames Research Center. The geometry required is represented as a closed, watertight, triangulated surface. From this triangulated surface, CART3D produces the volume mesh. The volume mesh is a topologically unstructured, adaptively refined, Cartesian mesh produced around the geometry. The user can control the initial mesh division, the number of refinement levels, and specify certain regions for more cell refinement to develop a useable volume mesh. Using the volume mesh, CART3D uses a domain-decomposition, scalable, multi-level solver to solve the inviscid flow Euler equations.

For more information, visit the CART3D home page at
http://people.nas.nasa.gov/~aftosmis/cart3d/cart3Dhome.html

4.7.8.4 GASP

The GASP Real-Gas Navier-Stokes code was the primary code for solutions accomplished at Ames Research Center. This code originated as a commercially available code developed at AeroSoft, Inc (ref ARC1), but has been modified at ARC to enhance both capability and robustness specifically for hypersonic reentry applications (ref ARC2, ARC3, ARC4).

The GASP Reynolds Averaged Navier-Stokes code is a three-dimensional (3D) finite-volume code. Upwind flux options exist for this code, but for the present solutions the van Leer (ref ARC5) inviscid flux formulation was applied in all three directions. A formally 3rd order upwind-biased MUSCL scheme combined with min-mod limiter is selected to provide higher order accuracy. Experience at ARC with this code has indicated that wall normal spacing is sufficient to obtain accurate heat transfer with the Van Leer flux formulation and 3rd order accuracy provided the wall node Cell Reynolds number is kept below a value of 5. For most of the calculations provided in the present work the wall node Cell Reynolds number is approximately 1, which yields the best results in convergence and accuracy. Time advancement to steady state is accomplished with either a 2D Approximate Factorization, AF2, in the nominal cross-flow plane with planar relaxation in the streamwise direction, or, alternatively, with a point-Jacobi algorithm with inner iterations. Experience at ARC has shown that these two time-advancement schemes as implemented in GASP are nearly identical in convergence, robustness and speed.

The 5-species finite reaction rate model for dissociating air of Park (ref ARC6) was used in these calculations using GASP. In this chemistry model, air is composed primarily of molecular nitrogen, N2, and molecular oxygen, O2, with the possibility of dissociation at high temperature into atomic nitrogen, N, and atomic oxygen, O, followed by formation of NO. For the high Mach number, high altitude portion of a low Earth orbit reentry trajectory as considered herein, the molecular oxygen, O2, present in the atmosphere will almost entirely dissociate into atomic oxygen, O, upon encountering the bow shock. However, N2 will undergo but slight dissociation with lesser amounts of N and NO formed. The reaction rates are typically slow enough that little recombination occurs for hypersonic flows prior to the exit boundary except for that due to the catalytic effect of certain thermal protection surface materials.

The real-gas air chemistry has an important effect on the hypersonic flow about the orbiter by altering the shock location since energy is required to dissociate the molecular oxygen through the shock, the temperature and density rise through the shock are not as great as would otherwise occur for a perfect gas thereby reducing the effective gamma for the real gas in the shock relations. A further real-gas effect is that chemical energy is released at the shuttle surface due to recombination of O to O2 as a consequence of the catalytic behavior of the RCG shuttle tile material. This catalytic wall effect yields a higher heating rate to the wall than for non-catalytic materials.

Species transport properties are calculated using Blottner relations with mixture properties calculated using Eucken relations. See ref ARC1 for further details.

Stewart (ref ARC7) characterized the surface catalytic recombination of air due to various thermal protection system insulation materials including RCG as used on the windward side of the shuttle orbiter. RCG and other

catalytic materials act to enhance the rate of recombination of atomic oxygen into molecular oxygen and of atomic nitrogen into molecular nitrogen. Molecular NO is assumed to experience no catalytic effect. In the process, additional thermal energy is released to the wall due to the chemical reaction occurring at the surface.

The primary wall boundary condition used for these shuttle calculations is that of radiative equilibrium combined with the above RCG catalytic behavior. In this viscous wall boundary condition, there is an assumption that the radiative heat transfer from the wall exactly balances the thermal energy transfer to the wall due to convective heat transfer combined with energy release to the wall due to the surface catalytic chemical reaction. The radiative equilibrium boundary condition requires the simultaneous solution of 4 species equations (molecular NO is not considered catalytic) combined with an equation for the energy balance, all of which are written at the wall node. To then solve this wall boundary condition for each Navier-Stokes solver iteration, a Newton-Raphson method achieves quadratic convergence.

Additional boundary conditions used include conventional point-to-point zonal boundaries, adiabatic viscous wall, free-stream, and a specified back-pressure outflow boundary condition. Point-wise boundary conditions can be specified optionally for any of the 6 faces of each grid block and were used for the vented cavity panel 9 solutions.

Most of the solutions delivered were laminar throughout the solution domain. However, some eddy-viscosity turbulence models calculations were conducted to establish approximate turbulence heating enhancements and for validation purposes. Turbulence models implemented into this code include the Baldwin-Lomax algebraic model of Baldwin-Lomax (Ref ARC7) and the 2-eq SST/K-Omega turbulence model of Menter(Ref ARC8). These models have compressibility corrections suitable for hypersonic flows and have been validated for heat transfer in hypersonic strong interactions as implemented in the ARC version of the GASP code(see Ref ARC3). A means for specification of turbulence transition is implemented in the code, but is not used for the present work.

The GASP code was run initially on a serial processor computer (Intel 2 GHz XEON processor running RedHat Linux v 7.3). These early runs were for fully catalytic solid surface rather than RCG on grids of approximately 3/4 million grid points and took 96 hours. To improve throughput, subsequent work was moved to the NAS parallel-processing cluster, chapman, which is based on up to 1024 SGI Origin O3K cpus. For the parallel processor runs, the grids were decomposed into as many as 48 grid blocks each of which was then run on a separate SGI processor in the NAS chapman cluster. With grids of 1.9 million grid points, the chapman parallel processor runs took approximately 48 hours.

Convergence criterion was based on examination of residual history, temperature and pressure history for selected surface points during the entire iteration sequence, and when convergence was nearly complete examination of delta T and delta P surface plots separated by 50 to 200 iterations. Typically the L2 residual would drop by 5 orders of magnitude and the selected surface temperatures and pressures would become constant. The delta T and delta P surface plots were facilitated by the gasptools package written by D. Prabhu and M. Wright of Ames and which is based on perl scripts making use of the GASP print utility and the Tecplot plotting package. Typically the delta T surface plots were examined for constant temperature within 5 degrees over the entire shuttle surface. Some of the damage cases exhibited some oscillation of approximately a 10 degree K magnitude which was deemed acceptable inasmuch as there existed a physical basis.

4.7.8.5 USA

The unified solution algorithm (USA) code is a very versatile flow solver that can be used to compute numerical solutions to a large class of aerodynamic and aerothermodynamic problems by solving the Euler or Reynolds averaged Navier-Stokes (RANS) equations. The discretization is of TVD formulation using finite volume framework. Various Riemann solvers can be used with the preferred one being the modified Lax-Freidrichs scheme. A multi-zonal structural grid bookkeeping method facilitates the treatment of complex geometric topologies. A real gas approach based on a finite rate chemistry formulation can be coupled or uncoupled with the fluid dynamics to treat reacting and non-reacting gaseous species. In this work, the approximate factorization scheme using the implicit time marching option was used. The simulations were speeded up using grid-sequencing. The convergence of flow simulations were confirmed by monitoring the time history of surface results.

5 AEROTHERMODYNAMICS

5.1 Introduction

5.1.1 Team Objective

The objective of the aerothermodynamics team was to define local and acreage predicted heating environments of the Orbiter for nominal and damaged configurations in support of the Columbia accident investigation. These environments were used to explain the anomalies in the flight data and were provided to the thermal structures team in support of various thermal analyses, Figure 5.1.3-1.

5.1.2 Aerothermodynamics Overview –Orbiter Perspective

The discipline of aerothermodynamics as applied to the Orbiter principally refers to the aerodynamically induced heating of the vehicle during high speed flight. Significant aerodynamic heating occurs at Mach numbers of 2 and above. For the Orbiter, the highest heating is observed during re-entry from orbit as it descends into the earth's atmosphere traveling at Mach numbers greater than 25.

The heating is a result of the conversion of Orbiter kinetic energy into thermal energy. As the Orbiter passes through the atmosphere at high Mach numbers a shock wave is formed in front of the vehicle, called the bow shock. The bow shock processes convert the kinetic energy into thermal energy by reducing the air speed while tremendously increasing its temperature. Just behind the shock wave, the air can reach temperatures as high as 10,000° F. At these temperatures, the majority of the molecules that make up air, N_2 and O_2, dissociate into their respective atomic constituents. Such dissociated gases are termed high temperature gases. After passing through the bow shock, the heated dissociated gas flows around the vehicle, and thus the energy of the gas will be convectively transferred to heat the surface. Because this heating is extreme during re-entry, a thermal protection system (TPS) is required.

In order to determine the rate at which the heat is transferred to the surface of a vehicle, the flow physics that the vehicle will encounter must be understood, i.e., bow shocks, wing shocks, shock interactions, surface boundary layers and boundary layer state (laminar, transitional, or turbulent), shock-boundary layer interactions, and boundary layer separation and reattachment zones. The heat transfer rate will be a function of the vehicle geometry, its orientation to the flow, the surface temperature of the vehicle, the trajectory being flown through the atmosphere, and the TPS properties. Lastly, at Mach numbers greater than about 5, in a regime called hypersonic, chemical reactions in the air due to the energy exchange are significant. These reactions not only affect the heating of the vehicle but also its aerodynamics.

Flow chemistry affects the shock waves, pressure distributions, and heating distribution around the vehicle. As mentioned previously, at the speeds of Orbiter atmospheric re-entry, all of the molecular oxygen and most of the molecular nitrogen dissociate into their atomic forms via an endothermic reaction. This dissociation occurs due to the heating caused by the initial bow shock. The flow chemistry within this dissociated region may be considered in either a chemical equilibrium or non-equilibrium state, which also has an effect on the heat transfer rate. Determining the state depends upon the speed of the chemical reactions compared with the speed of the vehicle. It is during the phase of re-entry in which the dissociated region of the flow is also in a chemically non-equilibrium state that interaction of the dissociated gas with the TPS surface material properties can have a significant impact on the amount of heat being transferred to the vehicle. Surfaces that are non-catalytic inhibit the recombination of atomic nitrogen and oxygen and thus minimize the amount of heat transfer, whereas fully catalytic surfaces maximize the heat being transferred from the gas to the surface. In the case of the Orbiter TPS, both the tiles and leading edge materials are considered partially catalytic and are closer to non-catalytic than fully catalytic. This low partial catalytic property was designed into the TPS system to reduce the amount of chemical recombination energy transferred to the surface.

All of these issues must be considered when providing heating environments to be used in follow-on analyses. For a more thorough discussion on aerothermodynamics and high temperature gas dynamics, please refer to the works of Bertin and Anderson.

5.1.3 Approach to Determining Required Environments

As mentioned, there are many factors that need to be understood in order to determine Orbiter heating environments. Most of the previous work on determining these environments focused on a nominal Orbiter configuration during the TPS design and certification. Determining the environments for a damaged Orbiter is a more difficult problem. First, the size, shape, and location of the original and progressing damage are unknown. Second, because the damage exposes internal structure and permits external gases to enter internal cavities, the problem becomes a mixed internal-external flow problem. Finally, the problem is further complicated by the fact that as the damage to the Orbiter progressed, both the external and internal geometry changed, and the free stream conditions were also continuously changing.

During the design and operation of the Orbiter, and the design of more advanced vehicles since, numerous tools and testing techniques have been developed, and they were applied in support of this investigation. These tools include engineering methods using simplified geometries (e.g., spheres for nose caps, cylinders for wing leading edges), computational fluid dynamics (CFD), direct simulation Monte Carlo techniques (DSMC), and wind tunnel testing along with the associated instrumentation. The certified Orbiter heating model was also used as the benchmark for the Orbiter external heating environment as well as existing computational and testing data. This certified heating model is described in Section 5.2.2. The tools and techniques utilized for the certified Orbiter heating model were applied to nominal configurations with as-designed outer mold line (OML) geometry lines. There have been very limited pre-accident studies involving heating of the internal structure as a result of a penetration in the TPS. Those particular studies dealt with micrometeoroid penetrations and not the larger scale damage being considered as the root cause of the Columbia accident. The consideration of large scale damage to the Orbiter represented a new area of engineering analysis, especially for the determination of the internal heating environments.

In order to provide the external and internal heating environments needed for the investigation, a team of engineers and scientists from government, industry, and academia was formed. Two sub-teams were then formed - one focusing on external heating environments and the other on internal heating environments. The team decided that the damage configurations to be assessed were to be treated as static or at most quasi-static, in order to reduce the complexity of the analyses being performed. Also, it was recognized that since there was no time for a formal verification process of the environments being provided, the use of engineering best practices, multiple solution sources, and team review of the data would be sufficient. The idea was that the data were to be used in support of determining the plausibility of a given scenario and not to define the exact environments, because the exact configuration of the damage would never be known.

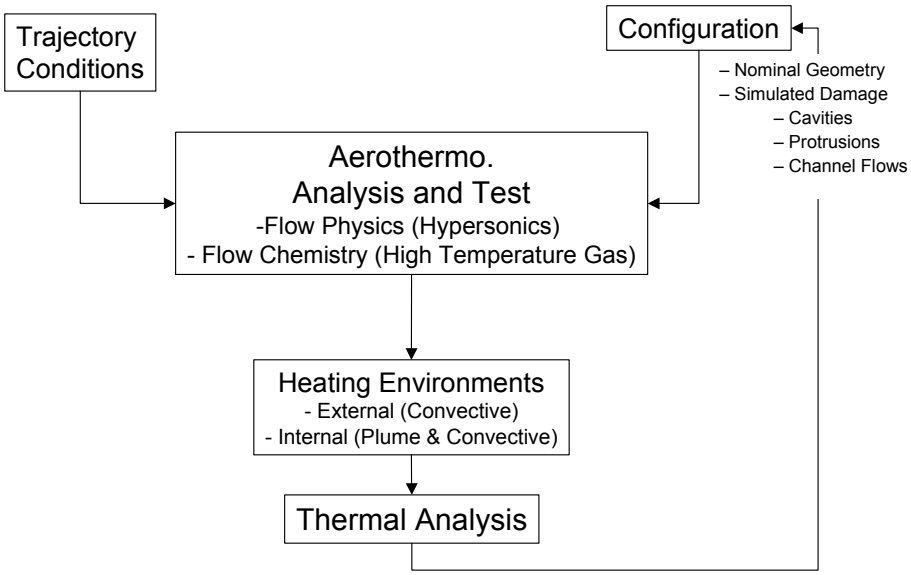

Figure 5.1.3-1 Aerothermodynamics Analysis Process

5.2 Orbiter External Aerothermodynamic Environments (Nominal & Damaged Configurations)

External aerothermodynamic environments for both nominal and damaged Orbiter configurations were needed for several aspects of the investigation. These include assessing the flight data using the aerothermodynamic results directly, qualitatively and/or quantitatively, or as input to the internal environments and thermal analysis teams. This section will review the relevant STS-107 flight data pertaining to the external environment and the working scenario, provide background on the certified Orbiter entry heating methodology, present the results from wind tunnel testing and computational analyses, and, finally, apply those data to the working scenario issues described in this section.

5.2.1 Orbiter OML/Skin Flight Data Observations

During the STS-107 re-entry, several off-nominal sensor readings on the Orbiter OML were recorded on the recovered Modular Auxiliary Data System (MADS) recorder. Also, several Orbiter Instrumentation (OI) sensors on the inner structure showed off nominal readings. Although there were a significant number of other off-nominal sensor readings in the MADS and OI data, those discussed in this section are pertinent relative to the external flow field and how they relate to the working scenario. The specific sensors to be discussed in this section include the surface thermocouples (T/Cs) on the left side fuselage and left OMS pod, the temperature sensors on the chin panel expansion seal, vacuum vent nozzle, water dump nozzle, and a surface T/C just behind the RCC Panel 9 and Panel 10 interface. Although not Orbiter flight data, the Kirtland photo image will be discussed in this section as it potentially shows a damaged Orbiter configuration.

5.2.1.1 Side Fuselage and OMS Pod

From the data available via the OI system, three measurements on the side fuselage indicated off nominal increased heating responses compared with previous flight data. The most significant of these increased heating responses was from V34T1106A, the location of which is shown in Figure 5.2.1-1. On the MADS there were 11 out of 14 surface T/Cs that indicated off-nominal response during the STS-107 re-entry prior to LOS. Those sensors showed both increased and reduced heating effects on the left side fuselage and OMS pod (locations depicted in Figure 5.2.1-1), as compared with previous flight data. Figure 5.2.1-2a – f show examples of these comparisons. The reduced heating was noted on the forward portion of the OMS pod and two sensors on the side fuselage-payload bay door area and began as early as 49:49 GMT (EI+340 sec). It is noteworthy that during this early part of the STS-107 flight, between 49:49 GMT (EI+340 sec) and about 52:09 GMT (EI+480 sec), only off-nominal low heating rates were

observed in any of the available side fuselage or OMS pod sensor data. Between 52:39 (EI+510 sec) and 53:09 GMT (EI+540 sec) the heating began to increase above the nominal range at various gauge locations compared with previous flights. This heating increase began with two measurements on the forward part of the OMS pod, V07T9978 and V07T9976. The different onset times for off nominal increased heating at the various gauge locations are a significant indicator of damage progression occurring on the Orbiter, Figure 5.2.1-1 and Figure 5.2.1-3.

An analysis was performed to back out the relative decrease or increase in heating that was observed. Since these were surface T/C's, an radiation equilibrium wall condition assumption can be made such that

$$\frac{\dot{q}_{STS-}}{\dot{q}_{Nominal}} \cong \frac{T^4_{STS-}}{T^4} .$$

In this relation, $\dot{q}$ is the heat transfer rate and T is the surface temperature in degrees Rankine. Using an average over previous flight data as a nominal value, a ratio of the disturbed to nominal heating was obtained. For all the sensors that experienced reduced heating during the early portion of the flight, before 52:09 GMT (EI+480 sec), the ratio of heating ranged from 0.6 to 0.8. The sensors on the OMS pod that showed reduced heating experienced heating ratios of 0.6 to 0.7 compared with previous flights. During the segment of the flight where off-nominal higher heating rates were observed, after 52:09 GMT (EI+480 sec), the heating ratios across several sensors on the side fuselage and OMS pod varied from 1.7 to 5.2.

A close examination of the temperature response of V07T9220 indicates at least two significant events during the period between 52:39 GMT (EI+510 sec) and 57:19 GMT (EI+850 sec), Figure 5.2.1-4. Observed debris events were co-plotted on the side fuselage and OMS pod data to investigate any correlation to the observed temperature increases, Figure 5.2.1-5, Figure 5.2.1-6, and Figure 5.2.1-7. The data for these gauges indicate that significant external changes were occurring on the Orbiter even before the first debris event was observed. Other flight data indicate that the wing spar had already been breached by the time the increased heating on the OMS pod was experienced. However, debris events 5 and 6 (with the flash) stand out as correlating well with changes in the slope of the temperature response. These data indicate a progression of damage on the wing that resulted from initial damage in the panel 5 through 9 region.

Finally, a check on the surface emittance of tiles recovered from the OMS pod region was performed to assess whether or not surface contamination could be the cause of the observed temperature response. If the heating environment were nominal, then the emittance of the TPS would have had to decrease to 0.3 from the nominal 0.85 value in order to match the temperature response, Figure 5.2.1-8. The emittance of these post-accident tiles was measured at NASA KSC and was shown to be nearly the same as a pristine tile. Therefore, the side fuselage and OMS pod measurements are believed to be accurate indicators of the reduced and increased heating.

5.2.1.2 Wing Surface T/C V07T9666A

V07T9666A is a surface T/C located on the lower wing immediately aft of the panel 9 / 10 interface, Figure 5.2.1-9. The data, Figure 5.2.1-10, indicate that this sensor begins to show an off-nominal behavior at 50:19 GMT (EI+370 sec). This start of off-nominal time is 30 seconds after the start of decreased heating recorded on the side fuselage and OMS pod. As can be seen in the figure, there were other flights in which an off-nominal temperature behavior can be observed for this T/C. However, the earlier off-nominal responses for the T/C are not of similar signature to the data seen for STS-107. No proven explanation can be provided for the previous off-nominal flight data but one theory is that the T/C temperature is demonstrating a sensitivity to the shock interaction. Shock interaction regions are areas within the flow field where two or more strong shock structures intersect. For the Orbiter, a very strong shock interaction occurs between the bow shock and wing shock, resulting in locally higher heating and pressure. In fact, the very high heating experienced on the Orbiter wing leading edge, in the region where the wing transitions from the strake section to the main wing section, results directly from the bow-

shock/wing-shock interaction. The heating produced by such an interaction can be very localized, implying very large surface heating gradients in the immediate vicinity of the interaction. The precise location of this interaction is a function of many variables related to high-speed aeroheating environments, and even small changes in these variables can cause significant changes in the actual position of the shock-shock interaction and hence the underlying heating experienced at the surface. No further discussion will be provided in this report on the off-nominal low data, but this information was noted here for completeness. The off-nominal high readings for STS-107 continue until the V07T9666A T/C fails at approximately 52:25 GMT (EI+496 sec).

The off-nominal trend for the V07T966A instrument occurs prior to any of the debris events that were observed, so no correlation can be made to observed debris. However, as was noted previously, instrumentation inside of the WLE and along the wing spar, i.e. V09T9910A, V12G9921A, V12G9169A, indicated that heating was already occurring in the WLE cavity when the off-nominal temperature at V07T9666A was noted. Thus, the temperature response of this gauge potentially indicates a worsening condition either inside the WLE cavity or at the original damage site itself.

5.2.1.3 Chin Panel and Vacuum Vent / Water Supply Dump Nozzles

Four additional temperature measurements indicated off-nominal behavior on the vehicle. However, these were located more forward on the fuselage than the sensors previously discussed. Additionally, these instruments are not surface thermocouples, but are instead Resistance Temperature Devices (RTDs) which were typically attached to structural elements of the Orbiter. The first of these was one of two RTDs located on the Nose Cap/Chin Panel expansion seal, Figure 5.2.1-11. The other three were located on the left side of the Orbiter; one associated with the vacuum vent nozzle and the other two with the water supply dump nozzle located just above the waste water dump nozzle, Figure 5.2.1-12.

The chin panel sensor, V09T9889A, was the first of these sensors to indicate off-nominal trends at 52:09 GMT (EI+480 sec) but it recovers to the “nominal” slope by 52:49 GMT (EI+520 sec), Figure 5.2.1-13. Note that V09T9880A, only 23 inches away on the centerline, did not show this off-nominal signature. Also in Figure 5.2.1-13, the vacuum vent, V62T0551A, and water supply dump nozzles temperature sensors, V62T0440A & 0439A (not shown), indicate similar behavior albeit at a slightly different start time of 52:32 GMT (EI+503 sec). However, the vacuum vent RTD recovered to the previous slope at 52:47 GMT (EI+518 sec), prior to the water supply nozzle RTD at 52.55 GMT (EI+526 sec). The slope of the temperature curves seen by these sensors essentially doubles between times 52:32 GMT (EI+503 sec) and 52.52 GMT (EI+523 sec). These vent nozzle temperature rise rate increases equate to an additional heat transfer rate of approximately 0.038 BTU/sec (40 Watts). Note that the nozzle temperatures were recorded via downlink on the OI system, and that off-nominal measurements were bounded by communication dropouts. The data dropouts were two of several unexplained communication blackouts (as noted by the gaps in the downlink data) that occurred prior to LOS.

As has been mentioned, the responses from these forward fuselage sensors are unusual in that their readings return to their nominal trends after a short period of off-nominal response. However, it is noted that the RTD response of the waste water dump nozzle, V62T0519A, located seven inches below the supply nozzle, V62T0520A, showed no indication of off-nominal response during the entire entry. Lastly, there was a surface T/C, V07T9522A, located just aft of and above the vent nozzle group that showed nominal behavior for the entire entry except for a sharp decrease in the data over one cycle. These data along with the observed debris data have been co-plotted in Figure 5.2.1-14. As can be seen, no clear relationship can be observed between the debris events and response of the sensors that performed nominally. Although not shown, the response of the chin panel gauge does coincide with the estimated time of the wing spar breach (see Section 6 for further details).

5.2.1.4 Kirtland Photo

As the Orbiter was passing over the Albuquerque, New Mexico area, images of the Orbiter were obtained from the Kirtland AFB Starfire Optical Range. Figure 5.2.1-15 shows the principle image of the set. Although a thorough analysis of the images was made (see Image Analysis Team Report), no direct evidence of damage to the Orbiter could be discerned. However, damage to the Orbiter, especially the WLE, could be inferred from the anomalous bulges noted on the left wing. The principle source of light

from an Orbiter re-entering the Earth's atmosphere is high temperature gas immediately behind the shock layer. It was hypothesized that the bulges in the light emission could be a result of a deformed wing shock or additional embedded shocks due to a damaged wing configuration, or additional illumination due to particulates in the flow field emanating from the damage site. Based upon the results of the analyses and testing presented below, this potential explanation will be discussed further in the external environments applications section.

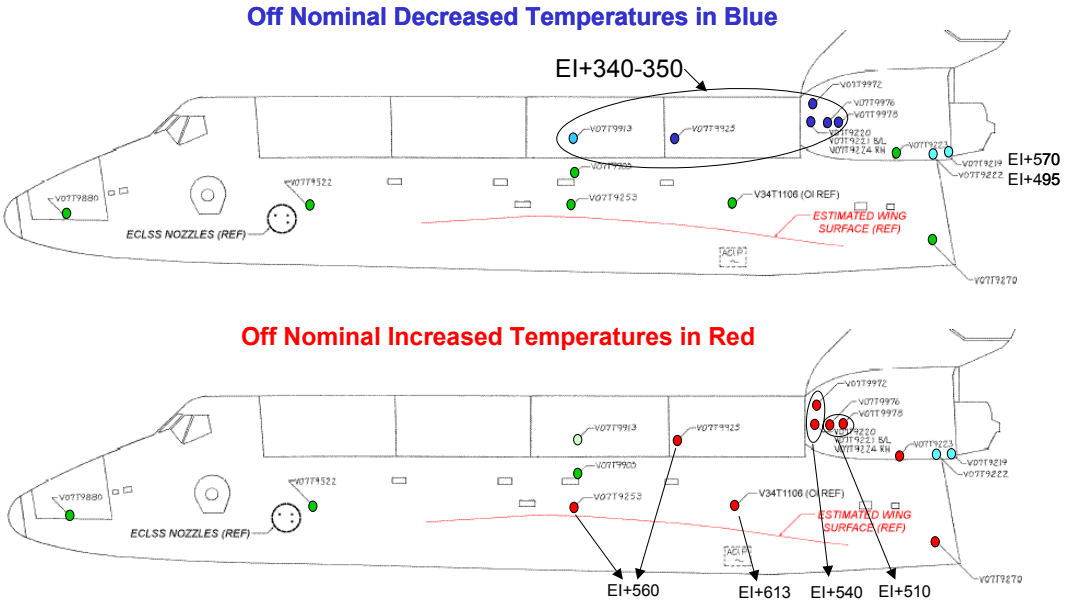

Figure 5.2.1-1 Left Side Fuselage and OMS Pod T/C locations. Times indicate when off nominal condition first observed.

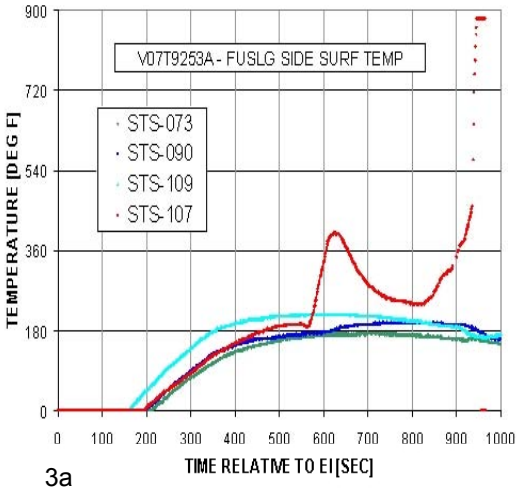

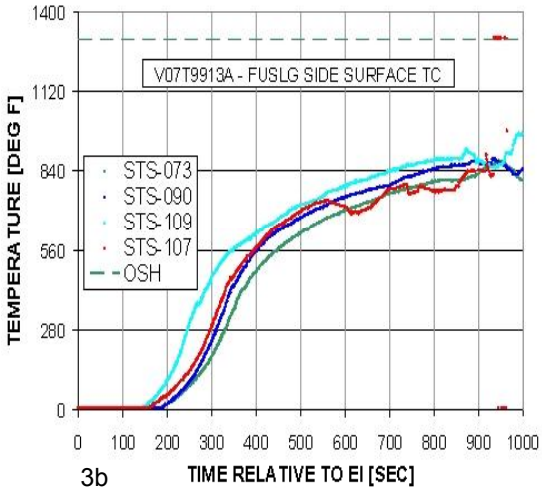

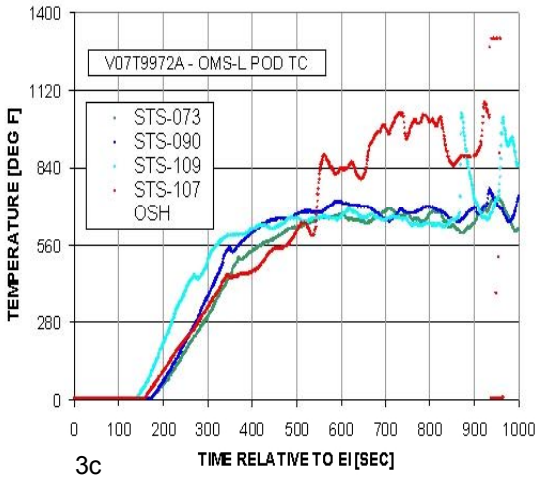

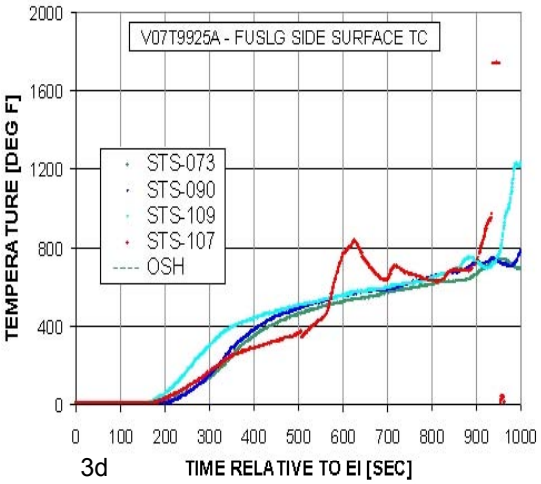

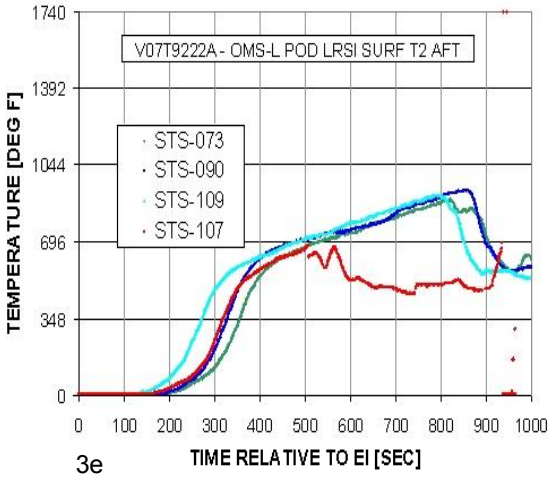

Figure 5.2.1-2a – 3e STS-107 Orbiter Side Fuselage and OMS Pod temperature comparisons with previous flights of Columbia.

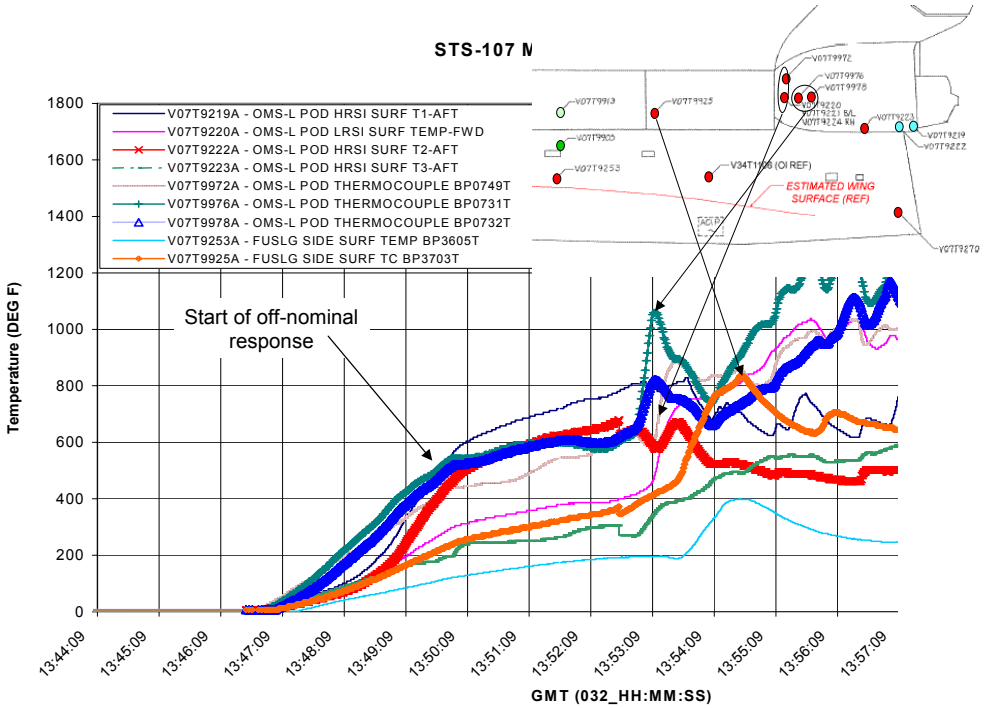

Figure 5.2.1-3 Left Side Fuselage and OMS Pod Off-Nominal Responses Indicate Aft to Forward Progression of Increased Heating

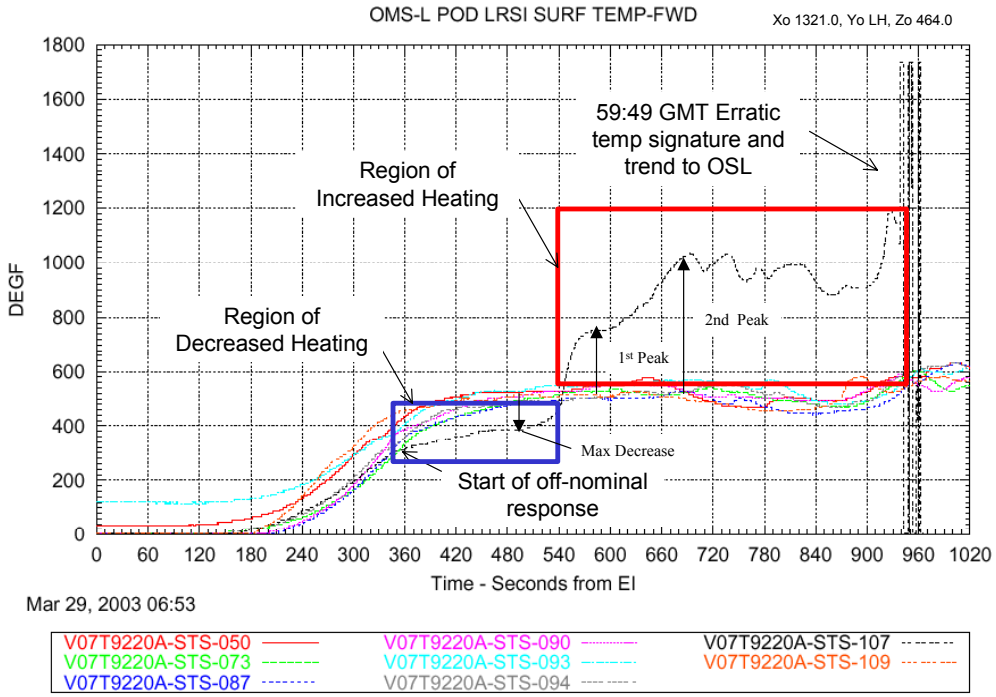

Figure 5.2.1-4 An example of Left OMS Pod temperature response that indicates at least two significant events during the period of increased heating

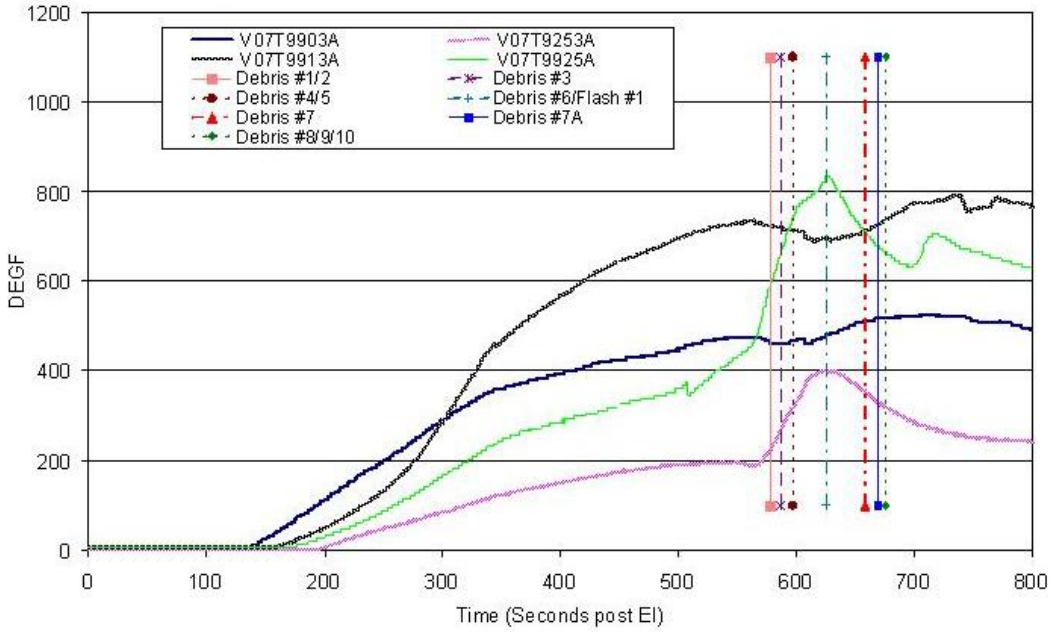

Figure 5.2.1-5 Mid Fuselage and Aft-Left Side Payload Bay Surface T/Cs response along with Debris Events 1 through 10

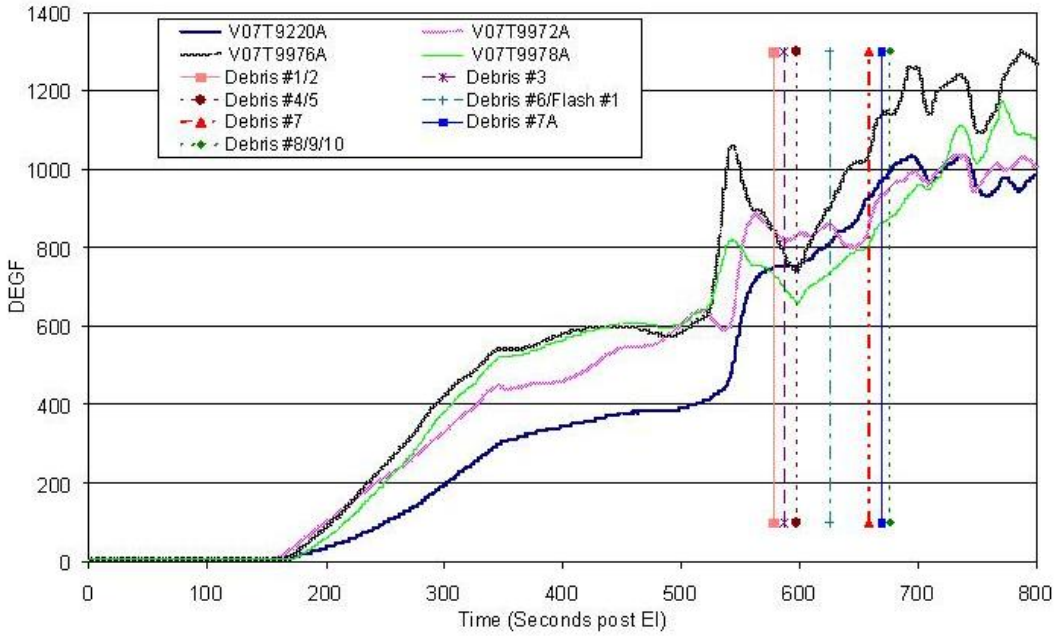

Figure 5.2.1-6 Forward Left OMS Pod Surface T/C responses along with Debris Events 1 through 10

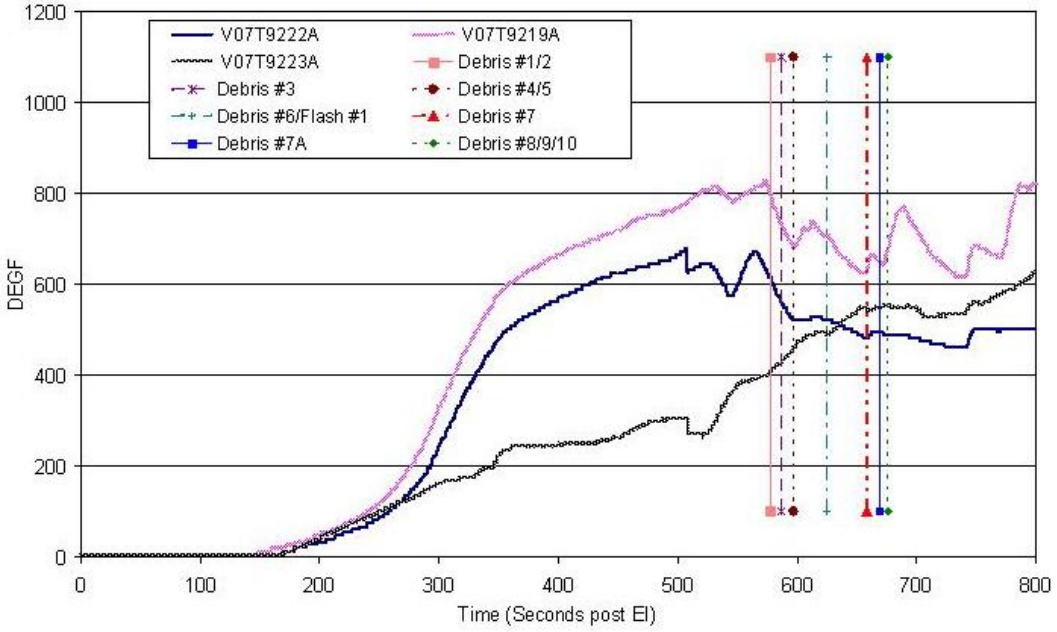

Figure 5.2.1-7 Mid and Aft Left OMS Pod Surface T/C responses along with Debris Events 1 through 10

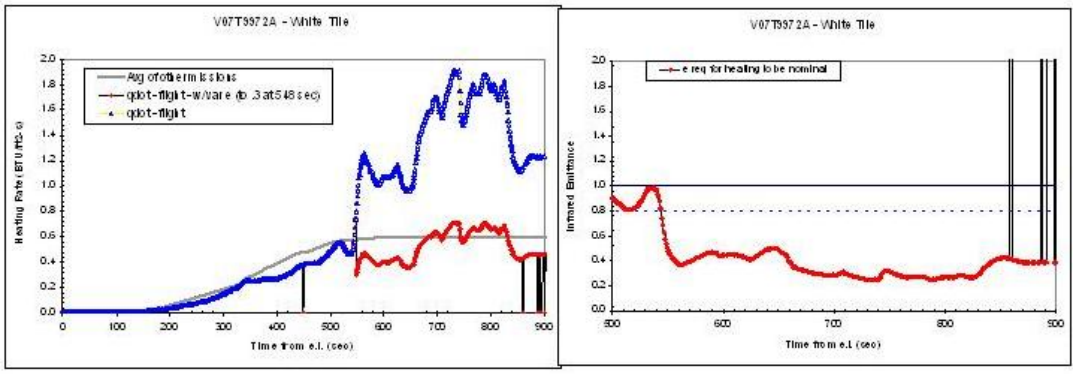

Figure 5.2.1-8 Emittance change needed to return inferred heating rates to previous flight average

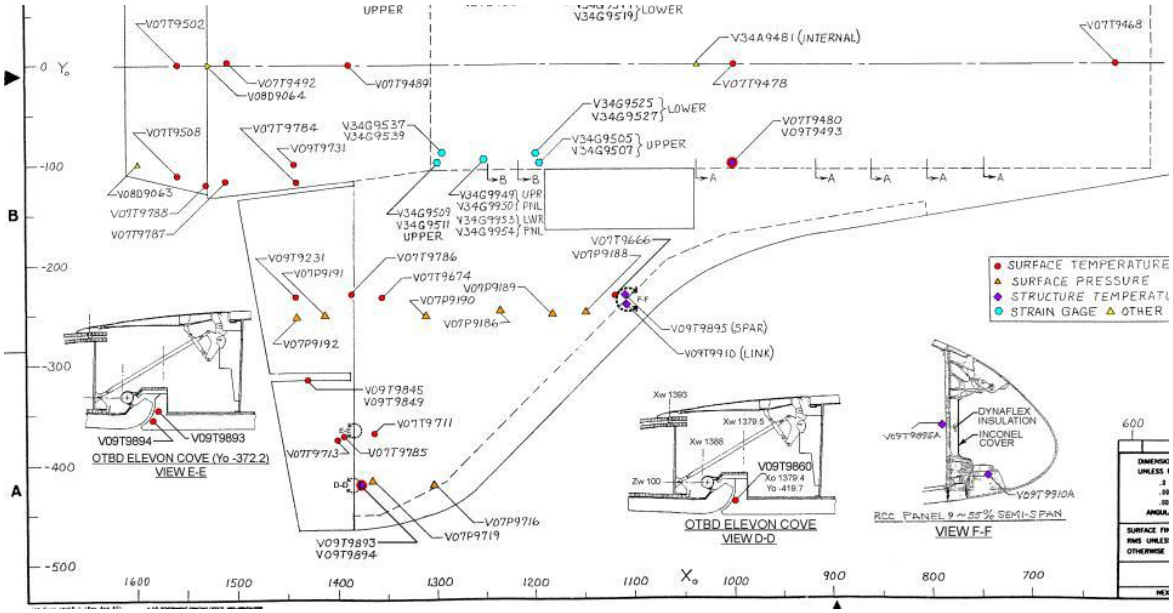

Figure 5.2.1-9 Lower Left Wing MADS instrumentation locations

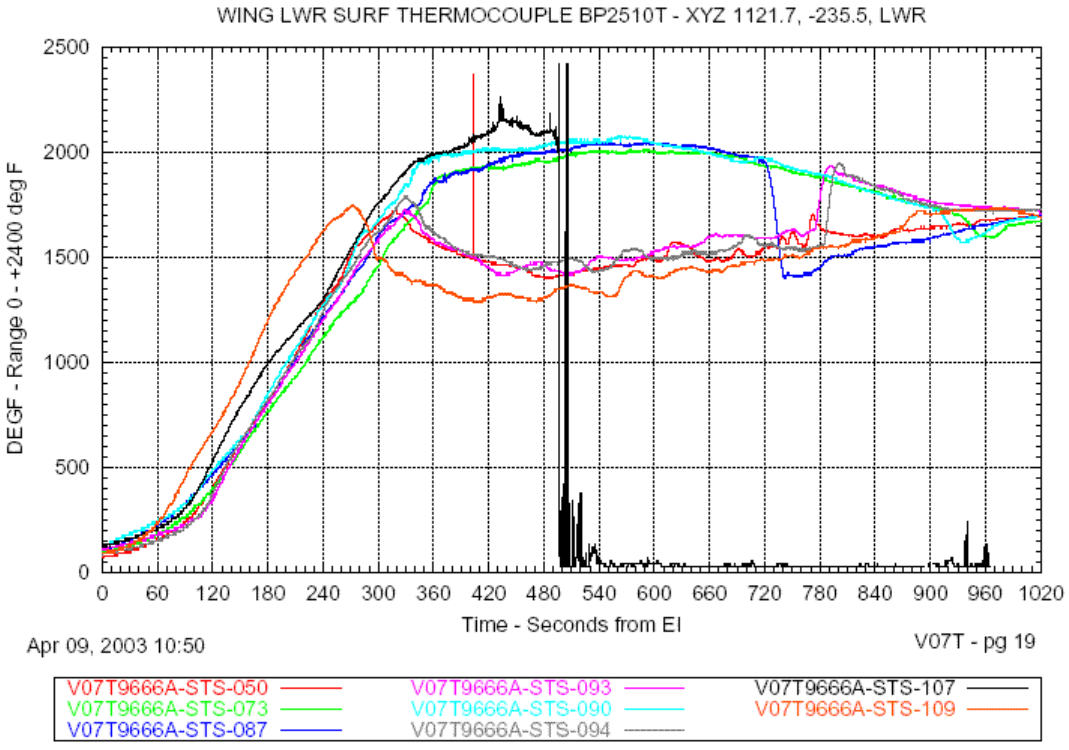

Figure 5.2.1-10 Temperature response of V07T9666A compared with previous flights of Columbia

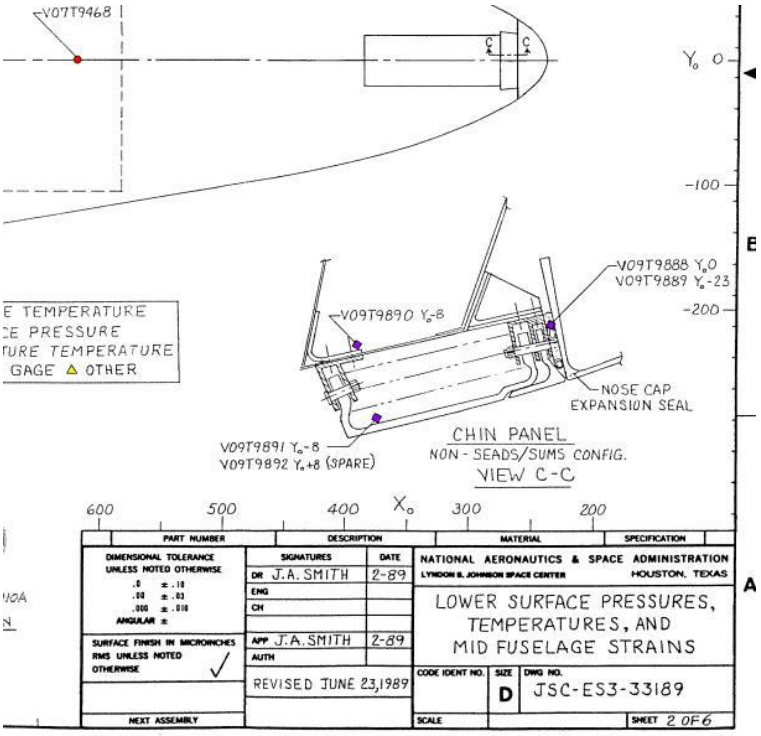

Figure 5.2.1-11 Nose Cap / Chin Panel Expansion Seal Instrument Locations

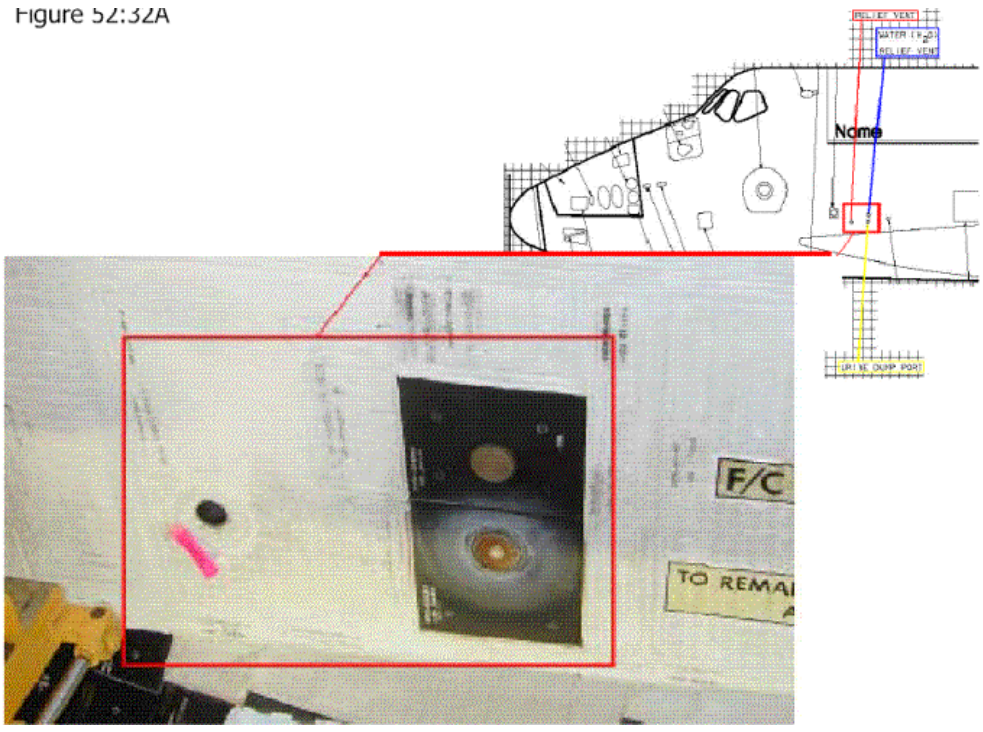

Figure 5.2.1-12 Vacuum Vent and Water Dump Nozzle Locations

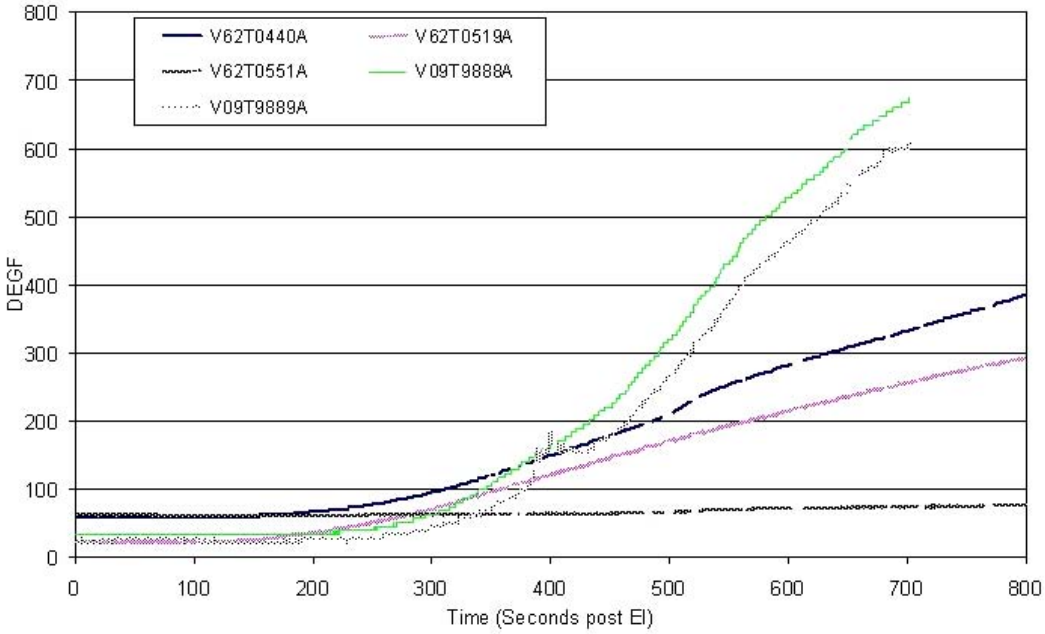

Figure 5.2.1-13 Chin Panel (V09T9880A and V09T9889A), Vacuum Vent (V62T0551A), Water Supply Dump Nozzle (V62T0440A), and Water Waste Dump Nozzle (V62T0519A)

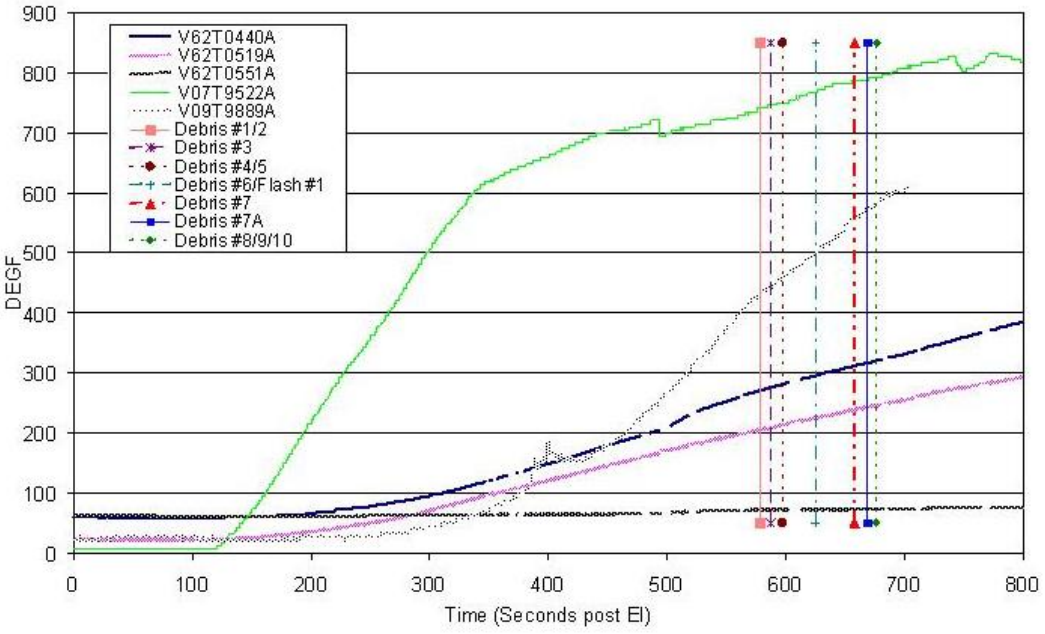

Figure 5.2.1-14 Chin Panel, Vent Nozzles, and local Surface T/C data plotted along with Debris Events 1 through 10.

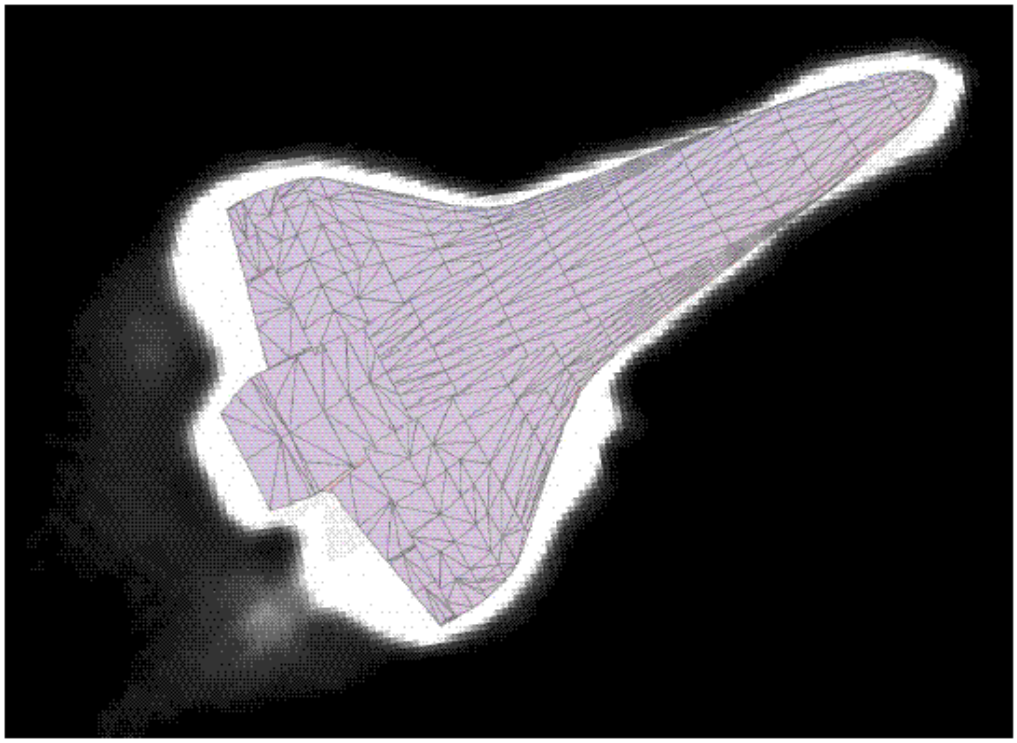

Figure 5.2.1-15 Kirtland AFB image taken at 13:57:14 GMT. Image has been enhanced and an Orbiter wire frame overlaid. View is of windward side of the Orbiter. Orbiter was in a left wing down roll attitude when this image was obtained.

5.2.2 Orbiter Certified Body Point Heating Methodology

5.2.2.1 Background on Body Point Heating Model Development

Entry aerodynamic heating of the Shuttle Orbiter is a result of the flow of air at high speed over the Orbiter. Friction between the air filaments as they stream over the orbiter surface, and compression near the stagnation regions of the nose and leading edges, convert kinetic energy of motion into heat. This heated gas environment envelops the Orbiter during its critical re-entry phase of flight.

Aerodynamic heating rates are influenced by all properties of the flow field as well as conditions at the body surface. In the external flow, the density, velocity, pressure, streamline pattern, and chemical composition must all be determined before heating calculations can be performed accurately.

The approach used for the development of Shuttle aerodynamic heating prediction methodology was to draw upon a vast knowledge available in the literature and combine it with Shuttle Orbiter wind tunnel data and Orbiter flight test data.

Use of wind tunnel data was strongly emphasized in the development of a heating prediction methodology. Where wind tunnel data were not available, analytical methods were used. It was the design philosophy (Figure 5.2.2-1) that, by proper use of wind tunnel data and analytical methods and by identifying and accounting for uncertainties in a logical manner, a minimum risk approach to the aerothermodynamic design of the Orbiter, without unnecessary conservatism, would be achieved. A nominal fairing/interpretation of wind tunnel data was used to develop the methodology. Verification of these methods was based on flow field solutions and data from developmental flight tests (OFT). A detailed description of the Orbiter entry heating prediction methods and database can be found in Rockwell International Document STS 83-0948 (1988).

5.2.2.2 Body Point Heating for Nose Cap, Wing Leading, Main Landing Gear Door

The basic approach for the Orbiter acreage is to break down the Orbiter into simple geometric shapes: sphere, cylinder, cones and wedges (Figure 5.2.2-2). These Simple Geometric Shapes (SGS) are correlated with wind tunnel data and adjusted to a nominal fit of the data. The SGS are then extrapolated to flight, while the adjustment factor is held constant. The adjustment factor accounts for Orbiter location, angle of attack, and Reynolds number variation. This approach works well for the Orbiter lower surfaces.

5.2.2.2.1 Fuselage Lower Surface (Nose Cap, Main Landing Gear Door)

The fuselage lower surface was divided into regions of both blunt body and slender body flows (Figure 5.2.2-3). The region of slender body flows was designated to be where the change in slope of the local velocity went to zero.

The bluntness of the Orbiter nose affects the downstream heating rate by altering the surface pressure distribution and by increasing the entropy of the flow at the boundary layer edge. For a cone, this bluntness causes the pressure to increase for a distance of one or two nose radii to a value greater than that for a sharp cone.

In the blunt body flow region, heat transfer film coefficients from wind tunnel data ratioed to reference sphere heat transfer values were applied to flight conditions adjusted by a slender body transfer factor. The reference sphere heating values were computed by the Fay & Riddell (1958) stagnation heating formulation with a variable Lewis number term. The heating distribution around the orbiter stagnation point at a 40^{o} angle of attack is shown in Figure 5.2.2-4.

At the stagnation point in the sonic flow zone, the slender body adjustment factors have a value of 1.0 and increase to the slender body value of 1.6 at X/L = 0.208 for alpha equal to 30^{o}. For angle of attack greater than 30^{o}, the slender body interaction zone is held constant at X/L = 0.20, although the adjustment factor is allowed to vary (Figure 5.2.2-5).

The slender body adjustment factors were determined by ratioing laminar flat plate theory values at flight to those at wind tunnel conditions. This resulted in the blunt to slender body transfer distribution of Figure 5.2.2-6.

The blunt body flow region is characterized by high pressure gradients, which, in the axial direction can be approximated by a Newtonian-Prandtl Meyer expansion (Figure 5.2.2-7), while the heat transfer can be approximated for wind tunnel conditions with a Cohen and Beckwith (1961) similar solution (Figure 5.2.2-8).

In the slender body region, a system was developed to modify Eckert's flat plate theory for streamline divergence by a series of factors as shown in Figure 5.2.2-9. Streamline patterns were obtained from oil flow data. To do this, wind tunnel data were compared with SGS using a nominal fit of the data, and laminar factors (LAMFACs) were developed. These laminar factors were allowed to vary with angle of attack. The LAMFACs were correlated with two angles of attack (α_{REF}) selected as reference conditions (1,2). Slopes of the LAMFAC (designated: Q_{SLOPE}) were developed about these two alphas, and reference laminar factors were established. This resulted in an angle of attack variation in equation form:

$$ALFAC = 1 + \frac{(\alpha - \alpha_{REF}) * Q_{SLOPE}}{LAMFAC_{REF}}$$

The SGS was adjusted by the product of ALFAC *$LAMFAC_{REF}$ to account for divergence. The assumption was made that both ALFAC and LAMFAC developed in the wind tunnel at $\gamma = 1.4$ and basically Mach 8 had the same variations and magnitude under flight conditions. An example of the variation in LAMFAC with angle of attack can be found in Figure 5.2.2-10 through Figure 5.2.2-12 for the lower surface body point 1600. Figure 5.2.2-11 shows the variation of wind tunnel test data and flat plate theory with angle of attack. When this information was converted to LAMFAC, the distribution in Figure 5.2.2-12 was obtained.

The origin of the flow used in the flat plate calculation was assumed to be at X/L = 0. When applied to points aft of X/L = 0.2, the small variation in angle of attack on stagnation point movement would be negligible in the wetted flow length. Forward of X/L = 0.2 (blunt body) the flow length did not fit directly into heating methodologies (heating ratios), although it is still of importance to boundary layer transition calculations.

Spalding and Chi (1964) turbulent flat plate values were adjusted using turbulent factors which were developed along similar patterns to the laminar factors. Turbulent factors also vary with angle of attack and body location and correlate similarly to the laminar factor equation.

Laminar factors were generally based on wind tunnel data from test OH39, OH49B and OH50B having model scales of 0.0175 and 0.04.

The existence of chemical non-equilibrium in the shock layer during much of the Orbiter's entry trajectory, coupled with the relatively non-catalytic behavior of the TPS materials, necessitate an additional correction to laminar equilibrium heating values on the nose cap and lower surface. This adjustment is in the form of a catalytic heating parameter (η) inferred from flight data:

$$(q_{wall})_{catalytic} = h_{eq}(i_r - i_w - \eta i_d)$$

where h_{eq} is the equilibrium heat transfer coefficient, i_r is recovery enthalpy, i_w is the wall enthalpy and i_d is dissociation enthalpy. Here, $\eta = 0$ implies equilibrium heating and $\eta = 1$ is equivalent to non-catalytic wall heating.

The catalytic resistance coefficient, η, is developed from a recombination rate constant dependent on surface recombination efficiency and gas properties at the surface. Thermocouple data from STS-2, STS-3 and STS-5 were used to determine the numerical form of the temperature dependent recombination

efficiency. Detailed discussion of the non-catalytic heating approach and correlation technique is presented in Miller (1984).

5.2.2.2.2 Wing Leading Edge Heating Methodology

In the philosophy of simple geometric theories, the wing leading edge would be thought of as a swept cylinder. However, there are several features that move this approach to only a starting solution for the problem. First, an airfoil attached to the leading edge affects the shock shape and thereby affects the effective radius of the cylinder. Second, the intersection of the bow shock with the leading edge shock (Figure 5.2.2-13) produces several features as discussed in various sources. The shuttle wing leading edge shock region was interpreted to experience a type V interference pattern (Figure 5.2.2-14). This type of shock interaction results in a new shock that strikes the leading edge at about 55% semi-span (dependent on angle of attack) and disturbs the wing lower surface. Also formed is a jet shear layer that strikes the outboard section of the wing, scrubbing both the upper and lower surfaces.

Based on wind tunnel data from wind tunnel test OH66, the effective radius variation with angle of attack was developed (Figure 5.2.2-15). By using this curve along with the modified swept cylinder equation, the effect of shock impingement can be determined (Figure 5.2.2-16). This figure represents the effect of shock impingement at 55% semi-span. Therefore, as the shock position moves with angle of attack, the maximum heating footprint moves leading to a maximum heating at the 55% semi-span between 35 and 40 degrees angle of attack. At the other angles of attack, maximum heating would occur at a different span-wise location.

Wind tunnel data applied directly to flight were used. Data were applied in terms of film coefficients (local to reference sphere ratio) as a function of angle of attack and leading edge location. For span locations where no data existed, the modified swept cylinder was used.

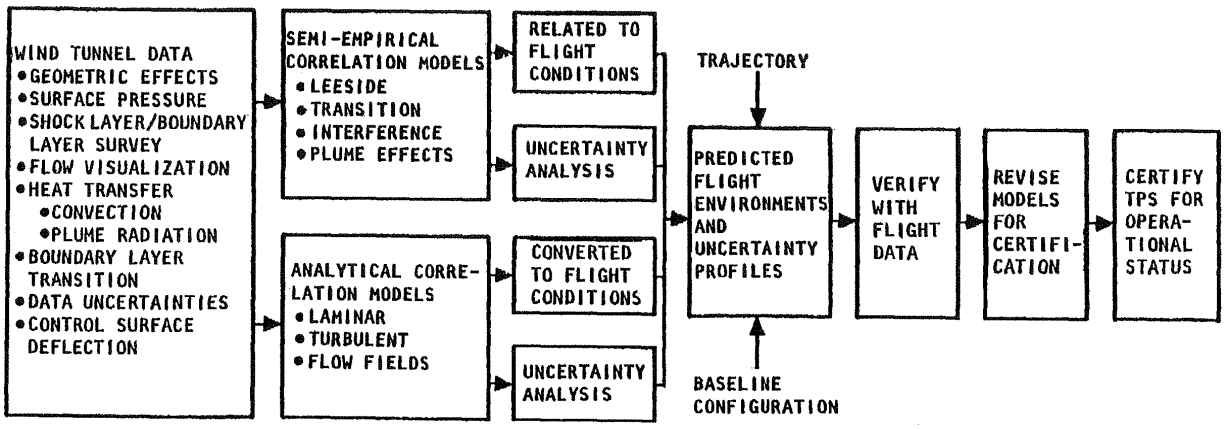

Figure 5.2.2-1 Orbiter Entry Heating Design and Certification Logic

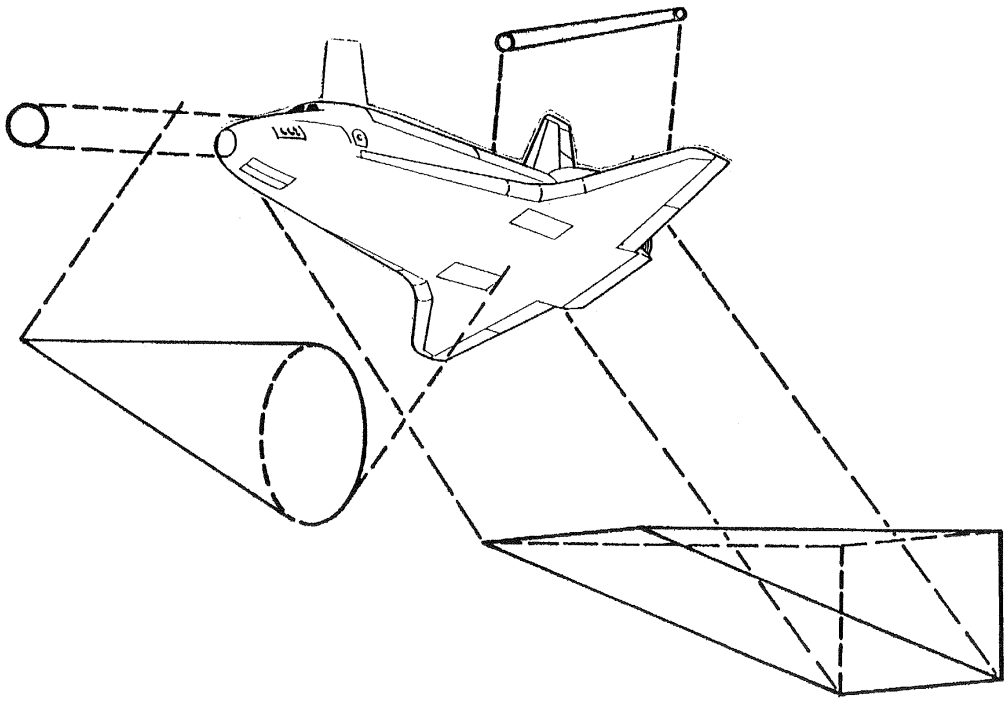

Figure 5.2.2-2 Simple Geometric Modeling (SGS)

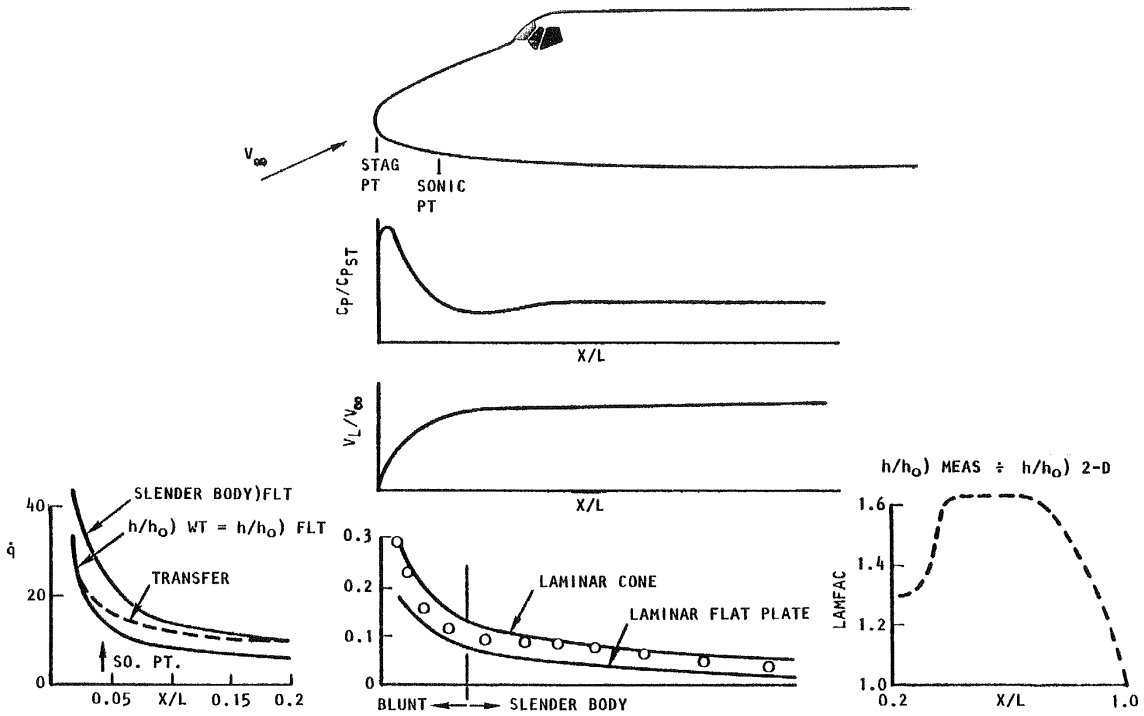

Figure 5.2.2-3 Fuselage Lower Surface Heating Extrapolation to Flight

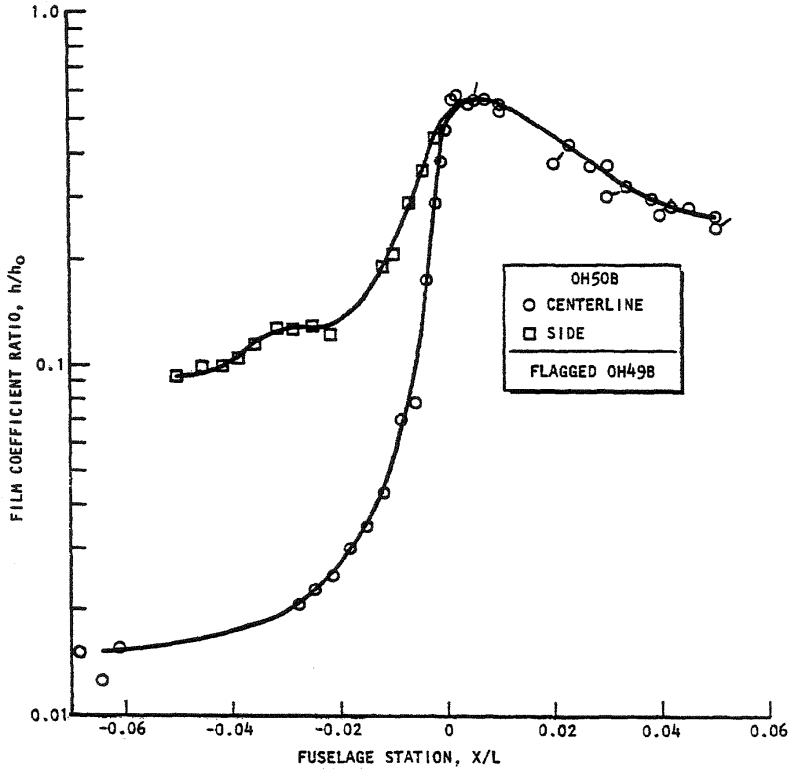

Figure 5.2.2-4 Heating Distribution Around the Orbiter Stagnation Point at Alpha = 40°

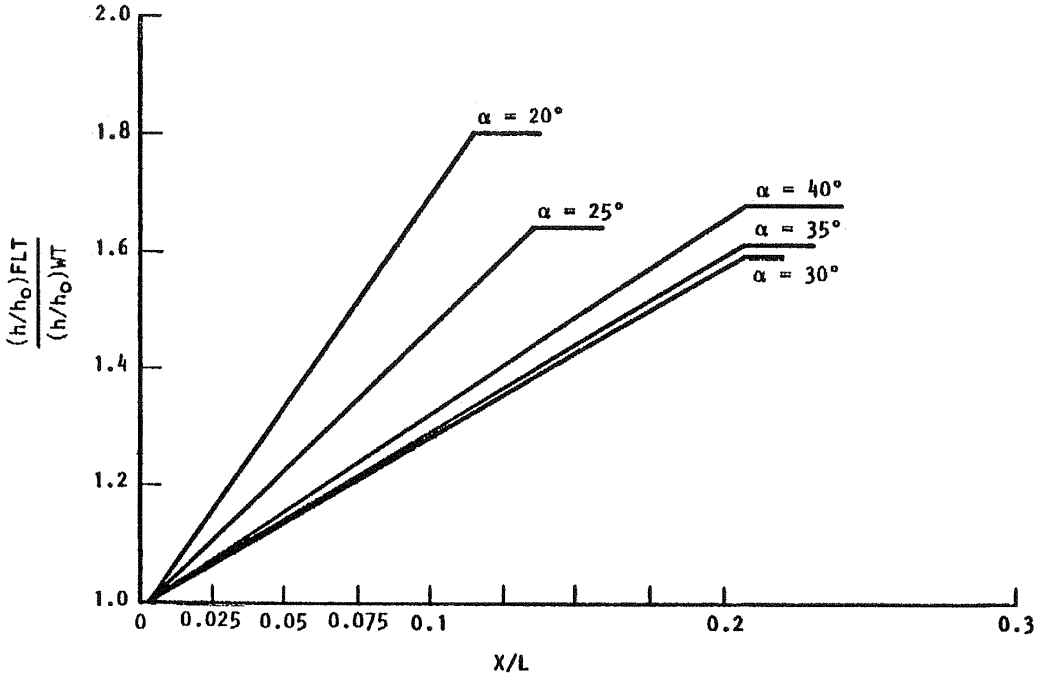

Figure 5.2.2-5 Wind Tunnel to Flight Scaling

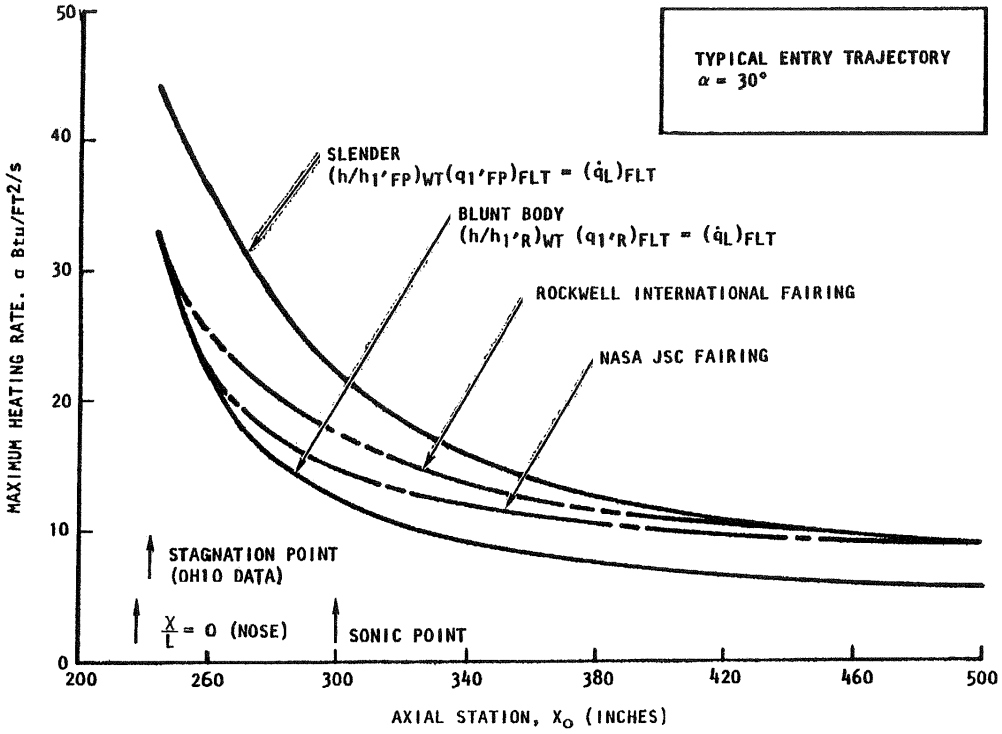

Figure 5.2.2-6 Blunt-Body-to-Slender Body Transfer Determination

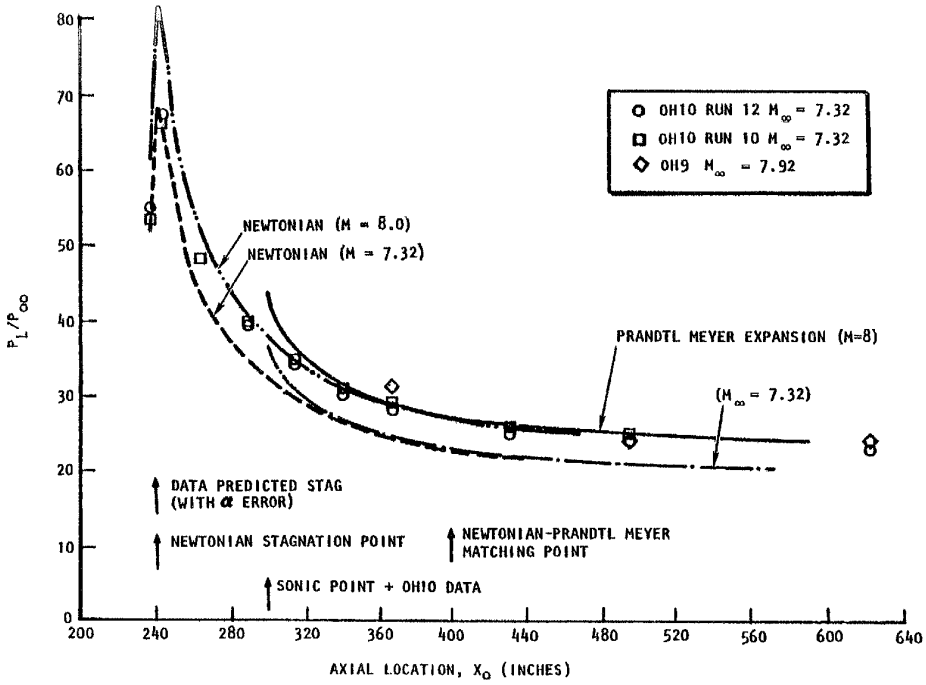

Figure 5.2.2-7 Forebody Pressure Modeling Under Wind Tunnel Conditions (Alpha = 30°)

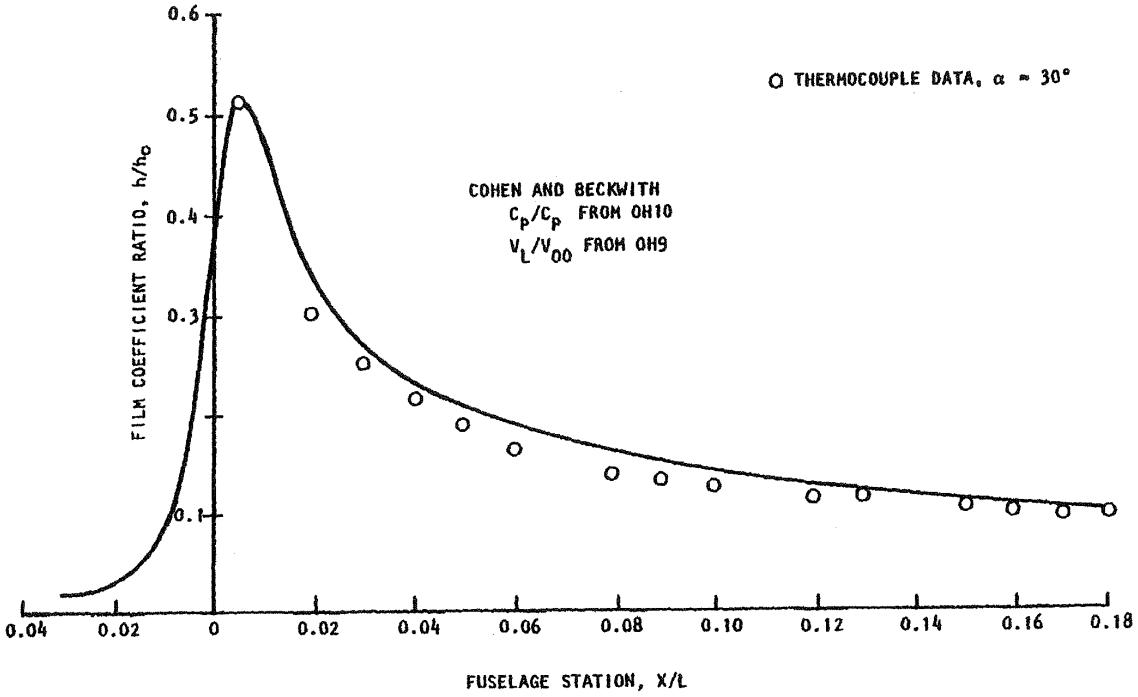

Figure 5.2.2-8 Cohen and Beckwith Modeling of Fuselage Forebody

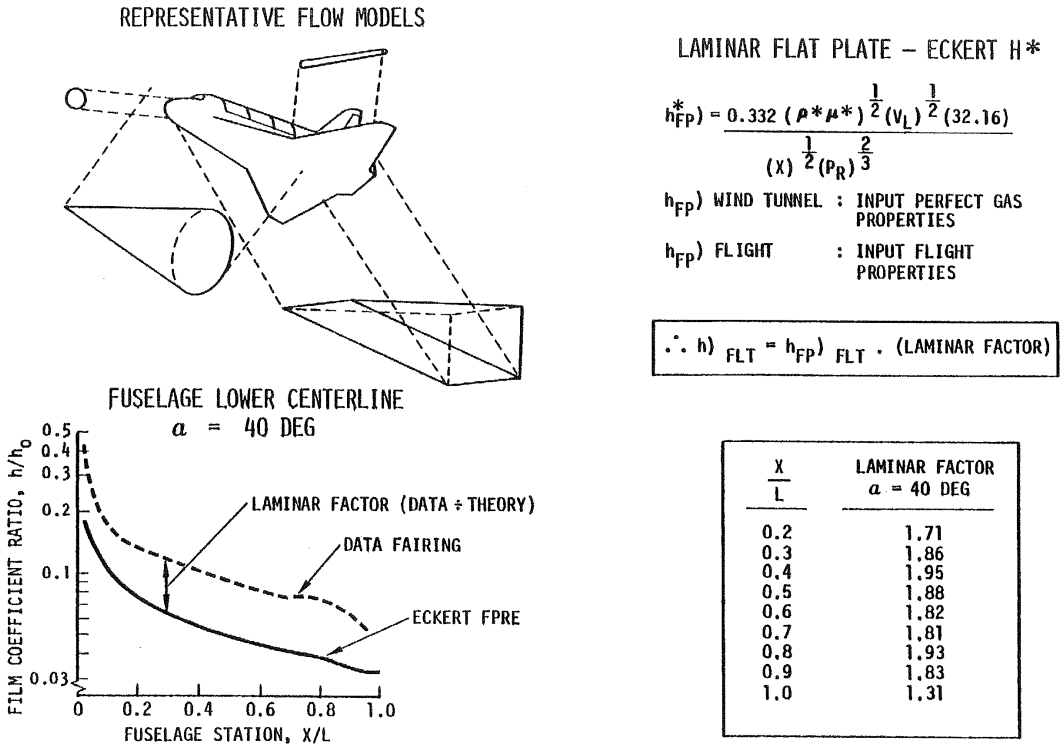

X/L	LAMINAR FACTOR α = 40 DEG
0.2	1.71
0.3	1.86
0.4	1.95
0.5	1.88
0.6	1.82
0.7	1.81
0.8	1.93
0.9	1.83
1.0	1.31

Figure 5.2.2-9 Orbiter Lower Surface Methodology, Slender Body Approach

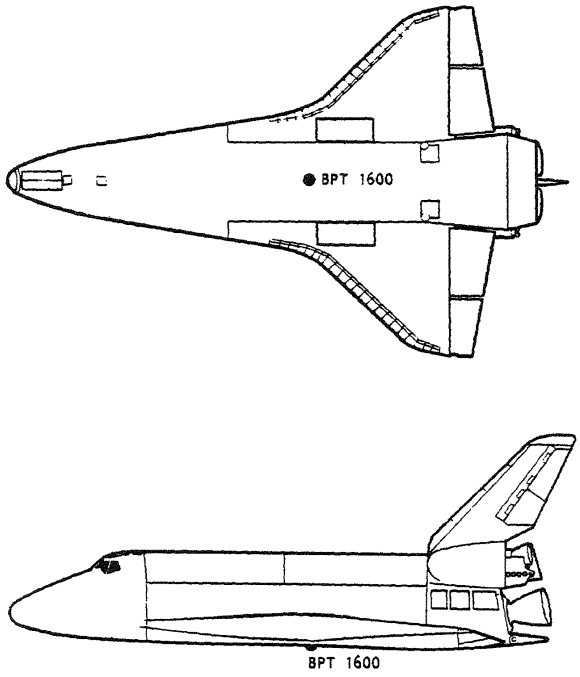

Figure 5.2.2-10 Typical Lower Surface Location

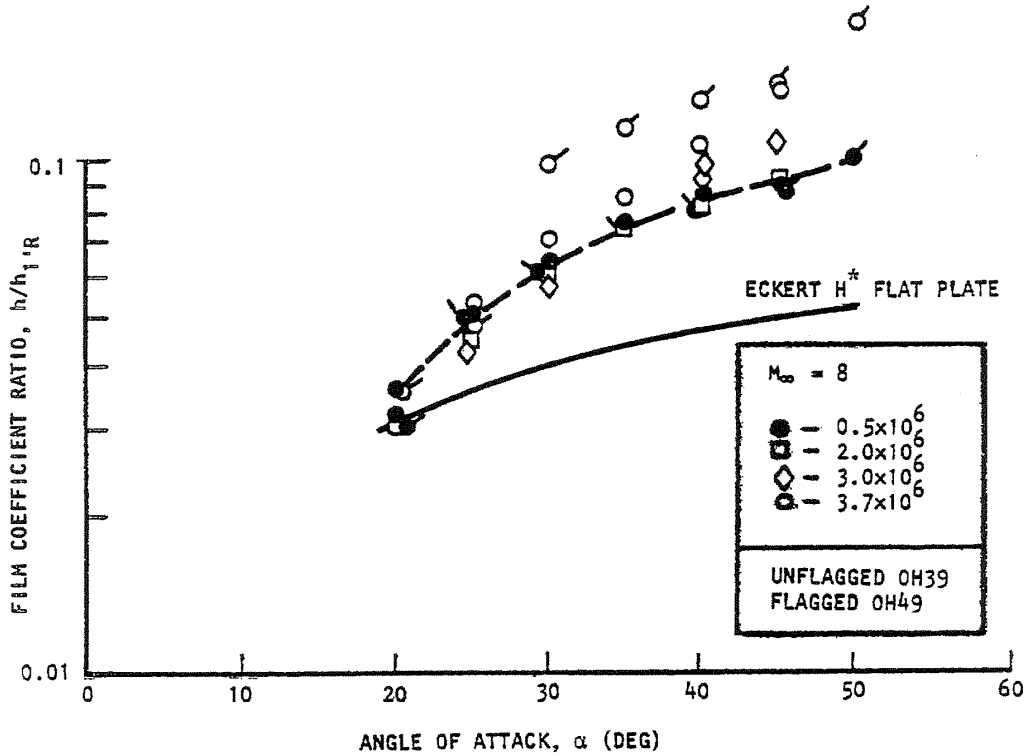

Figure 5.2.2-11 Local Heating Variation With Angle of Attack on Fuselage Lower Surface Centerline at X/L = 0.6

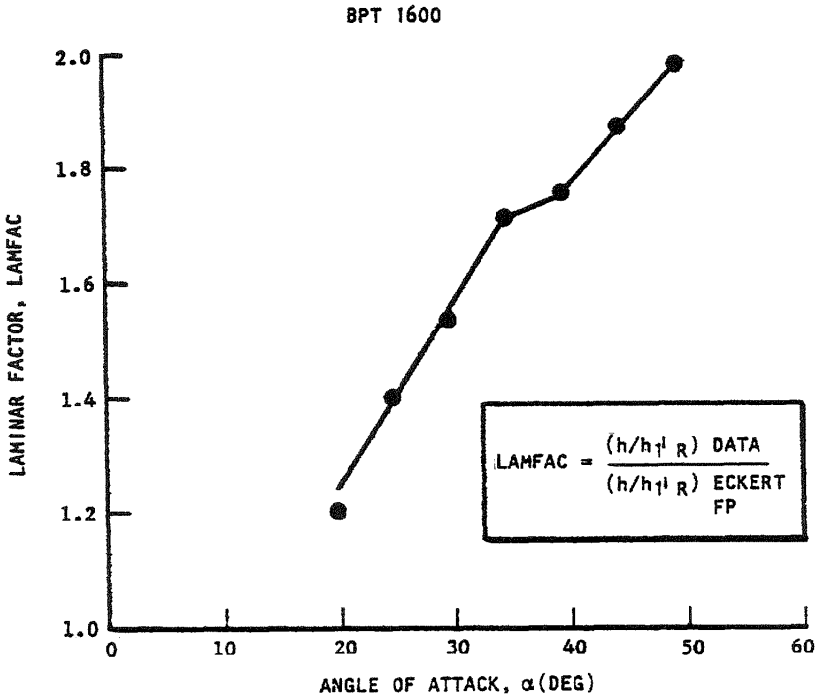

Figure 5.2.2-12 Fuselage Lower Surface Centerline Laminar Factor Laminar Variation With Angle of Attack

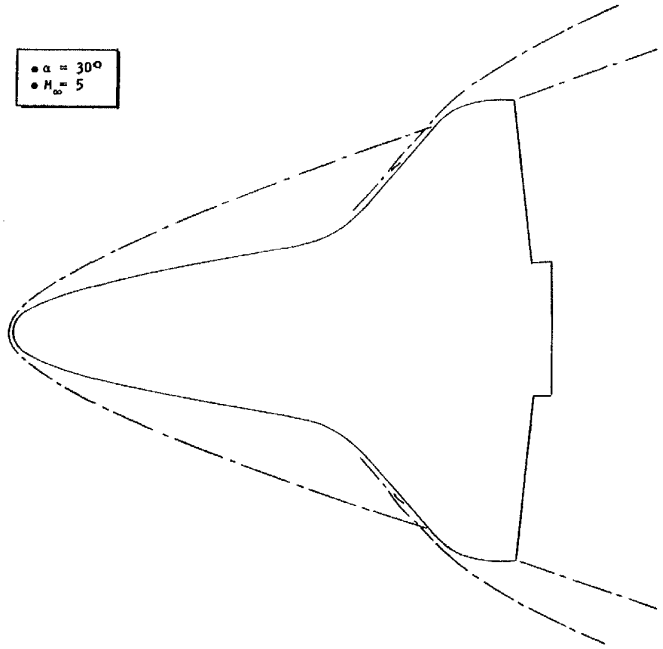

Figure 5.2.2-13 Shock Patterns Based on Wind Tunnel Shadowgraph

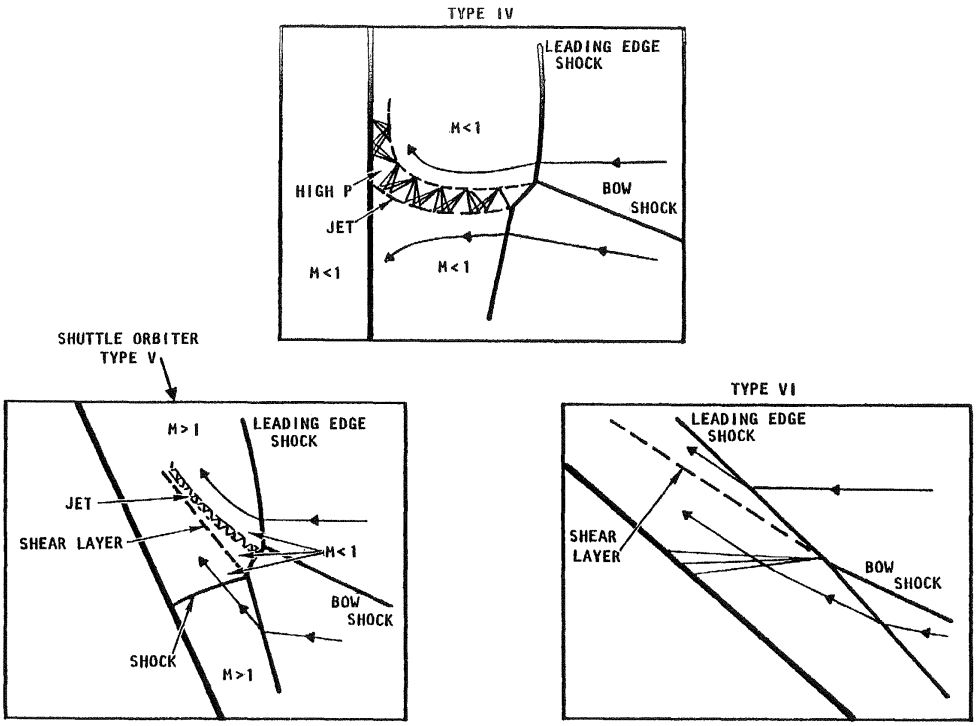

Figure 5.2.2-14 Variation in Shock Impingement Patterns

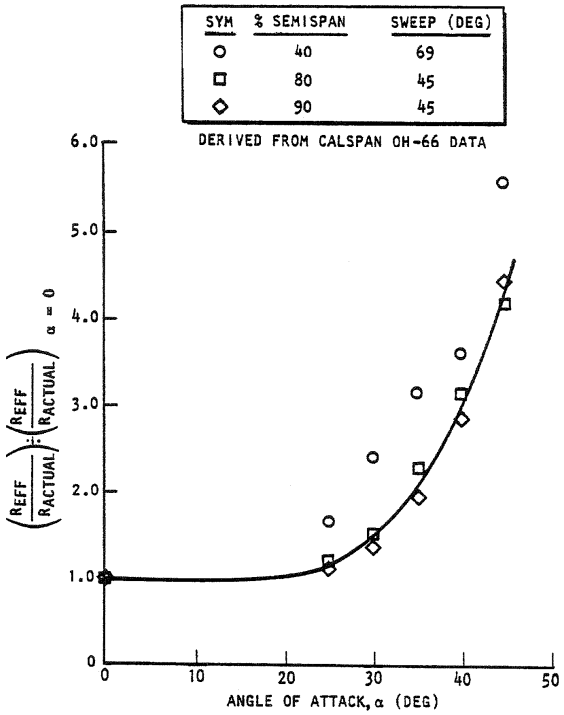

Figure 5.2.2-15 Angle of Attack Effect on Leading Edge Effective Radius

$$\text{SHOCK EFFECT} = \left(\frac{R_{EFF}}{R_{ACTUAL}}\right)_{\text{FIGURE 1-107}} \div \left(\frac{R_{EFF}}{R_{ACTUAL}}\right)_{\text{55\% SEMISPAN}}$$

DERIVED FROM CALSPAN OH-66 DATA

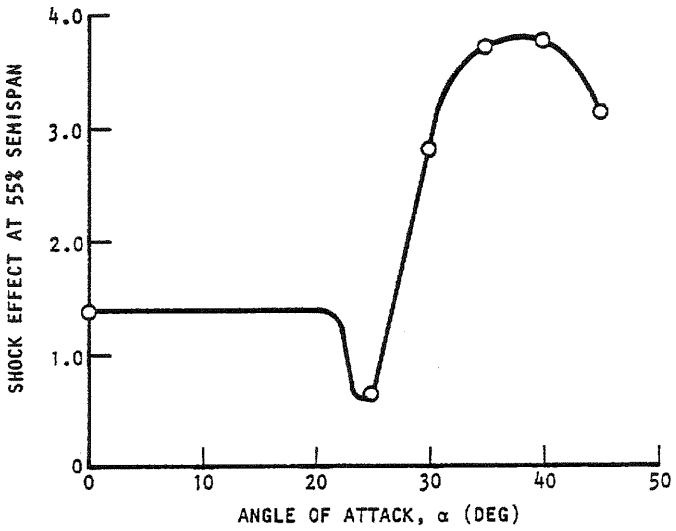

Figure 5.2.2-16 Angle of Attack Effect on Shock Impingement Effects

5.2.3 Wind Tunnel Testing

The purpose of this section is to describe the hypersonic aerothermodynamic wind-tunnel program conducted at the NASA Langley Research Center in support of the STS-107 accident investigation. The primary objective of the testing was to provide information regarding surface heating characteristics on scaled Orbiter models with surface perturbations to simulate various forms of localized damage to the thermal protection system (TPS). With very limited flight information available during the first weeks after the loss of STS 107, initial experimental testing covered a broad spectrum of TPS damage. As the investigation developed, increasing emphasis was placed on obtaining test data consistent with the subsequent body of recovered debris and extracted Orbiter OEX flight recorder data. Presentation of all heating test data associated with TPS damage, particularly that associated with early scenarios, has not been attempted in this section; emphasis has instead been placed on the data relevant to the working scenario involving damage to RCC panels 5-9.

Presently, the NASA has three active hypersonic wind tunnels (collectively referred to as the Langley Aerothermodynamics Laboratory) in the NASA LaRC inventory of ground-based facilities for hypersonic aerodynamic and aero-heating testing. Two facilities, the NASA LaRC 20–Inch Mach 6 Air and the 20–Inch Mach 6 CF_4 Tunnels, were utilized to characterize both heating and aerodynamic effects associated with damage scenarios. The high run productivity of the Mach 6 air tunnel was essential for assessments of damage scenarios involving large numbers of geometric parametrics. This initial screening capability was ideal for establishing test priorities and optimizing use of the more appropriate Mach 6 CF_4 tunnel. In addition, the wind tunnel results helped to focus application of higher fidelity CFD tools for damage simulations at flight conditions. Testing was not pursued in other facilities because appropriate testing techniques to perform rapid simultaneous aerodynamic and global aero-heating measurements on the Orbiter configuration were not available. Other NASA high enthalpy facilities or shock tunnels outside of NASA, while capable of generating high velocity/enthalpy conditions, were not amenable to the quick, parametric screening necessary for an investigation of this scope. The characterization of leeward flow fields in shock tunnels would also present challenges due to extremely short run times.

Documentation of global surface heat transfer, complimentary surface streamline patterns, and shock shapes are provided in this section for various simulated damage scenarios. Test parametrics include angles of attack from 38 to 42 deg, sideslip angles of $\pm$1 deg, unit Reynolds numbers from 0.05×10^6 to 6.5×10^6/ft, and normal shock density ratios of 5 (Mach 6 air) and 12 (Mach 6 CF_4). The model scale utilized in these studies was 0.0075 (approximately 10 inches).

5.2.3.1 Mach 6 Air and Mach 6 CF_4 Applicability Flight

Aeroheating events leading to the loss of Columbia occurred during hypervelocity entry at low Reynolds numbers and high Mach number (25 to 18) and enthalpy levels. This complex flight environment is characterized by the excitation of energy modes in the gas as it passes through the bow shock wave of the Orbiter. At high enthalpy conditions, high temperature effects result in dissociation, recombination, and ionization of the air, and these in turn dictate changes in the shock layer flow. An effect with large impacts on the flow field is the reduction of the ratio of specific heats (herein referred to as γ) relative to a non-reacting perfect gas. In hypervelocity flight, decreases in γ within the windward and leeward Orbiter flow field result in increases in the density ratio across shock waves. The change in density ratio produces differences in shock layer structure including shock inclination and standoff distances and hence, shock interaction locations. Larger degrees of flow compression and expansion can exist relative to a non-reacting gas and these changes have been shown to directly influence Orbiter aerodynamics. While it is recognized that a nominal Orbiter entry environment cannot be duplicated in any one ground-based facility, aeroheating effects due to localized damage are first and foremost the result of flow physics or fluid dynamic phenomena (e.g., boundary layer/shear layer transition, shock-shock and shock-boundary layer interaction, flow separation-reattachment) associated with a given vehicle geometry, attitude, and flight condition. High temperature chemistry effects at high flow enthalpy levels "alter" the aerodynamic or aeroheating characteristics due to flow physics, but do not add new flow physics phenomena or delete any.

Testing in the perfect gas environment of a Mach 6 air tunnel captures all pertinent flow physics phenomena but does not provide information as to how the results may be influenced by flow chemistry. To address the effects of flow chemistry, the experimental test program was designed to take advantage of the simulation capability of the 20–Inch Mach 6 CF_4 Tunnel. Orbiter damage scenarios were first screened in the Mach 6 air tunnel for aerodynamic and aerothermodynamic consistency; the most promising were then tested in the CF_4 tunnel. This conventional-type (as opposed to impulse-type) low enthalpy hypersonic tunnel has relatively long run times and avoids complex chemistry typically associated with high enthalpy facilities. Modeling of the effects of flow chemistry that occur at the actual flight conditions is accomplished by using a heavier-than-air test gas that exhibits a low ratio of specific heats and a correspondingly high normal shock density ratio characteristic of air at reacting hypersonic conditions. In conjunction with the Mach 6 air tunnel, this CF_4 tunnel provides the capability to test at the same free-stream Mach and Reynolds numbers, but at two values of density ratio (approximately 5 in air and 12 in CF_4). The Mach 6 CF_4 density ratio of 12 is relatively close to the values of 15-18 encountered near Orbiter re-entry peak. Thus, generating large density ratio values simulates many of the aerodynamic and aeroheating effects associated with a high temperature gas. Synergistic tests of the Orbiter in these facilities led Miller (1982) to conclude that the effects of density ratio on the non-dimensional windward surface heating at hypersonic entry angles of attack were small.

Prior to the application of CFD with complex reacting chemistry air, perfect-gas engineering codes were used quite successfully to predict aerodynamic/aero-heating characteristics at hypervelocity conditions where the effects of flow chemistry were significant. This was accomplished via modifications to the perfect gas equations by the introduction of an effective gamma to "account" for high temperature effects. The effective gamma (herein referred as γ_{eff}) was based on the normal-shock density ratio value and the free-stream Mach number (for Mach numbers > 10) at re-entry conditions. Thus, one method to bridge between perfect air and heavy gas hypersonic wind tunnels and flight is through the use of an effective gamma. Brauckmann (1995) used gamma defined as local enthalpy divided by internal energy to successfully characterize the STS-1 pitch-up anomaly by relating Orbiter aerodynamic measurements made in the CF_4 tunnel to flight predictions. For the Orbiter at flight Mach numbers above 18, γ_{eff} is approximately 1.11. In the Mach 6 CF_4 and air tunnels, the value is 1.13 and 1.40, respectively. A close agreement between flight prediction and measured windward bow shock inclination and standoff distance is shown in Figure 5.2.3-1. In addition, there is general agreement between the flight and Mach 6 CF_4 tunnel conditions for predicted pressure coefficients and non-dimensional heating distributions (and wing bow shock interaction locations) on the Orbiter windward surface (Figure 5.2.3-2). These two observations imply very good ground-based simulation capability of the Orbiter windward flow field.

Compressibility (Mach number) effects were not addressed explicitly via testing in the two facilities. However, during hypervelocity/hypersonic entry the Orbiter is at relatively high angles of attack and thus the local Mach number over a majority of the windward surface is supersonic (typically between 2 and 3). For blunt to moderately blunt configurations such as the Orbiter at entry angles-of-attack, aerodynamic characteristics are essentially independent of Mach number. In terms of viscous simulation in the continuum (Reynolds number) regime, the flight free stream Reynolds number based on vehicle length was below 0.5×10^6 up to the point of the first measured off-nominal heating event on the side fuselage and OMS pod regions. The free stream Reynolds number for STS-107 had increased to approximately 2.4×10^6 at loss of signal near M=18. In the Mach 6 air testing, Reynolds number based on model length was varied between 0.3×10^6 and 6.5×10^6, and the majority of testing occurred at 2.4×10^6. The length Reynolds number in the Mach 6 CF_4 tunnel was varied between 0.05×10^6 and 0.55×10^6 with most of the testing at 0.4×10^6. These Mach 6 CF_4 conditions are more representative of the flight conditions prior to loss of signal (higher altitude and Mach number). In the design of wind tunnel experiments, local conditions are often more appropriate when, for example, boundary layer correlations are sought. For the Orbiter at M=18 in flight, the edge Mach number at X/L=0.6 is approximately 3 with a post normal shock Reynolds number of 0.4×10^6 (Bouslog, 1995). The corresponding conditions for the Mach 6 air tunnel (at X/L=0.6) are 2.3 and 0.42×10^6, respectively. During a nominal Orbiter entry at Mach numbers greater than 18, the windward (Bouslog, 1995) and leeward (Throckmorton, 1995) flows are laminar. Wall-to-total temperature ratio was 0.60 and 0.45 for the air and CF_4 tunnels, respectively. Flight wall-to-total temperature ratio for the Orbiter near Mach 18 at flight conditions is generally within the range of 0.2 to 0.3.

In terms of facility limitations, it is recognized that acoustic disturbances are inherent for any hypersonic ground-based facility having a turbulent boundary layer on the nozzle wall. This fact may promote transition in an attached or separated wall boundary layer earlier than may occur in flight. Surface roughness related transition data provided to the investigation for correlation purposes were based upon a fully effective roughness criterion, whereby turbulence is initiated immediately downstream of the roughness element site. When vehicle surface roughness is present (a typical boundary layer transition bypass), it is generally accepted within the transition community that facility noise from conventional tunnels has little effect on transition as long as roughness heights are large enough to be considered effective.

One of the largest unknowns associated with the ground-based testing performed as part of the STS-107 investigation is the extrapolation to flight of wind tunnel based leeside flow field characteristics. Data derived from conventional air facilities regarding leeward flow separation, reattachment, transition of separated or attached leeward flow, and leeward vortex interactions all present significant scaling issues as discussed by Haney (1995). Historically, the CF_4 tunnel has not been heavily utilized for characterization of separated, leeward (or wake) flows. Rather, it has been used for aerodynamic studies associated with blunt planetary entry configurations where the inviscid forebody flow is primarily governed by the normal shock density ratio (Jones, 1969). If, in hypervelocity flight, the Orbiter leeside flow is non-reacting or frozen due to the rapid flow expansion around the leading edge, it is quite possible that the CF_4 simulation (with a free-stream $\gamma = 1.22$) will provide a rather good representation of coupled leeside flow physics and flow chemistry. It will be equally important in the future to determine how well CFD can accurately capture the "challenging" leeside flow physics (e.g., flow separation/reattachment, vortical flow) at wind tunnel conditions before the complexity of flow chemistry at flight conditions is introduced. In Mach 6 CF_4 results for the Orbiter, it has been observed that the spatial location of maximum OMS pod heating is closer to the location observed in flight (i.e., the high temperature black tile on the flight vehicle) relative to that inferred from test results in Mach 6 air. It is suggested by these observations that perturbations to the nominal leeward flow field from certain damage scenarios may also be better represented by the Mach 6 CF_4 tests (as opposed to Mach 6 air) as the disturbances generally originate from the windward surface.

5.2.3.2 Orbiter Configurations Tested

Baseline Orbiter Models

More than 70 cast ceramic models of the Orbiter configuration were manufactured as part of the investigation and they all share a common construction technique. Initially, during the first weeks of the investigation, existing ceramic 0.0075 scale models of the Orbiter from a prior NASA JSC/LaRC collaboration (Berry, 2002) were utilized. The expansive scope of aeroheating testing needed for the investigation, however, required additional models to be fabricated. To accomplish this quickly, a pre-existing epoxy based mold constructed from the 0.0075 scale metallic force & moment model (used during the early phases of the aerodynamic testing-see Section 4.3.1) was used to slip cast each new ceramic model. A magnesia ceramic was used to backfill the ceramic shells, thus providing strength and support to the base mounted sting support structure. Ceramic models used during simultaneous aerodynamic and aeroheating tests were constructed in a similar fashion, but were modified to accept a six-component balance. An overview of model fabrication used exclusively for thermal testing is shown in Figure 5.2.3-3. In order to obtain accurate heat-transfer data with the phosphor or IR technique, the ceramic models are cast with a material having low thermal diffusivity and well-defined, uniform, isotropic thermal properties. The phosphor coatings typically do not require refurbishment between runs in the wind tunnel and have been measured to be approximately 0.001 inch thick. Details concerning the model fabrication technique and phosphor coating can be found in Buck (1993, 2000). Fiducial marks were placed on the model side fuselage surface at the locations for RTDs V34T1106A and V09T1724A (Orbiter coordinates provided by NASA JSC) and axial stations X/L= 0.25, 0.50, 0.75, and 0.90. These fiducial marks were used to assist in more accurately determining spatial locations of surface heating features.

Modified Orbiter Models

Damage to the Orbiter was simulated on the ceramic models in several ways and was driven by the leading scenario(s) at the time of testing. Initial modifications to the model surface involved placing discrete protuberances at strategic locations on the windward surface (e.g., left main landing gear door) and along the left wing leading edge (along individual RCC or adjacent carrier panels). Subsequent

modeling of damage scenarios was more intrusive and involved machining cavities or holes through the wing. Damage in the form of a completely missing isolated RCC panel 6 was initially attempted with hand tools and later with milling operations. The approximate locations of RCC panels, carrier panels, and TPS damage for these early tests were taken from technical drawings of the TPS layout (Joels, 1982) and transferred to the model surface via transparency. A higher fidelity, more systematic approach to characterizing wing leading edge damage was undertaken and involved construction of 13 models (see Figure 5.2.3-3) each with an individual missing RCC panel (1-13). RCC panel and adjacent upper and lower carrier panel locations were provided in the form of a CAD file. These locations were transferred to the model as discrete points via the surface verification laboratory at NASA LaRC. Additional models were constructed to characterize thermal effects associated with multiple missing RCC panels, partially missing panels (with and without vent paths down the RCC channel or to the leeside) on the wing upper surface, and missing T-seals. The leading edge channel formed by the Orbiter RCC panels was not captured with the ceramic models. Thus, removal of an RCC panel or T-seal yielded solid walls and hence no lateral pressure relief.

Simulation of leading edge damage with a leading edge channel (lateral pressure relief) similar to the flight vehicle required a unique approach to model construction. A solid model CAD file (1997 definition-see sec 5.2.3.2) was modified to approximate the volume of the RCC channel (Figure 5.2.3-4). A rapid prototyping technique was used to "grow" a resin stereolithography (SLA) model. Thermal protection of the resin model was provided for by application of a ceramic coating to the resin model. Qualitative thermal imaging was accomplished via the phosphor thermography technique. To characterize the thermal effects associated with RCC channel venting to the leeside, a similar approach was taken. A resin model was internally modified (see Figure 5.2.3-5) to blow CF_4 or nitrogen gas through a continuous 0.01-inch vent gap along the upper wing near the RCC/carrier panel interface.

5.2.3.3 Results for Mach 6 Air

Wing Leading Edge Discontinuities

The sensitivity of global aeroheating distributions on the windward and side fuselage surfaces to several forms of simulated RCC panel 6 damage is summarized in Figure 5.2.3-6 and Figure 5.2.3-7, respectively. These results, obtained using IR thermography, all correspond to the same model residence time in the flow and indicate local areas of increased surface temperature relative to the nominal configuration. The typical surface protuberances placed along the wing leading edge would correspond to a 13-inch x 13-inch full scale surface raised 0.5-inch above the nominal outer mold line. While shown to be effective at promoting boundary layer transition on the windward surface, the raised disturbances along the leading edge did not produce temperature augmentations on the side fuselage at these Mach 6 air conditions. The temperature image corresponding to run 47 in Figure 5.2.3-7 was the first direct experimental evidence that simulated RCC panel damage in the form of a "notch" could produce a localized heating anomaly on the Orbiter side fuselage.

Missing Wing RCC Panel Survey

The sensitivity of Orbiter side fuselage surface heating to simulated RCC panel damage for completely missing individual panels is summarized in Figure 5.2.3-8. At the time of testing, the body of recovered debris did not refute the possibility of entire RCC panels missing and it was felt that this form of damage would be easier to model computationally. Higher fidelity, parametric removal of individual leading edge RCC panels 1-13 was undertaken to characterize the location and magnitude of the heating disturbance on the side fuselage. The results were obtained using phosphor thermography and indicate local areas of increased surface heating relative to the nominal wing leading edge. Global heating distributions are presented in terms of the ratio of enthalpy-based heat-transfer coefficients h/h_{REF}, where h_{REF} corresponds to the Fay and Riddell (1958) predicted sphere stagnation-point heating with a 1-ft radius at flight scale (i.e., radius equal to 0.09-inches at wind tunnel scale). Unless noted otherwise, a constant maximum color value of 0.25 was selected for data presentation to maintain consistency when viewing or comparing images. On the contour scale, the colors tending towards red indicate areas of higher heating (temperatures) while the colors towards blue represent areas of lower heating.

A localized heating disturbance on the side fuselage (Figure 5.2.3-8) was evident for all panel locations RCC (1-13). Although the heating magnitudes associated with the disturbance were generally insensitive to the location of the missing panel, the inclination of the heating pattern on the side fuselage was

dependent on the span-wise location of the RCC damage. The nearly vertical side fuselage heating footprint associated with missing RCC panel 1 approached a nearly horizontal orientation (parallel to the Orbiter reference waterline) as the systematic removal of individual RCC panels progressed outboard to missing RCC panel 12. A missing RCC panel at the location of the Mach 6 air wing/bow shock interaction (RCC panel 12) did not result in abrupt changes to the side fuselage heating footprint in terms of location or magnitude. In addition, no large location or magnitude changes to the surface heating associated with missing RCC panel 12 were observed for small changes in angle-of-attack (Figure 5.2.3-9), sideslip (Figure 5.2.3-10), or a factor of 4 increase in Reynolds number (Figure 5.2.3-11). Heating images taken from above the model (Figure 5.2.3-12) indicated that disturbances created from wing leading edge damage could produce leeward flow field perturbations strong enough to reduce the OMS pod heating for missing RCC inboard of panel 9. In contrast, local heating augmentations to the forward face of the OMS pod were measured for missing $9 \leq$ RCC panel ≤ 11. Comparison of Schlieren images revealed the local shock structure complexity associated with missing RCC panel 8 (Figure 5.2.3-13) relative to a baseline undamaged wing leading edge (Figure 5.2.3-14).

Holes Through Wing

Limited parametric studies of simulated damage in the form of a wing breach from the windward surface to the leeward surface were attempted in this facility and were primarily associated with aerodynamic testing (see Section 4.3.1). Initially, circular holes dimensionally consistent with the width of a carrier panel (approximately 4 inches full scale) were placed at the interfaces for carrier panels 5, 9, 12, and 16. The holes were found to force boundary layer transition on the windward surface to the damage site. The model and IR setup for the aerodynamic tests at this point in time precluded imaging the side fuselage. Since the model also incorporated damage in the form of missing RCC panel 6, it is believed that effects (if any) from the carrier panel holes would have been dominated by the disturbance from the missing RCC panel.

TPS damage in the form of a much larger breach through the wing was attempted, but the side fuselage heating measurements were considered qualitative due to compromised phosphor coatings on the models that were used. The holes were orientated normal to the wing chord and were located near the left main landing gear door. One hole location was approximately located at the center of the forward bulkhead (X=1040-inches in Orbiter coordinates) and the second location was near the center of the outboard bulkhead (Y=167-inches in Orbiter coordinates). At each location, the wing hole diameter was systematically changed from 0.0625 to 0.125 and 0.25-inch at wind tunnel scale (8.3, 16.7, and 33.3-inch full scale). While the compromised phosphor coating considerably degraded the image quality, it was evident that no change in side surface heating was apparent for any tested combination of location or diameter.

Aerothermodynamics Associated with Asymmetric Boundary Layer Transition

Boundary layer transition on the Orbiter during re-entry is known to introduce small changes in the aerodynamics of the vehicle. Thus, in order to assess the sensitivity of Orbiter aerodynamics to several forms of simulated damage, damage resulting in boundary layer transition was evaluated. The surface heating results complementing the companion aerodynamic tests (see Section 4.3.1) were obtained using IR thermography. The results indicated several surface protuberances (corresponding to a 6-inch x 6-inch full scale surface raised 0.5 to 1-inch above the nominal outer mold line) placed along the wing leading edge would effectively promote Asymmetric Boundary Layer Transition (ABLT) on the windward surface. As mentioned in Section 4.0, the corresponding aerodynamic data provided the first direct evidence that while ABLT could produce measurable aerodynamic increments consistent with the Orbiter ABLT model for flight, the trends were inconsistent with STS-107 flight data.

5.2.3.4 Results for Mach 6 CF_4

Windward Surface Protuberances

A limited data set was obtained in the Mach 6 CF_4 tunnel to determine (1) if the Orbiter windward surface boundary layer could be forced turbulent with discrete isolated roughness, and (2) if the results were positive, could they be mapped onto a previously developed Orbiter boundary layer transition correlation developed in the Mach 6 air tunnel (Berry, 2002). The forced boundary layer transition results are summarized in Figure 5.2.3-15. Surface protuberances were placed on the windward centerline near X/L of 0.26. This location corresponds to the location of a protuberance observed on flight STS-73 which

resulted in an "early" high Mach number (approximately 19) boundary layer transition event. The protuberances correspond to a 6 x 6-inch full scale surface raised approximately 0.5, 0.9, and 1.5-inch above the nominal outer mold line. Boundary layer edge conditions were computed with a method consistent with the Mach 6 air correlation and yielded protuberance height-to-boundary layer thickness ratio (k/δ) values of 0.2 to 1.75. The discrete data points in Figure 5.2.3-15 correspond to laminar, incipient and effective roughness and these Mach 6 CF_4 data are compared with previously correlated Mach 6 air perfect gas results (solid curves). This limited data set represents the first discrete roughness boundary layer transition data on the Orbiter acquired in the Mach 6 CF_4 facility. Because complicated effects interact to produce boundary layer transition, and a comprehensive study could not be carried out (due to time constraints) of how the current limited Mach 6 CF_4 data set relates to the previously developed correlation of Berry (2002) for Mach 6 air, assessments of boundary layer transition for STS-107 utilized the previously developed correlation.

Missing Wing RCC Panel Survey

The sensitivity of side fuselage heating distributions to RCC panel damage in the Mach 6 CF_4 facility for completely missing panels is summarized in Figure 5.2.3-16. At the time of this testing, the body of recovered wing debris suggested that loss of an entire RCC panel was not likely, except for RCC panel 9. Higher fidelity, parametric removal of individual leading edge RCC panels (1-13) was pursued to characterize the location and magnitude of the heating disturbance on the side fuselage and to compare with the Mach 6 air results. Similar to the previously obtained Mach 6 air data, the CF_4 results were obtained using phosphor thermography and indicate local areas of increased surface heating relative to the nominal configuration. As discussed previously, global heating distributions are presented in terms of the ratio of enthalpy-based heat-transfer coefficients h/h_{REF}, and unless noted otherwise, a constant color bar maximum value of 0.25 was selected with colors tending towards red indicative of areas of higher heating (temperatures).

A localized heating disturbance on the side fuselage (Figure 5.2.3-16) was evident for all RCC panel locations (1-13). The relationship of the heating pattern inclination on the side fuselage to missing panel span-wise location was different from that observed for Mach 6 air. The local disturbance in the Mach 6 CF_4 facility was "directed" at the OMS pod, resulting in heating augmentations to the forward face of the OMS pod for missing panel $1 \leq RCC \leq 10$ (in contrast to heating reductions in Mach 6 air). Similar to the Mach 6 air trends, however, heating magnitudes associated with the disturbance on the side fuselage were generally insensitive to the location of the missing panel. A missing RCC panel at the location of the wing/bow shock interaction for Mach 6 CF_4 (RCC panel 9) did not result in abrupt location or magnitude changes to the side fuselage heating footprint. Similar to the observation in Mach 6 air results, the side fuselage heating footprint approached a nearly horizontal orientation (parallel to the Orbiter reference waterline) as the systematic removal of individual RCC panels progressed outboard. No significant Reynolds number effects were observed for TPS damage in the form of missing RCC panels. Based upon the Mach 6 air results, no Mach 6 CF_4 heating sensitivity studies were attempted for angle-of-attack and sideslip.

The leading edge channel formed by the wing spar and RCC panels on the flight vehicle was not captured with the solid ceramic models. Removal of an individual RCC panel by a milling machine yielded solid walls and hence, no lateral pressure relief. Limited tests on ceramic-coated resin models with a leading edge channel were conducted to investigate this. Characterization of any differences in the leeside flow field associated with a missing RCC panel and lateral pressure relief along the wing leading edge was felt necessary. Although qualitative in terms of heating magnitudes, the comparison of side fuselage heating patterns associated with an open and closed leading edge channel (Figure 5.2.3-17) suggests that the local heating disturbance propagates further forward (i.e., further upstream) when the damaged cavity is allowed to vent down the RCC channel.

Partial RCC Panel Damage

As the debris recovery effort drew to a close, the body of evidence indicated that partially damaged RCC panels (as opposed to entirely missing panels) was likely. Sensitivity of the Orbiter side fuselage heating associated with several forms of RCC panel 9 damage are shown in Figure 5.2.3-18. At this wing leading edge location only a missing T-seal or a completely missing RCC panel lead to off-nominal heating disturbances on the side fuselage or OMS pod. The missing T-seal was located at the RCC 8/9 interface and was sized to simulate a gap taken from the leading edge back to the wing spar. The gap width was

approximately 1.3-inch full scale, which corresponds roughly to the correct width for a removed T-seal. In contrast to the completely missing RCC panel, the missing T-seal disturbance did not indicate any off nominal side fuselage heating and affected only the lower side surface of the OMS pod.

The various forms of lower RCC panel 9 damage did not result in side fuselage/OMS pod off nominal heating (Figure 5.2.3-18). However, this was not the case for all wing leading edge locations, as shown in Figure 5.2.3-19. The test results indicated that the extent of RCC panel damage in relation to the wing leading edge attachment line largely determines if the disturbance is "swept" to the leeside. Qualitative heating images associated with the companion force and moment tests indicated the threshold for disturbances propagated to the leeside from half RCC panel damage was between RCC 5 and 6 (see Section 4.3.1, Figure 4.3.16). In other words, half RCC panel damage at panels 1 to 4 produced fuselage side heating disturbances in the Mach 6 CF_4 facility, whereas half RCC panel damage outboard of panel 5 did not.

Holes Through Wing

Limited parametric studies for simulated damage in the form of a breach from the wing windward surface to the leeward surface were attempted in the Mach 6 CF_4 facility for dedicated aero-heating tests. Wing hole parametrics were primarily associated with the simultaneous aerodynamic/aero-heating testing (see sec 4.3.1). Similar to the Mach 6 air results discussed previously, holes through the wing (located at the center of carrier panels 6, 9, 12) were found to increase heating on the windward surface, a characteristic of boundary layer transition. With regard to the dedicated aeroheating tests, an early qualitative result with a single circular hole placed at the RCC/carrier panel 5/6 interface did not result in off-nominal heating to the side fuselage/OMS pod (Figure 5.2.3-20). Heating associated with missing RCC panel 6 is shown for comparison. The hole was orientated normal to the wing chord with the diameter dimensionally consistent with the width of a carrier panel.

Venting from Discrete Locations along Wing Upper Surface with RCC Panel Damage

Qualitative heating images associated with the companion force and moment tests indicated that disturbance propagation to the side fuselage with partial RCC panel damage (the lower surface missing) for panels outboard of RCC 5 was possible. In order to investigate a partial panel damage case that might lead to leeside heating effects, the stagnated flow in the damaged panel region was allowed to vent via a carrier panel slot (see Sec 4.3.1). This experimental evidence coupled with a developing understanding of recovered Columbia debris prompted an effort to qualitatively characterize the possible influence of mass addition on the leeside flow field. The ceramic-coated resin models that possessed a wing leading edge channel were further modified to include venting paths to the leeward surface. The total estimated venting area was first computed per unit panel; a series of circular holes with the per panel vent area were drilled into the leading edge channel near each RCC/carrier panel interface. The channel was allowed to pressurize via damage in the form of a completely missing RCC panel 9. No attempt was made to measure local pressure or mass flow rate along the wing leading edge. The qualitative data presented in Figure 5.2.3-21 reveals little effect of this venting via circular holes on side fuselage heating patterns. Since the model also incorporated damage in the form of missing RCC panel 9, it is believed that effects (if any) from the discrete carrier panel venting holes were dominated by the disturbance from the missing RCC panel.

Venting from Continuous Gap Along Upper Wing Surface with/without RCC Panel Damage

To isolate possible venting effects from major RCC damage that dominates the leeward flow field, qualitative tests were first conducted on a ceramic-coated resin model with an undamaged leading edge. In contrast to the previous resin model with discrete holes, new resin models with a continuous 0.01-inch wide vent gap running along the upper wing RCC/carrier panel interface were fabricated (see Figure 5.2.3-5). The gap width on the model was a limitation of the manufacturing process and is approximately a factor of 10 larger than the actual vent gap width at model scale. Gaseous CF_4 was fed to the gap internally via a free-stream flow field pitot tube and allowed to vent to the leeside through the gap. A pressure measurement inside the wing provided a pressure measurement for the flow being fed into the RCC channel. The internal gap pressure measurement divided by the computed surface pressure exceeded a factor of 2, indicating the flow was sonic at the gap (surface pressure predictions at wind tunnel conditions provided by methods detailed in Section 5.2.4). The qualitative data presented in Figure 5.2.3-22 suggests that mass addition (venting) to the leeside via this continuous vent gap behind RCC 1 to 22 forces wing flow separation and leeside flow field perturbations, resulting in off-nominal low

heating on both the side fuselage and the OMS pod. The maximum contour ratio of enthalpy-based heat-transfer coefficients h/h_{REF}, was changed to 0.10 for the leeward planform image to provide more detail associated with the heating patterns (h/h_{REF} = 0.25 for the side fuselage images).

Having demonstrated leeside flow field perturbations from venting, attempts at controlling mass flow rates using gaseous nitrogen were made. As with the previous CF_4 venting study, the qualitative heating tests were conducted on a ceramic-coated resin model with an undamaged leading edge. The objective of these tests was to correlate the off nominal low side fuselage/OMS pod heating using a local jet momentum to free-stream momentum ratio. The form of the momentum ratio was based on previous work by Stone and Cary (1972), and Zukoski and Spaid (1964). The experimental results shown in Figure 5.2.3-23 at two free-stream Reynolds numbers reveal off-nominal low side fuselage heating for momentum ratios > 0.35, and OMS pod heating reductions for momentum ratios > 0.80. These momentum ratios were determined by assuming sonic orifice conditions. The maximum contour ratio of enthalpy-based heat-transfer coefficients h/h_{REF}, was changed to 0.10 for these side fuselage images to provide more detail associated with the heating patterns. These results provide experimental data suggesting that a threshold scaling parameter ratio of about 0.3 or greater is required to cause side fuselage effects, and a threshold value of 0.5 or greater is required for OMS pod effects.

To conclude the wing venting characterization study, a cavity near the lower surface carrier panel of RCC panel 8 was machined into the previously tested resin model (Figure 5.2.3-24) permitting the wing leading edge channel to pressurize and vent to the wing leeward surface along the gap. The initial wing hole–to-vent gap area ratio was approximately 0.5. It has been previously shown that lower half panel RCC damage at this location (RCC panel 8) does not affect leeside heating, whereas the lower RCC panel damage shown in Figure 5.2.3-24 produces leeside heating effects. Similar to the previous venting scenarios, regions of off-nominal low heating were evident on the side fuselage/OMS pod as shown in Figure 5.2.3-24. In this image, the maximum contour ratio of enthalpy-based heat-transfer coefficients h/h_{REF}, was changed to 0.10 for the leeward planform image to provide more detail associated with the heating patterns (h/h_{REF} = 0.25 for the side fuselage images). Increasing the wing hole-to-vent gap area ratio to approximately 1 produced similar effects (not shown) on the off nominal heating.

5.2.3.5 General Experimental Observations

Description of Leeside Flow

The purpose of this section is to provide a brief overview of the Orbiter leeside flow field and to provide insight into how some of the RCC damage scenarios may have affected the side fuselage/OMS pod heating. An interpretation of the Orbiter leeside flow, Figure 5.2.3-25, taken from Baranowski (1983), captures the complexity of the three-dimensional flow structures that affect the Orbiter's leeward surfaces Figure 5.2.3-25 (a). The leeside is dominated by regions of strong flow expansions, flow separation/reattachment (which may be laminar, transitional, or turbulent), shock interactions, and vortical flow. For these reasons, the leeward flow field is highly sensitive to compressibility and viscous effects, and may be chemically frozen.

Flow features in the upper payload bay area with angles-of-attack less than 35 deg, are thought to be dominated by a vortex pair that interact along the centerline, Figure 5.2.3-25 (b, c, and d-1). At angles-of-attack between 35 and 45 deg, this vortex pair moves off the surface as depicted in Figure 5.2.3-25 (1d-2). Below this primary vortex pair a "quasi" boundary layer forms within which secondary or tertiary embedded vortices can develop. The so-called "vortex" scrubbing often used to describe the heating along the Orbiter side fuselage is, in actuality, reattachment of flow that has separated from the upper wing surface. It is this complex system of separated /re-circulating flow that is potentially perturbed by disturbances emanating from wing leading edge damage. Baranowski (1983), writes "…properties in the upper fuselage vortices are likely to be influenced by flow originating along the strake [wing] leading edge and impinging on the side fuselage." It is reasonable to assume that wing damage which alters the leading edge flow separation characteristics could have first-order effects on side fuselage/OMS pod heating.

Leeside Flow with Wing Leading Edge Damage

The effects of a missing RCC panel on Orbiter leeside flow as inferred from surface heating and corresponding streamline patterns are shown in Figure 5.2.3-26. Flow separation from the wing upper

surface and subsequent reattachment on the side fuselage as described by Baranowski (1983) is apparent from the surface oil flow streamline patterns. Locally displaced flow separations/reattachments (inferred from streamline patterns) are shown in Figure 5.2.3-26. Displacement of the embedded wing shock(s) as depicted in Figure 5.2.3-25 (1d-2) is also probable. It is believed that a jet-like plume originating from the wing leading edge damage is responsible for the observed heating augmentations. Until computational predictions demonstrate the ability to accurately capture the complex surface phenomenon (i.e., leeside wing separation, reattachment for both damaged and undamaged leading edges) as shown in Figure 5.2.3-26, the nature of the perturbed off-surface leeside flow remains speculative.

Off-Nominal Leeside Heating Trends

Side fuselage/OMS pod heating augmentations and reductions resulting from various damage scenarios have been identified from the ground-based tests. However, the off-nominal heating disturbances inferred from the experimental data were highly localized. In addition, the exact damage to Columbia is unknown and time dependent. These two factors are strong indicators that comparisons of wind tunnel derived augmentation/reduction factors to flight thermocouple and RTD magnitudes be performed with prudence.

The heating data presented in Figure 5.2.3-22 through Figure 5.2.3-24 suggest that in the absence of major leading edge damage (that tends to dominate the leeward flow field and results in *both* off-nominal high and low heating), mass addition via a degraded upper surface vent slot along the RCC 1-22/carrier panel interface can produce off-nominal low heating on both the side fuselage and OMS pod. As the heating data measurements were made on resin models, they are considered qualitative. However, it was determined that the side fuselage areas indicated in Figure 5.2.3-22 showed heating reductions of approximately 65% to 75% of the nominal surface heating. In terms of momentum ratio, a threshold for leeside venting effects was experimentally determined and should be correlated against flow field predictions involving both leading edge damage and leeside venting. However, the experimental data do suggest that a momentum ratio of at least approximately 0.3 is required to provide changes in leeside heating on the Orbiter.

Side fuselage heating augmentations associated with missing RCC panels were found to range from 2 to 12. In Mach 6 air, no changes to the surface heating associated with missing RCC panel 12 were observed for small changes in angle-of-attack (Figure 5.2.3-9), sideslip (Figure 5.2.3-10), or a factor of 4 increase in Reynolds number (Figure 5.2.3-11). Similar to the Mach 6 air trends, side fuselage heating peak magnitudes associated with missing RCC panels in Mach 6 CF_4 were generally insensitive to the location of the missing panel as shown Figure 5.2.3-16.

The test results in both facilities indicate that missing RCC panel damage outboard of RCC panel 10 leads to the heating footprint becomes nearly horizontal to the Orbiter reference waterline. In this orientation, the disturbance would act much like a “fluid fence” and would effectively prevent flow from flowing up through the elevon/fuselage gap to impinge on the lower aft corner of the OMS pod such as occurs with a nominal configuration (Haney, 1995).

Effect of Normal Shock Density Ratio on Heating Patterns

Side fuselage localized heating disturbances for normal shock density ratios of approximately 5 (γ_{eff} = 1.4) and 12 (γ_{eff} = 1.13) are contrasted in Figure 5.2.3-27 for individual missing RCC panels (1, 5, and 9). It has been noted earlier that for a missing RCC panel inboard of panel 10, the local heating disturbance on the side fuselage was more inclined from vertical in Mach 6 CF_4 than in Mach 6 air. That effect results in heating augmentations to the forward face of the OMS pod (see also Figure 5.2.3-16). For CF_4, it is speculated that local differences in γ on the leeside contribute to leading edge separation differences on the upper surface of the wing. It is not unreasonable to assume that differences in the wing embedded shock structure associated with air and CF_4 for a missing RCC panel would affect the flow to the leeside in a contrasting manner. Stronger flow expansions characteristic of a lower γ would imply larger flow turning angles as the separated flow off the wing is swept aft. If in flight, the Orbiter leeside flow is non-reacting or frozen due to the rapid flow expansion around the leading edge, it is quite possible that the Mach 6 CF_4 simulation (with a value of freestream γ limited to 1.22) provides a better representation than Mach 6 air (γ = 1.4) of coupled leeside flow physics and chemistry associated with hypervelocity flight.

Detailed computational and experimental studies of this topic would be required to address this question more comprehensively. However, at this time, the maturity of CFD to contribute significantly to a better characterization of the leeside flow field and γ effects is an open topic of discussion.

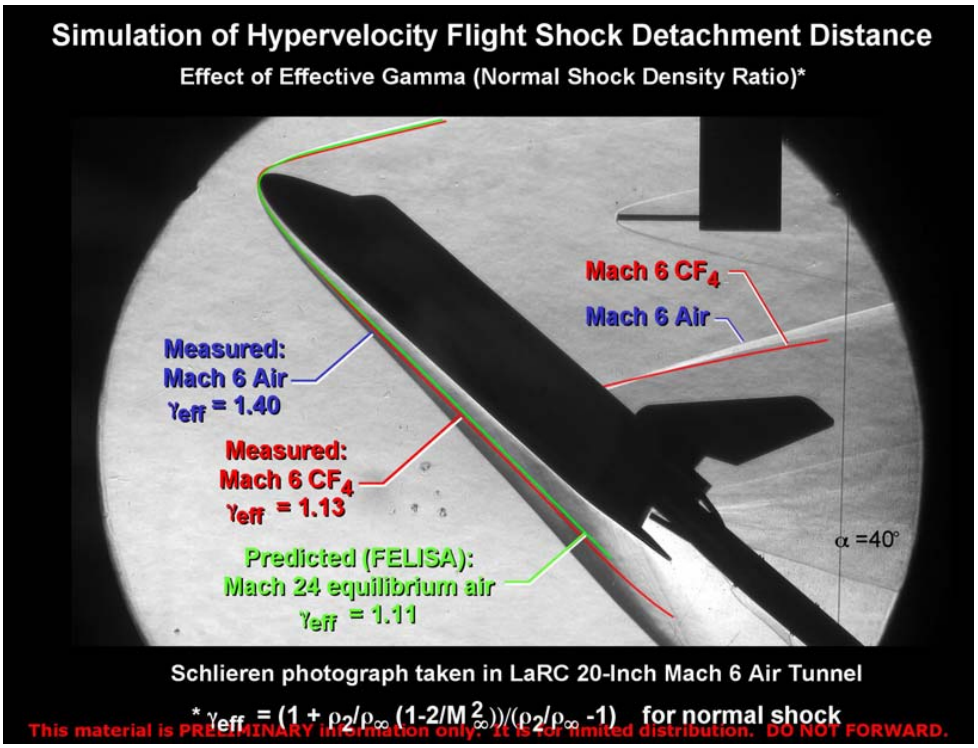

Figure 5.2.3-1 Simulation of Hypervelocity Flight Shock Detachment Distance

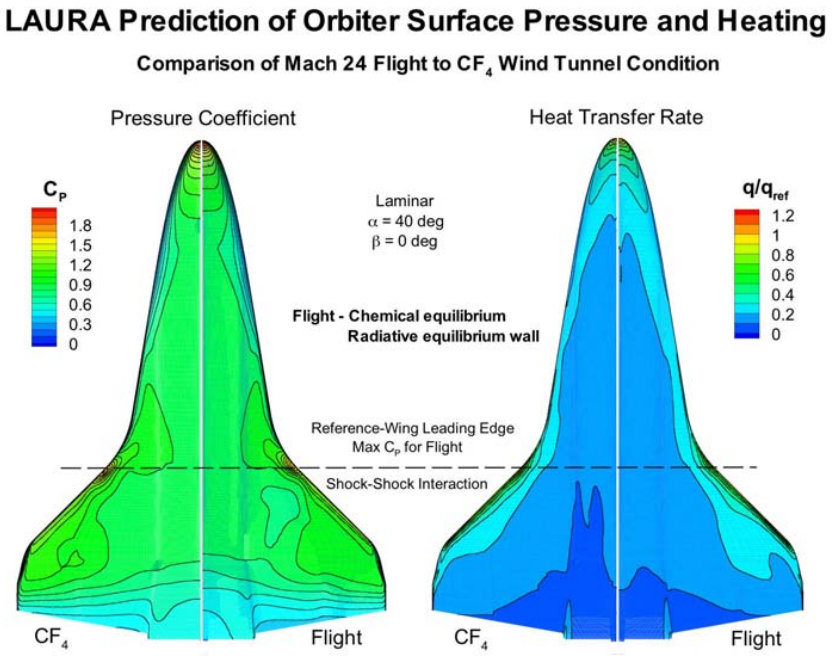

Figure 5.2.3-2 LaRC LAURA solutions of Orbiter windward surface pressure and heat flux

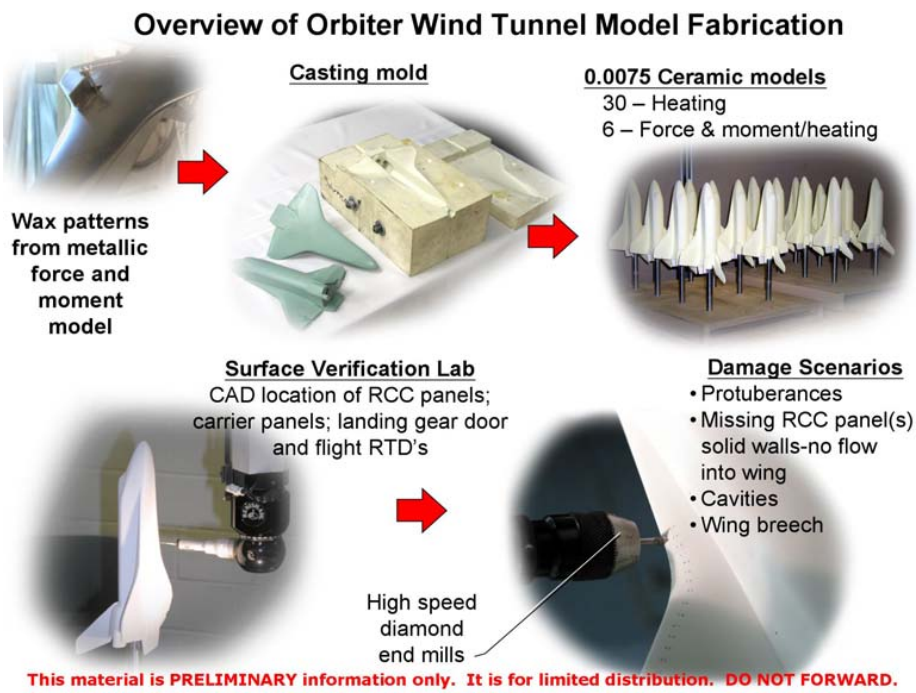

Figure 5.2.3-3 Ceramic model fabrication process

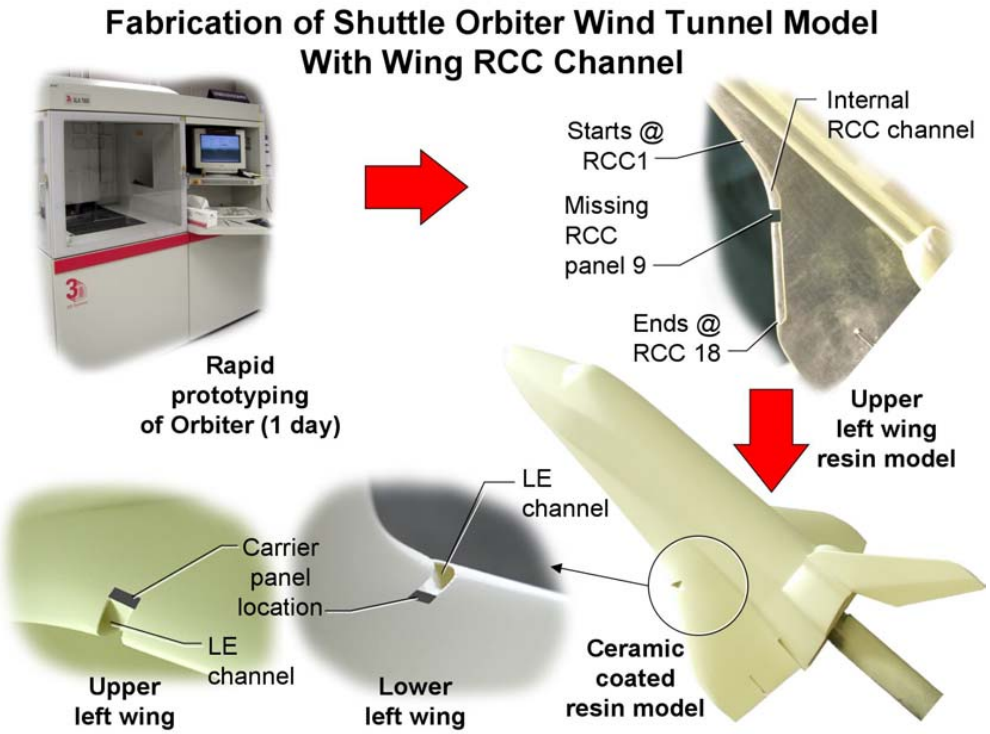

Figure 5.2.3-4 SLA model fabrication process of Orbiter with WLE cavity

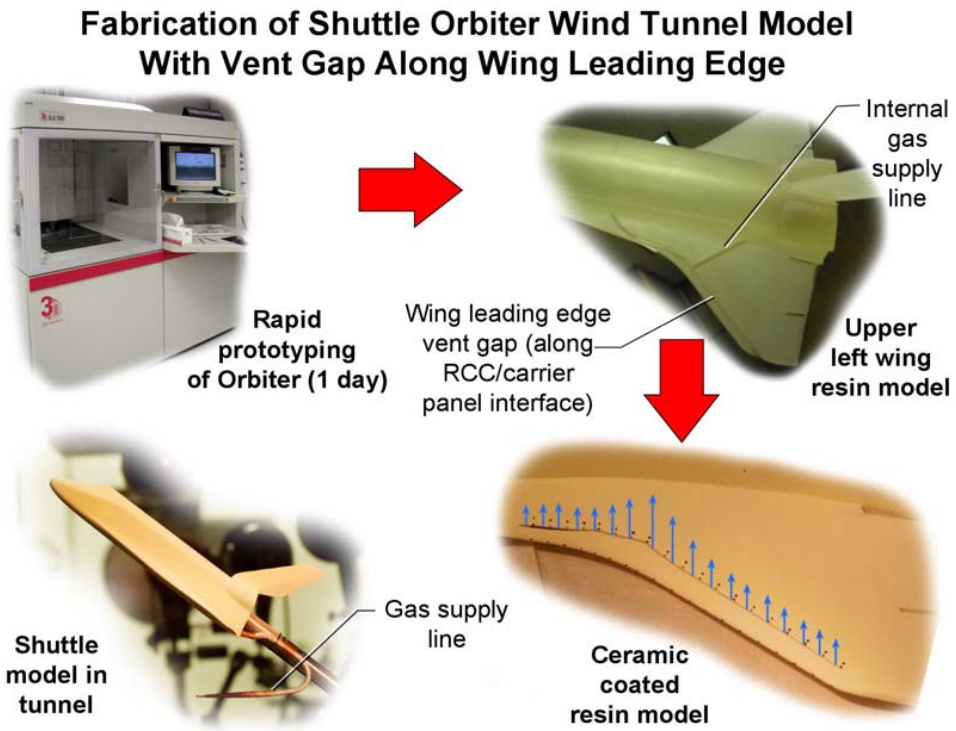

Figure 5.2.3-5 SLA fabrication process of Orbiter with WLE vented cavity and gas supply line

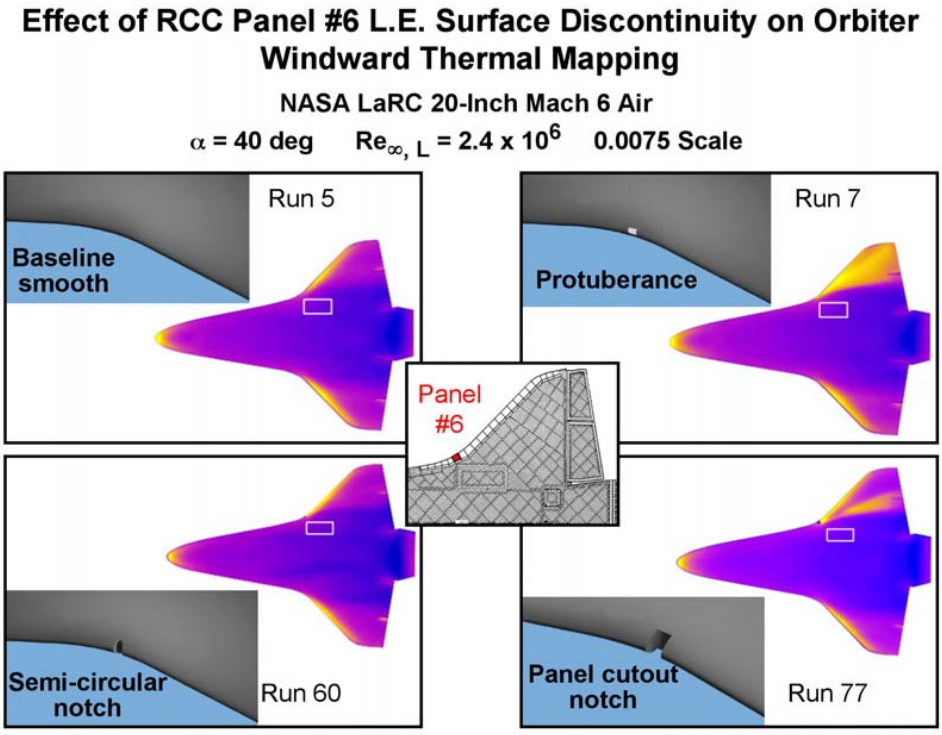

Figure 5.2.3-6 Effect of RCC Panel 6 surface discontinuity, windward view

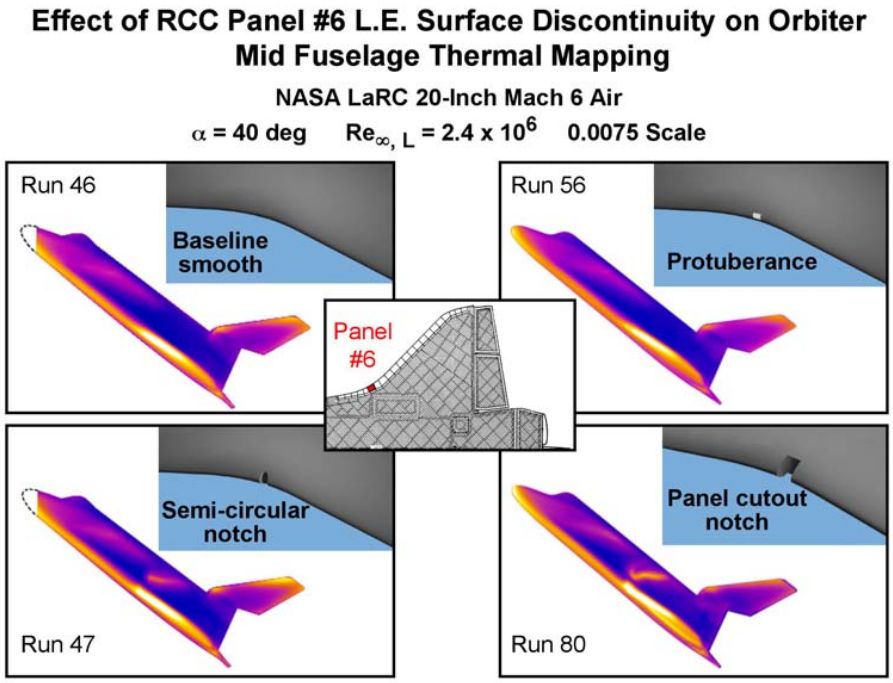

Figure 5.2.3-7 Effect of RCC Panel 6 surface discontinuity, side fuselage view

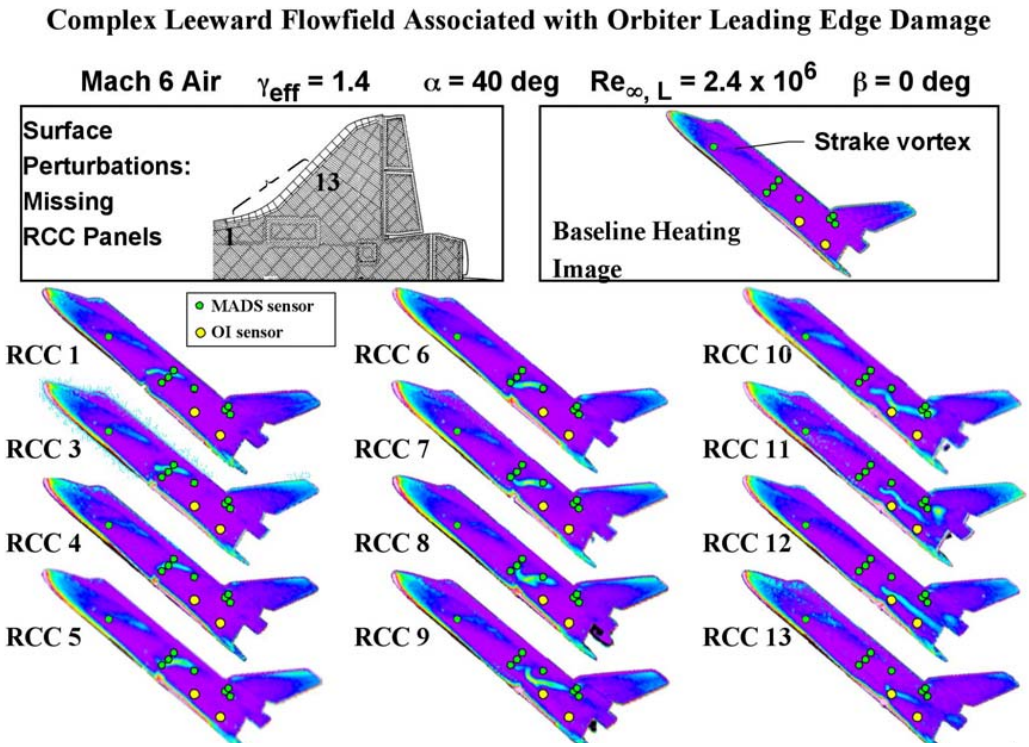

Figure 5.2.3-8 Mach 6 Air results of full RCC panel removed

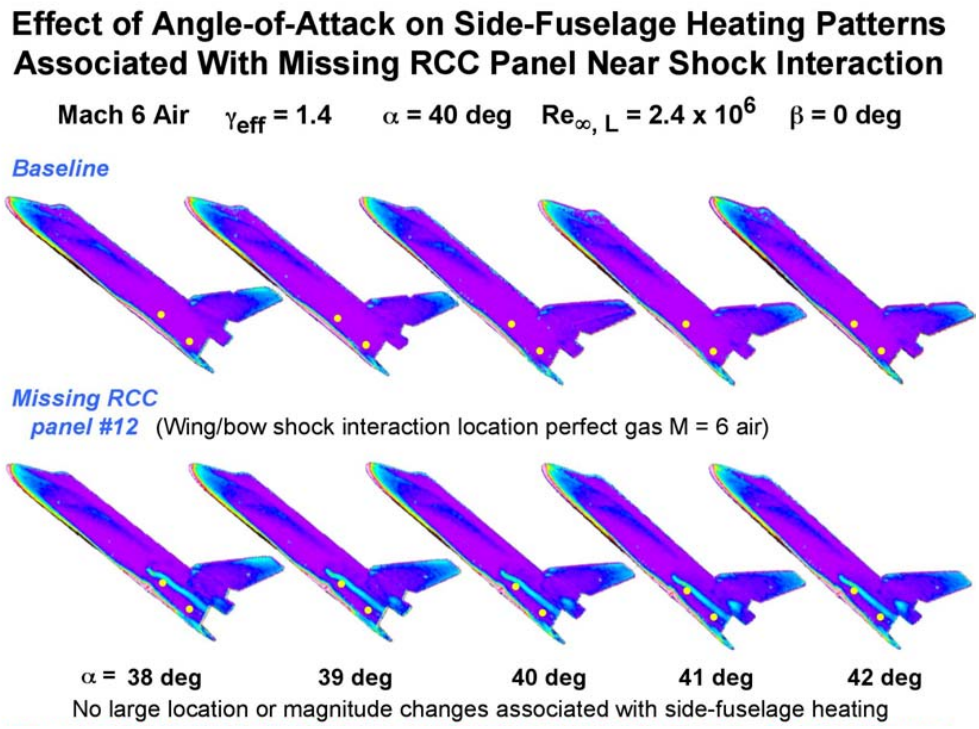

Figure 5.2.3-9 Assessment of the effect of angle of attack on side fuselage heating

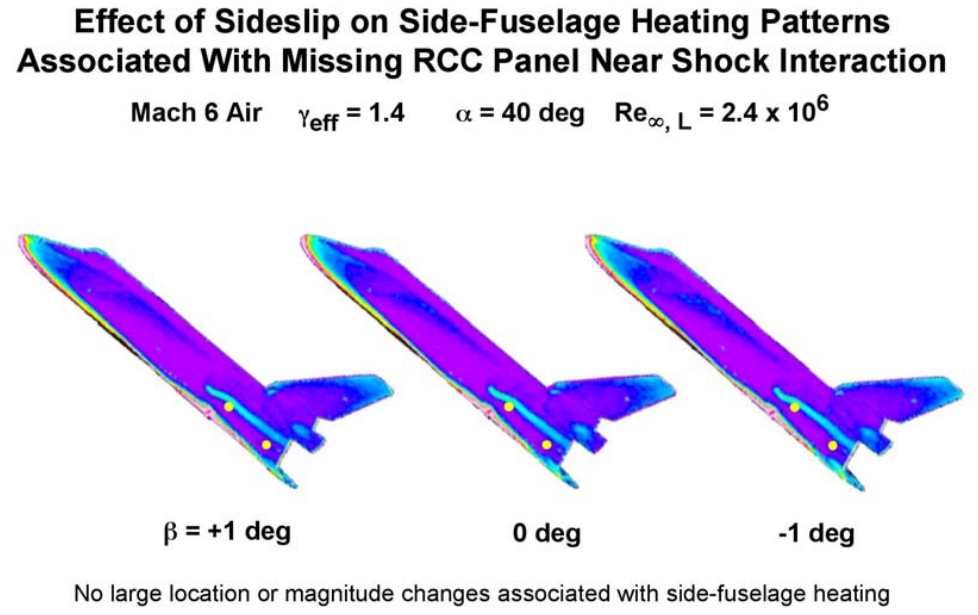

Figure 5.2.3-10 Assessment of the effect of angle of sideslip on side fuselage heating

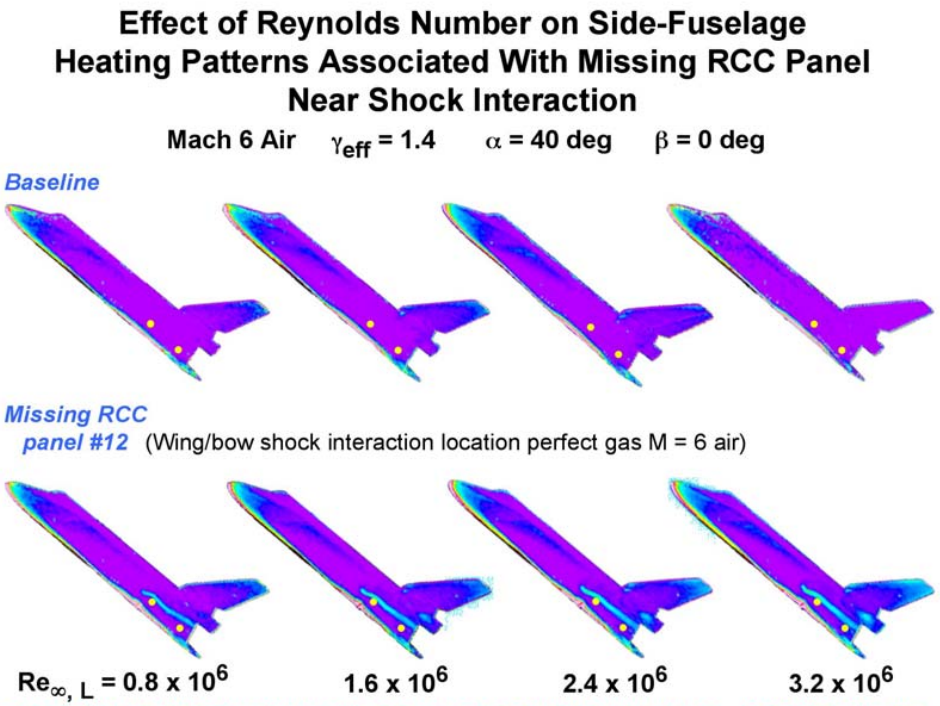

Figure 5.2.3-11 Assessment of the effect of Reynolds Number on side fuselage heating

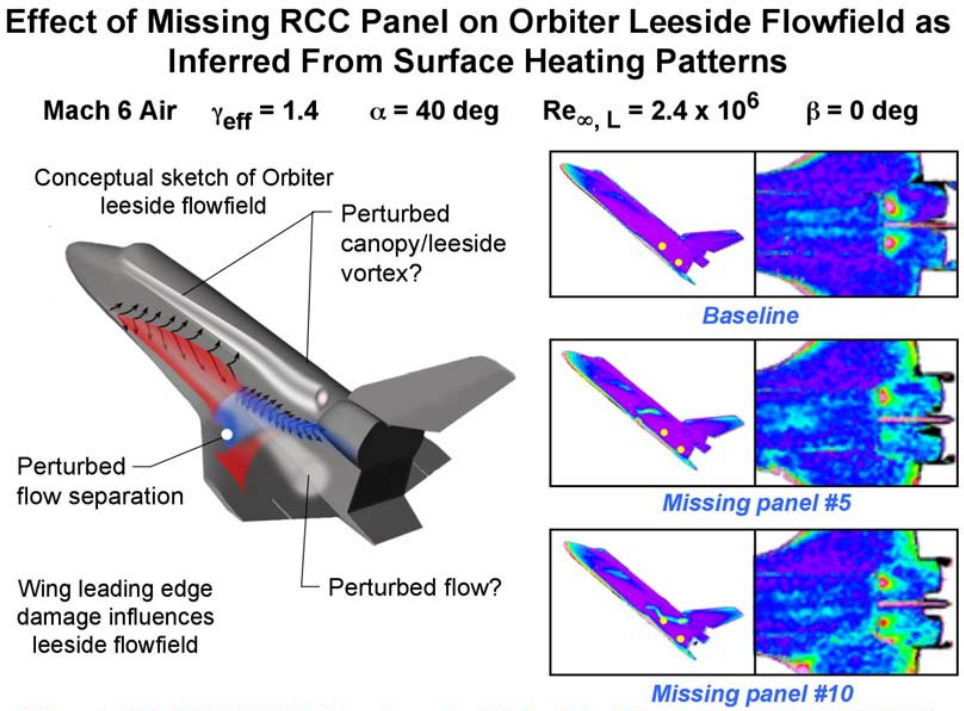

Figure 5.2.3-12 Orbiter leeside flow field changes as a result of WLE damage

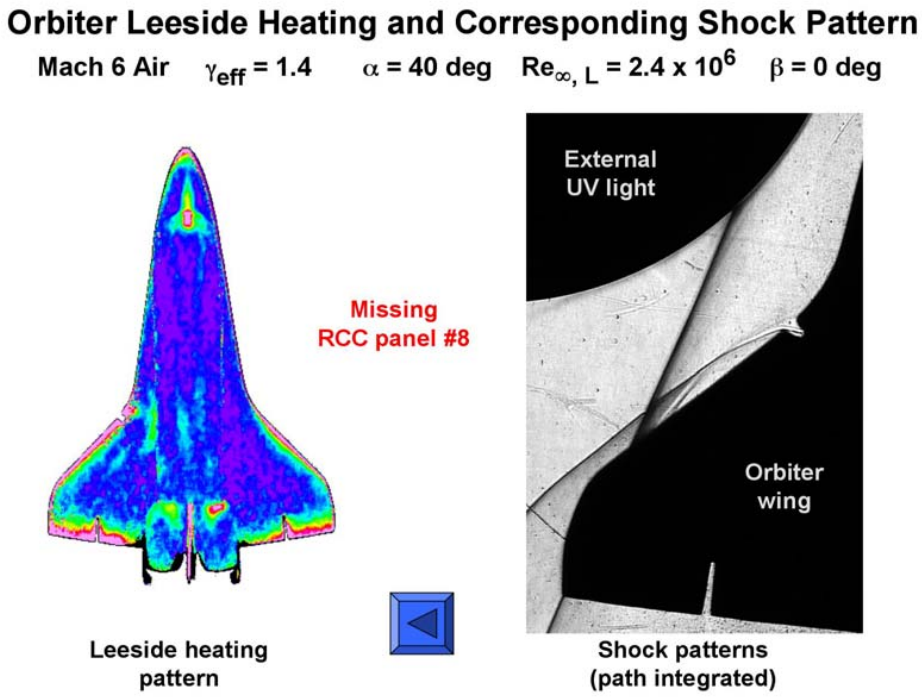

Figure 5.2.3-13 RCC Panel 8 Removed leeside heating and shock pattern

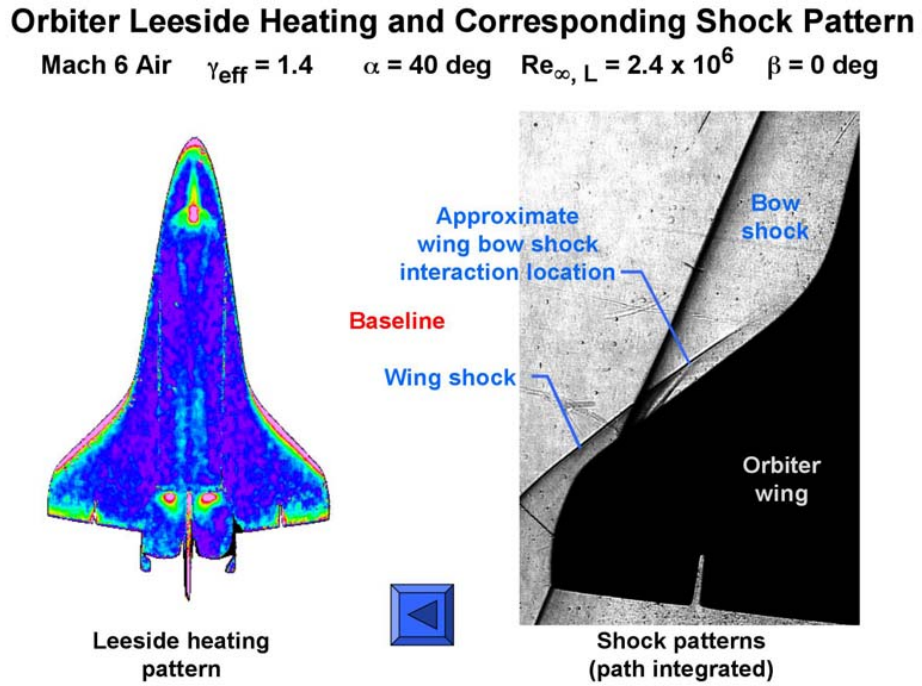

Figure 5.2.3-14 Baseline leeside heating and shock pattern

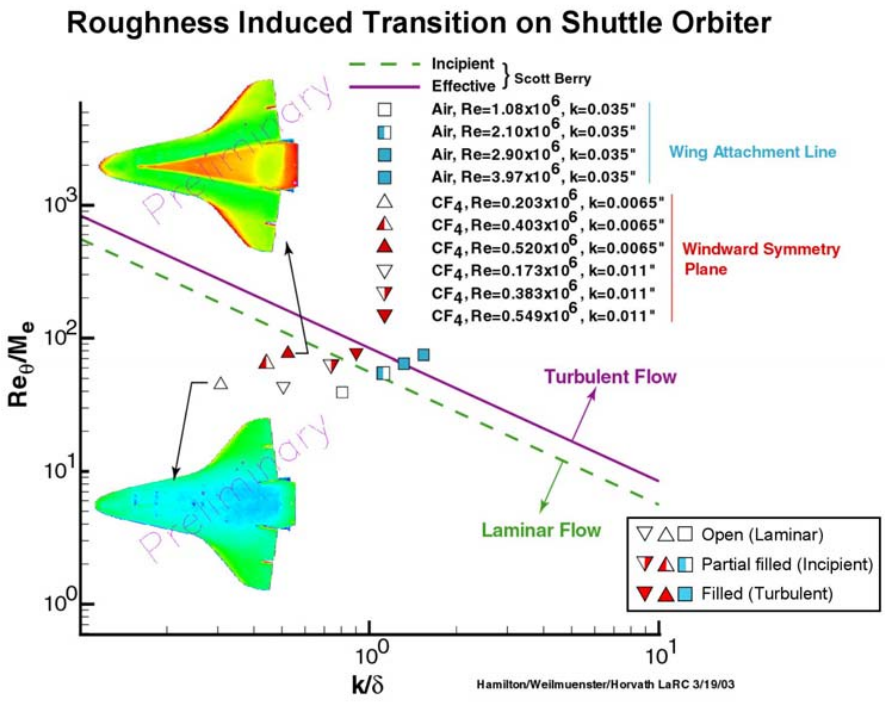

Figure 5.2.3-15 Roughness induced transition on the Orbiter. Berry correlation as compared to wind tunnel test results in both Mach 6 Air and Mach 6 CF_4

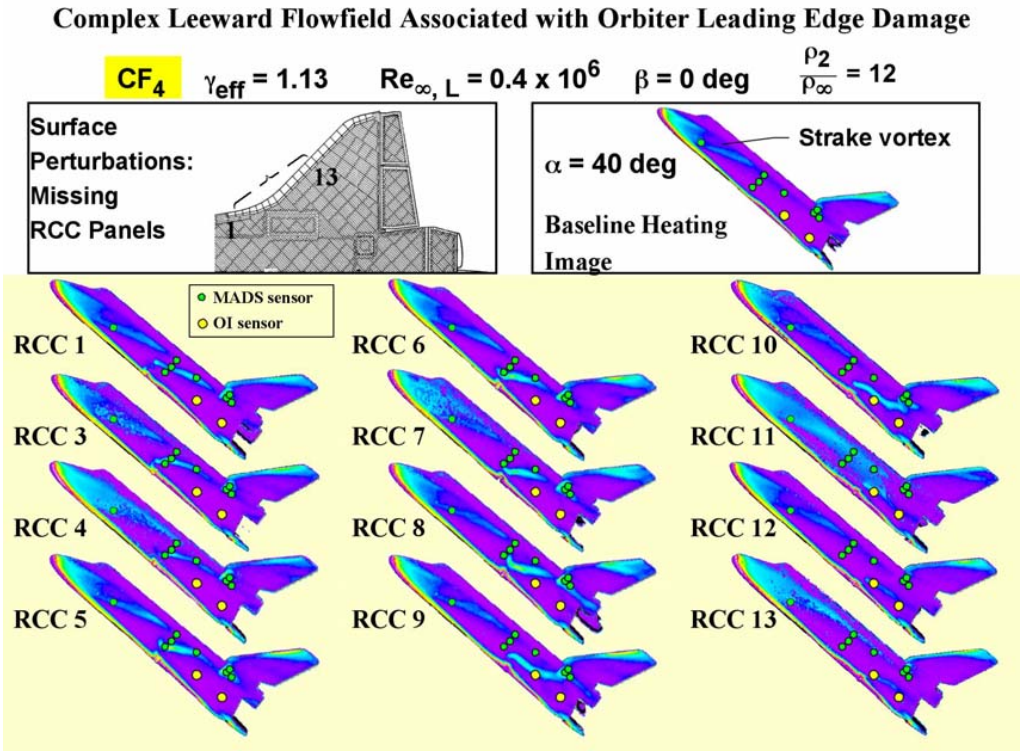

Figure 5.2.3-16 Mach 6 CF4 results for full RCC panels removed

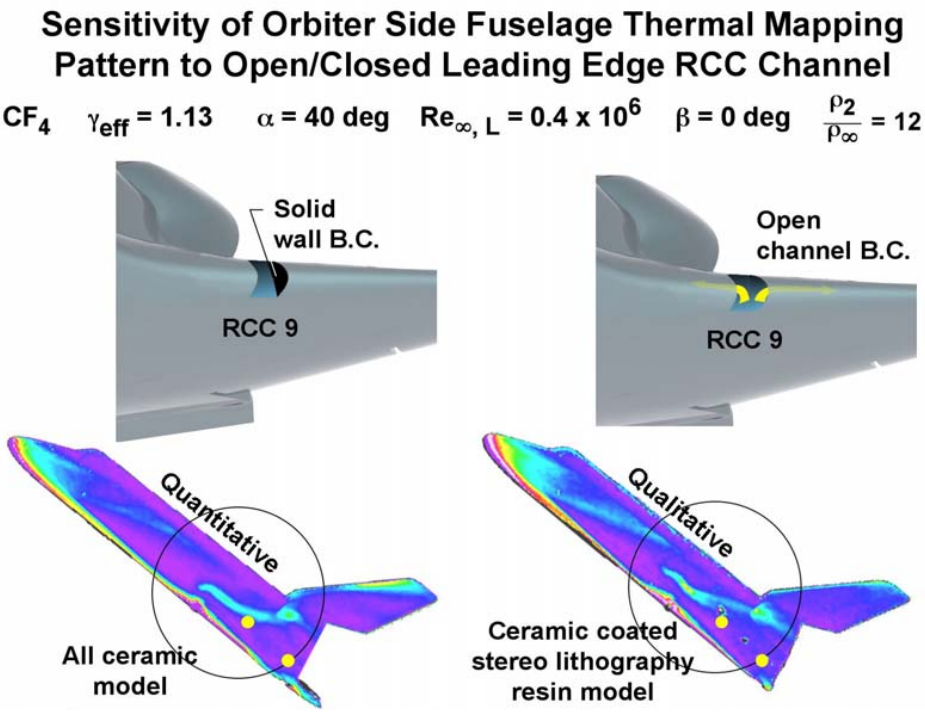

Figure 5.2.3-17 Effect of closed versus opened WLE cavity on side fuselage heating footprint

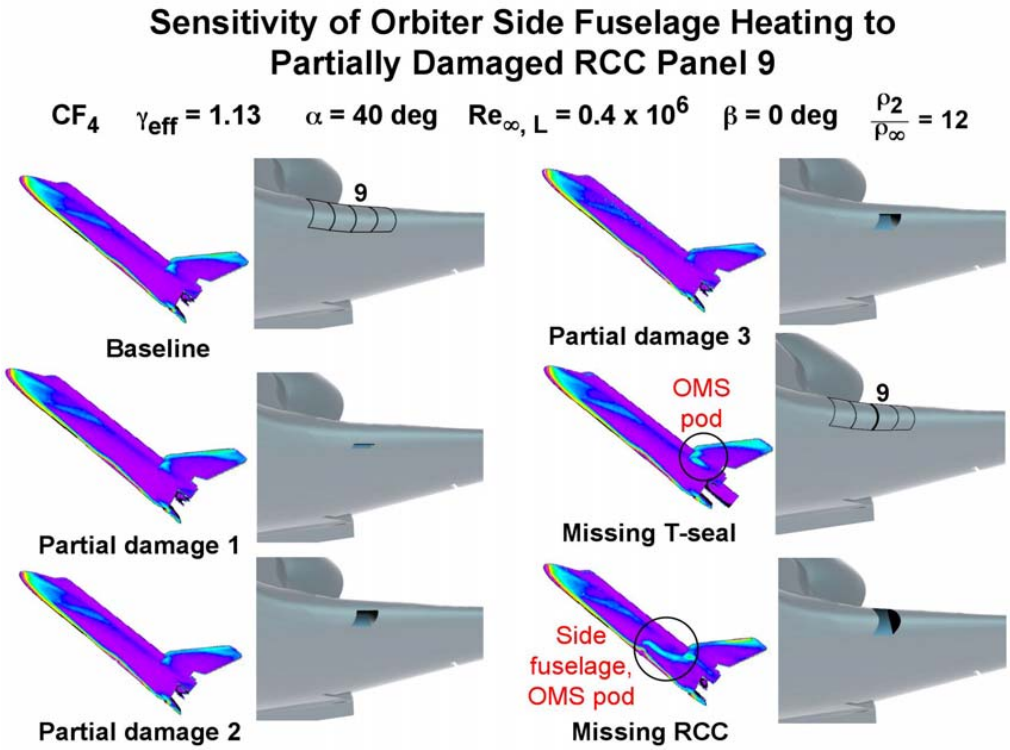

Figure 5.2.3-18 Effect of various types of panel 9 damage on side fuselage heating

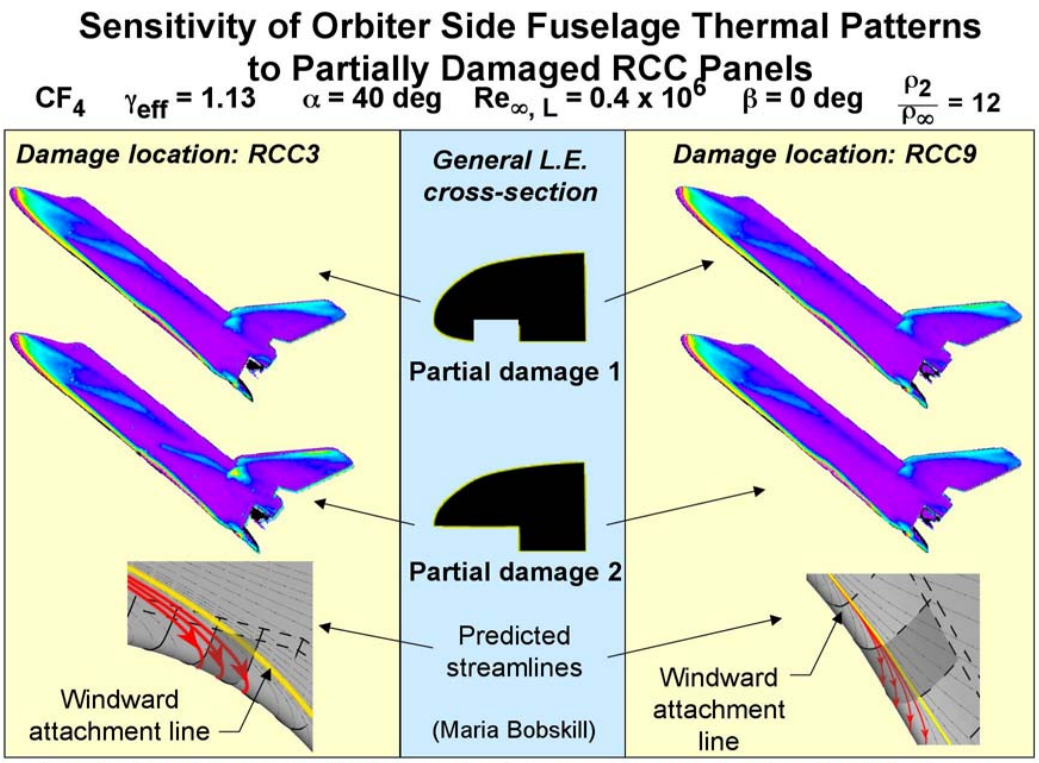

Figure 5.2.3-19 Partial panel damage assessment

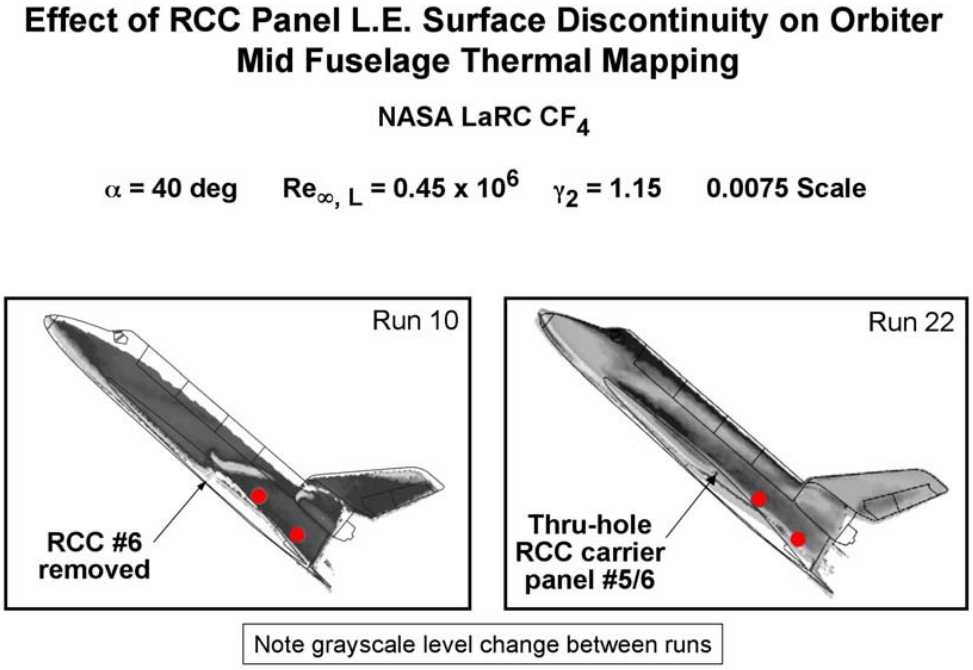

Figure 5.2.3-20 Hole through the wing assessment

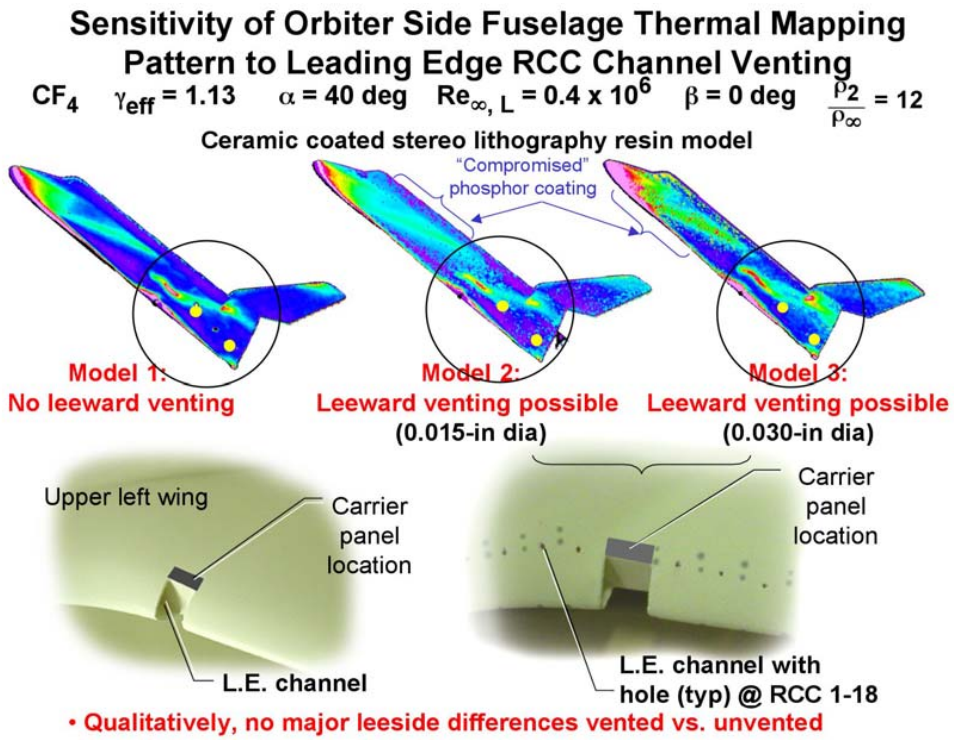

Figure 5.2.3-21 Initial assessment of venting with panel 9 missing and WLE cavity

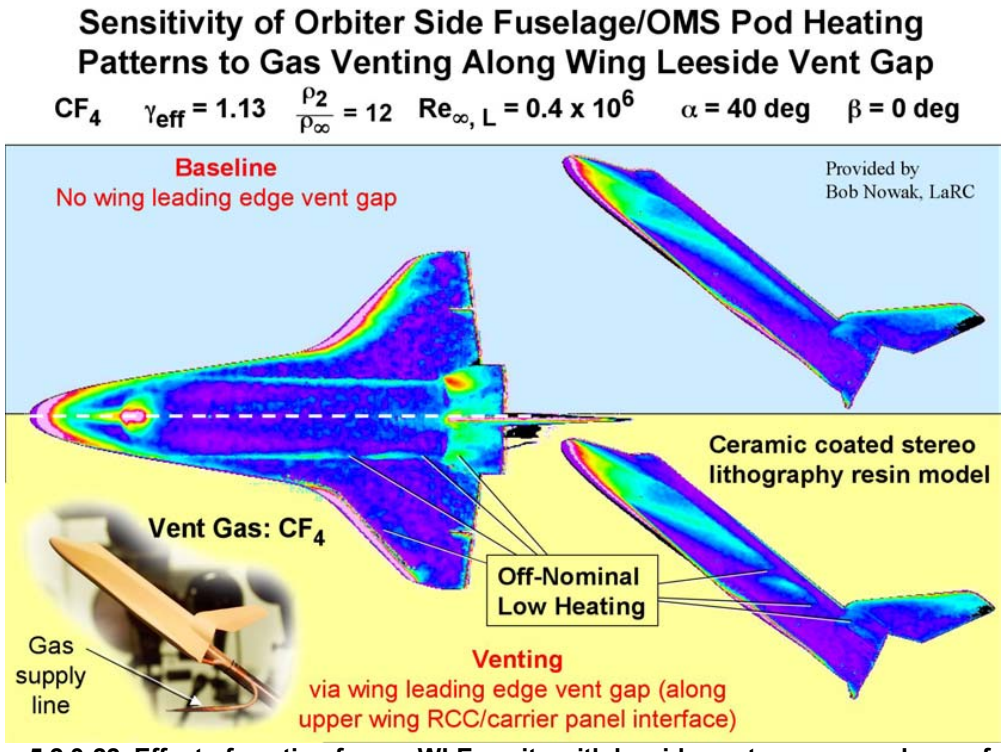

Figure 5.2.3-22 Effect of venting from a WLE cavity with leeside vents; gas supply was from a pitot probe in the flow field

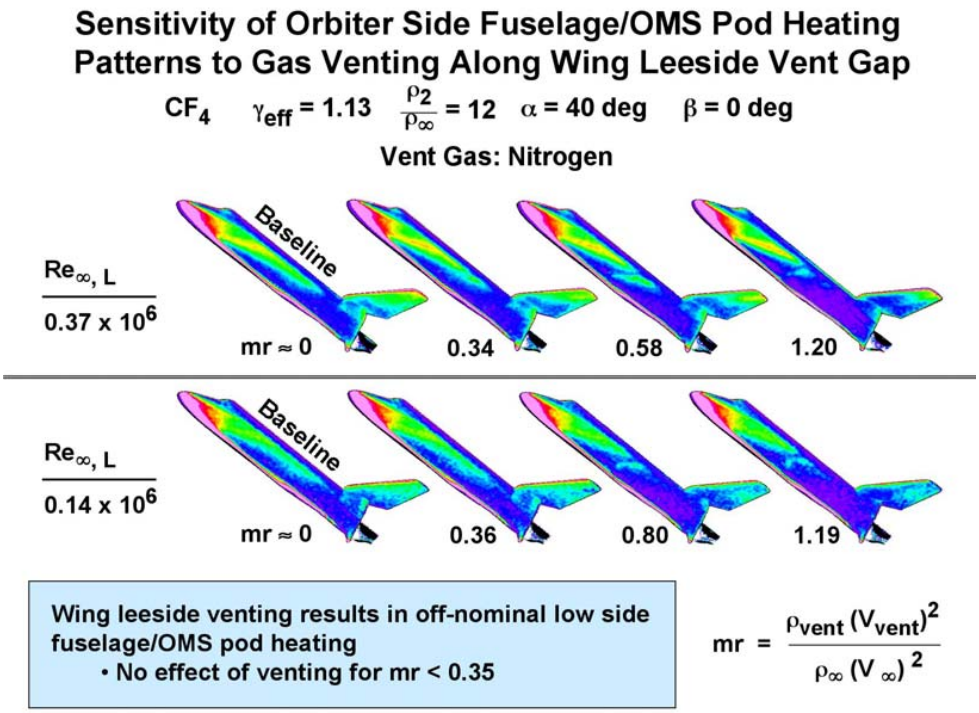

Figure 5.2.3-23 Reynolds Number and Momentum Ratio variation effects on side fuselage heating; gas supply from regulated GN2

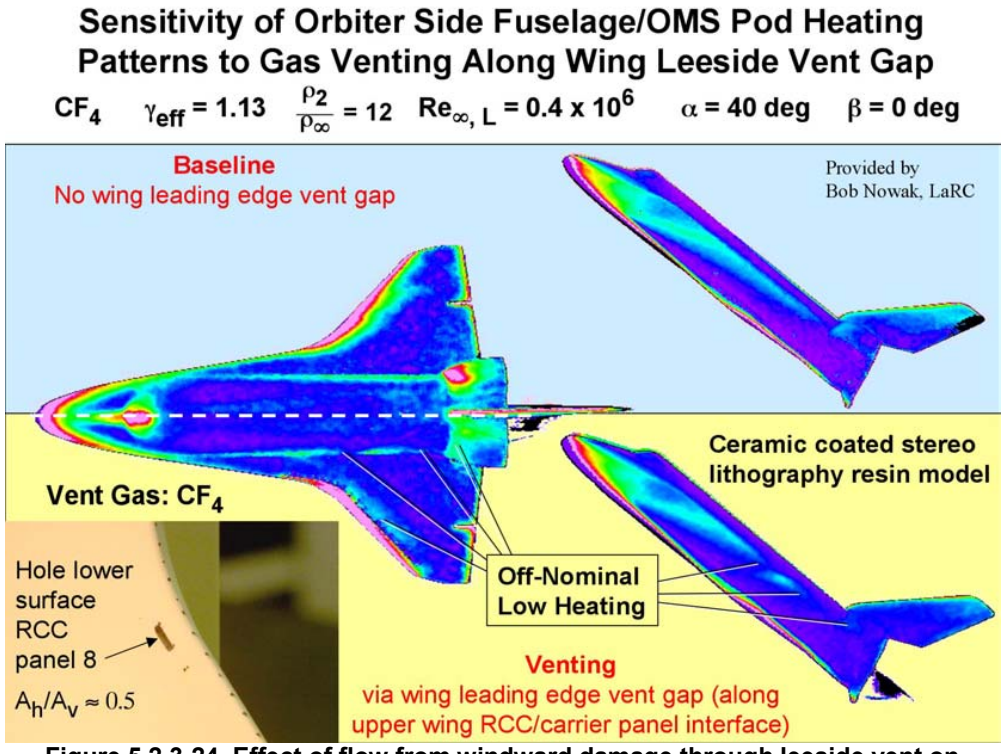

Figure 5.2.3-24 Effect of flow from windward damage through leeside vent on side fuselage heating

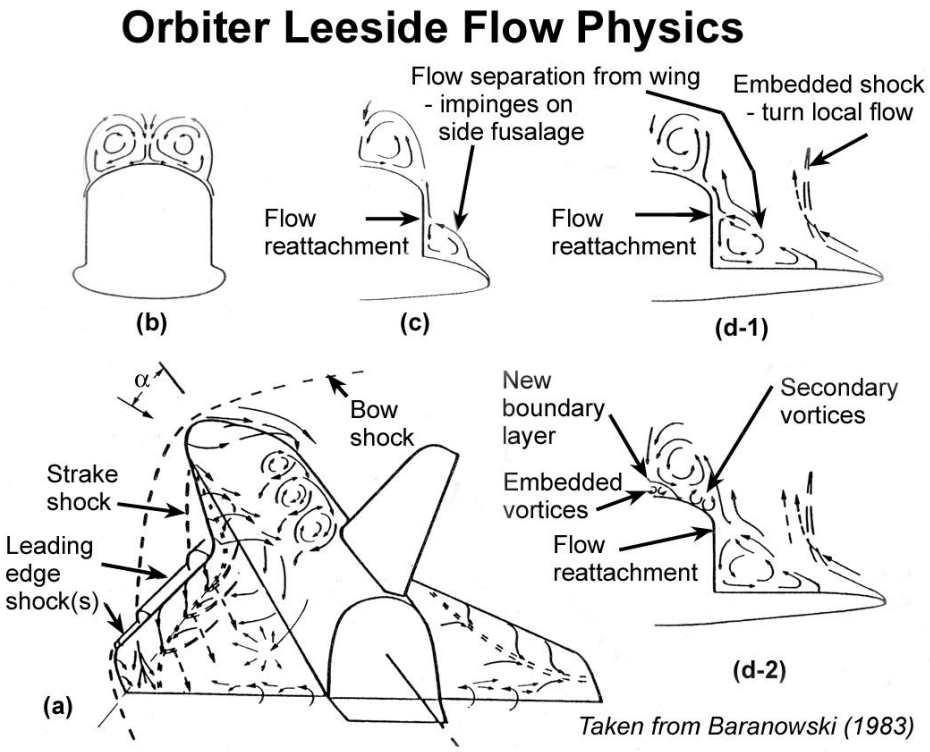

Figure 5.2.3-25 Orbiter Leeside Flow Physics

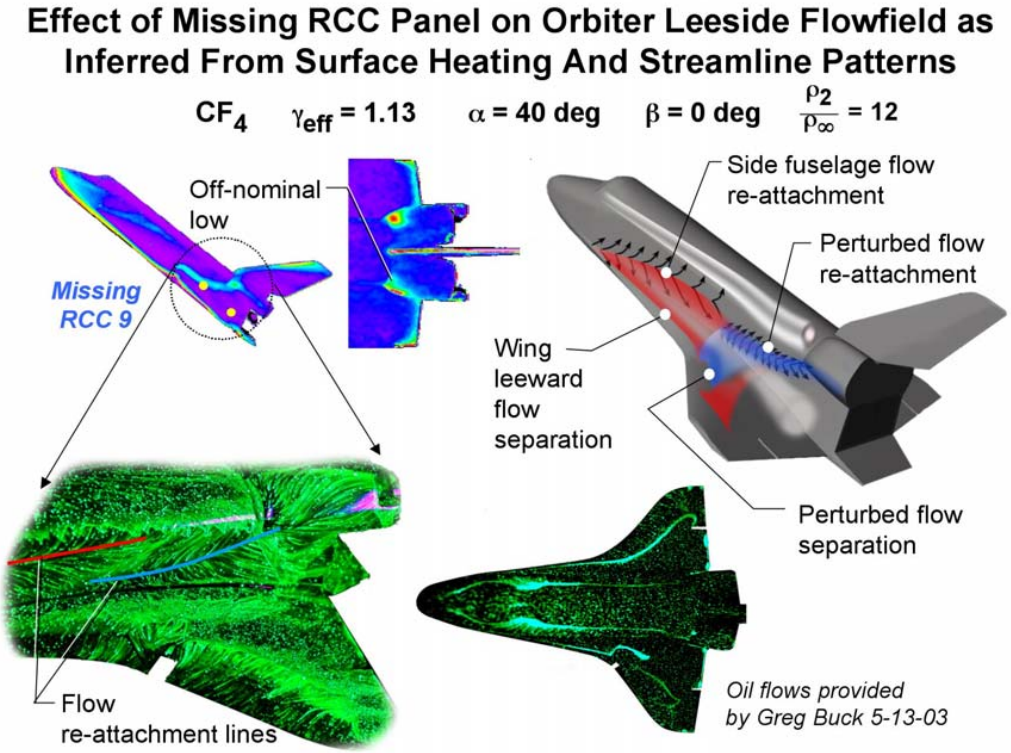

Figure 5.2.3-26 Phosphor Oil Flow showing leeside surface flow separation

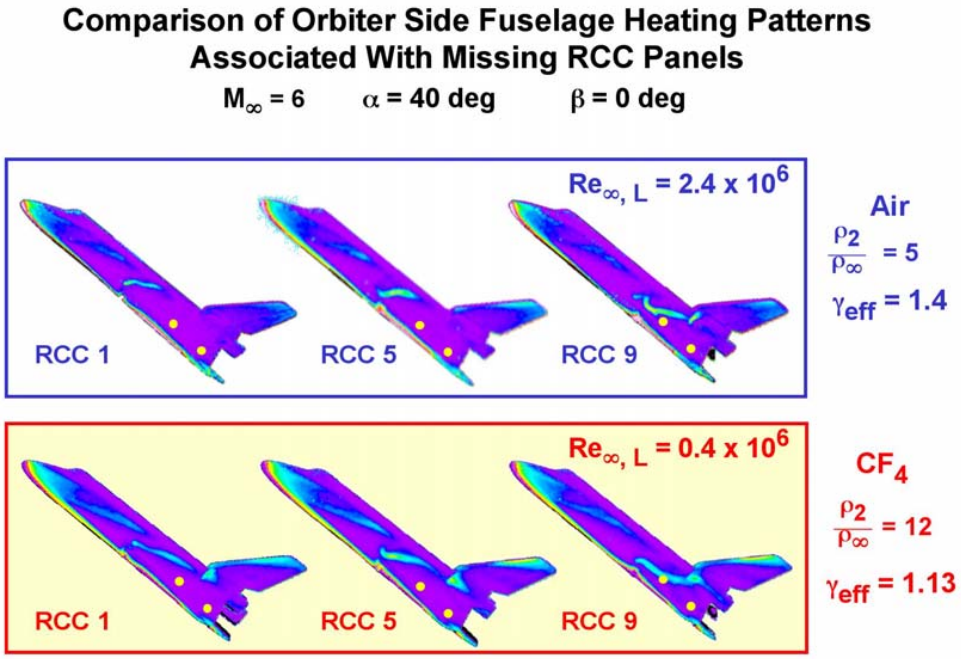

Figure 5.2.3-27 Comparison of Orbiter Side Fuselage Heating Patterns Associated with Missing RCC Panels

5.2.4 Computational Fluid Dynamics (CFD) and Direct Simulation Monte Carlo (DSMC)

5.2.4.1 Introduction for CFD and DSMC

Investigations of the Orbiter's external flow field encompassed several aspects of numerical analyses, from the high altitude rarefied regime to the lower altitude continuum regime. Since no ground-based facility can reproduce the Orbiter environments during hypervelocity re-entry conditions, the use of numerical simulations to understand the flow field at flight conditions was critical during the investigation. The analyses goals were primarily focused on two topics, providing nominal external flow field information supporting localized engineering analyses, and damaged configuration solutions to investigate changes in the aerodynamic and aerothermodynamic characteristics of the Orbiter. Because the magnitude of these analyses is daunting, a parallel effort across several organizations was required. The Navier-Stokes tools employed in the continuum regime analyses included GASP, LAURA, OVERFLOW, SACCARA and USA. The Direct Simulation Monte Carlo (DSMC) tools utilized in the rarefied regime included DAC and ICARUS. More details on each of the tools can be found in the Appendices.

Several concerns affected how the effort was approached, and effective utilization of the array of organizations and tools required the team to follow a staged route in the generation of the External Environments. Concerns with how the effort was approached center around aspects of validation and calibration of the numerical results. Information provided from STS-107 OI data highlighted the idea that significant efforts would be required to assess Orbiter leeside heating environments, yet no extensive leeside calibration effort has ever been performed with Orbiter flight data. In addition, concerns also exist about the validity of numerical simulations for damaged leading edge geometries. In light of these concerns, many leeside environment aspects and the damaged leading edge environment aspects from the numerical solutions must be viewed with an appropriate perspective. The perspective to take is that the solutions relied on established best practices at the time of the investigation. However, they are in essence uncalibrated for the leeside flow field and/or damaged leading edge configurations. Some effort was undertaken to assess the accuracy of the solutions by performing a comparison with STS-2 flight-derived surface temperatures and heat flux. Further information from that study is included in Section 5.2.4.3 (CFD/DSMC Validation). In addition, a study was initiated to characterize our ability to model the hypersonic leeside Orbiter flow field at wind tunnel conditions. Further information from that study is also included in Section 5.2.4.3 (CFD/DSMC Validation). Despite the concerns above about perspective and calibration, it is important to point out that the simulations can still provide much insight into the flow field characteristics and physical mechanisms at work on the Orbiter leeside. Also, an approach of using the results more in an engineering sense than in an absolute quantitative or scientific sense is what will drive interpretations of the CFD and DSMC numerical results to be presented in later sections.

As mentioned above, effectively utilizing the External Environment team's assets (tools, people and computers) to develop relevant CFD solutions required the use of a staged route. The first step in this staged route involved relying on established best practices to generate a suite of initial solutions on the undamaged Orbiter configuration with grid systems that were already available. However, the existing CFD grid systems from the various contributing organizations were markedly different in their intended purpose, resolution and even their Orbiter geometry representation. Thus, while these initial solutions were being generated for STS-107-specific re-entry conditions, an effort was undertaken to standardize the team on a single Orbiter CAD definition and generate a Common Baseline grid system that could be used to generate an extended set of solutions for both nominal and damage scenario configurations. Further information on this common grid generation effort can be found in Section 5.4.2 (Grid Development). Because of the difference in resolution requirements between DSMC and Navier-Stokes solutions, the Common Baseline grid developed for the Navier-Stokes studies was inappropriate for the DSMC analyses. For this reason, the decision was made to use a heritage DSMC Orbiter surface grid that has been shown to agree well with Orbiter aerodynamic flight data in previous studies. Later, as our understanding of the available flight data grew and was affected by a rapid and dynamic environment of investigation, the External Environments team simulations took on three distinct aspects. These aspects are nominal solution environments, to be covered in Section 5.2.4.4, providing damaged leading edge simulations, covered in Section 5.2.4.5, and providing simulations on other damage configurations that supported the effort to focus down to the Working Scenario. Those additional efforts will not be covered in any detail in this report, however.

5.2.4.2 Grid Development

Many aspects of numerical analyses are driven as much by process requirements as the particular physical modeling assumptions. In the simulation of hypersonic or hypervelocity flow fields, local changes in surface definition or grid density can affect the flow field results. These localized changes can be difficult to attribute specifically to either the surface definition or differences in results obtained by different tools and/or users. In order to move beyond discrepancies generated by differences in surface definition or grid resolution among the various numerical tools, an effort was undertaken to standardize the Aerodynamics and Aerothermodynamics teams on a common surface definition. In addition, the External Environments team standardized their Navier-Stokes simulations on a Common Baseline grid system. However, the DSMC simulations did not utilize the Common Baseline grid system. The Common Baseline grid developed for the External Environments Navier-Stokes studies was inappropriate for the DSMC analysis because of the resolution of the surface geometry. Over-discretization of the surface reduces the sampling count used to convert the microscopic events simulated by DSMC into macroscopic properties, thus increasing the statistical noise. Therefore, for the DSMC calculations, the decision was made to use a heritage DSMC Orbiter surface grid that has been shown to agree well with actual Orbiter flight data in previous studies. Efforts to standardize the Aerodynamics and Aerothermodynamics teams on a specific CAD definition are described in this section. In addition, details on the CAD definition developed as a standard for the Aerodynamics and Aerothermodynamics teams are provided. Also included is an overview of the Common Baseline grid system utilized by the External Environments team.

A majority of the viscous flow simulations performed for the Space Shuttle Orbiter Columbia accident investigation utilized structured volume grids. Structured grids are comprised of a logical or computational domain, characterized by three mutually orthogonal curvilinear coordinate directions. The orthogonal coordinates, in combination with a mapping that dictates how the points are placed on the surface of the vehicle, describe a vehicle to be analyzed. The mapping is referred to as a topology. It links the physical domain where the vehicle is typically described with Cartesian coordinates such as (x,y,z), to the computational domain where the coordinates are typically (i,j,k) and form a cube. In a structured grid, the most important issues to be addressed are the integrity of the outer mold lines that define the surface of the vehicle, the topology, and the quality of the grid with respect to the viscous flow solver to be used. Each of these issues will be discussed within the context of presenting our overall grid generation approach.

Initial computations performed by NASA (ARC, LaRC, and JSC), Boeing, and SNL made use of existing surface and volume grids for viscous flow simulations. The geometry description in use by most organizations prior to the STS-107 investigation was a version of the Shuttle Orbiter developed by Mississippi State University, under contract to NASA-JSC in 1997. This geometry, referred to as the ’97 definition, had several problematic regions on the vehicle, including an abnormally thick leading edge in the region of wing crank, and improperly modeled geometry at the wing tip/aileron junction. At the time of the accident, however, Navier-Stokes grids from the various organizations based on the ’97 definition were the most accurate available. Thus, these initial meshes were used to commence computational fluid dynamic (CFD) simulations.

Despite inaccuracies in the ’97 definition, NASA –LaRC developed a damaged RCC panel 6 geometry on that database. The volume grid was a modified version of an existing single-block volume grid, originally consisting of more than 9 million points. The damaged panel 6 geometry was estimated from existing Space Shuttle Orbiter Experimentation (OEX) documents. The surface and volumes of the previously existing grid system were modified to accommodate a damaged panel utilizing the “embedded” O-grid technique, and a new volume grid of 18 blocks and more than 18 million points was developed. This definition of panel 6 damage, referred to as the panel 6 “notch” grid, was used in many different computations performed at LaRC, Boeing, SNL, and JSC. It was so-named because the length of the missing RCC panel 6 was one half of the actual panel; hence it was a mere notch in the wing leading edge. Owing to its early availability, the panel 6 “notch” definition was used for many of the initial damaged RCC computations In addition, the generation of a volume grid on this early geometry definition provided extremely valuable insights towards developing structured volume grids for all subsequent leading edge damage scenarios.

In parallel with the CFD calculations that began on the pre-existing meshes, a new effort was initiated by the External Environments team to develop a common baseline grid. Following several discussions with representatives from all groups, an embedded O-grid topology was chosen. The embedded O-grid topology provides flexibility, enabling accurate computation of various damage scenarios with significantly reduced volume grid regeneration. As shown in Figure 5.2.4-1, there are three possible structured grid topologies. Each topology is so-named because of its structure; the O-grid looks like an O, and similarly for the C- and H-grids.

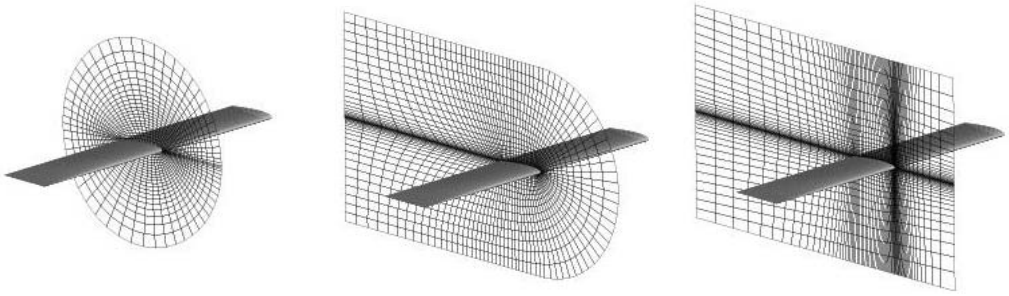

Figure 5.2.4-1 O-, C-, and H-grid topologies

For the common baseline grid, an O-grid wrapping around the entire vehicle from the top to the bottom was used as a starting point. The wings were then isolated topologically with C-grids so that grid resolution along the span of the wings would be completely independent of the main O-grid that wraps around the vehicle, as shown in Figure 5.2.4-3. This topology was chosen specifically because it permits blocks on the wing within the

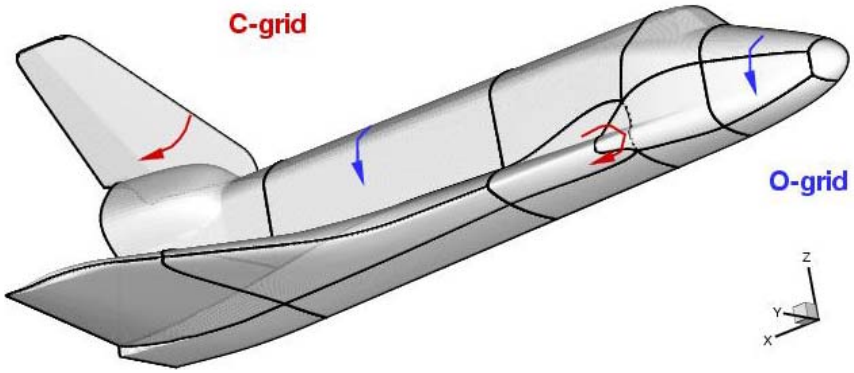

Figure 5.2.4-2
Figure 5.2.4-3 Common grid baseline topology

C-grid to be removed and replaced with an “embedded” O-grid, thus focusing grid points to a damaged leading edge area by altering the spacing and clustering.

Common baseline grid development began with the creation of a smooth outer mold line (OML) version that could be used to benchmark all the flow solvers from the various organizations. As noted previously, initial computations used the ’97 OML definition for the grid systems. The ’97 geometry definition had several accuracy issues, mentioned above, that needed to be addressed. These issues led to the development of a new, more accurate geometry description from computer-aided design (CAD) data provided by NASA -JSC to NASA-LaRC and ARC. The geometric description provided by NASA-JSC was not a complete geometry, as it had several regions where surfaces describing the wing and fuselage were not sealed. This produced holes where a grid could not be generated. Thus, the CAD representation was slightly modified to ensure that a solid model could be mathematically described with the data provided by NASA-JSC. To ensure a good solid model, the CAD representation was modified by filling in the “holes” and smoothing over gaps between the control surfaces and the respective hinge lines. In addition, the control surfaces were positioned based on initial STS-107 flight data. The resulting

surface definition became the '03-definition of the Space Shuttle Orbiter and it was utilized for the common baseline grid generation.

The process used in the common baseline grid generation, as well as many of the subsequent surface and volume grids used for viscous flow simulations is shown in Figure 5.2.4-4.

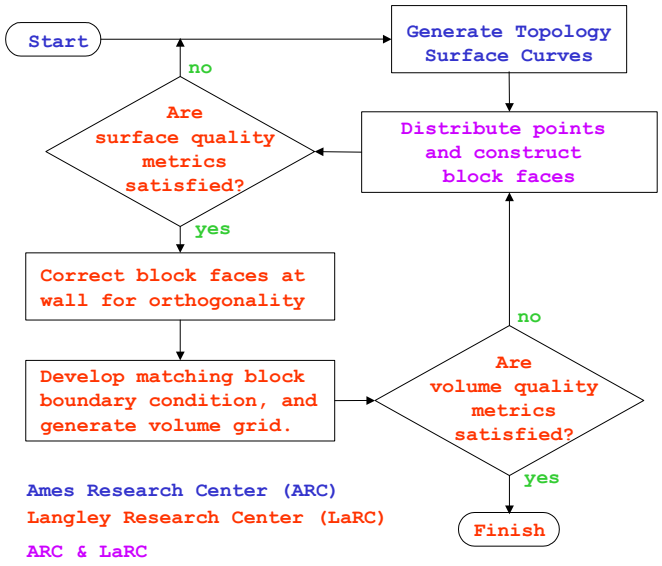

Figure 5.2.4-4 Grid generation process with ARC and LaRC

The first step in generating the common baseline grid system was the development of the basic grid topology. After the topology was developed, the next step involved the detailed generation of the surface meshes over the entire OML of the Orbiter. Next, initial block faces for all of the non-surface faces that defined the volume grid boundaries were created to produce a complete first sketch of the entire mesh. After these initial surfaces were constructed, the surface grids and initial block faces were evaluated for overall grid quality. Modifications were then made to ensure orthogonality of the grid lines emanating from the wall and to ensure that the grid metrics could be satisfied for grid stretching. Once an acceptable quality was reached for the OML surface and block interfaces, an initial volume grid was generated. Newly developed technologies were developed by LaRC to ensure slope continuity across matching block boundaries, producing superior grids that could meet grid quality metrics requirements established by the team. These requirements will be discussed in more detail later in this sub-section.

The primary grid generation software used at NASA-ARC was the GridGen software from Pointwise Inc., while NASA-LaRC utilized a combination of GridGen, the Volume Grid Manipulator (VGM), and the Three-Dimensional Grids about Anything using Poisson's Equations with upgrades from Ames and Langley (3DGRAPE/AL) for grid generation. NASA-LaRC also used the CFD Analyzer software from AMTEC Engineering Inc. for grid quality evaluations. The GridGen software was used to develop the initial surface grids by constructing grid lines on the baseline IGES-format database. GridGen was also used to construct the volume grids. However, due to limitations in GridGen, the interfaces of all blocks with edges coinciding with the OML were modified with VGM. This was done to ensure that the block interfaces were locally orthogonal to the vehicle OML. After block interface modification, the VGM software was used to develop a C-II continuous boundary condition across matching block volume grids. The volume grids were then elliptically smoothed in GridGen. In some rare instances where GridGen was unable to produce a volume grid with all positive cell volumes, the 3DGRAPE/AL software was used to generate the volume grid. After GridGen smoothing, all volume grids were modified and improved with VGM to reduce grid stretching. Finally, individual organizations re-positioned the outer boundary location of the baseline common grid to closely match the bow shock location for a given flight condition. The

repositioning of the outer boundary also allowed re-stretching in the normal direction to optimize the grid distribution in the shock layer.

The development of all surface and volume grids for the damage scenarios investigated by the External Environments team used the baseline common grid as a starting point. Several complete volume grids were generated to model various damage conditions of the Shuttle Orbiter, including Missing Main Landing Gear door tiles (MLG), a forward dump valve investigation, and Missing Reinforced Carbon-Carbon (RCC) panel 6 and Missing RCC panel 9 configurations. In addition, the Aerodynamics team used this grid system for portions of their Navier-Stokes analyses. In a general sense, therefore, each grid was generated with the same process identified in Figure 5.2.4-4. Also, as the damage scenarios varied, only the wing region was modified to accommodate a given damage scenario. This is illustrated in Figure 5.2.4-5, where the wing blocks and the attached fuselage blocks (shaded yellow) are modified to accommodate a damage scenario. This figure also shows the "embedded" O-grid, which encompasses the damage site. Using this topology, the center square on the wing leading edge representing a missing RCC panel was resolved with many more grid points than in the nominal geometry grid. However, this additional grid density did not affect any other portion of the vehicle. This approach made generation of new damage scenario volume grids easier and more efficient because only the wing leading edge region blocks needed to be re-constructed. All subsequent damage scenarios were generated with this type of topology, enabling the development of several different volume grids for the Shuttle Orbiter within a two-month period. It is estimated that this procedure saved 50% of the grid generation time compared with rebuilding a new volume grid each time a different damage scenario was considered.

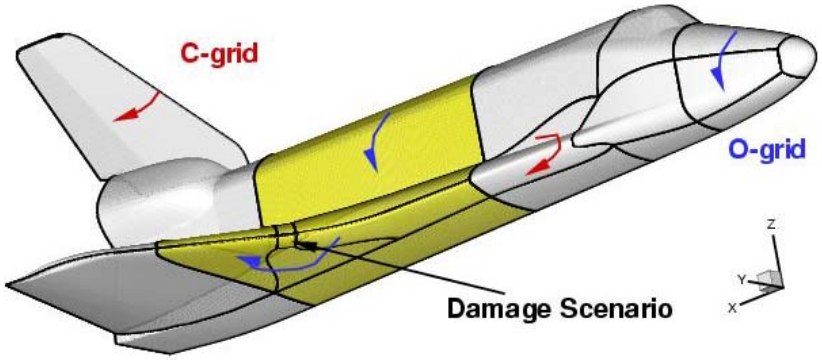

Figure 5.2.4-5 Damage scenario topology

Grid quality metrics used to assess the common baseline grid were defined based on extensive experience at NASA-LaRC in grid generation. The grid metrics used to determine the quality of the grid with respect to CFD include cell-to-cell stretching, interior and near-wall orthogonality, and cell volume. Based on previous work in structured grid generation, grid stretching should be less than a factor of 1.5 from one point to the next. Grid line orthogonality at the wall should be within 10 degrees of orthogonal, and cell volumes should be positive. These metrics are used to assess the grid quality by evaluating the maximum stretching, and minimum orthogonality, as well as the root mean square (RMS) and three-sigma values of the metrics, assuming a normal distribution. Based on anecdotal evidence obtained with the grids used for this effort, failure to adhere to reasonable limits for these metrics can result in inaccurate flow simulations. This evidence also suggests that grids with large values for these metrics will suffer from slower convergence of flow field residuals. Tabulated in Table 5.2.4-1 are the grid metrics for the common baseline grid, generated with the previously identified software and process. Note that the ξ-direction is streamwise from nose to tail, the η-direction is from top of the vehicle to the bottom, and the ζ-direction is from the wall to the outer bow-shock within the flow field. These directions represent the three mutually orthogonal computational coordinates that are used in the mapping of the grid to the geometry, using the topologies described. The common baseline grid contains nearly 3.5 million points and 20 blocks, and was suitable for computations by all viscous-flow CFD software used by the team.

Table 5.2.4-1 Baseline common grid quality metrics

	Minimum	Average ± 3σ	Maximum
I-Stretching (ξ)	1.000	1.048 ± 0.132	2.775
J-Stretching (η)	1.000	1.015 ± 0.132	2.775
K-Stretching (ζ)	1.000	1.013 ± 0.075	1.763
J-K Orthogonality (ξ)	0.018	0.671 ± 0.708	1.000
I-K Orthogonality (η)	0.042	0.729 ± 0.621	1.000
I-J Orthogonality (ζ)	0.023	0.836 ± 0.528	1.000

Additional Comments on Damage Scenario Meshes

Using the embedded-O mesh topology, the exterior grid resolution is focused toward the damage location. As previously noted, separate external meshes were created for the RCC panel 6 and panel 9 cases. The missing panel meshes allow the flexibility to assess a wide range of damage at a specific panel location. The inner perimeter of the focused embedded-O follows the OML at the RCC panel of interest. The External Environments team utilized two different topologies to investigate the damaged RCC panel parametrics. One group utilized a simple H-mesh interior for the missing RCC cavity. This topology required that Navier-Stokes spacing was achieved, tangential to the OML surface in the radial direction, as the external embedded-O mesh approached the perimeter of the damage location. The cavity itself is modeled with a simple H-topology that has Navier-Stokes spacing against each block face. The internal topology is broken out into a series of H blocks to permit various or progressive damage scenarios to be considered. For example the interior of an RCC panel removed cavity had separate H-grids for the carrier panels the RCC panel and the RCC channel interior. Each internal block maintained Navier-Stokes spacing against each of its six faces such that once the mesh was constructed any combination of upper/lower carrier panel and/or RCC panel could be computed without any re-gridding or re-stretching.

The second mesh topology used for damage scenarios employed a double-O mesh topology interior for the missing RCC cavity. While this topology required the creation of seven internal cavity blocks to ensure that Navier-Stokes clustering was obtained against all interior faces of the cavity, it did not require the Navier-Stokes clustering of the exterior grid except in the traditional normal direction. The inside of the cavity for the second option is constructed with a central H-mesh that is enclosed on six sides by unique blocks. Each of the surrounding six blocks has Navier-Stokes spacing against a single outward facing block face. This topology completely isolates the Navier-Stokes spacing, used against each of the interior walls, from propagating outside of the cavity region. However, the topology also requires interior cavity meshes (not the external mesh) to be constructed independently for the upper and lower panel out cases. Figure 5.2.4-6 shows a cut through the double-O interior mesh topology for the full panel 6 removed case. Similar interior mesh configurations were constructed for the full panel 9 out geometry and the two half panel out geometries.

For each damage grid option, the exterior mesh is built in two halves corresponding to upper and lower halves of the Orbiter, and is split at the wing leading edge water line. This split construction permits a missing upper half panel, a missing lower half panel, or a complete panel missing to be simulated from a single grid system. Furthermore, for each option the exterior meshes were clustered against all OML surfaces with Navier-Stokes spacing to meet a cell Reynolds number of approximately 1. Even the H-block that extends from the OML surface of the damage location to the outer boundary (present for both damage scenario topologies) has the same Navier-Stokes spacing. This exterior mesh construction, for either option, allows the various damage configurations such as smooth OML, half panel out and full panel out to be computed with changes only to the interior cavity mesh boundary conditions.

Both options allowed the region of the damaged RCC panel that vents into the leading edge channel to be modeled with an outflow boundary condition. The first option, with a simple H mesh interior to the cavity, was chosen for the LAURA simulations. It allowed the flexibility to easily re-distribute the grid to

satisfy a surface grid spacing criterion. However, this capability also resulted in a larger grid system due to the competing requirements of Navier-Stokes spacing in the radial/tangential direction along the perimeter of the damage location and the less than 1.5 point-to-point stretching ratio. The only way to meet both demands was to increase the number of points within the external common grid topology. The second option allowed the flexibility to model various damage scenarios using a single external grid system that could have considerably fewer points since there were no demands on Navier-Stokes spacing in the tangential/radial direction, but this flexibility was obtained at the expense of a topologically more complex internal cavity grid system and the need to have independent internal cavity meshes for either half- or full panel out scenarios. The two topologies are depicted in Figure 5.2.4-6 and Figure 5.2.4-7. Both topologies were utilized for the damaged RCC panel parametrics considered, and the various simulations performed with GASP and LAURA will be described in more detail in the damage scenario description of the CFD results.

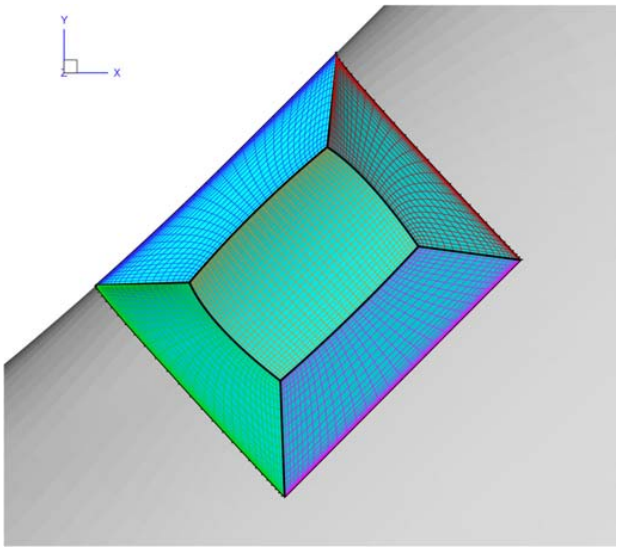

Figure 5.2.4-6 Cut through full panel out interior cavity mesh for GASP simulations

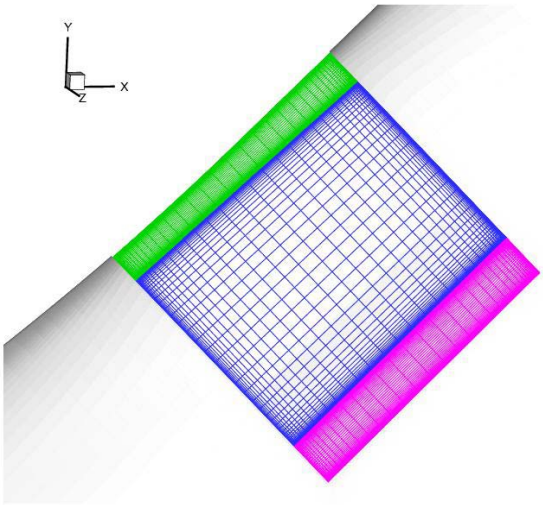

Figure 5.2.4-7 Cut through full panel out cavity mesh for LAURA Panel 9 simulation

5.2.4.3 CFD/DSMC Verification for the Orbiter Configuration

In order to determine laminar and turbulent heating rates and surface temperature uncertainty bands for the primary Navier-Stokes solvers used in the investigtion, researchers from Boeing Huntington Beach, NASA-ARC, and NASA-LaRC computed Navier-Stokes CFD solutions to compare against STS-2 flight data at three trajectory points, two laminar and one turbulent. Results from this study are provided in the following section. The CFD codes USA, LAURA, and GASP were used for the simulations by the Boeing-Huntington Beach, NASA-LaRC, and NASA-ARC groups, respectively, and are described in Section 5.6. Since this work was done prior to the completion of the common CFD grid, the grids available to each group at the time of STS-107 were used. They did not include body flap or elevon deflections and had been constructed primarily to capture windward side heating.

In order to make a comparison with flight data, three STS-2 trajectory points were simulated using the free-stream conditions shown in Table 5.2.4-2. The Mach 24 point was selected to approximate the conditions at the start of the peak heating region on the STS-107 trajectory. The Mach 18 point was selected to approximate the point on the STS-107 trajectory for which good GPS data were available. The Mach 7 point was selected to provide a turbulent comparison case.

Table 5.2.4-2 Freestream conditions for STS-2 computations

Case	M	V	ρ	T	alt.	Re/L
		(m/s)	(kg/m^3)	(K)	(km)	(1/m)
t = 75260 s	24.3	6920.0	5.7500E-05	202.00	72.400	28439
t = 75950 s	18.1	5617.0	1.6260E-04	240.60	64.400	56430
t = 76310 s	7.7	2486.0	1.9130E-03	256.90	45.070	278700
Case	**M**	**V**	**ρ**	**T**	**alt.**	**Re/L**
		(ft/s)	($slug/ft^3$)	(R)	(ft)	(1/ft)
t = 75260 s	24.3	22714.0	1.1152E-07	363.29	237670	8822
t = 75950 s	18.1	18430.0	3.1558E-07	433.07	211440	17958
t = 76310 s	7.7	8156.0	3.7094E-06	462.56	147870	88576

Comparisons between the computed and flight derived surface heat transfer rate data provide an additional measure of confidence in the numerical simulations at flight conditions. The results of these comparisons using the experimental data derived by Throckmorton and Hartung are discussed in the following paragraphs. Additionally, code-to-code comparisons are presented for predicted surface pressures. All calculations were made with a 5 species nonequilibrium chemistry model assuming thermal equilibrium. A radiative equilibrium wall boundary condition with the emissivity set to 0.90 was used. The RCG catalysis model from Stewart was used for the entire vehicle for each of the solvers. In the case of the Mach 7 condition,. NASA-LaRC used the Cebecci-Smith turbulence model, while NASA-ARC used the Baldwin-Lomax turbulence model.

Mach 24 Results

Figure 5.2.4-8 shows STS-2 flight data for surface heat flux plotted over the computed results for the windward side of the orbiter. The two tiles covered with a catalytic coating are indicated in the figure. The GASP and LAURA results are in general agreement, and the comparison with the data is good. The solutions are not expected to match the data in the body flap region since neither Ames nor Langley modeled the actual body flap deflection in their solutions.

Figure 5.2.4-9 gives a more quantitative comparison of the results along the windward centerline. The comparison between both predictions and the flight data is excellent for the non-catalytic locations

upstream of the body flap. A fully-catalytic GASP solution is also shown in Figure 5.2.4-9. The prediction matches the data at the downstream catalytic tile, but under-predicts the heating at the upstream catalytic tile. This under-prediction is not surprising since the computation is not modeling the physical situation of a catalytic tile surrounded by non-catalytic tiles. The heating on the isolated catalytic tile downstream of non-catalytic tiles should be higher than the heating at the same location downstream of catalytic tiles. The higher heating can be attributed to higher atomic species mass fractions in the boundary layer. The atomic species exist in higher quantities for the non-catalytic upstream tiles case because a lower-catalycity surface suppresses recombination of the atomic constituents. Thus, for an isolated catalytic tile in the vicinity of non-catalytic tiles, more atomic species exist in the approaching boundary layer, providing more potential for catalytic heat transfer.

The heating rate uncertainty, defined as the difference of the computed and flight derived heating rates divided by the flight derived heating rate, is shown in Figure 5.2.4-10 at every measurement location. The same data are also presented in Figure 5.2.4-11 as a function of axial co-ordinate down the Orbiter.

Figure 5.2.4-12 shows the computed heat transfer rates from GASP and LAURA on a slice through the Orbiter at a location of X = 1215 in Orbiter coordinates, which passes just downstream of the main landing gear (MLG) door. The agreement between the two codes on the wind side and around the wing leading edge is quite good. On the leeside, the results differ by as much as 100%, although this is not surprising since neither grid was optimized to capture leeside heating. In fact, the grid used for the GASP calculations is particularly coarse. The Z-location of RTD V34T1106 is indicated in the figure.

The heating results for a slice at Y = 167 in are shown in Figure 5.2.4-13. This slice is along the outboard edge of the MLG. On the wind side, the predictions of the two codes are within 10% of each other, and the heating rates on the WLE are within 2%. Figure 5.2.4-14 shows the predicted heating rates along the WLE. The codes are in good agreement except in the downstream region where the LAURA heating rates are about 30% higher than the GASP heating rates. Given the difference in grid resolution between the two solutions, a difference of 30% is not unreasonable. In addition, the shock-shock interaction region is a particularly difficult feature to resolve numerically. Because of this and the fact that a comprehensive calibration study using Orbiter wing leading edge heating flight data has not been performed, questions remain about what is required to obtain an accurate flight prediction.
The comparison of windward centerline pressure predicted by GASP and LAURA is shown in Figure 5.2.4-15. The two codes give similar answers, except for the wiggles in the GASP solution between $0.3 < X/L < 0.5$. These wiggles are caused by waves in the surface geometry used to create the GASP grid. Later comparisons for STS-107 cases computed on the common grid showed good agreement between the GASP and LAURA results.

Mach 18 Results

The results for Mach 18 are similar to the results for Mach 24. Figure 5.2.4-16 shows the computed and flight derived surface heat transfer rates on the windward side of the Orbiter. Figure 5.2.4-17 shows a comparison between the CFD predictions and the flight data on the windward centerline. Figure 5.2.4-18 and Figure 5.2.4-19 show the uncertainties in the computed data. The off-centerline results show the same trends as in the Mach 24 case. GASP and LAURA agree within about 10% of each other on the wind side, but differ on the lee side due to the differences in the grids.

Mach 7 Results

Figure 5.2.4-20 shows the computed and measured heat transfer rates for the Mach 7 turbulent trajectory point. In GASP the Baldwin-Lomax model was turned on at X/L = 0.4. In LAURA, the Cebecci-Smith turbulence model was turned on at X/L = 0.3. The flight data indicates transition in the region $0.3 < X/L < 0.5$. The GASP computation predicts higher heating than the LAURA computation. The higher heating in GASP can be seen clearly in Figure 5.2.4-21 where results on the windward centerline are presented. Figure 5.2.4-22 and Figure 5.2.4-23 show the uncertainties in the computed data.

Summary of STS-2 Surface Heating Comparisons

The agreement among the CFD codes utilized in this comparison to STS-2 flight derived heat flux data is generally very good considering that different codes and different meshes were used. There are some windward oscillations in the GASP solutions due to waviness in the surface grid. In addition, differences between the results from LAURA and GASP are apparent on the lee side. However, as mentioned previously, the grids were not tailored to capture leeside heating, and it is likely that lack of grid resolution is the reason for the differences among the codes. Only a comprehensive calibration study of leeside flow heating environments on the Orbiter can establish whether differences in leeside heating between the two solvers are due to grid resolution.

Table 5.2.4-3 shows the standard deviation of the computed heat transfer rates from the flight data for the windward surface gauges upstream of the body flap and elevons, forward of X = 1433.2 in. The laminar results are within about 15% of the data, while the turbulent results are within 30% of the data. The poorer than expected comparison with the turbulent results could be due to the fact that the radiative equilibrium assumption at the wall may not be valid. The flight data do show differences of up to 20% between the inferred radiative equilibrium heat fluxes and convective heat fluxes, suggesting that the surface is not in radiative equilibrium.

Table 5.2.4-3 Standard deviation of heating results

	LAURA	GASP	USA
M=24 Laminar	12.50%	12.60%	N/A
M=18 Laminar	11.20%	15.30%	N/A
M=7 Turbulent	27.70%	27.20%	N/A

Comparisons of Computed and Measured Surface Streamlines at Wind Tunnel Conditions

The simulation of leeside flows with computational fluid dynamics is a challenging endeavor, and the inclusion of leading edge damage parametrics into the activity makes the effort even more difficult. Most activities for the simulation of hypersonic flow fields have focused on the windward regions where surface heating drives the selection of thermal protection systems. In the case of the Space Shuttle Orbiter, no comprehensive leeside flow field calibration study has ever been performed. Because of this lack of historical base, the leeside results included in this report need to be looked at from an engineering perspective, as mentioned in Section 5.2.4.1. In order to provide some information on the quality of the leeside flow field results from the CFD simulations, LAURA computations were performed to simulate a wind tunnel experiment in the LaRC Mach 6 CF_4 wind tunnel. The computation was performed using the thin layer formulation of the Navier-Stokes equations assuming laminar flow and vibrational equilibrium. The grid used for these computations had 2 million cells, most of which were devoted to the vehicle windward side, and was derived from the '97 geometry definitions. The grid covered the leeward side and windward side of the vehicle but did not extend into the wake. The model scale for the computations was 0.75%. The angle of attack was 40 degrees and the sideslip angle was 0 degrees. A constant wall temperature boundary condition of 300 K was assumed, and the Mach 6 CF_4 CFD computation was run with the following free-stream conditions:

Mach = 5.902
Velocity = 889.84 m/s
Density = 1.9417e-2 kg/m3
Temperature = 198.38 K
Reynolds Number= 0.44 million/ft

The CF_4 wind tunnel experiment, run at 40 degrees angle of attack, had the following free-stream conditions:

Mach = 5.94
Velocity = 880 m/s
Density = 1.97e-2 kg/m3
Temperature = 190 K
Reynolds Number = 0.47 million/ft

The two sets of conditions are very similar, but are not an exact match because the CFD conditions were chosen before the wind tunnel experiment was performed. However, these free stream conditions are considered similar enough to provide a valid comparison. Computed and measured streamlines on the lee side of the vehicle are shown in Figure 5.2.4-24. The experimental streamlines, shown in the top of the figure, were obtained from post-run images using an oil flow technique. The lower images are computed surface streamlines from the LAURA simulation at the wind tunnel conditions listed above. While differences, possibly due to grid resolution, are observed in the computed and measured locations of the strake vortex separation line on the aft portion of the wing leeside, the code predicted the separation and reattachment line locations of the strake and canopy vortices. In general, good agreement was observed in this first comparison of leeside surface streamlines between the viscous solver LAURA and CF_4 wind tunnel measurements. The level of agreement in the streamline patterns between the experimental and numerical results demonstrates the confidence level that can be expected for the leeside flow simulation. Certain aspects of the flow field show quite reasonable agreement, e.g., the separation and reattachment locations on the fuselage and inboard wing regions, while others show less agreement, e.g., the outboard region of the wing leeside. The LAURA simulation was obtained using best practices available at the time of the accident, which do not include an a priori knowledge of what is necessary and sufficient to model the lee side of the Orbiter flow field. This statement is true for both wind tunnel and flight conditions. These results reinforce the statement made in Section 5.2.4.1 and reiterated here. Critical insight can be gained into the flow field characteristics and physical mechanisms at work on the Orbiter leeside. But, an approach towards interpreting the results more in an engineering sense than a scientific sense must be used for any of the leeside numerical results in this report because an established practice for obtaining accurate Orbiter leeside simulations is not known at this time.

Comments on DSMC Verification

A comparison of DSMC heating results with STS-2 flight data was also considered. After reviewing the available STS-2 data from Throckmorton and Hartung, it was decided that a comparison could not be made with the DSMC methodology. This was because the surface thermocouple data available showed little or no temperature response at the higher altitudes where it is reasonable to employ the DSMC method. Therefore, it was determined that an aerodynamic comparison previously made between STS-62 flight data and DSMC results would serve as verification that the surface geometry selected was acceptable to use for the DSMC analysis work done to support this investigation. More information on that study can be found in Boyles (2003). The Orbiter surface geometry used in the study by Boyles was also used for the 350,000 ft altitude DSMC solution performed for the STS-107 investigation, and the 300,000 ft altitude DSMC solution utilized a slightly finer resolution Orbiter definition. In addition to the conclusion to rely on the aerodynamic study as sufficient calibration for the STS-107 investigation, the judgment was made to accept the heating results obtained using the best practices available at the time of the accident. Therefore, to date, no comprehensive comparison has been made of DSMC heating results for the Orbiter at rarefied re-entry conditions.

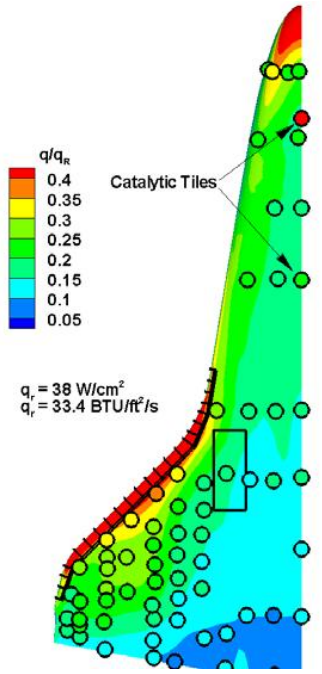

a) GASP

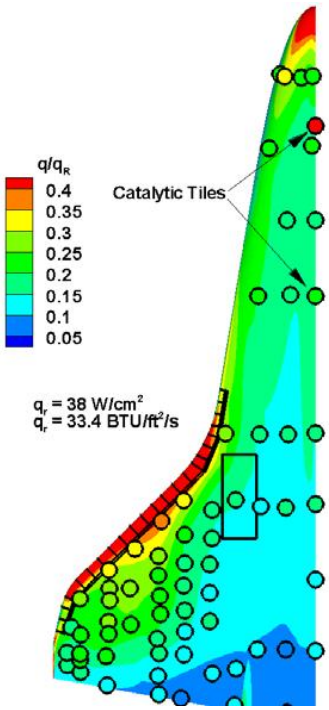

b) LAURA

Figure 5.2.4-8 Windward surface temperature predictions from GASP and LAURA compared with flight data at Mach 24. Experimental data are plotted inside the circular symbols. The symbol size is made larger than the measurement extent to aide visualization of the data.

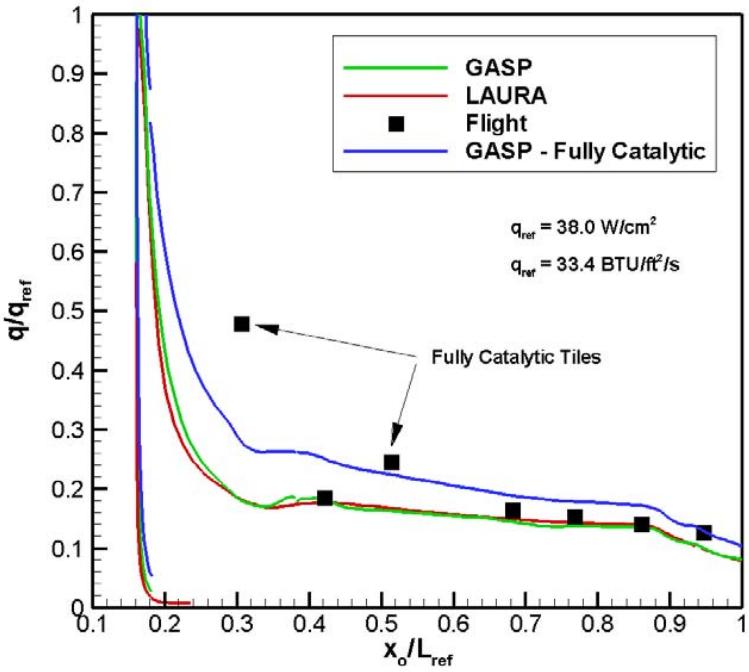

Figure 5.2.4-9 Windward centerline heat transfer rate for Mach 24. L_{ref} = 37.24 m = 1466 in

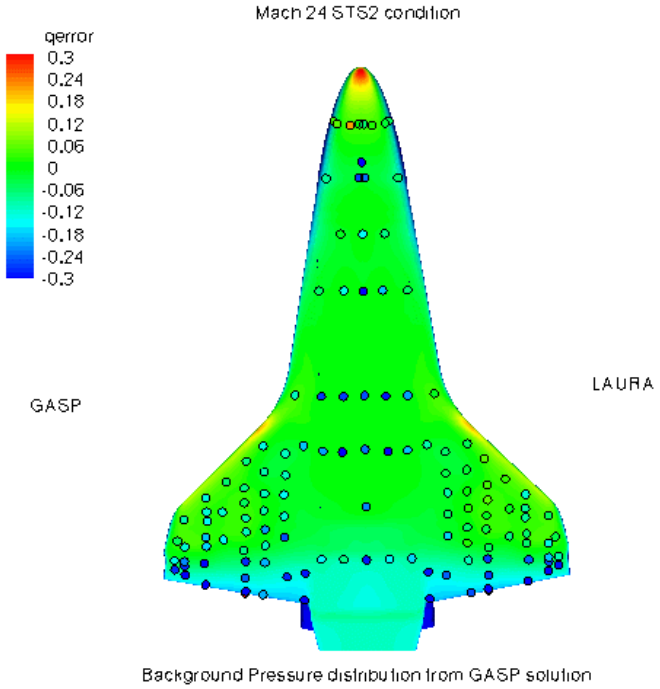

Figure 5.2.4-10 Windward heating rate uncertainty at Mach 24 plotted over pressure contours $q_{error} = (q_{cfd} - q_{flight})/q_{flight}$.

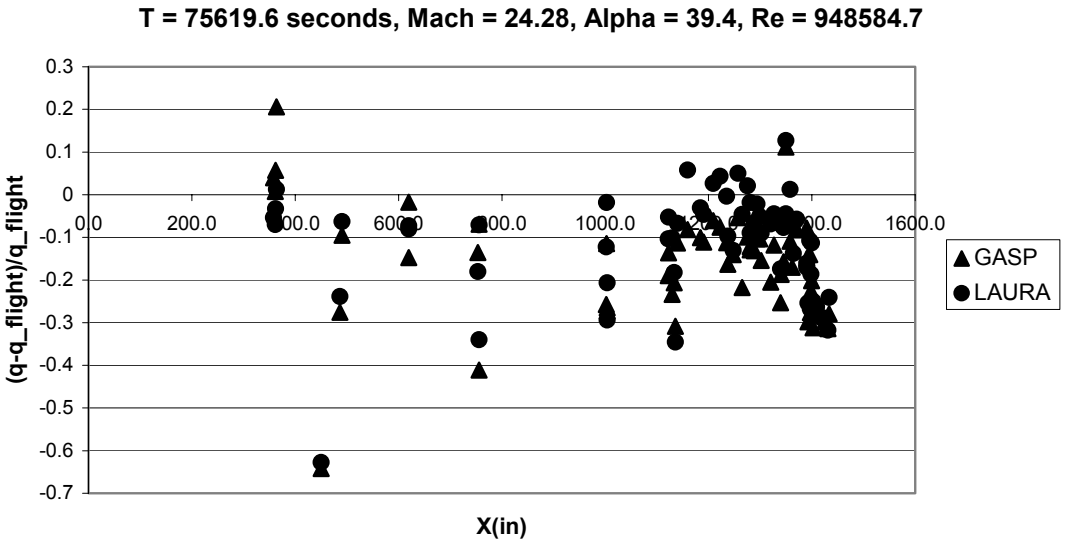

Figure 5.2.4-11 Heating rate uncertainty at Mach 24 as a function axial distance along the orbiter

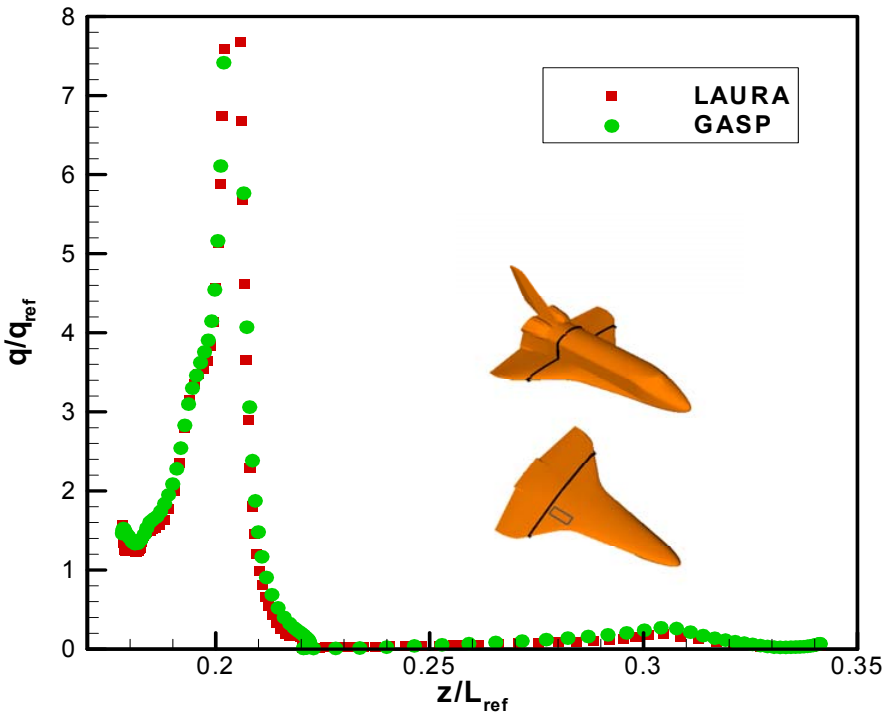

a) Wind side and lee side.

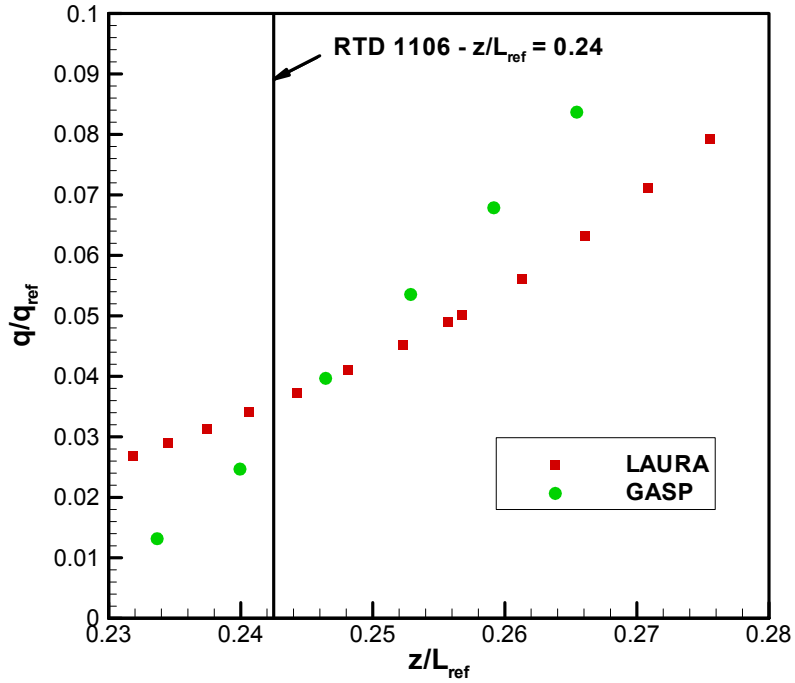

b) Zoom of leeside region.

Figure 5.2.4-12 Comparison of GASP and LAURA heat transfer rates along a cut at X = 1215 in. The location of the MLG is shown in the inset. q_{ref} = 3.55 W/cm^2 = 3.13 BTU/ft^2/s. L_{ref} = 37.24 m = 1466 in.

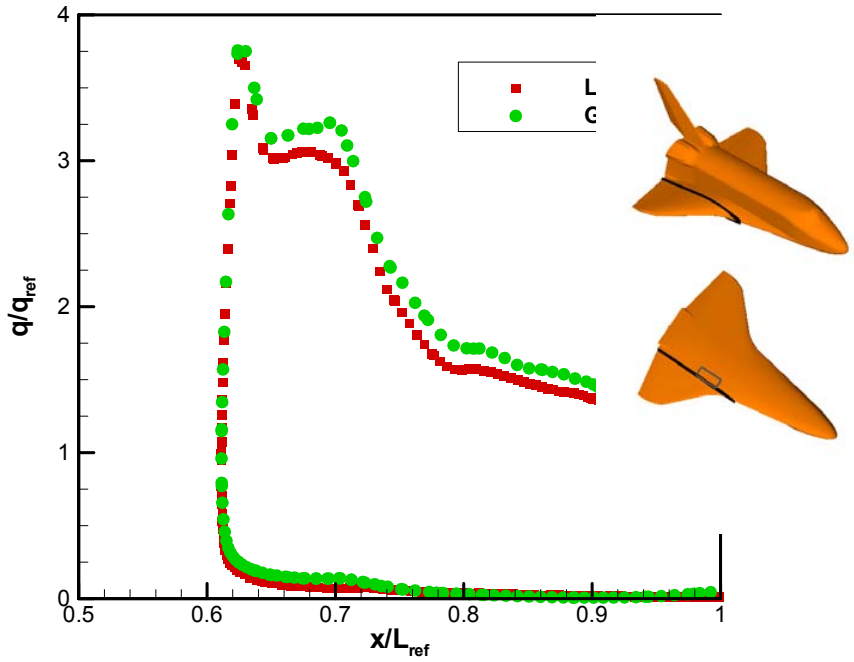

Figure 5.2.4-13 Comparison of GASP and LAURA heat transfer rates along a cut at Y = 167 in. The MLG location MLG is shown in the inset. q_{ref} = 3.55 W/cm^2 = 3.13 BTU/ft^2/s. L_{ref} = 37.24 m = 1466 in.

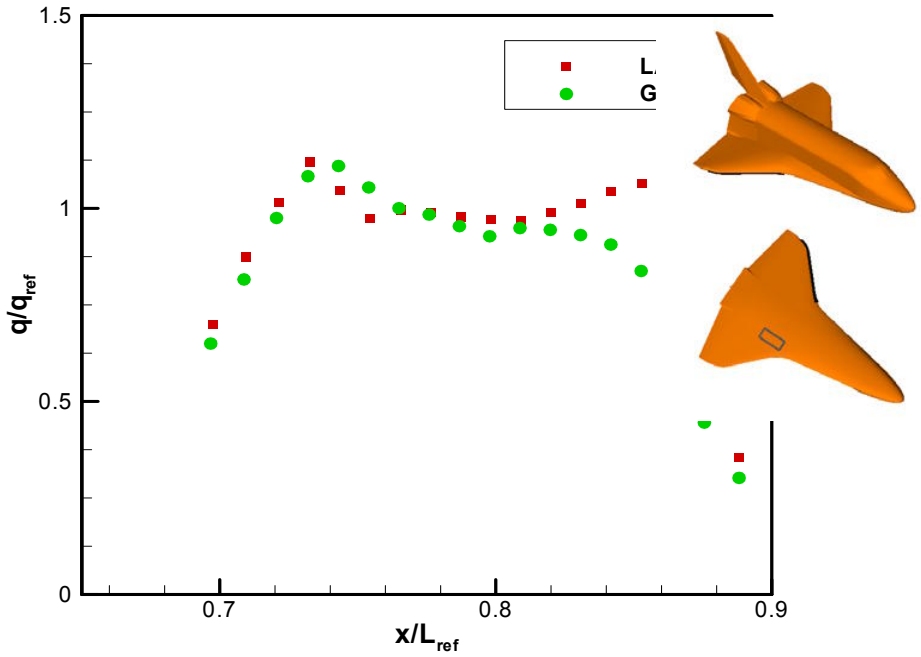

Figure 5.2.4-14 Comparison of GASP and LAURA heat transfer rates along the wing leading edge. q_{ref} = 37.8 W/cm^2 = 33.2 BTU/ft^2/s. L_{ref} = 37.24 m = 1466 in.

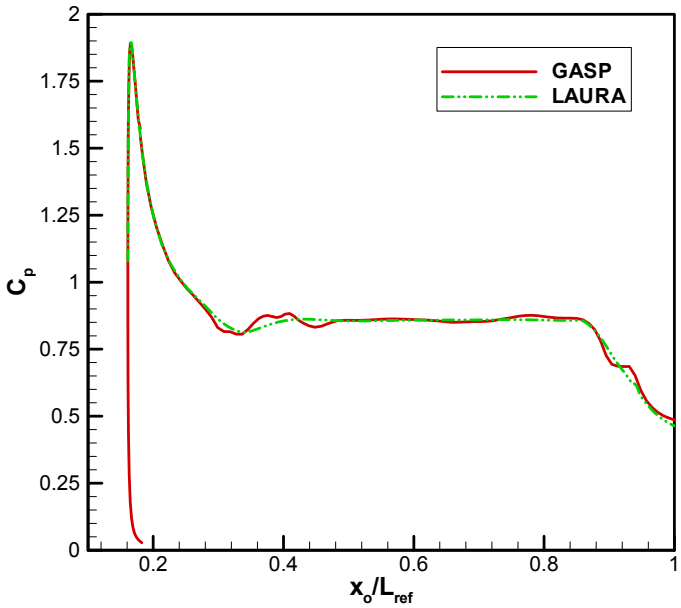

Figure 5.2.4-15 Computed windward centerline pressure distributions from GASP and LAURA. L_{ref} = 37.24 m = 1466 in.

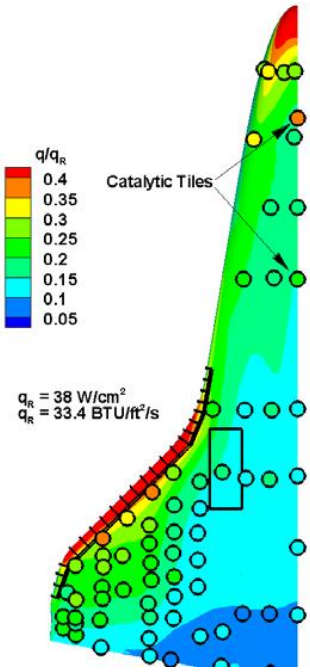

a) GASP

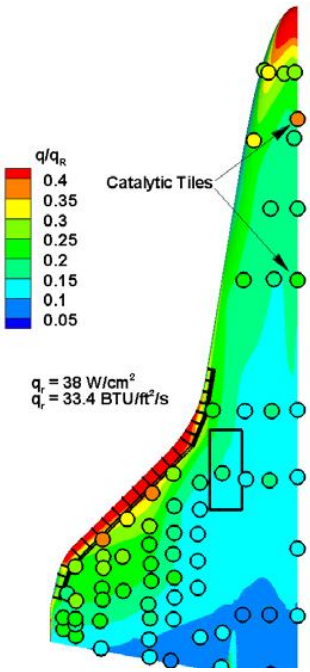

b) LAURA

Figure 5.2.4-16 Windward surface temperature predictions from GASP and LAURA compared with flight data at Mach 18. Experimental data are plotted inside the circular symbols. The symbol size is made larger than the measurement extent to aide visualization of the data.

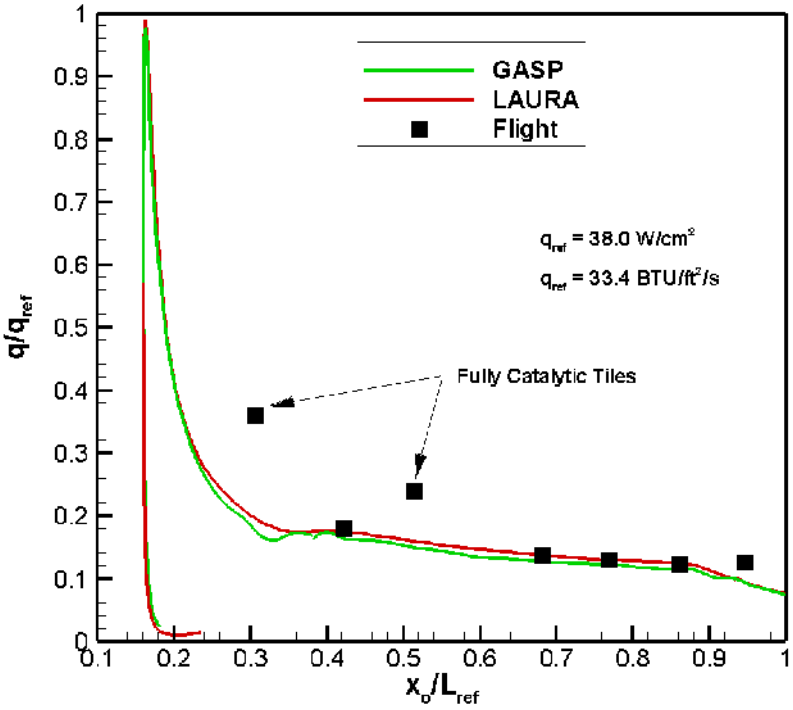

Figure 5.2.4-17 Windward centerline heat transfer rate for Mach 18. L_{ref} = 37.24 m = 1466 in.

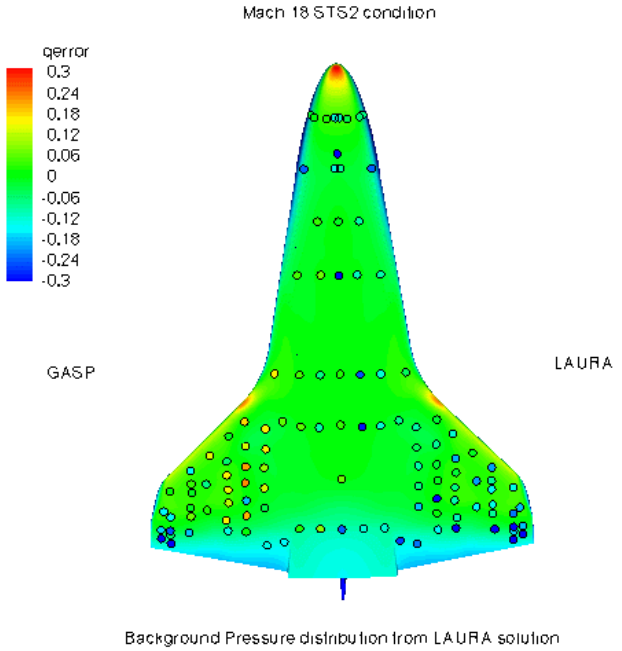

Figure 5.2.4-18 Windward heating rate uncertainty at Mach 18 plotted over pressure contours $q_{error} = (q_{cfd} - q_{flight})/q_{flight}$.

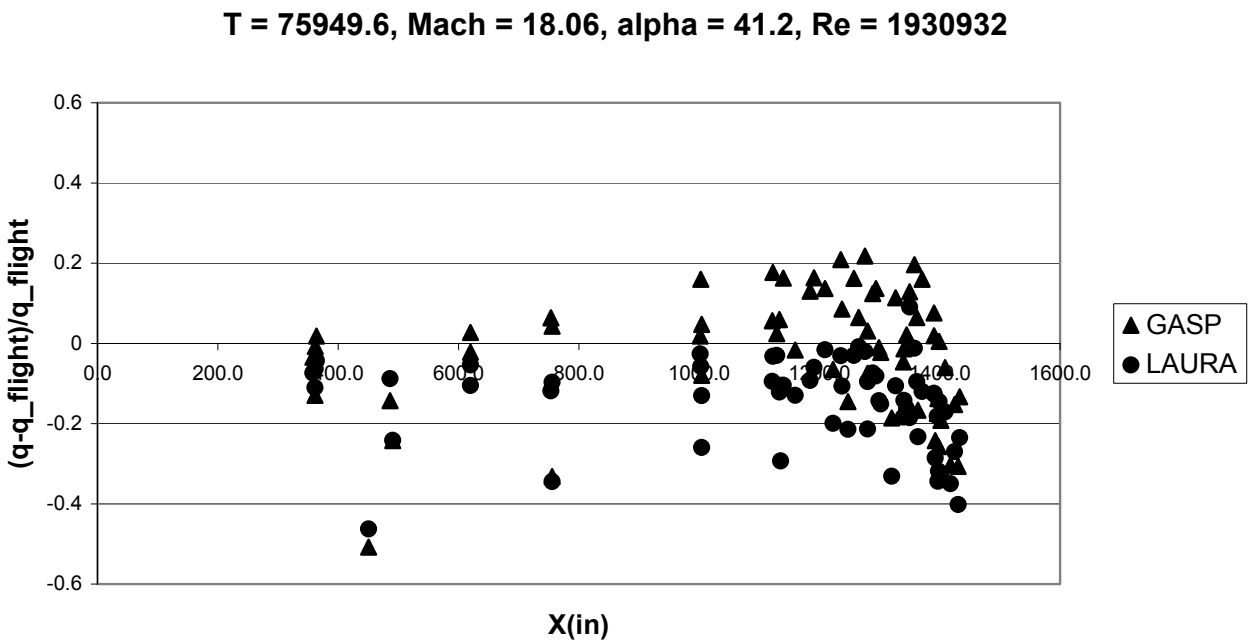

Figure 5.2.4-19 Heating rate uncertainty at Mach 18 as a function axial distance along the orbiter

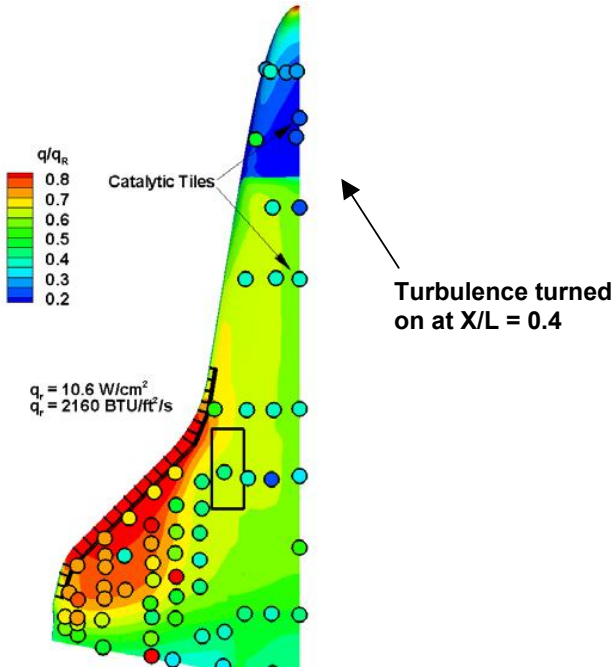

a) GASP

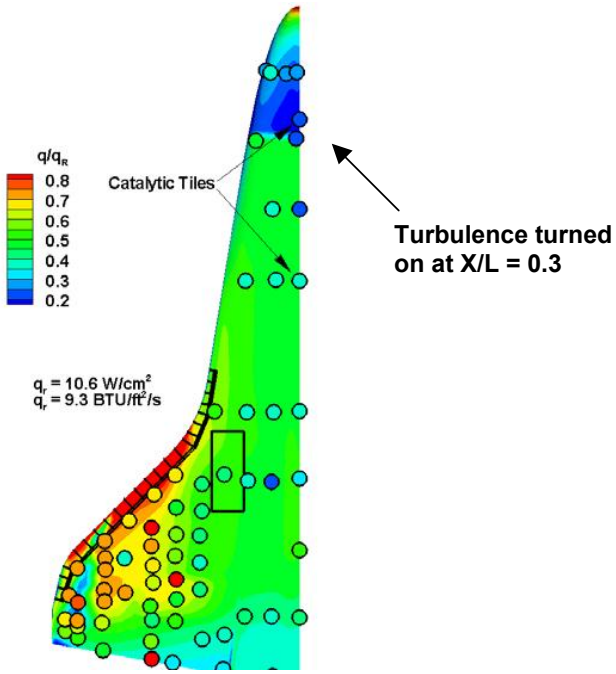

b) LAURA

Figure 5.2.4-20 Windward surface temperature predictions from GASP and LAURA compared with flight data at Mach 7. Experimental data are plotted inside the circular symbols. The symbol size is made larger than the measurement extent to aide visualization of the data.

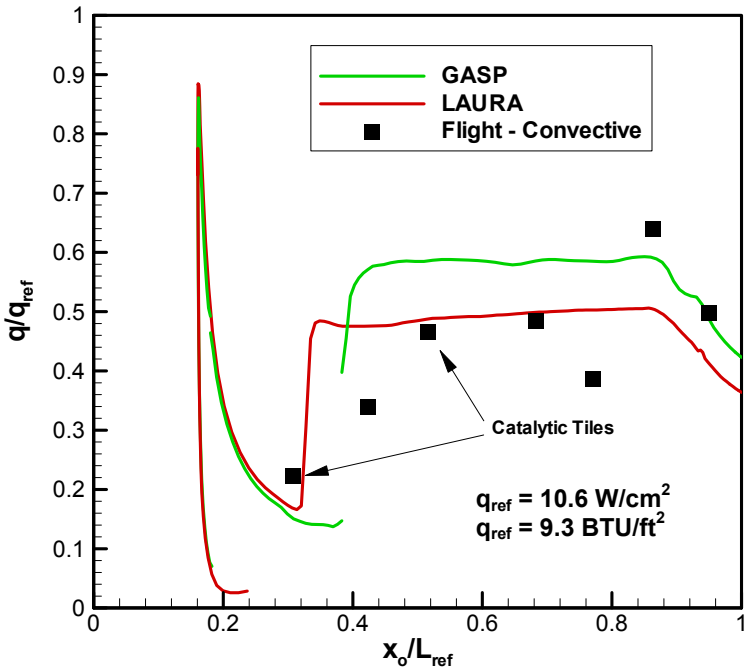

Figure 5.2.4-21 Windward centerline heat transfer rate for Mach 7. L_{ref} = 37.24 m = 1466 in.

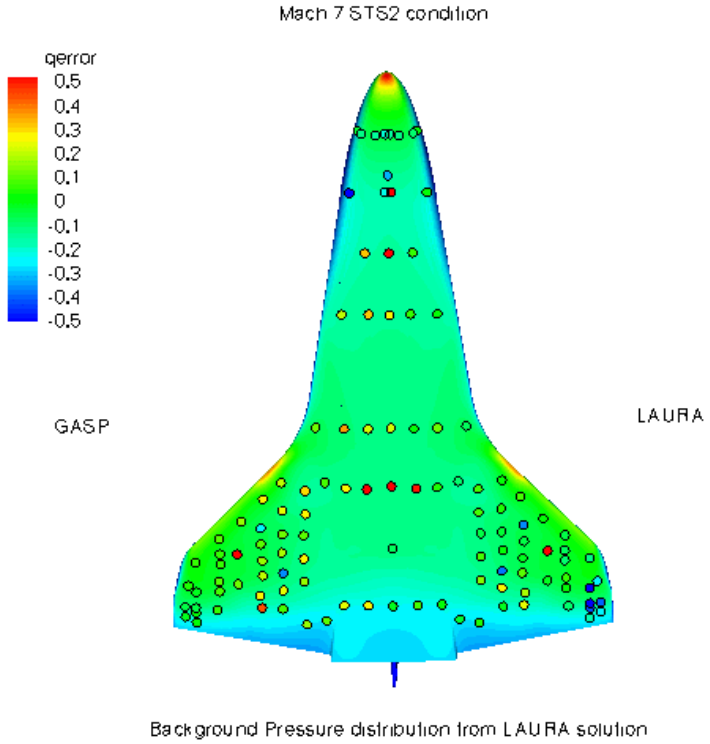

Figure 5.2.4-22 Windward heating rate uncertainty at Mach 7 plotted over pressure contours q_{error} = $(q_{cfd} - q_{flight})/q_{flight}$.

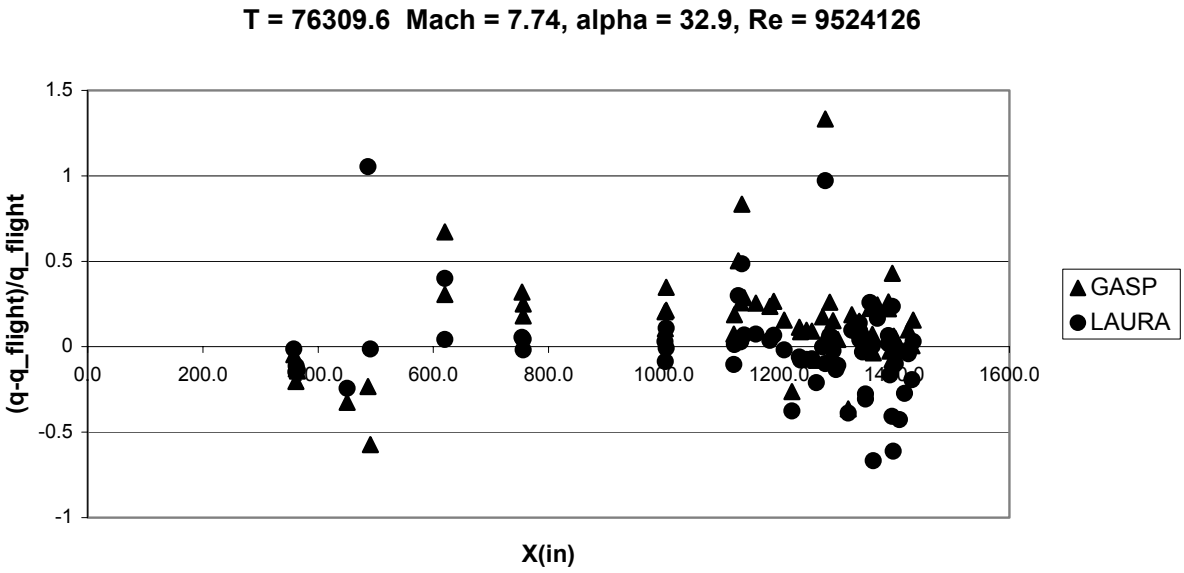

Figure 5.2.4-23 Heating rate uncertainty at Mach 7 as a function of axial distance along the orbiter

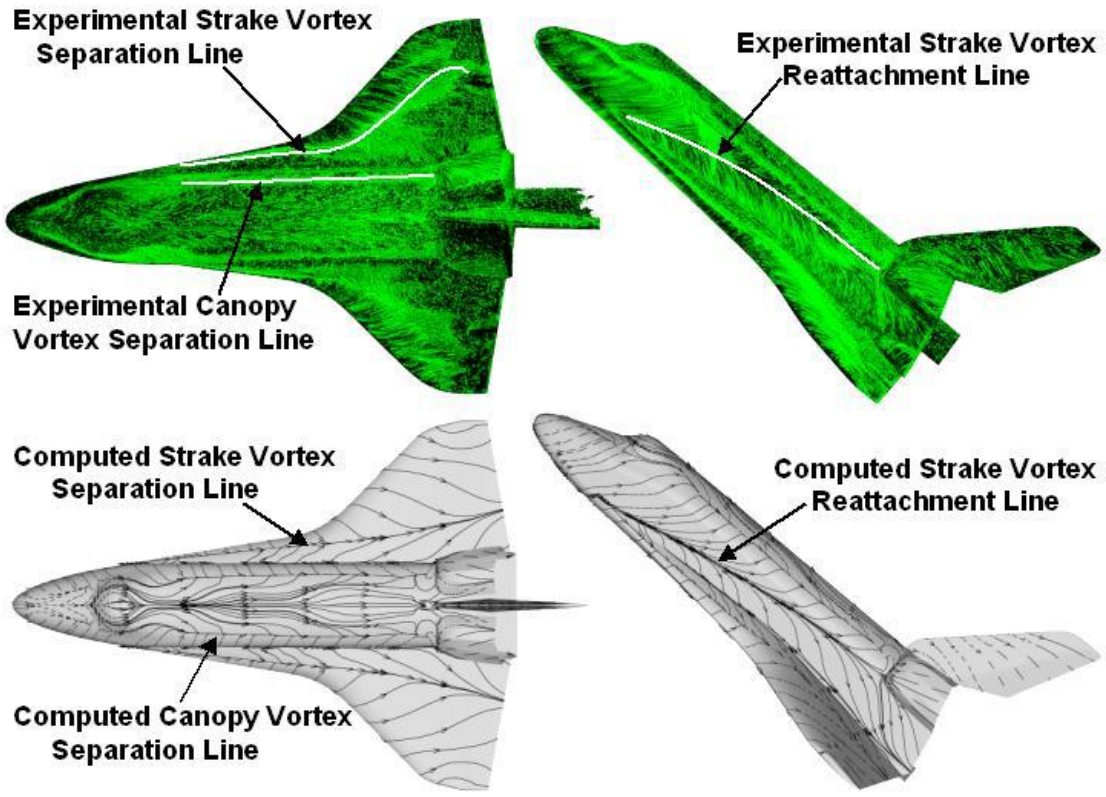

Figure 5.2.4-24 Comparison of Computed and Experimental Surface Streamlines on the Lee Side of the Baseline Orbiter in the CF_4 Wind Tunnel

5.2.4.4 Nominal Orbiter Configuration – Flight Environments

5.2.4.4.1 Introduction

The Orbiter re-entry environment exposes the vehicle to extreme high temperature gases, thus demanding as robust a thermal protection system as possible. The detailed physical features in the very complex Orbiter flow field during re-entry can be appreciated by examining high-fidelity CFD simulations calculated at the actual flight conditions. Thus, a need for understanding the details of local flow field features for the nominal Orbiter geometry led to the calculation of a suite of numerical solutions at STS-107-specific flight conditions. Details about the trajectory conditions identified to perform the simulations can be found in the Aerodynamics Section. The trajectory conditions cover the entire duration of the STS-107 entry trajectory, and as a whole provide a valuable database for the aero/aerothermal team. Because the Orbiter experiences conditions on re-entry that range from a very rarefied environment down to a fully continuum environment, the suite of nominal geometry solutions includes simulations appropriate to both regimes.

The external environment simulations along the STS-107 trajectory were performed by Boeing-Huntington Beach, NASA-ARC, NASA-JSC, NASA-LaRC and Sandia National Laboratories. The software tools used to perform these simulations included Navier-Stokes solvers (GASP, LAURA, SACCARA, USA) appropriate to the continuum regime, and DSMC software (DAC) appropriate to the rarefied regime. The database of solutions generated is provided in Table 5.2.4-4 , where the solutions obtained are listed by trajectory condition, grid basis, and software tool. The abbreviations for the entries correspond to 5-species chemical non-equilibrium using Reaction Cured Glass surface properties (Noneq), fully catalytic surface properties with 5-species non-equilibrium chemistry (FC), and equilibrium chemistry (Eq). The DAC solutions utilized a 6-species, non-equilibrium chemistry gas model, and a fully diffuse, non-catalytic surface with radiation equilibrium surface temperature boundary condition and an emissivity of 0.9. The Navier-Stokes simulations (GASP, LAURA, SACCARA and USA) all used laminar flow assumptions with a radiation equilibrium temperature boundary condition, and an emissivity of 0.9. Further details on the software tools can be found in the Appendices. As noted in the Grid Generation section, the initial nominal geometry grids mentioned in Table 5.2.4-4 were used to generate initial Navier-Stokes solutions immediately after the loss of Columbia. The common baseline grid was subsequently developed and was used to generate the additional solutions listed. The modified common baseline grid utilized for the SACCARA simulation used a grid system which had a resolution doubled in the streamwise and circumferential directions, and it encompassed only the front half of the Orbiter The DAC simulations utilized a surface definition already available at the time of the accident..

5.2.4.4.2 Description of the Nominal Orbiter Configuration Flow Field

Four of the flow field solutions shown in Table 5.2.4-4 were selected to present predicted surface pressure and thermal loads experienced by Columbia and to present the properties of the gas in close proximity to the Orbiter surface. The four solutions correspond to trajectory points with the following conditions:

CFD Point 1: EI+404 sec.; Mach = 24.9; Altitude = 243,000 ft; Alpha = 40°; Dyn. press. = 22.0 psf.
CFD Point 6: EI+921 sec.; Mach = 17.9; Altitude = 200,767 ft; Alpha = 40°; Dyn. press. = 83.5 psf.
DSMC Point A EI+197 sec.; Mach = 27.0; Altitude = 300,003 ft; Alpha = 40°; Dyn. press. = 1.6 psf.
DSMC Point AA EI+ 91 sec.; Mach = 25.1; Altitude = 350,274 ft; Alpha = 41°; Dyn. press. = 0.1 psf

Figure 5.2.4-25 presents the flow field Mach number distribution around the Orbiter as predicted by the LAURA code. Two views are shown – a pitch plane cut and a constant span cut through Panel 9. The first view shows that the bow shock is relatively close to the windward surface of the vehicle for the nominal 40-degree angle-of-attack re-entry. The second view shows that the distance between the Panel 9 wing leading edge surface and the shock is approximately 7 inches for a flight condition near Mach 25. Figure 5.2.4-26 and Figure 5.2.4-27 present the flow field number density distribution around the Orbiter for DSMC Points AA and A as predicted by the DAC code. The view shown is of the x-z plane down the centerline of the vehicle. Since the conditions of DSMC Points AA and A are more rarefied than the CFD points, the boundary layers shown in Figure 5.2.4-26 and Figure 5.2.4-27 merge with the shock layer,

creating a large compression region. This effect is more pronounced in Figure 5.2.4-26, with DSMC Point AA being the most rarefied.

Table 5.2.4-4 Nominal Geometry Hypersonic Orbiter Simulations at Flight Conditions

Trajectory Point		Common Baseline Grid			Modified Common Baseline Grid	Initial Grids	
	DAC	GASP	LAURA	USA	SACCARA	GASP	LAURA
AA	X	N/A	N/A	N/A		N/A	N/A
A	X	Noneq				Noneq & FC	Noneq
B		Noneq	Noneq	Eq		Noneq & FC	Noneq
1		Noneq	Noneq	Noneq & Eq		Noneq & FC	Noneq
2		Noneq				Noneq & FC	Noneq
3		Noneq	Noneq	Noneq & Eq		Noneq & FC	Noneq
4		Noneq				Noneq & FC	Noneq
5		Noneq				Noneq & FC	Noneq
6		Noneq				Noneq & FC	Noneq
VN					Eq		

Surface streamlines are presented in Figure 5.2.4-28 for the wing leading edge region at CFD point 1. An attachment line exists along the leading edge, which separates the flow that remains on the windward side from the flow that is swept over onto the leeward side of the vehicle. Note that the flow moves outboard along the attachment line. These streamlines provide an indication of where local disturbances on the surface will propagate downstream on the vehicle. Figure 5.2.4-29 through Figure 5.2.4-34 present the surface pressure distributions in the wing leading edge region for CFD Points 1 and 6 and DSMC Points AA and A, respectively. Absolute pressures in pounds per square foot (psf) are presented along with pressure coefficients. The pressure coefficient is defined as,

$$C_p = \frac{P_{local} - P_\infty}{\frac{1}{2}\rho_\infty V_\infty^2}$$

where P_{local} = local surface pressure, P_∞ = free stream atmospheric pressure, ρ_∞ = free stream atmospheric density, and V_∞ = relative velocity of vehicle. The pressure distributions for the CFD and DSMC flight conditions are very similar as depicted by the pressure coefficients. However, the wing leading edge peak pressure magnitudes change from ~0.001 psf at Mach 25.1 and 350,000 ft, ~0.01 psf at Mach 27.0 and 300,000 ft, ~35 psf at Mach 24.9 and 243,000 ft, and finally to ~140 psf at Mach 17.9 and 200,000 ft.

Figure 5.2.4-35 through Figure 5.2.4-40 present both the heat flux and Stanton number distributions on the wing leading edge region. The Stanton number is defined as,

$$St = \frac{q}{\rho_\infty V_\infty H_{total}}$$

where q = local heat flux, and H_{total} = total free stream enthalpy. The quantity $\rho_\infty V_\infty H_{total}$ is a measure of the total energy in the flow field and therefore the Stanton number provides an indication of how much of the total energy contained within the flow is transferred to the surface of the vehicle. Thus, a value of 1.0 for the Stanton number corresponds to complete energy accommodation to the surface. The results shown in Figure 5.2.4-35 Figure 5.2.4-36 , Figure 5.2.4-37 , and Figure 5.2.4-38 illustrate that the heating

distributions are very similar over the Mach 24.9 to 17.9 range, with the peak heat flux occurring along the attachment line of leading edge in the vicinity of RCC panels 8 and 9. Because the Orbiter GN&C attempts to guide the vehicle along a constant heat flux boundary between these Mach numbers, it should be expected that the peak heat flux remains fairly consistent in these illustrations. One additional observation is worthwhile. The Navier-Stokes results included here predict the magnitude of the peak heat flux in the region of leading edge panel 8 to be in the 38 to 40 Btu/ft^2-sec range. However, DeVenezia, et al. have shown that flight data typically indicate values of approximately 50 Btu/ft^2-sec for the same region. Clearly, the CFD results tend to under-predict the heating to this leading edge region of the vehicle. To date, no comprehensive Navier-Stokes calibration effort has ever been undertaken using the available Orbiter re-entry leading edge heating data.

However, an engineering code, XF0002, developed by Boeing and calibrated with Orbiter flight data can be used to predict peak heat fluxes to leading edge panel 9. The RCC panel 9 flight certified indicator in XF0002 is known as BP (Body Point) 5505. The XF0002 predicted heat flux and surface temperature histories are provided in Figure 5.2.4-41.

While the DSMC heating distributions at Mach 25.1 and Mach 27.0 are somewhat similar to those of the two CFD points, the area where the peak heat flux occurs along the attachment line of leading edge panels 8 and 9 is not as well defined, especially for DSMC Point AA. This lack of definition is due to the more diffuse nature of the flow under rarefied conditions. In addition, the significantly lower density at DSMC Points AA and A results in a peak wing leading edge heating rate of only about 2 Btu/ft^2-sec and 10 Btu/ft^2-sec, respectively. Note from Figure 5.2.4-35 and Figure 5.2.4-36 that the peak Stanton number for the continuum conditions is only 2 to 5%, while in Figure 5.2.4-38 and Figure 5.2.4-40 the peak Stanton number is approximately 25 to 50%. This is because at the rarefied high altitude conditions corresponding to DSMC Points AA and A, the flow is non-continuum. As a vehicle approaches completely rarefied conditions, where individual molecules do not interact, the Stanton number for a fully accommodated surface approaches 1 at the stagnation point. This rarefied flow effect is thus evident at the peak heating location on the wing leading edge, as illustrated in the DSMC heating figures.

Figure 5.2.4-42 presents radiation equilibrium surface temperature distributions for the wing leading edge region for CFD Points 1 and 6. The peak temperatures are along the leading edge attachment line and highest on Panels 8 and 9. As discussed previously, the peak temperatures predicted by the CFD codes are low and flight-calibrated values are presented in Figure 5.2.4-41. Figure 5.2.4-43 and Figure 5.2.4-44 show the radiation equilibrium surface temperature distribution for the wing leading edge region at DSMC Points AA and A. Note that no further discussion of the nominal geometry DSMC results will be included here, since the discussion to follow was important to the STS-107 investigation only for the continuum regime.

Another critical aspect of the flow environment experienced by the Orbiter during re-entry is the extreme gradients in flow field properties between the vehicle surface and the free stream. In order to illustrate these gradients, three locations in the leading edge (LE) region were selected to provide estimates of the local boundary-layer thickness, total enthalpy profiles, and static temperature profiles near the surface. Figure 5.2.4-45 provides a sketch describing the location of these three points – LE Panel 6, LE Panel 9 and Main Landing Gear Door forward outboard corner.

Figure 5.2.4-46 through Figure 5.2.4-51 provide predictions of the total enthalpy and static temperature variation of the gas near the surface of the Orbiter. These profiles for the CFD Point 1 flight condition, Mach 24.9 at an altitude of 243,000 feet, are provided in Figure 5.2.4-46 - Figure 5.2.4-48 for the locations shown in Figure 5.2.4-45 . On each of these plots the estimated boundary-layer thickness is noted. This estimate was obtained by locating the distance from the surface that the total enthalpy attains a value approximately 99% of the total free-stream value of 11,730 Btu/lb$_m$. For the 243,000 ft flight condition, the gas static temperatures are approximately 10,000 degrees Rankine at the boundary-layer edge. The thinnest boundary layer occurs at Panel 9. Figure 5.2.4-49 - Figure 5.2.4-51 provide the same information at the CFD Point 6 flight condition, Mach 17.9 and an altitude of 201,000 feet. For this flight condition, the boundary layer is considerably thinner at Panel 9 with a thickness of ~0.3 inches and the edge gas temperatures have decreased to about 7,000 degrees Rankine. This decrease in total enthalpy or total temperature corresponds to a decrease in kinetic energy of the Orbiter by approximately

40% between the conditions at CFD Point 1 and 6. Thus, roughly one-half the energy of the vehicle had been dissipated by the time Columbia reached LOS at about Mach 18.

Species concentration comparisons in the shock layer ahead of LE Panel 9 and the Orbiter nose stagnation point are provided in Figure 5.2.4-52 and Figure 5.2.4-53, respectively. These predictions were obtained from the LAURA solution at CFD Point 1. At the nose, the shock is approximately 2.5 inches from the surface and at Panel 9 it is about 7 inches from the surface. For both locations the oxygen is completely dissociated, thus only atomic oxygen is present in the shock layer. However, very near the surface some recombination occurs as the atomic oxygen mass fractions drop slightly. If the surface had been modeled as a fully catalytic surface instead of with the catalysis properties for the Reaction Cured Glass tile coating, full recombination of oxygen would have been predicted. For the nose shock layer, a significant amount of the nitrogen is dissociated with a peak atomic nitrogen mass fraction of about 0.38. This is in contrast to the Panel 9 shock layer, where the atomic nitrogen mass fraction is less than 0.1.

5.2.4.4.3 Orbiter Forebody CFD–Chin Panel / Vent Nozzle Cases

A focused set of simulations was conducted to investigate the anomalous chin panel and vent/dump nozzle instrumentation responses. See Section 5.2.1 for more information on the anomalous flight data characteristics. One theory to explain the increase in the temperature rise at the vent/dump nozzles is that an increase in sideslip angle moved the vortex at the wing body junction closer to the Orbiter fuselage, producing the increased heating. Thus, an effort to determine if the small changes in the angle of sideslip at those flight conditions could produce increased heating at the relevant vehicle OML locations was investigated. . In order to evaluate these anomalies, the common baseline grid of the nominal Orbiter was truncated at 50% of its length and additional grid, equivalent to what was removed by deleting the aft, was applied to the forebody. The resulting grid system had twice the resolution in the streamwise and circumferential directions compared with the baseline common mesh. The highly refined forebody grid were developed in order to provide the most accurate solution possible. In addition to flight simulations using the forward one-half of the Orbiter, a calibration was performed at wind tunnel conditions before attempting the flight simulations.

OH109 Orbiter Wind Tunnel Test Overview

Test OH109 was designed to investigate the effect of sideslip on heat transfer rate. The test was performed at Mach 8 for a range of Reynolds numbers and sideslip angles. A 0.04 scale thin-walled model of the shuttle was used in the experiment. The model was instrumented with thermocouples, and included thermocouples near the vent nozzles. These wind tunnel data provided a direct measurement of temperature rise rate near the vent nozzles and heat transfer data to benchmark the simulation tools.

The wind tunnel test measured the temperature rise rate on the surface of the model. The wind tunnel conditions were a Mach number of 8, side slip angle of –2.02°, -1.01°, -0.5°, 0.0°, angle of attack of 40.0, and a Reynolds number of $5x10^5$/ft. The flight vehicle was nominally at a Mach number of 24, angle of attack of 40°, a wind-corrected sideslip angle of 0.2°, and Reynolds number of $8x10^3$/ft when the instrumented vent nozzles recorded a doubling of the temperature rise rate. If the nominal temperature rise rate is measured at 0° sideslip, doubling the 0° sideslip temperature rise rate measured in the wind tunnel should produce a curve analogous to the off-nominal temperature rise rate observed in flight. In Figure 5.2.4-54 the white line near the wing-body junction is the vortex core location. Figure 5.2.4-55 shows the Orbiter forebody on the right and wind tunnel data comparisons on the left. The representative off-nominal curve shown in Figure 5.2.4-55 is the value the temperature rise rate would need to reach in order to match the increase observed in flight. The representative off-nominal curve is the dark line with no symbols. The arrow points to a line of thermocouples that are used for comparison in the image on the left. The red circles on the shuttle forebody are the location of the water dump, waste dump and vacuum nozzles. The plot on the left shows the temperature rise rate for sideslip angles from–2° to 0°. The wind tunnel data show only a moderate increase in temperature rise at a sideslip angle of –2°. The increase is approximately 20%, substantially less than the factor of two increase required to resemble the flight data. While the wind tunnel test did not match flight conditions and did not capture all the physical

phenomena that occurs in flight, the general data trend should be captured. Thus, the theory that the underlying cause of increased temperature rise rate is a sideslip effect is not supported by the available wind tunnel data. Even at an order of magnitude larger sideslip angle than the slip angle observed in flight, the increase in temperature rise rate from the wind tunnel data is only 20% of the flight observed increase.

Wind Tunnel Test OH109 Comparisons with Simulations

The experimental data taken in test OH109 provided an opportunity to benchmark the SACCARA prediction of heat transfer rates. A simulation was run on the truncated common baseline grid. The conditions computed matched the OH109 test: Mach number of 7.83, angle of attack of 40.04°, sideslip angle of -1.01°, Reynolds number of 4.938×10^5 and wall temperature of 505 °R. Figure 5.2.4-56 shows pressure contours along the centerline and the outflow boundary. Streamlines were placed near the wing-body junction vortex. Also, comparisons with the experimental data were made with a normalized heat transfer coefficient using the following definitions:

TT = tunnel total temperature, °R
QDOT = heat transfer rate, BTU/ft^2-sec
TW = wall temperature, °R
H(TT) = QDOT/(TT-TW), BTU/ ft^2-sec-°R
H(REF) = heat transfer coefficient derived from a Fay and Riddell based equilibrium stagnation point heating

Figure 5.2.4-57 shows the computed normalized heat transfer coefficient on both the in-wind side and the out-of-wind side, where the simulation results are co-plotted with the experimentally measured in-wind heat transfer coefficient. The Y- data were extracted from the simulation in-wind side and the Y+ data were extracted from the out-of-wind side. The comparisons are shown along the line of thermocouples indicated by the arrow shown in the right hand image. The diamonds depicted on the Orbiter fuselage represent the experimental data locations shown in the figure.

As illustrated in Figure 5.2.4-57, the in-wind and out-of-wind results have the same trends with a maximum change of approximately 20% in heat transfer coefficient. The simulation predicts a higher heat transfer coefficient that the experimental data. However, in comparison with the wind tunnel data, the predictions provide a conservative estimate of the heating rate. The in-wind and out-of-wind results show only modest differences in the heat transfer coefficient for the sideslip angle considered. An on-going study is under way to quantify the grid independence of the simulations. In addition, the experimental uncertainty in the OH109 data needs to be quantified before any conclusions can be drawn.

Simulation at flight conditions

One possible explanation for the flight observed temperature rise rate increase on the vent nozzles is that a gap or step located at the chin panel could have introduced a localized region of turbulent intermittency. The approach taken to examine this possible explanation was to run a simulation of the flight condition where the rise rate was observed, and to use the predicted surface quantities to determine where a disturbance would have to originate to affect the vent nozzles. Flight conditions for the simulation were selected based on the timesat which the vent nozzles were showing an increased rise rate, as in Section 5.1.2. The free stream conditions for this case use the VN (vent nozzle) identifier and are provided in the Aerodynamics section. Roughly, the conditions for the vent nozzle case are a Mach number of 24, altitude of 235,000 ft, with an angle of attack of approximately 40° and sideslip angle of -0.5°. The simulation was run on the same truncated common baseline grid used in the wind tunnel calibration study discussed above. Of particular interest in the flight simulation results is the behavior of the surface streamlines integrated from the surface shear stress vector. These streamlines should provide insight into the path a disturbance would follow. In Figure 5.2.4-58 , the water dump nozzle location and the vacuum vent location are indicated by the red circles, while the waste dump nozzle and thermocouple V07T9522A are shown in black. Figure 5.2.4-58 shows a number of streamlines on the Orbiter surface, along with colored contours of shear stress magnitude. The results show that the flight measurements are all located along the reattachment line. In relation to the attachment line, the vacuum nozzle is

located near its center, the waste dump nozzle is located below it, and the water dump nozzle and thermocouple are located above it. Figure 5.2.4-59 shows surface streamlines passing through the measurement locations for the vent/waste dump nozzle temperature instruments. The streamlines are tightly packed together until they reach the vacuum vent nozzle, where they begin diverging from one another. On the left of Figure 5.2.4-60 is an image of the front view, and on the right side is a close up of the nozzle. The front view shows that a disturbance in the chin panel region could propagate back to the nozzle locations. The close up of the nozzle locations shows that a disturbance could affect each nozzle differently, but with three streamlines passing the measurement locations, a clear case cannot be made. The simulation results do support the theory that a chin panel disturbance could have been the cause of the temperature rise rate. However, these results do not provide enough evidence to draw any conclusions. Since the temperature rise-rate returned to its nominal behavior after about 15 seconds of abnormality, it is very difficult to make any firm conclusions without additional data.

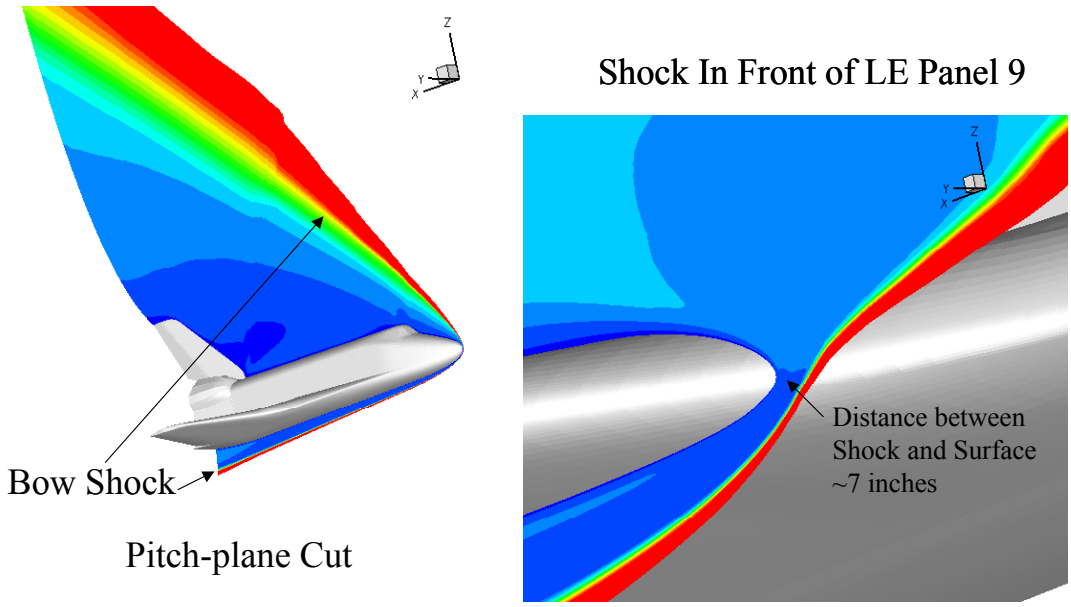

Figure 5.2.4-25 Shock Wave Structure around the undamaged Orbiter at CFD Point 1

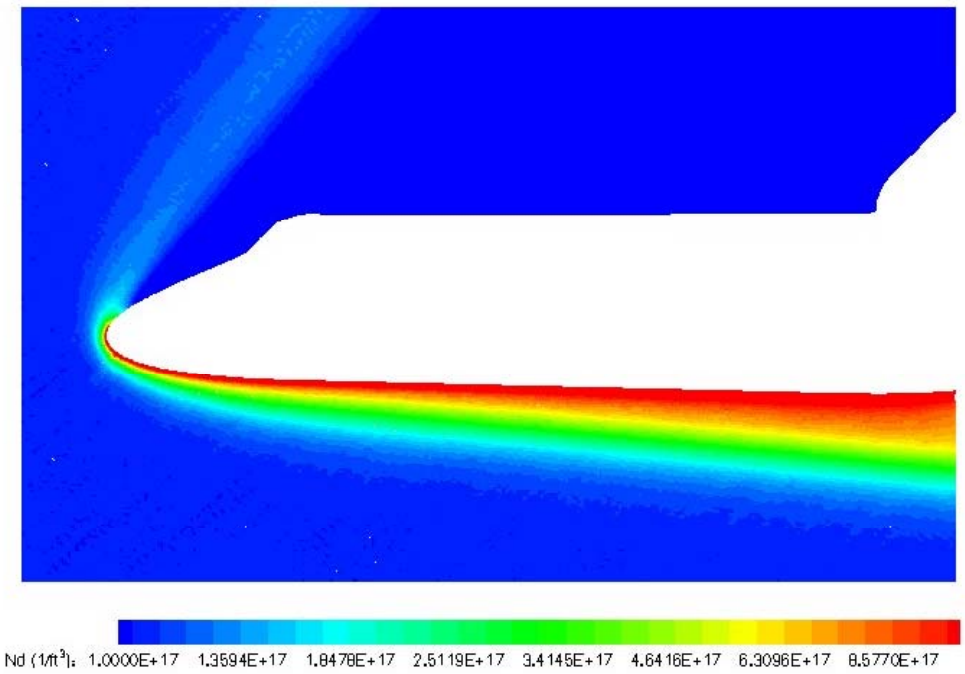

Figure 5.2.4-26 Number Density Distribution around Orbiter for DSMC Point AA

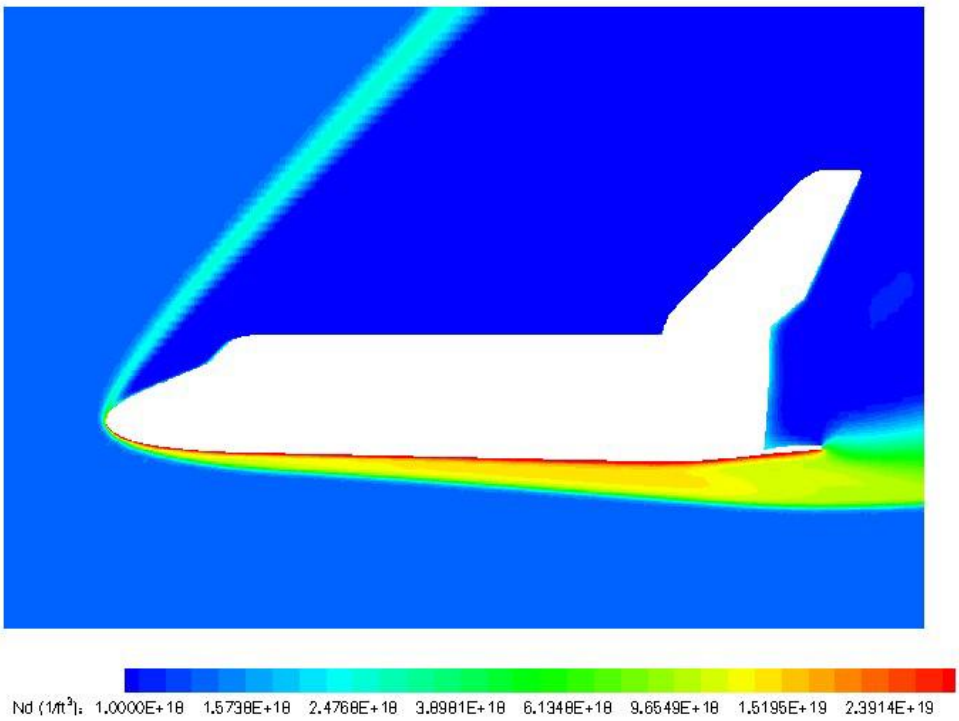

Figure 5.2.4-27 Number Density Distribution around Orbiter for DSMC Point A

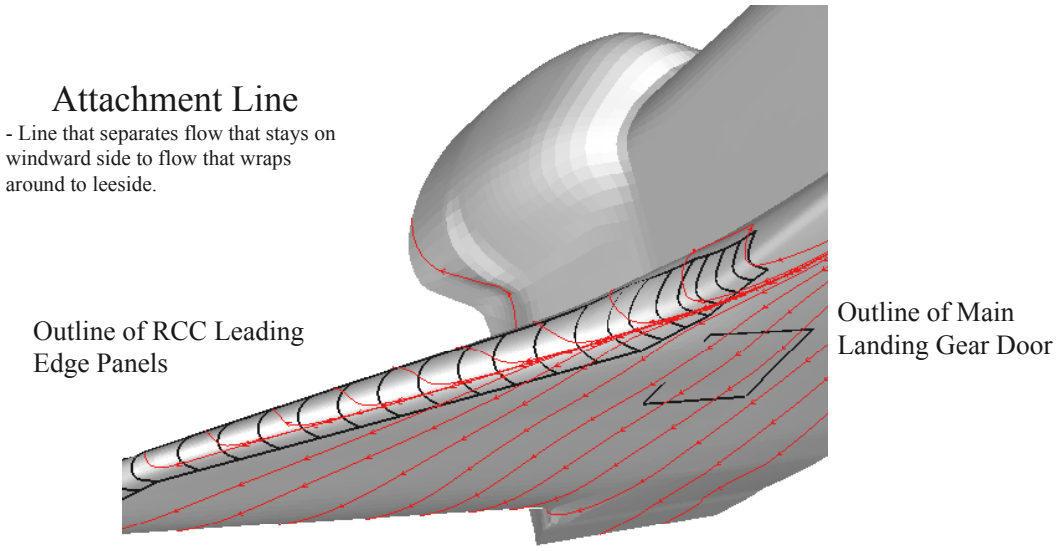

Figure 5.2.4-28 Surface Streamlines in the Wing Leading Edge Region

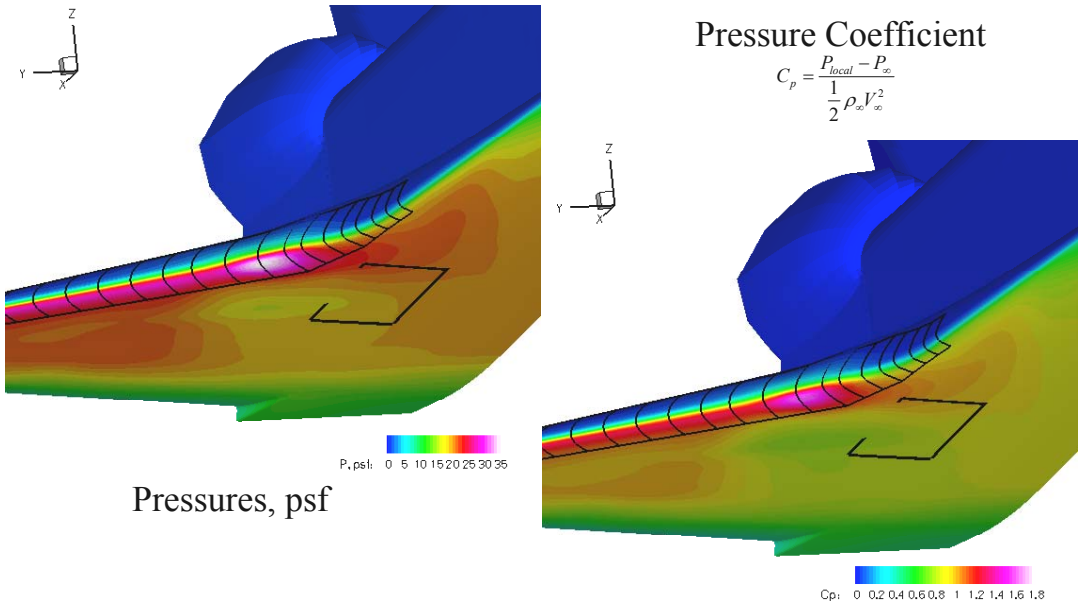

Figure 5.2.4-29 Surface Pressures for CFD Point 1, Mach 24.9

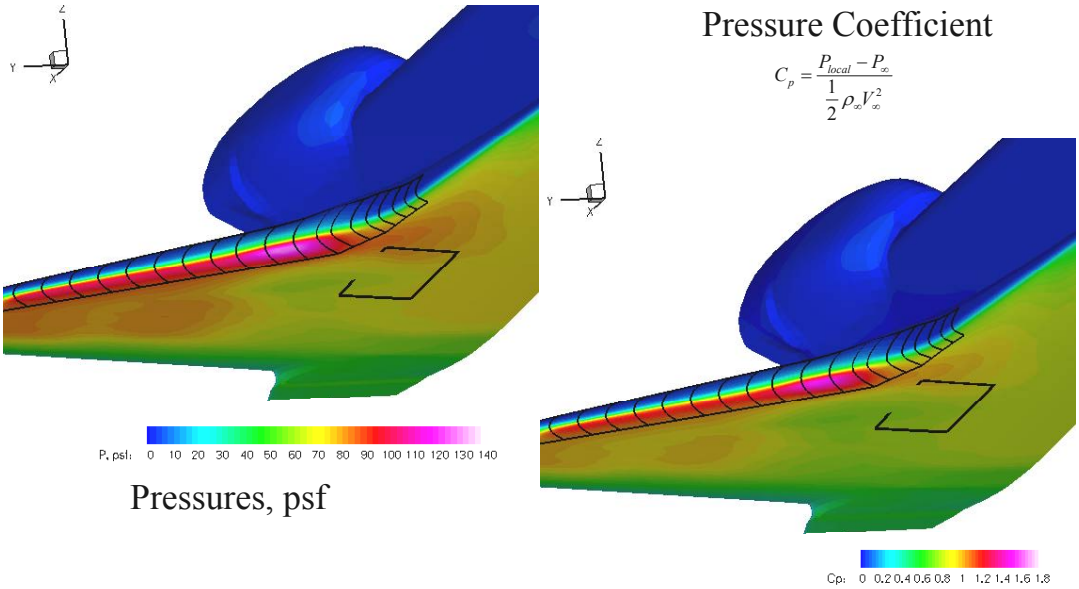

Figure 5.2.4-30 Surface Pressures for CFD Point 6, Mach 17.9

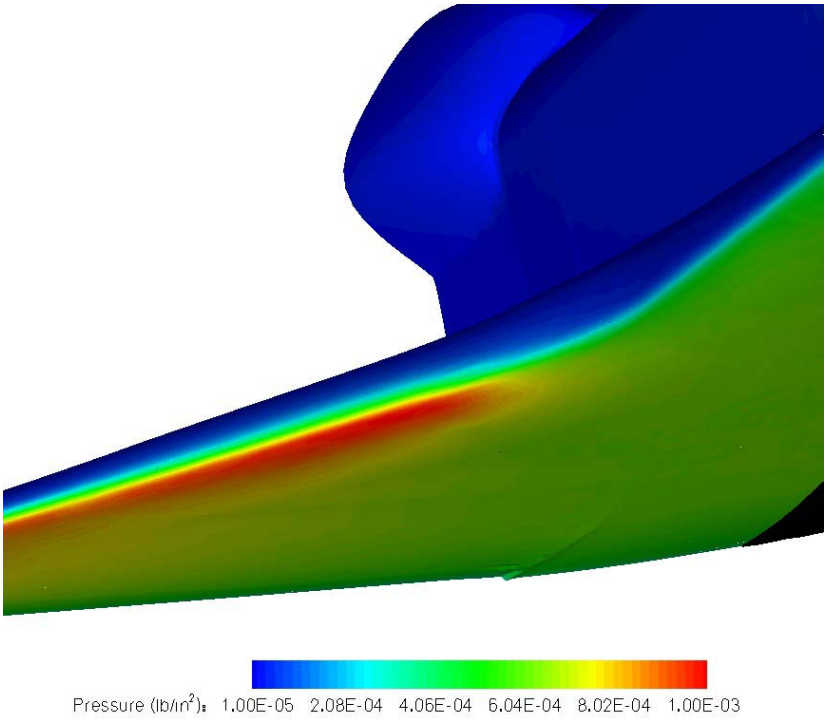

Figure 5.2.4-31 Surface Pressure for DSMC Point AA, Mach 25.1

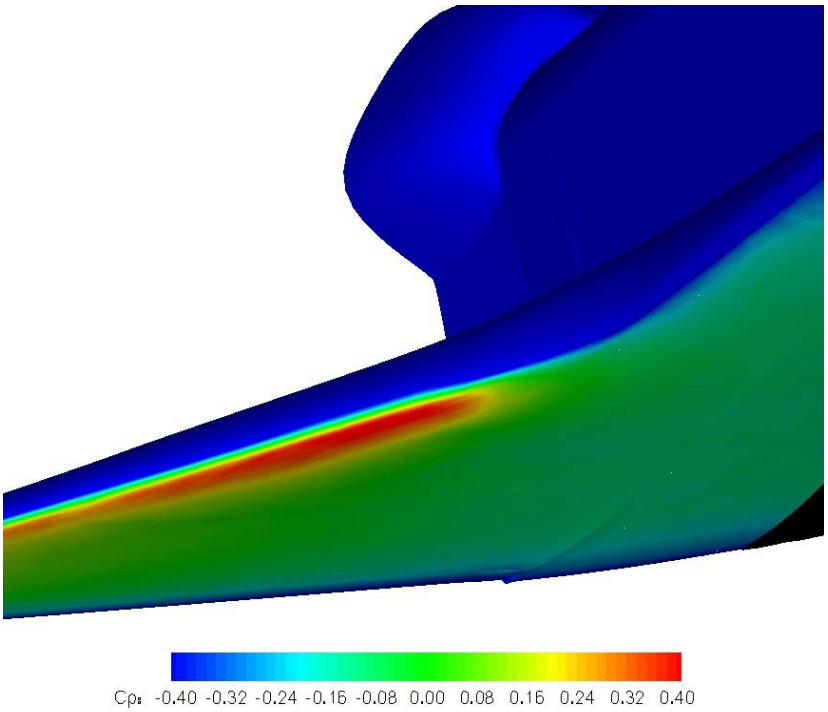

Figure 5.2.4-32 Surface Pressure Coefficient for DSMC Point AA, Mach 25.1

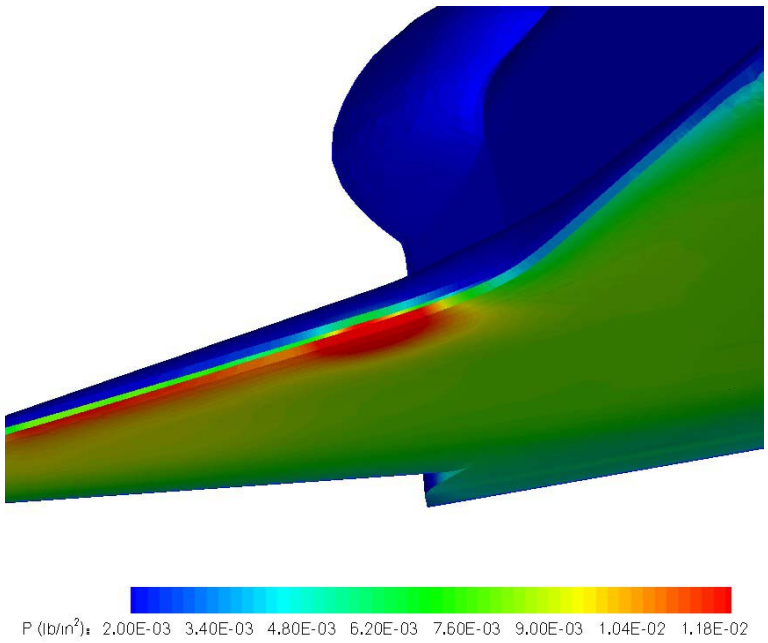

Figure 5.2.4-33 Surface Pressure for DSMC Point A, Mach 27.0

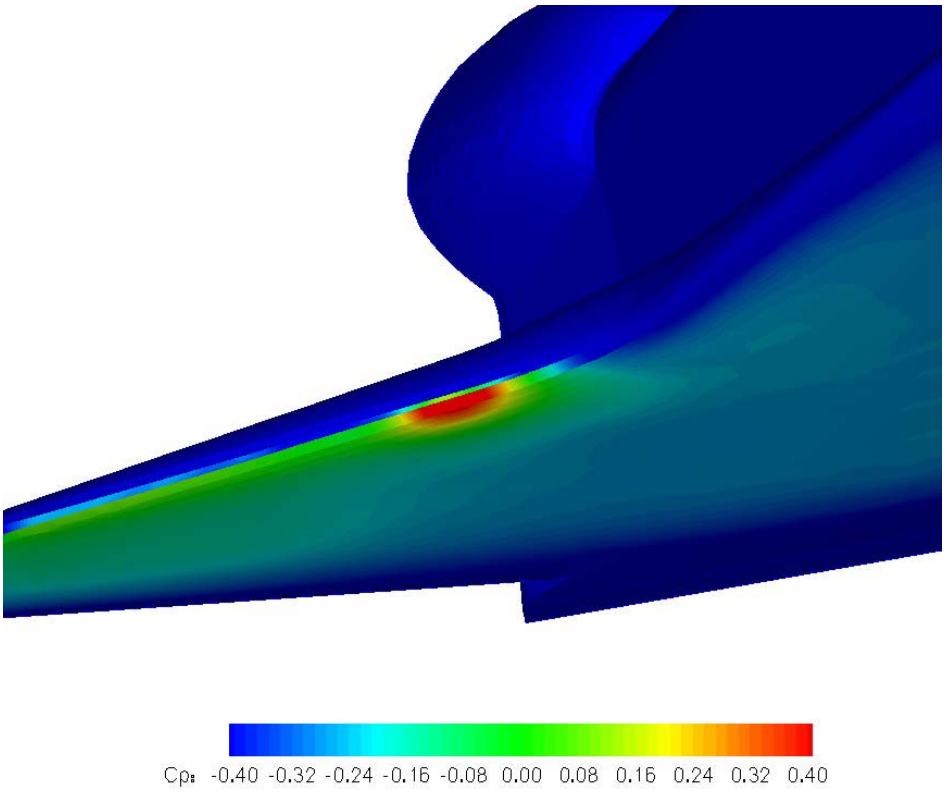

Figure 5.2.4-34 Surface Pressure Coefficient for DSMC Point A, Mach 27.0

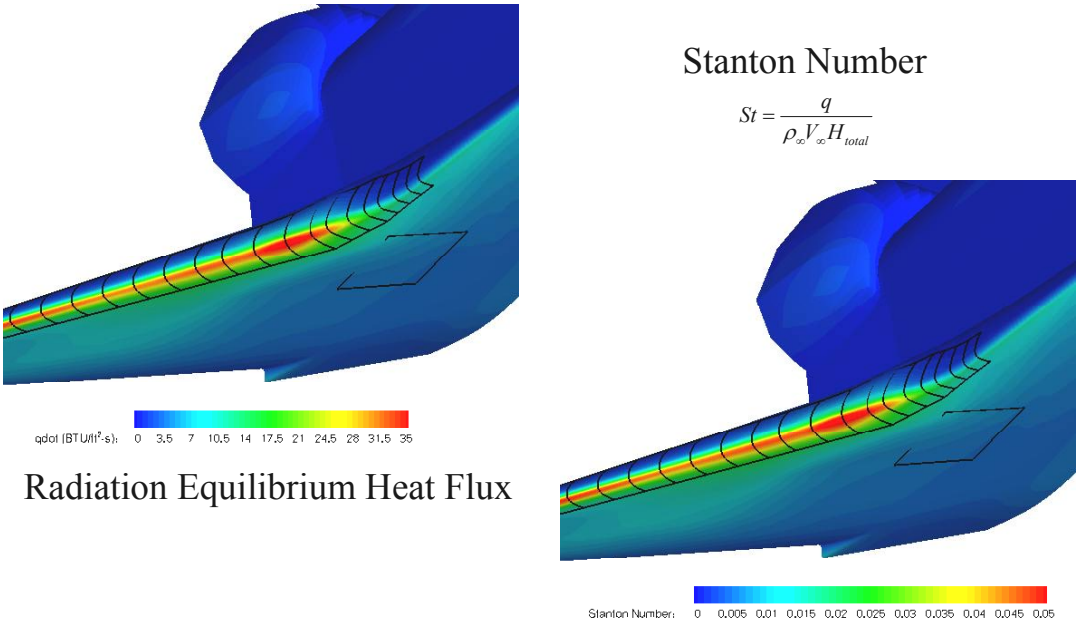

Figure 5.2.4-35 Surface Heat Flux Distributions for CFD Point 1, Mach 24.9

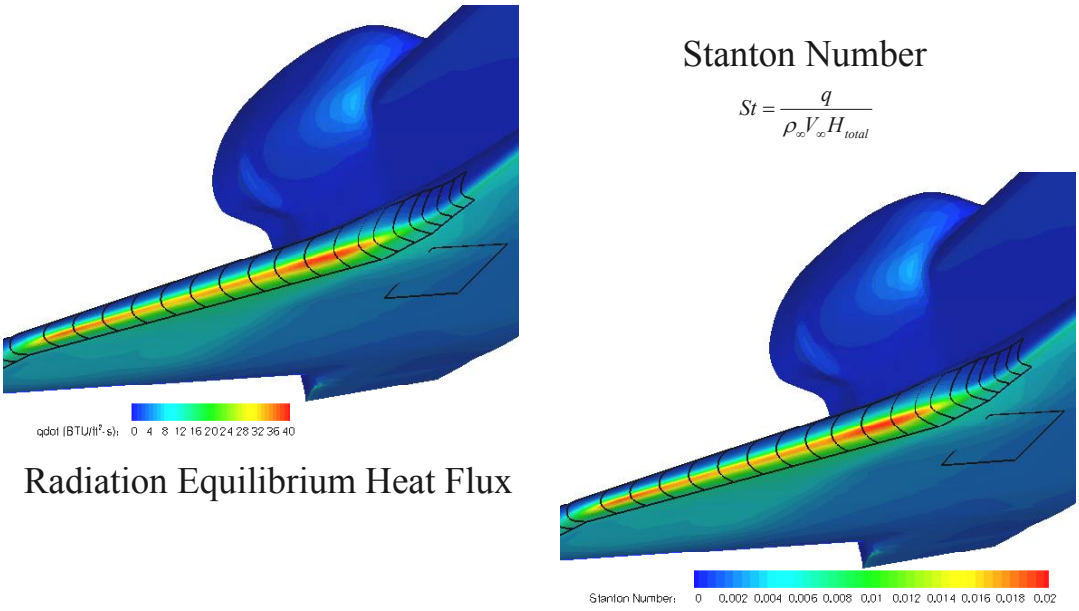

Figure 5.2.4-36 Surface Heat Flux Distributions for CFD Point 6, Mach 17.9

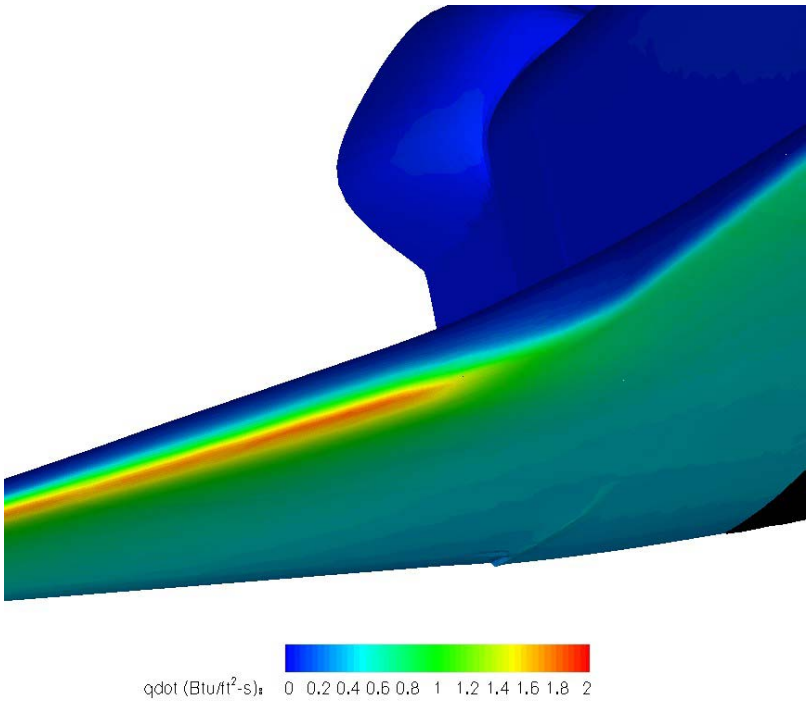

Figure 5.2.4-37 Surface Heat Flux Distribution for DSMC Point AA, Mach 25.1

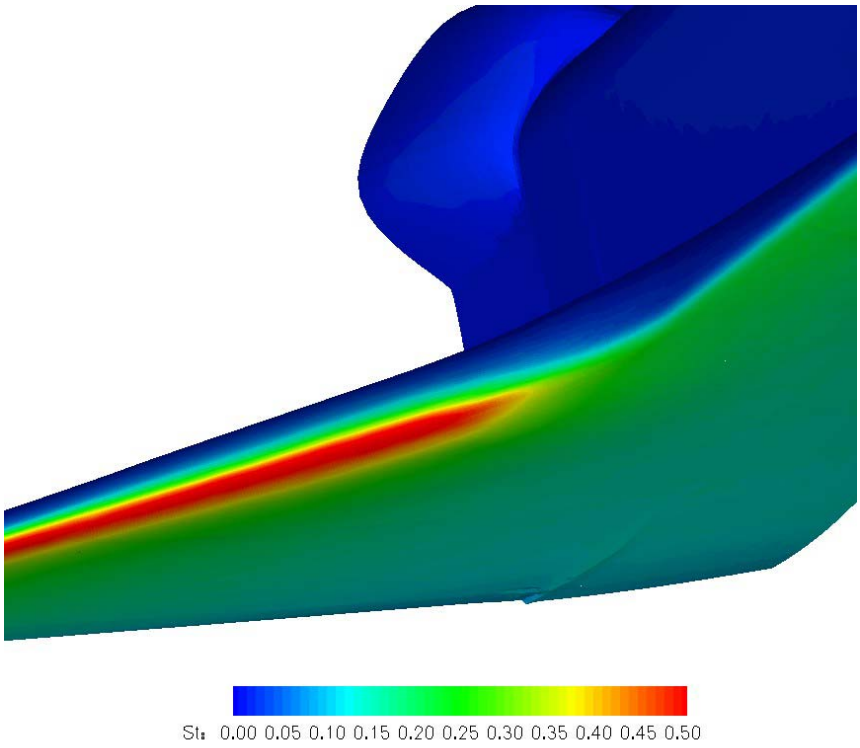

Figure 5.2.4-38 Stanton Number Distribution for DSMC Point AA, Mach 25.1

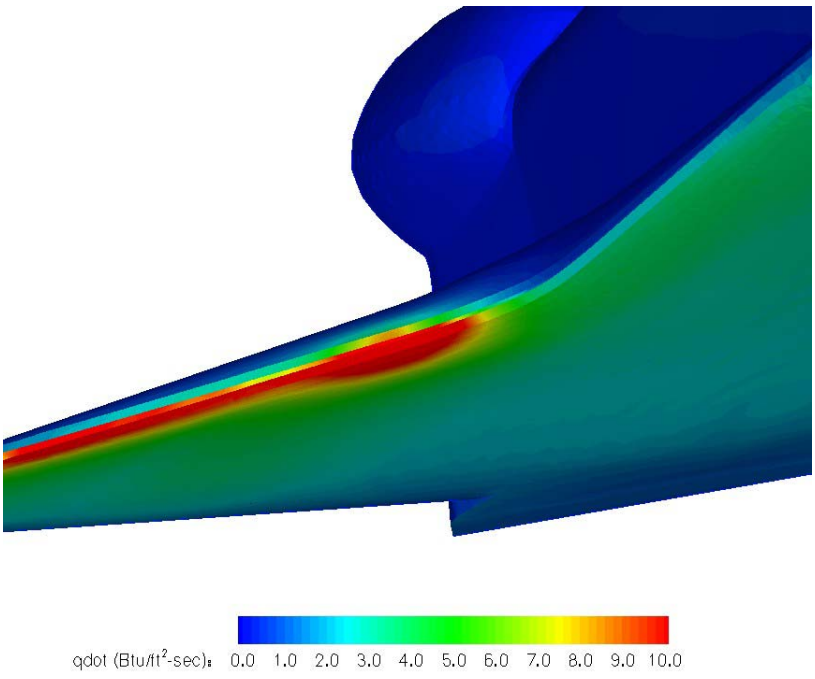

Figure 5.2.4-39 Surface Heat Flux Distribution for DSMC Point A, Mach 27.0

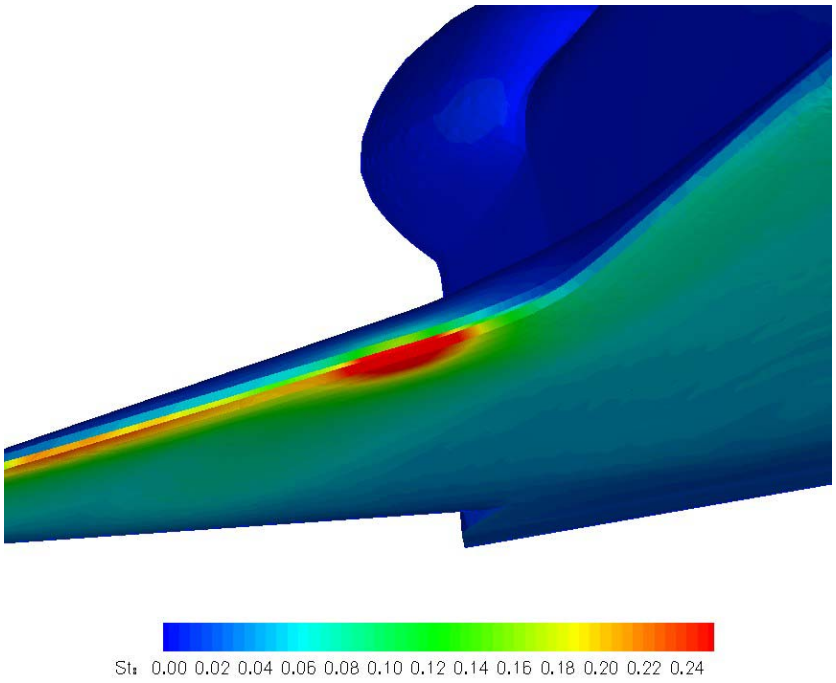

Figure 5.2.4-40 Stanton Number Distribution for DSMC Point A, Mach 27.0

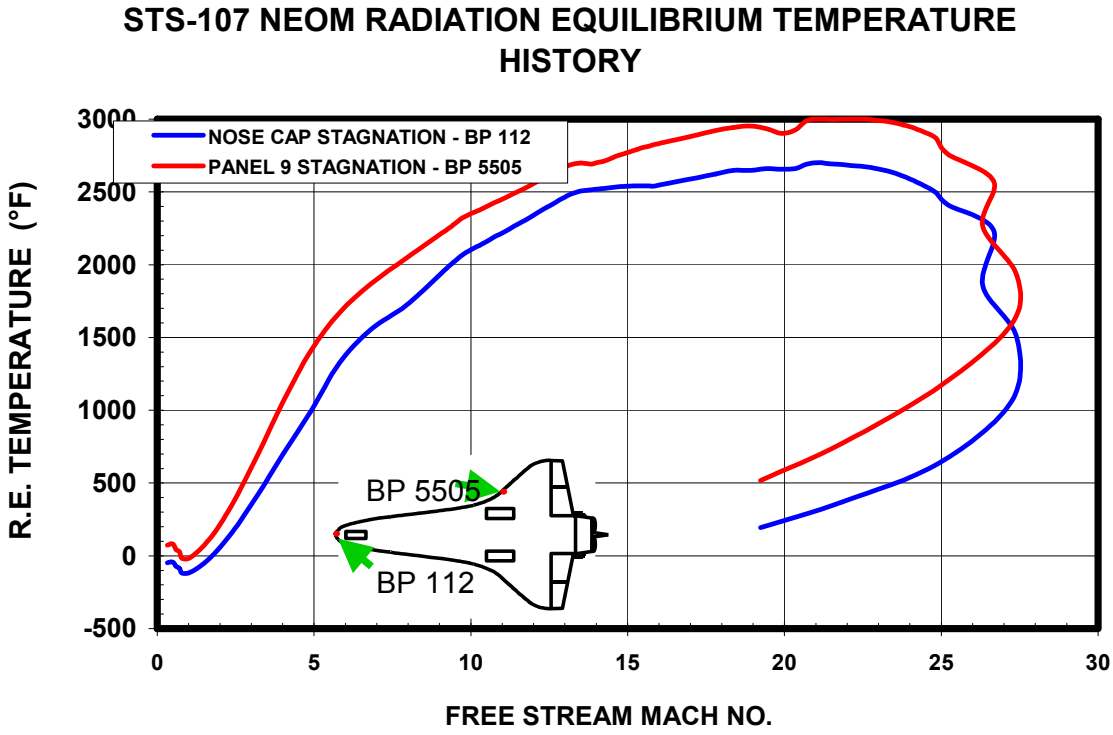

Figure 5.2.4-41 Flight Calibrated Estimate of Peak Heat Flux History on Panel 9

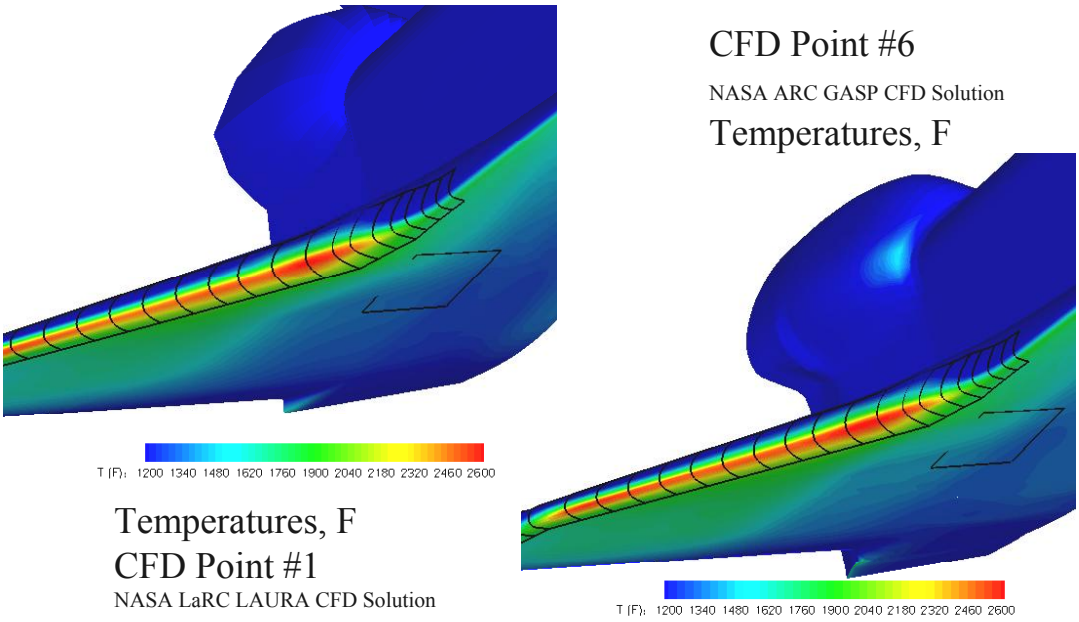

Figure 5.2.4-42 Radiation Equilibrium Surface Temperatures In the Wing Leading Edge Region

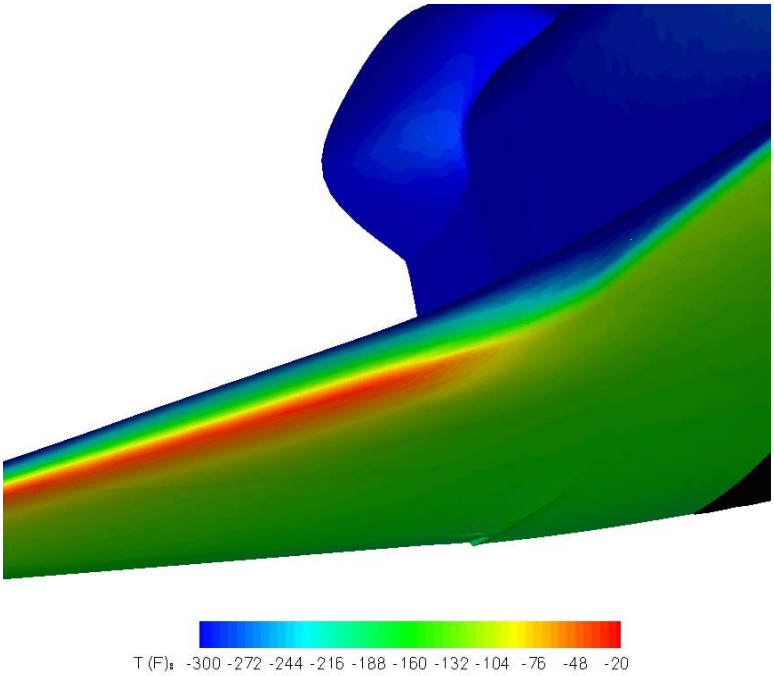

Figure 5.2.4-43 Radiation Equilibrium Surface Temperatures In the Wing Leading Edge Region for DSMC Point AA

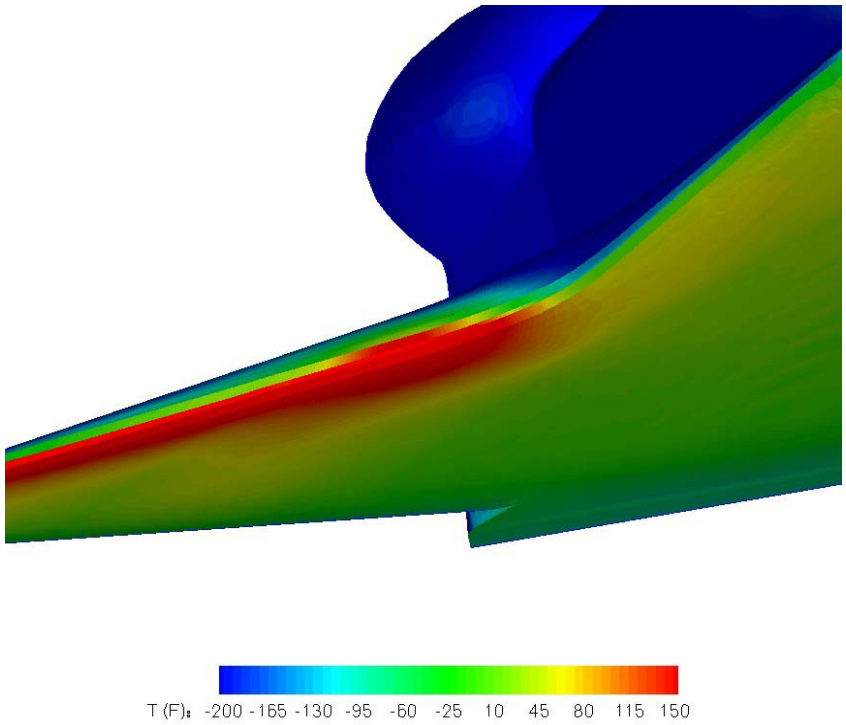

Figure 5.2.4-44 Radiation Equilibrium Surface Temperatures In the Wing Leading Edge Region for DSMC Point A

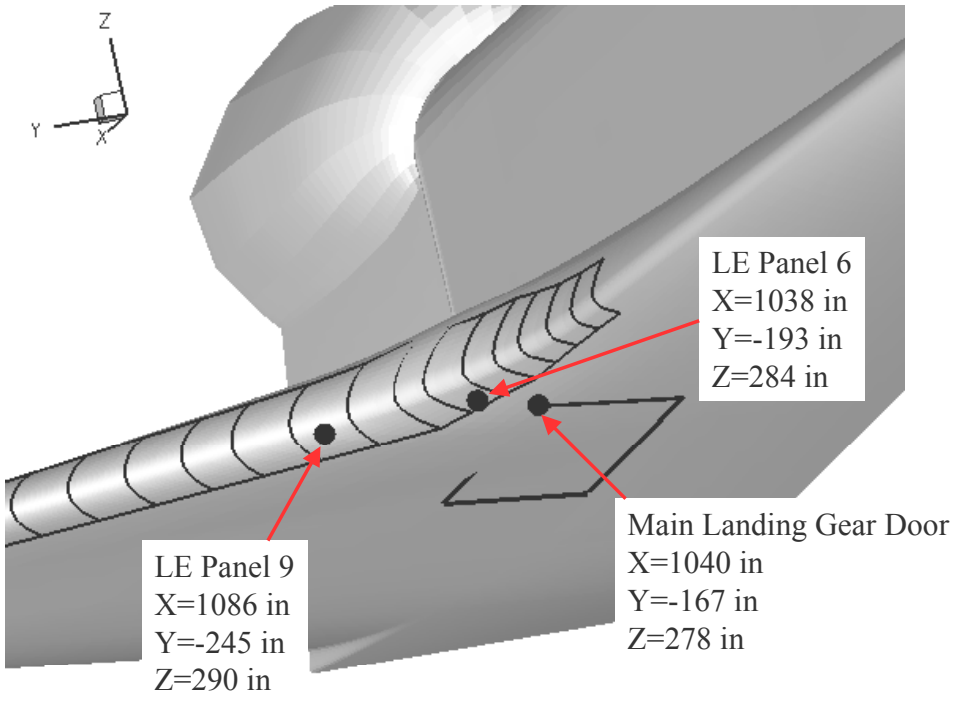

Figure 5.2.4-45 Boundary-layer Temperature and Enthalpy Profile Locations on Orbiter

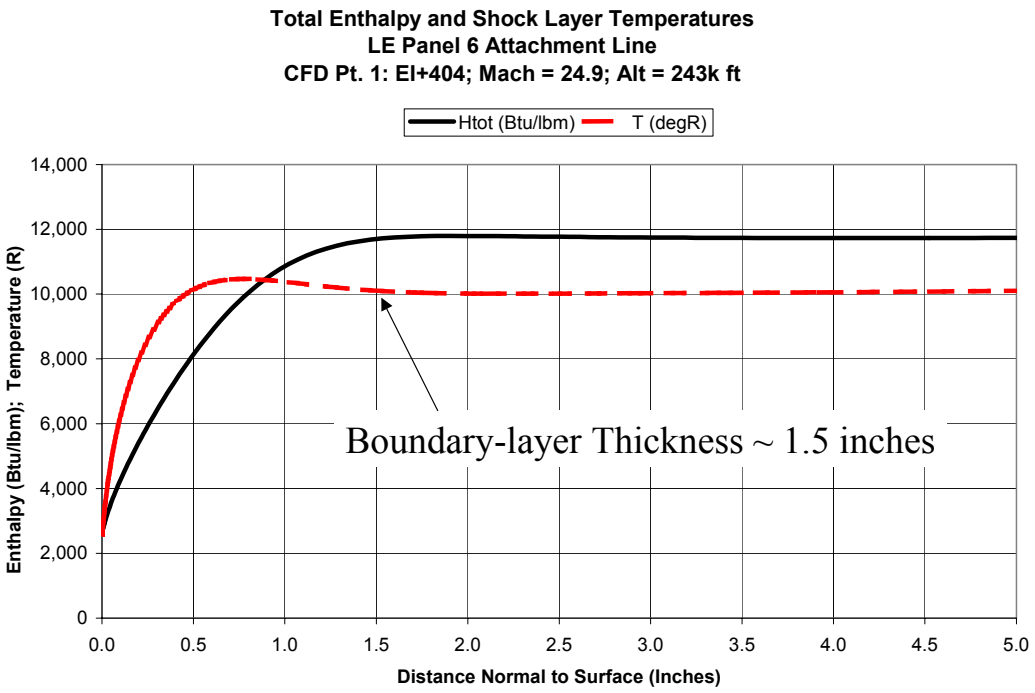

Figure 5.2.4-46 Total Enthalpy and Static Temperature Variation from LE Panel 6 Surface into Flow Field: CFD Point 1, Mach 24.9

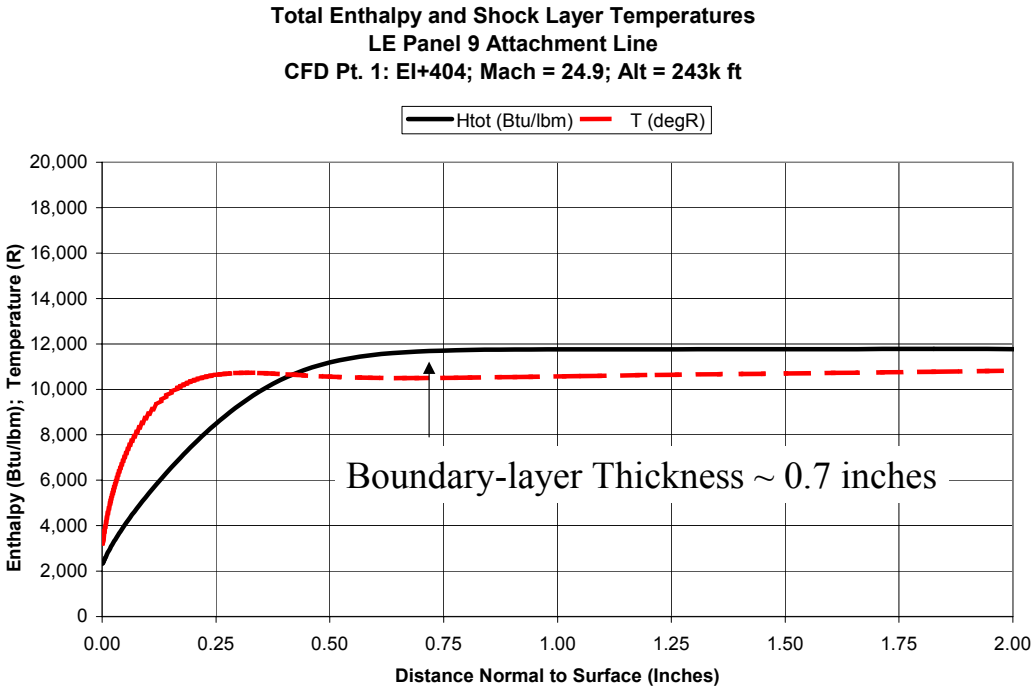

Figure 5.2.4-47 Total Enthalpy and Static Temperature Variation from LE Panel 9 Surface into Flow Field: CFD Point 1, Mach 24.9

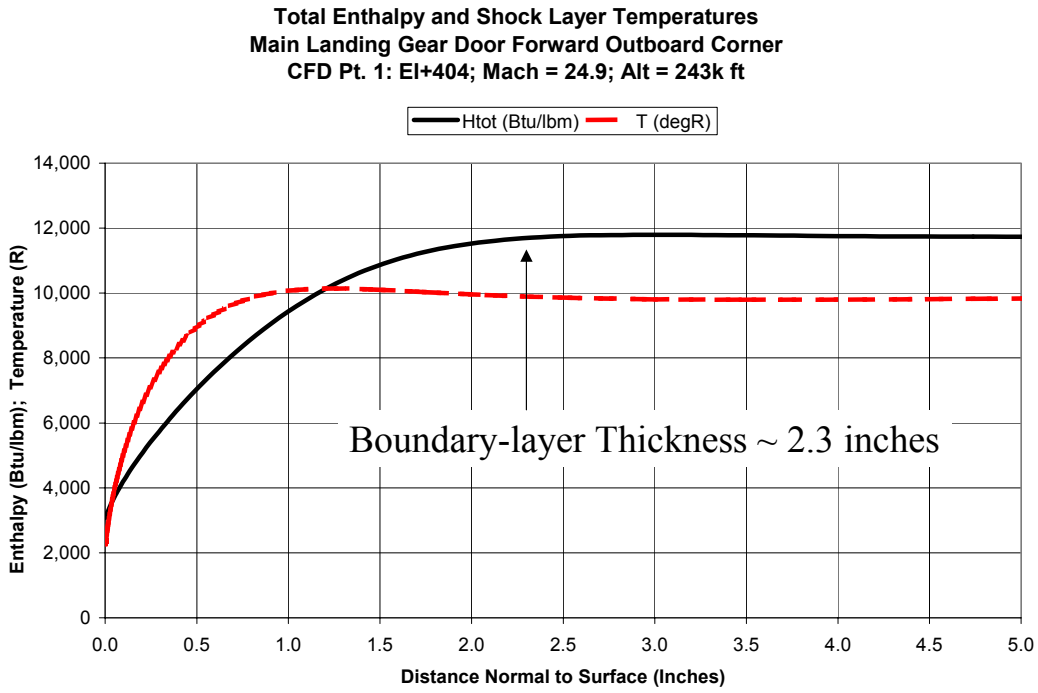

Figure 5.2.4-48 Total Enthalpy and Static Temperature Variation from Main LG Door Surface into Flow Field: CFD Point 1, Mach 24.9

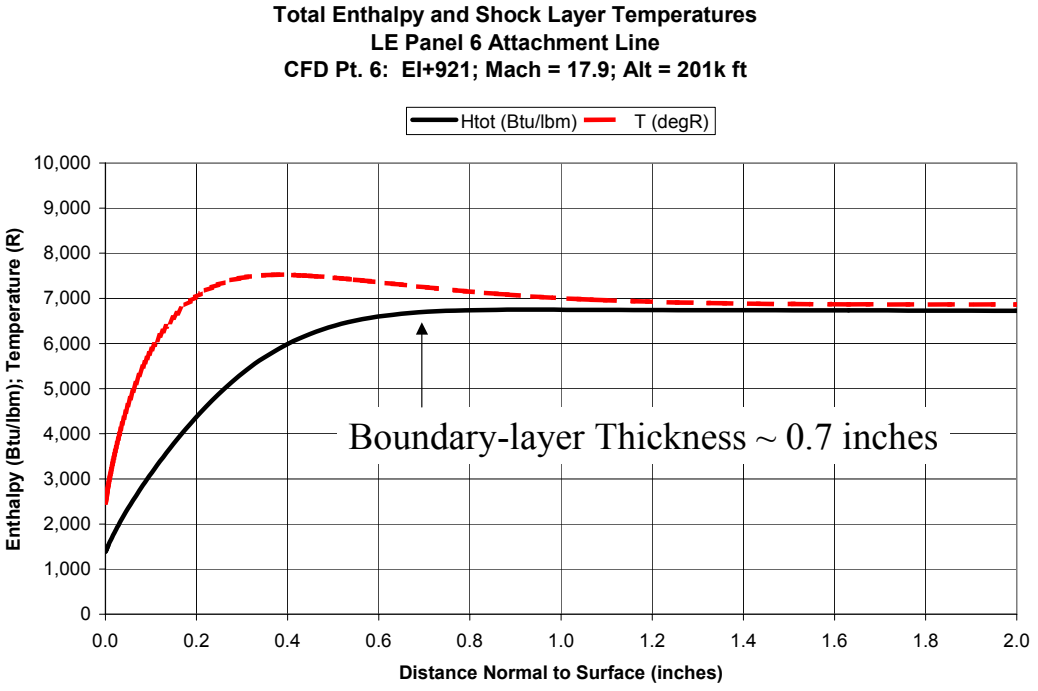

Figure 5.2.4-49 Total Enthalpy and Static Temperature Variation from LE Panel 6 Surface into Flow Field: CFD Point 6, Mach 17.9

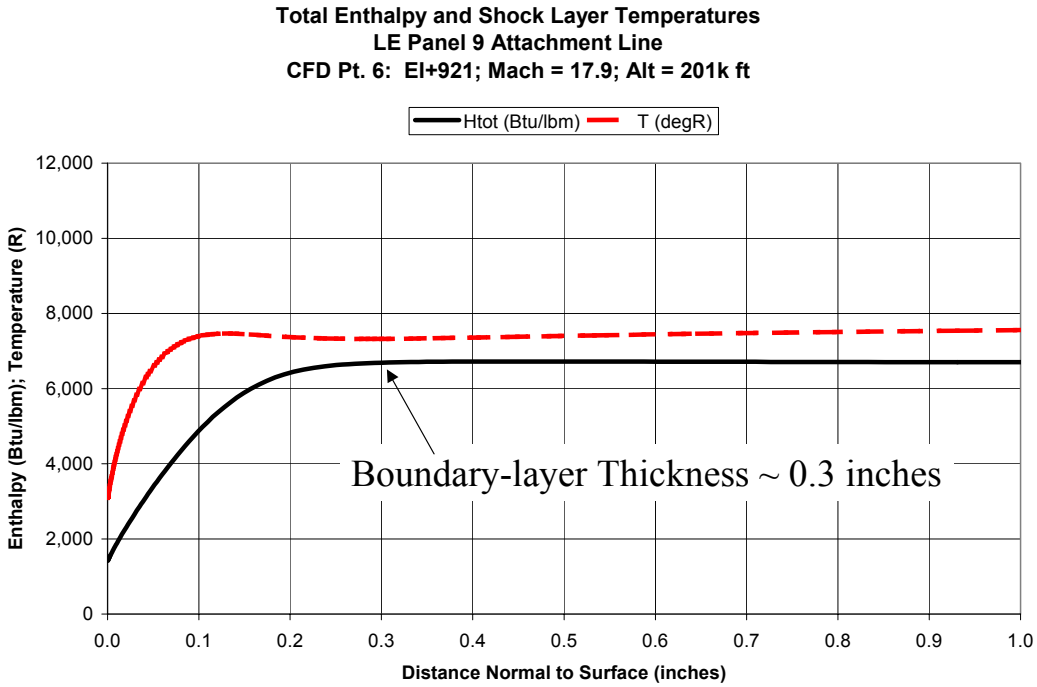

Figure 5.2.4-50 Total Enthalpy and Static Temperature Variation from LE Panel 9 Surface into Flow Field: CFD Point 6, Mach 17.9

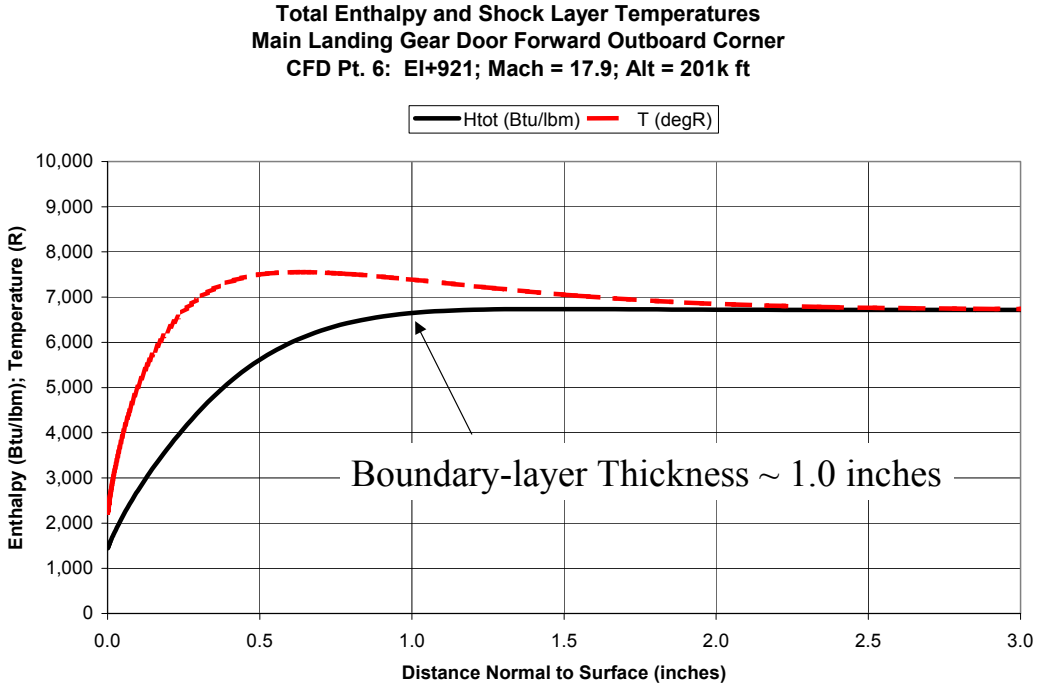

Figure 5.2.4-51 Total Enthalpy and Static Temperature Variation from Main LG Door Surface into Flow Field: CFD Point 6, Mach 17.9

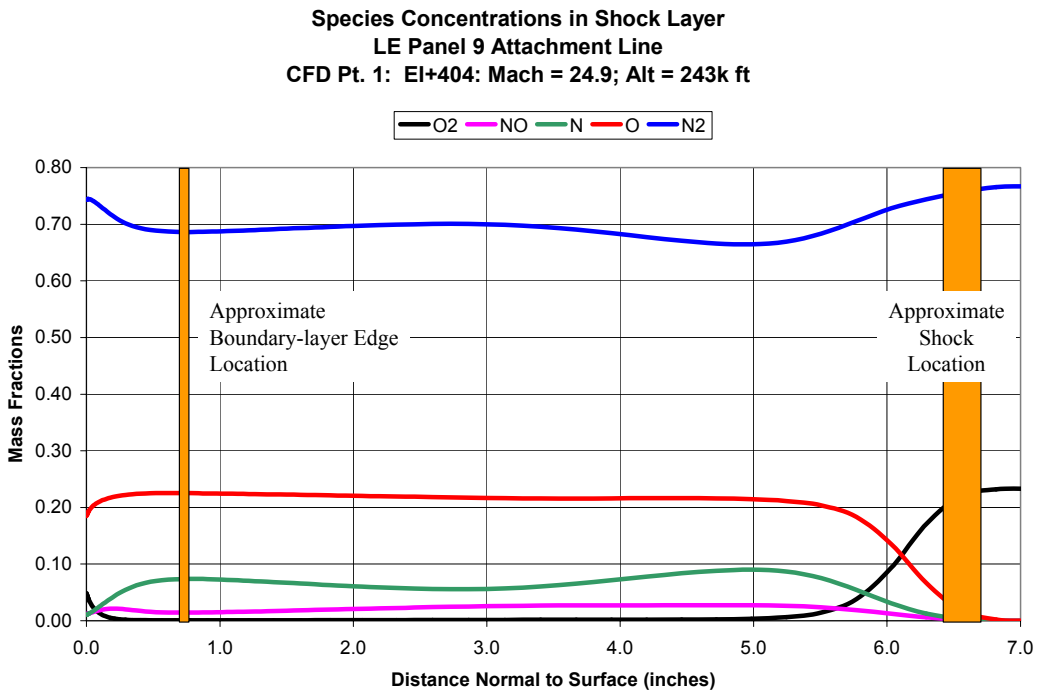

Figure 5.2.4-52 Predicted Species Mass Fractions in the LE Panel 9 Shock Layer: CFD Point 1, Mach 24.9

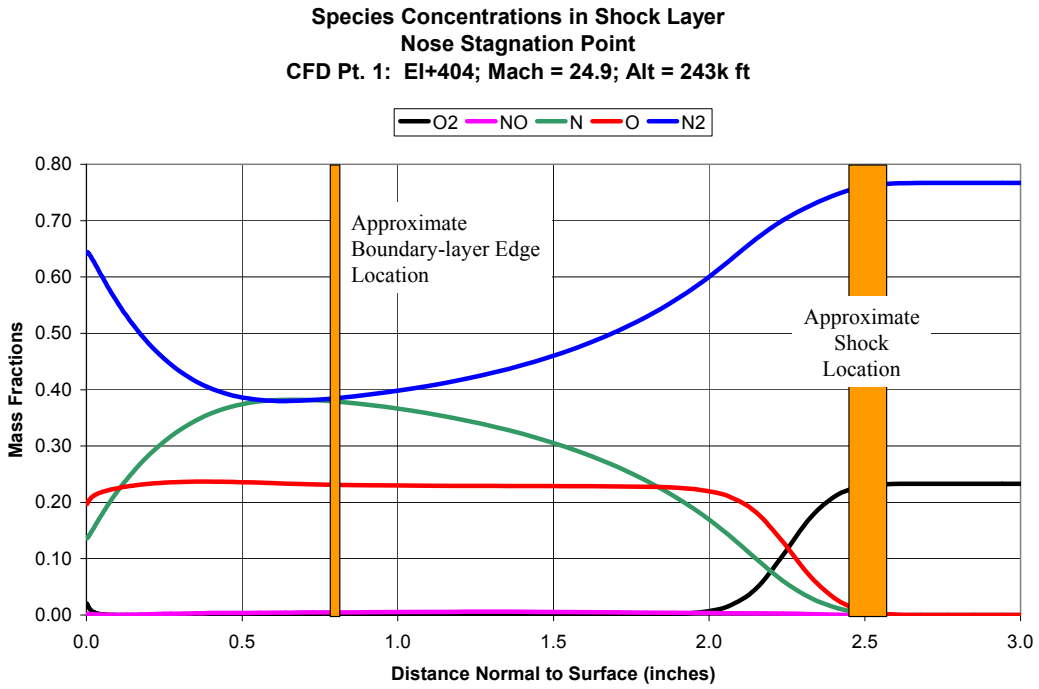

Figure 5.2.4-53 Predicted Species Mass Fractions in the Orbiter Nose Shock Layer: CFD Point 1, Mach 24.9

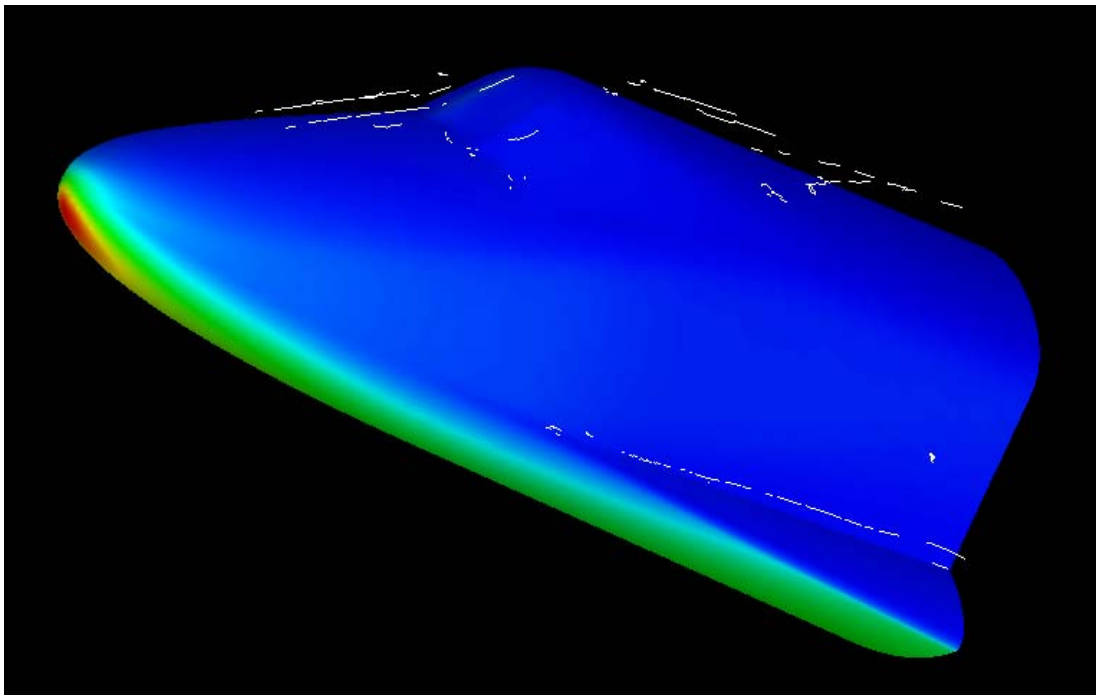

Figure 5.2.4-54 Pressure Contours and Vortex Location for wind tunnel conditions

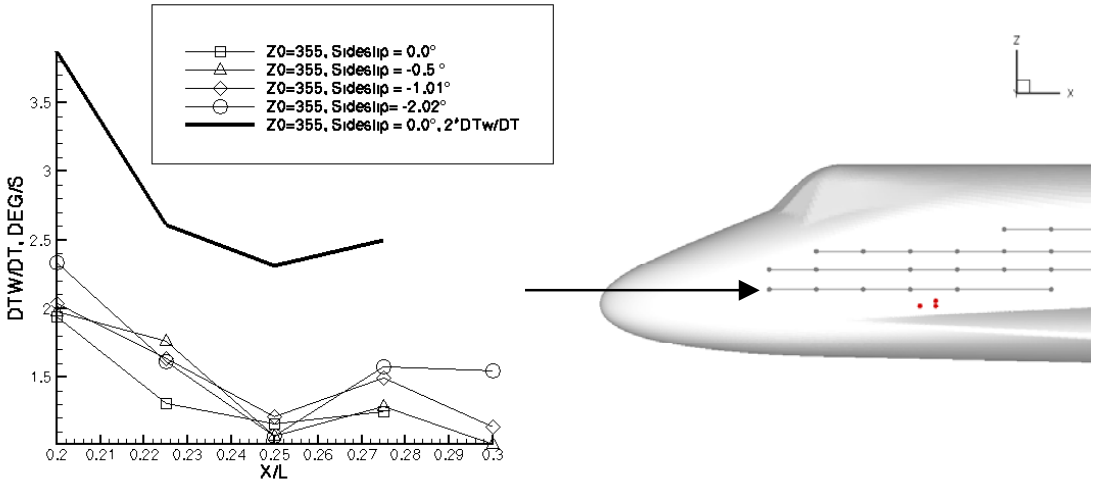

Figure 5.2.4-55 Wind Tunnel Measured Temperature Rise Rate

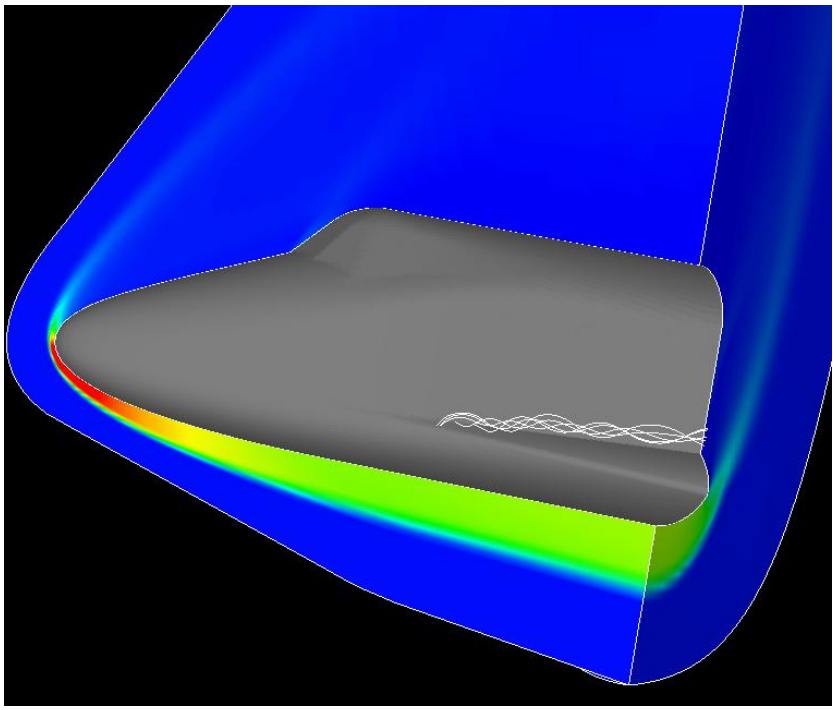

Figure 5.2.4-56 Pressure contour and vortex core location for wind tunnel conditions

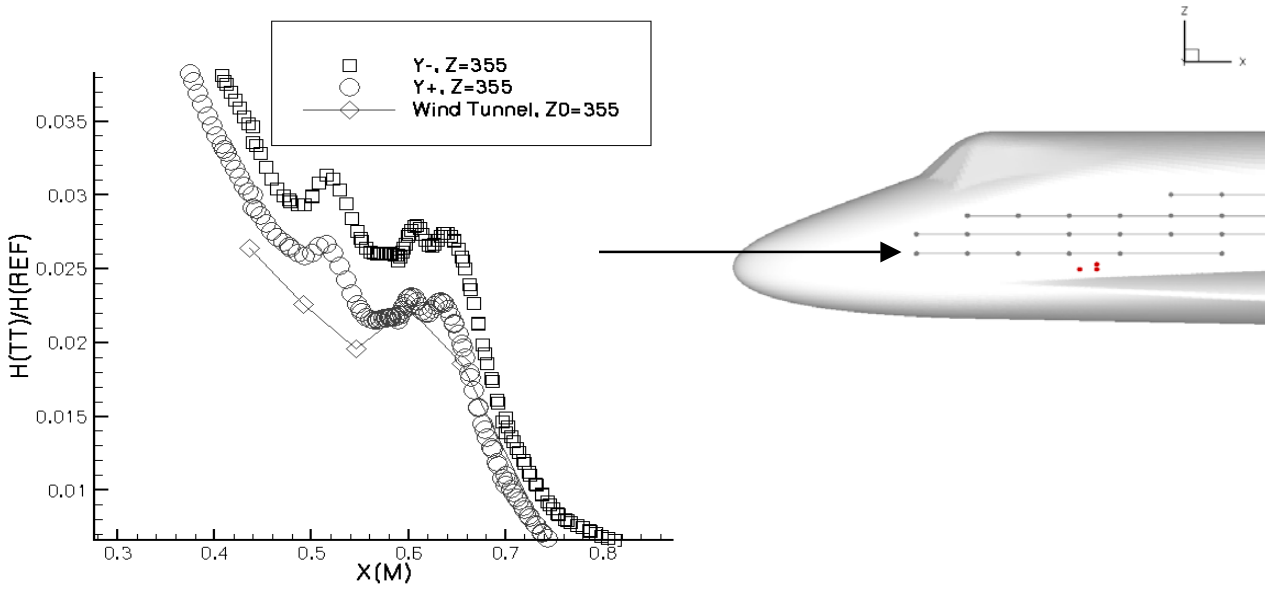

Figure 5.2.4-57 Comparisons with wind tunnel data

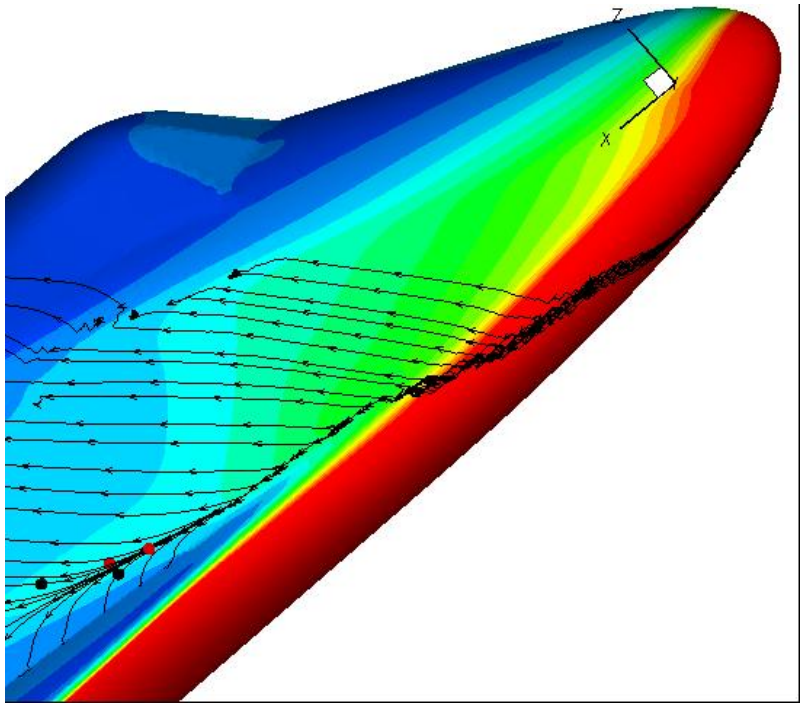

Figure 5.2.4-58 Shear stress contours and surface streamlines at flight conditions

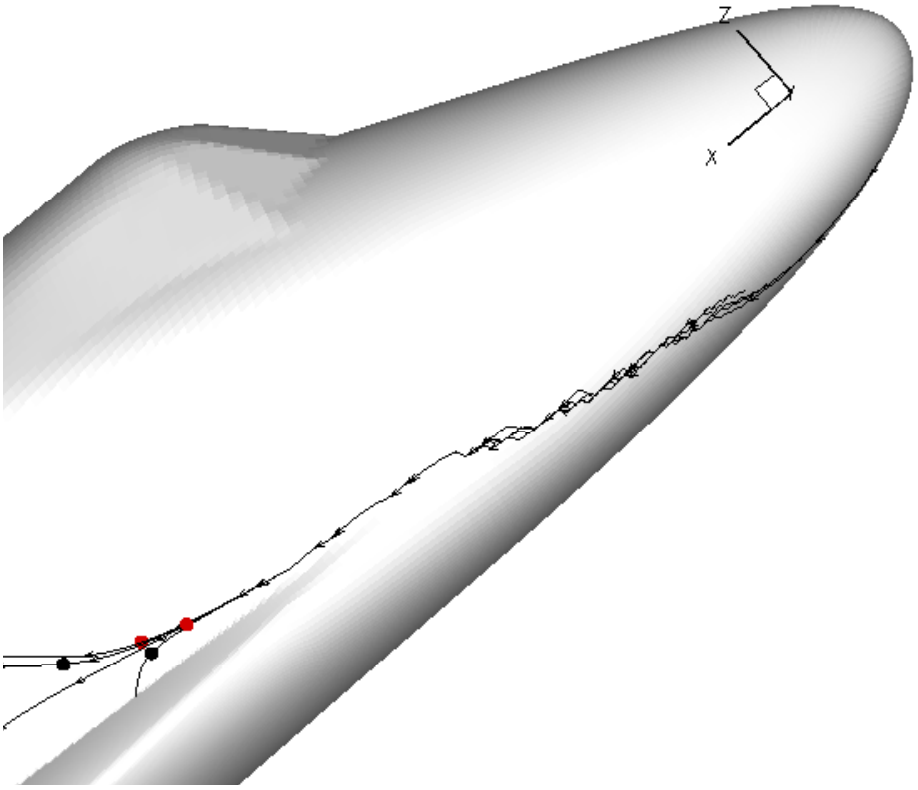

Figure 5.2.4-59 Nozzles and thermocouple streamlines at flight conditions

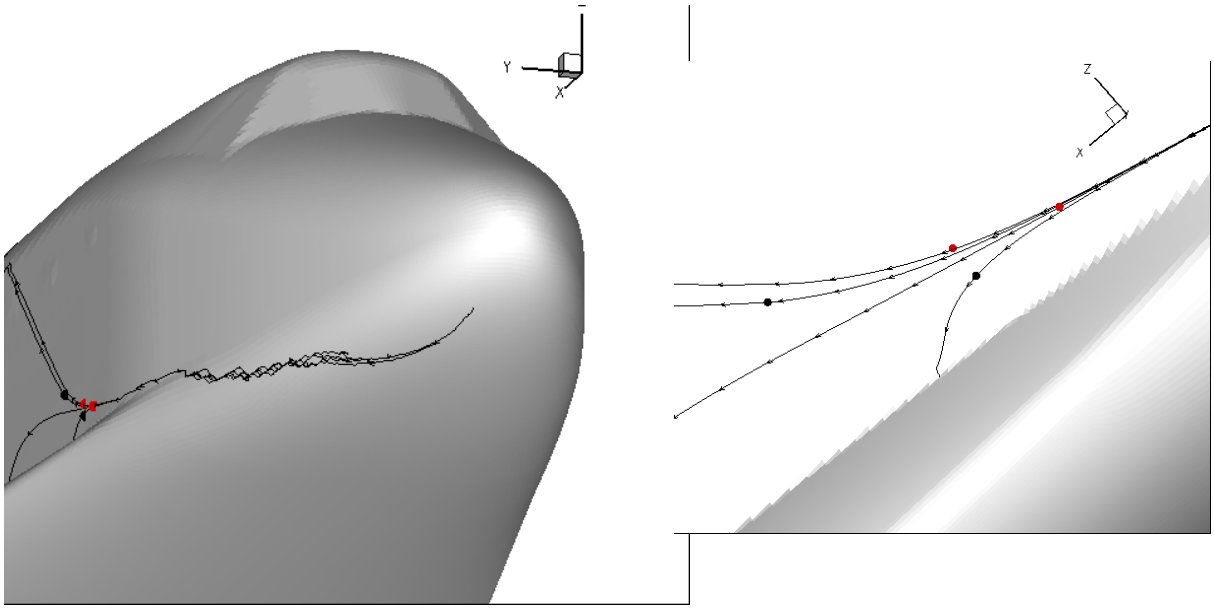

Figure 5.2.4-60 Front view and close-up of nozzles at flight conditions

5.2.4.5 *Damaged Orbiter Configurations Solutions*

5.2.4.5.1 Introduction

Computational aerothermodynamics was used to investigate the effects of damage to the Orbiter leading edge during Earth re-entry. The primary motivation in performing these RCC panel damage scenario CFD calculations was to gain a greater understanding of the detailed effects that various leading edge damage types and locations would have on overall vehicle dynamics and surface heating. Of particular interest in these CFD solutions was how the damage location and type would affect surface heating at the sensor locations on the side fuselage and OMS pod, where Columbia data were available. Another high priority aspect to be examined via the CFD solutions was the detailed off-body flow characteristics resulting from OML damage. Also, in order to aid the in the investigation of the delta aerodynamics (Section 4), these CFD solutions presented in this section were used to evaluate the damage effects on surface pressure and hence, on the integrated aerodynamic forces and moments. Obtaining a detailed understanding of RCC wing panel damage on the actual temperatures and heating for the wing spar, internal RCC channel insulation and other internal wing leading edge hardware was considered to be of secondary importance for these CFD computations. It is well understood that very small changes in damage topology or location will have very substantial effects on the actual heating values in the vicinity of the damage. The unknown nature of the actual STS-107 damage, combined with its likely rapid progression, makes quantitative internal cavity temperature and heating predictions virtually impossible. Furthermore, to attain even an engineering level of credibility on internal cavity heating, the cavity geometries would have to be more realistic and represent the actual internal wing leading edge hardware. Also, physically representative wall boundary conditions for the internal wing materials (emissivity and catalycity) and proper treatment of the internal radiative conditions would be necessary. Not only would these new kinds of boundary condition have to be implemented in our CFD codes, but they would have to be validated as well. Section 5.3 of this report focuses more on the interior heating details; thus this

section will not examine the physics or flow features within the cavities generated by removing RCC panels.

The studies described in this section were conducted at the start of peak heating where the external flow is characterized by high angle of attack, hypervelocity conditions: CFD case 1 condition (404 seconds from EI, free-stream Mach number = 24.83, angle of attack = 40.2 degrees, and altitude = 243,000 ft). Members of NASA-ARC Reacting Flow Environments (ASA) Branch and NASA-LaRC Aerothermodynamics Branch performed these computations using GASP (Appendix 5.6) and LAURA (Appendix 5.6), respectively. The entire flow field for these damage cases was assumed to be laminar and in a state of chemical nonequilibrium (5 reacting species), and in a state of thermal equilibrium. The boundary condition at all solid surfaces (both the OML and the internal cavity surfaces) used RCG catalysis assumptions developed by Stewart, radiative equilibrium, and an emissivity of 0.89. Complete details of the computational strategy and convergence acceptance and quality checking for both GASP and LAURA are provided in Appendix 5.6.

The damaged geometries considered in this work included an approximation of a complete missing panel 6 (herein referred to as the panel 6 “notch”), a fully removed and lower half removed panel 6, a lower half removed panel 9 with and without flow into the RCC channel, a complete missing panel 9 with and without flow into the RCC channel, and a lower half removed panel 9 with flow into the RCC channel and the upper carrier panel missing. These cases as well as the results observed from the computations are described more fully in the following sub-sections. A main point in considering the solutions below is that not all possible types of damage were explored nor were any thermal analyses performed to define in a precise way the actual damage experienced by STS-107. Rather the boundaries of a matrix of possible damage scenarios to the leading edge were explored. This matrix of damage solutions was used to establish the locations, extent and magnitude of associated temperature and heat flux anomalies that might credibly occur on the exterior surface of the Orbiter. Since special focus will later be placed on the effect that leading edge damage has on leeside heating of the fuselage side and the OMS pod, it is important to note the key parameters that appear to drive these effects: (1) the topology, size and location of any wind side wing leading edge damage, (2) the magnitude of venting into the interior wing, (3) the extent of venting to the lee side by hot gases within the RCC channel, and (4) the extent and nature of any breech that allows hot windside gases to pass directly to the leeward side of the vehicle. Thus, as mentioned in section 5.2.1.1, an engineering perspective is taken in the interpretation of these numerical results.

RCC Panel 6, Baseline Smooth OML Solution with Embedded-O Mesh (ARC)

The first in the series of GASP CFD computations for damaged RCC panel scenarios was that of the smooth OML panel 6 case. The computational mesh leaves both the upper and lower RCC half panels in place and therefore is simply another smooth OML solution. The main difference between this calculation at CFD condition 1 and the comparable GASP solution discussed in section 5.2.4.4.2 is the grid. The same forebody and aft body grids are used in the two GASP calculations, but the mid-body external grid for the current calculation uses an imbedded-O topology that focuses on the outer perimeter of RCC panel 6. Since this panel is left in place, the body surface face of the exterior H-grid that sits in the “eye” of the imbedded-O topology simply covers theRCC panel 6 OML. The calculation can be thought of as another comparison/validation case for the common baseline mesh solutions at CFD condition 1. Because of the use of the imbedded-O grid used in the earlier nominal GASP calculation (1.86 million for the current calculation, 1.06 million for the earlier nominal GASP calculation) its primary purpose here is to isolate possible solution problems related to the modified exterior grid or the complicated internal cavity grid. Also, when differences between the temperatures or heat fluxes of damaged and undamaged configurations are examined, the use of identical exterior meshes for both solutions greatly simplifies the differencing process.

Figure 5.2.4-68 and Figure 5.2.4-69 show side and top planform views of the normalized heating rates seen on the configuration for this nominal configuration case. These views shall be used repeatedly for all ARC-computed damage scenario CFD solutions presented later in this section. These images provide a viewpoint to understand changes in surface heating over regions of the vehicle where flight data were obtained during the STS-107 re-entry. The results of this computation are in very close agreement in

terms of temperature and heat flux compared with the corresponding solution obtained from the baseline common mesh discussed in section 5.2.4.4.2.

RCC Panel 6, Full "Notch" Out Solution with Solid Side Walls (LaRC)

For expediency in assessing the effects of leading edge damage, a grid approximating a missing RCC panel 6 was generated early in the investigation for the first damage scenario CFD case at flight conditions. Coordinates defining RCC panel 6 were estimated from existing literature since this work occurred prior to acceptance and distribution of a common CAD geometry within the investigation team. Subsequent comparison of the estimated panel 6 coordinates with the actual size and location revealed that the approximated missing panel was centered about the correct location but was roughly only 2/3 of the full panel. Figure 5.2.4-61 shows a planform view of the missing panel modeled in this work compared with the size and location of the actual RCC panels. The exterior grid for this "notched" panel 6 out case was developed at LaRC very early in the investigation before the common grid development had taken place. Details of the grid are presented in section 5.2.4.2. The grid uses an O-H topology to define the interiorof the missing RCC panel 6 cavity. This topology allows grid cells to be clustered against the solid side and back surfaces to capture viscous boundary-layer behavior. This current cavity grid can be thought of as a hybrid between two cavity grid alternatives described in section 5.2.4.2. The grid has an H topology in the spanwise direction and an O topology in the streamwise direction. The interior cavity grid was composed of 5 matching blocks, one in the center and four surrounding it with their outward faces forming the backplane and the matching faces to the RCC panel 6 OML. Each of the two spanwise faces of thesefive cavity blocks meets the side walls of the cavity. To construct the missing panel geometry, solid vertical surfaces were used to slice the nominal Orbiter geometry along the sidewalls and backplane, thereby forming the leading edge cavity. In reality, the sidewalls of a cavity formed by a missing RCC panel are hollow. This would allow flow into the channel on either side, but such venting was not modeled in the present computation. The backplane of the cavity is a rough approximation of the main wing spar in this simulation; however, no other internal geometry components (e.g., spanner bars, carrier panels, earmuffs) were modeled. The solution was obtained with LAURA using thin-layer Navier-Stokes equations on a grid that had been coarsened to one-half the available grid density in directions parallel to the surface, with full resolution normal to the Orbiter surface. This coarsened grid totaled approximately 8.5 million points, 2.5 million of them located within the missing RCC panel cavity.

Figure 5.2.4-62 shows one aspect of the resulting flow solution where a slice that crosses the RCC cavity has been extracted in the planform plane. The flooded contours on this figure show the flow field density levels for the case where the RCC panel is missing. It can be seen in the figure that shock waves are anchored at both the inboard and outboard leading-edge corners of the missing RCC panel. These embedded shocks are formed around the recirculating flow within the cavity at the inboard corner and from impingement of flow on the outboard corner. Both shocks form weak interactions with the wing bow-shock downstream of the cavity. Solid contour lines are overlaid on the figure to depict the density contours in this area for the case of a baseline geometry with no missing RCC panels. By comparison the presence of the cavity appears to have a very small effect on the outer bow shock and downstream flow in this plane. The only differences noted are the additional features described for the missing panel case. This observation regarding the downstream flow also held true for other planes around the leading edge.

While the missing RCC panel 6 "notch" effect was minimal along the wing leading edge, its impact was very evident in the wing leeside flow. Figure 5.2.4-63 through Figure 5.2.4-65 show temperature contours plotted in vertical planes that have been extracted from the flow field at three axial stations (at the missing RCC panel 6 "notch", midway between RCC panel 6 and the OMS pods, and at the front face of the OMS pods). These figures compare the flow fields of the nominal (i.e., undamaged) Orbiter geometry with the flow field predicted on the leeside with the RCC panel 6 "notch". The sequence of figures shows a jet flowing out of the cavity toward the side fuselage and then the subsequent flow development along the fuselage. In probing the computed flow field it can be ascertained that the jet flow leaves the cavity and travels across the wingspan toward the symmetry plane. Then, it impacts the fuselage at a nearly perpendicular angle. At the fuselage, the jet is turned abruptly downstream. The accompanying temperature increase in the flow field is due to both the hot gas flowing from the wind side and the impact of this jet on the fuselage.

The irregular flow effect on the Orbiter lee side is most evident in the surface pressure and heating experienced on the side fuselage. Figure 5.2.4-66 and Figure 5.2.4-67 illustrate these effects by showing contours of the increase in predicted surface pressure and heating rate over the nominal case. The pressure effect is computed as a difference in pressure coefficient and the effect on heat transfer is shown as a ratio of off-nominal to nominal heating. The area of pressure and heating increases are located almost directly transverse to the missing RCC panel 6. Both areas show an angled orientation sloping upward and aft. This result is in general agreement with wind-tunnel measurements of heating with missing RCC panel 6 geometry in terms of both location and orientation (Section 5.2.3). The maximum heating augmentation from the current prediction is ~5 times the nominal rate.

RCC Panel 6, Lower Half Panel Out Solution with Solid Side Walls (ARC)

The first damage scenario at flight conditions with an accurate definition of the RCC panels considered removing the lower half of RCC panel 6. A cavity was constructed into the wing leading edge by generating surfaces defining the spar, the inboard and outboard sides of RCC panel 6, and a constant waterline to define the vertical extent of panel loss. For the wing spar surface, a cutting plane was created that extends upward from the wing lower surface and parallel to the wing spar. The location of the vertical damage extent utilized a cutting plane that extends aft from the leading edge apex at a constant Z or waterline. Cutting planes between the edges that define the inboard and outboard RCC panel 6 side boundaries defined the width of the damage cavity. A pictorial representation of this geometry for a similar damage configuration at RCC Panel 9 is depicted in Figure 5.2.4-78. Solid wall RCG radiative equilibrium boundary conditions are applied along all of these interior cavity cut planes to fully define the boundary conditions.

The exterior mesh used for this calculation is the same as that used for the smooth OML RCC panel 6 case discussed above. It contained 1.86 million mesh points and 40 blocks, while the 7-block interior cavity mesh topology, which was described in detail in section 5.2.4.2 as the second alternative, contained 164 thousand points. Due to the short time frame allowed to complete this case and the long run times needed to converge a solution with leading edge damage, only a single CFD case was run. The conditions used for the GASP CFD code corresponded to point 1 in table 4.3-4 from section 4.3.2.2.

The cavity geometry is somewhat fictitious in that the inboard and outboard side walls should actually have vents into the RCC channel. Furthermore, the solid wall applied at the constant waterline cut plane actually has no physical basis. Finally, none of the internal RCC channel components such as the earmuffs, hardware insulation, or RCC panel attachment hardware were modeled. Instead, the interior of the RCC cavity was modeled with smooth straight walls. Nevertheless, to understand how significant windward RCC damage affects the leeside flow, this RCC half panel out cavity calculation was a helpful bounding case. In addition, an RCC half panel damage scenario solution at flight conditions helped to provide insight into differences between wind tunnel data and these flight simulations.

Figure 5.2.4-70 and Figure 5.2.4-71 show the analogous side and planform views of the damaged configuration with MADS (circles) and OI (boxes) sensors noted on the images. What is directly observable by comparing these images with the smooth OML images seen in Figure 5.2.4-68 and Figure 5.2.4-69, is that there is virtually no difference between the surface heating on the lee side, except for the region closest to the damage site. The conclusion from this solution is that having a lower half panel missing at the RCC panel 6 location has very little effect on the side fuselage or OMS pod heating. This result is consistent with the wind tunnel trends presented in Section 5.2.2. As a final note, the half RCC panel 6 out case calculation shows that there is some effect on the windward heating downstream of the damage region, although the images of this effect are not included in this report.

RCC Panel 6, Full Panel Out Solution with Solid Side Walls (ARC)

A follow-on to the RCC panel 6 half out case, simulated the loss of an entire RCC panel 6. Again cutting planes were constructed along the spar definition and at the RCC panel side boundaries. All of the new cavity-defining surfaces were specified as solid boundaries with RCG catalysis and radiative equilibrium. This cavity definition, as for the previous RCC half panel out case, was also somewhat flawed. No venting down the RCC channel was included, and hardware such as the insulating earmuffs and RCC panel retaining hardware was entirely missing. Both the backwall and the two side walls were modeled

as smooth featureless surfaces. Nevertheless, since our focus was on heating effects that occur away from the damage location, it provided a reasonable approximation of the loss of an entire RCC panel.

The mesh used for the exterior of the Orbiter was identical to that used for the two previous ARC RCC panel 6-related calculations. Inside the cavity, the 7-block interior mesh topology with 252 thousand points was used. CFD point 1 was used to define the conditions for GASP and only this single case was run.

Figure 5.2.4-72 and Figure 5.2.4-73 show the now familiar side and planform views of Orbiter leeside heating. Immediately evident from these images is that removal of the complete RCC panel 6 results in a rather significant heating change on the side fuselage and OMS pod. Figure 5.2.4-74 illustrates heat flux ratios on the side fuselage between the current complete-panel-removed solution and the smooth OML equivalent solution. Dramatic heat rate differences are indeed present. Very striking in the figure is the fact that locations of both significantly greater heating and moderate cooling relative to the undamaged OML solution are present on the vehicle. In particular, the OMS pod heating is dramatically reduced while a section on the side of the fuselage near the wing root and *ahead* of the actual damage location experiences heating levels that are dramatically higher than normal. Notice that the side fuselage region experiencing increased heating is quite large and that it is preceded upstream by a section of *reduced heating*. The increased heating of the side fuselage is due to impingement of the jet originating from the RCC cavity. The decreased heating on the OMS pod region may be due to changes in the position of the leeside wing-strake vortices, that normally run along paths that cause significant vortex scrubbing and hence heating effects on the OMS pod.

To illustrate the structure of the jet coming from the RCC cavity, Figure 5.2.4-75 through Figure 5.2.4-77 show temperature contours for cuts through the flow-field solution at three constant X locations. Side-by-side comparisons for both half RCC panel out and full RCC panel out with the smooth OML solutions are depicted. It is noted again that virtually no differences are seen in the leeside region for the half RCC panel out case. However, for the full panel out case, dramatic flow-field structures, not present in the smooth OML solution, are revealed. The very hot regions of these flow structures, which are especially evident at the X = 27 m and X = 30 m cuts, may be considered secondary shocks that are standing off the side of the fuselage. The shocks appear to be caused by an impinging jet hitting almost perpendicular to the side fuselage which emanates from the upper half of the RCC panel 6 removed cavity. The fact that the jet structure traverses the flow-field in the cross-stream direction while the free-stream flow is at Mach 25 emphasizes the strength of the jet. The removal of the panel can be thought of as creating a scoop down into the windside flow. The scoop turns the flow inward toward the body, and since on the leeside conditions are very nearly at a vacuum there is no resistance to this jet heading directly toward the side fuselage. Furthermore, once on the lee side, the jet must be traveling with considerable speed since it creates a secondary bow shock that stands off the side of fuselage. The temperature experienced by the flow as it traverses this secondary side-fuselage shock reaches levels that are near those present in the primary bow shock on the wind side of the vehicle. The cooler than normal region ahead of the jet impingement on the side of fuselage is a result of the jet flow moving aside the leeside flow that would normally be slowly accelerating along the side of body.

RCC Panel 9, Baseline Smooth OML Solution with Embedded-O Mesh (ARC)

In addition to the RCC panel 6 studies discussed above, studies at flight conditions focused on RCC panel number 9 were also conducted. Again an initial Ames solution using GASP for the smooth OML instance of the RCC panel 9 series was first conducted. The CFD case calculated was point 1 as defined in table 4.3-4. The mesh had an identical number of points to the equivalent RCC panel 6 case – 1.86 million points. For a comprehensive discussion on the motivation for running this case, the reader is referred to the RCC panel 6 equivalent case above. Figure 5.2.4-79 and Figure 5.2.4-80 show the side and planform views of the heating for this case. The images are very similar to those shown earlier for the smooth OML RCC panel 6 results, and thus will not be discussed in any more detail.

RCC Panel 9, Lower Half Panel Out Solution with Solid Side Walls (ARC)

The next case in the series of RCC panel 9 related CFD solutions, calculated with GASP at NASA Ames, follows the same sequence as that followed for the RCC panel 6 series. Specifically, the current case models a lower half RCC panel 9 out. A pictorial representation of the geometry for this damage

configuration at Panel 9 is shown in Figure 5.2.4-78. The construction of the lower half RCC panel out cavity used cutting planes just as in the corresponding half RCC panel 6 out case. The number of mesh points and the topological details of the mesh were also the same as those used for the RCC half panel 6 out case. A GASP simulation with the lower half RCC panel 9 removed and solid wall boundary conditions inside the resulting cavity is depicted in Figure 5.2.4-81 and Figure 5.2.4-82. Again, virtually nothing happens on the lee side, either on the upper wing surface or on the side of the body. A detailed examination showed that the differences in surface heating on the side fuselage and OMS pod, between the present case and the smooth OML RCC panel 9 case, are of the same order as the solution noise present for any calculation with the convergence tolerance used for this study. Thus, it can be concluded that the lower half RCC panel 9 damage case, at CFD flight condition 1, shows no leeside heating effect, within the tolerance of the CFD simulation. Note that the equivalent lower RCC half panel 6 out case discussed above showed slight but not negligible heating differences. The observation is that the attachment line along the leading edge that separates flow traveling to the lee side and the wind side moves higher with increasing span position. It is therefore expected that lower panel damage to the higher panel numbers will show less and less leeside influence. By the time lower RCC panel 9 is reached, essentially no leeside effects can be observed. Wind tunnel tests discussed earlier confirm this trend and demonstrate that rather sizeable leeside effects can be seen if the lower panel damage is as far inboard as RCC panel 3. Although it is not presented pictorially in this report, the RCC lower half panel 9 out does cause significant changes to the windside heating on the wing lower surface. However, these effects are well within the limits that can be tolerated by the RCG coated tiles.

RCC Panel 9, Lower Half Panel Out Solution with Vented Side Walls into the RCC Channel (ARC)

Solid sidewalls within the RCC cavity were used in the flight simulations discussed above, and it was recognized that those solutions could produce misleading results. Thus, an alternate CFD simulation of the lower half RCC panel 9 out scenario was conducted. There is one primary difference between this simulation and the previous RCC lower half panel 9 out case. Instead of the lower half panel out cavity being confined to the lower portion of the wing leading edge section, the entire extent of the RCC cavity bounded by the local RCC panel definition is modeled. This cavity modeling leaves the upper RCC half panel 9 hanging in space; its exterior OML side is exposed to the external flow and its interior cavity side is exposed to the interior flow. The actual RCC panel in this calculation is modeled as a zero thickness surface for the remaining upper section of RCC panel 9. The zero thickness approximation may not be appropriate to capture details of the internal cavity flow, but should suffice to model the leeside effects. In the actual case of a removal of just a lower half panel, a detached bow shock would form on the lip of what remains of the panel and disturb the flow inside the cavity in a way that is different from an attached shock caused by the infinitely thin edge used for the present calculation. This case also differs from the previous solutions in that the location of the RCC channel is defined, or scribed, on the sidewall mesh faces. The sidewall boundary conditions within the RCC channel regions are switched from being modeled as solid to being modeled as exit flow, with a (very low) fixed back pressure. By changing the sidewall boundary condition, we attempted to model the venting relief that occurs down the RCC channel in both spanwise directions. The upper left hand corner inset in Figure 5.2.4-91 shows details of the channel definition across which the exit/venting boundary condition is applied. The back pressure specified for these RCC channel vents was set to 0.1 lbf per ft^2.

The exterior mesh used for this case was identical to that used in the immediately preceding case. Again, only CFD point 1 was computed due to time and resource constraints. The interior mesh was actually identical to the next two full panel 9 out cases, using the 7-block internal topology with 252 thousand grid points. The side walls outside the vented regions, the back wall and the interior surface of the RCC 9 upper half panel were all model as solid walls with RCG catalysis, radiative equilibrium and an emissivity of 0.89.

The side and planform views of heating shown in Figure 5.2.4-83 and Figure 5.2.4-84 are indistinguishable from those shown in Figure 5.2.4-81 and Figure 5.2.4-82. The conclusion is that for the lower half RCC panel out case presented thus far, the details of the cavity modeling seem to have little leeside flow field influence. In general, for RCC panel 9, removal of the lower half does not propagate effects into the leeside flow. As noted previously leeside effects resulting from having a lower half panel out seem to increase as the removed half panel location is moved forward along the wing leading edge.

This result is consistent with experimental leeside heating data presented in Section 4.3.1 and 5.2.3. Lower wing heating differences were again observed but not examined in detail.

RCC Panel 9, Full Panel Out Solution with Solid Side Walls (ARC)

A damage scenario with all of RCC panel 9 removed, and the sidewall boundary conditions within the cavity returned to solid walls with RCG catalysis and radiative equilibrium, is considered next. The case is analogous to the simulation computed for the RCC panel 6 study at Ames. The grid was identical to that used in the preceding case. Figure 5.2.4-85 and Figure 5.2.4-86 show the heating levels from a side view and a planform view. Immediately clear from these figures is the presence of significant side fuselage heating. To reveal the details of this heating pattern more clearly, the heat flux ratio between this solution and the smooth OML panel 9 solution is depicted in Figure 5.2.4-87. Significantly increased heating levels are seen across a wide range of the lower part of the side fuselage, extending substantially upstream of the damage location. The peak heating increase shows a ratio of heating relative to the smooth OML case of above 50. Ahead of this increased heating region is a prominent section of reduced heating extending up and onto the payload bay doors. Unlike the full RCC panel 6 out with solid side walls solution that showed a decreased heating on the OMS pod, this full RCC panel 9 out solution shows a significant heating increase on the OMS pod. The differences in heating effects for RCC panel 6 missing and a RCC panel 9 missing show that leeside heating effects depend upon the actual leading edge damage location. Further information regarding leading edge panel parametrics with a much larger series of RCC panels removed can be found in the wind tunnel discussion of Section 5.2.3.

Figure 5.2.4-88 through Figure 5.2.4-90 show temperature contours across cuts through the solutions for the half and full panel solid sidewall RCC panel 9 damage scenarios. As in the RCC panel 6 equivalent images, the half RCC panel out case is virtually identical to the smooth OML solution. The solution with the full RCC panel 9 out shows very complex flow structures on the lee side above the wing. These “hot” flow structures interact with the side fuselage, resulting in surface heating similar to that seen in the Panel 6 plots of Figure 5.2.4-72 - Figure 5.2.4-77. The reader is referred back to the detailed discussion for the Ames full panel 6 out calculation to gather an understanding of the off body flow phenomena.

RCC Panel 9, Full Panel Out Solution with Vented Side Walls into the RCC Channel (ARC)

The next in the ARC series of panel 9 damage scenarios was the vented side wall version of the above RCC full panel 9 out calculation. In this computation the solid inboard and outboard sidewalls have been changed to the vented sidewalls boundary conditions. This boundary condition was analogous to what was already discussed above for the half RCC panel out cases. The mesh used in the previous computation was recycled for this case to compute CFD point 1. The objective of this simulation was to better understand the differences that RCC channel venting might have on the leeside flow field and surface heating.

Figure 5.2.4-101 and Figure 5.2.4-102 display the side and top planform views of surface heating. The figures show that a geometry with RCC channel venting also has very large heating increases on the lower part of the side fuselage, similar to the unvented full RCC panel 9 out case. Figure 5.2.4-103, illustrates the ratio of heat fluxes between the current case and the smooth OML case. A comparison with Figure 5.2.4-87 (RCC Panel 9 out unvented) leads to the observation that approximately the same side fuselage region experiences increased heating with or without RCC channel venting. However, the level of heating augmentation and the forward extent of the heating footprint are both somewhat reduced for the vented case compared with the unvented case. In addition, the vented RCC channel case experiences very significant cooling on the OMS pod region compared with the slight heating that was present in same location for the solid wall case. The conclusion is that venting down the RCC channel reduces the strength of the high-pressure jet emanating from the full RCC panel out cavity region. As a result, the effects on the side fuselage are less extreme than without the venting.

RCC Panel 9, Full Panel Out Solution with Vented Side Walls into the RCC Channel (LaRC)

A computational analysis of the flow field effects due to RCC panel 9 loss on the Orbiter was performed using the LAURA code. For this analysis, gas entering the cavity formed by the missing RCC panel was

allowed to flow into the outboard RCC channel by imposing vacuum conditions on the sidewall. Note that the previous GASP-calculated full RCC panel 9 out case used 0.1 psf back pressure instead of a hard vacuum. The inboard side of the cavity was modeled as a solid wall. For the vented outboard cavity surface, the solution remains independent of RCC channel back pressure as long as the back pressure is low enough to produce supersonic flow. This stipulation is true for all the vented cavity sidewall solutions. This is the only boundary condition that can be applied for a well-posed computation of flow through a sidewall without interior RCC channel modeling. The full scale computation at flight conditions was performed on a grid with 2 million cells where over half a million cells were located in the cavity.

An approximation of the RCC channel geometry was made for hardware exposed to the external flow by a missing panel 9. These features are shown in Figure 5.2.4-91. As noted in the illustration, the geometry modeled in the cavity extended to the main wing spar. This approach allowed for an approximation of the spanner beam/earmuff blockage, as well as the windward and leeward carrier panels. An additional detail modeled by this simulation was to maintain the height of the RCC rib exposed on panel 9. A vent area of about 312 square inches resulted after this rib surface was included in the geometry.

Figure 5.2.4-92 shows a cross-section of the flow field density at a constant waterline through the wing for the region surrounding RCC panel 9. Results for both the smooth OML geometry and the case of missing RCC panel 9 are shown. The density contours approaching the cavity are identical between the two solutions as expected, and a complex shock structure is observed in the cavity of the missing panel. At the upstream edge of the cavity an expansion fan propagates into the shock layer, accelerating and turning the flow into the gap. A weak recompression wave, also emanating from the upstream edge of the cavity, processes the over-expanded flow. On the outboard RCC rib, an embedded bow shock forms with one-half of the wave ingested into the RCC channel and the other half forming a second interaction with the downstream wing shock. The effects of this interaction with the wing shock appear to be very minor since the intersection angles of this secondary interaction are small and the incident wing shock is already weakened by ingestion of flow into the RCC channel. The shock layer thickness is approximately 20% smaller over the wing downstream of the missing panel. This is due to flow ingestion into the missing panel region, which is then convected into the outboard RCC channel, or is spilled over to the leeside of the wing.

A view of the missing panel cavity presented in Figure 5.2.4-93 illustrates the major surface and flow field features in the cavity. Color contours in the figure represent surface pressures, while volume streamlines are plotted to indicate flow direction. The streamlines illustrate that a substantial part of the flow entering the missing panel cavity also continues directly into the RCC channel. An attachment line is formed on the outboard RCC rib that separates flow going into the RCC channel from flow continuing onto the wing upper surface. The interior cavity, formed by the presence of upper and lower carrier panels and the spanner bar, produced additional flow features of note. Streamlines that flow into this cavity region are deflected toward the wing spar by the spanner bar (away from the outboard RCC channel). A circulation is formed within the volume encompassed by the interior cavity and the inboard sidewall. This recirculating flow is “spun” out the top of the missing RCC cavity into the leeside flow field.

Predicted heating rates to surfaces in the interior of the missing RCC panel area are presented in Figure 5.2.4-94. The heating contours closely follow the pressure contours shown in the previous figure except on the exposed edge of the lower carrier panel. It appears that heating in this area is elevated due to a thin boundary layer and high shear stresses. These two effects, in combination, lead to the highest heating rate observed in this simulation.

A simple view of the streamlines emanating from the leeside of the missing RCC panel is shown in Figure 5.2.4-95. The streamline patterns illustrate that the flow leaving the gap corner nearest the inboard sidewall and spar is directed straight toward the fuselage. Flow leaving the gap from other locations along the spar and toward the outboard cavity area is increasingly turned downstream. The end result is a small area of flow diverted low along the upper wing and toward the side fuselage in this simulation.

Temperature contours normal to the vehicle axis are shown in Figure 5.2.4-96 to Figure 5.2.4-99 for both the smooth OML and the missing RCC panel 9 solutions. The first figure, Figure 5.2.4-96, shows the temperature contours at X = 1051 inches which is 40 inches upstream of the missing RCC cavity. The

contours are symmetrical, illustrating that the cavity has no effect on the flow at this upstream station. The location at X=1051 inches is within a region of the volume grid which was significantly modified from the original common baseline grid. The solution's similarity for the nominal OML and the Panel 9 cavity grid demonstrate that the cavity modifications did not result in noticeable flow field differences in the computations forward of the damage site. Figure 5.2.4-97 shows the temperature contours at X = 1091 inches, corresponding to the inboard corner of the cavity. The missing RCC panel 9 solution produces a jet of hot gas which exits the cavity and scrubs the leeside of the wing in the direction of the fuselage. At this station, however, the side of the fuselage appears unaffected by the jet. Figure 5.2.4-98 shows the temperature contours at X = 1204 inches, halfway between the cavity and the OMS pod. At this downstream station, the jet from the cavity has been turned downstream and is scrubbing the side of the fuselage with the highest temperature gas near the intersection of the fuselage and the wing. Figure 5.2.4-99 shows the temperature contours at X = 1316 inches at the beginning of the OMS pod. The increased temperatures along the side fuselage persist at this station, although they have decreased somewhat. A region of off-nominal low temperature is also evident on the leeside surface of the wing for this missing RCC panel 9 solution. The most predominant feature, however, is the high temperature gas near the OMS pod surface. While both the baseline smooth OML and the missing RCC panel 9 solutions show hot gases in this region, a higher temperature gas occurs for the baseline solution. This effect can be noted by the white levels in the contours for the smooth OML solution, as opposed to the magenta contours in the missing panel 9 solution.

The leeside flow field perturbation seen in Figure 5.2.4-95 to Figure 5.2.4-99 causes the surface heating effect illustrated in Figure 5.2.4-100. Here the amplification of heating rate relative to the nominal (undamaged geometry) is plotted to isolate missing RCC panel 9 effects. As would be expected from the streamline patterns, the fuselage heating is increased in the area where the flow diverted through the missing panel gap strikes the fuselage. In this damage scenario, the heating augmentation pattern assumes a horizontal orientation and is confined near the wing-fuselage juncture. Augmentation factors up to 2 over the nominal heating case are predicted on the side fuselage. The effect on the OMS Pod is lower heating (approximately 70%) for the missing panel solution relative to the baseline. The results of other CFD simulations presented in this section, as well as the wind tunnel results in Section 5.2.3 with missing RCC panels have shown similar trends, but quantitatively different heating patterns. In many of those cases, the side fuselage heating augmentation is higher up on the fuselage, occurs more upstream, and the pattern assumes an angled orientation. Also, heating to the OMS pod in those cases generally increased. Differences in leeside surface heating characteristics between this simulation and the other results are primarily believed to be due to the amount of flow venting into the RCC channel and to the presence of an embedded cavity behind the missing RCC panel. This simulation illustrates the sensitivity to venting effects down the RCC channel, as well as the geometry of hardware in the RCC cavity.

RCC Panel 9, Half Panel Out Solution with Vented Side Walls into the RCC Channel and the Upper Carrier Panel Out (ARC)

The damaged RCC panel configurations discussed up to this point all involved permutations on the location of damage on the RCC panel, and different extents of vertical damage (i.e.., half or full panel). Concurrent with the development of the grid systems and the understanding developed from those CFD simulations, as well as on-going wind tunnel studies and observations from the debris, our understanding of the parametrics involved in wing leading edge damage increased dramatically. Late in the investigation, it became apparent that the extent of the initial wing leading edge damage was not likely to include large leeside sections of the RCC panels missing. Wind tunnel testing was indicating that some windward damage, together with some leeward damage near the RCC, could produce signatures consistent with the surface instrumentation responses during the early part (i.e., < EI + 480 seconds) of the STS-107 trajectory. With these observations from the later stages of the investigation in hand, a final solution at flight conditions was pursued with the lower half of RCC panel 9 removed, and an approximation of upper carrier panel damage. This configuration was deemed to be more representative of potential early timeline damage to Columbia, and complements a similar geometry considered in the wind tunnel testing (see Section 4.3.1). Similar to the more complicated half panel 9 out case discussed previously (i.e., with vented side walls and the complete RCC cavity modeled), the current case modeled the full RCC cavity with a zero thickness RCC upper half panel 9 and venting down the RCC channel through the inboard and outboard sidewalls. However, to model the desired upper carrier panel removed configuration, the last 4 inches of upper RCC panel 9 along the wing spar was also removed. Flow-

through boundary conditions were applied across this gap at the top of the RCC panel, allowing communication of the flow from the RCC cavity to the wing lee side. A graphic depicting the geometry is shown in Figure 5.2.4-104.

CFD condition 1 was calculated using GASP with the mesh remaining consistent with the other panel 9 out ARC cases. Figure 5.2.4-105 and Figure 5.2.4-106 show side and top planform views of the leeside heating. While the visible effects in these images are mild compared with those seen for the full RCC panel 6 or 9 out cases, the surface heating effects are still substantial compared with those seen on the previous half RCC panel out cases. Figure 5.2.4-107 depicts the ratio of the heat fluxes between the present case and the smooth OML panel 9 case. The figure shows that the primary leeside fuselage influence is a cooling effect on the OMS pod region. There is also some local increased heating near the wing-body intersection aft of the damage location.

5.2.4.5.2 Concluding damage scenario comments.

Because the exact damage to the wing leading edge of Columbia will remain unknown, a limited matrix of damage configurations were examined using CFD and focusing on RCC panels 6 and 9. These solutions suggest that initial damage to only the windside leading edge coupled with significant venting to the interior of the WLE cavity (possibly also with some open vent paths from the RCC channel to the lee side via T-seal gaps and upper carrier panel gaps) would result in only minor temperature anomalies on the fuselage, and potentially, decreased heating on the OMS pod. Also, as the damage geometry changed during the re-entry of Columbia, the footprint on the side fuselage and OMS pod would also have changed. Furthermore, a breach from the windward side via lower RCC panel damage coupled with significant upper carrier panel damage would be associated with initial moderate heating anomalies on the side fuselage. To experience extensive heating anomalies on the fuselage would require additional damage including either more upper carrier panel damage (e.g., more than a single upper carrier panel removed), loss of an entire RCC panel, or an equivalently large wing breach allowing windside flow to feed directly to the lee side. Venting to the interior of the wing leading edge (through the RCC channel) delays the extent of leeside anomalies. This is due to reduced mass flow to the lee side associated with the jet from the wind side to the lee side, emanating from the leading edge damage cavity. The existence of this jet due to wing leading edge damage is shown conclusively in the CFD simulations presented in this section. The character of that jet is such that, with sufficient damage to the wing leading edge, high temperature gas is driven toward the side fuselage of the Orbiter which can propagate *upstream* of the damage site. The most dramatic heating increases and the largest extent of surface heating effects occur when the leading edge cavity jet is driven by wing leading edge stagnation pressure due to a significant breach in the wing leading edge on the wind side. As a final comment on the damaged leading edge CFD simulations, it must be pointed out again that the nature of these simulations, and the conclusions to be drawn from them, should be restricted to an engineering perspective. The CFD simulations conducted as part of the investigation were performed on representative geometries. The particular geometries that have been assessed were chosen in a very dynamic environment of wind tunnel, CFD, flight instrumentation, and recovered debris investigations. The fact that these geometries were chosen for investigation does not mean that the damaged geometry experienced by Columbia is exactly represented in this suite of simulations. In fact the dynamic/progressive nature of the actual Columbia data coupled with the time responses for the sensors will likely mean that a direct one-to-one match between CFD simulations and instrumentation flight data will never be achieved.

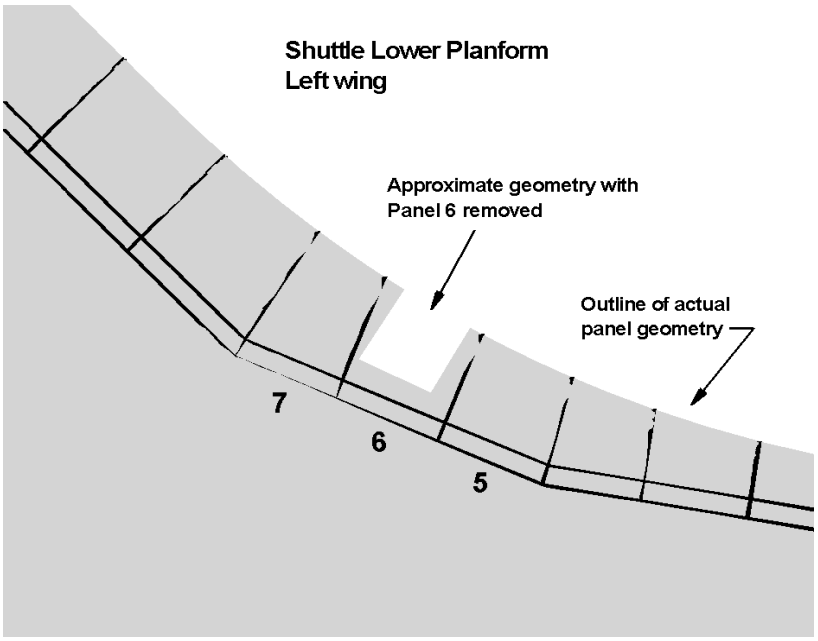

Figure 5.2.4-61 Planform view of missing panel 6 "notch"

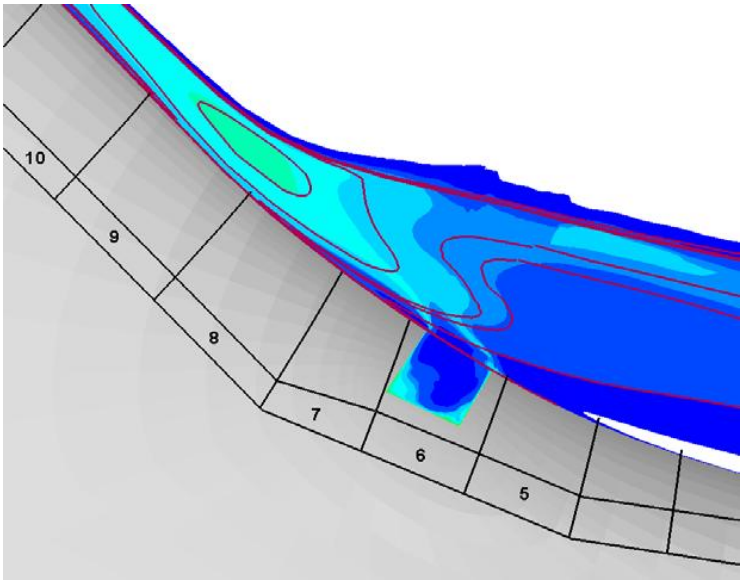

Figure 5.2.4-62 Planform view of flow field density contours for nominal geometry (contour lines) and for missing RCC panel 6 (flooded contours)

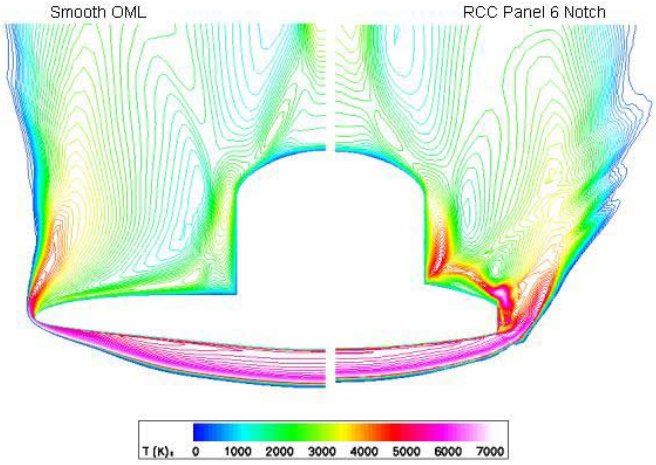

Figure 5.2.4-63 Temperature Contours at X = 1036 inches (through panel 6 notch)

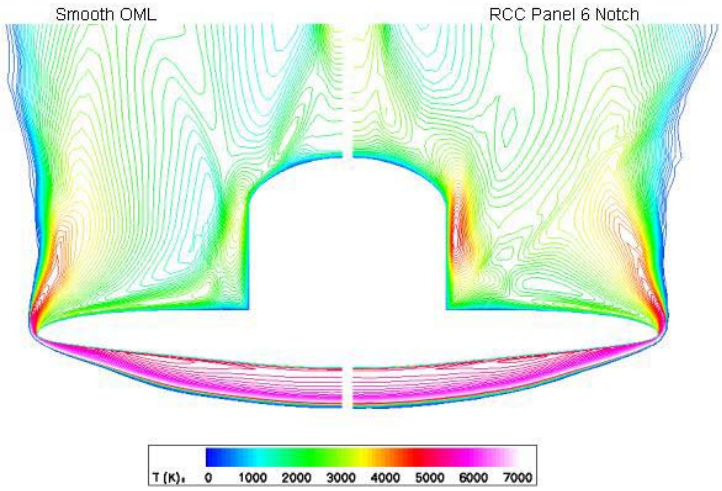

Figure 5.2.4-64 Temperature Contours at X = 1181 inches (halfway between notch and OMS pods)

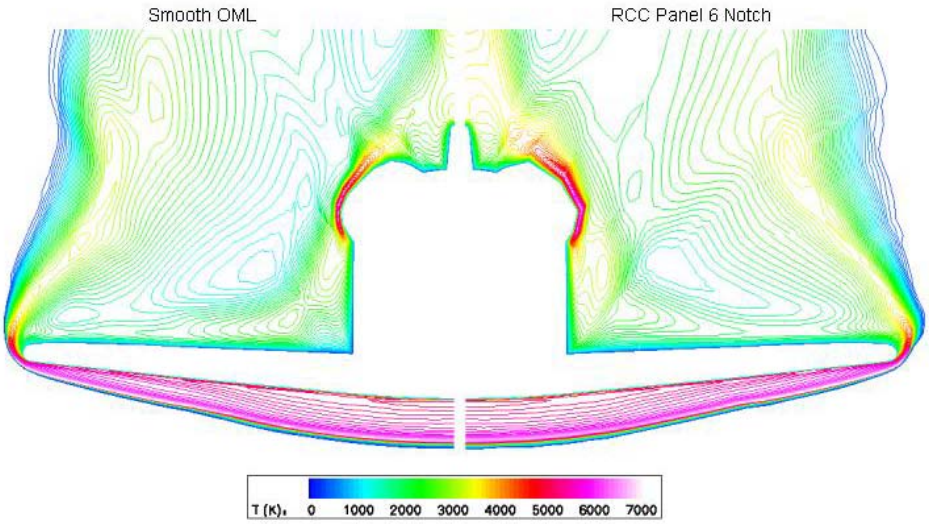

Figure 5.2.4-65 Temperature Contours at X = 1326 inches (forward face of OMS pod)

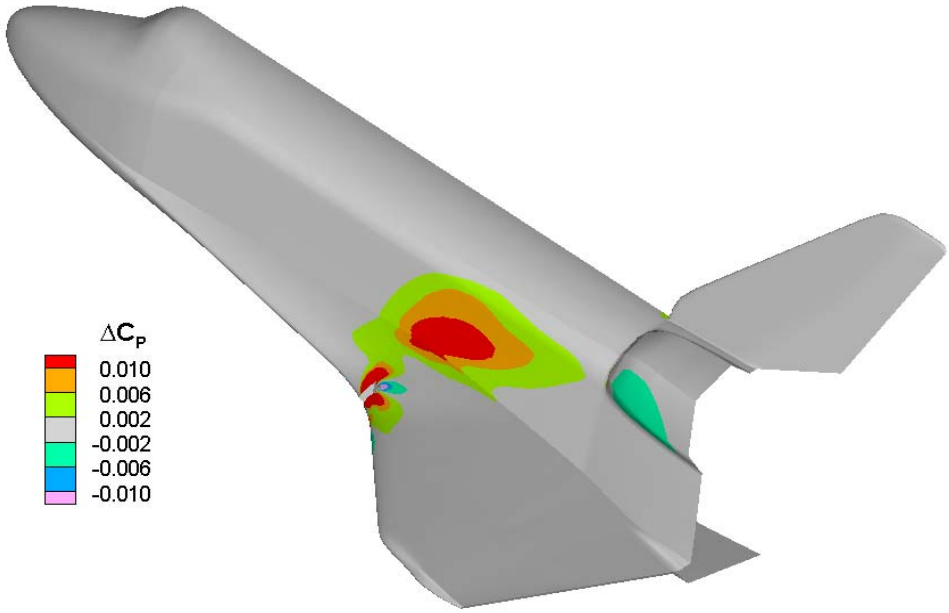

Figure 5.2.4-66 Difference in pressure coefficient due to missing RCC panel 6 "notch"

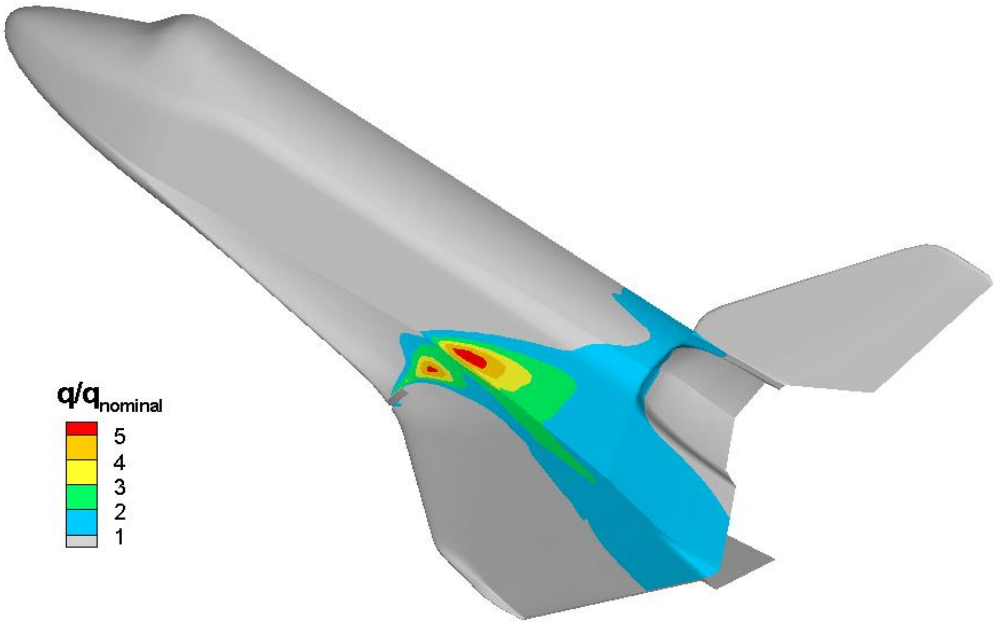

Figure 5.2.4-67 Heating augmentation due to missing RCC panel 6 "notch"

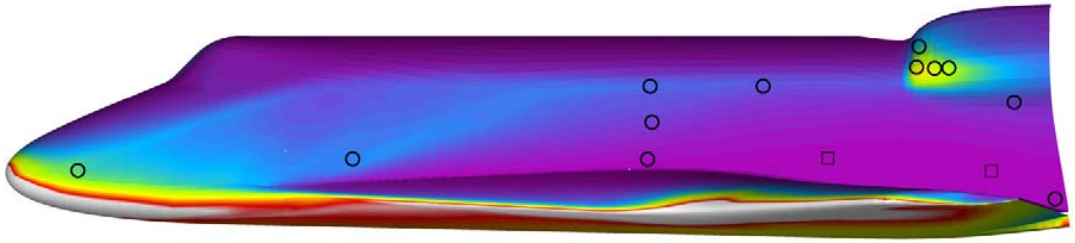

Figure 5.2.4-68 Smooth OML RCC Panel 6, Side View, Heating Rates

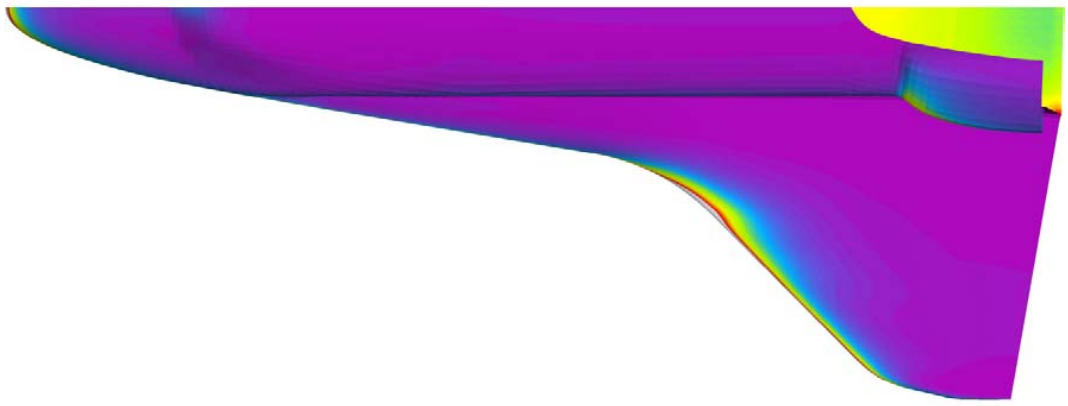

Figure 5.2.4-69 Smooth OML RCC Panel 6, Planform View, Heating Rates

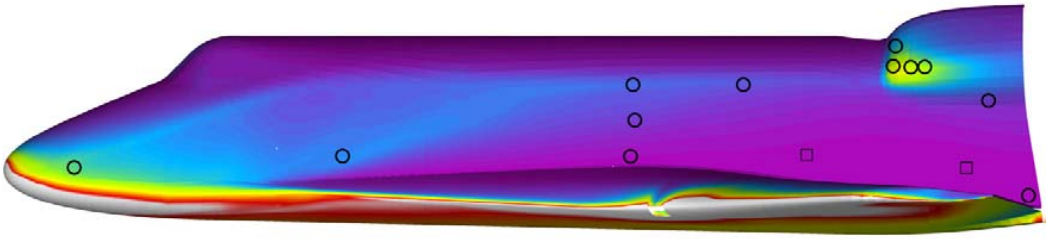

Figure 5.2.4-70 Lower Half RCC Panel 6 Out, Side View, Heating Rates

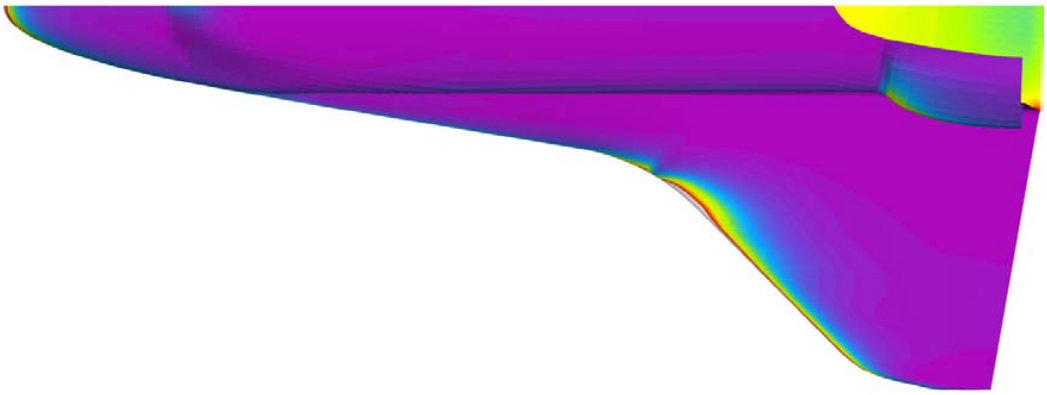

Figure 5.2.4-71 Lower Half RCC Panel 6 Out, Planform View, Heating Rates

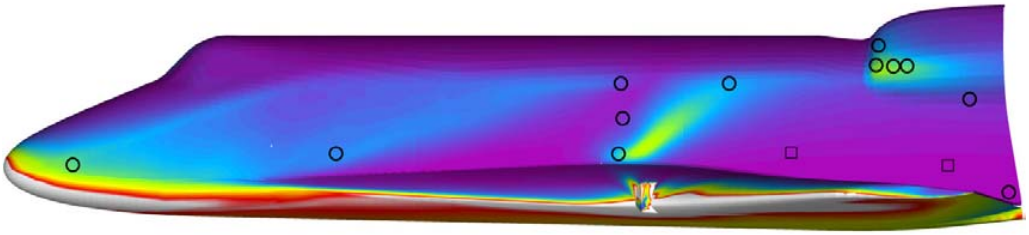

Figure 5.2.4-72 Full RCC Panel 6 Out, Side View, Heating Rates

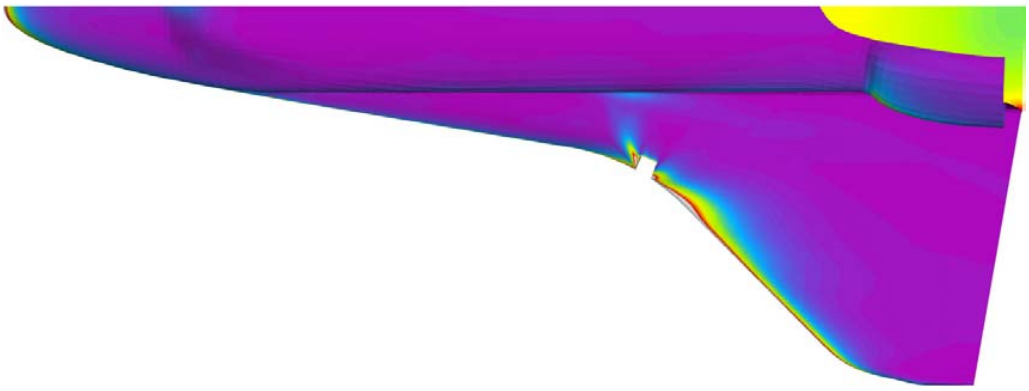

Figure 5.2.4-73 Full RCC Panel 6 Out, Planform View, Heating Rates

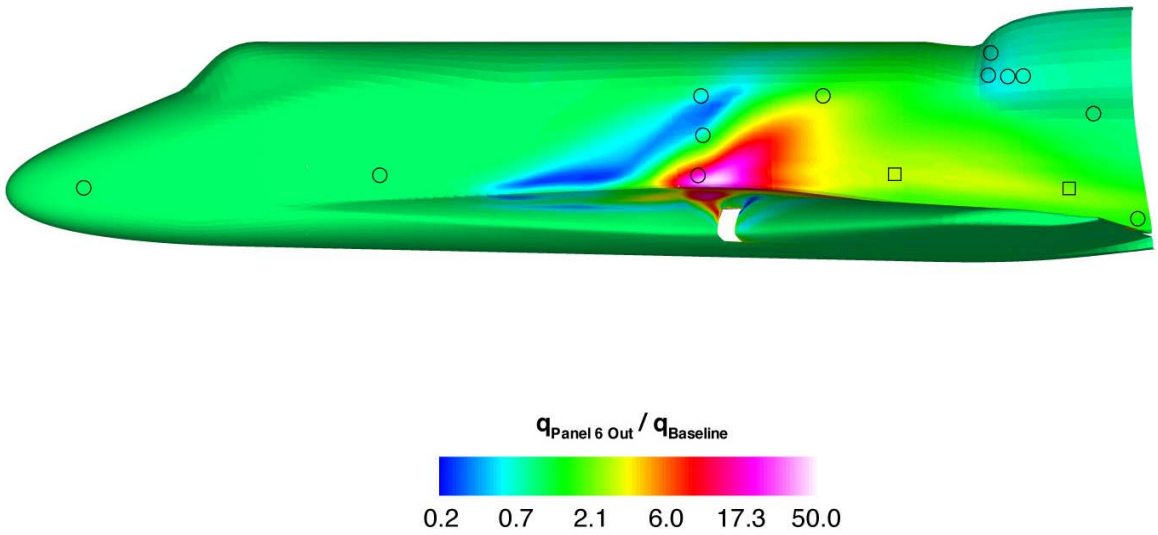

Figure 5.2.4-74 Full RCC Panel 6 Out, Side View, Ratio of Heat Fluxes

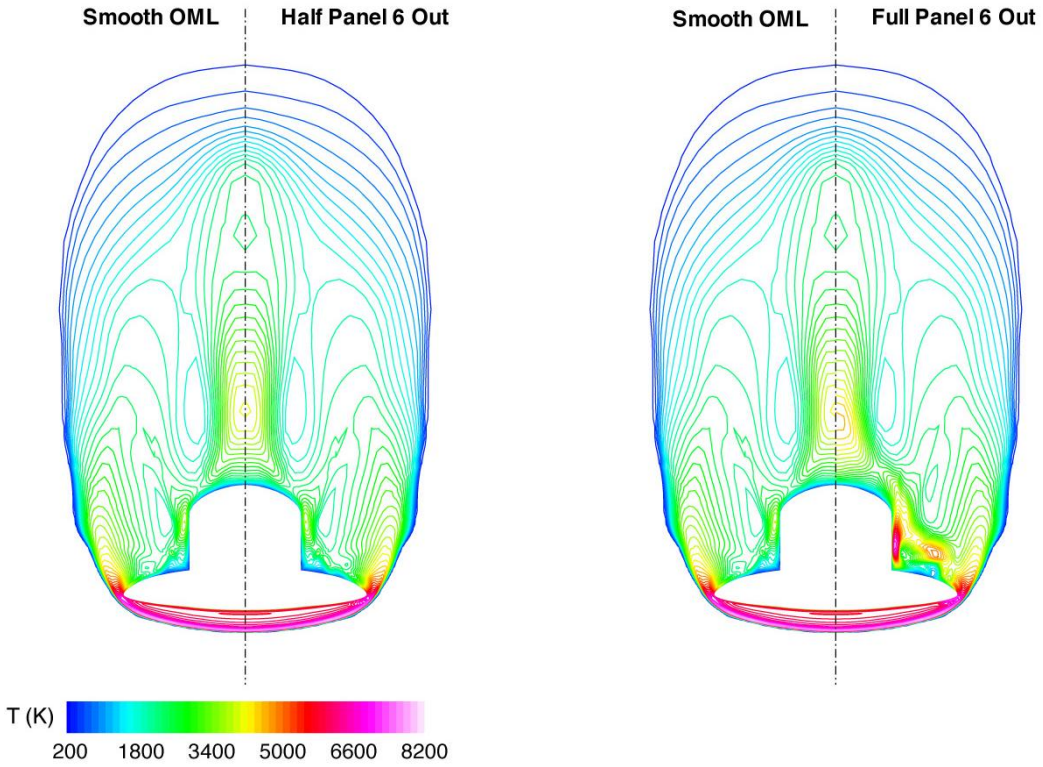

Figure 5.2.4-75 RCC Panel 6 Out, Y-Z Solution Cut at X = 27 m, Temperature Contours

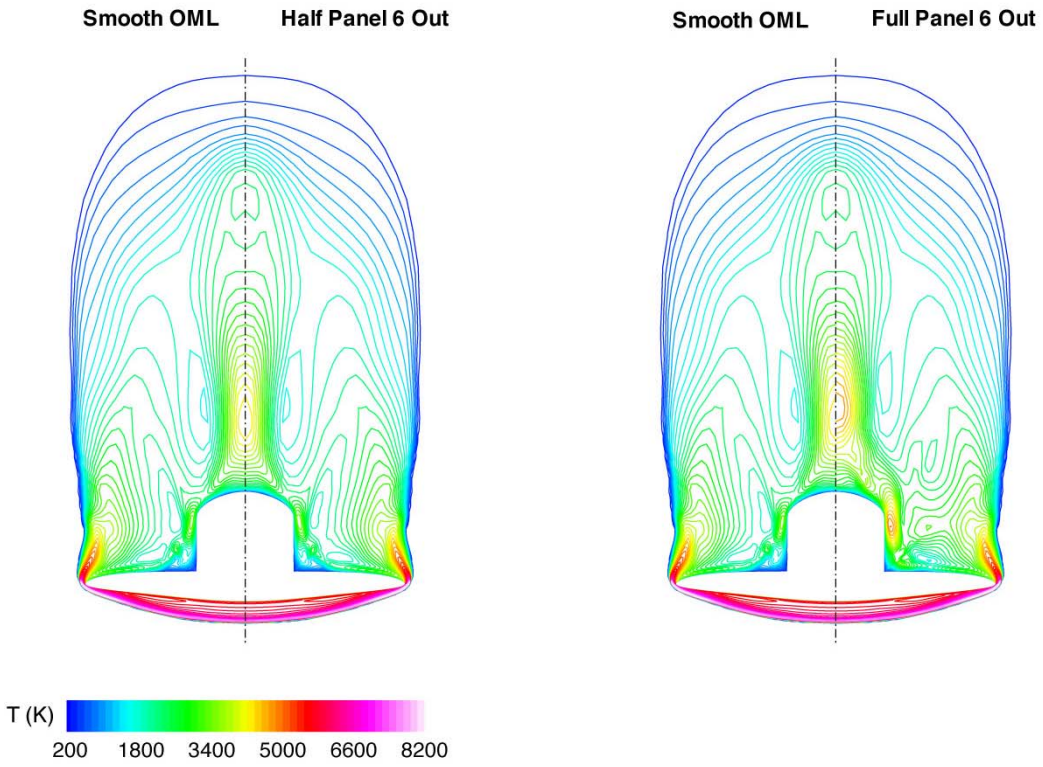

Figure 5.2.4-76 RCC Panel 6 Out, Y-Z Solution Cut at X = 30 m, Temperature Contours

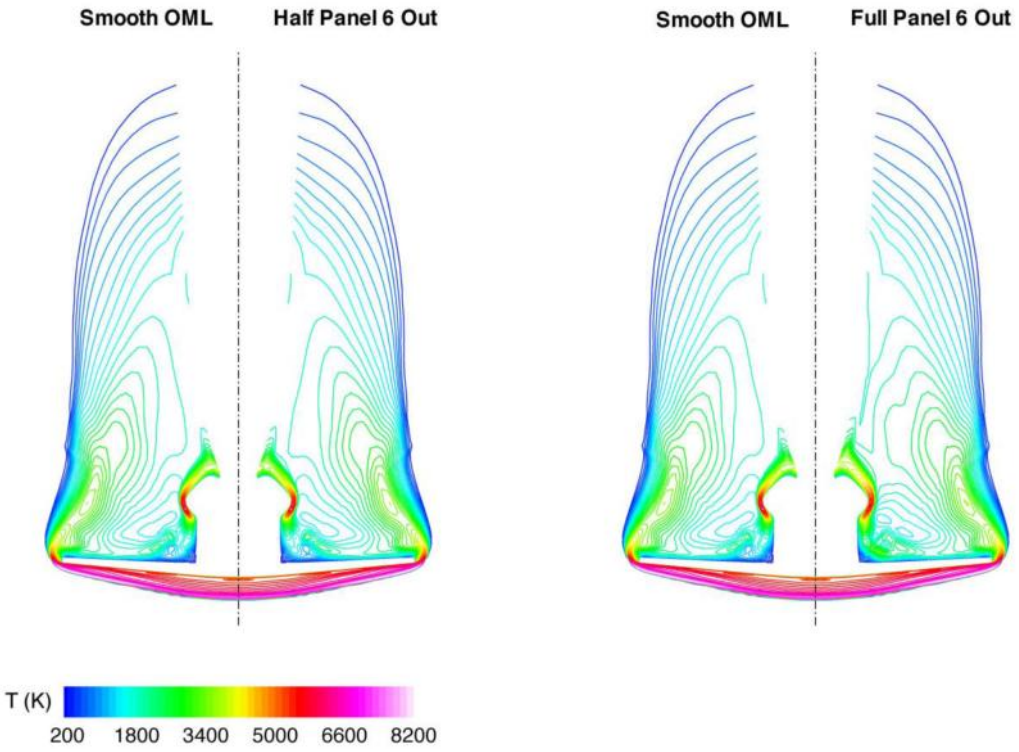

Figure 5.2.4-77 RCC Panel 6 Out, Y-Z Solution Cut at X = 35 m, Temperature Contours

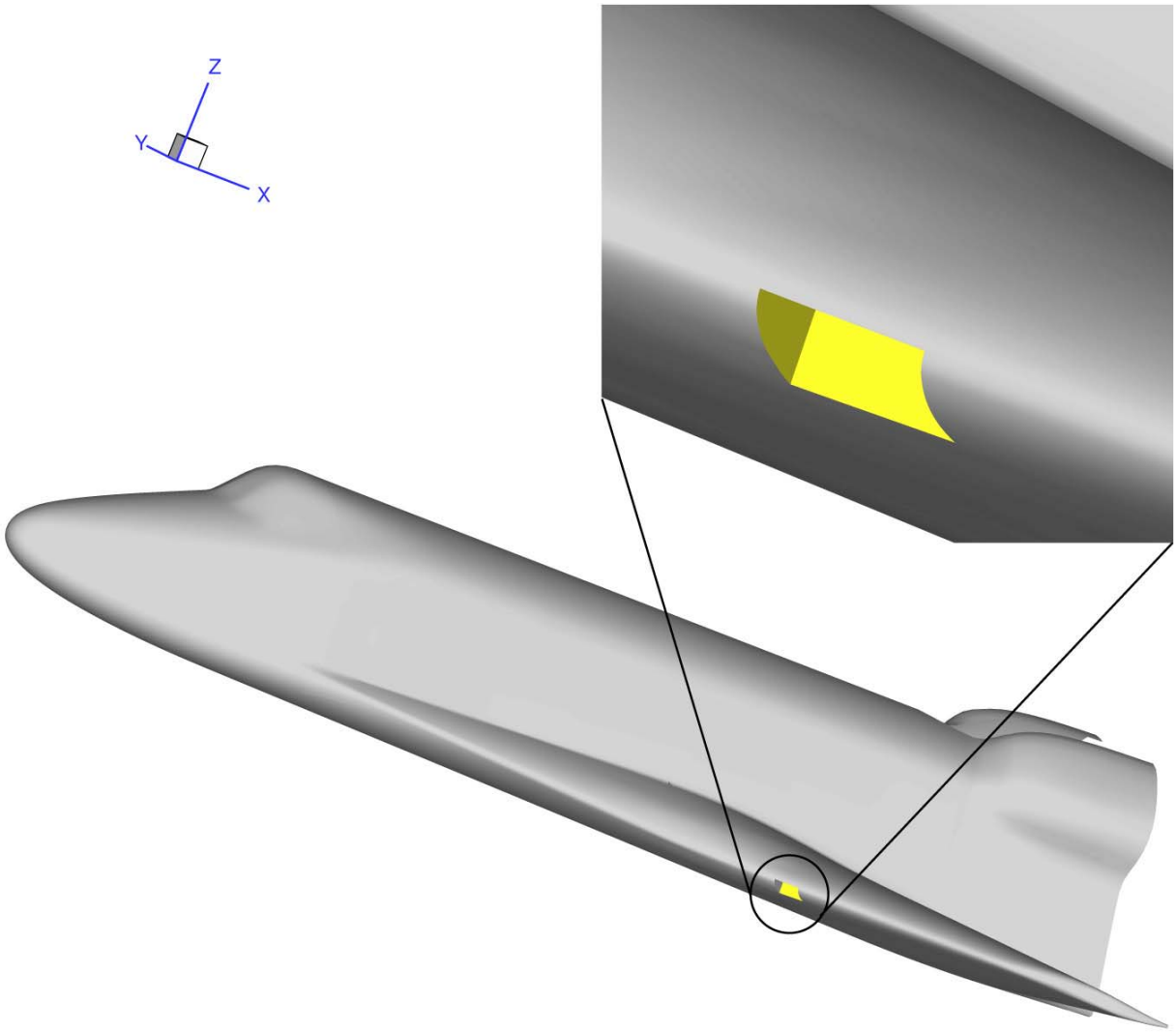

Figure 5.2.4-78 Lower Half RCC Panel 9 Out Geometry

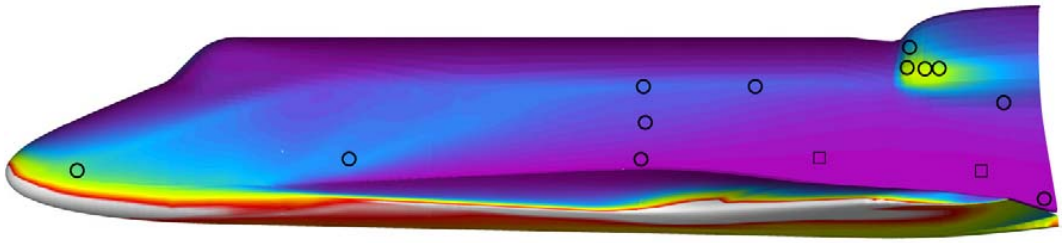

Figure 5.2.4-79 Smooth OML RCC Panel 9, Side View, Heating Rates

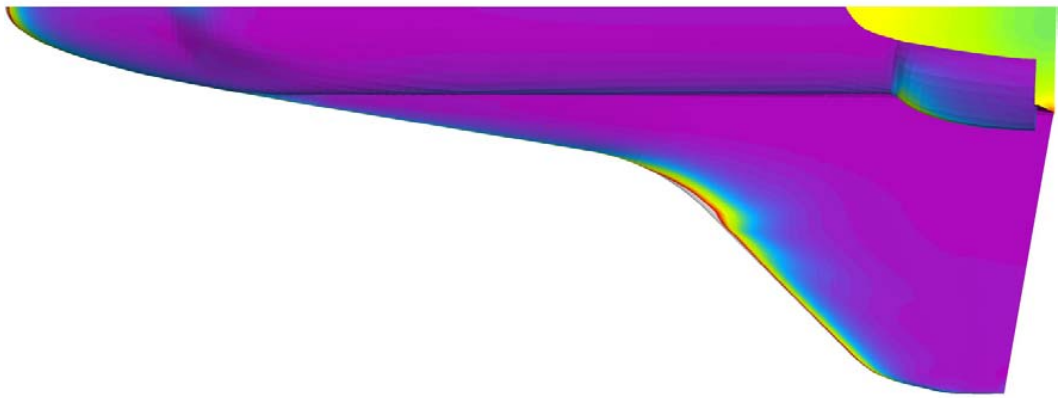

Figure 5.2.4-80 Smooth OML RCC Panel 9, Planform View, Heating Rates

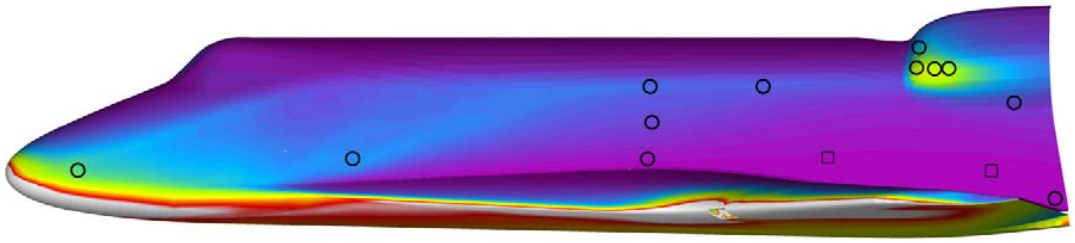

Figure 5.2.4-81 Lower Half RCC Panel 9 Out, with Solid Side Walls, Side View, Heating Rates

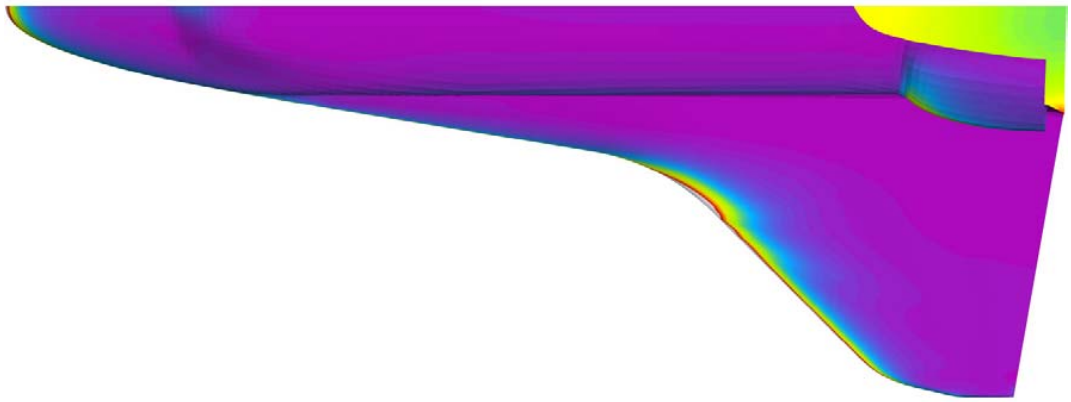

Figure 5.2.4-82 Lower Half RCC Panel 9 Out, with Solid Side Walls, Planform View, Heating Rates

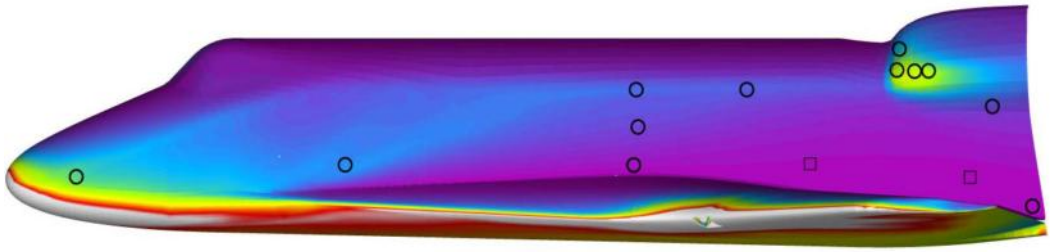

Figure 5.2.4-83 Lower Half RCC Panel 9 Out, with Vented Side Walls, Side View, Heating Rates

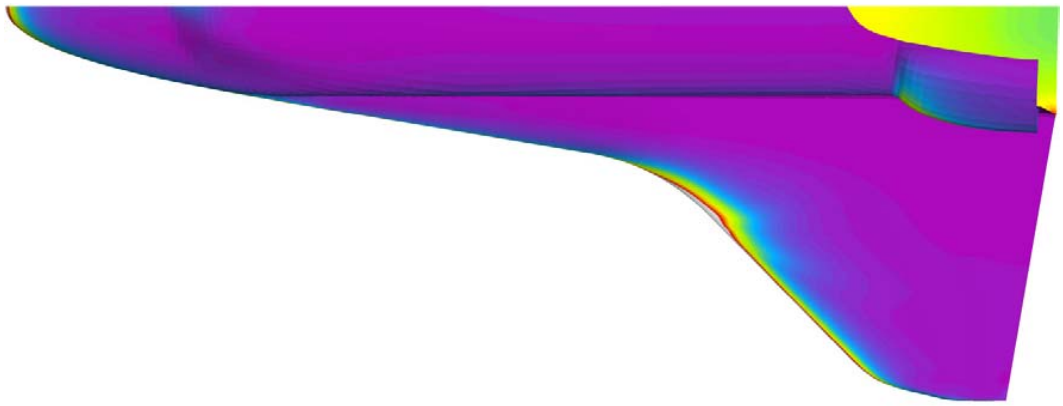

Figure 5.2.4-84 Lower Half RCC Panel 9 Out, with Vented Side Walls, Plan View, Heating Rates

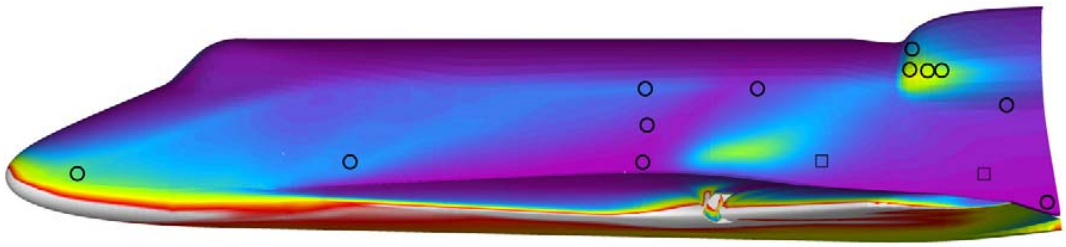

Figure 5.2.4-85 Full RCC Panel 9 Out, with Solid Side Walls, Side View, Heating Rate

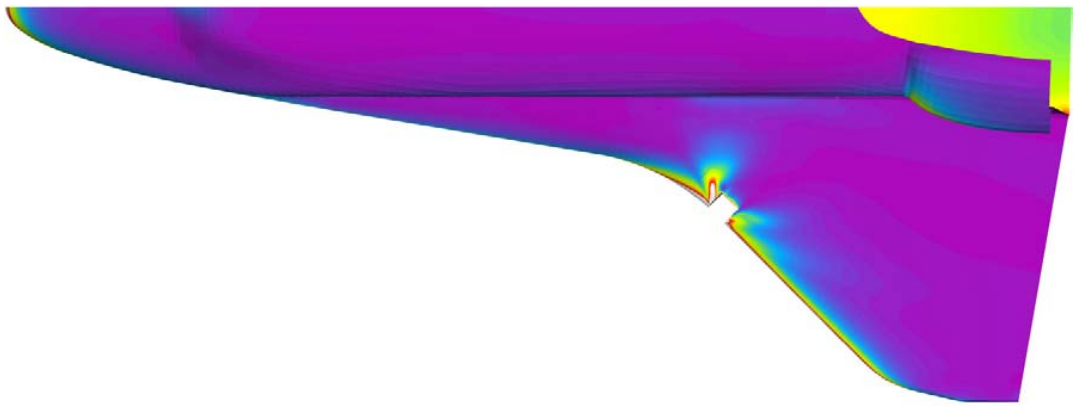

Figure 5.2.4-86 Full RCC Panel 9 Out, with Solid Side Walls, Planform View, Heating Rate

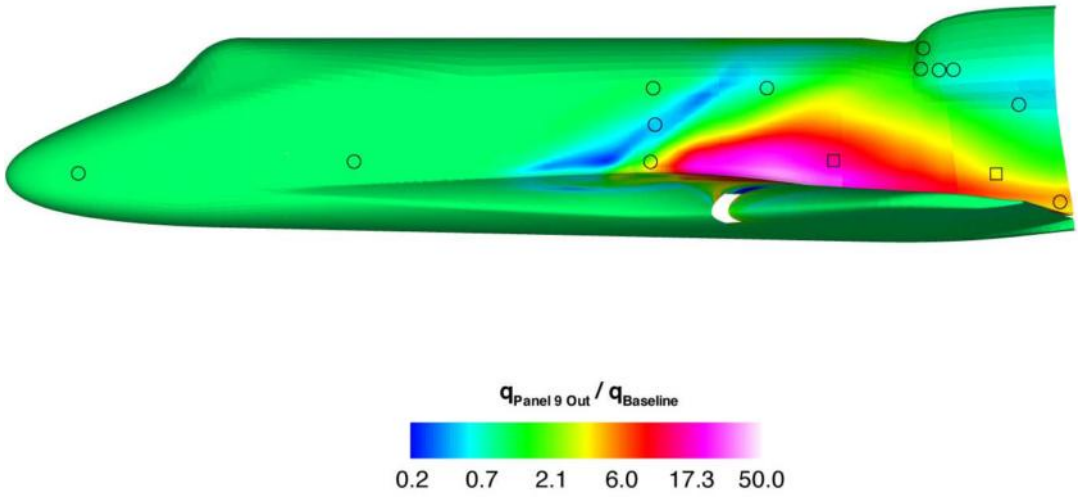

Figure 5.2.4-87 Full RCC Panel 9 Out, with Solid Side Walls, Side View, Ratio of Heat Fluxes

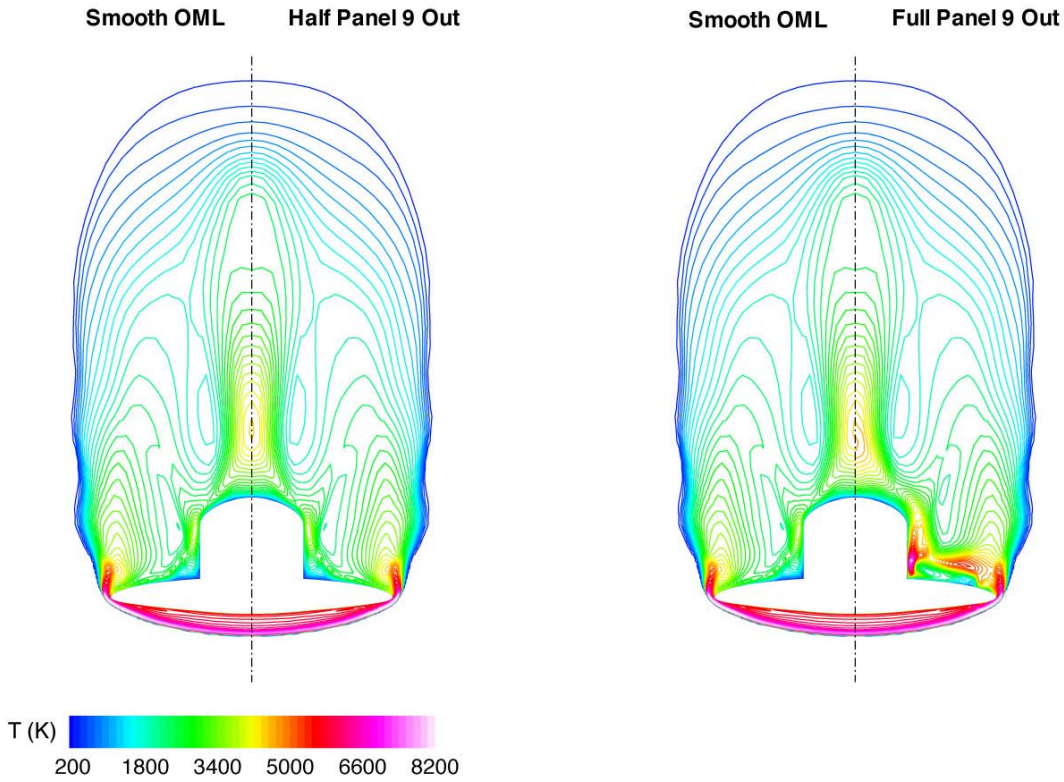

Figure 5.2.4-88 RCC Panel 9, Y-Z Solution Cut at X = 28.5 m, Temperature Contours

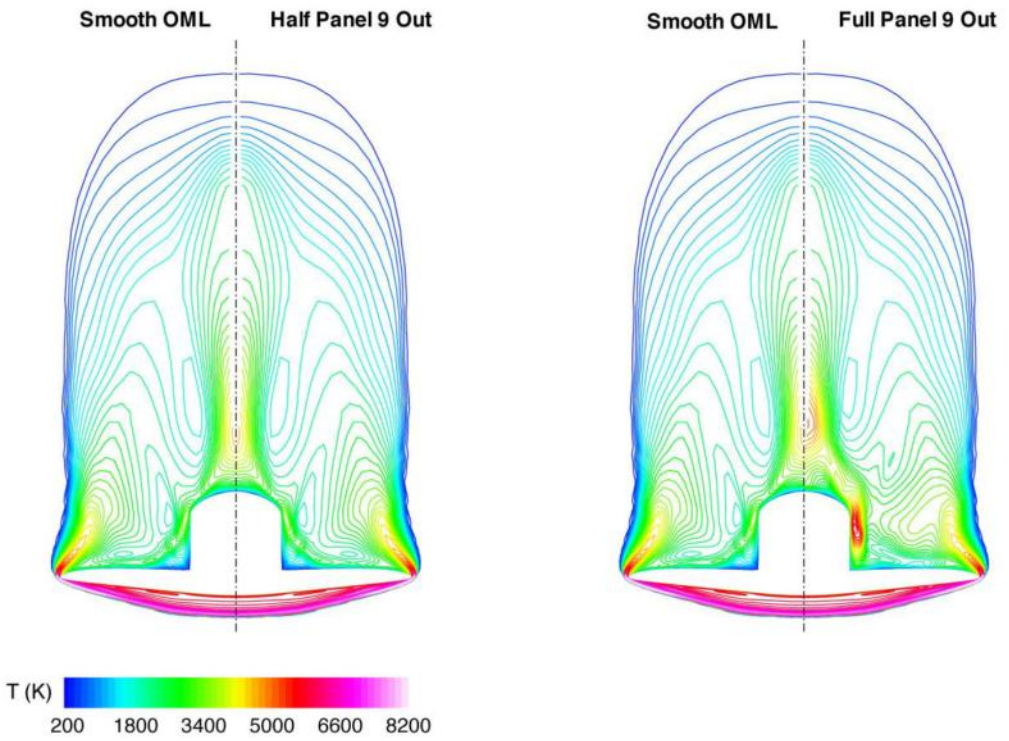

Figure 5.2.4-89 RCC Panel 9, Y-Z Solution Cut at X = 31.5 m, Temperature Contours

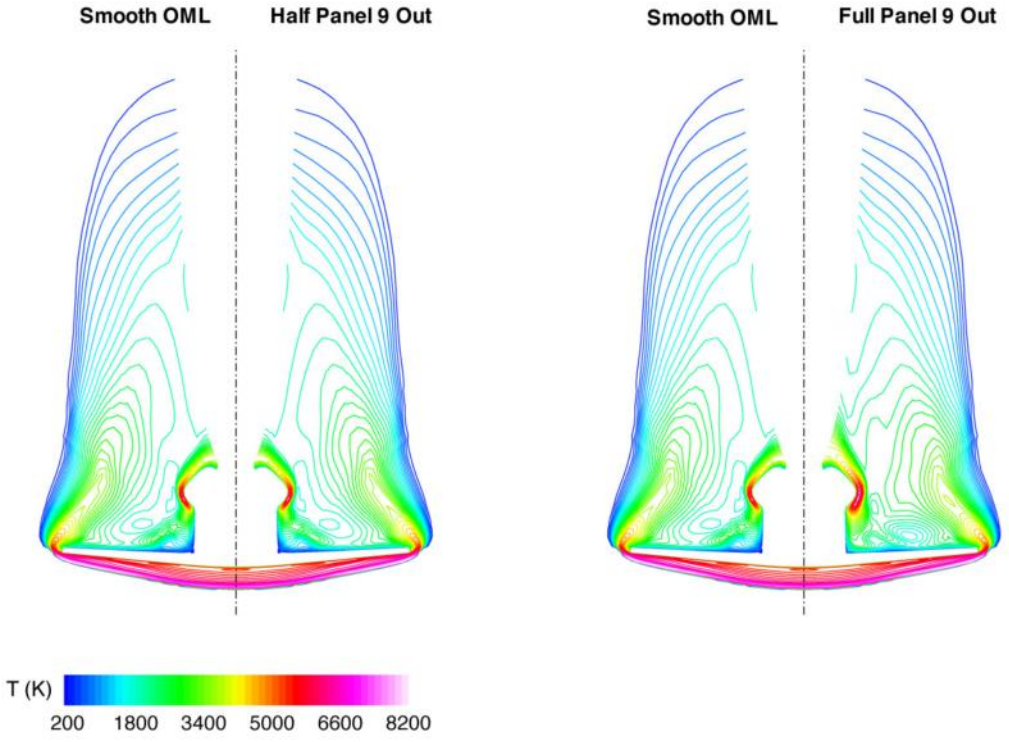

Figure 5.2.4-90 RCC Panel 9, Y-Z Solution Cut at X = 35.0 m, Temperature Contours

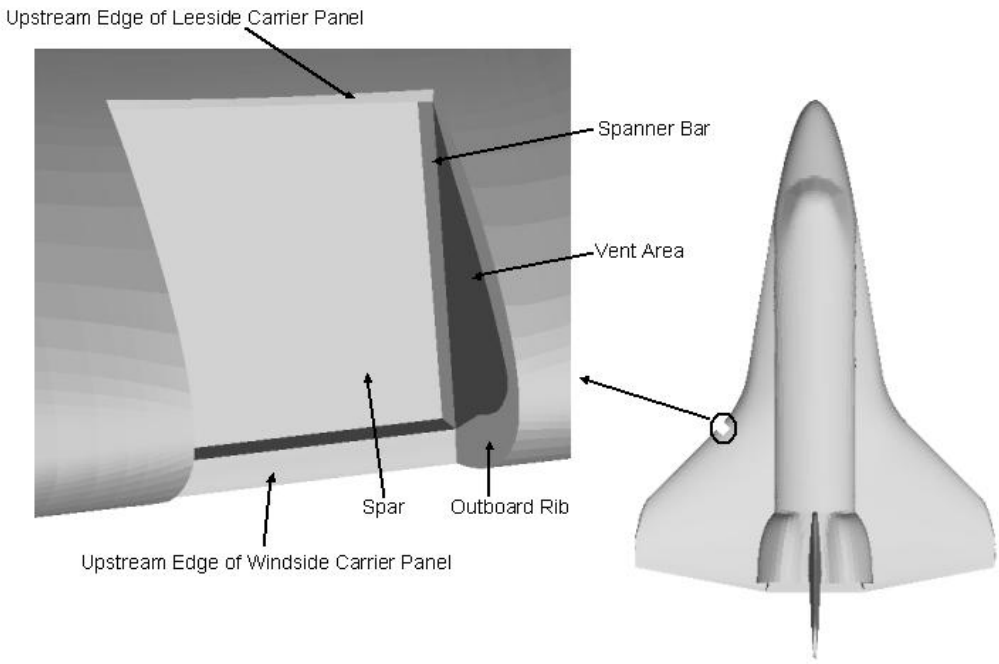

Figure 5.2.4-91 Geometry for Missing RCC Panel 9 with Venting in RCC Chamber

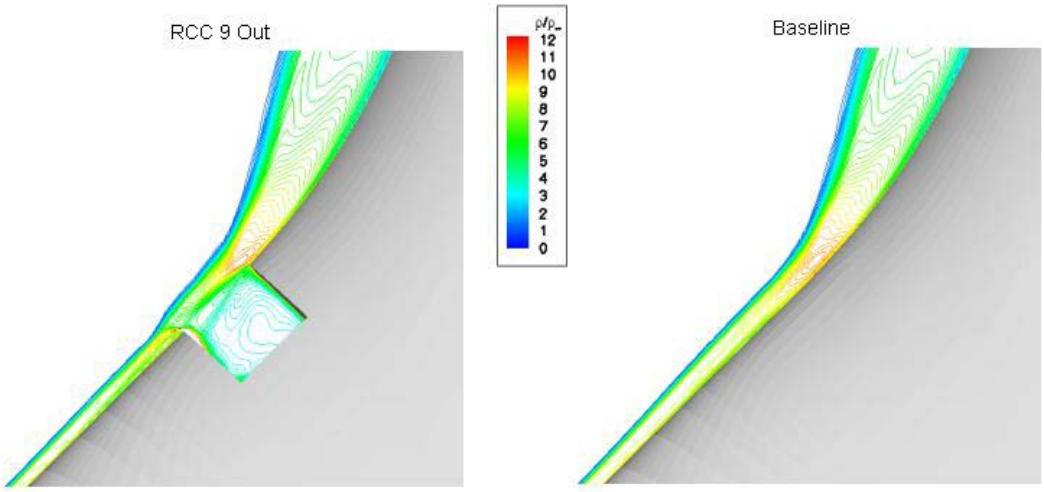

Figure 5.2.4-92 Comparison of Density Contours in Missing RCC Cavity and on Smooth OML Baseline Grid

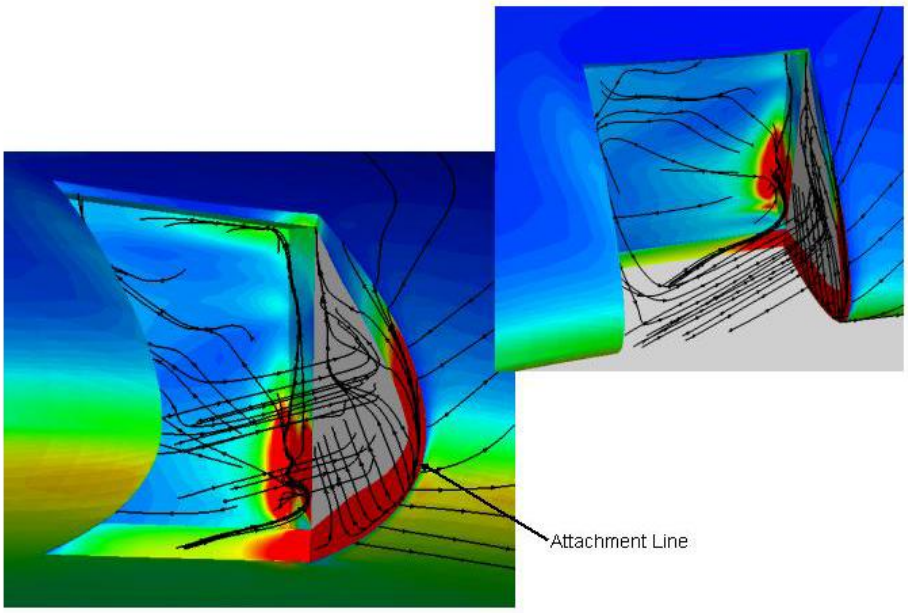

Figure 5.2.4-93 Pressure Contours, Volume Streamlines and Surface Streamlines in Vented RCC Panel 9 Cavity

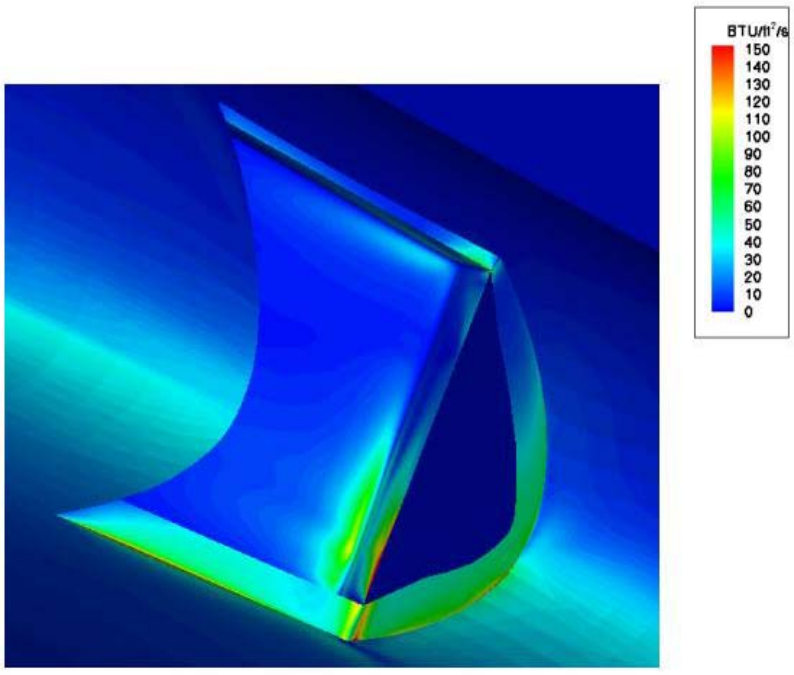

Figure 5.2.4-94 Heat Flux Contours in the Vented RCC Panel 9 Cavity

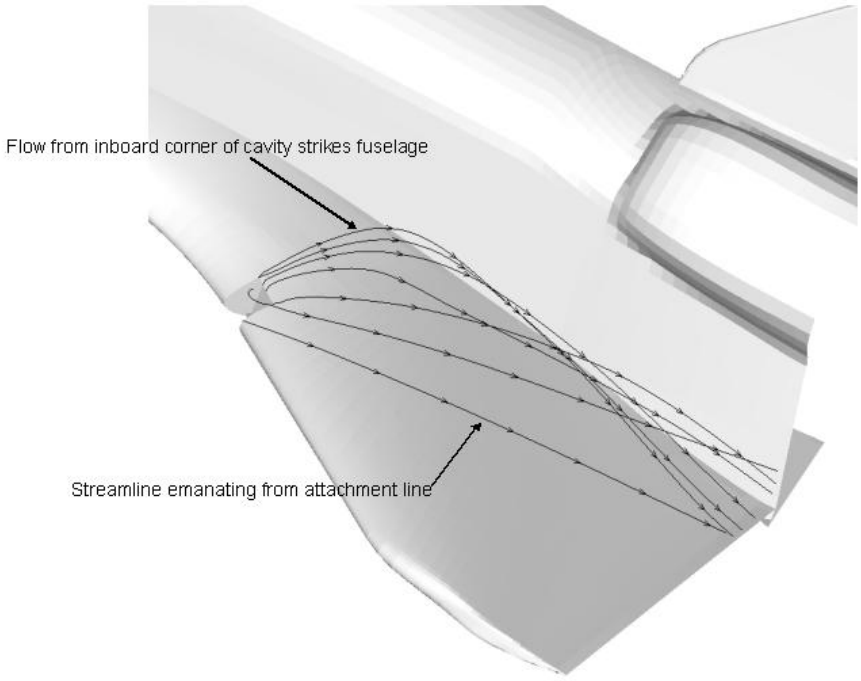

Figure 5.2.4-95 Streamlines on the Body Emanating from the RCC Panel 9 Cavity

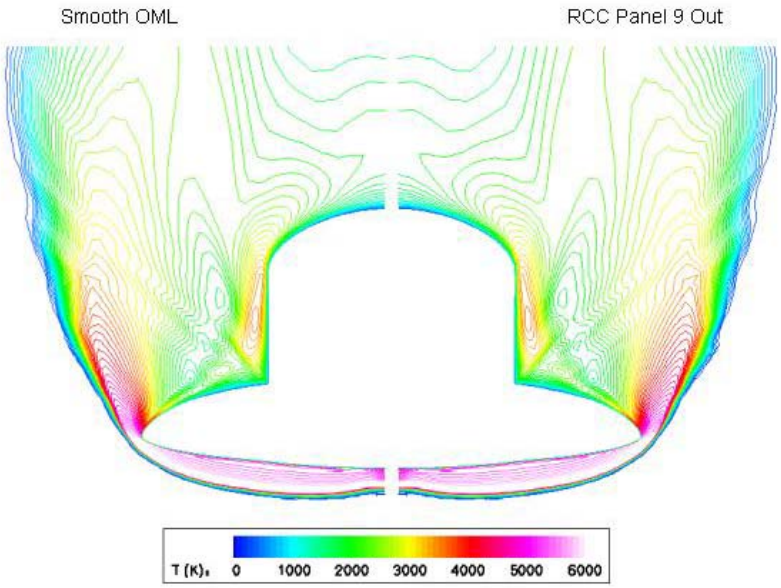

Figure 5.2.4-96 Temperature Contours at X = 1051 inches (40 inches upstream of RCC Panel 9 Cavity)

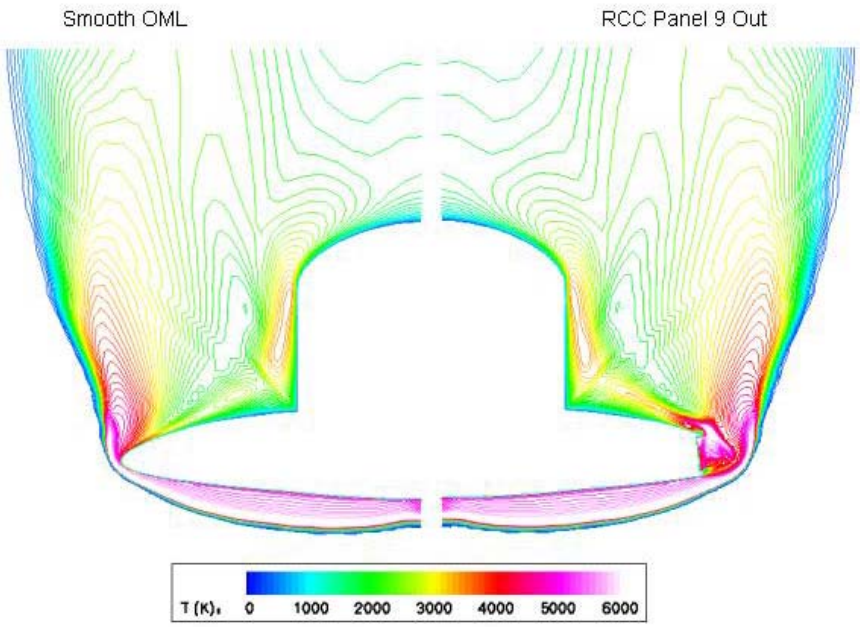

Figure 5.2.4-97 Temperature Contours at X = 1091 inches (at inboard corner of cavity)

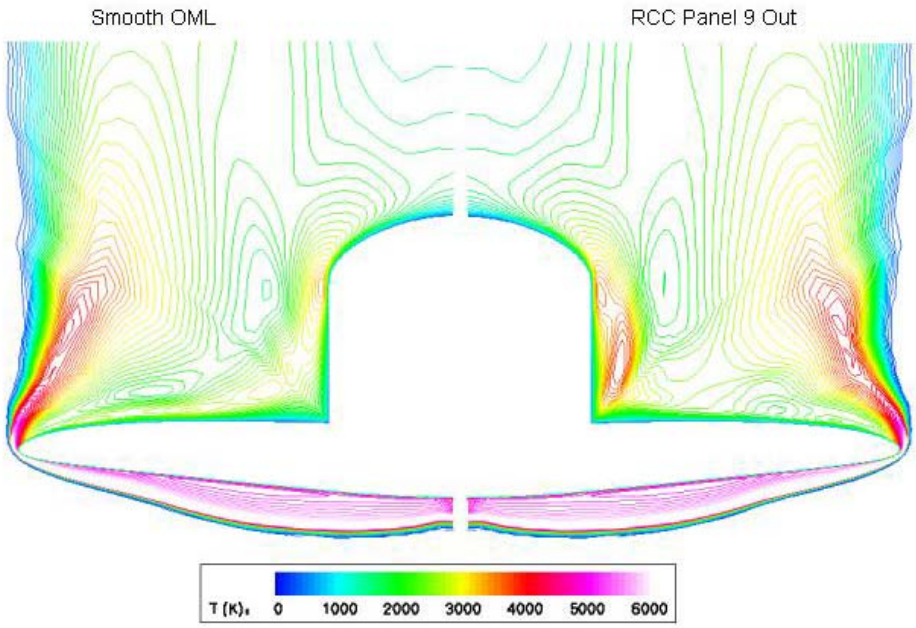

Figure 5.2.4-98 Temperature Contours at X = 1204 inches (halfway between cavity and OMS pods)

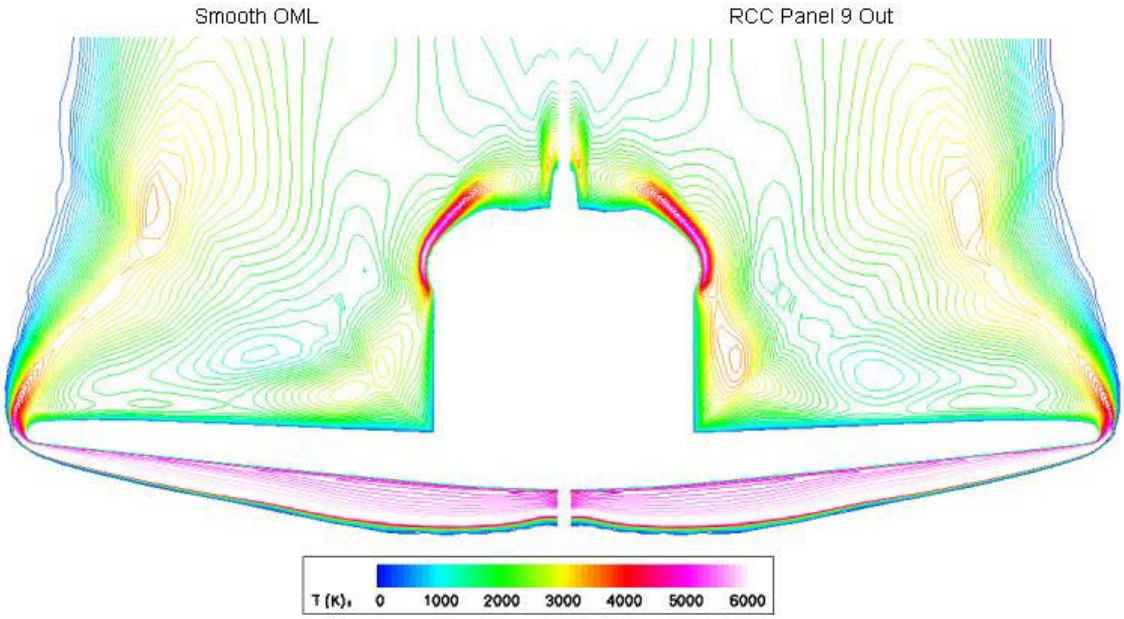

Figure 5.2.4-99 Temperature Contours at X = 1316 inches (at forward portions of OMS pods)

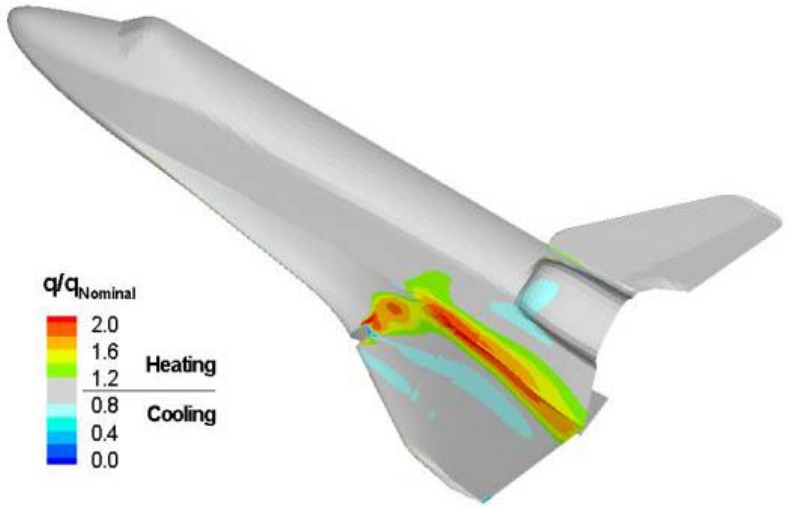

Figure 5.2.4-100 Magnification Factor for Missing RCC Panel 9 Heat Flux

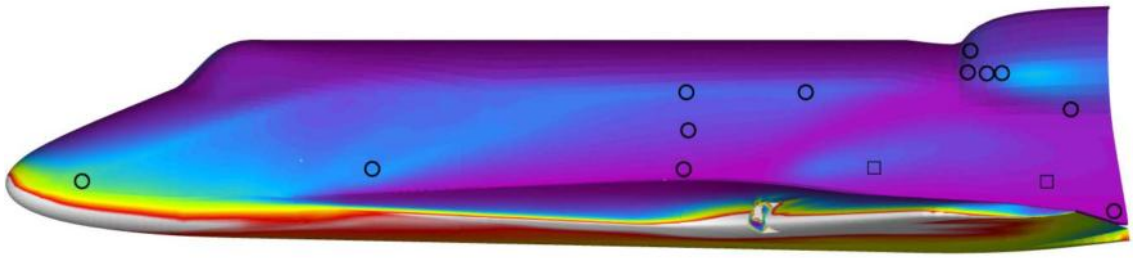

Figure 5.2.4-101 Full RCC Panel 9 Out, with Vented Side Walls, Side View, Heating Rate

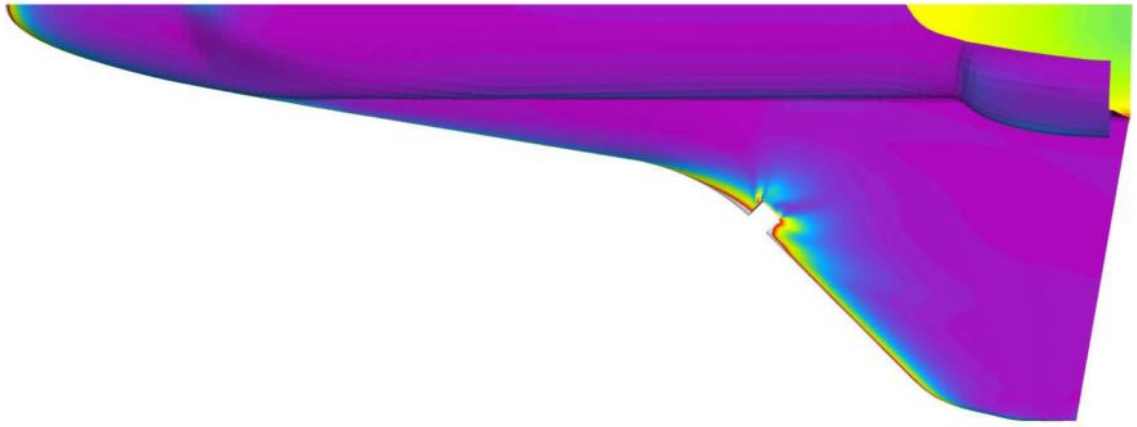

Figure 5.2.4-102 Full RCC Panel 9 Out, with Vented Side Walls, Planform View Heating Rate

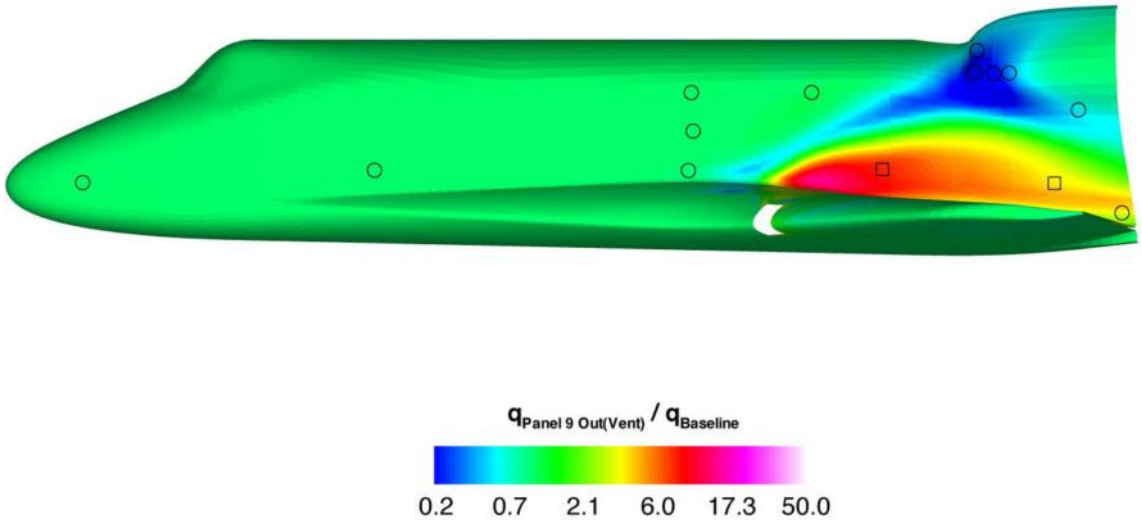

Figure 5.2.4-103 Full RCC Panel 9 Out, with Vented Side Walls, Side View, Ratio of Heat Fluxes

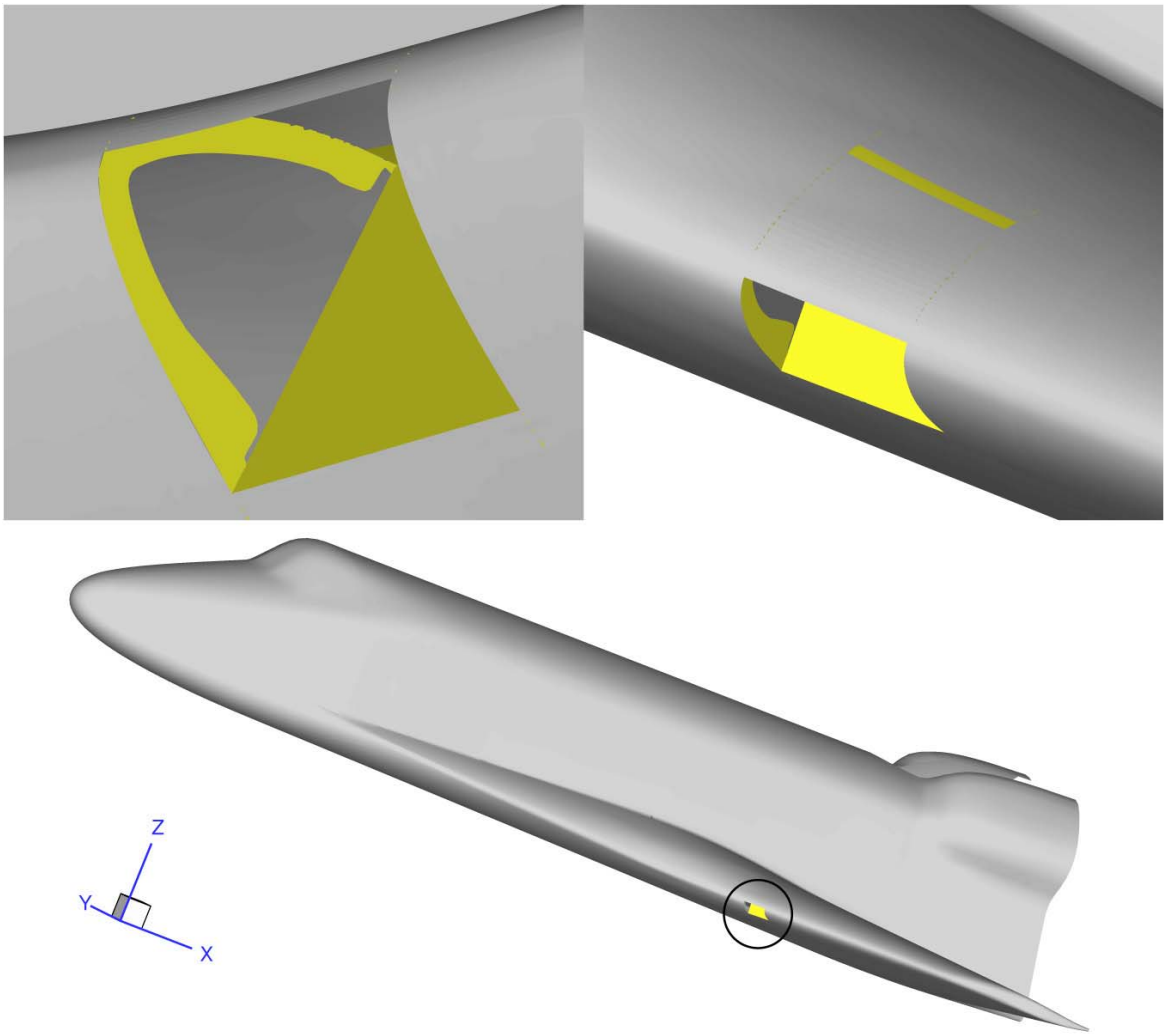

Figure 5.2.4-104 Lower Half RCC Panel 9 Out with Upper Carrier Panel Damage Geometry Used in GASP Simulations

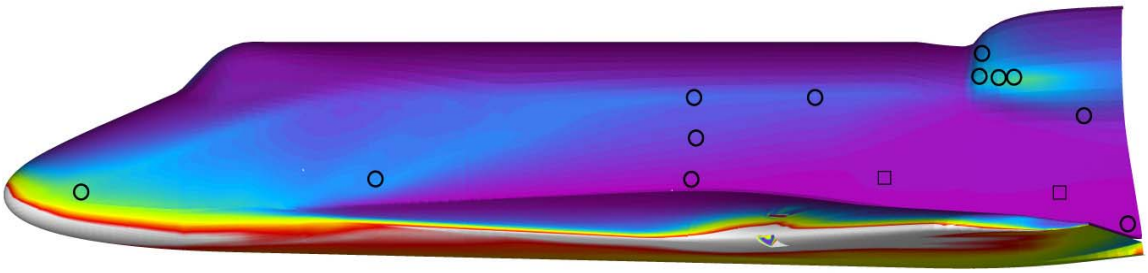

Figure 5.2.4-105 Lower Half RCC Panel 9 Out + Upper Carrier Panel 9 Out, with Vented Side Walls, Side View, Heating Rate

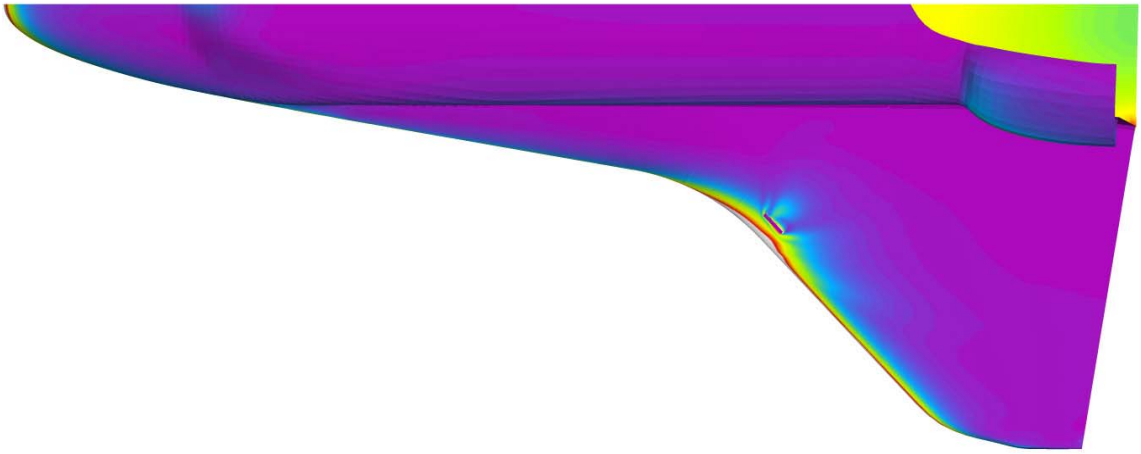

Figure 5.2.4-106 Lower Half RCC Panel 9 Out + Upper Carrier Panel 9 Out, with Vented Side Walls, Planform View, Heating Rate

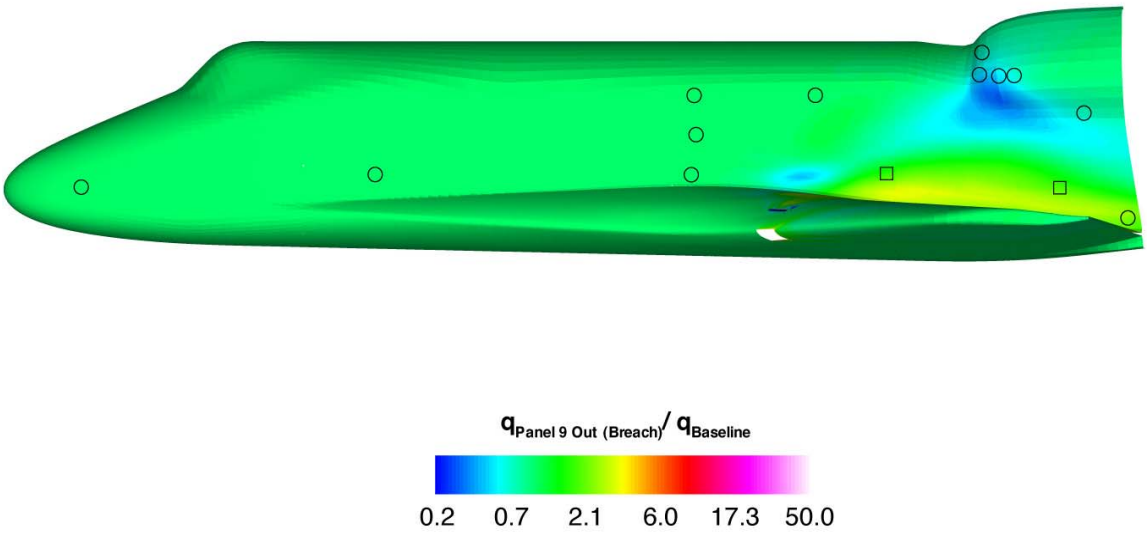

Figure 5.2.4-107 Lower Half RCC Panel 9 Out + Upper Carrier Panel 9 Out, with Vented Side Walls, Side View, Ratio of Heat Fluxes

5.2.5 Application of External Environments Data to the Working Scenario

The objective of this section is to provide a plausible explanation of the observed STS-107 flight data presented in Section 5.2.1 using the results from the various analyses and testing presented in sections 5.2.2 – 5.2.4 above or section 5.3 to follow.

5.2.5.1 Side Fuselage and OMS Pod

The decreased and increased temperature response on the side fuselage and OMS pod can be explained by the working scenario involving damage to the WLE, RCC panels 5 through 9. In Section 5.2.3, sufficient empirical evidence has been obtained to indicate that reduced heating exhibited early in flight (< EI + 480 sec) on the side fuselage and OMS pod sensors was due to changes in the leeside vortex field of the Orbiter, Figure 5.2.5-1, possibly coupled with the dynamics of flow emanating from the WLE damage which perturbs the WLE separation zone. For this reduced heating segment of the flight the most consistent result that matched the flight data was obtained by a case where there was flow through degraded RCC WLE cavity vents, Figure 5.2.3-22 through Figure 5.2.3-24. During this period of the flight, changes in the vortex field were likely caused by additional gas entering the leeside flow field through the vents designed into the upper RCC panel and T-seals, and in possible combination with small local upper carrier panel damage. The correlation of the vented flow to the lee side with flight data necessitates that there was a windside breach along the WLE in order to have the pressure necessary to drive the flow to the leeside with sufficient momentum. The momentum scaling, typically used for flows injected into a cross flow, was used to verify that a proper simulation of the flight environment was being performed and checked against various WLE breach CFD simulations, Figure 5.2.3-23. However, the slot in the wind tunnel model was an order of magnitude larger (1” width full scale, as opposed to 0.1” width full scale) than for the nominal Obiter WLE vent configuration. Therefore, local small damage to the vent area, which could easily occure where the RCC and upper carrier panels meet, has to be present to yield these leeside heating effects. The need for additional vent area was also confirmed using a coupled venting and thermal math model of the wing, Section 5.3.5, for a 10” diameter hole in the windward side of RCC panel 8. For this analysis, the hole existed at EI and the simulation was terminated at the estimated latest point of spar breach, Figure 5.2.5-2. Although mass flow rate is presented, the trend would be similar for momentum. The momentum scaling ratio is on the order of 0.6 from the coupled venting and thermal model. Venting of the RCC WLE cavity with a breach begins to increase significantly at the time the decreased temperature response is recorded on the Orbiter leeside instrumentation. However, the momentum ratio scaling parameter and the information from the wind tunnel tests and venting analyses allow the conclusion to be made, that the mass flow rates, and thus the momentum rates, out of the nominal 66 square inch leeside vent area would be too small to result in the initial side fuselage and OMS pod disturbance. Thus, before either the spar is breached or additional significant damage to the upper carrier panel occurs, the flow entering the WLE from the windward side was exiting through the leeside vents with locally damaged upper carrier panel(s), Figure 5.2.3-24.

The increase in side fuselage and OMS pod heating that occurred later in flight (> EI + 480 sec) can be explained by progressively worsening damage to the upper portion of the RCC panel, upper carrier, and eventually the upper wing skin. Although the increased side fuselage and OMS pod heating began as early as EI+510 seconds, significant changes in the off-nominal leeside temperature response can be attributed to the observed debris events. For instance, debris # 5 (considered to be more of a flash event than a debris event, as a result of ballistic coefficient and luminosity analyses) is closely tied to changes in the temperature response of gauges V07T9220, V07T9976, and V07T9978, Figure 5.2.1-6. Likewise, flash event 1/debris # 6 can be related to significant changes in slopes for gauges V07T9253 and V07T9925, Figure 5.2.1-5. It is important to note that debris # 5 is also closely correlated to the slope change in the delta rolling moment, discussed in Section 4. Therefore, significant changes in the increased heating signatures can be correlated to the observed debris events, which imply progressively worsening damage on the Orbiter.

During the increased heating period, the actual Orbiter configuration remains unknown; thus, multiple leading edge damage geometries, full and half panels, missing T-seal 8, and holes through the wing were evaluated in both the Mach 6 Air and CF_4 facilities. This information has been used to determine the

effect on side fuselage and OMS pod heating of different types of damage, Section 5.2.3. Since holes through the wing showed no evidence of sidewall and OMS pods heating augmentation, the focus turned towards some form of leading edge damage. Leading edge damage is required in order to provide the energy and pressure necessary to affect the leeside flow field. As can be seen in Figure 5.2.3-8 and Figure 5.2.3-16, the results from the Mach 6 air and CF_4 facilities show significant side fuselage and OMS pod disturbances for full RCC panel out cases 5 through 9 (Working Scenario). Overlaid on these figures are the MADS and OI measurement locations. As shown, the impingement footprint is dependent on the removed panel location and the facility. It was noted in the Mach 6 air results for panels 5 through 8 that although increased heating was indicated on the side fuselage, decreased heating was observed on the OMS pod. This combination is inconsistent with the flight data. However, when panel 9 was removed the results in the air facility were more consistent with the flight data. The results for the CF_4 facility showed that increased OMS pod heating was observed for all of the removed RCC panel cases. Setting aside the differences between the two facilities, there is substantial evidence that a damaged WLE will result in increased heating to the side fuselage and OMS pod. The testing results showed heating augmentation factors of from 2 to 10, whereas flight data indicated factors of 1.7 to 5.2 for the MADS data and up to 13 times for the OI V34T1106A gauge (Section 6).

However, the debris evidence indicates that most of the RCC panels were recovered with the exception of a majority of panel 9 and a large segment of panel 10. In addition, all the recovered RCC panel debris was found in Texas. It is believed that having substantial portions of the RCC missing as early as EI+510 seconds is not consistent with the vehicle flying all the way to Texas airspace. It is noted that the debris contains only a single interior tile for upper carrier panel 8 and that neither of upper carrier panels 9 and 10 was recovered. This lack of debris along with the above discussion on the reduced heating provides a consistent explanation for the initial cause of increased heating on the side fuselage and OMS pod. The explanation is that damage to the upper carrier panels became severe enough to allow substantial flow through the WLE vents, with at least a compromised vent path geometry. In order to demonstrate this, a half RCC panel 9 removed model configuration was modified to include the upper carrier panel missing. This geometry allows WLE damage to provide gas flow through the WLE and out the leeside venting location. The results of that wind tunnel test, shown in Section 4.3.1, indicated similar heating trends as the full panel out case.

As was stated above, a compromised upper surface geometry coupled with windward RCC damage was the most likely cause for the initial increased heating. Note that during this time the spar had already been breached and that significant damage was occurring to the wiring instrumentation along the spar and the wheel well. The analysis shown in the next section and the related results discussed in Section 6 will indicate that damage was also occurring to the intermediate wing structure. Since debris event 5 (flash 0) and flash event 1 / debris event 6 closely tie to changes in the side fuselage and OMS pod temperatures as well as the vehicle aerodynamics, it could be postulated that they are indications of upper wing skin breach in the intermediate wing area. The flash events are believed to be the release of small high temperature particles which rapidly decelerate in the Orbiter wake, as concluded from a ballistic coefficient. These particles, as will be shown, could have been combusting aluminum present in the intermediate wing interior, which was then vented to the exterior when the upper wing was breached.

A final question, that of determining which facility provides the more appropriate simulation of the Orbiter leeside flight environment for a damage configuration, may be addressed computationally Extensive aero/aerothermal calculations for the Orbiter with missing half and full RCC panels 6 and 9 were performed at CFD Case # 1 flight condition. Both the half panel out cases showed similar results to the wind tunnel in that no significant heating augmentation could be seen on the side fuselage and OMS Pod, although local disturbances do occur on the leeside of the WLE very near the damage location. The full RCC panel out cases with solid sidewall boundaries also showed side fuselage and OMS pod effects comparable to the wind tunnel results, and tend to favor the CF_4 measurements. However, because of uncertainties in grid resolution requirements and the physical modeling assumptions needed to simulate the leeside flow field accurately, it remains a judgment as to whether or not CFD solutions can be used to differentiate which facility best represents the Orbiter flight environment.

5.2.5.2 Wing Surface T/C V07T9666A

The response of V07T9666A is closely related to the events on the side fuselage and OMS Pod. As mentioned previously, the off-nominal trend for this T/C does not begin until after the indications of reduced side fuselage and OMS pod heating, off-nominal response of the spar temperature and strain gauge at RCC panel 9, and off-nominal clevis temperature response at the RCC panel 9/10 interface. There are two possible explanations for the V07T9666A measurement response. The first possibility is that an external flow disturbance caused by the damage site on the WLE propagated downstream to the measurement location via boundary layer transition. The second possibility is that disturbed flow came out of the WLE damage back onto the windward surface as a result of high temperature gas ingestion into the WLE cavity.

For the first possibility, a boundary layer transition analysis of the Orbiter near this point of the flight was performed. Figure 5.2.5-5 indicates that it would require a trip height of between 1.2" and 1.4" to result in an effective transition trip (see Appendix 5.6 for more information on effective trip calculation). At EI+370, the free stream Reynolds number for the Orbiter, presented in Figure 5.2.5-3, is approximately 5.0×10^5. Given a large enough damage site, a boundary layer disturbance could propagate downstream. No correlation is presented between the effectiveness of a protuberance versus that of a cavity, but a cavity would be more representative of a damaged WLE. However, protuberances are typically more effective at promoting boundary layer transition. For example, Figure 5.2.5-4 shows the limited downstream effect of a 6" diameter hole on the windward side of RCC panel 6. However, it will be shown that the damage necessary to cause the Columbia accident has been narrowed down to either a significant portion of a T-Seal, or RCC acreage damage on the order of 30 to 80 square inches. Moreover, this size of damage would be large enough to result in a locally disturbed flow extending from the damage site to this region of the wing given a high enough Reynolds number. Figure 5.2.5-6 presents a surface streamline plot of the Orbiter WLE region showing how the flow passes over the vehicle at EI+404 seconds. Since the working scenario addresses damage to the WLE in the area of RCC panels 5 through 9, this damage zone propagates streamwise effects which would pass over this gauge.

For the second possibility, the debris along with the above mentioned flight data provide a supporting rationale for the off-nominal temperature responses. As was noted, heating was already occurring in the WLE cavity at the time of leeside surface heating excursions. Therefore, flow was entering the cavity and exiting the WLE vent system (nominal configuration or damaged) prior to EI+370. Close inspection and reassembly of the debris in the RCC panel 8 and 9 area, Figure 5.2.5-7, indicated that flow out of the WLE cavity from a manufactured slot at the back corner of RCC panel 8 did occur. This flow is evidenced as well by the erosion on the RCC panel 9 lower carrier panel tiles. The answer for how flow can exit the WLE cavity to the lower surface of the wing is that the interior of the WLE cavity must be at a higher pressure than the local external pressure. At the high angle of attack during entry, the local pressure on the lower surface of the wing beyond the leading edge is approximately equal to the free stream dynamic pressure. In order to determine the relative pressure of the two regions given a damaged WLE condition, a coupled external / internal CFD of the Orbiter must be performed. This issue will be addressed in the section on internal aeroheating environments.

5.2.5.3 Chin Panel and Vacuum Vent / Water Supply Dump Nozzles

A possible explanation for the temperature responses of the chin panel and vacuum vent/water supply dump nozzles in flight is that a local disturbance to the flow, such as a protrusion, could have existed which then burned away over the period of time in question. For the chin panel gauge, the protrusion itself would have to be the gap between the nose cap and chin panel, exactly where the expansion seal resides. Preflight inspection of the gap, (see Boeing TM, ATA-TM-02-0009) indicated a small excursion of 0.002" beyond the equivalent roughness requirement of 0.120" just left of the vehicle centerline. Again referring to Figure 5.2.5-5, boundary layer transition analysis of the Orbiter at this point of the flight indicates that it would require a trip height of between 1" and 1.4" to result in an effective transition trip. Also, this trip had to be located at or outside the attachment line streamline such that the disturbance in the flow was swept overboard, because no disturbance was observed on any of the windward fuselage T/Cs downstream from the nose cap, see
Figure 5.2.5-8. Therefore, from an aerothermodynamic perspective, the response of the chin panel expansion seal gauge cannot be readily explained. Adding to that, as will be discussed in Section 6, is

the fact that the temperature response of the expansion seal gauge is non-physical with respect to how it recovers to the original slope of the curve.

For the vacuum vent and water supply dump nozzles, two possible explanations for the transient were proposed and investigated: (1) change in the vehicle orientation, and (2) a local flow disturbance just upstream from the two nozzles that flows along the same streamline. The nozzles are right above the beginning of the wing glove (forward wing extension). At this location the flow wraps around the chine of the wing glove, forming a vortex. This vortex is the source for the nominal heating in this region, Figure 5.2.5-9. Where the vortex scrubs the surface there is higher heating than where it does not; this can be seen in Figure 5.2.5-10. The location of this vortex is a function of the angle of attack and angle of sideslip, shown in Figure 5.2.5-11 and Figure 5.2.5-12, respectively. The variation in the angle of attack during this period is negligible with respect to the variation of the aeroheating environment. The variation of the angle of sideslip, although small, was investigated as a potential source for the off nominal events. As was seen in the aerodynamics section, this variation of sideslip was not outside previous flight experience of the Orbiter during this portion of the re-entry. CFD analysis of the Orbiter forebody showed insignificant changes in the heating due to variations in sideslip from 0 to –0.5 degrees.

From a local flow disturbance perspective, as can be seen in
Figure 5.2.5-9, the flow crossing both the vacuum vent nozzle and the water supply dump nozzle would also cross V07T9522, a surface T/C. Any disturbance strong enough to cause a change in the heating of the nozzle should have also disturbed the heating to this surface T/C. As was indicated previously, the only anomaly seen on this gauge is a sharp drop in temperature for one cycle during this time; otherwise, the response was determined to be nominal. Thus, again, from an aerothermodynamics perspective, the responses of the vent nozzle and water supply dump nozzle cannot be readily explained. Therefore, both the off-nominal events related to the chin panel and these nozzles should be listed as unexplained anomalies (UA).

5.2.5.4 Kirtland Photo

As was shown in Section 5.2.4, no dramatic changes to the windward and leading edge shock shapes could be discerned from the CFD solutions with RCC panel 6 or panel 9 removed. However, the source of the bulge in the light from the leading edge could have been either from embedded shocks in the damage zones or from additional particulates in the flow field as the damage progressed, or a combination thereof. No supporting evidence for the proposed particulate explanation exists. For the proposed imbedded shock explanation, Figure 5.2.5-13 is an example of the resultant embedded shocks due to WLE damage. The additional shocks would likely re-excite the N_2 first mode, which is the principle light source in the shock layer immediately around the vehicle. However, this explanation remains speculation, and thus there is no substantial evidence that can explain the Kirtland photo.

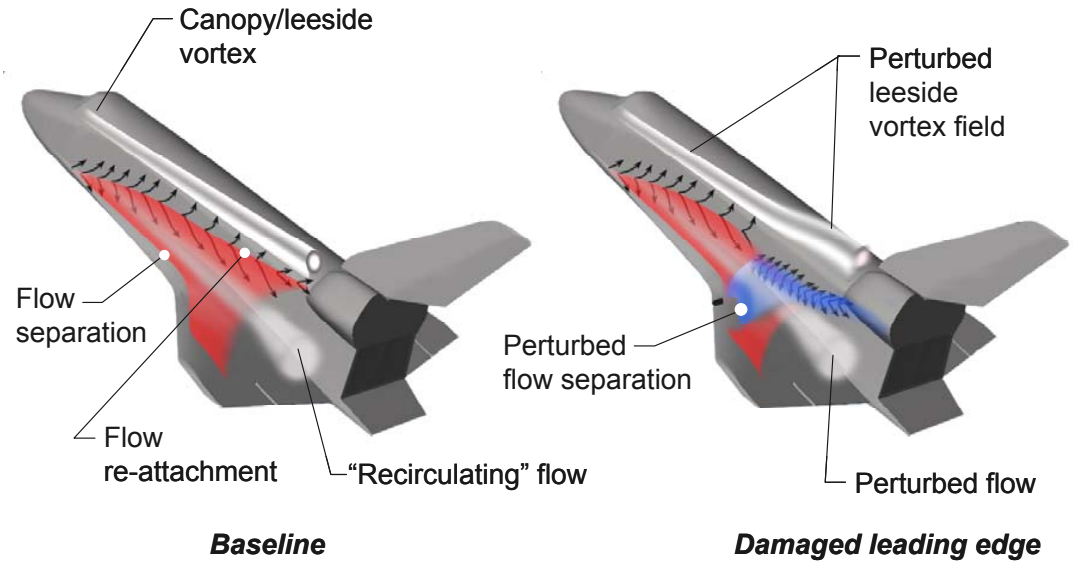

Figure 5.2.5-1 Postulated Orbiter Leeside Flowfield Associated With Wing Leading Edge Damage. Wing leading edge damage perturbs leeward flow separation and re-attachment locations as well as leeward embedded shocks (not shown).

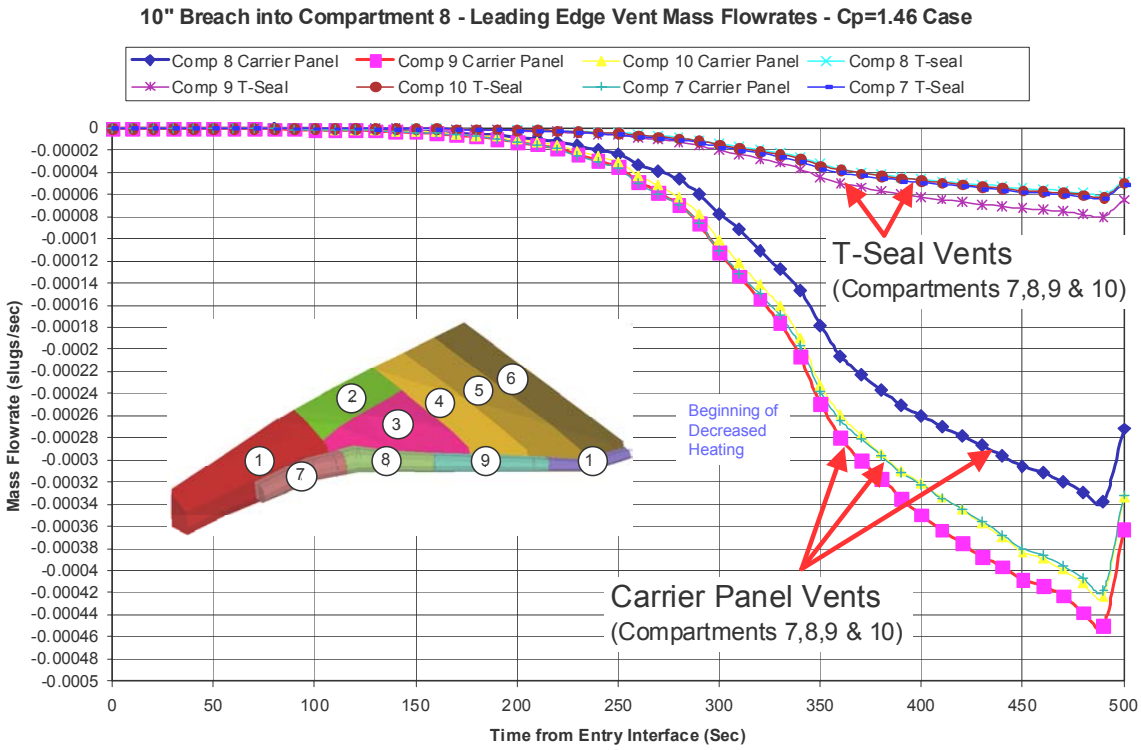

Figure 5.2.5-2 Leading Edge Vent Mass Flow-rate Summary - 10" Breach Cp=1.46. Results from MSFC-developed coupled venting and thermal wing model.

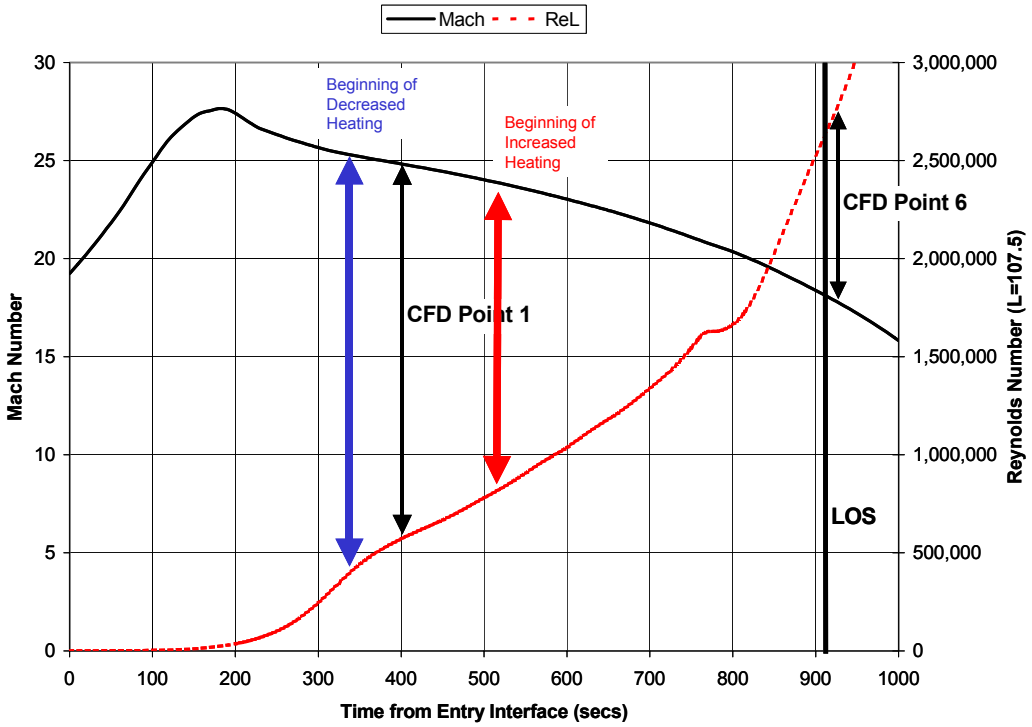

Figure 5.2.5-3 STS-107 entry trajectory, Mach No. and Reynolds No. from entry interface

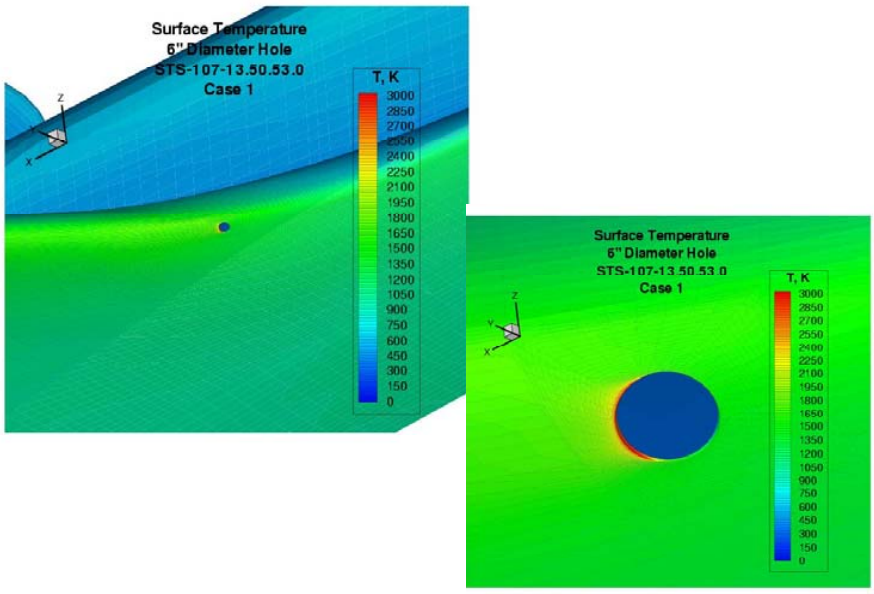

Figure 5.2.5-4 NASA LaRC LAURA CFD solution of a 6" hole on the windward side of Panel 6. Note the limited downstream disturbance of the flow.

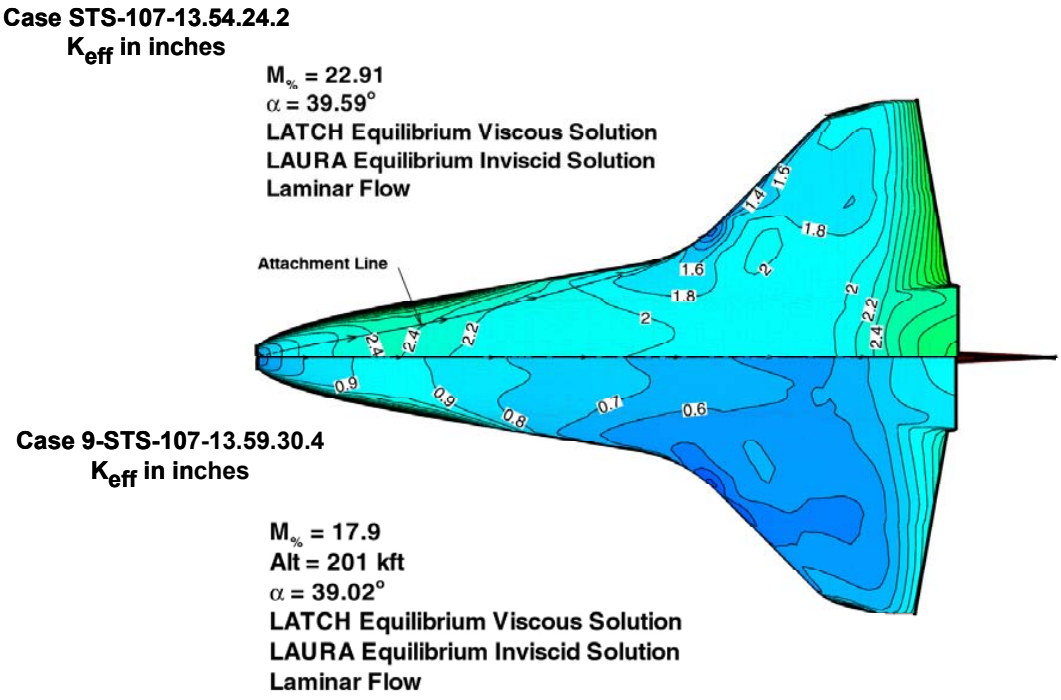

Figure 5.2.5-5 Effective Roughness Height for Transition

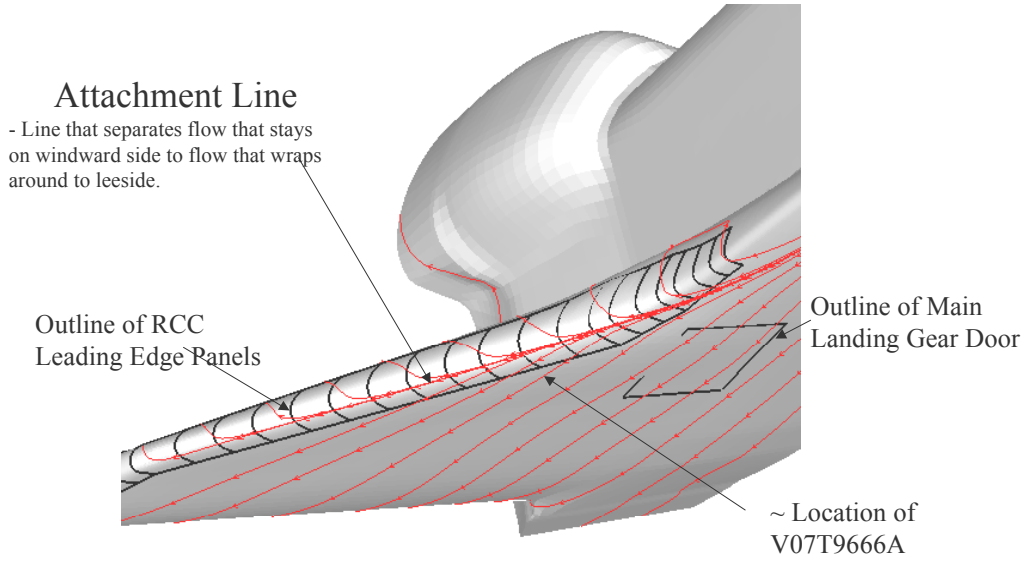

Figure 5.2.5-6 Orbiter surface streamlines. CFD Point 1, EI+404, Mach 24.9, 243 kft.

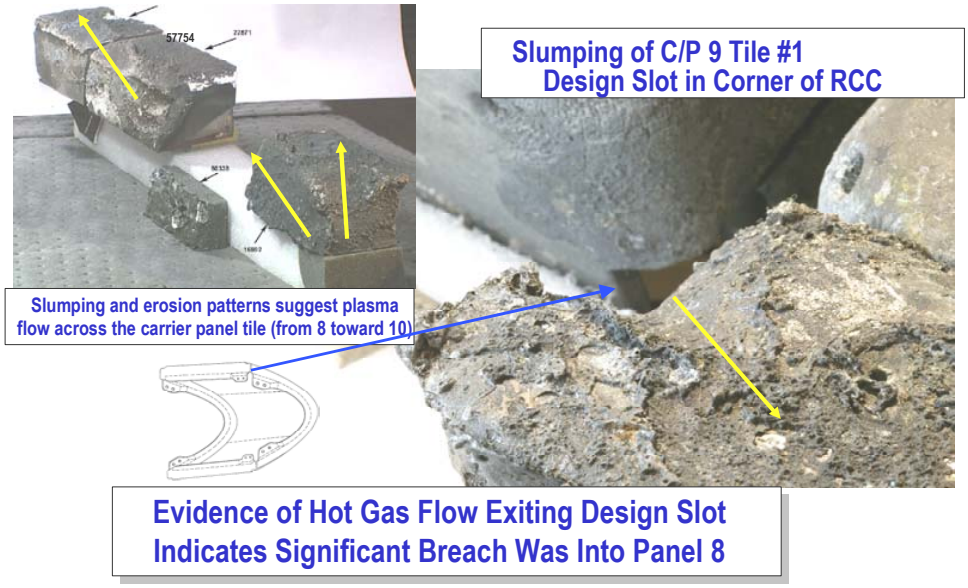

Figure 5.2.5-7 Hardware Forensics Team reassembly of RCC Panel 8 with RCC Panel 9 Lower Carrier Panel Tiles. April 28, 2003 presentation to the OVEWG.

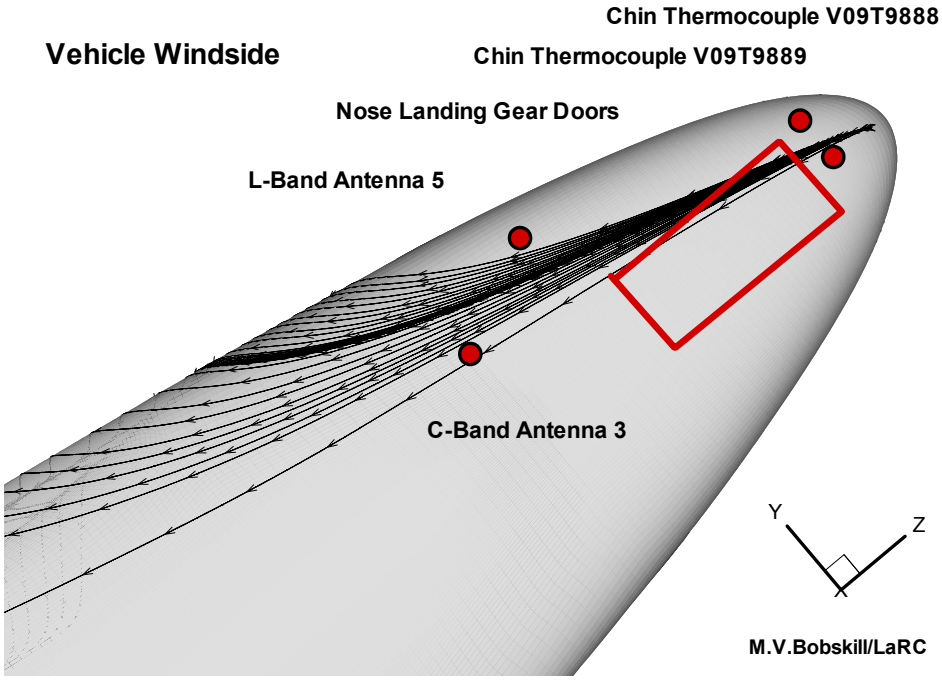

Figure 5.2.5-8 Orbiter surface streamlines crossing chin panel region.LaRC LAURA solution of CFD Case #1. CFD solution is of right side when angle of sideslip equals 0. Chin Panel gauges are in the correct relative position.

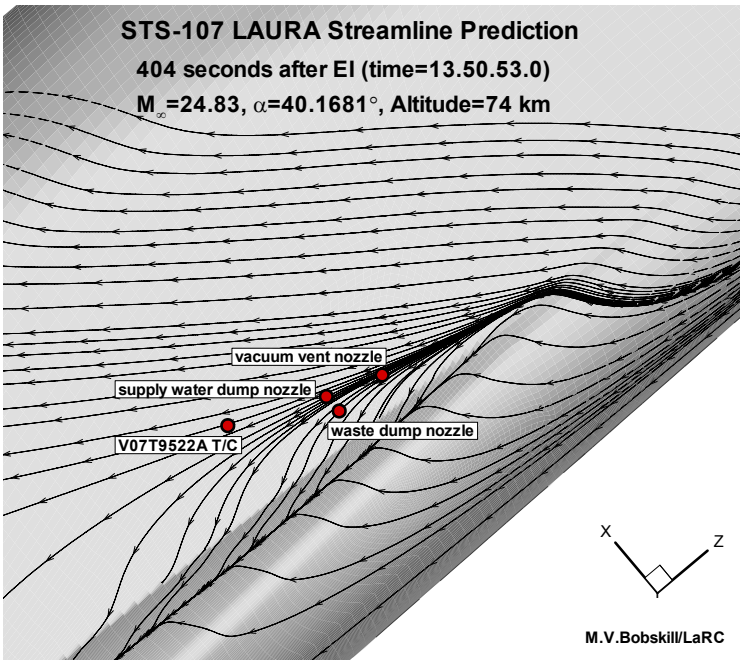

Figure 5.2.5-9 Orbiter surface streamlines in vent nozzle region. CFD solution is of right side when angle of sideslip equals 0. Nozzles are in the correct relative position.

.

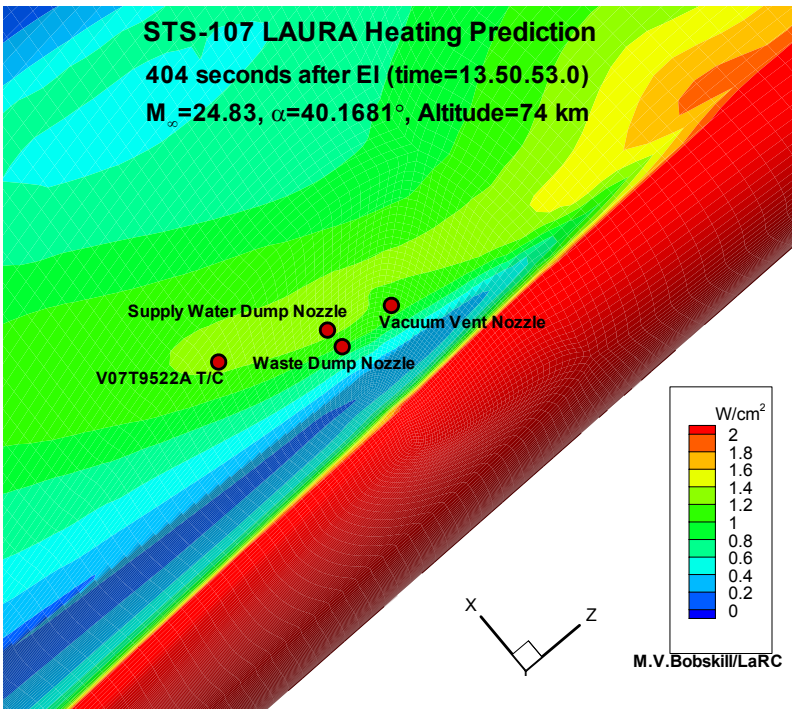

Figure 5.2.5-10 Orbiter surface heating in vent nozzle region. Note CFD solution is of right side when angle of sideslip = 0 deg. Nozzles are in the correct relative position.

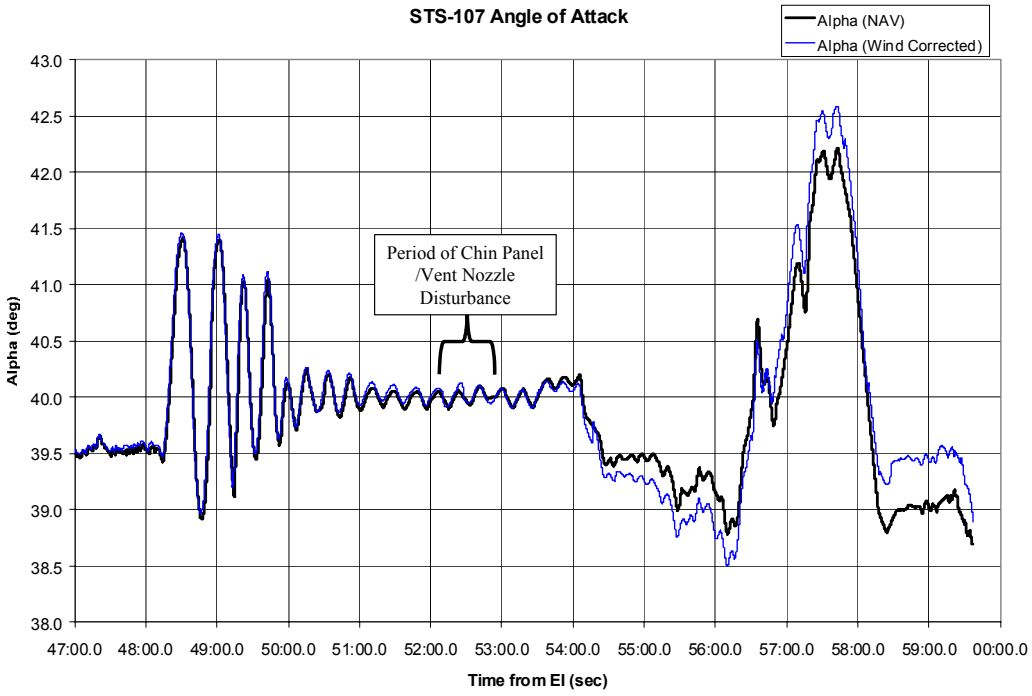

Figure 5.2.5-11 STS-107 Angle of Attack History with and without modeled winds. See Section 4.0 for further detail on model wind effects.

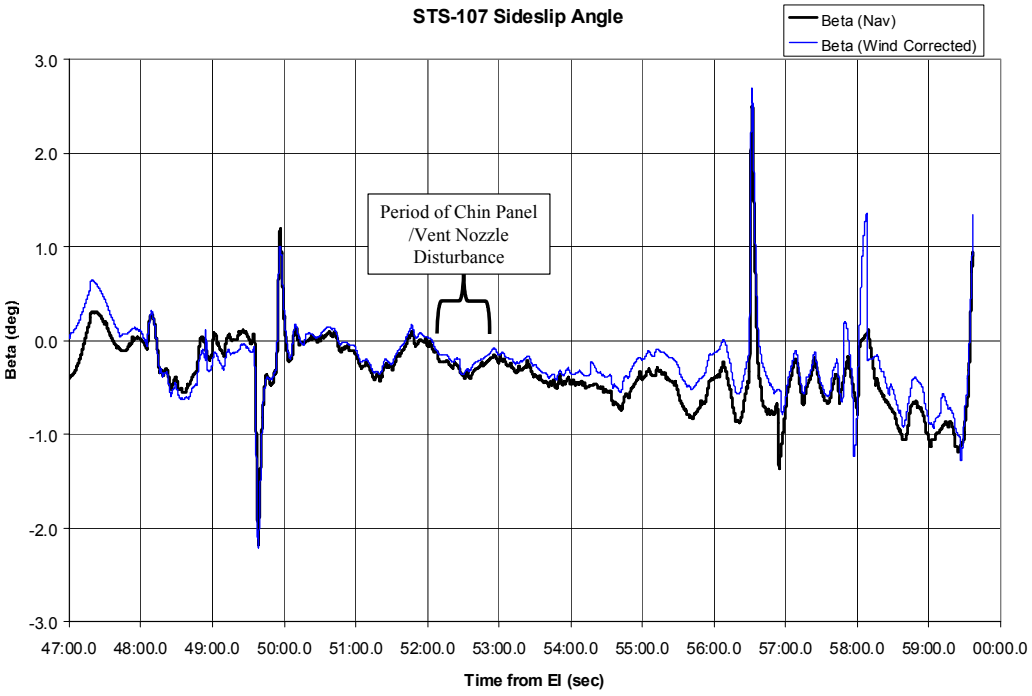

Figure 5.2.5-12 STS-107 Angle of Sideslip History with and without modeled winds. See Section 4.0 for further detail on model wind effects.

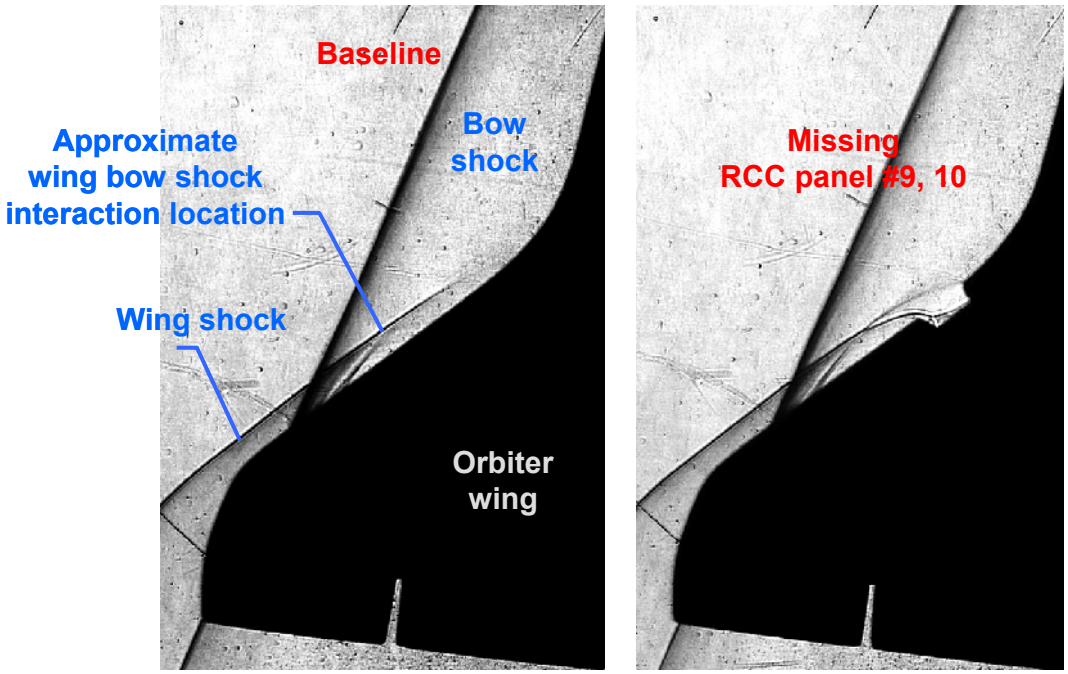

Figure 5.2.5-13 An example of imbedded shocks along the wing leading edge as a result of wing damage. Schlieren images taken in the LaRC Mach 6 Air facility. Note, shock locations are freestream Mach No. dependent.

5.3 Damaged Orbiter Internal Aerothermodynamic Environments

This section of the report details Internal Aerothermodynamic team activities contributing to the STS107-investigation working scenario. Internal environment team members focused on the analysis, investigation, prediction, and understanding of the complex, high temperature gas dynamics environment within the Orbiter wing following a breach of the external thermal protection system. From this point of view, the internal environment interfaced to the external environment activities, previously discussed, at the undisturbed outer mold line of the vehicle. Preliminary assessments, assuming independence of the two separate environments, proved to be inadequate, however, and required the complete integration and coupling of the exterior flow field with the internal breach environments. This direction led to the development and application of new aerothermal tools and techniques, which are discussed in the following sections below.

Section 5.3.1 will discuss the overall process of developing the internal environments used for thermal analysis as detailed in Section 6. Sections 5.3.2 through 5.3.6 detail the individual activities and tool development efforts required to produce integrated environments. Finally Section 5.3.7 will pull together the lessons learned and insight provided by the studies as an application to the present working scenario.

By the very nature of internal flow environments (that a hole has to exist before they come into play), the results of all analysis are highly scenario dependent. While insight and general understanding of the dominant fluid dynamics can guide engineering analysis, one must keep in mind that a small change in hole location or diameter may produce entirely different results. Given the degree of uncertainty regarding the actual damage, internal engineering predictions of heating were generally characterized with +/- 50% levels of uncertainty. These models were most useful for matching trends and understanding major phenomena. Refined CFD analyses, discussed in Section 5.3.6, emerged late in the investigation that locally produced peak heating rates several factors larger than engineering model results. The large heating rates predicted result from extreme flowfield gradients picked up in the finer grid solutions. Comparisons with the engineering distributions are presented in Section 5.3.7.

5.3.1 Process of Determining Internal Aerothermodynamic Environments

The use of Computational Fluid Dynamic tools for high temperature gas dynamic environments has progressed significantly over the last decade in the development of external aerothermal environments. With experienced CFD personnel and baselined tools, the external Aerothermodynamic teams were primed to get started within a relatively short time. Internal environments, however, were a different story. The following process was developed from scratch specifically for the STS107 investigation and drew on tremendous talent from across the country. (Note: the work covered in this report represents only a fraction of the total effort put forth by the Internal Flow team. Much of the unique and cutting edge analysis did not have direct bearing on the present working scenario, and thus, was not reported here. The remaining work will be reported in the future.)

5.3.1.1 Process Development

Immediately following the demise of Columbia, the aerothermal community came together and brainstormed activities required for understanding fluid dynamics of the entry event timeline leading to the loss of vehicle. In the process, a framework for constructing the necessary information and toolsets emerged with clear delineation between external and internal aerothermodynamics. The internal team was given the challenge of developing insight and tools to understand an environment involving multiple penetrations of supersonic, high temperature gases into complex geometries with coupled heat transfer to structures. The starting point for the process was identification of the types of analyses that would be required, identification of personnel and tools to perform the analysis, and establishment of a plan to meet all objectives in a short few months. Table 5.3.1.1-1 displays the five major fields of analysis identified and how they play together to provide a clear picture of three early scenarios. Given the unique nature of the investigation it was clear to the team that the required expertise to complete the analysis did not presently exist within the aerothermal community and would have to be developed.

At the outset the team developed a series of Unit Physics benchmarks, see Table 5.3.1.1-2, that separated the fully coupled, complicated problem into smaller pieces that could be individually simulated and compared to

calibration quality test data to assure the tools and capabilities could accurately simulate the necessary phenomena. These pieces would then be built upon through a series of increasingly complicated, more flight-like cases, leading to the fully coupled external/ internal failure simulation at true flight conditions. This process, as developed, is summarized in Figure 5.3.1-1.

Implementing the entire process shown in Figure 5.3.1-1 proved to be untenable within the time constraints of the investigation. Therefore, the majority of the internal team's CFD analysis relied on current best practices. However, for three specific failure scenario analyses the CFD did proceed through the key steps of this process. The CFD tools implemented for the two and three-dimensional T-Seal damage and the RCC Panel 8 10" breach (Sections 5.3.6.2.2, 5.3.6.2.4, 5.3.6.1.2, respectively) were benchmarked to the key Unit Physics and Unit Physics Extension relevant for those failure scenarios.

Thermal analysts require heating distributions and histories to assess structural temperatures and hardware failure times. Engineering methodologies for predicting internal environments were developed in parallel with the CFD techniques for the full-scale problem to meet thermal analysts data and schedule requirements. In order to provide greater consistency and accuracy, the interface for all internal tools was always the latest, most complete CFD analyses available from the external environments team. These additional tools include boundary layer extraction and mass/energy balance tools, venting and coupled thermal/venting tools, engineering plume impingement heating tools, and basic engineering support CFD for tool assessments. Figure 5.3.1-2 presents the internal environments process and some of the interactions between components.

	A. MLGD Penetration	**B. Wing Leading Edge Damage**	**C. Acreage Tile Loss**
1. Venting Analysis	1. Mass flow analysis 2. Energy balance 3. Penetration parametrics	1. Mass flow analysis 2. Energy balance 3. Penetration parametrics	1. Penetration location parametrics
2. Fluid Thermal Coupling	1. Flow past seal 2. Flow through crack	1. Flow past seal 2. Energy loss to wing structure	
3. Engineering Model CFD Support	1. 2D/Axi Jet modeling 2. Flow into cavities 3. Simplified 3D	1. Swept cylinder with hole 2. 2D into RCC cavity	1. Flow over cavity with penetration
4. Penetration flow engineering models	1. Modeling of Jet 2. Impingement modeling	1. Spar Impingement 2. Attach Hardware	1. Test data analysis 2. 3D heating factors
5. Large Scale CFD	1. Wheel Well Penetration 2. Door Ajar/Seal Breach 3. Vent ingestion	1. RCC Leading Edge penetration 2. Lower Seal breach 3. Missing panel	1. Wing Box Flow

Table 5.3.1.1-1 Internal Flow Team Analysis Matrix

Unit Physics	Benchmark Dataset	POC and Consolidator	Location or Date Available
High Enthalpy Flow (HEF)	Sphere Flows. LAURA Cases	P. Gnofo, 757 864 4380 p.a.gnoffo@larc.nasa.gov	simak.jsc.nasa.gov/pub/from_hermes/LargeInternalFlow/Continuum/Benchmarks/HEF/
Underexpanded Jet (UEJ)	Donaldson & Snedeker '71	Joe Ruf, 256 544 4942 Joseph.h.ruf.nasa.gov	simak.jsc.nasa.gov/pub/from_hermes/LargeInternalFlow/Continuum/Benchmarks/UEJ/
Shock – Shock Interaction (SSI)	Glass's Material	Kim Bey, 757 864 1351 k.s.bey@larc.nasa.gov	
Cavity Flow (CF)	1) Laminar, Hahn '68, & Wyborney,AGARD 2) Turbulent, 3) Pressure Gradient	Kim Bey, 757 864 1351 k.s.bey@larc.nasa.gov	simak.jsc.nasa.gov/pub/CavityFlow_Bey/
Wall Bounded Jet (WBJ)	In work -	Chris Glass, 757 864 1350 c.e.glass@larc.nasa.gov	Experimental Data being generated

Table 5.3.1.1-2 Unit Physics Benchmarks

Large Scale Wing Internal CFD Roadmap Overview

- Multiple Failure Scenarios to be assessed
  - Many similarities, some uniqueness
  - Basic fluid physics broken down to several Unit Physics
- Unit Physics Problems
  - Each addresses a unique set of physics
  - Codes are compared to available test data for each unit physics
- Unit Physics Extensions
  - Extend the Unit Physics problems to flight fluid properties
- Bridging Problems
  - Combine all relevant physics together in a geometrically representative problem
- CFD of the Failure Scenario
  - Lessons learned from the process applied to improve the result of the 'Large Scale Wing Internal CFD'

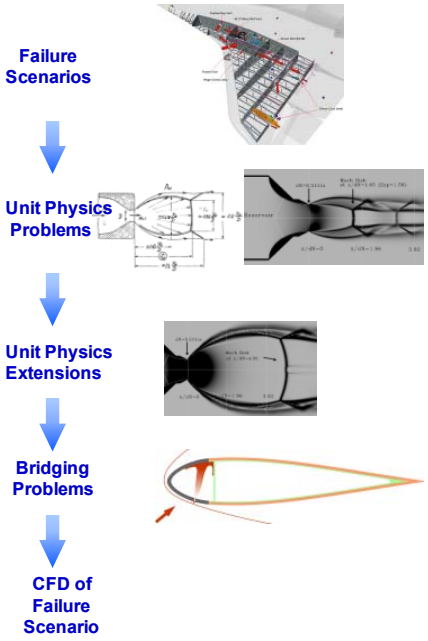

Figure 5.3.1-1 Large Scale Internal CFD Roadmap

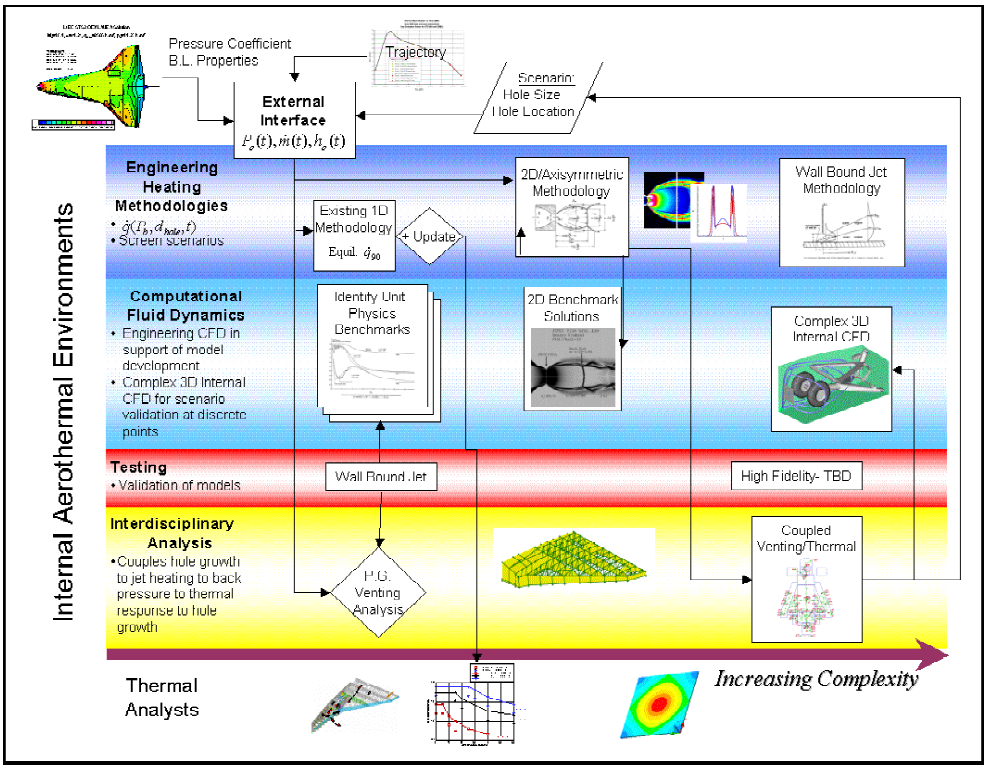

Figure 5.3.1-2 Internal Environments Flow

5.3.1.2 Tools

The unique application of aerothermodynamic analysis to the Orbiter internal environments required the development of a suite of unique capabilities and tools previously not available. A natural basis for much of the internal environment work involved the application of several CFD codes with diverse backgrounds. Each of the tools developed during this investigation for the assessment of the Orbiter, post breach, internal environment will be described in the following sections.

5.3.1.3 Integration

The original time-dependent, integrated analysis plan is given in Figure 5.3.1-3. In this original schematic, the intent was to fully assess a dynamic, multiple failure scenario leading to the STS-107 observed timeline. Within this schematic, the loop starts in the upper left with an assumed hole size, trajectory condition, and external properties from CFD solutions. This information is passed off to the external flow interface, which provides predictions of penetration mass and energy flux through the hole, as well as specifying fluid properties at the penetration. Fluid flow into the Orbiter through the penetration pressurizes the interior volume and transfers energy to the vehicle structure as modeled in the coupled venting thermal analysis loop. Once the quasi-steady internal properties are established, engineering predictions of jet impingement heating to internal structures are generated and fed to the detailed thermal models for local temperature predictions. Based on vehicle loads and material limits, breach and/or structural failure assessments are made and hole diameter/breach status is updated and the process starts the loop over again. The internal flow process, backed by the blue background, would be assessed at discrete time points by application of large-scale CFD solution methods and engineering validation for simplified jet impingement models.

This process was ultimately untenable within the time constraints of the investigation, given the distributed nature of the internal flow team. (Boeing Huntington Beach successfully implemented a similar process for their Progressive Failure Analysis as detailed in Section 6: provided a priori prediction for the hole diameter and internal heating distributions.) The present working scenarios are analyzed with fixed hole diameters up to

the point of structural failure, allowing specification of complete heating distribution histories to be computed and provided to thermal analysts for failure analysis.

Figure 5.3.1-4 presents the final integrated process for developing the internal heating environment for a breach into the wing leading edge RCC system. Starting in the upper left, the external team CFD solutions using LAURA are probed at the assumed hole location and values extracted as inputs to the external flow interface routines which generate bulk enthalpy values into the breach and into pressure inputs to the coupled thermal/venting methodology for the prediction of internal pressures and mass flow within the vehicle. Peter Gnoffo's LAURA calculations also serve as the basis for the fully coupled jet penetration calculations. *(Though larger holes were assessed later, the final environments produced utilized jet directions derived to match two-inch hole results.)* Potential penetration locations were screened along the predicted debris impact footprint to determine a worst-case penetration producing the peak impingement heating on the internal insulation surfaces. With the hole location specified, axisymmetric heating predictions are generated utilizing the previously calculated mass/energy flux and CFD predicted surface pressures. These results are then fed into the internal heating distribution methodology, which provides time histories of convective heating values over the internal volume of the RCC cavity. The final heating distributions and accompanying trajectory corrections are then provided to the thermal community. Use of large-scale CFD results is two-fold in this approach: 1) to independently assess the applicability of the final methodology, and 2) provide additional fluid insight in order to explain observed debris forensics.

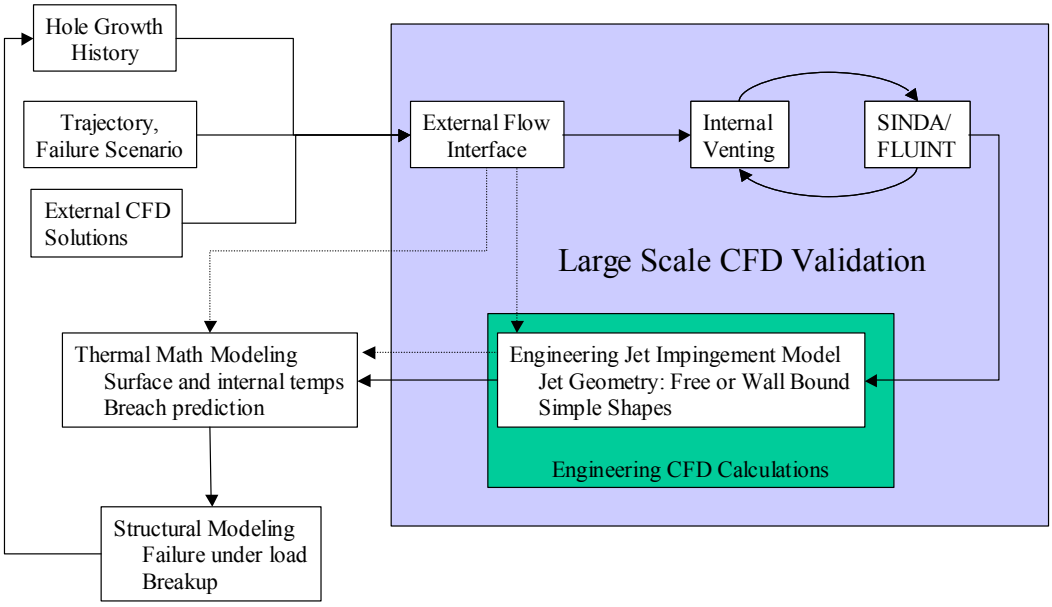

Figure 5.3.1-3 Closed Loop Integrated Analysis

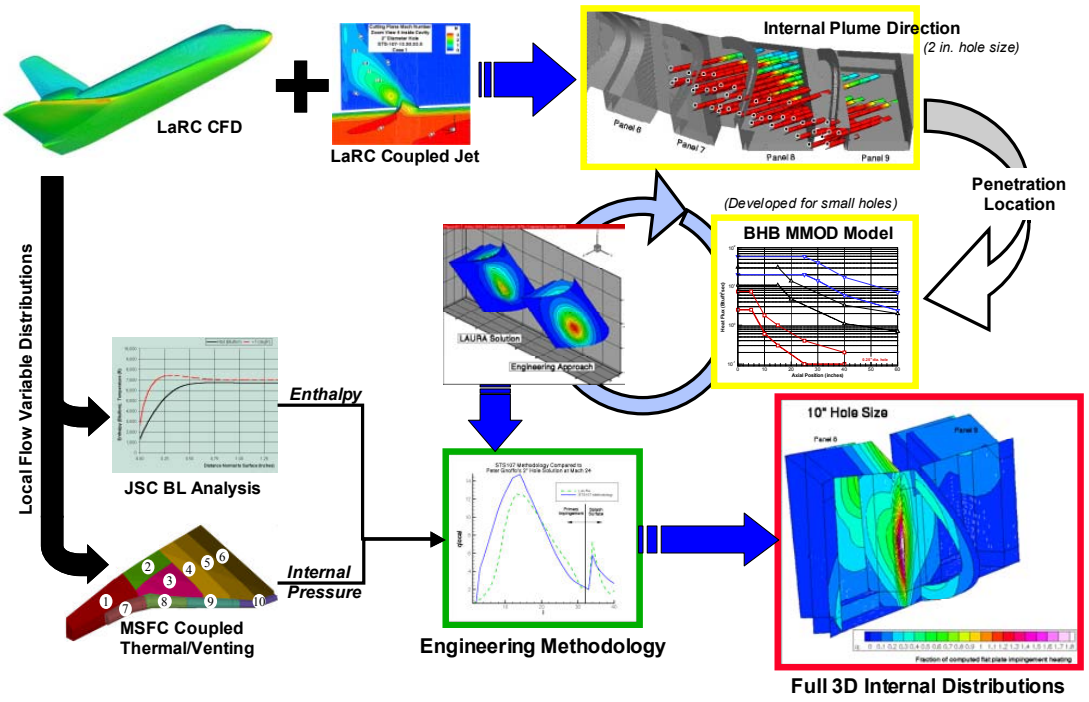

Figure 5.3.1-4 Integrated Internal Environments Schematic

5.3.2 External/Internal Environments – Engineering Analysis

In order to evaluate the effects of ingested reentry gases on the internal structure of the Orbiter wing, a method was needed that would provide the properties, e.g. mass flow rate and energy flux, of the ingested gas as a function of time through the trajectory. These values were needed as input to the 'plume' models that provided the local heating to internal hardware and as input to the coupled venting/thermal codes that modeled the flow and bulk heat transfer inside the wing. CFD solutions require significant resources to setup and then provide detailed data for only one or two free stream conditions. Therefore, selected CFD solutions were used to aid in the development of engineering tools that provided the histories of the ingested gas flow rate, bulk enthalpy and bulk temperature needed to evaluate the propagation of damage inside the vehicle.

5.3.2.1 Overview of Breach Hole Engineering Analysis Methodology

Figure 5.3.2-1 provides a sketch of the basic aspects of a breach flow field. Once a breach hole opens in the Orbiter aeroshell the pressure differential between the outside flow field and internal volume will cause reentry gases to enter the vehicle and generate a gas 'plume' that then impinges on internal structure. The flow rate and energy of the flow ingested depends on the size and shape of the hole and the properties of the gas just upstream of the hole. The gas properties in the external flow vary by location on the vehicle and by distance from the surface. For small breach holes, only a portion of the gas near the surface, as shown in Figure 5.3.2-1, is ingested. As the hole increases in size, more of the boundary-layer gas is ingested until the entire boundary layer is swallowed. Further increases in hole-size results in the boundary layer and a portion of the high enthalpy shock-layer gases to be ingested. The mass flow rate of gas through the breach hole is a function of the mass-averaged enthalpy of the boundary-layer gas that is ingested. Therefore, a mass balance between the gas flowing through the hole and that extracted from the external flow was used to obtain an engineering estimate of the mass flow rate and energy flux of the gas ingested.

The mass-flow rate through the hole was computed by the following isentropic relation from Shapiro:

$$\dot{m}_{hole} = Area\sqrt{\frac{\gamma}{R_{gas}}}\frac{P_o}{\sqrt{T_o}}\frac{M}{\left(1+\frac{\gamma-1}{2}M^2\right)^{\frac{\gamma+1}{2(\gamma-1)}}} \qquad (5.3.2\text{-}1)$$

where $\dot{m}_{hole}$ = mass flow rate through hole
Area = cross-sectional area of hole
γ = Ratio of specific heats
R_{gas} = Gas constant
P_o = External Pressure
T_o = Bulk temperature of ingested gas
M = Mach number at hole

The mass flow relation above has a maximum value when the Mach number is 1.0. The following isentropic relation was used to compute the Mach number as a function of the internal and external pressures, P_{int} and P_{ext}, respectively.

$$\frac{P_{ext}}{P_{\text{int}}} = \left(1+\frac{\gamma-1}{2}M^2\right)^{\frac{\gamma}{\gamma-1}} \qquad (5.3.2\text{-}2)$$

P_{ext} was used for the P_o value in Eqn. 5.3.2-1. The values γ, R_{gas}, *and* T_o are a function of the average gas properties of the flow extracted from the external flow field. To obtain these values it was assumed that chemical equilibrium air properties could be used given a pressure and an enthalpy. The average, or bulk, enthalpy of the ingested gas was obtained from the following relation:

$$H_{Bulk} = \frac{\int \rho u H dA}{\int \rho u dA} \qquad (5.3.2\text{-}3)$$

where H_{Bulk} = Bulk gas enthalpy
ρ = gas density in external flow field
u = gas velocity in external flow field
H = total gas enthalpy
dA = cross-sectional area of external flow ingested

The quantity ρudA is the mass flow rate through the cross-sectional area of the external flow streamtube that enters the hole. Therefore, to obtain the bulk enthalpy, the area of integration is enlarged until the quantity ρudA equals the mass flow rate through the hole, $\dot{m}_{hole}$. For this analysis, the local external flow properties were assumed to vary only in the y-direction normal to the surface. The area of integration was assumed to be

$$A_{st} = C\sqrt{A_{hole}}\int_0^y dy \qquad (5.3.2\text{-}4)$$

where A_{st} = cross-sectional area of external flow streamtube
C = constant derived from CFD solutions
A_{hole} = area of breach hole
y = normal distance from the surface

The value C was set to 0.4 to better match the ingested mass flow rate predicted by a CFD solution for a 2-inch diameter hole in Panel 6 (see Sec. 5.3.2.2). Therefore, the ingested streamtube had a rectangular cross-

sectional shape with a fraction of the square-root of the hole area defining the transverse dimension. The vertical distance was defined by integrating through the flow field until the value $C\sqrt{A_{hole}}\int_0^y \rho u dy$ equaled the hole mass flow rate, $\dot{m}_{hole}$.

Applying these assumptions for the ingested cross-sectional area, accounting for the enthalpy difference across the boundary layer, and non-dimensionalizing the values by the boundary-layer edge values, the bulk enthalpy relation used in the engineering analyses was obtained.

$$H_{Bulk} = \frac{\int_0^{y/y_e} \frac{\rho}{\rho_e}\frac{u}{u_e}\frac{(H - H_{wall})}{(H_e - H_{wall})} d\left(\frac{y}{y_e}\right)}{\int_0^{y/y_e} \frac{\rho}{\rho_e}\frac{u}{u_e} d\left(\frac{y}{y_e}\right)} + H_{wall} \qquad (5.3.2\text{-}5)$$

where the subscript *e* corresponds to the boundary-layer edge value and H_{wall} is the gas enthalpy at the wall temperature. As described in the next section, polynomial curve-fits for the quantities $\frac{\rho}{\rho_e}\frac{u}{u_e}$ and $\frac{\rho}{\rho_e}\frac{u}{u_e}\frac{(H - H_{wall})}{(H_e - H_{wall})}$ as a function of the non-dimensional distance, $\left(\frac{y}{y_e}\right)$, through the boundary layer were obtained from CFD solutions.

A FORTRAN computer code was used to solve for the breach hole gas mass flow rate, bulk enthalpy and bulk temperature using the relations above. The solution process included the following steps:

1) Compute the boundary-layer thickness and edge quantities as described in the next section.
2) Compute the bulk enthalpy and mass flux for the ingestion of the entire boundary layer and then compare the boundary-layer mass flux (denominator of Eqn. 5.3.2-5) to the hole flow rate (Eqn. 5.3.2-1). If the hole flow rate is greater than the boundary-layer mass flux, then it was assumed that more than the boundary layer was ingested into the hole. Outside of the boundary layer it was assumed that the gas properties are equal to the edge values. Increments of one-tenth of a boundary-layer thickness were used to find the vertical distance and therefore the external mass flux that best matched the flow rate through the hole.
3) If the hole-flow rate was less then the boundary-layer mass flux, then the vertical distance inside the boundary layer was varied by increments of one one-hundredth of a boundary-layer thickness to best match the flow rate through the hole.

5.3.2.2 Use of CFD Solutions

Two sets of CFD solutions were used to develop the engineering methods to estimate the ingested gas properties. The first set included two CFD solutions of the nominal undamaged Orbiter. These solutions were used to obtain curve-fits of flow field parameters just upstream of the assumed breach hole. The second set of CFD solutions were coupled external/internal flow field solutions for various size circular breach holes in the wing leading edge. These solutions were used to calibrate the engineering tool and to confirm its results.

5.3.2.3 External Flow Parameter Curve-fits

Two LAURA CFD solutions for the nominal Orbiter provided curve-fits for use in the breach hole gas ingestion engineering analysis. The CFD solutions for the following two flight conditions were chosen:

1) CFD Point 1: EI+404 secs.; Mach =24.9; Altitude = 243,000 ft; Angle-of-attack = 40 degs.; Dynamic pressure = 22.0 psf.
2) CFD Point 6: EI+921 secs.; Mach = 17.9; Altitude = 200,767 ft; Angle-of-attack = 40 degs.; Dynamic pressure = 83.5 psf.

For each of these 3-D flow field solutions, two points on the wing leading edge were selected – one on Panel 6 and one on Panel 8.

Panel	X (in)	Y (in)	Z (in)
6	1038	-193	284
8	1070	-211	294

At each of these points, predicted flow field properties were extracted from the CFD solutions as a function of the normal distance from the surface. Figure 5.3.2-2 presents the variation of gas temperature and enthalpy predicted by LAURA for the Panel 8 location at the CFD Point 1 flight condition. The boundary-layer thickness is 1.4 inches and was determined by selecting the first grid point from the wall where the total enthalpy value is approximately 99% of the free stream total enthalpy.

For use in the engineering analysis, curve fits of the quantities $\frac{\rho}{\rho_e}\frac{u}{u_e}$ and $\frac{\rho}{\rho_e}\frac{u}{u_e}\frac{(H-H_{wall})}{(H_e-H_{wall})}$ were defined using the extracted CFD values which were non-dimensionalized by the edge values. Figure 5.3.2-3 and Figure 5.3.2-4 present these curve-fits for the Panel 8 location. The extracted and curve-fit CFD values included both the CFD Point 1 and 6 data.

Since all of these values were non-dimensionalized by the boundary-layer edge values, relations also had to be developed to estimate the edge values as a function of nominal free stream parameters. Two values were needed – the boundary-layer thickness and the edge mass flux, $\rho_e u_e$. It was assumed that the boundary-layer thickness, δ, is a linear function of the square-root of the free stream Reynolds number, Re_L, based upon the length of the Orbiter (L=107.5 ft). Using the boundary-layer thickness values at the Panel 8 location from the two CFD solutions, the following relation was obtained.

$$\delta = \frac{1250}{\sqrt{\mathrm{Re}_L}} - 0.1617 \text{ (inches)} \qquad (5.3.2\text{-}6)$$

The edge mass flux , $\rho_e u_e$, was assumed to be a linear function of the free stream dynamic pressure, P_{dyn}, with the edge values for curve-fitting obtained from the two CFD solutions at the Panel 8 location.

$$\rho_e u_e = 1.0567E-03 P_{dyn} \text{ (slugs/ft}^2\text{-sec)} \qquad (5.3.2\text{-}7)$$

The relations and curve-fits presented are unique for the Panel 8 location. Additional relations of the same form were generated for the Panel 6 location.

5.3.2.4 Calibration of Engineering Tool

Several CFD solutions were generated for holes in the Orbiter wing leading edge. Four of these solutions described in Sec. 5.3.6.1.3 were used to calibrate and evaluate the engineering method for estimating the mass flow and energy flux of gas entering a leading edge breach hole. CFD solutions for 2, 4 and 6-inch diameter circular holes in Panel 6 and one for a 10-inch diameter hole in Panel 8 were reviewed and the predicted mass flow rate and energy flux flowing through the plane of the hole were computed. All of these values are for the same flight condition – CFD Point 1.

Case	Mass Flow Rate (lbm/sec)	Energy Flux (Btu/sec)
Panel 6: 2-in Dia. Hole	0.00152	9.4
Panel 6: 4-in Dia. Hole	0.00562	43.6
Panel 6: 6-in Dia. Hole	0.01247	110.9
Panel 8: 10-in Dia. Hole	0.04839	498.0

5.3.2.5 Properties of Flow into Breach Holes

The engineering method was exercised for four hole sizes in leading edge Panel 6 – 1, 2, 4, and 6 inches in diameter. Figure 5.3.2-5 presents the predicted fraction of the boundary layer that is ingested into the hole. Both the 4 and 6-inch diameter holes result in the ingestion of the entire boundary layer at later times in the trajectory. Figure 5.3.2-6 and Figure 5.3.2-7 present the predicted bulk gas temperature and enthalpy of the ingested gas. The gas temperatures are mostly between 9,000 and 10,000 R. Figure 5.3.2-8 and Figure 5.3.2-9 present the predicted mass flow rate and energy flux and compare the results to the values obtained from the CFD solutions for the holes in Panel 6. For the smaller holes – 2 and 4-inch diameter – the engineering method provides a very good estimate of the ingested flow rate and energy flux. However, as the hole is increased in size to the 6-inch diameter, the engineering methods tend to under predict the values.

Breach holes in Panel 8 were also analyzed with the engineering method. In this case, the external pressure used for the computation (C_p=1.46) was for a location slightly different from the location where the curve-fits were obtained. Figure 5.3.2-10 and Figure 5.3.2-11 present the predicted mass flux and energy flux into the holes. The values for the CFD solution with a 10-inch diameter hole are also plotted and indicate that the engineering method is under predicting the energy ingested into large breach holes.

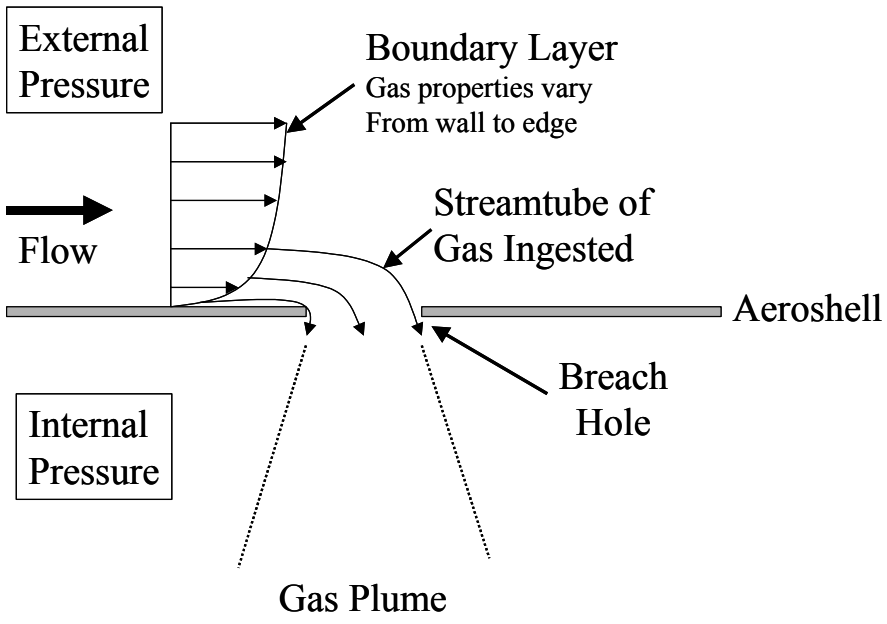

Figure 5.3.2-1 Sketch of Breach Flow Field

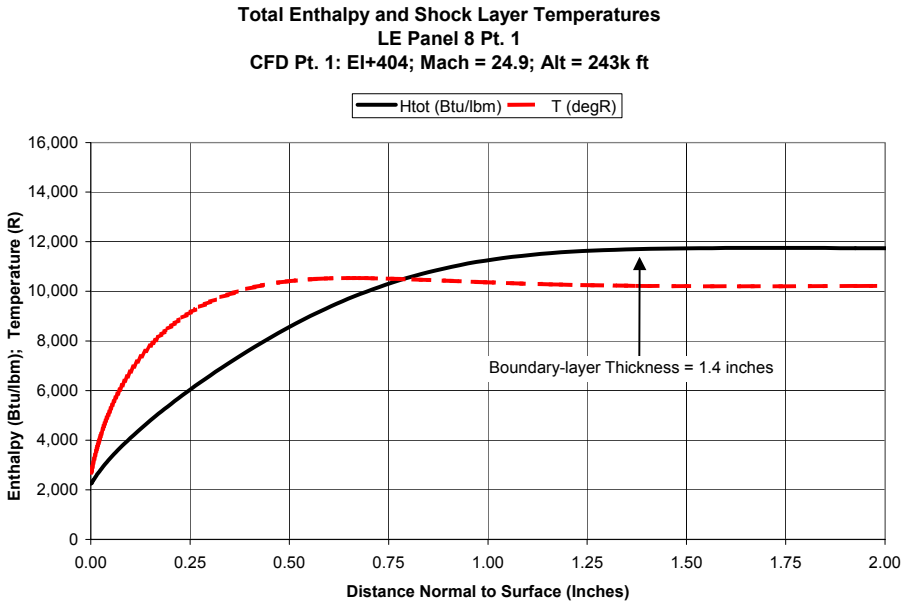

Figure 5.3.2-2 Total Enthalpy and Temperature Profiles at LE Panel 8 for Mach 24.9.

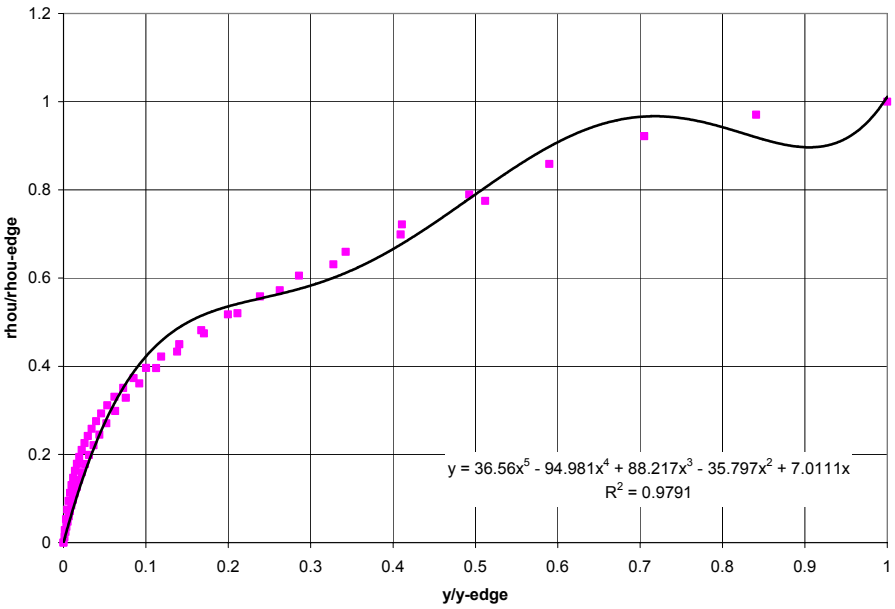

Figure 5.3.2-3 Boundary-layer Mass Flux, $\frac{\rho}{\rho_e}\frac{u}{u_e}$, Curve-fit for LE Panel 8.

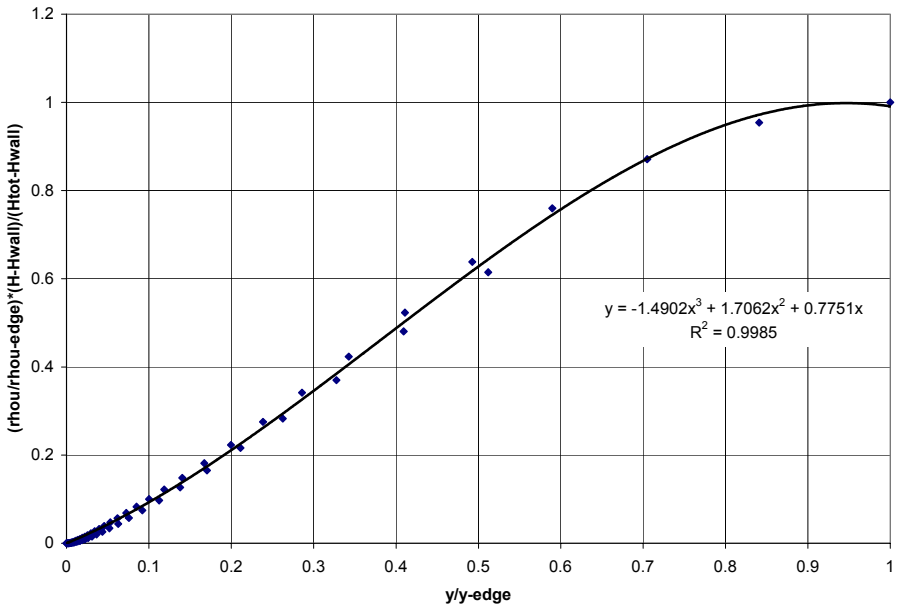

Figure 5.3.2-4 Boundary-layer Energy, $\frac{\rho}{\rho_e}\frac{u}{u_e}\frac{(H-H_{wall})}{(H_e-H_{wall})}$, Curve-fit for LE Panel 8

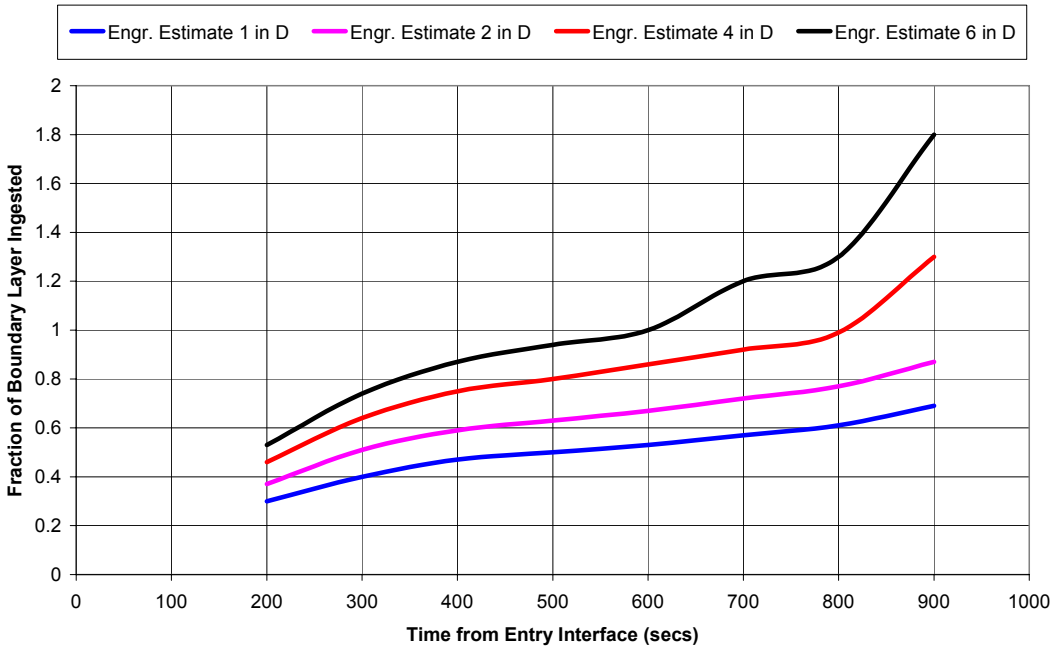

Figure 5.3.2-5 Predicted Fraction of Boundary-layer Thickness of Gas Ingested into Hole in LE Panel 6.

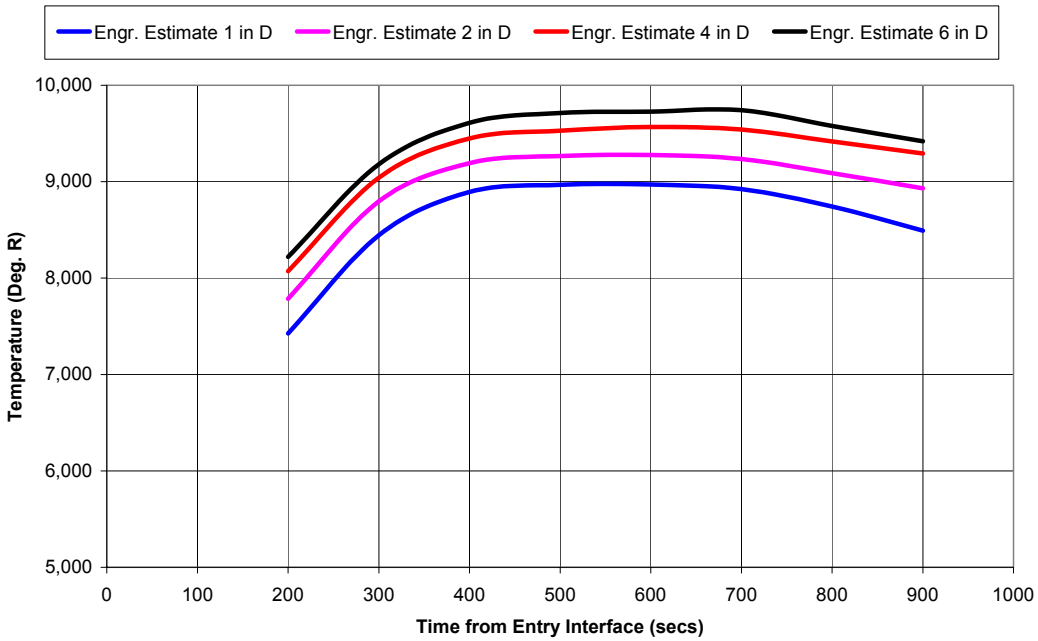

Figure 5.3.2-6 Predicted Bulk Temperature of Gas Ingested into Hole in LE Panel 6.

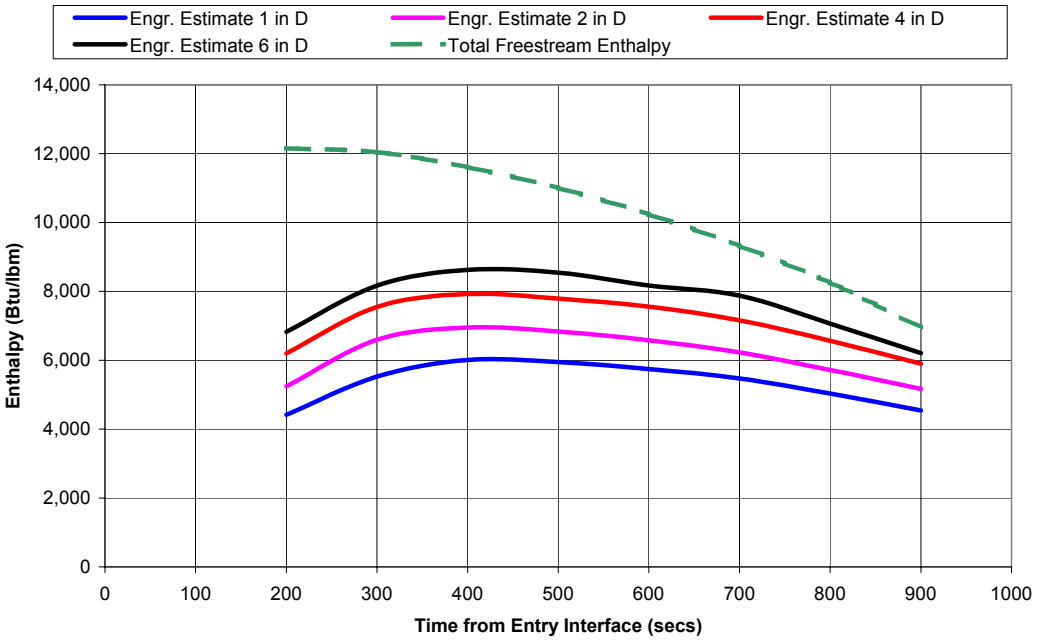

Figure 5.3.2-7 Predicted Bulk Enthalpy of Gas Ingested into Hole in LE Panel 6.

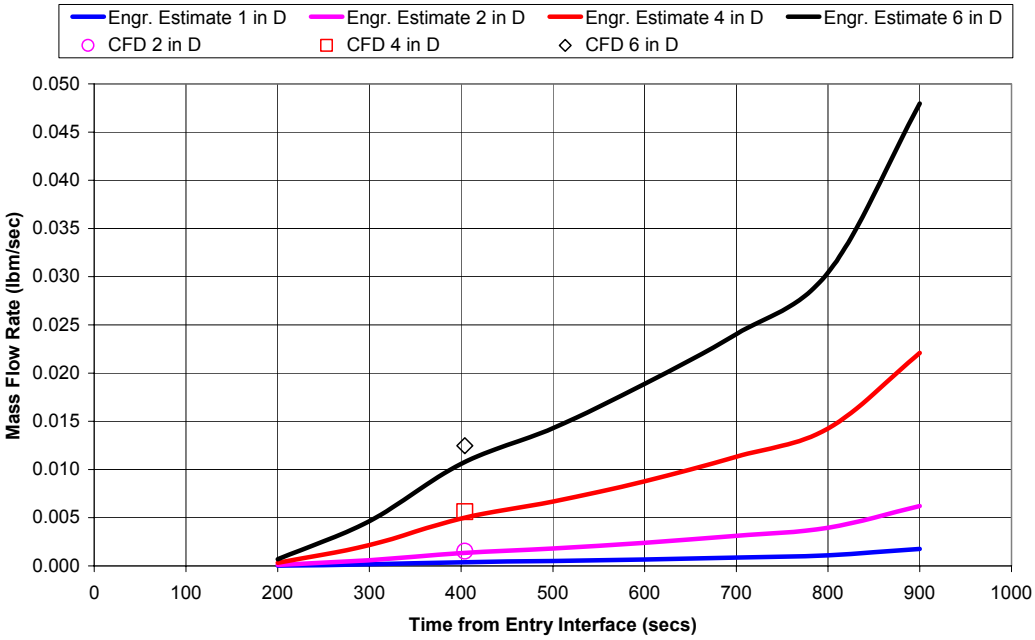

Figure 5.3.2-8 Predicted Mass Flow Rate of Gas into Hole in LE Panel 6.

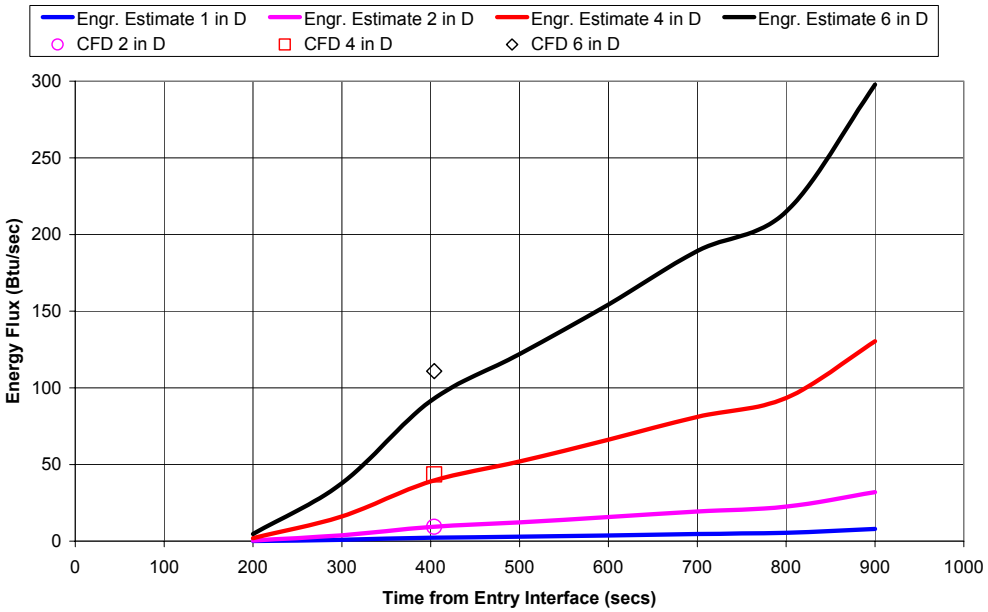

Figure 5.3.2-9 Predicted Mass Flow Rate of Gas into Hole in LE Panel 6.

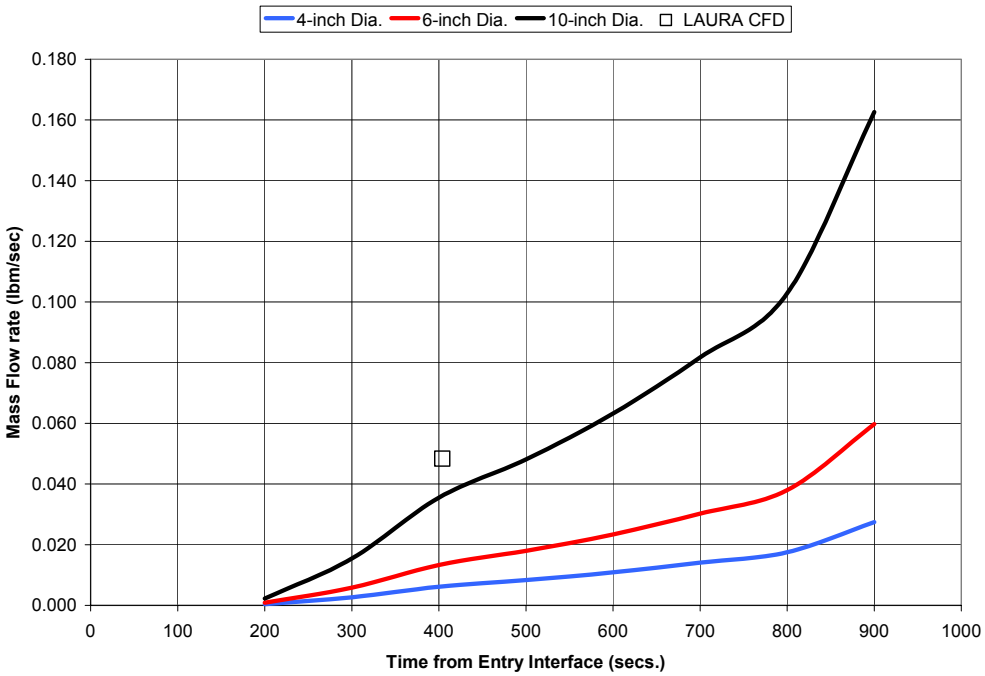

Figure 5.3.2-10 Predicted Mass Flow Rate of Gas into Holes in LE Panel 8.

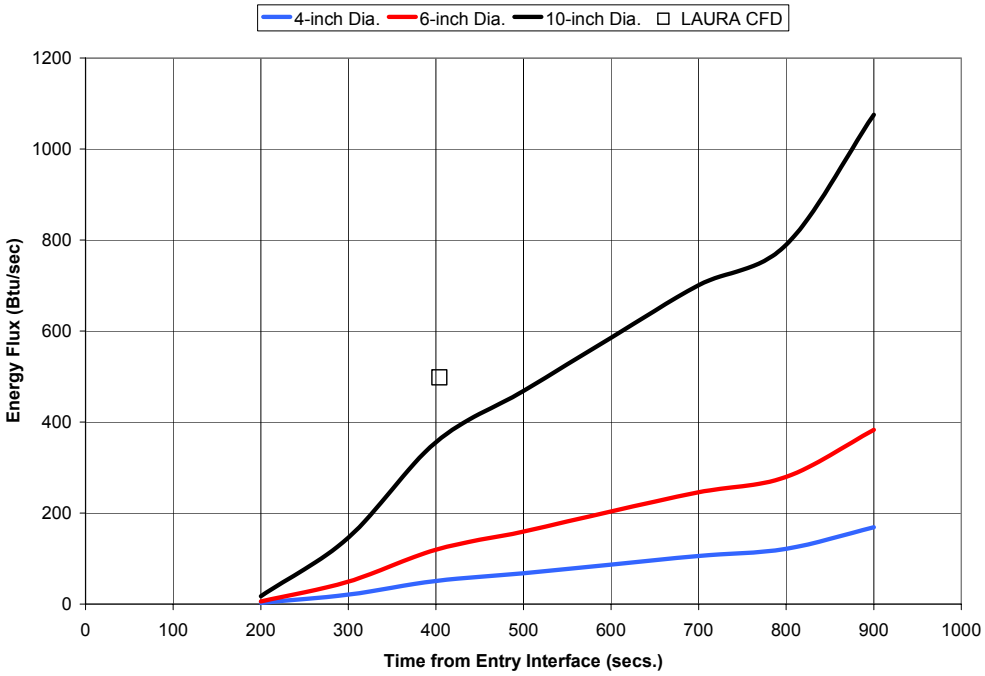

Figure 5.3.2-11 Predicted Energy Flux of Gas into Holes in LE Panel 8.

5.3.3 Plume Model Development

Engineering models of internal jet impingement heating are necessary to assess localized heating in the primary impingement zone for burn through and structural failure analysis. Heating distributions are produced based on:

1) Assumed hole diameter and shape
2) Assumed hole location
3) Freestream conditions
4) Internal pressure
5) Internal geometry
6) External boundary layer properties

The results must be in a form suitable for thermal analysis, typically closed form functions or tables that may be linearly interpolated. Computational results are very expensive to obtain and are only available at discreet points in the trajectory. Engineering models, though, if properly setup, allow for parametric studies in order to match flight data in terms of hole diameter, location, and jet direction. Such studies will be presented in the thermal analysis portion of the report. The following two sections describe the development of an engineering model to predict internal plume impingement values for circular holes, while the model developed to assess missing T-seal segments in described in Section 5.3.3.6.

5.3.3.1 Basic internal plume physics and impingement issues

The nature and structure of a free jet issuing into the Orbiter interior through a breach in the thermal protection system is dictated by the total pressure difference across the surface, the hole diameter, boundary layer properties, and local boundary layer edge Mach number. For small orifices, on the order of one inch, the jet may be assumed to enter normal to the internal surface with a sonic condition. For such a case the governing parameter that dictates shock structure and mixing of the jet is the ratio of external driving pressure to internal pressure. Bulk fluid properties are a function of the percentage of external boundary layer drawn off into the hole. For very small hole, the properties will be near wall conditions, whereas larger holes can produce internal flows with enthalpy levels approaching free stream total values. As the high-speed gas enters the cavity, it immediately starts mixing with the ambient fluid at the boundaries of the jet. This mixing zone gets larger as the jet progresses, until finally the core portion of the jet has been consumed and the jet has reached a fully developed condition. Depending on the conditions driving the jet, this may not occur until ten's of diameters downstream. In the highly under-expanded state, the jet shock structure is dominated by a normal shock downstream of the initial expansion called the Mach disk. Immediately downstream of the Mach disk the flow is subsonic, though it may re-expand to supersonic flow. Figure 5.3.3-1 displays variations in free-jet structure and with varying pressure ratios. Figure 5.3.3-2 shows the impact of pressure ratios in the range expected for Orbiter penetrations on computed flow structure.

Larger hole diameters display significant departure from this relatively simple structure as larger percentages of the highly energetic boundary layer are ingested and increased transverse momentum bends the jet over in the direction of the boundary layer edge flow. This effect was discovered with the first fully coupled, internal/exterior flow solution performed for a two-inch breach into RCC panel 6. Complete results are presented in Section 5.3.6.1.4. Larger diameter penetrations tend to carry highly supersonic, high temperature gases directly to the interior surfaces and produce highly complex shock/impingement structures that can significantly impact local heat transfer rates.

Two dimensional jet structure differs from that of the axisymmetric jet, primarily due to conservation constraints. The three-dimensional source flow falls off as $(1/r^2)$ versus $(1/r\ lnr)$. The effect of this can be seen in Figure 5.3.3-3 where the two-dimensional flow structure is quite different and maintains the first shock cell considerably further downstream.

Also, of note in predicting internal jet flow fields is the importance of modeling chemistry correctly. Jet structure and spreading are strongly a function of the ratio of specific heats of the gas. Additional considerations of chemistry are the energies absorbed in chemical reactions and the net energy transfer to the surface. This study will focus equilibrium chemistry options in internal flow computations in order to provide the most reasonable predictions of plume heating with sufficient conservatism.

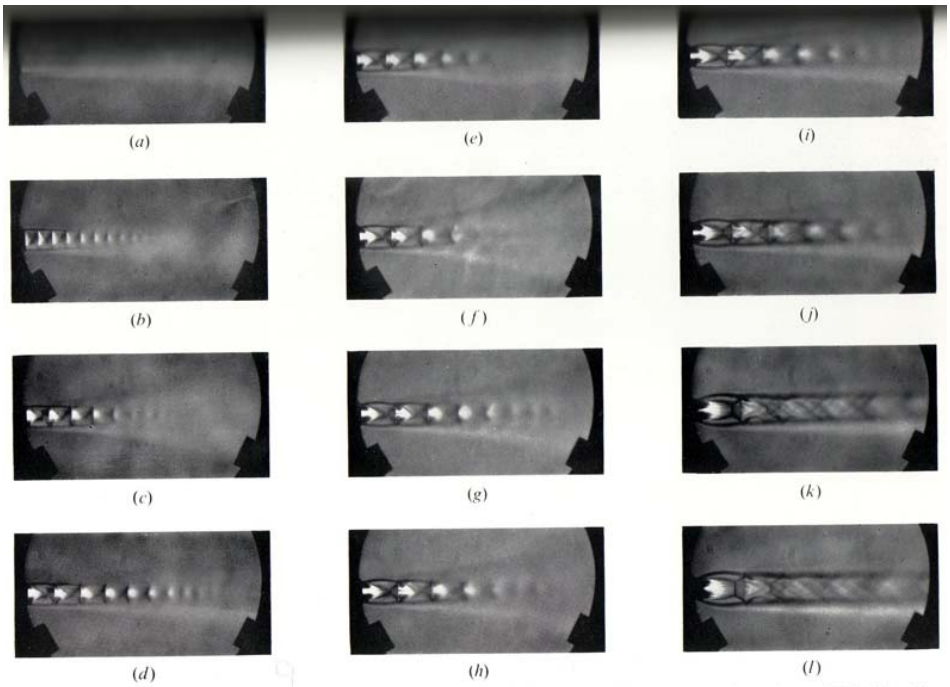

FIGURE 8. Free jet from convergent nozzle photographed with double-pass schlieren system. (a) $p_1/p_\infty = 1{\cdot}00$ (subsonic). (b) $p_1/p_\infty = 1{\cdot}15$. (c) $p_1/p_\infty = 1{\cdot}42$. (d) $p_1/p_\infty = 1{\cdot}59$. (e) $p_1/p_\infty = 1{\cdot}71$. (f) $p_1/p_\infty = 1{\cdot}84$. (g) $p_1/p_\infty = 2{\cdot}00$. (h) $p_1/p_\infty = 2{\cdot}13$. (i) $p_1/p_\infty = 2{\cdot}31$. (j) $p_1/p_\infty = 2{\cdot}59$. (k) $p_1/p_\infty = 3{\cdot}57$. (l) $p_1/p_\infty = 4{\cdot}09$.

Figure 5.3.3-1 Free jet mixing and structure with pressure ratio

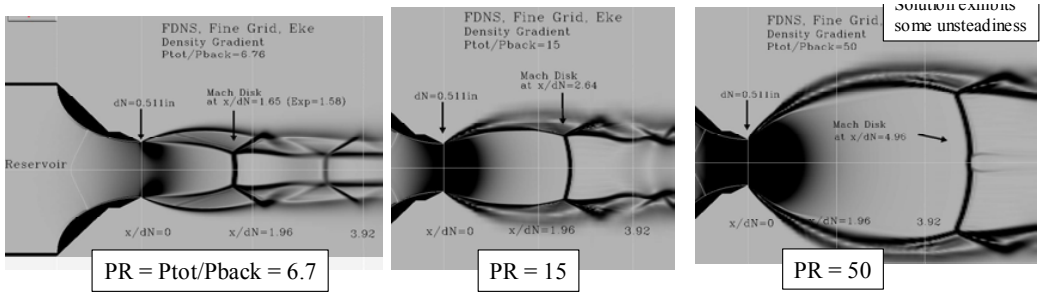

Figure 5.3.3-2 Computed pressure ratio effect on near orifice flow

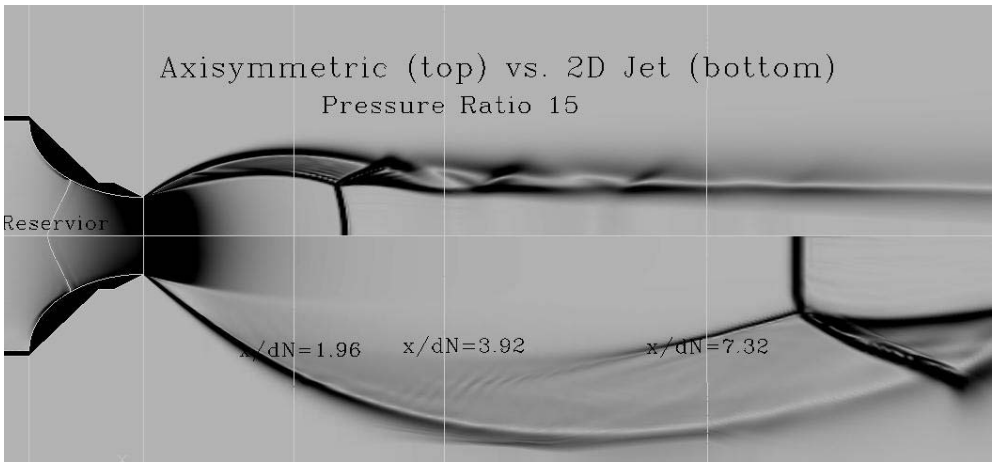

Figure 5.3.3-3 Axisymmetric vs. 2D Jet structure

5.3.3.2 1-D Axisymmetric Equilibrium Plume Heating Model

5.3.3.2.1 History

The plume model used to support the STS-107 accident investigation is a version of that originally developed to support Space Shuttle mission risk definition due to micrometeoroid and orbital debris hazards. The study objective, prompting the original model development, was to define levels of on-orbit impact damage that subsequently results in catastrophic loss of vehicle during entry. Under these conditions, on-orbit penetrations of the OML would result in ingestion of high enthalpy gas during reentry due to the pressure differential across the penetration. Heating environments due to this internal flow were required for thermal and structural analysis of the affected structure. As a result, a simplified internal jet flow model was developed to conservatively estimate time-dependent internal heating environments required for this study. During the course of this work, the analysis methodology and results were presented in 1997 to the National Research Council Review on Shuttle Meteoroid Risk Management.

For the STS-107 investigation, this model was employed for scenario feasibility and screening assessments.

5.3.3.2.2 Development

To provide the required time-dependent environments throughout an entry trajectory, it was desirable to develop a simplified method using closed form expressions to obtain characteristics of such internal flows, primarily impingement heating. The development of this method is described in this section.

5.3.3.2.3 Assumptions/limitations

- Due to the nature of the on-orbit impact hazard, the penetrations analyzed were limited to small holes of 1 inch diameter or less
- As a result, internal flow was modeled as an axisymmetric free jet issuing from a sonic orifice normal to the vehicle OML at the penetration location.
- Jet decay characteristics are based on empirical relations for properly expanded jets
- To maintain a conservative approach, internal heating levels were based on normal impingement angles for surfaces within the jet flow field

5.3.3.2.4 Theoretical Description of the Jet and Impingement Regions

To analyze the impinging jet, four distinct regions of flow are considered. First, a zone of flow establishment extends from the orifice to the apex of the potential core along the centerline of the jet. Within this core the velocity of the jet remains constant. It is surrounded by a region in which mixing occurs between the jet and ambient gas. In the second region, established flow in the direction of the jet beyond the apex of the potential core is characterized by a dissipation of the centerline jet velocity and temperature, and by a spreading of the

jet in the transverse direction. At this point, usually several nozzle diameters downstream from the orifice, the mixing region has spread inward enough to reach the centerline. Beyond this point the mixing region continues to spread as the velocity decays at a rate required to conserve axial momentum. These first two flow regions are shown in Figure 5.3.3-4. A third region is characterized by deflection of the jet from the axial direction at the impingement surface. At this point, local flow conditions on the jet centerline, including the effects of an impingement shock if present, are used to compute a stagnation heating level to a desired surface geometry, either a flat plate or cylinder in crossflow. In the final region of the jet the redirected flow increases in thickness as the boundary layer builds up along the solid impinged surface. Convective heating continues on these surfaces although at levels that progressively drop from the maximum achieved at the stagnation point at the jet centerline.

5.3.3.2.5 Analysis Methodology

Properties of the external flow ingested through the damaged OML are based on a bulk gas enthalpy defined by the method described in Section 5.3.2.1 and the local surface pressure at the hole. With the internal pressure within the RCC cavity controlled by the local pressure at the passive vent located on the upper surface of the wing, a small penetration in the RCC is expected to act as a choked sonic orifice. Flow at the exit of the orifice is based on the 1-D nozzle equation:

$$\begin{aligned} mdot &= \rho_j U_j A_{hole} C_D \\ &= p_s (1+((\gamma-1)/2)M_j^2)^{-(1+\gamma)/2(\gamma-1)} M_j (\gamma g/(zRT))^{0.5} A_{hole} C_D \end{aligned}$$

where $M_j = 1$ when $P_s/P_a \geq ((1+\gamma)/2)^{\gamma/(\gamma-1)}$, and P_a is the internal pressure within the RCC cavity.

Isentropically expanding this sonic flow to the required internal pressure produces an initial supersonic condition in the flow that is accompanied by a strong normal shock, or Mach disc, in highly underexpanded flows. A calculation procedure conserving mass, momentum and energy fluxes across a normal shock are used to account for the total pressure loss in the jet core due to this shock. High temperature equilibrium air properties are used in all flow property calculations.

A continued expansion to the established internal cavity pressure defines the conditions within the jet core downstream of the Mach disc. Although experimental values of potential core length reported in the literature vary from 4.7 to 7.7, a value of 6.5 orifice diameters was used in this analysis, close to the median reported in the literature. Beyond that point, decaying values of centerline velocity and temperature are given by:

$$U_{cl}/U_c = 6.5 / (X / D_{orifice})$$

$$T_{cl} = T_{ambient} + 0.722 (T_c - T_{ambient}) U_{cl}/U_c .$$

As illustrated in Figure 5.3.3-5, flow conditions approaching the impingement point represent the upstream properties for a normal shock solution, if required, to provide local and total flow properties downstream of the impingement shock. Based on the experimental work in the literature, post-shock properties are used in the calculation of laminar stagnation heat flux:

$$q_{fp} = 0.763\, g\, Pr^{-0.6} (\rho_s \mu_s U_{cl} / r_5)^{0.5} (\rho_w \mu_w / \rho_s \mu_s)^{0.1} (H_s - H_w)$$

$$q_{cyl} = 0.763\, g\, 2^{-0.5} (Pr)^{-0.6} (\rho_s \mu_s)^{0.4} (\rho_w \mu_w)^{0.1} (du/dx)^{0.5} (H_s - H_w)$$

$$\text{where } du/dx = R_{cyl}^{-1} [2 (p_s - p_j) / \rho_s]^{0.5}$$

The stagnation point velocity gradient for the flat plate is experimentally derived as reported in the literature, while that for the cylinder is based on modified Newtonian flow.

5.3.3.2.6 Results Summary

Early in the investigation, impingement heating levels were computed parametrically for various hole sizes on RCC panel 9, several impingement distances and two surface geometries, flat plate and cylinder. The results

of these calculations are shown in Figure 5.3.3-6. Stagnation heating values for ingested flow through large diameter holes in RCC panel 8 were also provided later in the investigation in support of the Working Scenario. Table 5.3.7.2-1 lists these heating values.

As described in Section 5.3.7, these values were used to create internal heating distributions within the RCC cavity.

5.3.3.2.7 Validation/Verfication

To gauge the usefulness of this simplified model, comparisons were made with available CFD solutions discussed in Section 5.3.3.4. Figure 5.3.3-7 shows the results of this comparison and indicates the simplified model off-axis heating profiles generally envelope CFD results and have much smaller rate of decay in radial direction.

Nomenclature

A	Hole area
C_D	Discharge coefficient
D	Hole diameter
H	Enthalpy
M	Mach no.
P	Pressure
Pr	Prandtl no.
q	Heat flux
r_5	Radial distance from jet centerline at $U=U_{cl}/2$
R	Gas constant, Geometric radius
T	Temperature
U	Jet axial velocity
z	Gas compressibility
γ	Ratio of specific heats
ρ	Gas density
μ	Gas viscosity

Subscripts

c	Core
cl	Center line
cyl	Cylinder
fp	Flat plate
j	jet
s	stagnation
w	wall

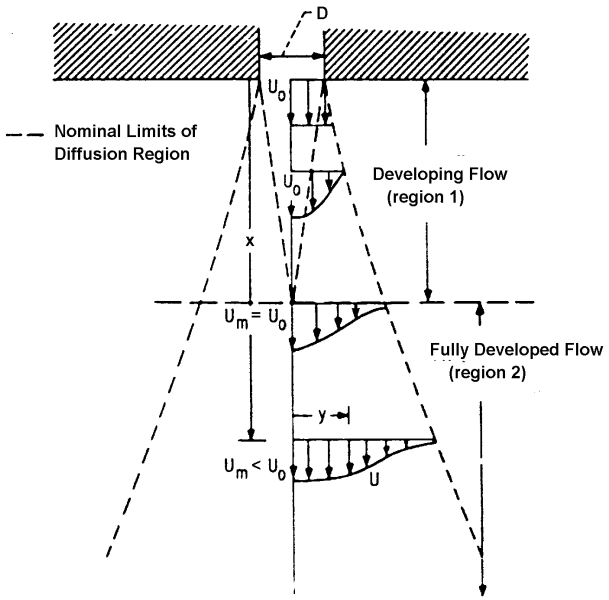

Figure 5.3.3-4 Flow Regions in Free Jet

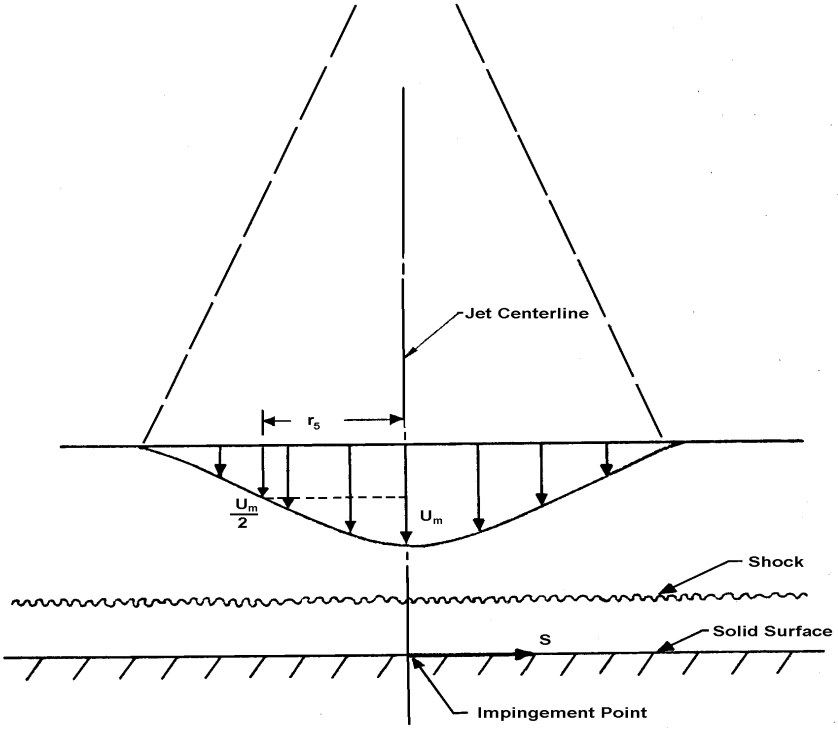

Figure 5.3.3-5 Jet Impingement Within Developed Flow Region

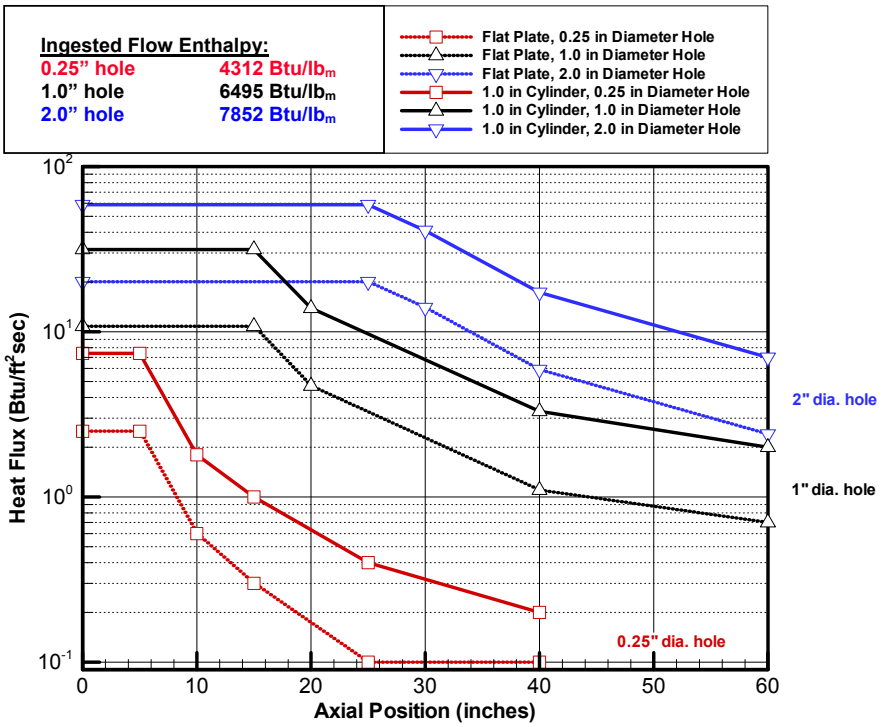

Figure 5.3.3-6 Simplified Plume Model Heating Results at 491 seconds After EI

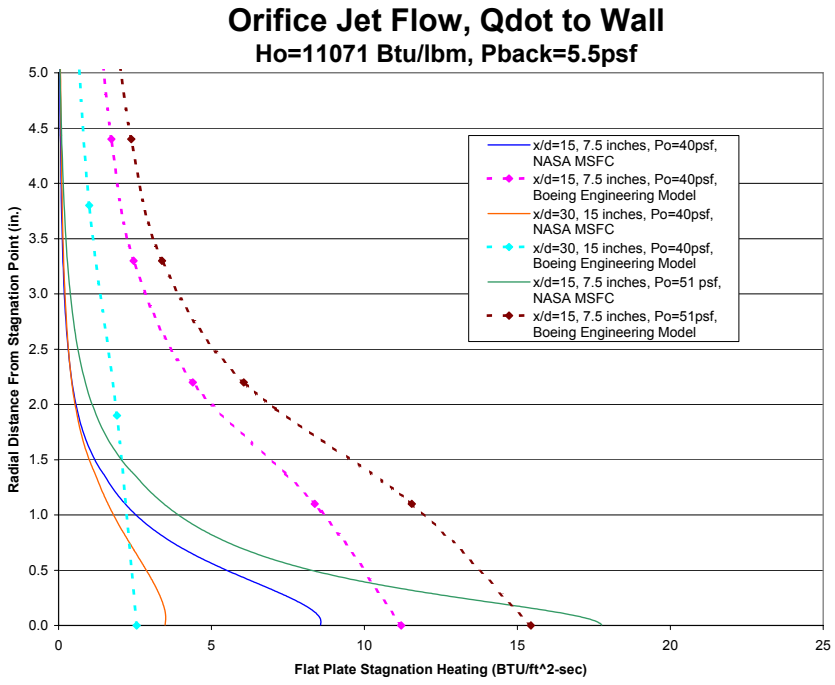

Figure 5.3.3-7 Comparison of Simplified Plume Model Results With NASA MSFC CFD Results

5.3.3.3 Engineering Corrections to Plume Model to Produce Heating Histories

The methodology of 5.3.3.2 allows the computation of stagnation heating to a flat plate, or cylinder, located along the axis of the jet, for fixed total conditions and a specified hole size. Early in the investigation process, the thermal community wanted a set of relations that would allow the assessment of heating distributions to flat plates and cylinders at arbitrary orientations to the jet orifice. The following analytical corrections allow the use of the data from Figure 5.3.3-6 for the assessment of burn-through times and hole sizes required to burn through in a specified time.

5.3.3.3.1 Radial coordinate correction

Axis values for stagnation heating are corrected for radial distance variation based on measured turbulent jet impingement heating characteristics with the distance to 50% of centerline velocity, r_5, as the similarity variable. r_5 is initially equal to the orifice exit radius, r_e, throughout the length of the undisturbed core and then slowly grows to reflect the entrainment and mixing with ambient air in the internal volume. Values from Table 5.3.3.3-1 are linearly interpolated to arrive at the ratio of local heating to centerline heating as a function of distance downstream, x.

r/r_5	$qdot/(qdot)_0$
0	1
1	0.748
2	0.392
3	0.219
4	0.154
5	0.119
6	0.1
7	0.0808
8	0.0615
9	0.0423

Table 5.3.3.3-1 Radial Jet Heating Correction

$$r_5 = r_e \qquad \text{for } x \le 7.0 r_e$$

$$r_5 = r_e + x \tan\left(\frac{\pi}{30}\right) \qquad \text{for } x > 7.0 r_e$$

5.3.3.3.2 Trajectory condition correction

Jet impingement heating values are directly dependent on the effective reservoir conditions driving the development of the plume. Figure 5.3.3-6 reflects the impingement heating values for 491 seconds from entry interface. In order to complete a thermal analysis, complete time histories of heating values must be computed. In order to do so, it is assumed that the internal heating scales with freestream dynamic pressure and the square of freestream velocity. This is equivalent to fixing the local Stanton number and scaling with mass flow through the hole (dynamic pressure) and enthalpy (velocity squared). The necessary equation is

$$\dot{q}\left(x,r,t,d_{hole}\right) = \dot{q}\left(x,0,491\sec,d_{hole}\right) \times \frac{\overline{q}(t)}{\overline{q}(491)} \times \frac{V_\infty{}^2(t)}{V^2{}_\infty(491)} \times \frac{\dot{q}(r)}{\dot{q}(r=0)}$$

5.3.3.3.3 Flat plate and cylinder attitude corrections

It is highly unlikely, given the geometry involved, that the jet will strike the impinged surface at a 90-degree angle. Therefore, corrections to the heating are required in order to reflect the known relationship between pressure and heating for more grazing angles. Using Newtonian theory for local pressures, the heating may be corrected by

$$q(x,r,t,d_{hole},\alpha) = q(x,r,t,d_{hole}) * \sin(\alpha)$$

For wire burn-through analysis, this equation takes the form of

$$q(x,r,t,d_{hole},\Lambda) = q(x,r,t,d_{hole}) * \cos(\Lambda)$$

where Λ is the sweep angle of the wire to the jet axis and is the complement to α, the local angle of attack.

5.3.3.3.4 Hole diameter effects

Holes greater than the two-inch diameter originally simulated can now be assessed for thermal effects through application of curve fit results for the 0.25, 1.0, and 2.0 inch holes. Notice that the exponent is not 2.0, which would be the case for area correction only. The larger exponent results from larger holes pulling off larger and larger portions of the boundary layer and much closer to the free stream total enthalpy.

$$q_{d_{hole}>2.0"} = q_{d_{hole}=2.0"} \times \left(\frac{d_{hole}}{2.0"}\right)^{2.6}$$

5.3.3.4 CFD Supporting the 1-D Axisymmetric Plume Model

CFD analysis was used to verify the Plume Model's (section 5.3.3.2.1) predicted heat transfer. The CFD tools were used to estimate axisymmetric plume impingement heating rates to a cold wall perpendicular to the plume axis. To facilitate the quick development of the Plume Model, the CFD analyses were set up based on past experience for what was required to produce accurate estimates of heat transfer. The CFD codes were not specifically benchmarked for conditions at which they were run. However, two CFD codes were run independently to develop confidence in the results.

5.3.3.4.1 General Boundary Conditions

The Plume Model support CFD analysis was done at conditions derived from the External CFD trajectory point #1, or EI +404 sec. These plume analyses assumed a reservoir condition which decoupled the plume flow from the external flow. Specifics of the boundary conditions for each case are given in the results section. Different chemistry models: frozen, finite rate and chemical equilibrium, were applied as needed. Two sets of plume CFD analyses were performed. The first was for a ½ inch orifice impinging on a flat plate 7.5 and 15 inches downstream from the orifice. The second set was for a six-inch orifice impinging on a plate 30 and 60 inches downstream. In all cases the downstream wall temperature was held at 540° R and was non-catalytic.

5.3.3.4.2 Laminar Flow

A key question about the plumes was whether the flow laminar or turbulent. This was important for two reasons. The first is that the heating rate of a turbulent plume would be higher than of a laminar plume. The second is that turbulent plumes are self-similar. That is, a solution for a plume from a small orifice, with the proper scaling, could be used to assess plume heating for other size orifices.

Mr. W. Dahm, NASA/MSFC, re-produced the Figure 5.3.3-8 from the literature. Although this chart maps plume characteristics for large pressure ratios (P_{total}/P_{back}) it was still useful for the relatively low pressure ratio plume calculations performed to support the Plume Model. The mapping of the plume character is done with Re_L, a Reynolds number based on the location of the plume Mach disk. It can be approximated by the orifice Reynolds number multiplied by the square root of the inverse of the total to static pressure ratio (equation shown in Figure 5.3.3-8).

The CFD plume heating calculations had orifice Reynolds numbers between 100 and 700 (Re_L between approximately 50 and 250) and pressure ratios of 5 to 15 and fell in the lower left had side of the graph. Reviewing Figure 5.3.3-9 the first observation is that for Re_L of 100 to 1000 the plume flow is laminar. The second observation is that the region of interest for the wing penetration was outside those regions in which the plumes would be self-similar. Two conclusions were made. One, the CFD analyses would be run laminar, and two, because the combinations of orifice Re and pressure ratio of interest were outside the regions of self similarity, the CFD results for one orifice size should not be scaled to other orifice sizes.

The three following calculations of a free jet (non-impinging) demonstrate the significant differences in plume structure due to different Re_L. The same total conditions were run for three different orifice sizes to assess the mixing characteristics of the resultant plumes. The orifices sizes were one-half, one and two inches

corresponding to Re_L of approximately 47, 86 and 178, respectively. As can be seen from the Mach number contours in Figure 5.3.3-9, the plume expanded to Mach 3.6 for the two-inch orifice, but only Mach 2.7 for the half-inch orifice. Additionally, the progression to fully developed flow took much longer (x=24") for the two-inch orifice than for the half-inch orifice (x=4").

5.3.3.4.3 Results

Two sets of plume heating rate calculations were performed. The first was done for a half-inch orifice with the freestream total conditions corresponding to a pressure coefficient of 1.5 at EI +404s. These conditions were, H_{total} =11071 Btu/lbm, P_{total} = 37 lbf/ft^2, T_{total}=10400 R. The back pressure was assumed to be 5.5 lbf/ft^2 resulting in a pressure ratio of 6.7.

Both NASA/MSFC and Sandia National Laboratory (SNL) personnel calculated heating rates for these conditions using the FDNS and the SACCARA codes, respectively.

This first set of heating calculations assumed frozen chemistry. The low density and rapid expansion of the gas from the orifice was the basis for this assumption. It was subsequently verified by a DSMC analysis at SNL, that few reactions occurred in these plumes. The gas was modeled as a single specie of average gas properties derived from the constituents of the disassociated gas at the total conditions. At these total conditions the equilibrium mole fractions of the constituents were N_2=0.2, N=0.55, O=0.25. The single specie molecular weight was 17.334 and the ratio of specific heats of was 1.59. Laminar flow was prescribed. Figure 5.3.3-10 shows a representative plume solution from FDNS.

Figure 5.3.3-11 shows the SACCARA and FDNS results for a subset of the cases run. For the half-inch orifice impinging on a plate 7.5 inches downstream the heating to the wall agreed within 20% between the two codes (comparing the solid blue line on the left with the solid red line on the right). Although the total conditions were slightly different, the conclusion drawn from this comparison was that the CFD codes were sufficiently accurate to provide verification for the Plume Model for a half-inch orifice.

The second set of CFD cases were run using the FDNS code. This set nominally modeled a six-inch hole in an RCC panel at EI +404s. The total conditions were based on average gas properties entering a six-inch hole in RCC panel 6 as calculated by a coupled external CFD solution (Section 5.3.6.1.3). Averaged properties of the flow entering the six-inch hole were used as total conditions. They were, H_{total} = 9004 Btu/lbm, P_{total} = 28 lbf/ft^2, T_{total} = 9796 R. At these conditions the equilibrium mole fractions were NO=0.0090, N=0.4151, O=0.2743, N_2=0.3097. The back pressure was set to 4.4 lbf/ft^2 based on the venting analysis (Section 5.3.5) for this size hole at this point in the trajectory. Frozen, finite rate and equilibrium chemistry models were run. The impinged plate was at 30 and 60 inches downstream from the orifice. Figure 5.3.3-12 shows a representative solution for these cases. Figure 5.3.3-13 shows the heating rates for the four calculations. Note that the equilibrium cases had significantly higher heating to the wall. This was a result of the full recombination of the species at the wall. Also note that the finite rate solution and frozen solution heating rates were essentially the same. The shape of the heating distribution indicates that the jet was not yet fully developed and possessed a large subsonic bubble on the axis at the impinged plate. Off axis peaks are the result of relatively high total pressure flow that has been processed through oblique shocks. Of particular interest is the comparison with engineering predictions under the same conditions. Here the model would predict that both the 30" and the 60" locations are still in the underdeveloped core region and hence have the same heating value - 30 Btu/ft^2sec. These results compare well with the peaks observed for both distances.

Nomenclature

x	axial station
d_N	Nozzle Diameter
H	Enthalpy
P	Pressure
Re	Reynolds Number
T	Temperature

Subscripts

L	Length to Mach Disk
total	total conditions

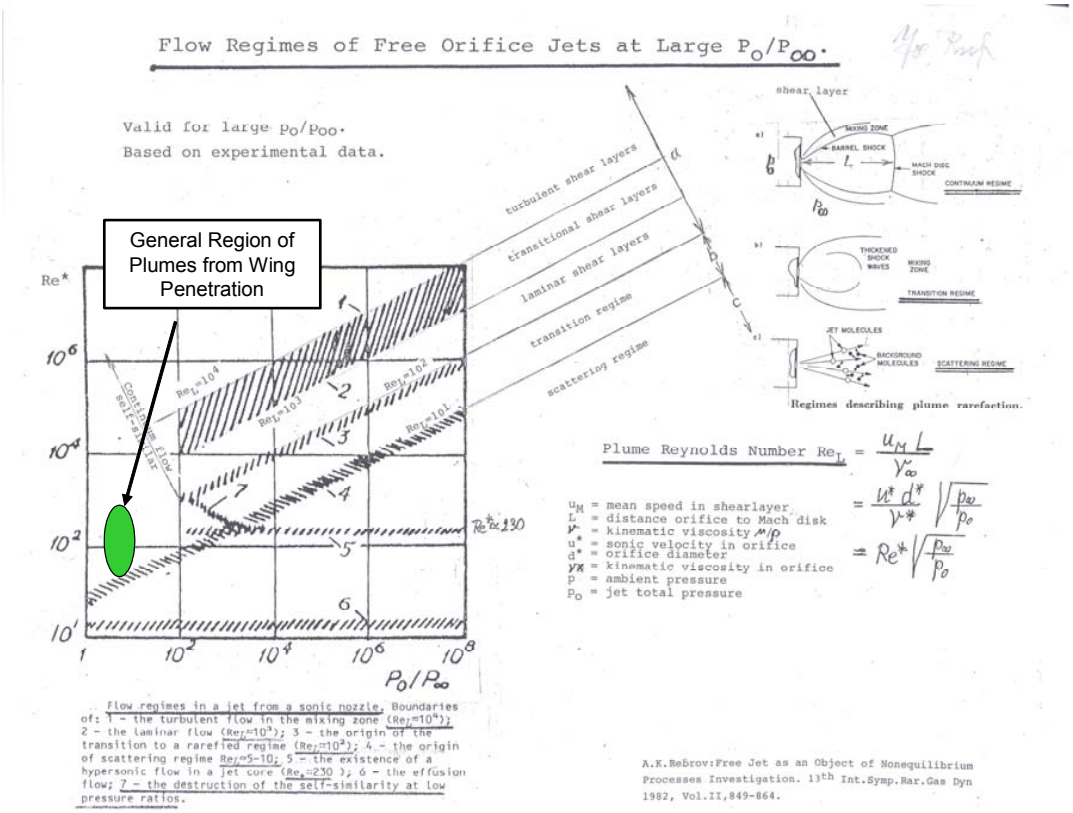

Figure 5.3.3-8 Flow Regimes of Free Jets from an Orifice.

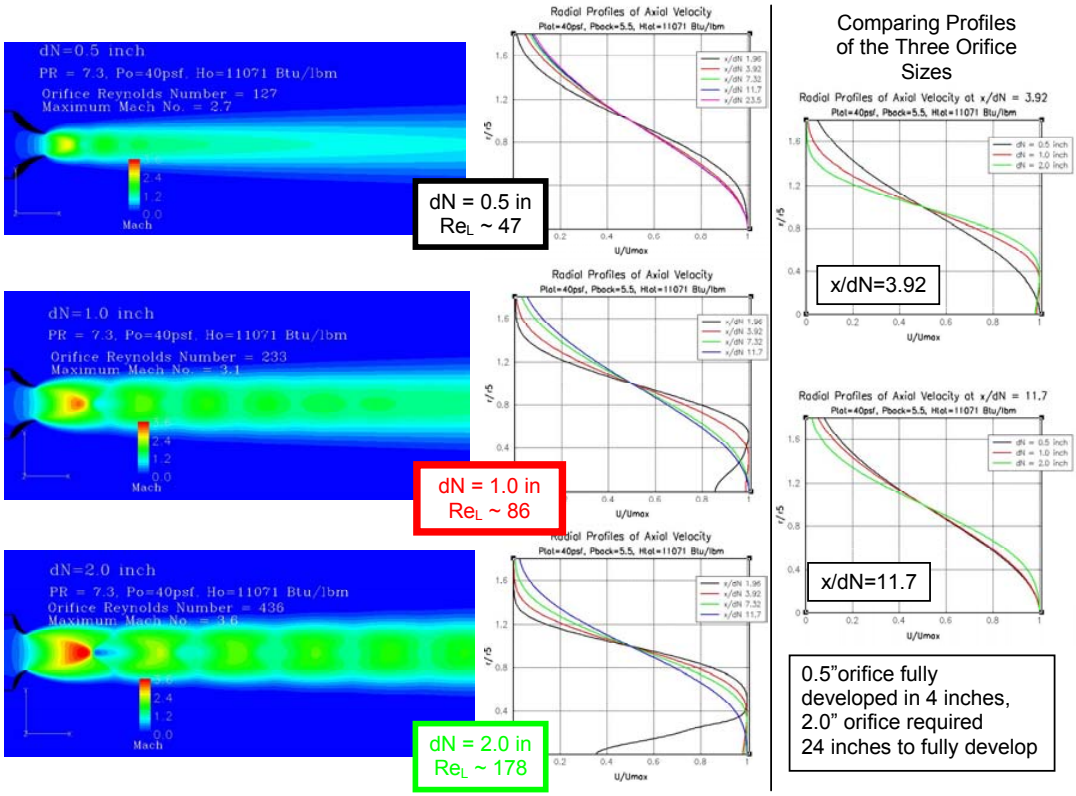

Figure 5.3.3-9 CFD Analysis of a Free Jet at Flight-like Total Conditions for Three Orifice Sizes.

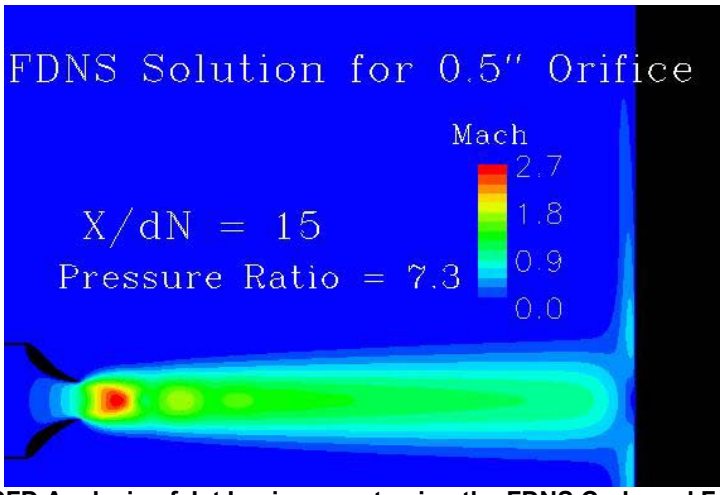

Figure 5.3.3-10 CFD Analysis of Jet Impingement using the FDNS Code and Frozen Chemistry.

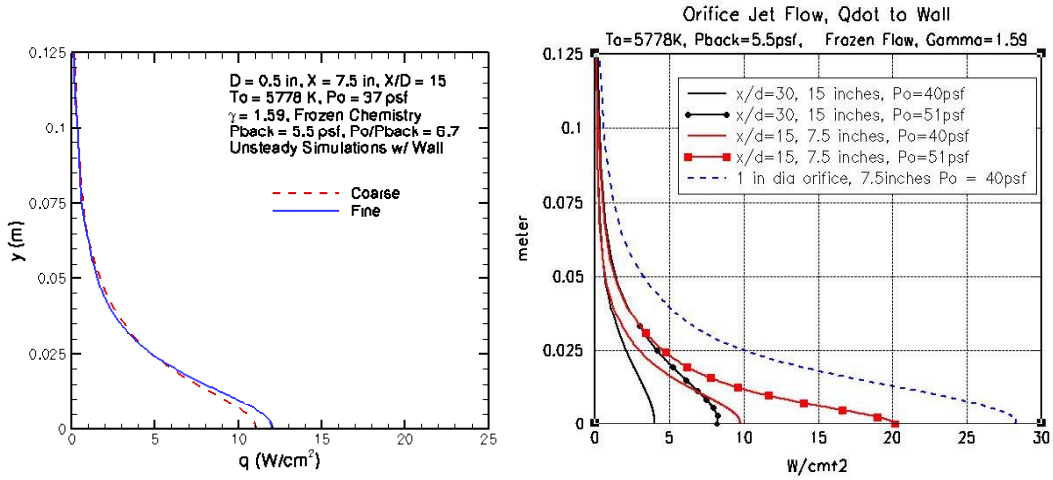

Figure 5.3.3-11 Heat Transfer for Half-Inch Orifice from SACCARA (left) and FDNS (right).

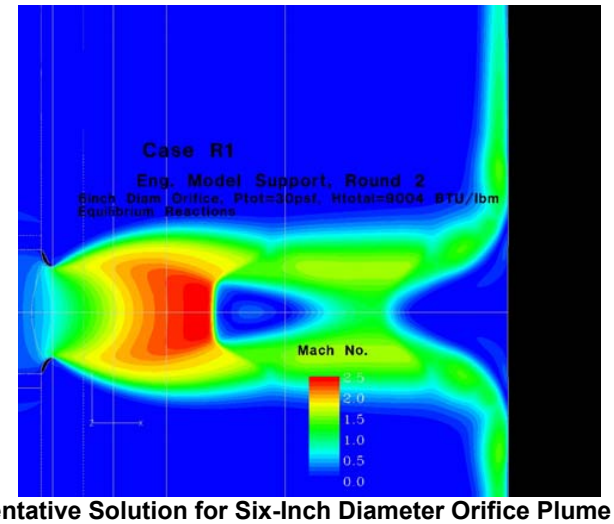

Figure 5.3.3-12 Representative Solution for Six-Inch Diameter Orifice Plume Impinging on a Plate 30 Inches Downstream.

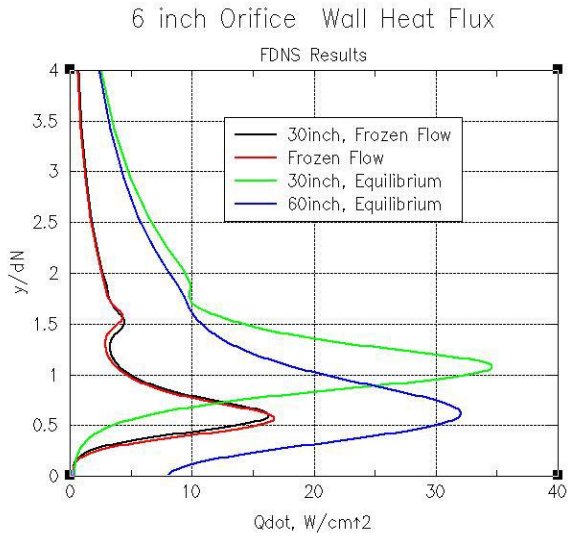

Figure 5.3.3-13 CFD Calculated Heating Rates for Six Inch Diameter Orifice Plume.

5.3.3.5 Arc-jet Test Data for Plume Heating Verification

5.3.3.5.1 Test Description

As described in Section 6.4, arc-jet tests were conducted in the NASA JSC facility to support the evaluation of effects of a breach hole in the Orbiter aeroshell. The test fixture, as sketched in Figure 5.3.3-14, was a rectangular cross-section box that was inserted into the flow exiting the arc-jet nozzle. Figure 5.3.3-15 shows the box with a hole in the front face and the location of test articles in the box downstream of the hole. Tests were conducted with a 1-inch and a 2-inch diameter hole in the front face. At the 15-inch test article location, pitot-probes, heat flux sensors and an instrumented cylinder were used to obtain data to verify the plume heating models.

Arc-jet test conditions were selected to be representative of those in flight by using total enthalpy and stagnation pressure as the simulation parameters. Figure 5.3.3-16 presents the STS-107 history of total enthalpy plotted as a function of the stagnation pressure. These values were derived from the STS-107 EOM3 trajectory simulation. A box is indicated on the plot that is labeled 'Zone of Interest' that corresponds to the range of total enthalpy and stagnation pressure for the time span of 300 to 600 seconds from entry interface. The two symbols on the plot indicate the total enthalpy and stagnation pressures that correspond to the two test conditions at which data were obtained. The arc-jet stagnation pressure was obtained from measurements of the pressure on the front face of the test fixture during runs. The arc-jet total enthalpy was derived from a combination of the stagnation pressure and the measured heat flux on a flat-face 1-inch diameter heat flux probe inserted into the arc-jet flow field at the same location at which the test fixture was located during runs. The following relation documented in Hiester and Clark was used with the measurements to obtain an estimate of the total enthalpy in the arc-jet flow field just upstream of the hole in the test fixture.

$$H_{total} = 24\dot{q}_{stag}\sqrt{\frac{R_{eff}}{P_{stag}}}$$

In this relation, R_{eff}, is the effective radius and is obtained by multiplying the flat-face cylindrical radius by a factor of 3.3, as recommended by Hiester and Clark.

The following table provides a summary of the two test conditions.

Test Configuration	Air Flow Rate (lb_m/sec)	Arc-jet Current (amps)	P_{stag} (psf)	q_{stag} (Btu/ft^2-sec)	H_{total} (Btu/lb_m)
1-inch Dia. Hole	0.3	1200	27	154	12,200
2-inch Dia. Hole	0.4	1200	35	139	9,700

5.3.3.5.2 Results

For the purpose of verifying plume-heating models, the most significant data obtained from this test series were pitot-pressure measurements and heat flux data on a 1.75-inch diameter cylinder at the 15-inch location downstream of the hole. The measured and predicted values are presented in the following table:

Test Configuration	P_{stag} (psf)	H_{total} (Btu/lb_m)	P_{box} (psf)	$P_{pitot-X=15"}$ (psf)	Measured q_{cyl} (Btu/ft^2-sec)	Predicted q_{cyl} (Btu/ft^2-sec)
1-inch Dia. Hole	27	12,200	0.88	2.02	4.7	21.1
2-inch Dia. Hole	35	9,700	0.68	3.18	12.1	39.3

The predicted values were obtained using the plume-impingement heating model described in Sec. 5.3.3.1. The test fixture stagnation pressures, P_{stag}, the box internal pressures, P_{box}, and a reduced total enthalpy were used as input to these predictions. It was assumed that the total enthalpy in the gas ingested through the test fixture hole was 84% of the arc-jet centerline total enthalpy, H_{total}, for the 1-inch hole case and 93% for the 2-inch hole case. These values were based upon mean temperature estimates for entry-length ducts, as described by Kays and Crawford. Clearly, the predicted values are significantly larger than those measured. It is believed that the test fixture box interfered with the free-jet flow field emanating from the hole and created shock waves inside the box. The simple plume impingement model was not created to predict heating in this type of flow field.

5.3.3.5.3 CFD Computation for Arc-jet Test Setup

At the time of report release, JSC was in the process of running CFD solutions for arc-jet conditions and the test hardware mockup. Preliminary results indicated that the test box walls constrained the plume expansion and created compression shocks that changed the plume flow field.

5.3.3.5.4 Conclusions

The breach hole arc-jet test provided valuable data about hole growth in aluminum plates and about the demise of flight-like instrumentation cable bundles. However, questions about the flow field inside the box prevent the impingement heating data to be used for verifying the plume impingement heating model.

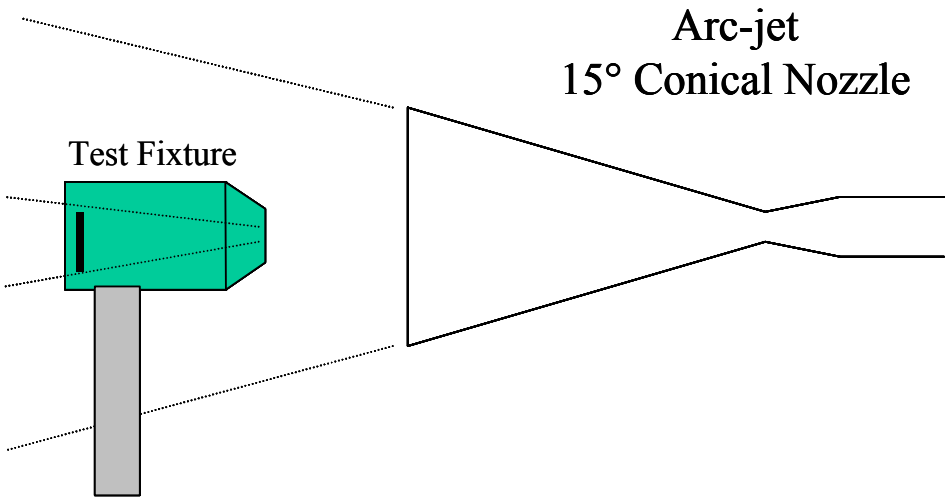

Figure 5.3.3-14 Sketch of Breach Hole Arc-jet Test Setup.

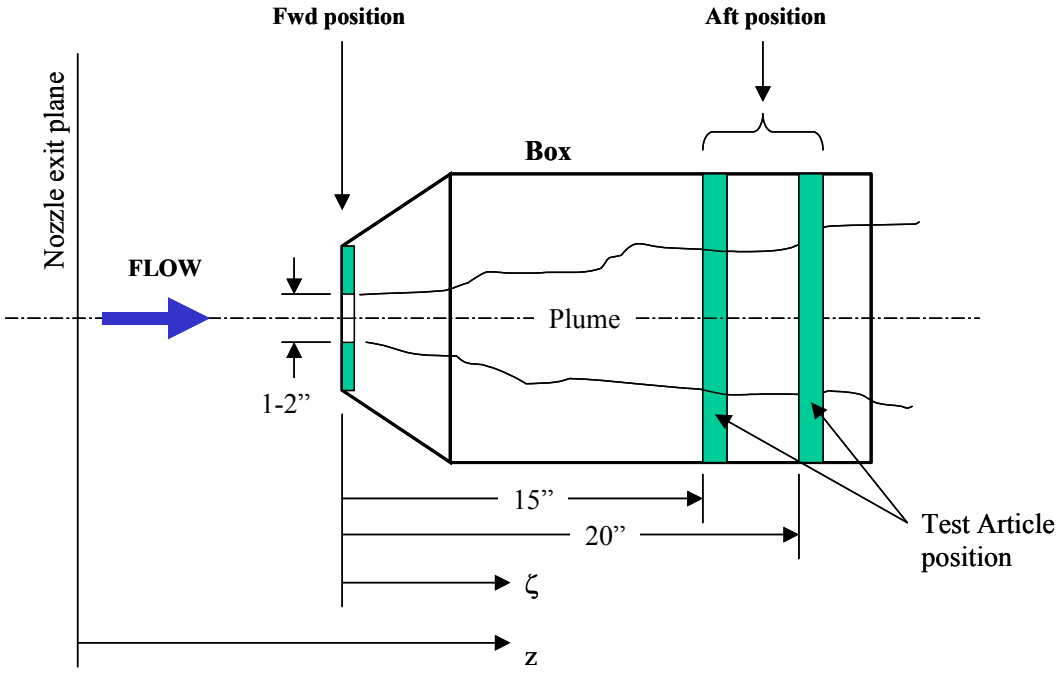

Figure 5.3.3-15 Sketch of Test Fixture and Locations of Test Articles

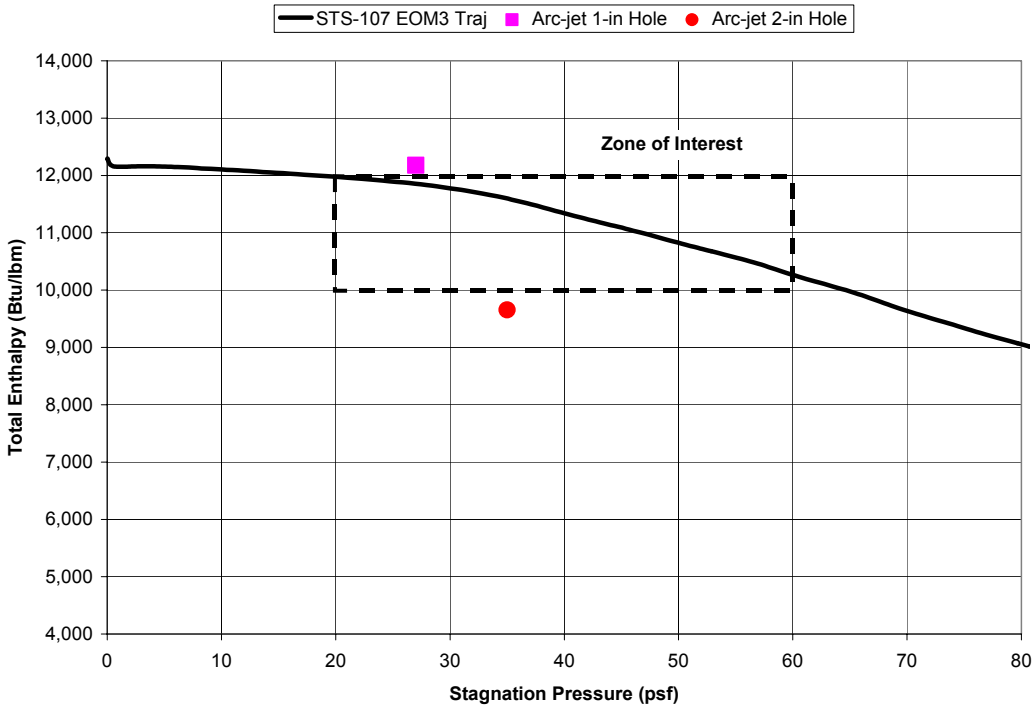

Figure 5.3.3-16 Comparison of STS-107 Flight Conditions and Arc-jet Test Conditions.

5.3.3.6 Slot Jet Heating Model (Missing Panel 8/9 T-seal)

5.3.3.6.1 Scenario Description

One of the damage scenarios evaluated was that the T-seal between leading edge panels 8 and 9 was damaged and missing at the beginning of the STS-107 reentry. In this instance it was postulated that only the lower portion of the T-seal between the apex and the beginning of the internal earmuff insulation was missing. Figure 5.3.3-17 provides a sketch of the geometry for this case. Panel 8 has been removed to permit a view of the internal structure.

5.3.3.6.2 CFD Predictions of Heating to Internal Hardware

Two sets of CFD solutions were used as the basis for developing the transient heating distribution to the earmuff insulation as a result of a missing T-seal between Panels 8 and 9. A 3-D Navier-Stokes CFD solution of the flow through the gap between panel 8 and 9 ribs for a missing 8-inch segment of T-seal has been provided by Boeing-Huntington Beach (see Sec. 5.3.6.2.3) for CFD Point 1:

> CFD Point 1: EI+404 secs.; Mach =24.9; Altitude = 243,000 ft; Angle-of-attack = 40 degs.; Dynamic pressure = 22.0 psf.

The heat flux distribution on the earmuff and spar insulation predicted by this solution is presented in Figure 5.3.3-18. The heat fluxes are for a wall temperature of 460° R. Note that the highest heating is concentrated at the edge of the earmuff closest to the rib channel outlet and quickly drops by a factor of ten on the rest of the earmuff front face. Heating to the earmuff sides and spar insulation is on the order of another factor of ten lower – less than 0.3 Btu/ft^2-sec.

Several 2-D Navier-Stokes CFD solutions were generated for the same flight conditions and for the perpendicular impingement of the flow emanating from the rib channel onto the earmuff insulation (see Sec. 5.3.6.2.1). Figure 5.3.3-19 shows the Mach number contours for the 2-D solution for a 5-inch distance between the rib outlet and the front face of the earmuff insulation. Cases were also run for 2-inch, 11-inch and 21-inch distances between the ribs and the earmuff. The resultant heat flux distributions predicted are presented in Figure 5.3.3-20 for a 1500° F wall temperature. The predicted heat fluxes on the edge of the earmuff are probably high due to a smaller than actual edge radius (0.25" modeled versus a 1.0" actual) used in these solutions. In order to apply the 2-D results to the actual hardware, lines perpendicular to the rib outer edge were projected to the earmuff front face centerline as shown in Figure 5.3.3-21. The radial distances between the rib and the earmuff were selected to approximate the perpendicular distances used in the 2-D CFD cases and the angles between the radial rays and the earmuff centerline were obtained. The 2-D CFD centerline heat flux values were then corrected by the cosine of the impingement angle. The resultant centerline heat fluxes are presented in the table below as a function of distance from the lower edge of the earmuff insulation.

Earmuff Location (inches)	Distance from Rib (inches)	Impingement Angle (degs)	CFD Prediction (Btu/ft^2-s)	Angle Corrected Heat Flux (Btu/ft^2-s)
2	2	70	46.7	15.9
6.5	5	70	17.5	6.0
12	11	65	7.1	3.0
20	18	55	3.1*	1.8

*Value derived by curve-fit since actual data were available for 2, 5, 11, and 21 inches.

5.3.3.6.3 Development of Engineering Model for Earmuff Insulation Heating

The CFD solutions provide heat flux predictions for a single flight condition – CFD Point 1. In order to conduct a thermal analysis and determine the response of the hardware, heat fluxes are needed as a function of time (varying flight conditions) and as a function of the surface temperature. Furthermore, the 3-D CFD solution was modeled with only an 8-inch length of the T-seal missing. Therefore, engineering judgment had to be used to estimate the effect of having a longer length of T-seal missing. The first step in the process of developing the engineering model was to assume that a majority of the heating was on the front face of the earmuff and then to establish the heating along the centerline of the earmuff in a local coordinate system. Figure 5.3.3-22 presents a sketch of the local coordinate system with an origin at the center lower edge of the earmuff and with the x-axis lying along the earmuff centerline from the lower to the upper edge. The z-axis is perpendicular to the earmuff front face.

The earmuff centerline heat fluxes in the local coordinate system are presented in Figure 5.3.3-23. Both the 3-D and corrected 2-D CFD values are shown. A best-estimate curve-fit is also provided that uses a reference maximum heating rate of 55 Btu/ft^2-sec at X_{local}= 0.25 inches.

$$q_{CL}(x) = \frac{0.412 q_{CL}(x = 0.25")}{x^{0.64}}$$

This curve-fit provided the basis for the earmuff centerline cold-wall heating distribution. In order to account for wall temperature effects and the energy available to heat the earmuff, the cold-wall heat fluxes were used to obtain enthalpy-based heat transfer coefficients. The final engineering model provides heat transfer coefficient and bulk enthalpy histories to use in calculating the transient heat flux to the earmuff.

$$q(x, y, t) = h(x, y, t)(H_{bulk}(t) - H_{wall}(T_{wall}))$$

In this relation, h, the heat transfer coefficient is a function of the location (x,y) and the time, t; H_{bulk} is the ingested bulk enthalpy of the flow through the rib channel as a function of time; and H_{wall} is the enthalpy of the gas at the wall temperature. Therefore, the centerline heat flux is defined by

$$q(x,0,t) = h(x,0,t)(H_{bulk}(t) - H_{wall}(T_{wall}))$$

with

$$h_{CL}(x,0,t) = \frac{0.412 h_{CL}(0.25",0,t)}{x^{0.64}}$$

The heat transfer coefficient at the reference point, h_{CL}(0.25",0,*t*) was obtained for *t*=EI+404 secs. from the peak cold-wall heat flux value of 55 Btu/ft^2-sec estimated from the CFD solutions and using a bulk enthalpy estimated from the 2-D CFD solutions.

$$h_{CL}(0.25",0,404\,\text{sec}.) = \frac{(5366 Btu/lbm) - H_{wall}(460R))}{55 Btu/ft^2 - \text{sec}} = 0.0105 lbm/ft^2 - \text{sec}$$

To obtain time dependent, and therefore flight condition dependent, values of the heat transfer coefficient at x=0.25" it was assumed that the heating varied as the square-root of the free-stream dynamic pressure. The rationale for this assumption is that impingement heating is proportional to the square root of the impingement pressure. In addition, the impingement pressure on the earmuff is driven by the wing leading edge external pressure which is a function of the dynamic pressure.

The variation of the bulk enthalpy with flight conditions was obtained by using the engineering analysis procedures discussed in Sec. 5.3.2. The effective gap width of the ingested flow was varied until the bulk enthalpy predicted by the engineering analysis matched that estimated from the 2-D CFD solution for t=404 seconds. The resultant bulk enthalpy history and the predicted maximum earmuff heating rate history are presented in Figure 5.3.3-24. The table below also presents the transient values.

EI Time (secs.)	**Ingested Enthalpy (Btu/lbm)**	**Dynamic Pressure (psf)**	$\sqrt{\frac{P_{dyn}}{P_{dyn,t=400s}}}$	**q_{CL}(x=0.25") Tw=460 R (Btu/ft^2-s)**	**h_{CL}(x=0.25") (lbm/ft^2-s)**
200	3781	1	0.23	8.81	0.0024
300	4861	8	0.65	32.26	0.0068
400	5366	19	1.00	55.00	0.0105
500	5387	25	1.15	63.34	0.0120
600	5273	33	1.32	71.20	0.0138
700	5095	41	1.47	76.63	0.0154
800	4741	48	1.59	77.02	0.0166
900	4334	69	1.91	84.23	0.0199

With the centerline heat transfer coefficients and bulk enthalpy values defined as a function of time, the lateral distribution of heat transfer on the earmuff was defined as a function of the centerline values using the results from the 3-D CFD solution. The non-dimensionalized values are presented in Figure 5.3.3-25 for five axial stations – x=0.25, 1, 2, 4, and 8 inches. Beyond 8 inches it was assumed that the distribution was the same as that for the 8-inch station.

Figure 5.3.3-26 presents a comparison of the cold-wall heat flux distribution on the earmuff front face from the 3-D CFD solution and that resulting from the engineering model. The acreage heating provided by the engineering model tends to be greater than that predicted by the CFD and that was done to provide an estimate of the effect of the increased length of the T-seal missing.

Heating to the sides of the earmuff and the spar insulation was assumed to be low and estimated to be below 0.5 But/ft2-sec at EI+404 seconds. Using this value a heat transfer coefficient of 0.0001 was estimated and the heat flux was then computed using the following relation:

$$q = 0.0001\sqrt{\frac{P_{dyn}}{P_{dyn,t=400s}}}(H_{ingested}(t) - H_{wall}(Tw))$$

5.3.3.6.4 Reduction of Heating with Distance from Rib Channel Outlet

In order to estimate the heating to hardware behind the earmuff after the earmuff is removed a relation was derived from the 2-D CFD solutions that provides an indication of the reduction in heating as a function of distance from the rib channel outlet. The relation is presented in Figure 5.3.3-27 and was obtained by curve-fitting the centerline heat flux predictions from the 2-D CFD solutions for a normal impingement.

This curve-fit was used to estimate the heating to a 1.75-inch diameter cylinder located 13 inches from the rib outlet. The cylinder represents an instrumentation cable bundle that would be located at the closest 13 inches from the rib channel outlet. Using the curve-fit from Figure 5.3.3-27, the heating to the front face of the earmuff would be approximately 4.7 Btu/ft^2-sec. However, the earmuff has a blunt front face with a width of 9 inches. To correct the heating for the difference in geometries between the earmuff and the cylinder the square root of the ratio of effective radii is used.

$$q_{cyl} = q_{earmuff-CL}\sqrt{\frac{R_{eff-earmuff}}{R_{eff-cyl}}}$$

The effective radius of the cylinder is half the diameter or 0.875 inches. With the blunt front face of the earmuff the effective radius is estimated to be 3 times the half-width or 13.5 inches. The estimated heat flux to the 1.75-inch cylinder would be 18 Btu/ft^2-sec. The factor of three is a typical ratio for scaling a flat-faced cylinder to an equivalent hemisphere as reported by Hiester and Clark.

This heating value was verified by extracting flow field properties from the 2-D CFD solution at a point 13 inches downstream of the rib channel outlet, and using a stagnation point relation also provided by Hiester and Clark to compute the heating.

$$q_{cyl} = \frac{H_{total}}{24}\sqrt{\frac{P_{stag}}{2R_{eff-cyl}}}$$

The factor of 2 in the relation is used for stagnation heating to cylinders. From the 2-D CFD solution the value of total enthalpy at 13 inches from the rib channel outlet was 5654 Btu/lb$_m$ and the stagnation pressure was determined to be 1.9 psf. Using these values, in the appropriate units, also results in a cold-wall heat flux on the cylinder of 18 Btu/ft^2-sec. This value contrasts with the results of section 6.0 in assessing the heating rate required to match the wire demise rate observed from flight of 89.6 Btu/ft^2-sec.

5.3.3.6.5 Heating to the Panel 8/9 Rib Channel with T-seal Removed

A 2-D CFD solution was also generated by Boeing-Rocketdyne for the detailed 2-D geometry of the channel between leading edge panels 8 and 9 for the CFD Point 1 flight conditions (see Sec. 5.3.6.2.2) with the T-seal removed. Figure 5.3.3-28 presents contours of the gas static temperature predicted by this solution. Three flow field regions were identified from these results – 1) separation region; 2) stagnation region; and 3) duct region. The flow along the Orbiter leading edge consists of a supersonic boundary layer that flows from inboard to outboard. When the flow encounters an open rib channel, the flow locally separates from the surface and then impinges on the downstream edge of the outboard rib. Some portion of the flow is turned inward and flows through the parallel ribs creating a flow similar to a two-dimensional duct. Using the characteristics of these flow regions and the heating distributions predicted by the 2-D CFD solution, an engineering model was developed to predict the local heat flux history in the rib channel for the STS-107 reentry trajectory.

The 2-D CFD solution provided heat flux distributions on the upstream and downstream rib surfaces in a local coordinate system shown in Figure 5.3.3-29. The CFD heat flux distributions for a wall temperature of 2900 R

were used to obtain enthalpy-based heat transfer coefficients, *h*, referenced to the heat transfer coefficient, h_{ref}, on the external surface of the leading edge.

$$\frac{h(s,t)}{h_{ref}(t)} = \frac{\dfrac{q(T_{wall} = 2900R)}{(H_{rec} - H_{wall}(T_{wall} = 2900R))}}{\dfrac{q_{ref}(T_{wall} = 2900R)}{(H_{fs-total} - H_{wall}(T_{wall} = 2900R))}}$$

To obtain the value h_{ref} the free stream total enthalpy, $H_{fs\text{-}total}$, was used. For the heat transfer coefficients inside the rib channel, the recovery enthalpy, H_{rec}, varied by the flow region. For the stagnation region, the recovery enthalpy was assumed to be equal to the free stream total enthalpy. For the separation and duct regions, the recovery enthalpy was assumed to be equal to the ingested bulk enthalpy found by the methods discussed in Sec. 5.3.2. The heat transfer coefficient distributions for the upstream and downstream surfaces were defined with linear segments based upon the local coordinate, *s*. A comparison of the heat fluxes derived from the engineering model with those provided by the CFD solution is presented in Figure 5.3.3-30. In order to obtain the transient variation of heat flux within the rib channel, values of the ingested enthalpy were provided as a function of time and it was recommended that the heat flux for BP 5505 on the leading edge of Panel 9 be used for the reference heat flux, q_{ref}. The resultant cold-wall heat flux histories for three locations in the rib channel are presented in Figure 5.3.3-31. These heat fluxes are very high since they use the high leading-edge heating associated with BP 5505 on Panel 9 (see Sec. 5.2.2).

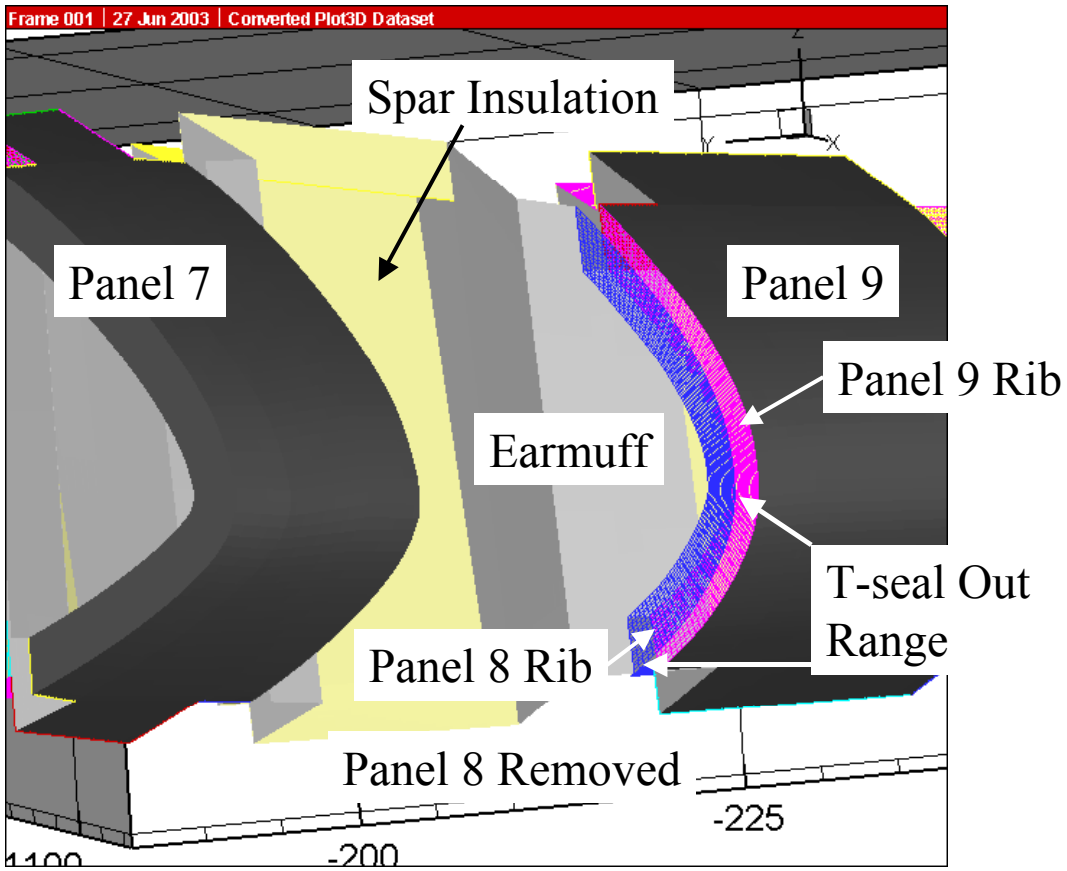

Figure 5.3.3-17 Sketch of Leading Edge Region for Panels 7, 8 and 9.

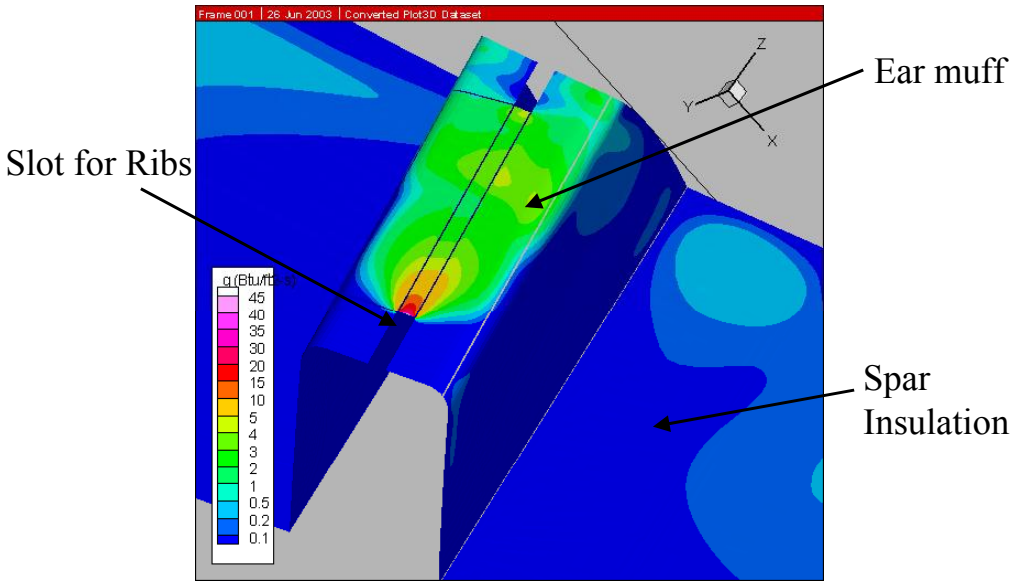

Figure 5.3.3-18 Earmuff and Spar Insulation Heating Predictions for CFD Point 1 from the Boeing-HB CFD Solution – Twall=460 R.

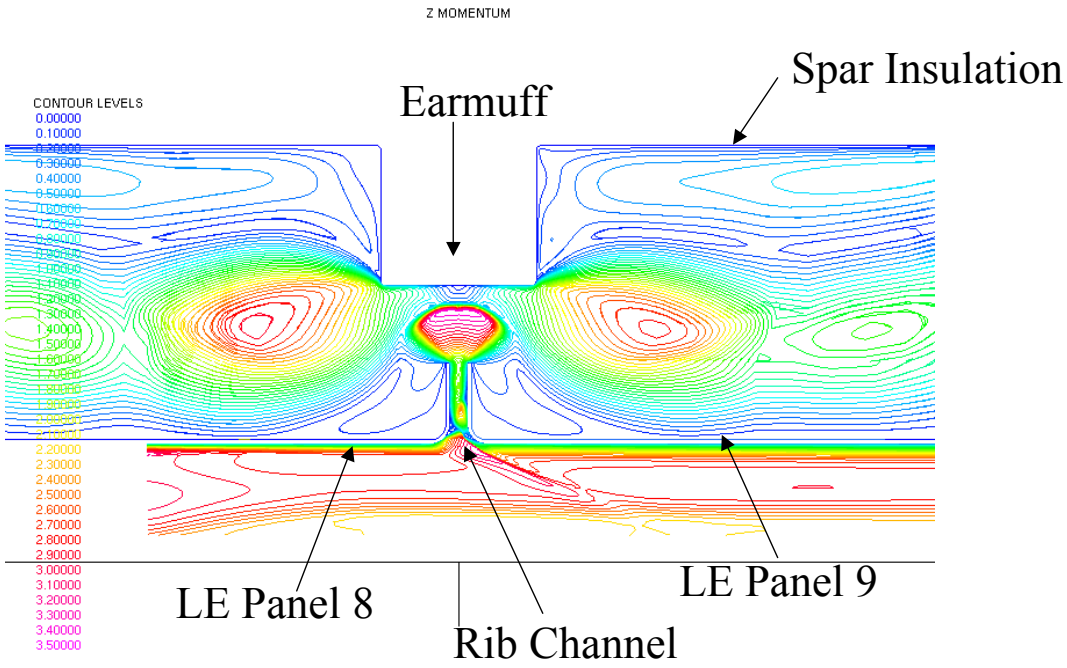

Figure 5.3.3-19 Mach Number Contours for 2-D flow impingement onto Earmuff and Spar Insulation – 5-inch Distance between Rib Channel Outlet and Earmuff.

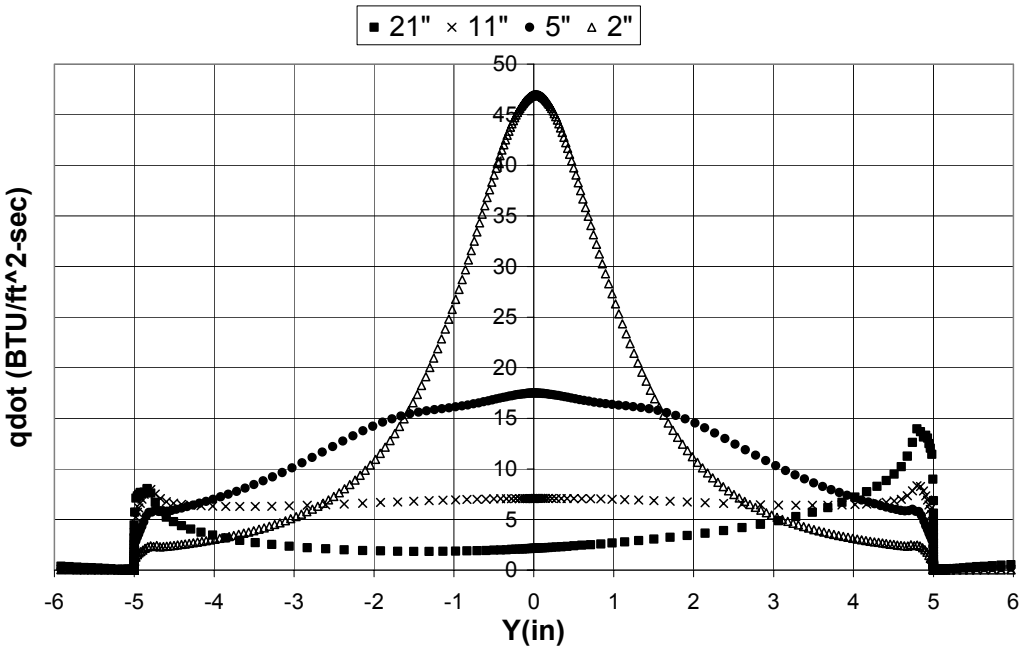

Figure 5.3.3-20 – Earmuff Heat Flux Distributions Predicted by the NASA JSC 2-D GASP CFD Solutions CFD Point 1.

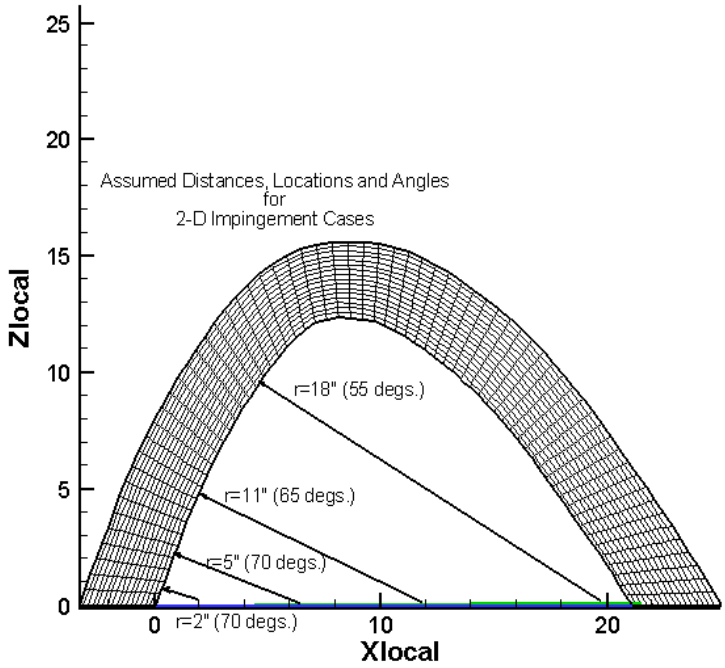

Figure 5.3.3-21 Application of 2-D CFD Solutions to the Actual Hardware

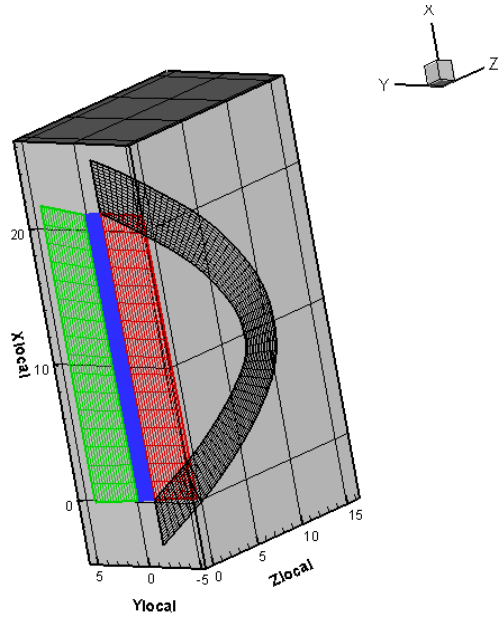

Figure 5.3.3-22 Local Earmuff Coordinate System
Figure 6 – Local Earmuff Coordinate System.

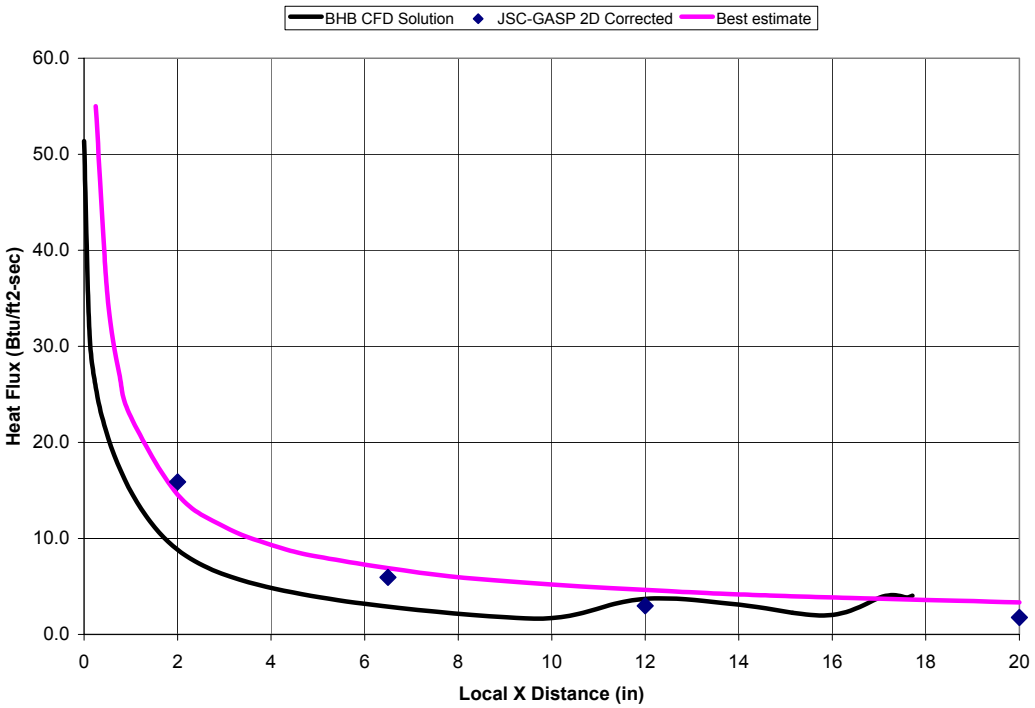

Figure 5.3.3-23 Comparison of Predicted Heat Fluxes on the Earmuff Centerline for CFD Point 1

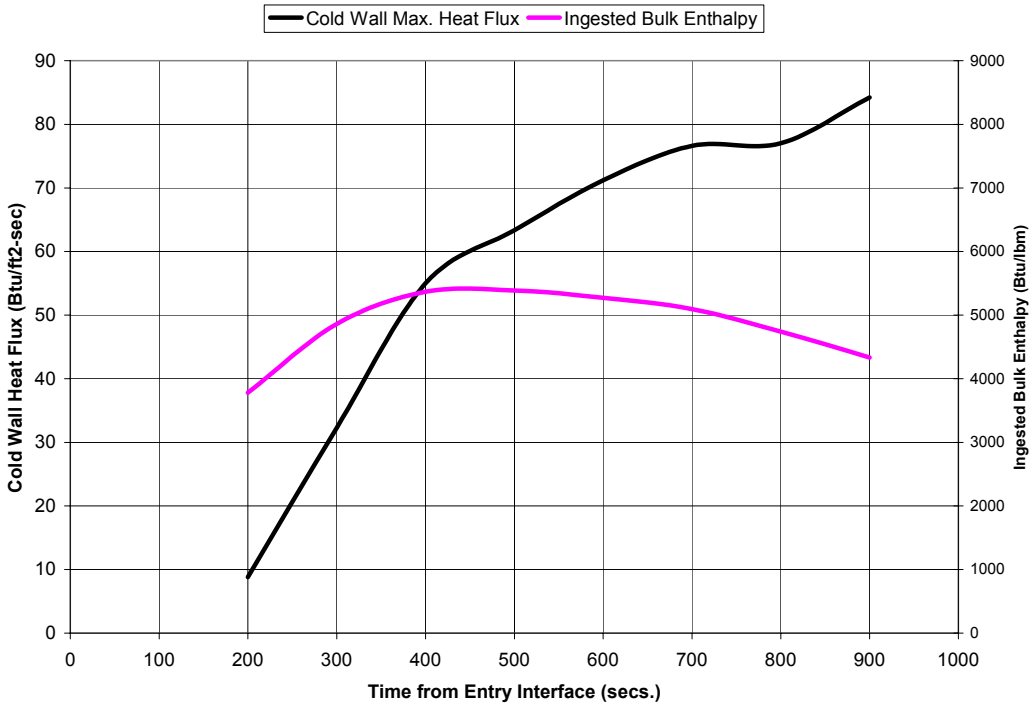

Figure 5.3.3-24 Predicted Maximum Cold-wall Heat Flux and Ingested Bulk Enthalpy Histories.

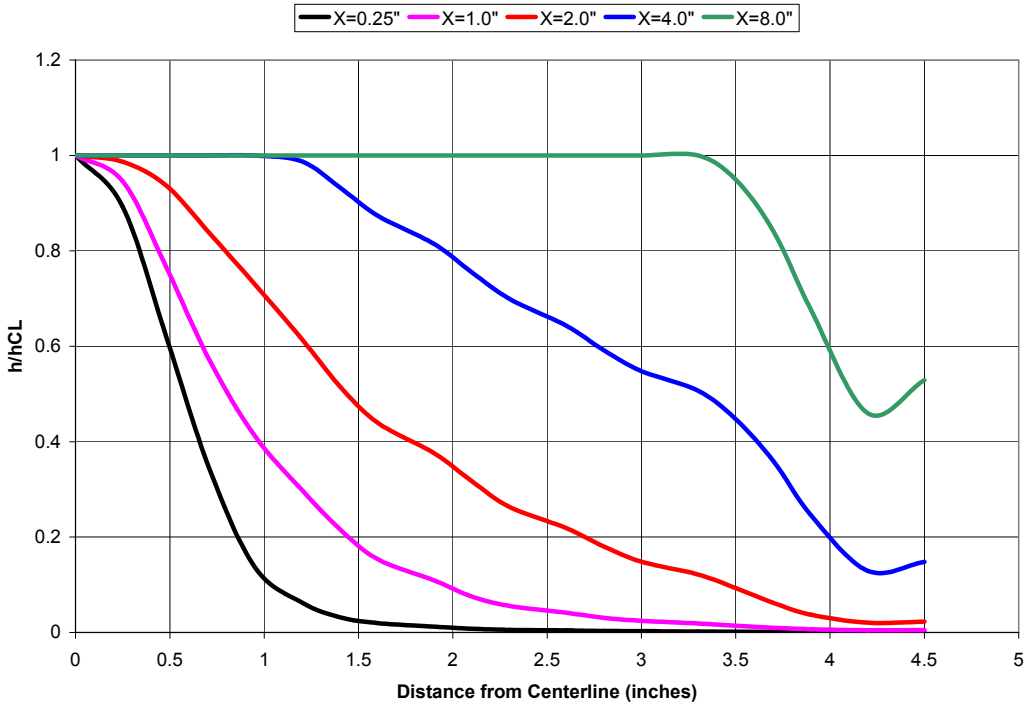

Figure 5.3.3-25 Predicted Maximum Cold-wall Heat Flux and Ingested Bulk Enthalpy Histories.

Twall=460 R

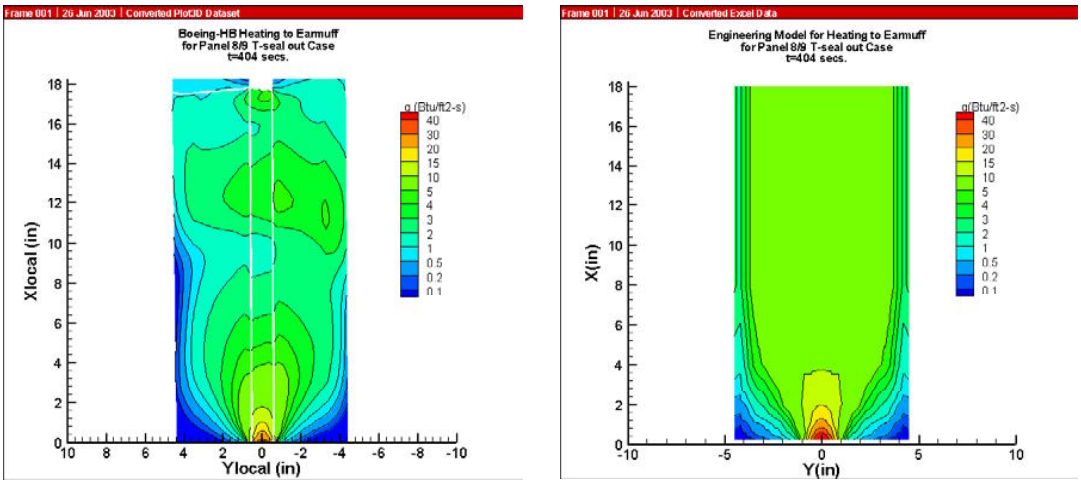

BHB 3-D CFD Results
8-inch T-seal out

Engr. Model Results

Figure 5.3.3-26 Earmuff Front-face Heating Comparison for EI+400 seconds. (Assumed results for 400 and 404 seconds are same.)

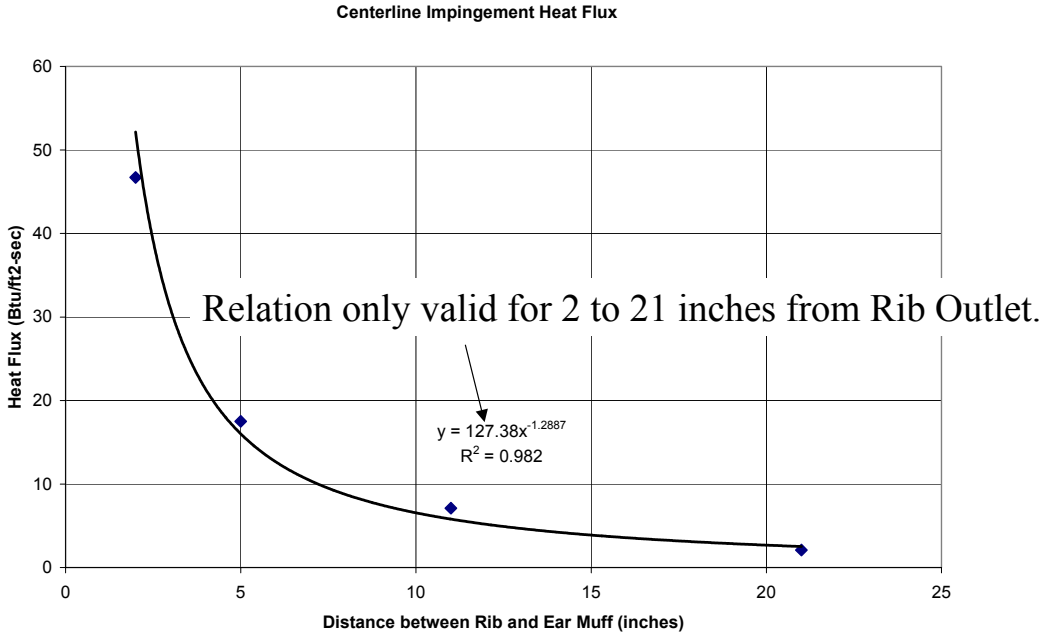

Figure 5.3.3-27 Relation for Estimating Reduction in Heating with Distance from Rib Channel Outlet.

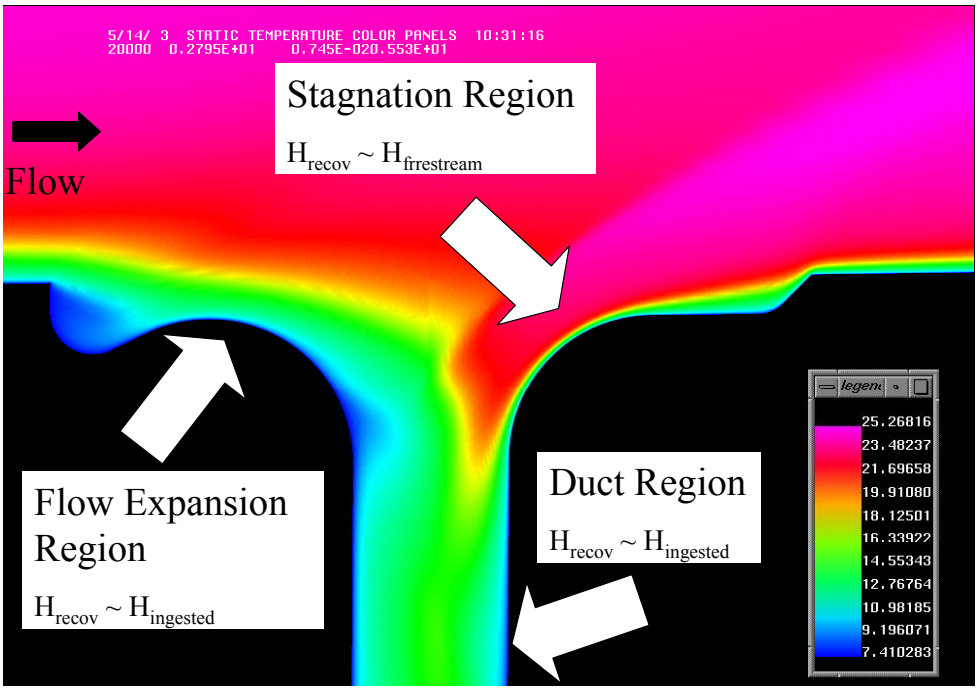

Figure 5.3.3-28 Regions of the Flow field in the T-seal Out Rib Channel.

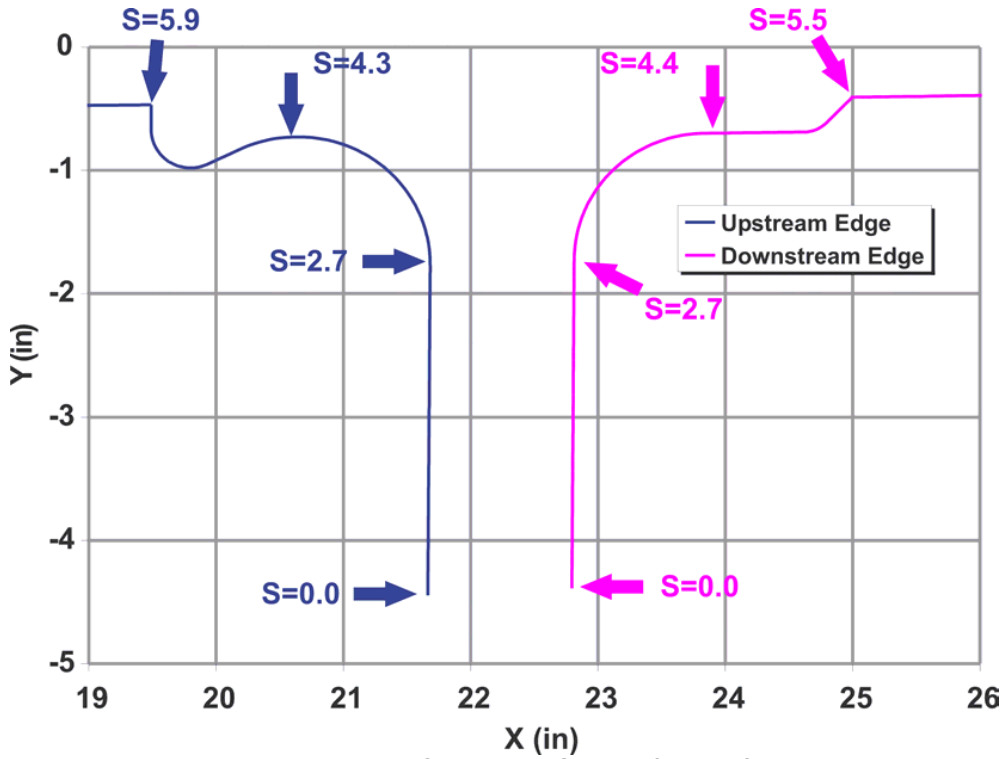

Figure 5.3.3-29 Local Coordinate System for Rib Channel.

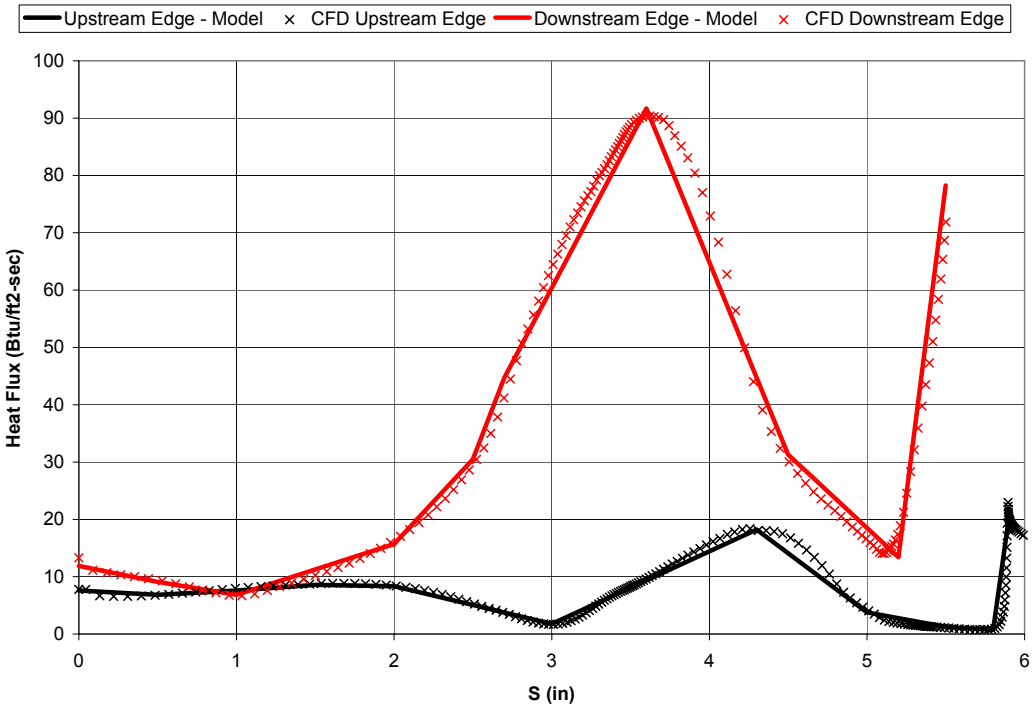

Figure 5.3.3-30 Comparison of Engineering Model Heat Fluxes with CFD Results.

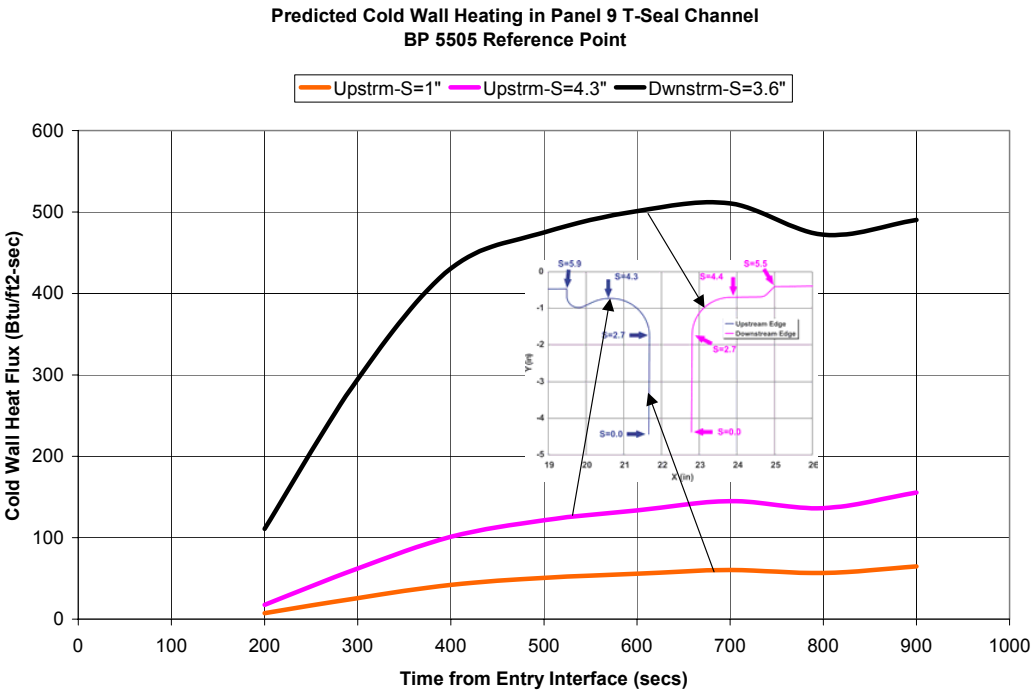

Figure 5.3.3-31 Predicted Cold-wall Heat Flux History for Locations in the Panel 8/9 Rib Channel

5.3.4 Effects of Burning Aluminum

In order to evaluate the effects of aluminum combustion on the STS-107 accident, a team was formed that included the following personnel:

NASA JSC Engineering Directorate Personnel (EG and ES Divisions)
NASA White Sands Test Facility Personnel
Boeing Huntington Beach Engineering Personnel
Lockheed Martin Space Operations Personnel
Sandia National Laboratories Personnel
Princeton – Dr. I. Glassman
Stanford – Dr. J. Jeffries
CalTech – Dr. P. Dimotakis

First, this team reviewed the aerothermodynamic environments associated with the STS-107 reentry. These environments are summarized in the following section. After reviewing these environments it was recognized that there was very limited experience with the exposure of aluminum to the high-temperature and low-pressure air resulting from a breach during reentry. Therefore, an air/aluminum chemical analysis that would determine the key reactions that would occur for the pressure and temperature range of the reentry gases was deemed necessary. Based upon the results of this analysis the heats of formations of the key reactions would be used to determine the additional energy available for propagating damage within the structure of the Columbia wing. A pictorial of the damage propagation process is provided in Figure 5.3.4-1.

5.3.4.1 Overview of STS-107 Aerothermal Environments

During the STS-107 reentry the total free stream energy of the gas surrounding the Columbia varies from about 12,000 Btu/lb_m-air in the early part of the reentry to about 7,000 Btu/lb_m-air at the time the vehicle was lost. Over this same time frame, pressures acting on the vehicle vary from near vacuum to less than 0.1 atmospheres. The resultant gas temperatures range from 6,000 R to over 10,000 R. A breach into the aeroshell exposes the aluminum structure to air at these pressures and temperatures. A more complete description of the STS-107 aerothermal environments is provided in Section 5.2.3.4.

5.3.4.2 Air/Aluminum Chemistry Analysis

5.3.4.2.1 Approach

The NASA Glenn Research Center's computer program for calculation of complex chemical equilibrium compositions and applications developed by S. Gordon and B. J. McBride was used to determine the chemical reactions that occur when aluminum is exposed to high-temperature air. This program was used to determine if the aluminum-oxygen reaction dominates the process or if aluminum-nitrogen reactions are prevalent enough to require consideration and was used to determine the appropriate heat of reaction to use in the plume energy calculations.

Several iterations of the Gordon-McBride program were run in which aluminum and air were present in stoichiometric proportions (phi=1), in fuel-lean proportions (phi=0.5), and in fuel-rich proportions (phi=2). For each fuel/oxidizer ratio a temperature-pressure problem was run in which the final temperature of the reactants were fixed at various temperatures ranging from 8000 to 520 R and the pressure was varied to represent the stagnation pressure at 8 points during re-entry (1.0, 5.1, 15.2, 35.5, 47.6, 76.0, 88.2, and 131.7 psf). More than 50 species were considered in this system including aluminum, oxygen, atomic oxygen, ozone, nitrogen, atomic nitrogen, aluminum oxide (various forms and states), and aluminum nitride (various forms and states).

Next, for each fuel/oxidizer ratio an enthalpy-pressure problem was run in which the initial temperature was input and the enthalpy was held constant for each of the 8 pressures. This calculation provided the adiabatic flame temperature of the reactants. This calculation was performed to provide a value to compare to the literature value of adiabatic flame temperature and thus provide a "sanity check" for the results.

5.3.4.2.2 Results and Conclusions

The results for the stoichiometric case (phi=1) indicate that the primary product of the reaction is Al_2O_3. Figure 5.3.4-2 presents the mole fractions for the 15.2 psf case. Figure 5.3.4-3 presents the enthalpy (energy) required to maintain the mixture at the specified temperatures. Note that for temperatures above ~5000 R energy is required to be input into the mixture to maintain the state and no aluminum oxide is formed. Below ~5000 R aluminum oxide is formed and energy is released.

These results were also confirmed in the fuel-lean case (phi=0.5). In the fuel-rich case (phi=2), aluminum nitride did appear, but it was observed that the presence of aluminum nitride did not significantly affect the calculated heat of reaction. Therefore, it was agreed by the team to use the heat of reaction of Al_2O_3 (1589 Btu/mole-Al_2O_3 (1676 kJ/mole-Al_2O_3) for subsequent calculations (see Glassman's text).

The calculated adiabatic flame temperatures in all cases compared favorably with the adiabatic flame temperatures provided by Glassman and were observed to be below the dissociation temperature of Al_2O_3 (6840 R (3800 K)). Figure 5.3.4-4 presents the flame temperatures for the stoichiometric case.

5.3.4.2.3 Additional notes

It was agreed by the team that aluminum burns if it is directly subjected to the ingested high-temperature 'plume' gases, but structural elements not directly impinged by the plume or not very near the plume will not necessarily sustain combustion. It is necessary to expose those aluminum structures to extreme heating conditions in order to get them to burn. Therefore, while the burning of aluminum contributes to the development of the breach hole and the propagation of damage inside the wing, it is not tangible for the entire wing structure to develop self-sustained burning simply as a result of that single, localized plume. It is important to realize that there are many conditions in which aluminum structural parts will not support self-sustained combustion. Factors that will hinder self-sustained burning of structural aluminum are as follows:

1) Thermal diffusivity: The thermal diffusivity of aluminum is very high enabling aluminum to rapidly conduct heat away from the burning region.
2) Radiative heat transfer: The energy radiated from a plume of hot air with burning aluminum is being distributed to a very large surface area at significant distances from the plume.
3) Fluid dynamics: The flow velocities of the plume are high. In such cases the molten and vaporized and burning aluminum will be rapidly blown downstream carrying much of the heat away from the high-temperature zone of the hole.
4) Protective oxide coating: In cases where the protective Al_2O_3 layer is not forcibly removed or penetrated, the ignition temperature of aluminum increases from the melting point of aluminum (1679 R (933 K)) to the point where the Al_2O_3 layer is breached. For systems with no mechanical disruption of the layer this is usually associated with the melting point of the oxide (4172 R (2318 K)) (see Werley et al).
5) Experience Base: WSTF has significant experience with the burning of structural aluminum and has many examples where aluminum did not support self-sustained combustion even in pure oxygen environments (see Newton and Stradling). The quenching of self-sustained combustion in these cases was clearly a function of heat transfer away from the burning region of the material.

5.3.4.3 Energy Comparison

Given the conclusion that the formation of aluminum oxide was the dominant reaction that would occur due to the exposure of aluminum structure to the reentry environments, an analysis was conducted to determine the maximum energy released by the reaction and compare that energy to the energy already in the reentry gases entering a breach into the aeroshell. As previously mentioned the heat of formation of aluminum oxide is (1589 Btu/mole-Al_2O_3 (1676 KJ/mole-Al_2O_3). Assuming that the reaction is limited by the available oxygen the energy released can be computed on a per mass of oxygen basis.

$$\left(\frac{1676 kJ / mole - Al_2O_3}{48 gm - O / mole - Al_2O_3} \right) = \frac{35 kJ}{gm - O} \text{ or } 14{,}982 \frac{Btu}{lb_m - O}$$

Using this value and the mass flow of air into a breach hole, the maximum energy flux due to aluminum combustion can be computed and compared to the energy flux associated with the high-temperature air. Of course this assumes that sufficient aluminum is available to react with all available oxygen. If the reaction is aluminum limited, then the energy released is

$$\left(\frac{1676kJ \,/\, mole - Al_2O_3}{54gm - Al \,/\, mole - Al_2O_3} \right) = \frac{31kJ}{gm - Al} \text{ or } 13{,}340 \frac{Btu}{lb_m - Al}$$

Assuming a 6-inch diameter hole into the leading edge spar, a quantitative comparison between the air energy flux and the aluminum combustion energy flux limited by the available oxygen is presented as a function time during the STS-107 trajectory in Figure 5.3.4-5. It is readily noted that the energy of the high-temperature air entering the breach hole is much greater than the energy released by the combustion of aluminum. At 600 seconds from entry interface, the reentry gas has a total enthalpy of 10,286 Btu/lb_m and flows into the 6-inch diameter hole at a rate of 0.038 lb_m/sec which results in an energy flux of 389 Btu/sec. Assuming that air is approximately 23% oxygen by mass, the energy flux associated with aluminum combustion is 133 Btu/sec or approximately one-third of the energy in the reentry gas. In order to compute the total energy available to heat wing internal structure due to a breach, the specific quantity of aluminum being heated must be considered since the energy required to raise the aluminum to the temperature at which it will begin to combust must be subtracted from the reentry gas energy.

5.3.4.4 Conclusions

Based upon this study several conclusions can be made. First, the ingestion of high-temperature reentry gases into the Columbia wing can result in the vaporization and subsequent combustion of aluminum with the primary reaction being the formation of aluminum oxide, Al_2O_3. Second, the energy released from this reaction is limited by the available amount of oxygen flowing into the wing. The aluminum combustion energy is approximately one-third of the energy already in the ingested reentry gas for the early portion of the reentry (less than 600 secs. from entry interface). Third, aluminum combustion occurs only for that portion of the wing structure being directly heated by the ingested reentry gases.

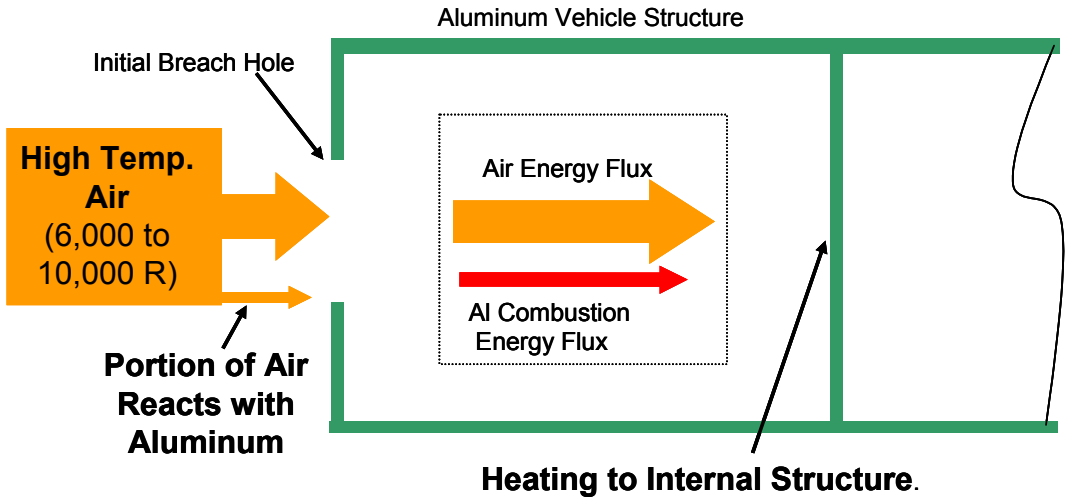

Figure 5.3.4-1 Breach Hole Scenario.

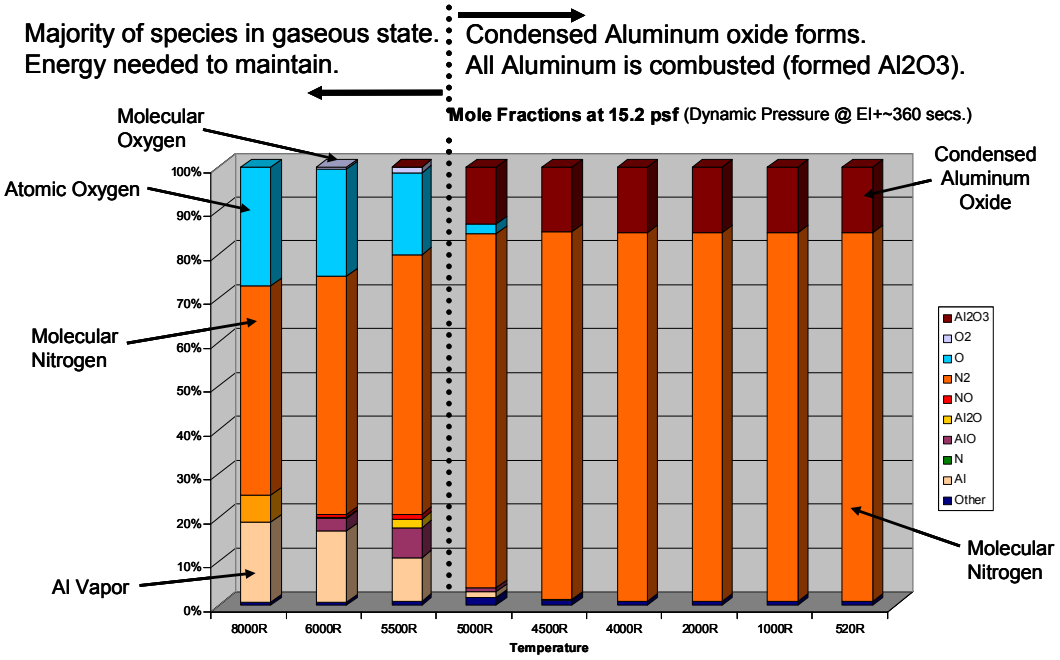

Figure 5.3.4-2 Aluminum/Air Mixture Mole fractions at 15.2 psf for Stoichiometric Conditions.

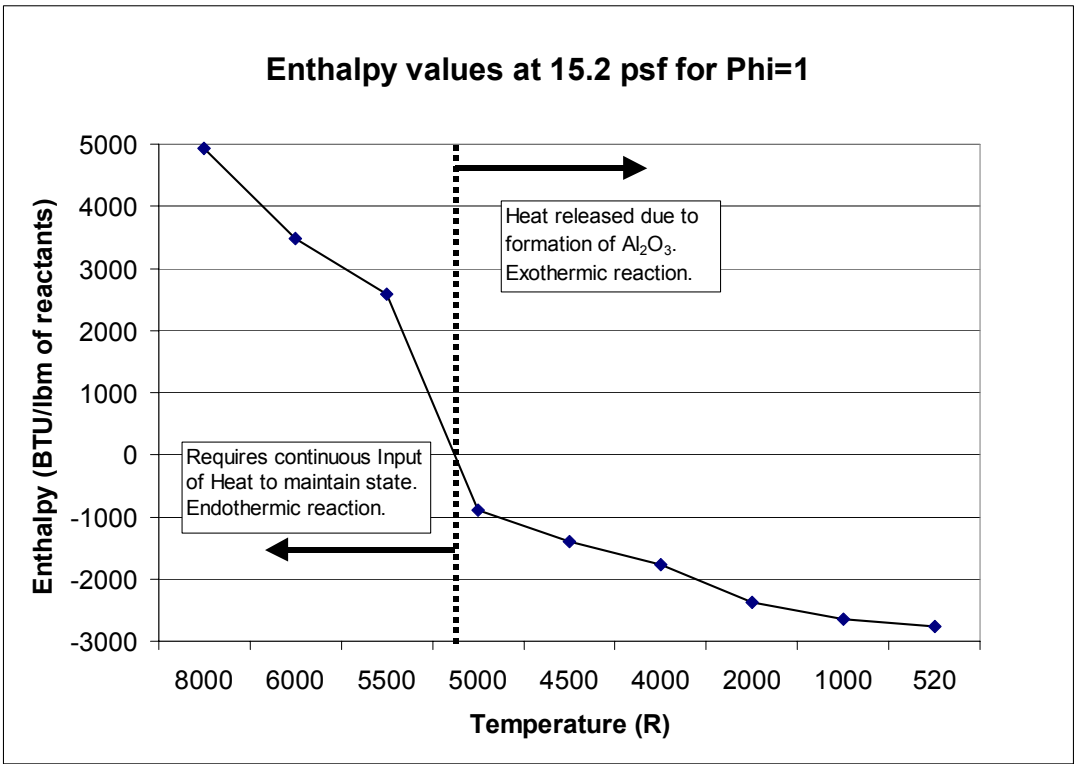

Figure 5.3.4-3 Energy Required to Maintain Air/Aluminum Mixture in Equilibrium State.

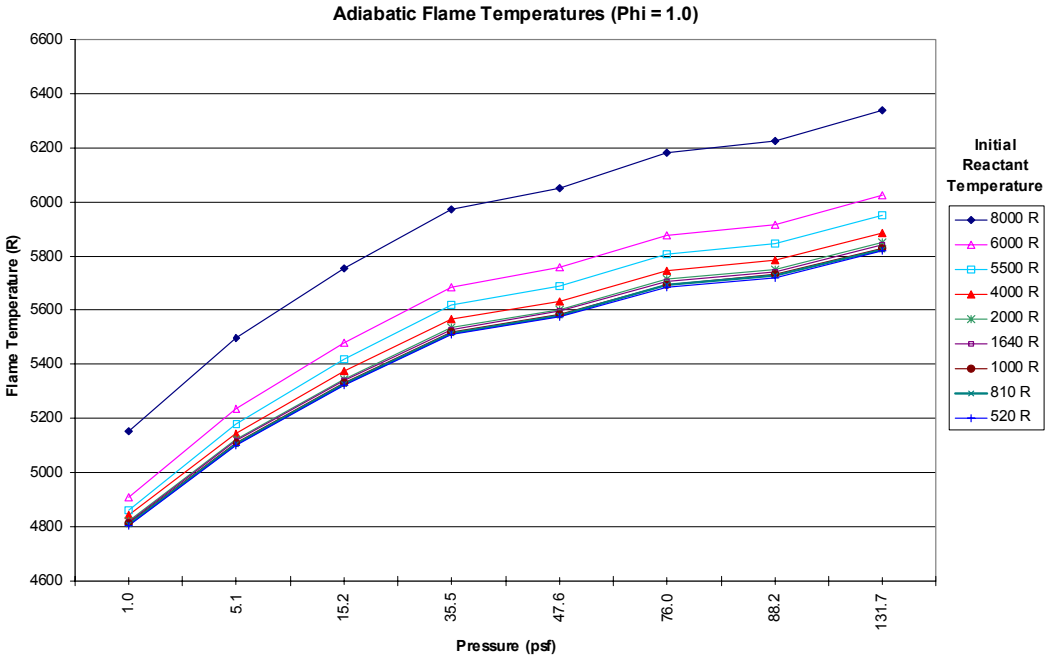

Figure 5.3.4-4 Adiabatic Flame Temperatures of Al Combustion.

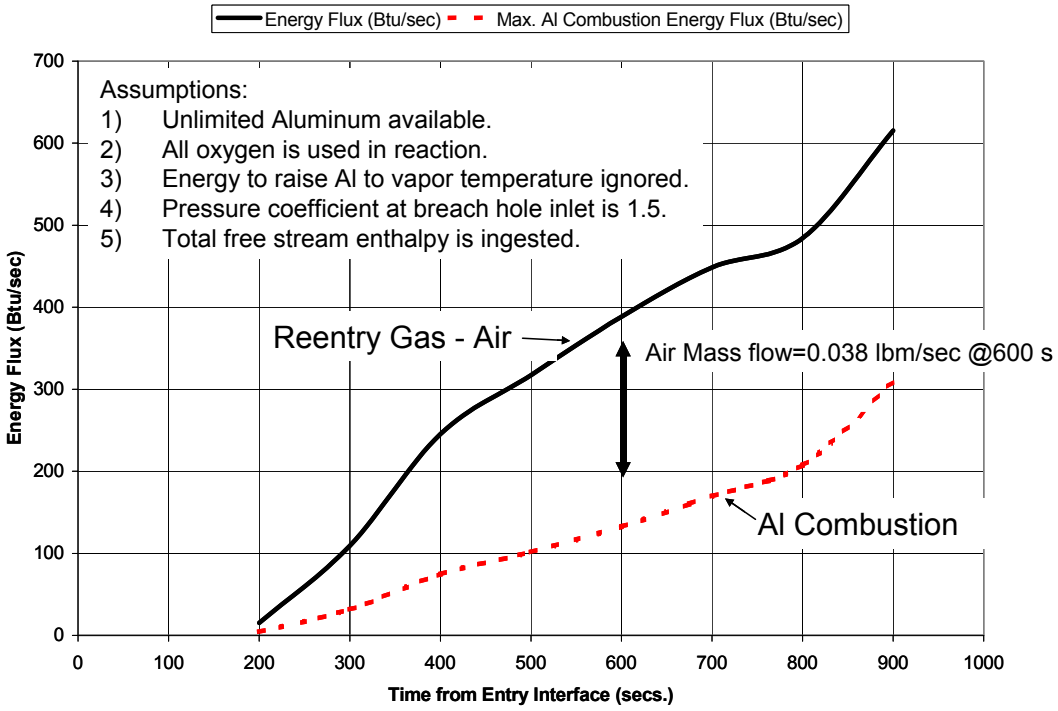

Figure 5.3.4-5 Comparison of Reentry Gas Energy Flux and Al Combustion Energy Flux for 6-inch Diameter Breach Hole in Leading Edge.

5.3.5 Coupled Venting and Thermal Model of Wing

5.3.5.1 Introduction

The objective of this analytical effort was to develop a tool capable of analyzing bulk flow in the STS-107 port wing for various breach scenarios. The intent was to utilize this transient modeling capability to provide pressure and flow rate boundary conditions to steady-state detailed CFD modeling and to screen the case matrix to isolate the more probable scenarios and decrease the number of cases for the more time intensive CFD work.

Originally, the scope was to utilize ideal gas venting codes (both CHCHVENT and FLUINT) and combine this venting model with a thermal representation (SINDA) of the wing for a coupled venting/thermal capability. Once preliminary results were achieved, the scope was increased to include the effect of dissociation and ionization of the ingested air, which was done assuming equilibrium air chemistry properties of the air as a function of air pressure and temperature instead of the ideal gas assumption.

5.3.5.2 Modeling Tools-Capabilities And Limitations

5.3.5.2.1 CHCHVent Program

Program CHCHVENT (see documentation by Fay) models the flow of a mixture of ideal gases with constant specific heats in the continuum flow regime between compartments arbitrarily connected by vents. It is primarily used to model launch vehicle compartment and payload venting environments. The program is based on the conservation equations of mass and energy with heat transfer in the chambers modeled as adiabatic, isothermal, or finite rate with a user-specified heat transfer coefficient.

Flow through the vents is assumed one-dimensional, isentropic, and is determined from the following equations (where subscripts U and D denote properties in the upstream and downstream compartments):

$$\dot{m} = C_d A P_U \sqrt{\frac{\gamma}{R T_U}} \frac{M}{\left[1 + \frac{\gamma - 1}{2} M^2\right]^{\frac{\gamma+1}{2(\gamma-1)}}}$$

where

$$M = \sqrt{\frac{2}{\gamma - 1}\left[\left(\frac{P_U}{P_D}\right)^{(\gamma-1)/\gamma} - 1\right]}$$

where:

$\dot{m} =$ Mass Flowrate

$C_d =$ Discharge Coefficient

$A =$ Flow Area

$P =$ Pressure; U=Upstream; D=Downstream

$M =$ Mach Number

$\gamma =$ Ratio of Specific Heats

$R =$ Gas Constant

T_U = Upstream Temperature

If the Mach number (*M*) is calculated to be greater than one, the program sets the Mach number to one (choked flow). A discharge coefficient (C_d) is used to correct the isentropic mass flow rate predicted from the

above equations. The C_d correction options included in CHCHVENT are: constant value, pressure-ratio dependent, and pressure-ratio-and-cross-flow dependent.

The program explicitly advances in time by numerical integration with the user having choices of 1st order Taylor series, 2nd order Modified Euler, 4th order Runge-Kutta and Runge-Kutta-Merson routines. Local pressure coefficients and local Mach numbers (which are specified as functions of free stream Mach number, vehicle angle of attack, and roll angle) and the trajectory parameters can be specified by the user.

The venting simulation is initialized by specifying pressures and temperatures for all chambers in the model. The total mass and internal energy derivatives with respect to time for a particular chamber are determined by summing the contributions from all vents connected to the chamber. These derivatives are used in the numerical routine to determine the chamber mass and internal energy at the next time, from which the remaining chamber properties are determined:

$$\rho = m / Vol \qquad T = U / mC_v \qquad P = \rho RT$$

where:

$\rho =$ Density
$m =$ Mass
$Vol =$ Compartment Volume
$T =$ Temperature
$U =$ Internal Energy
$C_V =$ Constant Volume Specific Heat
$P =$ Pressure
$R =$ Gas Constant

Using these chamber properties, the above procedure is repeated for the next time step.

5.3.5.2.2 SINDA/FLUINT Program

The Simplified Improved Numerical Differencing Analyzer (SINDA) with Fluid Integrator (FLUINT) is a software package, developed under contract to NASA, for solving lumped parameter network representations of heat transfer and fluid flow problems that are governed by conservation equations. For heat transfer problems, the physical system is partitioned into a Resistance-Capacitance (R-C) network that is analogous to an electrical circuit inasmuch as heat flows between nodes of unequal temperature, current flows between nodes of unequal potential (voltage) in an electrical circuit. Nodes within the thermal network represent discretized portions of the physical system and, in a transient simulation, may store or lose energy much like capacitors in an electrical circuit. Similarly, fluid systems are discretized into lumps and connectors where pressure differences between lumps and the resistance of the connectors determine both the magnitude and direction of the flow. The thermal and fluid networks may be seamlessly integrated through convective ties between fluid lumps and thermal nodes. The coupled thermal/fluid network is solved simultaneously by SINDA/FLUINT, thereby increasing stability and temporal accuracy.

Specifying the mass (or capacitance) of the thermal nodes and/or the volume of the fluid lumps permits transient as well as steady state simulations. A semi-implicit 2nd order forward-backward differencing scheme is used to advance the solution in time. The time-step is dynamically determined by the program to ensure stability with a user defined output interval available to provide results. The transient thermal network is solved such that the energy flows between nodes as well as the energy gained or lost by each node balance over the time-step. The transient flow network is solved such that conservation of mass and energy are maintained at each lump while momentum is conserved within each connector. FLUINT can handle compressible and incompressible flows up to the sonic limit (supersonic flows may be computed in special cases) and choked flows are automatically identified and computed by the program.

Connector-device models exist within FLUINT to allow the user to model a wide variety of flows. The orifice device is used almost exclusively in subsequent SINDA/FLUINT based analyses to describe the connectivity between flow compartments in the orbiter wing and associated volumes in the payload bay or fuselage. The orifice device is pictured below with the important input/output parameters noted. The subscripts U, D, and TH denote the upstream, downstream, and throat conditions, respectively. FLUINT automatically determines the direction of flow and the upstream and downstream conditions are derived from the fluid lumps between which the orifice device is connected. The throat conditions are only used in choking calculations and are determined by assuming an isentropic expansion from the upstream conditions. AORI is the actual physical area of the orifice and ATH is the effective area determined from AORI and a user specified discharge coefficient, CDIS. AF is the upstream area (generally intended for pipe flow) and is set to ten times the actual orifice area for the large freely vented volumes of the orbiter wing.

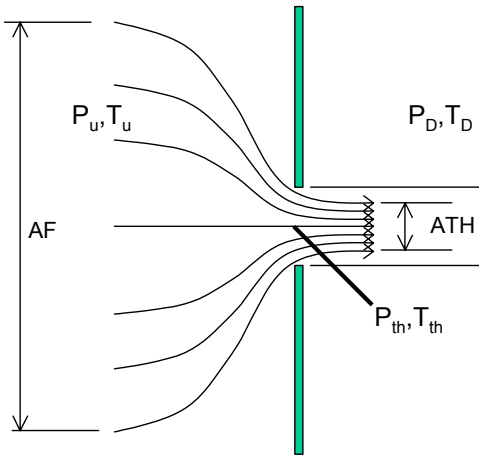

where:
AFTH = Throat Area (ATH)
CDIS = Discharge Coefficient
Cv = Velocity Coefficient
AORI = Orifice Area
P = Pressure (U=upstream; D=downstream; th=throat)

$$AFTH = \frac{CDIS}{C_V} AORI$$

$$C_V = .98$$

The internal algorithm for determining whether the flow-rate through the orifice device is choked is illustrated below. First, isentropic expansion from the upstream conditions and a velocity equal to the speed of sound at the throat are used to determine the critical (choked) flow-rate through the orifice. Next, the actual flow-rate through the orifice is determined from the pressure difference, average density, and a K-factor based upon the geometry of the orifice. Finally, comparing the actual flow-rate to the critical flow-rate yields the correct flow-rate.

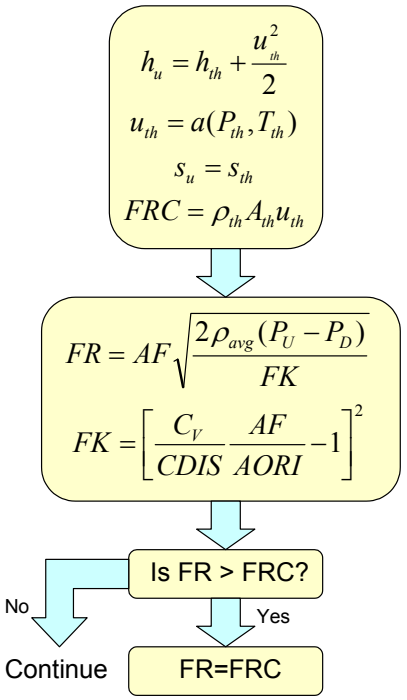

where:
h = enthalpy
u = internal energy
a = speed of sound
s = entropy
FRC = Critical Flowrate (for choking)
AF = Flow Area
FK = loss coefficient
FR = mass flowrate

5.3.5.3 Modeling Assumptions

5.3.5.3.1 Trajectory

The analysis is based on the STS-107 End of Mission 3 (EOM3) trajectory, where time zero corresponds to Orbiter Entry Interface (EI). The pertinent quantities used in the analysis are plotted in Figure 5.3.5-1 and Figure 5.3.5-2.

5.3.5.3.2 Discharge Coefficients

Two orifice discharge coefficient (C_d) corrections were used in the analysis. One is a pressure-ratio dependent C_d for a sharp-edged circular orifice from Shapiro, where C_d is a function only of the pressure ratio across the orifice. The second correction is a pressure-ratio-and-cross-flow dependent C_d for a circular orifice that is from CHCHVENT, which is based on experimental data documented by Haukohl and Forkois. The C_d in this correction is a function of both the pressure ratio across the orifice and the local external Mach number flowing past the orifice. Shapiro's correction is incorporated as a 5th order polynomial curve fit and is depicted in Figure 5.3.5-3. The pressure-ratio-and-cross-flow correction is incorporated as a bi-variant lookup and is depicted in Figure 5.3.5-4. For the high aspect ratio leading edge vents (carrier panel and T-seals), the Haukohl and Forkois data were consulted. Since the leading edge vents are choked for all the cases, the empirical data showed a less than 5% difference compared to the sharp-edged circular orifice correlations, so the circular orifice correlations were used in lieu of computing the family of curves needed to generically account for high aspect ratio vents.

5.3.5.3.3 Local Pressure Coefficients

The local pressure of the flow just outside a vent, leak, or possible penetration is crucial to the venting analysis because it is frequently very different from the freestream pressure. Local pressure coefficients (C_p) computed from LAURA CFD analyses were used as inputs to the venting programs for determining the local external surface pressures. These CFD solutions were completed by Langley Research Center for STS-2, and two solutions (Mach=18.1, angle of attack=41.2 degrees and Mach=24.3, angle of attack=39.4 degrees) were made available by Gnoffo.

In CHCHVENT, the C_p value at a particular location is determined by linearly interpolating between the C_p values for the two Mach numbers, 18.1 and 24.3. Since these C_p values were similar and in an effort to

expedite the process of adding this capability to FLUINT, the C_p values for the two Mach numbers were averaged in the FLUINT models. Also, since the vehicle angle of attack in the EOM3 trajectory is approximately 40 degrees from EI through EI+1000 seconds, the C_p values were considered virtually constant over this range. To validate this assumption, the CHCHVENT model was run with both linearly varying and constant averaged C_p values with negligible change in the results. Contour plots for the windward and leeward sides of the vehicle for the Mach=18.1 solution are depicted in Figure 5.3.5-5 and Figure 5.3.5-6, respectively.

5.3.5.3.4 Breach Boundary Conditions

The derivation for the local boundary conditions for a large breach is based upon the assumption that either all or a sizable fraction of the free stream total enthalpy is ingested at the breach or penetration. The flow through the large breach is modeled by the orifice device (within SINDA/FLUINT) and conditions at the upstream lump (or plenum) are updated each time-step based upon the assumed trajectory.

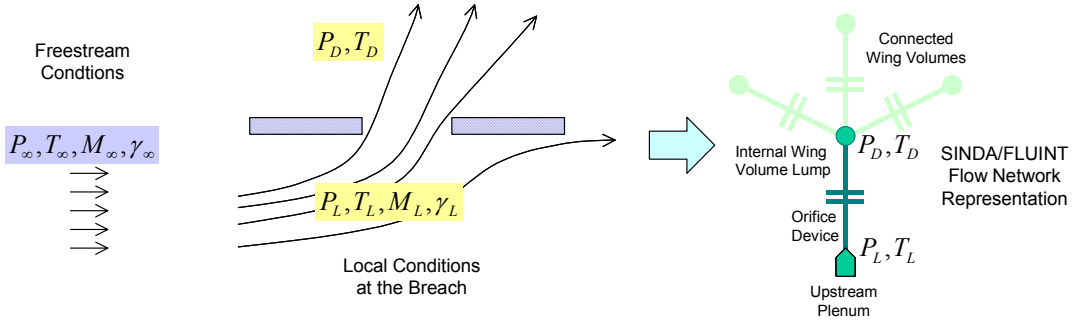

To determine the local conditions for the upstream boundary, the local enthalpy is scaled to the free-stream enthalpy (or taken from the engineering analysis described in Sec. 5.3.2.1) and the local pressure is derived from the free-stream pressure through an externally supplied pressure coefficient. Iteration within the equilibrium air property tables is required to determine the local conditions as a function of enthalpy and pressure for a real gas while a closed form solution exists for a perfect gas. An alternate model was created to more accurately model the period after the internal spar breach, where the local pressure from the jet impinging on the spar is assumed to equal the local external pressure. Also, the bulk enthalpy ingested through the leading edge hole was assumed to be ingested through the spar breach (consistent with jet flow through the breach).

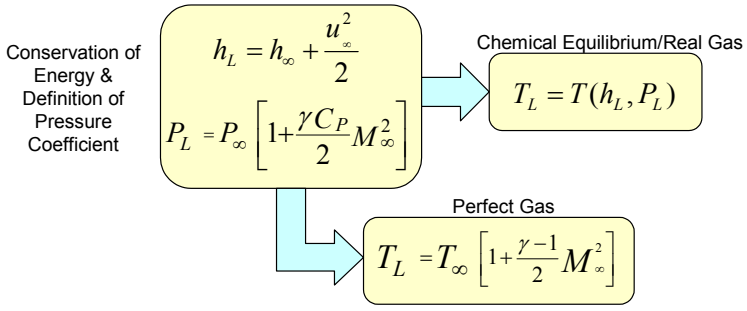

The derivation for the local boundary conditions for a small breach or vent is based upon the assumption that the flow into the small breach or vent is greatly influenced by the surrounding structure which necessitates the use of the local Mach number and the static conditions at the breach.

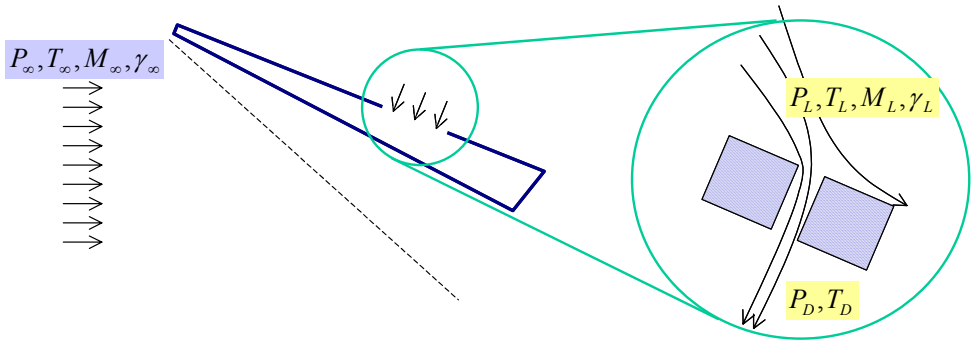

As in the case of the large breach, the local pressure is derived from the free-stream pressure via an externally provided pressure coefficient. The remaining state condition is determined by assuming constant entropy between the free-stream conditions and those locally at the breach or vent. This is not strictly correct if shock waves are present in the flow, but engineering judgement dictates that for wing locations away from the leading edge, the entropy increase through the shock will be largely offset by an entropy decrease due to the non-adiabatic nature of the flow over the wing. Determining the actual energy lost by the non-adiabatic flow to the wing structure is problematic for non-CFD based venting analyses and, for locations away from the leading edge of the wing (such as the windward elevon seals), it is anticipated that only a very small fraction of the free-stream enthalpy would be ingested. As before, a closed form solution exists for an ideal gas while a real gas demands use of the property tables.

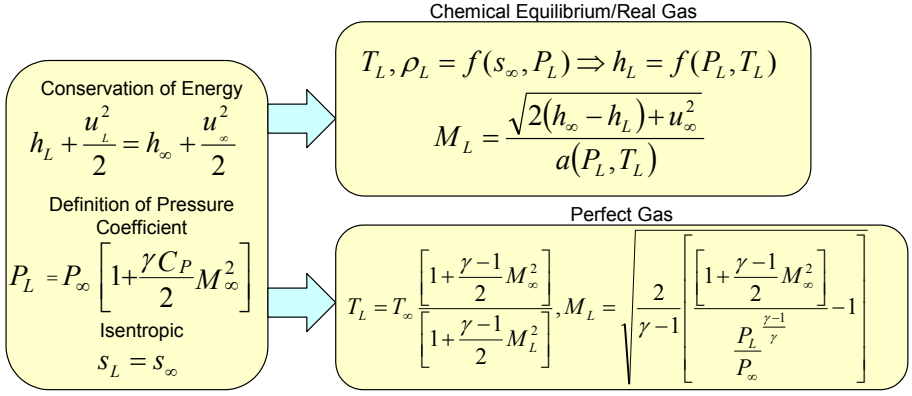

5.3.5.4 Vent-Only Model Development

5.3.5.4.1 Development/Description

The venting model was developed primarily from Rockwell International's 1994 "Orbiter Entry Venting Substantiation Report" by Wong, and a report documenting an integrated venting model for OV-102, Flight 27, STS-109 by Cline. The models used in the Substantiation Report were based on one-half of the Orbiter; whereas, the geometry was extended to include the complete vehicle to account for the non-symmetric nature of a possible breach in the left wing. The venting model was later modified based on results of a structural leakage test done for this investigation (Cline and Torres), suggested modifications from the JSC Aerothermal Internal Flow team, and estimated leading edge vent areas from Computer Aided Design (CAD) drawings. A graphical representation of the venting model is depicted in Figure 5.3.5-7.

Comparison Of CHCHVENT And FLUINT (Adiabatic/Ideal Gas)

FLUINT did not initially have the capability to calculate local external pressures from pressure coefficients or contain the discharge coefficient models included in CHCHVENT; therefore, these capabilities were added to FLUINT and comparisons between CHCHVENT and FLUINT were made for validation purposes. A typical plot from the comparisons is shown is Figure 5.3.5-8, where the predicted net rate of change of mass in the

left main gear wheel well assuming a 20 in^2 breach into the left wing front glove compartment (section between bulkheads 807 and 1040) is shown. This comparison was made assuming the air as an ideal gas with constant specific heats in both CHCHVENT and FLUINT. In addition, the boundary-condition temperatures used in the comparison cases only were calculated from isentropic equations. For the breach, the local ingested gas temperature was assumed to be the free-stream stagnation temperature and calculated from:

$$\frac{T_{local}}{T_{freestream}} = \left[1 + \frac{\gamma - 1}{2} M^2_{freestream}\right]$$ (Ideal Gas Case Only – Not used in Final Results)

For all other locations where gas could be ingested (i.e. lower elevon seals, wheel doors, etc.) the following equation was used for the ingested gas temperature:

$$\frac{T_{local}}{T_{freestream}} = \frac{\left[1 + \frac{\gamma - 1}{2} M^2_{freestream}\right]}{\left[1 + \frac{\gamma - 1}{2} M^2_{local}\right]}$$ (Ideal Gas Case Only – Not used in Final Results)

5.3.5.5 Chemical Equilibrium Air Properties

SINDA/FLUINT Property (FPROP) tables were generated using FORTRAN 90 property routines for chemical equilibrium air obtained from the NASA Langley Research Center (LaRC). Six property tables (all as a function of pressure and temperature) were generated from the property routines: specific volume, enthalpy, speed of sound, entropy, absolute viscosity, and thermal conductivity. Entropy was obtained by numerically integrating the enthalpy tables at constant pressure.

SINDA/FLUINT requires entropy as a function of pressure and temperature for choking calculations in real gas simulations. Entropy tables were generated from the LaRC routines by numerically integrating the relevant *Tds* equation along lines of constant pressure:

$$Tds = dh - vdP$$

$$\int_1^2 ds = \int_1^2 \frac{dh}{T} - \int_1^2 \frac{v}{T} dP$$

$$P = const$$

$$s_2 = \frac{T_1 + T_2}{2T_1T_2}\left[h_2 - h_1\right] + s_1$$

An arbitrary reference entropy of 10,000 J/kg-K (2.39 Btu/lb_m-R) was chosen for the pressure equal to 0.001 Pa (9.9e-09 atms) and temperature equal to 200 K (360 R). Initial conditions for the integration were based upon ideal gas estimates of the entropy at 200 K and for a pressure range of 0.002 Pa (1.97e-08 atms) through 101325 Pa (1 atm). The trapezoidal integration was performed row-by-row with each succeeding entropy numerically integrated from the previous row's entropy at the same pressure. The real gas properties of air are markedly different from those of a perfect gas as evidenced by the entropy versus temperature plot shown in Figure 5.3.5-9. The almost cyclical changes in entropy with increasing temperature indicate a pattern of dissociation/ionization as new species are continually formed.

Also to aid choking calculations, a frozen speed of sound was computed from the specific heat ratio and an effective gas constant ($R_{EFF}=P/\rho T$). SINDA/FLUINT utilizes internal routines to provide fluid properties either by direct interpolation or by iteration if not requested as a function of pressure and temperature (i.e. T=T[s,P]).

Several of the interpolation/integration routines were rewritten to remove any dependency on ideal gas assumptions and/or to remove the additional logic present for two-phase fluids.
The property tables were generated over a range of 200 K (360 R) to 9100 K (16,380 R) and from 0.001 Pa (9.9e-09 atms) to 101325 Pa (1 atm). At very low density (due to extreme temperature or low pressure), the LaRC property routines issued cautions. Some thermal conductivity and viscosity data were discarded and replaced with data obtained from the routines at a higher pressure (this is assumed reasonable given the range of pressure profiles expected in this analysis).

5.3.5.6 Thermal Model Development

Thermal representation of the main structure comprising the port wing was developed in order to determine the thermal coupling effects of the structure on the venting model. The model was developed in SINDA/FLUINT format with geometric modeling being performed in Thermal Desktop. The stand-alone thermal model was initially set up utilizing STS-5 re-entry environments (Hartung and Throckmorton) and compared to results from the Dryden Flight Research Center's STS-5 analyses (Gong et al). The model was then modified to STS-107 environments and convectively coupled to the vent models.

Configuration details for the SINDA/FLUINT thermal math model of STS-107 Columbia's left wing were obtained from several sources (Figure 5.3.5-10), Computer Aided Design (CAD) models developed by the STS-107 Accident Investigation Structures Team, Shuttle Drawing System (SDS) – Boeing North America (BNA), Shuttle Operational Data Book on the NASA Human Space Flight website, Space Shuttle Entry Heating Data Book, Volume III – STS-5 (Hartung and Throckmorton), and Dryden Flight Research Center's Space Shuttle SPAR wing model (Gong et al).

5.3.5.6.1 Thermal Model Description

The three-dimensional thermal model consists of six internal wing volumes (sections 1-6) and four wing leading edge volumes (sections 7-10) corresponding to the venting models. Details of the thermal model are shown in Figure 5.3.5-11 and outlined below.

- Wing internal geometry based on CAD model – model includes the wing spars but the struts are omitted.
- Landing gear/wheel assembly derived from CAD model and specifications.
- Spar, fuselage and wheel well closeout panels assumed to be 0.1 inch thick Al-2219.
- Skin Al and Al-honeycomb panel representations are included. Al-honeycomb core is thermally modeled based on X-33 leeward aeroshell skin.
- Leeward honeycomb is 1.15 inches thick including inboard and outboard face-sheets of 0.025 and 0.045 inches, respectively.
- Windward honeycomb is 0.75 inches thick. The face-sheets are the same thickness as the leeward side. Remaining wing skin was assumed to be 0.1 inch thick Al-2219.
- TPS is represented on both windward and leeward sides. Leeward TPS was assumed to be 0.16 inches of FRSI throughout. (LRSI tiles were not modeled). Windward TPS assumed to be HRSI. Thicknesses averaged for each wing section based on the Dryden model data (Gong et al).
- SIP and RTV layers are included.
- Internal radiation is included (Optical properties from Dryden model or estimated from material.)
- Leading edge geometry based on vent volumes in venting models and the spar geometry from the CAD model.
- STS-107 wing leading edge, windward and leeward heat rates for STS-107 End of Mission (EOM) 3 trajectory were supplied by Boeing-Houston.
- Material properties taken from (in order of preference) NASA RP-1193 or TPSX database (NASA ARC).
- Time dependent pressure arrays (required to interpolate pressure and temperature dependent property arrays) estimated from STS-107 EOM3 trajectory profiles, STS-2 LAURA windward and leeward C_p profiles.

5.3.5.6.2 Fluid/Structure Coupling

The lumps representing the air in each of the compartment volumes in the vent models were tied convectively to the internal wing structural nodes in the thermal model. Convection coefficients for each tie were derived from laminar flow, flat plate Nusselt Number correlations (Incropera & Dewitt) utilizing the total flow entering each compartment, the cross-sectional area at the centroid of each volume (roughly normal to the perceived main flow direction), the path length through the centroid (along the perceived main flow direction) and the fluid properties (evaluated at the average of the wall and lump temperatures). The thermal model was later modified to include convective coupling between the leakage into the wheel-well area through the MLG door seal and the door structure. Also, convective coefficients for compartment 3 were later derived from FLUENT CFD modeling of this flow (Sec. 5.3.6.3). A correction factor was derived between the flat-plate Nusselt relation and the CFD at time point 404-sec after entry interface and used for correcting the Nusselt relation for the remainder of the transient simulation.

5.3.5.7 Thermal/Venting Results

The results in this section were generated over several weeks as the modeling assumptions were evolving. The following matrix summarizes the cases for which results are presented in this report with the major assumptions at the time of that modeling effort. Many additional cases were generated, but are not included for brevity, but are available upon request.

Case #	Assumptions	Purpose
1	10”, 6” and 4” diameter RCC Breach hole with Cp=1.46 6” diameter internal Spar Breach hole at 490-sec after EI Ingested Enthalpy = 76% of freestream (based on Gnoffo CFD at 404-s) Local Pressure at Spar Breach calculated based on bulk compartment 8 pressure response. Flat Plate empirical Nusselt correlation for internal heat transfer	Assess leading edge pressure history for CFD boundary conditions and internal wing temperature response
2	10” diameter RCC Breach hole with Cp=1.46 10” diameter internal Spar Breach hole at 487-sec after EI Ingested Enthalpy based on Sec. 5.3.2 calculations. No heat transfer to leading edge structure – all ingested into spar breach. Local Pressure at Spar Breach assumed equal to external pressure (Cp=1.46). Flat plate empirical Nusselt correlation for internal heat transfer except for compartment 3, which uses FLUENT CFD heat transfer coefficient factor from Sec. 5.3.7.	Assess leading edge pressure history for CFD boundary conditions and internal wing temperature response
3	10” & 6” diameter RCC Breach Hole Cases with Cp=1.46 Ingested Enthalpy based on Sec. 5.3.2 calculations No internal Spar Breach	Provide pressure differential across leading edge spar for structural loads failure analyses.

5.3.5.7.1 Leading Edge Pressure Profiles

Case 1

The leading edge compartment pressures were of general use to providing CFD boundary conditions for various breach analyses. The Case 1 results are shown in Figure 5.3.5-12 for the three breach hole diameters. Prior to the EI+490-sec internal spar breach, the pressures represent the balance of flow coming in via the breach and the outflow from the T-seal and Carrier Panel vents of the leading edge. The pressure drop after the spar breach is due to flow into the low pressure compartment 3 volume.

Case 2

For Case 2, the leading edge was not modeled, but rather the spar breach local pressure was set equal to the external RCC pressure (assumed equal to jet impingement pressure). This approach results in a much higher local pressure to the spar breach as shown in Figure 5.3.5-13.

Case 3
The intent of Case 3 was to provide bulk pressure differentials across the leading edge spar, so the jet impingement local pressure to the spar was not appropriate. Therefore, this case models the leading edge bulk compartments (same as Case 1 except no internal spar breach). The pressure differentials for a 6" diameter and 10" diameter RCC hole are shown in Figure 5.3.5-14.

5.3.5.7.2 Internal Volume Pressure Profiles
The internal wing pressures are largely uninfluenced by the leading edge breach since there is only a very small nominal leak around the leading edge spar, but these pressures are dramatically increased by the subsequent internal spar breach at 487-seconds as shown in Figure 5.3.5-15 for both Case 1 and 2. The Case 2 post-spar breach pressures are much higher due to the larger local pressure and the 10" diameter spar breach instead of the 6" diameter breach in Case 1. The bulk of the wing is freely vented, but the forward wing-glove and wheel well compartments are slightly lower due to the large venting through the Payload Bay vent in the wing-glove as illustrated by the close-up of the Case 2 pressures in Figure 5.3.5-16.

5.3.5.7.3 Leading Edge Air Temperature Profiles

Case 1
The leading edge compartment temperatures are shown in Figure 5.3.5-17 for Case 1. Compartment 8 is the hottest due to the breach inflow and the other compartments are lower in temperature due primarily to the energy lost to structure (i.e., the RCC and leading edge spar insulation) and outflow from the leeside vents.

Case 2
As previously stated, Case 2 does not include the full representation of the leading edge, but rather just Compartment 8 treated as a plenum of local conditions for the spar breach. The air temperature for this plenum is illustrated in Figure 5.3.5-18. This is much higher than Case 1, which included the loss of energy to structure, where Case 2 assumes the jet energy carries through the internal spar breach. Therefore, the compartment 8 temperature represents the assumed bulk temperature of the flow entering the wing through the spar.

5.3.5.7.4 Internal Wing Air Temperature Profiles

Case 1
The internal wing compartment air temperatures are shown in Figure 5.3.5-19 for Case 1. The temperatures remain low until the leading edge spar breach at 490-seconds. Compartment 3 has the highest values since this is the compartment that the spar breach flows into directly. Temperatures in the other compartments are lower due to loss of energy to the wing structure. Compartment 1 has the next highest temperatures which is consistent with the mass flow and spar structural temperature results presented later.

Case 2
The internal wing compartment air temperatures for Case 2 are shown in Figure 5.3.5-20. These values are much higher than those for Case 1 due to the larger breach hole and much higher ingested enthalpy. The wheel well (Compartment 2) shows an elevation in temperature prior to the spar breach. This is due to an inflow from the payload bay, which is also at elevated temperature. This is an artificial effect since the standard leaks causing the elevated payload bay temperature would in reality lose energy to structure through those leaks, which the vent-only modeling does not capture. This effect is not a factor after the spar breach because the wheel well pressurizes with respect to the payload bay shortly thereafter.

5.3.5.7.5 Leading Edge Mass Flow Rate and Energy Rate In/Out
The leading edge RCC breach mass flow rate history is plotted in Figure 5.3.5-21 for Case 1. The Case 1 carrier panel and T-seal vent mass outflow is shown in Figure 5.3.5-22. The corresponding energy flux into the breach and out of the vents as well as heat transfer to the RCC and Cerachrome insulation is shown in

Figure 5.3.5-23. The mass flow through the spar breach for both Case 1 and 2 is compared in Figure 5.3.5-24 and the corresponding energy inflow is shown in Figure 5.3.5-25. The Case 2 mass and energy inflow are much higher due to the larger 10" hole instead of the 6" diameter and since energy is not transferred to structure before flowing through the spar breach in Case 1 as was shown in Figure 5.3.5-23.

5.3.5.7.6 Internal Wing Mass Flow Rate and Energy Rate In/Out

The forward and aft Compartment 3 vents (at Xo=1040 and Xo=1191) and wheel well forward Xo=1040 vent mass flow rates are plotted in Figure 5.3.5-26. The corresponding energy rates are shown in Figure 5.3.5-27.

The wheel well is of particular interest based on the flight data. The energy rates in/out from various vents/leaks for Case 1 is shown in Figure 5.3.5-28 and for Case 2 in Figure 5.3.5-29. Note the addition of energy into the wheel well prior to spar breach from the main landing gear door juncture leakage for Case 1. This energy is significant for Case 1 but not for Case 2 due to the much higher energy flux entering the wing for Case 2. Also, Case 2 reveals a brief inflow through the forward vent after the breach, but then the flow begins to outflow almost immediately. This transient is most likely due to the rapid pressurization of the wheel well from Compartment 1.

5.3.5.7.7 Leading Edge and Internal Wing Mach Number Histories

The RCC breach hole, the leading edge vents and the internal spar breach hole are almost immediately choked for all cases, so the plots of Mach Number are not presented. The Case 1 vent Mach Numbers for the Xo=1040, Xo=1191 and wheel well forward vents are plotted in Figure 5.3.5-30. The Case 2 results are shown in Figure 5.3.5-31.

5.3.5.7.8 Internal Wing Heat Transfer Coefficient Histories

Case 1 and 2

The heat transfer coefficients in Compartment 3 for Cases 1 and 2 are shown in Figure 5.3.5-32 and Figure 5.3.5-33, respectively. Case 2 includes the FLUENT CFD-based correction factors on these values. The wheel well (Compartment 2) Case 1 and 2 heat transfer coefficients are plotted in Figure 5.3.5-34 and Figure 5.3.5-35. The Case 2 values are higher primarily due to higher velocity flow rates.

Solid Wall Temperature Histories for the Leading Edge

The leading edge spar is insulated with Cerachrome that has a thin outer layer of Inconel. The Inconel temperature for Case 1 is plotted in Figure 5.3.5-36. Local heating effects caused by the leading-edge breach jet impinging on the insulation are not modeled and therefore the resultant temperatures for Compartment 8 are lower than what would be expected. However, for compartments away from the breach (7, 9, and 10) the predicted Inconel temperatures are considered realistic and indicate that the insulation would remain intact. The spar behind this insulation is plotted in Figure 5.3.5-37 and shows that the insulation performs very well.

Solid Wall Temperature Histories for Internal to the Wing

The Compartment 3 wall skin temperatures are shown in Figure 5.3.5-38 and Figure 5.3.5-39 for Cases 1 and 2, respectively. The wheel well wall temperatures are plotted in Figure 5.3.5-40 and Figure 5.3.5-41 for Cases 1 and 2, respectively. Case 2 temperatures are dramatically higher due to the larger hole in the spar, and the much higher ingested enthalpy. Note that the Case 2 temperatures exceed the aluminum melting point for many of the areas, which is known not to be the case from the telemetry data. This indicates that the Case 2 includes too much energy flowing into the wing (as compared to actual) due to either too large a size of the breach holes or the ingested enthalpy with local pressure assumptions being too high. The actual results are somewhere between the Case 1 and Case 2 predictions.

The spar temperatures for the remaining wing compartments are compared to Compartment 3 in Figure 5.3.5-42. The results indicate that heat is removed from the flow as it passes through the wing and that Compartment 1 structural temperatures are the next highest compared to Compartment 3. This trend is consistent with the higher flow rates through the 1140 vent into Compartment 1.

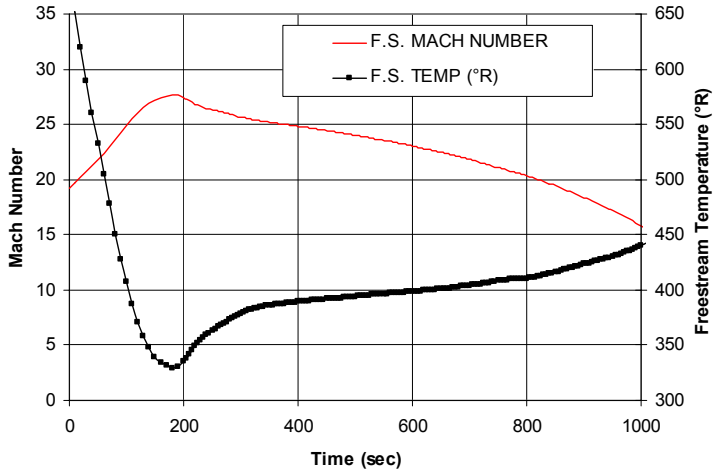

Figure 5.3.5-1 EOM3 Trajectory – Free-stream Mach Number and Temperature History.

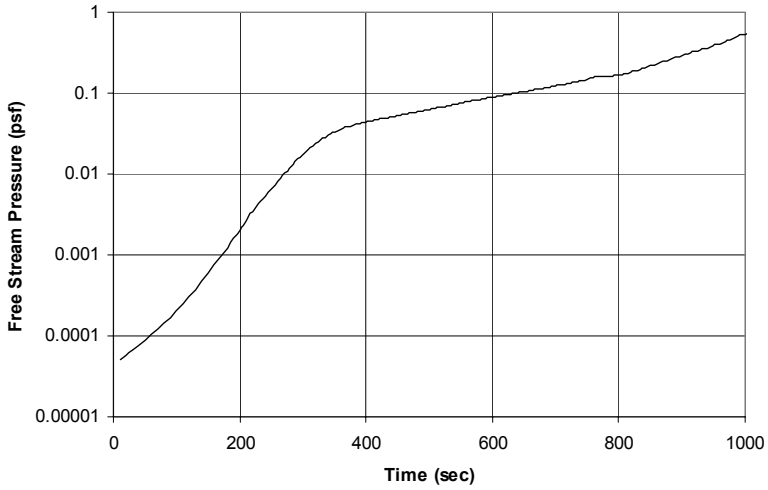

Figure 5.3.5-2 EOM3 Trajectory – Free-stream Pressure History.

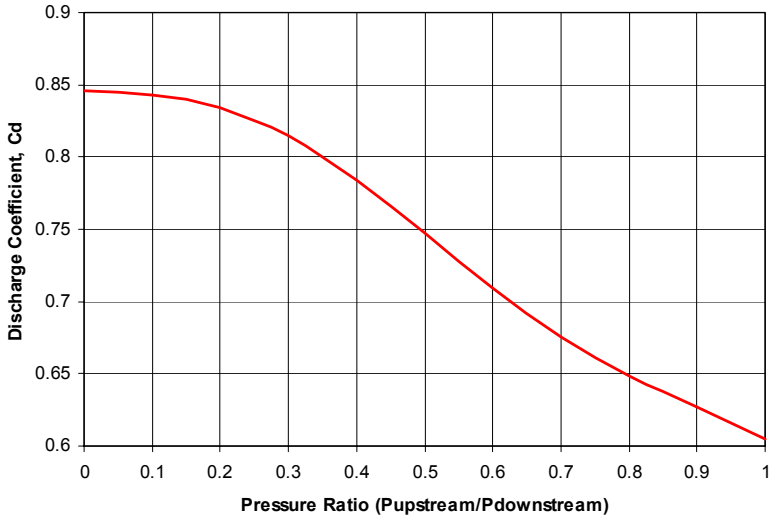

Figure 5.3.5-3 Pressure-Ratio Dependent Sharp Edge Orifice Discharge Coefficient .

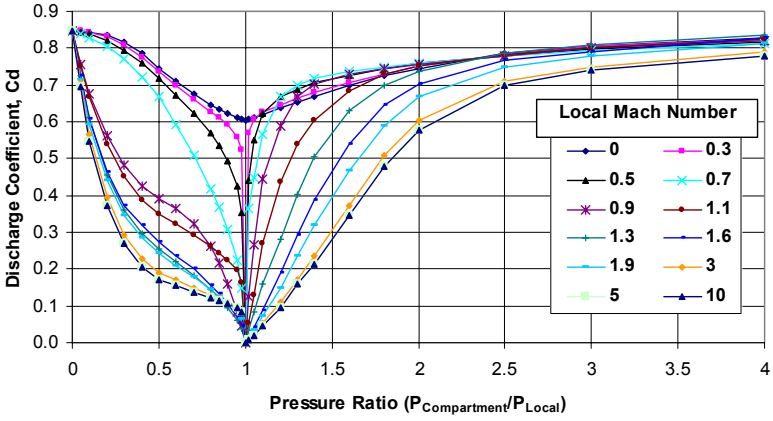

Figure 5.3.5-4 Pressure-Ratio-and-Cross-Flow Dependent Discharge Coefficient.

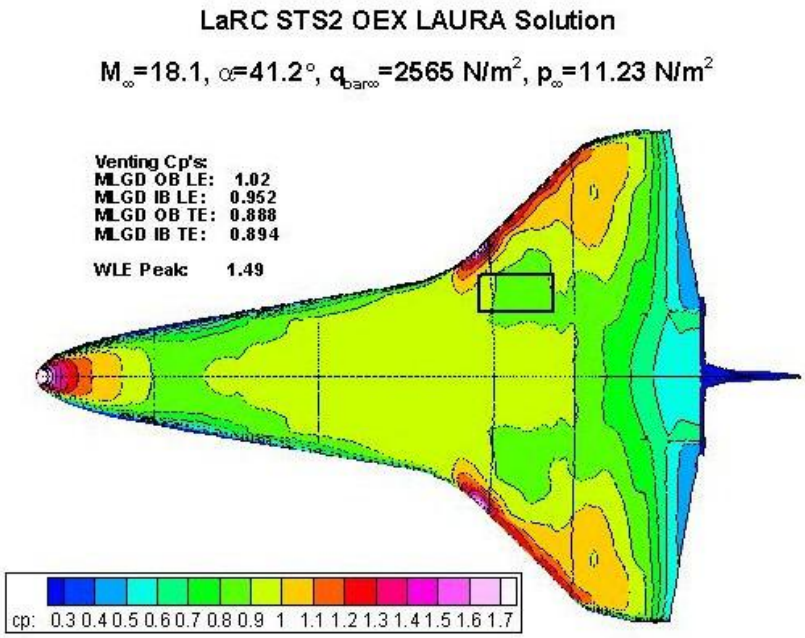

Figure 5.3.5-5 Windward LAURA Solution (STS-2, Mach 18) Surface Pressure Coefficient Contours.

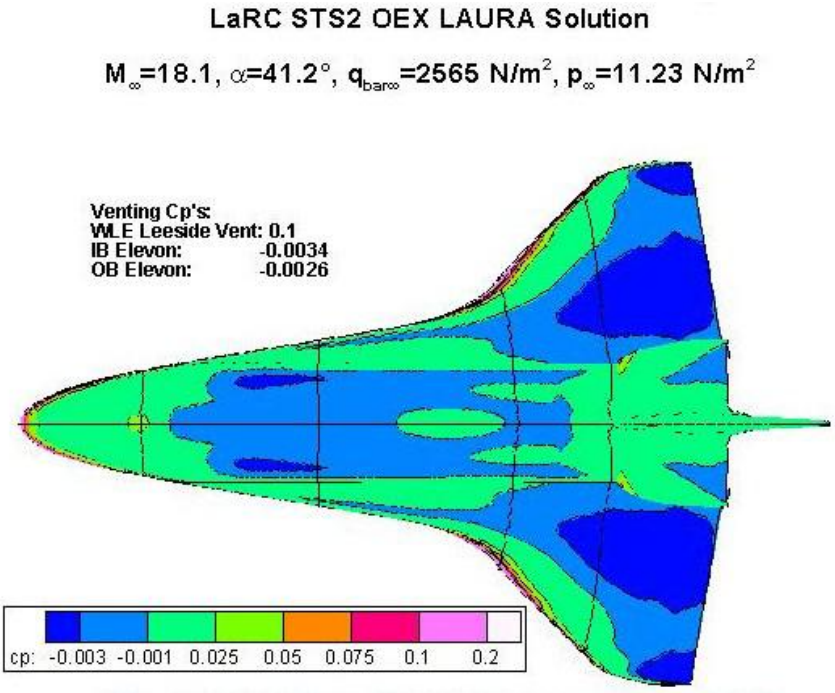

Figure 5.3.5-6Leeward LAURA Solution (STS-2, Mach 18) Surface Pressure Coefficient Contours.

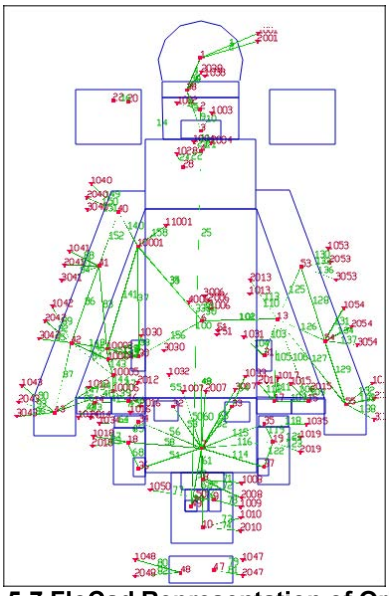

Figure 5.3.5-7 FloCad Representation of Orbiter Venting Model.

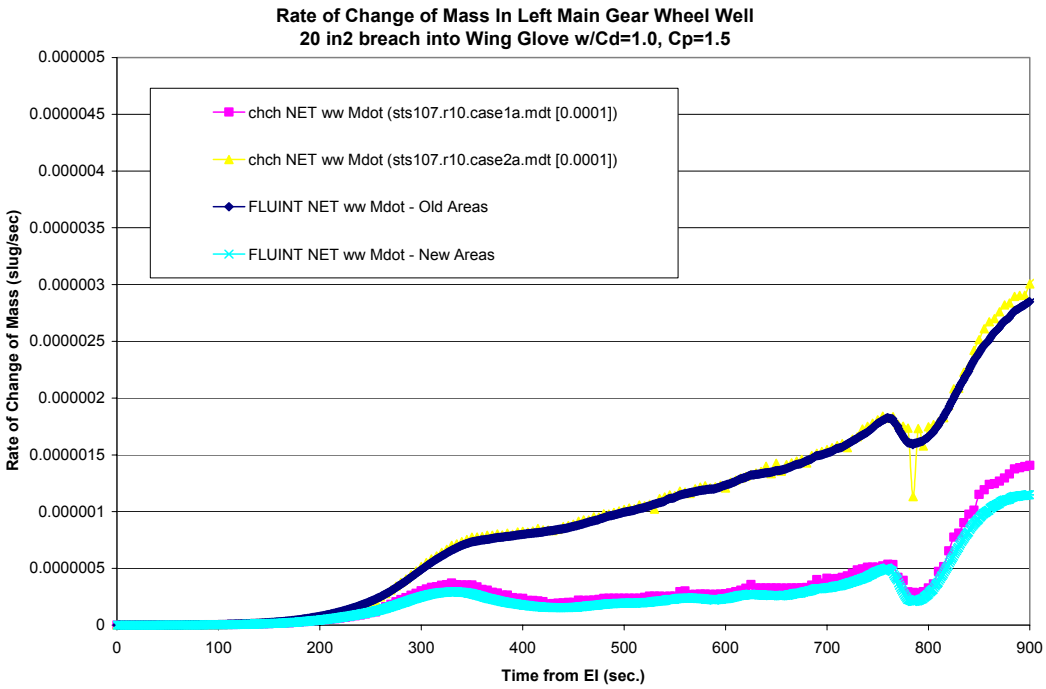

Figure 5.3.5-8 CHCHVENT and FLUINT Venting Comparison.

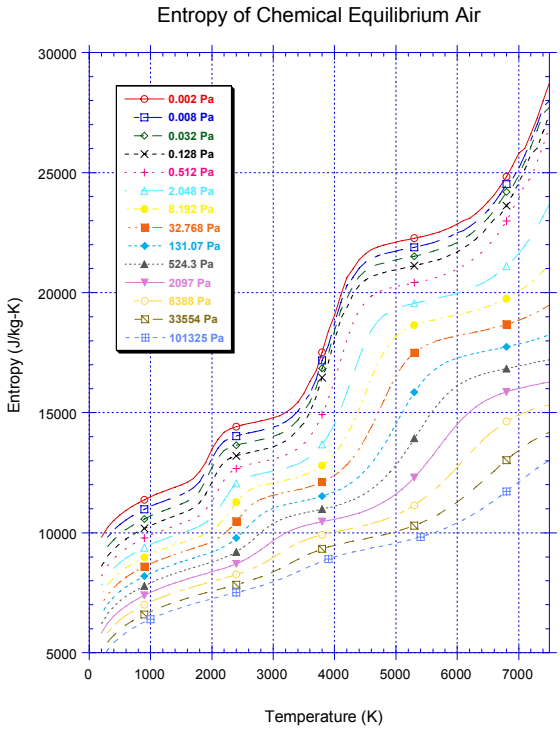

Figure 5.3.5-9 Equilibrium Air Entropy Variation with Temperature.

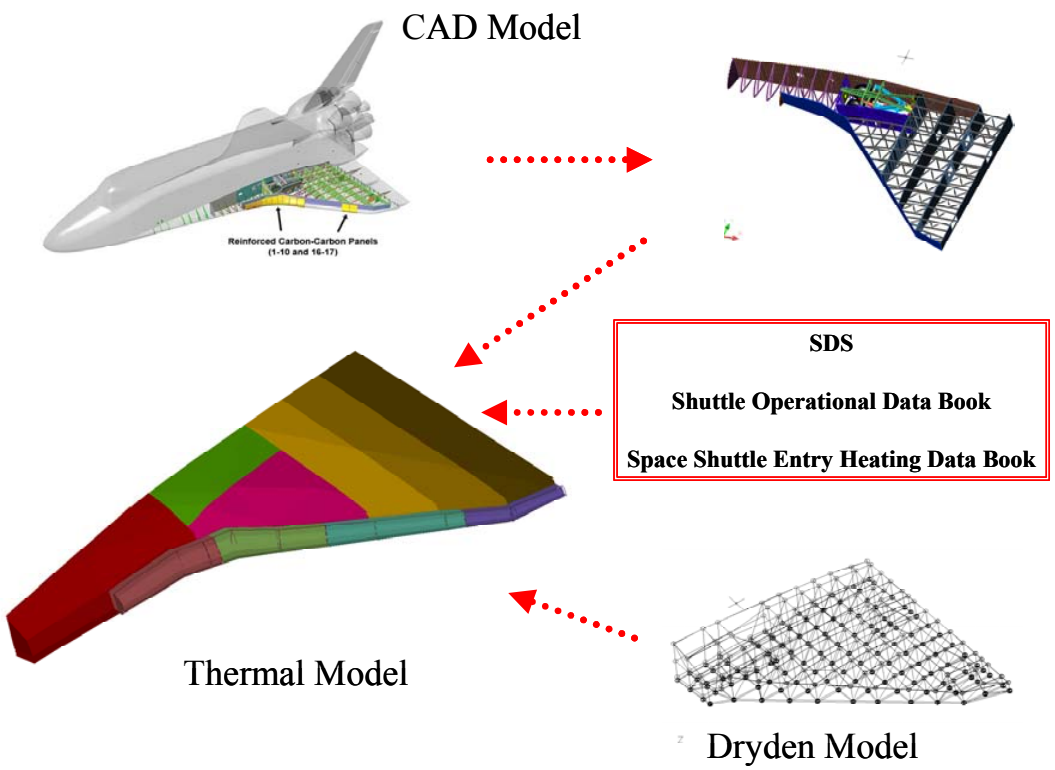

Figure 5.3.5-10 Orbiter Thermal Model Development Heritage.

RCC Leading Edge

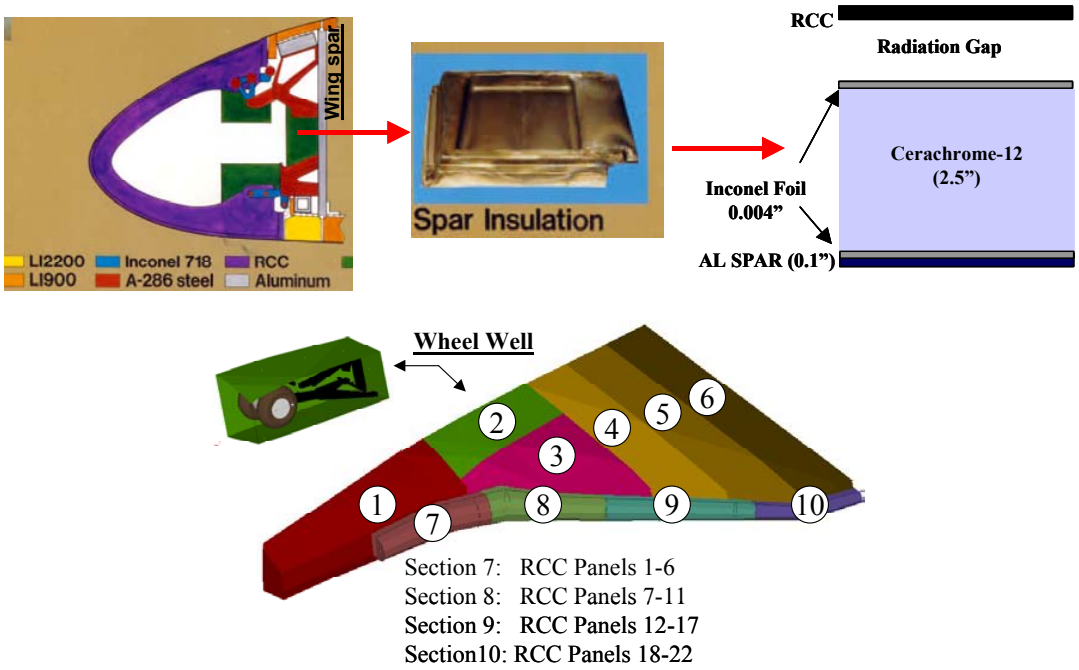

Figure 5.3.5-11 Thermal Model Configuration Details.

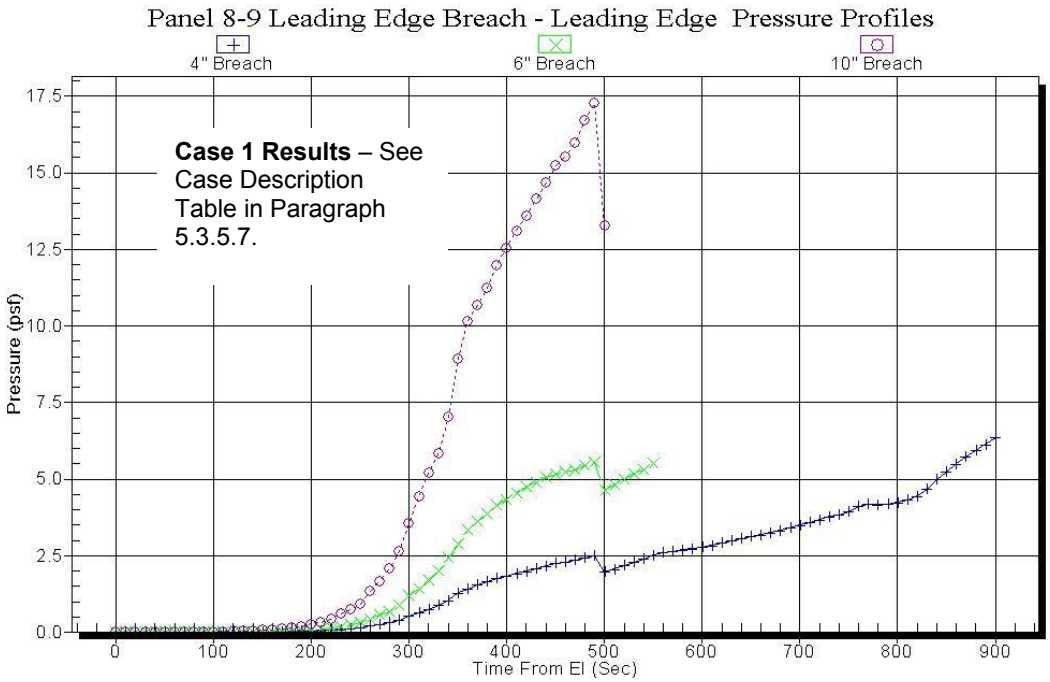

Figure 5.3.5-12 Case 1 Leading Edge Pressure History Plot for 4", 6" & 10" Diameter Breach

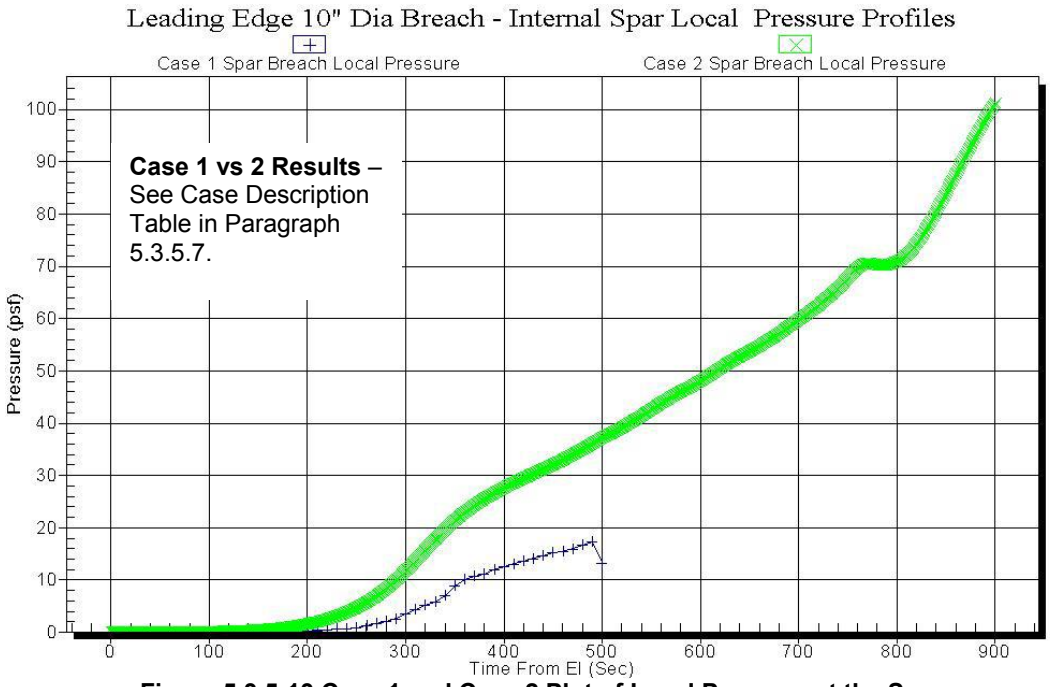

Figure 5.3.5-13 Case 1 and Case 2 Plot of Local Pressure at the Spar

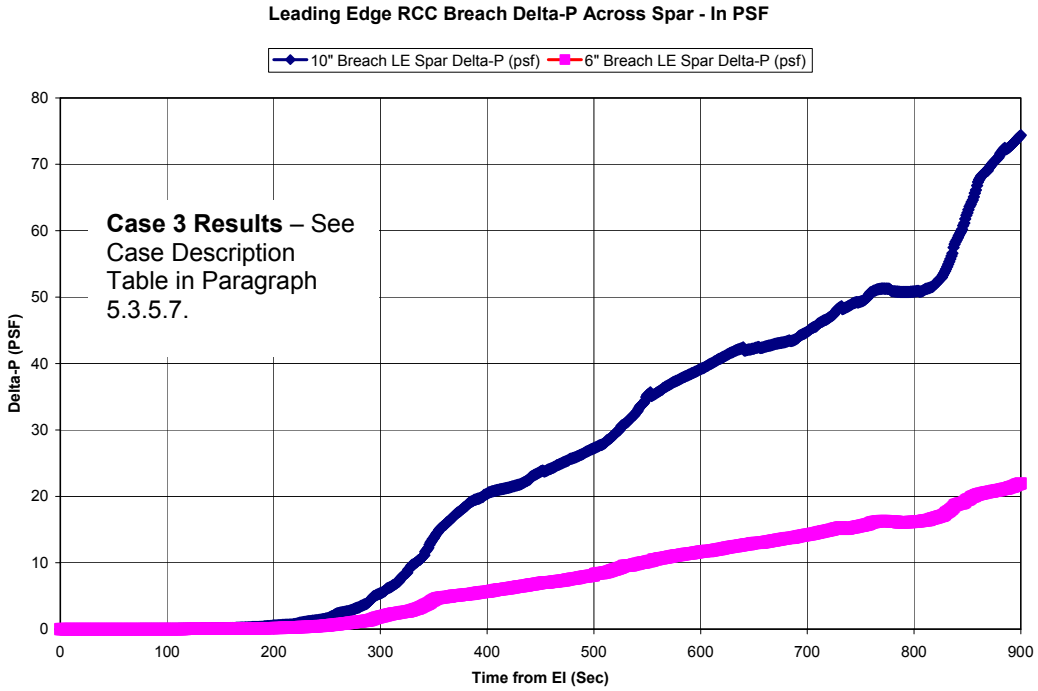

Figure 5.3.5-14 Case 3 Plot of Differential Pressure Across Leading Edge Spar for 6" and 10" Diameter Breach

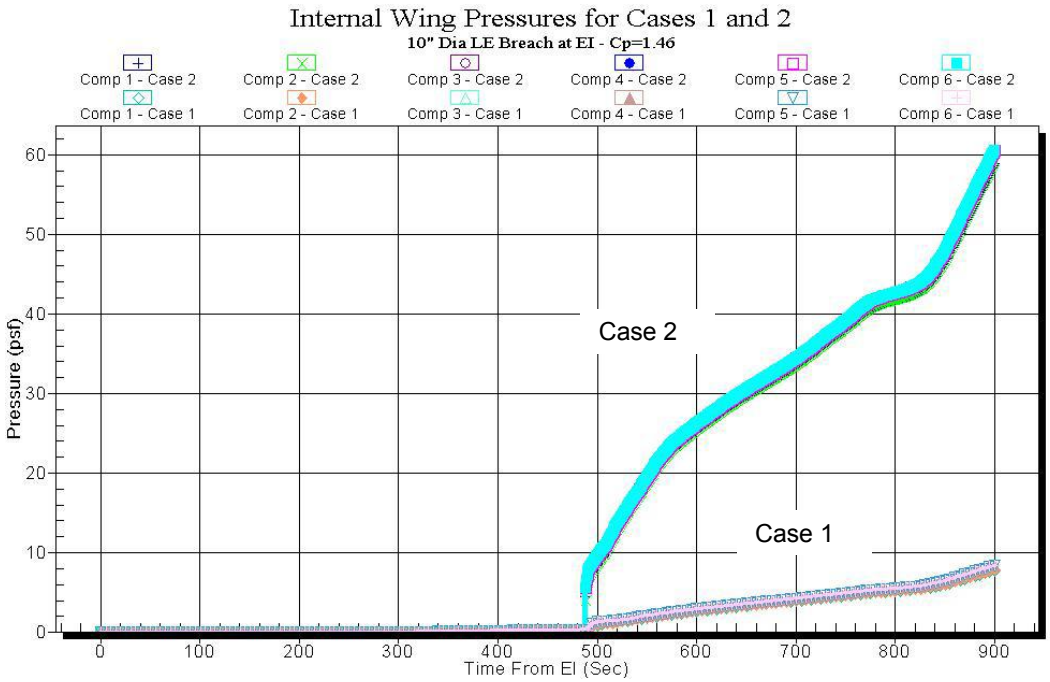

Figure 5.3.5-15 Internal Wing Pressure Histories for Cases 1 and 2

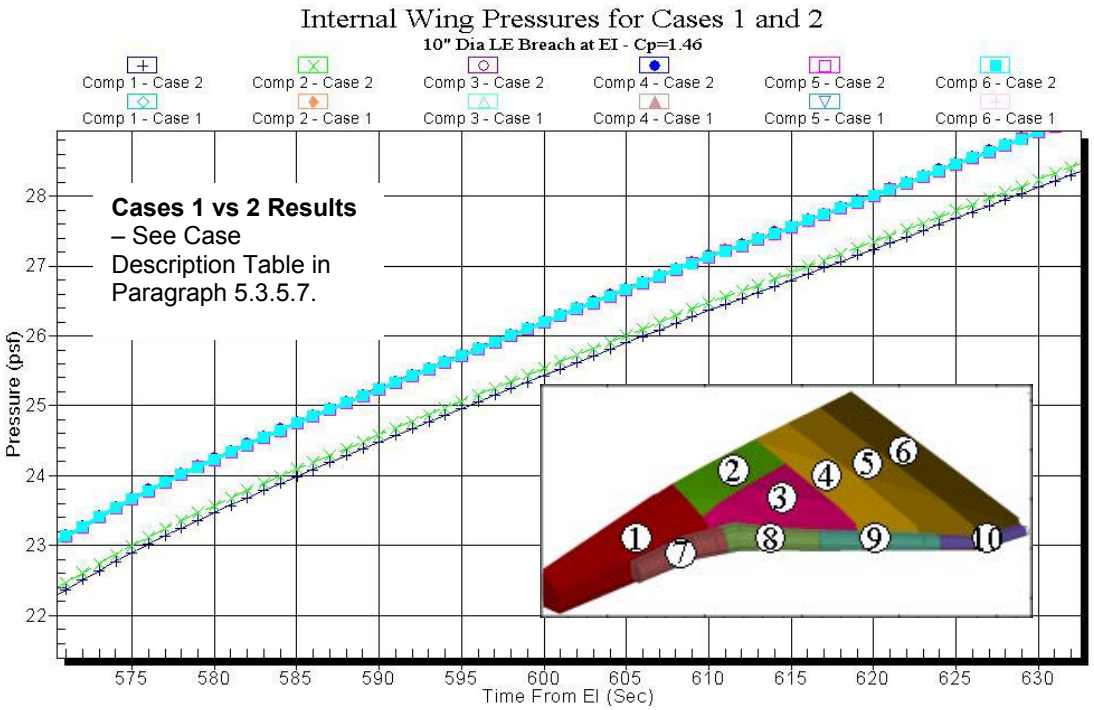

Figure 5.3.5-16 Detail Time-slice of Internal Wing Pressure Histories for Case 2

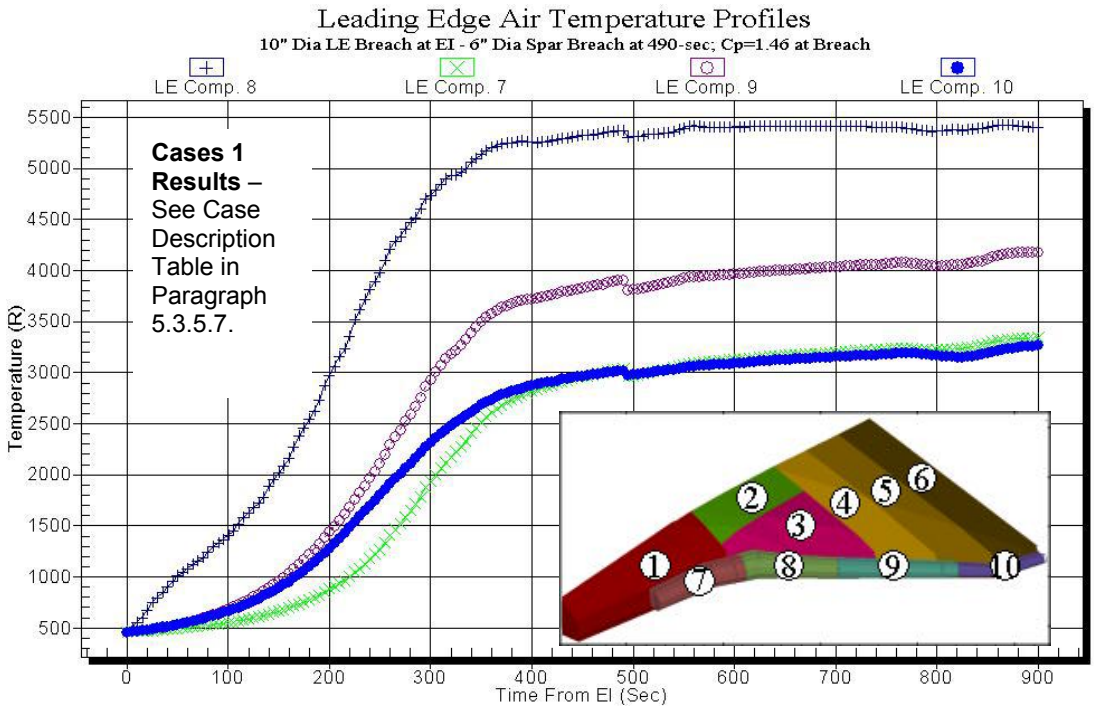

Figure 5.3.5-17 Leading Edge Air Temperature Histories for Case 1

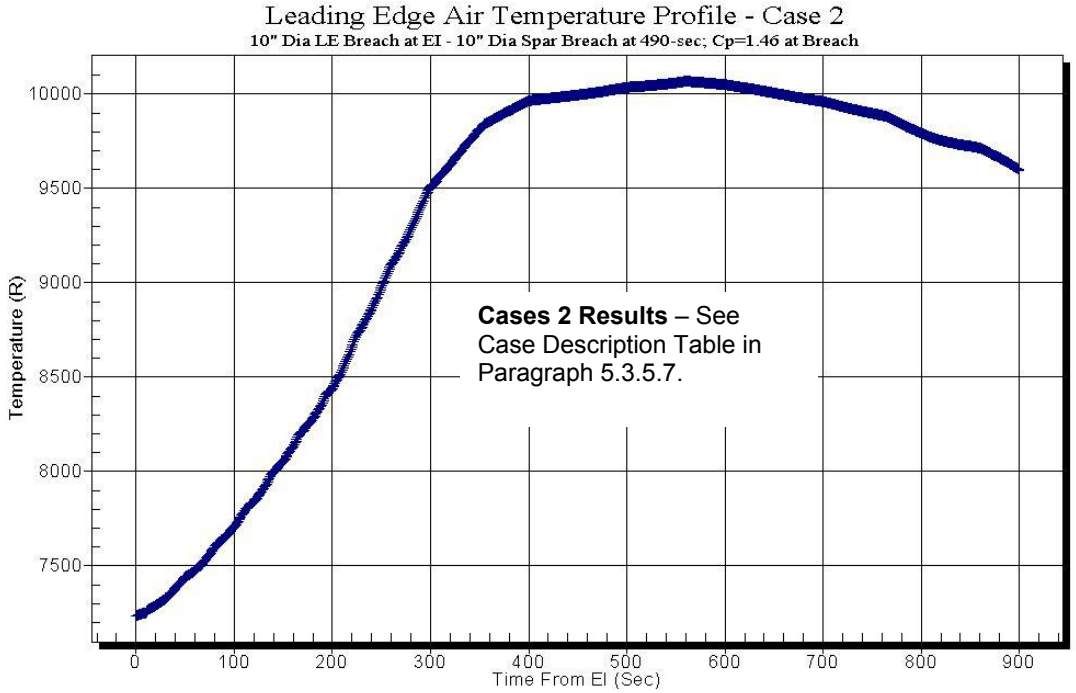

Figure 5.3.5-18 Leading Edge Air Temperature Histories for Case 2

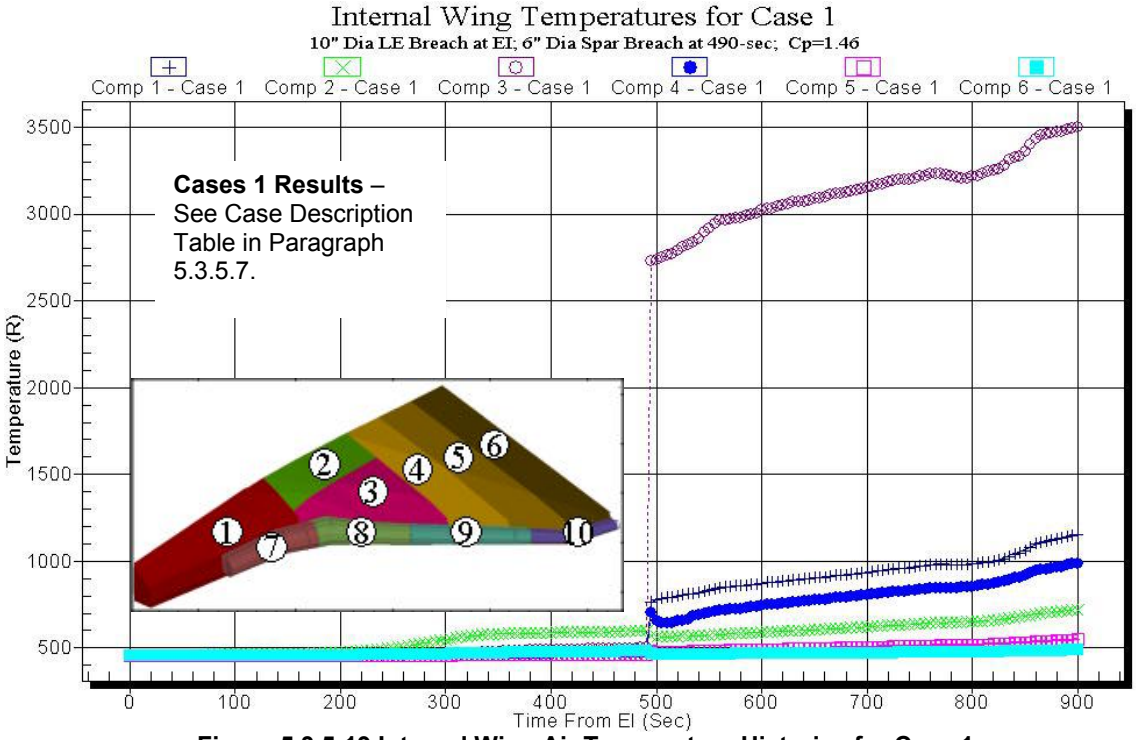

Figure 5.3.5-19 Internal Wing Air Temperature Histories for Case 1

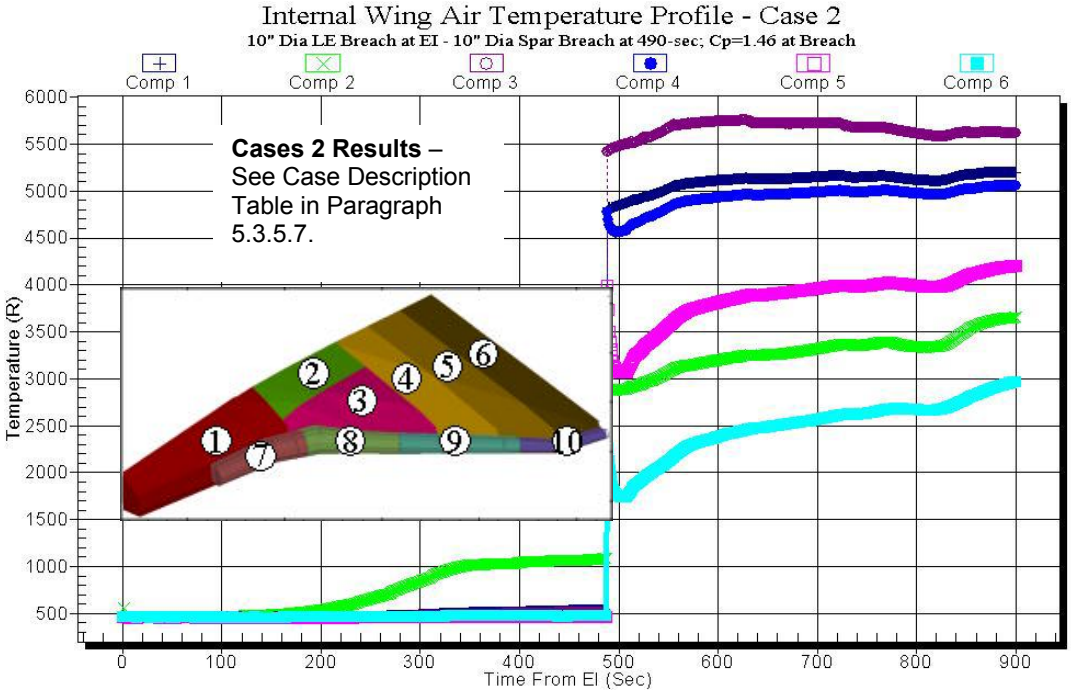

Figure 5.3.5-20 Internal Wing Air Temperature Histories for Case 2

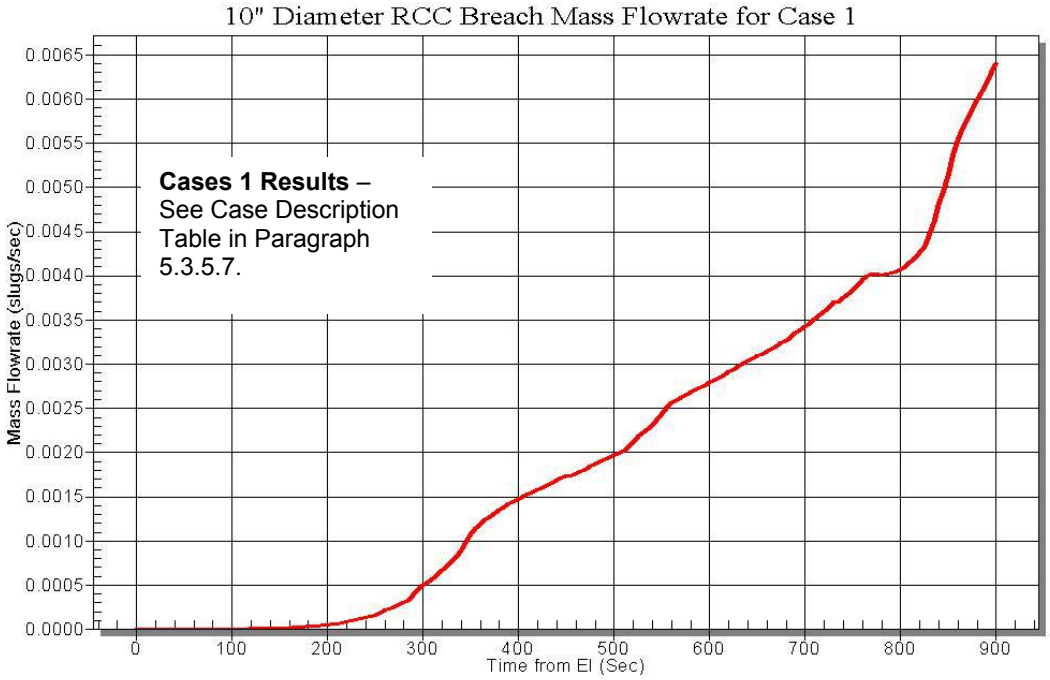

Figure 5.3.5-21 Leading Edge Breach Mass Flowrate for Case 1

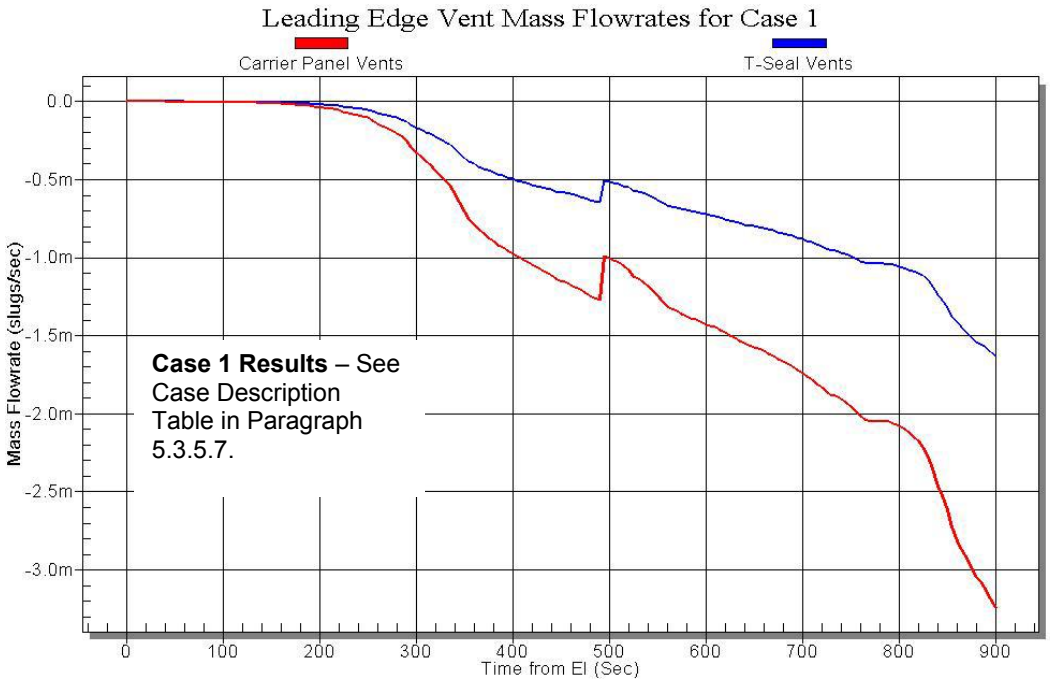

Figure 5.3.5-22 Leading Edge Vent Mass Flowrates for Case 1

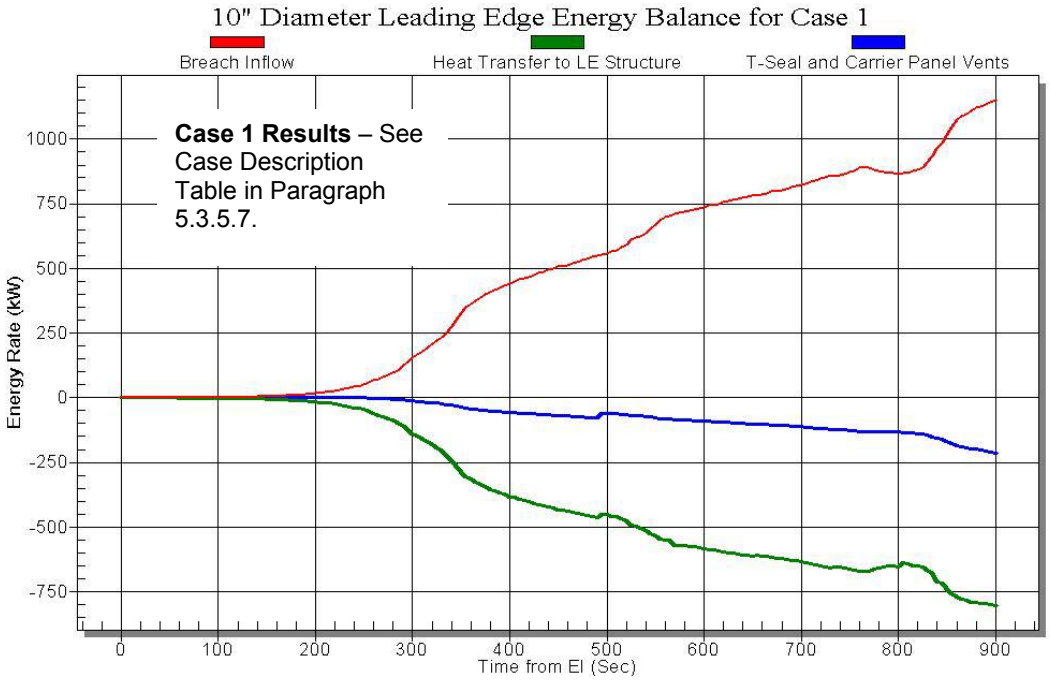

Figure 5.3.5-23 Leading Edge Breach Energy Inflow and Vent Outflow for Case 1

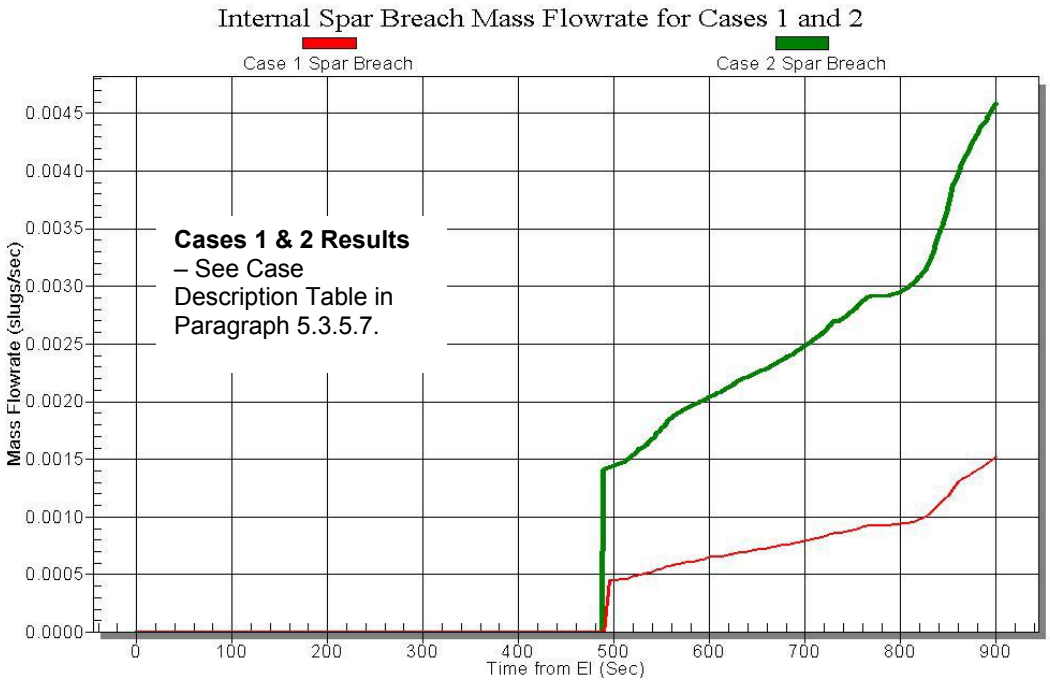

Figure 5.3.5-24 Spar Breach Mass Flowrate Comparison Between Case 1 and 2

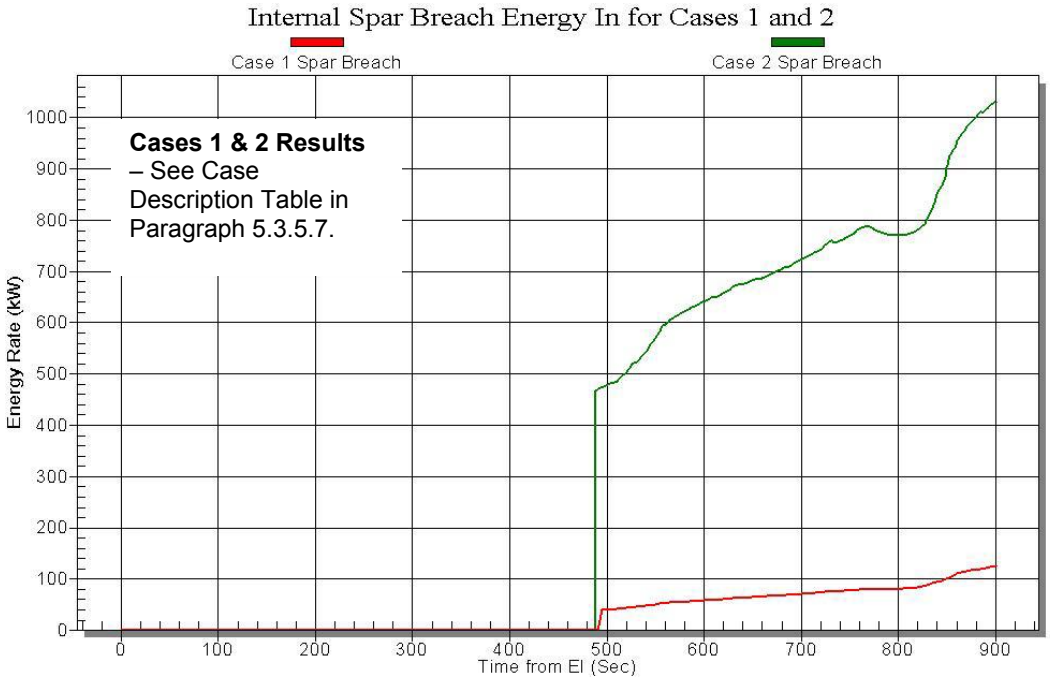

Figure 5.3.5-25 Spar Breach Energy Inflow Comparison Between Case 1 and 2

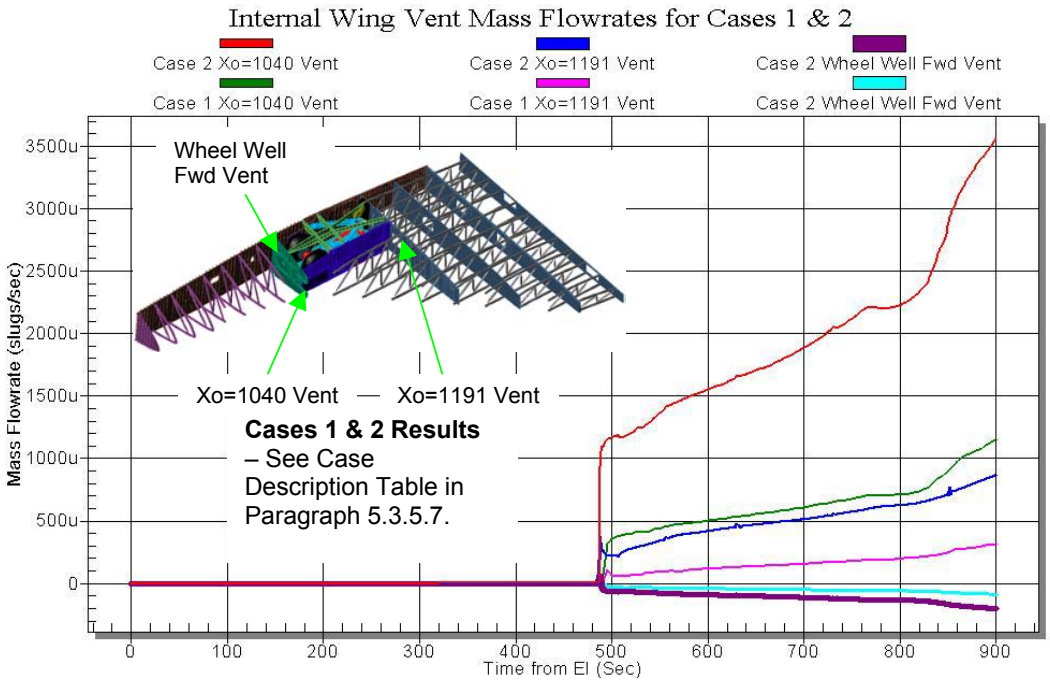

Figure 5.3.5-26 Internal Wing Vent Mass Flowrates for Cases 1 and 2

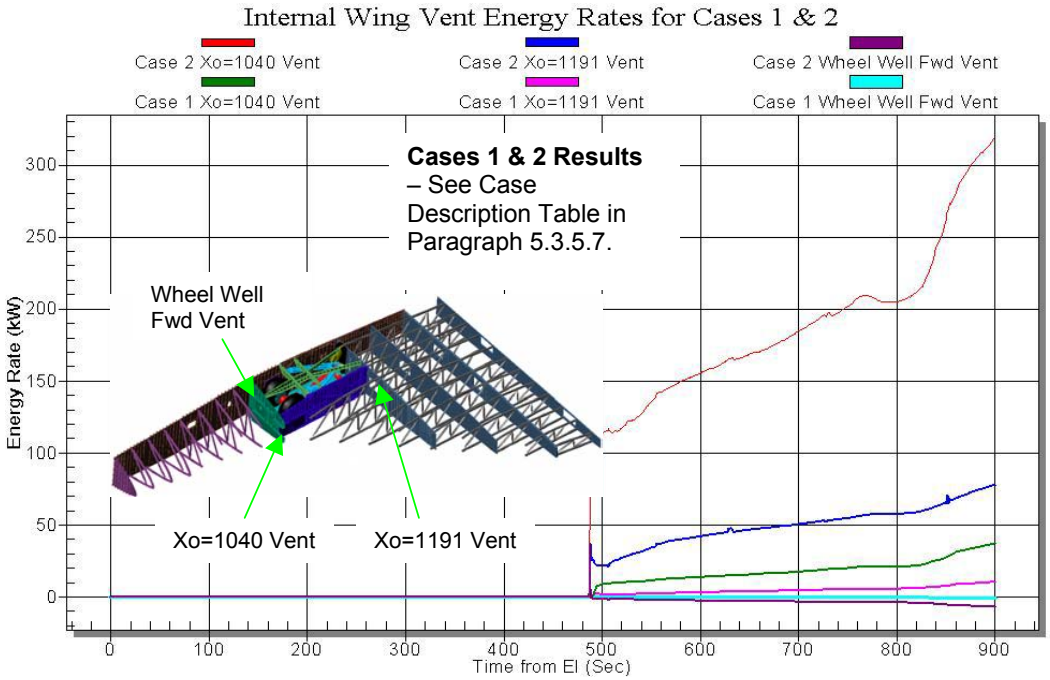

Figure 5.3.5-27 Internal Wing Vent Energy Inflows for Cases 1 and 2

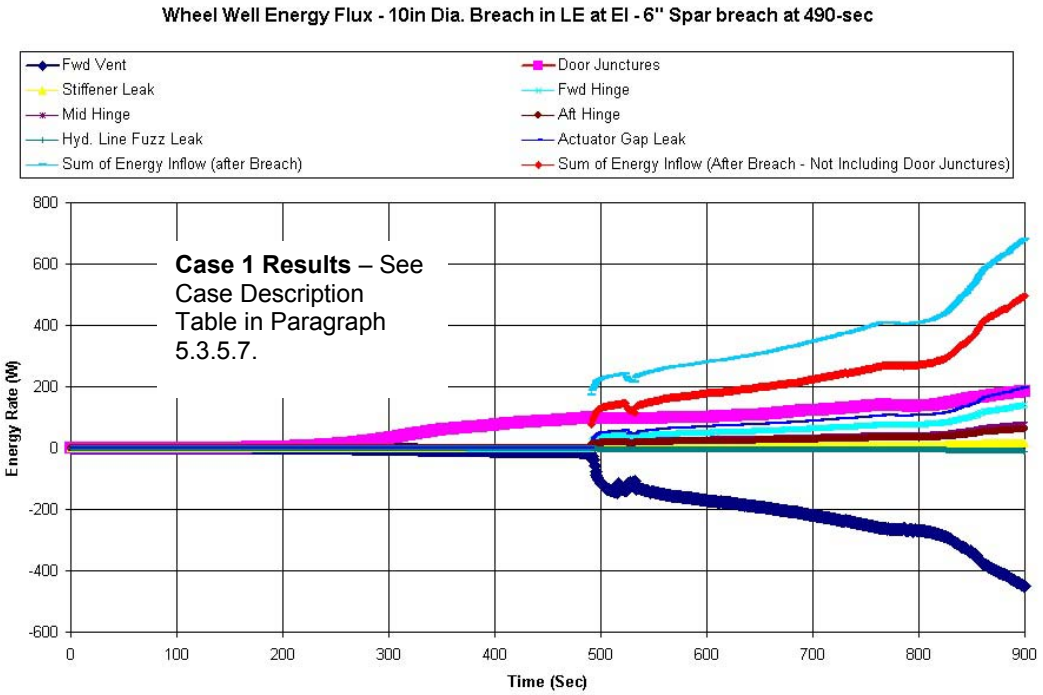

Figure 5.3.5-28 Wheel Well Energy Inflows for Case 1

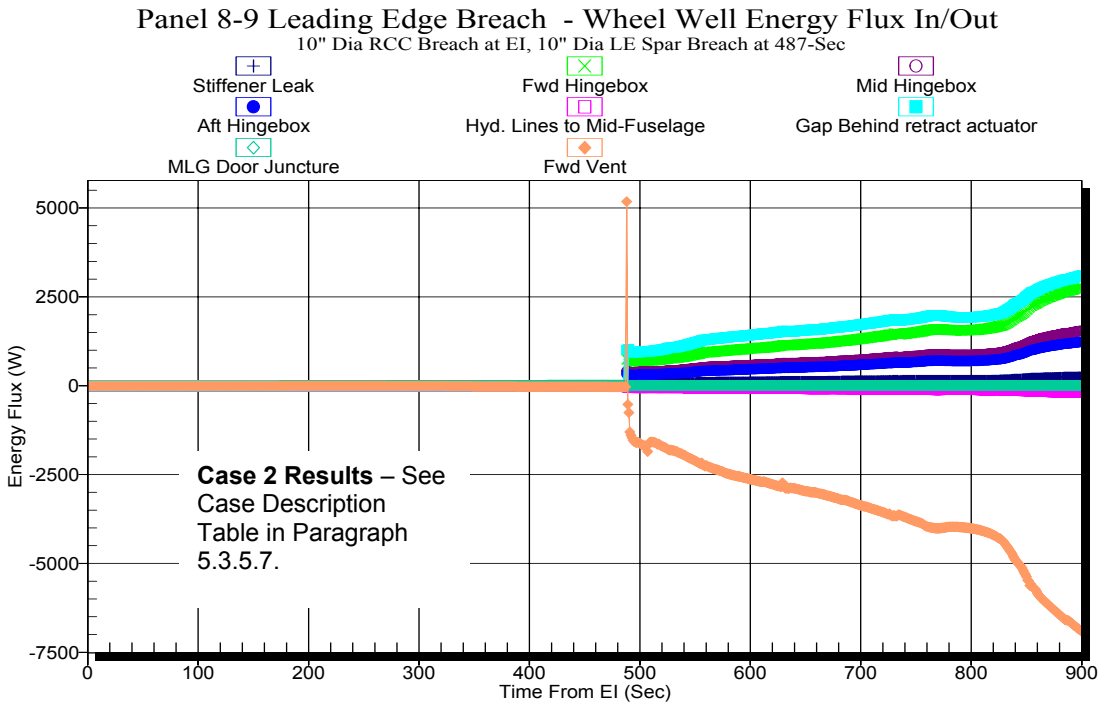

Figure 5.3.5-29 Wheel Well Energy Inflows for Case 2

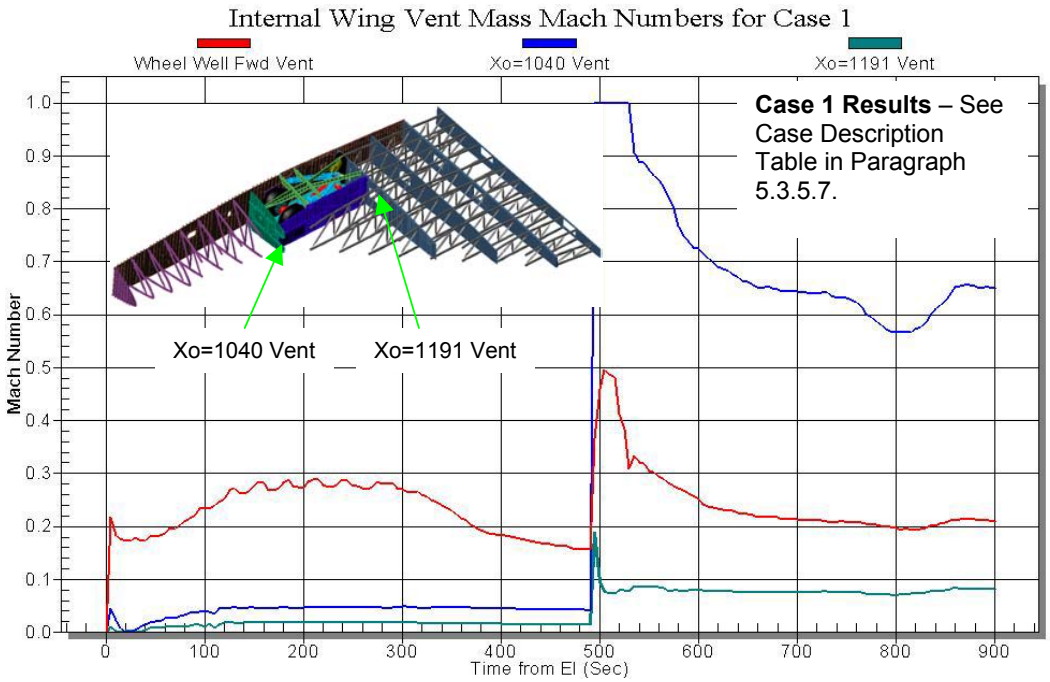

Figure 5.3.5-30 Internal Vent Mach Numbers for Case 1

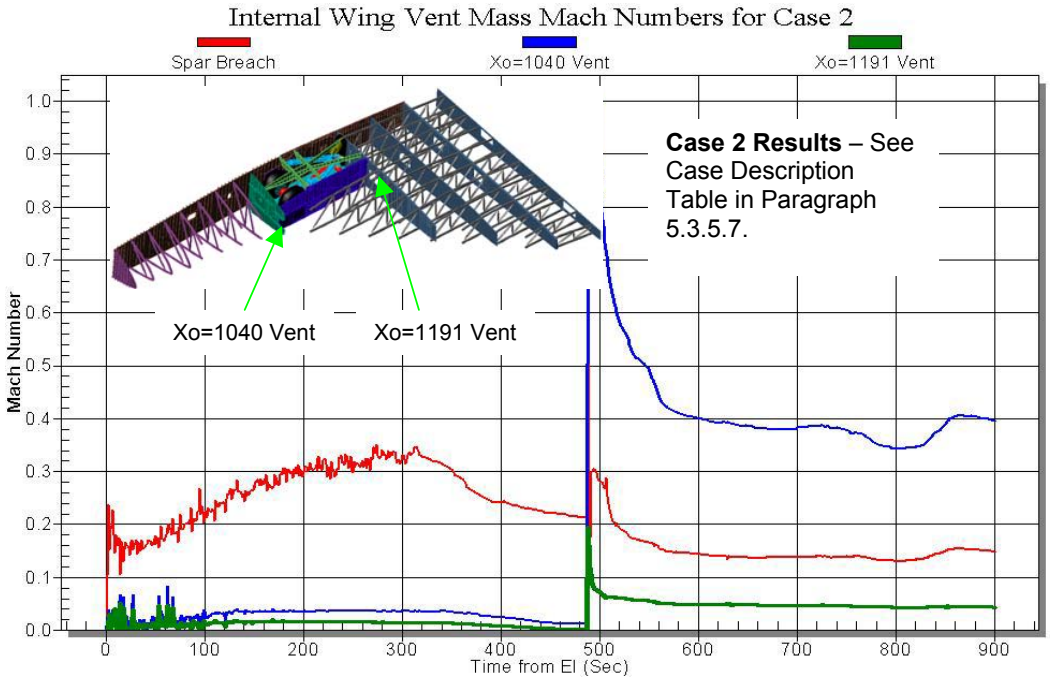

Figure 5.3.5-31 Internal Vent Mach Numbers for Case 2

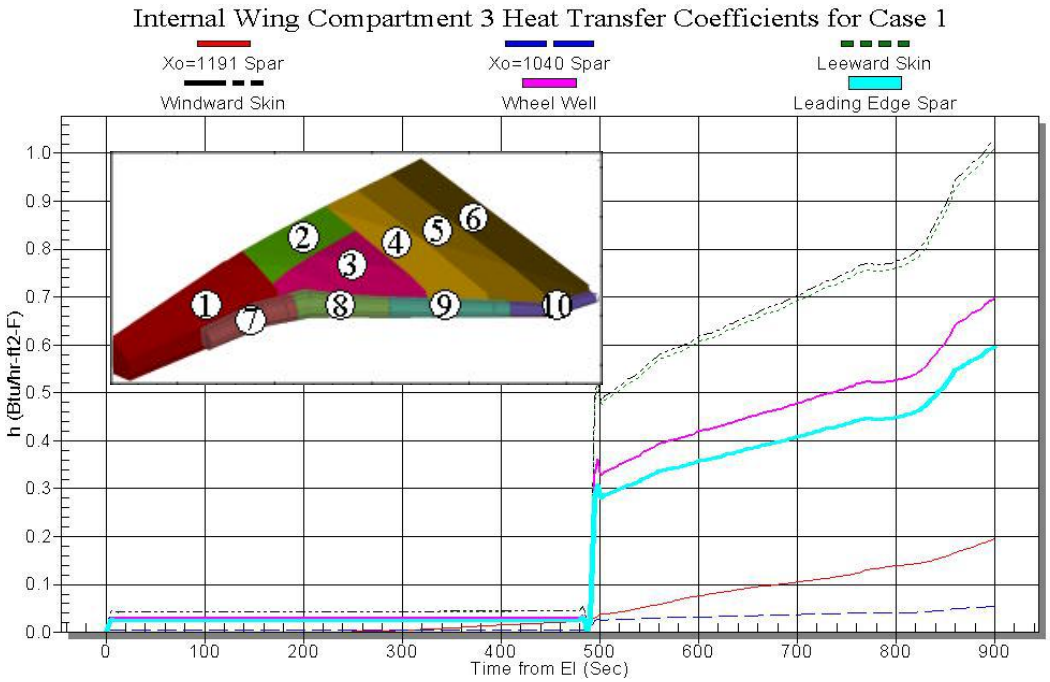

Figure 5.3.5-32 Compartment 3 Heat Transfer Coefficients for Case 1

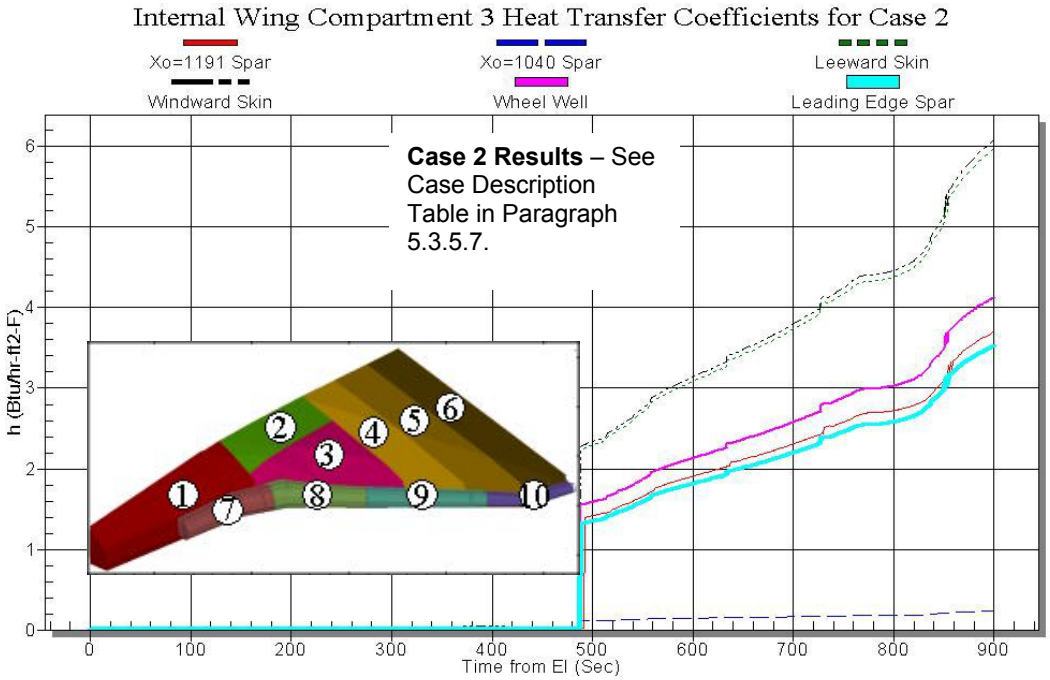

Figure 5.3.5-33 Compartment 3 Heat Transfer Coefficients for Case 2

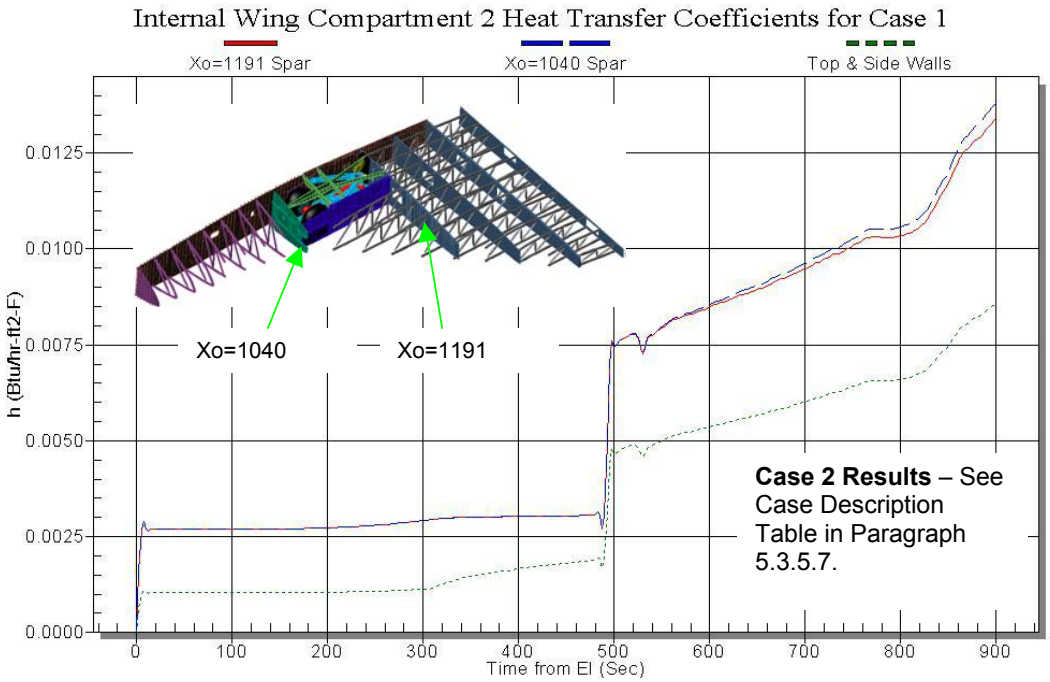

Figure 5.3.5-34 Wheel Well Heat Transfer Coefficients for Case 1

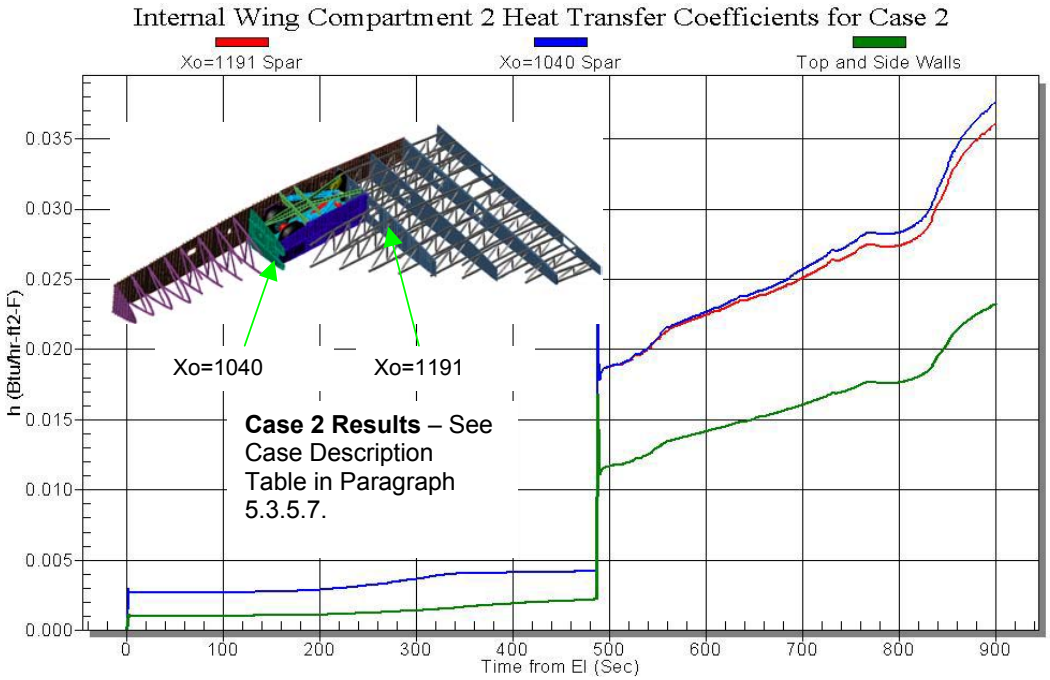

Figure 5.3.5-35 Wheel Well Heat Transfer Coefficients for Case 2

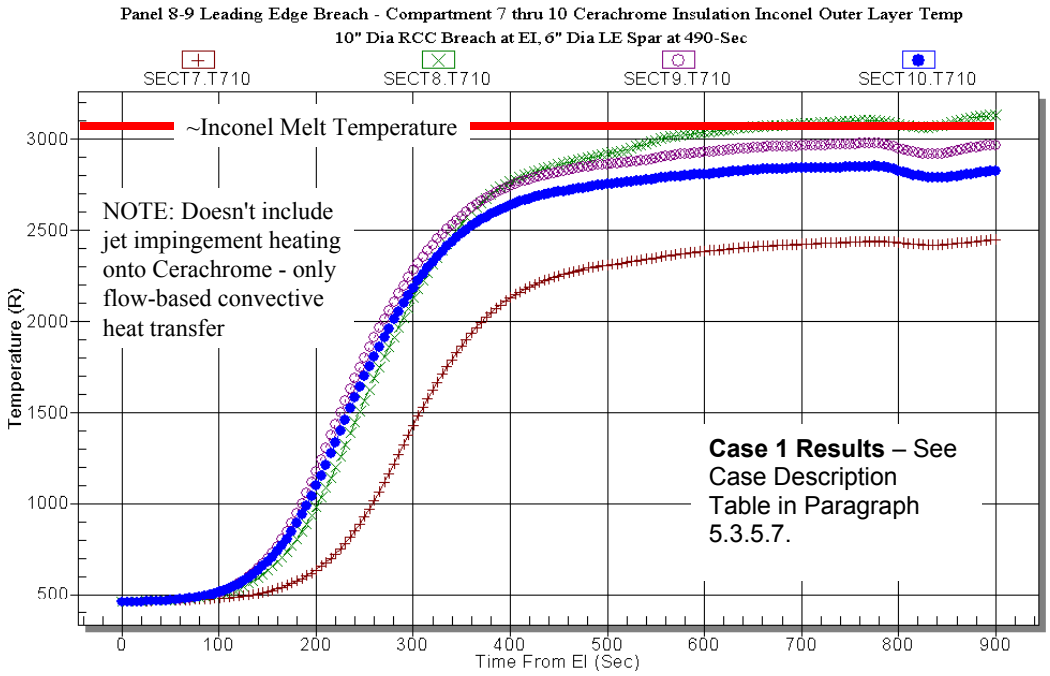

Figure 5.3.5-36 Leading Edge Cerachrome Insulation Inconel Outer Layer Temperature

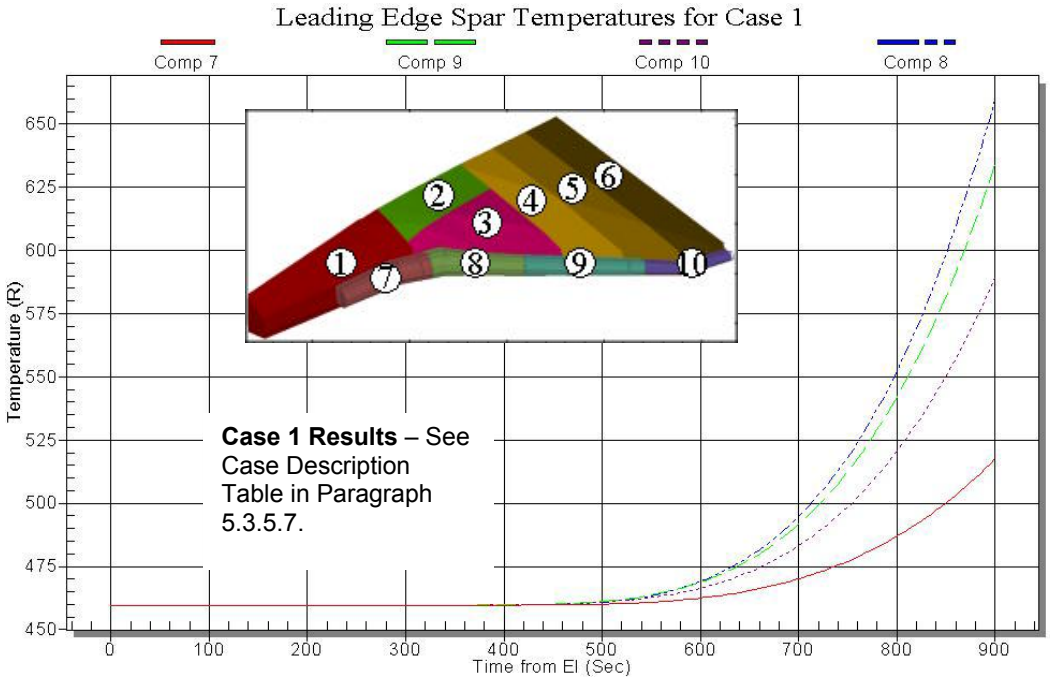

Figure 5.3.5-37 Leading Edge Structural Spar Temperature

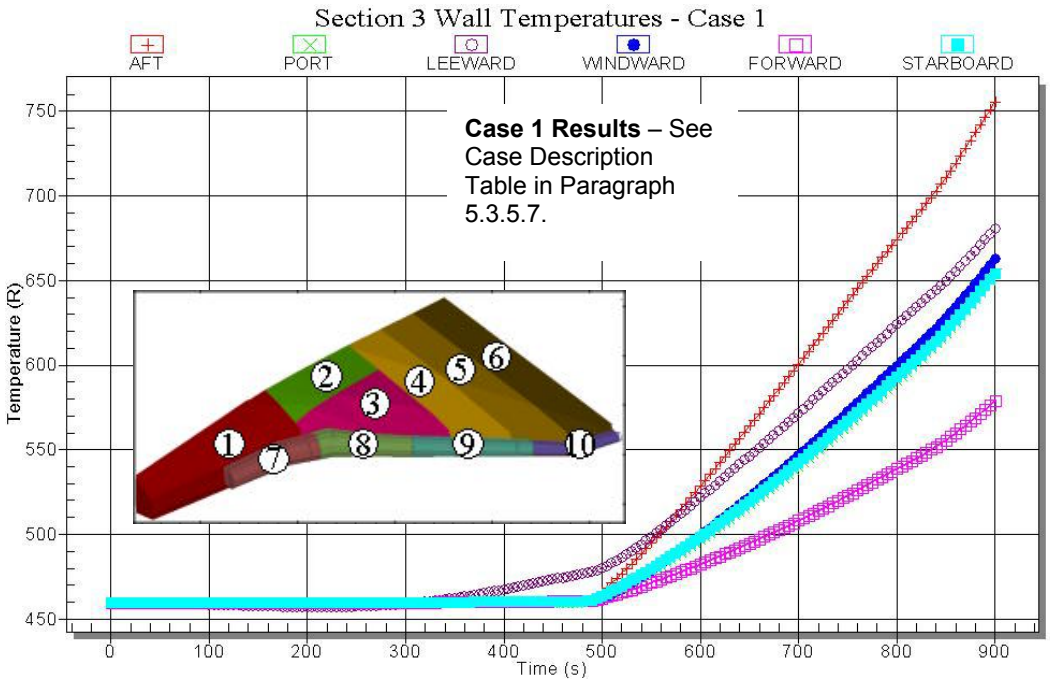

Figure 5.3.5-38 Compartment 3 Spar and Wall Skin Temperatures for Case 1

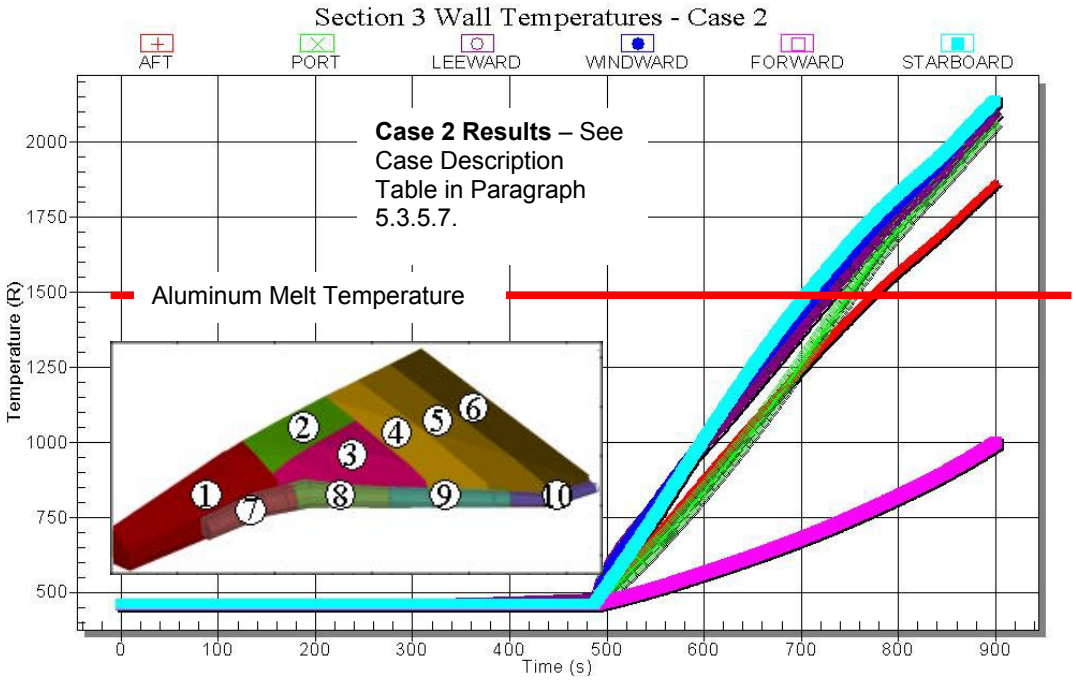

Figure 5.3.5-39 Compartment 3 Spar and Wall Skin Temperatures for Case 2

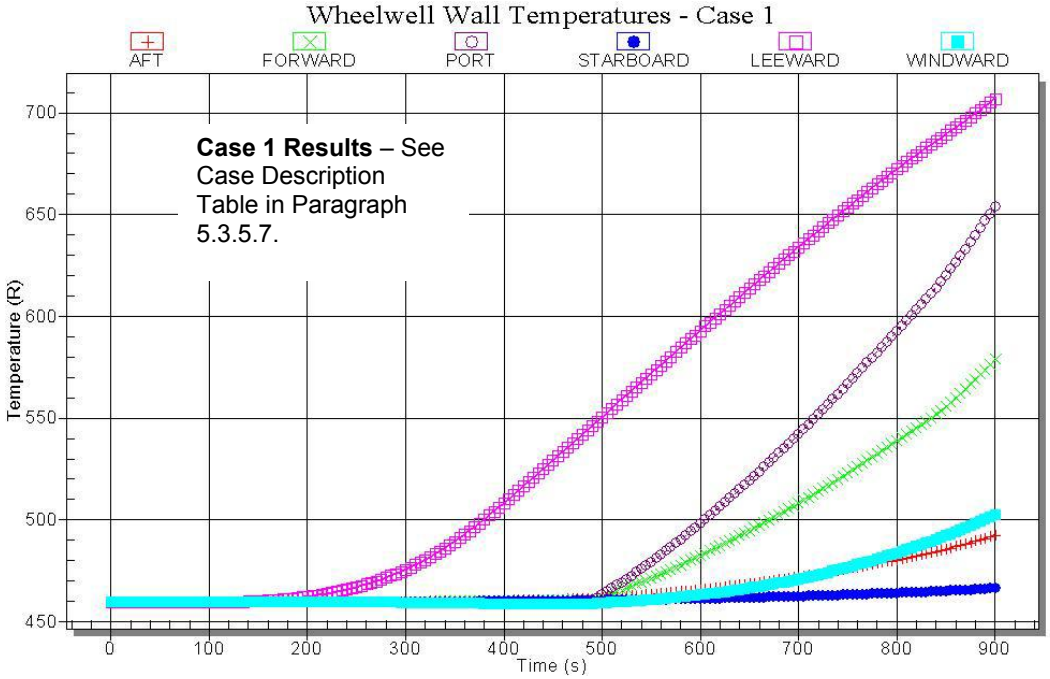

Figure 5.3.5-40 Compartment 2 Spar and Wall Skin Temperatures for Case 1

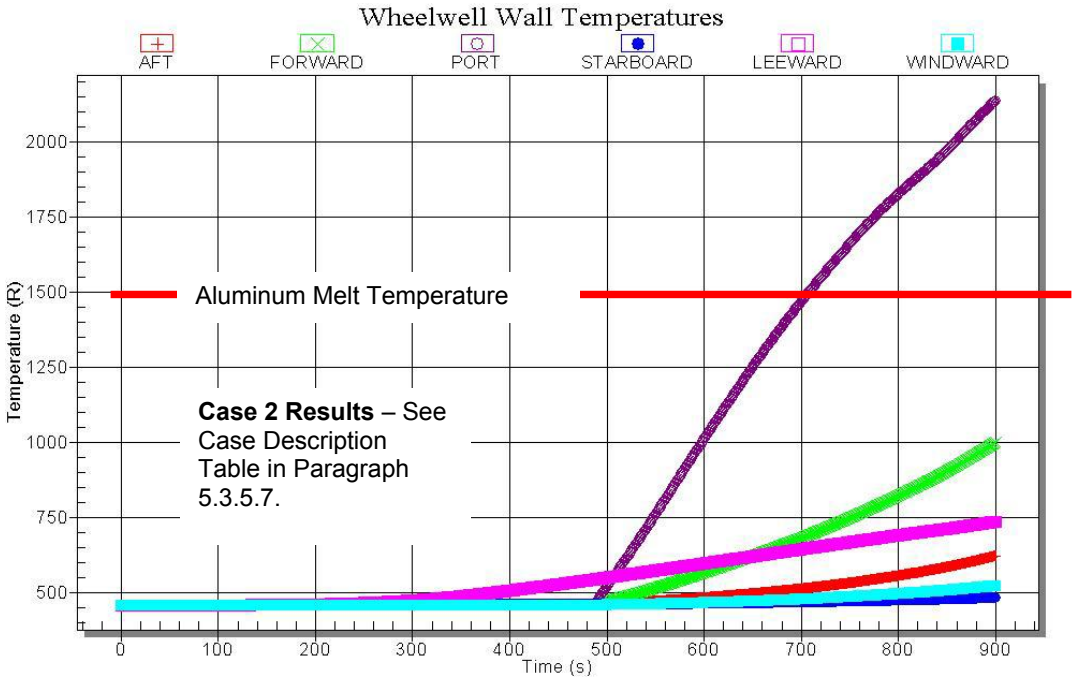

Figure 5.3.5-41 Compartment 2 Spar and Wall Skin Temperatures for Case 2

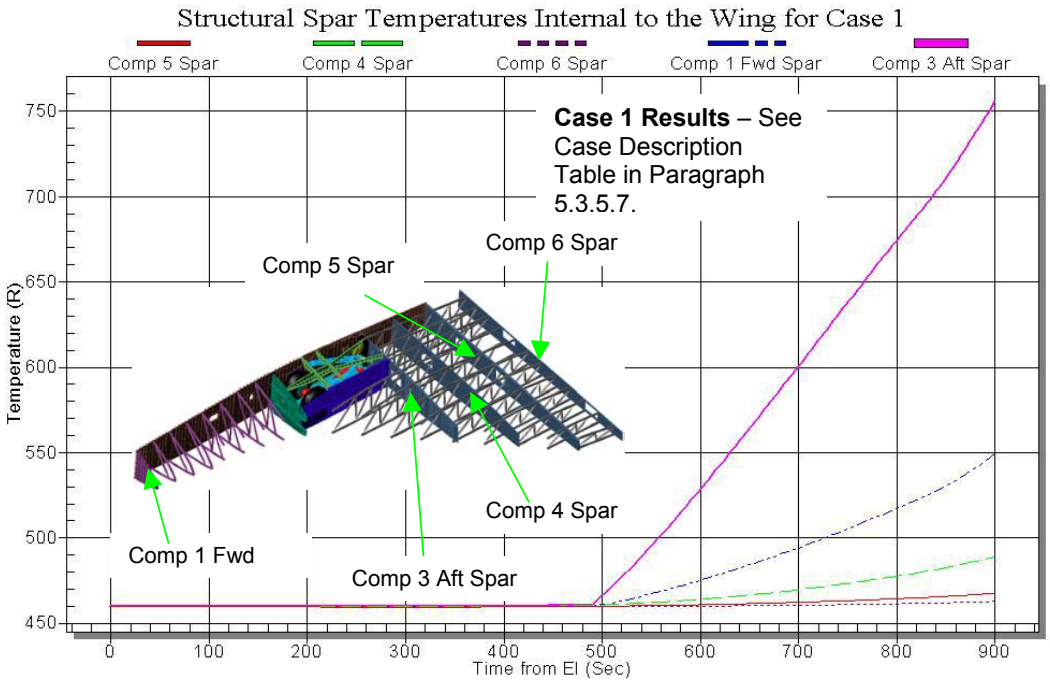

Figure 5.3.5-42 Internal Wing Spar Temperatures for Case 1

5.3.6 3D CFD & DSMC of Wing Leading Edge Cavity

5.3.6.1 CFD of RCC Panel Acreage Damage

5.3.6.1.1 Panel 7 6" Hole Decoupled Solution

5.3.6.1.1.1 Case description

This effort focused on a 6" diameter hole in RCC Panel 7 located on the attachment line at the panel midpoint (X = 1048 in, Y = -217 in, Z = 291.6 in). The attachment line location was determined from nominal geometry hypersonic Navier-Stokes solutions at approximately 40 degrees angle of attack. This study was conducted in two stages using the Unified Solution Algorithm (USA) flow solver with equilibrium air chemistry. The grid models were generated using ICEM/Hexa software. The first stage of the simulation involved a computational domain limited to the hole inlet and a section of the RCC channel from Panels 5-9, and is referred to as the decoupled internal flow case. Coupled external/internal flow simulations were performed next in the second stage. This decoupled internal flow simulation provided initial jet plume flow field information and convective heating environments to internal structure in the leading edge volume.

5.3.6.1.1.2 Geometry and Grid Definition

The CFD grid model used in this simulation included the ribs on both sides of Panel 7. Figure 5.3.6-1 show the surface grid. For the volume grid the wall spacing is 0.0005 inch to ensure a cell-Reynolds number of 1 or less. Rectangular openings to simulate the T-seal vent gaps were modeled on the leeside between Panels 5 and 6; Panels 6 and 7; Panels 7 and 8; and Panels 8 and 9. The respective areas of these vents are 0.5556, 0.642, 0.7704 and 0.642 square inches. These leeside rectangular vents of 0.2 inch width were modeled between the RCC panels in a chordwise orientation 2 inches ahead of upper carrier panels. To account for the vents in Panels 1-4, a circular vent of area 22.03 square inches was modeled at the inboard end of the Panels 5-9 channel. Similarly, another circular vent of area 55.29 square inches was modeled on the outboard end of the Panels 5-9 channel to account for the vents on Panels 10-22. The total vent area of about 80 square inches was purposely made to be about 20% larger than 66.4 square inches of all the documented spanwise vents in front of the upper carrier panels and the chordwise vents between RCC Panels just ahead of upper carrier panels.

5.3.6.1.1.3 Boundary Conditions

For the decoupled internal flow simulation the total conditions at the hole inlet were obtained from the Orbiter nominal geometry Navier-Stokes solutions for STS-107 CFD Point 2 flight condition (491.4 sec from Entry Interface). In this laminar simulation with equilibrium air chemistry, a pressure of 38.6 psf and temperature of 18,375° R were specified as the reservoir conditions at the hole inlet. This results in a total enthalpy of 27,500 Btu/lbm whereas the actual total enthalpy is 11,175 Btu/lbm for the flight condition at 491.4 sec after EI. The interior surfaces were kept at 0° F. A back-pressure of 0.5 psf was specified at the vents for the simulation.

5.3.6.1.1.4 Results

Figure 5.3.6-3 shows Mach contours of the jet plume with the corresponding jet pressure contours illustrated in Figure 5.3.6-4. The total enthalpy contours are shown in Figure 5.3.6-5. The pressure results on the RCC channel and the front spar are shown in Figure 5.3.6-6 and Figure 5.3.6-7, respectively. Similarly, Figure 5.3.6-8 and Figure 5.3.6-9 illustrate the heating on the RCC channel surfaces and on the front spar, respectively. The results discussed thus far in this section were obtained with a 2 million-cell grid model. Another simulation with a denser grid model of about 15 million cells was also conducted to evaluate grid convergence effects. Figure 5.3.6-10 and Figure 5.3.6-11 show the surface pressure and heating distributions, respectively, on the front spar and the RCC cavity from the 15 million-cell model simulation. The heating results are as high as twice the results from the 2 million-cell model simulation. The jet plume is probably better resolved as seen in the flow field Mach and pressure distributions illustrated in Figure 5.3.6-12 and Figure 5.3.6-13, respectively. The decoupled internal flow CFD heating results are higher than predictions from engineering models calculated at the same conditions. Nevertheless, the decoupled internal flow simulation provided a lead-in to the coupled external/internal flow simulations.

5.3.6.1.2 Panel 7 6" Hole Coupled External/Internal Flow Solution

5.3.6.1.2.1 Case description

Two coupled external/internal flow simulations were conducted during the second stage of this study for a 6-inch diameter hole in leading edge panel 7 using the freestream flow conditions from flight at 404 sec after EI. The first simulation used a finer grid but did not model the internal earmuff insulation between Panels 7 and 8. The second simulation used a coarser grid but the earmuff insulation between both panels 7/8 and panels 8/9 was modeled.

5.3.6.1.2.2 Geometry and Grid Definition

The grid models used for the coupled simulation included the RCC channel, vents and the 6” hole, as well as the Orbiter external flow grid in order to generate coupled external/internal flow solutions. In addition, the grid model used in the first coupled external/internal flow simulation included the ribs on both sides of RCC Panel 7 and Panel 8, along with the earmuff insulation between Panels 8 and 9. The far and close-up views of the surface grid of the external and internal flow regimes are shown in Figure 5.3.6-14 and Figure 5.3.6-15, respectively. Figure 5.3.6-16 and Figure 5.3.6-17 illustrate further the details of the geometry inside the RCC cavity, whereas a cross-section of the grid is shown in Figure 5.3.6-18. The wall spacing is 0.0005 inch to ensure the cell-Reynolds number of 1 or less on the surface.

5.3.6.1.2.3 Boundary Conditions

In this equilibrium air chemistry simulation, the RCC interior surfaces were kept at 0° F, whereas the Orbiter exterior surfaces were specified with radiative equilibrium temperature boundary condition. The vent areas and pressure boundary conditions used in the decoupled simulation were also applied to these simulations.

5.3.6.1.2.4 Results

Figure 5.3.6-19 and Figure 5.3.6-20 show the Mach and Pressure contours, respectively, in the jet plume for a planar cut through the leading edge cavity. Figure 5.3.6-21 illustrates the pressure contours in the flow field whereas the Mach contours in flow field are shown in Figure 5.3.6-22 and Figure 5.3.6-23 for a constant-z cut. The surface pressure distributions are shown in Figure 5.3.6-24 and Figure 5.3.6-25 on the RCC channel and the front spar, respectively. Similarly, the heating results are illustrated in Figure 5.3.6-26 and Figure 5.3.6-27 for the RCC channel and the front spar, respectively. These results are from a dense grid model with about 15 million cells. The heating environment inside the RCC cavity is converged, except on the front spar where there are some small variations. The secondary impingement of

the jet on the front spar is probably not a steady-state phenomenon, but the level of heating on the spar is not very high. The earmuff insulation between Panels 7 and 8 were not modeled in this simulation, because the jet was thought to be going straight toward the earmuff between RCC Panels 8 and 9. This simulation however showed that the jet hits primarily the outboard rib of RCC Panel 7 and the rib redirects the jet toward the region of the earmuff insulation between RCC Panels 7 and 8. The second coupled external/internal flow simulation in this study conducted included the earmuff insulation between RCC Panels 7 and 8.

Figure 5.3.6-28 and Figure 5.3.6-29 illustrate the external flow grid model for this simulation whereas the internal flow grid model is shown in Figure 5.3.6-30, Figure 5.3.6-31 and Figure 5.3.6-32. The results for this simulation using a grid model of about 2 million cells are discussed below. Figure 5.3.6-33, Figure 5.3.6-34 and Figure 5.3.6-35 show pressure distributions on the RCC channel, whereas similar heating distributions are illustrated in Figure 5.3.6-36, Figure 5.3.6-37 and Figure 5.3.6-38. Also, pressure contours in flow field are shown in Figure 5.3.6-39 and Figure 5.3.6-40, whereas Figure 5.3.6-41 and Figure 5.3.6-42 illustrate Mach contours in the flow field. The jet hits the outboard rib of Panel 7, then the outboard edge of the earmuff insulation between RCC Panels 7 and 8, and then the front spar behind RCC Panel 8.

• RCC Panels 5-9 with leeside vents modeled. (Side vents represent vents for other panels either side).

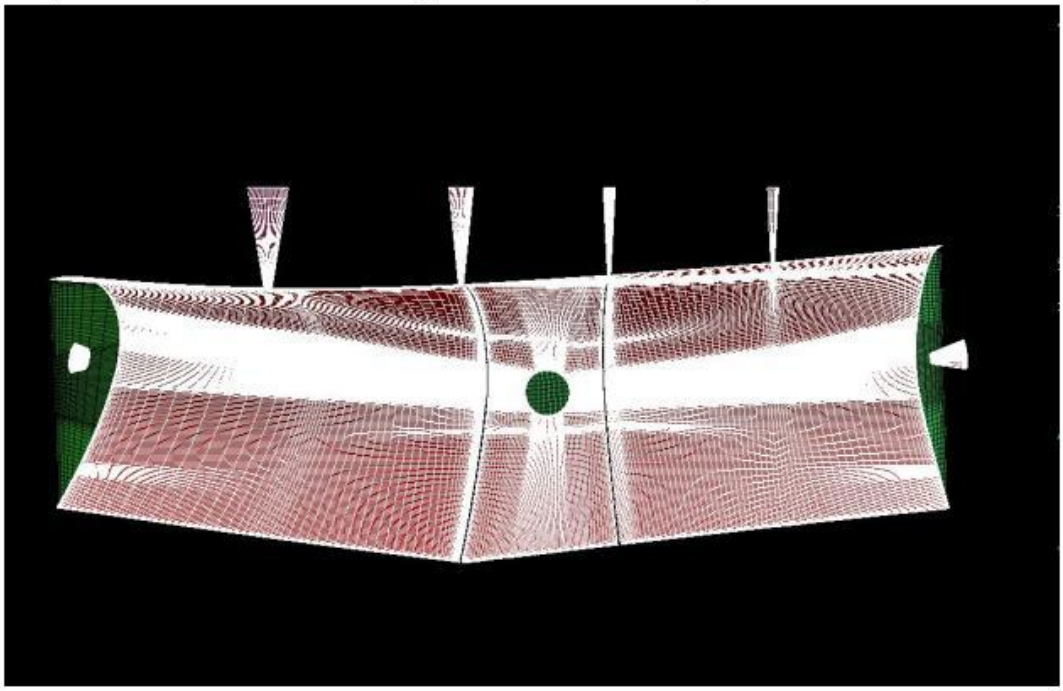

Figure 5.3.6-1 Grid Model for Panel 7 Hole Internal Flow Simulation

• Vents are connected to a fictitious dump chamber where back-pressure from leeside specified. (Brackets modeled either side of Panel 7)

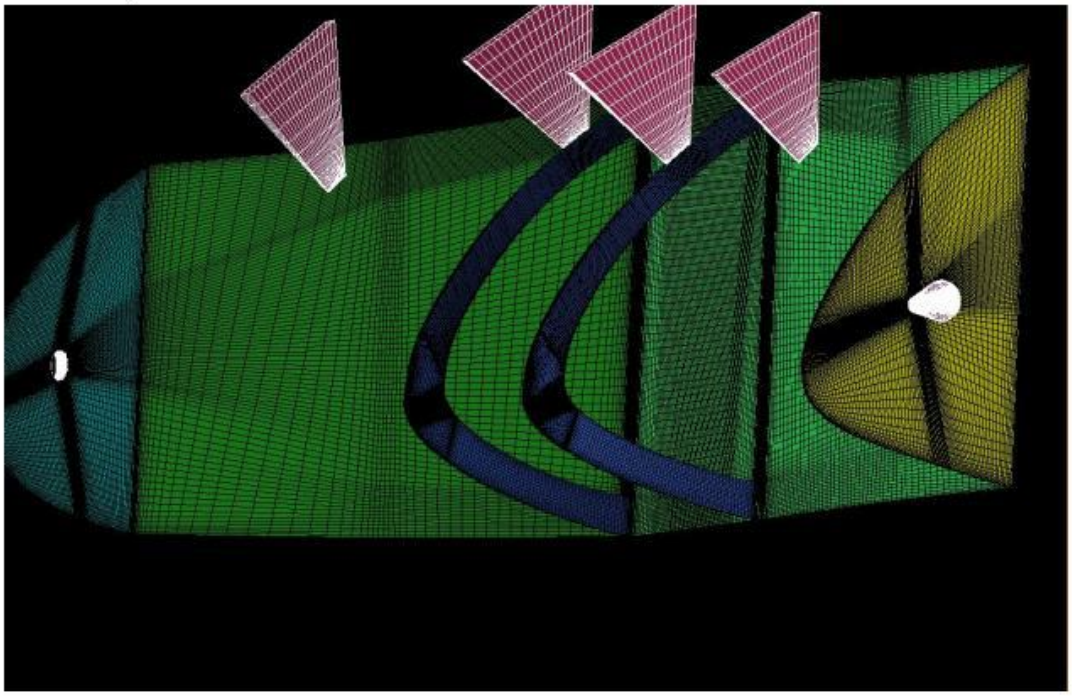

Figure 5.3.6-2 Grid Model for Panel 7 Hole Internal Flow Simulation

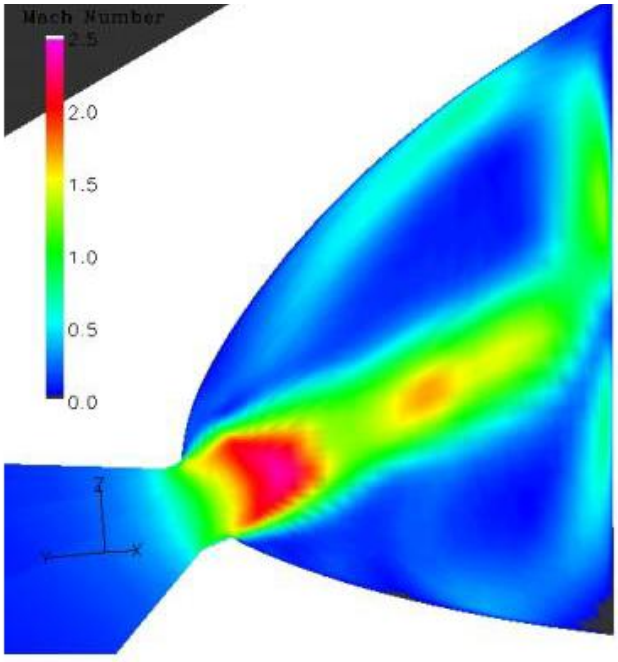

Figure 5.3.6-3 Mach Contours for Panel 7 Hole Internal Flow Simulation with 2 million-cell Model

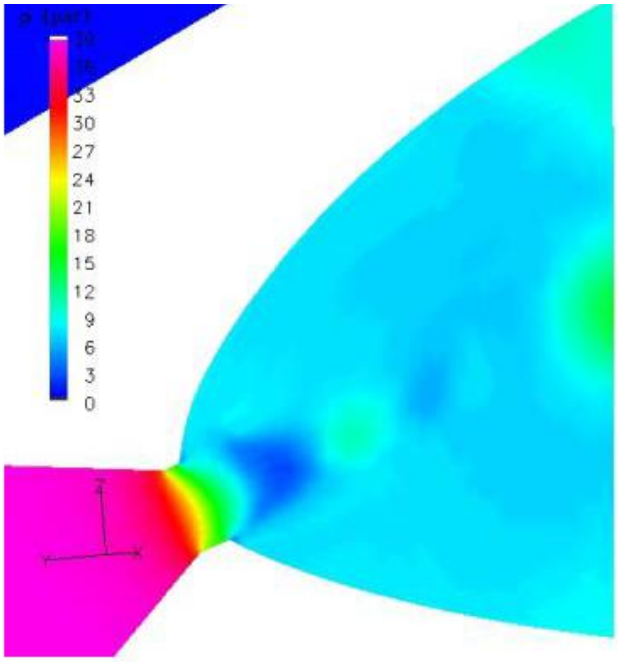

Figure 5.3.6-4 Pressure Contours for Panel 7 Hole Internal Flow Simulation with 2 million-cell Model

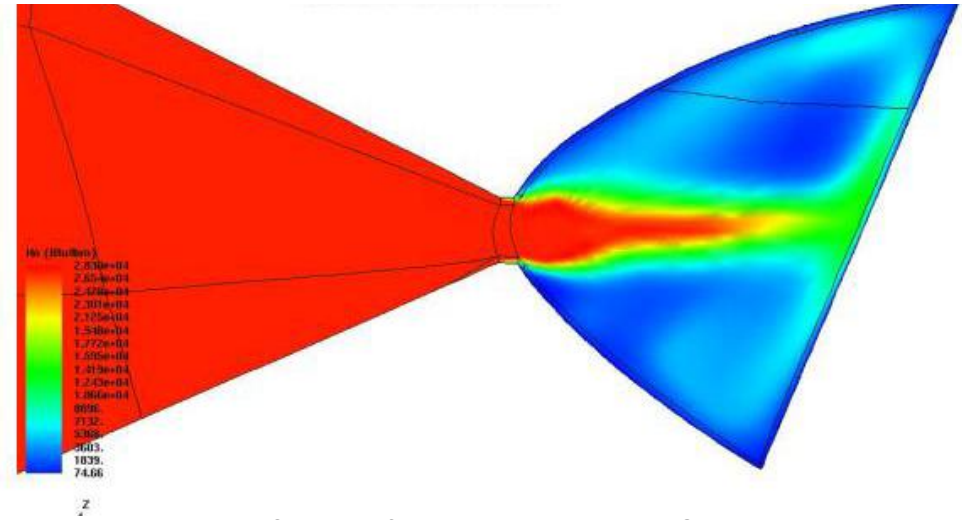

Figure 5.3.6-5 Total Enthalpy Contours for Panel 7 Internal Flow Simulation with 2 million-cell Model

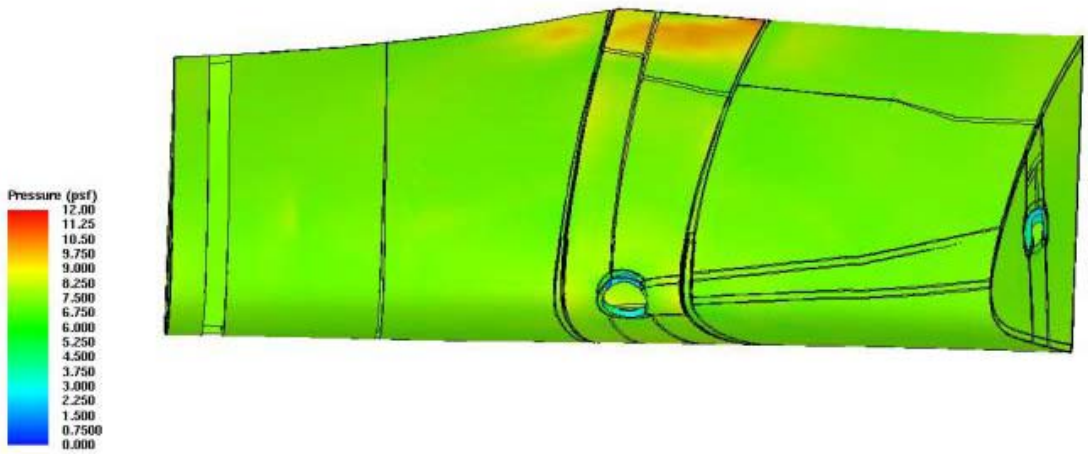

Figure 5.3.6-6 Pressure Contours on RCC Channel from Panel 7 Hole Internal Flow Simulation with 2 million-cell Model

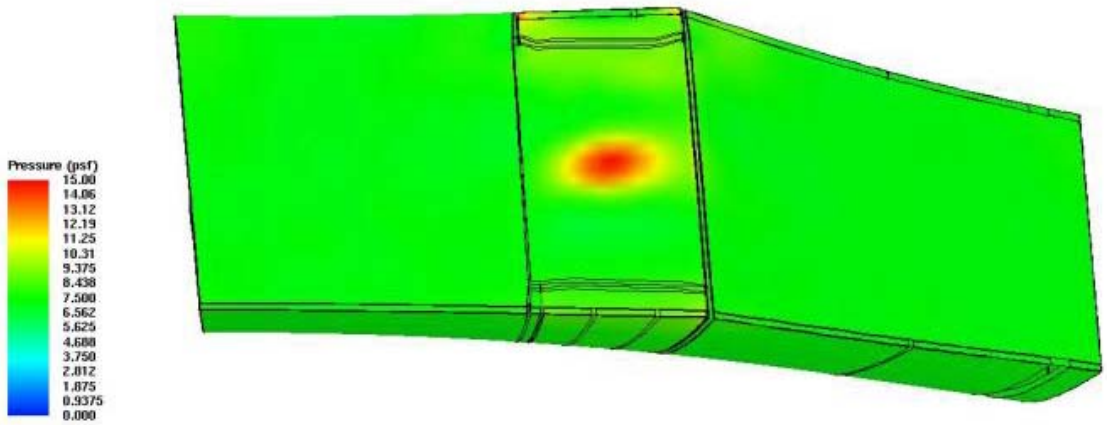

Figure 5.3.6-7 Pressure Contours on Front Spar from Panel 7 Hole Internal Flow Simulation with 2 million-cell Model

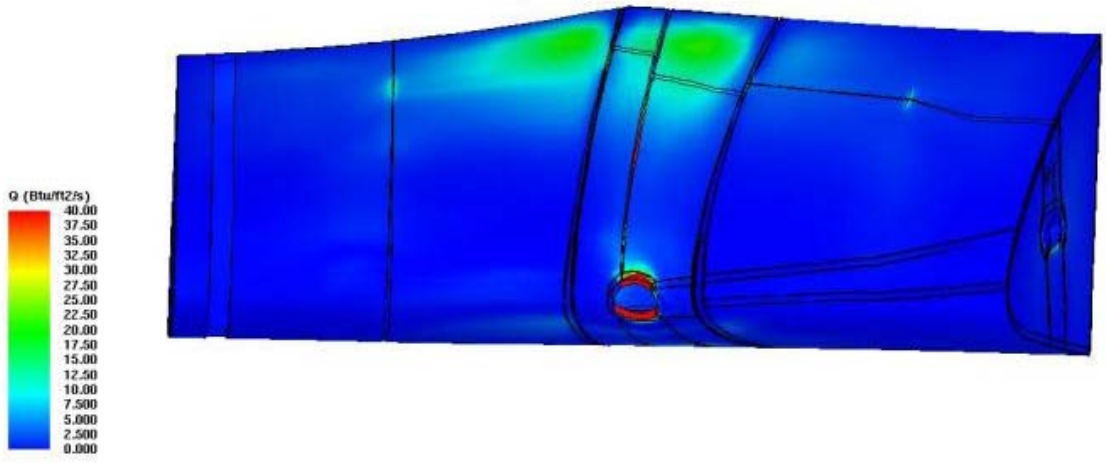

Figure 5.3.6-8 Heating Contours on RCC Channel from Panel 7 Hole Internal Flow Simulation with 2 million-cell Model

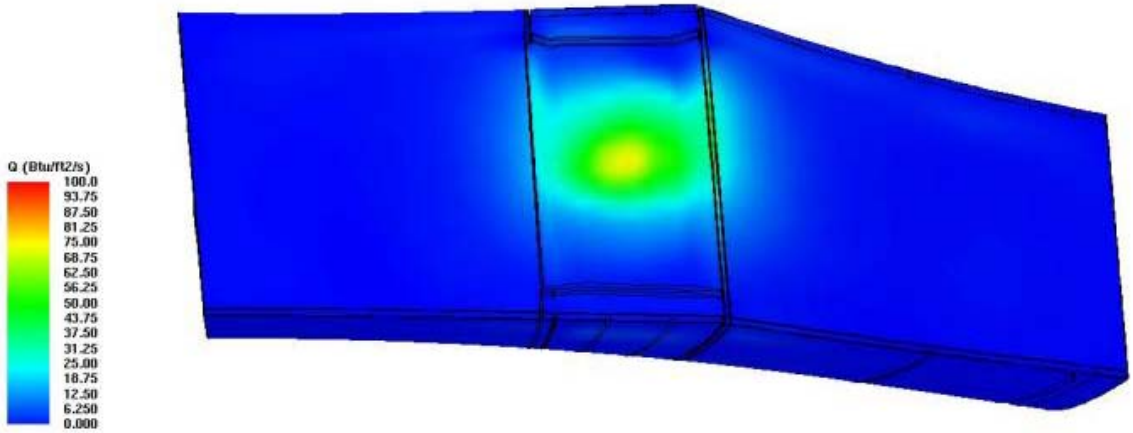

Figure 5.3.6-9 Heating Contours on Front Spar from Panel 7 Hole Internal Flow Simulation with 2 million-cell Model

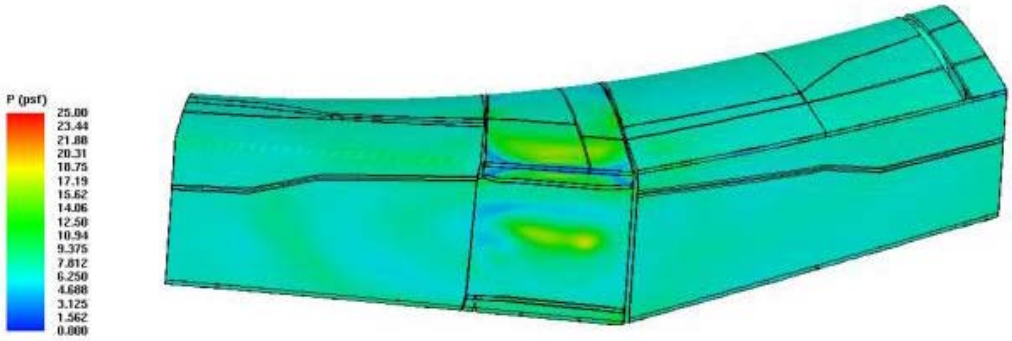

Figure 5.3.6-10 Pressure Contours on Front Spar and RCC Cavity from Panel 7 Hole Internal Flow Simulation with 15 million-cell Model

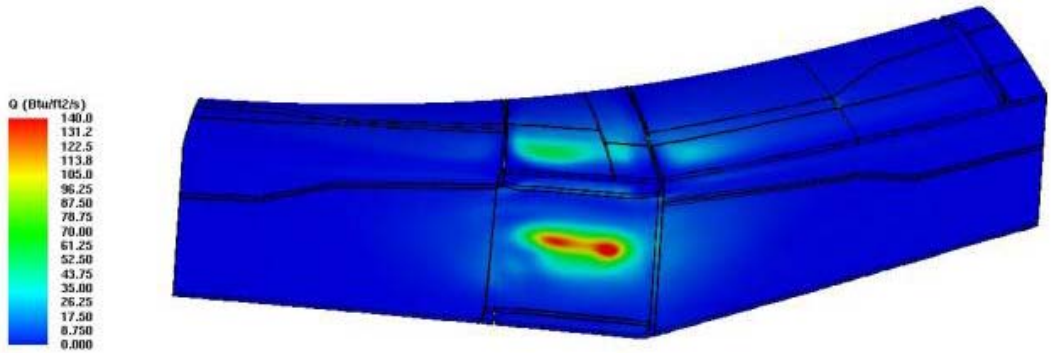

Figure 5.3.6-11 Heating Contours on Front Spar and RCC Cavity from Panel 7 Hole Internal Flow Simulation with 15 million-cell Model

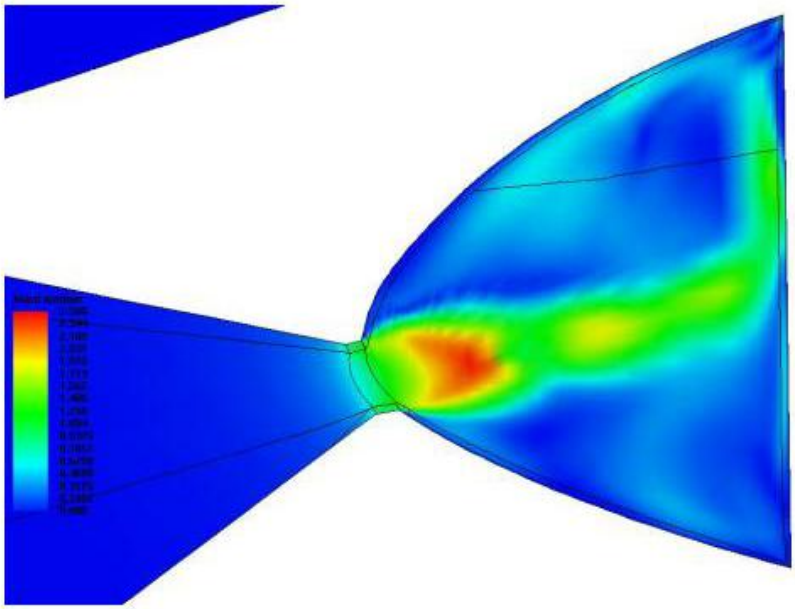

Figure 5.3.6-12 Mach Contours for Panel 7 Hole Internal Flow Simulation with 15 million-cell Model (Post-processed with every other points)

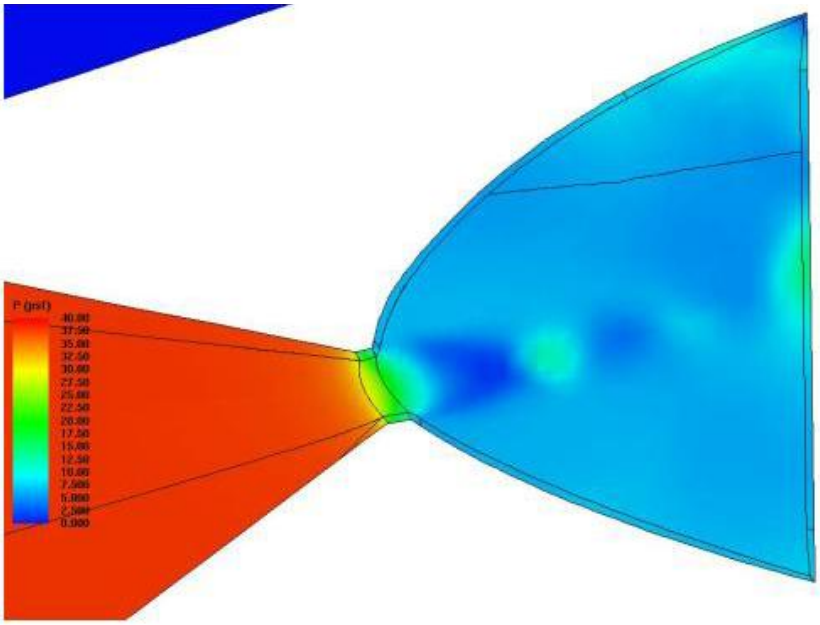

Figure 5.3.6-13 Pressure Contours for Panel 7 Hole Internal Flow Simulation with 15 million-cell Model (Post-processed with every other points)

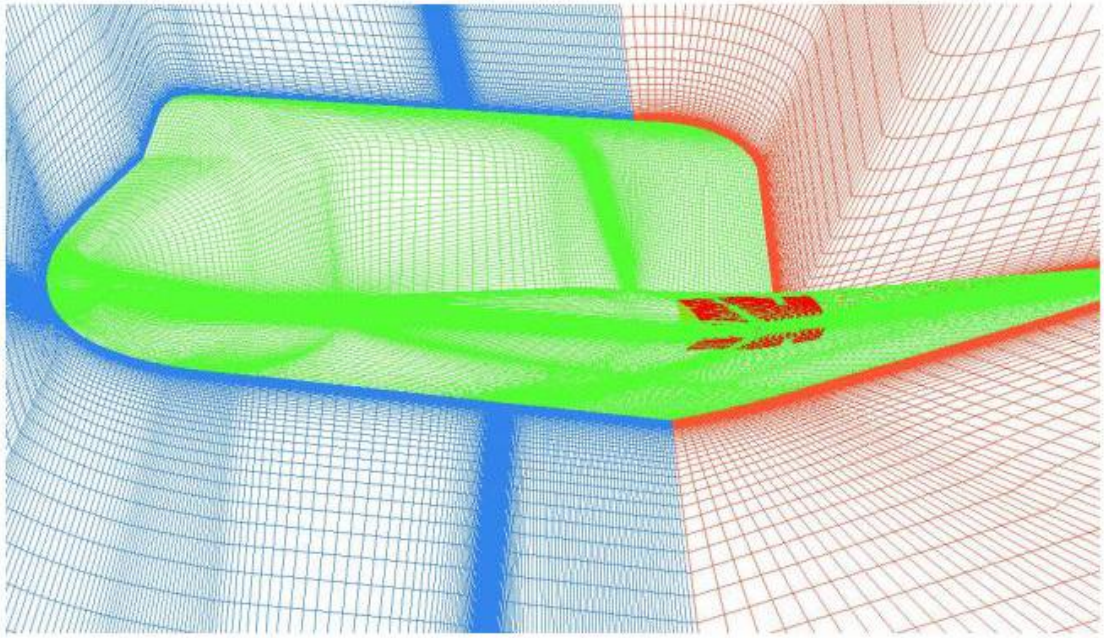

Figure 5.3.6-14 Grid Model for Panel 7 Hole Coupled External/Internal Flow Simulation I

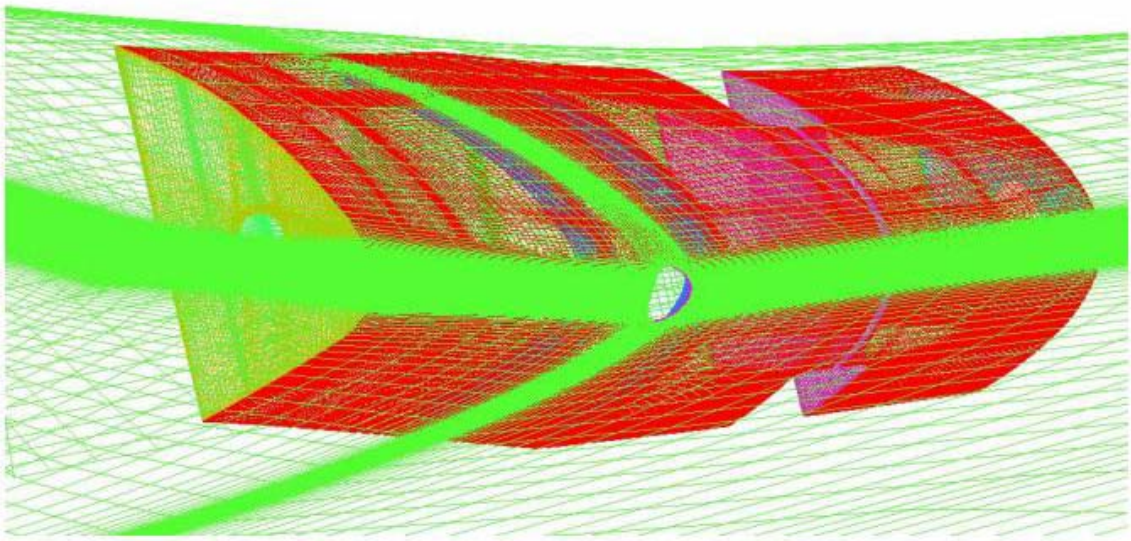

Figure 5.3.6-15 Grid Model for Panel 7 Hole Coupled External/Internal Flow Simulation I

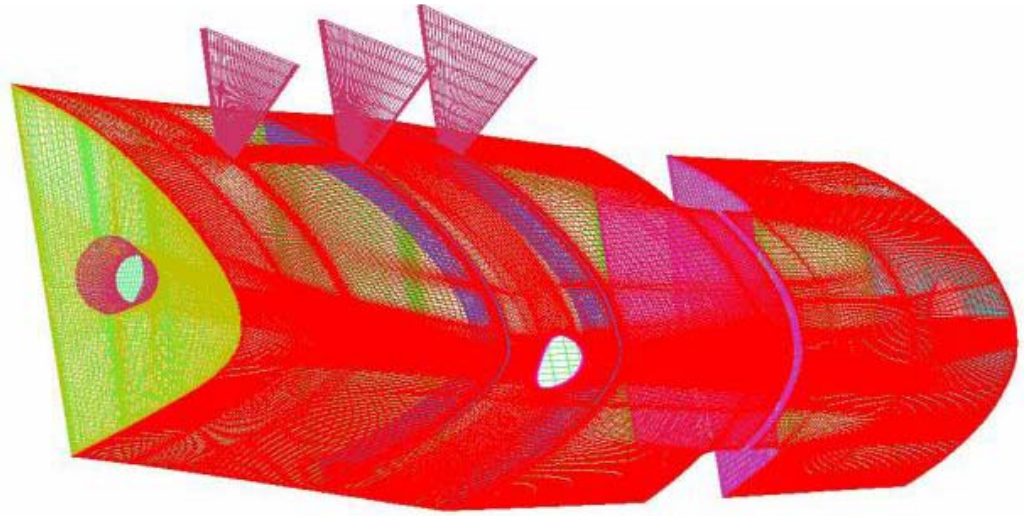

Figure 5.3.6-16 Grid Model for Panel 7 Hole Coupled External/Internal Flow Simulation I

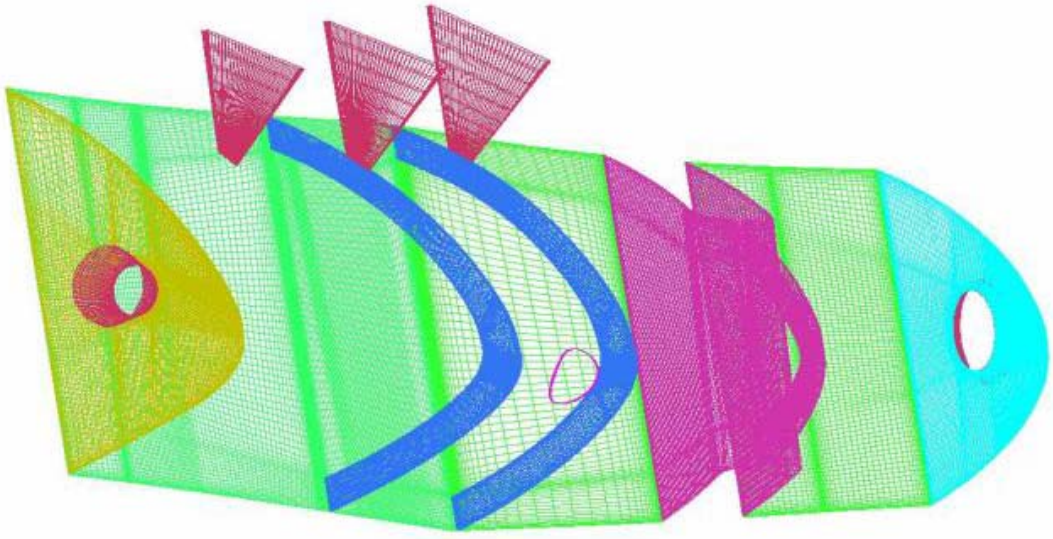

Figure 5.3.6-17 Grid Model for Panel 7 Hole Coupled External/Internal Flow Simulation I

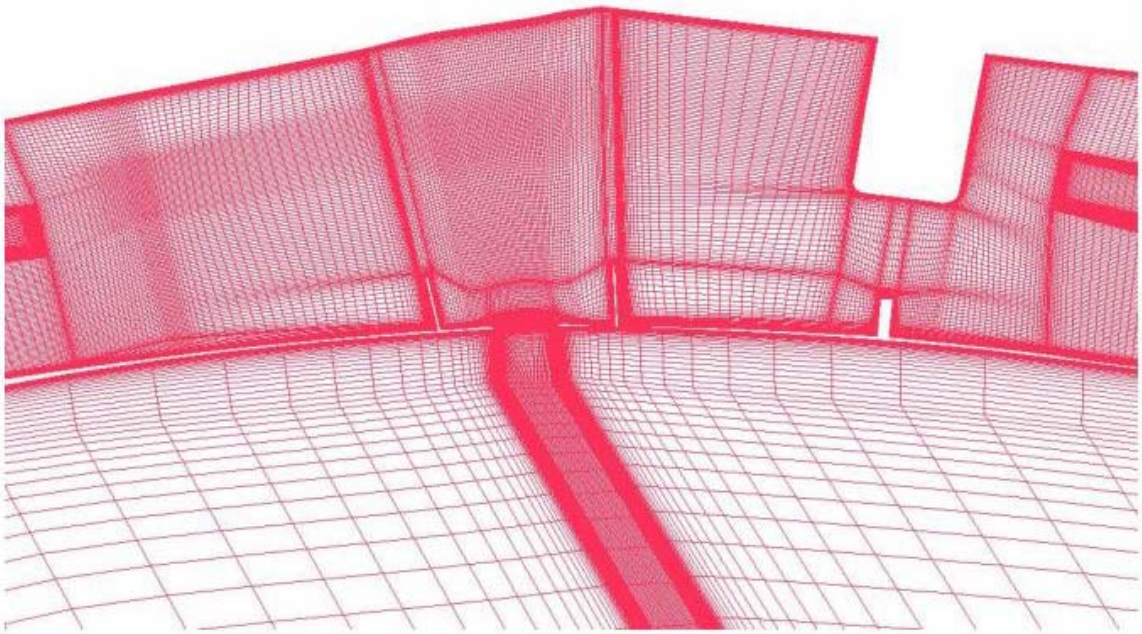

Figure 5.3.6-18 Grid Model for Panel 7 Hole Coupled External/Internal Flow Simulation I

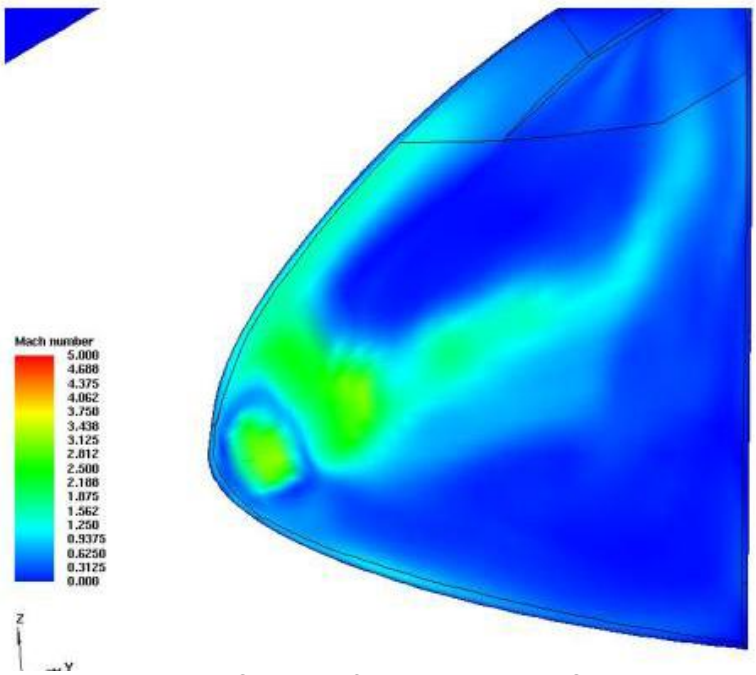

Figure 5.3.6-19 Mach Contours from Panel 7 Hole Coupled External/Internal Flow Simulation I (Postprocessed using every other points)

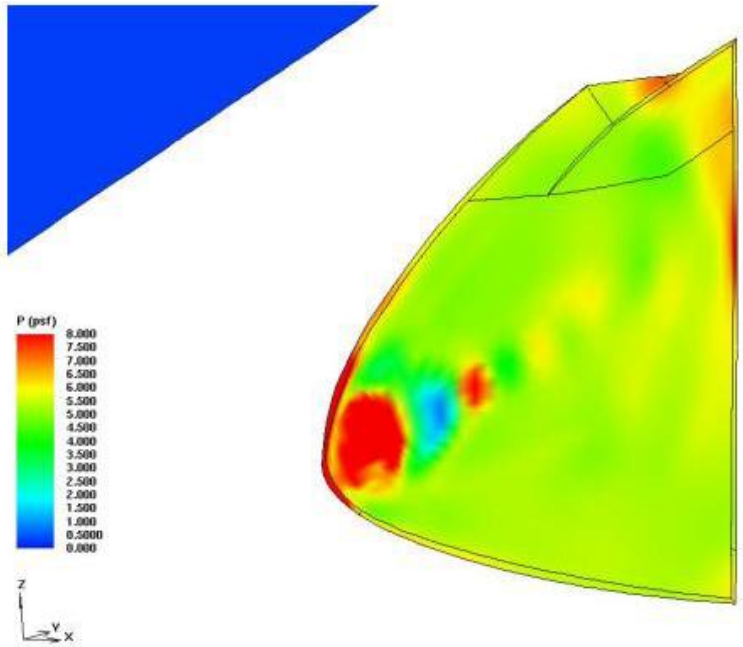

Figure 5.3.6-20 Pressure Contours from Panel 7 Hole Coupled External/Internal Flow Simulation I (Postprocessed using every other points)

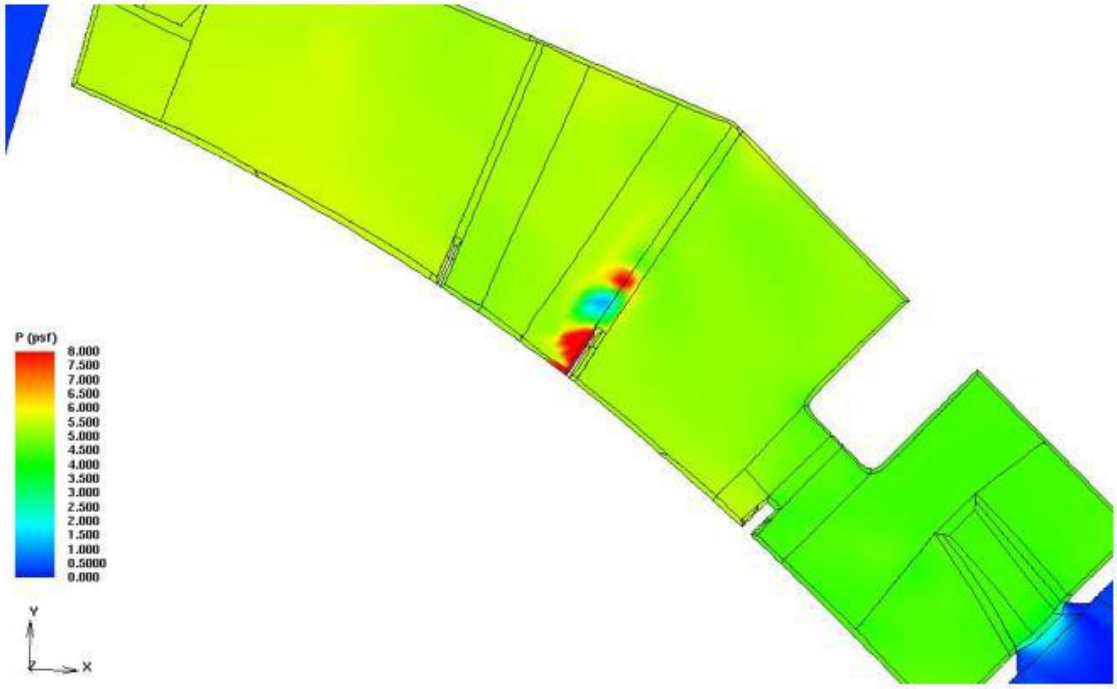

Figure 5.3.6-21 Pressure Contours from Panel 7 Hole Coupled External/Internal Flow Simulation I (Z=297.3; Postprocessed using every other points)

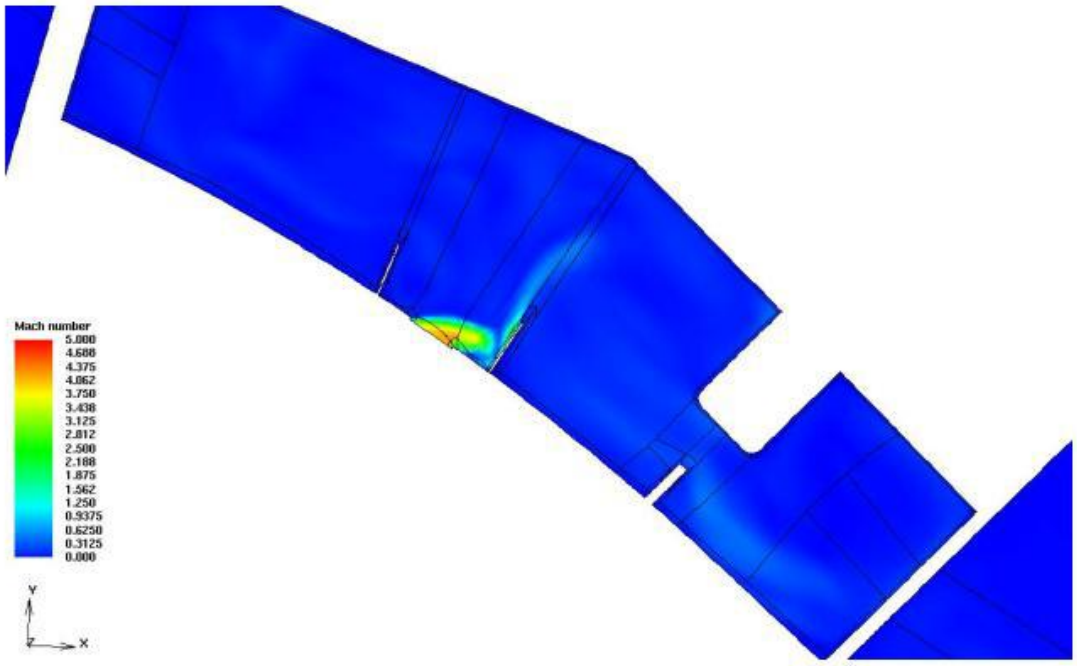

Figure 5.3.6-22 Mach Contours from Panel 7 Hole Coupled External/Internal Flow Simulation I (Z=291.6; Postprocessed using every other point)

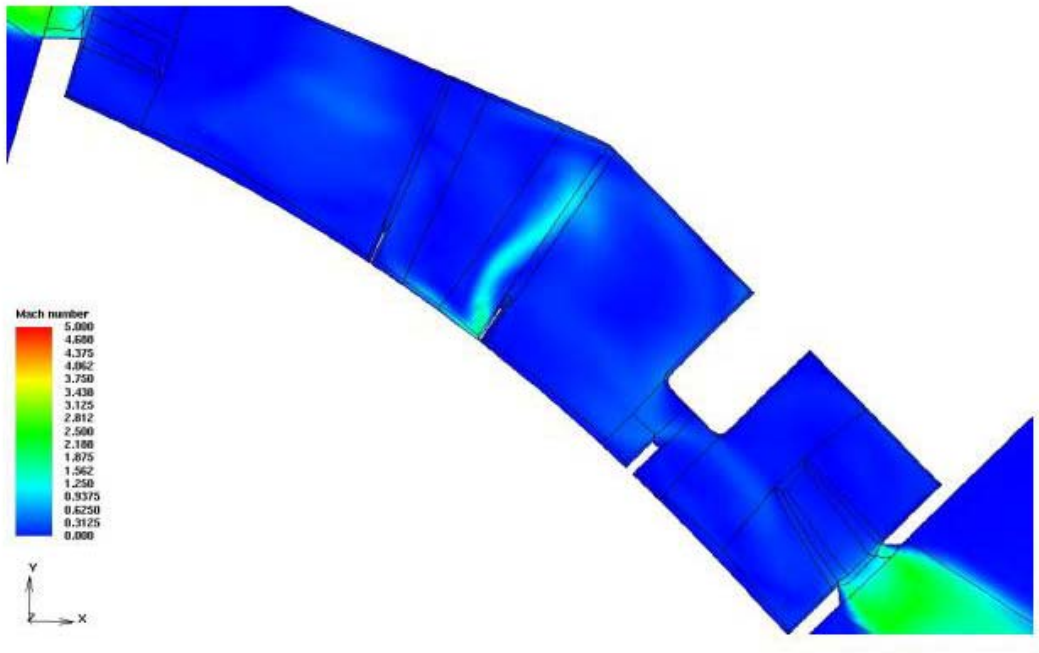

Figure 5.3.6-23 Mach Contours from Panel 7 Hole Coupled External/Internal Flow Simulation I (Z=301.6; Postprocessed using every other point)

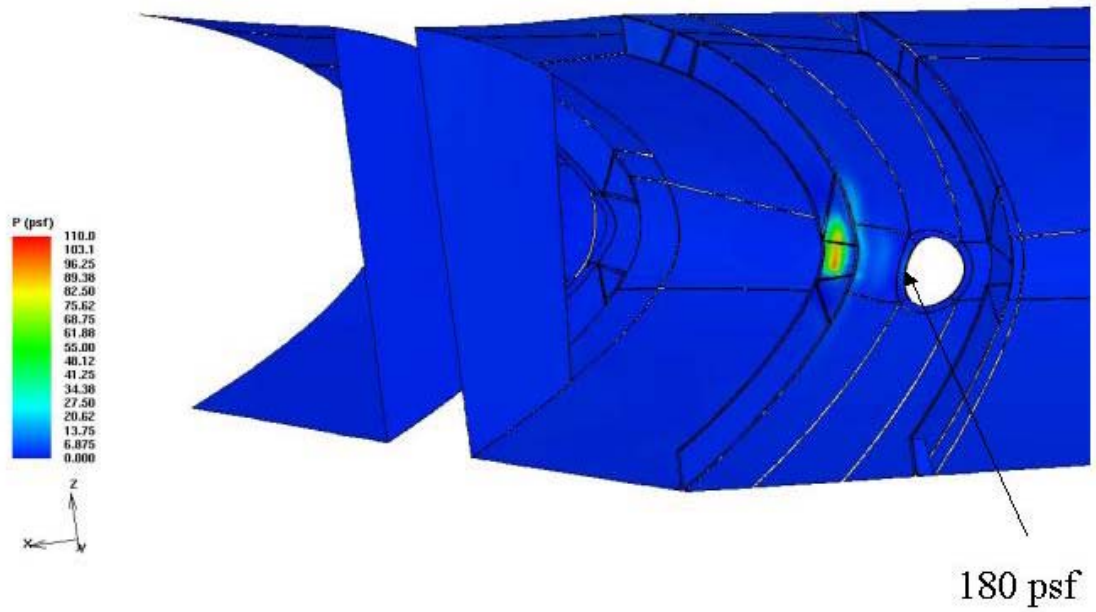

Figure 5.3.6-24 Pressure Contours on RCC Channel from Panel 7 Hole Coupled External/Internal Flow Simulation I

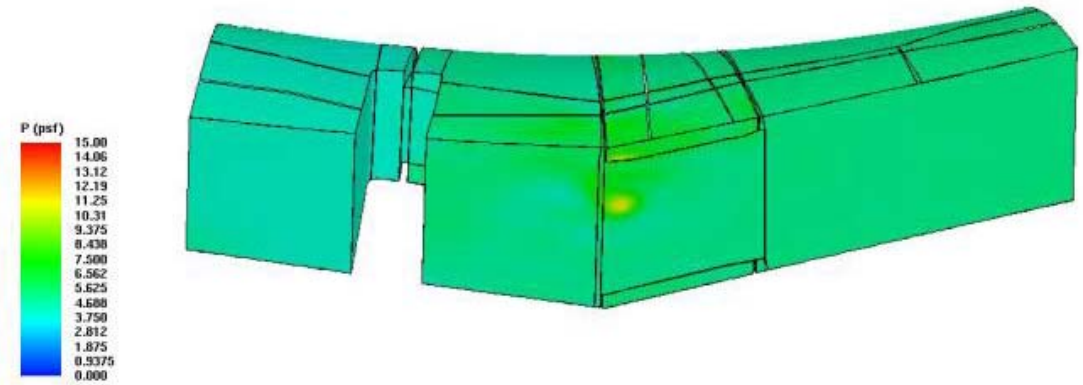

Figure 5.3.6-25 Pressure Contours on Front Spar from Panel 7 Hole Coupled External/Internal Flow Simulation I

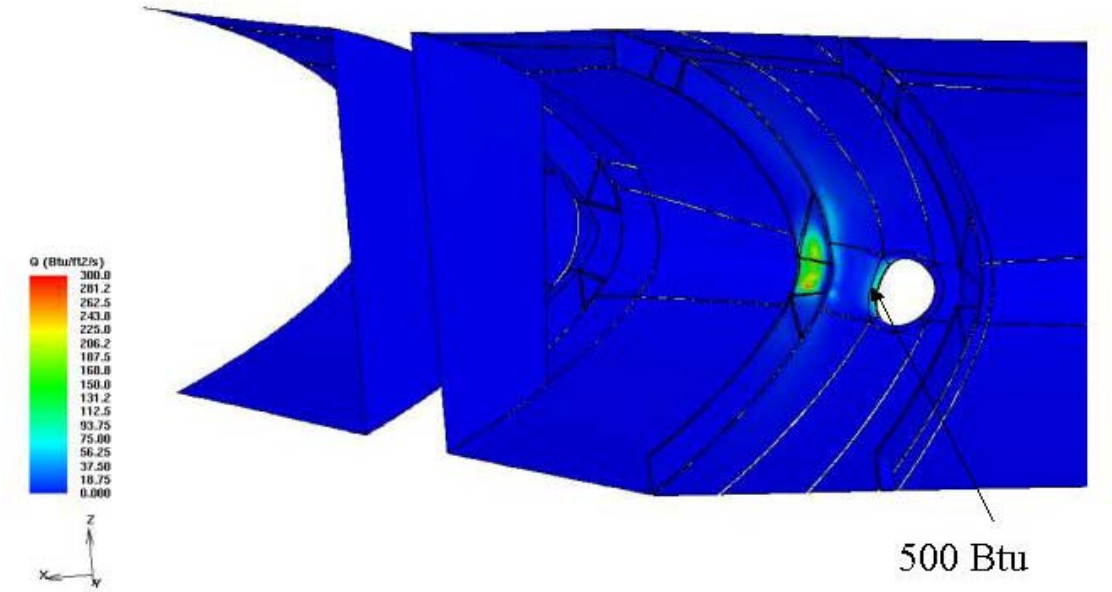

Figure 5.3.6-26 Heating Contours on RCC Channel from Panel 7 Hole Coupled External/Internal Flow Simulation I

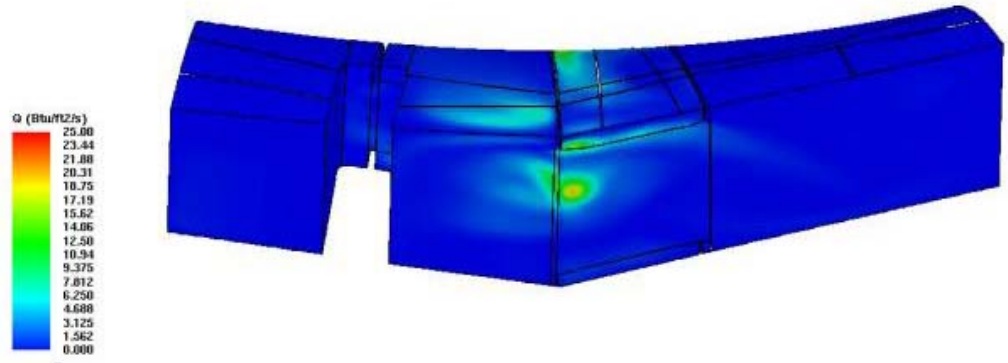

Figure 5.3.6-27 Heating Contours on Front Spar from Panel 7 Hole Coupled External/Internal Flow Simulation I

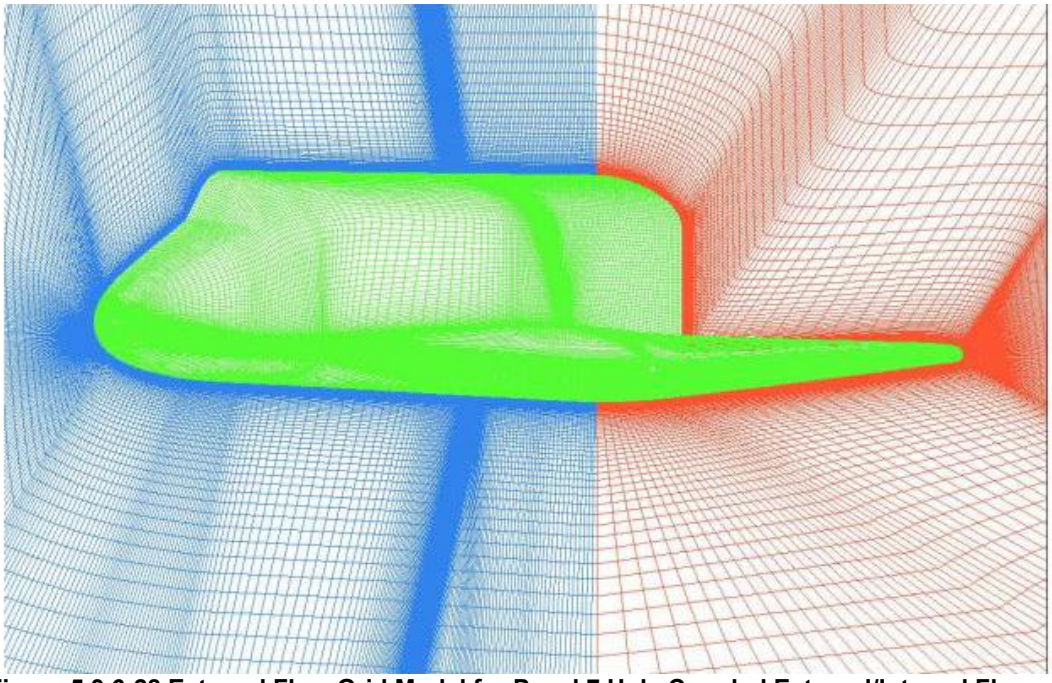

Figure 5.3.6-28 External Flow Grid Model for Panel 7 Hole Coupled External/Internal Flow Simulation II

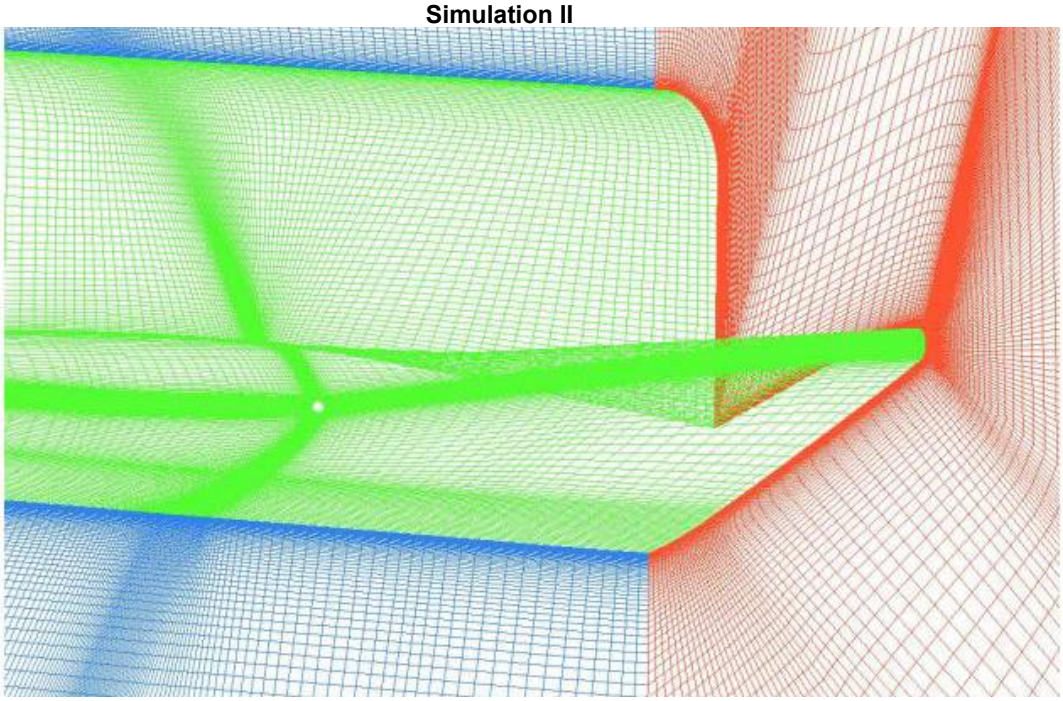

Figure 5.3.6-29 External Flow Grid Model for Panel 7 Hole Coupled External/Internal Flow Simulation II

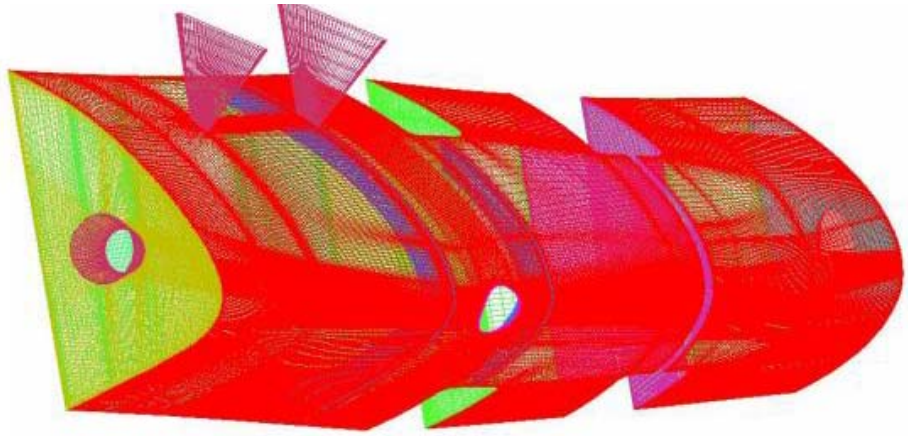

Figure 5.3.6-30 Internal Flow Grid Model for Panel 7 Hole Coupled External/Internal Flow Simulation II

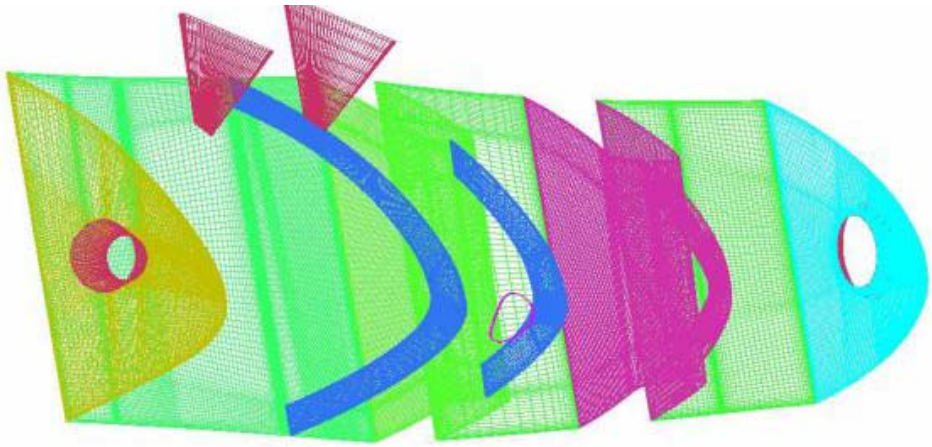

Figure 5.3.6-31 Internal Flow Grid Model for Panel 7 Hole Coupled External/Internal Flow Simulation II

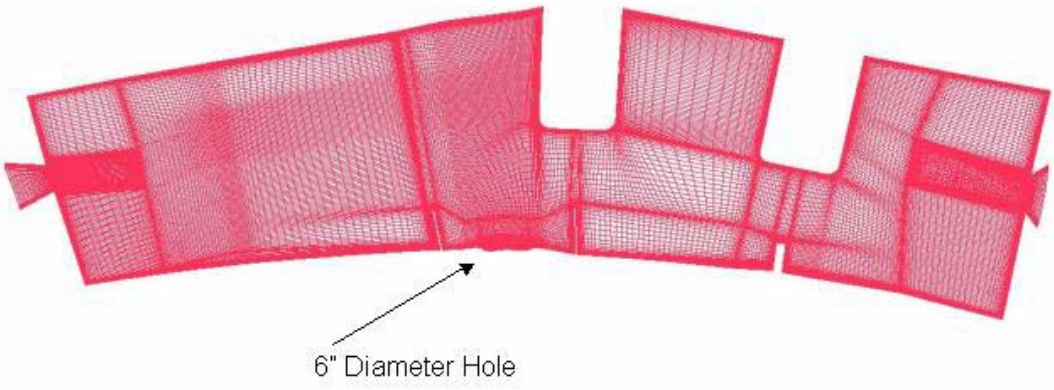

Figure 5.3.6-32 Internal Flow Grid Model for Panel 7 Hole Coupled External/Internal Flow Simulation II

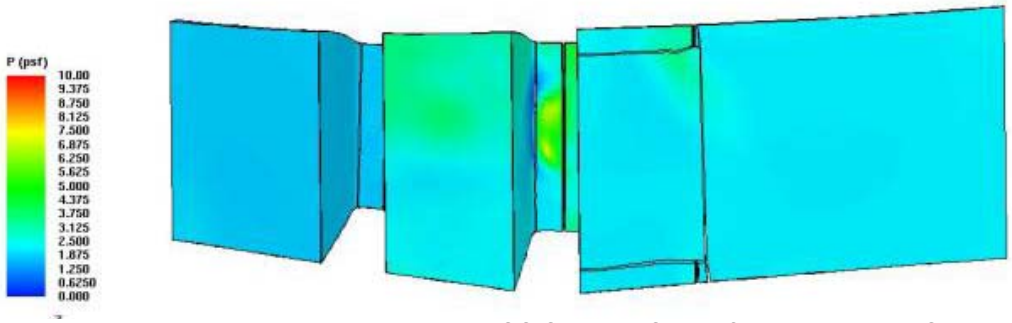

Figure 5.3.6-33 Pressure Distribution on RCC Channel Cavity for Panel 7 Hole Coupled External/Internal Flow Simulation II

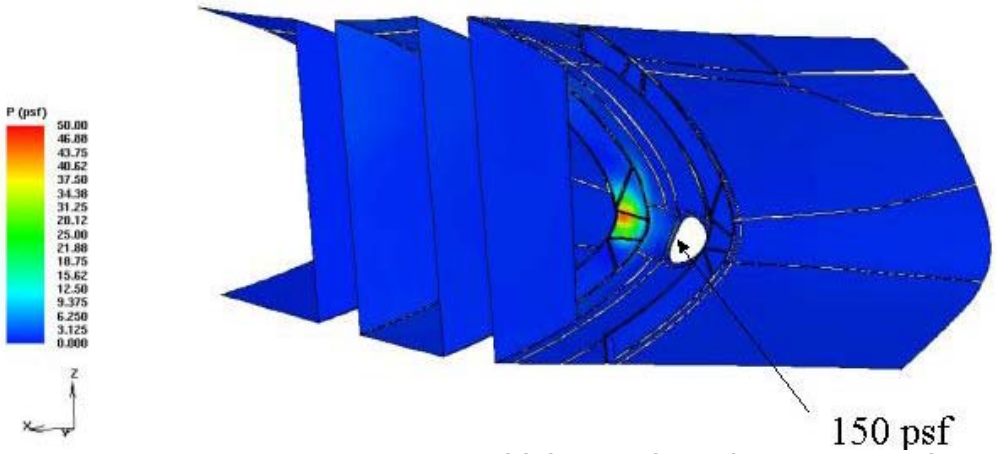

Figure 5.3.6-34 Pressure Distribution on RCC Channel Cavity for Panel 7 Hole Coupled External/Internal Flow Simulation II

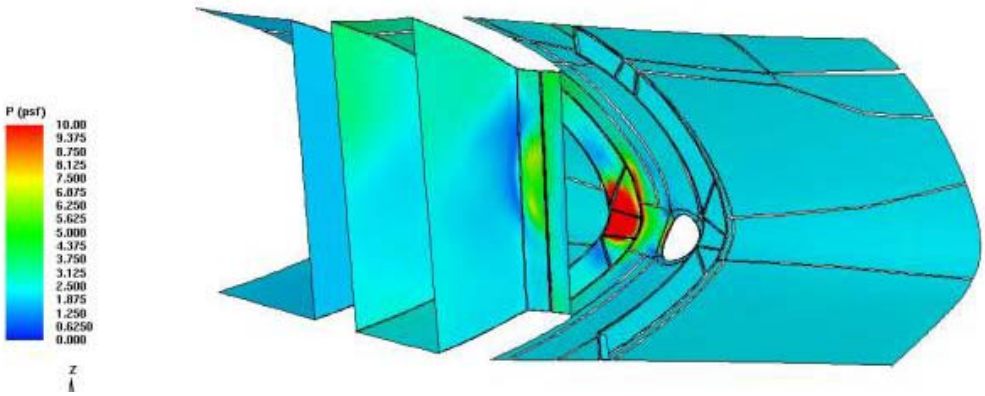

Figure 5.3.6-35 Pressure Distribution on RCC Channel Cavity for Panel 7 Hole Coupled External/Internal Flow Simulation II

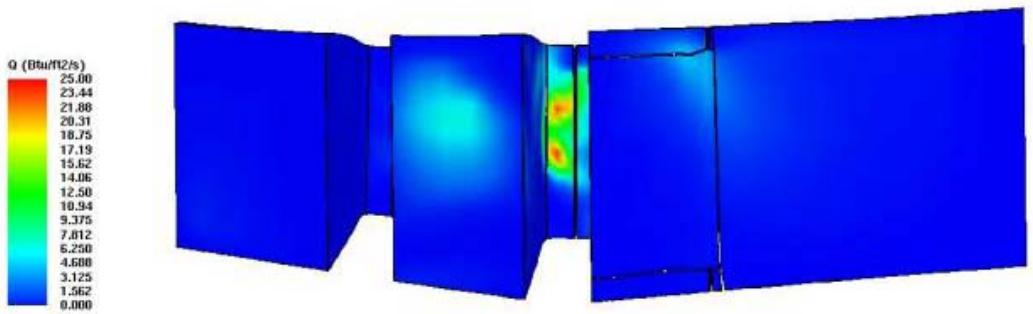

Figure 5.3.6-36 Heating Distribution on RCC Channel Cavity for Panel 7 Hole Coupled External/Internal Flow Simulation II

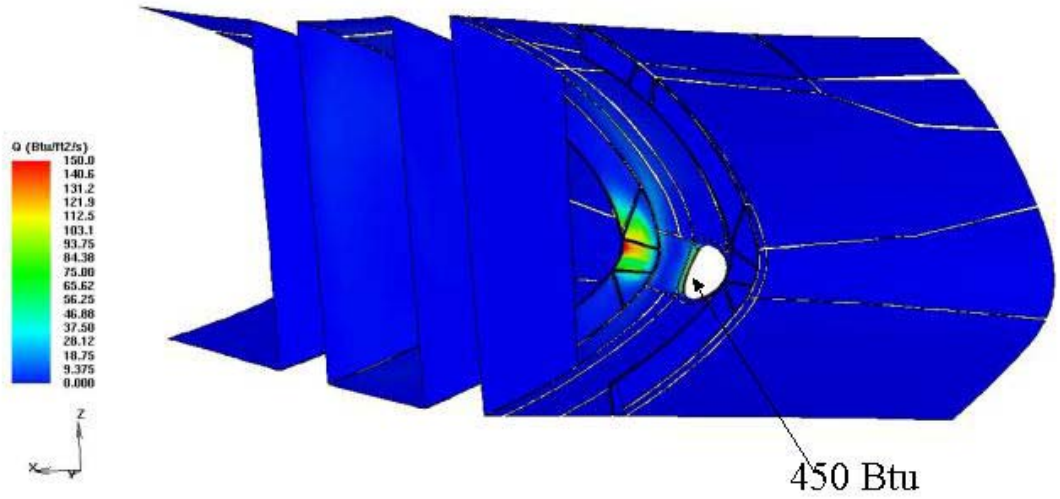

Figure 5.3.6-37 Heating Distribution on RCC Channel Cavity for Panel 7 Hole Coupled External/Internal Flow Simulation II

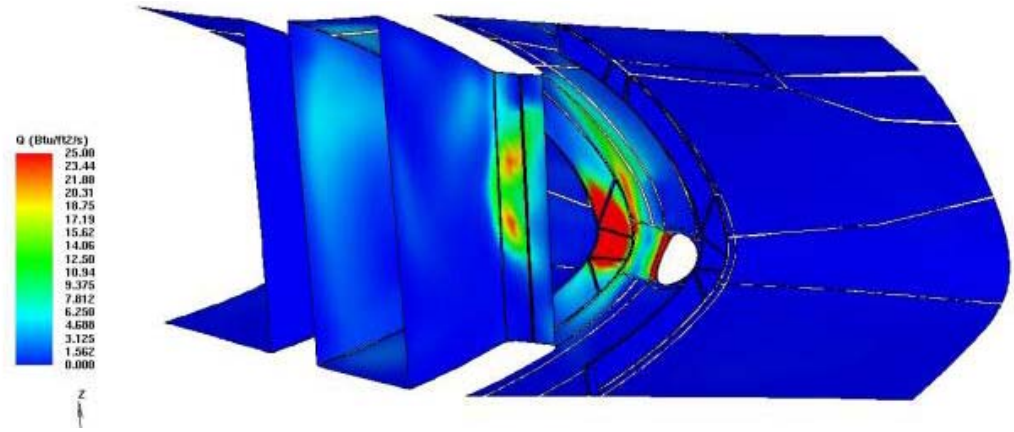

Figure 5.3.6-38 Heating Distribution on RCC Channel Cavity for Panel 7 Hole Coupled External/Internal Flow Simulation II

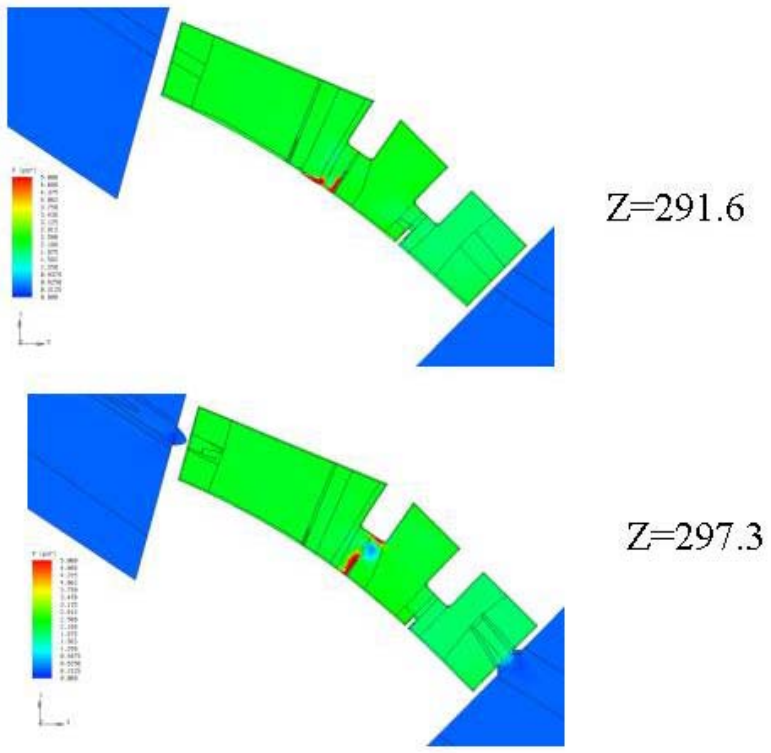

Figure 5.3.6-39 Pressure Contours in flow field for Panel 7 Hole Coupled External/Internal Flow Simulation II

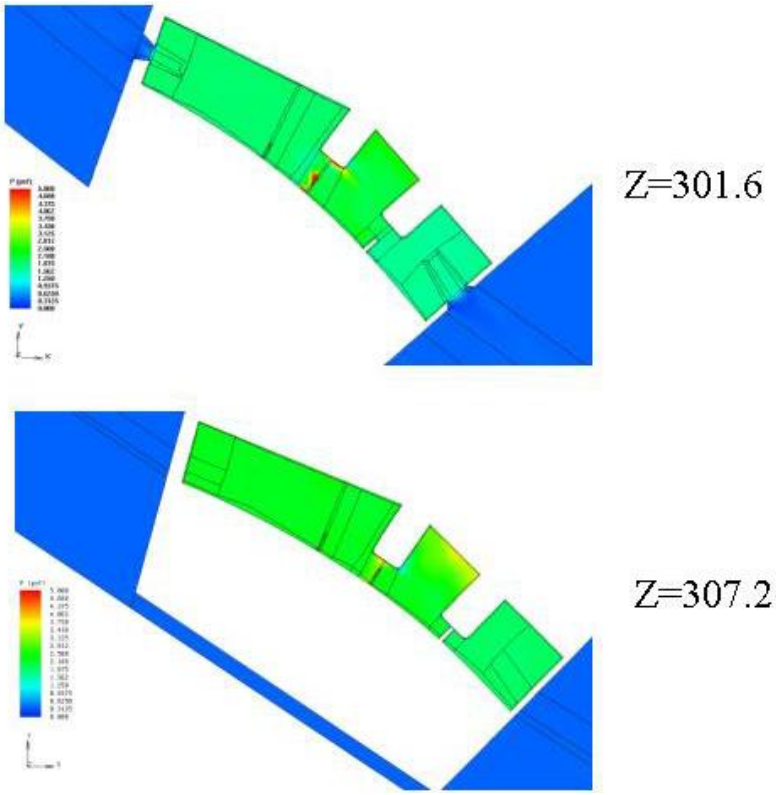

Figure 5.3.6-40 Pressure Contours in flow field for Panel 7 Hole Coupled External/Internal Flow Simulation II

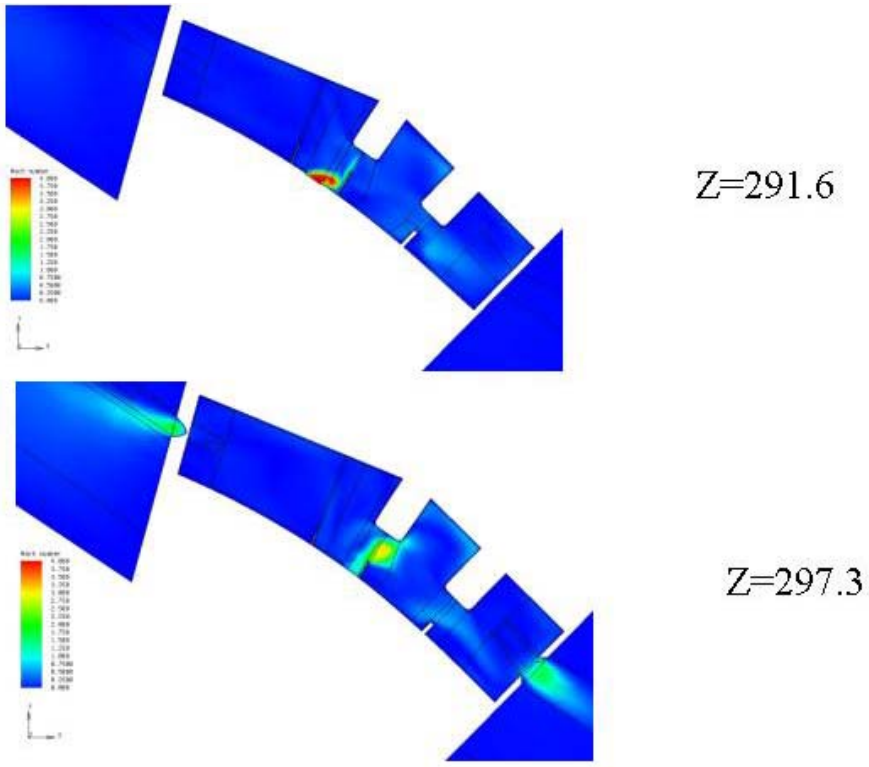

Figure 5.3.6-41 Mach Contours in flow field for Panel 7 Hole Coupled External/Internal Flow Simulation II

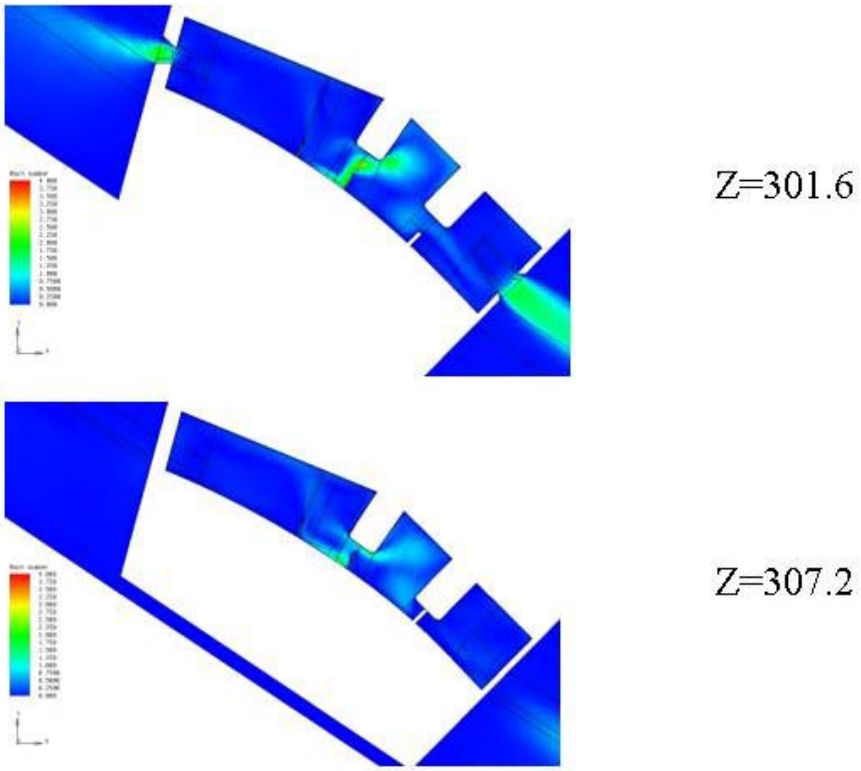

Figure 5.3.6-42 Mach Contours in flow field for Panel 7 Hole Coupled External/Internal Flow Simulation II

5.3.6.1.3 RCC Panel 8 10" - Boeing Rocketdyne

5.3.6.1.3.1 Case Description

The objective of this analysis was to compute convective heating rates on the Leading Edge Structural Subsystem (LESS) cavity internal surfaces. The intended application of the data was to enhance the engineering heat transfer models and to improve understanding of this flow field structure.

A 10 inch diameter hole was located at coordinates X=1066.00, Y=-214.75, Z=234.6 as shown in Figure 5.3.6-43. Also shown is a jet penetration analysis by NASA JSC based on a NASA LaRC LAURA external flow solution. This indicates that impingement will occur on the inboard side of the RCC 8/9 spanner beam insulators (earmuffs) given a hole at this location. These results were used as a guide for grid clustering in this analysis.

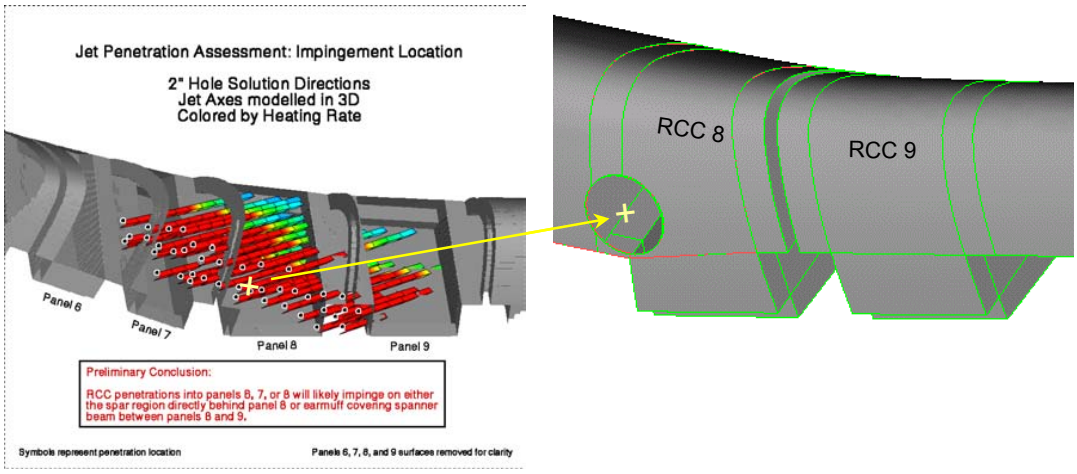

Figure 5.3.6-43 - 10 inch Hole Location Compared to Jet Penetration Analysis

5.3.6.1.3.2 *Grid/Solution Development*

The JSC model mentioned above was selected as the internal surface geometry for this analysis. This model had the benefits of possessing the RCC 7/8, 8/9, 9/10 earmuffs and the forward spar insulators (hot tubs) in between them. The hot tubs had been specifically requested for this analysis, while all three earmuffs were deemed desirable based on the anticipated flow field in this region. The negative aspects were that all of the edges are sharp, which conflicted with other models and photographs. Dimensions of key components, such as the earmuffs and hot tubs, were also somewhat uncertain since the JSC dimensions conflicted with a model used by Boeing Huntington Beach and some photographs. Due to time constraints however, the JSC model was employed while a more accurate model of the LESS was started using the Pro/Engineer CAD system. Extruded "dump" regions were added on either side of RCC 8 and 9 to enable the application of constant pressure outflow boundary conditions. The dimensions of these regions were based on the results of the 2-D T-Seal analysis (Section 5.3.6.2.2). Previous analyses had shown that a high degree of coupling existed between the internal and external flow fields. For a hole of this size, the external flow is capable of negotiating the opening while remaining supersonic. The LAURA external solution was used to provide the necessary coupling, but only a small two-zone (37 and 38) portion of it. This was carefully selected to reduce the size of the model while preserving the external solution in the region of interest (Figure 5.3.6-44).

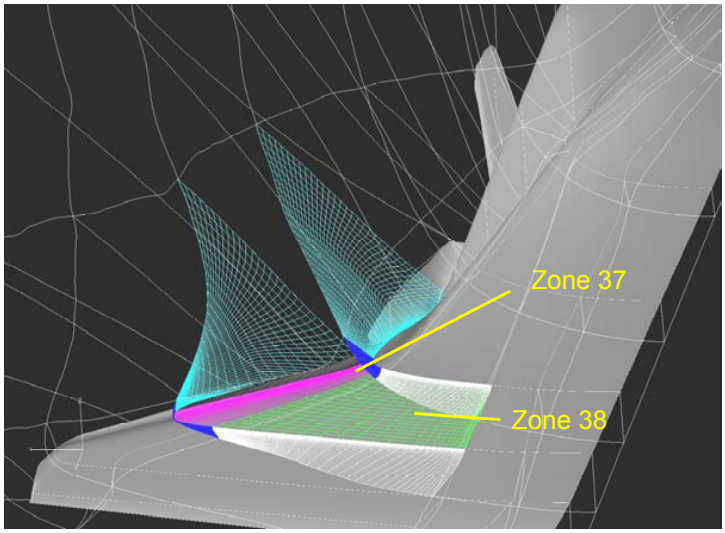

Figure 5.3.6-44 - LAURA Solution Zones Used as External Domain

The Boeing APPT system was used to generate the hybrid viscous unstructured computational grid. The unstructured approach greatly reduces the time required to generate the grid and eliminates wasted clustering cells in complex internal regions. After a number of revisions, final grids (Figure 5.3.6-45) were produced containing 4.1M elements with a wall spacing of $1.0e^{-4}$ inches (medium grid), and 4.9M elements with a wall spacing of $1.0e^{-5}$ inches (fine grid). The solutions were obtained using the Boeing ICAT code. Fully laminar flow was assumed based on the extremely low Reynolds numbers present. Liu-Vinokur equilibrium air thermochemistry and Tannehill transport properties were used. The convergence criteria were to drive net fluxes to an initial steady-state and also to drive integrated heat load in key areas to steady-state. Contours of heat flux in key areas were also plotted at different time steps.

The CFD Condition 1 trajectory point was used to define the freestream conditions. All wall temperatures were set to 3,000ºR. This corresponds to the melting temperature for the Inconel 601 outer layer of the Dynaflex surfaces such as the earmuffs and hot tubs. The pressures on the cavity outflow surfaces were established from the venting analysis (Section 5.3.5) and are presented in Table 5.3.6.1-1.

Cavity Outflow Pressure					
Cp	P/Pinf	*psf*	*psia*	*N/m^2 (Pa)*	
0.188	82.198	4.177	0.0290	200	Boeing Huntington Beach RCC7 6 inch hole
0.567	246.593	12.531	0.0870	600	This analysis

Table 5.3.6.1-1 – RCC Cavity Outflow Boundary Pressure

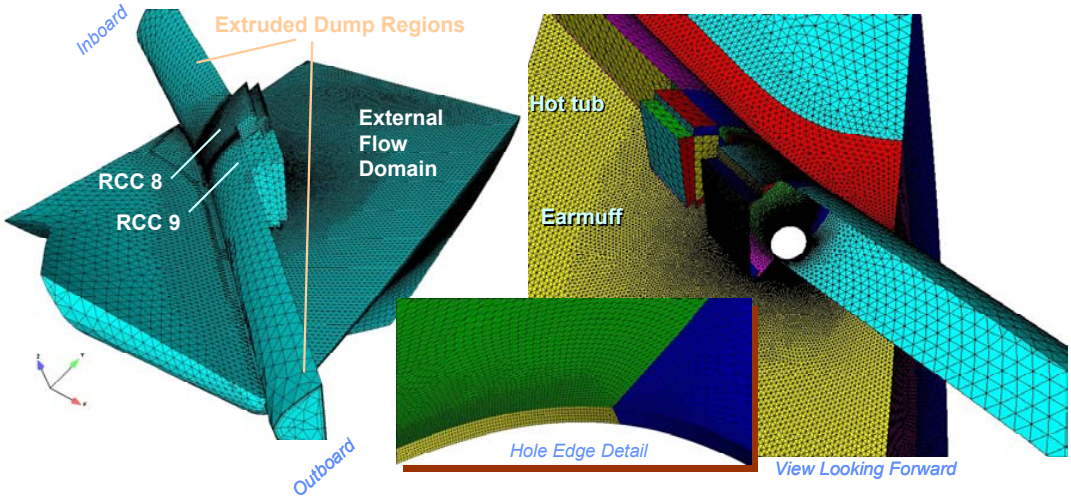

Figure 5.3.6-45 - Hybrid Viscous Unstructured Grid

5.3.6.1.3.3 Results

Major flow-structure comments

Figure 5.3.6-46 shows the flow inside the LESS cavity. The walls are colored by static pressure and the streamtubes are colored by Mach number. The primary jet issuing from the hole impinges on the inboard side of the RCC 8/9 earmuff. The jet makes a near constant-pressure turn (as observed by the small change in Mach number) and splits into two supersonic tails. This behavior was consistently observed in the T-Seal 2-D solutions (Section 5.3.6.2.2). The weaker tail (#2) impinges in upper corner of hot tub, while the stronger tail (#1) impinges in lower corner of hot tub. The latter impingement creates a transonic "re-tail" that impingements on RCC 7/8 earmuff outboard surface then shocks down to subsonic conditions. Entrainment of a subsonic vortex by the primary jet creates small supersonic impingement on RCC 8 rib. These features account for all of the supersonic flow inside the LESS cavity, and hence all of the high pressure and heat flux areas. Once subsonic, the flow twists into complex vortical patterns and makes its way to the outflow boundaries.

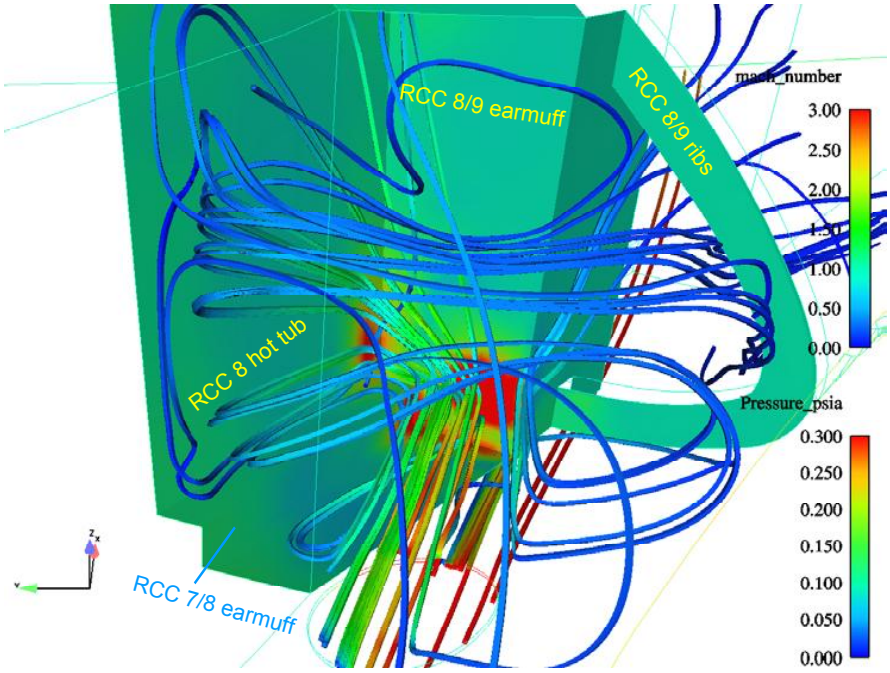

Figure 5.3.6-46 – Mach-colored Streamtubes and Wall Static Pressure Viewed from in Front of Leading Edge

Figure 5.3.6-47 shows static pressure on the walls and Mach number on a cutting plane. The cutting plane includes the internal and external flow fields. The external flow captured by the hole includes all of the wing boundary layer and some of the local freestream. Recall that the local freestream has been processed through the vehicle shock envelope that is oblique in this area. The captured flow expands through a 10° turn into the hole and forms the primary jet. The jet expansion is small internally since the pressure ratio due to the turn is only about 1.9. The primary jet then encounters a near-normal (80°) impingement onto the RCC 8/9 earmuff. The resulting stagnation pressure exceeds freestream-normal shock pressure due to recompression by oblique vehicle shock. Supersonic tail #2 is observed moving vertically along the earmuff.

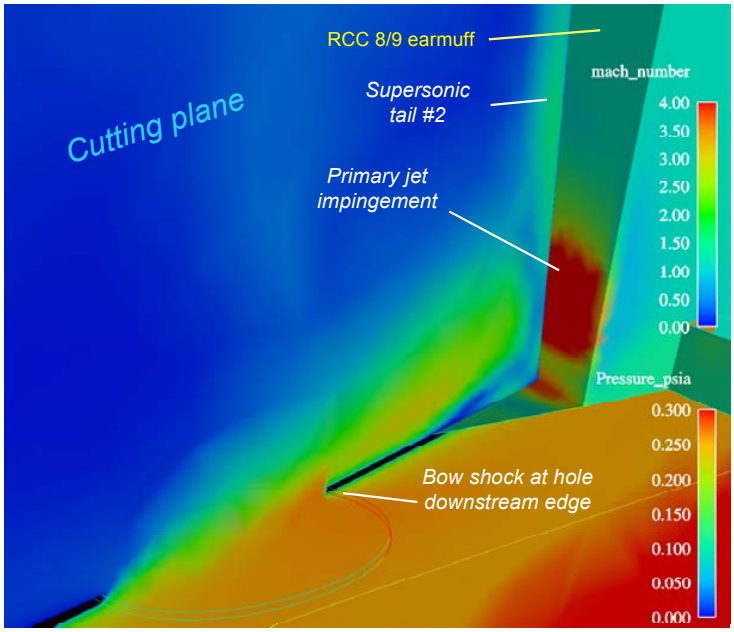

Figure 5.3.6-47 - Mach-colored Cutting Plane and Wall Static Pressure Detail View From in Front of Leading Edge

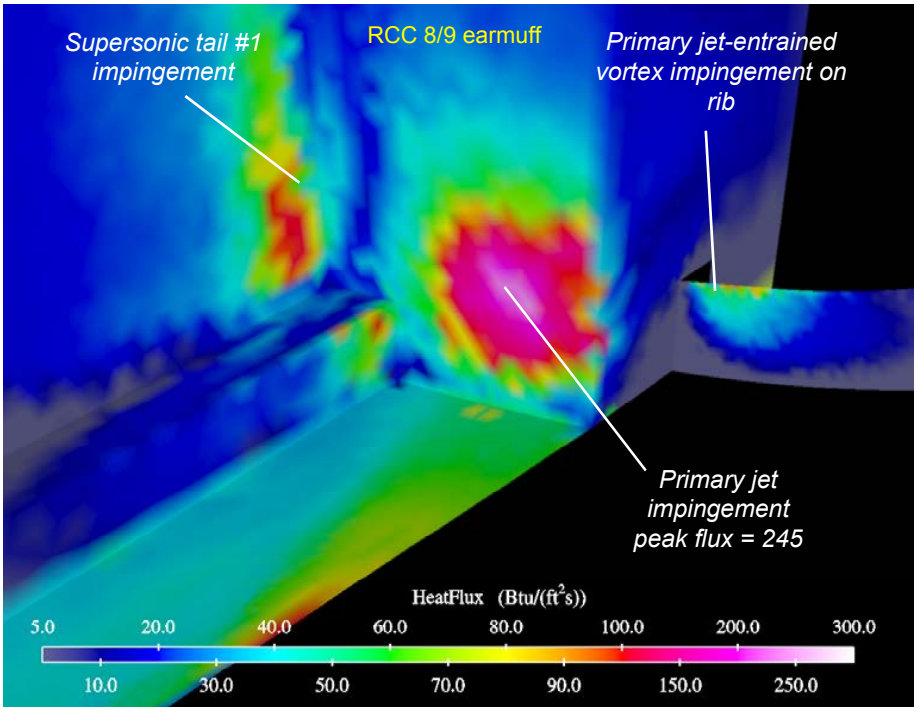

Figure 5.3.6-48 – Surface Heat Flux Detail View From in Front of Leading Edge – Medium Grid Solution

Surface heating and pressure comments

Figure 5.3.6-48 shows surface heat flux for the medium grid solution in the region where the RCC 8/9 earmuff and the RCC 8 hot tub intersect. This is the area of highest heating, as would be expected based on the pressure and Mach fields observed. The primary jet impingement produces the highest heating, while supersonic tail #1 produces the second highest. The tail flow has lost some total pressure due to shock waves encountered in the turning process that created it (Figure 5.3.6-48) so its stagnation pressure

and heat flux are lower. The RCC 8 rib encounters some heating do to the impingement of vortical flow that was reaccelerated to supersonic velocity via entrainment in the primary jet. Flow field animations were used to reveal this phenomenon as the source of that heating.

The fine grid solution is shown in Figure 5.3.6-49. The peak heat flux is 14% lower, however this occurs at a single surface cell. The integrated heat load in the regions of interest differs by only 2.3% with the fine grid solution having the lower value. Based on the proximity of these results, grid independence can be claimed. The medium grid solution was run a total of 30,000 time steps, while the fine grid solution was run a total of 32,000 time steps. Both were monitored periodically using flow visualization. No indication of unsteady flow was found, however there is still a possibility that this could occur. Many more time steps would be needed to be certain.

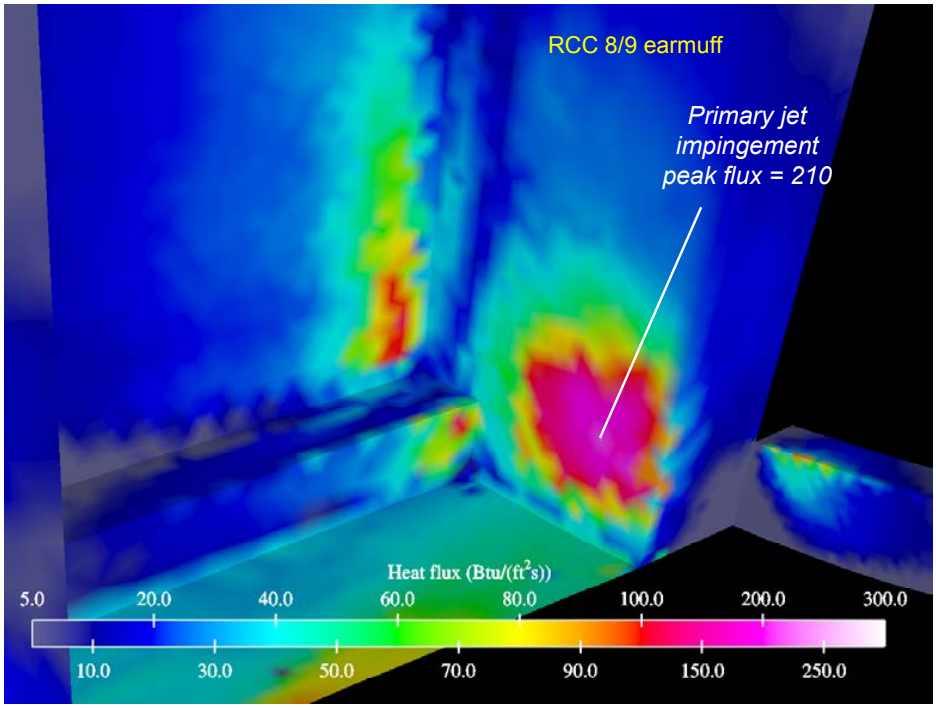

Figure 5.3.6-49 – Surface Heat Flux Detail View From in Front of Leading Edge – Fire Grid Solution

An equilibrium thermochemistry model was employed for computational efficiency based on the historical equivalence of surface heat flux from solutions using equilibrium air and those using finite-rate chemistry with a fully catalytic wall. The Dynaflex material covering the earmuff and hot tub surfaces has a 0.004" thick Inconel 601 foil. Figure 5.3.6-50 from Goulard shows that metals are highly catalytic under these conditions. The actual catalycity of the Inconel 601 and underlying materials under these conditions is not known at this time, however. Actual heat fluxes can range from 25%-80% less than the fully catalytic value if the materials have a lower catalycity.

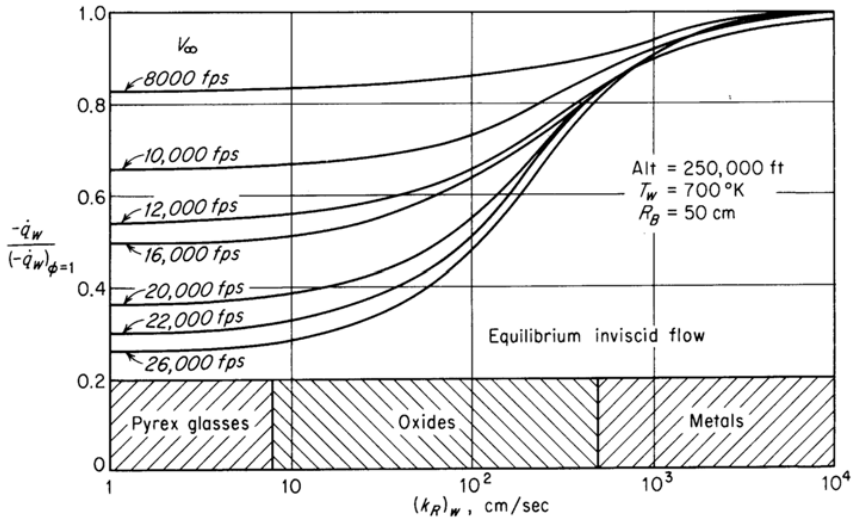

Figure 5.3.6-50 - Effect of Wall Material on Heat Flux (Goulard)

5.3.6.1.4 LaRC Solutions of Various Hole Size and Locations

The Langley Aerothermodynamic Upwind Relaxation Algorithm (LAURA) [NASA TM 4674, NASA TP 2867] was applied to external and internal flow simulations for the Columbia investigation. LAURA is a high fidelity analysis tool, specialized for hypersonic re-entry physics, utilizing state-of-art algorithms for computational fluid dynamic (CFD) simulations. Previous simulations of STS 1,2 and 5 with LAURA to resolve questions of a pitching moment anomaly (STS 1) and to validate heating predictions were published in the AIAA Journal of Spacecraft and Rockets in 1994 [JSR Vol. 31 No. 3]. All of the current simulations specify laminar flow of air in chemical nonequilibrium (N, O, N_2, O_2, NO) and thermal equilibrium. Only CFD point 1 is simulated with freestream conditions: V_∞ = 24,116 fps (7350.6 m/s), ρ_∞ = 7.5681 x 10^{-8} slugs/ft^3 (3.9005 x 10^{-5} kg/m^3), T_∞ = 391.2° R (217.3 K), α = 40.1681 deg., and time = 13.50.53.0 GMT. The external flow simulations are implemented on the shared, baseline grid developed for the External Environments Team. The baseline grid is modified to allow coupling of the external flow with flow through a breach in the wing entering a vented cavity.

The simulations described in this section were generated relatively quickly and early in the investigation on the NAS Cray SV1 because simplifications were made to the leading edge cavity geometry. These simplifications enabled (1) a very quick grid generation procedure; and (2) high fidelity corroboration of jet physics with internal surface impingements ensuing from a breach through the leading edge, fully coupled to the external shock layer flow at flight conditions.

5.3.6.1.4.1 Holes in Panel 6

The following material is the first application of LAURA to flow in a vented cavity. Consequently, geometric complexity was incrementally added to better understand ensuing flow physics and effects of boundary condition specification.

Initially, quarter inch deep holes with varying diameters were inserted into the baseline, external flow solution at Panel 6. (See Figure 5.3.6-51.) The boundary condition at the bottom of the hole used a zero-order extrapolation from interior points for density and velocity and a specified reservoir pressure equal to

2 p_∞ (approximately 0.1 psf). The flow through this boundary evolved to be substantially supersonic for hole-sizes greater than two inches. The vent backpressure is sufficiently low to maintain at least sonic conditions through the vent and is characteristic of leeside levels.

The two-inch-hole simulation was then expanded to include an internal cavity extruded from the backside of panel 6. The cavity was roughly 1ft x 1ft x 1ft but its shape evolved from an ad-hoc grid generation process. A two-inch vent hole was included at the far end of the cavity. Flow through the breach is fully coupled to the external flow and the vent boundary condition was transferred to its new location.

Methodology
An in-house utility to insert structured grids defining Reaction Control System (RCS) jets through the outer mold lines (OML) of hypersonic vehicles was modified to define a quarter-inch deep, circular hole through the leading edge of shuttle orbiter wing. The modified surface grid blends smoothly with the baseline external grid as shown in Figure 5.3.6-52. A detail of the surface grid defining the hole is shown in Figure 5.3.6-53.

Taking the inserted, rectangular domain surrounding the breach shown in Figure 5.3.6-52 and creating a quarter-inch offset orthogonal to the OML produced the near wall of the cavity. This surface was extruded into the interior in a direction defined by the axis of the hole. An initial cell size taken from the external flow domain was applied. A constant growth factor (1.20) grows the grid off the wall for 32 cells and then an inverse factor is applied for another 32 cells to resolve a boundary layer on the opposite wall. Sidewall boundary-layer resolution is achieved with a similar procedure in which additional points are added in directions defined by an extrapolated coordinate line. A view of this extruded cavity is shown in Figure 5.3.6-54.

Immediate vent (No internal cavity)
These simulations provided early evidence that the flow through a two-inch diameter (or larger) breach entered the cavity with significant retention of external flow directionality. A normal jet into the cavity was not an appropriate model for these conditions at CFD Point 1 (Mach 24). The breach diameters were of the same order or larger than the local, external boundary-layer thickness. High impingement heating and pressures on the downstream lip of the breach are computed. It is likely that hole shape would evolve as a slot cut in the direction of the external streamlines as shown in Figure 5.3.6-51. In the case of the six-inch diameter breach the boundary layer is fully ingested. Summary of results follow.

Two-inch hole
The contour plot of total enthalpy in Figure 5.3.6-55 shows the boundary edge as the transition from orange to red color. The total enthalpy above the boundary layer edge, outside of viscous dissipation effects, is a constant. The boundary layer thickness is roughly ¾ of the hole diameter. The pressure field and streamlines entering the breach (Figure 5.3.6-56) indicate significant retention of streamwise momentum after processing by a Prandtl-Meyer expansion emanating from the sonic line in the boundary layer. Surface heating rates exceed 264 Btu/ft^2-sec (300 W/cm^2) (Figure 5.3.6-57) and surface temperatures approach 5400° R (3000 K) (Figure 5.3.6-58) at the downstream lip of the breach where impingement is strongest. Ingested mass and energy rates are 0.00152 lb_m/s (0.000689 kg/s) and 9.4 Btu/s (9.92 kW), respectively. Boundary conditions (radiative equilibrium, finite catalytic wall) and examination of near surface grid quality (Re_{cell} of order 10 at impingement) suggest this heating rate is a lower bound. More data on grid convergence tests will be provided in the Panel 8 results to follow.

Four-inch hole
The contour plot of total enthalpy in Figure 5.3.6-59 is repeated for the four-inch diameter hole. The boundary layer edge impinges on the downstream lip. The pressure field and streamlines entering the breach (Figure 5.3.6-60) indicate even more retention of streamwise momentum as compared to the previous case for the smaller hole. Surface heating rates again exceed 264 Btu/ft^2-sec (300 W/cm^2) (Figure 5.3.6-61) and surface temperatures exceed 5400° R (3000 K) (Figure 5.3.6-62) at the downstream lip of the breach where impingement is strongest. Ingested mass and energy rates are 0.00562 lb_m/s (0.00255 kg/s) and 43.6 Btu/s (46 kW), respectively.

Six-inch hole
The contour plot of total enthalpy in Figure 5.3.6-63 is repeated for the six-inch diameter hole. The boundary layer edge and some inviscid flow at the maximum freestream total enthalpy above it are

completely ingested. The lip is impacted by streamlines carrying the total freestream enthalpy and a relatively large total pressure. The pressure field and streamlines entering the breach (Figure 5.3.6-64) show the same trends for retention of streamwise momentum as compared to the previous case for the four-inch hole. Surface heating rates again exceed 264 Btu/ft^2-sec (300 W/cm^2) (Figure 5.3.6-65) and surface temperatures exceed 5400° R (3000 K) (Figure 5.3.6-66) at the downstream lip of the breach where impingement is strongest. Of the three hole sizes, the present case should exhibit the largest heating because it is seeing undissipated flow from above the boundary layer edge. Ingested mass and energy rates are 0.0125 lb_m/s (0.00566 kg/s) and 111 Btu/s (117 kW), respectively.

Vented internal box

These simulations allowed the jet to develop naturally within the cavity and to view initial impingement and deflections of flow to other surfaces. Jet orientation is a strong function of hole depth to diameter ratio. Summary of results follow.

Two-inch hole to vented box

Figure 5.3.6-67 shows streamlines entering the breach and the ensuing reflected wave pattern producing compressions and expansions in the jet core. The jet is non-orthogonal to the back plane of the breach. It has a significant directional component defined by the external flow direction. An expansion off the upstream side of the hole overtakes a shock off the downstream side of the hole. The shock forms in response to supersonic flow from the upper portion of the boundary layer and the boundary layer edge impinging on the downstream lip. The Mach number distribution in Figure 5.3.6-68 provides additional detail of the jet entering the cavity. A sonic line sets up behind the inner edge of the breach lip shock indicating a choked condition. The interesting feature here is that the sonic line does not span the back plane of the hole but rather spans a smaller area defined by convergence of the streamlines entering from the circular border. Pressure coefficients in Figure 5.3.6-69 indicate the ambient pressure level in the cavity of approximately (1/8) $\rho_\infty V_\infty^2$. This level is attained at the back plane of the hole. The dependence of cavity ambient pressure on vent hole size has not been explored. It is interesting to note that a specification of the vent pressure immediately behind the back plane of the hole results in approximately the same ambient pressure level in the cell preceding the outflow boundary. Pressures exceeding the external pressure of approximately (1/2) $\rho_\infty V_\infty^2$ (C_p = 1) would effectively block ingestion of external flow.

The temperature in the shock over the downstream lip approaches 14,400° R (8000 K) in Figure 5.3.6-70. The corresponding total enthalpy profile is shown in Figure 5.3.6-71 that corresponds to the earlier result in Figure 5.3.6-55 except now the cavity beneath the hole is included. Conditions just below the boundary layer edge impact the lip to drive the large surface heating rates and surface temperatures (Figure 5.3.6-72). The impingement heating on the edge will tend to cut a slot along the surface in the external streamline direction.

The oxygen content of ingested flow is almost fully dissociated as indicated in Figure 5.3.6-73. A strong catalytic heating effect would be expected on metallic cavity walls but the finite catalytic boundary condition on the external surfaces was continued into the cavity. Also, the radiative equilibrium wall boundary condition assumes cavity walls can radiate to free space whereas the actual closed environment would restrict radiative cooling. Conductive cooling through metallic walls is not considered. Given these conditions (expected to produce lower heating rates) the surface temperatures on the cavity walls (Figure 5.3.6-74) exceed the melting point of pure aluminum at the impingement zone. Note that the breach hole through the lower surface is not visible in this figure. The vent hole on the top surface still sees temperatures that would melt aluminum.

Quarter-inch hole to vented box

A quarter-inch diameter hole was simulated to provide reference conditions in which the hole diameter was not larger than the hole depth and all hole dimensions were smaller than the local boundary layer thickness. In this case, the jet develops in an orthogonal direction to the wall as seen in the Mach number contour of Figure 5.3.6-75. Impingement heating and temperatures on the downstream lip are much more benign (Figure 5.3.6-76) because the energy content and total pressure of the impinging streamlines emerging from deep within the boundary layer is significantly dissipated. Temperatures entering the cavity (Figure 5.3.6-77) exceed 1800° R (1000 K).

5.3.6.1.4.2 Ten-inch Hole in Panel 8

These simulations were initiated in mid-May to complement ongoing simulation work on higher fidelity internal grids and to insure that sufficient corroborating data for engineering analyses could be made available as quickly as possible. However, greater fidelity to the internal geometry was requested (as compared to the ad-hoc cavity) so that jet development lengths and splash to adjoining internal surfaces may be better simulated.

A simulation plan was developed to maximize productivity in the limited, remaining time. First, the simulation of a ten-inch hole in Panel 8 into the ad-hoc cavity as described in the previous section was produced. (The grid in this case had to be post-processed by the VGM utility to compensate for problems associated with the larger ratio of local effective radius to hole diameter.) This simple simulation would next be used to initialize the cavity flow in a more realistic "chunnel" geometry generated concurrently. A grid sequencing process is used to complete the simulation and significant sharpening of the jet was observed in the transition from moderate to fine grid. When the jet boundaries sharpened, it was noted that the impingement location was under-resolved. An additional grid-processing step was required to bring a factor ten finer resolution on the wall at impingement.

The chunnel geometry was built off of the ad-hoc cavity and expanded to include the domain behind panels 7-9. The back plane was defined by the actual spar location. Two vent slots with combined area of 66 in^2 were included on the leeside, back surface. An internal core system of blocks was approximately bounded by the inner extent of ribs at the panel interfaces to accommodate possible future extensions of internal complexity. A combination of an O- and C- grid topology was used to accommodate the complex internal structure. The C-grid provides the ability to capture the rib and spar geometry while offering a decoupling of the grid requirements for stretching and clustering at the internal wall surfaces. As shown in Figure 5.3.6-78 and Figure 5.3.6-79, the C-grid easily captures the necessary chunnel features. Within the C-grid, in the bottom block, the hole in the RCC is accommodated by simply replacing the block of the C-grid with an "embedded" O-grid, which enables accurate modeling of the flow entering the chunnel. The O- and C-grid junction enables the accurate modeling of the existing geometry while offering the expandability to increasing geometric complexity without restructuring and regenerating the entire chunnel volume grid.

In the final simulation, the top vents were closed and the side core vents (combined area 79.3 in^2) were opened to enable the splash from an impinging jet to spill over a rib and through a vent. Summary of results follow.

Vented internal box

Mach number and streamlines entering the box through the ten-inch hole in panel 8 are shown in Figure 5.3.6-80. Streamlines exit a ten-inch diameter vent at the top of the box. The flow is strongly supersonic entering this cavity. The most interesting details of this simulation (that remain true for the subsequent chunnel simulations) are the high temperatures and pressures in the shock layer over the downstream lip of the hole. The high temperature (approaching 21,600° R (12000 K) in Figure 5.3.6-81) is easily explained because the lip is bathed in flow that carries the full freestream total enthalpy. The local pressure coefficient (C_p = 10) is higher than the stagnation point because the local streamlines here were processed by an oblique shock so that total pressure losses are less than those experienced in crossing a normal shock. Computed heating rates exceed 704 Btu/ft^2-sec (800 W/cm^2) in this case. When considering the factor of increase in pressure and factor decrease of local radius of curvature relative to the stagnation point one may expect this rate (ignoring ablative cooling) is a lower bound.

Chunnel with slotted leeside vents

Results in this section discuss the solution after adaptation of the finest grid to concentrate more mesh to the jet impingement point. Error norms had dropped to order 0.4 (a five to six order of magnitude decrease from the initial solution off the coarse grid). Some unsteadiness is evident when monitoring the solution but there was insufficient time to gather meaningful statistics on frequency. The jet impingement point has moved very little over about 10000 relaxation steps and it is believed that the basic flow physics presented here are correct.

Details of the jet in the cutting plane through the chunnel are presented in Figure 5.3.6-82 (total enthalpy), Figure 5.3.6-83 (Mach number), and Figure 5.3.6-84 (temperature). A tongue of high enthalpy flow persists up to the impingement point. A high temperature shock layer forms above this location. The jet initially scrapes the surface and then rises above it.

A "strip" of high pressure (Figure 5.3.6-85) and high heating rate (Figure 5.3.6-86) is evident at the relatively narrow impingement location. These figures show the sharpening of the profile associated with refinement from the medium grid to the fine grid (a factor of 2 in the i, j, and k directions). Review of solution metrics at the impingement showed high cell Reynolds number and large jump between imposed wall temperature (900° R (500 K)) and boundary cell center temperature (5184° R (2880 K)). Consequently, a grid adaptation was implemented to provide a target factor of 10 finer grid at the wall (i-direction) using a greater stretching factor for the same number of cells in the near wall blocks. Even with this refinement, the worst-case cell center temperature next to the wall was (2088° R (1160 K)). The convergence of peak impingement heating on these three sequential cases (not located at exactly the same surface mesh point) progressed from 102 Btu/ft^2-sec (116 W/cm^2) (medium grid) to 265 Btu/ft^2-sec (301 W/cm^2) (fine grid) to 635 Btu/ft^2-sec (721 W/cm^2) (adapted fine grid, Figure 5.3.6-87).

Chunnel with side vents

This side vent case (top vents now closed) was initialized from the previous top vent case with the finest grid and adaptation of grid on the impingement boundary.

The error norm for this case jumped about 4 orders of magnitude from the previous converged solution and returned to order 1 values at this "snapshot". An attempt to force the solution to advance more quickly with a constant, large time step eventually diverged. A smaller constant time step was again applied and the solution began to recover but insufficient time remained to drive it to convergence. The solution posted here is thought to have a jet impingement point that will continue to rise toward the side vent. The magnitude of jet oscillations cannot be estimated from the solution generated to date. A representative jet structure is presented in Figure 5.3.6-88 (total enthalpy) and Figure 5.3.6-89 (pressure). The basic structure is very similar to that observed in the previous case. The expansion process to sonic conditions at the side vent is displayed in Figure 5.3.6-90 (pressure) and Figure 5.3.6-91 (Mach number) in the impingement zone.

Top vent versus side vent internal surface pressures are compared in Figure 5.3.6-92. The equivalent heating comparison is presented in Figure 5.3.6-93 and Figure 5.3.6-94. Heating at impingement on the finest grid has remained between 440 and 616 Btu/ft^2-sec (500 and 700 W/cm^2).

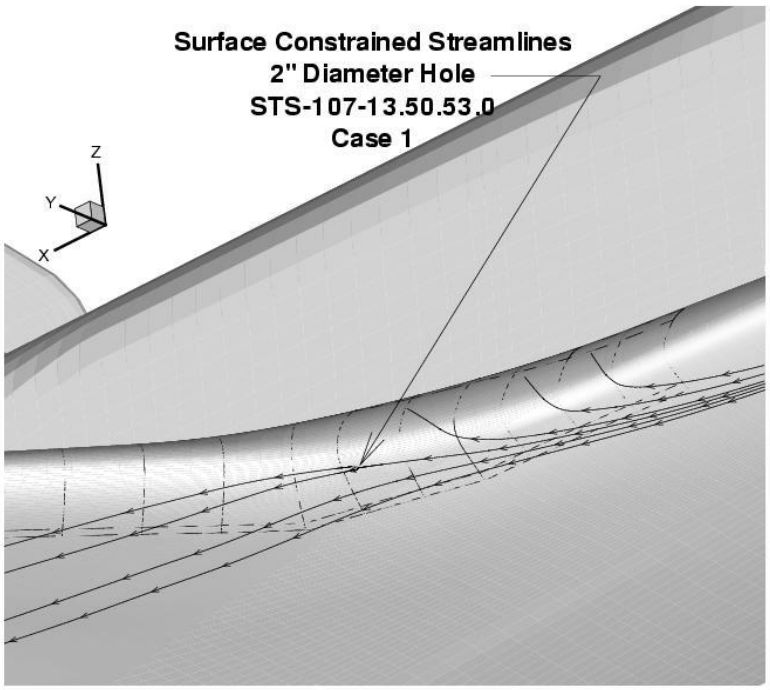

Figure 5.3.6-51 Streamlines over RCC panels on the leading edge and the location of the circular breach through the wing in panel 6.

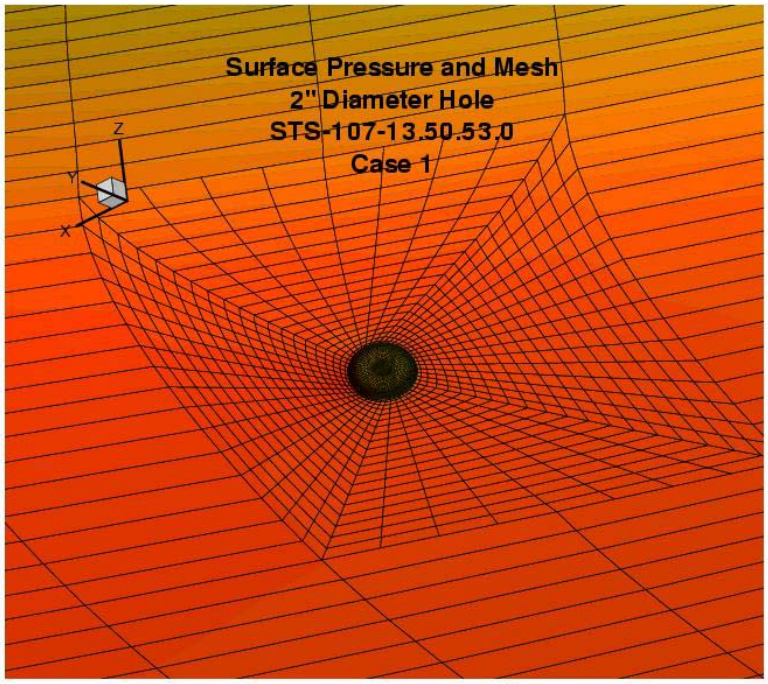

Figure 5.3.6-52: Modified surface grid in the vicinity of the hole.

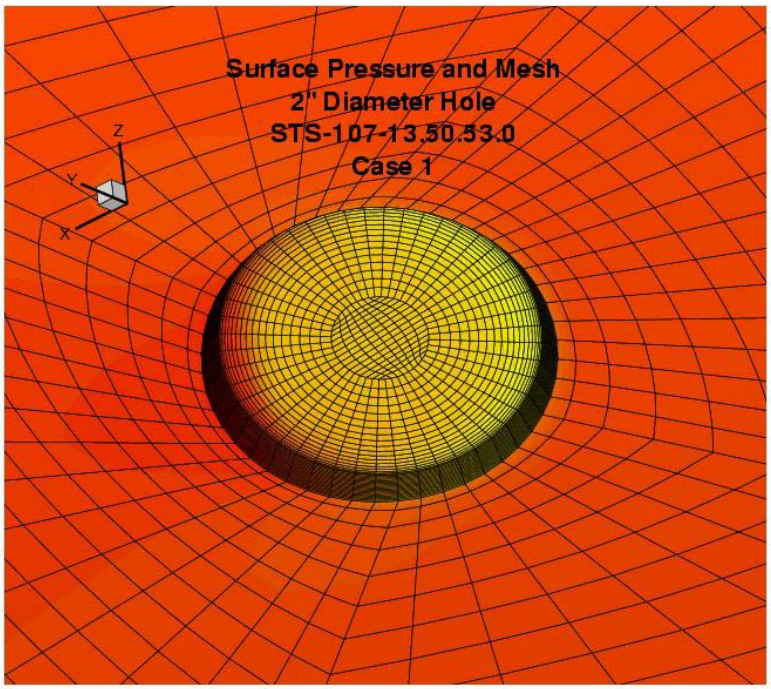

Figure 5.3.6-53: Structured grid within hole, approximately 20 cells deep and 60 cells across.

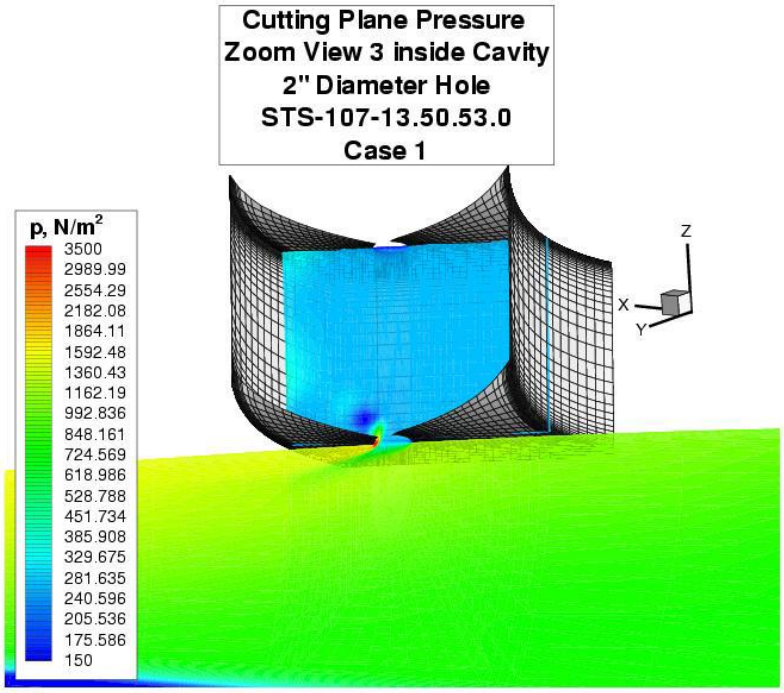

Figure 5.3.6-54: Pressure in cutting plane across breach and view of surface grid defining the vented cavity.

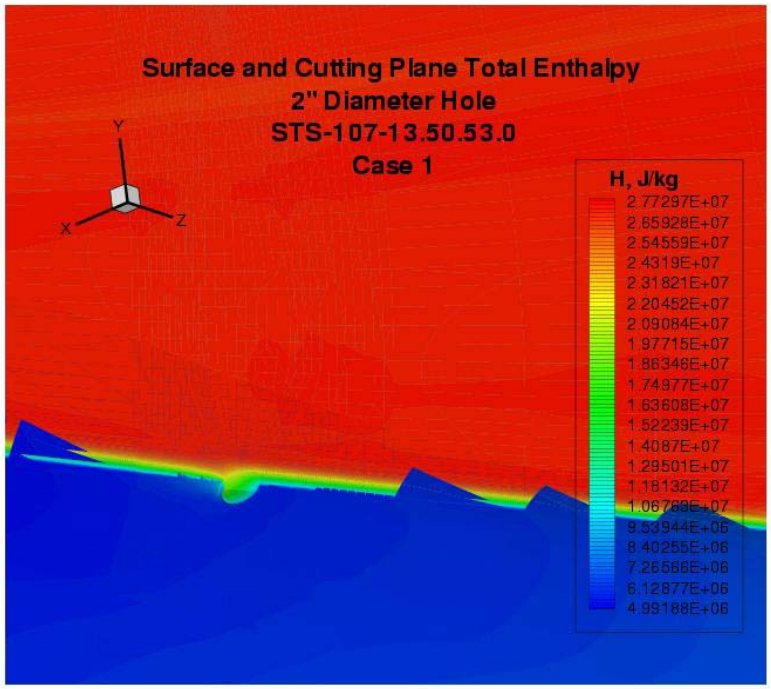

Figure 5.3.6-55: Total enthalpy in cut plane above hole showing partial ingestion of the boundary layer. (Blue jags are artifact of picture format conversion.)

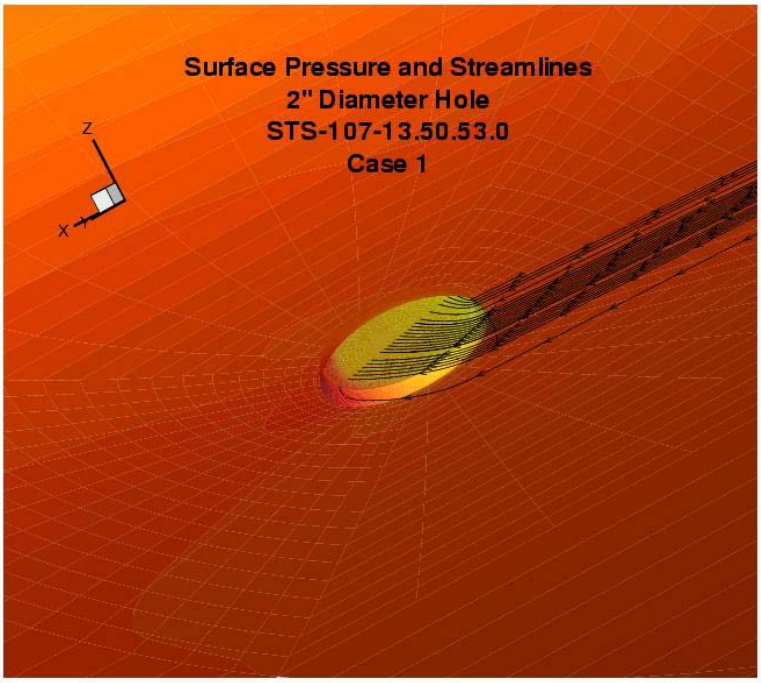

Figure 5.3.6-56: View of streamlines entering breach showing significant retention of external streamwise momentum.

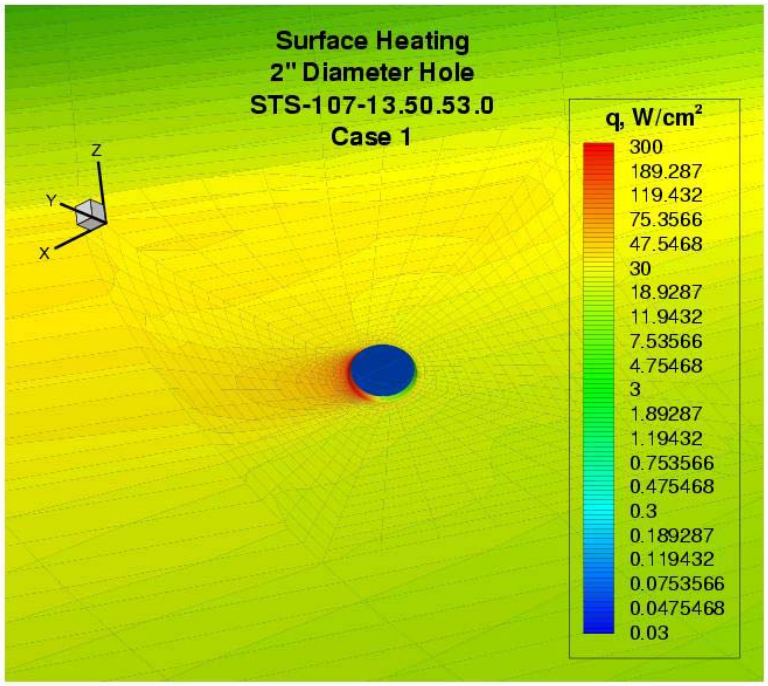

Figure 5.3.6-57: Surface-heating contours in the vicinity of the two-inch hole in Panel 6.

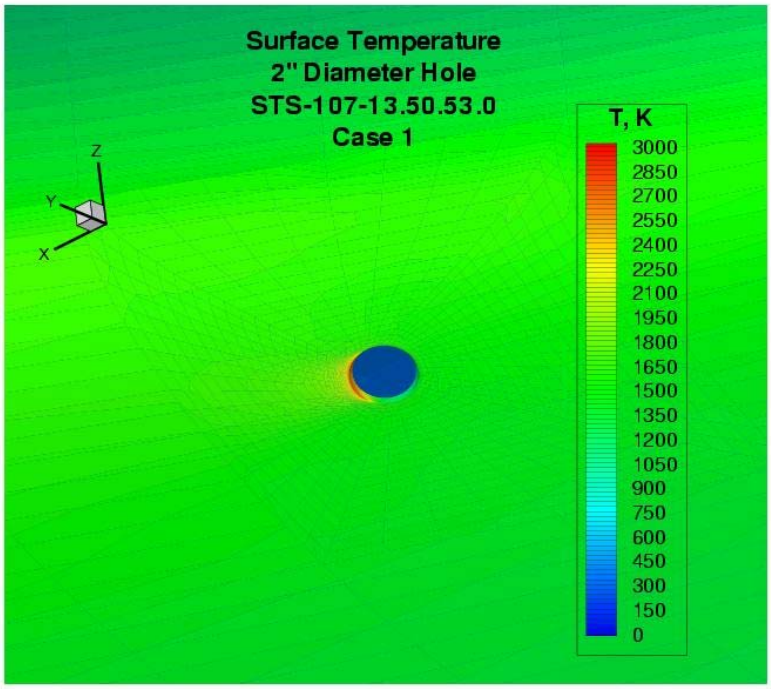

Figure 5.3.6-58: Surface temperature contours in vicinity of the two-inch hole in Panel 6.

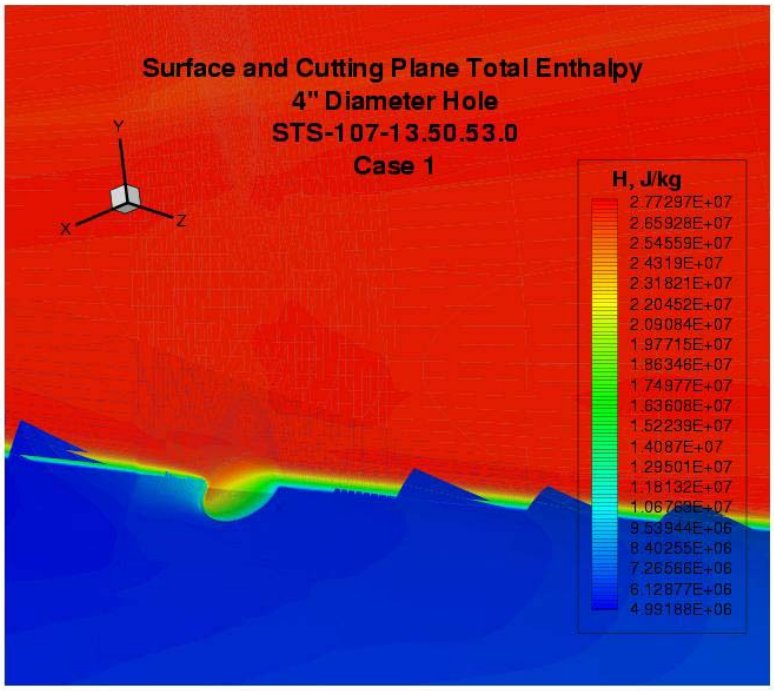

Figure 5.3.6-59: Total enthalpy in cut plane above four inch hole showing significant ingestion of the boundary layer. (Blue jags are artifact of picture format conversion.)

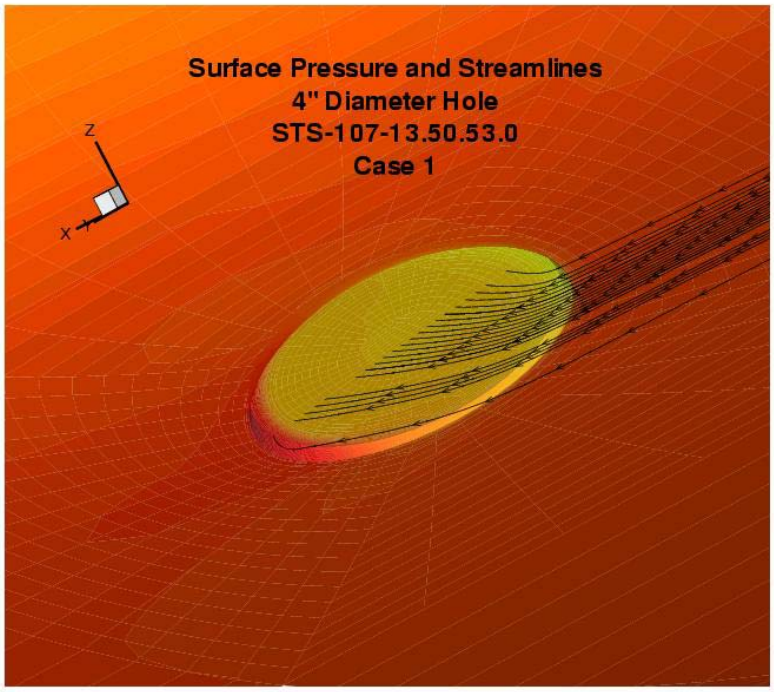

Figure 5.3.6-60: View of streamlines entering four-inch breach showing significant retention of external streamwise momentum.

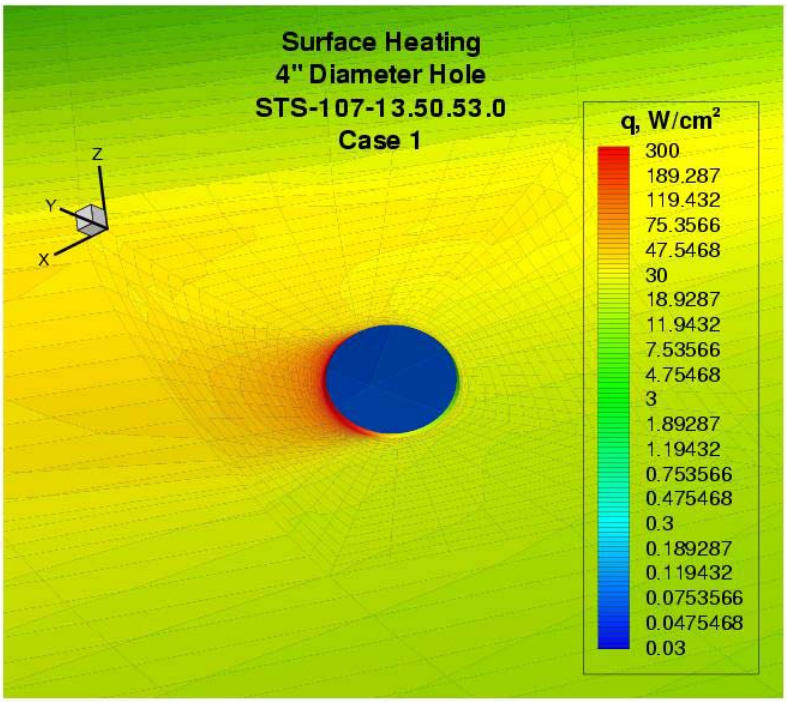

Figure 5.3.6-61: Surface-heating contours in the vicinity of the four-inch hole in Panel 6.

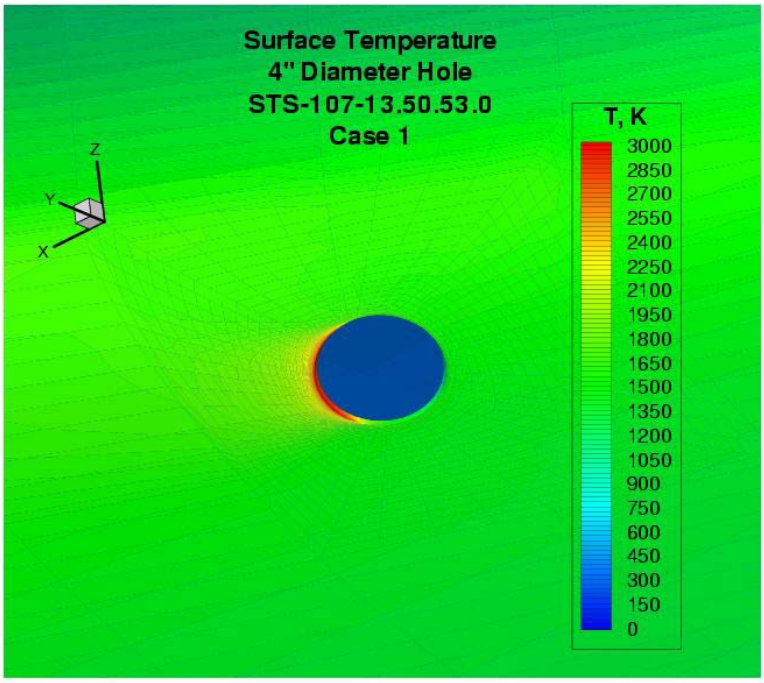

Figure 5.3.6-62: Surface temperature contours in vicinity of the four-inch hole in Panel 6.

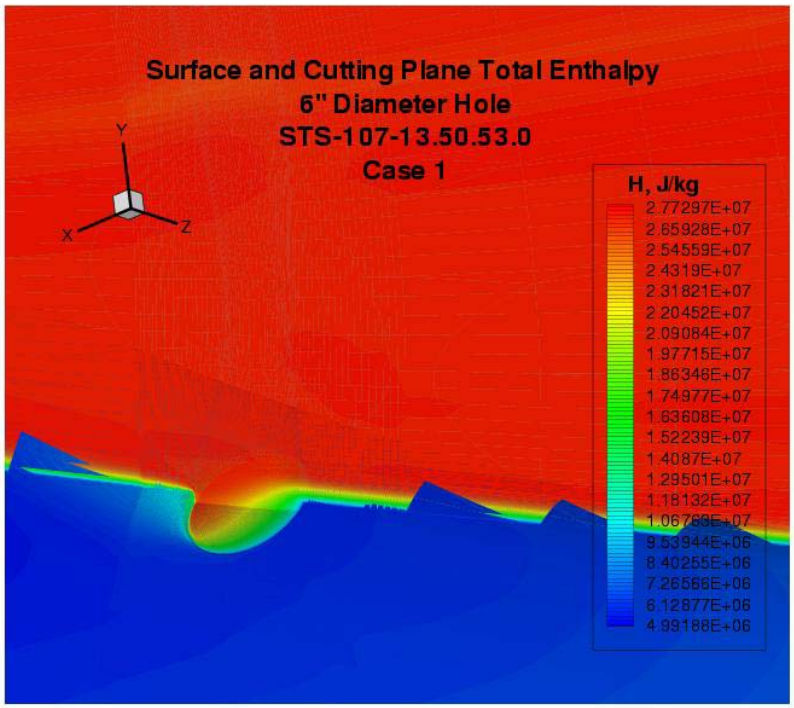

Figure 5.3.6-63: Total enthalpy in cut plane above six inch hole showing complete ingestion of the boundary layer. (Blue jags are artifact of picture format conversion.)

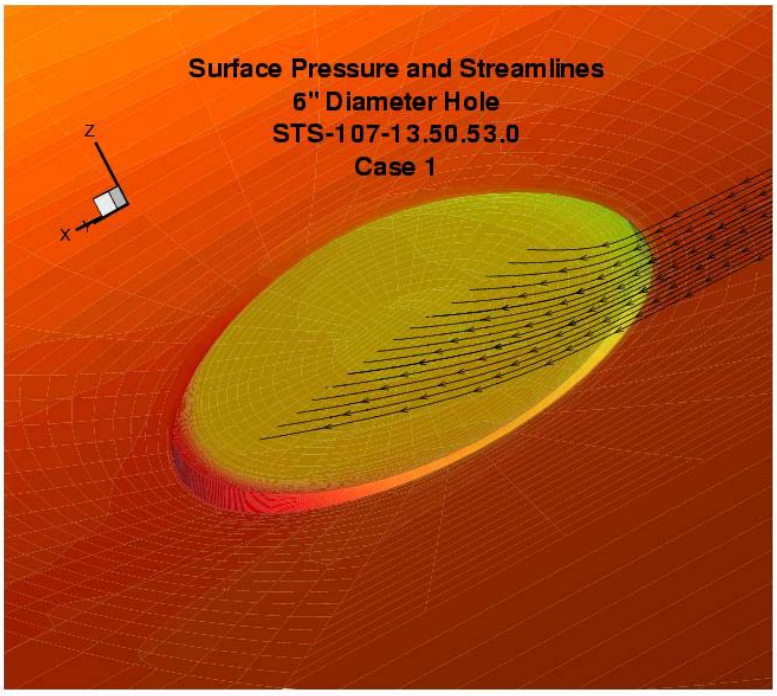

Figure 5.3.6-64: View of streamlines entering six-inch breach showing significant retention of external streamwise momentum.

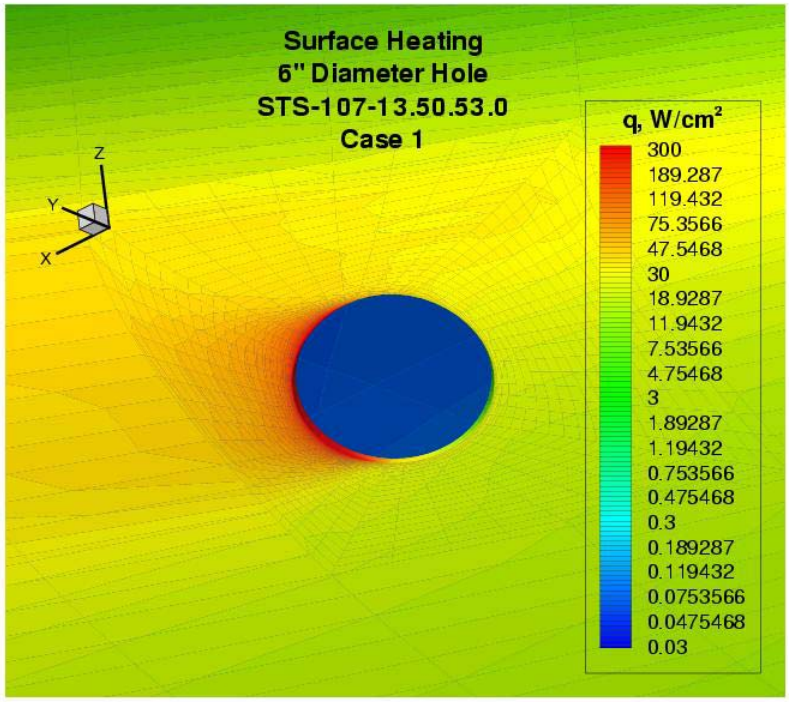

Figure 5.3.6-65: Surface-heating contours in the vicinity of the six-inch hole in Panel 6.

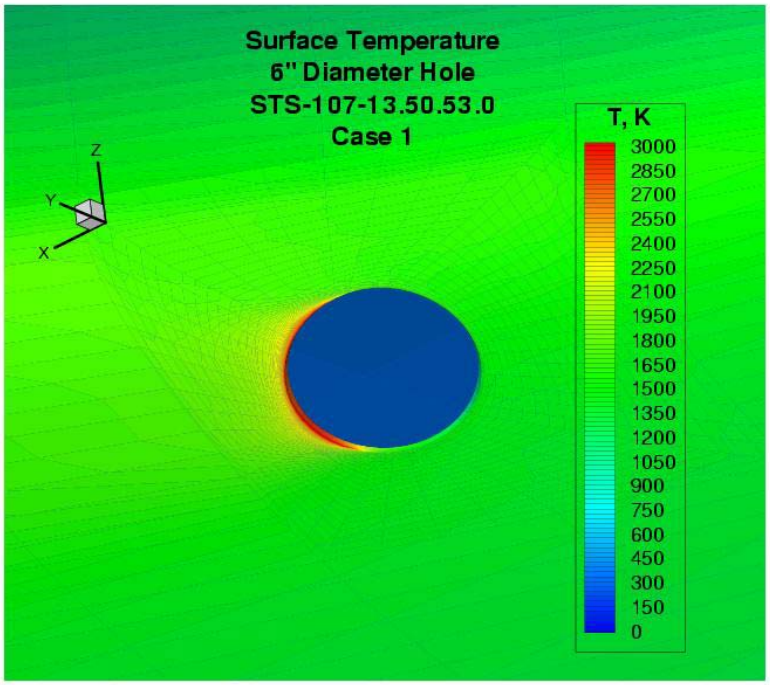

Figure 5.3.6-66: Surface temperature contours in vicinity of the six-inch hole in Panel 6.

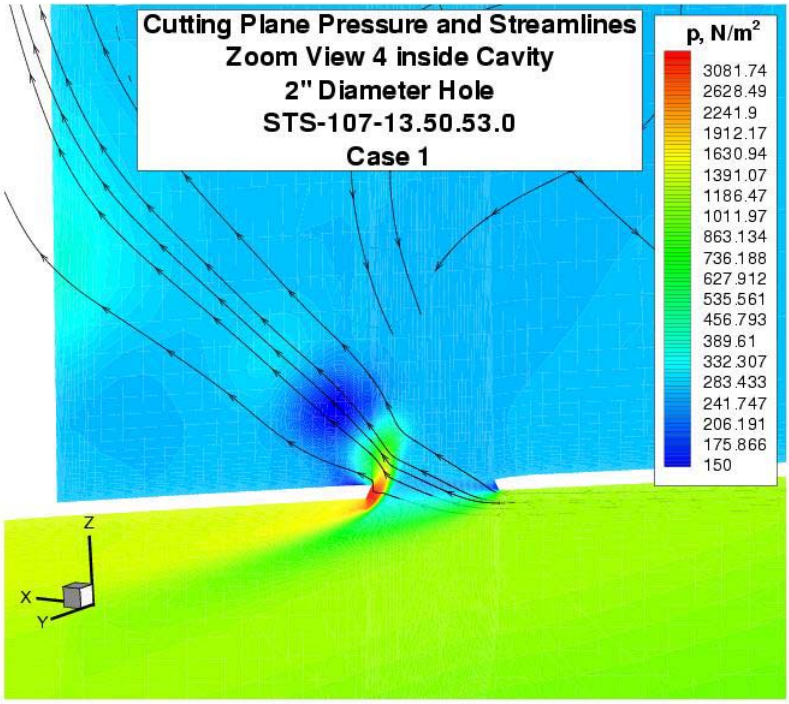

Figure 5.3.6-67: Streamlines entering the breach and pressure levels in the cutting plane. External flow direction is from the right to the left.

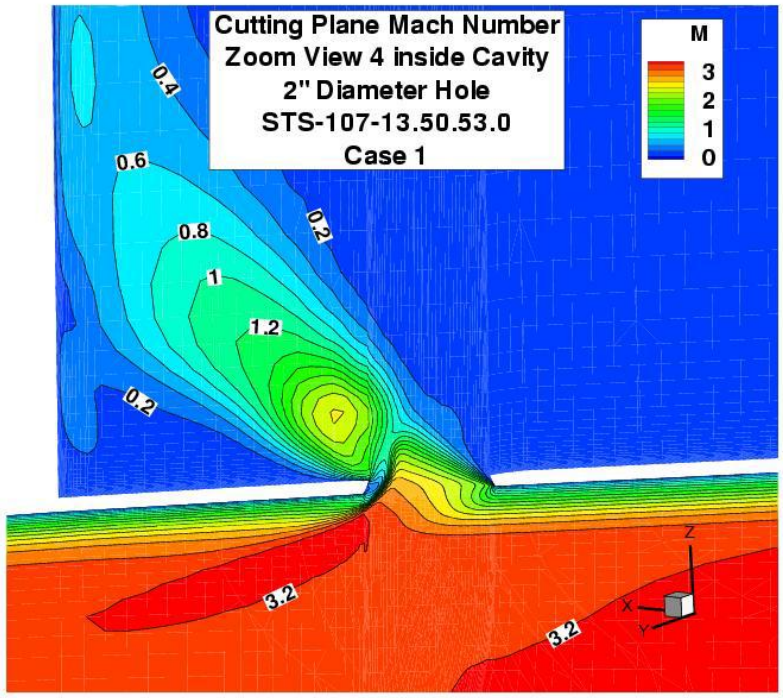

Figure 5.3.6-68: Mach number contours across the breach and in the jet entering the cavity. A sonic, choked condition sets up behind the lip shock over the downstream lip of the breach.

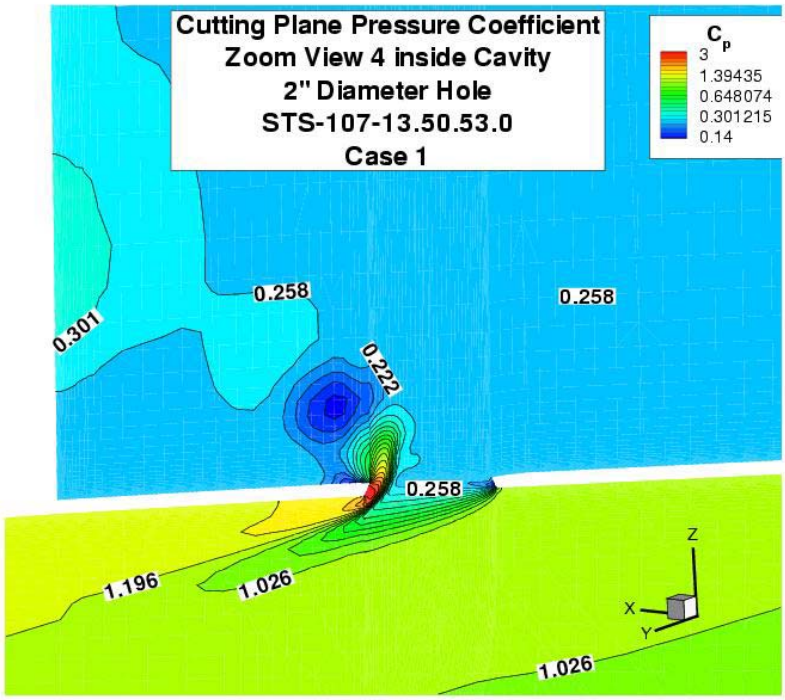

Figure 5.3.6-69: Pressure coefficient in vicinity of the breach.

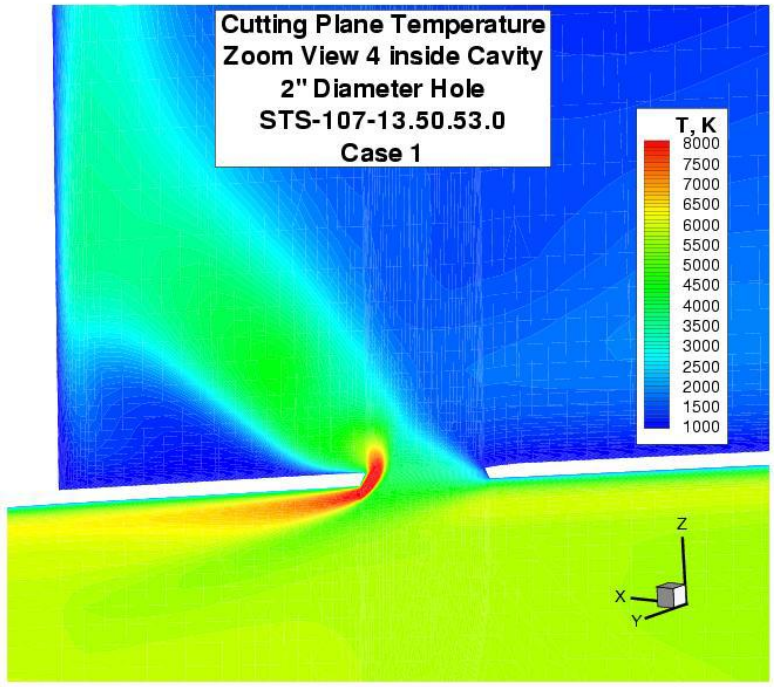

Figure 5.3.6-70: Temperature in vicinity of the breach.

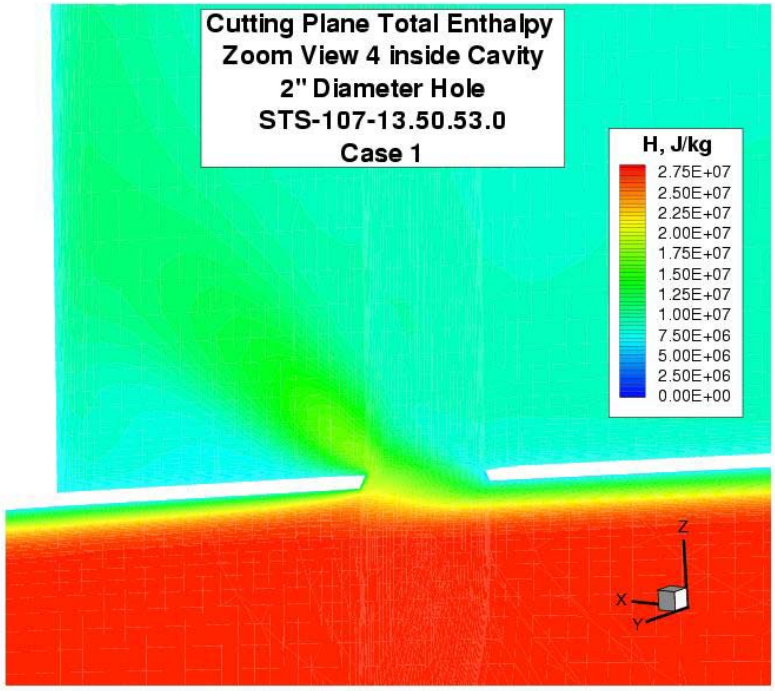

Figure 5.3.6-71: Total enthalpy in vicinity of breach indicating level of ingestion of the external boundary layer.

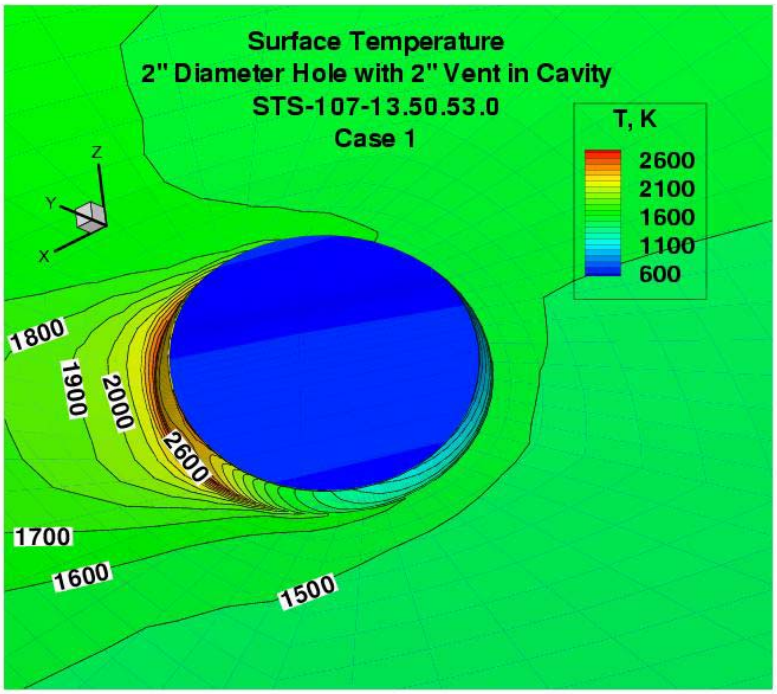

Figure 5.3.6-72: Surface temperatures in vicinity of downstream lip of two-inch hole over cavity.

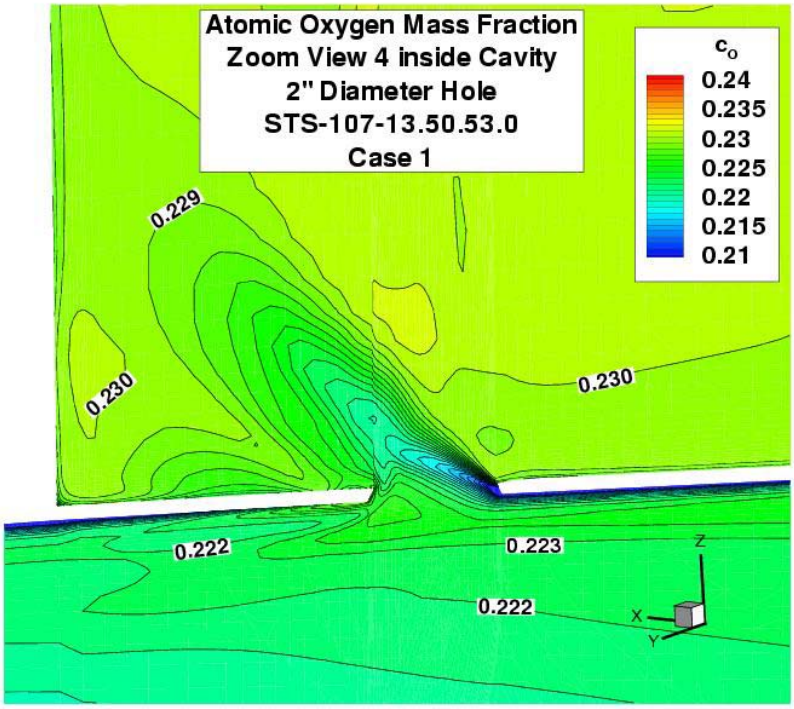

Figure 5.3.6-73: Atomic oxygen mass fraction ingested through breach.

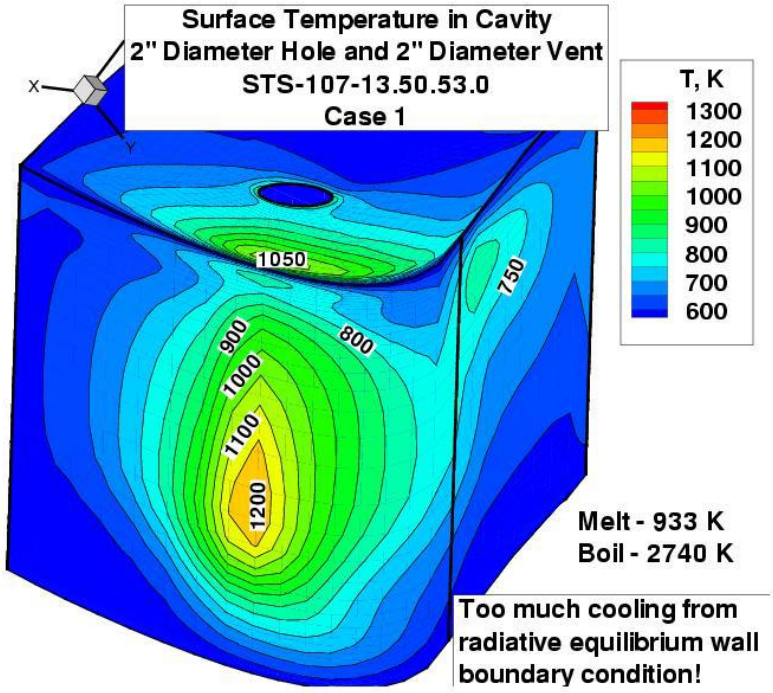

Figure 5.3.6-74: Surface temperature on cavity walls with identical cooling mechanisms as used for external flow.

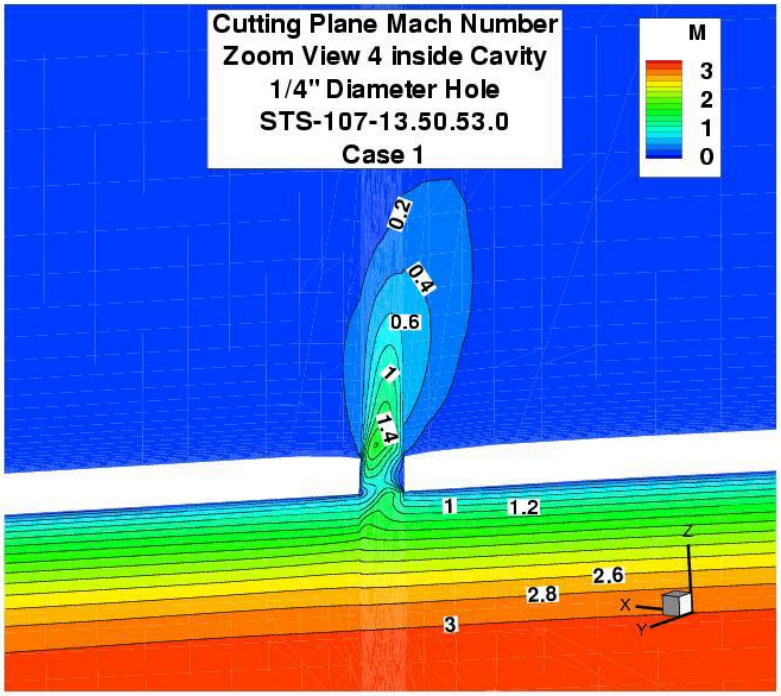

Figure 5.3.6-75: Mach number contours of jet entering cavity through quarter-inch diameter hole.

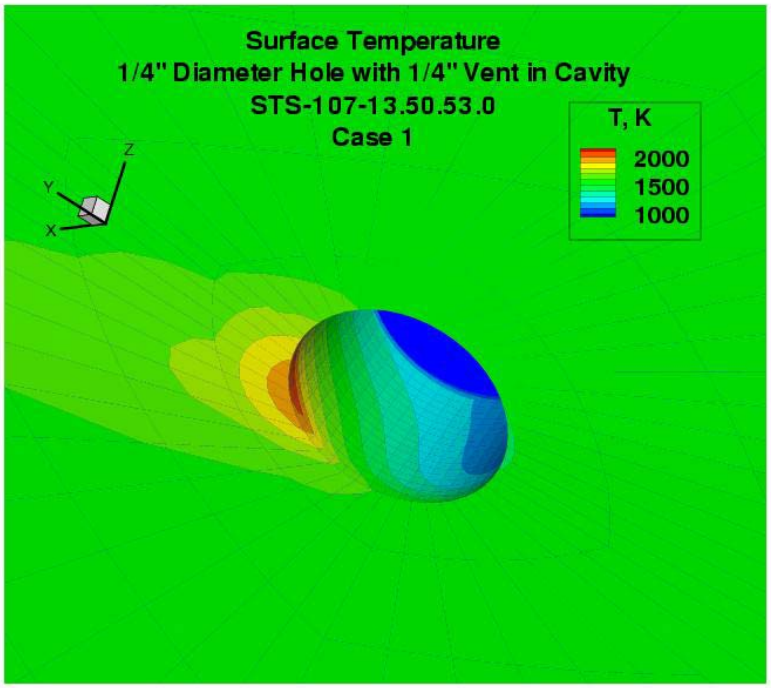

Figure 5.3.6-76: Surface temperatures in vicinity of quarter-inch hole.

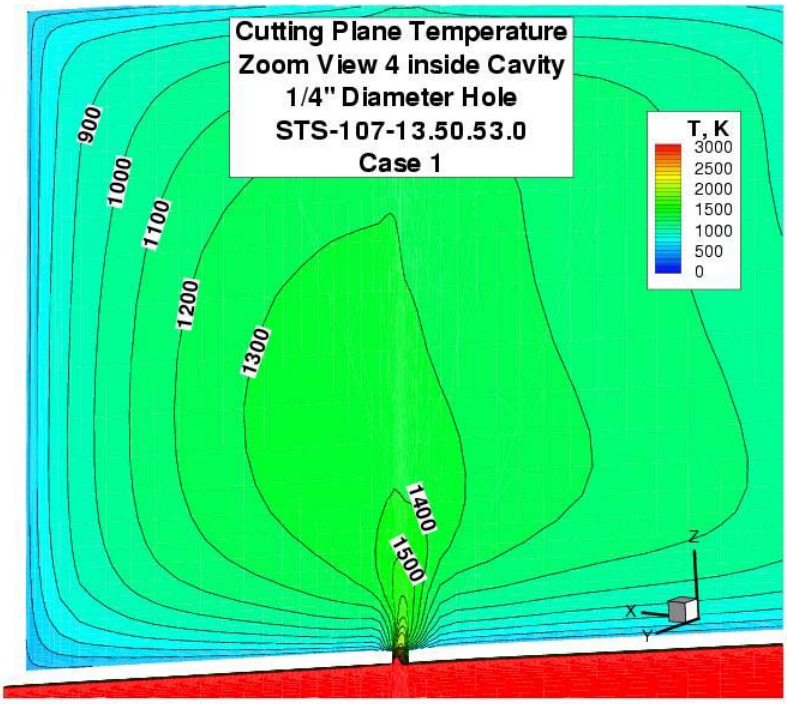

Figure 5.3.6-77: Jet temperatures in cavity bled from bottom of external boundary layer.

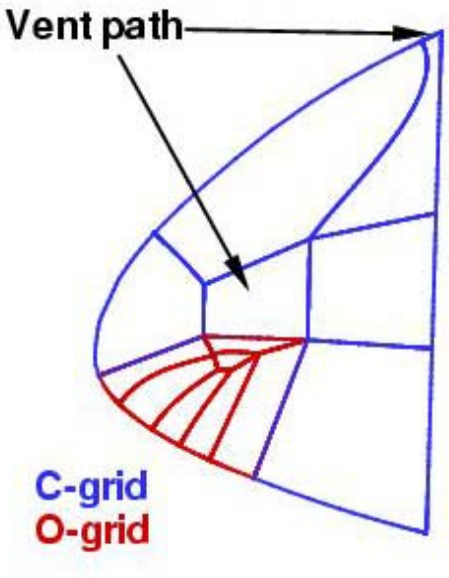

Figure 5.3.6-78: Internal block structure merging ad hoc cavity and chunnel showing relative vent positions.

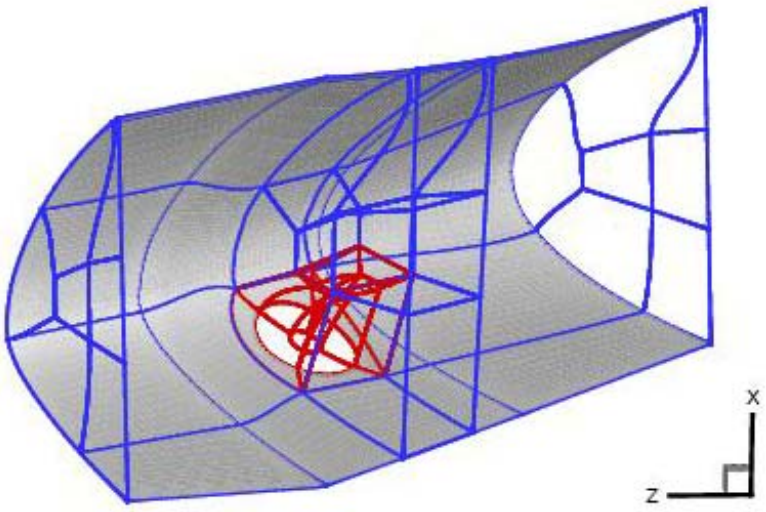

Figure 5.3.6-79: Global view of chunnel block structure.

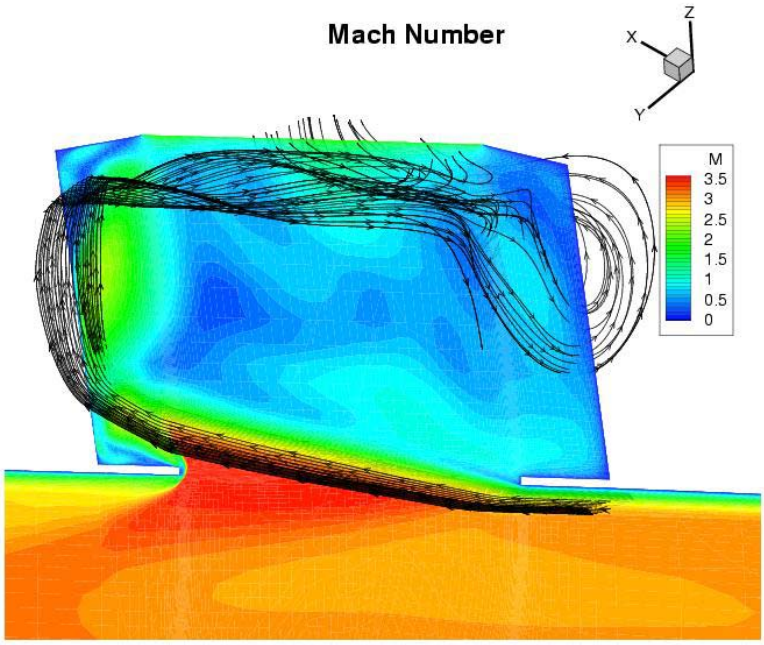

Figure 5.3.6-80: Mach number and streamlines in cavity behind panel 8 with ten-inch diameter hole and ten inch diameter vent.

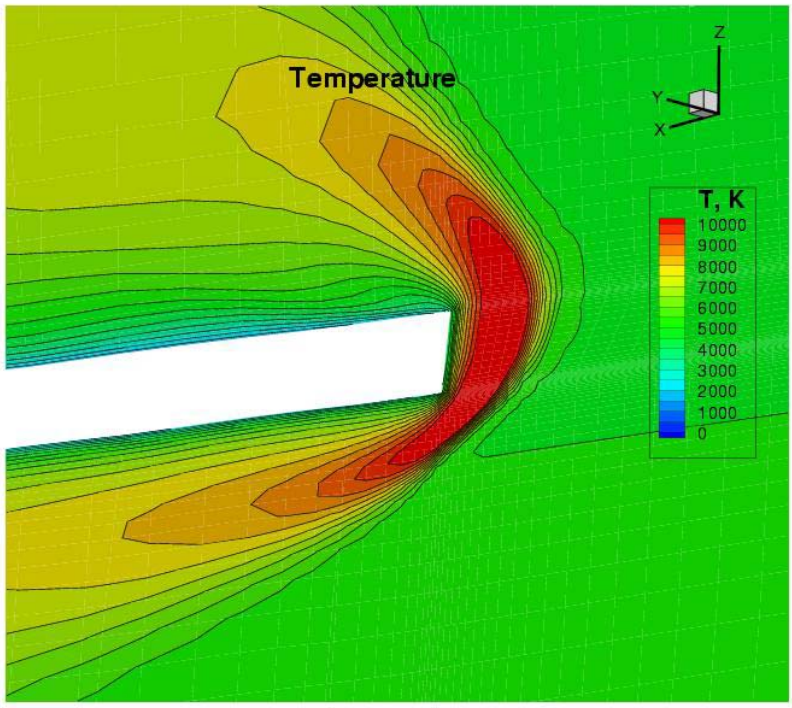

Figure 5.3.6-81: Details of temperature in shock layer over downstream lip with ten-inch breach through panel 8.

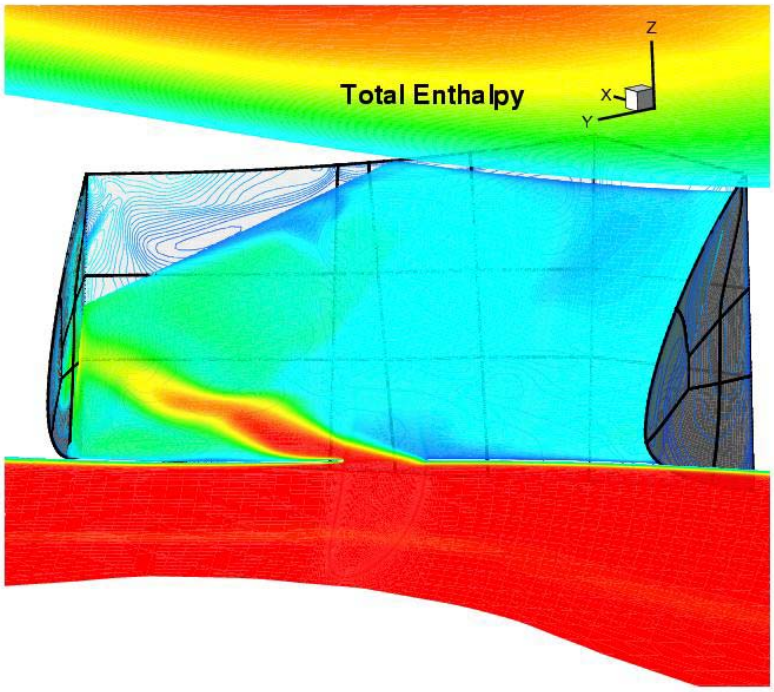

Figure 5.3.6-82: Total enthalpy entering chunnel through Panel 8. Venting is through slots on top of chunnel.

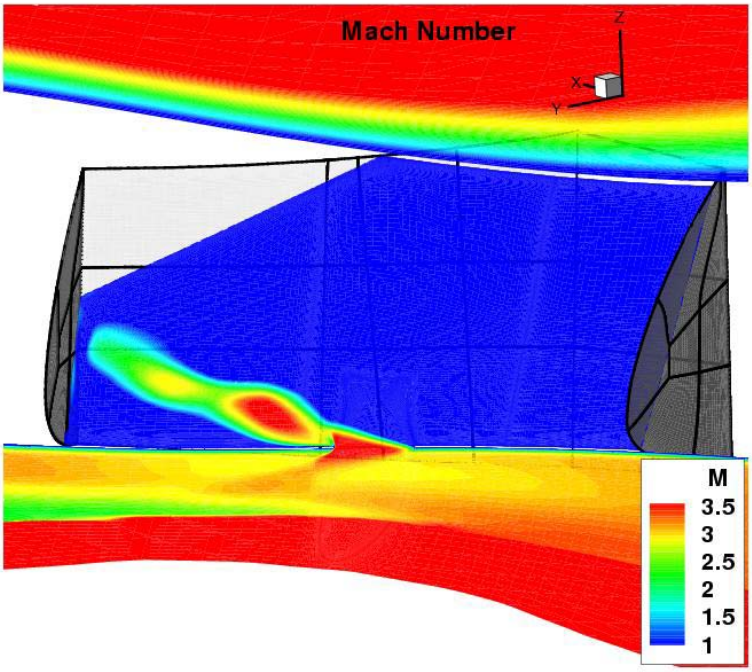

Figure 5.3.6-83: Mach number contours focused on supersonic domain.

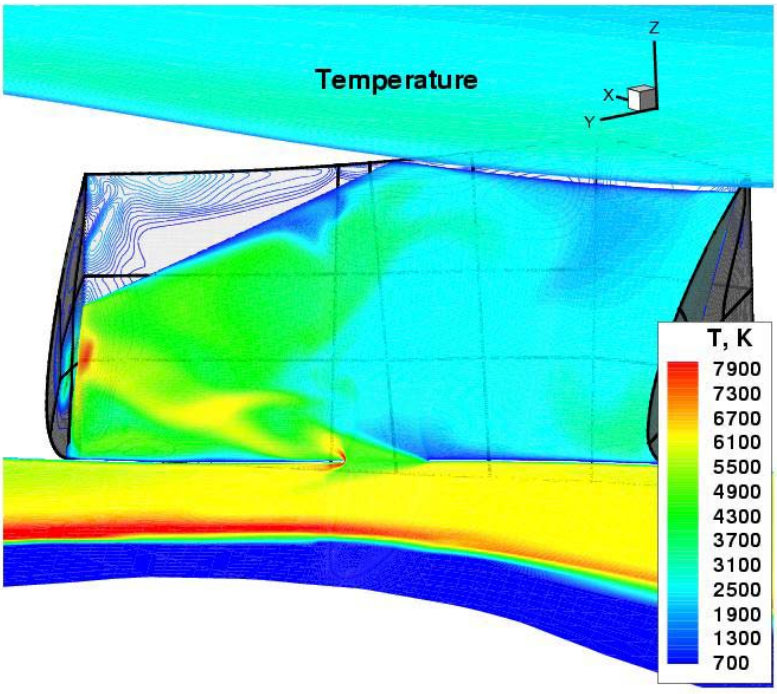

Figure 5.3.6-84: Temperatures in cutting plane through chunnel showing high temperatures at impingement of jet on the side wall.

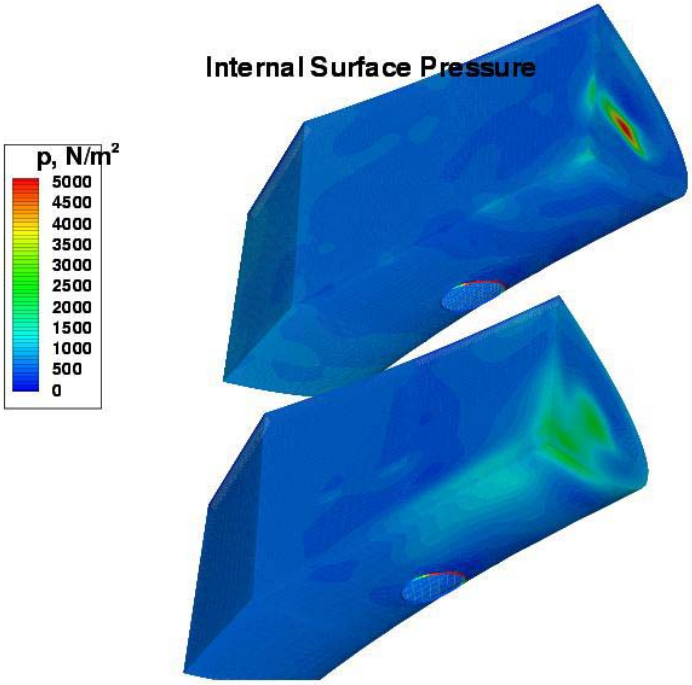

Figure 5.3.6-85: Comparison of chunnel surface pressures from medium grid and unadapted fine grid.

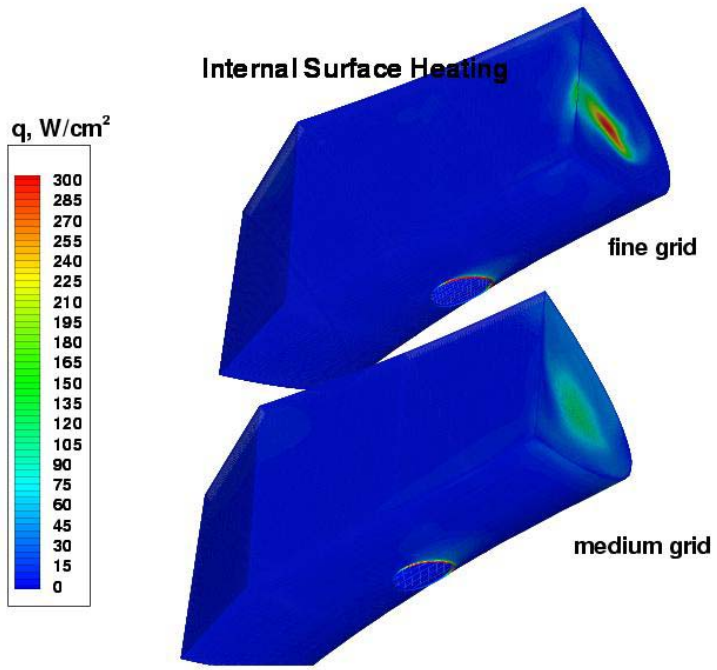

Figure 5.3.6-86: Comparison of chunnel surface heating from medium grid and unadapted fine grid.

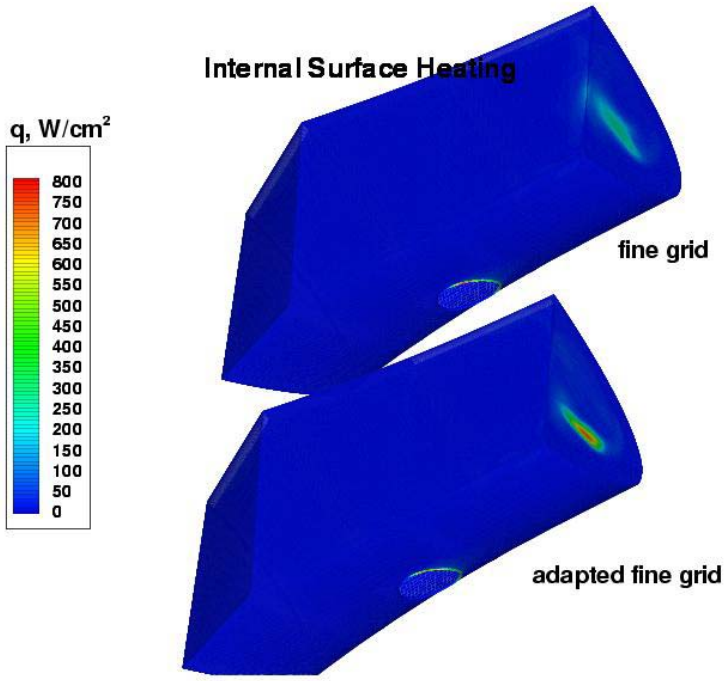

Figure 5.3.6-87: Comparison of chunnel surface heating from unadapted fine grid and adapted fine grid on impingement surface.

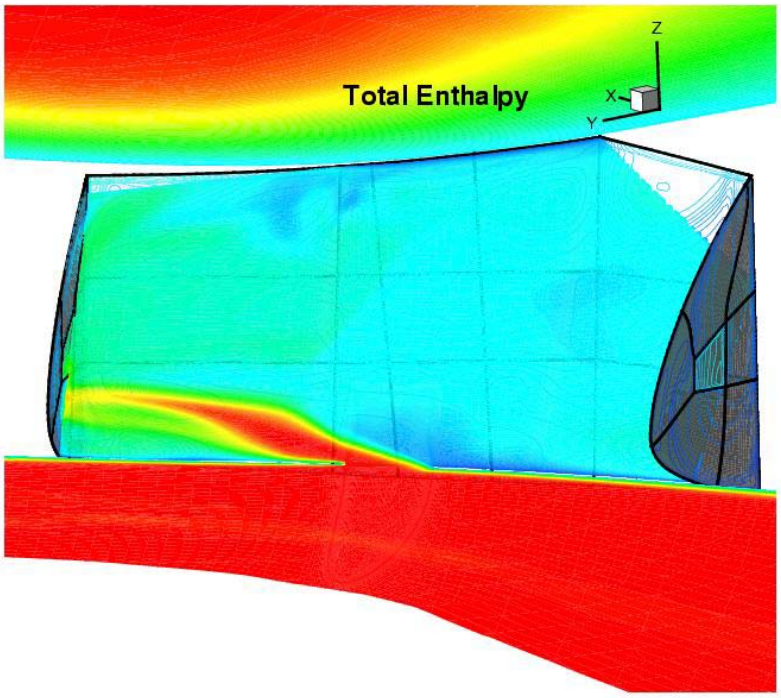

Figure 5.3.6-88: Total enthalpy in chunnel with side vents.

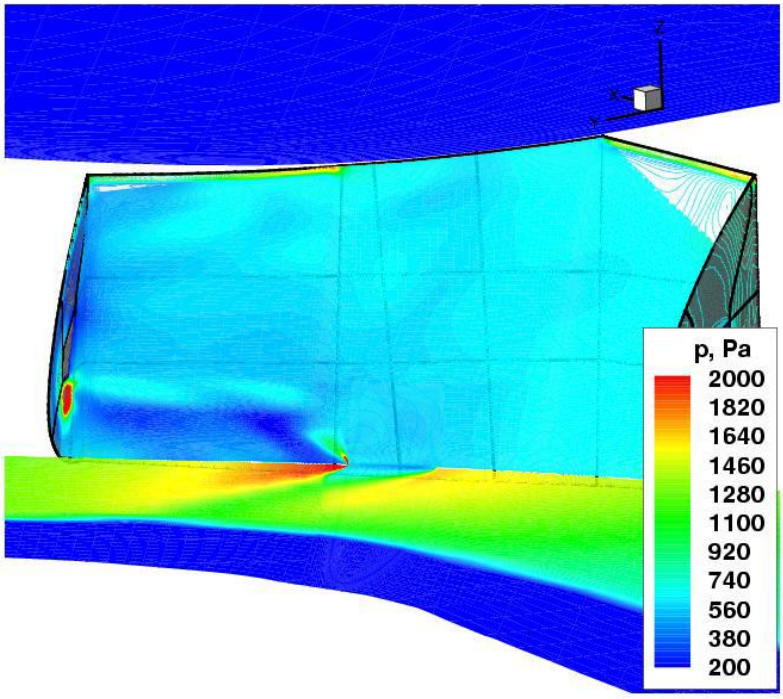

Figure 5.3.6-89: Pressures in chunnel with side vents.

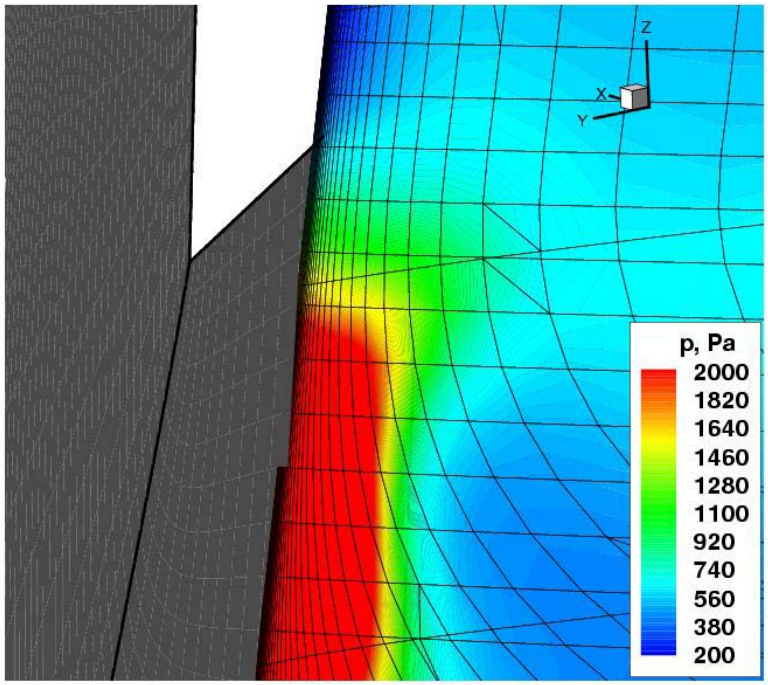

Figure 5.3.6-90: Detail of pressure at impingement location below side vent with supporting grid in the cut plane.

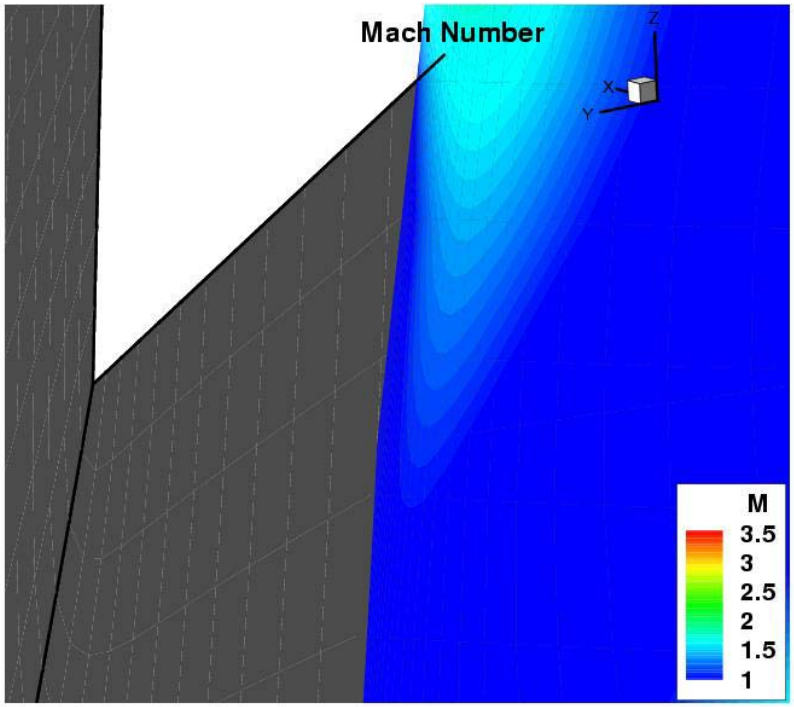

Figure 5.3.6-91: Magnified view of Mach number expanding to sonic condition at side vent.

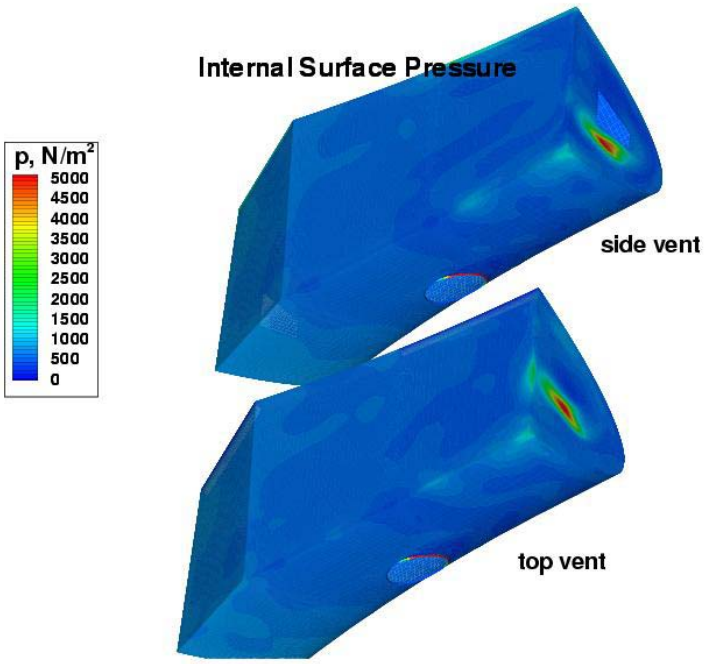

Figure 5.3.6-92: Comparison of chunnel surface pressures with top and side vents.

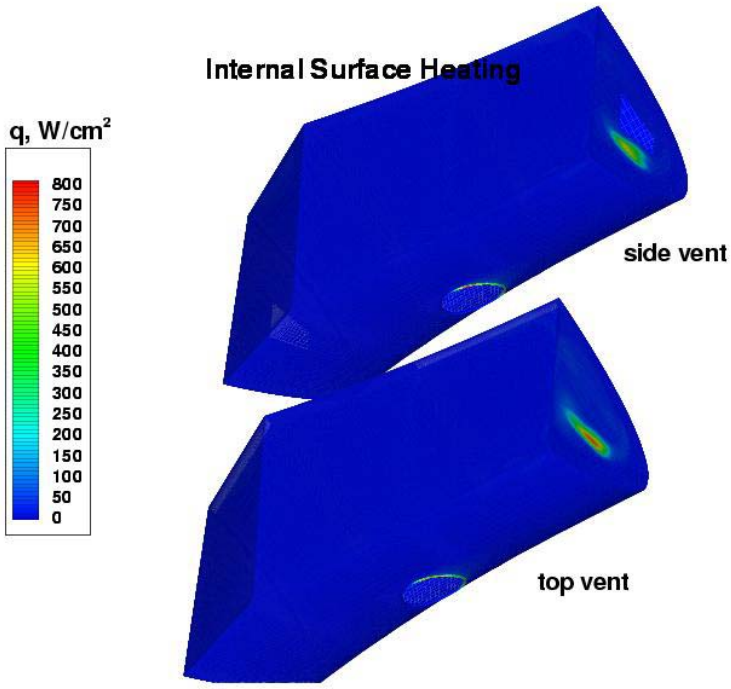

Figure 5.3.6-93: Comparison of chunnel surface heating with top and side vents.

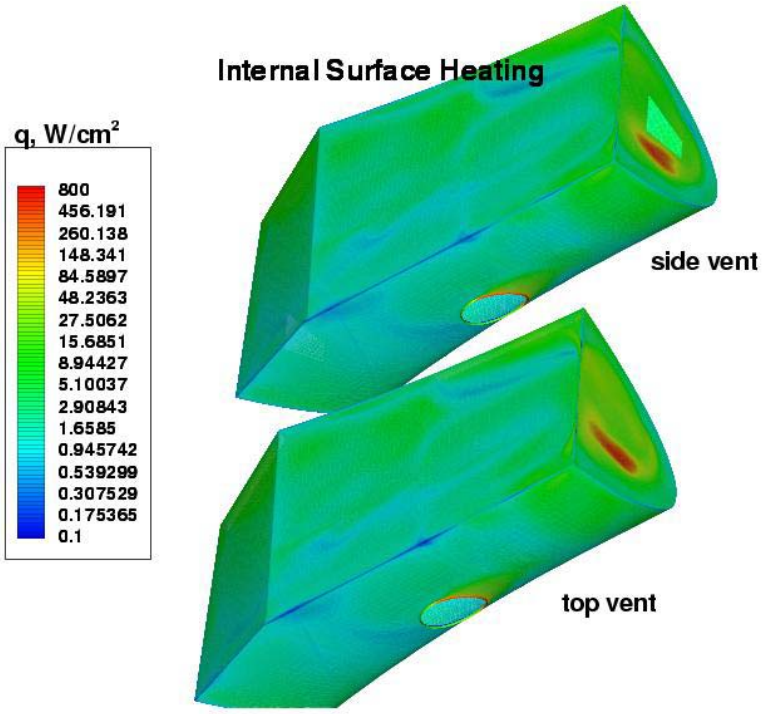

Figure 5.3.6-94: Logarithmic scaling of surface heating.

5.3.6.1.5 DSMC – Panel 8 10" Hole

5.3.6.1.5.1 Case Description

Using the DSMC Analysis Code, a DSMC case was run to simulate internal flow behind RCC panels 7, 8, and 9 due to a 10-inch hole in RCC panel 8. In this case, inflow boundary conditions were extracted from the previously run DSMC external flow solutions at an altitude of 350,274 and 300,000 feet. Vents were also applied to each side of the geometry with a total area equivalent to 66 inches squared.

5.3.6.1.5.2 Grid Development

Surface Grid
A heritage CAD definition for the RCC cavity was obtained from Jim Greathouse (NASA-JSC). This definition includes wing geometry from the leading edge back to the wing spar and includes a definition for the earmuffs between panels. The geometry used in this case was developed using the GridGen grid generation tool. After importing the CAD into GridGen, a 10-inch hole was generated in RCC panel 8 at a location of X = 1065 inches, Y = -219 inches, and Z = 286 inches in the orbiter coordinate system. Vent holes were included on each side of the geometry. It was assumed that the RCC thickness was uniform at ¼ inch, so the 10-inch hole in RCC panel 8 was given a thickness of approximately ¼ inch.

Since a DSMC solution had already been obtained for a nominal case at an altitude of 350,274 feet, it was felt that it was not necessary for a full-length shuttle case to be run for this failure scenario (1). Instead, an external flow field box-like "geometry" was created that connected to the hole from the external flow side. Great care was taken to create an external flow field geometry large enough so that the hole geometry would not significantly affect the flow at the upstream boundary, but small enough so that the case would run in a timely manner. The external flow field geometry was created to connect to a corresponding

portion of the outer RCC surface, which in turn, connected to the surface representing the thickness of the hole. Two different views of the surface geometry are displayed in Figure 5.3.6-95 and Figure 5.3.6-96.

In DAC, the surface geometry is represented as a collection of unstructured triangular elements and the entire surface geometry must be created to be "watertight" and possess continuous connectivity among triangles. In this case, the surface geometry contained approximately 53,000 surface triangles. Each individual surface triangle has specific boundary conditions associated with it. The triangles representing the surfaces of the wing were given the "solid wall" boundary condition, which means that no molecules are produced at the wall and none pass through. The triangles representing the vents were given the "outflow" boundary condition, which means that any molecules that hit the surface will disappear. Finally, the triangles representing the external flow field surface were given the "inflow" boundary condition. An inflow boundary creates molecules on the flow field side of the triangle, but any molecules that hit the surface will disappear.

Flow field Grid
The computational domain was specified to encompass the surface geometry created in this case and the boundary conditions of the computational domain were specified as vacuum. For the 350 kft case the internal flow field was discretized with Level-I Cartesian cells and each cell was specified to have a length of 1.18 inches (0.03 meters). The flow field grid was refined to the mean free path resolution though an adaptation process. After the adaptation process, the total number of cells in the computational domain was approximately 0.86 million cells. For the 300 kft case the Level I discretization employed cells of 0.059 inches (0.0015 meters). The total number of cells after the adaptation was approximately 40 million.

5.3.6.1.5.3 Input Parameters

The solution was run fully diffuse and the surface wall temperature was assumed to be 540° R (300 Kelvin). A chemistry model for high temperature reacting air was used that contained six molecular species – O_2, N_2, O, N, NO, and Argon. The mole fractions of these species were obtained from the 1976 Standard Atmosphere Model[1]. Number density, velocity, and freestream temperature were obtained from STS-107 flight data. To obtain the inflow boundary conditions from the full-length shuttle case already run at an altitude of 350,274 feet, the Surface Tools Plus (STP) DAC utility code was used to interpolate flow field properties onto the inflow geometry.

5.3.6.1.5.4 Results

Figure 5.3.6-98 and Figure 5.3.6-99 display a Y-slice of the flow field number density for the 350kft and 300 kft cases respectively. Due to the fact that the SLICE code (the DAC post-processing code that extracts the flow field properties of a certain plane) only has the capability to extract properties in a constant x, y, or z plane, Figure 5.3.6-97 was included to display a visual picture of the Y-direction cutting plane chosen. In Figure 5.3.6-98 and Figure 5.3.6-99, the streamlines shown depict the movement of the flow as it enters the hole in panel 8 and begins re-circulating inside the cavity. Figure 5.3.6-100 through Figure 5.3.6-103 (front and back view for the 350 and 300 kft cases, respectively) show the heating distribution in the RCC cavity while and Figure 5.3.6-104 through Figure 5.3.6-107show the corresponding pressure distribution. For the 350 kft case both the heating and pressure values shown in the legends on the right side of the figures have been normalized by reference heating and pressure values chosen from a point near the hole in panel 8 on the upstream RCC external surface. For the 300 kft case the heating and pressure were normalized by the free stream values at 300 kft. From these figures, it is evident that the area of highest pressure and heating due to the breach is near the earmuff between panels 8 and 9. In Figure 5.3.6-100 through Figure 5.3.6-103, a splash effect is shown on the panel 8 spar surface. As the flow hits the corner of the earmuff, a shock is formed and the flow is seen to splash onto the spar. Elevated heating levels are also seen near the earmuff between panels 7 and 8.

As was mentioned previously, mean free path resolution was obtained in the flow field grid for the 350 kft case. Historically, solutions that have reached mean free path resolution in their flow field grids have compared well with experimental data. The 300 kft case proved more challenging and although the available computational resources were exhausted mean free path resolution was not achieved throughout the domain. (That would have required a total number of cells in excess of 100 million). However, most cells were concentrated near the walls to capture the surface properties as accurately as possible.

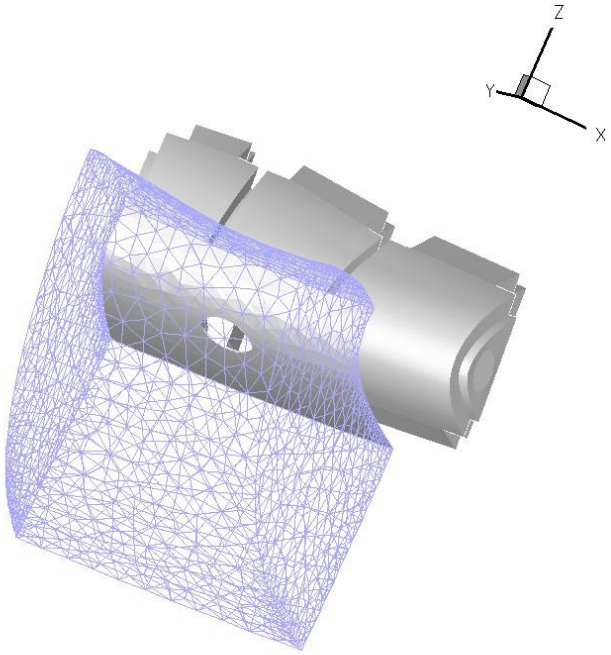

Figure 5.3.6-95 External (Triangulated) and Internal (Solid) Computational Domains – Front View

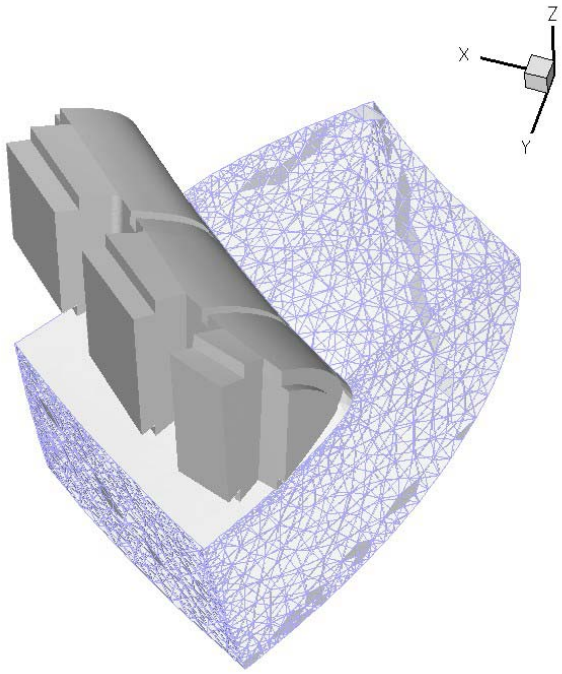

Figure 5.3.6-96 External (Triangulated) and Internal (Solid) Computational Domains – Back View

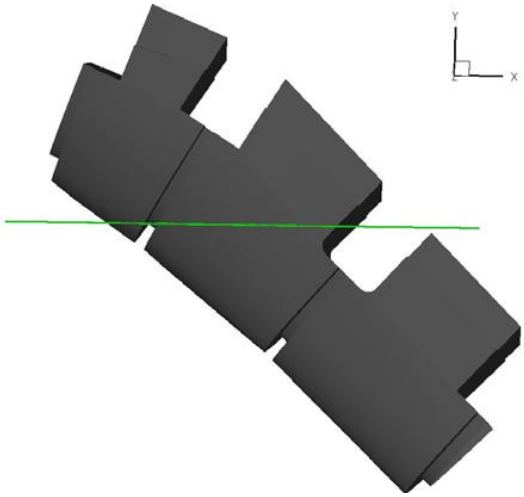

Figure 5.3.6-97 Visual of Cutting Place Chosen for Figure 5.3.6-98 and Figure 5.3.6-99

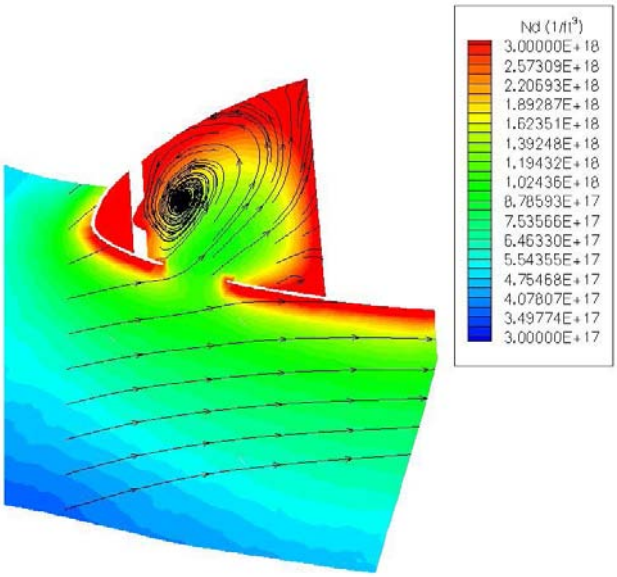

Figure 5.3.6-98 350kft Case-Number Density in Flowfield with Streamlines (Slice in Y-Direction)

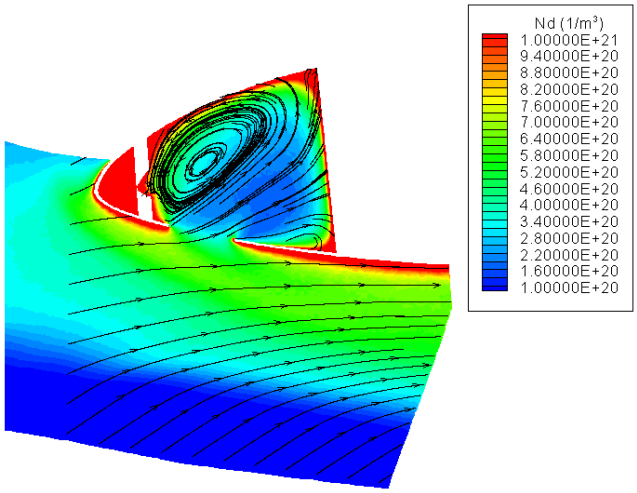

Figure 5.3.6-99 300kft Case-Number Density in Flowfield with Streamlines (Slice in Y-Direction)

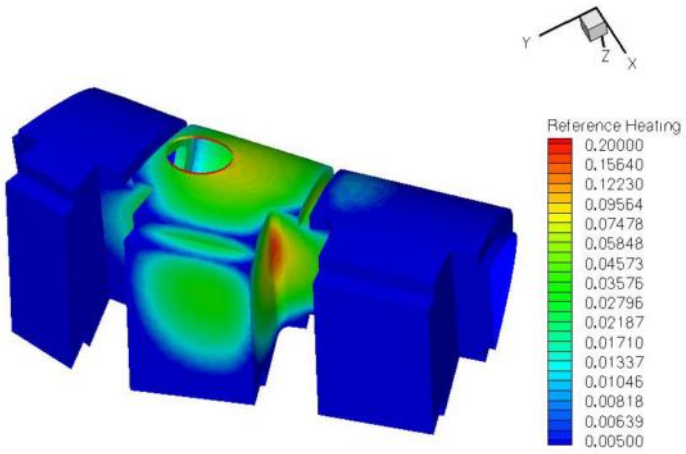

Figure 5.3.6-100 350kft Case-Reference Heating Distribution in RCC Cavity - Front View

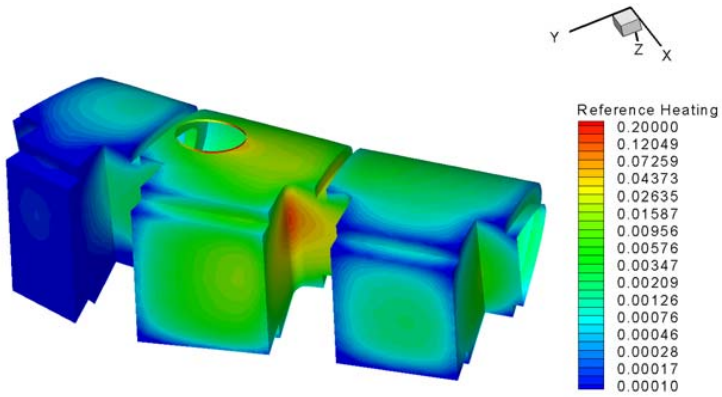

Figure 5.3.6-101 300kft Case-Reference Heating Distribution in RCC Cavity - Front View

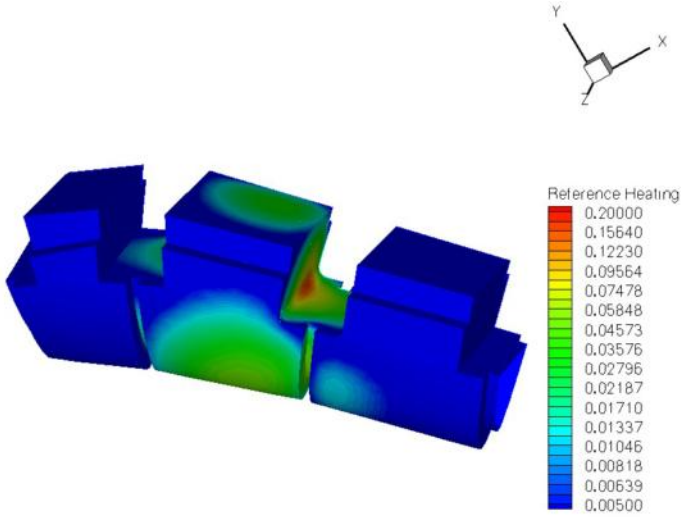

Figure 5.3.6-102 350kft Case-Reference Heating Distribution in RCC Cavity – Back View

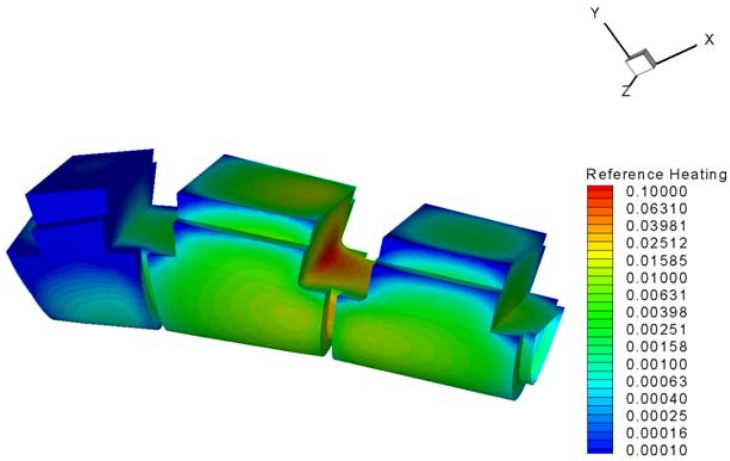

Figure 5.3.6-103 300kft Case-Reference Heating Distribution in RCC Cavity – Back View

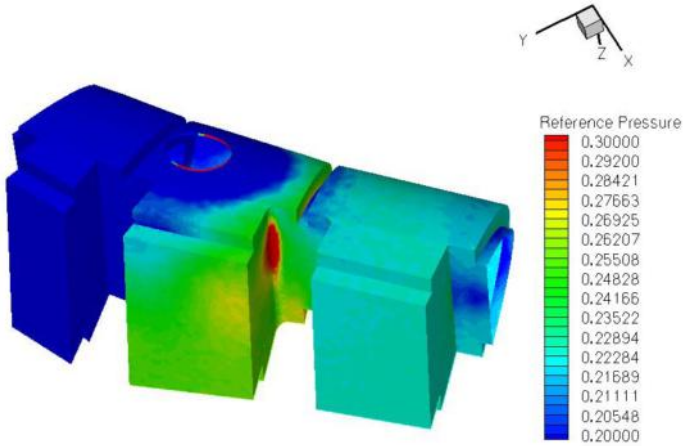

Figure 5.3.6-104 350kft Case-Reference Pressure Distribution in RCC Cavity – Front View

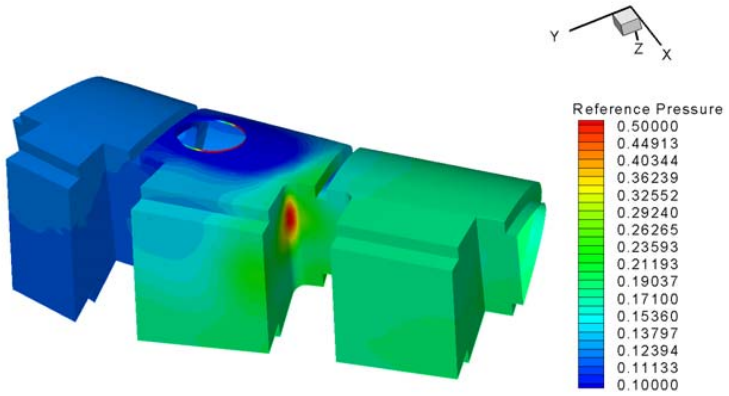

Figure 5.3.6-105 300kft Case-Reference Pressure Distribution in RCC Cavity – Front View

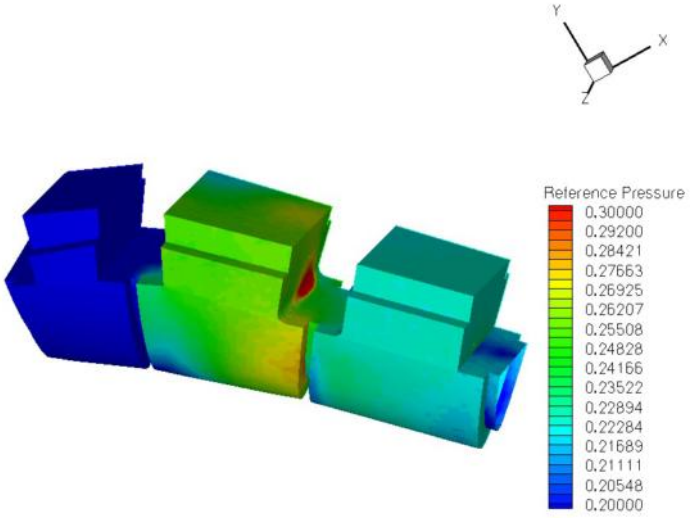

Figure 5.3.6-106 350kft Case-Reference Pressure Distribution in RCC Cavity – Back View

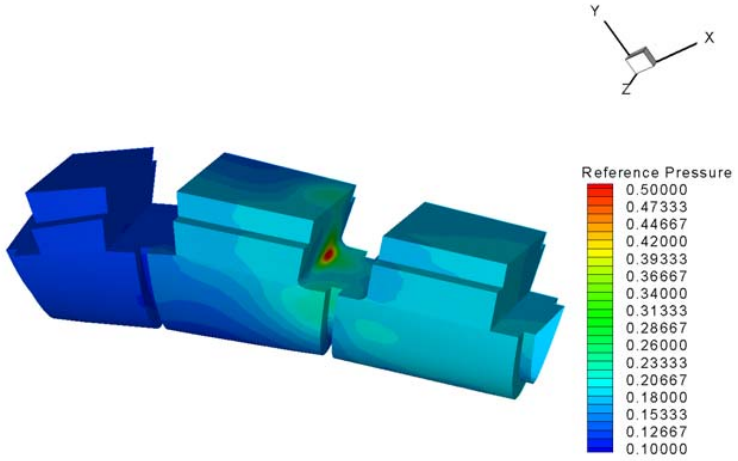

Figure 5.3.6-107 300kft Case-Reference Pressure Distribution in RCC Cavity – Back View

Footnotes

1. The value of the Knudsen number (a ratio of the molecular mean free path to a reference length) is often used as an indicator of rarefied flow. A Knudsen number of 0.01 or less is typically used to describe continuum flow, whereas higher Knudsen numbers indicate more rarefied flow. In this case, the Knudsen number is an order of magnitude larger when simulating only the portion of the flow field near the leading edge of the wing, than when simulating the entire flow field around the full-length vehicle. This corresponds to fewer computational resources needed due to fewer flow field molecules simulated.

5.3.6.2 CFD of RCC T-Seal Damage (Missing Portion of T-Seal)

5.3.6.2.1 JSC GASP 2D Solutions

5.3.6.2.1.1 Brief CFD Intro / Application Description

Two-dimensional simulations were done with GASP to model the internal wing flow field around the earmuff with a T-seal missing. Figure 5.3.6-108 is a representation of this simplified geometry. The true wall contour on the windward surface was not modeled in the GASP simulations. Instead, the windward surface was just a straight wall (black line instead of blue line in Figure 5.3.6-108).

GASP 4.1 with the overset grid option was used to expedite grid generation. Figure 5.3.6-109 shows the grid system. Sixteen grids were used with no overlap on the viscous surfaces. The upstream boundary was obtained by interpolating from a solution provided by the LAURA code from CFD point 1. The exact point to interpolate the boundary layer profile from was found by locating the attachment line on the wing leading edge and then locating the point between panels 8 and 9 that interested the attachment line. Figure 5.3.6-110 shows streamlines across the wing leading edge. The center of the red square is where the boundary layer profile was interpolated.

The interpolated boundary layer profile was in 3-D coordinate space, which was not the same coordinate system as the two-dimensional model problem. To transform the profile to the two-dimensional coordinate system the three-dimensional vector was dotted with the surface normal (along the attachment line) to get the x-component of the 2-D profile and dotted with the surface normal at the interpolation point to get the y-component of the 2-D profile. Figure 5.3.6-111 shows the boundary layer profile by components.

The out of page component is the velocity that would be out of the page in the 2-D simulation. It is small in comparison for the entire profile so it was ignored. The Mach number was used to limit the height of the profile that was used. The computational domain was limited to about 6.3 inches (0.16 meters) above the windward surface. Beyond that, the shock affected the Mach number profile.

5.3.6.2.1.2 Case Definition

The inlet to the simulation, as stated above, was a boundary layer profile from the LAURA code (CFD point 1). The internal back pressure was taken to be 0.835 psf (40 Pa). This was the leeside pressure above the leading edge from the same LAURA simulation (where the actual wing venting occurred). The internal wall temperature (on the earmuff) was held at 1500° F (fully catalytic surface). The external wall used the wall temperature from the LAURA solution (2794° F, partially catalytic surface).

5.3.6.2.1.3 Configurations Analyzed

The original geometry called for the internal surface to be 45” away from the windward surface of the wing. This made the distance from the earmuff to the T-seal exit to be 31” in the simulation. Four other cases were ran, with the distance from the earmuff to the T-seal exit being 21”, 11”, 5”, and 2”. The purpose for the fives cases was to create an earmuff heating model that varied as a function of distance from the T-seal exit to the earmuff. To speed up the running of the extra 4 cases, the original 31” solution was interpolated to each of the new grid systems (21”, 11”, 5”, and 2”) and the solution was ran from there. This saved the time of the flow setting up into the T-seal inlet. This was a legitimate way of running the cases because the flow out of the T-seal exit was supersonic thus the flow through the T-seal inlet never changed even when the earmuff was moved closer.

5.3.6.2.1.4 Heating Results

The heating distribution on the earmuff is shown in Figure 5.3.6-112. As the earmuff approaches the T-seal exit, the jet expands less, thus the heating on the earmuff is more localized and the peak heating is

much higher. The heating on the corners of the earmuff seems to increase slightly as the earmuff gets further from the T-seal exit.

5.3.6.2.1.5 Observations and Conclusions

The distance from the T-seal exit to the earmuff surface largely affects the plume structure. Figure 5.3.6-113 shows Mach contours for the 31" case. Figure 5.3.6-114 shows the mach contours for the 5" case. The maximum Mach number in the plume is at least 25% lower for the 5" case than the 31" case. Figure 5.3.6-115 shows the T-seal inlet flow structure. As the plume passes through the nozzle created by the missing T-seal, the flow directionality of the freestream is mostly washed away. This is evident by the symmetric flow at the exit of the T-seal.

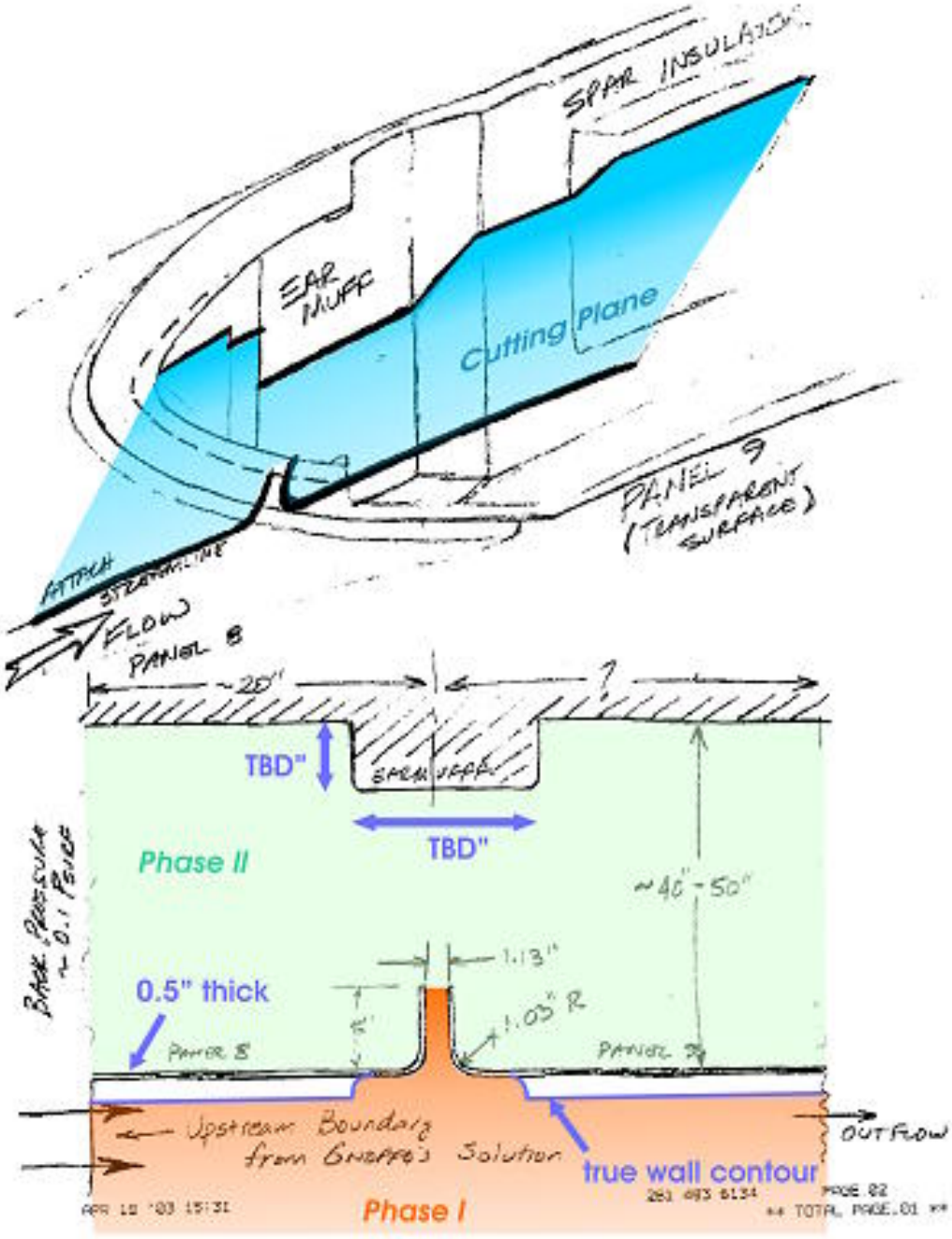

Figure 5.3.6-108 Representative T-seal geometry

a) Overview of Grid System

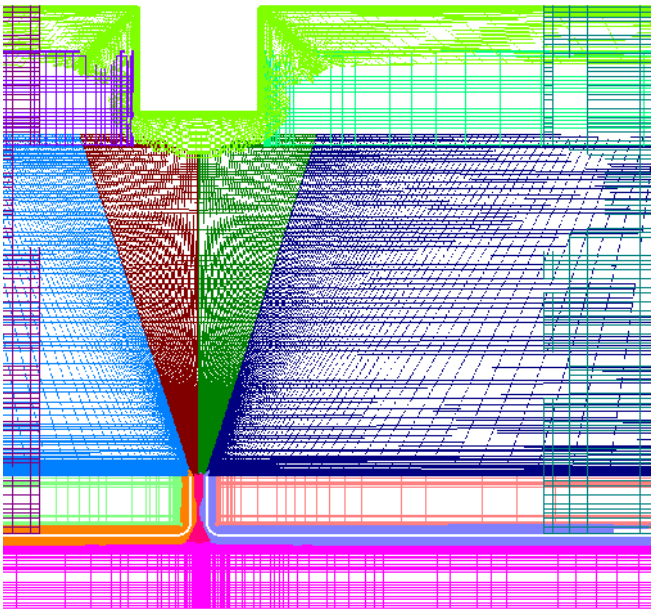

b) Close up of Earmuff Region

Figure 5.3.6-109 T-Seal Grid System

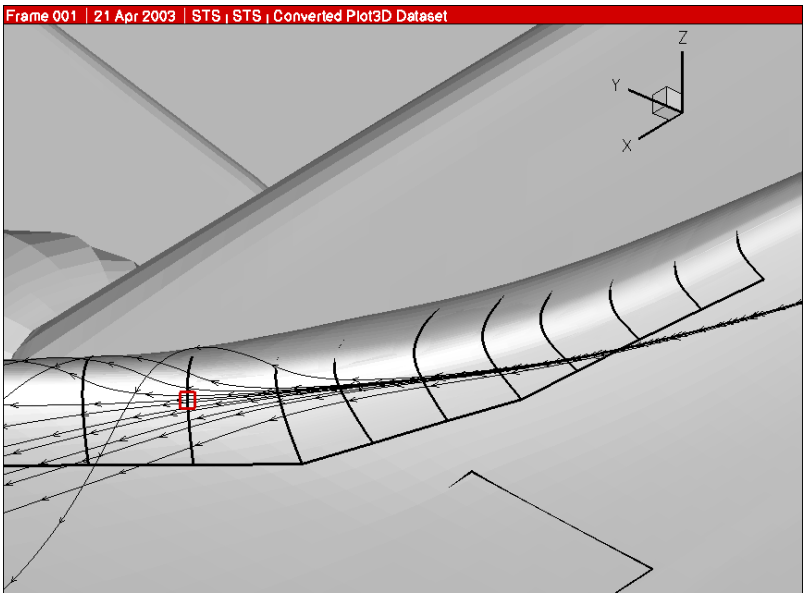

Figure 5.3.6-110 Panel 8 Attachment Line

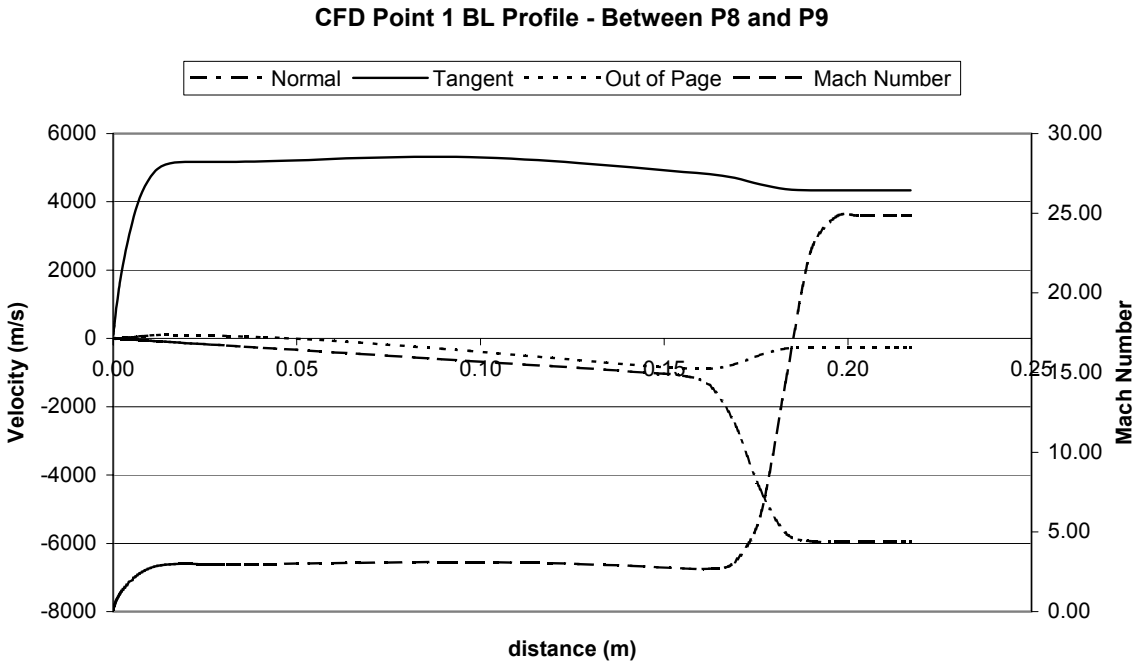

Figure 5.3.6-111 Transformed Boundary Layer Profile

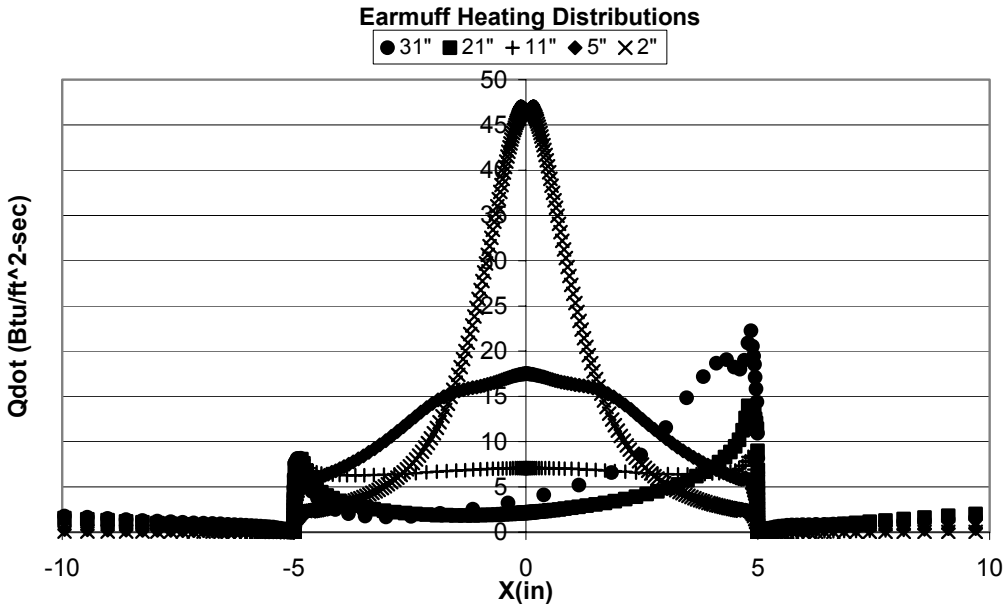

Figure 5.3.6-112 Earmuff Heating Distributions for Varying Distances

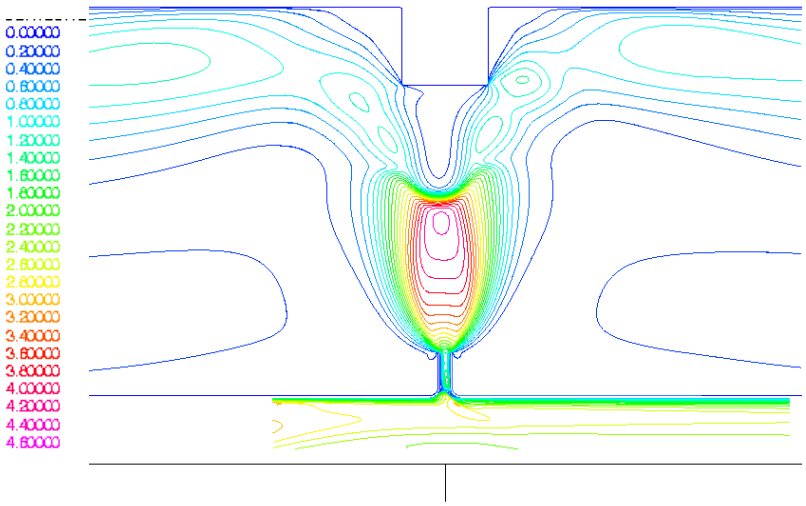

Figure 5.3.6-113 Mach contours for the 31" separation case

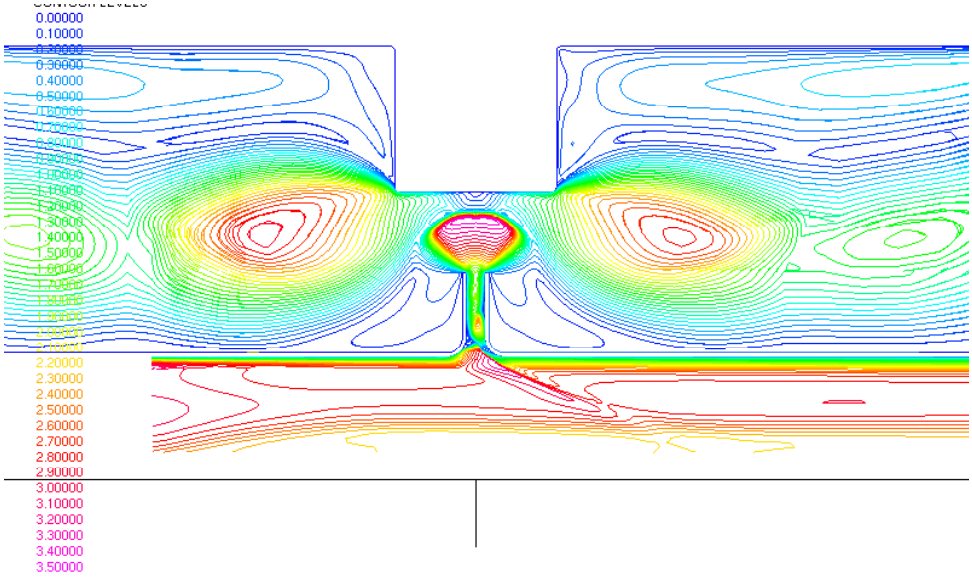

Figure 5.3.6-114 Mach contours for the 5" separation case

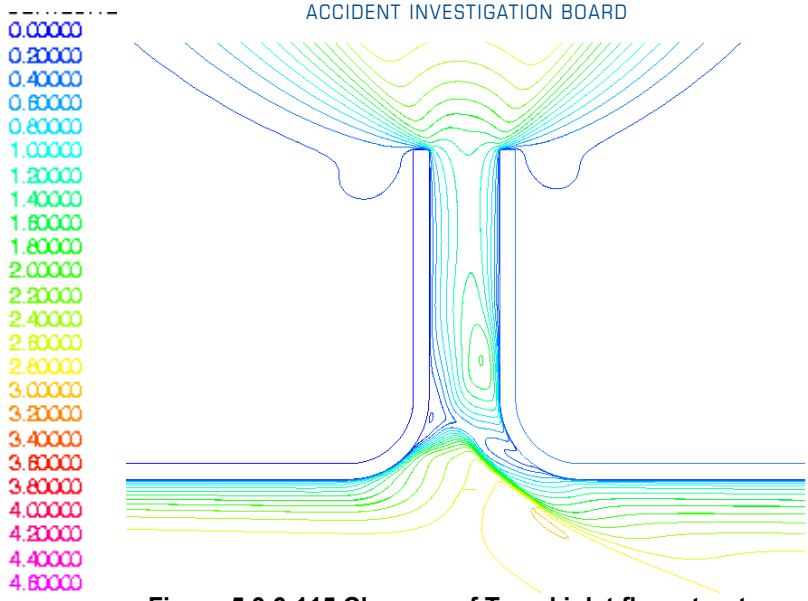

Figure 5.3.6-115 Close up of T-seal inlet flow structure

5.3.6.2.2 Rocketdyne 2-D T-Seal solution

5.3.6.2.2.1 Case description

The objective of the Rocketdyne 2-D CFD analyses was to compute convective heating rates on the RCC T-seal cavity and rib channel areas as well as on the spanner beam insulation directly behind the T-seal (RCC 8/9 "earmuff"). The motivation for these analyses was to create a "bridge" between the unit physics validation problems and the full 3-D failure scenario simulations. The experience obtained from these analyses was intended to improve the understanding of the flow field and heat transfer mechanisms applicable within the T-seal cavity and on the earmuff. The experience gained would be directly applied to constructing the models for 3-D failure scenarios. In order to obtain solutions in a timely manner and break down the complexity of the problem further, a two-phase approach was implemented for the 2-D analyses. The first phase examined only the external surface, T-seal cavity, and rib channel flow fields and heat fluxes. The second phase expanded upon the first phase to examine the flow field inside the RCC panel cavities and the heat fluxes the earmuff would be subjected to.

5.3.6.2.2.2 Grid/Solution development

A planar cut of the RCC T-seal cavity on the underside of the wing provided the geometry used to generate the grid. The cut was made through a Pro-E subassembly of RCC panels 8 and 9. A sketch of the flow domain and subassembly are shown below in Figure 5.3.6-116. External LAURA CFD solutions helped determine the appropriate placement of the planar cut to ensure that the flow was mostly perpendicular to the edge of the T-seal.

The grids for both phases were block structured and created using the Boeing APPT system. In the first phase, a dummy "dump" zone was added to the grid at the end of the T-seal rib channel to improve convergence time. The wall spacing used was 1.0e-4 in., and the grid was "wrapped" around the external surfaces and T-Seal cavity to maintain a consistent grid clustering normal to the walls. The phase I grid consisted of four zones, contained 38, 788 cells, and is shown in Figure 5.3.6-117.

The second phase grid was more or less identical to the first phase grid over the external region, T-Seal cavity, and rib channel, but several zones were created to replace the dump zone with a representation of the RCC panel internal geometry. Dimensions for the earmuff and some other geometrical information were extracted from the sketch in Figure 5.3.6-116 as well as the 2-D grid discussed in Sec. 5.3.6.2.1. Consequently, the representation of the wing leading edge internal geometry is not exact. Furthermore, the earmuff is modeled with sharp corners. This does not correspond to the actual geometry and does have an appreciable affect on the heat transfer as discussed in the results section below. The geometry, however, is good enough to provide a feel for the flow field and heat transfer. The outflow areas of the grid for phase II were expanded to include "dump" regions to allow the application of constant pressure boundary conditions. The wall spacing used was 1.0e-4 in. It should also be noted that the grid

coordinate system for phase II was different from that of phase I although this has no effect on the results. The phase II grid consisted of seven zones, contained 115,355 cells, and is shown in Figure 5.3.6-118.

For both phases of the 2-D analyses, solutions were obtained using the USA structured solver. Fully laminar flow was assumed based on the extremely low Reynolds numbers present. In phase I, Liu-Vinokur equilibrium air thermochemistry and Tannehill transport properties were used. In phase II, a finite rate thermochemistry model with five species and seventeen reactions was used and fully catalytic walls were assumed. The transport properties were determined using Sutherland's law. Additionally, a laminar Schmidt number of 0.52 was used. Also, for both phases of the 2-D analyses, the CFD Condition 1 trajectory point data provided the freestream conditions, and the external LAURA flow solution established the external flow boundary conditions. Three different wall temperature boundary conditions for the RCC external walls (2900° R – STS-5 nose temperature, 3523° R – approximate RCC coating loss temperature, and 5273° R – approximate RCC oxidation temperature) were run in both the first and second phases to obtain a "database" of wall heat fluxes versus temperature and wall location. In the second phase, a 3000°R boundary condition was applied to the earmuff wall. This specific temperature was chosen because it was assumed there was enough heating on the earmuff surface to melt the material and that insulation material has an external layer of Inconel, which has a melting point of 3000° R. The "databases" created by these analyses were intended to aid any subsequent radiation analyses. Furthermore, three different cavity backpressure values were set at the end of the extended outflow region (Cp = 0.02, Cp = 0.06, and Cp = 0.10) for phase II, while the phase I outflow condition was set to be supersonic outflow. In phase I, the convergence criterion was to drive the net fluxes to steady state. Phase II retained that same criterion, but also added another – steady state heat flux on the earmuff windward surface.

5.3.6.2.2.3 Results

5.3.6.2.2.3.1 Major flow structure comments

Figure 5.3.6-119 shows all the major flow structure features of interest from the phase I solutions. The image is for the 2900° R solution – all the other flow fields are similar in nature so only data from the 2900° R solution is presented. There are changes to the flow field with temperature, but the effects are negligible. There is a high degree of internal/external flow coupling and all of the captured flow is from the external boundary layer. Large recirculation regions exist in the T-Seal cavity corners, as is expected for laminar flow. There is also a "bow shock" on the downstream side of the T-Seal cavity as the flow in the boundary layer turns and hits the T-Seal rib cavity walls. Of particular interest is the aerodynamic throat in the T-Seal channel that is formed by this bow shock and the separation area on the upstream side of the rib channel. This aerodynamic throat chokes the incoming flow and leads to expanding supersonic flow leaving the rib channel. This, in turn, affects the heat transfer environment inside the RCC cavity.

In phase II of the 2-D analyses, the external flow field changes very little from that obtained in the phase I 2-D analyses. The internal RCC panel flow field structure, however, varies significantly depending upon the backpressure boundary condition chosen. The flow is not, however, particularly sensitive to external or internal wall temperatures. As a result, most of the following discussion focuses on the changes in flow structure arising from different backpressure boundary conditions.

In phase I, it was clearly established that the flow exiting the rib channel would be supersonic based upon an assumed low backpressure within the cavity. The pressure differential between the flow reaching the cavity exit and the RCC cavity backpressure would provide more than enough energy to accelerate the flow to supersonic speeds. Given such circumstances (a backpressure such that Cp <= 0.10), the rib channel flow becomes a supersonic jet fired into the RCC panel cavity, and some sort of plume expansion expected. The results of the phase II analyses showed that the amount of plume expansion in the cavity is closely tied to the cavity backpressure. Consequently, the higher the backpressure, the more mass flow that impinges on the "earmuff" and the larger the expected heat flux on the earmuff windward surface (given that the incoming jet flow does not unchoke). The following six figures (Figure 5.3.6-120 through Figure 5.3.6-125) clearly show the differences in the plume and shock structures of the RCC cavity jet flow as the backpressure varies. All three backpressures exhibit very large-scale separated regions resulting in large-scale constant pressure regions. Such separated regions are, again, expected because of the laminar nature of the flow. Similarly, all three backpressures have a canted stagnation streamline due to the asymmetric flow in the rib channel. In addition, supersonic "tails" develop in the interior of the RCC panel cavity. How those tails impinge upon the interior surfaces changes with the backpressure in a minor

way. Furthermore, those tails turn almost 90° while staying supersonic due to the constant pressure recirculation regions they see on either side of the earmuff.

Figure 5.3.6-120 and Figure 5.3.6-121 demonstrate that low backpressures (Cp = 0.02) result in a large plume expansion. Most of the incoming jet does not impinge on the earmuff, and the normal shock occurs at a considerable distance from the earmuff surface.

Similarly, Figure 5.3.6-122 and Figure 5.3.6-123 show that a slightly higher backpressure (Cp = 0.06) results in as much as a third of the incoming jet impinging on the surface. Furthermore, a complicated shock pattern develops and the normal shock is much closer to the earmuff surface. Unfortunately, the solution on the earmuff seems unsteady and goes through cycles. This adds uncertainty to the validity of any heat flux information that may be extracted. See the discussion in the section below for more detail.

Finally, in Figure 5.3.6-124 and Figure 5.3.6-125 when the highest backpressure is run (Cp = 0.10), all of the incoming jet impinges on the surface. Once again, there is a complicated shock pattern that develops and the standoff distance of the normal shock from the earmuff surface is at a minimum leading one to expect a higher temperature gradient and thus a larger heat flux.

5.3.6.2.2.3.2 Surface heating and pressure comments

The heart of these 2-D analyses is to help determine the heating environments on various internal structures of the orbiter wing and aid the heat transfer analysts by providing them insight into the flow field and heat transfer mechanisms. In the simplest terms, the largest heat fluxes occur where the largest temperature gradients reside. Most often, the largest temperature gradients occur at the geometrical features with the smallest radii (sharp corners, etc.) because more often than not such features thin or destroy the thermal and viscous boundary layers. This trend is observed in both the phase I and phase II results. As mentioned in Section 5.3.6.2, some parts of the geometry were modeled as having sharp corners even though pictures of the actual hardware indicated that the corners are actually rounded. One would expect to over-predict the heat flux at those corners, and indeed, large localized spikes in heat flux do occur in both the phase I and phase II solutions at any geometrical corner or feature with a small radius. Figure 5.3.6-126 shows the arc length coordinate system that is used to describe the positional heat flux along the walls of interest while Figure 5.3.6-127 shows the actual heat flux values along the T-Seal cavity from the Phase I solutions and Figure 5.3.6-128 shows a comparison of the phase I and phase II solutions on the external and T-Seal cavity surfaces. The heat flux predicted in phase II is quite a bit less almost over the entire length of the external, T-Seal cavity and rib channel walls, roughly 55% of the phase I solution. More importantly, except for at the sharp corners and other geometrical features with small radii, it is a consistent. The explanation for most of this difference lies in the different thermochemical and transport models used.

Figure 5.3.6-129 presents the heat flux predictions on the surface of the earmuff. Note the sharp spikes in heat flux at the sharp corners of either side of the top surface of the earmuff due to the thinning of the thermal boundary layer. There was a problem, however with the data obtained on the earmuff windward surface. For a backpressure of Cp = 0.06 (and probably Cp = 0.10), even though the solution seemed to have converged, there was a slow oscillation in the position and magnitude of the peak heat flux and pressures on the earmuff surface. In order to explain this discrepancy, the solver was allowed to run through twenty cycles (800 time steps each) of this oscillation. The data from the twentieth such cycle is shown in Figure 5.3.6-130. As is easily visible, the oscillation is not trivial and leads to a great deal of uncertainty in the results for $Cp \geq 0.06$. Even more unsettling is the fact that there is 13-fold change in the peak heat flux during the oscillations. This behavior points to unsteady behavior in the flow.

In summary, the Phase I and Phase II bridging problems provided a wealth of useful information and helped troubleshoot the CFD process for implementing full 3-D failure scenarios.

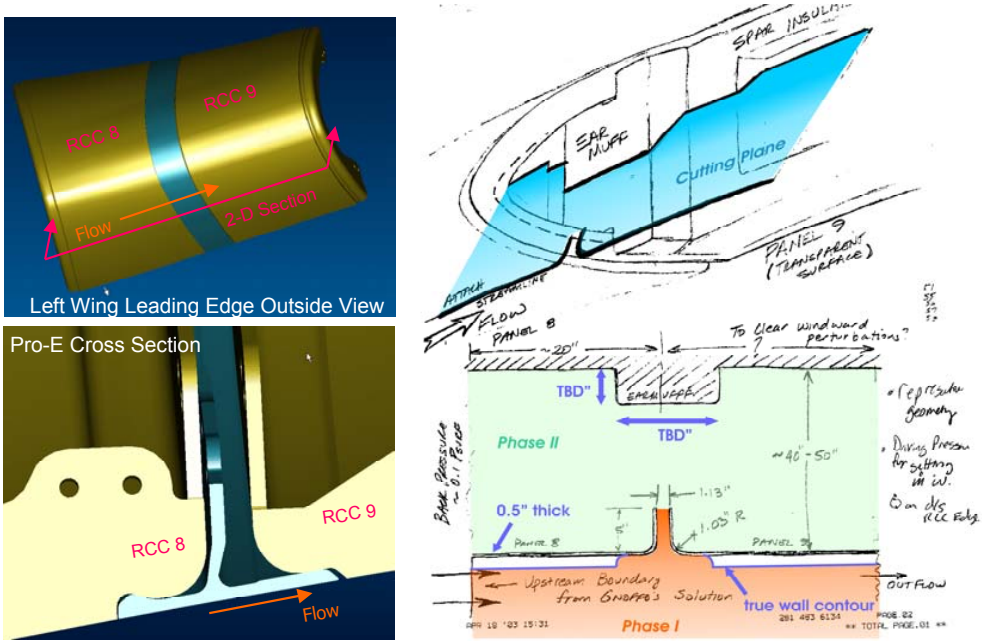

Figure 5.3.6-116 Assumed geometry and 3-D Pro/E subassembly

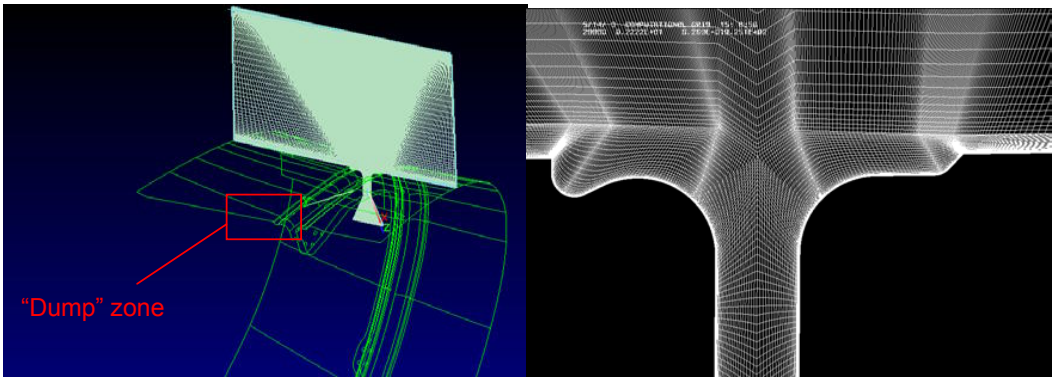

Figure 5.3.6-117 Phase I grid

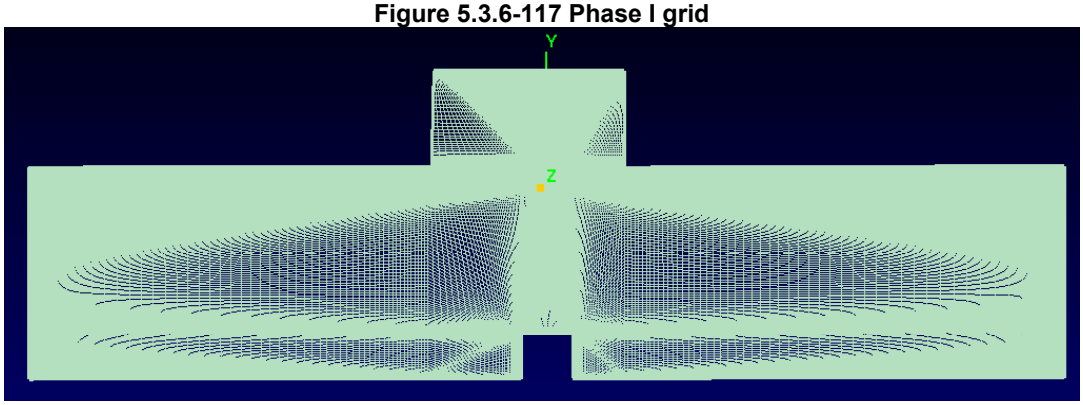

Figure 5.3.6-118 Phase II Grid

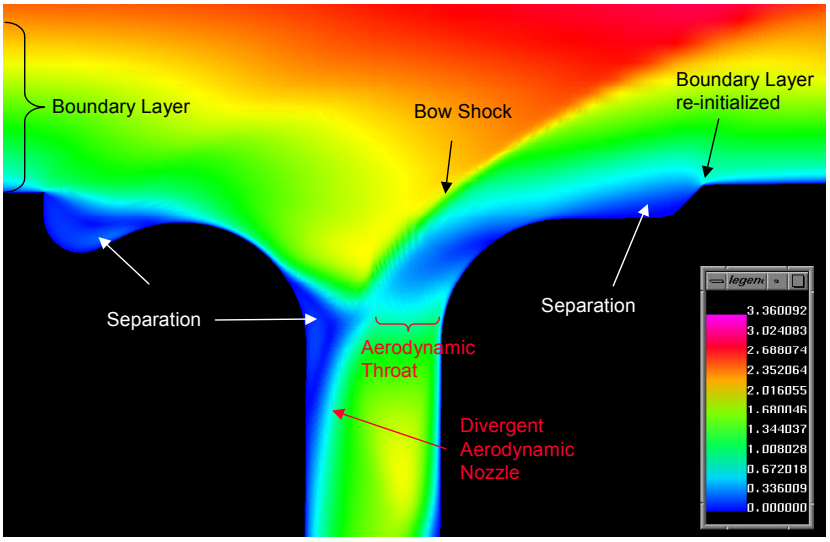

Figure 5.3.6-119 Mach Contours for T = 2900°R, phase I

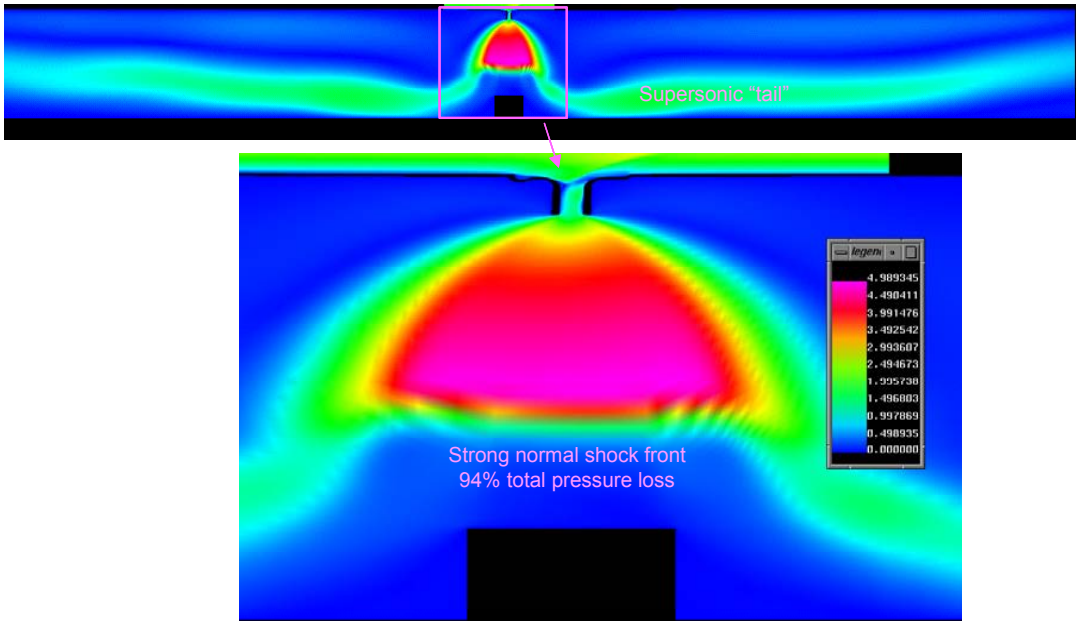

Figure 5.3.6-120 – Mach Contours for T = 2900°R and Cp = 0.02, phase II

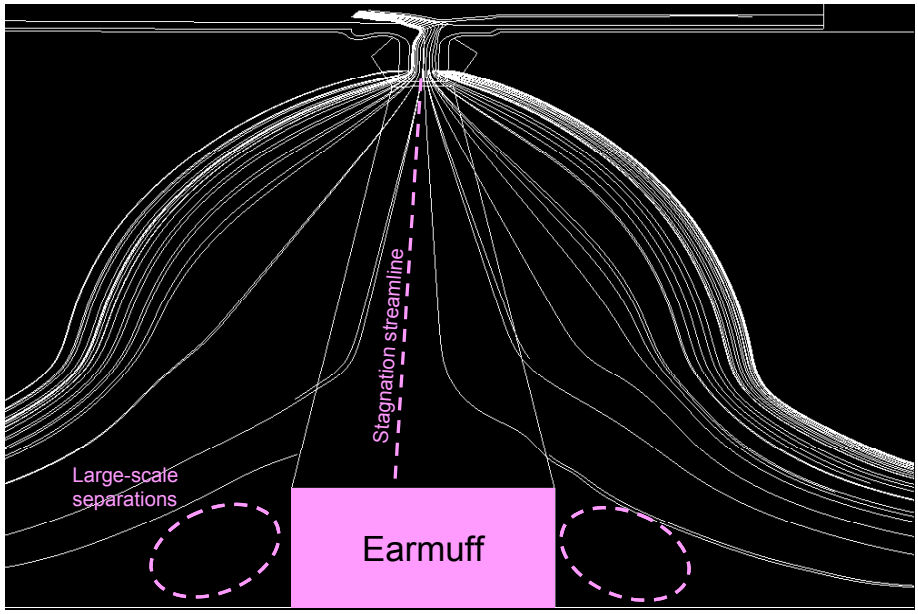

Figure 5.3.6-121 Streamlines for T = 2900°R and Cp = 0.02, phase II

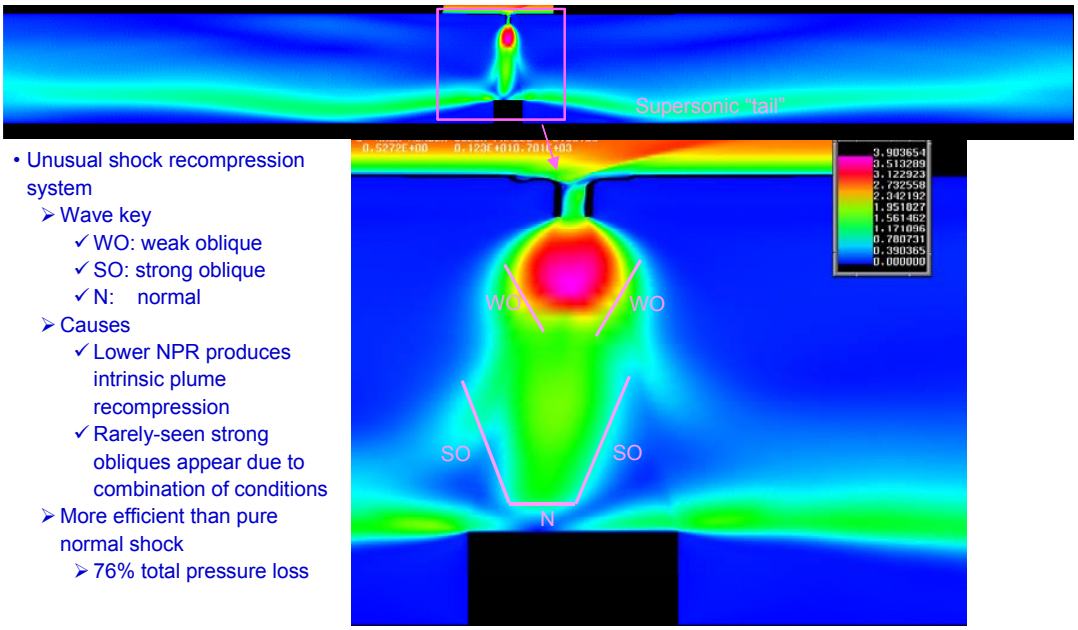

- Unusual shock recompression system
  - Wave key
    - ✓ WO: weak oblique
    - ✓ SO: strong oblique
    - ✓ N: normal
  - Causes
    - ✓ Lower NPR produces intrinsic plume recompression
    - ✓ Rarely-seen strong obliques appear due to combination of conditions
  - More efficient than pure normal shock
    - 76% total pressure loss

Figure 5.3.6-122 – Mach contours for T = 2900°R and Cp = 0.06, phase II

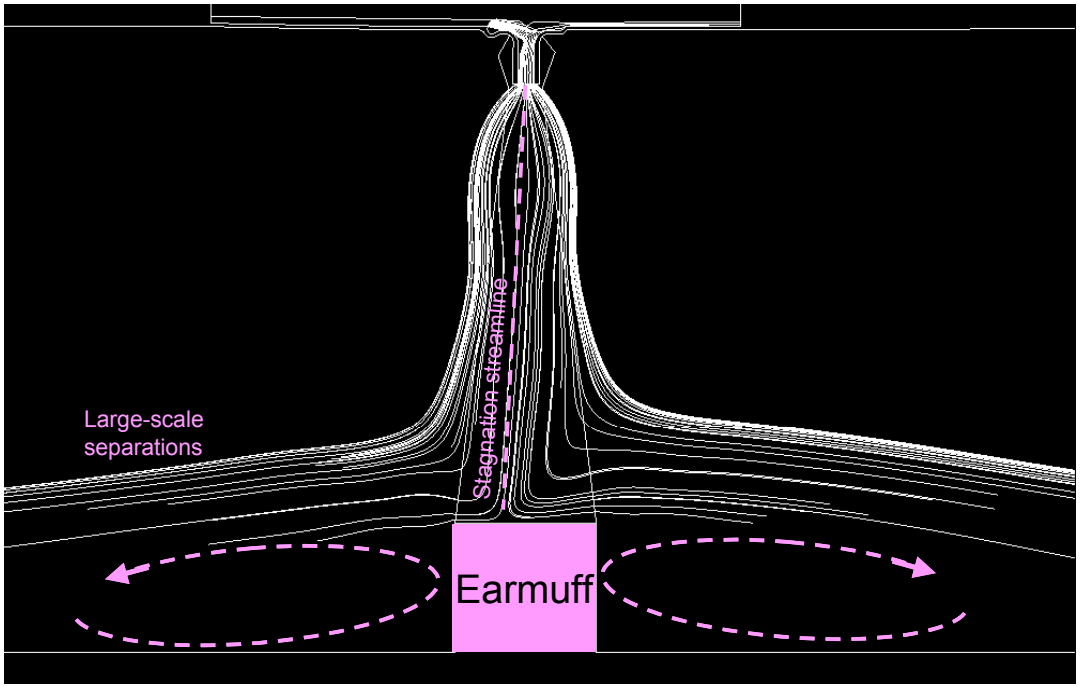

Figure 5.3.6-123 Streamlines for T = 2900°R and Cp = 0.06, phase II

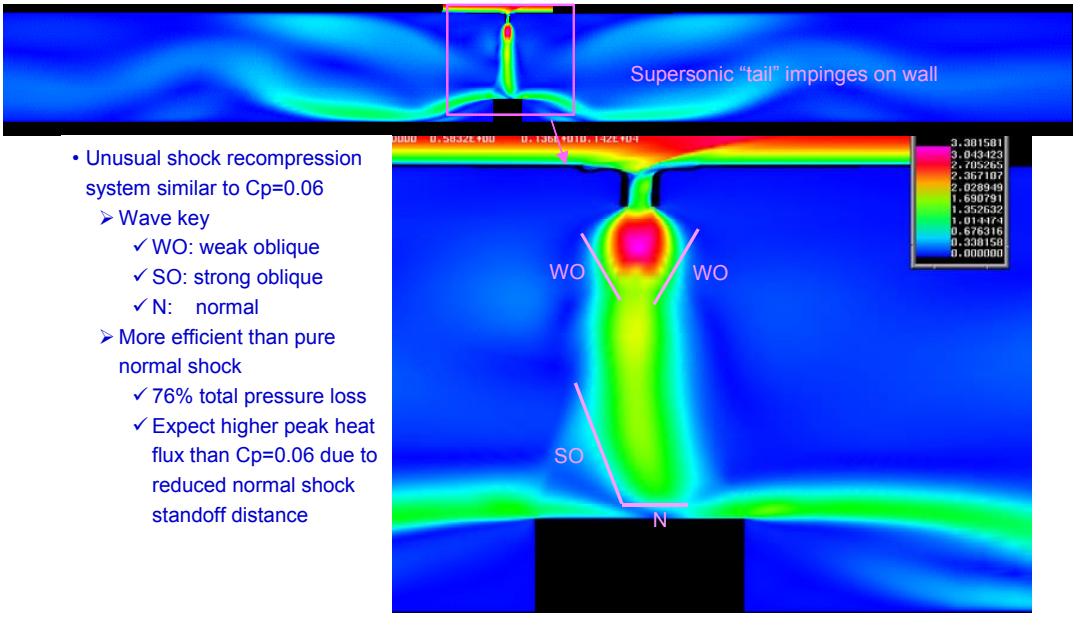

Figure 5.3.6-124 Mach contours for T = 2900°R and Cp = 0.10, phase II

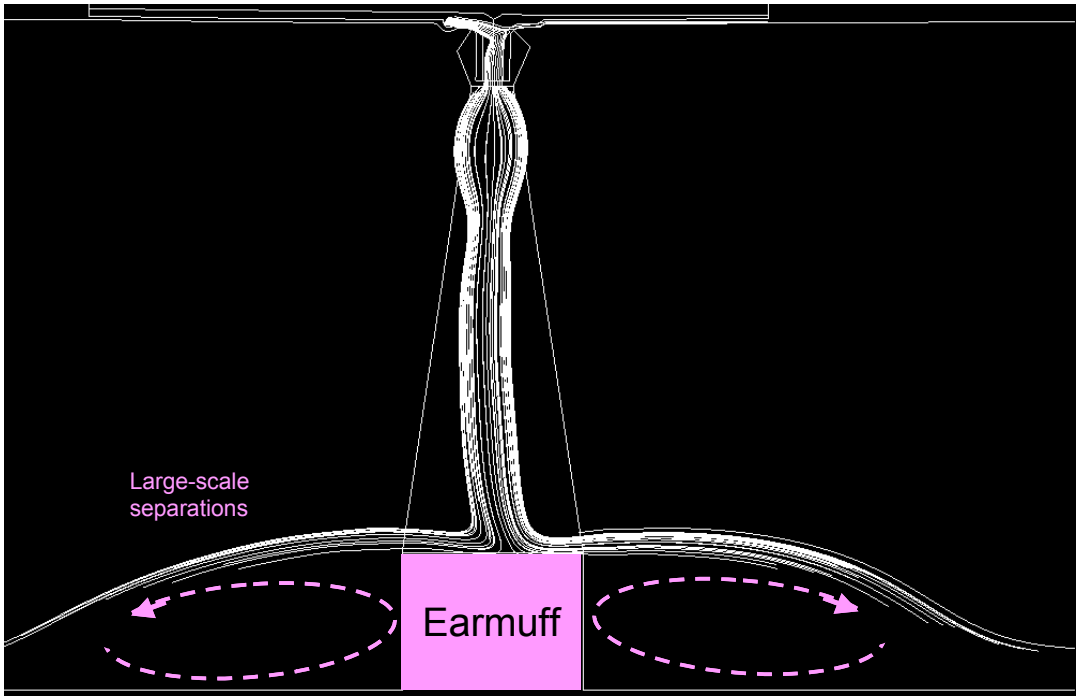

Figure 5.3.6-125 streamlines for T = 2900°R and Cp = 0.10, phase II

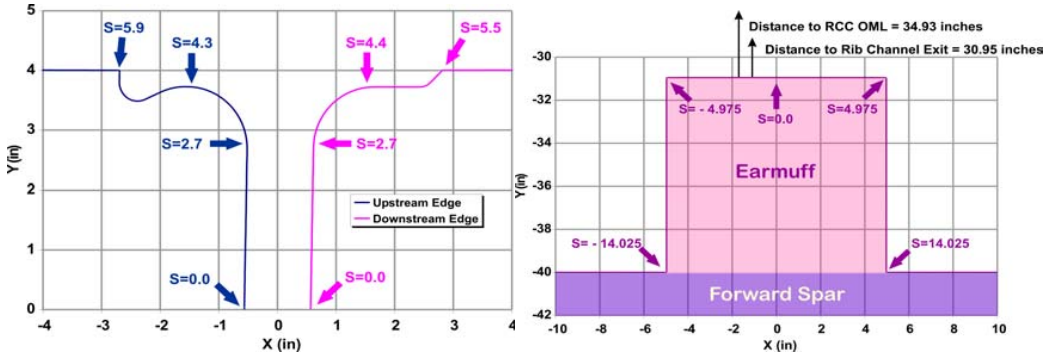

Figure 5.3.6-126 Arc length coordinate systems, phase I & II

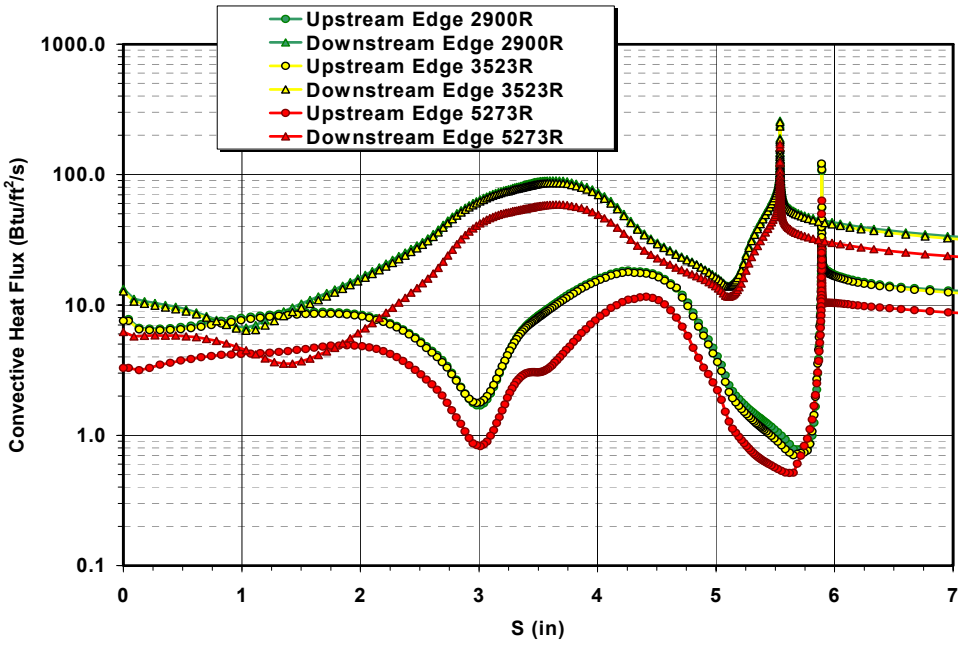

Figure 5.3.6-127 Convective heat flux on T-seal Cavity Surfaces, phase I & II

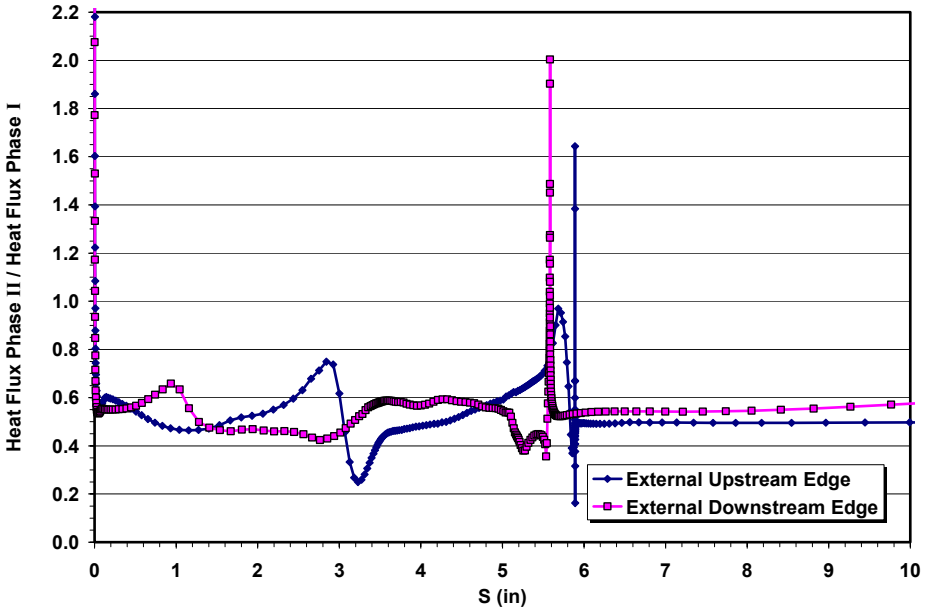

Figure 5.3.6-128 Phase I and phase II Comparison of T-seal Cavity Convective heat flux, T = 2900°R

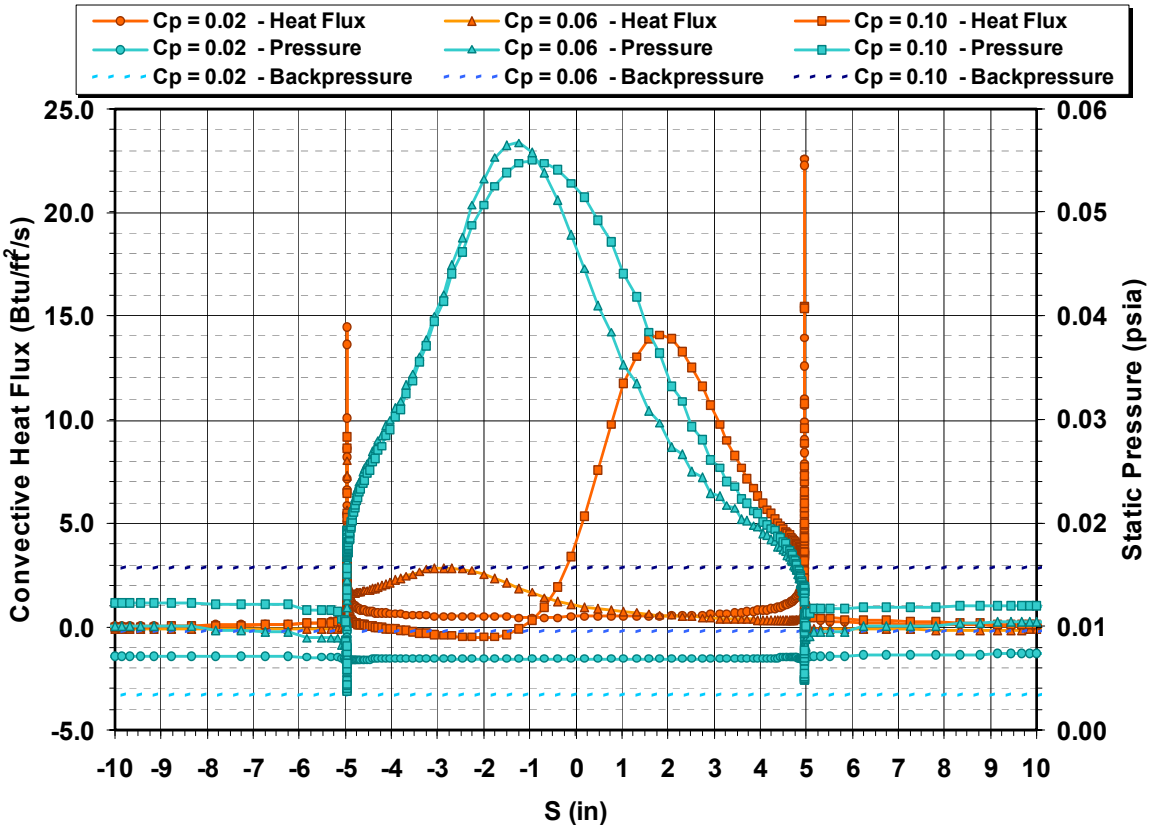

Figure 5.3.6-129 Earmuff Convective heat flux for T = 3000°R and Back-pressures, Phase II

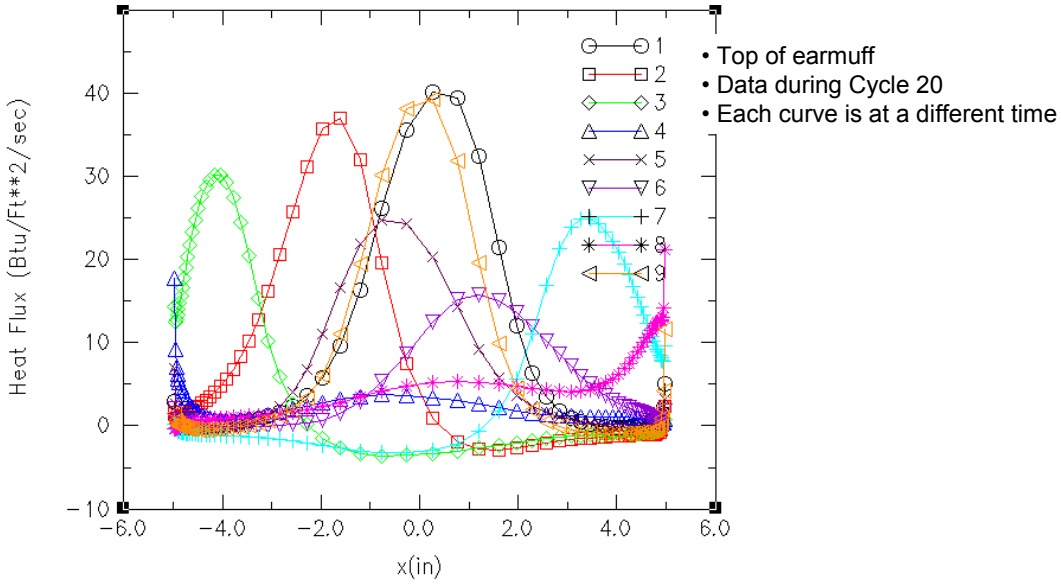

Figure 5.3.6-130 Earmuff Heat Flux Distribution Unsteadiness, phase II

5.3.6.2.3 BHB 3-D Panel 8/9 T-seal Damage

5.3.6.2.3.1 Case Description

T-seal damage between RCC Panels 8 and 9 was also one of the scenarios considered. This numerical study conducted with the USA flow solver at Boeing, Huntington Beach modeled a rectangular opening of 8" by 1.13" between the ribs of RCC Panels 8 and 9 on the windward side approximately 8" from the aft end of the lower carrier panel. This simulation included the ribs and the earmuff insulation between RCC Panels 8 and 9.

5.3.6.2.3.2 Geometry and Grid Definition

The external surface grid is illustrated in Figure 5.3.6-131, Figure 5.3.6-132 and Figure 5.3.6-133. Figure 5.3.6-134 and Figure 5.3.6-135 show the surface grid for the internal leading edge cavity. The volume grid was generated such that the wall spacing is 0.0005 inch to ensure the cell-Reynolds number of 1 or less near the surface. Solutions with both 2 and 15 million grid cells were generated.

5.3.6.2.3.3 Boundary Conditions

This equilibrium air chemistry simulation was conducted at the CFD Point 1 flight condition corresponding to 404 seconds after entry interface. The RCC interior surfaces were kept at 0° F, whereas for the Orbiter exterior surfaces a radiation equilibrium temperature boundary condition was applied.

5.3.6.2.3.4 Results

The flow field pressures are shown in Figure 5.3.6-136 and Figure 5.3.6-137 for chordwise and spanwise vertical cuts, respectively, through the T-seal damage. The corresponding Mach number distributions are illustrated in Figure 5.3.6-138 and Figure 5.3.6-139. The surface pressure and heating on the earmuff and the ribs in the vicinity of the T-seal damage are illustrated in Figure 5.3.6-140 and Figure 5.3.6-141 for the 2 million-cell model simulation. Similarly, Figure 5.3.6-142 and Figure 5.3.6-143 present the pressure and heating distributions for the 15 million-cell model simulation. The 15-million cell model results show as high as twice the heating levels, compared to the 2 million-cell model. The jet in this case acts like a wall-jet right next to the earmuffs.

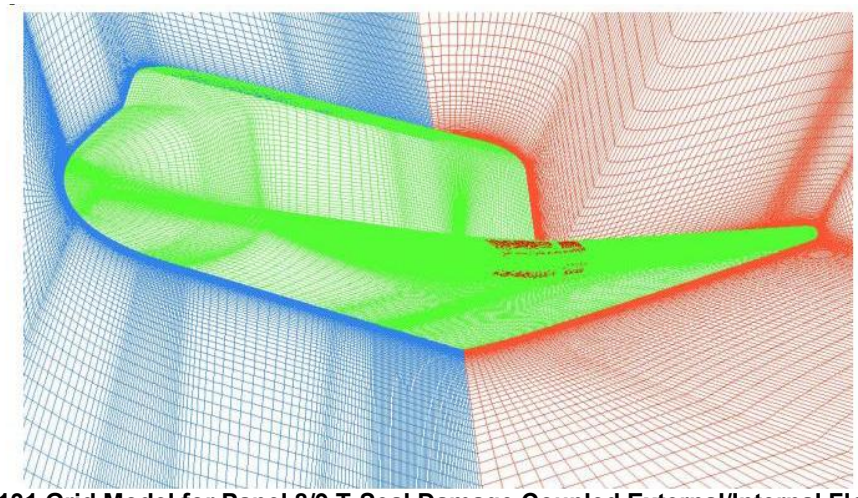

Figure 5.3.6-131 Grid Model for Panel 8/9 T-Seal Damage Coupled External/Internal Flow Simulation

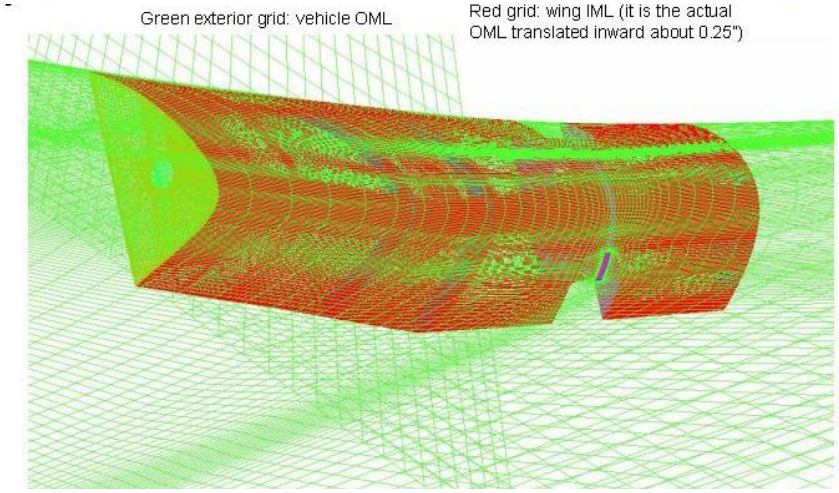

Figure 5.3.6-132 Grid Model for Panel 8/9 T-Seal Damage Coupled External/Internal Flow Simulation

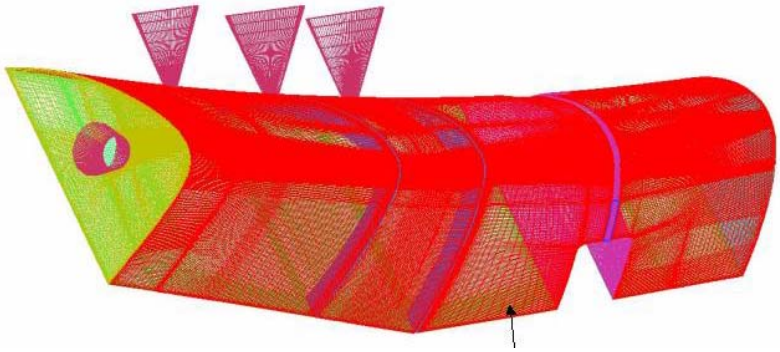

Figure 5.3.6-133 Grid Model for Panel 8/9 T-Seal Damage Coupled External/Internal Flow Simulation

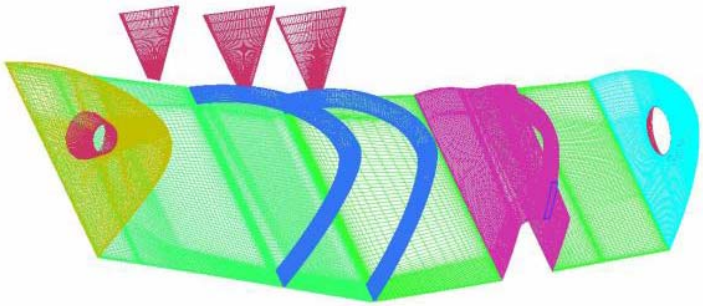

Figure 5.3.6-134 Grid Model for Panel 8/9 T-Seal Damage Coupled External/Internal Flow Simulation

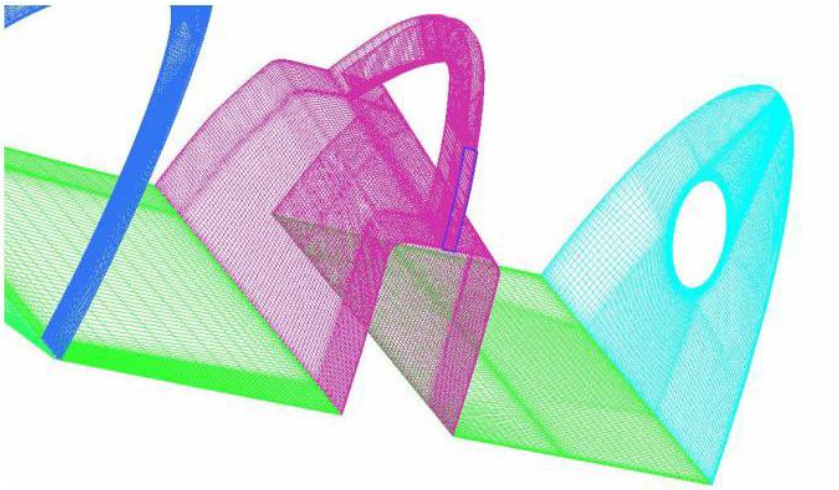

Figure 5.3.6-135 Grid Model for Panel 8/9 T-Seal Damage Coupled External/Internal Flow Simulation

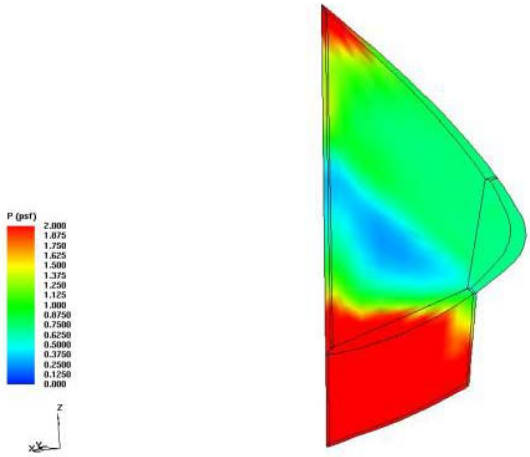

Figure 5.3.6-136 Pressure Contours from Panel 8/9 T-Seal Damage Coupled External/Internal Flow Simulation (15 million-cell Model; Postprocessed using every other points)

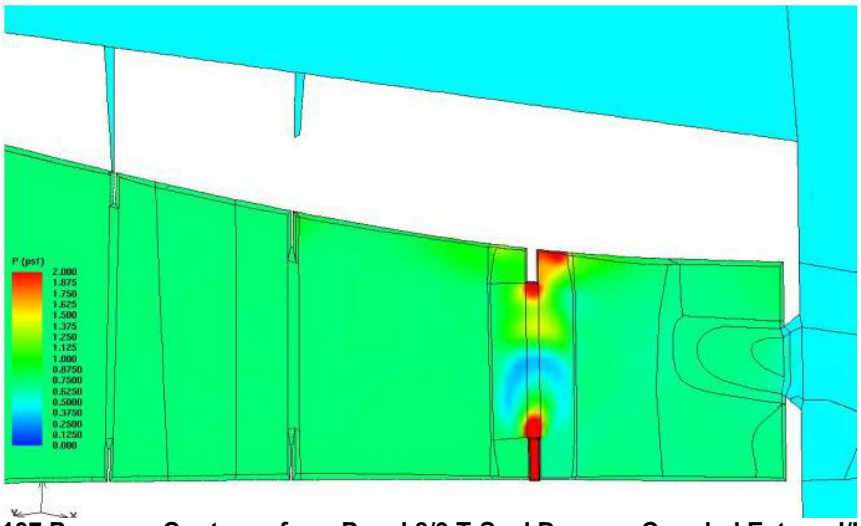

Figure 5.3.6-137 Pressure Contours from Panel 8/9 T-Seal Damage Coupled External/Internal Flow Simulation (15 million-cell Model; Postprocessed using every other points)

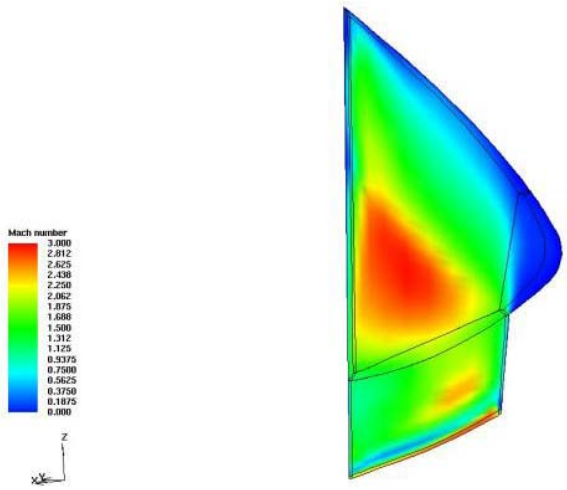

Figure 5.3.6-138 Mach Contours from Panel 8/9 T-Seal Damage Coupled External/Internal Flow Simulation (15 million-cell Model; Postprocessed using every other points)

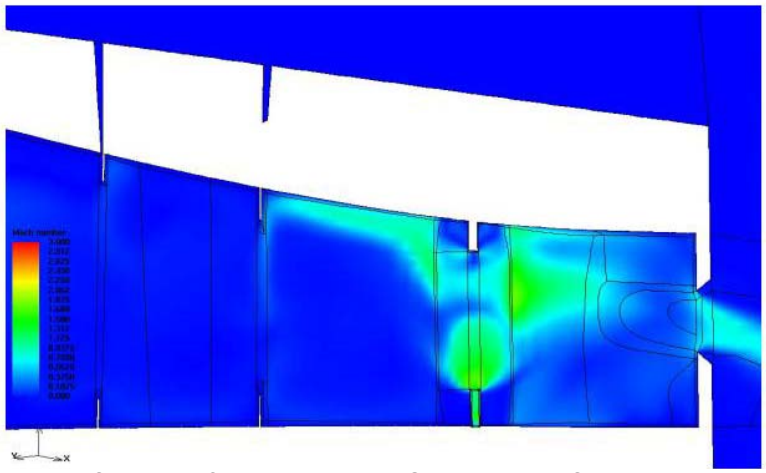

Figure 5.3.6-139 Mach Contours from Panel 8/9 T-Seal Damage Coupled External/Internal Flow Simulation (15 million-cell Model; Postprocessed using every other points)

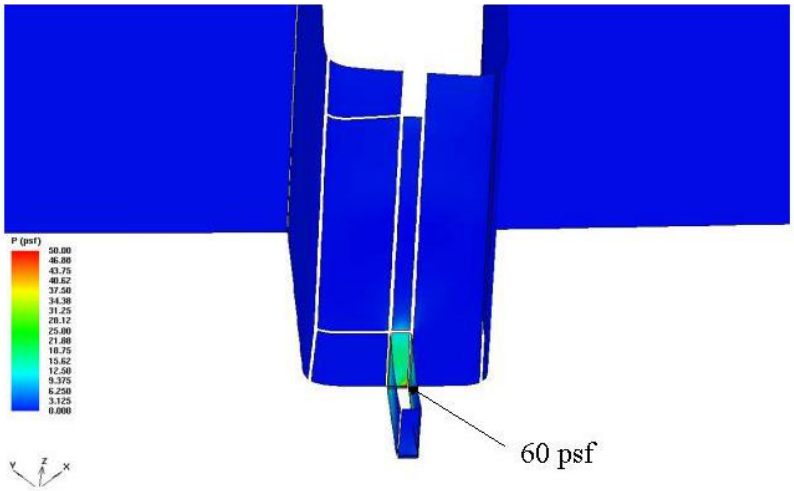

Figure 5.3.6-140 Pressure Contours on Earmuff Insulation and Rib Channel from Panel 8/9 T-Seal Damage Coupled External/Internal Flow Simulation (2 million-cell Model)

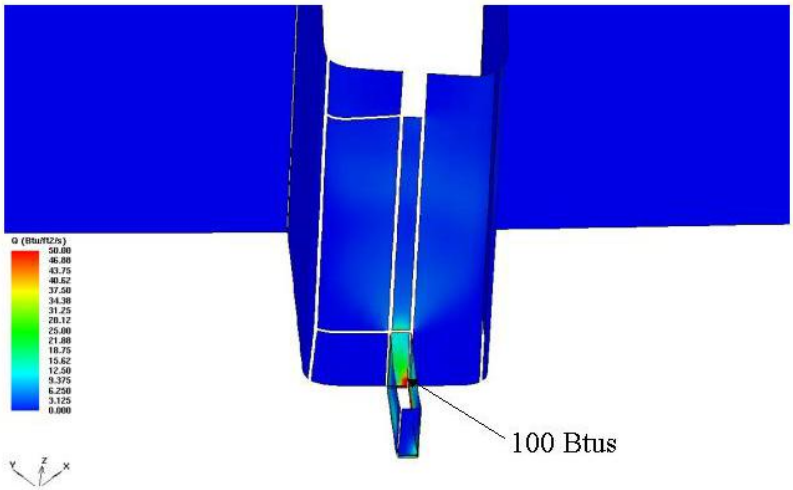

Figure 5.3.6-141 Heating Contours on Earmuff Insulation and Rib Channel from Panel 8/9 T-Seal Damage Coupled External/Internal Flow Simulation (2 million-cell Model)

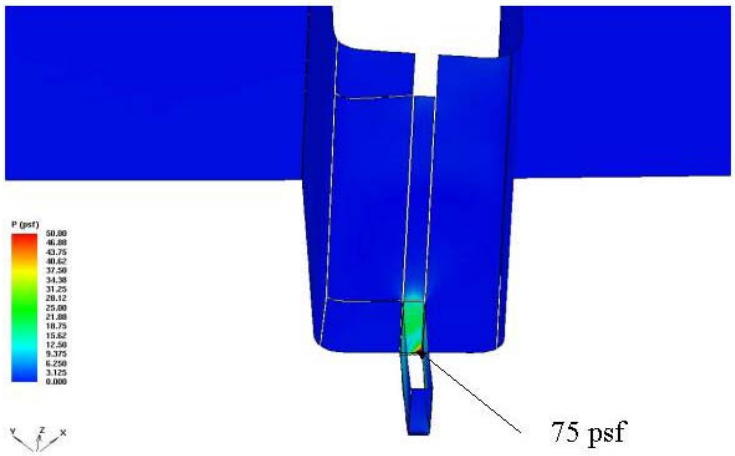

Figure 5.3.6-142 Pressure Contours on Earmuff Insulation and Rib Channel from Panel 8/9 T-Seal Damage Coupled External/Internal Flow Simulation (15 million-cell Model)

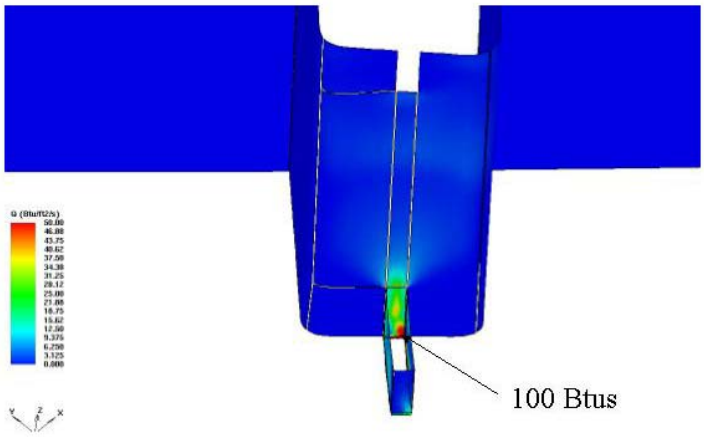

Figure 5.3.6-143 Heating Contours on Earmuff Insulation and Rib Channel from Panel 8/9 T-Seal Damage Coupled External/Internal Flow Simulation (15 million-cell Model)

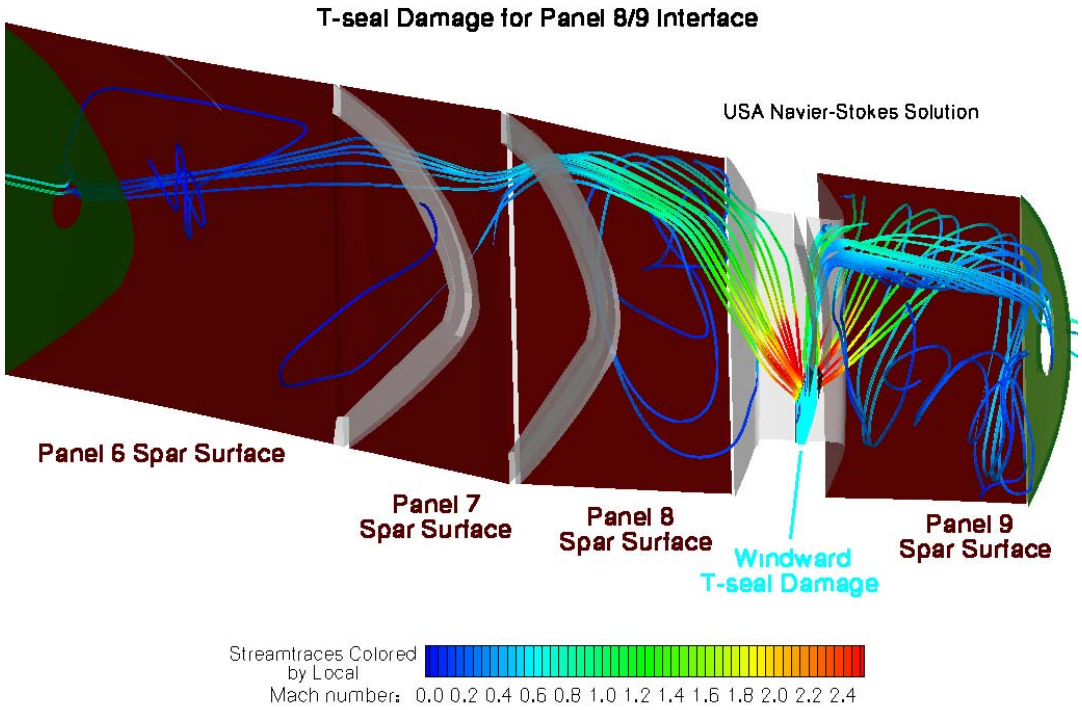

Figure 5.3.6-144 BHB Panel8/9 T-seal Damage Internal Streamtraces

5.3.6.2.4 BRPP 3-D Panel 8/9 Damaged T-Seal Solution

5.3.6.2.4.1 Case Description

The first objective of this effort was to compute convective heating rates on key surfaces of the Leading Edge Structural Subsystem (LESS) for the scenario of a damaged T-Seal in the RCC 8/9 location. These included:

- RCC T-Seal
  - Cavity
  - Rib channel
- Internal insulation units:
  - Forward spar insulator units (hot tubs)
  - Spanner Beam Insulator units (earmuffs)

The T-Seal damage was assumed to be a piece missing from the intersection of the T-Seal and the lower edge of the earmuff to the geometric leading edge as shown in Figure 5.3.6-145.

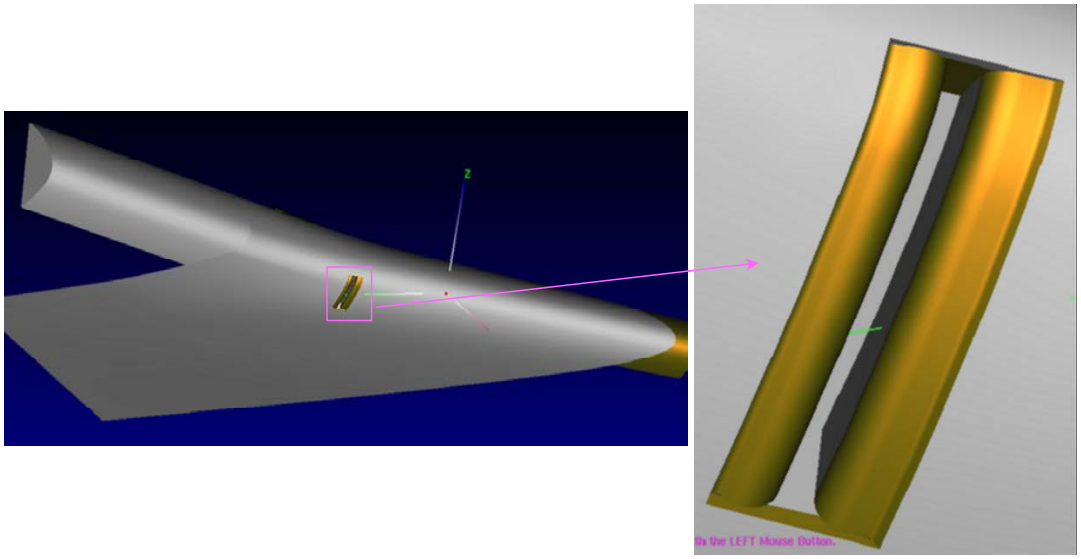

Figure 5.3.6-145 – Damaged T-Seal Geometry

The intended application of the data was to enhance the engineering heat transfer models and to improve understanding of this flow field structure. The second objective of this effort was to construct an accurate CAD model of the LESS components that would serve as a universal model usable for all types of multidimensional analysis via IGES export. This would possess clean, "watertight", trimmed surfaces for import to modeling software.

5.3.6.2.4.2 Grid/Solution Development

The universal CAD model was constructed with the Pro/Engineer parametric CAD system. Sources for geometry included imported CAD models for the RCC panels, forward wing spar, and RCC attachment brackets. Design specifications combined with photographs were used for the earmuffs, hot tubs, and wick insulators. No detailed drawings for the latter three components have been located to date. The model has been completed however issues precluded its use for CFD grid generation. The imported RCC parts were too complex for analysis use. They contained over 1,000 surfaces per RCC panel as well as duplicate surfaces. In addition, the model architecture requires a large amount of prep work prior to export for analysis grid generation due to the grouping of surfaces with solids. It was anticipated that an additional 1-2 weeks would be required to complete this task. A fallback plan was implemented in which development of the universal CAD model would continue, while the NASA JSC-based model for internal region used in for the 10" Leading Edge Breach would be modified for use in this analysis. The T-Seal channel geometry was extracted from the Pro/E CAD model and integrated into the JSC model (Figure 5.3.6-145). As discussed in Section 5.3.6.1.4, the JSC model included the RCC 7/8, 8/9, 9/10 earmuffs and the hot tubs in between them. The negative aspect of this model was that all of the edges were sharp, which conflicted with other models and photographs. Dimensions of key components, such as the earmuffs and hot tubs, were also somewhat uncertain since the JSC dimensions conflicted with a model used by Boeing Huntington Beach and some photographs.

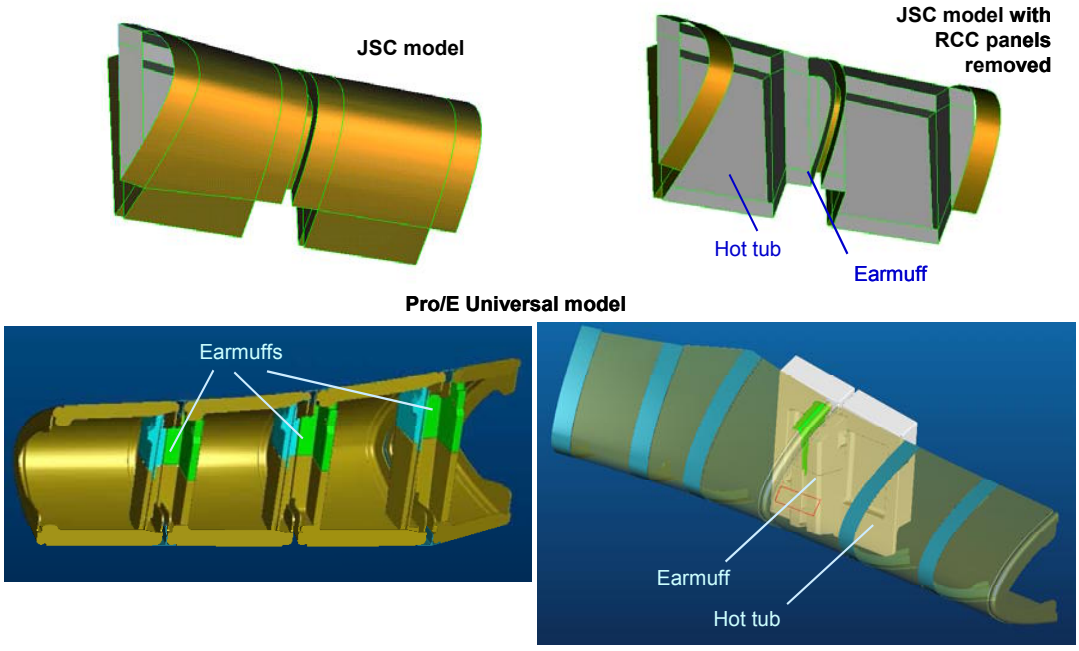

Figure 5.3.6-146 – Internal Region Geometry Models

The JSC and the Pro/E Universal model are compared in Figure 5.3.6-146. Extruded "dump" regions were added on either side of RCC 8 and 9 to enable the application of constant pressure outflow boundary conditions. The dimensions of these regions were based on the results of the 2-D T-Seal analysis of Sec.5.3.6.2.2.

Previous analyses had shown that a high degree of coupling existed between the internal and external flow fields. A NASA LaRC LAURA external flow solution was used to provide the necessary coupling, but only a small three-zone portion of it. This was carefully selected to reduce the size of the model while preserving the external solution in the region of interest (Figure 5.3.6-147). Not all of Zone 36 was required so it was sectioned with a cutting-plane interpolation.

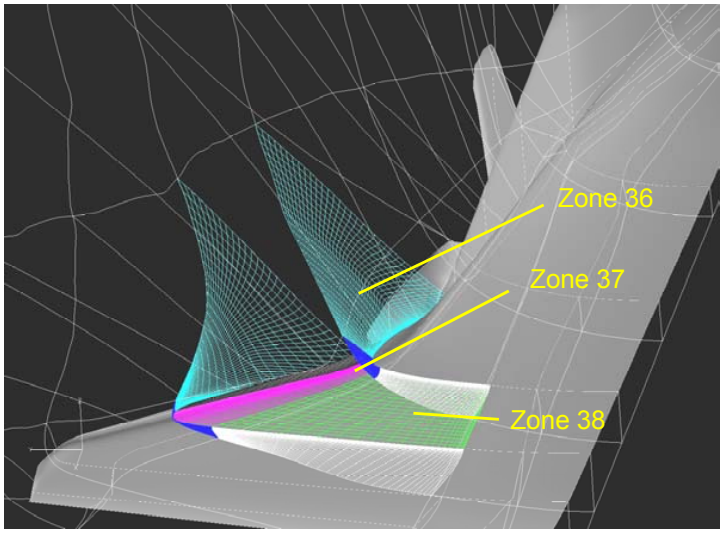

Figure 5.3.6-147 - LAURA Solution Zones Used as External Domain

The Boeing APPT system was used to generate the hybrid viscous unstructured computational grid. The unstructured approach greatly reduces the time required to generate the grid and eliminates wasted clustering cells in complex internal regions. After a number of revisions, final grids (Figure 5.3.6-148) were produced containing 4.1M elements with a wall spacing of $1.0e^{-4}$ inches, and 5.7M elements with a wall spacing of $1.0e^{-5}$ inches. Results from the 2-D T-Seal analysis (Sec. 5.3.6.2.2) along with a cardboard model and discussion among compressible flow experts were used to determine the clustering of elements in the internal region.

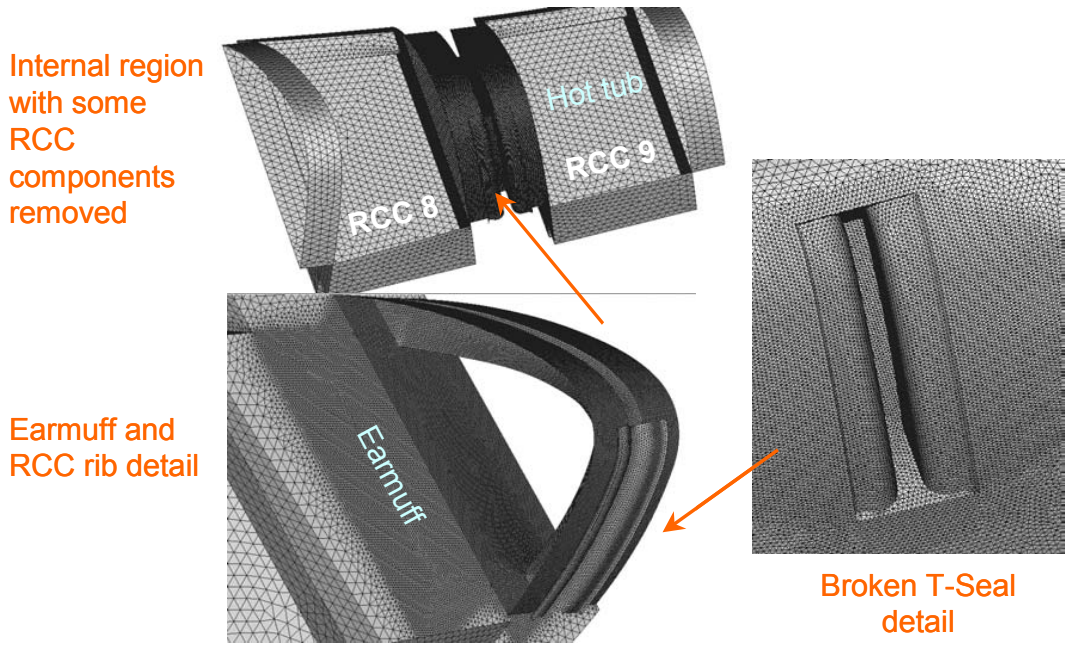

Figure 5.3.6-148 – Hybrid Viscous Unstructured Grid

The solutions were obtained using the Boeing ICAT code. Fully laminar flow was assumed based on the extremely low Reynolds numbers present. Liu-Vinokur equilibrium air thermochemistry and Tannehill transport properties were used. The convergence criteria were to drive net fluxes to an initial steady-state and also to drive integrated heat load in key areas to steady-state. Contours of heat flux in key areas were also plotted at different time steps.

The CFD Condition 1 trajectory point was used to define the freestream conditions. All wall temperatures were set to 3,000º R. This corresponds to the melting temperature for the Inconel 601 outer layer of the Dynaflex surfaces such as the earmuffs and hot tubs. The pressure on the cavity outflow surfaces was set according to Table 5.3.6.1-1. These values were established from venting analysis. Note that the values have evolved over time as has the venting analysis. The current level of 10.8 psf (517 Pa) is the result of the 2-D T-Seal computations being fed back into the venting analysis.

5.3.6.2.4.3 Results

5.3.6.2.4.4 Major flow structure comments

Figure 5.3.6-149 shows the flow inside the LESS cavity. The walls are colored by static pressure, and the streamlines are colored by Mach number and are launched from the center of rib channel. Subsonic flow is observed exiting the rib channel into the LESS cavity. This is due to the high cavity backpressure of .075 psia vs. ~.060 psia at the rib channel exit. The latter number comes from examination of the T-Seal 2-D solutions (Sec. 5.3.6.2.2) and represents the rib channel exit pressure without the influence of backpressure. Overexpanded laminar flow, such as this, easily separates, and normal shock structures reduce the flow to subsonic and also reduce total pressure. Both of these effects reduce the capability of the flow to generate heat flux on impingement surfaces. The majority of the LESS cavity flow is large-scale subsonic vortices.

Figure 5.3.6-150 shows the flow in the RCC rib channel. Again, the walls are colored by static pressure, and the streamlines are colored by Mach number, however this time they are launched from a boundary layer rake in the external flow. This flow field has features similar to the 2-D T-Seal solutions (Sec. 5.3.6.2.2). These include the aerodynamic throat, the upstream edge separation, and the downstream edge bow shock. Surface pressures are also close to the 2-D solutions.

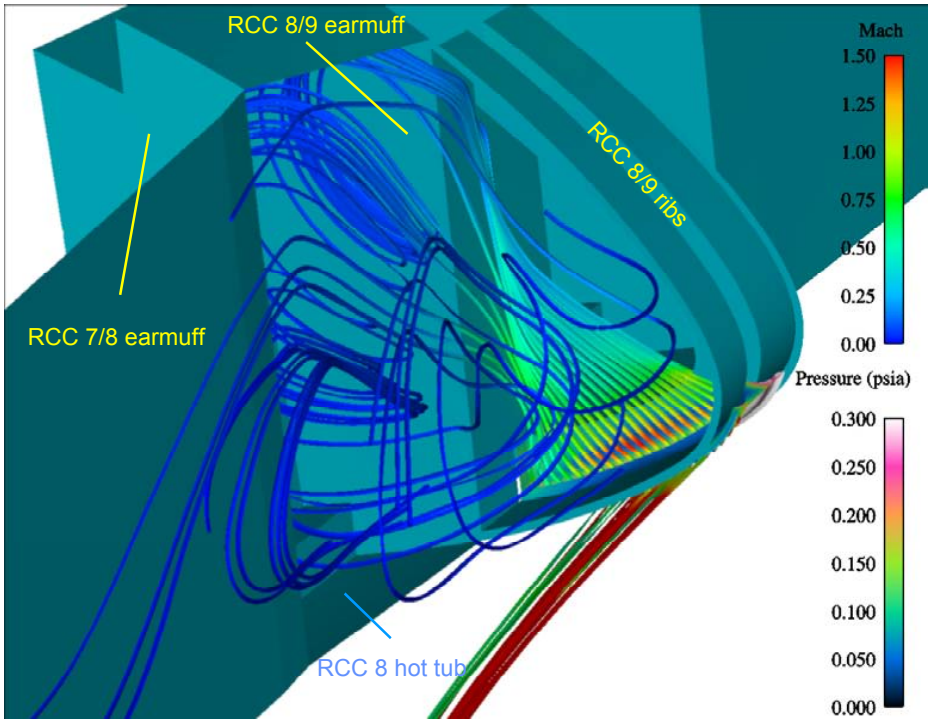

Figure 5.3.6-149 - Mach-colored Cutting Plane and Wall Static Pressure Detail View From in Front of Leading Edge

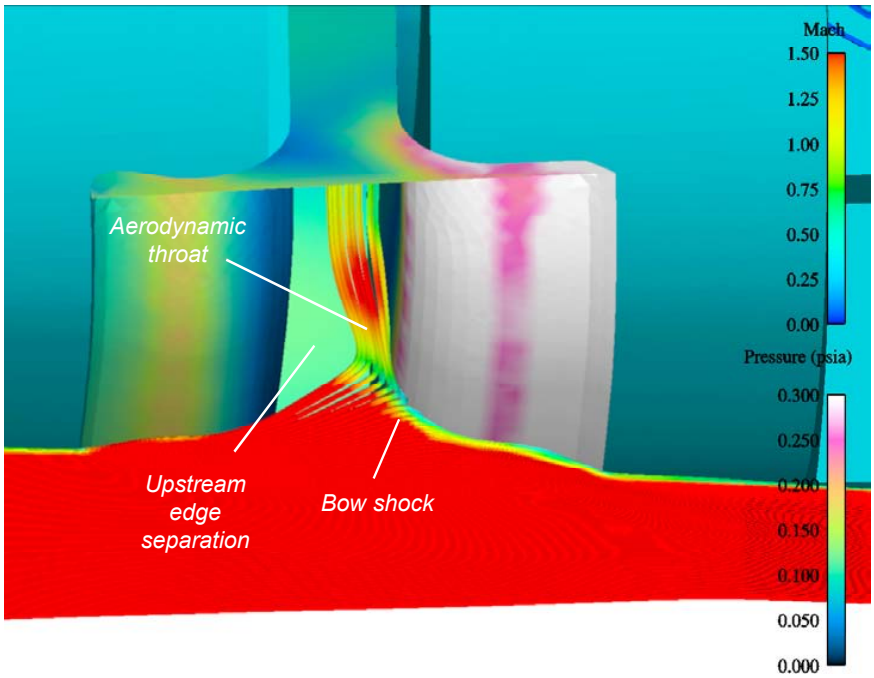

Figure 5.3.6-150 – View Into RCC Rib Channel

5.3.6.2.4.5 Surface heating and pressure comments

Figure 5.3.6-151 shows surface heat flux in the region where the RCC 8/9 earmuff and the RCC 8 hot tub intersect. This is the area of highest heating on the earmuff and hot tub surfaces, as would be expected based on the pressure and Mach fields observed. The levels are low compared to the peaks observed for the 2-D T-seal solution (Sec. 5.3.6.2.2) where supersonic flow is impinging on the earmuff. Heat fluxes in the rib channel closely match the USA 2-D T-Seal solutions (Sec. 5.3.6.2.2). The medium grid solution was run a total of 28,000 time steps. The solution was monitored periodically using flow visualization. No indication of unsteady flow was found, however there is still a possibility that this could occur. Many more time steps would be needed to be certain.

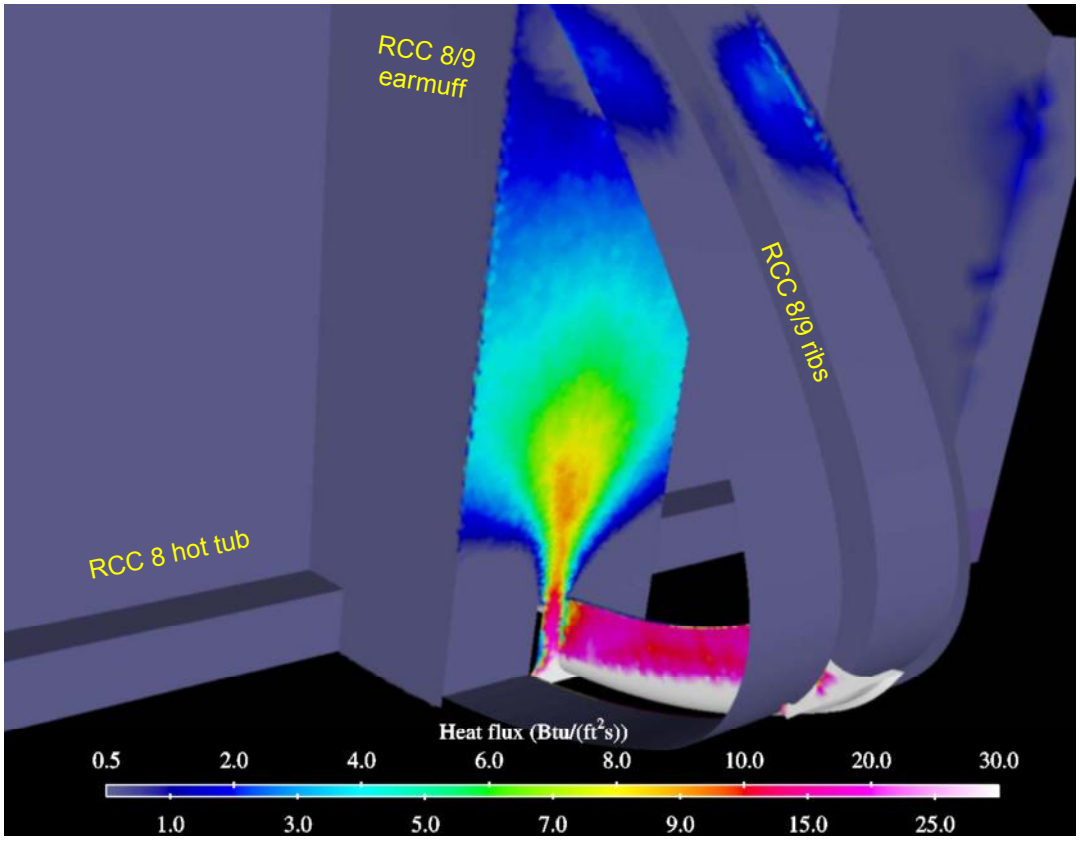

Figure 5.3.6-151 - Surface Heat Flux Detail View From in Front of Leading Edge

5.3.6.3 CFD of Simplified Internal Wing Geometry

5.3.6.3.1 Methodology and Philosophy of "Insight CFD"
CFD was used not only to help characterize fine details in the flow field with large, detailed CFD models, but also to help understand some of the larger scale flow phenomenon. For this purpose a few large scale, simplified models were created to understand the flow patterns once a breach of the internal wing cavity was initiated. These models were primarily used to visualize flow patterns within the wing cavity. They were not relied upon for detailed information such as wall heat fluxes, heat transfer coefficients, surface temperatures, or transient calculations.

Two simplified models were created. The first was a simplified model of the entire left wing aft of the 1040 wing spar and without the wheel well cavity. Wing spar designations are shown in Figure 5.3.6-153 for reference. This model did not include the RCC cavity along the wing leading edge. The purpose of this model was to visualize the flow field within the wing cavity immediately after the leading edge spar breach. This model assumed that the flow coming onto the wing cavity was normal to the spar. The second "insight" CFD model was a 2-D model of the left wing cavity and the RCC cavity. This model was used to visualize the flow through the RCC breach, through the wing spar breach, then into the wing cavity directly outboard of the wheel well. The purpose of this model was to verify whether or not it was possible for the flow to come into the wing cavity normal to the leading edge spar or not.

Models are "simplified" in the sense that only the necessary surfaces needed to characterize the flow field satisfactorily are included. The 3-D wing model has none of the internal circular struts connecting the upper and lower wing surfaces. Only the internal spars and spar vents and the wing upper and lower surfaces are included. The wing upper and lower surfaces were generated based solely on the spar outlines; therefore some of the finer details in the wing curvature were not captured in the models. All walls within the models are smooth walls, which in reality is not the case, particularly in the area of the wheel well walls.

FLUENT 6.1 was the CFD code used to model these simplified geometries. FLUENT 6.1 is a commercial Navier-Stokes solver for unstructured meshes. It is a cell-centered, finite-volume code. FLUENT's three solvers can be used to compute the flow and heat transfer for all flow regimes, from low subsonic via transonic and supersonic to hypersonic. The unstructured grid capability in FLUENT allows for modeling of complex geometries similar to the geometry found in the wing and wheel well areas of Columbia. A more detailed description of FLUENT can be found in the Appendix and in [1].

5.3.6.3.2 3-D Solution Cases

5.3.6.3.2.1 <u>3-D Wing Model, 6 inch and 10 inch Spar Breach</u>
The purpose of the analysis was to determine the flow path of the plume entering the wing through the wing leading edge spar. A steady state analysis was done using boundary conditions corresponding to the time immediately following the wing spar breach, approximately 490 seconds after entry interface.

A simplified model of the left wing of Columbia was created, Figure 5.3.6-152, and shows the outer wall boundaries of the model including the wing upper and lower surfaces and the leading edge spar. A circular breach hole was located in the wing spar leading edge at the intersection of RCC panels 8 and 9. Two different spar breach hole diameters were modeled - circular breach sizes of 6 inches and 10 inches diameter were chosen based upon other analyses performed as part of the investigation. An assumption was made that the flow coming into the wing area would be normal to the spar.

Figure 5.3.6-153 shows the internal spars and vents not visible in Figure 5.3.6-152. Three flow exit areas are included in the wing model and are shown in Figure 5.3.6-153. A rectangular vent area of 180 in^2 is located in the 1040 wing spar. The internal wing volume forward of the 1040 spar was not included in the model, instead pressures obtained from the MSFC analyses outlined in Section 5.3.5.7 were used to set the conditions at that interface. The other two flow exits are located at the rear of the model at the 1365 spar location. These vents are located at the approximate locations where the inboard and outboard elevons penetrate the 1365 spar. Vent areas were 2.55 in^2 and 5.5 in^2 for the inboard and outboard

elevons, respectively. Four internal vents allow for flow between the various internal wing compartments and are shown along with their areas in Figure 5.3.6-153.

The wing geometry was simplified in order to reduce the computational expense of the model. None of the tubular struts supporting the upper and lower wing surfaces were included in the model. As mentioned previously, the wing volume forward of the 1040 spar was not included. The wheel well volume was not included due to the complex geometry in the wheel well and because the primary focus of the analysis was flow paths within the wing, not the wheel well area. Another area of simplification was the wing surfaces. These were not imported directly from CAD geometry, but were created within the FLUENT geometry generation program. This means that there may be subtle differences between the FLUENT wing surfaces and the actual wing surface geometry, however due to the overall size of the model it is not anticipated that this difference would have a significant effect on the results. The size of the 3D wing model computational domain was approximately 340,000 cells.

Boundary conditions for the 3-D model are shown in Figure 5.3.6-154 for the 6-inch breach case and in Figure 5.3.6-155 for the 10-inch breach case. Pressure boundary conditions were applied at the breach hole and three flow exit boundaries. These pressure values were obtained from the MSFC venting model discussed in Section 5.3.5.7. The pressures correspond to the boundary pressures at 500 seconds after entry interface. This time is 10 seconds after the estimated spar breach time of 490 seconds.

The standard k-e turbulence model available in FLUENT was activated for all of the 3-D and 2-D analyses. The working fluid was air modeled as an ideal gas. No attempt was made to model the chemical reactions occurring within the gas at these elevated temperatures using FLUENT. A correlation for determining the specific heat of air as a function of temperature from 495 ^{o}R to 10400 ^{o}R was used in the all of the 2-D and 3-D FLUENT models due to the large variation of specific heat over this temperature range. This correlation was input into FLUENT as a piecewise-polynomial function, and a plot of this correlation versus the data used to generate it can be found in Figure 5.3.6-156. The models were run until convergence was met on the net mass flow in and out of the domain, and pressures reached a steady state value.

5.3.6.3.2.2 Results – 3D Model, 6 inch Breach hole

Results of the 3-D internal wing flow case with a 6-inch diameter spar leading edge breach are shown in Figure 5.3.6-157 through Figure 5.3.6-161. Figure 5.3.6-157 is a contour plot of velocity magnitude on a plane cut horizontally through the entire wing. The plot shows that the flow does not penetrate significantly beyond the 1191 spar, and that it tends to circulate within the cavity outboard of the wheel well and exit through the 1040 spar vent. Some flow does penetrate all the way to the rear elevon vents, and Figure 5.3.6-158 shows this with a velocity contour plot with a different scale.

Mass flow rates and Mach numbers for the flow inlet and three flow exits are shown in Table 5.3.6.3-1. The mass flow rates indicate that 78% of the incoming gas exits the wing cavity through the 1040 spar vent.

Table 5.3.6.3-1 6-inch Breach Hole Mass Flow Rates and Mach Numbers

Vent	Mass Flow Lb/min	Flow direction	Mach Number
6” Dia breach Hole	0.686	In	1.06
1040 Spar Vent	0.535	Out	0.105
Inboard elevon	0.0667	Out	0.83
Outboard elevon	0.0835	Out	0.39

Figure 5.3.6-159 shows pathlines (colored by velocity magnitude) to indicate the flow paths of hot gas entering the wing cavity. The pathlines begin at the breach hole location. The flow impinges directly on the outboard wheel well wall then turns 180 degrees and the majority of the flow exits through the 1040 vent hole. A small percentage of the flow does penetrate all the way to the rear of the wing but at a much slower velocity than seen in the cavity outboard of the wheel well.

Figure 5.3.6-160 shows a contour of static pressure within the wing. The figure indicates that the pressure at the 1040 spar vent drives the resulting static pressure. This is due to the large size of that vent in relation to the two smaller rear vents. Figure 5.3.6-161 shows a contour plot of static temperature within the wing.

5.3.6.3.2.3 3D Model, 10 inch Breach hole

Results of the 3-D internal wing flow case with a 10-inch diameter spar leading edge breach are shown in Figure 5.3.6-162 through Figure 5.3.6-166. Figure 5.3.6-162 and Figure 5.3.6-163 are contour plots of velocity magnitude on a plane cut horizontally through the entire wing using two different scales to help visualize both the higher speed flow outboard of the wheel well and the low speed flow rear of the 1191 spar. The plots shows that even with the higher energy flow coming in the breach, the flow still does not penetrate significantly beyond the 1191 spar. Table 5.3.6.3-2 lists the mass flow rates and Mach numbers that again indicate that the majority of the flow (87%) entering the wing exits forward through the 1040 spar vent.

Table 5.3.6.3-2 10-inch Breach Hole Mass Flow Rates & Mach Numbers

Vent	Mass Flow Lb/min	Flow direction	Mach Number
6” Dia breach Hole	7.13	In	1.06
1040 Spar Vent	6.19	Out	0.75
Inboard elevon	0.29	Out	0.95
Outboard elevon	0.65	Out	0.95

Figure 5.3.6-164 shows pathlines (colored by velocity magnitude) to indicate the flow paths of hot gas entering the wing cavity. The flow impinges directly on the outboard wheel well and exits primarily through the 1040 vent hole, similar to the 6-inch breach case. As in the 6-inch breach case some flow penetrates the cavity aft of the 1191spar. Figure 5.3.6-165 shows a contour of static pressure within the wing. Figure 5.3.6-166 shows a contour plot of static temperature within the wing. Comparing the temperature contour plots between the 6-inch breach (Figure 5.3.6-161) and the 10-inch breach case (Figure 5.3.6-166), the area behind the 1191 spar is much warmer in the 10-inch case. The larger breach hole size is able to push more flow beyond the 1191 spar vent into this region.

5.3.6.3.3 2-D Simplified Wing Model Solutions

The purpose of the analysis was to trace the flow path of the plume as it enters the RCC cavity and impinges on the RCC attach hardware, then passes through a breach hole in the wing spar. It was assumed that the plume would be deflected by the RCC attach hardware and burn a hole through the spar, entering the wing cavity in the direction approximately normal to the spar. The analysis is an attempt to support the 3-D model assumption that flow is entering the wing cavity normal to the spar. A steady state analysis was done using boundary conditions corresponding to the time immediately following the wing spar leading edge breach, approximately 490 seconds after entry interface.

A simplified 2-D model of the left wing of Columbia was created and is shown in Figure 5.3.6-167. The view is looking up from below the left wing. The model consists of the wing cavity bounded by the wheel well outer wall, the 1040 spar, the 1191 spar, and the leading edge spar. This wing geometry was derived from the 3-D model. A section representing the RCC cavity was added along the length of the wing leading edge spar. The 2-D RCC cavity geometry was approximated with a 29-inch deep channel. A 10-inch diameter hole was located on the leading edge of the RCC cavity in the approximate location of panel 8. The green lines shown in Figure 5.3.6-167 represent interior zones in the domain and are not hard walls.

Four flow exit areas are included in the wing model. A pressure outlet is located in the 1040 wing spar, and another pressure outlet represents the vent in the 1191 spar that allows flow to pass to the rear cavities of the wing. The RCC cavity has two pressure outlets located at either end of the RCC cavity. These openings were sized based upon leakage areas obtained from the MSFC venting model discussed in Section 5.3.5.7

Figure 5.3.6-167 also shows the simplified RCC attach hardware used in the model. The attach hardware (representing the spanner beam insulation) in the model represents the hardware associated with RCC panel #8, and the breach hole in the spar is located directly adjacent to this attach hardware.

Boundary conditions for the 6 inch and 10 inch breach hole 2-D models are shown in Table 5.3.6.3-3. Static pressure boundary conditions were applied at the four flow exit boundaries. These pressure values were obtained from the MSFC venting model discussed in section 5.3.5.7. The pressures correspond to the boundary pressures at 500 seconds after entry interface.

Table 5.3.6.3-3 2-D Model Boundary Conditions

RCC Leading Edge Breach	Breach Pressure Lb/ft^2	Breach Temperature ^oR	1040 Spar Vent Lb/ft^2	1191 Spar Vent Lb/ft^2	RCC Fwd Vent Lb/ft^2	RCC Rear Vent Lb/ft^2
6 inches	37	6000	0.92	1.04	13.2	13.2
10 inches	37	6000	8.6	9.65	13.2	13.2

The flow entering the RCC cavity was redirected to impinge directly at the corner of the RCC attach hardware. This assumption was supported by other coupled external/internal CFD analyses which show the RCC inlet plume impinging directly on the corner of the attach hardware. All walls of the domain were set at a constant temperature of 50 ^oF, and the same turbulence models and specific heat correlations were used as in the 3-D models.

5.3.6.3.3.1 2-D Results - 6 inch Spar Breach

Results of the 2-D internal wing flow case are shown in Figure 5.3.6-168 and Figure 5.3.6-169. The velocity contour plot of Figure 5.3.6-168 shows the flow does penetrate the spar approximately normal to the spar. This figure as well as the pathlines of Figure 5.3.6-169.shows how the spanner beam insulation hardware turns the flow. Both plots support the assumption made in the 3-D model that initially the flow coming into the wing cavity was normal to the spar. There are some differences in the flow patterns compared with the 3-D model results, and this is likely due to the restrictions on the flow imposed by the 2-D geometry. In the 3-D case the flow can circulate around the wing cavity by splitting and traveling over and under the incoming jet, while in the 2-D model the flow is blocked from doing this by the incoming jet. The flow direction into the wing cavity at a later time would depend upon the length of time that the RCC attach hardware remained in place.

5.3.6.3.3.2 2-D Results - 10 inch Spar Breach

Results of the 2-D internal wing flow case are shown in Figure 5.3.6-170 and Figure 5.3.6-171. As in the 6-inch wing spar breach case, the velocity contour plot of Figure 5.3.6-170 shows the spanner beam insulation hardware turns the flow so it enters the wing approximately normal to the spar. This is also indicated in the pathline plot of Figure 5.3.6-171. Both plots support the assumption made in the 3-D model that initially the flow coming into the wing cavity was normal to the spar.

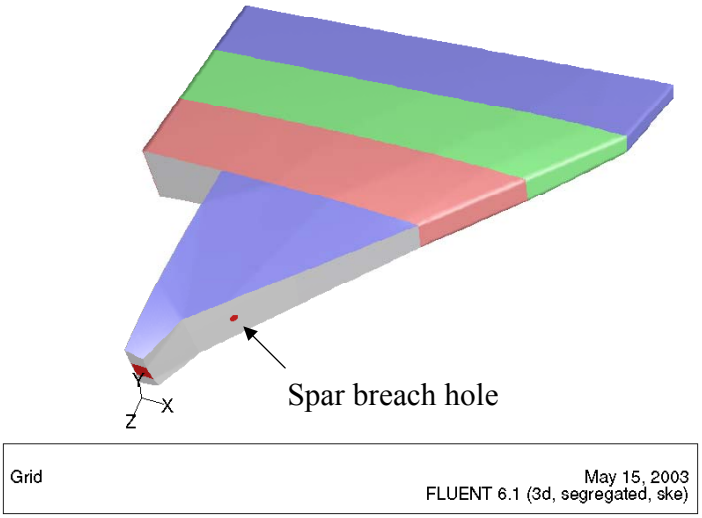

Figure 5.3.6-152 3-D Simplified Wing Geometry

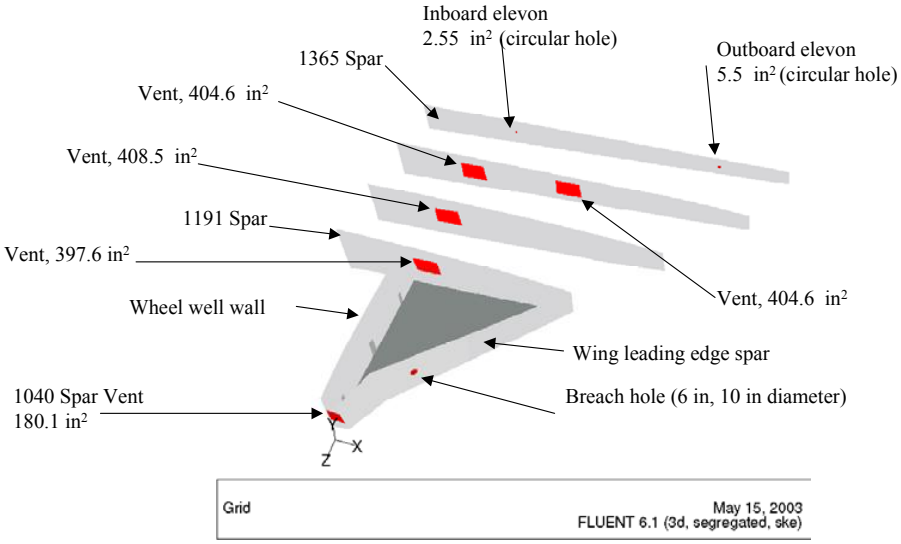

Figure 5.3.6-153 3-D Model Vent sizes

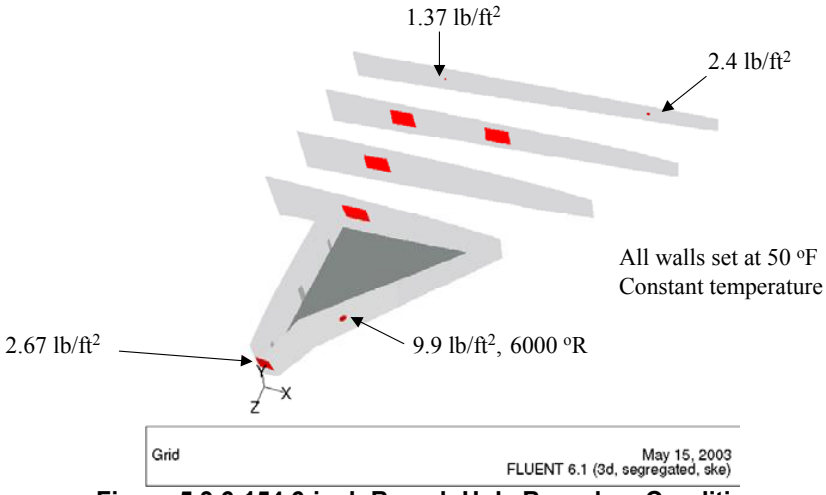

Figure 5.3.6-154 6-inch Breach Hole Boundary Conditions

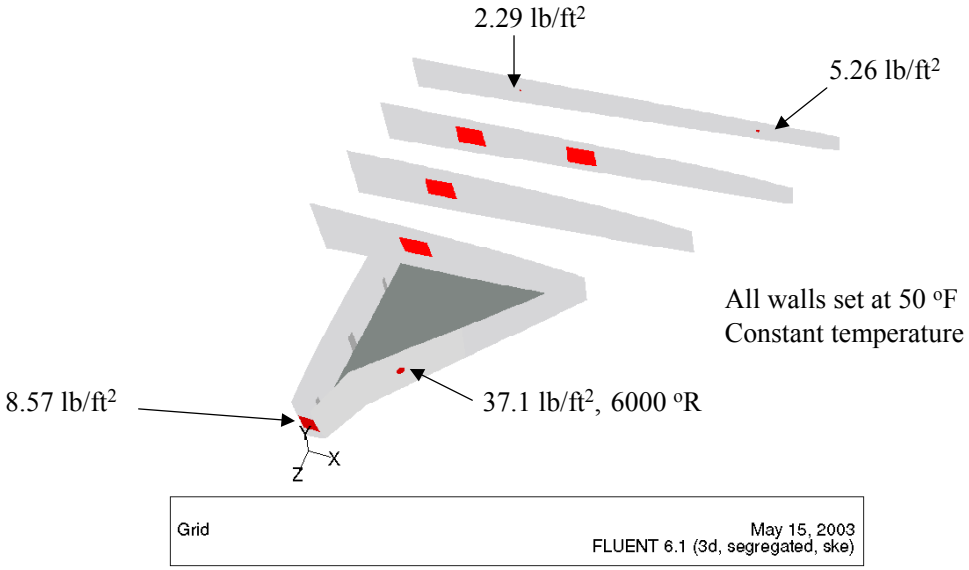

Figure 5.3.6-155 10-inch Breach Hole Boundary Conditions

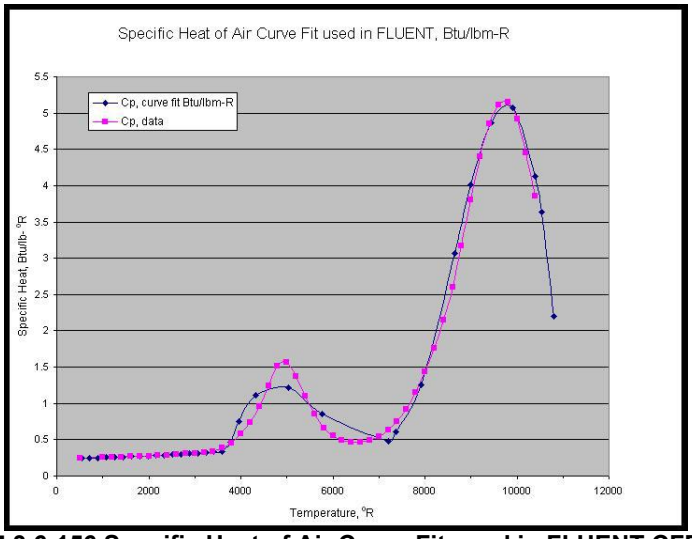

Figure 5.3.6-156 Specific Heat of Air Curve Fit used in FLUENT CFD Cases

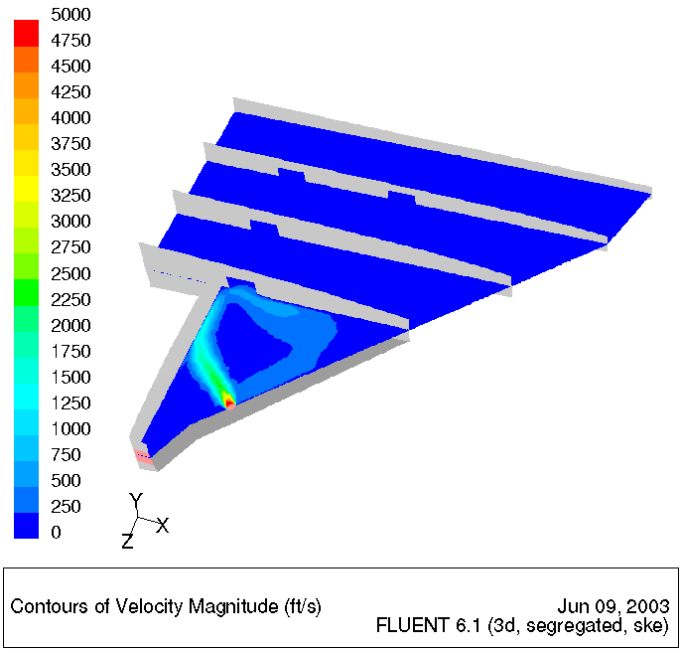

Figure 5.3.6-157 6-inch Breach hole, Velocity Contour Plot

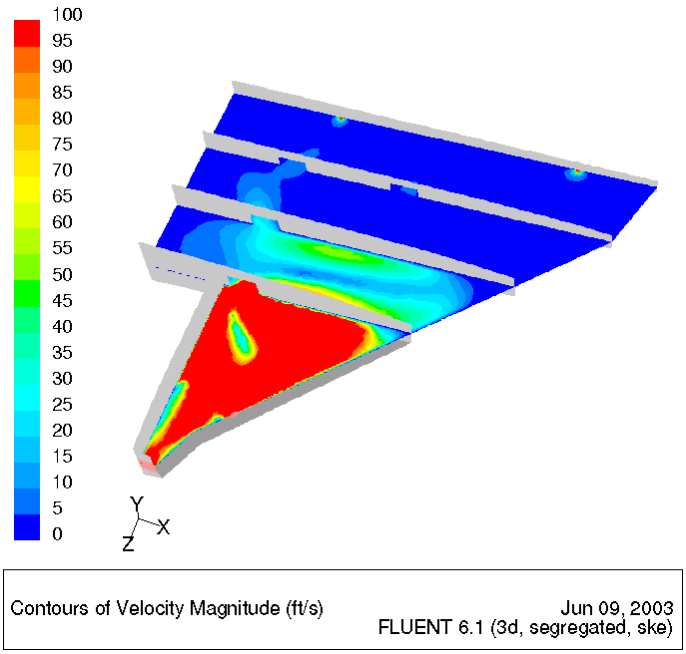

Figure 5.3.6-158 6-inch Breach Hole, Velocity Contour Plot

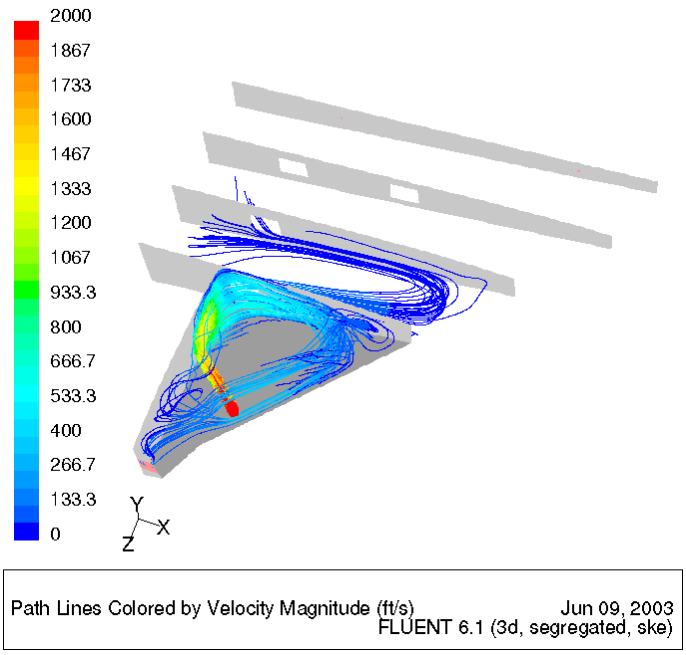

Figure 5.3.6-159 6-inch Breach Hole, Pathlines

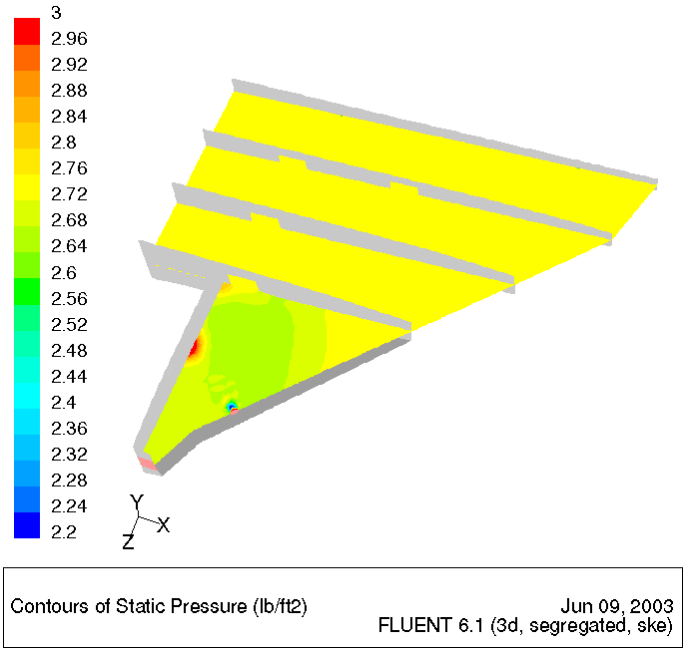

Figure 5.3.6-160 6-inch Breach Hole, Static Pressure

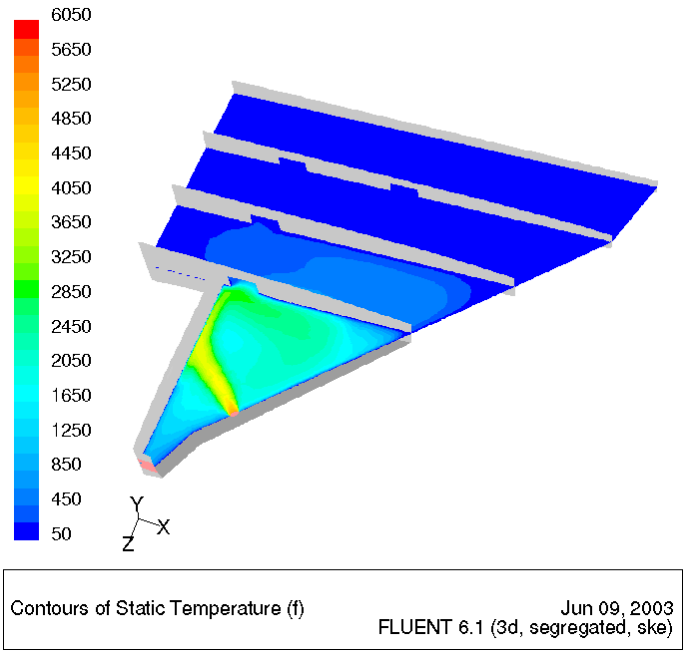

Figure 5.3.6-161 6-inch Breach Hole, Static Temperature

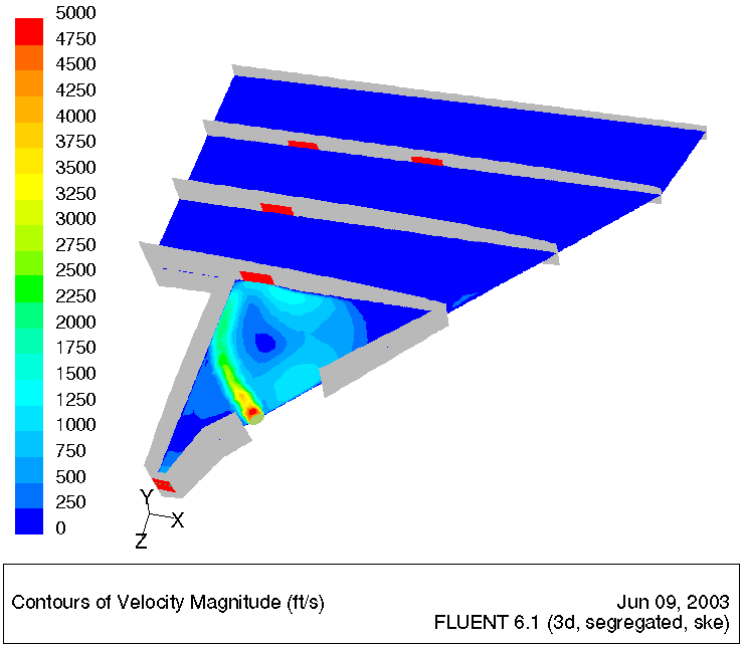

Figure 5.3.6-162 10-inch Breach Hole Velocity Contours

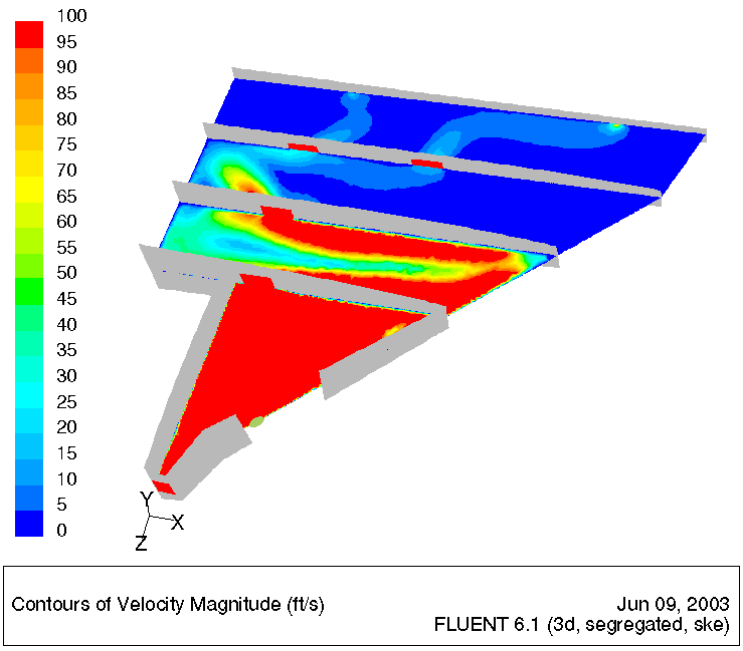

Figure 5.3.6-163 10-inch Breach Hole Velocity

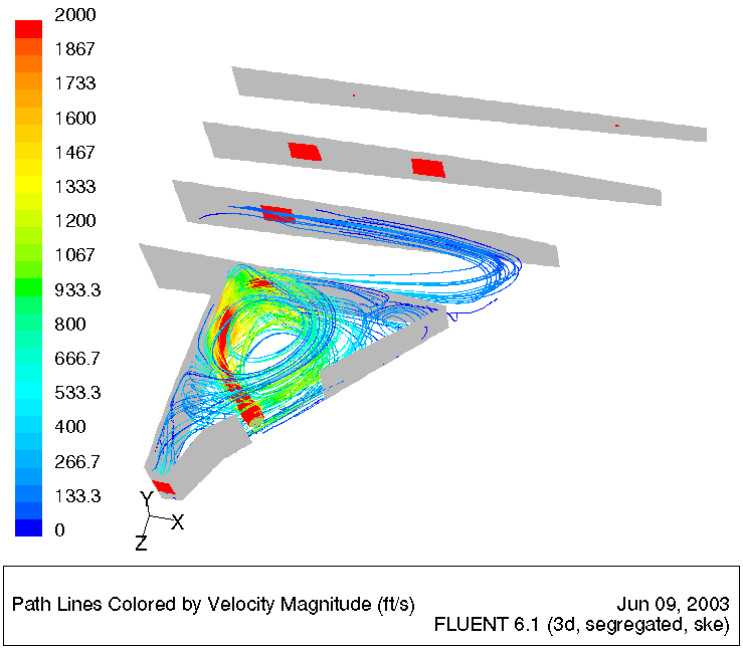

Figure 5.3.6-164 10-inch Breach Hole, Pathlines

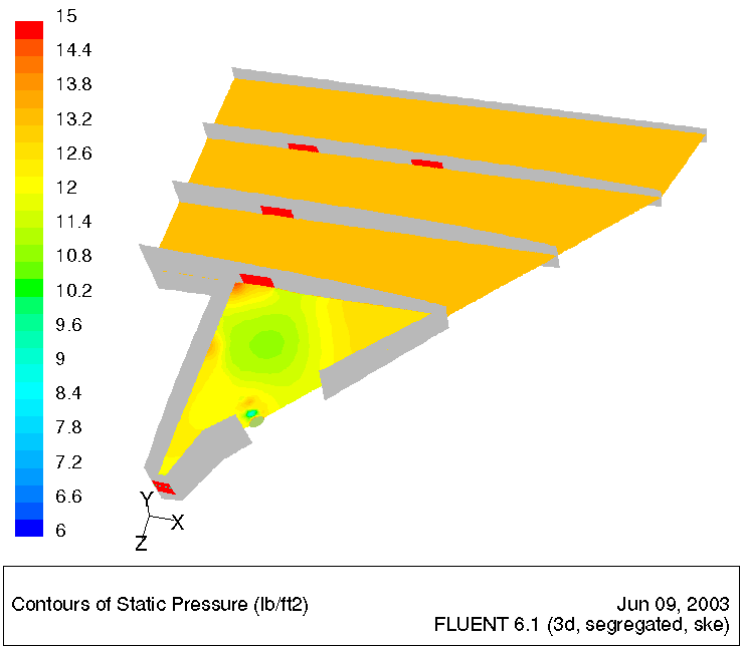

Figure 5.3.6-165 10-inch Breach Hole, Static pressure Contours

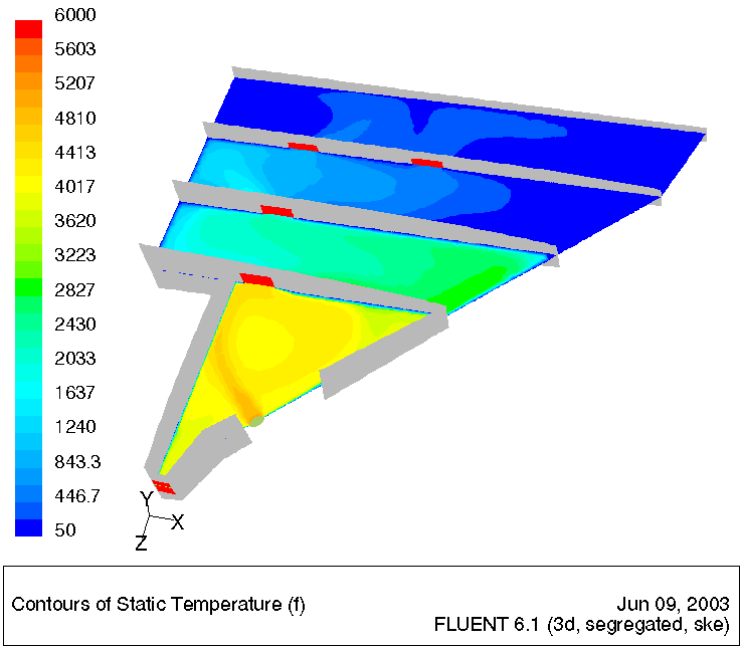

Figure 5.3.6-166 10-inch Breach Hole, Static Temperature Contours

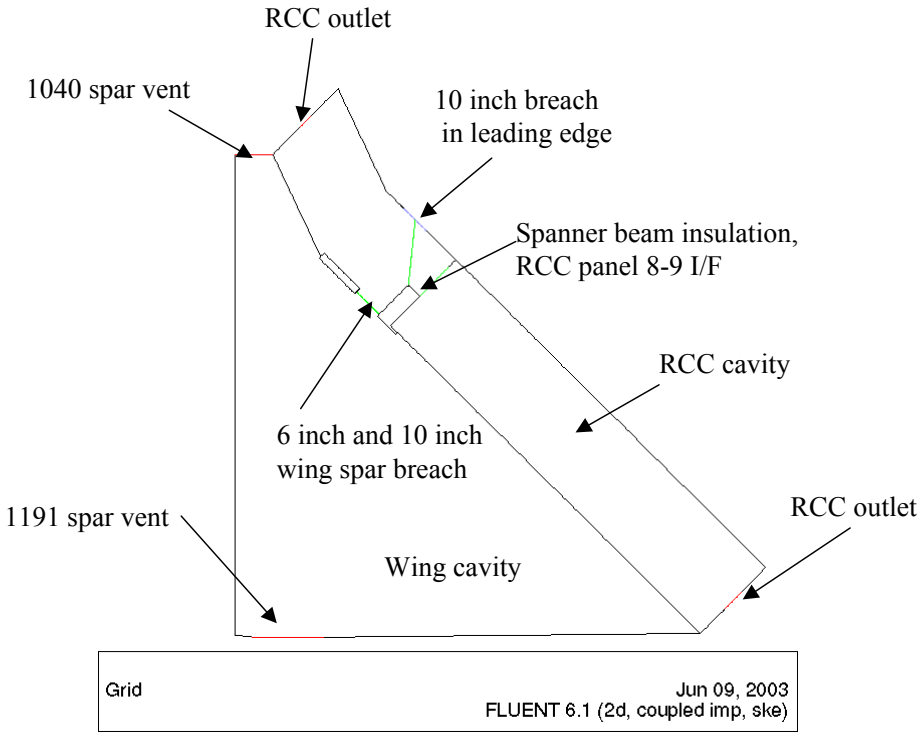

Figure 5.3.6-167 2-D Model Geometry – 10 inch Breach in RCC Leading Edge, 6 and 10-in Spar Breach

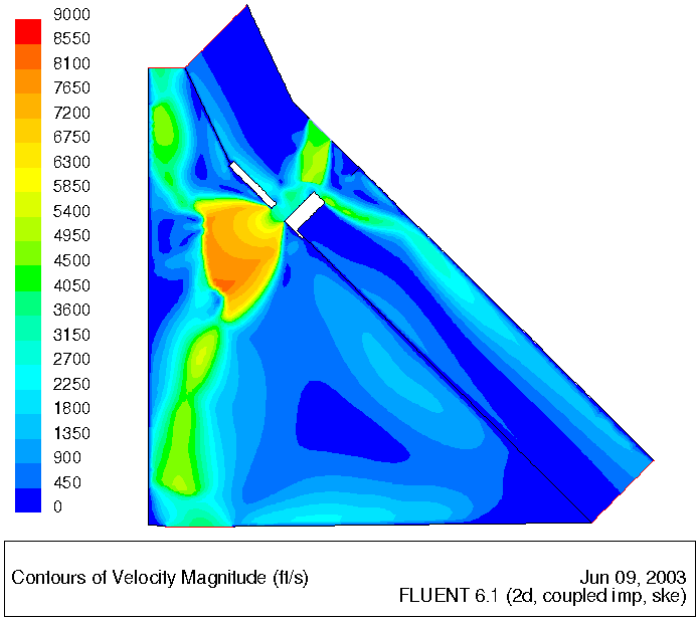

Figure 5.3.6-168 2-D Model, 6-inch Breach in Wing Spar, Velocity Contours

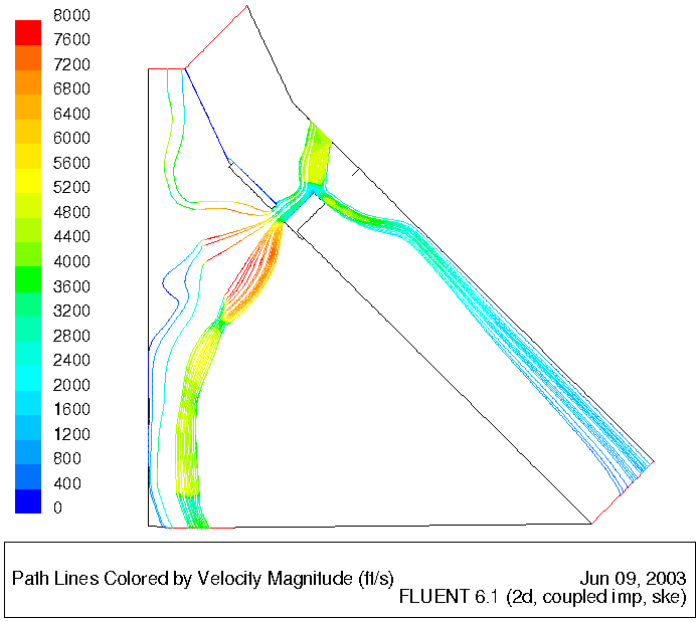

Figure 5.3.6-169 2-D Model, 6-inch Breach in Wing Spar, Pathlines

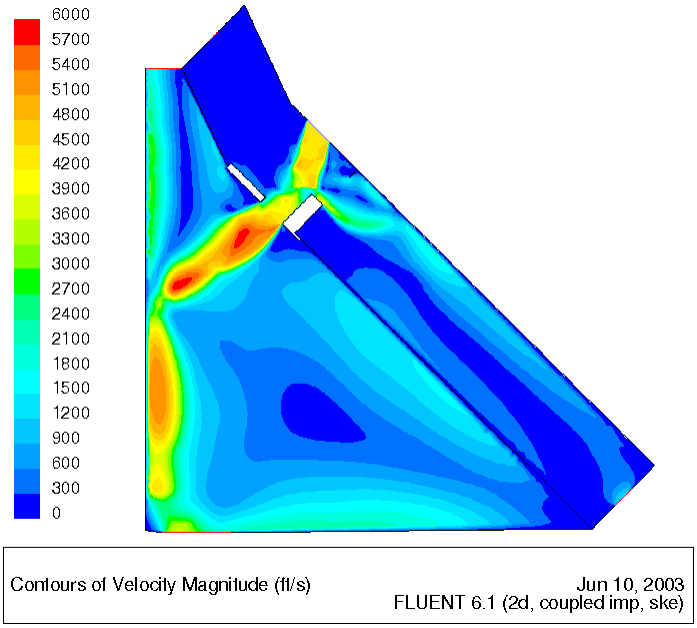

Figure 5.3.6-170 2-D Model, 10-inch Breach in Wing Spar, Velocity Contour

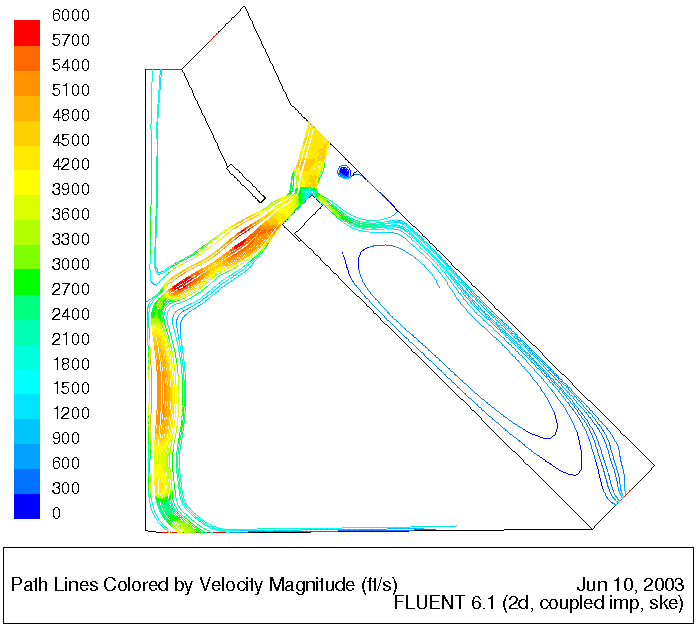

Figure 5.3.6-171 2-D Model, 10-inch Breach in Wing Spar Pathlines

5.3.7 Application of Data to the Working Scenario

5.3.7.1 Plume impingement angle in WLE

The insight provided by the CFD results for RCC penetrations with coupled flow fields allowed the adjustment of the assumed jet internal direction from normal to the interior surface to an angle reflective of the transverse momentum ingested into the RCC penetration. Figure 5.3.7-1 displays the two-inch penetration solution in RCC panel 6 by Peter Gnoffo. The streamlines turn into the hole initially at a 20-degree angle, that then interacts with the downstream lip shock resulting in a final flow turning angle of 41 degrees. It is desired to take advantage of this solution to generalize the internal jet direction to any penetration location. In doing so, the panel 6 results are assessed for a simple correlating parameter. A

local velocity based coordinate system is defined, as shown in Figure 5.3.7-1, with one component aligned with the velocity vector at the boundary layer edge and the other along the inward normal to the surface. Directional components were then assigned to the vectors. Many combinations of momentum components were tried, but with the uncertain impact of the lip shock, a simple correlation of boundary layer edge dynamic pressure (q_e) and surface static pressure (p_e) was chosen. The initial 20-degree flow turning angle was well reproduced with the ratio of static pressure over average ingested dynamic pressure. Boundary-layer edge properties are used to simplify the application to the entire wing. Figure 5.3.7-2 shows the process used to derive the correlation parameter, ***C***, to apply to the edge properties in establishing the flow turning into a penetration. Therefore, once the local coordinates are established, the predicted internal jet direction can be calculated as

$$\vec{J} = \left(0.176 \times \bar{q}_e\right)\vec{V} + p_e\vec{P}$$

With this definition established, a series of points along the projected debris path were chosen as illustrated in Figure 5.3.7-3 with the symbols. The ***J*** vectors are represented in three dimensions in the accompanying views of Figure 5.3.7-3, with the view from inboard on top and the view looking down on the RCC outlines on the bottom. Due to the double delta shape of the Orbiter wing, and the projected impact path at the juncture, the vectors primarily point to the spar region behind panel 8.In Figure 5.3.7-4 a representation of the RCC insulation system has been added in investigating the impact points of the selected jet penetrations. Due to the vector alignment and insulation configuration the conclusion is that the most likely primary impingement location for an RCC penetration along the predicted foam path is the spar region behind panel 8 or the earmuff region between panels 8 and 9. Table 5.3.7.1-1 provides the selected penetrations and the associated jet direction unit vectors.

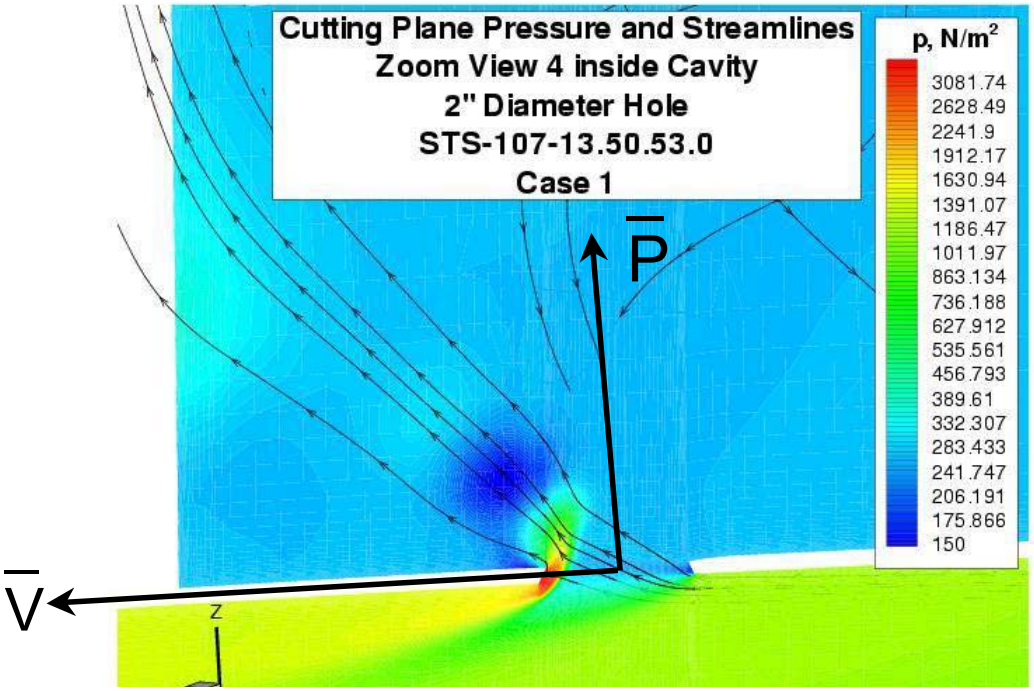

Figure 5.3.7-1 Panel 6 penetration and Jet direction coordinate system.

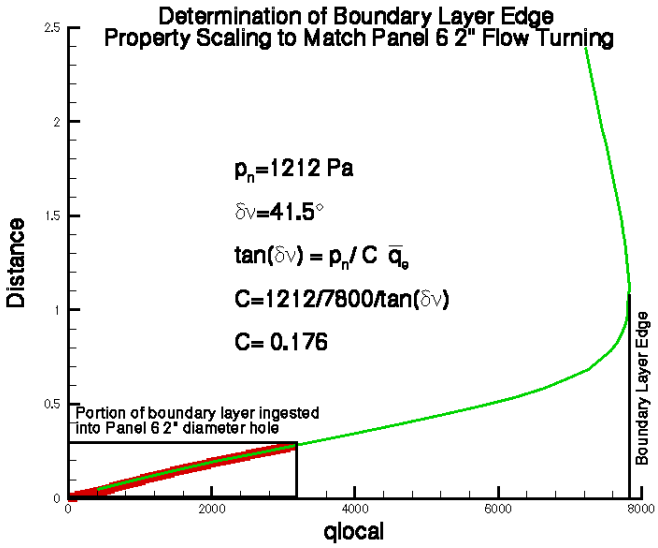

Figure 5.3.7-2 Jet direction correlation parameter derivation

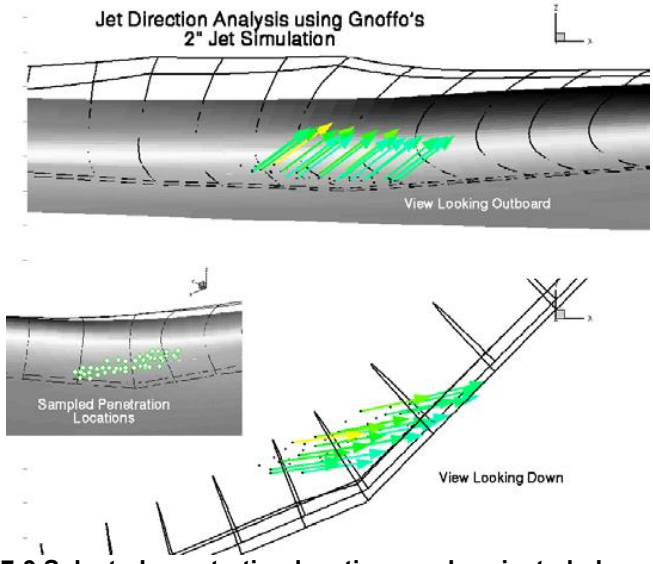

Figure 5.3.7-3 Selected penetration locations and projected plume directions

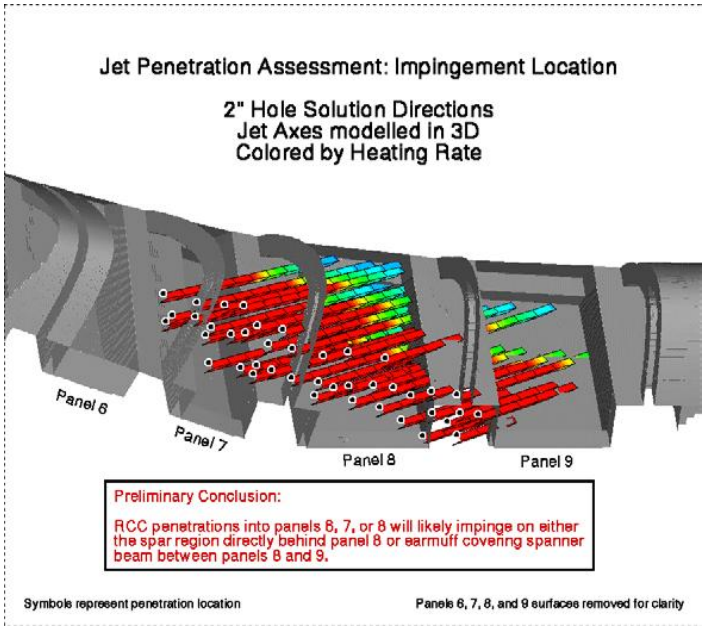

Figure 5.3.7-4 Jet penetration assessment

X	Y	Z	JetX	JetY	JetZ
1087.40	226.40	283.69	0.773	0.185	0.607
1088.09	221.74	282.61	0.775	0.173	0.608
1085.12	224.67	283.66	0.775	0.178	0.606
1082.34	226.31	284.54	0.776	0.179	0.605
1085.03	222.34	283.15	0.776	0.173	0.607
1084.47	218.03	282.33	0.777	0.165	0.607
1082.20	221.60	283.44	0.778	0.169	0.605
1079.10	223.87	284.55	0.779	0.169	0.603
1077.42	221.25	284.19	0.780	0.164	0.604
1079.82	217.54	282.90	0.780	0.159	0.605
1075.67	216.60	283.35	0.782	0.156	0.604
1074.39	220.23	284.52	0.783	0.157	0.602
1069.58	222.38	286.20	0.778	0.164	0.606
1071.82	218.29	284.50	0.784	0.151	0.602
1071.67	214.38	283.50	0.784	0.149	0.603
1067.86	213.76	284.04	0.786	0.145	0.601
1069.25	215.53	284.25	0.785	0.147	0.601
1064.78	218.99	286.31	0.785	0.149	0.601
1062.50	215.94	285.84	0.785	0.149	0.602
1065.37	212.72	284.25	0.788	0.141	0.600
1061.87	210.19	284.23	0.790	0.137	0.598
1058.09	213.32	286.04	0.792	0.135	0.596
1066.90	210.78	283.45	0.787	0.142	0.601
1058.65	208.86	284.49	0.792	0.134	0.596
1054.96	211.26	286.07	0.794	0.129	0.594
1051.40	211.92	287.24	0.797	0.121	0.592
1054.82	214.19	287.20	0.796	0.124	0.592
1050.94	209.88	286.56	0.797	0.122	0.591
1054.97	205.85	284.35	0.794	0.130	0.594
1057.20	206.49	284.10	0.793	0.132	0.595
1049.54	208.27	286.30	0.798	0.121	0.591
1045.30	210.44	288.34	0.801	0.104	0.590
1047.57	212.37	288.55	0.803	0.102	0.588
1046.34	206.93	286.58	0.798	0.119	0.590
1043.32	206.24	287.06	0.800	0.114	0.589
1041.77	207.76	288.11	0.806	0.104	0.583
1040.48	202.72	286.38	0.802	0.107	0.588
1036.79	205.16	288.31	0.810	0.087	0.581
1040.43	203.92	286.85	0.801	0.108	0.589
1046.73	205.56	285.99	0.797	0.119	0.591
1050.73	202.89	284.32	0.795	0.126	0.593
1056.37	207.78	284.63	0.793	0.132	0.595

Table 5.3.7.1-1Jet penetration directions

5.3.7.2 Plume heating distribution

As the investigation team narrowed in on a preferred working scenario, the internal flow team was asked to pull together internal heating distributions for assumed penetration locations that incorporate not only the primary impingement heating, like that described in 5.3.3.2, but also convective heating rates to the

surrounding internal TPS surfaces. Based on an assumed hole location and size, internal plume impingement environments were created that incorporate heating distributions for the panel 8/9 region based on assumed internal direction (5.3.7.1), degree of secondary splash heating, and geometric flow shadowing effects. Full 3-D CFD results for panel 7/8 penetrations were not yet complete, so the best fully coupled CFD solution with internal heating was used as a basis. Given the degree of engineering involved in producing the environments, uncertainty values of +/- 50% were applied to the final results and additional comparisons to higher fidelity CFD results were pursued to provide independent assessment of the expected internal heating.

5.3.7.2.1 Selection of assumed hole location

The present working scenario includes penetration of RCC from panels 6-9 with subsequent spar breach at 488 seconds from entry interface. The team chose a single penetration location for complete analysis in order to ballpark the hole size required to match the flight data for the panel 9 spar and clevis temperature measurements and the spar breach time of 488 seconds from E.I. Given similar heating analysis completed early in the investigation using the basic MMOD plume model, 5.3.3.2, hole sizes of 4, 6, and 10 inches in diameter were chosen and anticipated to bound the data. Hole location was chosen to maximize the predicted primary impingement heating rate, based on the internal flow direction analysis of 5.3.7.1. Using the simple 1-D plume heating model, the plume vectors of Table 5.3.7.1-1 were assessed and vector # 18 chosen and colored red in Figure 5.3.7-5. The anticipated heating rates at the primary impingement point are increased both by the short distance to the earmuff and the small radius of curvature on the TPS edge. The coordinates of the assumed penetration are X=1065 in, y=-219 in, and z= 286.3 in.

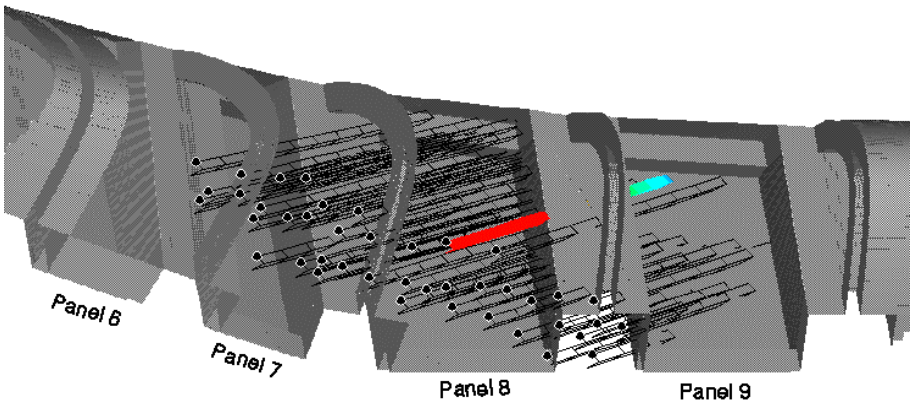

Figure 5.3.7-5 Panel 8 lower surface penetration location

5.3.7.2.2 Distribution methodology

Internal heating distributions are based on a modification of the baseline engineering methodology for holes as outlined Section 5.3.3.3 and take advantage of ingested flow enthalpy calculates using the methodology in Section 5.3.2 and a computed internal pressure using the methodology of Section 5.3.5. The local axis of the plume is assumed to align along the predicted direction of 5.3.7.1, independent of the hole diameter. This assumption was made due to the lack of available internal CFD at the time. (In truth, the larger holes will allow more transverse momentum to enter the hole and cause the jet to hug the interior RCC surface more than the present methodology based on 2" diameter hole results, but the heating distribution will only be shifted in space with little impact on peak heating values.) The radial position correction of the baseline methodology is replaced with computed three-dimensional factors as a function of hole size, which are presented in the results section below. Trajectory corrections remain the same, resulting in a final equation of

$$\dot{q}(x,y,z,t,d_{hole}) = \dot{q} \Big/ \dot{q}_{plate}(x,y,z,d_{hole}) \times \frac{\bar{q}_{\infty}(t)}{\bar{q}_{\infty}(488)} \times \frac{V_{\infty}^{2}(t)}{V^{2}{}_{\infty}(488)} \times \dot{q}_{plate}(d_{hole})$$

The baseline heating values, q_{plate}, are given for each hole size, computed for a trajectory time of 488 seconds from E.I., in Table 5.3.7.2-1.

10” Hole	55.9 Btu/ft^{2}sec for plate
6” Hole	30.1 Btu/ft^{2}sec for plate
4” Hole	27.1 Btu/ft^{2}sec for plate

Table 5.3.7.2-1 Panel 8 penetration heating values

5.3.7.2.3 Correlation and geometry correction factors

The methodology was adjusted based on the LAURA 2” diameter hole panel 6 penetration calculation of Section 5.3.6.1.4.1. Interior surface heating rates are extracted for the primary impingement region and the secondary splash surface. Corrections to the baseline model are made to bring the results into line with the CFD results. Comparison lead to a narrowing of the distribution by raising the values of Table 5.3.3.3-1 to the 1.6 power (also indicated by the comparisons in Figure 5.3.3-7) and the development of a splash heating approach to account for flow turning and secondary stagnation flows anticipated in the RCC cavity. Examination of the LAURA results indicated flow physics similar to a forward-facing step. Forward-facing step amplifications of 3.5 times the undisturbed value are appropriate for the observed internal Mach numbers and produced a good comparison on the splash surface of Figure 5.3.7-6. Secondary stagnation values are within 20% and the engineering methodology remains conservative as the flow moves down the surface.

In addition to secondary splash factors, other corrections to the baseline methodology are applied to account for “shadowing,” where the flow cannot directly impinge on the surface, local surface radius of curvature effects to earmuff edges and a general convective heating equal to three percent of peak values. The final geometry corrections are presented in Figure 5.3.7-7. Spar and carrier panel surfaces behind panel 8 are assumed to be secondary splash surfaces with a preference for the flow to splash on the upper surface and hence have amplification factors from 1 to 3.5. The edge of the panel 8/9 earmuff facing the assumed breach location shows high amplification factors to correct for local radius of curvature effects. The region behind panel 9 cannot be directly impinged upon from the assumed location and therefore has shadowing corrections that decrease the heating.

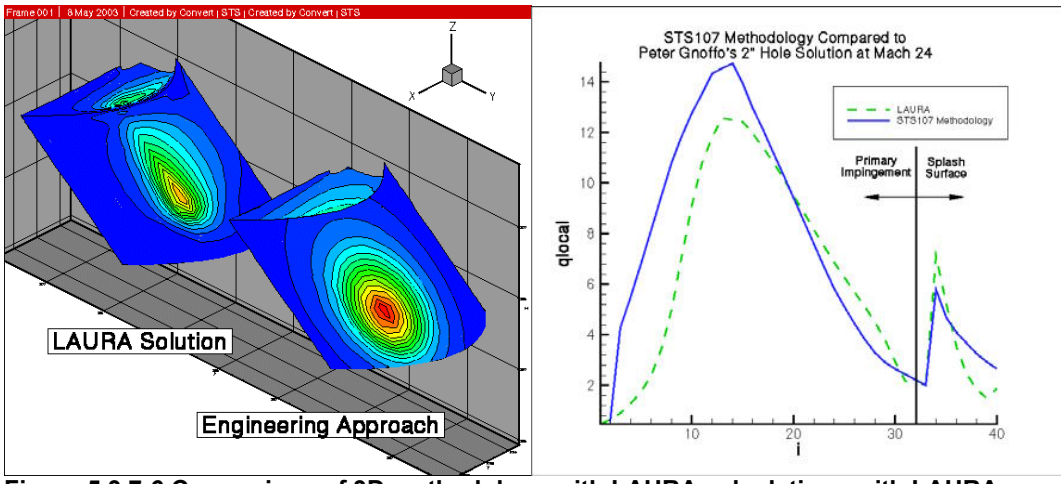

Figure 5.3.7-6 Comparison of 3D methodology with LAURA calculations with LAURA

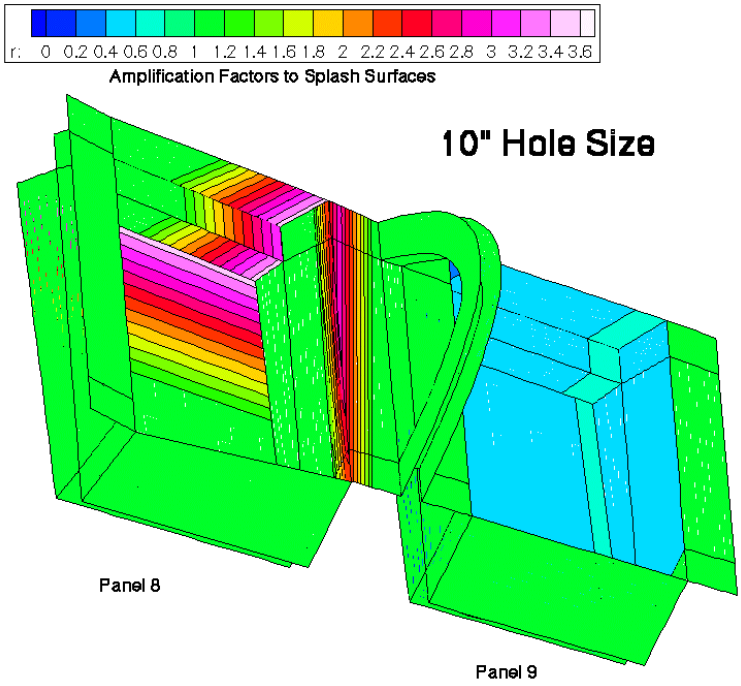

- Corrections given on a zone by zone basis to partially account for
  1. Secondary splash surface (based on forward facing step and panel 6 hole comparisons)
  2. Radius of curvature corrections to modeled geometry (Spanner beam insulation modeled with square corners, corrected to 1" radius heating)
  3. Line of sight shadowing and separation (panel 9 spar heating)
  4. Background heating values of 3% assumed on backward facing surfaces (on par with panel 6 and T-seal simulations)

Figure 5.3.7-7 Geometry correction for heating

5.3.7.2.4 Resulting Distributions

Engineering predicted heating distribution factors are presented in Figure 5.3.7-8 through Figure 5.3.7-10. All cases show a peak heating point on the earmuff between panels 8 and 9 at the edge of the TPS along the jet axis. By comparison, as the hole grows larger, so does the high heating region, with higher splash heating factors to secondary surfaces. Peak amplification factors do not change since the driving factor on the earmuff edge is local curvature, which is consistent between predictions. Keeping the previous equation and Table 5.3.7.2-1 in mind, however, shows that while the geometry amplification factors are the same, the 10" hole will experience significantly higher heating to the entire internal geometry.

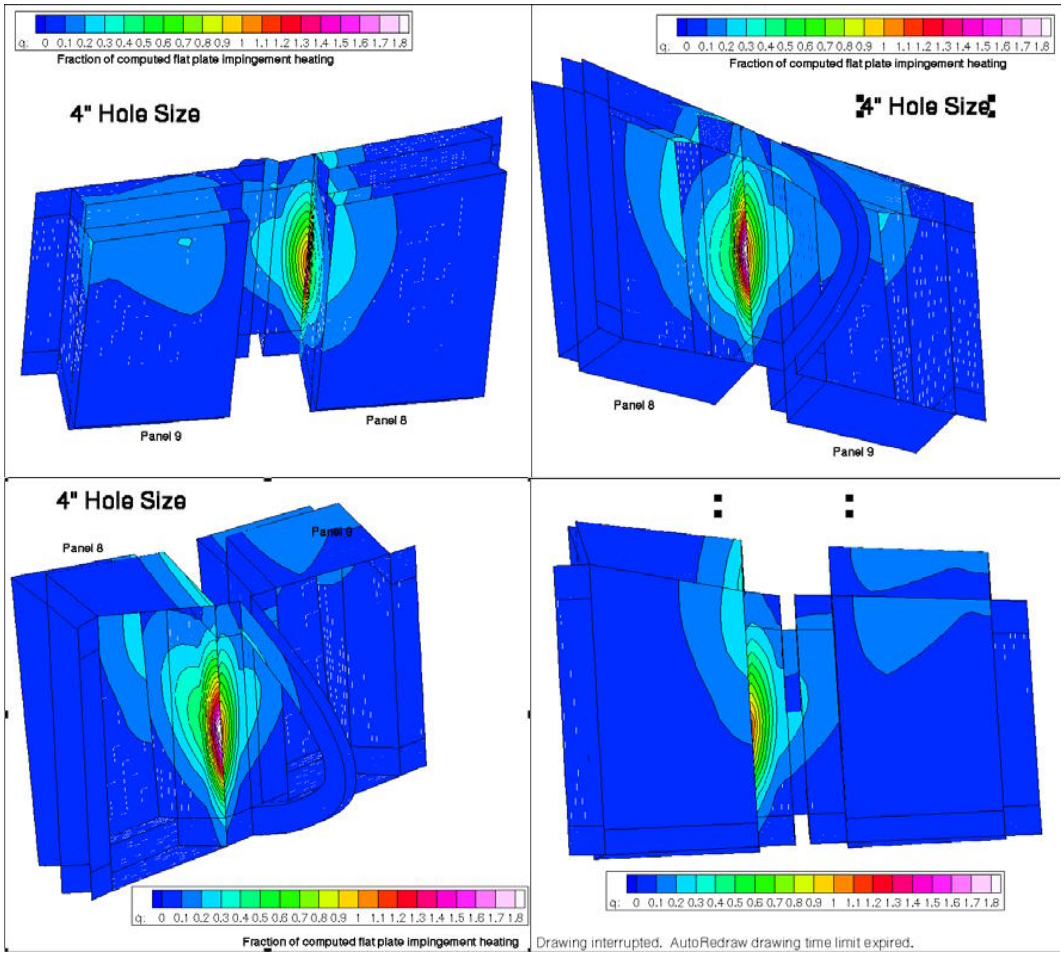

Figure 5.3.7-8 Heating factors for a 4" diameter hole in panel 8 lower surface

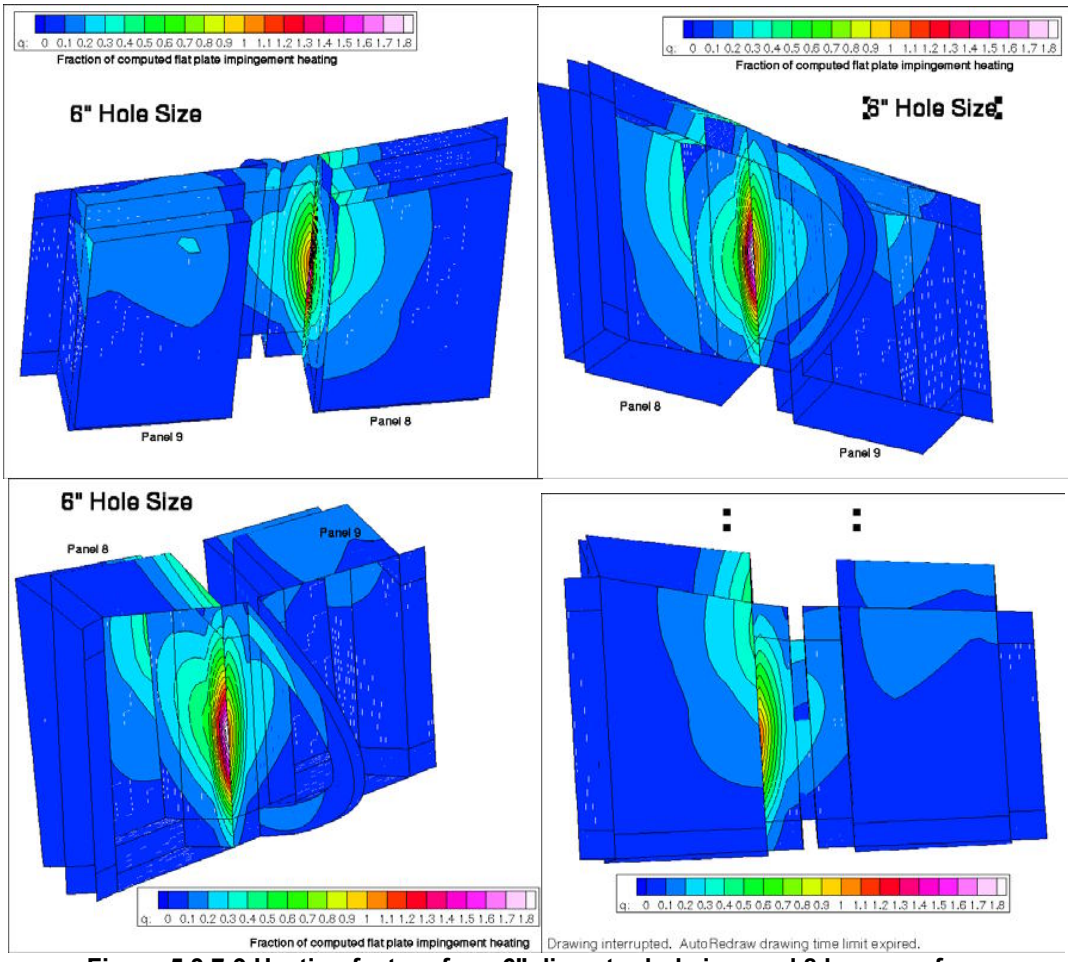

Figure 5.3.7-9 Heating factors for a 6" diameter hole in panel 8 lower surface

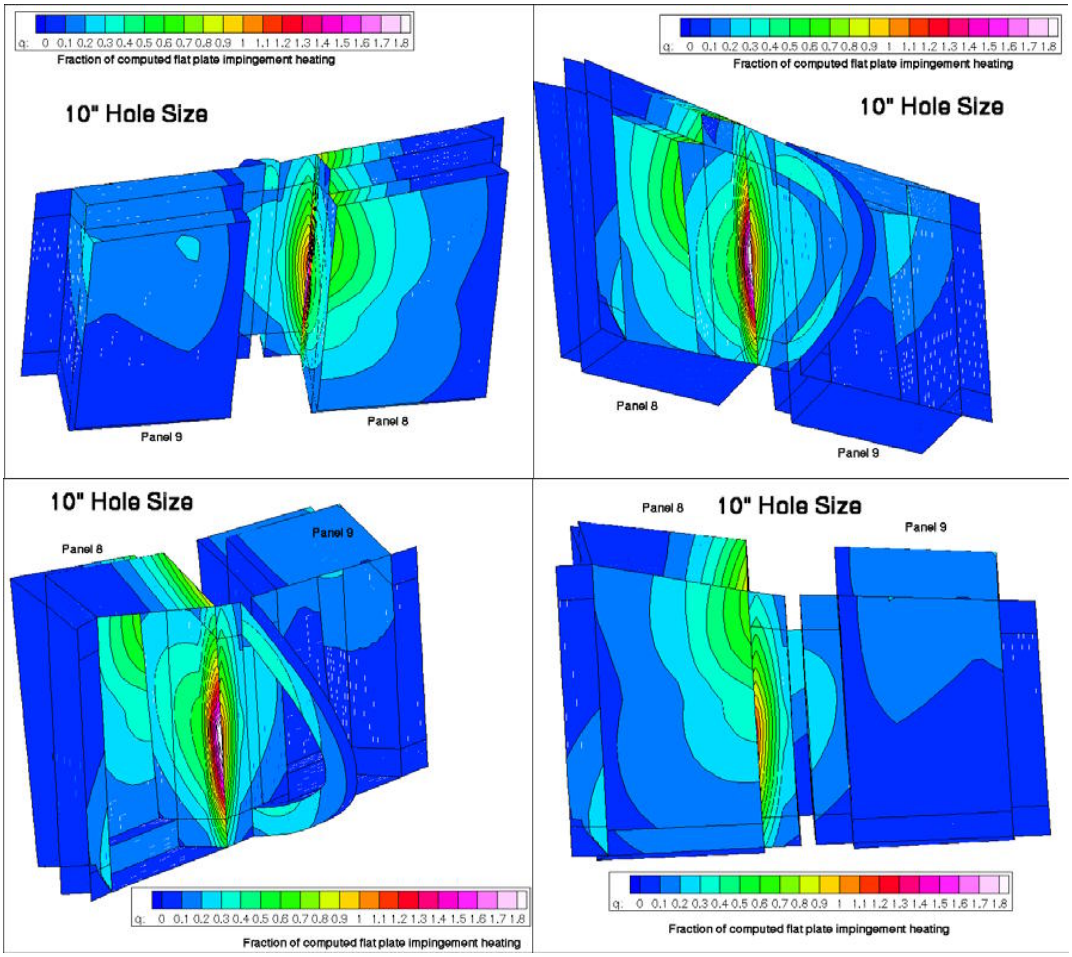

Figure 5.3.7-10 Heating factors for a 10" diameter hole in panel 8 lower surface

5.3.7.2.5 Comparison with 3D CFD/DSMC

The final STS-107 3-D plume heating methodology was developed based on very limited CFD results and represented a "highly engineered" environment for thermal analysis. It was desired to compare the engineering methodology to high fidelity CFD results for STS-107 type of geometries and assess the quality of the engineering predictions used for the subsequent thermal analysis. Given the complexity of the problem, the comparisons represent more of an independent assessment than a validation of the methodology, primarily since time did not allow a second loop through the process incorporating CFD lessons learned. Rather, the comparisons focused on gross fluid dynamic features and qualitative assessments. Comparisons with previously presented CFD results are given in Figure 5.3.7-11 through Figure 5.3.7-14.

Two types of comparisons with the DSMC results of 5.3.6.1.5 are displayed in Figure 5.3.7-11. On the left of the figure, both sets of data have been normalized by the peak impingement heating values on the panel 8/9 earmuff. The DSMC results fully couple the internal and external flow fields and provide additional support for the predicted internal jet direction since both methodologies predict peak heating values in the same location. DSMC results also provide an independent source for secondary splash heating to the spar region behind panel 8, again inline with the engineering methodology. Shadowing of the panel 9 spar region and some enhanced heating to the panel 9/10 earmuff are also predicted by the DSMC results inline with engineering assumptions. The right side of the figure provides a comparison of predicted heating magnitudes with the STS-107 engineering methodology. The engineering method predicts higher heating by roughly a factor of two. However, the engineering methodology is based on continuum assumptions and the calculations are made at rarefied condition so the conservatism is not surprising. Furthermore, the engineering method heat flux scaling appears to represent the physics well, given the two order of magnitude change in dynamic pressure.

Application of the engineering approach to the uncoupled panel 7 6" hole case, section 5.3.6.1.1, is displayed in Figure 5.3.7-12. Adjustments to the engineering methodology were made to account for the normal flow through the penetration, due to the uncoupled nature of the solution, and correction for total enthalpy variance. Comparison with two levels of grid refinement highlights a couple of conclusions. First, the STS-107 engineering methodology achieves qualitative agreement in terms of the size of the impinging jet, matching the spreading as the jet expands into the interior of the RCC. Peak heating values achieve excellent match with the medium grid results on the left. However, as more flow structure is captured with mesh refinement, the jet peak heating region changes shape and amplitude due to secondary flow patterns acting to self-focus the jet, enhancing peak heat transfer rates. While there remains a moderate level of unsteadiness in the results, as much as a factor of two increase over the engineering methodology is indicated. This phenomenon is independently predicted in the panel 8 results of section 5.3.6.1.4.2. The engineering methodology does not account for these flow interactions.

Figure 5.3.7-13 points out the dramatic change in internal heating distribution due to the external flow coupling. Here the same hole location produces a very concentrated, high enthalpy flow impingement on the interior rib surface of panel 7 just downstream of the hole. Examination of the engineering methodology indicates that the jet would, indeed, impact the rib, there is no automatic correction applied to account for it. The flow that strikes the rib has all of its downstream momentum arrested and winds up producing only moderate heating to the spar behind panel 7 while the STS-107 methodology shows a panel 8 spar impingement with elevated heating rates. Figure 5.3.7-14 shows the impact of local geometry changes to the distribution once more, as the earmuff between panels 7/8 is added and greatly changes the result. Fortunately, the additional interaction of the rib splash flow with the earmuff geometry produces heating distributions and magnitudes in line with the engineering methodology. While this is clearly a case of two wrongs make a right, it lends support to the use of the engineering approach for thermal analysis and does not negate the resulting outcome the thermal analysis to the panel 8 and 9 spar surfaces. RCC rib heating is handled by a separate modeling approach; section 5.3.3.6.5.

Overall, thermal analysis performed with the provided internal heat flux distributions will produce results consistent with CFD results, given the high levels of uncertainty applied to the approach. Final results may slightly change the hole size or hole location, but not invalidate the scenario.

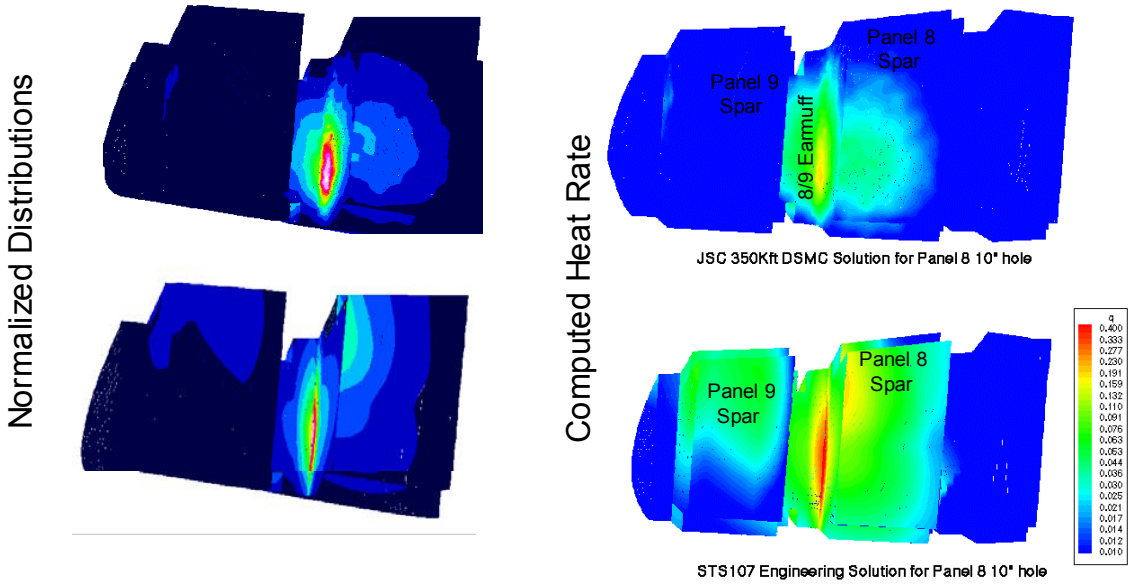

Figure 5.3.7-11 Comparison of engineering methodology with DSMC calculations at 350,000 feet

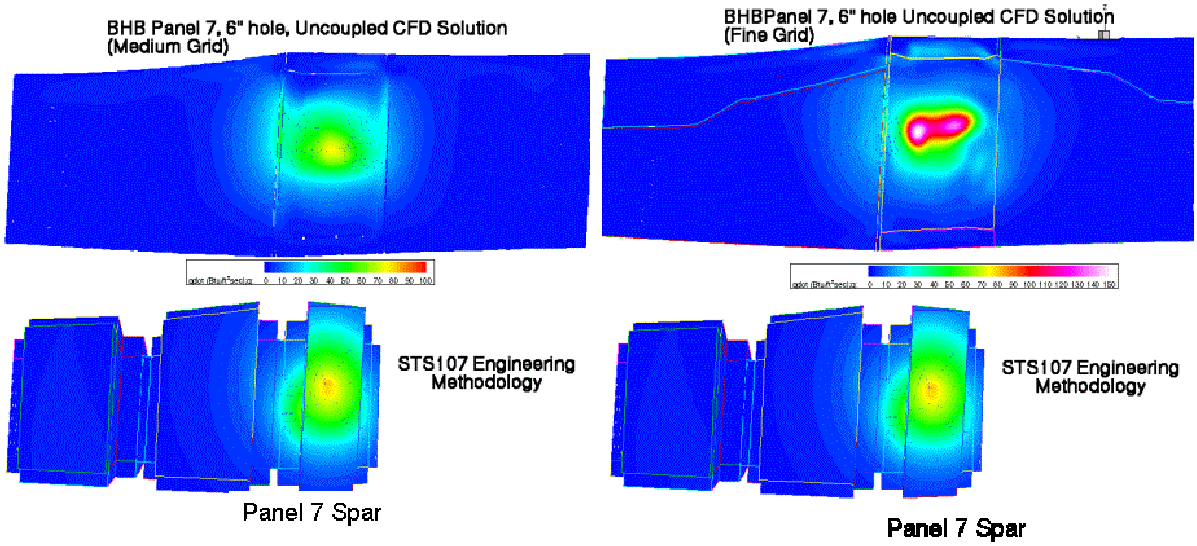

Figure 5.3.7-12 Comparison of STS107 methodology with panel 7 6” uncoupled CFD

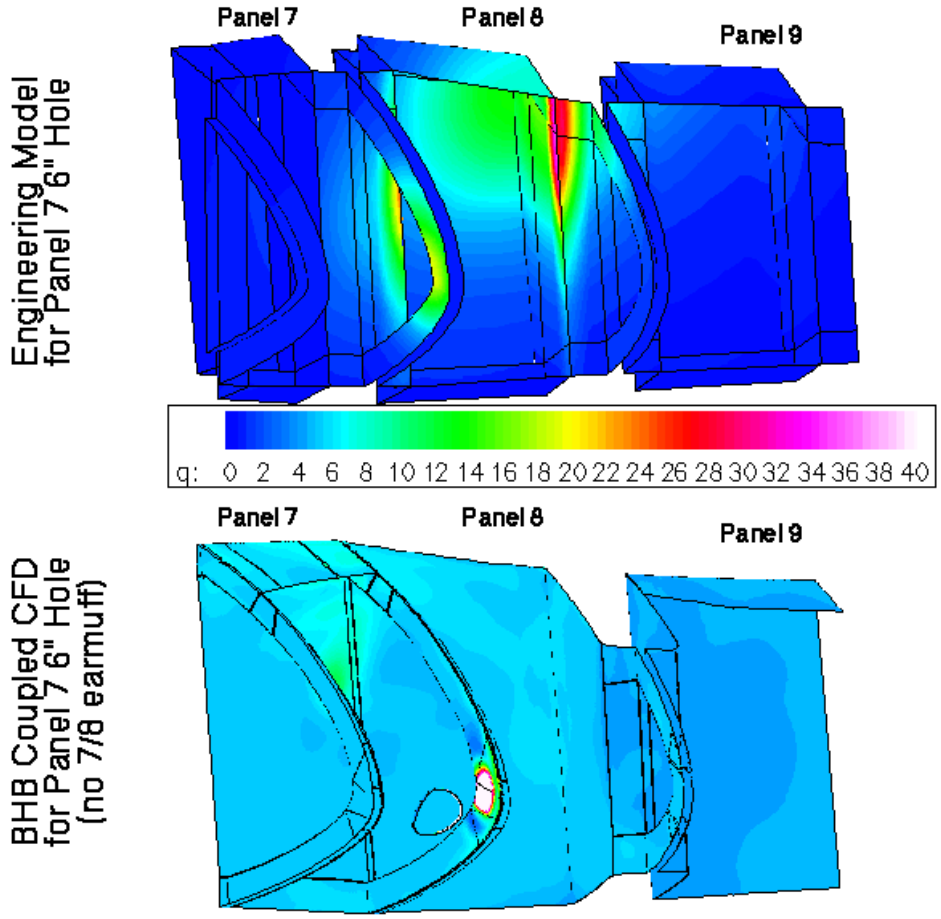

Figure 5.3.7-13 Comparison of STS107 methodology with panel 7 6” coupled CFD

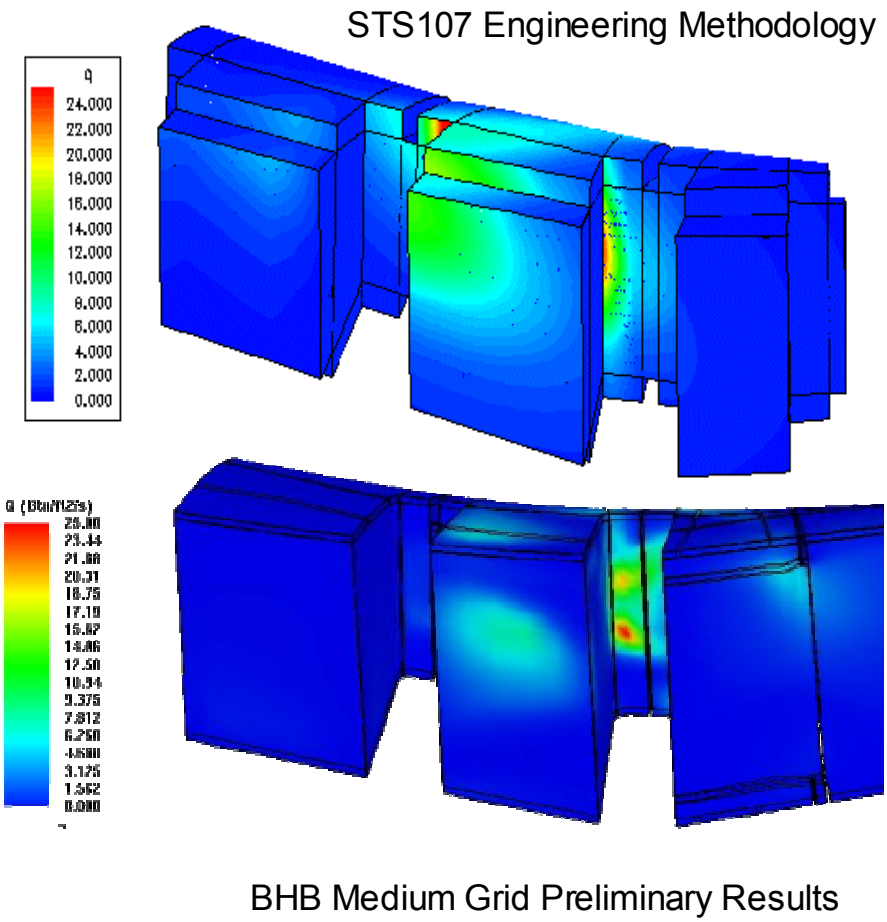

Figure 5.3.7-14 Comparison of STS107 methodology with panel 7 6" coupled CFD with earmuff

5.3.7.3 Assessment of Secondary Plume/Spar Breach

Thermal analysts keyed into wire burn-through times early in the investigation as a piece of known information that may be use to identify breach time, location, and size. The plume methodology of section 5.3.3.3 has been utilized in such assessment with one large, early assumption: that the plume enters through the spar normal to the surface. Early investigation activities, in fact, depended on the direction assumption with no conflicting information until the first coupled CFD results came out of Langley (5.3.6.1.4.1). With the additional knowledge that a significant fraction of transverse momentum is carried through the RCC breach, the question was raised about the secondary breach direction.

Secondary breach fluid dynamics are significantly different than RCC penetration for several reasons: 1) the internal RCC cavity geometry offers many surfaces to arrest momentum, 2) the highest heating point to the spar insulation is likely in a stagnant flow, high pressure region, 3) internal shock structures absorb significant portions of available flow energy, and 4) the flow must turn through several inches of structure and insulation rather than just 0.25 inches of RCC. With this information in hand, investigative activities continued assuming normal jet penetration. Final CFD calculations have continued to support the conclusion that the jet, at least initially, penetrated the spar normal to the surface.

Figure 5.3.7-15 represents the insight CFD results where the jet penetration direction was assumed normal to the spar. In the solution the jet structure remains coherent and impinges on the wheel well wall before being turned downstream and circulating through the mid wing volume. Figure 5.3.7-16 displays similar fluids dynamics from a two dimensional CFD solution where the flow initially carries streamwise momentum through the RCC breach and impacts internal geometry in the region where a hole is placed in the spar. This computed internal flow direction and mid wing fluid dynamic structure match the Figure 5.3.7-15 results quite well. While the two dimensional results modeled a large structural interference, the

BHB results of Figure 5.3.7-17 illustrate that even a relatively small geometric feature, in this case an RCC rib, can sufficiently absorb momentum to cause the jet to change direction completely. Any secondary burn-through of the spar in this case would clearly produce a normal jet through the breach.

In providing this assessment, however, the best that can be said is that **initially** the jet was certainly produced normal to the secondary breach surface. Given heating rates many times external values, eventually the primary impingement zone will be completely melted to the dimensions of the jet and there is then nothing to inhibit the free flow of the jet into the mid wing volume with full momentum. The time required to achieve such a state is entirely dependent on the initial damage and the TPS surface that is directly impinged.

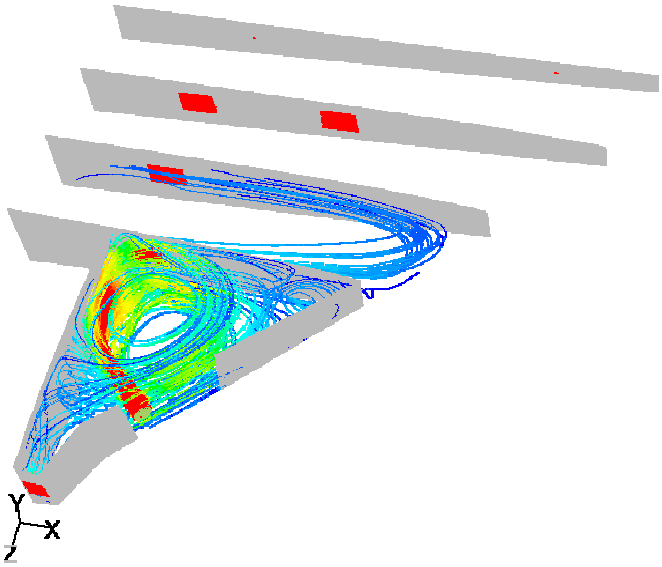

Figure 5.3.7-15 Assumed normal direction flow field

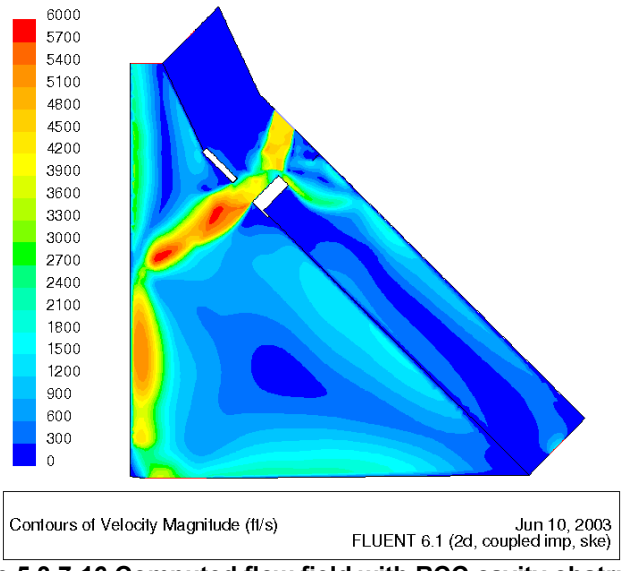

Figure 5.3.7-16 Computed flow field with RCC cavity obstruction

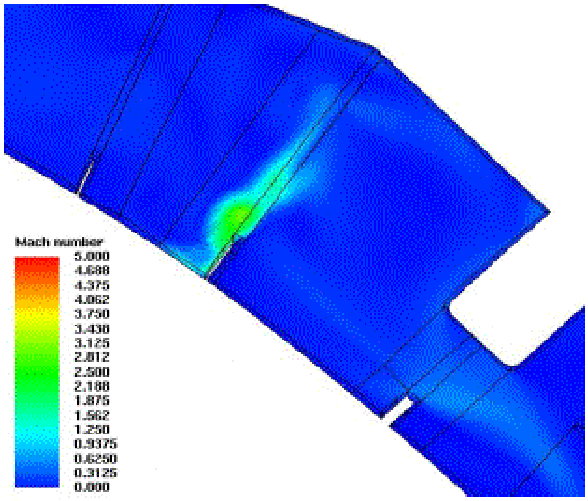

Figure 5.3.7-17 BHB Panel 7, 6" hole coupled internal flow field

5.3.7.4 Panel 8 penetration fluid dynamics and forensic evidence

Full three-dimensional CFD solutions for the panel 8 penetration provide invaluable insight into the flow inside the RCC that led to the eventual demise of the wing structure. Examination of the fluid dynamics and flowfield properties provides an explanation for, and independent verification of, hardware forensic evidence of a panel 8 breach. Figure 5.3.7-18 displays the internal streamline patterns for a 10" breach into the lower panel 8 surface. A supersonic stream of high-energy flow enters and directly impinges on the 8/9 earmuff, producing locally high pressures and heat rates. The flow re-expands and creates a supersonic "splash" flow that jets inward and upward into the panel 8 spar region before recirculating around to the panel 8 upper RCC inner surface and eventually exiting through the vents. This resultant flow field directly explains four key forensic features seen in the debris.

5.3.7.4.1 Inconel deposits on panel 8 inner surface

The initial deposits on the backside of the surviving panel 8 RCC have been analyzed and identified as Inconel nodules. The flow field predicted by BRPP provides the transport mechanism for the Inconel deposits. Initially high speed, high temperature flows impinge on the Dynaflex insulation, melting the outer Inconel surface. The melted/vaporized Inconel is deposited to the back of the panel as the supersonic tail jets scrub the panel 8 spar insulation and then the back side of panel 8.

5.3.7.4.2 Panel 8 and 9 rib erosion (knife-edging)

The BHB panel 7 CFD solution predicted heating rates over 200 Btu/ft^2-sec to the panel 7 interior rib surface in the primary jet impingement zone. BRPP results to the 8/9 earmuff are also over 200 Btu/ft^2-sec for the panel 8 penetration. Examination of Figure 5.3.7-18 shows how a slight adjustment of hole location would place the primary jet impingement heating region directly on the RCC rib. The directional aspect of the knife-edging observed in the debris can only be explained with a jet flowing internally from panel 8.

5.3.7.4.3 Erosion of panel 9 lower carrier panel tiles

Examination of panel carrier panel tiles shows clear indications of flow out from the corner of RCC panel 8, through the horse-collar seal and out and over the panel 9 lower carrier panel with significant erosion patterns. In order to produce such a flow, the internal pressure must be significantly higher than the lower surface pressure. In addition that erosion pattern indicates a coherent jet. Figure 5.3.7-19 shows the local pressure field for the panel 8 breach in the outboard lower panel 8 corner. Pressure values of 0.3 psia are greater than 2.5 times the external surface pressure at the same location on the lower surface of the Orbiter, more than sufficient to drive highly energetic flow out through the horse-collar. Of great significance is the localized aspect of the distribution: regions merely inches from the secondary stagnation point in the corner of the panel do not possess sufficient pressure to drive flow out onto the lower surface.

5.3.7.4.4 Panel 8 upper carrier panel "chimney" tile

Preferential jet splash patterns off of the earmuff surface and up and into the panel 8 spar region focus high temperature gases directly into the RCC leeside vents at the upper carrier panel. With the poor

radiation relief of tile to RCC, enhanced heating will quickly elevate the tile surface above the slump temperature and open the vent even more. Debris forensic evidence contains a panel 8 upper carrier panel tile with deposit buildup consistent with the internal insulation materials over 0.4" thick. Examination of Figure 5.3.7-20 shows the jet shape as it comes off the earmuff clearly heading directly into the region where the tile would be located, carrying with it any melted/vaporized material for deposit to the relatively cooler surface of the tile.

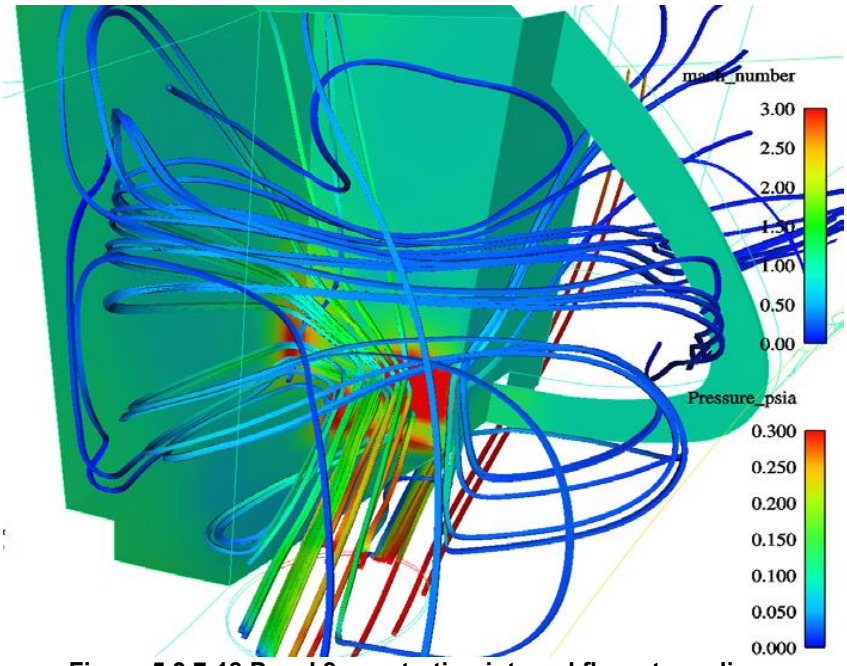

Figure 5.3.7-18 Panel 8 penetration internal flow streamlines

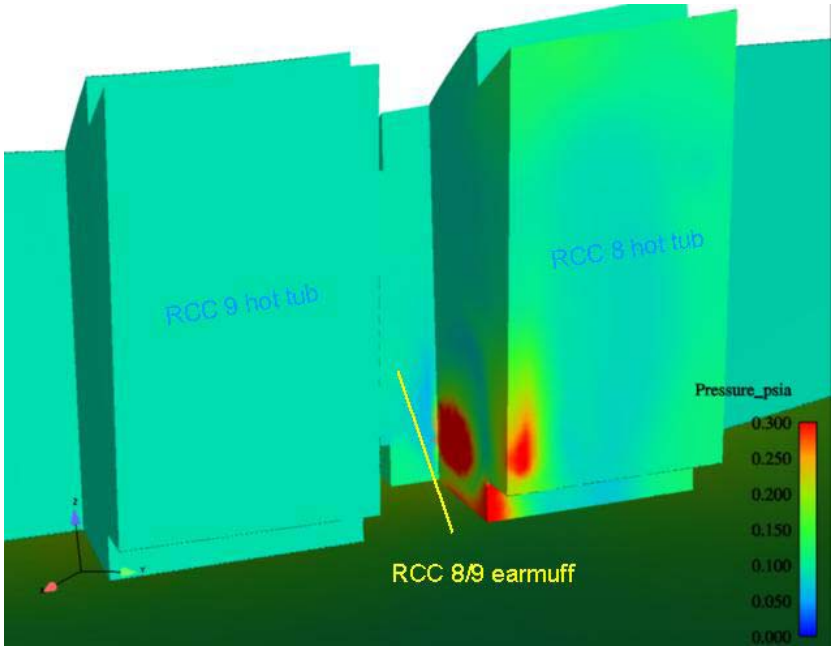

Figure 5.3.7-19 Panel 8 penetration internal stagnation pressures

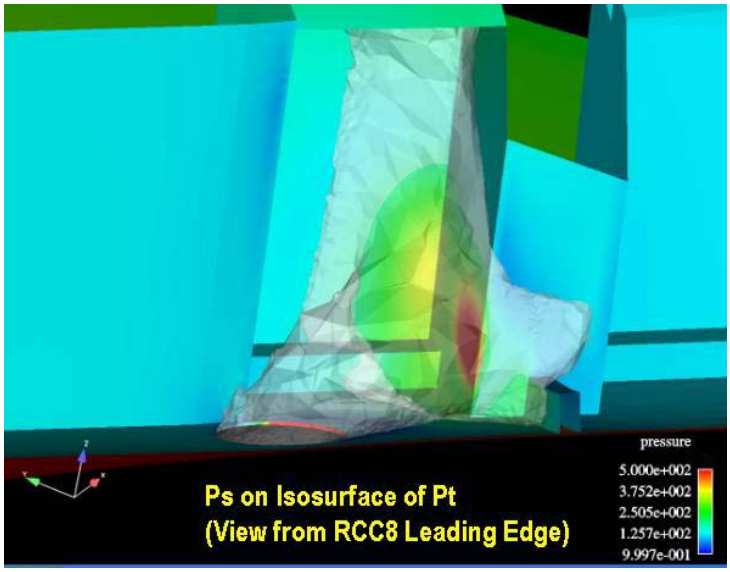

Figure 5.3.7-20 Panel 8 penetration internal jet shape

5.4 Aerothermodynamic Environments Summary

Aerothermodynamic analysis and testing has been conducted in support of the STS-107 Columbia accident investigation. The work presented above (in sections 5.1 – 5.3) explored various off-nominal external and internal aerothermodynamic events experienced by STS-107. The external aerothermodynamic analysis examined changes to the external Orbiter environment that result from a large matrix of possible damage types and locations. The internal aerothermodynamic analysis examined environments due to high temperature gas ingestion from the varying extent, location and type of damage. These analyses and test data were used to provide substantiating evidence in support of the Working Scenario: Damage to RCC Panels 5 through 9. In order to be considered as substantiating, the aerothermodynamic data had to be, (1) consistent with the results of data provided by the other technical disciplines and reported in this document, (2) consistent with evidence gathered through the recovered Columbia debris and data mapping, and (3) consistent with any other relevant evidence that became available during the investigation. Particularly important in this process of substantiating the aerothermodynamic data was correlating the aerothermodynamic team's analysis results with the data obtained from the STS-107flight instrumentation. Since the exact size, shape, and location of the damage was unknown, the process taken was to assume a damage configuration and evaluate the results on the aerothermodynamic environment. This was done by comparing the analysis or test results with the available flight data, as in the case of the surface thermocouples, or by providing the environments for thermal analysis to determine if the provided heating environment, coupled with the thermal model, was consistent with other data from the Orbiter.

Investigations of changes to the external environments through wind tunnel and numerical analyses have yielded much critical information. Although the chin panel and vent nozzle data could not be explained by these results, the side fuselage and OMS pod surface temperature and skin temperature responses were shown to be consistent with progressive wing leading edge damage. The extensive amount of wind tunnel test data obtained at Mach 6 Air and CF_4 facilities was mostly qualitative; however, the testing methods allowed for the rapid evaluation of multiple damage configurations and guided the focusing of the damage scenarios that were examined with computational analysis. High quality numerical simulations of the Orbiter with wing leading edge damage provided engineering information on leeside flow field features and surface heating. The combined efforts of numerical analyses and wind tunnel testing demonstrate that the reduced heating effect seen from the early part (< EI + 480 sec.) of the STS-107 flight instrumentation was caused by high pressure flow entering a hole on the windward side of the left wing leading edge and exiting to the lee side either through the leeside RCC channel vents or in combination with some localized leeside RCC/upper carrier panel breach. Analysis of the mass flow rates exiting the tested vent area

indicate that a hole size on the WLE windward side on the order of 80 square inches at flight scale was required to provide sufficient flow to affect leeside surface heating in a way that was consistent with flight data. The test and analyses data also showed that the increased leeside heating (side of fuselage and OMS pod) that occurred after EI + 480 seconds had to be associated with a significantly damaged leading edge; either severely damaged or missing upper carrier panels (more than one), the loss of significant portions of upper RCC panel(s), or even upper wing skin just aft of the WLE.

Supporting evidence for these damage geometries was generated with CFD tools, providing critical information at flight conditions. These CFD simulations represent a substantial effort, but they succeed in identifying the source of increased side fuselage heating as a jet emanating from a damaged RCC leading edge. This jet convects high-temperature/high-pressure gas onto the Orbiter leeside where, in sufficient strength, it both severely perturbs the leeside vortex flow field and impinges directly on the side fuselage. This side fuselage jet impingement was demonstrated to generate surface heating increases of more than a factor of ten. Damage configurations involving mass and energy convection to the Orbiter lee side, with less strength due to smaller leeside damage area, lack the strong coherent jet that impinges on the side fuselage. However, this weaker leeside flow disturbance still generates perturbations to the leeside vortex structure leading to movement of the wing strake vortices and the heating footprints associated with their flow structures. The identification of leeside surface heating differences was critical to interpreting these two classes of STS-107 flight data. The first being the early decrease in OMS pod and side fuselage heating, and the second being a substantially increased side fuselage heating together with moderate OMS pod heating increases.

The accuracy of leeside flow field computational simulations remains a concern for several reasons: (1) A comprehensive effort to validate leeside heating predictions has never been attempted. (2) The actual shape, location of the damage will never be known. (3) The progressive nature of the damage and the complicated mixed internal/external flows implies rapidly changing time dependent phenomena and hence unsteady solutions. (4) Details of modeling the proper internal cavity geometry and surface boundary conditions (both within the cavity and on the lee side) are beyond the scope of the currently available CFD methods. Nevertheless, the CFD simulations provided critical flow field information at flight conditions that allowed for an engineering perspective to draw the previously discussed conclusions. Similarly, questions remain about whether the Mach 6 air or Mach 6 CF_4 facility provide a more accurate representation of the high Mach number re-entry conditions of the Orbiter leeside flow field. However, these questions are less critical when considering the data in an engineering context and noting that the computational techniques are solving the equations for the conservation of mass, momentum, and energy and that both facilities reproduce the same basic physics of hypersonic flow.

In order to provide the internal heating environments in support of thermal analysis, new tools and techniques were developed. These included a process for the calibration and verification of the plume heating model, the development of a coupled equilibrium air venting and thermal model of the entire left wing, and the application of available CFD and DSMC computational tools on internal flows with complex geometry. As was discussed, the heating to an object is a function of its geometry. This problem is made even more difficult when the size, shape, and location of the original penetration is unknown, the internal configuration is complex and not designed for a convective environment, and the configuration is changing over the period in question. Thus, in order to provide internal heating environments, a static geometry strategy was pursued. For cases where a penetration in RCC panel acreage was assumed, a round hole was evaluated for simplicity. The area of the hole was the more critical factor because it determined the amount of energy ingested.

The engineering plume heating model used in the investigation had been previously applied for evaluation of micro-meteoroid penetrations of 0.25” to 1.0 “. For this work, holes as large as 10” in diameter were assessed. Experimental data for impinging plumes in a relevant environment were not readily available. This demanded that a process be developed to verify the applicability of the model to these larger diameter penetrations. The first step in the process was to analyze a series of relevant plume flows with two CFD codes. As there were no experimental data available, the CFD analysis relied on current best practices to estimate heat rates due to impinging plumes. Two CFD codes were run independently to develop confidence in the plume heating results. With confidence in the CFD established, the CFD results were compared to the engineering plume model at the same conditions. The engineering plume heating model was shown to compare to within +/- 30% of the CFD solutions. This plume model was used to evaluate plume heating on the wire bundles, wheel well wall, and the interior of the upper wing skin, as well as the

primary penetration in the WLE cavity. Arc jet tests were pursued to provide another source of verification of the plume model, the results of which are currently being evaluated.

An equilibrium air coupled venting and thermal model of the entire left wing of the Orbiter was developed principally to provide the best assessment possible of where the mass and energy of the high temperature gas was propagating within the wing outside of the direct plume impingement zone. This allowed for the evaluation of various penetration sizes and their effect on the interior surfaces and mass and energy distribution. This tool showed the internal compartment pressure and temperature effect that result from primary and secondary penetrations on the WLE, as discussed above, and a penetration of the wing spar. For the case of a 10" diameter hole in the wing spar behind RCC panel 8, it was shown that there was sufficient energy ingested to result in significant thermal damage to the interior of the intermediate wing prior to LOS. The case was used as substantiation for the configurations that were assessed for structural deformation. It also showed that the majority of the high temperature gas would flow towards the wing glove payload bay vent. These results provided the boundary conditions for CFD analysis of the interior wing volume.

CFD analysis was performed on the flow of the wing interior to provide insight into how the high temperature gases entering the wing from a breach of the spar behind RCC panel 8 would behave. The results of these analysis showed that a plume would remain coherent until impacting the wheel well wall and a majority of the flow would circulate back towards the 1040 spar vent as discussed above. The data from this analysis were used to update the heat transfer coefficients in the coupled vent / thermal analysis tool. Also, the analysis was used to assess whether or not an obstruction in the WLE cavity would be enough to redirect the flow such that it would enter into the wing interior normal to the spar. This assessment is important in that it would dictate the size of hole necessary to burn the wire bundle at the observed rate because of the distance involved in reaching the bundle from the WLE spar. The results indicated that any hardware impinged upon by the primary plume would be enough to arrest the momentum and redirect the flow. Since the interior geometry of the WLE cavity and the exact location, size, and shape of the WLE damage location remain unknown, it is likely that the plume entering the WLE did come in normal to the spar even if the flow entered the WLE cavity with some momentum.

Another concern of the internal heating group was the additional energy produced by the combustion of the aluminum that makes up the structure of the Orbiter. There was some concern that the combustion of aluminum could provide more than twice the energy available from only the ingested high temperature gas. Although more applicable to oxygen rich atmospheres, an analysis was performed to provide an estimate of the additional energy available at the high altitudes where the Orbiter was flying prior to breakup. The results showed that prior to EI+600 seconds only 30% additional energy could be released due to aluminum combustion and that variations in the breach hole size would result in larger changes in the total energy ingested. Given the uncertainty in the breach hole size, and therefore, the energy of the reentry-gas ingested, and the uncertainty in the predicted heating rates to the internal structures, the additional heating due to aluminum combustion was enveloped by these uncertainties.

In order to evaluate various size damage configurations of the WLE in support of the working scenario, an engineering heating distribution model of the internal WLE cavity was developed. This was needed not only to assess the direct plume impingement heating but also to provide secondary plume heating or "splash" effects. These "splash" environments were required in order to assess the thermal response of the RCC panel 9 clevis and spar temperature gauges, and again to establish consistency of the assumed damage size and location. But prior to this model's development, the question of, given a large enough hole, how does the external environment couple into the internal WLE cavity environment (i.e., does the plume come in normal to the penetration surface or does it flow in with momentum), had to be understood. The first ever coupled external / internal CFD analysis of the Orbiter was performed having only a simple one-foot vented cube as the interior volume. The results showed that for hole sizes 2" in diameter and greater, the majority of the upstream boundary layer was ingested into the interior volume. This result meant that the gases outside of the shock layer, at > 10,000° F, were being pulled into the WLE cavity. It also showed that the flow coming in carried with it its momentum and thus the plume no longer came in normal to the surface. This was critical for determining the location of plume impingement from a penetration in the acreage of an RCC panel. The initial engineering model was checked against these initial CFD solutions and provided to the thermal group for use in their analysis.

Additional CFD and DSMC analysis of the interior of the WLE was pursued to confirm the engineering model further and to include various degrees of complexity in the interior geometry of the WLE cavity. These involved holes in RCC panels 7 and 8 with and without the complex interior geometry and also partially missing T-Seal cases. All involved coupling the external flow field to the WLE interior. Each case provided further insight into the flow field of the interior WLE cavity. Several significant items resulted from these cases: (1) the heating rate on the edge of the RCC hole was an order of magnitude greater than the peak heating on the exterior of the Orbiter; (2) without a structural obstruction, the interior plume heating rate was an order of magnitude greater than the peak heating on the exterior of the Orbiter; (3) if obstructed, the momentum of the incoming gas would be arrested and redirected towards the spanner beam and spar insulation; (4) the heating distributions from the DSMC and CFD cases with obstructions agreed well with the engineering model; and (5) the heating from a partially missing T-Seal would be enough to burn through the spanner beam insulation but rapidly drops off as the flow reaches the spar. The latter indicated that although there was enough energy to get through the spar in the time required, there was not enough energy available to burn a wire bundle at the observed rate. Thus, the damage site was more likely either on the RCC panel acreage or a combination of panel acreage and T-Seal and less likely a partially missing T-Seal alone.

5.5 References

Bertin, John J. (1994), ”Hypersonic Aerothermodynamics,” American Institute of Aeronautics and Astronautics, Inc., Washington, DC.

Anderson Jr., John D. (1989), “Hypersonic and High Temperature Gas Dynamics,” McGraw-Hill, Inc., New York, NY.

NSTS-37384 Image Analysis Team Final Report projected completion date June 25, 2003

NSTS-37376 Data Review and Timeline Reconstruction Team Final Report in support of the Columbia Accident Investigation, June 3, 2003

NSTS-37379 Starfire Team Final Report in support of the Columbia Accident Investigation, June 3, 2003.

NSTS-37383 Vehicle Data Mapping Final Report in support of the Columbia Accident Investigation, June 18, 2003

NSTS-37385 Hardware Forensics Team Final Report in support of Columbia Accident Investigation projected completion, June 20, 2003

STS-107 Mishap Investigation – Combined Master Timeline, Revision 19.

NSTS-37397 Vehicle Reconstruction Team Final Report in support of the Columbia Accident Investigation, June 25, 2003

NSTS-60502 Columbia Working Scenario Final Report, projected completion date July 1, 2003

Chao, D. C. (2002), ”STS-107 Pre-Flight Aeroheating Report,” Boeing Technical Memorandum, Boeing NASA Systems – Houston, No. ATA-TM-02-0009.

Fay, J. A. (1958), and Riddell, F. R. “Theory of Stagnation Point Heat Transfer in Dissociated Air,” Journal of the Aeronautical Sciences, Vol. 25, No.2.

References for Section 5.2.2

“Orbiter Entry Heating Prediction Methods and Database,” Rockwell International Document STS 83-0948, Rev. 1, July 1988.

Fay, J.A. (1958) and Riddell, F.R., "Theory of Stagnation Point Heat Transfer in Dissociated Air," Journal of the Aeronautical Sciences, Vol. 25, No. 2, pp 73-85.

Beckwith, J.E. (1961), and Cohen, N.B., " Application of Similar Solutions to Calculation of Laminar Heat Transfer on Bodies with Yaw and Large Pressure Gradients in High Speed Flow," NASA TND-625.

Eckert, E.R.G. (1955), "Engineering Relations for Friction and Heat Transfer to Surfaces in High Velocity Flow," Journal of the Aeronautical Science, pp 585-587.

Spalding, D.G. (1964), and Chi, S.W., "The Drag of a Compressible Turbulent Boundary Layer on a Smooth Flat Plate with and without Heat Transfer," Journal of Fluid Mechanics, Vol. 18, pp 117-143.

Miller, B.A. (1984), "An Engineering Approach for Estimating Aeroheating to the Partially Catalytic STS Orbiter TPS Surface," Rockwell International Document STS 84-0015.

Holden, M.S. (????), "Boundary Layer Displacement and Leading Edge Bluntness Effects on Attached and Separated Laminar Boundary Layer in a Compressible Corner, Part I; Theoretical Study," AIAA Journal, Vol. 8, No. 12, pp 2179-2188, and "Part II: Experimental Study," AIAA Journal, Vol. 9, No. 1, pp 84-93.

Keys, J.W. (1973), and Hains, F.D., "Analytical and Experimental Studies of Shock Interference Heating in Hypersonic Flows," NASA TND-7139.

Bertin, J.J. (1975), Graumann, B.W. and Goodrich, W.D., "High Velocity and Real Gas Effects on Weak Two-Dimensional Shock Interaction Patterns," Journal of Spacecraft, Vol. 12, No. 3, pp 155-161.

Bertin, J.J. (1976), Mosso, S.J., Bacrette, D.W. and Goodrich, W.D., "Engineering Flowfields and Heating Rates for Highly Swept Wing Leading Edges," Journal of Spacecraft, Vol. 13, No. 9.

References for Section 5.2.3

Stone, David R. (1972), and Cary, Aubrey M. jr, "Discrete Sonic Jets Used as Boundary-Layer Trips at Mach Numbers of 6 and 8.5", NASA TN D-6802.

Zukoski, Edward E. (1964), and Spaid, Frank W., "Secondary Injection of Gases into a Supersonic Flow", AIAA J., vol. 2, no. 10, pp. 1689-1696.

References for Section 5.2.4

Steinbrenner, J. P. (1990), Chawner, J. R., and Fouts, C. L., "The GRIDGEN 3D Multiple Block Grid Generation System," WRDC-TR-90-3022, Wright Research and Development Center Report.

Alter, S.J. (1997), "The Volume Grid Manipulator (VGM): A Grid Reusability Tool," NASA CR-4772.

Sorenson, R.L. (1995), and Alter, S.J., "3DGRAPE/AL Users' Manual," NASA RP-1377, October 1995.

AMTEC Engineering Inc., (2002), "CFD Analyzer 3.0: User's Manual."

Olynick, D.D.R. (1996), "Importance of 3-D Grid Resolution and Structure for Calculating Reentry Heating Environments," AIAA Paper 96-1857.

Strang, W.Z. (1988), "QBERT: A Grid Evaluation Code," AFWAL Technical Memorandum 99-193, Wright Research and Development Center Report.

Thompson, J.F. (1985), Warsi, Z.U.A., and Mastin, C.W., *Numerical Grid Generation Foundations and Applications*, pp. 171-184, North-Holland, 1st ed.

Bird, G.A. (1976), Molecular Gas Dynamics, Clarendon Press, Oxford.

Boyles, K.A. (2003), LeBeau, G.J., Lumpkin, F.E., Wilmoth, R.G., "The Use of Virtual Sub-Cells in DSMC Analysis of Orbiter Aerodynamics at High Altitudes Upon Reentry", *41st AIAA Aerospace Sciences Meeting and Exhibit*, Reno, NV.

Stewart, D. (1997), "Surface Catalysis and Characterization of Proposed Candidate TPS for Access-to-Space Vehicles," NASA TM 112206.

DeVenezia, J. (1995), Wang, K.C., and Caram, J.M., "Space Shuttle Orbiter Wing Leading Edge Heating Predictions and Measurements," NASA CP 3248, Part 2, pp.741-809.

Baranowski, L. C. (1983), and Kipp, H. W., "A Study of Leeside Flow Field Heat Transfer On Shuttle Orbiter Configurations," NASA Contract NAS1-16839.

Berry, S.A. (2002), Hamilton, H.H., "Discrete Roughness Effects on Shuttle Orbiter at Mach 6," AIAA Paper 2002-2744.

Bouslog, S.A. (1995), An, M.Y., and Derry, S.M., "Orbiter Windward-Surface Boundary-Layer Transition Flight Data," Orbiter Experiments (OEX) Aerothermodynamics Symposium, NASA CP 3248, Part 2, pp. 703-740.

Brauckmann, G.J. (1995), Paulson, J.W., and Weilmuenster, J.K., "Experimental and Computational Analysis of Shuttle Orbiter Hypersonic Trim Anomaly," *Journal of Spacecraft and Rockets*, Vol. 32, No. 5, pp. 758-764.

Buck, G.M. (1989), "Automated Thermal Mapping Techniques Using Chromatic Image Analysis," NASA TM 101554.

Buck, G.M. (2000), "Rapid Model Fabrication and Testing for Aerospace Vehicles," AIAA Paper 2000-0826.

Buck, G.M. (1993), and Vasquez, P., "An Investment Ceramic Slip-Casting Technique for Net-Form, Precision, Detailed Casting of Ceramic Models," U. S. Patent 5,266,252.

Daryabeigi, K. (2003), Berry, S.A., Horvath, T. J., and Nowak, R. J., "Finite Volume Numerical Methods for Aeroheating Rate Calculations From Infrared Thermographic Data," AIAA Paper 2003-3634.

Fay, J.A. (1958), and Riddell, F.R., "Theory of Stagnation Point Heat Transfer in Dissociated Air," *Journal of Aeronautical Sciences*, Vol. 25, No. 2.

Haney, J.W. (1995), "Orbiter Pre STS-1 Aeroheating Design Data Base Development Methodology: Comparison of Wind Tunnel and Flight Test Data," Orbiter Experiments (OEX) Aerothermodynamics Symposium, NASA CP 3248, Part 2, pp. 607-676.

Joels, M.K. (1982), and Kennedy, G.P., "The Space Shuttle Operators Manual," Ballantine Books, New York.

Jones, R.A. (1969), and Hunt, J.L., "Use of Tetrafluoromethane to Simulate Real-Gas Effects on the Hypersonic Aerodynamics of Blunt Vehicles,", NASA TR 312.

Merski, N.R. (1998a), "Reduction and Analysis of Phosphor Thermography Data With the IHEAT Software Package," AIAA Paper 98-0712.

Merski, N.R. (1998b), "Global Aeroheating Wind-Tunnel Measurements Using Improved Two-Color Phosphor Thermography Method" *Journal of Spacecraft and Rockets*, Vol. 36, No. 2, pp. 160-170.

Miller, C.G. (1982), “Experimental Investigation of Gamma Effects on Heat Transfer to a 0.006 Scale Shuttle Orbiter at Mach 6,” AIAA Paper 82-0826.

Miller, C.G. (1999), “Development of X-33/X-34 Aerothermodynamic Data Bases: Lessons Learned and Future Enhancements,” NATO Research and Tech. Org., Applied Vehicle Technology Symposium Aerodynamic Design and Optimization of Flight Vehicles in a Concurrent Multi-Disciplinary Environment, paper no. 32.

Miller, C.G. (1990), “Langley Hypersonic Aerodynamic/Aerothermodynamic Testing Capabilities - Present and Future,” AIAA Paper 90-1376.

Throckmorton, D.A. (1995), “Orbiter Leeside Surface Aeroheating Environment Characterization,” Orbiter Experiments (OEX) Aerothermodynamics Symposium, NASA CP 3248, Part 2, pp. 811-822.

Hartung, L.C. (1988), and Throckmorton, D.A., “Space Shuttle Entry Heating Data Book: Volume I – STS-2,” NASA RP 1191.

Stewart, D., (1997), "Surface Catalysis and Characterization of Proposed Candidate TPS for Access-to-Space Vehicles", NASA TM 112206.

References for Section 5.3.2

Shapiro, A.H. (1953), “The Dynamics and Thermodynamics of Compressible Fluid Flow,” John Wiley & Sons, Inc.

References for Section 5.3.3

Hiester, N.K. (1966), and Clark, C.F., “Feasibility of Standard Evaluation Procedures for Ablating Materials,” NASA CR-379.

Kays, W.M. (1980), and Crawford, M.E., “Convective Heat and Mass Transfer”, McGraw-Hill Book Company, 2nd Edition.

Shapiro, A. (1958), "The Dynamics and Thermodynamics of Compressible Fluid FLow – Volume 1", 1953.
Moeckel, W. and Weston, K. "Composition and Thermodynamic Properties of Air in Chemical Equilibrium", NACA TN 4265.
Hrycak, P. (1970), et al., "Experimental Flow Characteristics of a Single Turbulent Jet Impinging on a Flat Plate", NASA TN D-5690.

Abramovich, (1963), "Theory of Turbulent Jets".

O'Connor, T. J. (1965), Comfort, E. H., and Cass, L. A. "Turbulent Mixing of Axisymmetric Jets of Partially Dissociated Nitrogen and Ambient Air", AVCO Corp Report RAD-TR-65-18.

Donaldson, C. DuP. (1971), and Snedeker, R. S. "A Study of Free Jet Impingements, Parts 1 & 2", J. Fluid Mechanics, Vol 45.

Rebrov, A.K. (1982), “Free Jet as an Object of Non-equilibrium Processes Investigation”, 13th International Symposium on Rarified Gas Dynamics, Vol II, pgs 849-864.

Chen, Y.-S. (1993), Liaw, P., Shang, H.-M. and Chen, C. P., “Numerical Analysis of Complex Internal and External Viscous Flows with a Second-Order Pressure-Based Method,” AIAA Paper 93-2966.

Roy, C. J. (2002), McWherter-Payne, M. A., and Oberkampf, W. L., “Verification and Validation for Laminar Hypersonic Flowfields Part 1: Verification,” manuscript submitted to the AIAA Journal.

References for Section 5.3.4

Gordon, S. (1994), and McBride, B.J., "Computer Program for Calculation of Complex Chemical Equilibrium Compositions and Applications," *NASA Reference Publication 1311*, National Aeronautics and Space Administration.
Glassman, I. (1977), "Combustion," Third Edition, Academic Press.

Werley, B. (1993), Barthelemy, H., Gates, R., Slusser, J.W., Wilson, K.B., and Zawierucha, R., "A Critical Review of Flammability Data for Aluminum," Flammability and Sensitivity of Materials in Oxygen-Enriched Environments, ASTM STP 1197, D.D. Janoff and J.M. Stoltzfus, Eds., American Society for Testing and Materials.

Newton, B. (2000), Hull, W., Stradling, J., "Failure Analysis of Aluminum-Bodied Medical Regulators," Flammability and Sensitivity of Materials in Oxygen-Enriched Environments, ASTM STP 1395, T.A. Steinberg, B.E. Newton, and H.D. Beeson, Eds., American Society for Testing and Materials.

References for Section 5.3.5

Fay, J.F. (1993), "Program CHCHVENT Version 5 User's Manual and Software Description." Sverdrup Technology/MSFC Group, Report 631-001-93-007.

Gnoffo, P.A. (1995), Weilmuenster, K.J., and Alter, S.J., "A Multiblock Analysis for Shuttle Orbiter Re-entry Heating from Mach 24 to Mach 12," NASA CP 3248.

Shapiro, A.H. (1953), The Dynamics and Thermodynamics of Compressible Fluid Flow, Volume 1, New York: John Wiley & Sons.

Haukohl, J. (1972), and Forkois, J.L. "Inflow Venting Orifice Efficiency Test Report." Lockheed Missiles & Space Company Report LMSC-HREC D225598, January.

Wong, LC. (1994), et al, "Orbiter Entry Venting Substantiation Report." Rockwell International Space Systems Division, SSD94D0275.

Cline, D.E. (2002), "As Built OV-102, Flight 27, STS-109 Integrated Vent Model," Boeing Company-Houston, DWC-2002-003.

Cline, D.E. (2003), and Torres, "Main Gear Wheel Well Leakage Mapping and Model," presentation to Aero-Thermal Mishap Investigation team, Boeing-PVD.

Hartung, L.C. (1988), Throckmorton, D.A., "Space Shuttle Entry Heating Data Book, Volume III – STS-5", NASA RP-1193.

Gong, L. (1984), Ko, W.L., Quinn, R.D., "Thermal Response of Space Shuttle Wing During Reentry Heating", NASA TM-85907, June 1984.
Thermal Protection Systems Expert and Material Property Database (TPSX), Web Edition Version 3, NASA Ames Research Center, 2003.

Incropera, F.P. (1985), Dewitt, D.P., "Fundamentals of Heat and Mass Transfer", Second Edition, John Wiley and Sons, Inc..

References for Section 5.3.6

Anon. (1976), U.S. Standard Atmosphere, 1976, National Oceanic and Atmospheric Administration, NASA, and U.S. Air Force.

"RCC 8-9 T-Seal Coupled Internal/External 2-D Bridging Phase II Results", Boeing Rocketdyne Propulsion and Power, CFDPUB00862.

"High Enthalpy Flow Benchmark Results", Boeing Rocketdyne Propulsion and Power, CFDPUB00822.

"High Enthalpy Flow Benchmark Extension Results", Boeing Rocketdyne Propulsion and Power, CFDPUB00865.

"Underexpanded Jet Benchmark Results", Boeing Rocketdyne Propulsion and Power, CFDPUB00866.

"RCC8 10in Leading Edge Breach Results", Boeing Rocketdyne Propulsion and Power, CFDPUB00867.

"Hybrid Viscous Unstructured CFD Mesh Technology", Boeing Rocketdyne Propulsion and Power, CFDPUB00756.

"Application of ICAT/BCFD in the Rocketdyne Design Environment", Boeing Rocketdyne Propulsion and Power, CFDPUB00752.

Goulard, R., "On Catalytic Recombination Rates in Hypersonic Stagnation Heat Transfer," Jet Propulsion, vol. 28, no. 11, 1958, pp. 737-745.

FLUENT 6.1 Users Guide, Volumes 1-24. Fluent Incorporated, 10 Cavendish Court, Centerra Resource Park, Lebanon, N.H. 03766.

References for Section 5.6.3

Gnoffo, P.A. (1989), Gupta, R.N., and Shinn, J., "Conservation Equations and Physical Models for Hypersonic Air Flows in Thermal and Chemical Nonequilibrium," NASA TP 2867.

Cheatwood, F.M. (1996), and Gnoffo, P.A. "Users Manual for the Langley Aerothermodynamic Upwind Relaxation Algorithm (LAURA)," NASA TM 4674.

Roe, P.L. (1981), "Approximate Riemann Solvers, Parameter Vectors, and Difference Schemes," Journal of Computational Physics, Vol.43, pp357-372.

Yee, H.C., (1986), "On Symmetric and Upwind TVD Schemes," NASA TM-88325.

Weilmuenster, K.J. (1994), Gnoffo, P.A., Greene, F.A., "Navier-Stokes Simulations of Orbiter Aerodynamic Characteristics Including Pitch Trim and Bodyflap," Journal of Spacecraft and Rockets, Vol. 31, No. 3, pp355-366.

Gnoffo, P.A. (1994), Weilmuenster, K.J., Alter, S.J., "Multiblock Analysis for Shuttle Orbiter Re-entry Heating from Mach 24 to Mach 12," Journal of Spacecraft and Rockets, Vol. 31, No. 3, pp367-377.

Kleb, W.L. (1994), Weilmuenster, K.J., "Characteristics of the Shuttle Orbiter Leeside Flow Dring a Re-Entry Condition," Journal of Spacecraft and Rockets, Vol. 31, No. 1, pp8-16.

Orbiter Experiments (OEX) Aerothermodynamics Symposium (1995), Edited by David Throckmorton, NASA Conference Publication 3248, Part I and II.

Wong, C.C. (1995), Soetrisno, M., Blottner, F.G., Imlay, S.T., and Payne, J.L., "PINCA:A ScalableParallel Program for Compressible Gas Dynamics with Nonequilibrium Chemistry," SAND 94-2436, Sandia National Laboratories, Albuquerque, NM.

Wong, C.C., Blottner (1995), F.G., Payne, J.L., and Soetrisno, M., "Implementation of a Parallel Algorithm for Thermo-Chemical Nonequilibrium Flow Solutions," AIAA Paper 95-0152.

Hassan, B. (1998), Kuntz, D.W., and Potter, D.L., "Coupled Fluid/Thermal Prediction of Ablating Hypersonic Vehicles," AIAA Paper 98-0168.

Kuntz, D.W. (1999), Hassan, B., and Potter, D.L., "An Iterative Approach for Coupling Fluid/Thermal Predictions of Ablating Hypersonic Vehicles," AIAA Paper 99-3460.

Yoon, S. (1988), and Jameson, A., "An LU-SSOR Scheme for the Euler and Navier Stokes Equa-tions," AIAA Paper 87-0600.

Peery, K.M. (1986), and Imlay, S.T., "An Efficient Implicit Method for Solving Viscous Multi-Stream Nozzle/Afterbody Flow Fields," AIAA Paper 86-1380, June 1986.

Steger, J.L. (1981), and Warming, R.F., "Flux Vector Splitting of the Inviscid Gasdynamic Equations with Applications to Finite Difference Methods," *Journal of Computational Physic*s, Vol. 40, pp. 263-293.

Van Leer, B. (1979), "Towards the Ultimate Conservative Difference Scheme. V. A Second Order Sequel to Godunov's Method," *Journal of Computational Physic*s, Vol. 32, No. 1, pp. 101-136.

Payne, J.L. (1999), and Hassan, B., "Massively Parallel Computational Fluid Dynamics Calculations for Aerodynamics and Aerothermodynamic Applications," Proceedings of the 1998 HPC-CP/CAS Workshop, NASA/CP 1999-208757, pp. 111-116.

Srinivasan, S. (1986), Tannehill, J.C., and Weilmuenster, K.J., "Simplified Curve Fits for the Thermodynamic Properties of Equilibrium Air," ISU-ERI-AMES-86041, Iowa State University.

Roy, C.J. (2000), McWherter-Payne, M.A., and Oberkampf, W.L., "Verification and Validation for Laminar Hypersonic Flowfields," AIAA Paper 2000-2550.

Roy, C.J. (2002), McWherter-Payne, M.A., and Oberkampf, W.L., "Verification and Validation for Laminar Hypersonic Flowfields Part 1: Verification," manuscript submitted to the *AIAA Journa*l.

Payne, J.L. (1995), and Walker, M.A., "Verification of Computational Aerodynamic Predictions for Complex Hypersonic Vehicles using the INCA TM Code," AIAA Paper 95-0762.

Roy, C.J. (2002), Gallis, M.A., Bartel, T.J., and Payne, J.L., "Navier-Stokes and DSMC Simulations for Hypersonic Laminar Shock-Shock Interaction Flows," AIAA Paper 2002-0737.

Roy, C.J. (2002), Gallis, M.A., Bartel, T.J., and Payne, J.L., "Navier-Stokes and DSMC Predictions for Laminar Hypersonic Shock-Induced Separation," manuscript to be submitted to the *AIAA Journa*l.

Alter, S.J. (1997), "The Volume Grid Manipulator (VGM): A Grid Reusability Tool," NASA CR-4772,.

Taubin, G. (1995), "A Signal Processing Approach to Fair Surface Design," SIGGRAPH.

Bartel, T.J. (2001), Plimpton, S.J., and Gallis, M.A., "Icarus: A 2-D Direct Simulation Monte Carlo (DSMC) Code for Multi-Processor Computers: User's Manual - v 10.0," Sandia Report SAND2001-2901, Sandia National Laboratories, Albuquerque, NM.

Bird, G.A. (1994), *Molecular Gas Dynamics and the Direct Simulation of Gas Flows*, Clarendon Press, Oxford.

Wagner, W. (1992), "A convergence proof for bird direct simulation Monte-Carlo method for the Boltzmann-equation," *J. Stat. Phys.*, **66**(3-4), pp.1011-1044.

Gallis, M.A. (2001), Torczynski, J.R., and Rader, D.J., "An approach for simulating the transport of spherical particles in a rarefied gas flow via the direct simulation Monte Carlo method," *Phys. Fluids*, **13**(11), pp.3482-3492.

Gallis, M.A. (2002), Torczynski, J.R., and Rader, D.J., "Calculations of the near-wall thermophoretic force in rarefied gas flow," *Phys. Fluids*, **14**(12), pp.4290-4301.

Torczynski, J.R. (2002), Gallis, M.A., and Piekos, E.S., “Comparison of methods for simulating gas forces on moving microbeams,” ASME Paper IMECE2002-33788.

Roy, C. J. (2002), Gallis, M. A., Bartel, T. J., and Payne, J. L., “Navier-Stokes and DSMC Simulations for Hypersonic Laminar Shock-Shock Interaction Flows,” AIAA Paper 2002-0737.

Roy, C. J. (2002), Gallis, M. A., Bartel, T. J., and Payne, J. L., “Navier-Stokes and DSMC Predictions for Laminar Hypersonic Shock-Induced Separation,” manuscript to be submitted to the *AIAA Journa*l.

Shufflebotham, P.K. (1995), Bartel, T.J., Berney, B., “Experimental validation of a direct simulation by Monte Carlo molecular gas flow model,” *J. Vac. Sci. Technol. B*, **13**(4), pp. 1862-1866.

Johannes, J.J. (1997), Bartel, T.J., Hebner, G.A., Woodworth, J., Economou, D.J., “Direct simulation Monte Carlo of inductively coupled plasma and comparison with experiments,” *J. Electrochem. Soc.*, **144**(7), pp. 2448-2455.

Gallis, M.A. (1999), and Bartel, T.J., “Direct simulation Monte Carlo modeling of viscous interactions,” AIAA Paper 99-3453.

Chakravarthy, S.R. (1985), and Osher, S., Computing With High-Resolution Upwind Schemes for Hyperbolic Equations, Proceedings of the 1983 AMS-SIAM Summer Seminar on Large-Scale Computations in Fluid Mechanics, published by American Mathematical Society in Lectures in Applied Mathematics, Vol. 22.

Rajagopal, K. (1997), Numerical Simulation of Flow Inside an Orbiter Wing Section during Entry through a Hole from a Possible On-Orbit Debris Impact Damage, AIAA Paper No. 97-2227.

Bird, G.A. (1976), *Molecular Gas Dynamics*, Clarendon Press, Oxford (1976).

Wilmoth, R.G. (1996), LeBeau, G.J. and Carlson, A.B., “DSMC Grid Methodologies for Computing Low-Density, Hypersonic Flows About Reusable Launch Vehicles”, AIAA Paper No. 96-1812.

LeBeau, G.J. (1999), "A Parallel Implementation of the Direct Simulation Monte Carlo Method", Computer Methods in Applied Mechanics and Engineering, Vol. 174, pp. 319-337.

LeBeau, G.J. (2001), and Lumpkin III, F.E., “Application highlights of the DSMC Analysis Code (DAC) software for simulating rarefied flows”, *Computer Methods in Applied Mechanics and Engineering*, Vol. 191, Issue 6-7, pp. 595-609.

References for Section 5.6.4

Steinbrenner, J.P. (1990), Chawner, J.R., and Fouts, C.L., “The GRIDGEN 3D Multiple Block Grid Generation System,” WRDC-TR-90-3022, Wright Research and Development Center Report.

Alter, S.J. (1997), “The Volume Grid Manipulator (VGM): A Grid Reusability Tool,” NASA CR-4772.

Sorenson, R.L. (1995), and Alter, S.J., “3DGRAPE/AL Users’ Manual,” NASA RP-1377

AMTEC Engineering Inc. (2002), “CFD Analyzer 3.0: User’s Manual.”

Olynick, D.D.R. (1996), “Importance of 3-D Grid Resolution and Structure for Calculating Reentry Heating Environments,” AIAA Paper 96-1857.

Strang, W.Z. (1988), “QBERT: A Grid Evaluation Code,” AFWAL Technical Memorandum 99-193, Wright Research and Development Center Report.

Thompson, J.F. (1985), Warsi, Z.U.A., and Mastin, C.W., *Numerical Grid Generation Foundations and Applications*, pp. 171-184, North-Holland, 1st ed.

Alter, S.J. (1997) "The Volume Grid Manipulator (VGM): A Grid Reusability Tool," NASA CR-4772.

Taubin, G. (1995), "A Signal Processing Approach to Fair Surface Design," SIGGRAPH.

5.6 Appendix for Aerothermodynamics

5.6.1 Engineering Tools

5.6.1.1 XF0002

XF0002/Exact Attitude Aerothermal Heating Computer Program is the main tool utilized for predicting re-entry heating of the Orbiter. The XF0002 Aeroheating Computer Program was formulated as a design tool for predicting ascent or re-entry heating to geometrically simple vehicle shapes. The program accurately predicts local properties and heat fluxes within the scope of the many user selected options. The options were obtained through the application of open literature publications on the subject and have been modified as required.

For re-entry, 2008 body points (aeroheating models) are used to cover the whole Orbiter body. The models are correlated with wind tunnel test data and the flight data from STS-1 through 5. The technical approaches and the body point heating methodology used in this program are described in Section 5.2.1.

XF0002 is under configuration control by Boeing Orbiter Vehicle Engineering Office.

5.6.2 Wind Tunnel Facilities & Measurement Techniques

The purpose of this section is to provide brief descriptions of the hypersonic aerothermodynamic wind-tunnel facilities and global heating measurement techniques at the NASA Langley Research Center utilized in support of the STS-107 accident investigation. Details regarding these facilities can be found in Miller (1990,1999).

5.6.2.1 Mach 6 Air

Heated, dried, and filtered air is used as the test gas. Typical operating conditions for the tunnel are: stagnation pressures ranging from 30 to 500 psia; stagnation temperatures from 760 deg to 1000 deg R; freestream unit Reynolds numbers from 0.5 to 8 million per ft., freestream and post normal shock gamma of 1.4, and a normal shock density ratio of 5.3. A two-dimensional, contoured nozzle is used to provide nominal freestream Mach numbers from 5.8 to 6.1. The test section is 20.5 by 20 in; the nozzle throat is 0.399 by 20.5 in. The test core varies from 12 to 14 inches depending on the operating condition. A floor-mounted model injection system can insert models from a sheltered position to the tunnel centerline in less than 0.5 s. For heat-transfer and flow visualization tests, the model residence time in the flow is only a few seconds; nominal run time for force & moment testing is approximately 60 to 120 s in this facility although longer run times are possible. Table 1 (sec 4.3.2) summarizes the nominal test conditions for the tests performed for this investigation.

5.6.2.2 Mach 6 CF4

Heated, dried, and filtered carbon tetrafluoride (CF_4 or Freon 14; molecular weight of 88 which is three times heavier than air) is used as the test gas. Typical operating conditions for the tunnel are: stagnation pressures ranging from 60 to 2000 psia, stagnation temperatures up to 1300 R, freestream unit Reynolds numbers from 0.01 to 0.55 million per ft., freestream gamma of 1.21 and a post normal shock gamma of 1.1, and a normal shock density ratio of 11.7. A contoured axisymmetric nozzle is used to provide a nominal freestream Mach numbers from 5.9 to 6.0. The nozzle exit diameter is 20 in with the flow exhausting into an open jet test section; the nozzle throat diameter is 0.466 in. The test core varies from 12 to 14 inches depending on the operating condition. A floor-mounted model injection system can inject models from a sheltered position to the tunnel centerline in less than 0.5 s. For heat-transfer and flow visualization tests, the model residence time in the flow is only a few seconds; nominal run time for force &

moment testing is approximately 20 s. Table 1 (sec 4.3.2) summarizes the nominal test conditions for the tests performed for this investigation.

5.6.2.3 IR Thermography

Model surface temperatures were measured using a FLIR SC2000 infrared imaging system having an un-cooled microbolometer-based focal plane array detector with 320 × 240 detector elements. The imager has a field of view of 24° × 18°, and is sensitive to infrared radiation in the 7–12 micrometer range of the electromagnetic spectrum. An eight-inch diameter zinc selenide window with a transmittance of 0.98 in the 7-14 micrometer spectral range was used for optical access to the test section. The measured infrared radiation was converted to actual surface temperatures using the emittance of a target, which for the phosphor-coated fused silica model was determined to be 0.906. The imager produces 30 frames of images per second, while the data acquisition hardware used with the infrared imaging system was only capable of real–time digital storage of approximately 6 frames per second. With temperature images acquired at different times during a wind-tunnel run, global heat-transfer images are computed assuming one-dimensional semi-infinite heat conduction formulation with convective boundary conditions. Details regarding the test methodology can be found in Daryabeigi, (2003).

5.6.2.4 Phosphor Thermography

With the two-color relative-intensity phosphor thermography technique (Buck, 1989; Merski, 1998a-b), ceramic wind-tunnel models are fabricated and coated with phosphors that fluoresce in two regions of the visible spectrum when illuminated with ultraviolet light. The fluorescence intensity is dependent upon the amount of incident ultraviolet light and the local surface temperature of the phosphors. By acquiring fluorescence intensity images with a color video camera of an illuminated phosphor model exposed to flow in a wind tunnel, surface temperature mappings can be calculated on the portions of the model that are in the field of view of the camera. A temperature calibration of the system conducted prior to the study provides tables used to convert the ratio of green and red intensity images to global temperature mappings. With temperature images acquired at different times during a wind-tunnel run, global heat-transfer images are computed assuming one-dimensional semi-infinite heat conduction. The primary advantage of the phosphor technique is the global resolution of the quantitative heat-transfer data. Such data can be used to identify the heating footprint of complex, three-dimensional flow phenomena (e.g., boundary layer transition locations, flow separation and reattachment locations, etc.) that are extremely difficult to resolve by discrete measurement techniques.

5.6.2.5 Flow Visualization

Flow visualization in the form of schlieren and oil-flow techniques was used to complement the surface heating and force & moment tests. The LaRC 20-Inch Mach 6 air and CF_4 Tunnels are equipped with a pulsed white-light, Z-pattern, single-pass schlieren system with a field of view encompassing the entire test core. Images were recorded on a high-resolution digital camera.

Surface streamline patterns were obtained using an oil-flow technique. Orbiter models were coated with a phosphorescent material dispersed in a thin layer of silicon oil. After the model surface was prepared, the model was injected into the airstream and the development of the surface streamlines was recorded with a conventional video camera. The model was retracted immediately following flow establishment and formation of streamline patterns, and post-run digital photographs were taken.

5.6.3 CFD/DSMC Tools

5.6.3.1 GASP (ARC)

The GASP Real-Gas Navier-Stokes code was the primary code for solutions accomplished at Ames Research Center. This code originated as a commercially available code developed at AeroSoft, Inc, but has been modified at ARC to enhance both capability and robustness specifically for hypersonic reentry applications.

The GASP Reynolds Averaged Navier-Stokes code is a three-dimensional (3D) finite-volume code. Upwind flux options exist for this code, but for the present solutions the Van Leer inviscid flux formulation was applied in all three directions. A formally 3rd order upwind-biased MUSCL scheme combined with min-mod limiter is selected to provide higher order accuracy. Experience at ARC with this code has indicated that wall normal spacing is sufficient to obtain accurate heat transfer with the Van Leer flux formulation and 3rd order accuracy provided the wall node Cell Reynolds number is kept below a value of 5. For most of the calculations provided in the present work the wall node Cell Reynolds number is approximately 1, which yields the best results in convergence and accuracy. Time advancement to steady state is accomplished with either a 2D Approximate Factorization, AF2, in the nominal cross-flow plane with planar relaxation in the streamwise direction, or, alternatively, with a point-Jacobi algorithm with inner iterations. Experience at ARC has shown that these two time-advancement schemes as implemented in GASP are nearly identical in convergence, robustness and speed.

The 5-species finite reaction rate model for dissociating air of Park was used in these calculations using GASP. In this chemistry model, air is composed primarily of molecular nitrogen, N2, and molecular oxygen, O2, with the possibility of dissociation at high temperature into atomic nitrogen, N, and atomic oxygen, O, followed by formation of NO. For the high Mach number, high altitude portion of a low Earth orbit reentry trajectory as considered herein, the molecular oxygen, O2, present in the atmosphere will almost entirely dissociate into atomic oxygen, O, upon encountering the bow shock. However, N2 will undergo but slight dissociation with lesser amounts of N and NO formed. The reaction rates are typically slow enough that little recombination occurs for hypersonic flows prior to the exit boundary except for that due to the catalytic effect of certain thermal protection surface materials.

The real-gas air chemistry has an important effect on the hypersonic flow about the orbiter by altering the shock location since energy is required to dissociate the molecular oxygen through the shock, the temperature and density rise through the shock are not as great as would otherwise occur for a perfect gas thereby reducing the effective gamma for the real gas in the shock relations. A further real-gas effect is that chemical energy is released at the shuttle surface due to recombination of O to O2 as a consequence of the catalytic behavior of the RCG shuttle tile material. This catalytic wall effect yields a higher heating rate to the wall than for non-catalytic materials. Species transport properties are calculated using Blottner relations with mixture properties calculated using Eucken relations.

Stewart characterized the surface catalytic recombination of air due to various thermal protection system insulation materials including RCG as used on the windward side of the shuttle orbiter. RCG and other catalytic materials act to enhance the rate of recombination of atomic oxygen into molecular oxygen and of atomic nitrogen into molecular nitrogen. Molecular NO is assumed to experience no catalytic effect. In the process, additional thermal energy is released to the wall due to the chemical reaction occurring at the surface.

The primary wall boundary condition used for these shuttle calculations is that of radiative equilibrium combined with the above RCG catalytic behavior. In this viscous wall boundary condition, there is an assumption that the radiative heat transfer from the wall exactly balances the thermal energy transfer to the wall due to convective heat transfer combined with energy release to the wall due to the surface catalytic chemical reaction. The radiative equilibrium boundary condition requires the simultaneous solution of 4 species equations (molecular NO is not considered catalytic) combined with an equation for the energy balance, all of which are written at the wall node. To then solve this wall boundary condition for each Navier-Stokes solver iteration, a Newton-Raphson method achieves quadratic convergence.

Additional boundary conditions used include conventional point-to-point zonal boundaries, adiabatic viscous wall, free-stream, and a specified back-pressure outflow boundary condition. Point-wise boundary conditions can be specified optionally for any of the 6 faces of each grid block and were used for the vented cavity panel 9 solutions.

Most of the solutions delivered were laminar throughout the solution domain. However, some eddy-viscosity turbulence models calculations were conducted to establish approximate turbulence heating enhancements and for validation purposes. Turbulence models implemented into this code include the Baldwin-Lomax algebraic model of Baldwin-Lomax and the 2-eq SST/K-Omega turbulence model of Menter. These models have compressibility corrections suitable for hypersonic flows and have been validated for heat transfer in hypersonic strong interactions as implemented in the ARC version of the GASP code. A means for specification of turbulence transition is implemented in the code, but is not used for the present work.

The GASP code was run initially on a serial processor computer (Intel 2 GHz XEON processor running RedHat Linux v 7.3). These early runs were for fully catalytic solid surface rather than RCG on grids of approximately 3/4 million grid points and took 96 hours. To improve throughput, subsequent work was moved to the NAS parallel-processing cluster, chapman, which is based on up to 1024 SGI Origin O3K cpus. For the parallel processor runs, the grids were decomposed into as many as 48 grid blocks each of which was then run on a separate SGI processor in the NAS chapman cluster. With grids of 1.9 million grid points, the chapman parallel processor runs took approximately 48 hours.

Convergence criterion was based on examination of residual history, temperature and pressure history for selected surface points during the entire iteration sequence, and when convergence was nearly complete examination of delta T and delta P surface plots separated by 50 to 200 iterations. Typically the L2 residual would drop by 5 orders of magnitude and the selected surface temperatures and pressures would become constant. The delta T and delta P surface plots were facilitated by the gasptools package written by D. Prabhu and M. Wright of Ames and which is based on perl scripts making use of the GASP print utility and the Tecplot plotting package. Typically the delta T surface plots were examined for constant temperature within 5 degrees over the entire shuttle surface. Some of the damage cases exhibited some oscillation of approximately a 10 degree K magnitude which was deemed acceptable inasmuch as there existed a physical basis.

5.6.3.2 LAURA (LaRC)

The Langley Aerothermodynamic Upwind Relaxation Algorithm (LAURA) was applied to external and internal flow simulations for the Columbia investigation. LAURA is a high fidelity analysis tool, specialized for hypersonic re-entry physics, utilizing state-of-art algorithms for computational fluid dynamic (CFD) simulations. Key elements of LAURA include Roe's averaging and Yee's Total Variation Diminishing (TVD) formulation of second-order, inviscid flux. Yee's TVD formulation has been found to be exceptionally robust and Courant-number-independent using point-implicit relaxation for hypersonic flow simulations. The TVD algorithm uses a non-linear, minmod function as a flux limiter that maintains second-order accuracy away from extrema but can admit limit cycles in the convergence process, particularly in the vicinity of captured shocks. This occurrence usually manifests itself as a stalling of convergence at a very low error norm, essentially a benign ringing in the solution at a level that has no impact on aerothermodynamic quantities. Viscous flux is computed using central differences.

Previous simulations of STS 1,2 and 5 with LAURA to resolve questions of a pitching moment anomaly (STS 1) and to validate heating predictions were published in the AIAA Journal of Spacecraft and Rockets in 1994. Some of this material was also presented in an ITAR restricted document with more detail and dimensions. All of the current simulations specify laminar flow of air in chemical nonequilibrium (N, O, N_2, O_2, NO) and thermal equilibrium. Only CFD point 1 is simulated for internal cavity flow simulations with freestream conditions: V_∞ = 7350.6 m/s, ρ_∞ = 3.9005 10^{-5} kg/m^3, T_∞ = 217.3 K, α = 40.1681 deg., and time = 13.50.53.0. The external flow simulations are implemented on the shared, baseline grid developed for the External Environments Team. The baseline grid has been modified to allow coupling of the external flow with flow through a breach in the wing entering a vented cavity.

5.6.3.3 SACCARA (SNL)

The Sandia Advanced Code for Compressible Aerothermodynamics Research and Analysis, SACCARA, was developed from a parallel distributed memory version of the INCA code, originally written by Amtec Engineering. SACCARA employs a massively parallel distributed memory architecture based on multi-block structured grids. The solver is a Lower-Upper Symmetric Gauss-Seidel scheme based on the works of Yoon et al., and also Peery and Imlay, which provides for excellent scalability up to thousands of processors.

For the current simulations, SACCARA was used to solve the Navier-Stokes equations for conservation of mass, momentum, and energy. The convective fluxes at the interface were calculated using the Steger and Warming flux vector splitting scheme. Second-order reconstructions of the interface fluxes were obtained via MUSCL extrapolation. A flux limiter was employed which reduces the spatial discretization to first order in regions of large second derivatives of pressure and temperature. This limiting process is used to prevent oscillations in the flow properties at shock waves. The use of flux limitiers results in a mixture of first- and second-order spatial accuracy. In this study three different equations of state were used depending on the physics that where being modeled.

The simulations for wind tunnel conditions assumed a perfect gas equation of state. The ratio of specific heat and the gas constant were specified and the remaining state variables were calculated. The viscosity was calculated using Keyes curve fit for air and conductivity was determined by assuming a constant Prandtl number. An iso-thermal, no-slip wall boundary condition was applied to the shuttle surface. This boundary condition enforces a zero velocity condition at the surface and keeps the wall temperature fixed at specified a value, while also assuming a zero pressure gradient at wall. The supersonic inflow boundary condition allows the user to specify inflow variables which remain fixed during the simulation. The outflow boundary condition assumes a zero order extrapolation.

A number of the simulations at flight conditions assumed equilibrium air. Tannehill's curve fits were used to determine the pressure and temperature from the known energy and density. The viscosity was calculated using Sutherland's law for air. The conductivity was calculated by assuming a constant Prandtl number. A radiative-equilibrium, no-slip wall boundary condition was applied to the shuttle surface. The wall temperature was calculated using an emissivity of 0.9. Remaining boundary conditions were as stated above.

The solutions were assumed to be converged when the residuals dropped by six or more orders of magnitude. The iteration histories of the quantities of interest were also carefully examined

A number of code verification studies provide confidence that the SACCARA code is free from coding errors. These studies included comparison to established numerical benchmark solutions as well as code-to-code comparisons with Navier-Stokes and Direct Simulation Monte Carlo approaches.

5.6.3.4 USA (BHB)

The unified solution algorithm (USA) code is a very versatile flow solver that can be used to compute numerical solutions to a large class of aerodynamic and aerothermodynamic problems by solving the Euler or Reynolds averaged Navier-Stokes (RANS) equations. The discretization is of TVD formulation using finite volume framework. Various Riemann solvers can be used with the preferred one being the modified Lax-Freidrichs scheme. A multizonal structural grid bookkeeping method facilitates the treatment of complex geometric topologies. A real gas approach based on a finite rate chemistry formulation can be coupled or uncoupled with the fluid dynamics to treat reacting and nonreacting gaseous species. Additional information on the USA code can be obtained in Chakravarthy (1985). In this work, the approximate factorization scheme using the implicit time marching option was used. The simulations discussed in Sections 5.3.6.1.1 and 5.3.6.2.2 modeled laminar flow conditions using equilibrium air chemistry model. The external flow surface had radiative equilibrium temperature boundary condition whereas the internal surfaces were kept at cold wall temperature of 0 degree F. The simulations were speeded up using grid-sequencing. The convergence of flow simulations were confirmed by monitoring the time history of surface heating results. An additional reference for the framework in which the USA code was applied can be found in Rajagopal (1997).

5.6.3.5 ICAT (B-RKDN)

ICAT is a general Navier-Stokes code that extends the well-validated numerical algorithms and physical models found in the structured USA code into an unstructured solver. ICAT can be used to compute a numerical solution to a large class of aerodynamic and aerothermodynamic problems by solving the Euler or Reynolds averaged Navier-Stokes (RANS) equations, and offers most of the chemistry, boundary condition and solver features of USA. However, the unstructured grid solver available in ICAT offers the advantage of being able to use hybrid viscous grids, which take an order of magnitude less time to create than structured grids, for complex geometries. The use of ICAT, along with Boeing grid generation tools, enabled the modeling and solution of complex orbiter wing and internal geometries in days, rather than in the weeks required for a comparable structured grid model and solution. The most important features of ICAT are currently being integrated into BCFD, Boeing's next generation structured/unstructured solver.

5.6.3.6 FLUENT (LMSC)

FLUENT 6.1 is a commercial Navier-Stokes solver for unstructured meshes. It is a cell-centered, finite-volume code. It is easy to use and the license entails full technical support, as well as two meshing programs called "Gambit" and "TGrid". Users can add their own functionality and models to FLUENT through the use of C-programs, with
Fluent providing a wide range of looping macros for accessing cell centers and face centers.

FLUENT's three solvers can be used to compute the flow and heat transfer for all flow regimes, from low subsonic via transonic and supersonic to hypersonic. The turbulence can be modeled by means of the Spalart-Allmaras model, the k-epsilon or k-omega families, the Reynolds Stress Model, the LES model, or the DES model. The software includes an integrated postprocessing suite.

FLUENT's broad range of physical models, designed to work on unstructured grids, is what differentiates it from other codes. The physical models include combustion models and associated multi-species capability, multiphase models, and radiation models. Finally, problems in which object boundaries move with respect to each other (e.g., stage
separation and store separation) are treated via FLUENT's moving-deforming mesh model.

Fluent Inc. also offers two finite-element solvers - FiDAP and PolyFlow
for engineers working with low-Reynolds number flows, i.e., materials
processing applications, viscoelastic flows, etc.

5.6.3.7 DAC (JSC)

DAC represents NASA's state-of-the-art implementation of the Direct Simulation Monte-Carlo (DSMC) method for simulating rarefied gas dynamic environments. Different than traditional CFD techniques, the DSMC method is a more direct physical simulation of a gas at the molecular level. Molecules are tracked as they move in space and time, colliding with surfaces and other molecules. The move and collision phases are decoupled, allowing molecules to move linearly a distance corresponding to the product of the molecule's velocity and the size of the time step, before collisions are considered. The microscopic quantities tracked during the simulation are converted to more familiar flowfield quantities of density, velocity and temperature by statistically sampling the ensemble of particles in the simulation. Although DSMC solutions are continuously unsteady, steady-state results are achieved by averaging an ensample of samples once a pseudo steady-state condition is achieved. Often, the cells of the grid used to group the molecules for collisions are also used as sampling zones for the flowfield quantities. This provides a distribution of the flowfield quantities throughout the computational domain. Likewise, the molecule-surface collisions simulated at the microscopic level are also converted macroscopic quantities by employing appropriate sampling techniques. For example, the pressure on a surface element is simply the time-rate-of-change of momentum for molecules impacting the surface element, divided by the area of the element. Similar techniques are used to obtain shear stress and heating on surface elements. Further details on the DSMC method can be found in the Reference section.

The DAC Series can simulate 2D, axi-symmetric and 3D problems using a handful of programs that perform specific tasks in the analysis process. The software employs a two level embedded Cartesian grid system that is used to both pair neighboring molecules, and for sampling of the macroscopic quantities. Embedded within the flowfield grid is the surface geometry. DAC represents the surface geometry as a collection of unstructured triangular elements, which also act as sampling zones for surface properties. Each triangle in the surface geometry may be assigned a specific boundary condition type. There are five types of boundary conditions: 1) a solid wall, 2) an outgassing wall, 3) an inflow boundary, 4) an outflow boundary, and 5) as a freestream. A solid wall means no molecules are produced at the wall and none pass through. An outgassing wall is the same as a solid wall, except molecules are created on the flowfield side of the triangle at a rate that matches the specified flux. An inflow boundary also creates molecules on the flowfield side of the triangle, but any molecules that hit that surface will disappear, as will those that hit an outflow boundary or a freestream boundary. Three types of boundary conditions can also be applied to edges of the computational domain: 1) vacuum, 2) freestream, and 3) a symmetry plane.

The rectangular bounding box for the computational domain is specified by the user, as is the discretization in each of the three Cartesian directions. The cells created by this uniform Cartesian grid are referred to as Level-I Cartesian cells – or simply Level-I cells. Each of these Level-I Cartesian cells can be further refined by its own embedded Cartesian grid. These embedded Cartesian grids allow varying degrees of refinement from one Level-I cell to the next as required by the local flowfield properties in that region of the computational domain. These embedded Cartesian grids form Level-II Cartesian cells – or simply Level-II cells. While the Level-II cells may be much smaller than their parent Level-I cell, they may be no larger than the parent Level-I cell, which would be the case if a Level-I cell was refined by a 1x1x1 Level-II grid.

The two-level embedded Cartesian grid system permits variable refinement throughout the computational domain, which is essential for meeting the local mean-free-path cell size requirement. The catch-22 here is that in order to create an appropriate grid, you need to know the local flowfield properties. But in order to accurately predict the flowfield properties, you have to have an appropriate grid. This issue is addressed in DAC through an adaptation process that allows the solution on one grid system to be used as the basis for the creation of a new more appropriate grid. This is an iterative process typically requiring one and sometimes two adaptations. Metrics provided by the post-processing software can be used to determine if additional adaptation in warranted. Figure 5.6.3-1 displays the ratio of the local mean-free-path to the flowfield cell size for the DSMC Point AA solution. As is shown in the figure, mean-free-path resolution was obtained near the body and greater-than-mean-free-path resolution was obtained everywhere else in the computational domain. Historically, solutions that have reached mean free path resolution in their flowfield grids have compared well with experimental data. It should be noted that for the DSMC Point A solution, the mean-free-path resolution requirement was approximated but not satisfied due to the excessive computational load that this would result in. Violation of this rule results in overestimation of the transport properties and the heat flux to the walls (the viscosity and heat conductivity of the flow is overestimated). Based on convergence analysis performed on these solutions the error should not exceed 10%, so the heat fluxes given Section 5.4 should be interpreted as maximum values.

In addition to controlling grid refinement, the adaptation process is also used to automatically specify other simulation parameters throughout the computational domain. The DSMC method also has very specific requirements for the size of the time step used in the simulation, and for having each cell be populated with an adequate number of simulated molecules. The DAC software efficiently addresses these requirements by allowing the time step and ratio of real-to-simulated molecules to be specified independently within each Level-I cell as needed.

In addition to the preprocessor (PREDAC) and the run code (DAC), the DAC Software also contains two post-processing codes, SLICE and SPROP, for viewing flowfield and surface properties, and a utility code, Surface Tools Plus (STP), which can be used for importing different file types, modifying boundary conditions, managing groups, manipulating geometry and performing diagnostic testing of the user created surface grids.

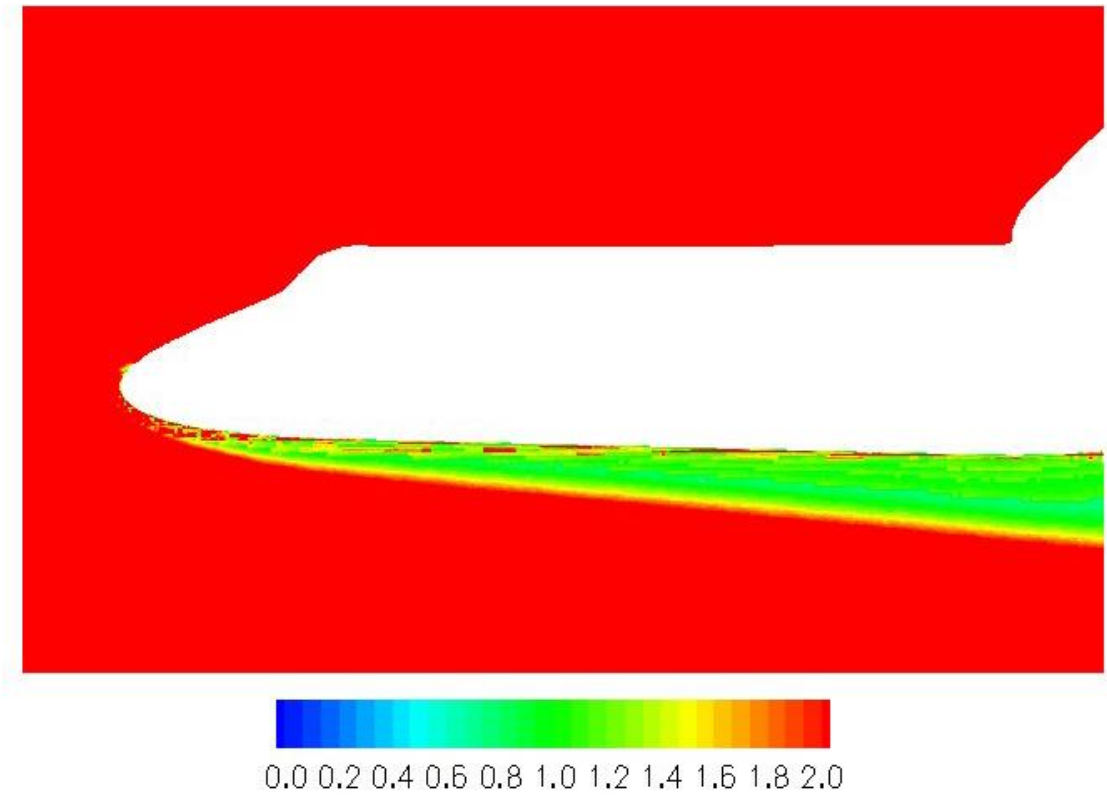

Figure 5.6.3-1 Ratio of Local Mean-Free-Path to Flowfield Cell Size for Nominal Orbiter Configuration DSMC Point AA.

5.6.3.8 ICARUS (SNL)

Icarus is a 2D gas dynamics code developed at Sandia by Bartel *et al.* based on the direct-simulation Monte Carlo (DSMC) method of Bird. It can model flowfields ranging from the continuum to the free molecular regime on Cartesian and axisymmetric grids. Icarus was optimized for a parallel computational environment with thousands of processors.

The DSMC method has been shown to approximate the Boltzmann equation. It employs computational particles that each represent a number of real molecules. During each time step, these particles undergo a deterministic move followed by a stochastic collision process. Collisions can involve multiple species, internal energy modes (rotation and vibration), and chemistry. Macroscale variables, such as temperature and velocity, are obtained by taking appropriate moments over the statistically-represented distribution functions.

The simulations of jet expansion were performed using both Cartesian and axisymmetric grids. The jet was modeled by introducing a constant flux of a given temperature, species mole fraction, and temperature. A vacuum condition was enforced at the outlet by deleting all particles that contact the boundary. The remaining boundaries were modeled as symmetry planes or solid surfaces, as the geometry required. Solid surfaces were treated as isothermal with full thermal accommodation.

The simulations of cavity flow were performed with Cartesian grids. A freestream boundary condition with a specified temperature, pressure, and velocity was enforced at the inflow edge. A vacuum was enforced at the outflow edge. Solid surfaces defining the wing and an open cavity were treated as isothermal with a specified thermal accommodation coefficient. In some calculations a vent was opened in the cavity with a specified outlet pressure.

The solutions were deemed steady-state when the total number of particles on the domain reached an asymptote. Statistical sampling then commenced and continued until the scatter was reduced to an acceptable level for all required quantities.

Extensive code verification studies have been performed on Icarus. These studies include comparison to data from analytic solutions, independent codes, and wind tunnel measurements.

5.6.3.9 VGM (LaRC)

The Volume Grid Manipulator (VGM) software was utilized on the Shuttle Orbiter Columbia Accident Investigation to modify, improve, refine, etc., structured surface and volume grids for viscous flow simulations. The software was developed in the late 1990's based on a set of existing grid manipulation tools. The suite of tools shared one specific drawback – they each required input and output which was the slowest part of operating on a grid. A grid manipulation language to couple the suite together was developed, and the VGM code was produced. Since its inception, the software has found application beyond its original intent, including the removal of negative celled volumes, feature based grid adaptation, and volume grid extrusion.

For the Columbia Accident Investigation, the VGM software was used to:

Correct negative celled volumes.

Transfer and adapt an existing solution to an entirely different topological grid.

Impose an orthogonal boundary condition on a block boundary attached to the wall of the shuttle orbiter.

Implement a C-II continuous matching block boundary condition in three dimensions.

Smooth surface and volume grids produced from adapting a grid to a specific solution.

Increase and decrease grid dimensionality to improve flow simulation accuracy without having to reconstruct the entire volume grid.

Expand existing volume grids to ensure outer bow-shock and entire flow field capture.

Reduce grid stretching and increase grid line intersection orthogonality to improve grid quality for flow simulations.

Smooth solution adapted grids through the implementation of method suggested by Taubin, but extended to fully three-dimensional problems.

The VGM language consists of 10 commands, where each command may have as many as 10 different options with up to 3 different settings for each option. Exercising each command with each option and setting produces a language with over 1000 individual operations. Coupling the individual operations enables the user to expand the capabilities of VGM to do extremely complex manipulations efficiently and with very few commands. Overall, the software provides a set of capabilities that do not exist in any other tool. As such, the user of this software can solve problems posed with structured grids that cannot be solved with any other grid generation software.

5.6.4 Hypersonic Boundary Layer Transition Effective Trip Height Calculation

The effective trip heights shown in Figure 5.2.5-15 were computed at Mach Numbers of 22.91 and 17.9 along the STS-107 flight path. The computations were based on a Euler/approximate boundary layer technique and on a Shuttle ground test boundary layer transition correlation (Berry,2002). Effective trip heights are defined in the study as the height required to move transition onset to the trip location. The transition correlation is presented by Berry as the momentum thickness Reynolds Number divided by the local Mach Number as a function of the roughness height divided by the boundary layer thickness (Figure 5.3.2.15). To establish the correlation, transition data were obtained on a Shuttle model over a range of

parameters including free stream Reynolds Number, angle of attack and roughness heights. The Euler/approximate boundary layer technique was used to compute the flow conditions to form the correlation parameters. Note that in Figure 5.3.2.15 the line defined as incipient transition relates to a trip height that promotes transition downstream of the disturbance(as opposed to occurrence at the trip). Data below the incipient line denote laminar flow, and data above the effective line represent turbulent conditions. Also, the data for the wing attachment line shown in the figure were obtained in the current study. The correlation results were extended to the two fight conditions shown in Figure 5.2.5-15 by first computing the momentum thickness Reynolds Number to Mach Number ratio over the Shuttle and mapping at the same locations the corresponding effective roughness height to boundary layer thickness ratio. For the computed values of boundary layer thickness, the appropriate effective trip heights were then computed and shown in the figure.

5.6.5 STS-107 End of Mission (EOM) 3 Pre-Entry Trajectory

STS-107 EOM3 1/22/03 KSC15 FEBRUARY WT/234200 XCG/1079.1 INC/39.0 D/L 8 XR								
Time (Seconds)	Altitude (Feet)	Velocity (Feet/Sec)	Alpha (Degrees)	Beta (Degrees)	Δ Elevon (Degrees)	Δ Body Flap (Degrees)	FS Density (Slugs/Ft^3)	FS Temp (°R)
0	399984.1	24639.3	39.53	0.46	1.98	-4.40	3.84E-11	682.9
10	395245.6	24651.6	39.71	0.43	1.98	-4.40	4.57E-11	650.9
20	390509.6	24661.4	40.09	0.38	1.98	-4.40	5.48E-11	619.8
30	385776.5	24668.6	40.20	0.31	1.98	-4.40	6.60E-11	589.7
40	381047.2	24672.2	40.00	0.23	1.98	-4.40	7.98E-11	560.5
50	376322.3	24671.4	39.46	0.13	1.98	-4.40	9.71E-11	532.1
60	371602.0	24668.9	39.40	0.01	1.98	-4.40	1.19E-10	504.6
70	366887.2	24663.7	39.54	-0.13	1.98	-4.40	1.47E-10	477.7
80	362178.4	24656.2	39.91	-0.30	1.98	-4.40	1.84E-10	450.7
90	357476.6	24646.7	40.10	-0.31	1.98	-4.40	2.30E-10	427.2
100	352782.9	24635.5	39.64	-0.03	1.98	-4.40	2.91E-10	406.8
110	348097.6	24623.6	39.44	0.28	1.98	-4.40	3.71E-10	387.3
120	343421.9	24612.9	39.82	-0.05	1.98	-4.40	4.76E-10	370.8
130	338757.1	24603.3	39.52	0.45	1.98	-4.40	6.12E-10	358.3
140	334104.5	24595.3	39.56	-0.12	1.98	-4.40	7.89E-10	348.4
150	329465.6	24589.4	39.63	0.20	1.98	-4.40	1.02E-09	339.5
160	324842.9	24585.3	39.61	-0.29	1.98	-4.40	1.32E-09	334.1
170	320238.7	24583.5	39.59	-0.30	1.98	-4.40	1.70E-09	331.5
180	315656.4	24583.6	39.59	-0.42	1.98	-4.40	2.18E-09	329.1
190	311100.3	24584.5	39.57	-0.39	1.98	-4.40	2.80E-09	330.0
200	306575.6	24585.9	39.55	0.21	1.98	-4.40	3.56E-09	334.9
205	304327.1	24586.9	39.59	0.25	1.98	-4.40	4.01E-09	338.2
210	302089.3	24587.8	39.59	0.04	1.98	-4.40	4.50E-09	341.7
215	299863.2	24588.6	39.56	-0.31	1.98	-4.40	5.05E-09	345.4
220	297649.9	24589.0	39.55	-0.30	1.98	-4.40	5.65E-09	348.9
225	295450.7	24589.2	39.58	-0.36	1.98	-4.40	6.31E-09	352.1
230	293267.3	24587.7	39.57	-0.03	-0.10	-4.40	7.03E-09	354.9
235	291100.9	24584.5	39.56	0.01	-2.15	-3.15	7.81E-09	357.0
240	288953.2	24580.9	39.58	-0.31	-4.24	-1.82	8.66E-09	358.9
245	286825.9	24576.9	39.62	-0.53	-6.32	-1.82	9.58E-09	360.7
250	284720.9	24572.3	39.82	-0.45	-7.28	-3.59	1.06E-08	362.7
255	282640.6	24567.1	40.46	-0.62	-5.80	-4.69	1.17E-08	364.6
260	280587.2	24561.0	41.26	-0.36	-2.87	-6.35	1.29E-08	366.5
265	278564.2	24551.6	41.32	-0.07	-1.52	-6.35	1.42E-08	368.2
270	276574.4	24541.8	40.55	-0.05	-2.32	-6.35	1.57E-08	369.8
275	274620.0	24531.8	39.45	-0.37	-4.80	-6.35	1.72E-08	371.3
280	272703.3	24520.6	39.16	-0.21	-5.63	-6.35	1.89E-08	372.8
285	270827.1	24508.2	40.17	-0.21	-3.08	-7.73	2.07E-08	374.2
290	268996.3	24494.3	41.21	-0.36	-0.63	-8.16	2.27E-08	375.6
295	267216.2	24479.3	41.08	-0.27	-0.48	-8.16	2.47E-08	377.1
300	265491.1	24463.8	40.01	-0.30	-2.70	-6.44	2.69E-08	378.3
305	263823.5	24448.1	39.37	-0.17	-3.70	-6.44	2.91E-08	379.6

310	262216.6	24431.6	39.99	-0.29	-2.10	-6.44	3.14E-08	380.7
315	260676.1	24413.5	40.77	-0.07	-0.60	-5.58	3.38E-08	381.7
320	259207.7	24394.4	40.44	-0.24	-2.02	-3.87	3.61E-08	382.5
325	257815.7	24375.1	39.80	-0.14	-4.02	-3.02	3.85E-08	383.2
330	256503.1	24355.2	40.10	-0.09	-2.47	-3.02	4.09E-08	383.8
335	255274.6	24333.9	40.51	-0.05	-2.00	-3.02	4.32E-08	384.3
340	254135.1	24311.9	40.22	0.04	-2.68	-3.02	4.55E-08	385.0
345	253087.5	24289.6	40.19	-1.99	-2.41	-3.02	4.77E-08	385.4
350	252135.7	24266.0	40.72	-0.41	-0.41	-2.40	4.97E-08	385.9
355	251278.6	24241.6	40.27	-0.29	-1.81	-1.03	5.17E-08	386.3
360	250503.9	24217.5	39.83	0.67	-2.30	0.39	5.35E-08	386.8
365	249792.7	24193.1	39.67	0.32	-3.60	0.39	5.52E-08	387.1
370	249134.9	24168.1	39.98	0.27	-3.27	0.39	5.69E-08	387.5
375	248524.0	24142.2	40.14	0.18	-3.34	0.39	5.85E-08	387.8
380	247953.5	24115.8	40.05	0.21	-3.52	0.39	6.00E-08	388.1
385	247417.5	24089.3	40.01	0.21	-3.36	0.39	6.15E-08	388.5
390	246911.2	24062.9	39.98	0.16	-3.45	0.39	6.29E-08	388.8
395	246430.6	24036.0	40.06	0.12	-3.38	0.39	6.42E-08	389.0
400	245973.2	24008.5	40.08	0.05	-3.49	0.39	6.56E-08	389.3
405	245536.9	23980.5	40.02	-0.06	-3.22	0.39	6.69E-08	389.5
410	245119.6	23952.3	39.96	0.01	-3.35	0.39	6.81E-08	389.8
415	244718.0	23923.6	40.03	-0.05	-3.32	0.39	6.94E-08	390.1
420	244329.6	23894.3	40.09	-0.02	-3.04	0.39	7.06E-08	390.3
425	243951.4	23864.7	40.00	-0.09	-3.17	0.39	7.18E-08	390.5
430	243581.0	23834.7	39.94	0.01	-3.36	0.39	7.30E-08	390.7
435	243215.1	23804.4	40.02	-0.07	-3.26	0.39	7.42E-08	391.0
440	242851.1	23773.4	40.04	-0.01	-3.04	0.39	7.54E-08	391.2
445	242485.7	23742.3	39.94	0.08	-3.20	0.39	7.67E-08	391.4
450	242116.3	23710.7	39.96	0.05	-2.85	0.39	7.80E-08	391.7
455	241741.2	23678.6	40.04	0.07	-3.11	0.39	7.93E-08	391.9
460	241359.5	23645.9	40.00	0.05	-3.43	0.39	8.07E-08	392.1
465	240971.8	23613.0	39.92	0.02	-3.24	0.39	8.21E-08	392.4
470	240579.1	23579.7	40.00	-0.01	-3.25	0.39	8.36E-08	392.6
475	240183.4	23545.8	40.03	-0.02	-2.90	0.39	8.51E-08	392.8
480	239787.2	23511.4	39.94	-0.11	-3.24	0.39	8.66E-08	393.1
485	239393.0	23476.7	39.96	-0.10	-3.23	0.39	8.82E-08	393.4
490	239002.9	23441.3	40.05	-0.15	-2.91	0.39	8.98E-08	393.6
495	238618.7	23405.3	39.98	-0.15	-3.29	0.39	9.13E-08	393.8
500	238241.2	23369.0	39.92	-0.18	-3.07	0.39	9.29E-08	394.0
505	237870.2	23332.3	39.98	-0.14	-2.87	0.39	9.45E-08	394.3
510	237504.4	23294.8	40.01	-0.11	-2.77	0.39	9.61E-08	394.5
515	237141.4	23256.9	39.94	-0.01	-2.95	0.39	9.77E-08	394.7
520	236777.7	23218.7	39.91	-0.06	-3.14	0.39	9.94E-08	394.9
525	236411.6	23179.8	40.00	0.01	-2.89	0.39	1.01E-07	395.1
530	236040.2	23140.4	39.95	0.05	-3.12	0.39	1.03E-07	395.4
535	235662.3	23100.6	39.90	0.06	-3.04	0.39	1.05E-07	395.6
540	235277.9	23060.2	40.00	0.07	-2.91	0.39	1.06E-07	395.8
545	234888.7	23019.0	39.98	0.03	-2.94	0.39	1.08E-07	396.0
550	234498.6	22977.4	39.92	-0.09	-2.90	0.39	1.10E-07	396.3
555	234112.4	22935.3	39.95	-0.12	-2.67	0.39	1.12E-07	396.5

560	233734.7	22892.3	39.98	-0.17	-3.18	0.39	1.14E-07	396.7
565	233369.4	22849.0	39.93	-0.19	-2.78	0.39	1.16E-07	397.0
570	233018.4	22805.0	39.91	-0.22	-2.87	0.39	1.18E-07	397.2
575	232681.6	22760.6	39.94	-0.20	-2.79	0.39	1.20E-07	397.4
580	232356.9	22715.7	39.92	-0.14	-2.84	0.39	1.22E-07	397.6
585	232039.2	22670.3	39.94	-0.04	-2.81	0.39	1.24E-07	397.8
590	231722.1	22624.3	39.92	0.04	-2.81	0.39	1.26E-07	398.0
595	231399.7	22578.0	39.93	0.08	-2.84	0.39	1.27E-07	398.2
600	231067.7	22531.0	39.95	0.12	-2.93	0.39	1.29E-07	398.4
605	230723.7	22483.6	39.91	0.09	-2.43	0.39	1.32E-07	398.6
610	230368.9	22435.8	39.74	0.04	-2.91	0.39	1.34E-07	398.9
615	230007.4	22387.5	39.82	-0.07	-2.56	0.39	1.36E-07	399.1
620	229646.0	22338.7	39.65	-0.10	-2.71	0.39	1.38E-07	399.3
625	229290.8	22289.6	39.71	-0.18	-2.27	0.39	1.41E-07	399.6
630	228946.8	22239.9	39.51	-0.22	-2.89	0.39	1.43E-07	399.9
635	228616.4	22189.9	39.58	-0.22	-2.21	0.39	1.45E-07	400.1
640	228299.4	22139.4	39.54	-0.18	-2.40	0.39	1.47E-07	400.4
645	227992.3	22088.4	39.54	-0.07	-2.44	0.39	1.49E-07	400.6
650	227689.0	22036.9	39.54	-0.03	-2.39	0.39	1.51E-07	400.9
655	227383.4	21985.1	39.55	0.02	-2.47	0.39	1.54E-07	401.1
660	227070.9	21932.6	39.55	0.00	-2.38	0.39	1.56E-07	401.4
665	226748.5	21879.6	39.56	0.04	-2.39	0.39	1.58E-07	401.7
670	226414.7	21826.1	39.55	0.00	-2.41	0.39	1.61E-07	402.0
675	226070.6	21772.1	39.59	-0.05	-2.25	0.39	1.63E-07	402.3
680	225719.2	21717.4	39.56	-0.10	-2.43	0.39	1.66E-07	402.6
685	225363.4	21662.0	39.57	-0.06	-2.74	0.39	1.69E-07	403.0
690	225005.7	21606.1	39.58	-0.14	-2.37	0.39	1.71E-07	403.3
695	224649.0	21549.6	39.56	-0.15	-2.45	0.39	1.74E-07	403.6
700	224294.1	21492.3	39.59	-0.11	-2.30	0.39	1.77E-07	404.0
705	223939.5	21434.5	39.58	-0.10	-2.44	0.39	1.80E-07	404.4
710	223582.2	21376.0	39.59	-0.06	-2.66	0.39	1.83E-07	404.7
715	223218.1	21316.9	39.59	-0.02	-2.38	0.39	1.86E-07	405.1
720	222843.4	21257.2	39.56	-0.03	-2.45	0.39	1.89E-07	405.5
725	222455.1	21196.6	39.60	0.00	-2.22	0.39	1.93E-07	405.9
730	222052.1	21135.4	39.59	0.00	-2.43	0.39	1.96E-07	406.3
735	221634.7	21073.3	39.51	-0.09	-2.50	0.39	2.00E-07	406.7
740	221205.8	21010.7	39.55	-0.07	-2.22	0.39	2.04E-07	407.1
745	220767.2	20947.2	39.54	-0.07	-2.15	0.39	2.08E-07	407.6
750	220320.4	20882.8	39.49	-0.07	-2.39	0.39	2.12E-07	408.1
755	219866.1	20818.0	39.47	1.91	-1.69	0.39	2.17E-07	408.5
760	219416.1	20750.2	39.74	0.39	-1.39	1.22	2.21E-07	408.9
765	219064.8	20683.0	39.21	-0.22	-1.59	2.88	2.25E-07	409.2
770	218859.4	20616.0	39.23	-0.30	-1.80	2.88	2.27E-07	409.5
775	218768.1	20549.0	39.22	-0.16	-2.22	2.88	2.28E-07	409.6
780	218696.7	20482.4	39.41	-1.77	-3.45	2.88	2.29E-07	409.6
785	218569.9	20414.7	39.91	-0.13	-3.75	2.88	2.30E-07	409.7
790	218392.9	20345.5	40.30	-0.07	-3.76	1.95	2.32E-07	409.9
795	218166.4	20274.7	40.60	-0.03	-3.31	1.02	2.34E-07	410.2
800	217889.0	20203.2	40.65	-0.04	-3.48	1.02	2.37E-07	410.4
805	217555.9	20130.6	40.84	-0.12	-3.62	1.02	2.41E-07	410.7

810	217162.0	20057.2	40.83	-0.20	-3.58	0.30	2.45E-07	411.1
815	216705.4	19982.2	41.03	-0.09	-3.44	0.09	2.51E-07	411.6
820	216190.2	19906.1	41.04	-0.14	-3.35	0.09	2.56E-07	412.1
825	215621.9	19828.7	41.04	-0.09	-3.67	0.09	2.63E-07	412.7
830	215009.4	19749.8	41.01	-0.09	-3.61	0.09	2.70E-07	413.2
835	214362.1	19669.6	40.86	-0.05	-3.29	0.09	2.78E-07	413.9
840	213690.7	19588.8	40.72	0.01	-3.23	0.09	2.87E-07	414.6
845	213005.6	19506.7	40.57	0.02	-3.18	0.09	2.95E-07	415.3
850	212313.4	19423.8	40.40	-0.10	-2.86	0.09	3.04E-07	416.0
855	211617.7	19339.5	40.27	-0.02	-2.91	0.09	3.14E-07	416.7
860	210923.6	19254.1	40.11	-0.02	-2.81	0.09	3.23E-07	417.5
865	210234.9	19167.5	39.99	-0.08	-2.75	0.09	3.33E-07	418.3
870	209553.6	19079.7	39.87	-0.08	-2.69	0.09	3.43E-07	419.0
875	208882.0	18990.7	39.75	-0.04	-2.77	0.09	3.53E-07	419.7
880	208222.7	18900.2	39.72	-0.08	-2.42	0.09	3.63E-07	420.4
885	207576.7	18808.7	39.64	-0.04	-2.59	0.09	3.73E-07	421.1
890	206944.3	18715.7	39.54	-0.06	-2.41	0.09	3.83E-07	421.8
895	206326.2	18621.5	39.55	-0.04	-2.39	0.09	3.93E-07	422.5
900	205722.0	18525.8	39.55	-0.10	-2.46	0.09	4.04E-07	423.2
905	205129.3	18428.6	39.54	-0.03	-2.47	0.09	4.14E-07	423.8
910	204545.9	18330.0	39.55	-0.08	-2.45	0.09	4.24E-07	424.4
915	203967.2	18230.1	39.55	-0.05	-2.46	0.09	4.35E-07	425.1
920	203388.7	18128.8	39.56	-0.04	-2.48	0.09	4.45E-07	425.8
925	202806.1	18026.1	39.55	-0.04	-2.51	0.09	4.56E-07	426.4
930	202213.9	17922.2	39.55	-0.10	-2.54	0.09	4.68E-07	427.1
935	201606.7	17816.8	39.65	-0.06	-2.59	0.09	4.80E-07	427.7
940	200980.4	17709.5	39.68	-0.06	-2.37	0.09	4.92E-07	428.5
945	200330.4	17600.9	39.75	-0.14	-2.52	0.09	5.06E-07	429.3
950	199653.1	17489.9	39.85	-0.07	-2.72	0.09	5.20E-07	430.0
955	198950.2	17377.0	39.92	-0.05	-2.90	0.09	5.35E-07	430.9
960	198224.3	17261.9	39.90	-0.10	-2.71	0.09	5.52E-07	431.8
965	197476.9	17144.9	39.98	-0.04	-2.77	0.09	5.69E-07	432.7
970	196710.1	17025.8	39.93	-0.08	-3.00	0.09	5.87E-07	433.7
975	195925.2	16904.5	40.01	-0.09	-2.91	0.09	6.06E-07	434.6
980	195124.4	16781.0	39.95	-0.03	-2.84	0.09	6.25E-07	435.8
985	194310.2	16656.0	39.99	-0.06	-3.13	0.09	6.46E-07	436.8
990	193484.9	16529.1	39.96	-0.08	-3.08	0.09	6.68E-07	438.0
995	192649.8	16400.4	39.94	-0.03	-3.07	0.09	6.90E-07	439.2
1000	191807.3	16269.1	39.94	-0.07	-3.00	0.09	7.14E-07	440.4
1005	190957.4	16135.7	39.98	-0.06	-3.12	0.09	7.38E-07	441.7
1010	190100.0	16000.1	39.95	-0.05	-3.02	0.09	7.63E-07	443.0
1015	189235.4	15862.3	39.95	-0.09	-3.26	0.09	7.89E-07	444.3
1020	188362.9	15722.2	39.93	-0.07	-3.49	0.09	8.16E-07	445.6
1025	187481.4	15579.5	40.00	-0.06	-3.56	0.09	8.45E-07	447.0
1030	186589.8	15434.7	39.97	-0.05	-3.53	0.09	8.74E-07	448.4
1035	185686.8	15287.5	40.03	-0.06	-3.61	0.09	9.05E-07	449.8
1040	184770.8	15137.9	40.06	-0.05	-3.89	0.09	9.37E-07	451.2
1045	183839.6	14985.8	40.10	-0.08	-4.09	0.09	9.71E-07	452.5
1050	182888.3	14831.0	40.17	-0.06	-4.19	0.09	1.01E-06	454.0
1055	181913.1	14673.7	40.19	-0.07	-4.57	0.09	1.04E-06	455.3

1060	180910.5	14513.1	40.36	-0.36	-4.71	0.09	1.09E-06	456.6
1065	179889.1	14350.3	40.21	-0.08	-4.64	0.09	1.13E-06	457.9
1070	178918.9	14186.9	39.91	0.21	-4.86	0.09	1.17E-06	459.1
1075	178067.7	14023.6	39.67	0.19	-4.56	0.09	1.21E-06	460.1
1080	177347.1	13860.6	39.52	0.03	-4.68	0.09	1.24E-06	460.9
1085	176724.9	13697.9	39.43	-0.13	-4.90	0.09	1.27E-06	461.6
1090	176152.3	13536.1	39.39	-0.16	-4.82	0.09	1.30E-06	462.2
1095	175593.1	13374.4	39.46	-0.10	-5.16	0.09	1.33E-06	462.8
1100	175031.4	13213.0	39.50	-0.08	-5.51	0.09	1.36E-06	463.5
1105	174461.4	13051.5	39.58	-0.05	-5.86	0.09	1.39E-06	464.1
1110	173878.9	12890.1	39.66	-0.07	-6.34	0.09	1.42E-06	464.8
1115	173276.2	12728.6	39.73	-0.05	-6.69	0.09	1.45E-06	465.5
1120	172645.7	12567.1	39.79	-0.05	-6.89	0.09	1.48E-06	466.1
1125	171982.4	12405.4	39.90	-0.03	-6.49	-0.86	1.52E-06	466.9
1130	171283.6	12244.0	39.84	-0.04	-6.75	-0.86	1.56E-06	467.7
1135	170547.6	12082.6	39.84	-0.08	-6.61	-0.86	1.60E-06	468.5
1140	169773.5	11921.5	39.83	-0.06	-6.99	-0.86	1.65E-06	469.3
1145	168966.5	11760.6	39.75	-0.06	-7.13	-0.86	1.70E-06	470.2
1150	168134.2	11599.5	39.69	-0.04	-7.35	-0.86	1.75E-06	471.1
1155	167281.4	11438.7	39.65	-0.03	-7.33	-0.86	1.81E-06	471.9
1160	166408.7	11278.1	39.59	-0.04	-7.40	-0.86	1.87E-06	472.8
1165	165514.7	11117.6	39.47	-0.05	-7.45	-0.86	1.93E-06	473.5
1170	164596.2	10957.6	39.34	-0.08	-7.39	-0.86	2.00E-06	474.2
1175	163649.5	10798.0	39.21	-0.06	-7.59	-0.86	2.07E-06	474.8
1180	162672.1	10638.6	39.10	-0.34	-7.24	-0.86	2.15E-06	475.5
1185	161677.1	10477.8	39.06	-0.24	-7.18	-0.86	2.23E-06	475.9
1190	160830.2	10316.7	38.82	-0.20	-6.97	-0.86	2.30E-06	476.1
1195	160265.4	10156.2	38.73	-0.10	-6.93	-0.86	2.35E-06	476.2
1200	159937.2	9996.5	38.68	-0.05	-7.19	-0.86	2.38E-06	476.2
1205	159630.2	9840.8	38.65	0.21	-8.15	-0.86	2.41E-06	476.3
1210	159171.9	9686.7	38.84	0.22	-7.97	-2.72	2.46E-06	476.3
1215	158523.9	9534.9	38.76	0.19	-7.55	-2.76	2.52E-06	476.3
1220	157702.7	9385.1	38.64	0.10	-7.61	-2.76	2.60E-06	476.3
1225	156769.7	9237.0	38.31	-0.20	-7.54	-2.76	2.69E-06	476.3
1230	155801.8	9091.0	37.98	-0.30	-7.25	-2.76	2.80E-06	476.3
1235	154846.5	8947.1	37.61	-0.26	-7.07	-2.76	2.90E-06	476.4
1240	153910.6	8805.3	37.26	-0.12	-6.93	-2.76	3.01E-06	476.6
1245	152971.8	8665.4	36.89	0.03	-6.59	-2.76	3.12E-06	476.8
1250	151997.5	8527.8	36.58	0.09	-6.64	-2.76	3.23E-06	477.1
1255	150968.2	8391.9	36.26	0.09	-6.35	-2.76	3.36E-06	477.3
1260	149885.0	8257.8	35.92	0.02	-6.47	-2.76	3.51E-06	477.3
1265	148768.0	8125.5	35.51	-0.09	-6.15	-2.76	3.66E-06	477.2
1270	147644.2	7994.6	35.13	-0.15	-5.97	-2.76	3.83E-06	476.8
1275	146532.0	7865.3	34.77	-0.17	-5.66	-2.76	4.00E-06	476.1
1280	145434.1	7737.4	34.33	-0.08	-5.61	-2.76	4.19E-06	475.1
1285	144338.0	7611.0	33.93	-0.02	-5.39	-2.76	4.38E-06	474.0
1290	143225.8	7486.2	33.58	0.01	-5.26	-2.76	4.58E-06	472.7
1295	142085.4	7362.9	33.18	-0.02	-5.15	-2.76	4.81E-06	471.4
1300	140912.7	7241.0	32.78	-0.06	-5.00	-2.76	5.05E-06	470.2
1305	139708.6	7120.4	32.39	-0.06	-4.60	-3.61	5.31E-06	468.8

1310	138474.9	7001.0	31.91	0.00	-4.52	-3.69	5.59E-06	467.6
1315	137213.0	6883.0	31.49	-0.02	-4.32	-3.69	5.89E-06	466.3
1320	135927.7	6766.3	31.05	-0.07	-4.05	-4.61	6.21E-06	464.9
1325	134625.6	6650.7	30.60	-0.05	-4.23	-4.61	6.56E-06	463.5
1330	133313.5	6534.3	30.44	-0.06	-3.76	-5.53	6.94E-06	462.1
1335	131989.1	6418.4	29.99	0.03	-3.55	-5.83	7.34E-06	460.6
1340	130641.9	6303.3	29.54	-0.02	-3.06	-7.37	7.78E-06	458.9
1345	129273.4	6189.6	29.02	-0.04	-3.27	-7.37	8.25E-06	457.1
1350	127888.4	6077.3	28.53	-0.04	-2.97	-7.50	8.76E-06	455.3
1355	126494.6	5965.6	28.07	-0.04	-2.65	-9.19	9.32E-06	453.3
1360	125095.7	5855.4	27.57	-0.03	-2.59	-9.19	9.91E-06	451.3
1365	123694.3	5746.2	27.08	-0.03	-2.59	-9.19	1.06E-05	449.2
1370	122292.7	5637.8	26.66	-0.02	-2.38	-10.10	1.12E-05	447.2
1375	120891.7	5530.4	26.15	-0.02	-2.25	-11.01	1.20E-05	445.2
1380	119488.9	5424.5	25.68	0.00	-2.31	-11.01	1.27E-05	443.2
1385	118083.1	5319.7	25.24	-0.04	-2.44	-11.01	1.36E-05	441.1
1390	116676.7	5215.7	24.84	-0.01	-2.59	-11.01	1.45E-05	439.1
1395	115269.8	5112.6	24.36	-0.04	-2.76	-11.01	1.54E-05	437.0
1400	113861.7	5010.4	23.89	-0.03	-2.78	-11.01	1.64E-05	434.9
1405	112454.1	4909.3	23.38	-0.01	-2.57	-11.01	1.76E-05	432.8
1410	111049.2	4809.3	22.88	0.00	-2.48	-11.01	1.87E-05	430.6
1415	109649.6	4710.2	22.40	0.00	-2.53	-11.01	2.00E-05	428.4
1420	108257.4	4612.0	21.98	0.59	-2.03	-11.01	2.14E-05	426.2
1425	106943.1	4512.5	21.62	0.15	-1.82	-11.01	2.27E-05	424.1
1430	105846.0	4412.5	21.20	0.12	-1.91	-11.01	2.39E-05	422.4
1435	104929.4	4313.0	20.92	-0.18	-2.00	-11.01	2.50E-05	420.9
1440	104021.4	4215.3	20.63	-0.01	-2.55	-11.01	2.61E-05	419.5
1445	103047.8	4119.0	20.47	0.03	-2.24	-11.01	2.73E-05	418.1
1450	102006.9	4024.6	20.19	-0.02	-2.48	-11.01	2.87E-05	416.5
1455	100890.1	3930.9	20.03	0.01	-2.38	-11.01	3.03E-05	414.8
1460	99695.7	3838.1	19.74	-0.03	-2.14	-11.01	3.21E-05	413.1
1465	98427.7	3746.1	19.43	0.01	-1.80	-11.01	3.42E-05	411.3
1470	97103.3	3655.7	18.97	0.00	-1.69	-11.01	3.64E-05	409.5
1475	95739.6	3566.6	18.56	0.00	-1.36	-11.01	3.89E-05	407.7
1480	94355.4	3477.7	18.15	0.01	-1.01	-11.01	4.16E-05	406.0
1485	92967.9	3389.3	17.72	0.04	-0.55	-11.01	4.46E-05	404.4
1490	91587.4	3301.5	17.29	0.04	-0.48	-11.01	4.77E-05	402.7
1495	90220.6	3214.1	16.78	0.01	-0.21	-11.01	5.10E-05	401.1
1500	88871.4	3127.4	16.35	0.03	-0.15	-11.01	5.45E-05	399.6
1525	82491.2	2702.0	14.77	0.03	-1.47	-11.01	7.49E-05	392.1
1550	76943.2	2283.9	13.52	0.20	-3.26	-11.01	9.92E-05	386.9
1575	72271.4	1882.0	11.73	0.10	-4.83	-11.01	1.26E-04	381.3
1600	66475.0	1568.7	10.26	0.10	-6.25	-11.01	1.72E-04	373.1
1625	59398.3	1276.8	9.30	0.17	-2.91	-11.01	2.52E-04	365.6
1650	52749.6	1010.9	8.98	0.27	2.18	-11.01	3.50E-04	368.7
1675	46737.0	848.5	10.47	0.28	7.04	-7.42	4.61E-04	378.1
1700	40406.4	777.7	11.07	-0.35	6.16	0.35	6.04E-04	392.0
1725	31130.9	801.1	10.03	-0.03	0.08	8.62	8.64E-04	420.0
1750	25762.5	735.9	8.30	-0.01	0.74	4.90	1.04E-03	441.3
1775	22151.3	675.3	8.16	-0.02	1.19	4.90	1.17E-03	455.9

1800	18315.8	636.5	7.52	-0.12	2.44	9.85	1.32E-03	470.8
1825	13676.3	604.1	7.19	-0.23	3.71	12.31	1.53E-03	485.9
1850	8865.0	593.3	5.14	-0.05	6.47	1.16	1.78E-03	500.7
1875	4352.1	544.0	5.17	-0.10	6.62	0.35	2.05E-03	511.1
1900	474.5	526.8	7.25	-0.07	2.96	0.35	2.31E-03	521.9
1923.48	-168.8	365.5	9.00	-0.02	2.14	0.35	2.35E-03	524.1

6 THERMAL

6.1 Panel 8/9 Spar & Clevis Thermal Analysis

A thermal analysis was conducted to compare the flight data instrumentation of the spar (V09T9895) and clevis (V09T9910) to the predicted thermal response in a plume heating environment of each of these panel 9 locations. The wing leading edge (WLE) cavity is shown in Figure 6-1. Two independent thermal math models, one from JSC and the other from Boeing Huntington Beach (B-HB), were utilized to perform this analysis.

The B-HB RCC panel 9 finite element model includes the entire RCC panel/T-Seal, internal insulation and metallic hardware including the spar aluminum honeycomb. Radiation between the RCC IML and internal insulation was simulated using the Thermal Radiation Analyzer System (TRASYS) software. Radiation was also simulated from the aluminum spar to the wing cavity using an existing structural model of the upper and lower wing without damage. The RCC inner mold line (IML), internal insulation, and metallic hardware, at the thermocouple locations, were compared to flight data to assure accuracy of the model. The flight certified model is used to support RCC mission life evaluation. This TMM was modified to simulate RCC damage with 6 and 10 inch holes at the center of the RCC panel. STS-107 nominal End-Of-Mission2 (EOM2) was utilized for the outer mold line (OML) heating. Internal plume heating, to be discussed later in detail, was taken from reference heating mapped on the internal RCC and insulation components with stagnation heating of 1.9 times the entering plume and significantly reduced over the spanner beam and spar insulation. As the internal components' material temperature limit exceeded its melting point the analysis was stopped in order to re-configure the TMM. A new geometry was developed to account for missing components and additional heating. The internal component material melting points used in the analysis are listed; Inconel (2500°F), Nextel Fabric (3000°F), Cerachrome (2600°F), and Aluminum (1000°F).

A simplified finite element TMM of the spar, spar insulation, and RCC fitting was developed by the JSC for this investigation. The spar is made entirely of Aluminum 2024-T6 with 0.03-inch thick facesheets that are adhesively bonded to a 1.0-inch thick honeycomb core. The Generic Honeycomb Modeling Tool was used to generate the effective heat transfer properties for the honeycomb spar. The honeycomb attributes for the spar in the region of panel 8 and 9 were gathered from stress report STS89-0537. These effective properties were then used to model the spar in the simplified finite element thermal model of the spar. The embedded aluminum fitting support bars are also included in the model. The spar insulation was modeled and an emittance of 0.85 was used for the outer Inconel foil material. The aluminum/cerachrome interface was assumed to be in intimate contact with no temperature difference at the gap. The four RCC attach fittings are made of steel A-286 and attached to the clevis hardware on the RCC. The RCC attach fittings were modeled each as a single diffusion node. The fitting temperatures are representative of the clevis temperatures and are reported as the clevis temperatures. Nominally, the clevis temperatures do not change until after 550 sec; well after STS-107 V09T9910 went off scale low. During this time, conduction from the RCC is insignificant and the only paths for heat to flow to the clevis are from the RCC fittings and through additional convective heating. The radiative boundary conditions for entry were based on the entry RCC inner mold line (IML) temperatures predicted for STS-107 by the Boeing Houston aero-thermal group. These boundary conditions were applied to the outer spar insulation surface. On the backside of the spar, where the inner wing structure is located, a constant boundary temperature of 22°F is used.

For the ascent thermal analysis using the JSC model, the boundary conditions are changed to the predicted ascent RCC IML temperatures. On the backside, the radiative boundary temperatures decreased from 55°F to 30°F. The backside spar ascent boundary conditions were determined by correlating the data to STS-109, since they had identical initial temperatures prior to the temperature increases at 300 seconds from launch.

The plume heating estimates for stagnation are and distributions within the cavity are discussed in section 5.3.3 and results summarized here for varying breach hole sizes in panel 8. Using equation (6-1), the time varying heat rate on panel 9 was generated.

$$\dot{q}(x,y,z,t,d_{hole}) = \dot{q}/\dot{q}_{plate}(x,y,z,d_{hole}) \times \frac{\bar{q}_{\infty}(t)}{\bar{q}_{\infty}(488)} \times \frac{V_{\infty}^{2}(t)}{V^{2}{}_{\infty}(488)} \times \dot{q}_{plate}(d_{hole}) \quad (6\text{-}1)$$

where;

$\dot{q}_{plate}(d_{hole})$ is 27.1, 30.1, 55.9 BTU/ft^2-sec for a 4 inch, 6 inch, and 10 inch hole respectively.

Figure 6-2 shows how $\dot{q}/\dot{q}_{plate}(x,y,z,d_{hole})$ varies for a 10 inch hole. The average distribution factor of the stagnation heating value over panel 9 for a 4 inch, 6 inch, and 10 inch hole are .02, .08, and .12, respectively. Additional heating behind the spar insulation, directly on the aluminum near bottom clevis locations, is also considered as a fraction of the panel 9 heating.

The ascent heating for internal flow impingement on the spar insulation was determined by normalizing the panel 8 stagnation heating with body point 5505 entry heating. The normalization factors are then applied to the STS-107 predicted ascent heating for body point 5505. The normalization factors used for the 4 inch, 6 inch, and 10 inch holes are 0.89, 1.0, and 1.8, respectively. The same distribution factors are then applied to the panel 9 spar insulation for ascent heating.

The thermal math models were solved using the Systems Improved Numerical Differencing Analyzer (SINDA). The B-HB model results are shown in Figure 6-3, through Figure 6-5. Figure 6-3 suggests that the heating through a 10 inch hole will produce a temperature rise on the back of the panel 9 spar that matches flight data V09T9895. The assumption of sneak flow directly onto the clevis, on the order of 1%, is necessary to match the flight data of V09T9910 as shown in the comparison of Figure 6-4 and Figure 6-5.

The JSC model predictions in Figure 6-6 and Figure 6-7 are shown for a 6 inch, and 10 inch hole. Figure 6-6 shows the instrumentation location on Panel 9 thermal response to varying hole sizes. A hole size between 6 inch and 10 inch will match the flight data V09T9895. The JSC model also requires a sneak flow assumption of 10% to match the clevis flight data, V09T9910 as shown in Figure 6-8. In Figure 6-9, sensitivity analysis of the thermal response was considered for a 50% variation in the heating data due to uncertainties.

The results from the ascent analysis are shown in Figure 6-10. Here it is shown that the predicted spar temperature rise during ascent is slightly higher with a pre-existing hole in the wing leading edge. STS-109 (undamaged condition) and STS-107 (presumably damaged condition) flight data are compared to these analytical results. It can be surmised that the thermal response of the STS-107 flight data is consistent with the analytical predictions for a damaged wing leading edge during ascent.

6.1.1 Damaged Tee-seal

An auxiliary analysis was performed to assess the feasibility for a damaged tee-seal between panel 8 and panel 9 to cause the observed flight data in the Panel 8/9 region. This analysis assumed that the tee-seal was damaged to the extent that it was completely missing for a 20 inch length on the lower portion of the seal. The same methodology as described in section 6.1 was used to compute the spar breach time and temperature response of the flight measurements using the heating rates described in section 5.3.3.

Analysis results using the Boeing-HB thermal math model is shown in Figure 6-11. This figure shows the computed temperature transients for the spar insulation immediately behind the tee-seal. This insulation does not have the Nextel fabric under the inconel foil and therefore has a lower failure temperature of about 2,600°F. Here the insulation fails within 400-500 seconds. The temperature response for the aluminum spar behind the insulation is predicted to fail at 360 seconds. This is earlier than the estimated actual spar breach time of 487 seconds.

Figure 6-12 shows the spar temperature transient prediction compared to the measured flight data. Here it is seen that the predicted temperature rise is much quicker than the flight data. Note that this analysis

is invalid after about 500 seconds because hot gases know to be within the wheel well at this time were not simulated. Figure 6-13 shows the analytical clevis temperature compared to the flight data. Here it is seen that the analytical prediction rises slightly earlier than the flight data but is not totally out of proportion.

This analysis and the analysis presented in section 6.5.1 suggests that a damaged tee-seal is not a likely scenario for initial damage to the wing leading edge.

6.2 Spar Burn Through Analysis

Several scenario-based and flight data-based data suggest that the wing leading spar experienced a breach during the mission. The most significant of these is the failure of the wire cables which run along the backside of the wing leading edge. Figure 6-14 shows a picture of this region and summarizes the failure times for each of these cables. Thermal analysis and torch testing has shown that the time for failure of one of these cables is less than three seconds. Therefore it is believed that the cable failure time gives a good indication of the when the spar is breached immediately in front of the cable. Since the cables do not provide full coverage of the spar and the original location of the breach is unknown, the exact time of the breach is uncertain but occurred no later than 487 seconds.

A geometric analysis was used to determine if the hole size as a function of time could be determined from the cable failure times. The result of this assessment is shown in Figure 6-15. Here it is predicted that the spar hole could reach a size of 580 in^2 by 520 seconds. It can be rationalized that the hole growth is eventually stunted and arrested as shown by the analysis due to the following factors:

- High mass of the spar embedded aluminum fitting support bars effectively “frames out” a rectangular limit for the hole
- Plume effect on the spar from the wing leading edge hole is arrested by the limited growth of the hole in the RCC.

A parametric analysis was also performed with this model to determine the initial breach time. Here the initial location was parametrically varied and the initial breach time computed. From these analyses, the spar could have been breached from 478 to 487 seconds from entry interface. Although the strain measurements and associated structural analysis suggest that the breach occurred between 420 and 470 seconds from entry interface, supporting data for a spar breach in this time frame comes from:

- Bundle 3 wire harness failure (before 498 sec)
- Bit flip in wheel well (488 sec)
- PNL 8/9 thermal analysis (490 sec)

6.3 Wheel Well Thermal Analysis

A thermal analysis was used to compare predicted heating to the flight data instrumentation summarized in Table 6-1 for the wheel well. Here a hot gas plume originating from the wing leading edge spar is assumed to impact the outboard wheel well wall. The hot outboard wall then conducts heat into the adjoining walls and radiates into the main landing gear (MLG) wheel well and the associated sensors within.

Table 6-1 - Wheel Well Sensor Summary

MEAS. NO.	DESCRIPTION
V58T0125A	SYS 1 LMG UPLK ACT UNLK LN
V58T0405A	L H MLG STRUT ACTUATOR
V58T0841A	SYS 2 L AFT BK SW VLV RTN
V58T0842A	SYS 3 L FWD BK SW VLV RTN
V58T1700A	L MLG BRK HTR LN 1 SYS 1&3
V58T1701A	L MLG BRK HTR LN 3 SYS 2&3
V58T1702A	L MLG BRK HTR LN 2 SYS 1&3
V58T1703A	L MLG BRK HTR LN 4 SYS 2&3

A thermal math model shown in Figure 6-16 was developed directly from computer aided design (CAD) models and used to predict the sensor responses in this presumed scenario. Shell elements were used where possible for simplicity with the remaining geometry represented by solid tetrahedral elements. Main Landing Gear (MLG) components were then thermally connected by combining nodes at joint locations. This allowed for faster analysis since arbitrarily low conductors (which is a common method to join components) can significantly reduce the time step in order to maintain a required accuracy. Internal radiation was also modeled using the Monte Carlo technique with 16000 rays per node. All of the nodes representing sensor locations had an initial temperature corresponding to the flight data. The rest of the components and the wheel well walls had an assumed initial temperature of 80°F.

The predicted plume heating distribution model is described in section 5.3.3. The heating was calculated for a 5 inch diameter hole in the wing leading edge spar assumed to appear instantaneously at EI+488sec (13:52:17 GMT). The plume impinged upon the outboard wheel well wall at location xo=1105, zo=309 and at a distance of 56 inch from the spar. Correction factors were applied for the 31.5 degree off normal impact angle as well as the internal wing pressure. The center of the plume had a heating rate of 22.1 BTU/ft^2-sec with the heating dropping off radially from the centerline. Melting of the outboard wall was not modeled, therefore, once a node reached melting temperature (935°F) it was then held at this temperature.

The thermal math model was solved using the Systems Improved Numerical Differencing Analyzer (SINDA). Predicted temperatures for the hydraulic lines and the strut actuator were obtained and are shown in Figure 6-17 through Figure 6-24. Initially, all the sensors begin to trend towards 80°F from radiation exchange with the 80°F surrounding structure. At 488 sec (GMT 13:52:17) the plume heating is applied to the outboard wall and the temperatures begin to trend upward at a rate dependant on their view factor to the outboard wall.

Table 6-2 - Sensor location and view factor summary

Sensor	Location	View Factor
V58T1700A	Bottom of strut	Good
V58T1701A	Bottom of strut	Good
V58T1702A	On inboard wall	Partial
V58T1703A	On inboard wall under debris shield	Poor
V58T0841A	On inboard wall under debris shield	Poor
V58T0842A	On inboard wall	Poor
V58T0125A	On upper wall behind structure	Poor
V58T0405A	Aft inboard corner of wheel well	Partial

At first glance sensors V58T1700A and V58T1701 correlate very well with the flight data. However, past EI+510 sec (GMT 13:52:39) the low mass honeycomb access panel has reached its melting temperature in the analysis as shown in Figure 6-25. This would allow hot gases to enter the wheel well and deposit energy through convection directly on the MLG components. However, one could argue that this convective energy then replaces radiative energy but CFD would have to confirm this. After EI+586 sec (GMT 13:53:55) the wall at the center of the plume reached its melting temperature as shown in . At this point the area available for hot gases to enter the wheel well increases rapidly as more of the outboard wall melts. The assumption of holding the wheel well wall at its melting temperature (935°F) is no longer valid for this analysis and CFD is required to determine the hot gas flow inside the wheel well in order to account for the convective heating.

From this analysis, it is possible to conclude that a portion of the hydraulic line temperature increase seen in the flight data can be attributed to radiation from the outboard wheel well wall being heating by a plume due to a spar breach.

6.4 Wire Bundle Burn-Through Tests

An Arc jet test program designed to simulate the flow of superheated air through a breach in the Space Shuttle Orbiter's Wing Leading Edge was performed at the Johnson Space Center's (JSC) Atmospheric Re-entry Materials and Structures Evaluation Facility (ARMSEF). Several of the test objectives listed in the test plan were met in this program. These objectives were:

- obtain test data to correlate and validate the axisymmetric plume heating methodology;
- obtain the failure mechanism characteristics, failure initiation time, failure rate, and burn-through time of a cable bundle when subjected to hot gas impingement with representative reentry plume environment;
- evaluate aluminum hole growth rates for aluminum flat plates;
- and evaluate aluminum burning phenomena and the effect of potential exothermic reactions on plume heating.

The test was accomplished through the use of a specially designed water-cooled "plume box" which was inserted in the arc jet flow field. The box was designed with interchangeable front plates with different hole sizes cut into them to represent the breach. The tests performed with this box show that a high enthalpy flow passing thorough a breach in Columbia's wing structure is not only capable of causing failures in flight-type wire bundles similar to what was seen flight, it is also capable of exacerbating the problem by rapidly increasing the size of the breach.

A total of three cable bundle tests were performed in this program. Each test was accomplished with a different plume box configuration. These configurations were, one-inch diameter hole in a cooled copper plate (the cooled plate resulted in a constant hole diameter), a two-inch diameter hole in a cooled copper plate, and a one-inch diameter hole in an uncooled aluminum plate. The arc heater power level for each test configuration were as follows: 3.27 MW for the one-inch hole test and 3.63 MW for both two inch hole tests. The one inch hole test resulted in a total of 6 wire failures in 837 seconds. That failure rate, a much lower rate than seen in the flight, necessitated an increase in heater power for the subsequent test runs. The increased power with a two-inch diameter fixed hole resulted in 33 wire failures (the total number of wires monitored) in 538 seconds. That rate approached what was experienced in the flight. The uncooled aluminum plate resulted in all 33 wires failing in 68 seconds as well as a complete disintegration of the bundle. The hole in the plate also grew from 1 inch in diameter to over 4 inches in diameter in approximately 13 seconds. This agreed well with pre-test analytical predictions.

Several calibration test runs were made to support the development of the analytical math models used to characterize the plume generated within the box. These test runs consisted of taking pressure and heat flux measurements along the centerline of the plume at different distances from the front hole. The heat flux and pressure of the arc jet free stream, the pressure on the front of the box, the static pressure within the box, and the static pressure of the test chamber were also measured. To estimate the heat flux that the cable bundle experienced, a tube calorimeter was built. The calorimeter consisted of a stainless steel thin walled tube with the same diameter as a cable bundle. To the inside of this tube were attached fine-gage thermocouples in a grid-like pattern. This tube was mounted inside the box in the same orientation as the cable bundles then exposed to the same environment. The response of the thermocouples was used to back out the absorbed flux.

Each cable bundle test article was approximately 1.75 inches in diameter and constructed to simulate the cable bundles that are routed along the Orbiter wheel well in the left wing. Each test bundle consists of 290 cables, of these, 33 cables were monitored with an auxiliary data system. Conductor-to-conductor resistance within each of the 33 cables was recorded during test operations. Each cable in the bundle was a Kapton insulated, 24 AWG, twisted, shielded, pair. Aluminum clamps from the vehicle installation were used to hold the bundle of cables together and for attachment to the box. A picture of the cable bundle test article is shown in Figure 6-27.

Previous test programs demonstrated the failure mode for Kapton insulated cables when subjected to extreme heating – a short circuit develops between the two conductors within a twisted shield pair cable. This occurs because the Kapton insulation breaks down and changes from an insulator to a resistor over a finite period of time. This means the resistance between the two conductors within a twisted pair cable changes from a very high value to a low value. An example of this from a previous test program is shown

in Figure 6-28. The cables of interest are connected to various sensors (temperature, pressure, strain). Measurements of conductor to conductor resistance are normalized by converting them to what the Orbiter signal conditioner would output for a –75 to 250°F hydraulic temperature sensor channel assuming initial actual temperature of 100°F and a short of this magnitude occurring in the cable. An example of the results from this conversion are shown in Figure 6-29. Note that this plot is similar to the actual sensor data observed from STS-107.

This test program was performed in Test Position #2 (TP2) of the ARMSEF. A video camera mounted on the test chamber was used to visually monitor the flow field and interior of the test chamber. This video was used to help determine if and when a particular test run should be terminated. A camera was also available to monitor the front of the box when a destructive test of that front plate was performed. A smaller camera was mounted inside the plume box and used to monitor the test specimens and determine if and when a particular test run should be terminated.

This test program was intended to simulate an internal convective plume resulting from penetration damage to the Orbiter wing. To facilitate a re-creation of this environment, a water-cooled copper box was fabricated and mounted to a specially designed insertion arm. The box was made of a stainless steel frame with 0.25-inch thick copper plates making up the walls and 0.25 inch diameter copper tubes were brazed to these walls to provide cooling. These walls also protect the test articles from the heating associated with reflected shocks within the test chamber. The front of the box had a 10”x10” square opening over which interchangeable faces could be attached. This position was designated the forward position. Four types of plates were manufactured to occupy this position. They were:

- Water-cooled copper plate with a 1-inch diameter hole
- Water-cooled copper plate with a 2-inch diameter hole
- Aluminum plate with a 1-inch diameter hole
- Aluminum honeycomb with a 1 inch diameter hole

Stainless steel brackets were mounted inside the box at 15 inches and 20 inches from this forward plate. The various test articles, cable bundles, calorimeters, etc., were attached to these brackets. These locations were designated the aft positions. Figure 6-30 gives a sketch of this set-up and Figure 6-31 shows the configuration and design of the box. Also within the box was mounted a video camera to record the response of the test article.

The test program consisted of two distinct phases: the calibration phase and the engineering test phase. Two different sized holes in the forward position provide two different plume geometries and two different ζ positions for the test article provide an array of test locations for this test program.

The test conditions attempted to match the arc jet flow free stream stagnation pressure and centerline enthalpy to the flight stagnation pressure and total enthalpy. The targeted conditions and results of arc jet calibration runs are shown graphically in Figure 6-32. The resultant heat rate at these conditions was measured. The calibration data for the flowfield free stream is compiled in Table 6-3

Table 6-3 – Test Conditions

Date	Run Number	Z-distance (in)	Current (amps)	Mass Flow (lbm/s)	Bulk Enthalpy (BTU/lbm)	Power (MW)	CL Pressure (psf)	CL Heat Rate 1" D (BTU/ft2-s)	CL Enthalpy (BTU/lbm)
05/01/2003	2-2509-3	10	530	0.2	3600	1.25	not measured	not measured	not calculated
05/01/2003	2-2509-3	10	1200	0.4	5400	3.62	not measured	not measured	not calculated
05/05/2003	2-2510-3	21.25	530	0.2	4100	1.25	15	52	5517
05/05/2003	2-2510-3	21.25	1400	0.4	6200	4.27	36	198	13560
05/05/2003	2-2510-3	21.25	1200	0.6	4700	4.44	46	149	9027
05/05/2003	2-2510-3	21.25	1300	0.67	4800	5.1	52	162	9231
05/05/2003	2-2510-3	21.25	1300	0.8	4500	5.43	60	not measured	not calculated
05/06/2003	2-2511-3	21.25	1000	0.3	5500	2.8	25	120	9862
05/06/2003	2-2511-3	21.25	1200	0.3	6400	3.26	27	154	12178
05/06/2003	2-2511-3	21.25	530	0.2	4080	1.26	15	60	6366
05/28/2003	2-2516-3	20.05	1200	0.4	5450	3.63	32	139	10097

Calibration runs were also performed to collect data on the plume generated within the box. The centerline pressure and heating rate of this plume was measured at specific test points established in the flow field calibration phase. In addition, a specially designed calorimeter was used to measure the heating distribution on a cylinder the same diameter as a cable bundle. This consisted of a 1.75-inch diameter thin-walled stainless steel tube to which several small gauge thermocouples were attached in a grid like pattern. The response of these t/c's to the plume environments was recorded and from this data the heat flux was determined. All of this data will be used to refine the thermal models used to analyze the cable bundle response to the breach environment. The results of these calibration runs are presented in Table 6-4.

Table 6-4 – Test Condition Summary

Arc-jet Parameters		Arc-jet Flow Conditions					Box Measurements							
Current	Flow Rate	Bulk Enthalpy	Chamber Pressure	q-4" FF	q-1" FF	P-4" FF	Hole Dia.	P-front	P-internal	Ppitot-10"	Ppitot-15"	q-probe-10"	q-probe-15"	q-cyl stag-15"
(amps)	(lbm/sec)	(Btu/lbm)	(psf) /w box in flow	(Btu/ft2-s)	(Btu/ft2-s)	(psf)	(inches)	(psf)	(psf)	(psf)	(psf)	(Btu/ft2-s)	(Btu/ft2-s)	(Btu/ft2-s)
1000	0.3	5800	0.902	62	122	26	1	28	0.78	2.06	No Data	No Data	No Data	4.3
1200	0.3	6600	0.966	74	154	27	1	29	0.88	No Data	No Data	No Data	No Data	4.7
1000	0.3	5800	0.902	62	122	26	2	28	0.47	1.45	2.06	No Data	11	7.9
1200	0.3	6600	0.966	74	154	27	2	29	0.42	1.49	2.02	No Data	13	9.4
1200	0.4	5500	1.153	71	139	35	2	35	0.68	2.18	3.18	No Data	16	12.1

Three runs with a cable bundle were performed at the test conditions shown in Table 6-5. After arc jet activation, the insertion arm with box and cable bundle inside were inserted into the flow field while cable resistance was monitored. When sufficient cable failures were observed or other arc jet constraints were reached, the arc jet was deactivated and the arm was moved to remove the box from the flow field.

Table 6-5 – Test Configuration Summary

Item	Run 1	Run 2	Run 3
Box Forward Plate Type	Cooled	Cooled	Uncooled
Forward Plate Orifice Diameter (in)	1 in	2 in	1 in (starting)
Bundle Distance Aft of Orifice (in)	15 in	15 in	15 in
Arc Jet Current (amps)	1200	1200	1200
Arc Jet Mass Flow (lb/sec)	0.3	0.4	0.3

Run 1: The test set-up incorporated a 1-inch diameter orifice in the forward position of the box with the cable bundle 15 inches aft. The relatively low heating rate of run 1 produced only a few cable failures, but all were on the cable side facing the plume.

Run 2: The test set-up incorporated a 2-inch diameter orifice in the forward position of the box with the cable bundle 15 inches aft. Higher heating rates of run 2 produced failures faster and the entire cable bundle failed. Photographs in Figure 6-37 shows the appearance of the bundle before and after the test.

Run 3: The test set-up incorporated an uncooled aluminum, 0.1 inch thick flat plate in the forward position box. This plate had a 1 inch diameter orifice on the centerline with the cable bundle 15 inches aft. The test demonstrated a rapid erosion of the uncooled aluminum orifice. The orifice grew to an estimated 4 inch dia in approximately 13 seconds. Orifice growth was somewhat arrested after 4-5 inch due to a heat sink designed around the perimeter. The cable bundle showed a very rapid and increasing failure rate as orifice diameter increased.

Figure 6-34 and Figure 6-35 shows a comparison of cable failure rates for this test series and that observed on the vehicle. Based on the various observed cable failure rates, heating rate for the vehicle cable bundle must have been between those of Run 2 and Run 3.

Table 6-6 – Test Results Summary

Item	Run 1	Run 2	Run 3
Cable Run Time (sec)	837	538	68
Heating Rate from Calibration (BTU/ft^2-sec)	4.69	12.13	Greater and increasing during run, but could not be measured
Time When First Cable Begins Failure (sec)	107	14	13
Time When Last Cable Begins Failure (sec)	635	351	66
Total Cables Failed (33 monitored)	6	33	33

Cable bundles were tested at three different test conditions. Test results showed the arcjet-induced heating produces the same cable failure mechanism as occurred during previous cable overtemperature tests - a short circuit between the two conductors within a twisted shield pair cable. Data obtained for cable failure rate as a function of heating rate can be used to validate thermal models of the vehicle cable bundles for the STS-107 Columbia investigation. These models can be utilized to determine the heating rate which the STS-107 bundle experienced. This in turn can be used to gain a better understanding of the vehicle failure scenario.

6.5 Wire Bundle Burn-Through Thermal Analysis

A thermal analysis was performed on the wire bundles, MLG wheel well wall, and wing upper skin shown in Figure 6-39. Separate Thermal Desktop TMM's were created for each hardware region. These math models were used to calculate the required breach sizes and breach locations along the wing leading edge spar that would cause failure of each item. Their best estimated failure times were determined from the flight data. The results of each analysis were mapped against each other at defined zones along the wheel well to determine if a common breach size and location could explain their collective failure. The zones and panel locations are defined in Figure 6-40.

The spar breach hole size is assumed to be constant with no growth for the purposes of this comparative analysis. In addition, any oxidation and combustion effects were not modeled. The plume is assumed to be perpendicular to the respective spar. In each analysis it is assumed to impinge directly upon the object (wire bundle, wheel well, upper wing). This is significant in that the wheel well wall should always have a direct impingement while the bundle will not necessarily have a direct plume impingent. The spar breach is assumed to be at EI+487 seconds.

The flat plate plume heating induced from a wing leading edge breach at EI+491 seconds as a function of hole size and distance was used in this analysis and is discussed in section 5.3.3. Figure 6-41 and Figure 6-42 show the heating rates for impingement on a flat plate and a 1-inch diameter cylinder, respectively. A heating factor time array was included to adjust the heating to represent a breach earlier in the re-entry profile. Also, adjustments were made for increased hole sizes and distances. The plume heating adjustment for breach hole sizes greater than 2-inch diameter are shown in equation 6-2 while plume heating adjustments for breach distances greater than 60 inches are shown in equation 6-3.

$$qdot(d_{hole}) = qdot_{2.0"hole} \cdot \left(\frac{d_{hole}}{2"} \right)^{2.6} \quad \textbf{(6-2)}$$

$$qdot(x) = qdot_{dist} \cdot \left(\frac{dist}{x} \right)^{2} \quad \textbf{(6-3)}$$

Corrections for local pressure coefficients, off-normal angle impingements, and radial distribution from the stagnation point are shown in Figure 6-43 though Figure 6-45. Plume impingement on the bundle was also adjusted for radius and circumferential distribution as shown in Figure 6-46 and Figure 6-47.

The wire bundles are comprised of several harnesses each comprised of cables. Each cable consists of 2, 3, or 4 wires as shown in Figure 6-48. The lost in-flight measurements experienced were due to cable failure.

Testing as described in section 6.4 was performed to correlate and gain confidence in the wire bundle TMM. Here, 1¾ inch diameter bundles were subjected to 8.08 BTU/ft^2-sec (large propane torch test), 4.69 BTU/ft^2-sec (arc jet test #1), and 12.13 BTU/ft^2-sec (arc jet test #2) heating rates (determined through calorimeter test runs). The TMM bundle failure rate test predictions were mapped against their respective test results in Figure 6-49 and Figure 6-50.

The wire bundle TMM represented the bundle as a lumped mass rather than a group of individual cables. A specific heat of 0.225 BTU/lb$_m$-F and thermal conductivity (along the length of the bundle) of 166 BTU/hr-ft-F were used. The density was calculated by dividing the bundle mass per unit length (0.197 lb$_m$/inch) by its cross sectional area. A factor of 2.14 was applied to account for the additional surface area present in the bundles but not in the TMM. A radiative boundary condition of 70°F (emittance = 0.88) was used. Bundle radial heat transfer and cable failure temperatures (800°F) were determined through large propane torch testing. How the cable failure temperature is determined is shown in Figure 6-51.

Heating was applied via film coefficients and a 1700°F flame recovery temperature during the large propane test correlation but was adjusted to the plume configuration for the arc jet test TMM simulations.

The test correlated TMM was adjusted to flight conditions by applying the corrected plume heating. It was also modified to represent flight bundle 3 as shown in Figure 6-52 by adjusting the mass per unit length to 0.303 lb$_m$/inch. A flight radiative boundary condition of 20°F was used (emittance = 0.88). Flight bundle 3 is assumed to have failed completely due to the likelihood that the measured failed cables are distributed throughout the bundle. The heating required to match flight bundle 3 failure rate was determined to be 89 BTU/ft^2-sec. This was used to determine the required spar breach sizes and locations.

The wheel well wall is constructed of ribbed aluminum 2024-T6 surfaces of varying thicknesses. Effective thicknesses were used along the wall to capture the appropriate thermal mass response as shown in Figure 6-53. Radiative boundary conditions were assumed to be 70°F based on wing structural temperatures. Koropon primer (emittance = 0.86) was assumed to be present during the duration of the analysis. A failure temperature of 935°F was assumed. Wall burn through was assumed at EI+599 due to the first indicated temperature rises of the wheel well. A failure time of 112 seconds (EI+599 – EI+487) was used to determine spar breach sizes and locations.

The upper wing is made up of Aluminum 2024-T6 honeycomb structure (melting temperature of 935°F). The thicknesses of the honeycomb facesheets and core are 0.025 and 0.9684 inches respectively. The Generic Honeycomb Modeling Tool was used to generate the effective conductivity through the honeycomb core. An adiabatic upper surface boundary condition and a lower surface radiative boundary condition (70°F) were assumed. A Koropon coating (emittance = 0.86) was applied and assumed to be present throughout the analysis. Upon burn through of the lower facesheet, heating is applied to the upper facesheet. The FRSI layer attached to the upper surface of the wing is assumed to fail when or slightly before the wing structure fails. A burn through time of EI+536 seconds is assumed due to a plateau in the wire bundle failure rate. Spar breach hole sizes and locations were determined using a failure time of 49 seconds (EI+536 – EI+487).

The TMM spar breach results for flight wire bundle 3, the wheel well wall, and the upper wing (for the partitioned zones of the wheel well) are compared in Figure 6-54 through Figure 6-57. Since the assumed failure times of the wheel well and the upper wing are not exact, error bars are included for the wall in zone 2 to indicate the sensitivity of the comparison to the chosen failure times. The locations of highest probability for the plume impingement are zone 1 (panel spar 6 and 7 coverage) and zone 2 (panel spar 8 coverage).

In this analysis, the most probable spar breach diameters ranges from 2 to 6 inches. This estimated hole size in the spar is not entirely consistent with the analysis described in section 6.1. It should be realized that this analysis had to make gross assumptions for the plume characteristics which biased the heating rates on the high side. Application of these heating rates resulted in demise rates for the cable which were higher than actually observed in flight. Therefore, from the cable demise rates which were correlated to the observed flight data, the estimated spar hole size should be considered as a lower bound.

6.5.1 Tee-seal scenario

In addition to the damaged tee-seal analysis comparison to the flight data in the panel area described in section 6.1.1, the damaged tee-seal scenario was evaluated for wire cable bundle burn rates. In the case of a damaged tee-seal where the flow entrance area aspect ratio is high in comparison to a round-shape hole, the plume heating drops off much quicker along the flow axis (refer to section 5.3.3). To bound this analysis in terms of feasibility, assumptions were biased to predict the most rapid burn rate for the cable bundle. The bundle was assumed to be directly behind the spar although the closet bundle is actually at least 12 additional inches away from the spar. Using the heating rate profile shown in figure 5.3.2-27, the predicted wire burn rate is shown in Figure 6-58. In comparison to the burn rate observed in flight, this analytically predicted burn rate is lower due to rapid drop in heating rate. This analysis coupled with the panel 8/9 thermal analysis provides evidence that a damaged tee-seal scenario is not consistent with the flight data and observations.

6.6 Orbiter Sidewall Bondline Thermal Analysis

A thermal analysis was performed on the area surrounding OV102's V34T1106 sidewall bondline temperature sensor. The sensor is located on the inboard surface of the port sidewall at XO: 1215.5, ZO: 355.5 as shown in Figure 6-59. A Thermal Desktop TMM was created to determine whether its temperature rise during the re-entry was produced by increased external heating, by the addition of internal heating, or by the loss of the FRSI layer. The assumptions used in the analysis, the TMM correlation with flight data, the analysis and its results are discussed below.

The sidewall is an aluminum honeycomb structure with a layer of FRSI on the outboard surface as shown in Figure 6-60. Conduction was assumed to be 1-D through the sidewall. Internal and external convection were negligible. Radiation heat loss was assumed from the FRSI (emittance = 0.8) to the external air temperature and from the inboard facesheet (emittance = 0.86) to the Orbiter internal structure. The internal structure temperatures are shown in Figure 6-61 and Figure 6-62 for STS-109 and STS-107 respectively. Conduction through the honeycomb core (density = 3.8 lb/ft^3) was assumed to be 0.095 BTU/hr-in-F. The honeycomb facesheet densities were adjusted to account for the honeycomb adhesive. The RTV density surrounding the sensor was modified to account for the sensor mass (1.5 g).

The inner facesheet, outer facesheet, and RTV densities became 223, 201.7, and 278.4 lb/ft^3, respectively.

Confidence in the TMM was obtained through correlation with STS-109 flight data as shown in Figure 6-63. Nominal STS-109 external heating can be seen in Figure 6-64 and corresponding pressure profiles were used in the analysis. To achieve correlation a factor of 1.986 was applied to the inboard RTV density to account for missing thermal mass.

Upon correlation, the TMM was used to investigate the possible STS-107 heating cases shown in Figure 6-65. Nominal STS-107 external heating and pressure profiles were applied except as otherwise noted.

The study showed that the temperature rise can be explained by an external heating 13x nominal applied after EI+600 seconds or the application of internal fuselage heating (0.16 Btu/ft2-sec) after EI+648 seconds. These heating profiles are shown in Figure 6-66 and Figure 6-67 respectively. The temperature rise, however, cannot be explained by the loss of the FRSI layer under nominal external heating. The results of the three cases studied are mapped against STS-107 re-entry flight data in Figure 6-68 (external heating case), Figure 6-69 (internal heating case), and Figure 6-70 (loss of FRSI case).

6.7 Damaged Wing Leading Edge Coupled Aero-Thermal-Structural Analysis

A multidisciplinary process was developed to simulate the initiation and propagation of thermal/structural failure in the left wing during reentry. The objective of the analysis was to evaluate the plausibility of RCC damage in the form of 6 or 10 inch diameter holes near the apex of panel 7 in leading to the observed pattern of thermal/structural failure established for STS-107. Critical conditions assessed during the simulation included front wing spar burn-through time, panel 8 spar rear facesheet temperature response, and eventual failure of the RCC panels and attachments.

The process, depicted in Figure 6-71, consisted of defining external and internal aerodynamic heating and airloads environments throughout the entry, generating high fidelity thermal response of the internal insulation blankets, wing and spar structure, and RCC panels, and performing a detailed structural failure analysis of the thermally and mechanically loaded system. Multiple failure mechanisms were examined including failure of wing spar insulation, aluminum melting, honeycomb face sheet/core debond and loss of structural integrity, and loss of RCC wing leading edge attachments. This section of the report describes the analysis methodology and solution results for a damage scenario consisting of vehicle reentry with a 6 or 10 inch diameter hole in the left wing leading edge. Predicted temperature distributions and structural analysis results showing material failure and damage propagation during entry are presented and compared with available flight data.

To provide a common basis for the multidisciplinary analysis, a detailed finite element model of the wing leading edge covering RCC panels 6 through 8 was developed and is shown in Figure 6-72. In addition to the RCC panels, the model encompassed the associated honeycomb wing spar, internal insulation blankets and earmuff, representative attachment fittings and spanner beam, surrounding wing acreage TPS and underlying honeycomb wing structure.

Utilizing a CFD solution derived from the Orbiter common grid system described in Section 5.2.4.2 and trajectory flight condition at 491.4 seconds after entry interface, external aerodynamic heating and pressure distributions were mapped onto the finite element model as analysis boundary conditions. These values were scaled with STS-107 trajectory-based reference stagnation heating and freestream dynamic pressure levels, respectively, to provide time-dependent external environments for analysis. On surfaces inside the RCC cavity, an internal convective heating distribution described in Section 5.3.7.2 – scaled with reference stagnation heating - and internal pressure level predicted by the coupled flow CFD solution described in Section 5.3.6.1.2 - scaled with freestream dynamic pressure - were applied to the model to serve as time-dependent internal environments.

Using the SINDA thermal analyzer code (Ref 6-3), transient temperature distributions were computed throughout the model due to the internal and external aerodynamic heating. Although absent from the finite element model due to their complexity, surrogate surfaces were added in the thermal model to represent T-seals, completing the internal radiation enclosure within the leading edge. Other features of the analysis included:

- Radiation from external surfaces to space at 0°F
- Surface-to-surface radiation within the RCC cavity, earmuff/spanner beam cavity, wing bay cavity, and spar honeycomb structure
- Temperature-dependent material properties

To simulate the melting failure of affected surfaces within the limited schedule available for the analysis, internal convective heating was applied to interior portions of the model as outer surfaces reached their melting temperature limits. This avoided the time-consuming process of node removal and, coupled with the imposition of temperature limits for failed nodes to prevent nonphysical levels during the analysis, served as a reasonable approximation to the actual structural heating during failure. The heat of fusion for the materials was not accounted for in this study. Resulting temperature histories throughout the insulation and spar are shown in Figure 6-73 for both the 6-inch and 10-inch damage cases.

Next, time-dependent temperature distributions were coupled with pressure-based mechanical loads during structural analysis to determine the sequence and timing of structural failure within the model. NASTRAN structural solutions were coupled with a with a progressive failure analysis and life prediction software code, Generalized Optimizer and Analyzer (GENOA, Ref. 6-5) to provide detailed information on temperature and stress distributions within the structure and consequent levels of physical damage such as fracturing, melting and displacement within the structure. Solutions were generated at ten-second time intervals throughout the entry. Upon achieving measurable levels of structural damage, subsequent solutions were processed using equilibrium analysis at each succeeding time step, allowing removal of melted/failed material and redistribution of mechanical loads to surviving structure.

To accommodate the challenging schedule associated with this effort, the present analysis contains a number of limitations and uncertainties. The use of panel 7 as the site of the initial RCC breach was based on the most current working scenario at the time of the analysis. More recent thinking during the investigation has placed the likely hole location at panel 8 with the bulk of internal thermal damage occurring at the junction of panels 8 and 9. This analysis is thought to be relevant even for this scenario by considering the damaged panel in the model as representative of panel 8 and viewing the results occurring between panels 8 and 9. Consistent with such an approach, the OEX flight data for the panel 9 spar rear facesheet thermocouple, V09T9895, has been compared with the thermal response of a comparable panel 8 location in the model as discussed in the Results section below. Other analysis limitations are reflected in the uncertainties surrounding the internal convective heating environment, the approximate nature of the RCC attachment fittings, the absence of inertial loads, and the absence of T-seals in the structural model.

Several events observed during the course of the solutions were considered particularly significant with respect to the overall structural failure of the wing leading edge. In order of occurrence they are listed below:

- Melting of the Inconel 601 foil overwrap on the internal insulation blankets indicated the onset of thermal failure of the insulation, eventually allowing convective heating to approach the spar.
- Initiation of wing spar damage and fracture.
- Melting of the rear facesheet indicated breach of the spar has occurred.
- RCC panel failure.

Analysis results at these conditions are shown in Figure 6-74 through Figure 6-77 for the 10 inch case and Figure 6-78 through Figure 6-81 for the 6 inch case. Predictions for both damage cases show eventual failure of RCC panels through fracturing and breakup.

A comparison of the times at which these critical events occur during the entry is shown in Table 6-7. As expected, failure times are accelerated for the 10 inch case compared with the 6 inch due to the higher levels of internal heating. Thermal response of instrumentation within the left wing of STS-107 have suggested the initial breach through the spar occurred at 491 seconds after entry interface. With a predicted spar breach time of 470 seconds, the 6 inch provides a better comparison to flight data than the 10 inch case. As shown in Figure 6-82, better agreement for the 6 inch damage case can also be seen by comparing the temperature response of V09T9895 (panel 9 spar rear facesheet thermocouple) from the OEX flight data with the model predictions at an analogous location on panel 8 (in this case panel 8 in the model is used as a surrogate for panel 9 as noted previously). The average predicted temperature of two nodes on the rear facesheet are used in the comparison for each damage case. Up to

the flight estimated time of spar breach at approximately 490 seconds the predicted thermal response for the 6 inch case is in reasonable agreement. After this point, the predicted temperature rise rates are much slower than flight data, indicating the effect of convective heating experienced during flight in this area from the hot gas jet expanding into the wing interior. Modeling of such heating was not included in this analysis.

Table 6-7 - Critical Failure Times For 6 Inch and 10 Inch Damage Cases

Critical Event	*10 inch hole*	*6 inch hole*	*Time difference*
Failure of Inconel 601 foil overwrap on thermal insulation.	***210 seconds***	***230 seconds***	***20 seconds***
Heating is applied to the aluminum spar surface. Initial structural failure of spar.	***320 seconds***	***380 seconds***	***60 seconds***
Initial spar breach. Inside now exposed with small gaps, growing into a large spar breach (28 inches x 4 inches; 38 inches is spar height).	***380 – 410 seconds***	***470 – 510 seconds***	***90 – 100 seconds***
Fracturing of RCC Panels Evident	***450 seconds***	***500 seconds***	***50 seconds***

6.8 Chin Panel Temperature Anomaly

Starting at 490 seconds from entry interface, a temperature measurement on the RCC chin panel recorded a sharp rise in temperature followed by a drop. Eventually, the temperature measurement recorded a trend that followed the expected nominal transient. The transient is shown in Figure 6-83. It has been concluded that this transient had to have been caused by a data system anomaly rather than an anomaly with the chin panel hardware of thermal environment.

- The anomalous transient picks up the thermal profile where it left off is unlikely for a real transient. This is very coincidental for a thermal transient since there is no reason for the temperature to return to the previous slope and absolute value (extrapolated).
- The recorded temperature actually cools down repeatedly during the transient. It is very difficult to cool this structure during entry because:
  - The surrounding hardware contributing to the radiation environment is getting hotter and the convection environment during this time period is heating (not cooling)
  - Thermocouple is on a heavy piece of hardware interior to the chin panel
- Anomalous behavior occurs after wing breach at 487 seconds. Postulate that the hot gases and associated heating and/or free electrons cause a data system malfunction.

6.9 Truss Tube Thermal Analysis

A thermal sensitivity study was performed on OV-102's left wing truss tubes. A Thermal Desktop TMM was created to gain an understanding if and when the tubes would fail if exposed to plume heating caused by a breach in the wing leading edge spar. Tubes at various distances from the spar were chosen as shown in Figure 6-84. The size of the breach was varied.

The tubes are aluminum 2024-T6. For analysis sake they are designated tubes 1 through 4. Table 6-8 shows their differences in outer diameter, wall thickness, length, and distance from spar panel 8.

Table 6-8 – Tube Summary

Tube	Outer Diameter (in)	Wall Thickness (in)	Length (in)	Distance (in)
1	3.75	0.048	48.41	15.94
2	3.75	0.031	39.04	96.44
3	2.00	0.018	38.37	37.80
4	2.25	0.020	38.02	94.49

Their diameters and wall thicknesses were assumed to be constant throughout their respective lengths. Their distances were measured in plane from their midpoints to the spar.

A radiative boundary condition of 20°F was assumed. The tubes were coated with Koropon (emittance = 0.86) throughout the duration of the analysis.

A spar breach is assumed at EI+488 seconds. It was assumed to be in spar panel 8 and to be constant in size. Oxidation and combustion effects were ignored. The plume was assumed to impact the middle portion of the tubes directly. Plume heating methodologies similar to section 6.5 were incorporated in this analysis. Correction for panel 8's local pressure coefficient, off-normal angle impingement, and radial distribution from the stagnation point were applied. The plume heating used is shown in Figure 6-85 and the heating correction for angular impingement is shown in Figure 6-86. Plume impingement on the tubes was also adjusted for radius and circumferential effects.

Failure was determined when the entire cross section of the tube at the point of plume impingement reached a temperature of 935°F. The failure times of the 4 tubes are shown in Figure 6-87 for varying breach hole sizes.

6.10 RCC Knife Edge Tests

STS-107 recovered debris for reinforced carbon-carbon (RCC) panels 8 and 9 showed "knife-edge" erosion. A test program was initiated in order to confirm uncoated RCC sharpening and determine if coated RCC will sharpen as seen in Columbia debris of RCC Panels 8/9 rib sections.

Two test fixtures were designed and developed for this test and are shown in Figure 6-88. The single plate fixture was used to simulate flow impinging onto a breach edge with an angle of 20°. The dual plate fixture was used to simulate flow impinging onto a near-normal (70°) surface representative of the RCC panel ribs.

RCC test specimens were prepared from an existing RCC panel rib section and RCC plate. The RCC test plates for the single plate fixture were 2.5"x3" in dimension and .25-inch thick. Closeout RCC pieces were used to prevent flow from entering into the copper holder and were of the same thickness of the single plate test specimen. Two uncoated specimens and one coated specimen were tested.

The RCC test plates for the dual RCC plate test fixture were 3"x3" in dimension and .375-inch thick. Smaller plates were used to model an offset RCC rib and were 1.6"x3" with an equivalent thickness. A coated and uncoated offset RCC plate was tested.

This test program was performed in test position #2 of the JSC Atmospheric Reentry and Structures Evaluation Facility (ARMSEF). Inside this facility, test gases (77% nitrogen and 23% oxygen) are head by a segmented constricted arc heater and injected into a vacuum chamber through a water-cooled 5-inch diameter nozzle that has a 15-degree half angle. While tests are in progress the facility vacuum chamber is maintained below 200 microns of mercury. Test models are mounted on a two water-cooled, remotely actuated sting arms that allow them to be inserted after test conditions are stabilized. The stagnation pressures experienced by test specimens were determined with a 0.5-inch diameter water-cooled pitot probe prior to specimen insertion.

Laser pyrometers monitored the center of the test specimens away from the edge to evaluate the gross temperature response of the RCC using an emissivity of 0.9. In addition, a stroboscopic camera was used to monitor the RCC test specimen edge for knife-edging. This camera provided real-time video data, which eliminated the effects of temperature on the image.

The test conditions were defined by enthalpy and pressure. The test points were derived from the predicted STS-107 RCC hole edge impact pressure and total enthalpy provided by JSC/EG. Three test conditions were established based on the profile shown in Figure 6-89.

A dual calibration model with a 1" flat face heat rate sensor and a pitot probe measurement was used to determine the heat rate and pressure. The actual test points that were calibrated for in the arc jet simulation are shown in Table 6-9.

Table 6-9 – Target Test Conditions

	Test Conditions	
	Pressure (psf)	Bulk Enthalpy (BTU/lb)
Condition #1	75	11200
Condition #2	129	10800
Condition #3	147	7400

The three test conditions were used to simulate a flight profile. For the first two tests, only condition #1 was used. Based on the results from these tests, conditions #2 and #3 were added and the flight profile developed. Figure 6-90 illustrates the simulated flight profile used during testing. It should be noted that the enthalpy specified is the centerline enthalpy and should be multiplied by a factor of two to correspond to the targeted total enthalpy.

In evaluating the results of the testing, the boundary conditions should be taken into account. The RCC test specimens were mounted in water-cooled copper holders, thus, slightly affecting the three mounted edges of RCC through conduction. There was an effort to minimize radiative losses from the back of the specimens using insulation and graphfoil (used to prevent any chemical reactions). However, both test fixtures could not prevent the large view factors from the front of the main RCC pieces to the chamber walls. The test run configurations are shown in Table 6-10.

Table 6-10 – Test Run Configuration

Run #	Angle	# of Plates	Offset	Coating
1	70	2	no	coated/coated
2	70	2	yes	coated/uncoated
3	20	1	n/a	uncoated
4	70	2	yes	coated/uncoated
5	20	1	n/a	coated

Test #1 produced no knife-edging since the conditions could not generate temperatures on the RCC specimen greater than 3250°F. Pre- and post-test photos are shown in Figure 6-91.

Test #2 used the same test conditions as Test #1, but the front specimen was exchanged with an offset RCC plate representing an offset RCC rib. Condition #1 could not produce temperatures greater than 3250°F on the SiC coating, but did oxidize the exposed carbon, leaving a white residue from the impregnated TEOS, as seen in Figure 6-92.

Test #3a utilized the simulated flight profile with conditions #1 though #3. Condition #1 did not create knife-edging, only localized oxidation on the exposed carbon. Condition #2 began after 200 seconds in

the stream, and created temperatures on the edge above 3250°F and initiated knife-edge like erosion. After 69 seconds at Condition #2, the environment was changed to condition #3. Condition #3 was a significant reduction in heating compared to condition #2, and the knife-edge features began to blunt. The decision was made to preserve the knife-edge features created in Condition #2 by removing the sting arm out of the flow. The pre- and post-test photos are shown in Figure 6-93.

Test #3b used another uncoated piece of RCC with the same simulated flight profile. The test, although, not required to run, reproduced the results in Test #3a with the same knife-edging.

Test #4 involved the same specimens tested in Test Run#2 in the dual plate fixture since there was minimal oxidation on the exposed edge and a limited amount of test specimens. The simulated flight profile was used, but the copper test fixture could not withstand the high heating rates at condition #2. Prior to the sting arm being removed from the flow, the SiC coating began eroding at the center of the front offset RCC piece. This suggests that the hottest portion of the RCC at this condition was not at the edge and that erosion would have propagated from the center outward. It must be noted that the front of the copper holder could have influenced the flow field and altered the heating distribution along the plate. Pre- and post-test photos are shown in Figure 6-94.

Test #5 used the single plate fixture with a coated RCC specimen. Knife-edging was produced on the main RCC specimen as shown in Figure 8. Test conditions did produce temperatures above 3250°F. The test condition profile was stopped at condition #2 in order to preserve the knife-edging features for posttest evaluation. A diagram showing the approximate dimensions of the knife-edging is shown in Figure 6-95.

In addition to the main RCC knife-edging on Test #5, the closeout RCC pieces also produced knife-edging as seen in Figure 6-96. The closeout pieces prevent flow from entering the copper test fixture. The erosion occurred from a secondary shock impinging on the closeout pieces. The knife-edging was sharper than what occurred on the main RCC piece.

The test facility was able to simulate predicted environments on RCC ribs and breach edge on six RCC test specimens. Knife-edging was apparent on specimens where the temperature on the SiC coating was above 3250°F. Knife-edging was also apparent on the closeout piece in test #5. This data along with the results from previous RCC testing suggests that under stagnation flow with temperatures above 3250°F, the RCC will erode in a knife-edge manner. If hot gases flowed into the wing leading edge through a breach with sufficient enthalpy and impact pressure, the RCC would have eroded in a similar manner as seen in the debris.

6.11 Leading Edge Reinforced Carbon-Carbon (RCC) Hole Growth Thermal Analysis

A prediction of RCC hole growth was performed using JSC arc jet test data obtained from hypervelocity impacted RCC test specimens when subject to a high temperature entry environment. The objective of the arc jet testing was to establish the oxidation characteristics of RCC with thru holes obtained from hypervelocity impacts. The specimens were exposed to constant heating conditions at temperatures of 2500 and 2800F and pressures of 50 to 180 psf. Correlations were developed from the data for use in trajectory simulations to predict hole growth and hot gas flow through an enlarging hole into the wing leading edge cavity.

A 0.75 inch diameter hole in the RCC was assumed for analysis purposes. Figure 6-97 shows the heat flux and pressure environment at the hole while Figure 6-98 shows the resulting RCC surface temperature as a function of time. The predicted RCC temperature of approximately 4800°F is assumed to be consistent with a diffusion-limited erosion regime for bare or uncoated RCC. With this assumption, the erosion or hole growth rate measured for the 2800°F arc jet tests can be used for erosion rate estimates here. The erosion rate in this flight environment and regime is .0032 in/sec. Figure 6-99 reveals the results of the analysis and shows the predicted growth to a final OML diameter of 4.0 inches. The predicted IML (back-face) diameter is slightly smaller at 3.0 inches. Extrapolation of this analysis to higher RCC temperatures (sublimation regime) or larger initial hole diameter is not recommended since the data base is very limited.

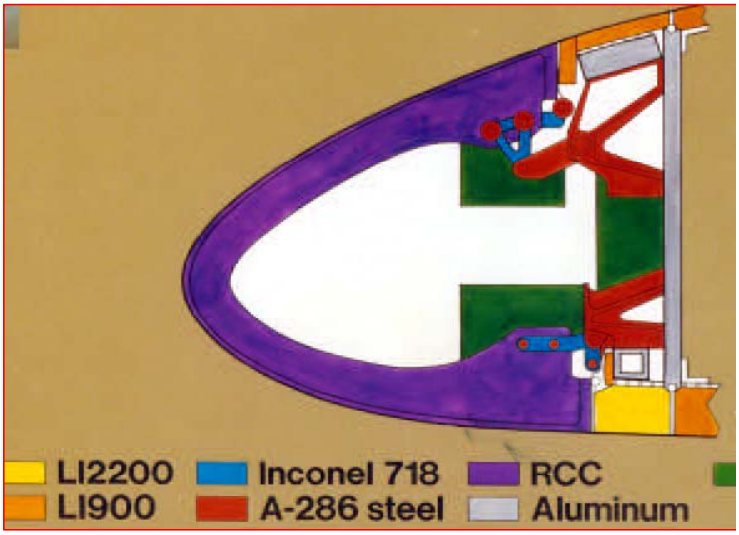

Figure 6-1 - Wing Leading Edge Cross-section

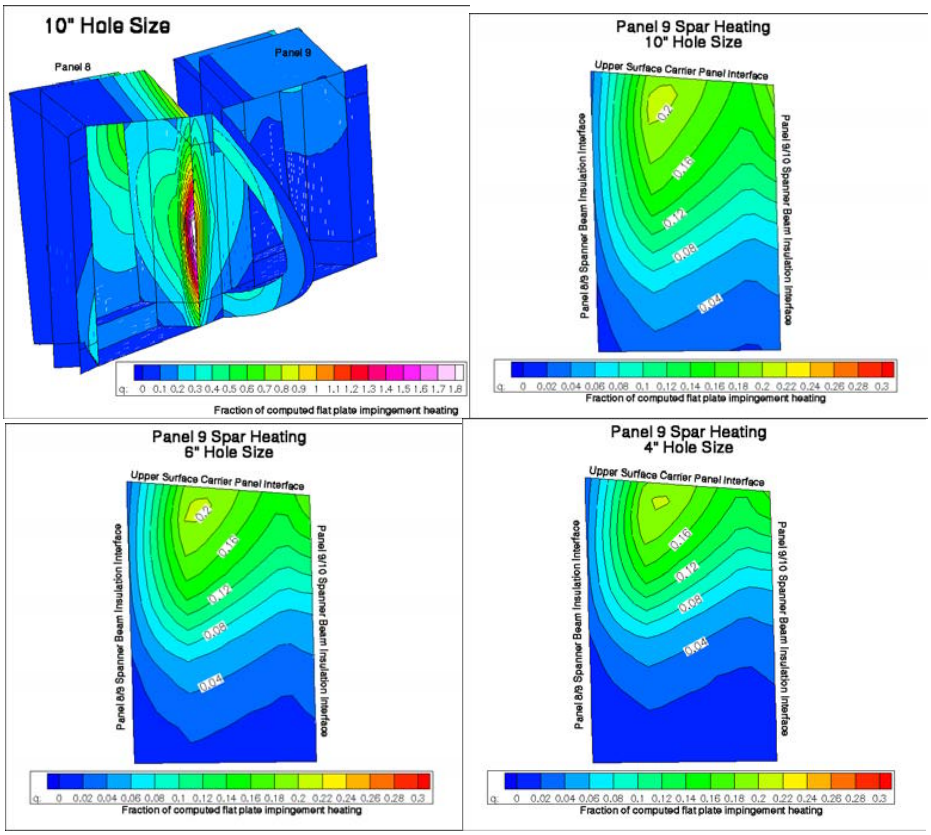

Figure 6-2 - Heating Distribution

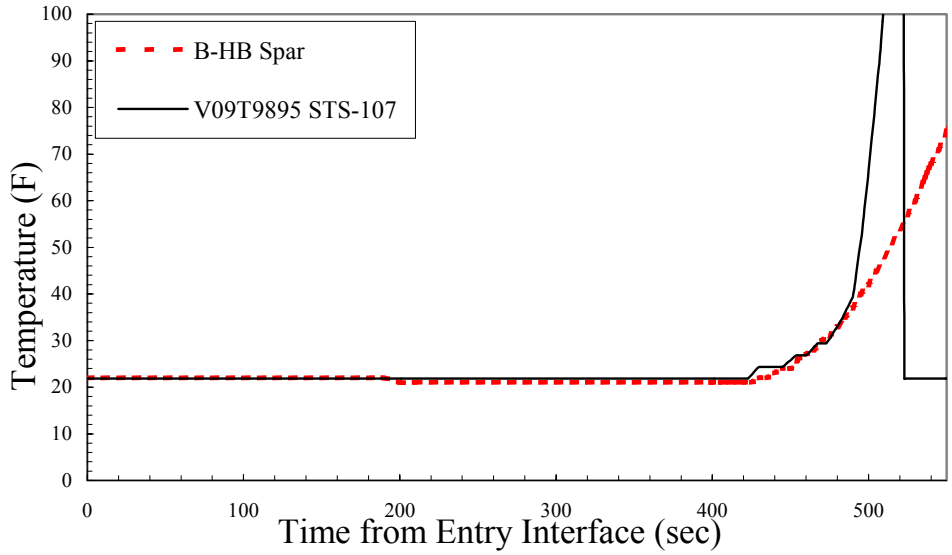

Figure 6-3 - Spar Temperature Prediction vs. Flight Data

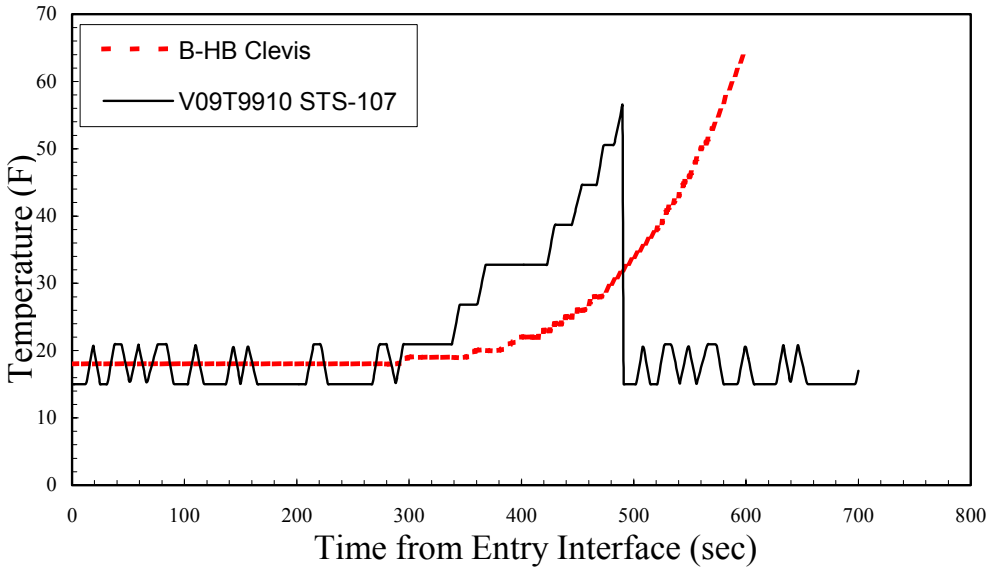

Figure 6-4 - Clevis Temperature Prediction vs. Flight Data

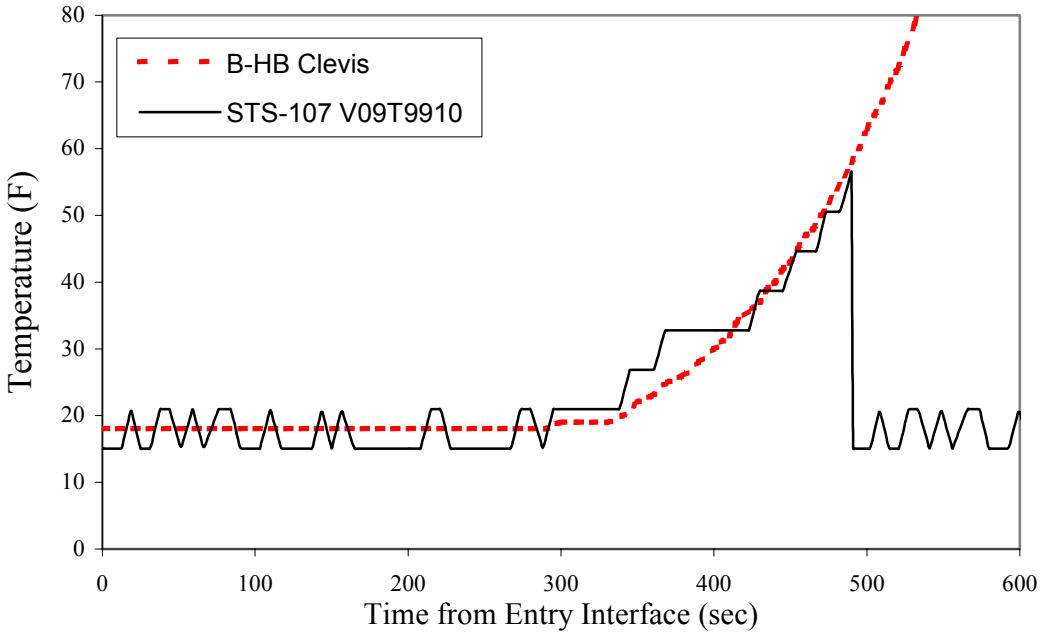

Figure 6-5 - Clevis Temperature Prediction vs. Flight Data

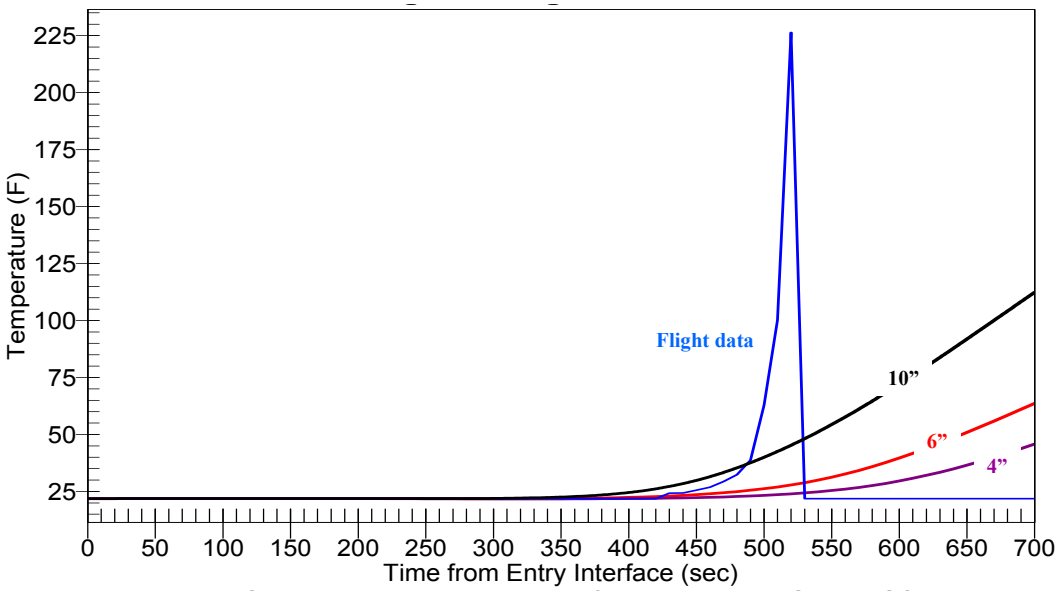

Figure 6-6 - Spar Temperature Prediction for Varying Hole Size – JSC TMM

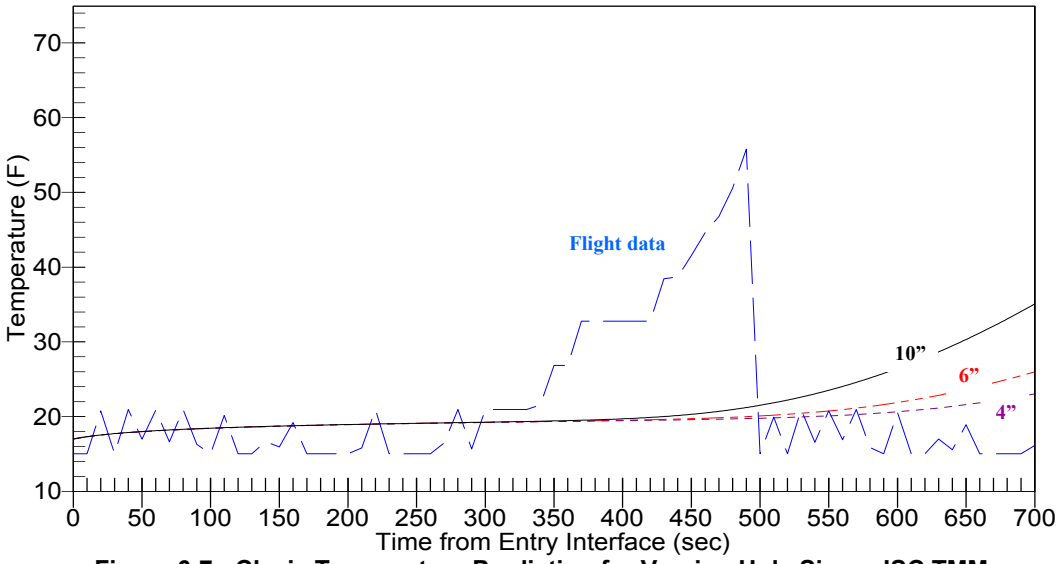

Figure 6-7 - Clevis Temperature Prediction for Varying Hole Size – JSC TMM

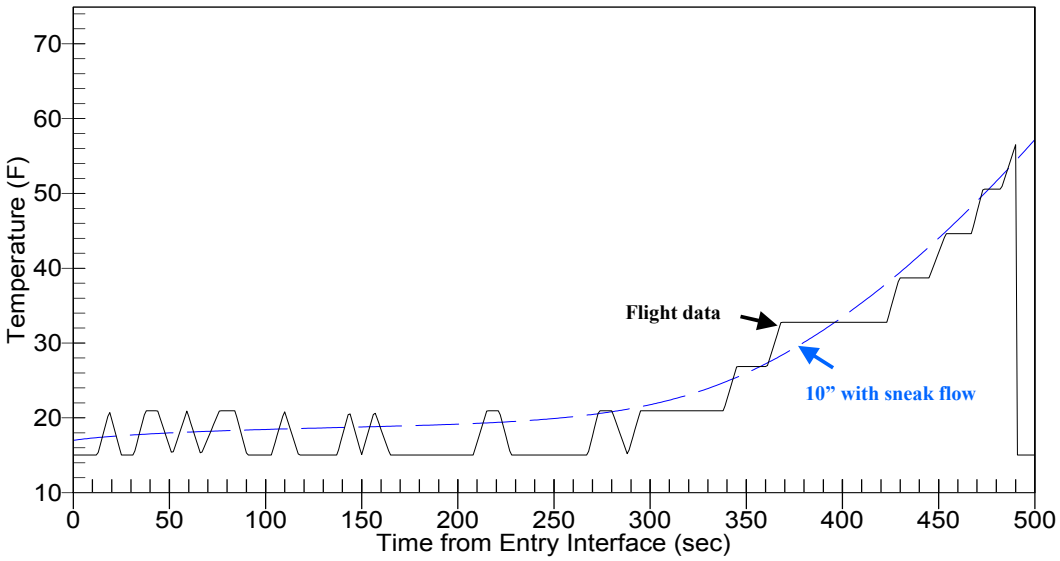

Figure 6-8 - Clevis Temperature Prediction (with 10% Sneak Flow) – JSC TMM

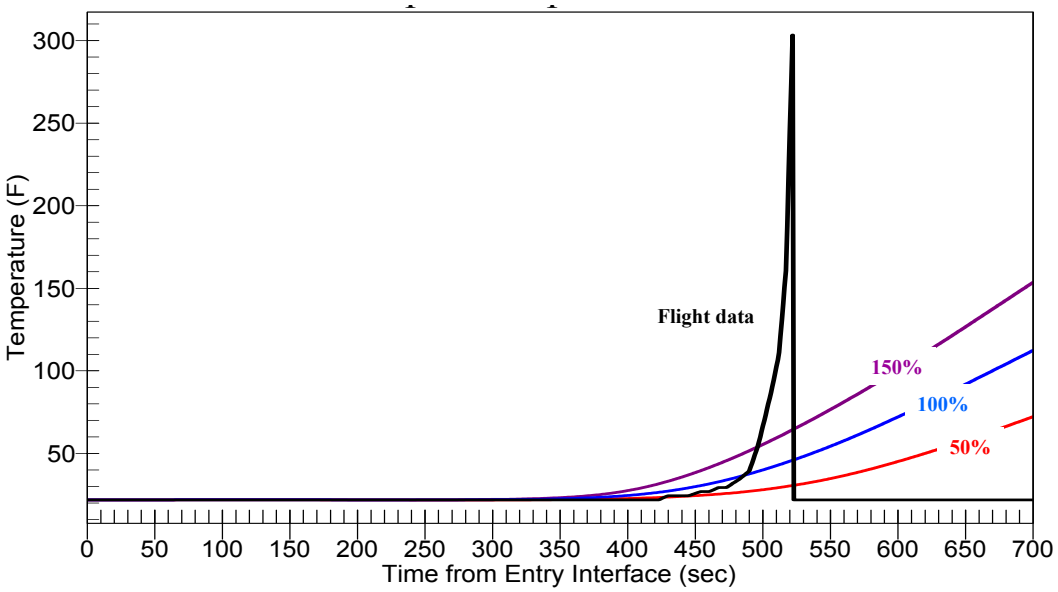

Figure 6-9 - Spar Temperature Predictions with Heating Uncertainties

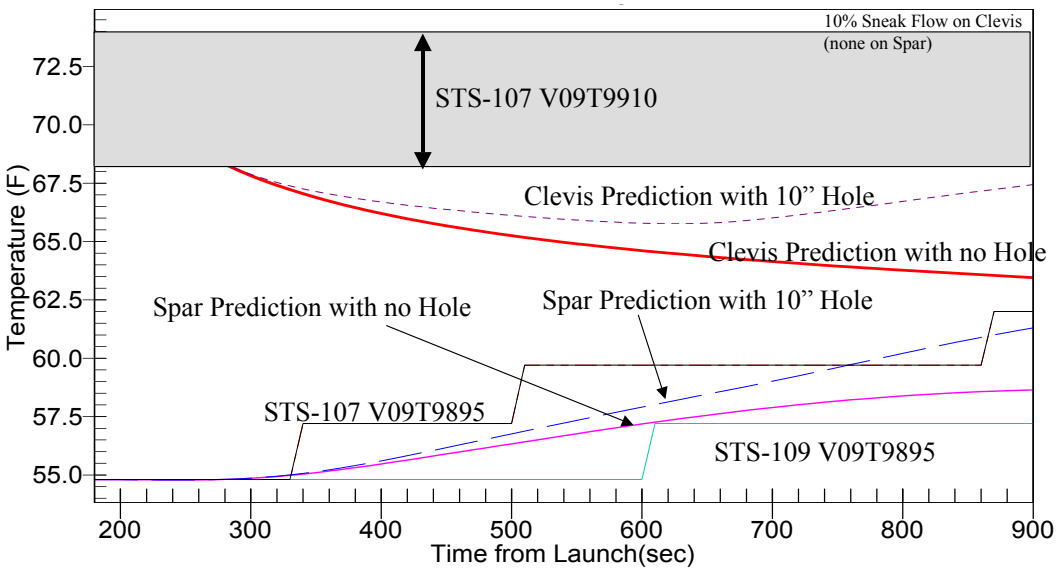

Figure 6-10 - Spar and Clevis Ascent Predictions Compared to Flight Data – JSC TMM

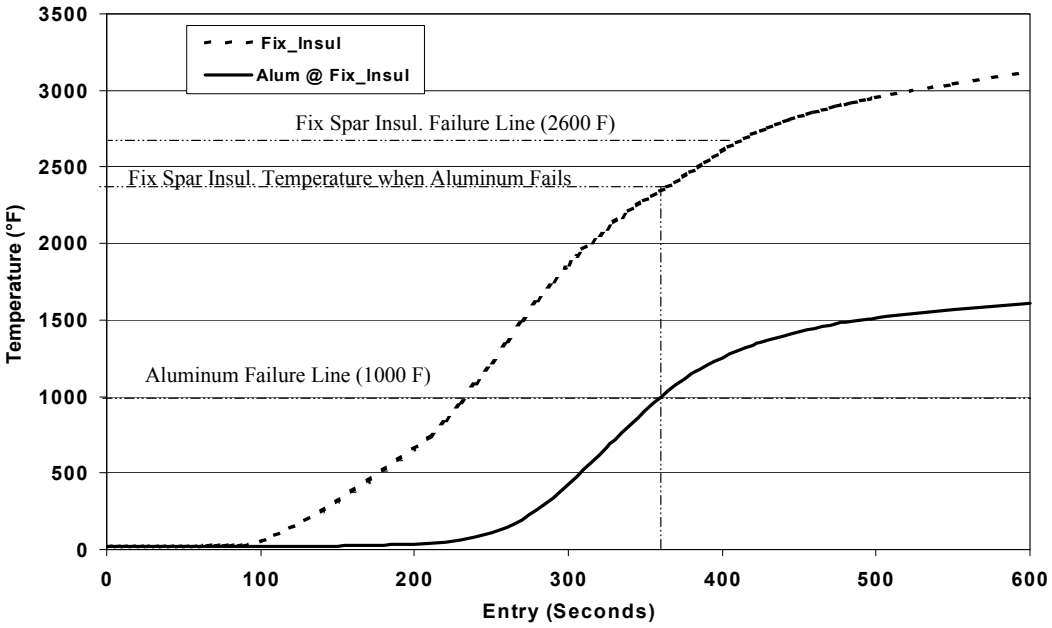

Figure 6-11 - Damaged Tee-Seal - Spar Insulation Transients

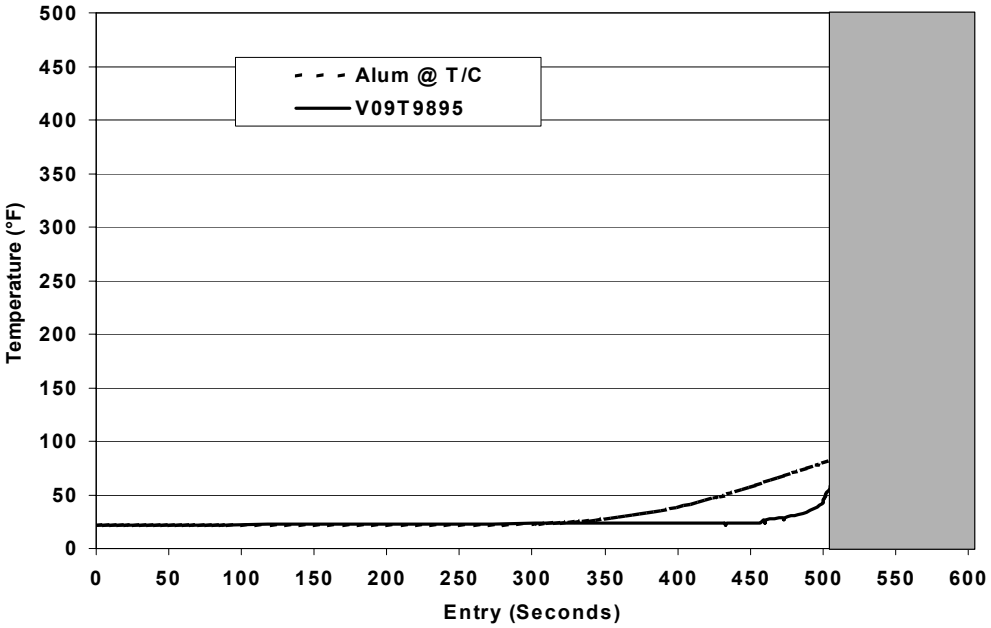

Figure 6-12 - Damaged Tee-seal - Spar Temperature Transients

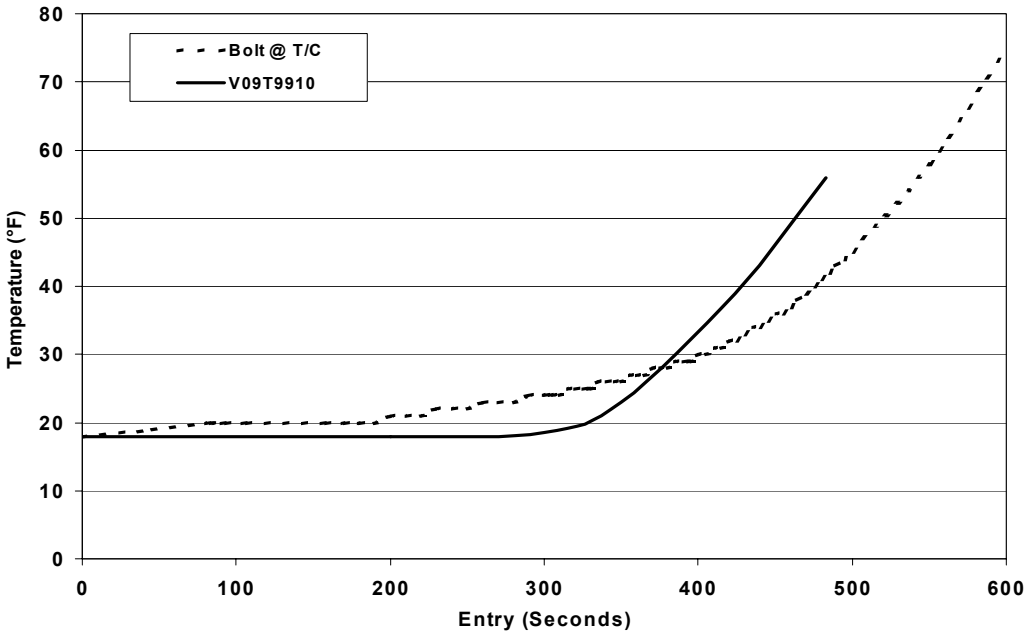

Figure 6-13 - Damaged Tee-seal - Clevis Transients

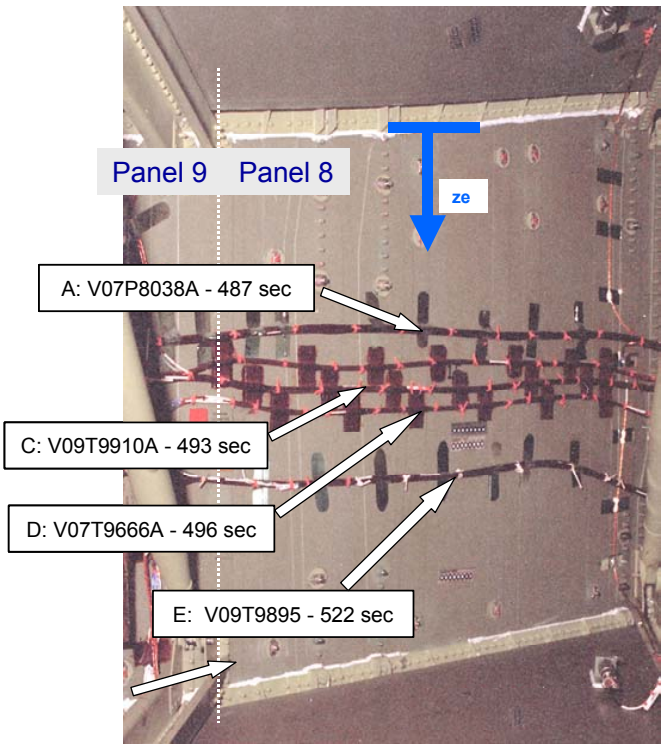

Flight data

	Time from e.i. (sec)	ze (in)
A	487.0	16.5
C	493.0	19.8
D	496.0	21.3
E	522.0	25.8
B		18.3

Figure 6-14 – Leading Edge Spar (view from within wing looking fwd)

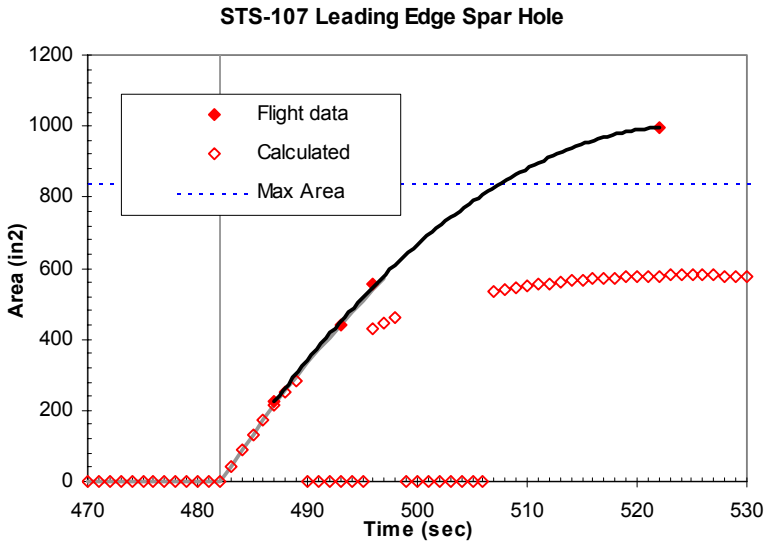

Figure 6-15 – Spar Hole Growth Analysis

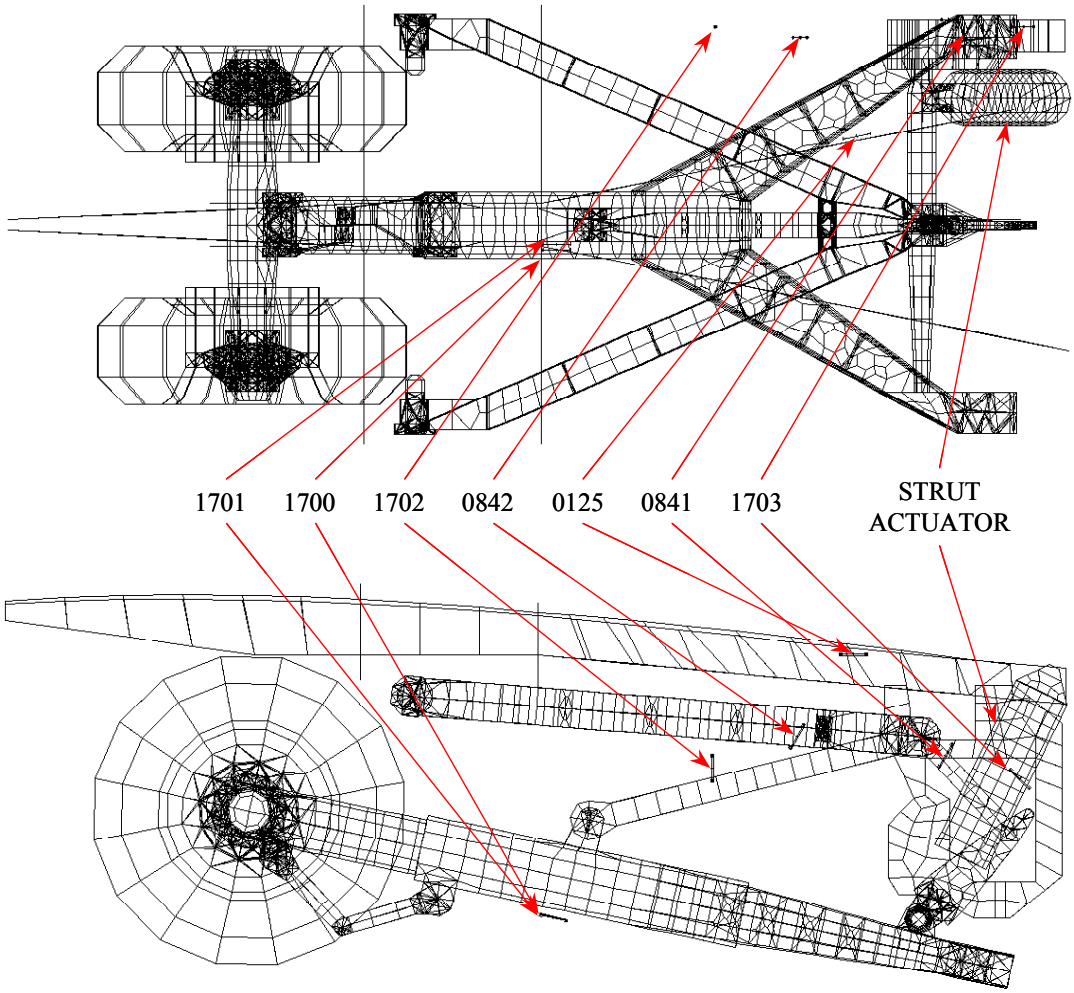

Figure 6-16 – Left Main Landing Gear Sensor Locations

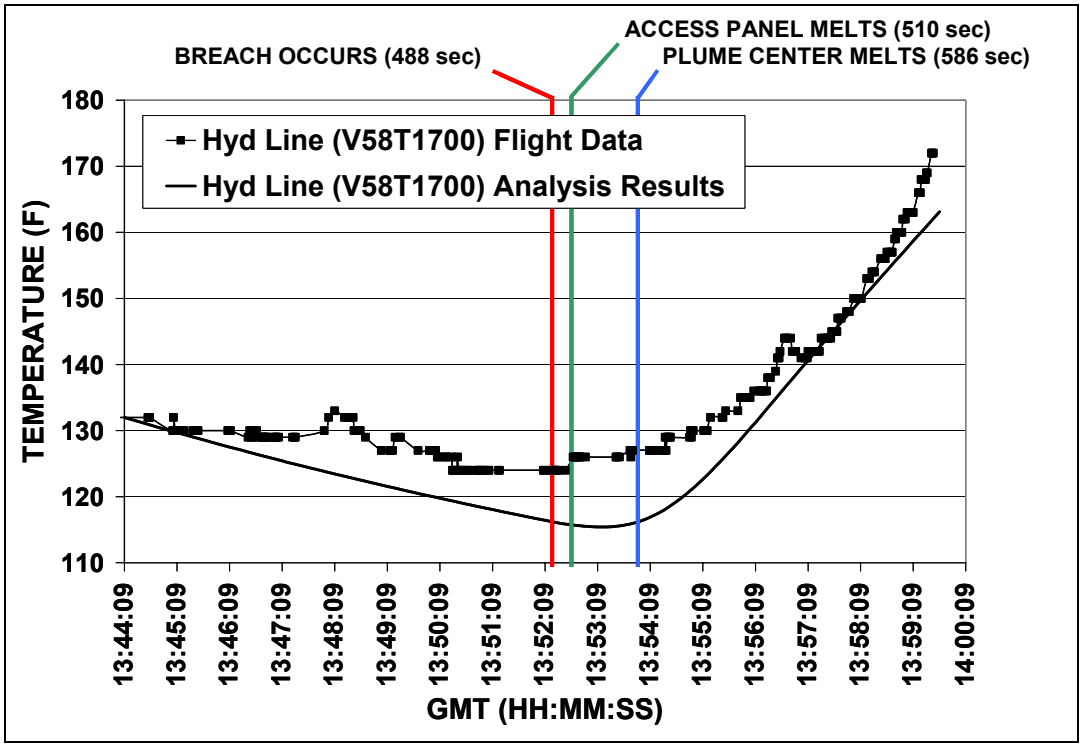

Figure 6-17 - V58T1700A analysis results

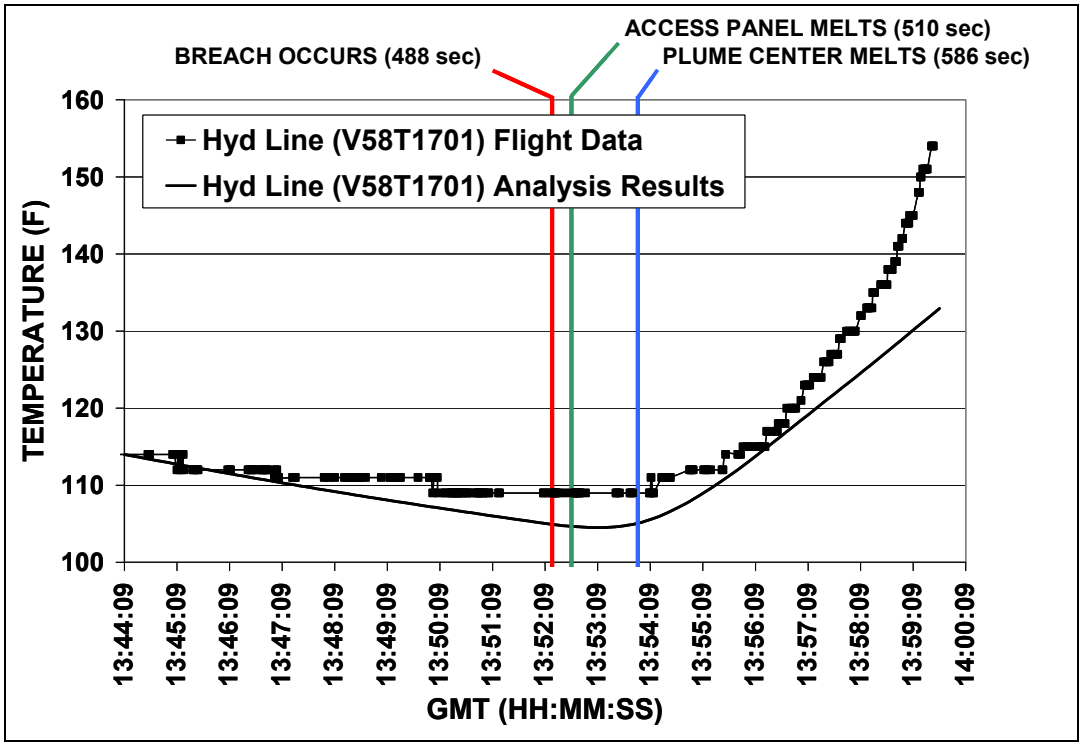

Figure 6-18 - V58T1701A analysis results

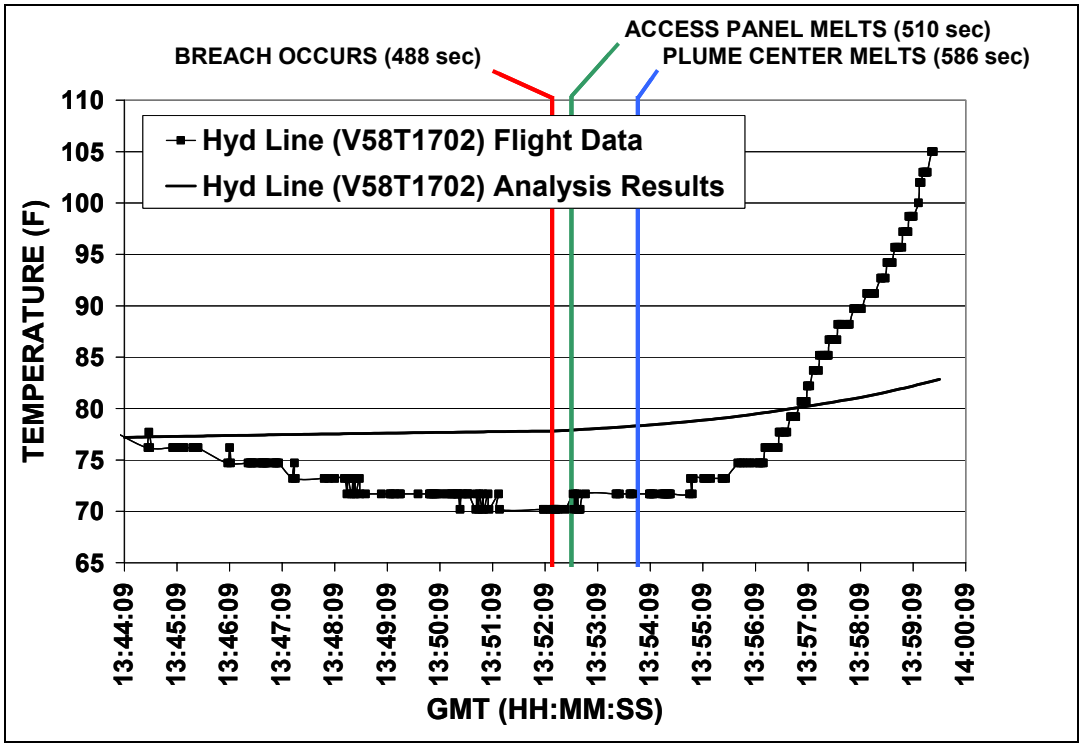

Figure 6-19 - V58T1702A analysis results

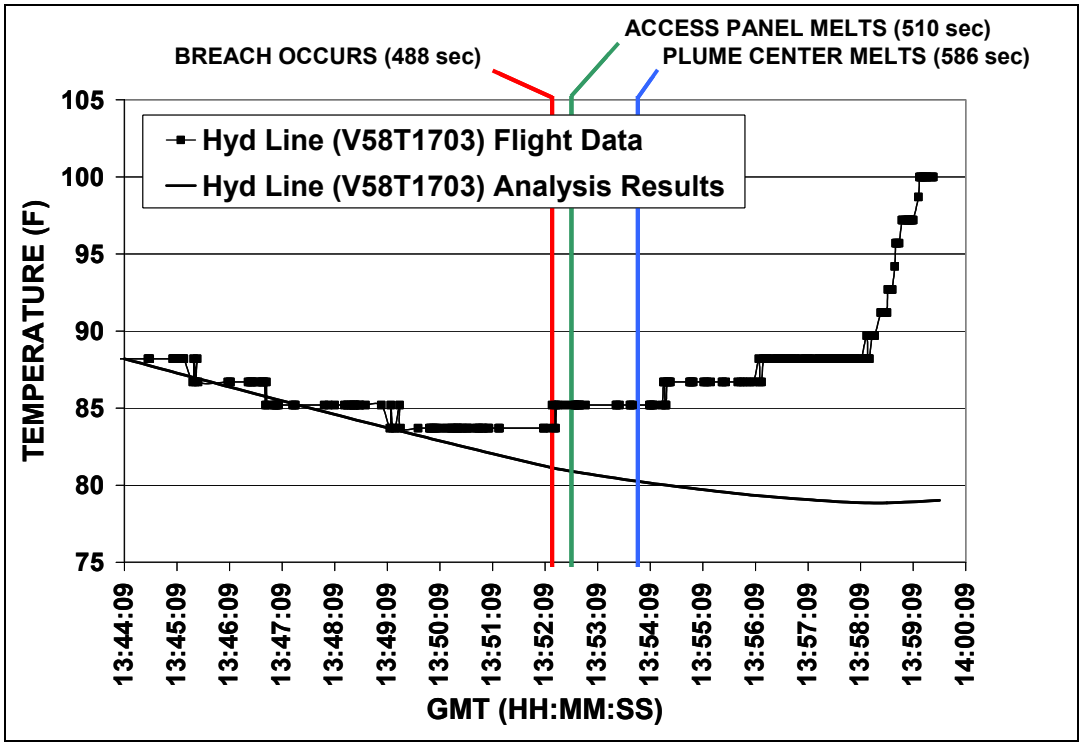

Figure 6-20 - V58T1703A analysis results

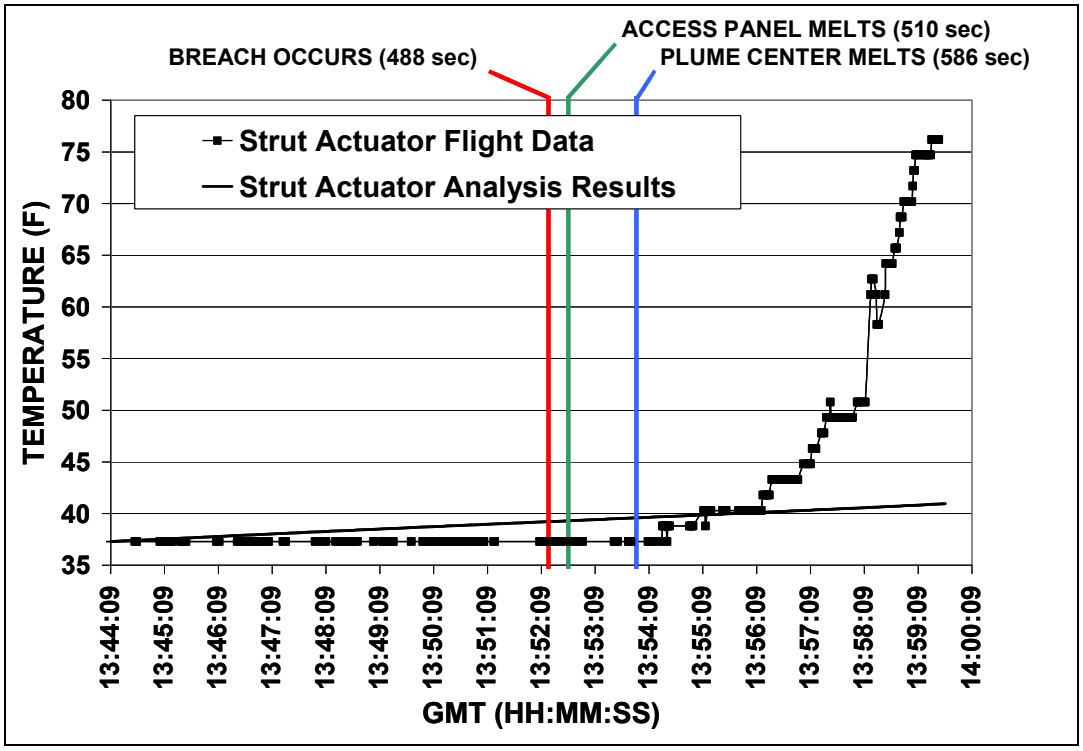

Figure 6-21 - V58T0405A (strut actuator) analysis results

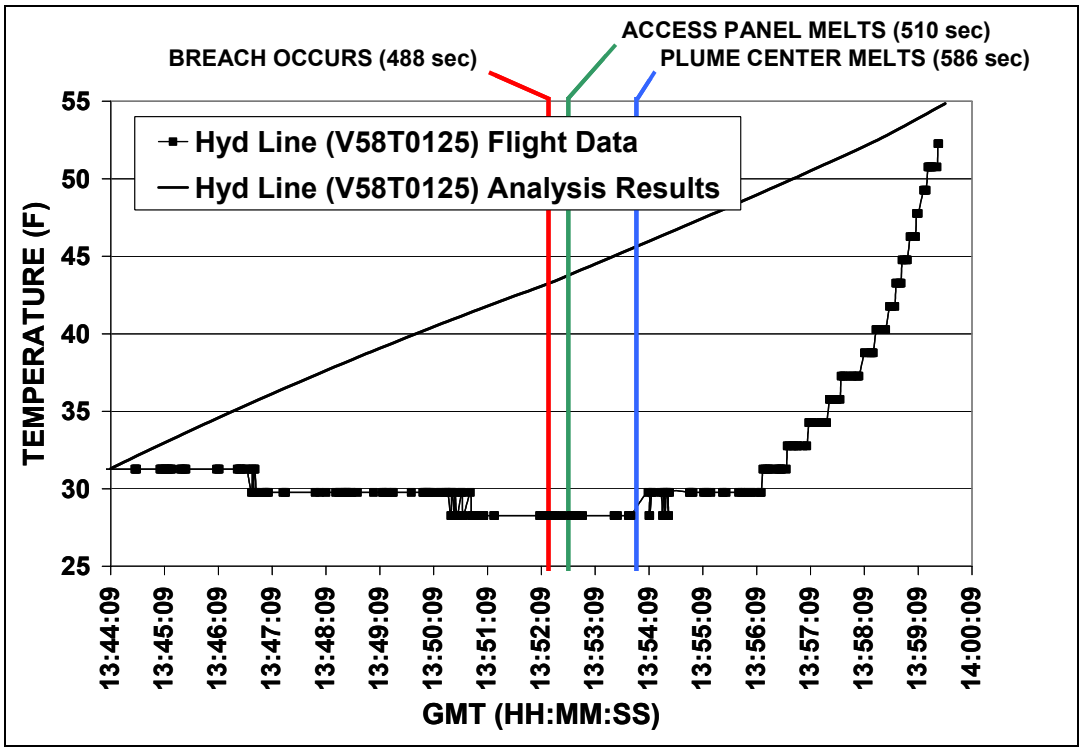

Figure 6-22 -V58T0125A analysis results

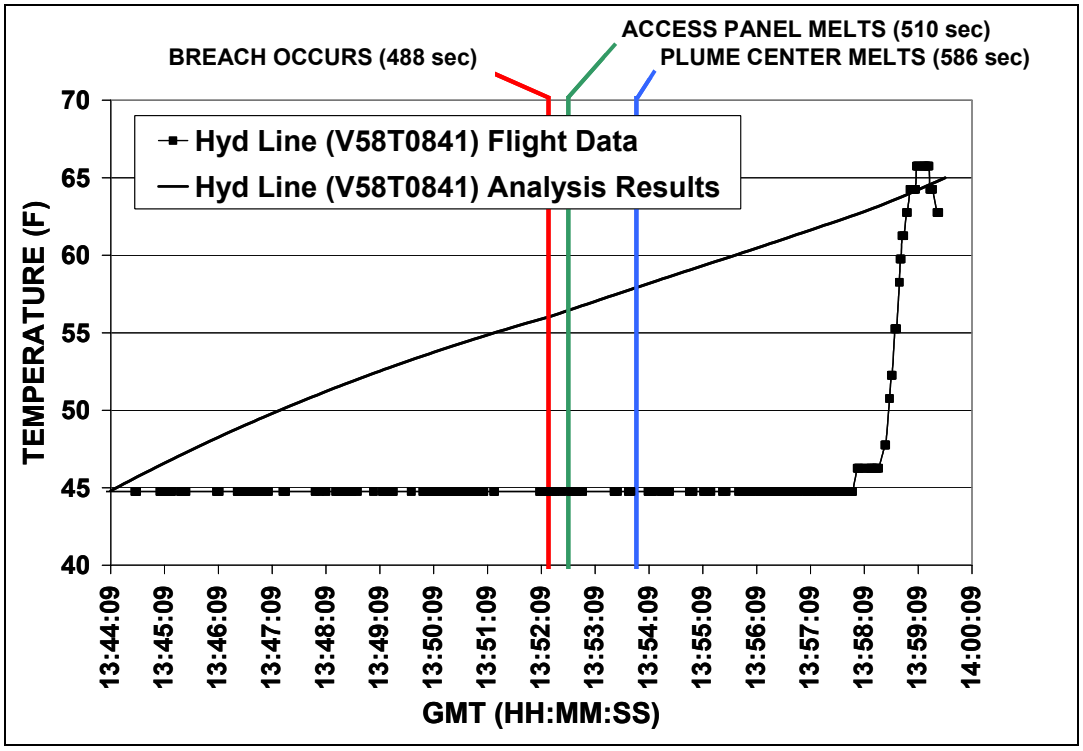

Figure 6-23 - V58T0841A analysis results

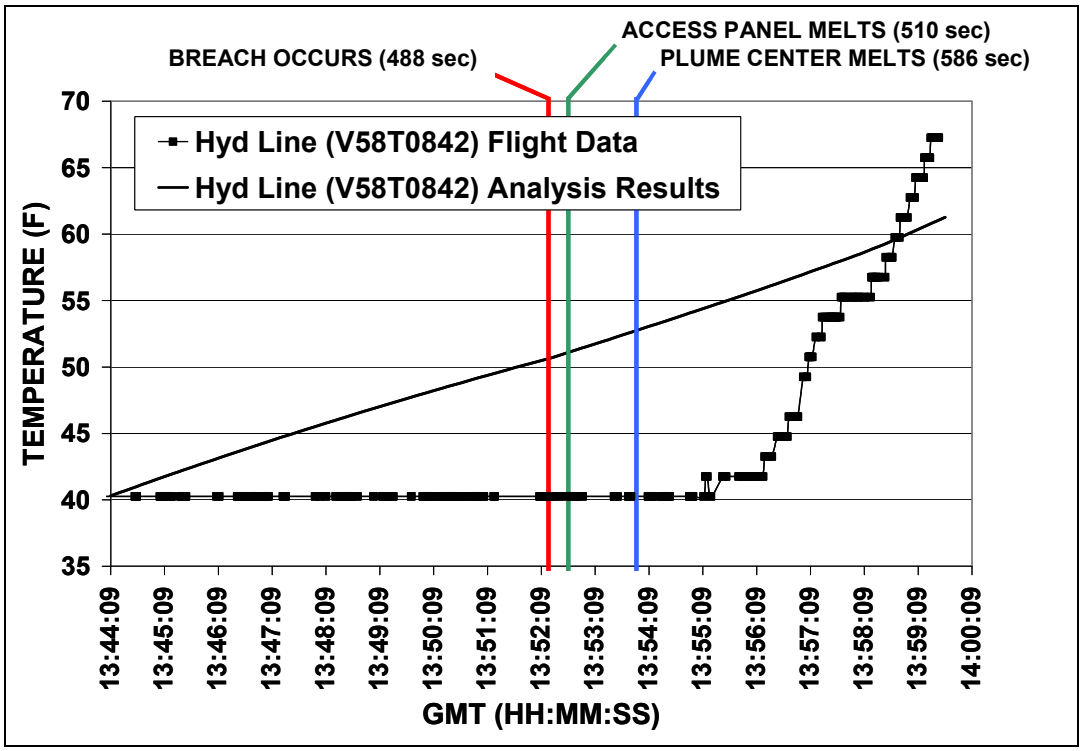

Figure 6-24 -V58T0842A analysis results

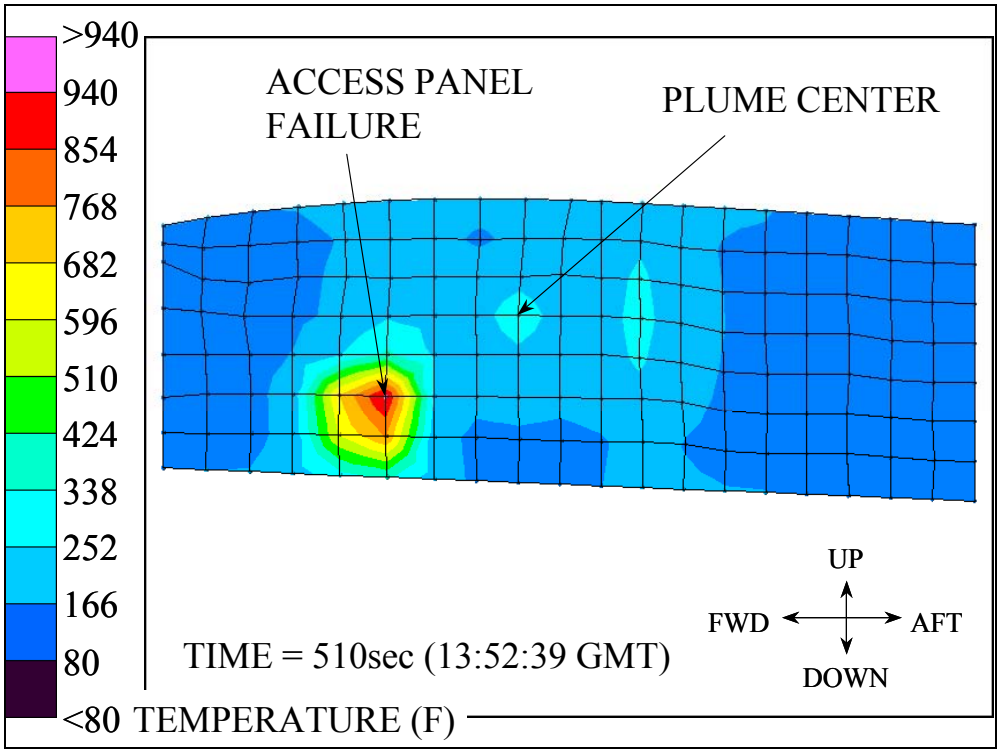

Figure 6-25 - Outboard wheel well wall temperature at 13:52:39 GMT

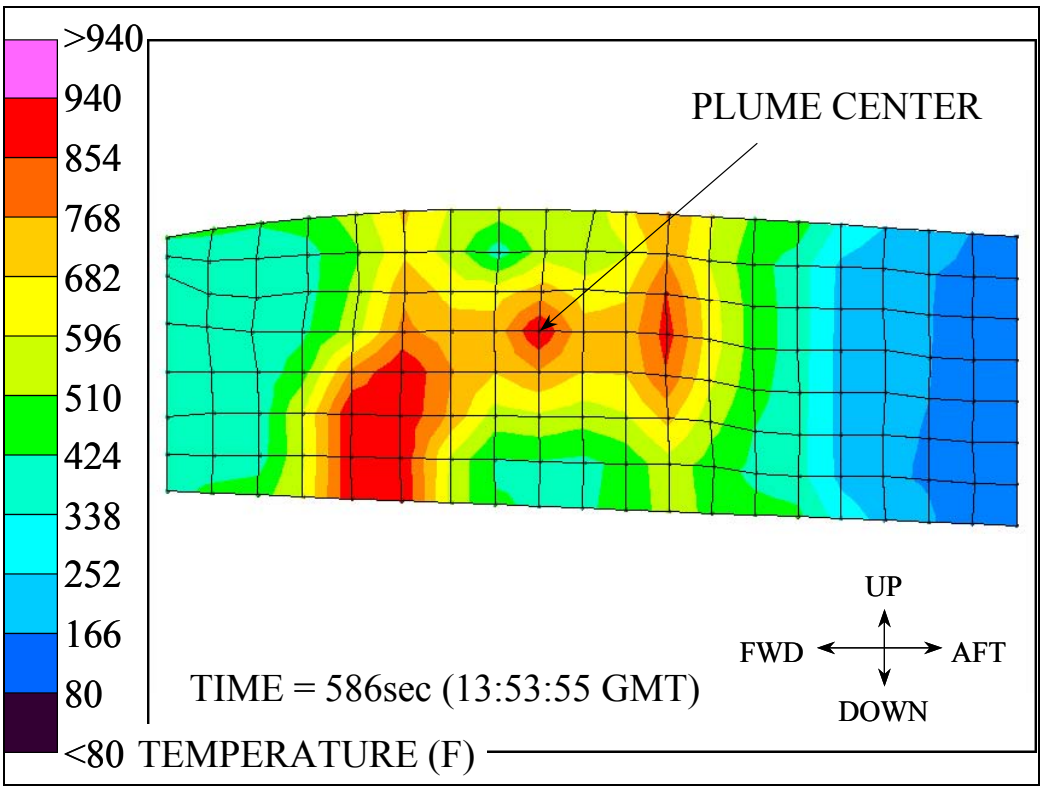

Figure 6-26 -Outboard wheel well wall temperature at 13:53:55 GMT

Figure 6-27 – Cable Bundle Test Article

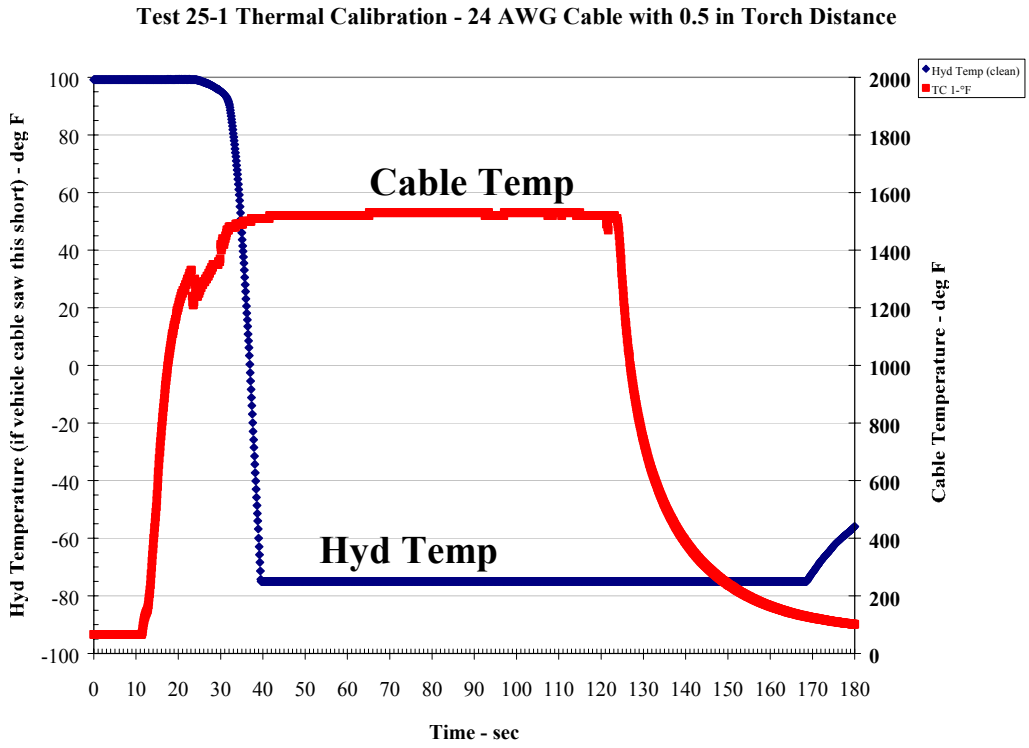

Figure 6-28 – Cable Failure Signature

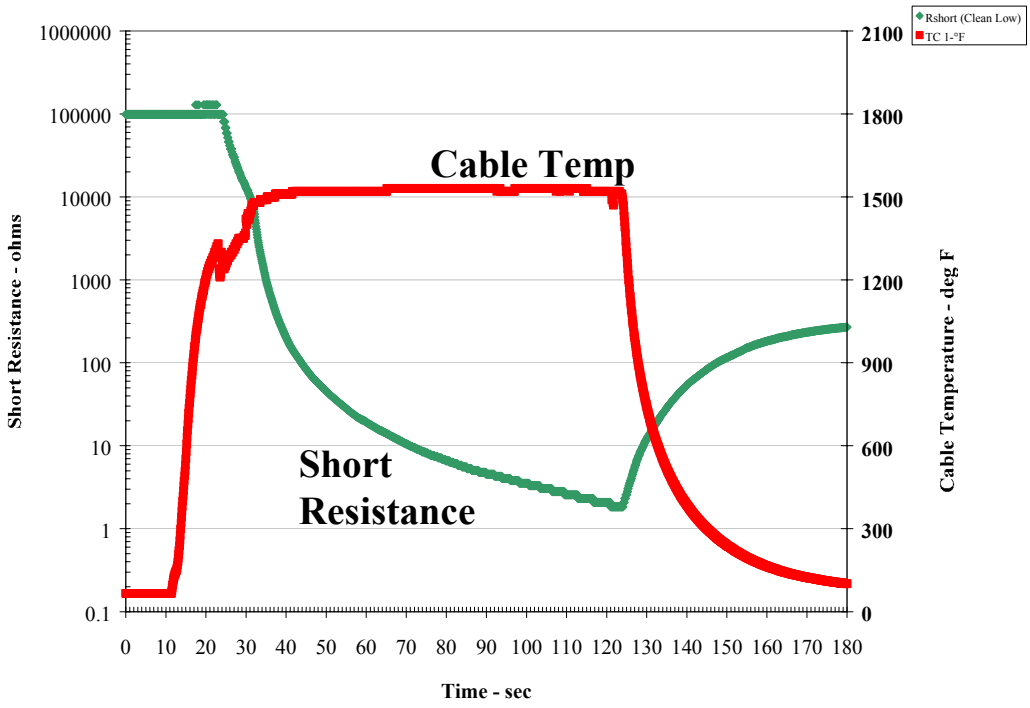

Figure 6-29 – Cable Failure Signature

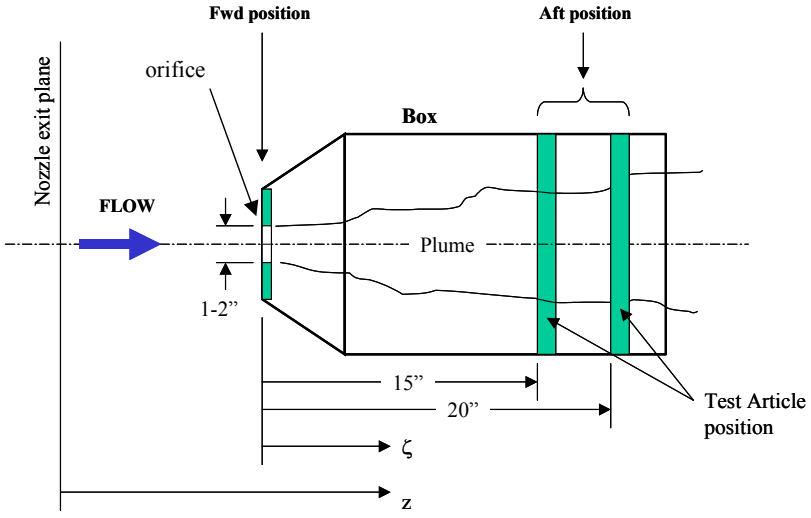

Figure 6-30 – Box Test Support Equipment

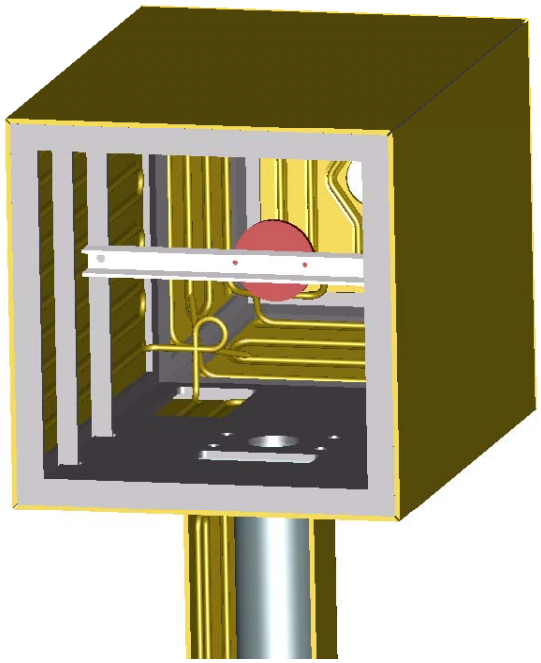

Figure 6-31 – Box Test Support Equipment

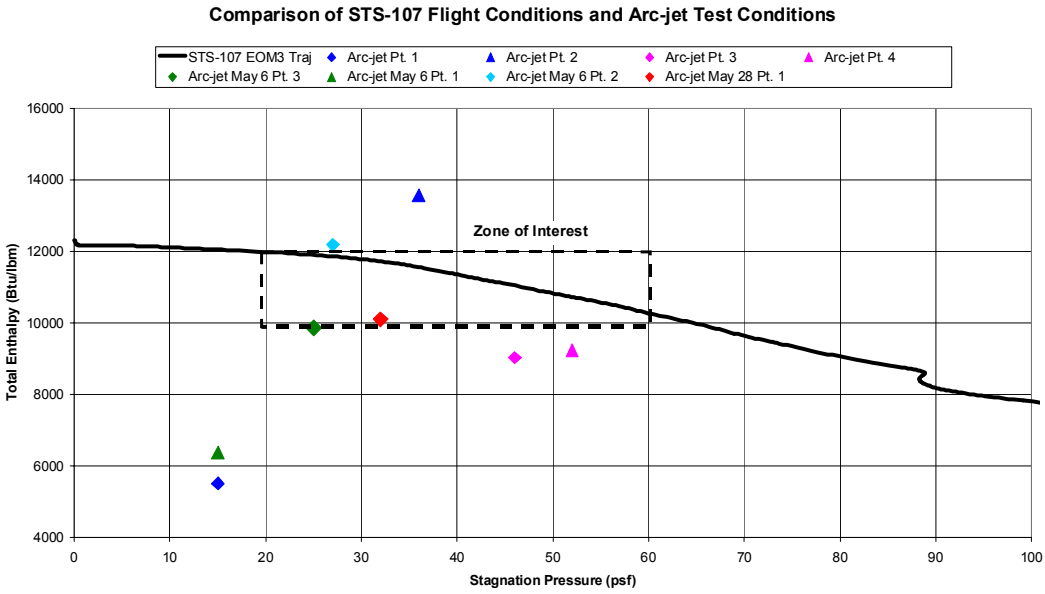

Figure 6-32 – Arc-Jet Test Conditions

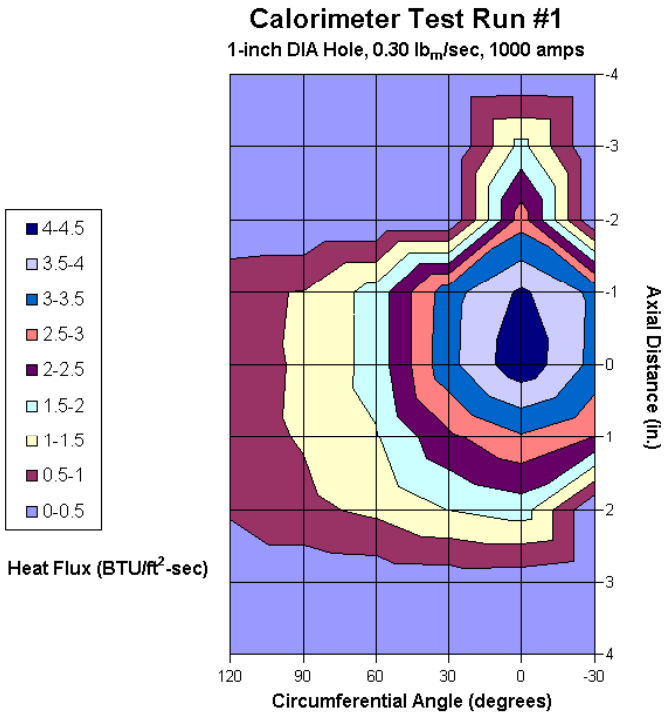

Figure 6-33 - Calorimeter

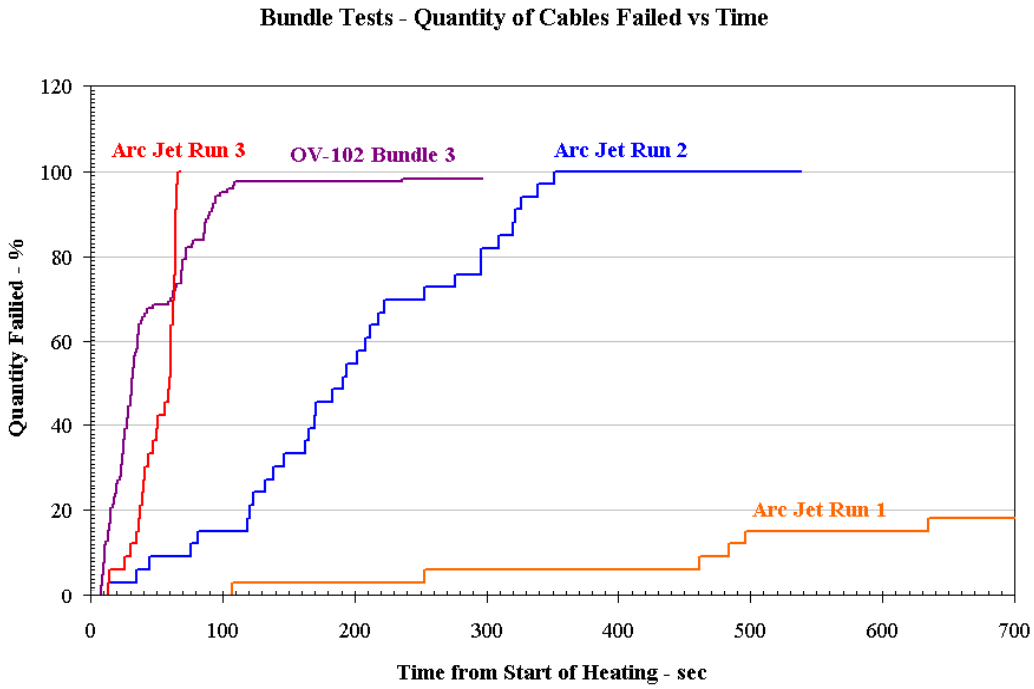

Figure 6-34 – Cable Failure Rates

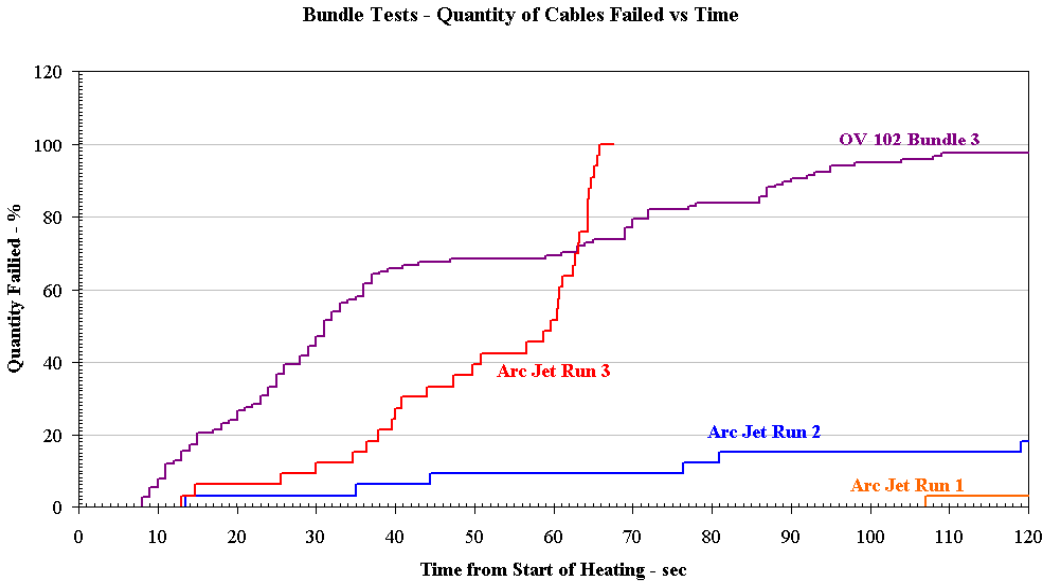

Figure 6-35 – Cable Failure Rates (expanded)

Figure 6-36: Wire bundle arc jet testing (before test)

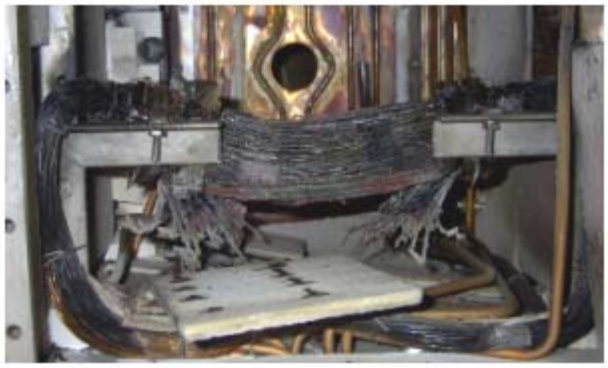

Figure 6-37 – Cable Bundle Post-Test Run #2

(1)
Test Article Inserted

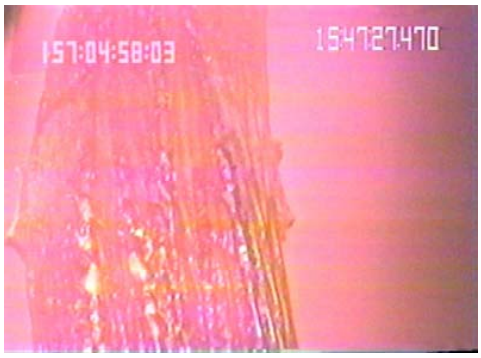

(2)

(3)

(4)

(5)

(6)

Figure 6-38 – Video Sequence of Cable Bundle Test (Run #3)

Figure 6-39 - MLG outboard sidewall (looking fwd)

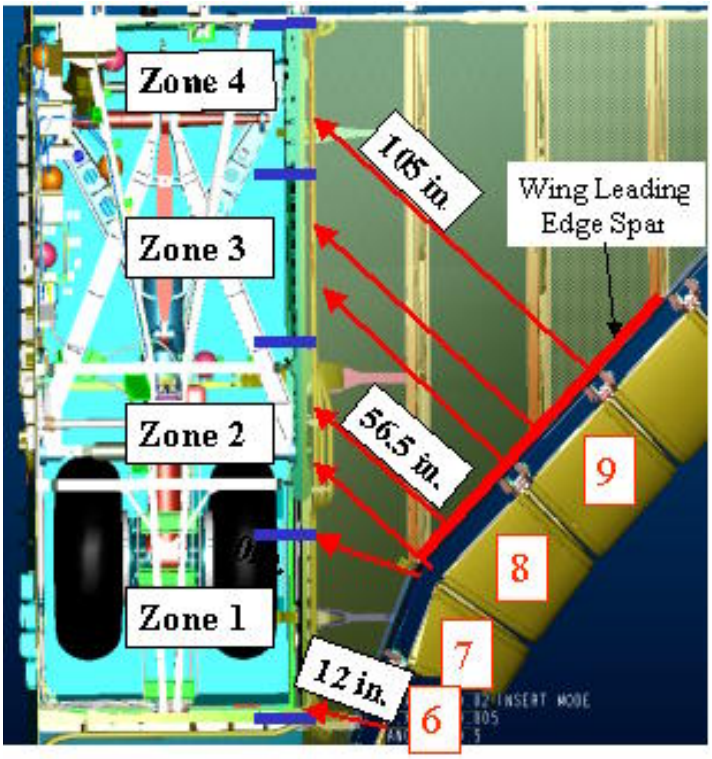

Figure 6-40 - MLG wheel well wall partitioning (view from top)

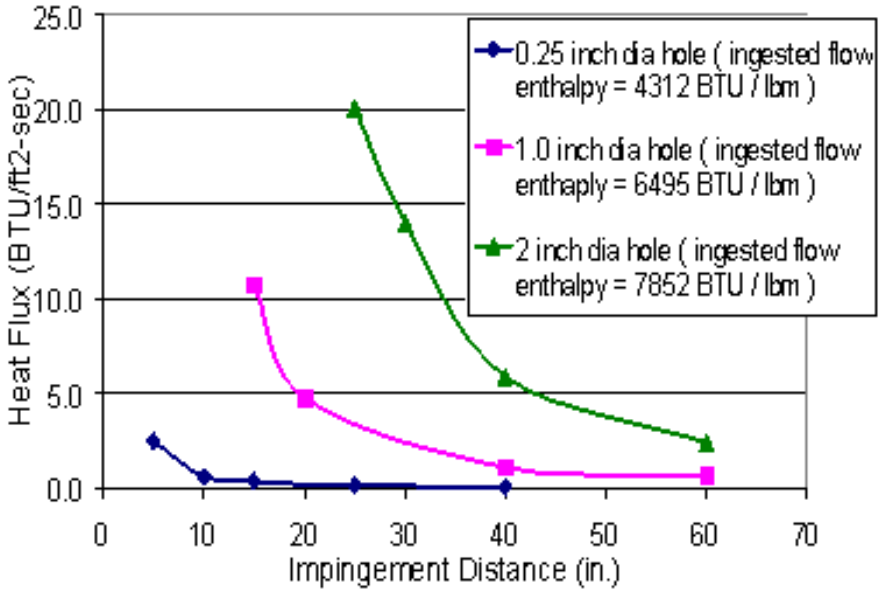

Figure 6-41 - Panel 9 internal plume flat plate impingement heating at EI+491 seconds

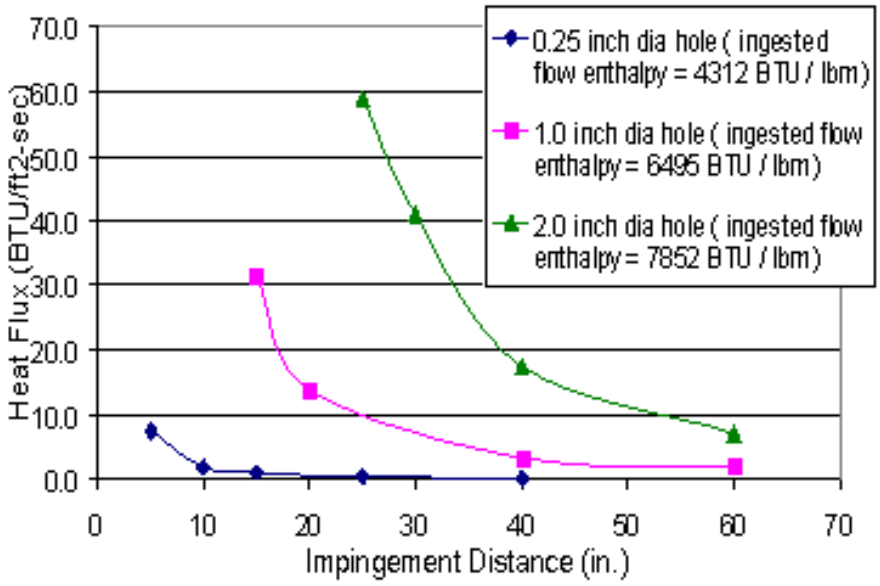

Figure 6-42 - Panel 9 internal plume impingement heating on 1" diameter cylinder at EI+491 seconds

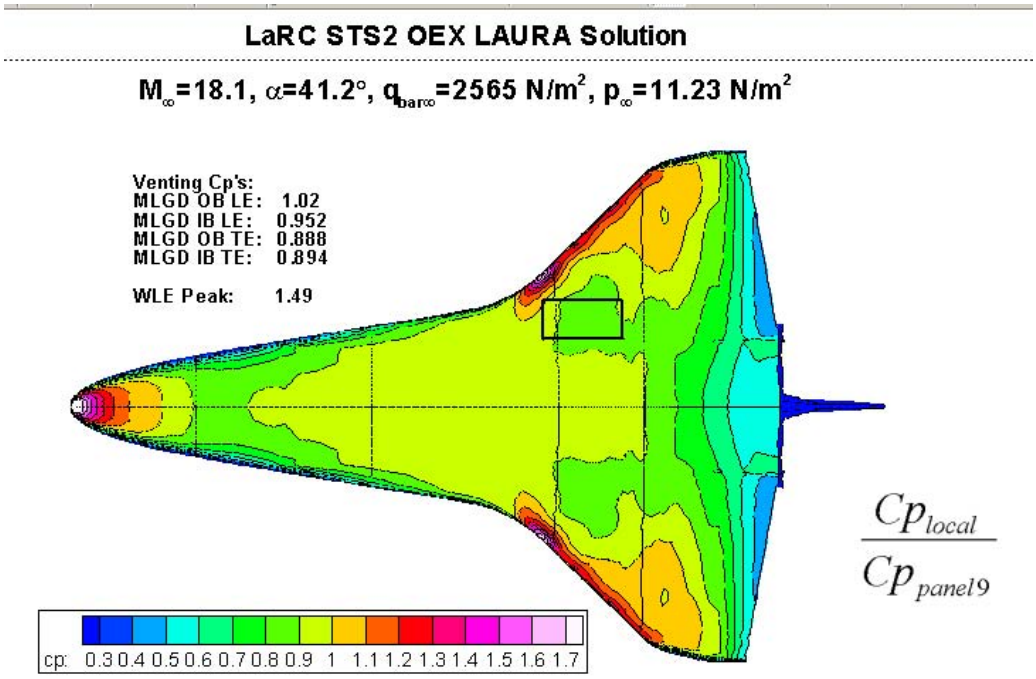

Figure 6-43 - Plume heating correction for local pressure coefficient

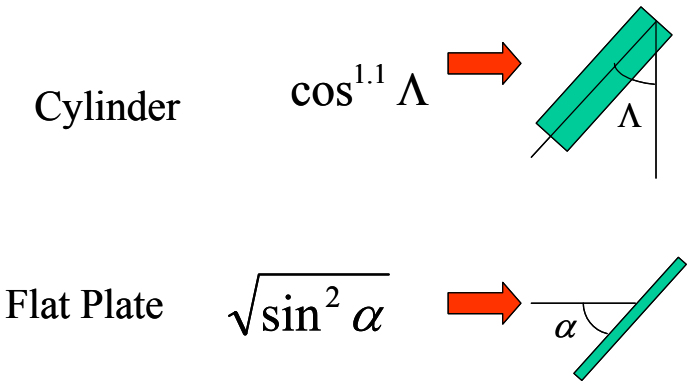

Zone	a	L
1	67.5	22.5
2	58.5	31.5
3	58.5	31.5
4	58.5	31.5

Figure 6-44 - Off-normal angle impingement plume heating correction for a cylinder and flat plate

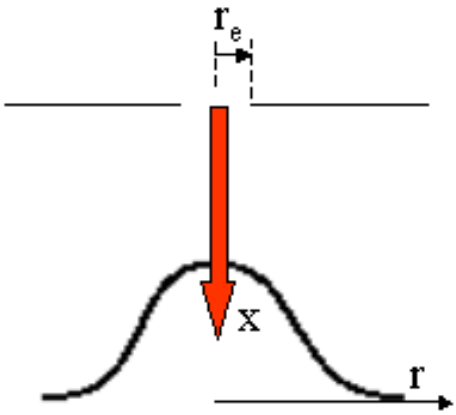

r/r_s	$qdot/(qdot)_0$
0	1.000
1	0.748
2	0.392
3	0.219
4	0.154
5	0.119
6	0.100
7	0.0808
8	0.0615
9	0.0423

$$r_S = r_e \quad \text{for } x \le 7.0 r_e$$

$$r_S = r_e + x \tan\left(\frac{\pi}{30}\right) \quad \text{for } x > 7.0 r_e$$

Figure 6-45 - Plume heating corrections for radial distribution from the stagnation point

$$\frac{\sqrt{r_{1"diametercylinder}}}{\sqrt{r_{bundle}}}$$

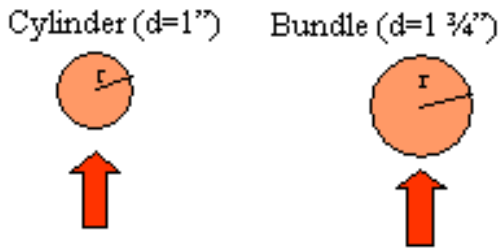

Figure 6-46 -Correction of plume heating due to radius effects

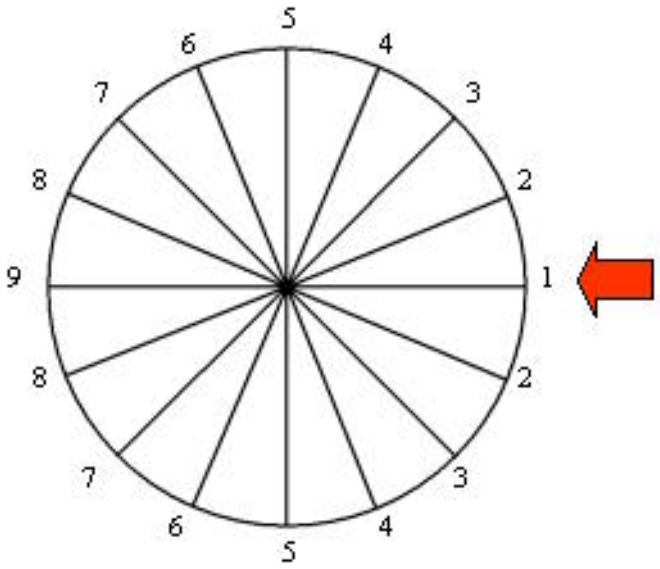

station	qdot/(qdot)$_0$
1	1.0000
2	0.9155
3	0.7080
4	0.4490
5	0.2230
6	0.0830
7	0.0320
8	0.0325
9	0.0370

Figure 6-47 - Circumferential plume heating corrections

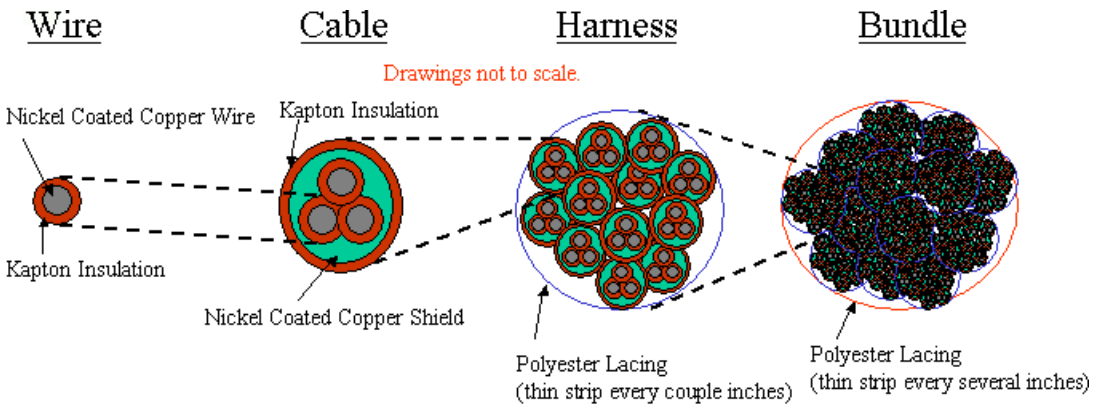

Figure 6-48 - Wire bundle configuration & terminology

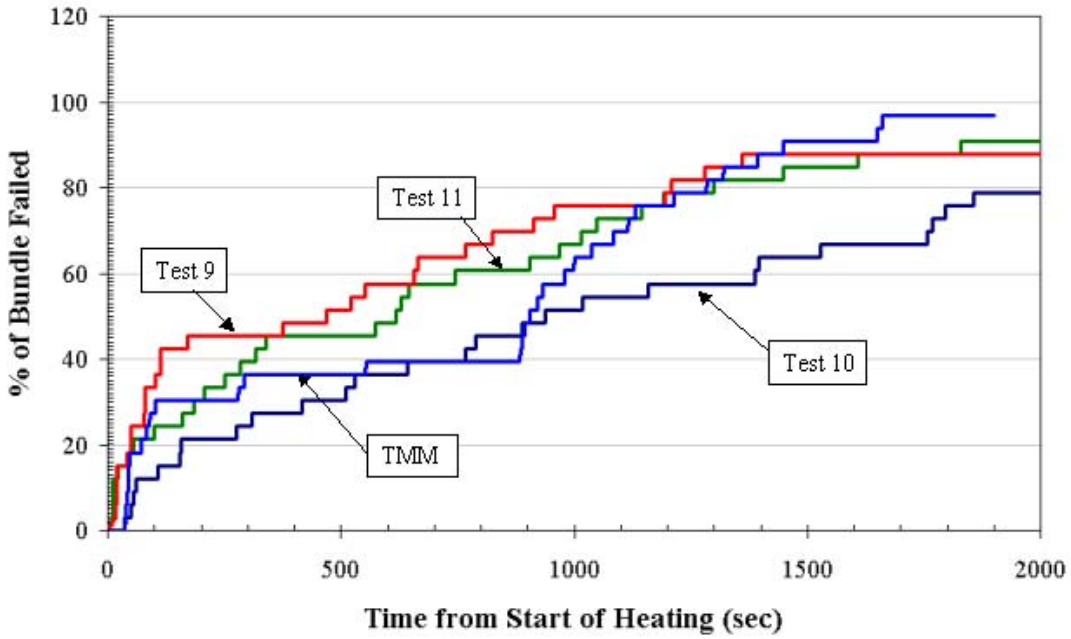

Figure 6-49 - Large propane torch test results vs. TMM test predictions

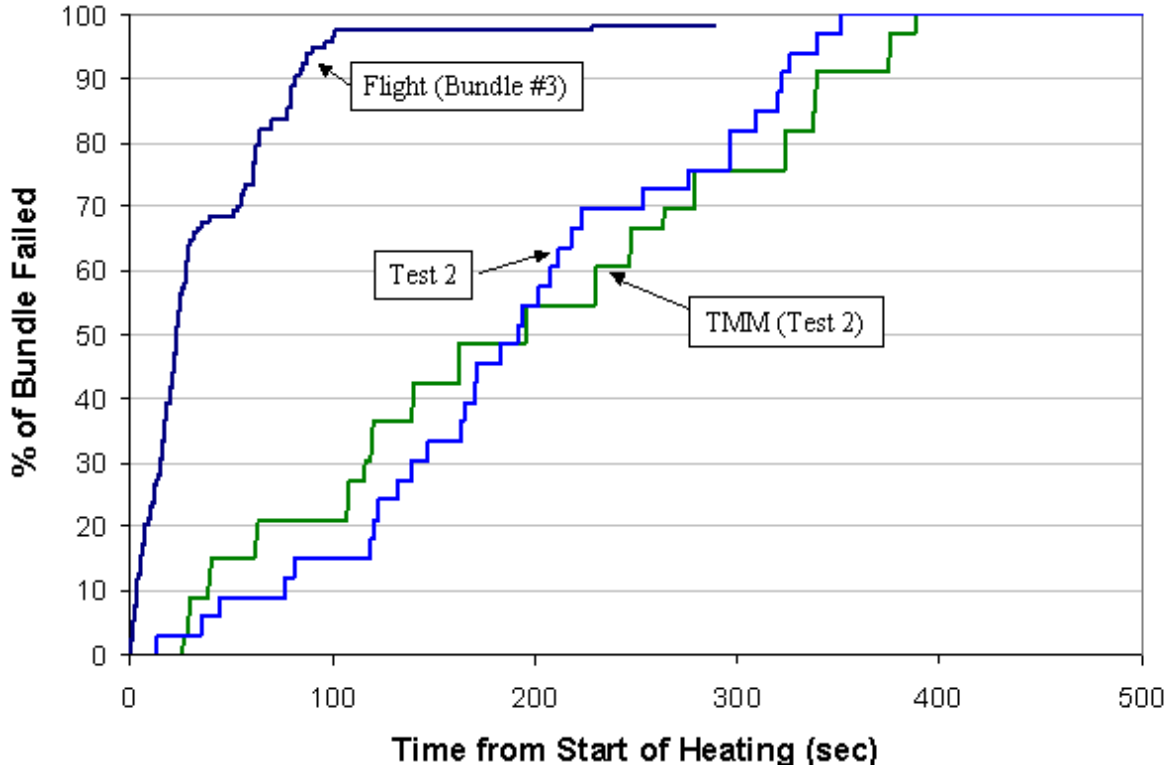

Figure 6-50 - Arc jet test 2 results vs. TMM test predictions

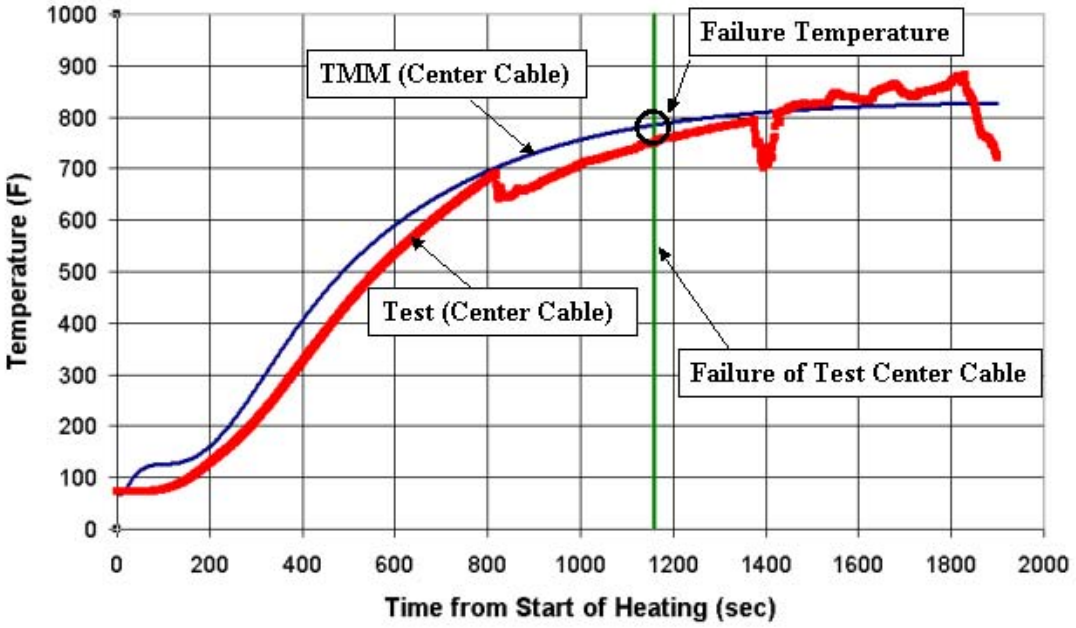

Figure 6-51 - TMM cable failure temperature determined through large propane torch testing

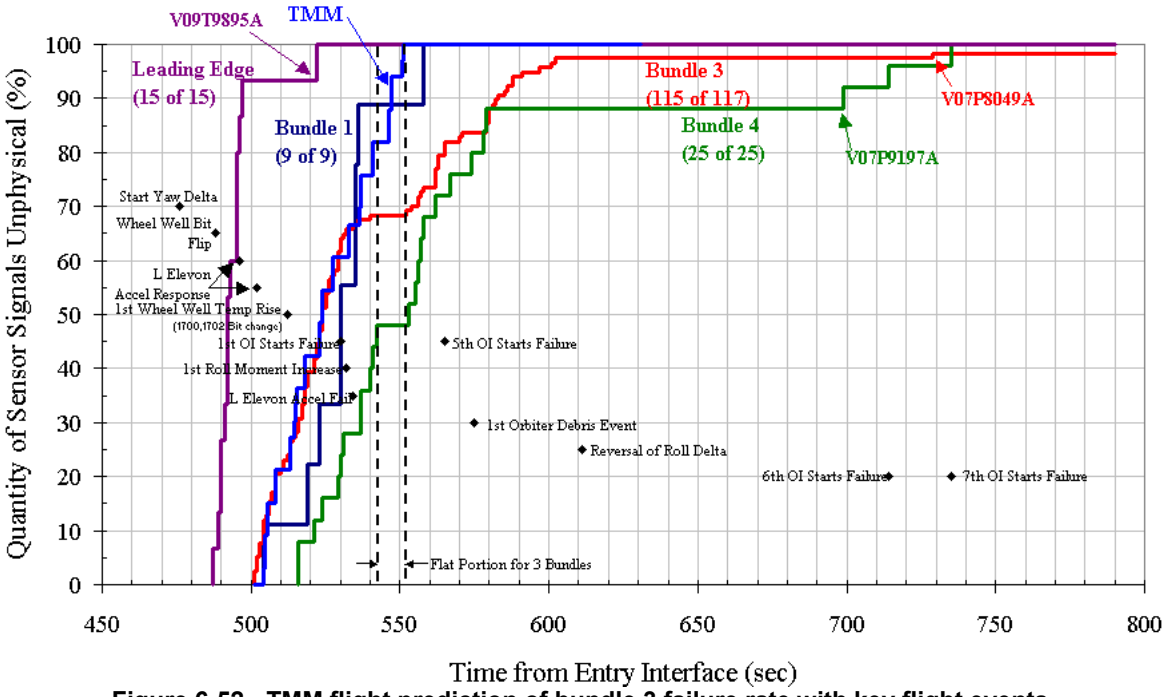

Figure 6-52 - TMM flight prediction of bundle 3 failure rate with key flight events

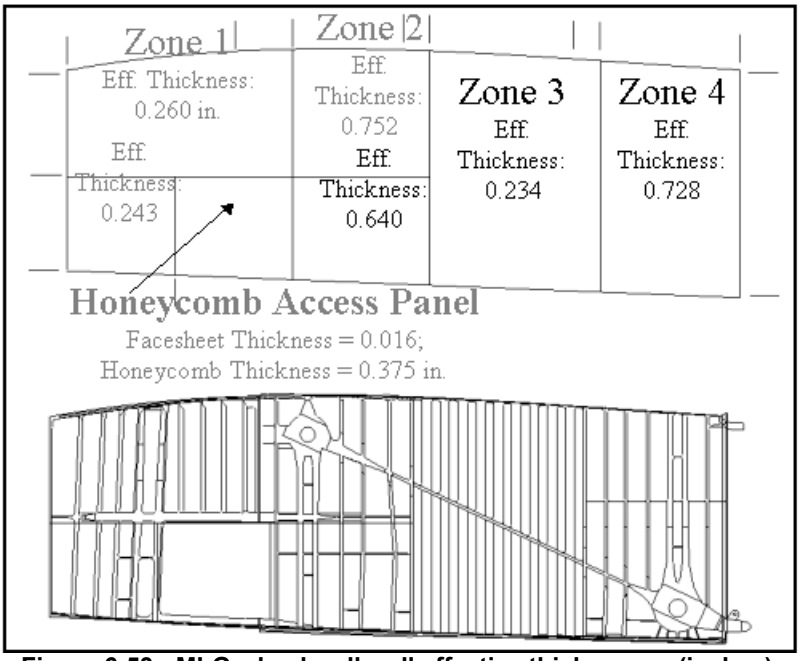

Figure 6-53 - MLG wheel well wall effective thicknesses (inches)

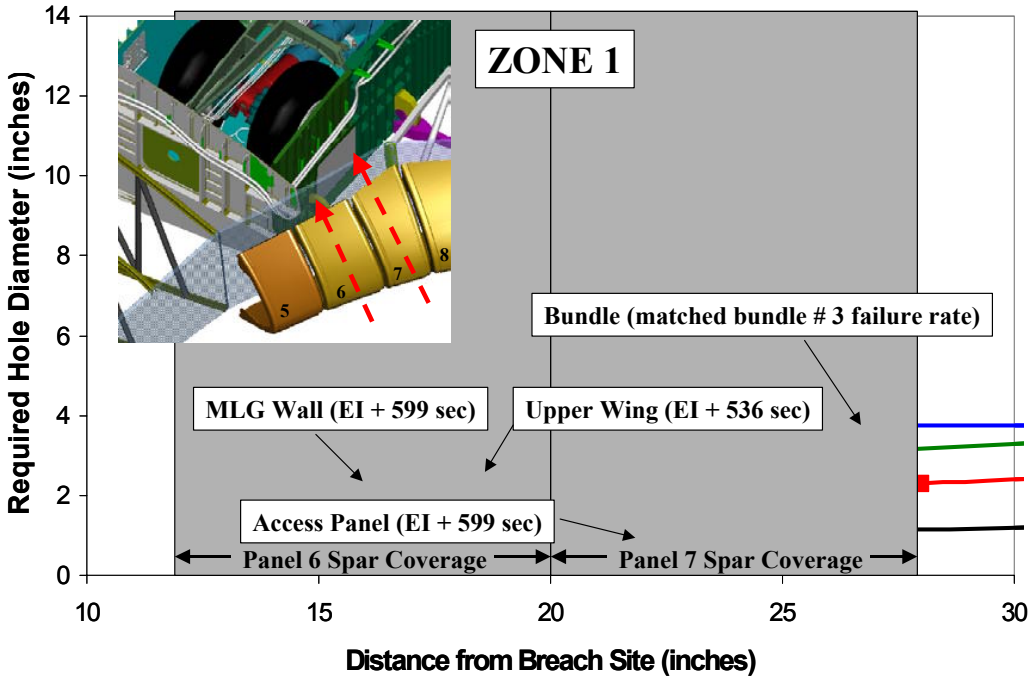

Figure 6-54 - Zone 1 plume heating result comparisons

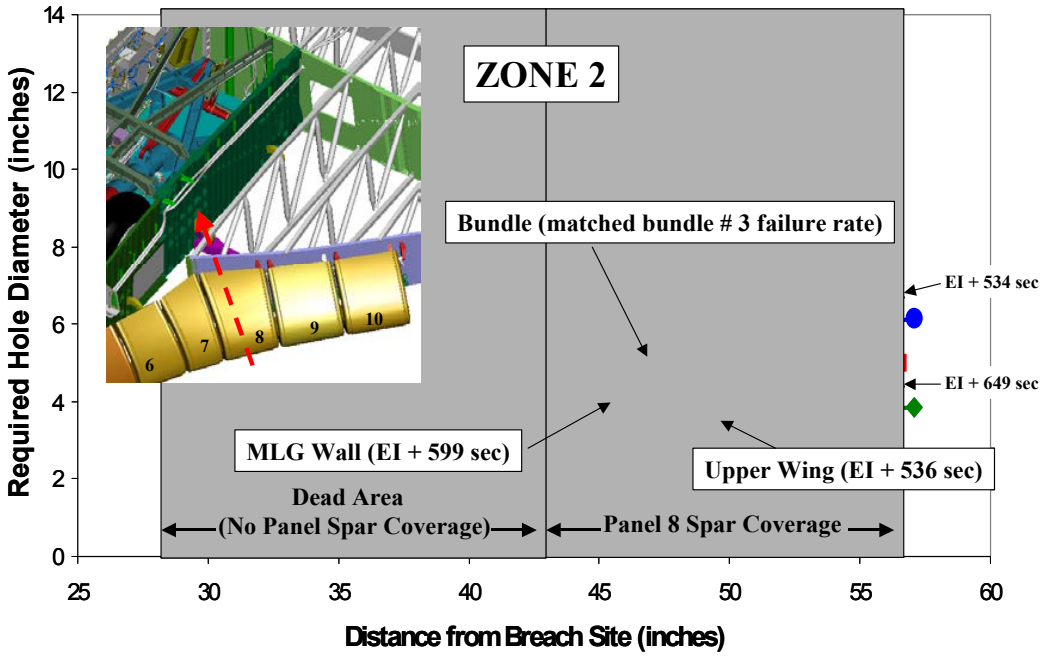

Figure 6-55 - Zone 2 plume heating result comparisons

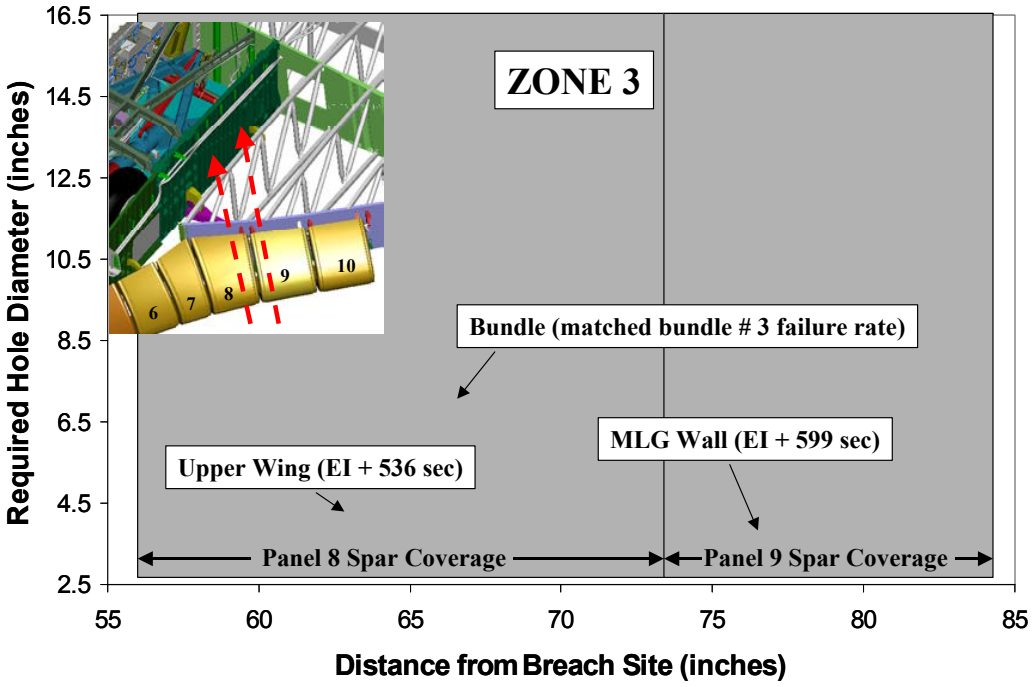

Figure 6-56 - Zone 3 plume heating result comparisons

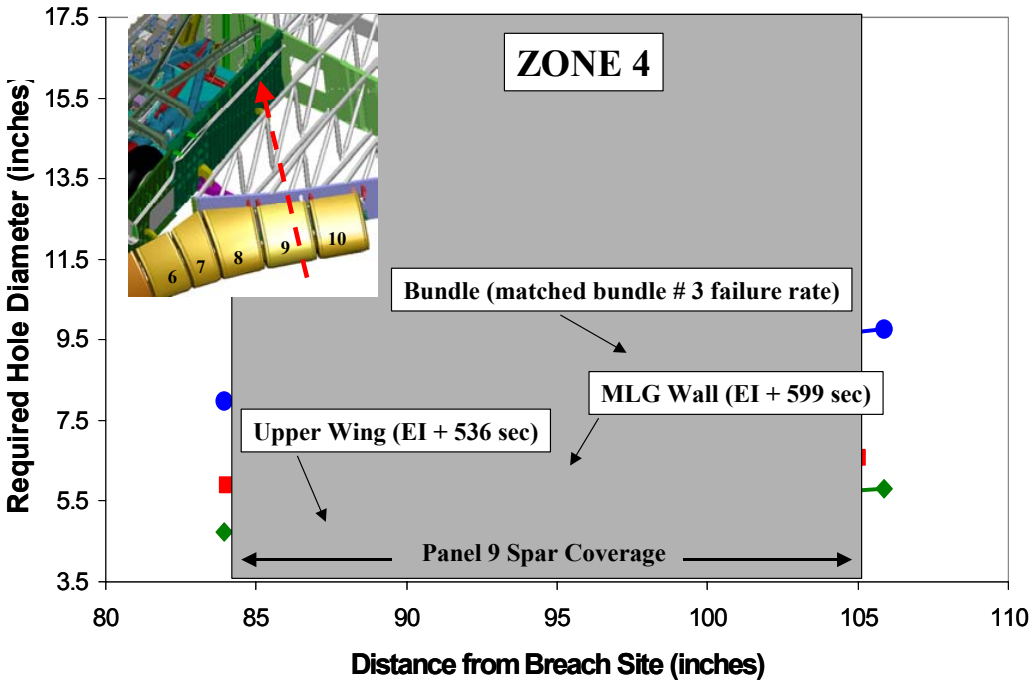

Figure 6-57 - Zone 4 plume heating result comparisons

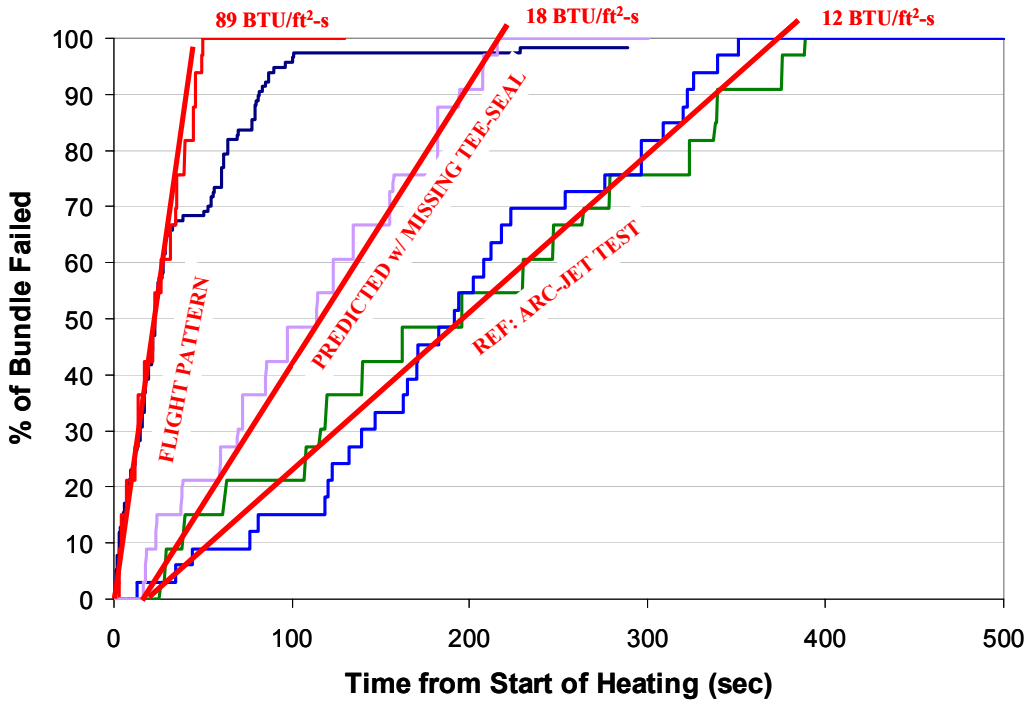

Figure 6-58 - Damaged Tee-Seal Bundle Failure

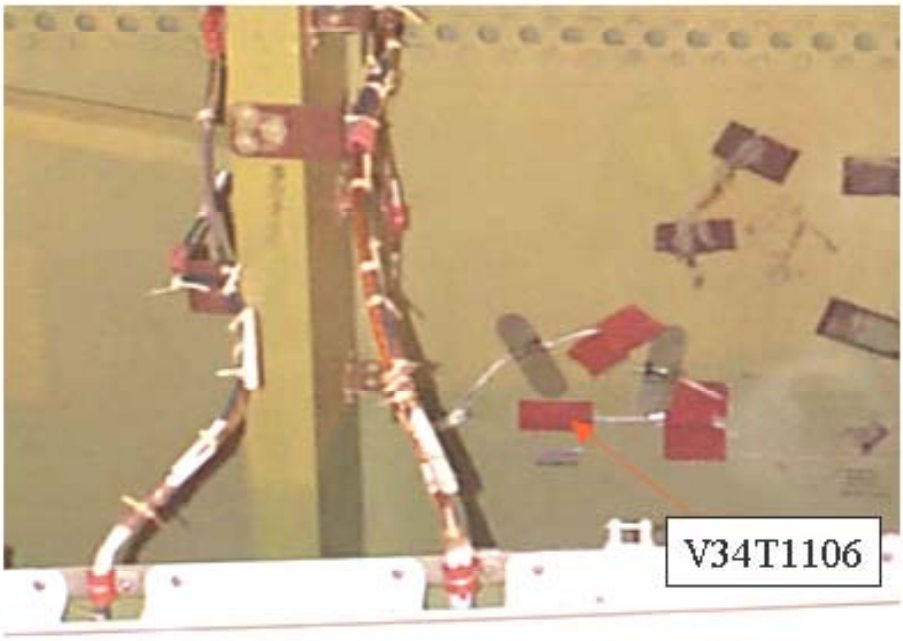

Figure 6-59 - OV-102 V34T1106 Temperature Sensor (looking outboard)

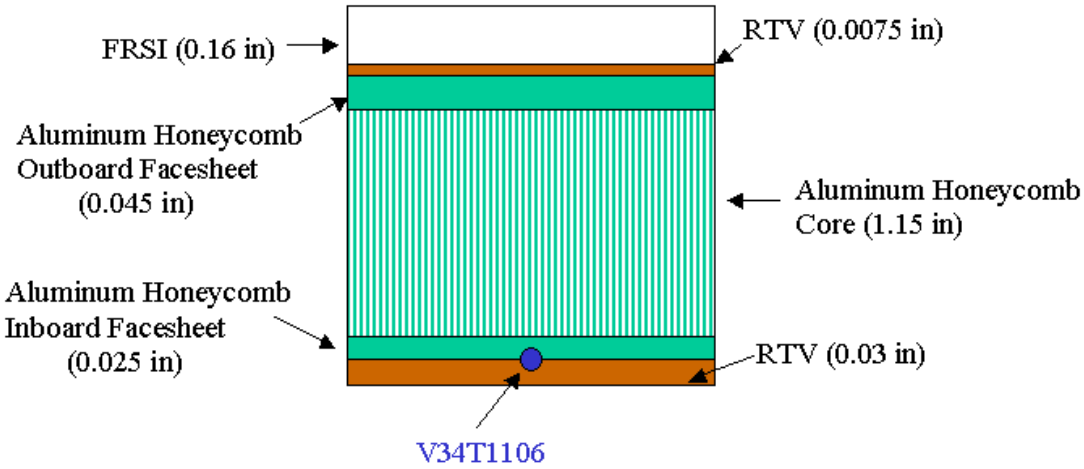

Figure 6-60 - OV-102 V34T1106 Port Sidewall Configuration for TMM

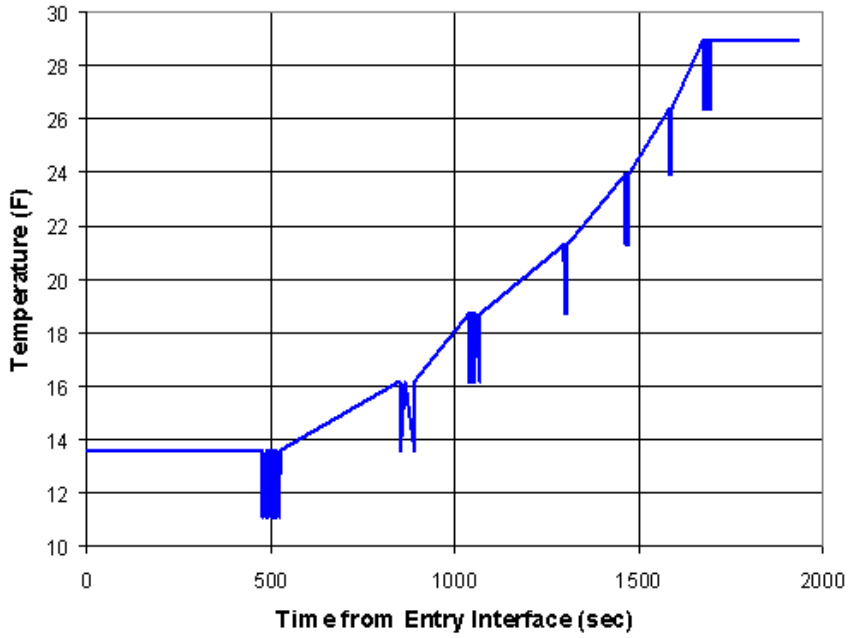

Figure 6-61 - STS-109 V34T1118 Structure Temperature Flight Data

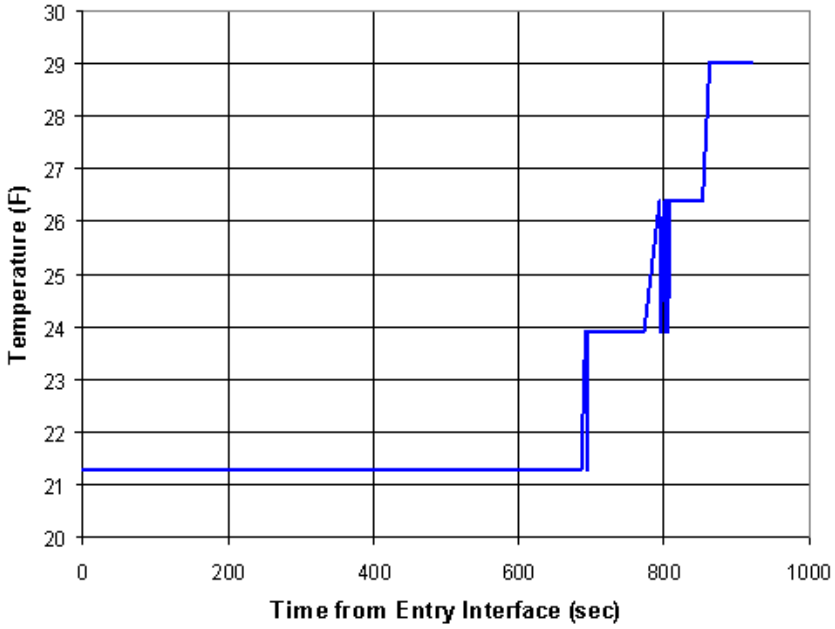

Figure 6-62 - STS-107 V34T1118 Structure Temperature

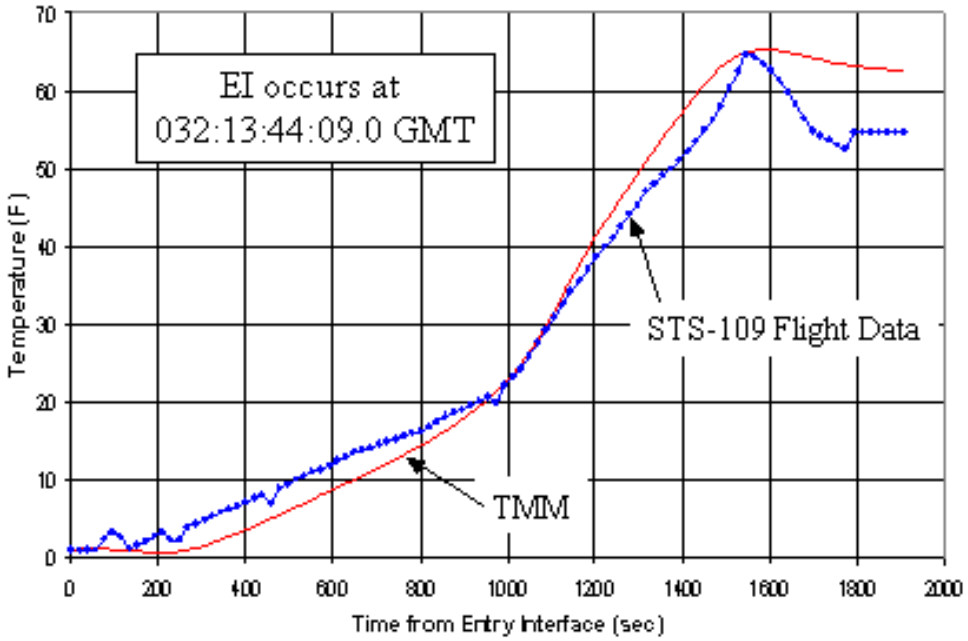

Figure 6-63 - STS-109 TMM Correlation to Flight Data

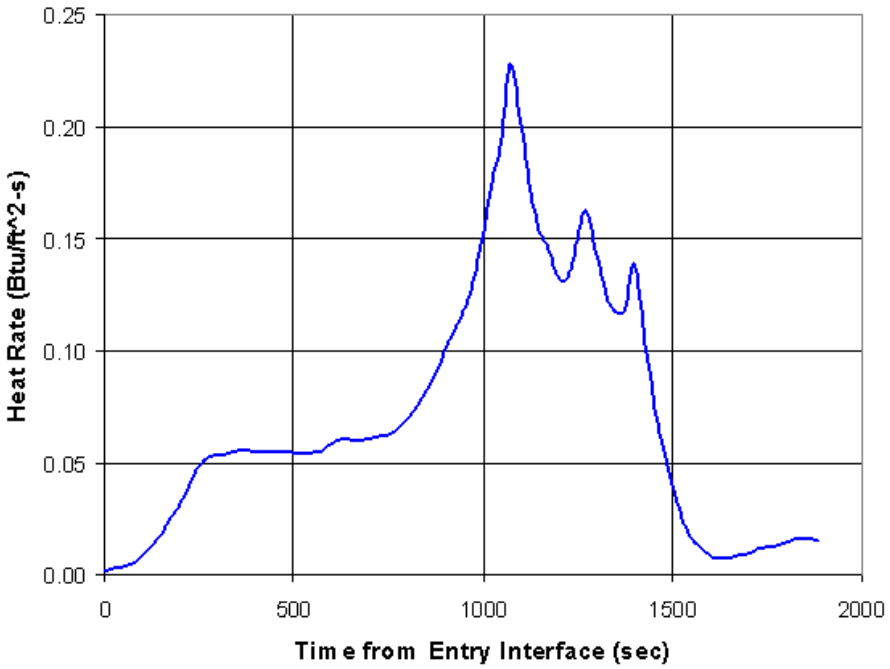

Figure 6-64 - STS-109 Nominal Aerothermodynamic Heating

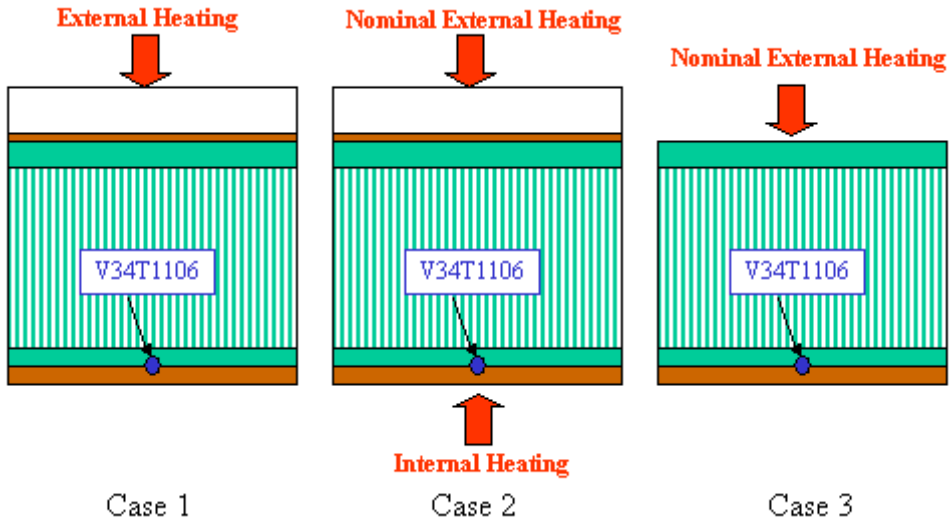

Figure 6-65 - Sidewall Heating Cases

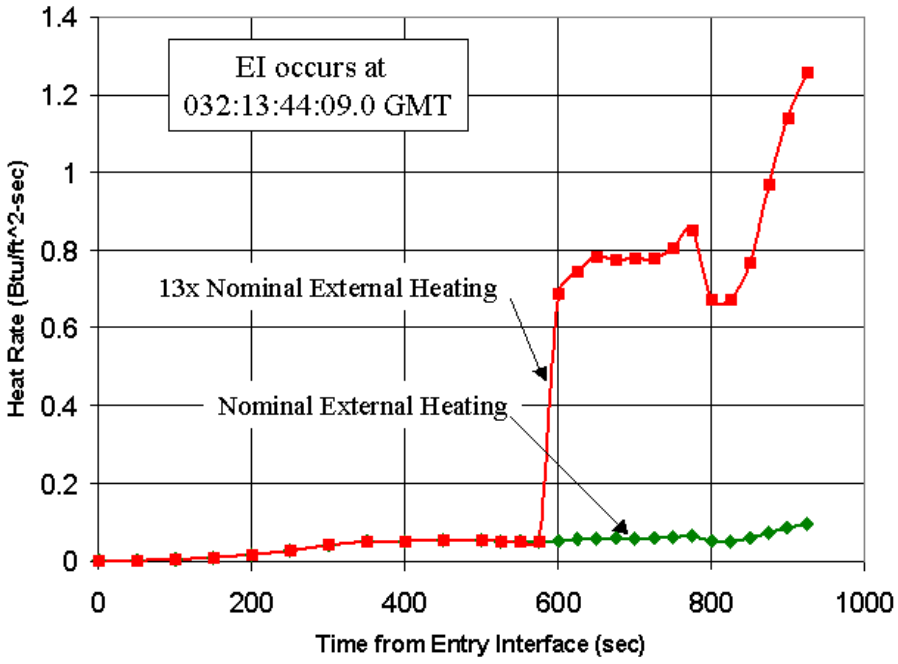

Figure 6-66 - STS-107 Aerothermodynamic Heating

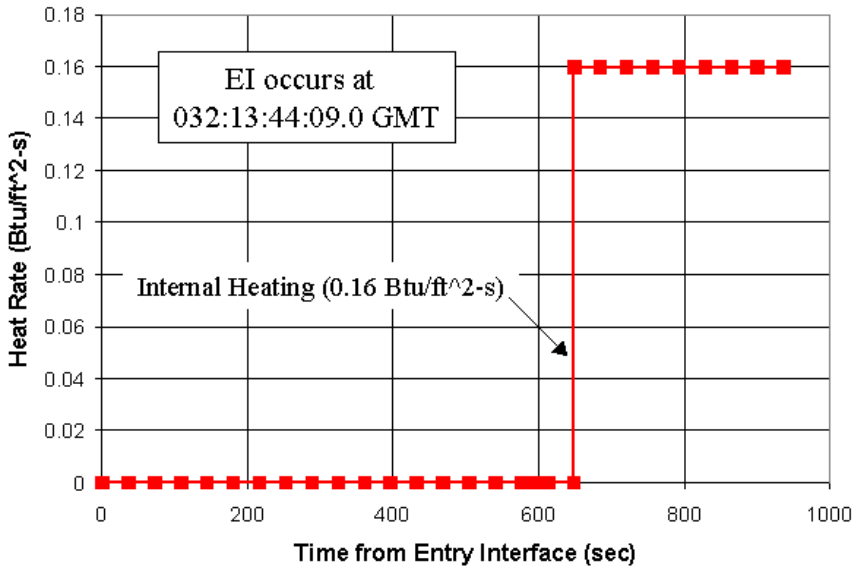

Figure 6-67 - STS-107 Internal Fuselage Heating

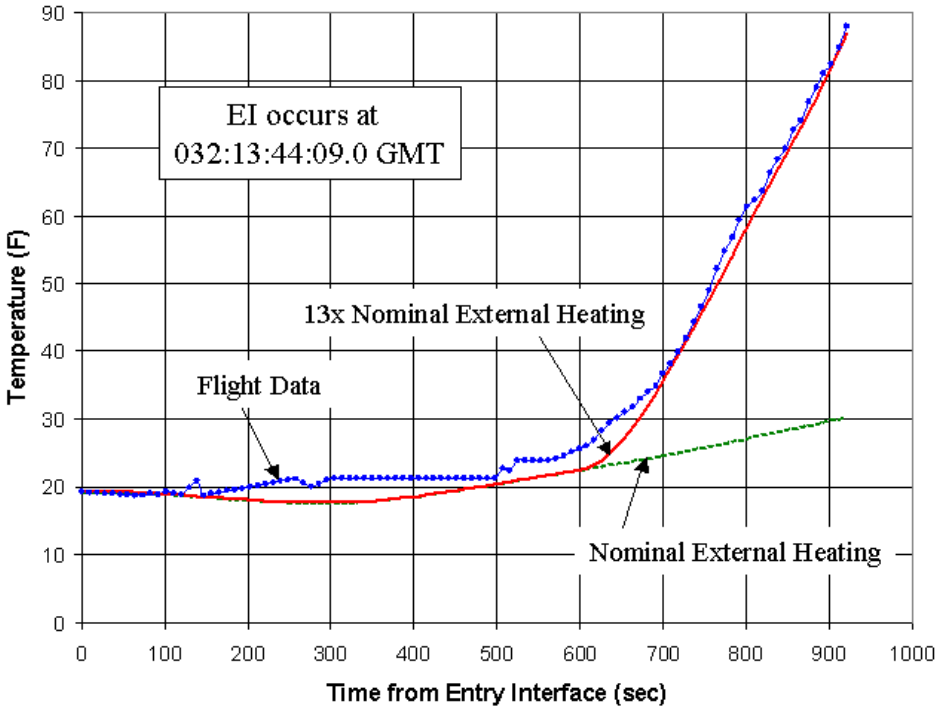

Figure 6-68 - Case 1: TMM Comparison to STS-107 Flight Data

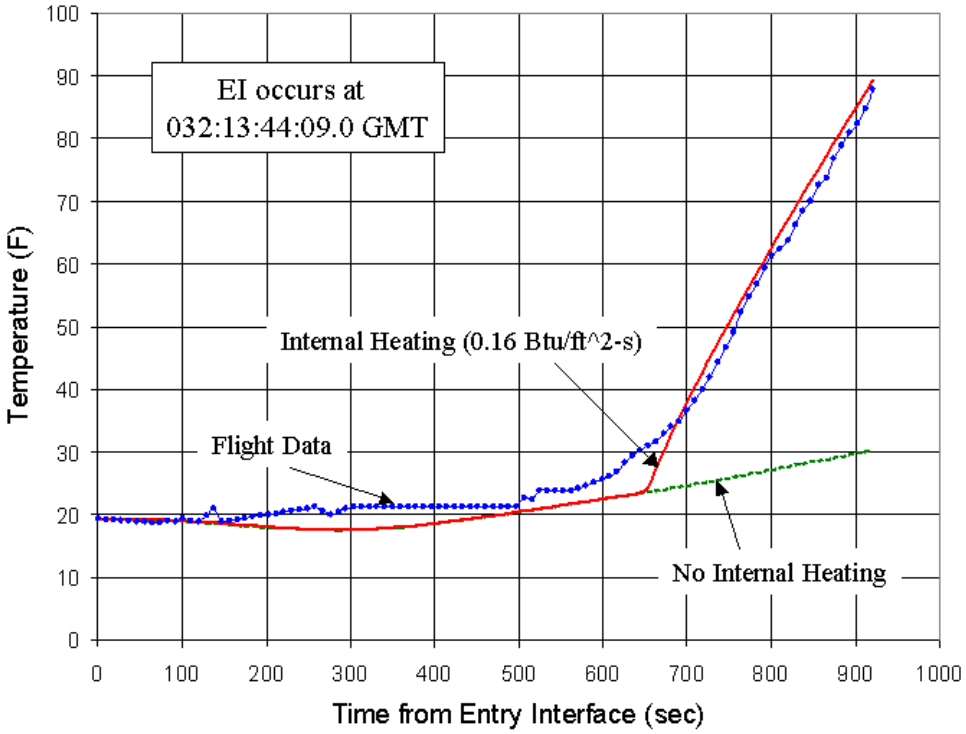

Figure 6-69 - Case 2: TMM Comparison to STS-107 Flight Data

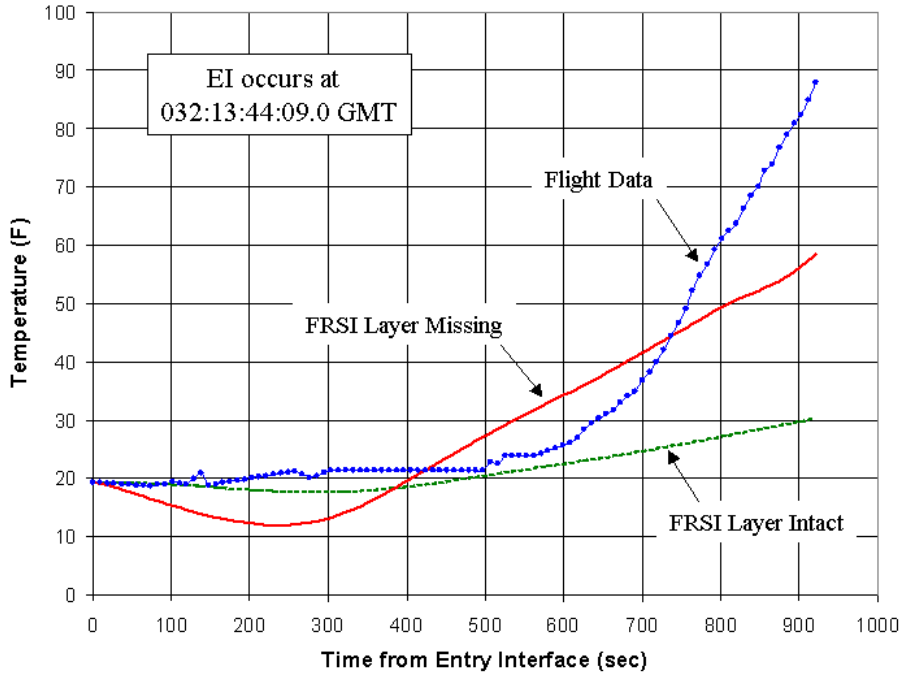

Figure 6-70 - Case 3: TMM Comparison to STS-107 Flight Data

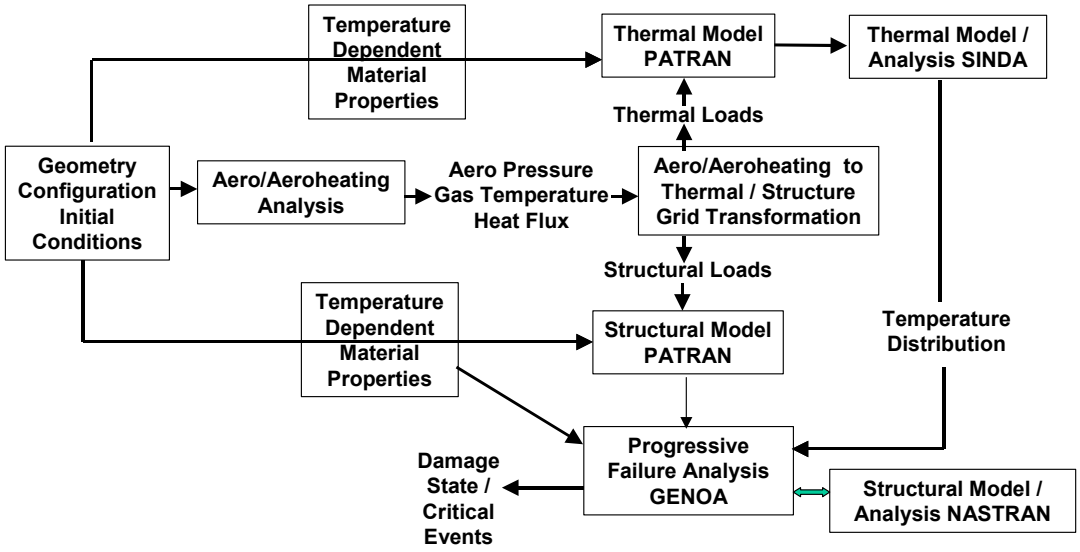

Figure 6-71 - Wing Leading Edge Failure Analysis Methodology

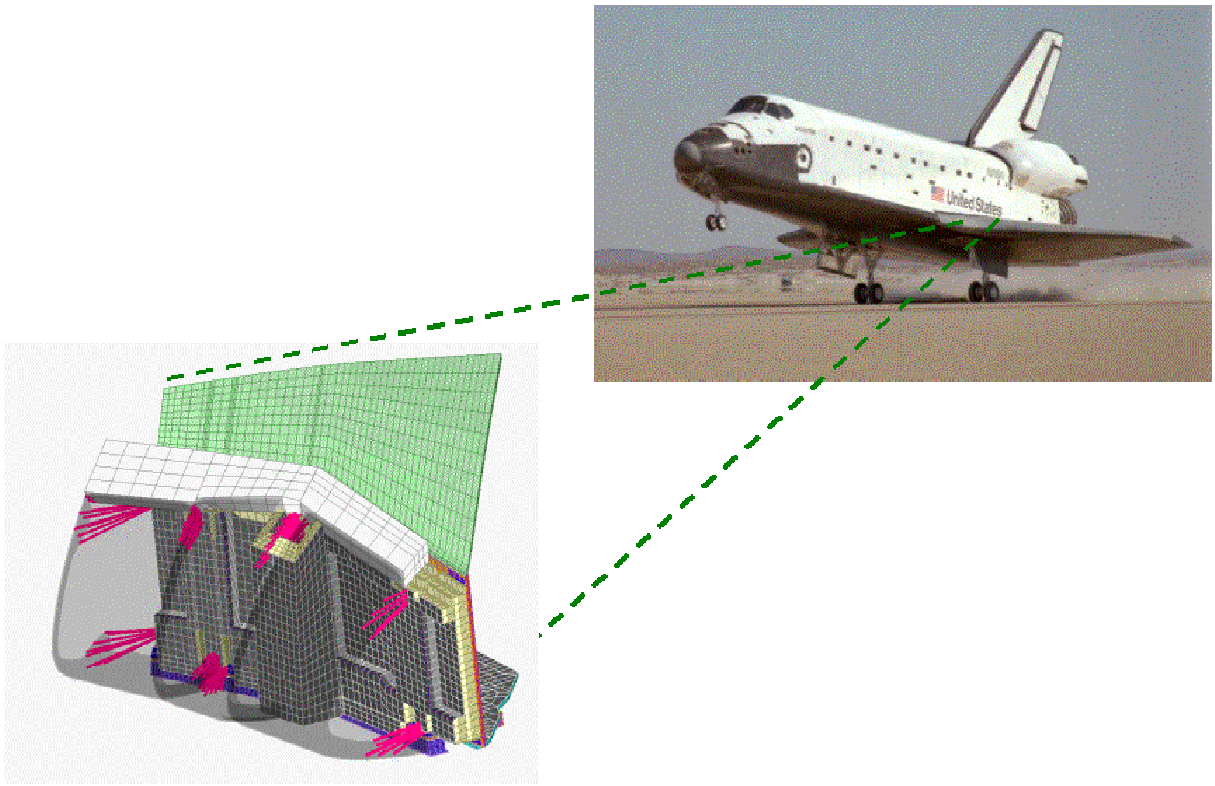

Figure 6-72 - Wing Leading Edge Finite Element Model

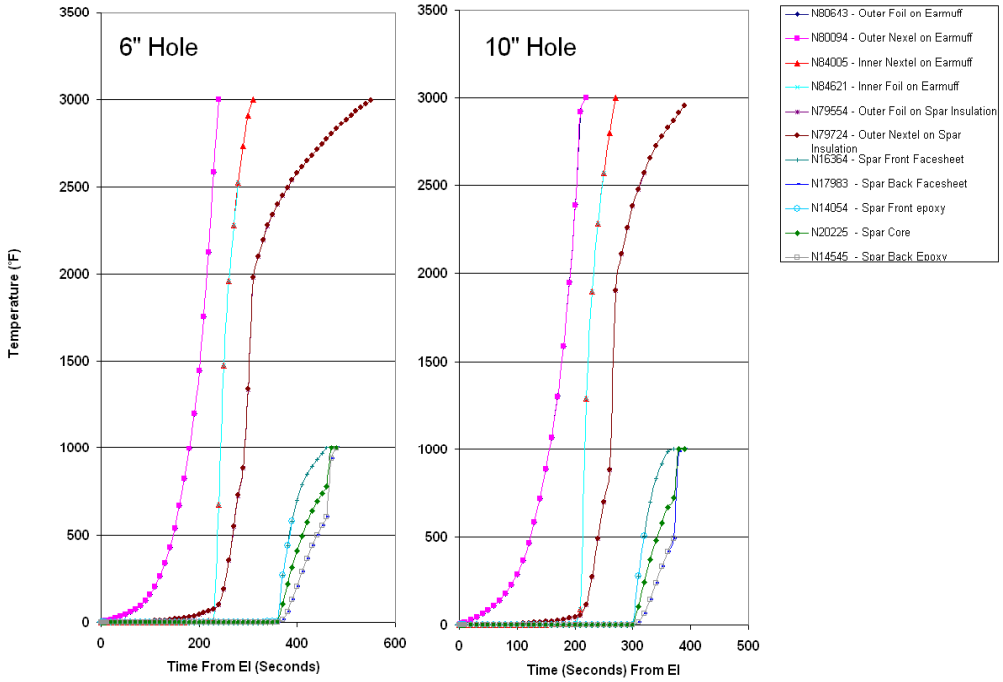

Figure 6-73 – Predicted Wing Spar Insulation and Structure Transients

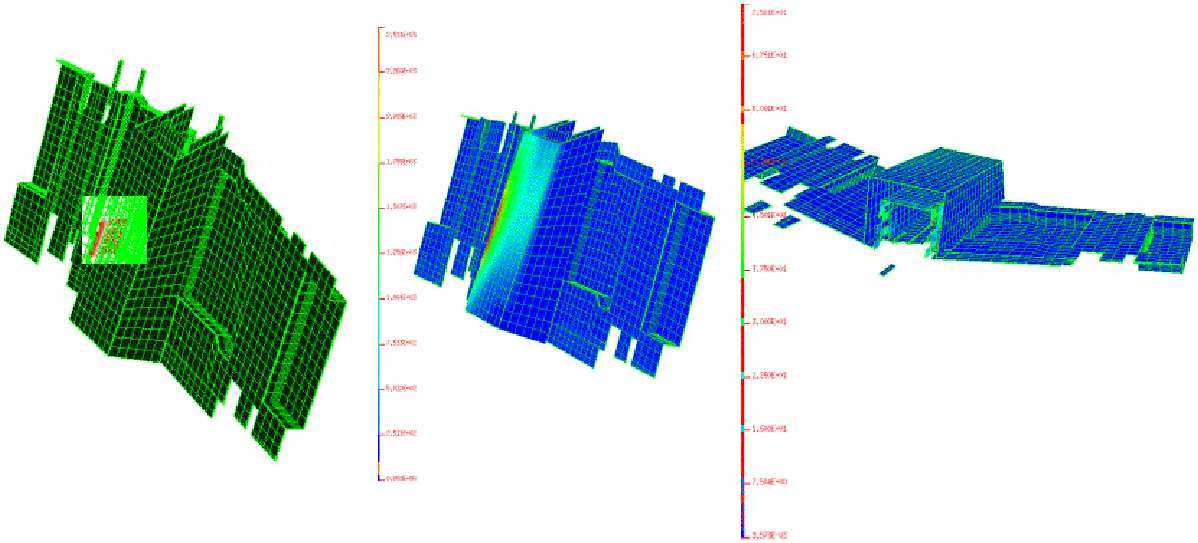

Figure 6-74 - Earmuff Insulation Analysis Results for 10 Inch Hole at t=210 Seconds

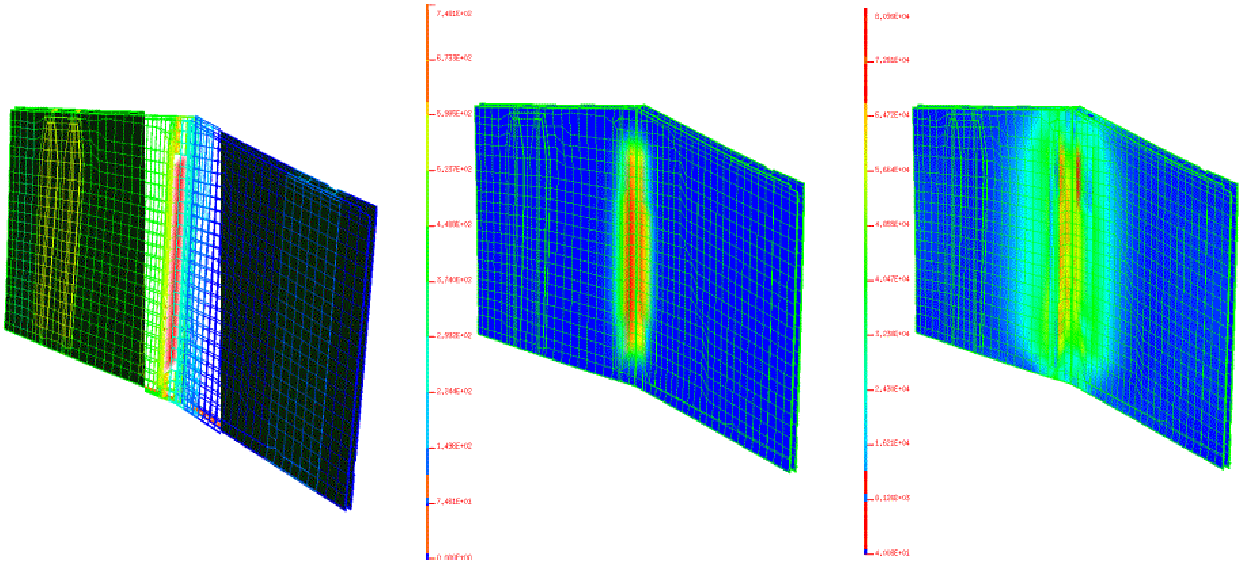

Figure 6-75 - Front Facesheet Analysis Results for 10 Inch Hole at t=320 Seconds

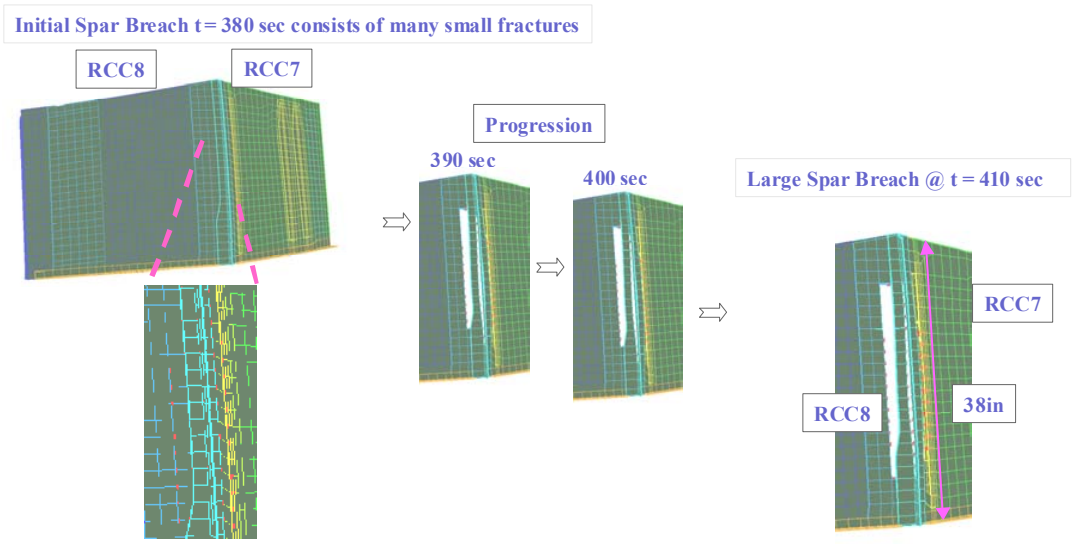

Figure 6-76 Rear Facesheet Analysis Results for 10 Inch Hole at t=380 Seconds (View of Spar From Inside Wing)

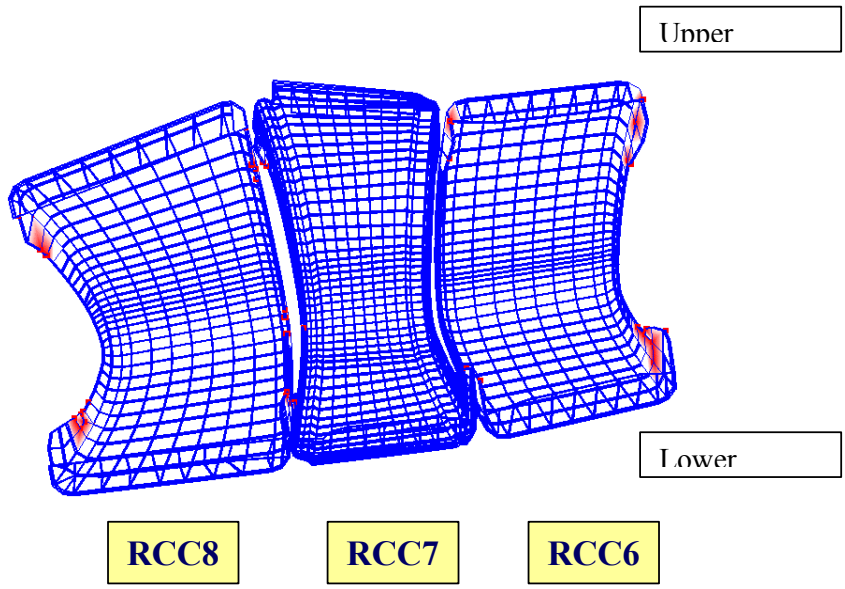

Figure 6-77 - RCC Panel Fracturing at 450 Seconds With 10 Inch Hole (View Looking From Inside RCC Cavity

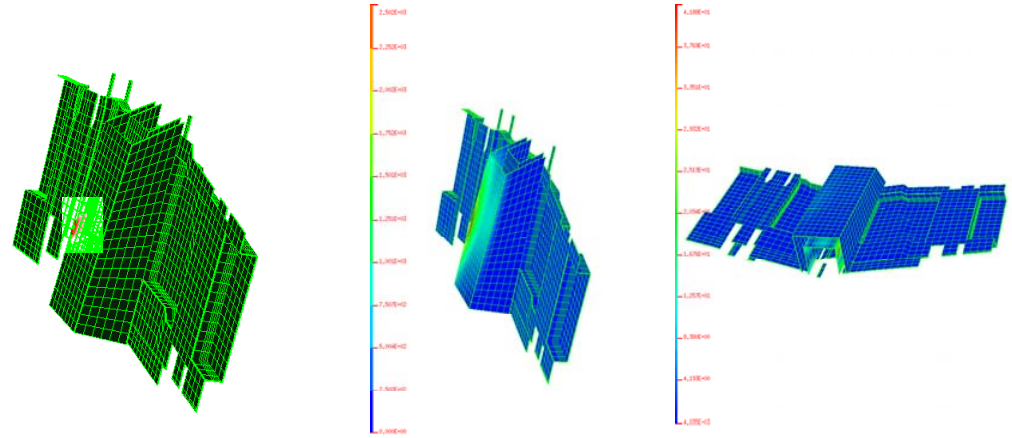

Figure 6-78 - Earmuff Insulation Analysis Results for 6 Inch Hole at t=230 Seconds

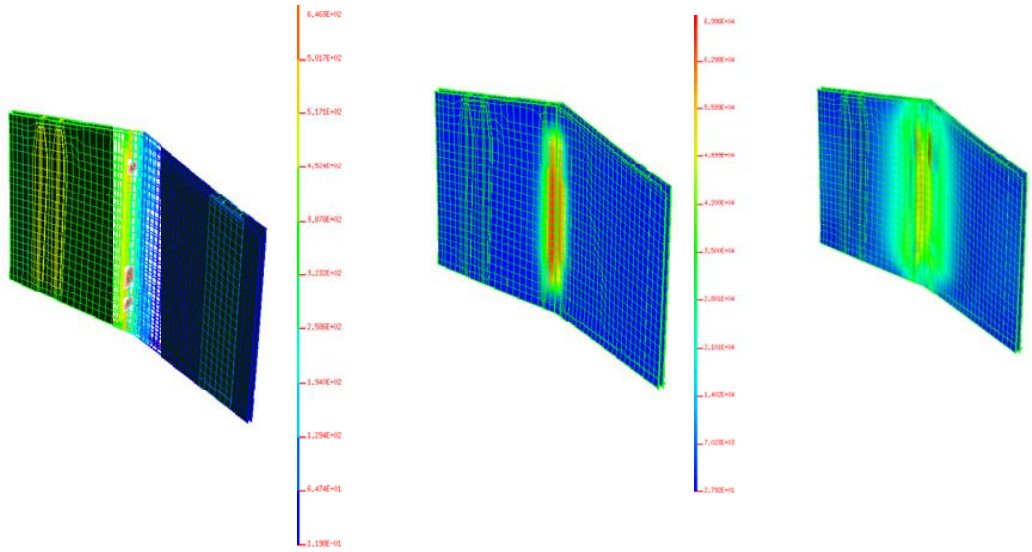

Figure 6-79 - Front Facesheet Analysis Results for 6 Inch Hole at t=380 Seconds

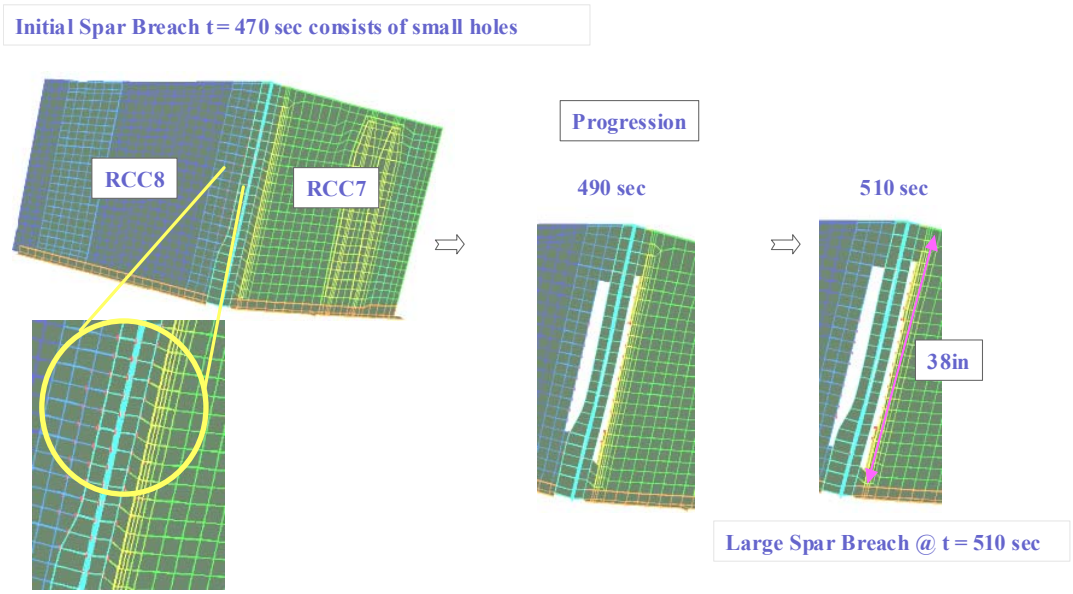

Figure 6-80 - Rear Facesheet Analysis Results for 6 Inch Hole at t=470 Seconds (View of Spar From Inside Wing)

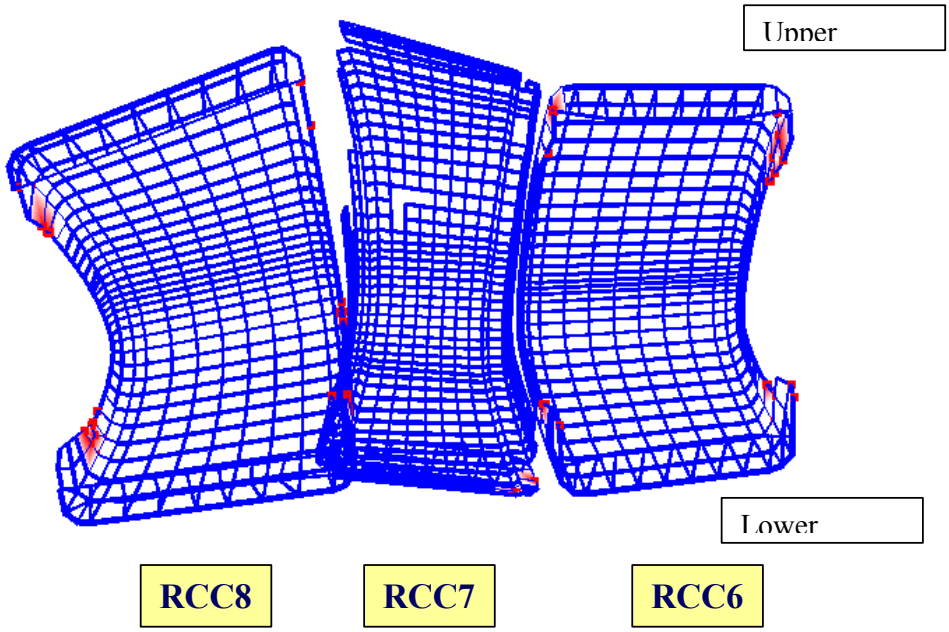

Figure 6-81 - RCC Panel Fracturing at 500 Seconds With 6 Inch Hole (View Looking From Inside RCC Cavity

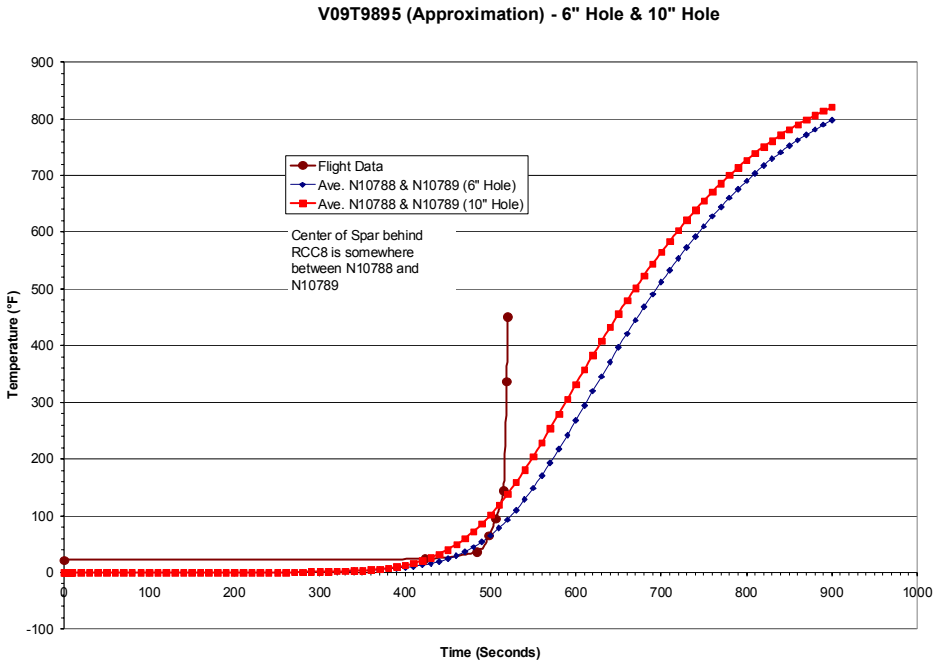

Figure 6-82 - Comparison of Panel 8 Rear Spar Temperature Prediction with Panel 9 Flight Data (V09T9895)

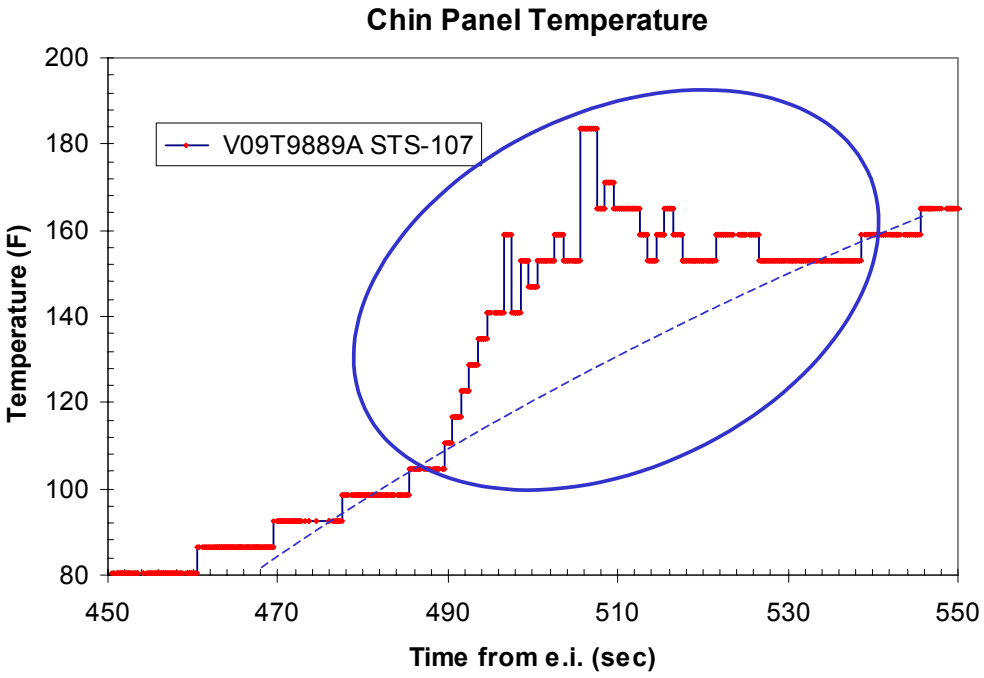

Figure 6-83 - Chin Panel Temperature Anomaly

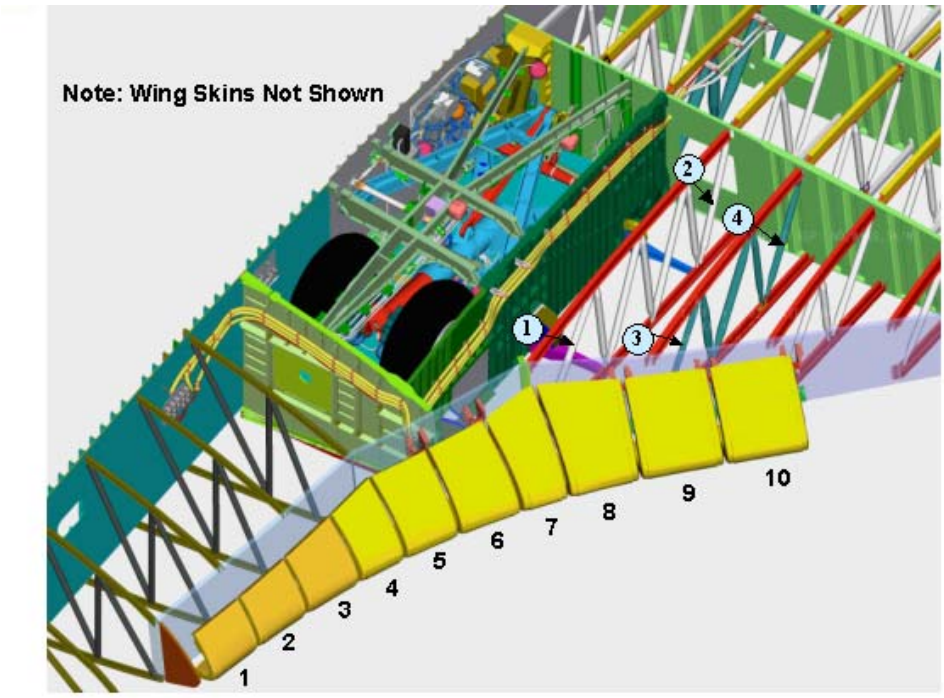

Figure 6-84 - Location of truss tubes (labeled 1-4) studied

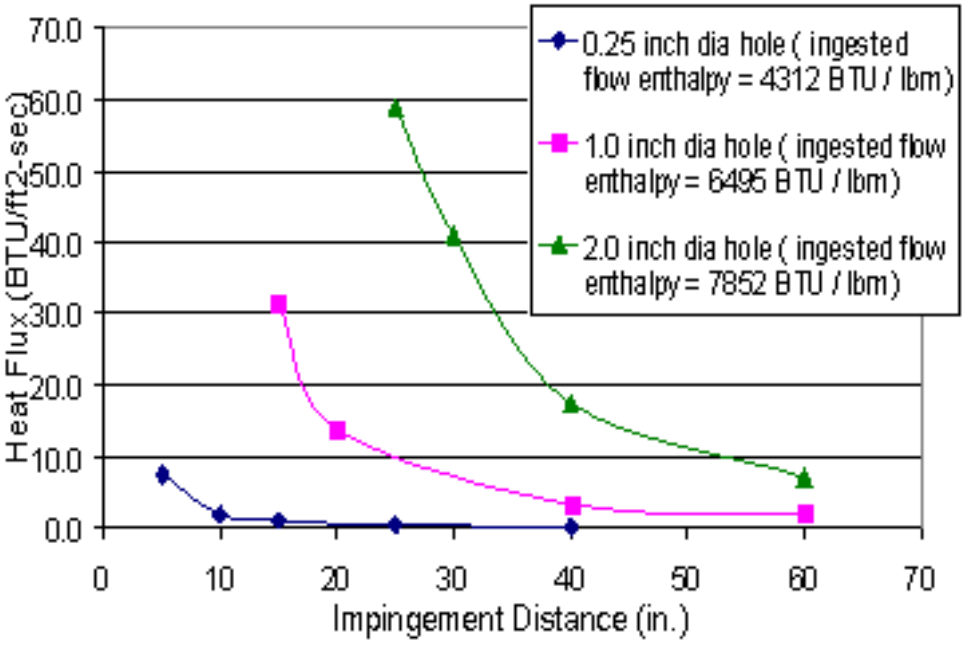

Figure 6-85 - Panel 9 internal plume impingement heating on 1" diameter cylinder at EI+491 seconds

$$\cos^{1.1}\Lambda_1 \cdot \cos^{1.1}\Lambda_2$$

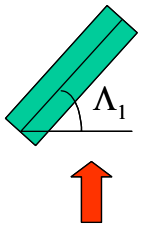

Tube	L_1	L_2
1	31.5	48
2	31.5	60
3	73.73	50
4	64.53	56

L_2 is out of the page

Figure 6-86 – Heating Correction for Angular Impingement

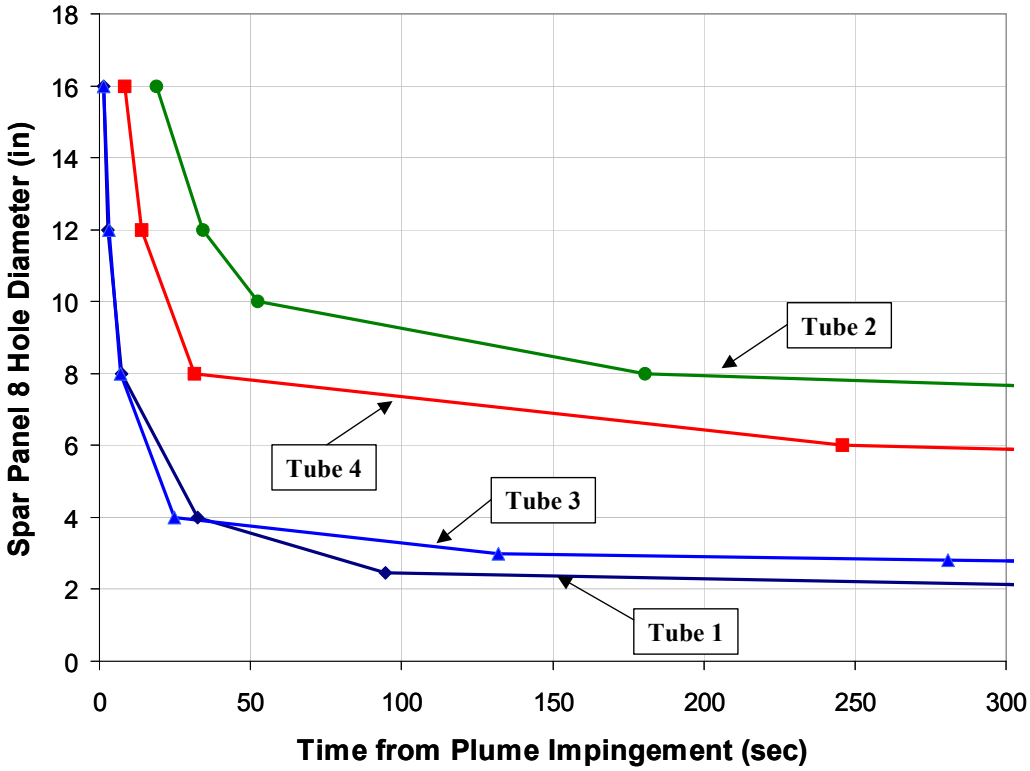

Figure 6-87 - Wing truss tube failure times with respect to breach sizes

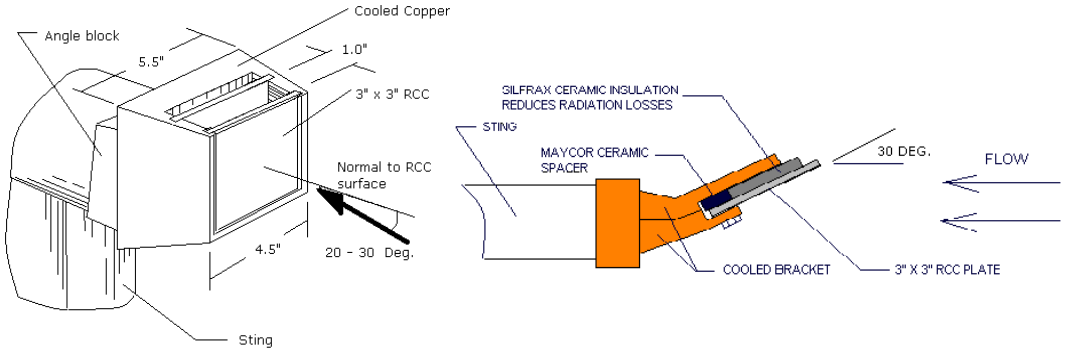

Figure 6-88 – Test Fixtures

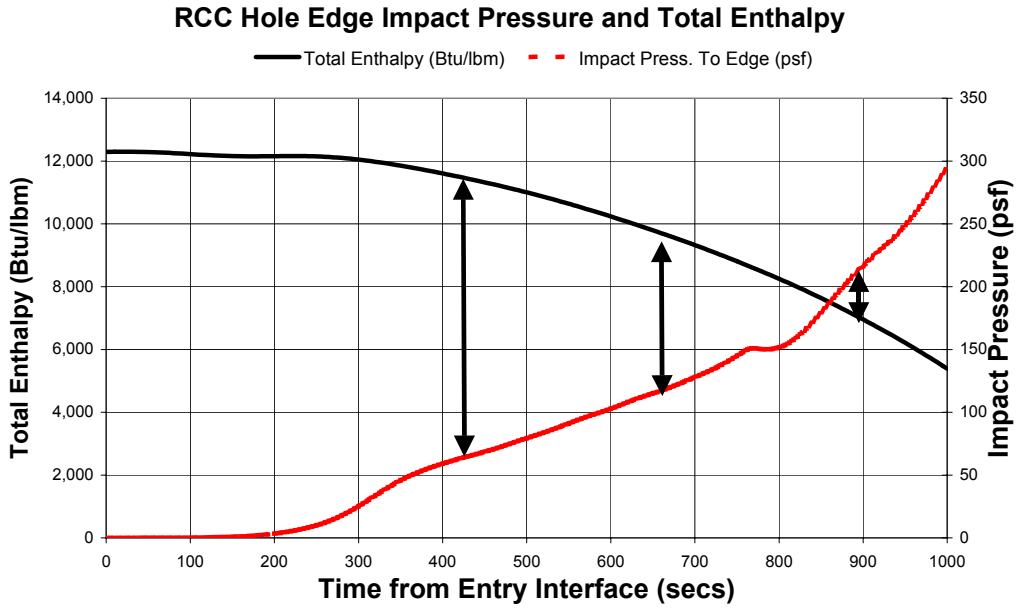

Figure 6-89 – Flight Environment

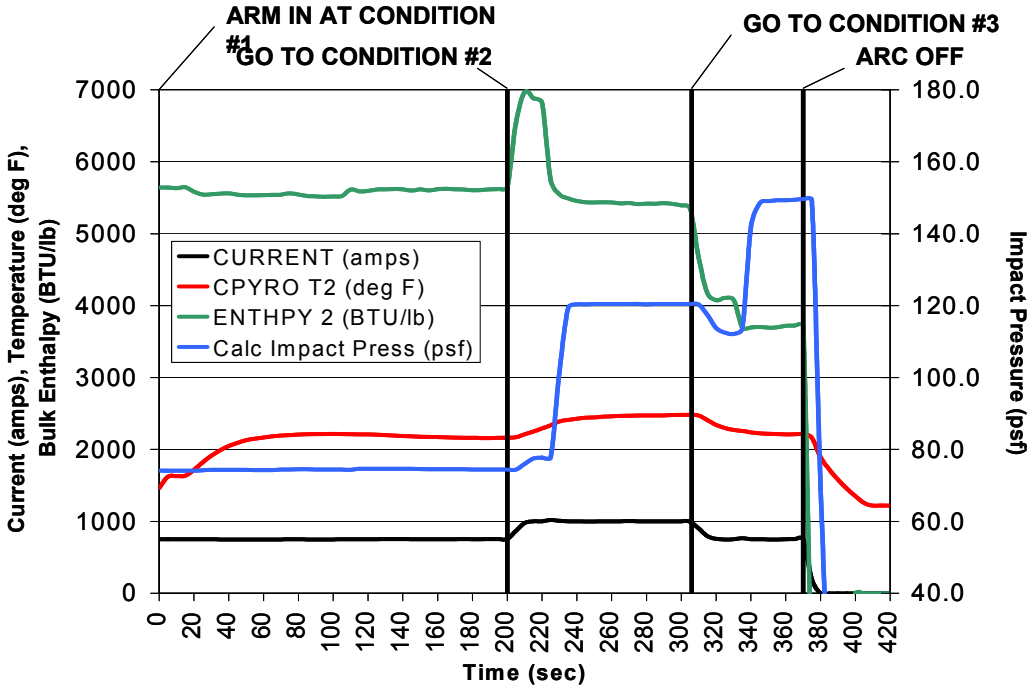

Figure 6-90 -Test Run #__ Actual Profile

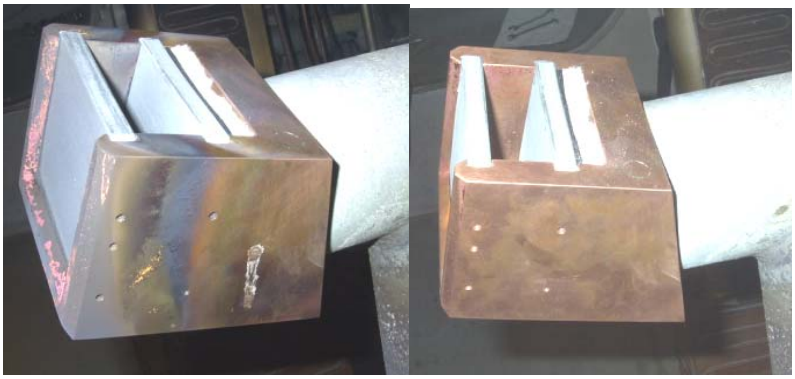

Figure 6-91 -Test #1 Pre and Post Test

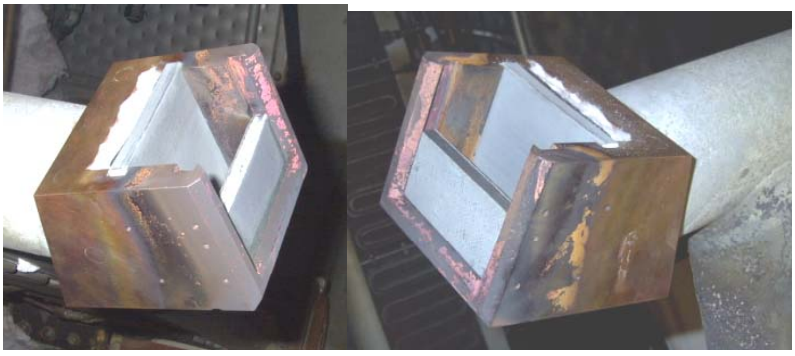

Figure 6-92 -Test #2 Pre and Post Test

Figure 6-93 -Test #3 Pre and Post Test - Knife-Edging Apparent

Figure 6-94 -Test #4 Pre and Post Test

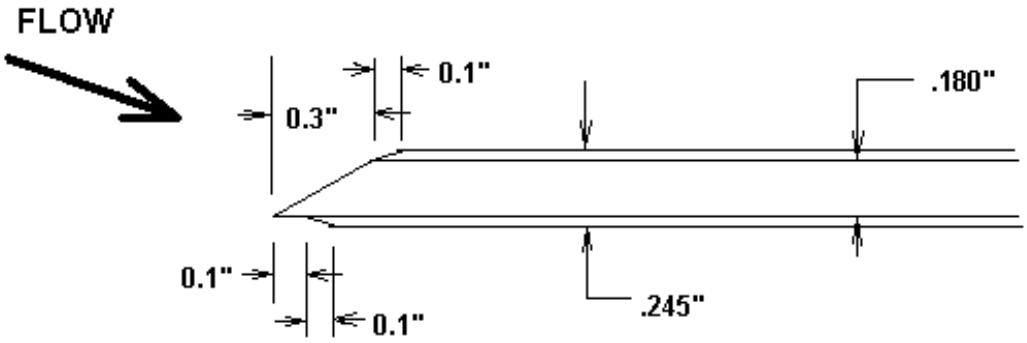

Figure 6-95 – Schematic of knife-edging dimensions

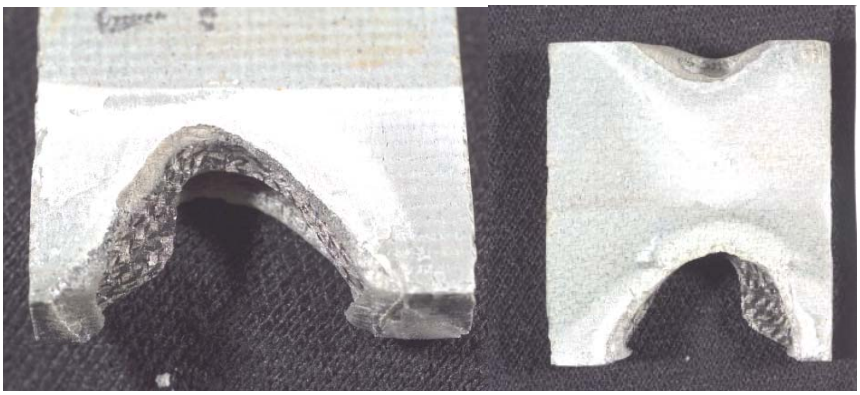

Figure 6-96 -Test #5 Closeout RCC Pieces with Knife-Edging

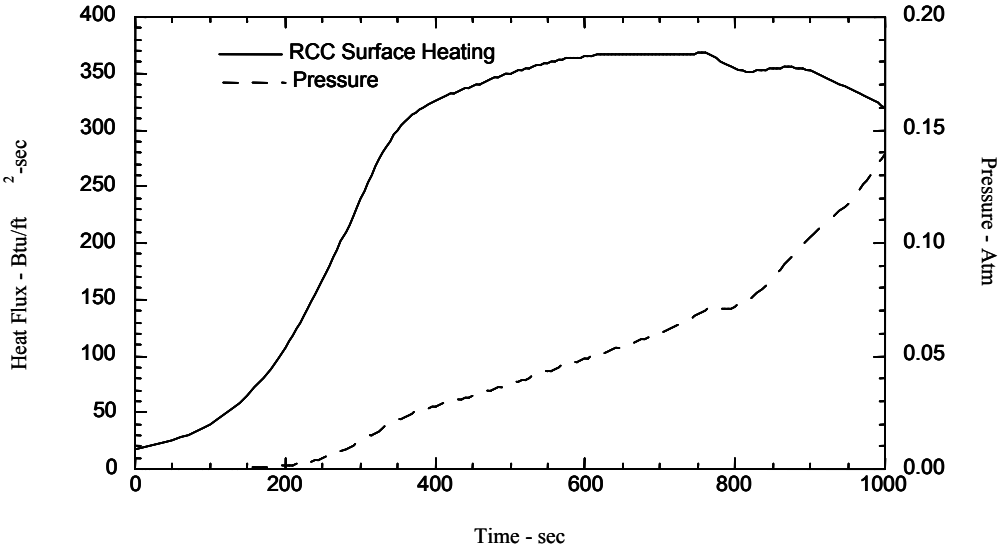

RCC Surface Heat Flux & Pressure History

Figure 6-97 – RCC Hole Environment

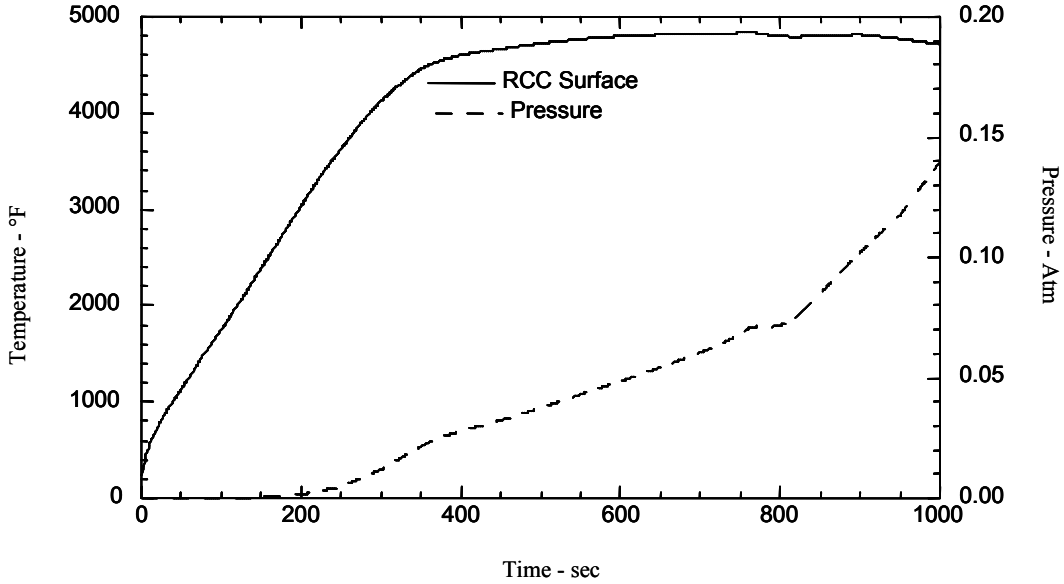

RCC Surface Temperature & Pressure

Figure 6-98 – RCC Temperature Response

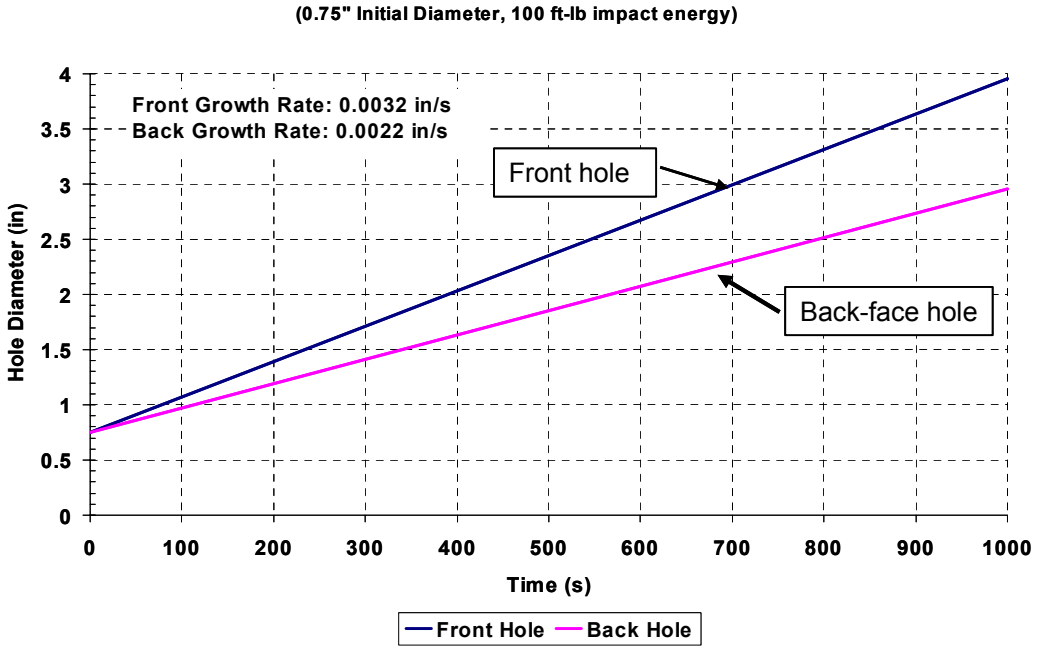

Figure 6-99 – RCC Hole Growth Calculation

References - Thermal

6-1. Generic Honeycomb Modeling Tool.
6-2. Stress report - STS89-0537
6-3. SINDA/FLUINT Version 4.4, C&R Technologies, Littleton CO.
6-4. Alpha Star Corporation, “Phase II Final Report, GENOA Progressive Failure Analysis of X-37 Reusable Launch Vehicle (RLV) Program”, June 24, 2000.
6-5. GENOA

7 STRESS

7.1 Panel 9 Spar Strain Gauge Evaluation

7.1.1 Analysis Objective

The objective of this analysis was to determine how a significant thermal event in the WLE spar would influence shear strain readings in the spar web shown in Figure 7.1-1. The location of the strain gage is shown in Figure 7.1-11. Primary focus was placed on thermal loading because mechanical loading would not produce the type of shear strain responses seen; maneuver type loads would have been seen on other strain gages and would have registered on the flight control systems. Mechanical load deviations would also be of relatively short duration. Pressure differentials across the WLE spar web would produce out of plane bending, but would not contribute to the shear strains in the web.

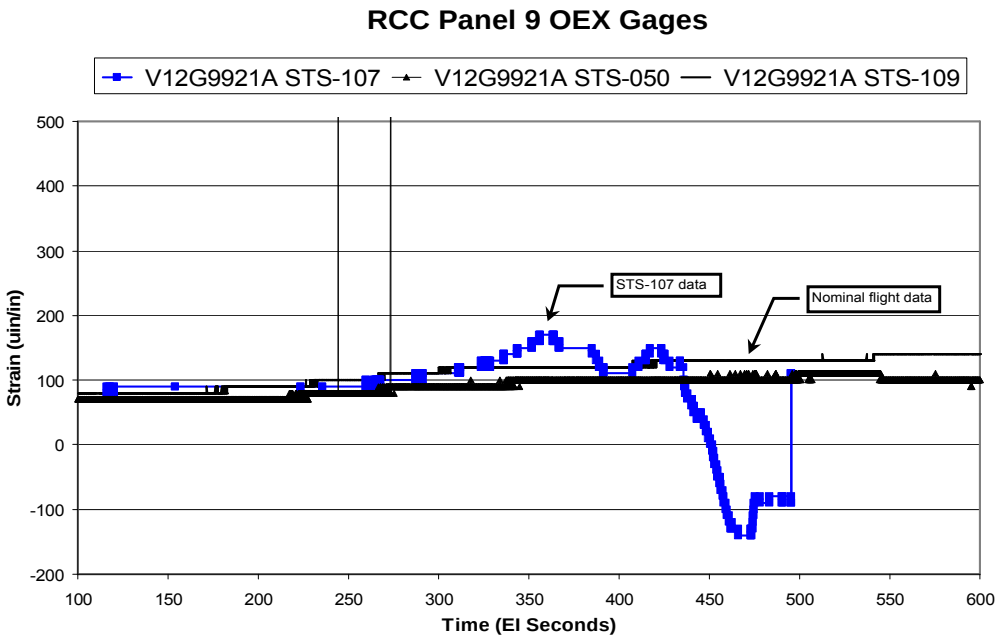

Figure 7.1-1 STS-107 V12G9921A strain gage data overlay with nominal strain gage flight data.

The two primary characteristics of the curve that need to be explained are the increase in shear strain with a sudden sign reversal. In addition to recreating the shear strain trends, interest was placed on how close to the thermal event would shear strain gage V12G9921A need to be to record the type of signal seen on STS-107. This gage is located roughly in the middle of the spar web near WLE panel 9. The thermal effects will register on the WLE spar strain gage even though it is some distance from the thermal event. Thermal sensors in the vicinity of panel 9 did not respond to a thermal event until much later. The quick response of the strain gage compared to the thermal sensors allows it to be used as a remote thermal sensor as shown in Figure 7.1-2. Near the boundary of a local thermal event, peak strains are expected because of the large thermal gradient. With increased distance from the thermal event the load will redistribute as illustrated and the influence of the thermally induced strain will eventually become negligible compared to the mechanical strain.

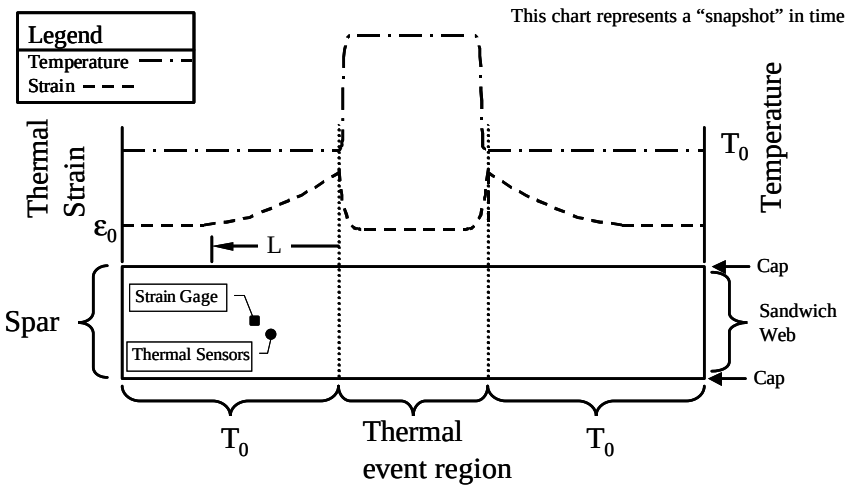

Figure 7.1-2 Temperature measurements lag strain measurements

7.1.2 Analytical Approach

A finite element model of the local wing area of interest was used because of the complex structural response to the thermal loading conditions. A total of 5 different assumed load cases were run. Initially a simple symmetric distribution was chosen. Because the strain gage is located near the middle of the WLE spar web, the shear strain response for a uniform thermal field is low. A number of unsymmetrical thermal fields were then analyzed, which created comparatively large shear strain responses similar to those seen during flight. The shear strain responses at the middle of the spar web were analyzed from the edge of the thermal event outward for each case. Based on the findings a possible scenario was then developed.

7.1.3 Model Description

The existing ASKA/NASTRAN loads finite element model of the wing was modified to perform a local analysis on the WLE spar. The coarse mesh on the original model in the WLE area near panel 9 was refined, as shown in Figure 7.1-3, to determine the local response of the structure to the thermal load cases being analyzed. In addition material properties were updated to include temperature dependent effects.

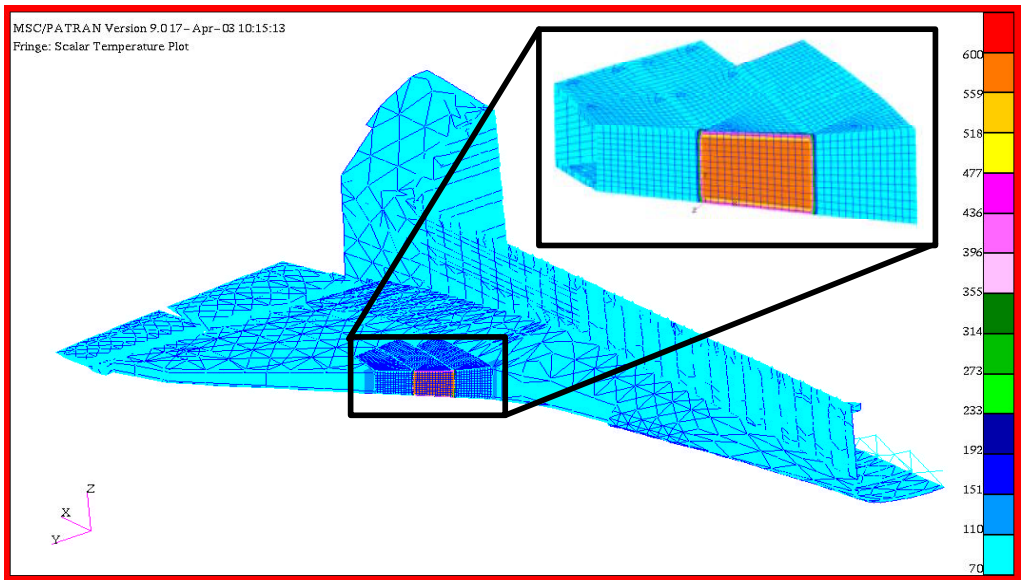

Figure 7.1-3 Refined region of wing used in thermally induced strain analysis

7.1.4 Thermal Profiles

Thermal profiles used in the analysis were assumed to be high heating events with large gradients between thermally protected and unprotected structure to induce large strain deviations from nominal flight data. A temperature of 600°F was chosen as the maximum temperature because reliable material properties were not available for higher temperatures. Also, since a uniform temperature region was used, this represented a reasonable average of temperatures ranging from melting of the aluminum (>900°F) to more moderate temperatures at the edge (400°F). Five different assumed thermal profiles were analyzed in developing the scenario.

Initially a temperature of 600°F was applied on WLE web while the spar caps were at 400°F. The rest of the structure was taken to be 70°F.

The second case assumed that the upper half WLE sees primary heating and it is initially heated to 300°F on upper half of WLE spar web and cap. Temperature from the middle of the WLE to the bottom of the WLE cap is linearly distributed from 300°F to 70°F and the rest of the structure is at 70°F. This case is an intermediate case between nominal heating and load case three.

For case three the upper half of the WLE sees continued primary heating up to 600°F on upper half of WLE spar web and cap with the temperature being linearly distributed from 600°F to 70°F at middle of WLE web to the bottom WLE cap. The rest of the structure is at 70°F.

For the fourth case a burn through is assumed on upper half WLE spar web. A temperature of 600°F is applied on upper WLE cap, wing skin, and wing ribs up to 16 inches from WLE. A linearly distributed temperature of 600°F to 70°F was applied from the edge of burn through (middle of WLE web) to bottom WLE cap. A temperature of 70°F was applied to the rest of structure.

The final case is a continuation of the fourth case. A burn through is now assumed on upper half WLE spar web and spar cap. A temperature of 600°F is applied on upper wing skin and wing ribs up to 16 inches from WLE. A linear temperature distribution of 600°F to 70°F from the edge of burn through (middle of WLE web) to bottom WLE cap is applied and the rest of the structure is sees 70°F. Contour plots of all five temperature profiles are shown in Figure 7.1-4 through Figure 7.1-7 below.

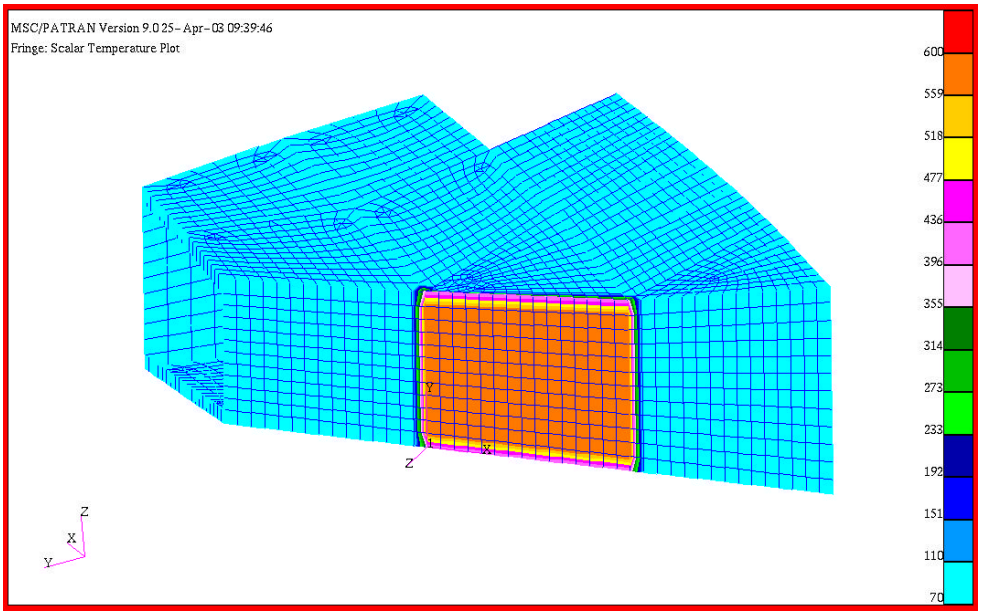

Figure 7.1-4 Contour plot of the initial symmetric temperature profile.

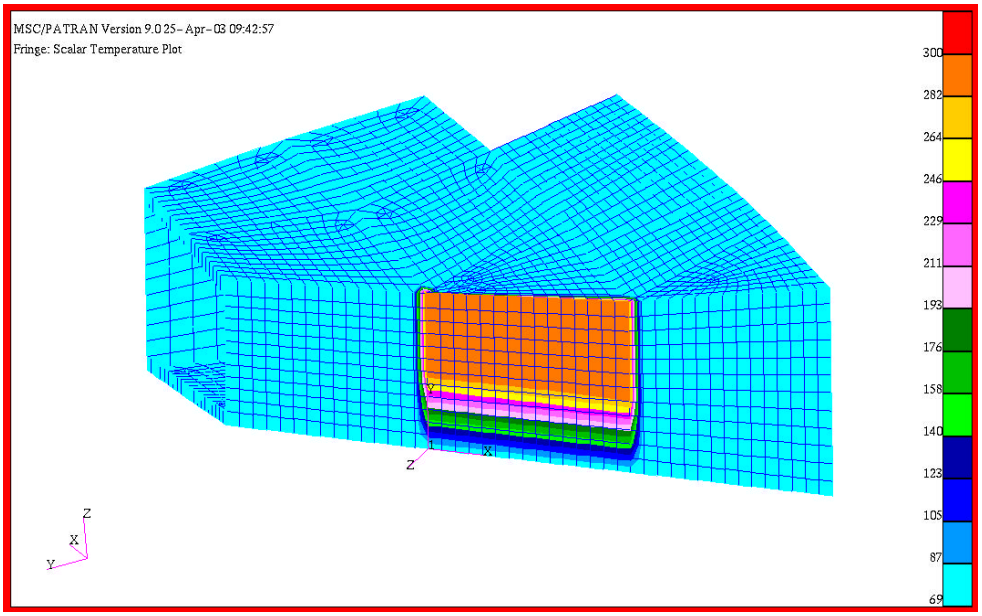

Figure 7.1-5 Temperature plot for the initial heating of WLE upper spar, second thermal profile.

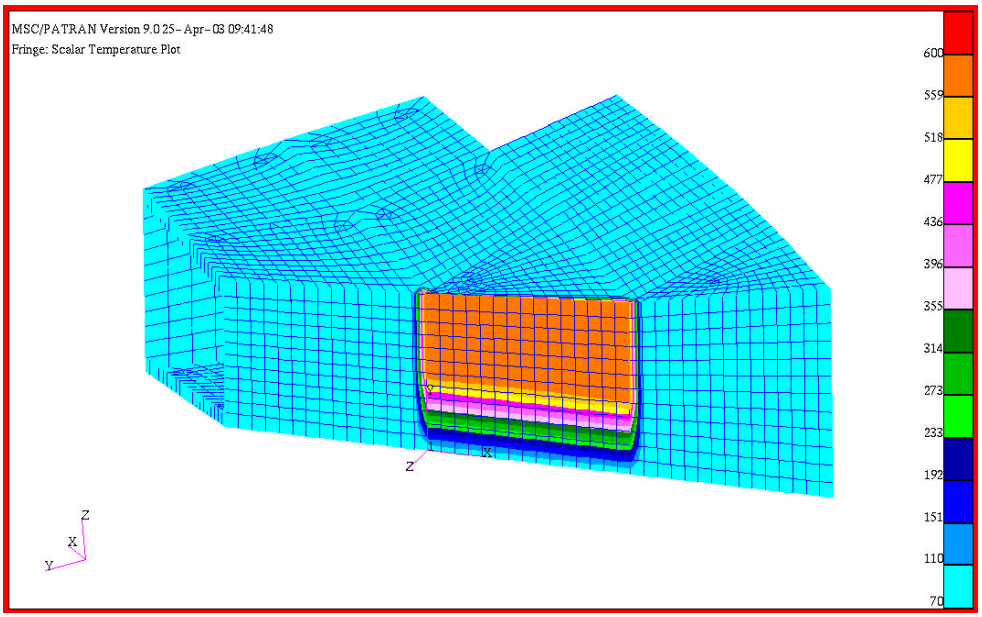

Figure 7.1-6 Contour plot for continued WLE upper spar heating, temperature profile three

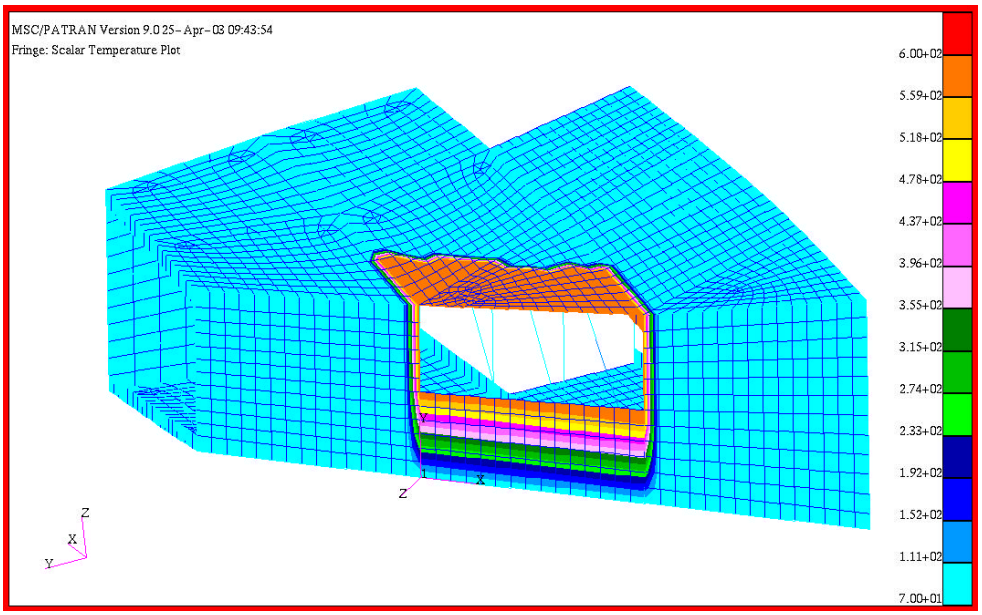

Figure 7.1-7 Temperature contour for WLE spar burn through, profiles four and five

7.1.5 Results

The shear strain results along the mid-span of the WLE spar outside of the thermal event for the five cases are shown in Figure 7.1-8 . The dashed lines on the chart show the amount of increase in shear strain that was seen during STS-107.

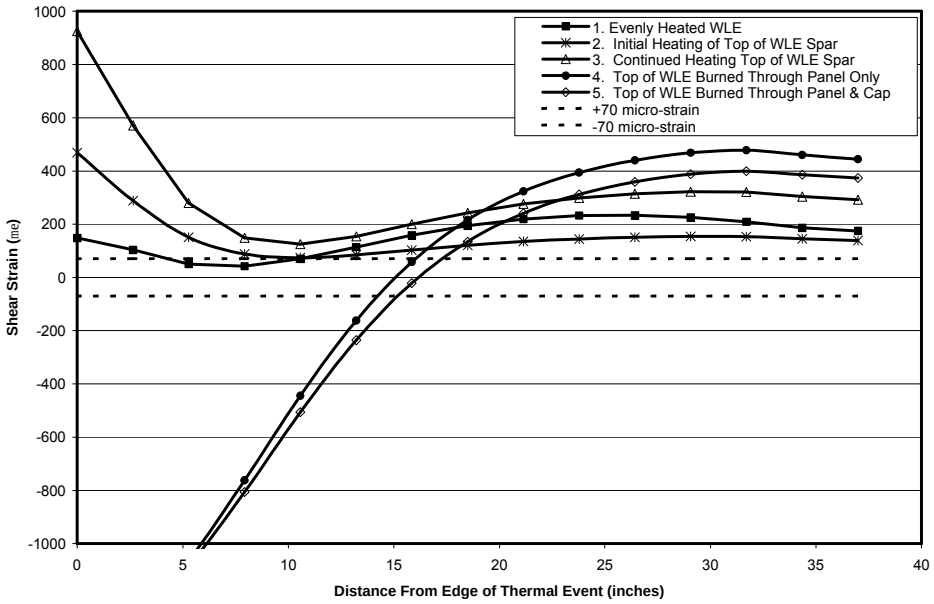

Figure 7.1-8 Shear strain results along midspan of WLE spar outside of the thermal event.

Thermal case one shows an increase in shear strain magnitude along the middle of WLE from the edge of thermal event outward but no significant magnitude. It is also noted that the sign remains the same for all locations plotted.

Thermal event two does show a significant rise in shear strain magnitude near the thermal event boundary that reduces with increased distance from the thermal event boundary. At distances greater than 18 inches from the thermal event boundary shear strain magnitude changes little. As with case one there is no change in sign of the shear strain at any distance from the thermal event.

Case three trends are very similar to case two trends but the magnitude of the shear strains has increased.

Case four produces the first reversal in shear strain sign. Even more than cases two and three there is a significant rise in shear strain magnitude near thermal event boundary. For distances less than 15 inches from thermal event boundary strain sign is negative. More importantly the shear strain from 15 to 19 inches reverses sign with magnitudes similar to the third case. There is a decrease in shear strain magnitude with increased distance from thermal event boundary as seen before. Shear strain magnitude changes little at distances greater than 26 inches from thermal event boundary.

Thermal event five is very similar to case four with increased magnitude. At distances less than 16 inches from the thermal event boundary the shear strain sign is negative and for the range of 16 to 23 inches from the boundary the shear strain is less than noted in the undamaged structure. With increased distance from the thermal event boundary the shear strain magnitude decreases and is relatively unchanging at distances greater than 26 inches from the thermal event boundary.

The results of cases four and five are significant findings. First it shows that a loss of the WLE spar structural capability is needed for a reversal of the shear strain sign seen on the gage. Additionally the results help bound the location of where the strain gage may be located. For both cases four and five sign reversals are see up to 15 or 16 inches away from the thermal event boundary, which establishes an outer limit location for this scenario.

7.1.6 Conclusions

Scenario Description

Based on the results of the five thermal cases coupled with previous OEX strain gage flight data, STS-107 strain gage and STS-107 thermal data, a possible scenario has been developed. It is hypothesized that a partial breech in a WLE RCC panel allowed hot gas impingement on WLE spar causing an unsymmetric temperature increase on WLE spar web and cap. The onset of this thermal event was slow to occur, probably due to the presence of WLE insulation, but caused shear strains to begin to deviate around 270 seconds as shown in a comparison to of STS-107 data with prior nominal flight data, Figure 7.1-9. The upper WLE spar web and cap were then subjected to heating and a temperature gradient occured on WLE spar from top to bottom. This increased shear strain gage readings until about 360 seconds from EI; during this time the structure remained intact. Shear strain data between approximately 360 to 400 seconds indicated the increasing temperatures were beginning to soften the structure but it was still carrying load in the heat affected region. Between 400 and 425 seconds there was a rise in shear strain that could be caused by heating at a second location closer to the strain gage; possibilities include a sudden loss of a large piece of insulation on the WLE spar or rapid temperature increase in the aft facesheet of the WLE sandwich panel. At 425 seconds, loss of structural capability was initiated causing the shear strain sign reversal. The loss could initially be attributed to debond on the facesheet of the WLE sandwich or significant loss of modulus (T>800°F) and, later, melting of the aluminum. Thermal stresses were relieved and the damage size continued to grow from this point on. The strain data is not considered reliable after about 470 seconds.

In summary, the main conclusion of this hypothetical scenario is that a loss of WLE spar structure is needed to reverse strain. Although this probably started as a facesheet debond or loss of modulus, it eventually proceeded to loss of the aluminum through melting. Secondly, the strain gage would need to be located in close proximity to the thermal event to record the type of signal seen for STS-107. For this scenario the strain gage would be located within 15” of edge of thermal as shown in Figure 7.1-8.

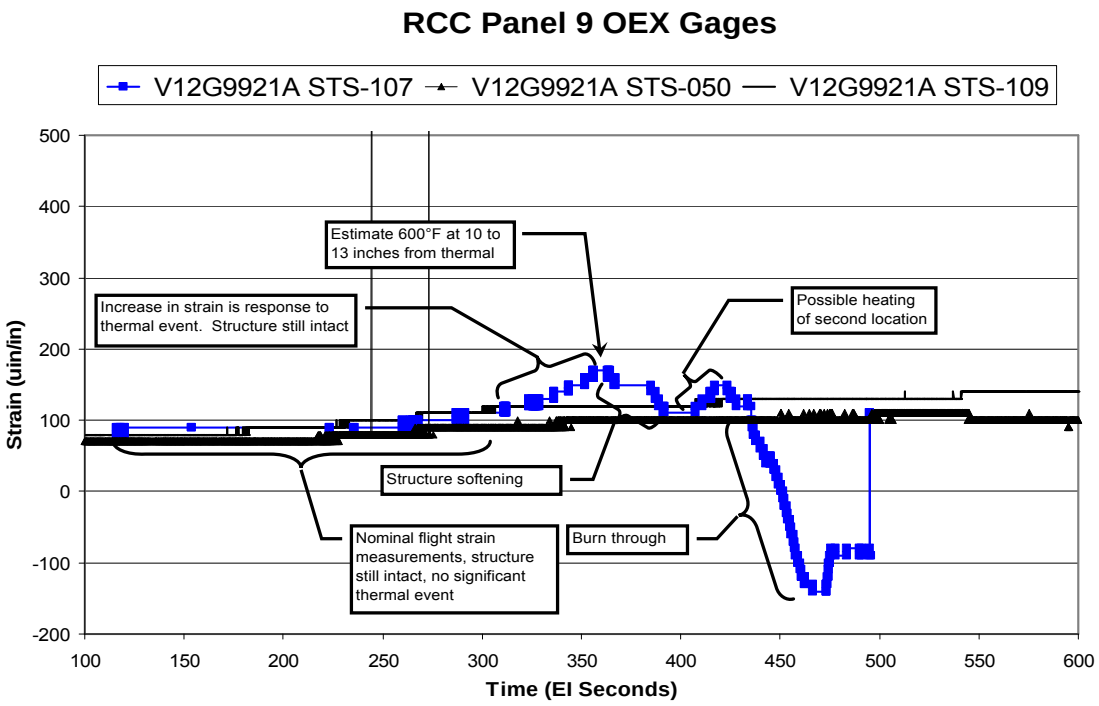

Figure 7.1-9 Scenario description overlay with nominal strain OEX strain gage data

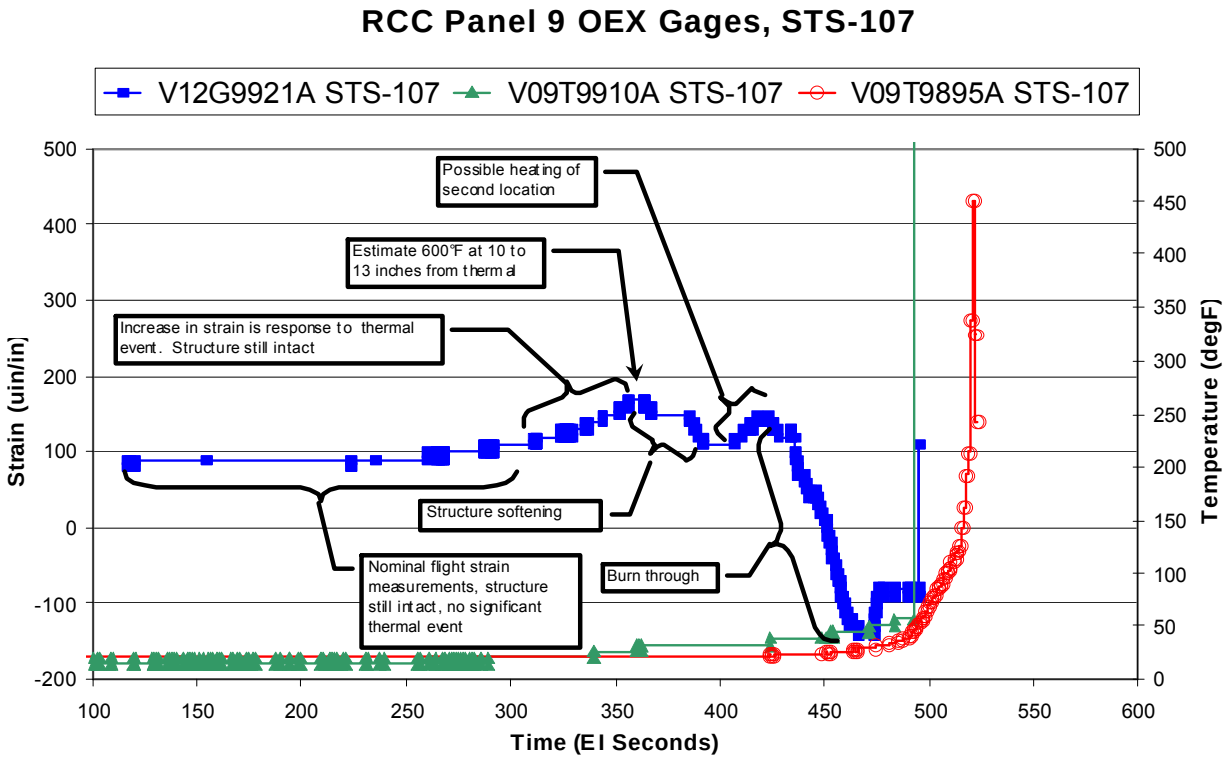

Figure 7.1-10 Scenario description overlay with STS-107 thermal flight data.

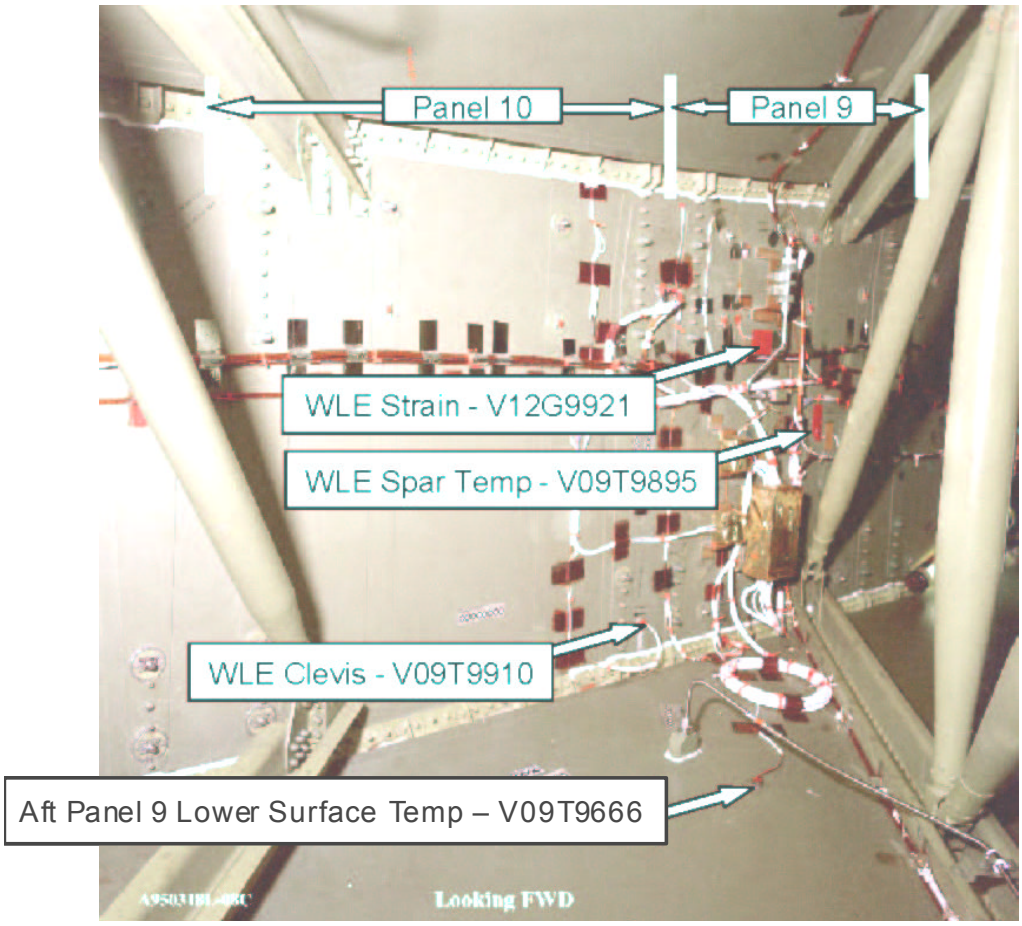

Figure 7.1-11 Location of WLE Strain Gage

7.2 1040 Spar Strain Gauge Evaluation

7.2.1 Analysis Objective

This analysis seeks to provide explanation for observed off-nominal strain signatures in gages V12G9048A and V12G9049A during STS-107 entry. Mechanical loading, pressure loading, load redistribution, thermally induced strain, and instrumentation malfunction were all considered as potential contributors. Strain due to local thermal effects in the region of the two gages is considered the most rational explanation, and is the primary focus of the analysis effort.

7.2.2 Analysis Inputs, Models, Assumptions, and Approach

7.2.2.1 Background

Axial strain gages V12G9048A and V12G9049A are located on the lower and upper caps of the left wing Xo1040 spar, respectively. The Xo1040 spar is the forwardmost of five major wing spars. Forward lies the wing glove area. Aft lie the main landing gear wheel well (behind the section of the spar inboard of the Yo167 rib), and the main wing cavity (behind the section of the spar outboard of the Yo167 rib). The outboard section of the spar includes a cutout that provides a path through to the main cavity of the left wing. There is also a cutout in the inboard section of the spar providing access to the MLG wheel well. Just forward of the Xo1040 spar on the Yo105 sidewall is a vent into the main fuselage. Figure 7.2-1 provides an illustration of the area.

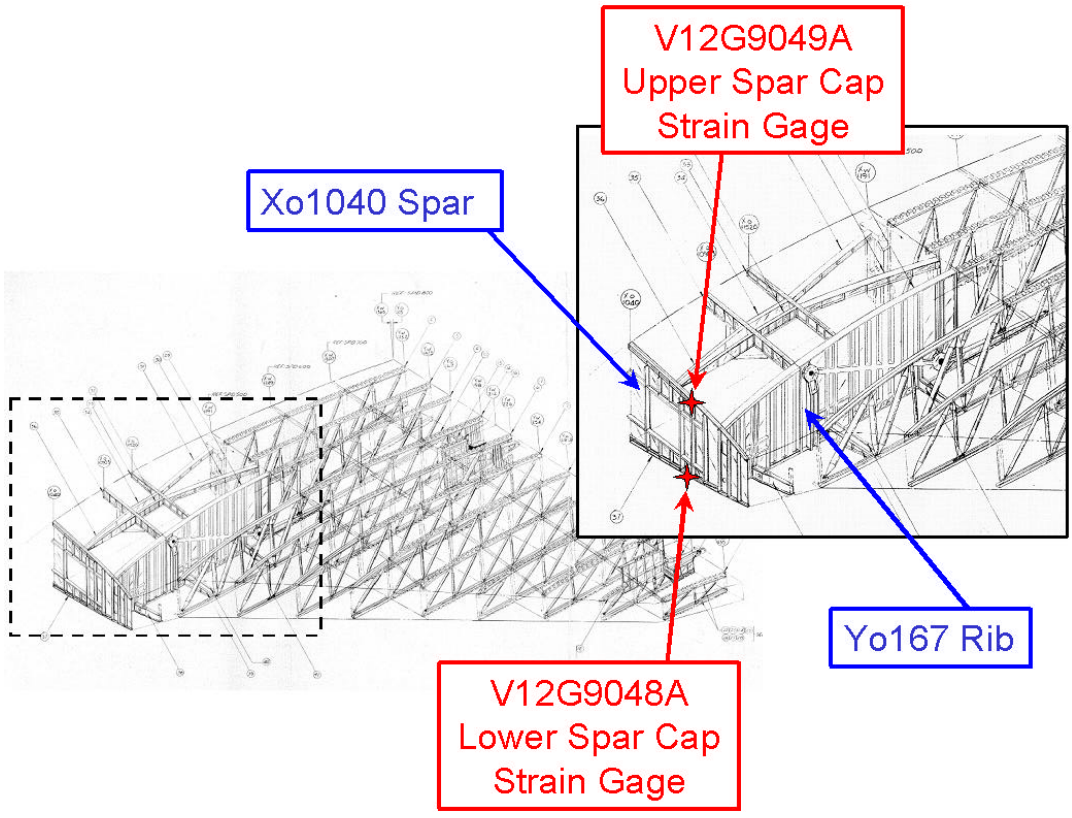

Figure 7.2-1 Xo1040 Spar Cap Strain Gage Locations

7.2.2.2 STS-107 Data Analysis & Reconstruction

As-recorded STS-107 data was refined in order to isolate suspected off-nominal behavior from nominal loading effects. To do so, a nominal profile, based on STS-109 (previous OV-102 flight) was compared with the recorded data. EI+488 seconds was chosen as an initial data point, up to which STS-107 data is considered nominal. The offset between STS-109 data and STS-107 data at this time was removed to generate a reconstructed nominal profile. Figure 7.2-2 illustrates the as-recorded STS-107 data versus the reconstructed nominal profile, based on STS-109.

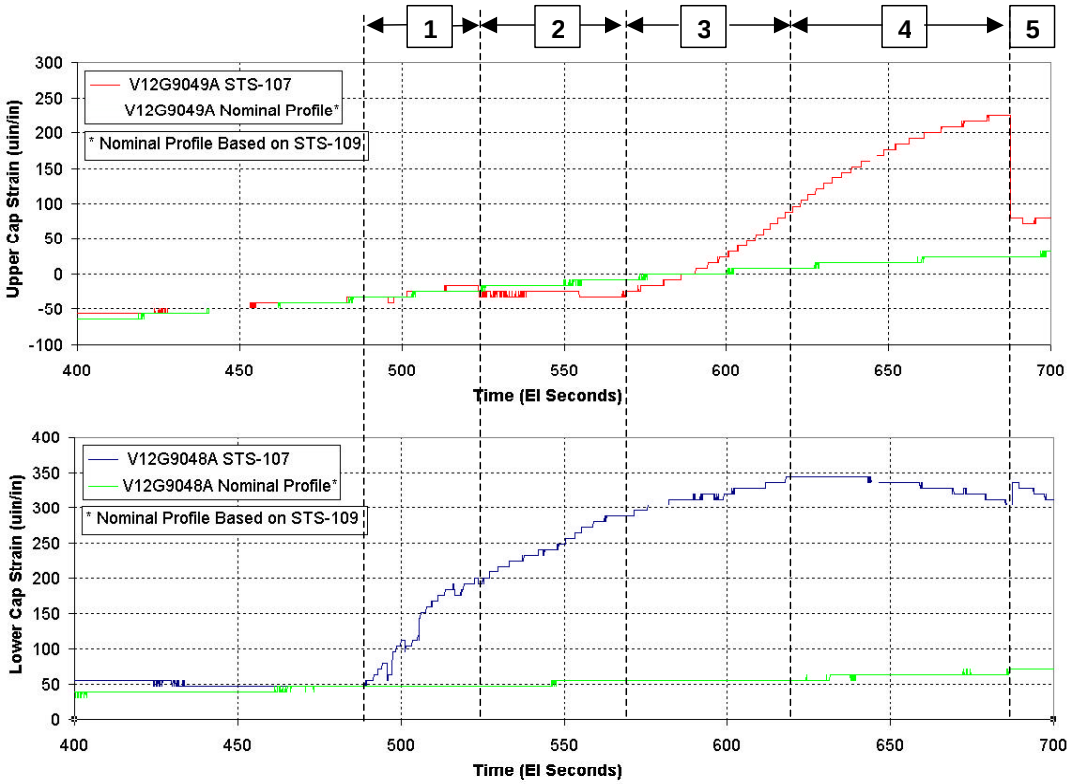

Figure 7.2-2 Observed STS-107 Strain Data versus Reconstructed Nominal Profile

Differentials between the nominal profile and the as-recorded profile represent strain values due to off-nominal loading during STS-107.

An illustration of the complete STS-107 Xo1040 spar cap strain data reconstruction is included for reference as Figure 7.6-2 of the Stress Appendix, Section 7.6.

The anomalous data profile has the following approximate timeline:

1. (EI+488 to EI+523 seconds)
   Minimal tension (8 µin/in) builds in the upper spar cap.
   Significant tension (152 µin/in) builds in lower spar cap.

2. (EI+523 to EI+569 seconds)
   Reversal causes minimal compression (-16 µin/in) in the upper spar cap.
   Tension continues to build to 232 µin/in in the lower spar cap.

3. (EI+569 to EI+618 seconds)
   Another reversal causes significant tension (72 µin/in) in the upper spar cap.
   Tension builds to a maximum (288 µin/in) in the lower spar cap.

4. (EI+618 to EI+687 seconds)
   Tension builds to a maximum (200 µin/in) in the upper spar cap.
   Tension reduces to 232 µin/in in the lower spar cap.

5. (EI+687 seconds)
   Instantaneous, high magnitude strain decrease (-144 µin/in) in the upper spar cap.
   Instantaneous, low magnitude strain increase (32 µin/in) in the lower spar cap.

Data following the instantaneous change at EI+687 seconds has not been conclusively verified as reliable strain data. There has been no instrumentation malfunction identified in these measurements at this time, or any time prior to EI+930 seconds. However, the instantaneous changes at EI+687 seconds are not considered rational from a real strain perspective. As such, there is no conclusive explanation for the instantaneous changes in strain values at that time. Without such an explanation, data beyond this point must be considered suspect, and therefore was not considered in the analysis that follows.

The observed off-nominal strain signatures during STS-107 are believed to be the result of instrumentation malfunction, thermally induced strain, or a combination of these two factors. Mechanical loading, pressure loading, and load redistribution were also evaluated as potential causes, but are believed to be unlikely explanations.

The primary evidence refuting mechanical loading, or more specifically, wing bending, is the agreement in sign between the off-nominal strains. That is, both the upper and lower caps show tensile loading. A nominal entry plot for these two gages from STS-109, included for reference as Figure 7.6-1 of the Stress Appendix, Section 7.6, illustrates that under significant wing bending loads in the TAEM portion of entry, the spar cap strains are of opposite sign; tension on the lower cap, compression on the upper cap. It should also be noted, however, that in the nominal profile, tensile loads exist in both spar caps during the period of entry in which off-nominal trends were recorded on STS-107. This phenomenon is attributed to the influence of upper skin heating, which generates a tensile effect in the upper cap that counteracts the mechanical compression load. The thermal effect on the lower cap is nominally much less pronounced.

An internal pressure load would not be consistent with the observed strain data, as the initiation times of off-nominal trends in the upper and lower spar caps, respectively, are not consistent with one another. Load redistribution also is largely unsupported by the data. The lower spar cap, for example, shows a reduction of tensile loading after EI+618 seconds, following the initial off-nominal rise. This would not be the expected behavior of a structure that had compensated for failure elsewhere by taking on additional load, namely as it would imply some sort of regaining of previously lost capability.

This evidence leaves localized thermal effects as the most reasonable explanation for the observed off-nominal strains. The analysis that follows considers thermal effects arising from intrusion of hot gas into the main wing cavity, which subsequently vents into the area in front of the Xo1040 spar. In combination with heating of the upper wing skin, due to breach into the main wing cavity and/or the MLG wheel well, localized heating in these regions could potentially give rise to temperature differentials that drive the observed spar cap strains.

7.2.2.3 Finite Element Model

The OV-102 Orbiter NASTRAN finite element model, based on the ASKA certification model, was used for assessment of localized heating. Selected FEM nodes were held at higher temperatures than others in order to produce thermally induced strain. FEM elements corresponding to the locations of the strain gages were then checked for strain response to the applied loads.

All elements in the model were assigned a default thermal expansion coefficient of a=0.000013/°F, and a default reference temperature of 70°F. Node temperatures by default were set to 70°F, with selected nodes raised to higher temperatures. It is important to note that the analysis does not attempt to model actual structural temperatures, but rather to gage structural response to local temperature differentials. The following structural areas were selected for application of local elevated temperature fields:

- Xo1040 Spar Web
- Xo1040 Upper Spar Cap
- Xo1040 Lower Spar Cap
- Wing Upper Skin, immediately forward of Xo1040
- Wing Lower Skin, immediately forward of Xo1040
- Wing Upper Skin between Xo1040 and Xo1090, Yo167 and Yo193
- Wing Lower Skin between Xo1040 and Xo1090, Yo167 and Yo193
- Wing Upper Skin between Xo1040 and Xo1090, Yo105 and Yo167
- Wing Leading Edge between Yw198 and Yw226 ribs
- Yo167 Rib Web between Xo1040 and Xo1098

Numerous combinations were run in order to assess the effects of different heating inputs on spar cap strains. These results were then compared to the observed strains to develop potential scenarios to explain the observed behavior.

Illustrations of the complete FEM, as well as specific areas of emphasis, are included for reference as Figure 7.6-3 to Figure 7.6-5 of the Stress Appendix, Section 7.6.

7.2.3 Results

The following table provides a qualitative summary of analyzed FEM cases and results:

Table 7.2-1 Qualitative FEM Results Summary

Case	Description	Upper Cap Reaction	Lower Cap Reaction
4A	Calibration (all nodes @ 70°F)	None	None
4B	Equal heating of spar web, forward upper and lower skins	Significant tension (20% higher than lower cap)	Significant tension
4C	Heating of outboard, aft, upper skin only	Significant tension	Very low tension
4D	Combined 4B and 4C	Significant tension (effects additive)	Significant tension (effects additive)
4F	Heating forward lower skin only	Very low compression	Significant tension
4G	Heating of WLE nodes	Very low compression	Low compression (2x upper cap)
4H	Heating of outboard, aft, lower skin only	Very low compression	Very low tension
4I	Heating of spar web nodes only	Very low tension	Low tension (2x upper cap)
4J	Heating of Yo167 rib sections	Very low tension	Very low tension
4L	Heating of upper spar cap only	Significant compression	Very low compression
4M	Heating of aft upper skin only	Significant tension	Very low compression

Numerical results from each of the load cases may be found in the Table 7.6-1 summary table of the Stress Appendix, Section 7.6.

The qualitative trends above were utilized to guide development of several temperature profiles that produce strains as observed in the STS-107 flight data. These profiles were screened versus scenario

evidence from the accident investigation team in order to define the most reasonable profile that could have produced the observed strains. The preferred profile, included in the scenario timeline that follows, corresponds to sequences 1-4 from the observed data timeline.

These results indicate that local temperature gradients on the order of 100-200°F could potentially explain the observed strains. These gradients may be consistent with scenarios involving hot gas intrusion from the wing cavity, passing in front of the Xo1040 spar enroute to the mid-fuselage, combined with heating of the wing upper skin just aft of the Xo1040 spar.

The major assumption of the selected temperature profile is that the lower spar cap has less heating than the structure around it; namely the upper spar cap, spar web, and wing skins immediately forward of Xo1040. The temperature rise in the lower spar cap thereby lags behind that of the adjacent structure and the upper spar cap. Note that sections A2 and A3 of the temperature profile indicate a transition from heating of the upper skin outboard of Yo167 to the upper skin atop the MLG wheel well, inboard of Yo167. This is one of a number of ways that a significant change in upper skin heating characteristics may be represented. The same effect could also be achieved, for example, by continued higher heating on the outboard section. It should be noted that the initiation of significant upper spar cap tension at this time is attributed to some substantial change in upper skin heating, but not necessarily by this particular means.

Scenario Timeline

1. (EI+488 to EI+523 seconds)
   Following WLE spar breach, hot gas vents into the region forward of the Xo1040 spar, providing heating to the spar web, nearby forward wing skins, and the upper spar cap. The lower spar cap temperatures lag behind the upper spar cap. Heating is also present in the upper wing skin just aft of the Xo1040 spar and outboard of the Yo167 rib.

2. (EI+523 to EI+569 seconds)
   Hot gas flow continues to drive temperature differentials in front of the Xo1040 spar, as the lower spar cap slowly begins to react. Heating to the upper wing skin outboard of Yo167 is effectively lost. Heating is now present only along skin at the top edge of the Yo167 rib.

3. (EI+569 to EI+618 seconds)
   Hot gas flow continues to drive temperature differentials in front of the Xo1040 spar. The lower cap is still slowly catching up. Breach into the MLG wheel well allows heating along the upper wing skin of the MLG well.

4. (EI+618 to EI+687 seconds)
   Xo1040 spar web, forward wing skins, and upper spar cap reach temperature equilibrium. Lower spar cap is slowly catching up, with continued heating of the upper wing skin above the MLG wheel well.

Table 7.2-2 Scenario Timeline FEM Results

Case	Description	Upper Cap Reaction	Lower Cap Reaction	Scenario
A1	+40°F applied to spar web, forward upper & lower skins, and upper spar cap +75°F applied to outboard, aft, upper skin	13 µin/in **(8 µin/in) (Recorded strain)**	146 µin/in **(152)**	Heating in front of spar and aft upper skin.
A2	+75°F applied to spar web, forward upper & lower skins, and upper spar cap +120°F applied to aft, upper skin along y167 rib +5°F applied to lower spar cap	-11 µin/in **(-16)**	225 µin/in **(232)**	Continued heating in front of spar and aft upper skin. Some heating in lower spar cap.
A3	+105°F applied to spar web, forward upper & lower skins, and upper spar cap +145°F applied to aft, upper skin above MLG wheel well +10°F applied to lower spar cap	73 µin/in **(72)**	291 µin/in **(288)**	Continued heating in front of spar and aft upper skin. Continued heating in lower spar cap.
A4	+105°F applied to spar web, forward upper & lower skins, and upper spar cap +190°F applied to aft, upper skin above MLG wheel well +20°F applied to lower spar cap	200 µin/in **(200)**	237 µin/in **(232)**	Thermal EQ in spar web, forward skins, and upper cap. Continued heating in lower cap. Continued heating of aft upper skin.

7.2.4 Conclusions

It is possible that the observed strains on V12G9048A and V12G9049A were a result of local thermal effects in the region of the Xo1040 spar. Given appropriate temperature gradients, the upper and lower spar caps are subjected to significant thermally induced strain, and could produce the observed strain gage signatures.

The STS-107 strain gage data offers some support for failure scenarios that involve intrusion of hot gas from the wing cavity into the glove area and/or the MLG wheel well. The timing of strain gage events shows some alignment with suspected breach times of the WLE and MLG well in these scenarios. Magnitudes of the observed strains, arising from local temperature gradients, could reasonably be generated by the suspected heat sources.

The strain gage data does not, however, conclusively indicate these scenarios. Numerous potential temperature profiles exist that would produce the observed strains. While a reasonable temperature profile has been suggested based upon corroborating evidence, this profile requires significant assumptions about the heat transfer properties of the local structure, the heat sources, and their combined ability to generate thermal gradients. A conclusive assessment would require conclusive identification of local structural temperatures, and significantly developed corroborating thermal analysis.

7.3 Overall Wing MADS Evaluation

7.3.1 Analysis Objective

This analysis compared recorded Modular Auxiliary Data System (MADS, a.k.a. OEX) wing strain gage measurements for STS-107 versus the same data for selected previous flights of the OV-102 vehicle. Both ascent and entry regimes were reviewed. Where appropriate, anomalous strain gage responses were identified, categorized, and in several cases, selected for additional in-depth analysis efforts.

7.3.2 Analysis Inputs, Models, Assumptions, and Approach

The OV-102 vehicle contained significantly greater MADS wing strain gage instrumentation than other vehicles in the STS fleet. There were 247 total strain gages available on the wings (Gage MSIDs begin with V12G); 121 of these gages were on the left wing, with the remaining 126 on the right. Additionally, 52 gages were located on the elevon structure, divided equally with 26 on each side of the vehicle (Gage MSIDs begin with V13G). In general, strain gage locations were symmetric between the two sides of the vehicle. Figure 7.6-23 and Figure 7.6-24 of the Stress Appendix, Section 7.6 illustrate strain gage locations on the vehicle. References in section 7.7 list relevant installation drawings.

OV-102 MADS strain gage data was recorded on three Pulse Code Modulation (PCM) data channels. Wing gages associated with channels PCM1 and PCM2 had continuous data recording at 10 samples per second for both ascent and entry flight regimes. There were 131 wing strain gages (45 left wing, 86 right wing) on channels PCM1 or PCM2. Gages associated with channel PCM3 had continuous 10 samples per second data recording during the ascent flight regime. During entry, PCM3 gage data was recorded in “snapshot mode” at periodic 1-minute-on, 4-minutes-off intervals (data rate during on-time was 10 samples per second). Elevon gages (PCM1 for right wing, PCM2 for left wing) had continuous data recording at 10 samples per second for the ascent regime. For entry, 20 of 52 gages (10 on each side) had continuous recording. The remaining 32 gages (16 on each side) were recorded in snapshot mode.

Seven previous OV-102 flights were selected for comparison with STS-107. These selections were made based upon similar mass properties and similar inclinations, starting with the most recent flights. Comparison flights were as follows:

STS-109, STS-093, STS-090, STS-087, STS-094, STS-073, and STS-050.

Comparison plots showing STS-107 data versus each of these previous flights were generated using in-house tools developed specifically for the STS-107 accident investigation. Comparison plots showed the entire duration of the ascent regime, and the first seventeen minutes of the entry regime, beginning at entry interface. This time frame includes all available data for STS-107, prior to loss of the vehicle and the end of data recording.

Comparison plots for each of the MADS strain gages were individually reviewed and assessed. Where appropriate, tabular point-by-point data was extracted, and additional analysis performed. Trends amongst gages were assessed, and gage response categories were defined.

7.3.3 Results

7.3.3.1 Ascent

All STS-107 MADS PCM strain data, without exception, was nominal during the ascent flight regime. No significant anomalies were noted. Comparison of ascent strain gage load indicators showed STS-107 ascent loads to be within the family of previous OV-102 flight experience. There was no discernable evidence of an impact load to the vehicle near MET +81.7 seconds. At the PCM sample rate of 10 samples per second, no such evidence is expected to be present. Both the extremely short duration of the impact load (0.003 to 0.005 seconds), and the range of wing modes (6 Hz and above) preclude such evidence. An interesting signature near this time was evident in some strain gages. The response was noted on left wing, right wing, and vertical tail gages. Further study and scrutiny showed that the signature was inconsistent with impact loading, and attributable to a nominal ascent load response. A review of accelerometer data did show signatures consistent with impact loading. This assessment is discussed in Section 7.4.

For reference, a typical PCM ascent strain gage comparison plot is shown in the Stress Appendix, Section 7.6, as Figure 7.6-6. Figure 7.6-7 illustrates the interesting signature noted near the suspect debris impact event, in comparison to data from STS-109, the previous flight of OV-102.

7.3.3.2 Entry - General

Comparison plots for the entry flight regime showed STS-107 data to be appreciably off-nominal versus previous flight experience after EI+490 seconds. Numerous anomalies were noted, most significantly on the left wing and elevon gages.

Due to the snapshot mode data recording on channel PCM3, data for these strain gages was largely not helpful in providing significant inputs to the analysis effort. Without continuous data, reliable conclusions regarding structural responses were not possible. Where possible, implications of off-nominal trends were identified, and data provided to the timeline team. This was the extent of the analysis effort for PCM3 strain gages.

Two sample PCM3 plots are included in the Stress Appendix, Section 7.6. Figure 7.6-8 shows a typical PCM3 comparison plot. Figure 7.6-9 illustrates a PCM3 gage with an apparent off-nominal trend.

The analysis effort focused on PCM1 and PCM2 gages that provided continuous data during the entry flight regime. This includes all PCM1 and PCM2 gages on the left and right wings, and 20 gages (10 on each side) on the elevon structure.

Loading levels during the initial stages of entry, prior to observation of significant off-nominal trends, were nominal as compared to previous flight experience. Maximum entry loading levels are nominally recorded during the TAEM region of flight, as shown by example in Figure 7.6-21.

7.3.3.3 Entry - Right Wing

In general, right wing strain gages showed nominal responses on STS-107 versus previous flights until immediately prior to loss of data (approximately 930 seconds after entry interface). Most, 49 of 85, right wing gages show this typical, nominal response, along with 8 of 10 right wing elevon gages. A sample plot is included for reference as Figure 7.6-10.

There were 19 right wing gages that show evidence of a brief, low magnitude off-nominal response initiating at EI+500 seconds. This signature is characterized by a 1 or 2 bit discrepancy versus previous flight experience, lasting as long as approximately 30 seconds. Following this time, strain values return to nominal tracking. This response was also noted on two right wing elevon gages. No instrumentation

malfunction has been identified in these gages at this time. The only reasonable hypothesis from a real strain perspective is internal pressurization following initial breach of the wing leading edge spar (both wings and the mid-fuselage share common venting). However, this hypothesis would not be consistent with the almost immediate return to nominal readings. The source of this phenomenon therefore is not conclusively understood at this time. A sample plot is included for reference as Figure 7.6-11.

There were 17 right wing gages that show an off-nominal response, initiating near EI+500 seconds, which creates a subsequent data offset versus previous flight experience. This signature is characterized by an off-nominal slope change of approximately 120 seconds duration, followed by a return to nominal tracking with a built-in offset, up to the loss of data. Again, this phenomenon may be explained by a transient internal pressurization effect, instigated by initial WLE spar breach, and relieved by a secondary external breach that subsequently reduces internal pressure. No instrumentation malfunction has been identified in these gages at this time. A sample plot is included for reference as Figure 7.6-12.

One right wing gage, V12G9653A (right wing upper skin at Xo1218, Yo245) showed a nominal response during ascent, but had no data recorded for entry. This gage is presumed to have failed at some point during the on-orbit period of STS-107. This type of on-orbit gage failure is not unusual in previous flight experience.

7.3.3.4 Entry - Left Wing

In contrast, the majority of left wing gages show indications of failure initiating between EI+486 seconds and EI+590 seconds. The vast majority, 42 of 45, of left wing gages, and all 10 left elevon gages show this typical response. The gage failure signature is characterized by sudden, rapid slope change driving strain to off-scale band edge values. In many instances, the gage signature oscillates between off-scale high and off-scale low values before settling at a “flatline”, steady-state response. This steady-state value is dictated by the instrumentation bias of a particular gage, and may or may not equal zero. Numerous gages show an off-nominal slope change that significantly precedes the dramatic off-scale event. The off-scale event, as well as the preceding off-nominal slope change, is attributed to burning of the strain gage wiring. These events are not consistent with literal strain responses to mechanical, thermal, or pressure loading. No significant correlation was found between strain gage location on the vehicle and initiation time of strain gage failure, as illustrated in Figure 7.6-22.

Significant unpredictability in the burning phenomenon dictates that individual gages show unique manifestations of the failure event. For example, not all gages “flatline” following the off-scale excursions. The period or number of oscillations between upper and lower band edge values also is variable from gage to gage.

Following the initial off-scale excursion, or off-nominal inflection toward such an excursion, strain gage data is considered invalid, due to the wire burning condition. Subsequent data therefore is an indication only of the wire-burning phenomenon, and not of structural strain gage responses.

Several representative samples of left wing and left wing elevon strain gage failure comparison plots are included for reference in the Stress Appendix, Section 7.6. Please refer to Figure 7.6-13 through Figure 7.6-17.

The remaining three left wing strain gages were the subjects of significant additional analysis effort. V12G9921A, located on the wing leading edge spar near RCC panel #9, showed the earliest off-nominal response of any strain gage, initiating near EI+270 seconds. Numerous slope changes and a change in sign of the strain value followed, prior to initiation of a gage failure signature after EI+470 seconds. Off-nominal strain values for this measurement are attributed to localized, thermally-induced strain and structural failure. This analysis is discussed separately in Section 7.1. The comparison plot for V12G9921A is included for reference as Figure 7.6-18.

Gages V12G9048A and V12G9049A, located on the lower and upper Xo1040 spar caps, respectively, in the center of the wheel well forward wall (Yo135) were the only two left wing gages that did not clearly indicate failure prior to EI+930 seconds. As these gages did not join wire bundles until just prior to

penetration of the mid-fuselage sidewall, this data would suggest an absence of direct plume impingement in the glove area forward of the wheel well. Both of these gages showed significant off-nominal trends, however, at earlier times. V12G9048A showed initiation of an off nominal trend at EI+489 seconds, which continued to the loss of data. Likewise, V12G9049A first showed initiation of an off-nominal trend at EI+568 seconds, again continuing until loss of data. These off-nominal trends are likely attributable to local thermal effects, possibly combined with instrumentation malfunction, as discussed separately in Section 7.2. Comparison plots for V12G9048A and V12G9049A are included for reference as Figure 7.6-19 and Figure 7.6-20, respectively.

7.3.4 Conclusions

Comparison of STS-107 MADS PCM strain gage data to previous flight data offers strong evidence and support for the STS-107 accident investigation. Specifically, the strain data offers support for failure scenarios with breach of the wing leading edge spar outboard of the Yo167 rib.

PCM strain gage data from the ascent regime shows no indications of off-nominal structural loads. Load levels for ascent are within the family of previous OV-102 flight experience.

During the entry regime, significant off-nominal behavior was identified. This off-nominal behavior is attributed primarily to combined influences of instrumentation failure and localized off-nominal thermal effects.

The typical left wing entry signature is indicative of instrumentation failure due to burning of wires inside the left wing. This failure pattern corroborates wire bundle burn-through scenarios developed in the previous analysis of telemetered OI data.

Significant early off-nominal strains in V12G9921A provide evidence of localized thermal effects in the area of RCC Panel #9.

Gages V12G9048A and V12G9049A, unlike all other left wing strain gages, do not show clear indications of instrumentation failure prior to loss of data. These two gages' wiring join bundles further forward than all other strain gages. Again, this data supports evidence of wire burning in the main left wing cavity. Off-nominal strains due to local thermal effects in these gages provide further clues regarding hot gas venting following initial intrusion into the left wing cavity.

7.4 Accelerometer Evaluation

Accelerometer and higher sample rate strain gage responses during STS-107 are studied during ascent and entry phases of the flight to identify any anomalous response. They were also compared to STS-109 and other OV-102 flight data to determine if the responses are within the family experience.

7.4.1 Ascent

The locations of the accelerometers are shown In Figure 7.4-1. They include 15 accelerometers on the wing/elevons, body flap and vertical tail/rudders, and 11 measurements on the longeron. In addition, there are 36 strain gages in the vertical tail and OMS deck area.

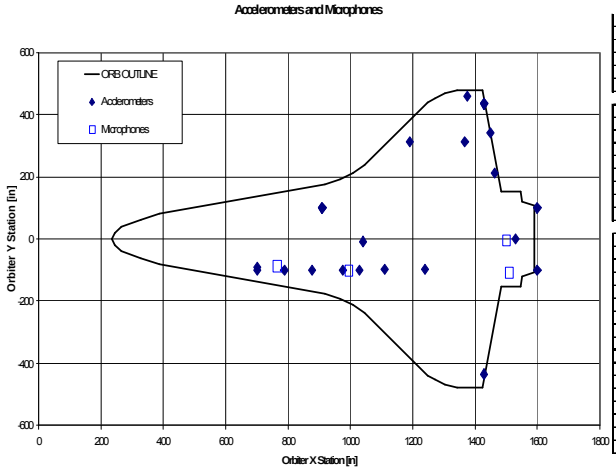

MISD	DFI	NOMENCLATURE	X	-Y	Z
		Microphones			
V08Y8006A	MADS	LH PAYLOAD BAY VENT #3 X765	765.3	-86.5	382.6
V08Y8039A	MADS	PAYLOAD BAY LH VENT NO 5 X994	994.0	-100.0	
V08Y9684A	MADS	AM ON HT SHLD Y-100 Z320 MAF004	1510.1	-107.3	316.4
V08Y9686A	MADS	AM AFT FUS HS CTR YO Z400 MAF006	1499.6	-2.4	384.9
		Accelerometers			
V34A9432A	MADS	LH LNGN ACCEL Z-AXIS X976	976.5	-101.5	407.5
V34A9460A	MADS	LH LNGN ACCEL Y-AXIS X701	701.2	-100.8	407.0
V34A9461A	MADS	LH LNGN ACCEL Z-AXIS X701	701.2	-91.3	407.5
V34A9464A	MADS	LH LNGN ACCEL Z-AXIS X877	877.2	-101.3	407.5
V34A9481A	MADS	KEEL ACCEL V-AXIS X1040,Y=0	1040.0	-8.5	LWR
V34A9482A	MADS	LH LNGN ACCEL Z-AXIS X790	788.3	-101.3	407.5
V34A9483A	MADS	LH LNGN ACCEL X-AXIS X1029	1029.0	-101.3	407.7
V34A9484A	MADS	LH LNGN ACCEL Z-AXIS X1110	1110.0	-96.8	407.3
V34A9485A	MADS	LH LNGN ACCEL Z-AXIS X1229	1238.7	-97.0	407.5
		Accelerometers			
V08D8037A	MADS	RH LONGERON Y-AXIS VIB	910.0	99.4	409.0
V08D8038A	MADS	RH LONGERON Z-AXIS VIB	910.0	99.4	409.0
V08D9062A	MADS	LFAF BF AFT-R Z-VIB AOB-16	1600.0	100.0	
V08D9063A	MADS	LFAF BF AFT-L Z-VIB AOB-17	1600.0	-100.0	
V08D9064A	MADS	LFAF BF HL CTR Z-VIB AOB-18	1530.0	0.0	
V08D9699A	MADS	LFAF L OTBD ELEV OTBD Y-VIB	1429.4	435.0	
V08D9729A	MADS	LFAF R OTBD ELEV OTBD Z-VIB	1428.6	-435.0	
V08D9737A	MADS	LFAF R OTBD ELEV OTBD Z-VIB	1428.6	435.0	
V08D9738A	MADS	LFAF R OTBD ELEV INBD Z-VIB	1449.1	342.5	
V08D9764A	MADS	LFAF R WING TIP AFT Z-VIB	1376.0	460.0	
V08D9765A	MADS	LFAF R WING OTBD-MID Z-VIB	1191.0	312.5	
V08D9766A	MADS	LFAF R WING X1365,Y312 Z-VIB	1367.0	312.0	
V08D9784A	MADS	LFAF R INBD ELEV-CTR Z-VIB	1462.6	212.0	
V08D9694A	MADS	LFAF V/S RSS262 A SPAR Y-VIB	1569.9	LH	710.0
V08D9789A	MADS	LFAF V/S RSS158 F SPAR Z-VIB	1459.9		671.5
V08D9795A	MADS	LFAF R SP BK UPR BOT Y-VIB	1620.9	RH	633.0
V08D9797A	MADS	LFAF R SP BK LWR TOP Y-VIB	1600.4	RH	593.2

Figure 7.4-1 Measurement Locations

In general, the responses from STS-107 and STS-109 are very similar for the most part. Shown in Figure 7.4-2 is a comparison of typical accelerometer responses. The magnitude is very comparable throughout the flight. The large amplitude responses at near M=1 are also very similar. (The peak response noted at ~82 seconds will be discussed later in detail) The RMS (Root Mean Square) values of all accelerometers for wing and tail accelerometers are shown in Table 7.4-1 and illustrate the overall amplitude is very similar. The PSD's of three measurements (Left outboard elevon, Right wing tip, Body flap) are shown in Figure 7.4-3. The results computed using 20-80 second data block demonstrate no significant change in the magnitude and frequency contents between the two flights.

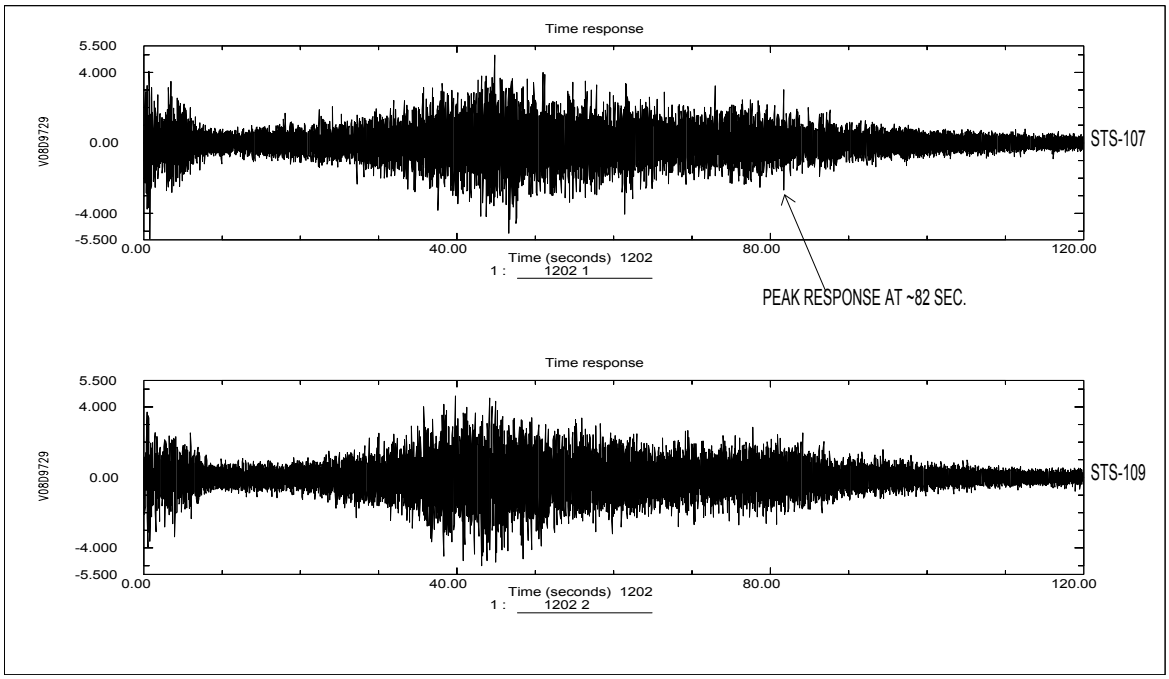

Figure 7.4-2 Comparison of Left Outboard Elevon Response (STS-107 VS. STS-109)

Table 7.4-1 Summary of RMS Acceleration

	T= 0-120 sec		T= 20-80sec.	
	STS107	STS109	STS107	STS109
VO8D9729A (L. OB Elevon)	.74	.78	.92	.98
VO8D9737A (R. OB Elevon)	.75	.75	.95	.95
VO8D9738A (R. OB Elevon)	.78	.75	.99	.95
VO8D9784A (R. IB Elevon)	.91	.90	1.23	1.22
VO8D9764A (R. Wing)	.73	.74	.92	.92
VO8D9766A (R. Wing)	.42	.41	.52	.51
VO8D9765A (R. Wing)	.35	.35	.40	.39
VO8D9064A (Body Flap)	.74	.85	.96	1.09
VO8D9062A (Body Flap)	3.51	3.79	4.85	5.09
VO8D9063A (Body Flap)	1.74	1.78	2.03	1.90
VO8D9699A (Vertical Tail)	.40	.36	.44	.37
VO8D9795A (Upper R. Rudder)	.52	.52	.68	.67
VO8D9694A (Vertical Tail)	.30	.28	.38	.33
VO8D9789A (Vertical Tail)	.43	.39	.52	.44
VO8D9797A (Lower R. Rudder)	---	---	---	---

Left Outboard Elevon Accelerometer

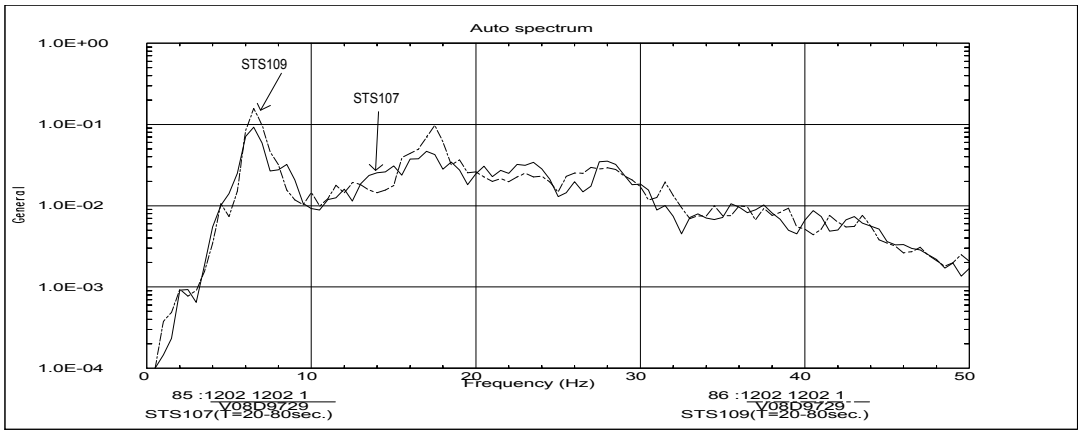

Right Wing Tip Accelerometer

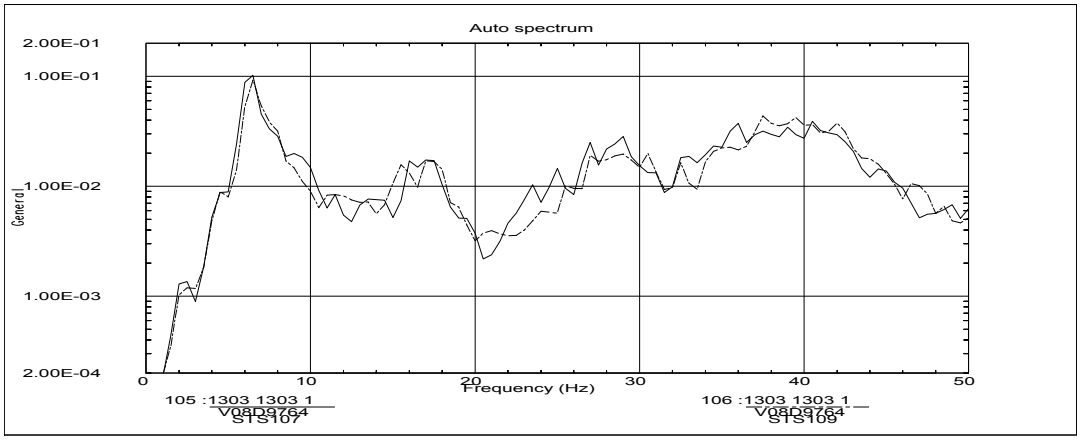

Body Flap Accelerometer

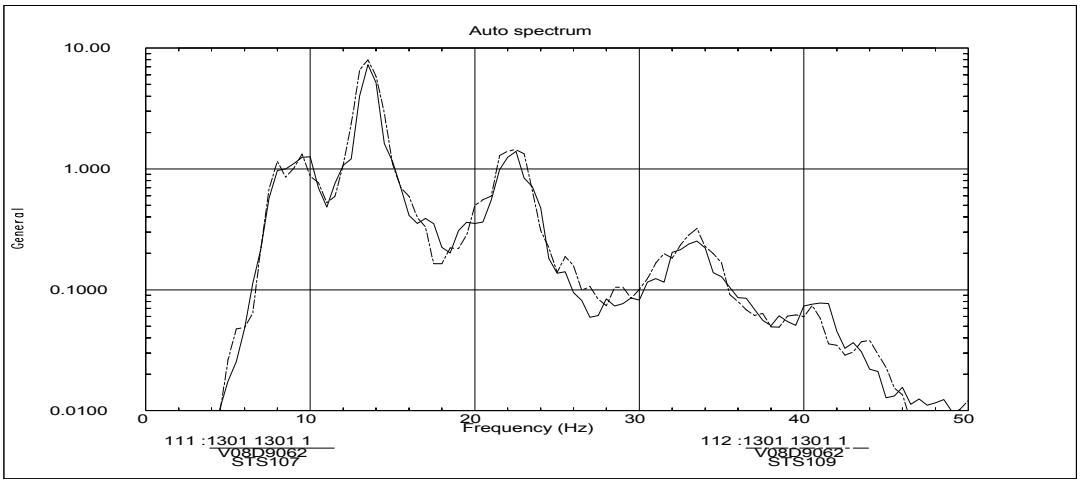

Figure 7.4-3 PSD's Comparison (STS-107 VS. STS109)

The only notable differences in the RMS acceleration are the three tail accelerometers, which are highlighted in the table. They show approximately 15-20% higher response during STS-107 compared to STS-109 results. The reason for the increase is the difference in the tail response near 40-42 second range, as noted in Figure 7.4-4. The PSD's during this time period shown in Figure 7.4-5 verify significantly higher response of the tail's 2nd and 3rd bending modes at the 20 to 40 Hz range.

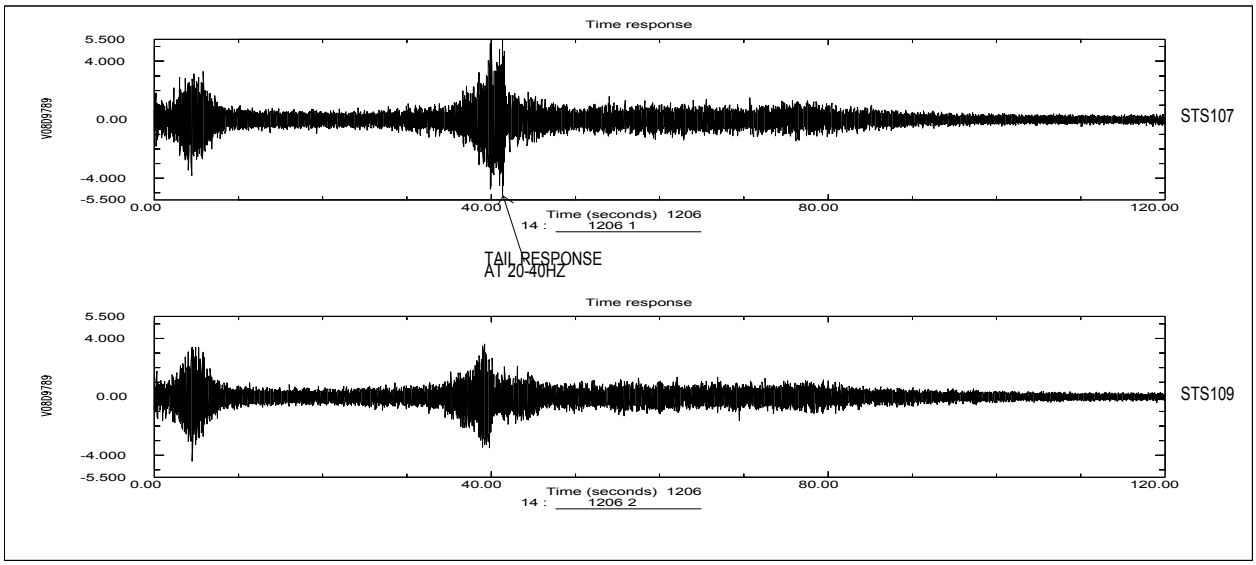

Figure 7.4-4 Vertical Tail Response during Ascent (STS-107 VS. STS-109)

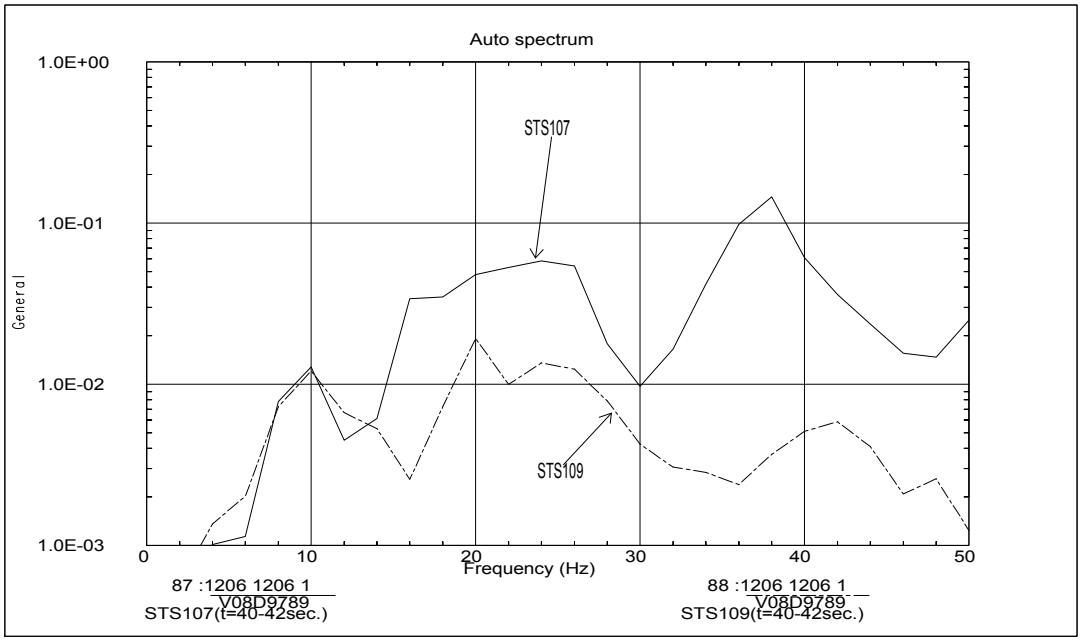

Figure 7.4-5 PSD Comparison of Vertical Tail Response at T=40-42 sec. (STS-107 VS. STS-109)

This type of variation in response is considered a normal behavior of tail reacting to buffeting environment near M=1, where the turbulent effect of the air is the greatest. The degree of turbulence level and the frequency content in air flow can vary flight to flight, which can result in different types of modes being excited. A similar characteristic was observed during STS-87 as presented in Figure 7.4-6. The PSD's from two flights are remarkably similar in magnitude and frequency contents. The results indicate the excitation of higher order tail mode during STS-107 is not unique and is considered within the family experience.

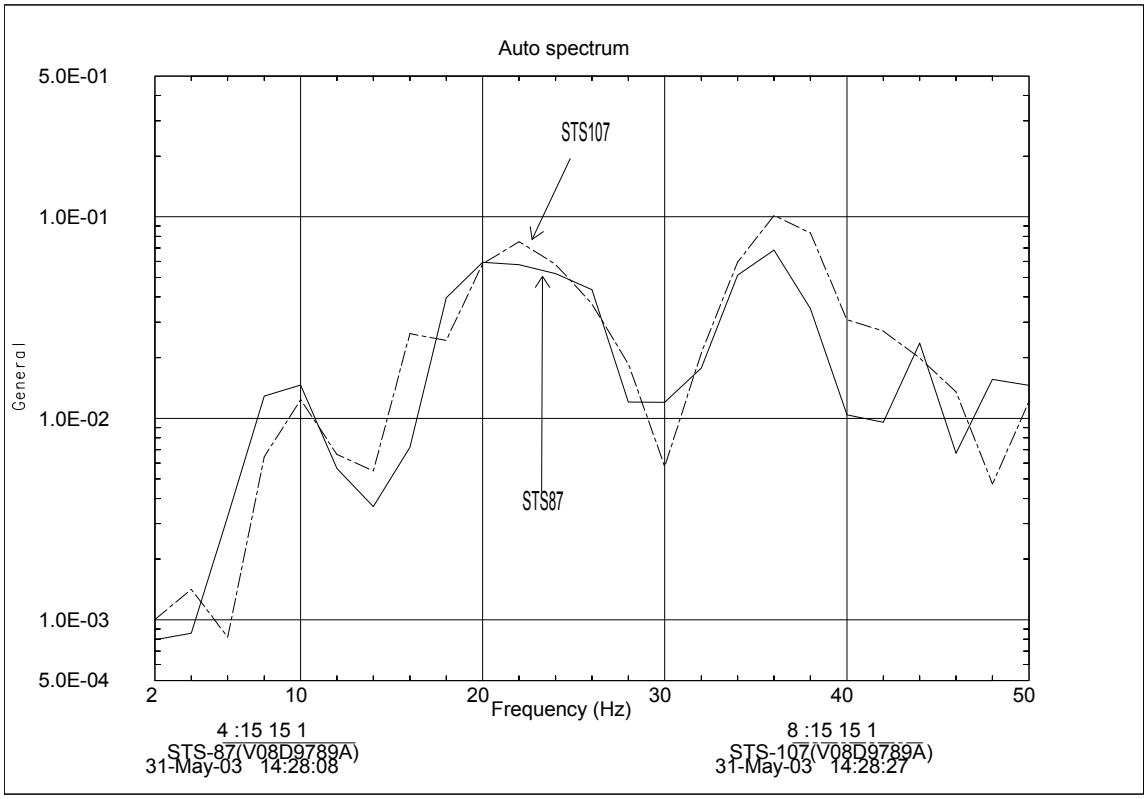

Figure 7.4-6 PSD Comparison of Tail Responses (STS-107 VS. STS-87) (T=40-42 sec.)

7.4.1.1 Evaluation of Peak Response at ~82 Seconds

An in-depth study was made to investigate if the peak responses observed at the left outboard elevon accelerometer at ~82 seconds is due to the debris impact. Normally, sharp spikes in acceleration are observed at times during the ascent phase of the flight due to buffeting event(s). The buffeting load is most significant during the transonic region. However, it still exists at higher Mach numbers, which results in structural excitation. Shown in Figure 7.4-7 is the left and right outboard elevon comparison for the 10 second period near 82 seconds. The peak response is noticeable only for the left outboard location. Filtered responses presented in Figure 7.4-8 verify several wing/elevons were excited at 82 seconds. The 2nd wing bending response constitutes the largest component of the peak amplitude. In addition, the responses of 3rd wing bending and elevon torsion modes contributed to the peak response.

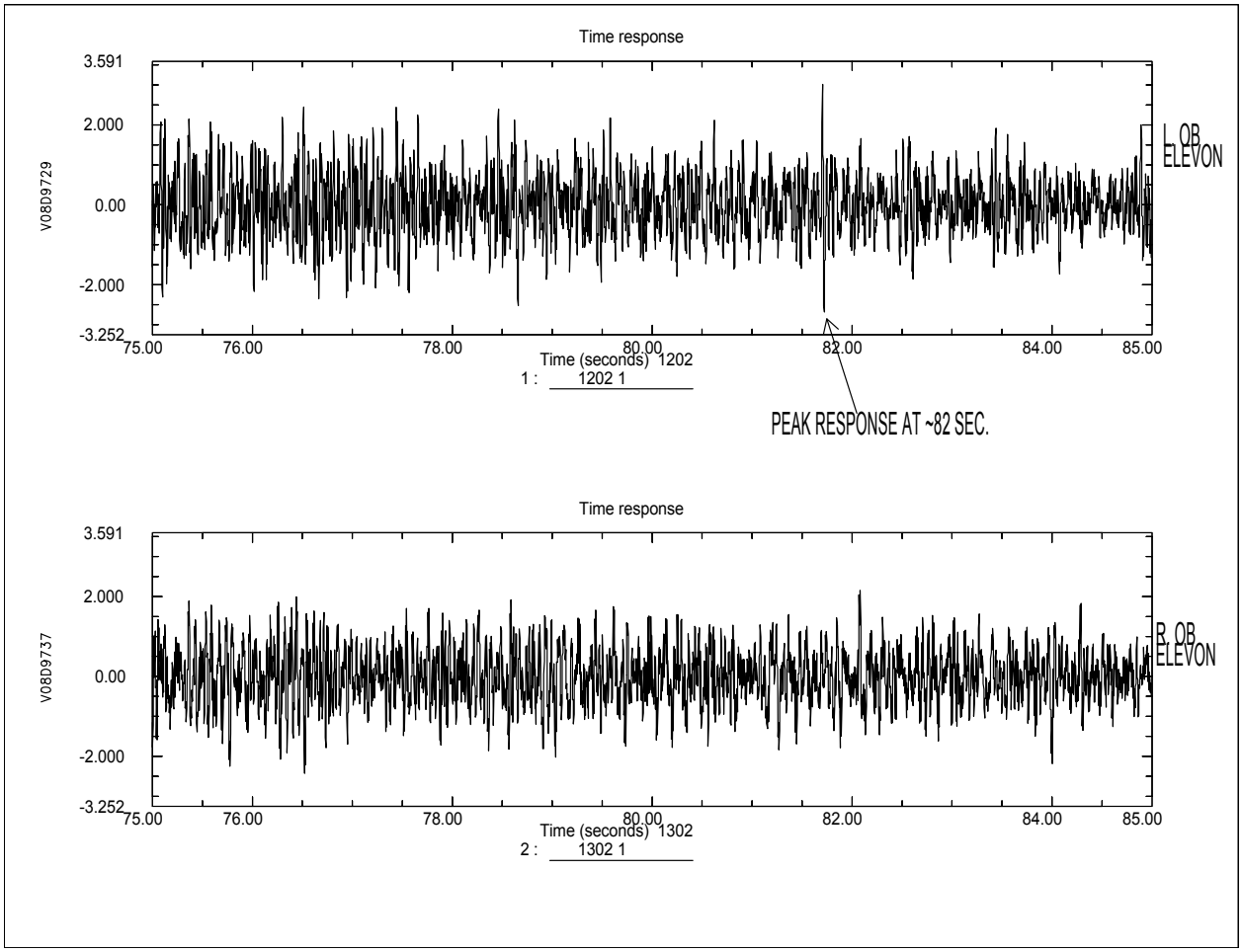

Figure 7.4-7 Right and Left Outboard Elevon Response at ~82 seconds

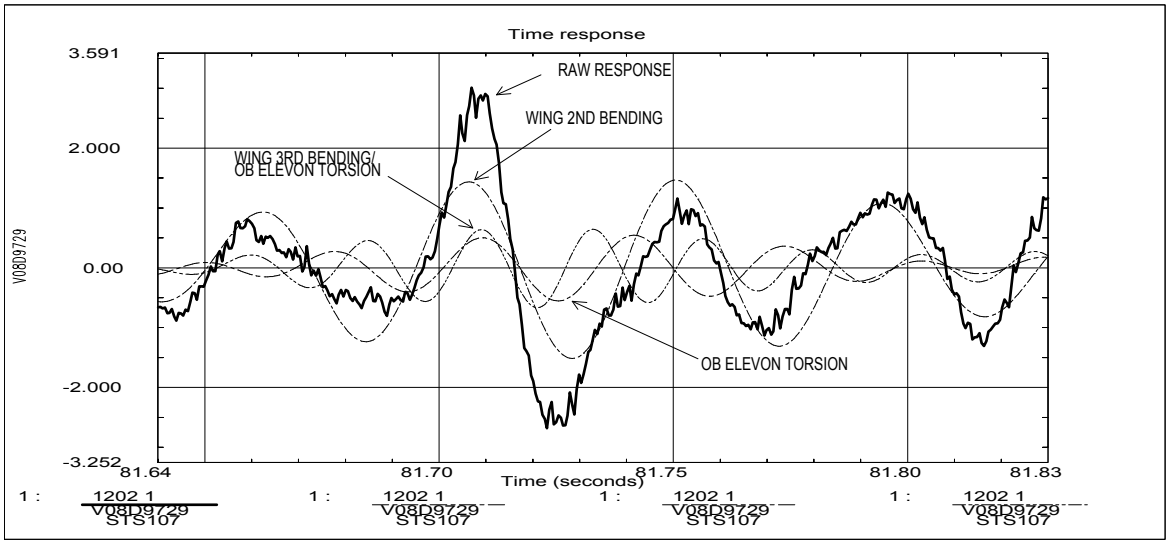

Figure 7.4-8 Excitation of Various Wing/Elevon Modes at ~82 sec. (Left Outboard Elevon)

To determine if the debris impact can cause the type of responses observed in the flight data, analyses were performed using the FEM model of the wing combined with the reduced model of the Orbiter, which provides the back-up structure's stiffness and mass (Figure 7.4-9). An impulse of 3,000 lbs force (with 0.005 second duration) in Z-direction was applied to the node closest to the RCC panel #8. The impulse of this magnitude is reasonable for a 1.5 lb object with a velocity of 530 MPH impacting the surface at 15 degrees inclination.

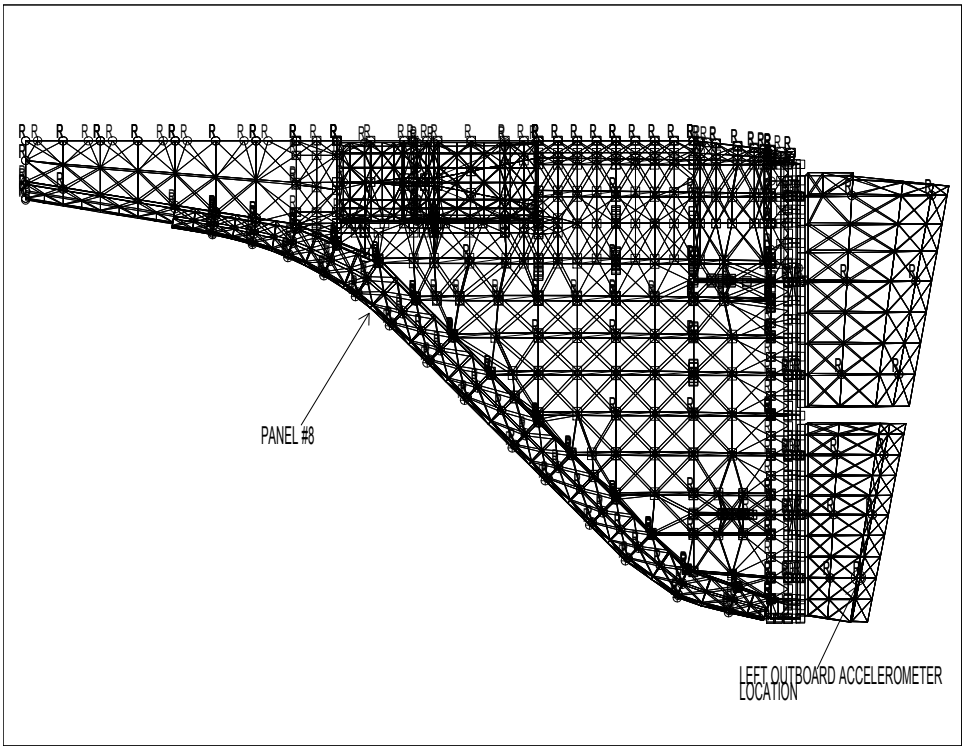

Figure 7.4-9 FEM Model of Wing Structure

Shown in Figure 7.4-10 is the recovered acceleration at the left outboard elevon location from the transient analysis. The FFT (Figure 7.4-11) of the response indicates excitation of several wing modes, including wing's 2nd and 3rd bending modes. The filtered responses shown in Figure 7.4-12 illustrate the 3rd wing bending mode constitutes the majority of the peak amplitude, while the 2nd wing bending and elevon torsion modes also contribute to the peak response. The acceleration computed using the FEM model is shown along with the flight measured data in Figure 7.4-13. The shapes of acceleration signatures are comparable at the onset of debris impact. The frequency from the analysis is higher, since the 3rd wing bending mode is excited the most compared with the 2nd wing bending mode experienced during STS-107. More pronounced 3rd wing bending response from analysis could be attributed to possible deviations from the assumed location and duration of impact event, and some uncertainty in the FEM models for higher order wing modes. Nevertheless, similar acceleration signature and the excitation of higher order wing modes from the analysis indicate that the debris impact quite possibly could have caused the peak acceleration on the left outboard elevon at ~82 seconds in addition to other aerodynamic disturbances, such as buffeting and shocks. An absence of additional sensors on the left wing make it difficult to make conclusive remarks.

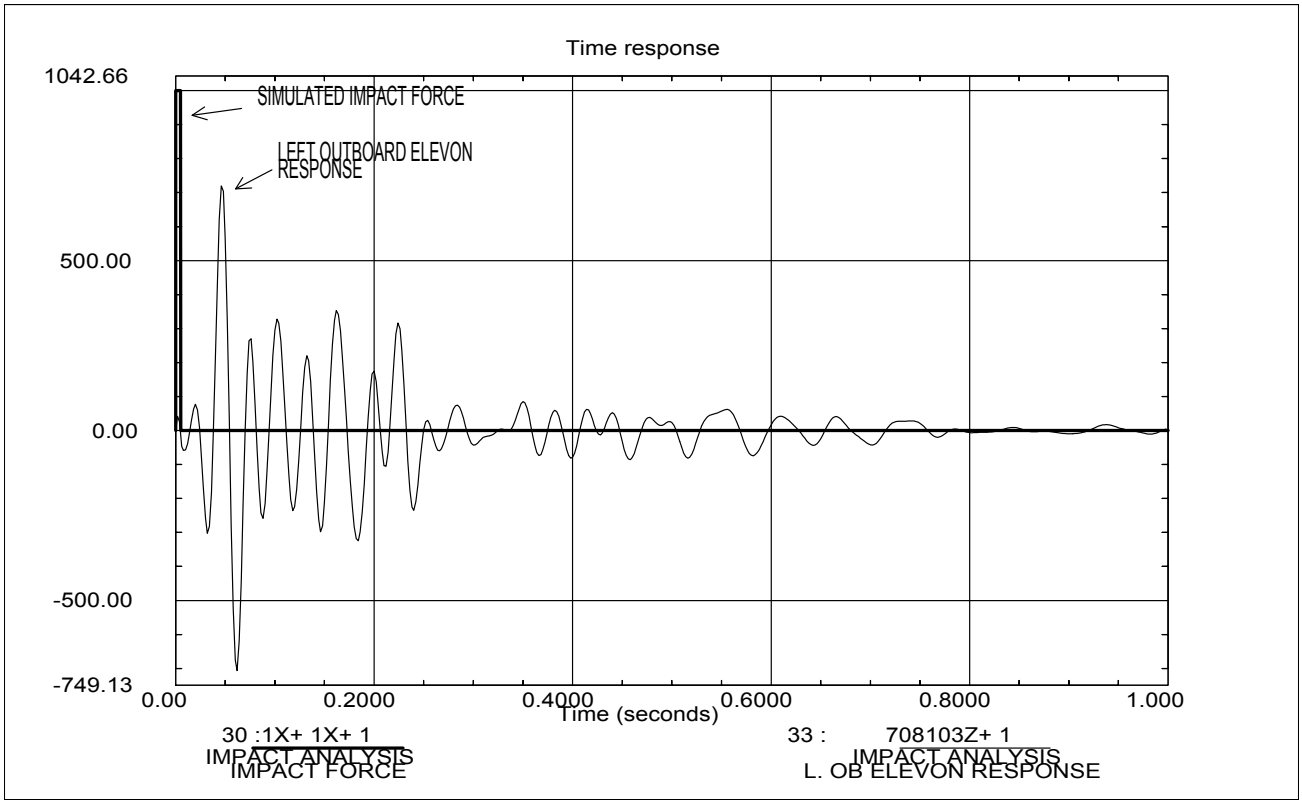

Figure 7.4-10 Outboard Elevon Response from Impact Analysis

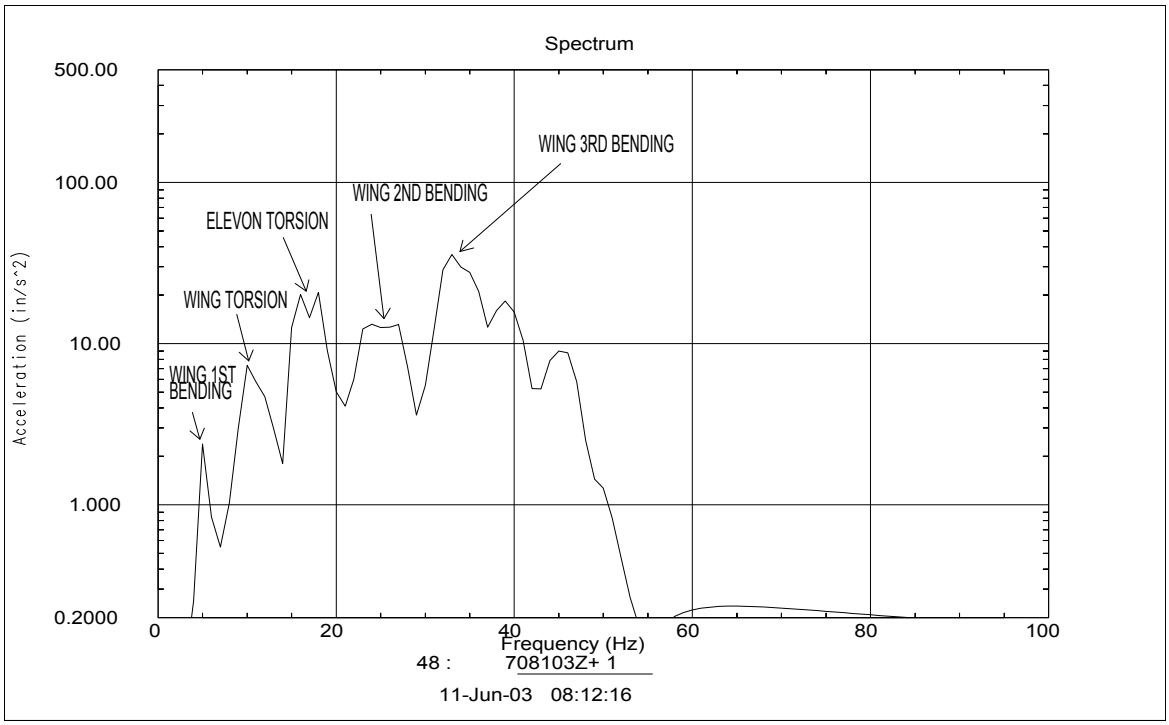

Figure 7.4-11 FFT at Outboard Elevon Location (Impact Analysis)

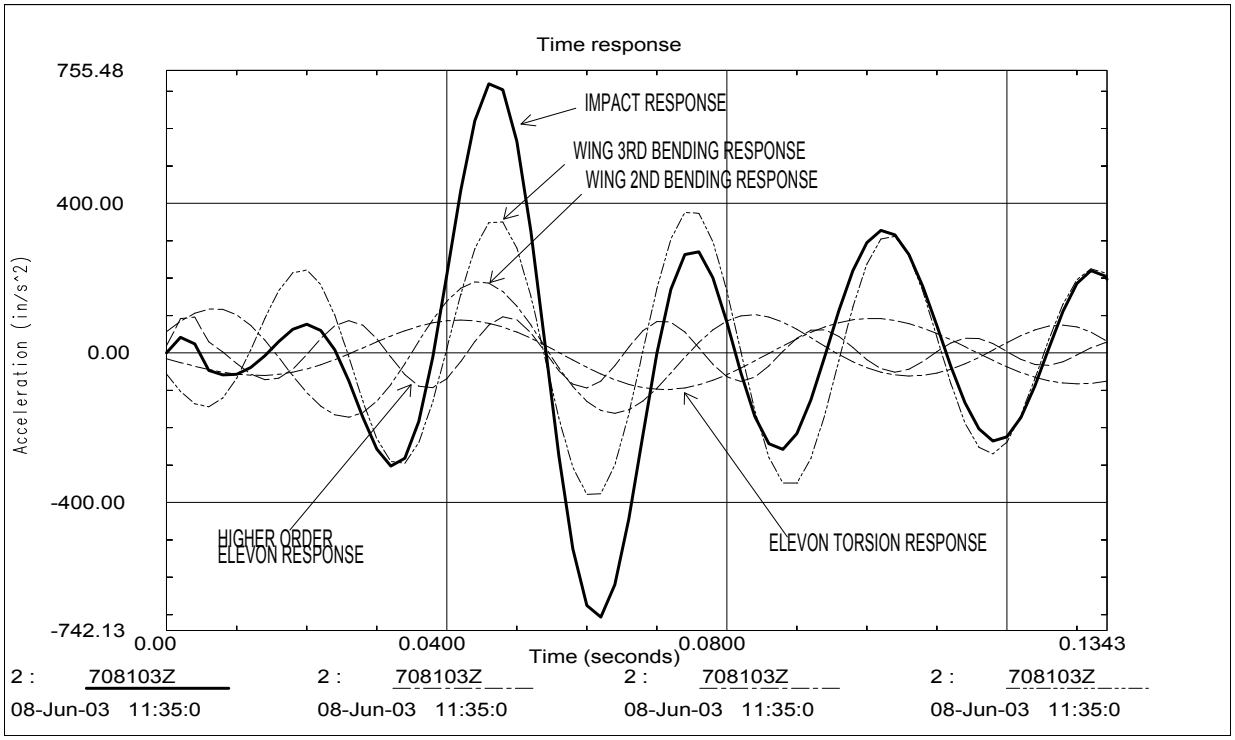

Figure 7.4-12 Excitation of Various Wing/Elevon Modes (Impact Analysis)

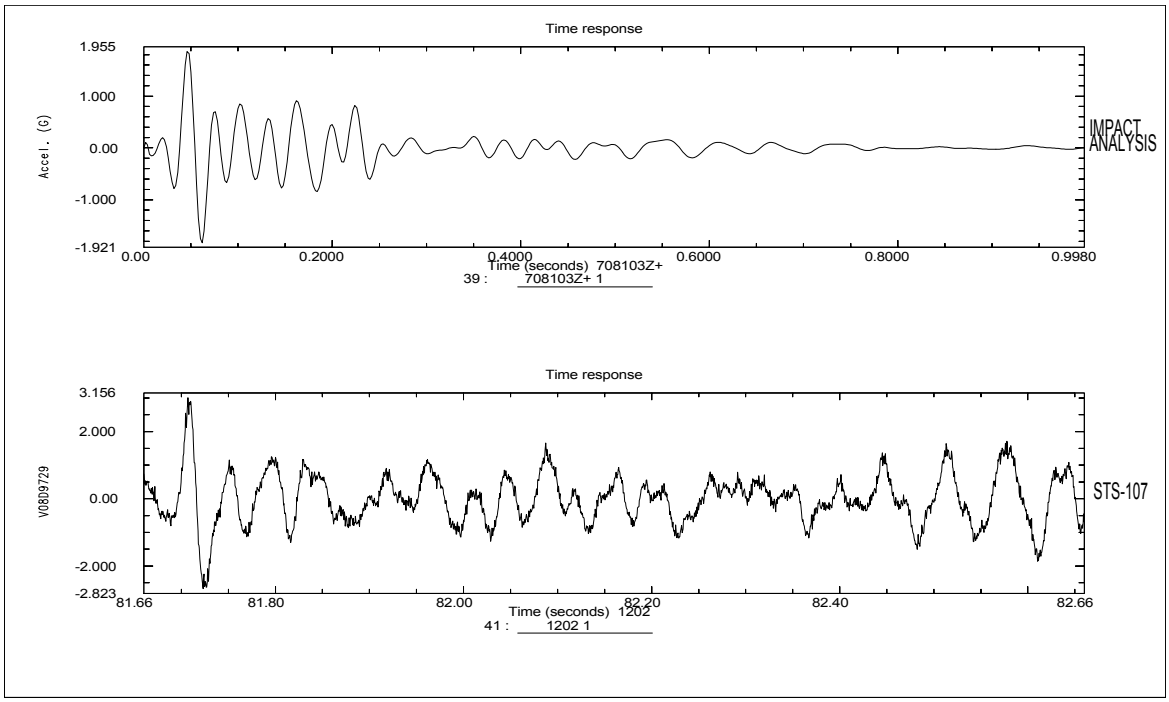

Figure 7.4-13 Comparison of Analysis and Flight Measurement

7.4.1.2 Flutter Assessment

A flutter assessment was made using wing and tail accelerometers. Previous flutter analysis had indicated the tail is the most critical component of the Orbiter for flutter instability. Flutter typically involves a coalescence of bending and torsion modes and is considered most critical near M=1. To determine if flutter had occurred during STS-107, PSD's from tail accelerometers were computed at various times during ascent. The results displayed in Figure 7.4-14 show distinct peaks for the 1st bending mode of tail at 3-4 Hz and the torsion mode at 10-11 Hz throughout the flight. This demonstrates that the mode coalescence did not occur and the tail was stable. Shown in Figure 7.4-15 are the filtered responses of the lower rudder. The raw accelerometer responses are filtered so that predominantly the bending and torsion responses are displayed. The figure illustrates that the response for critical modes always decayed after external disturbances. Also, the responses of the tail's bending and torsion mode are clearly visible, which verify that two modes did not coalesce and, consequently, the flutter instability did not occur.

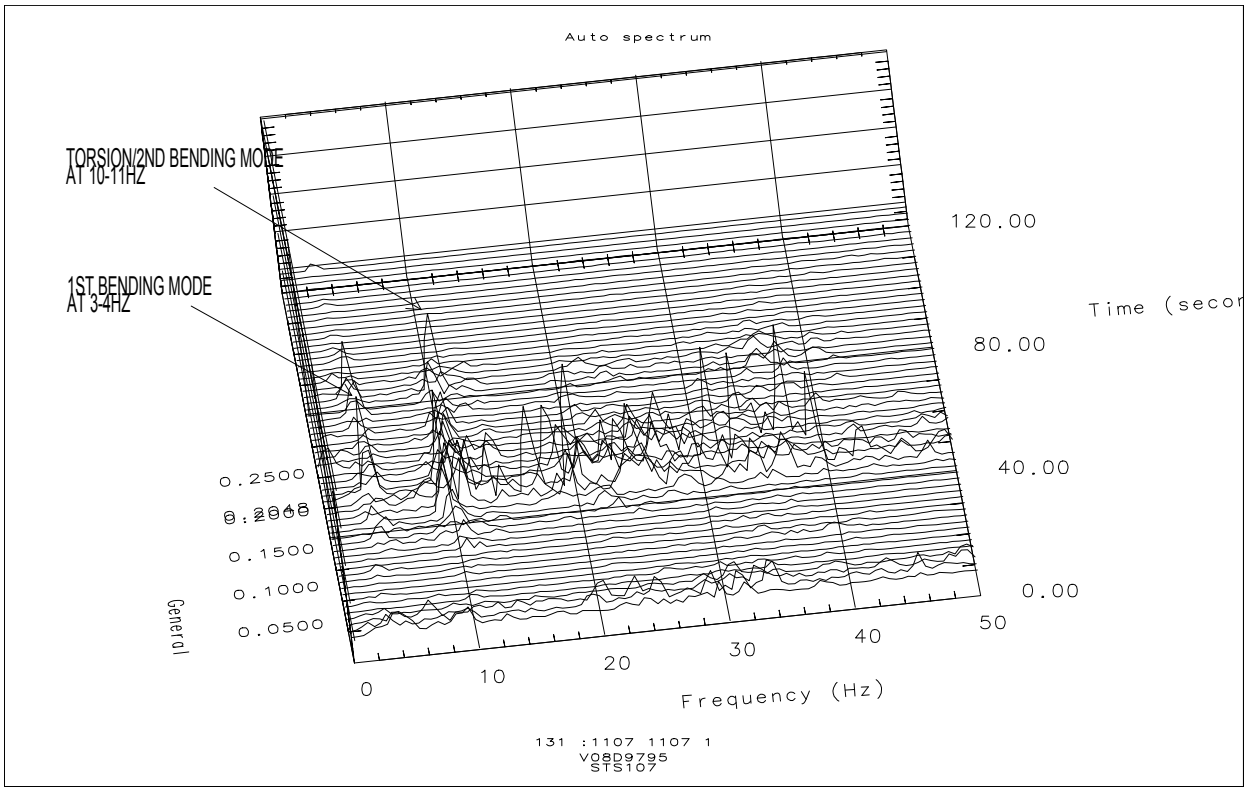

Figure 7.4-14 Vertical Tail Modes during STS-107

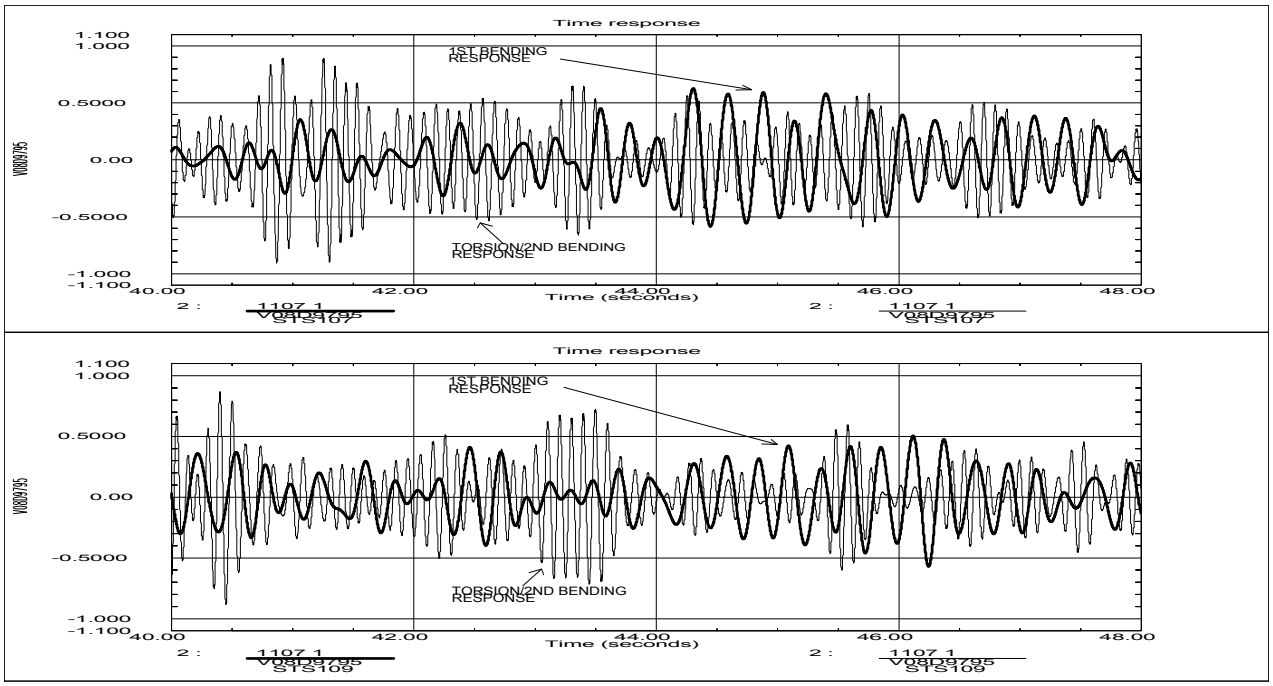

Figure 7.4-15 Filtered Response of Lower Rudder (STS-107 and STS-109)

For assessment of wing flutter instability, a similar process was employed. Presented in Figure 7.4-16 are the PSD's of the left outboard elevon accelerometer for STS-107 and STS-109. The distinct peaks for the 1st bending mode at ~6 Hz and torsion mode at ~8 Hz near M=1 are clearly visible. Thus, the mode coalescence did not occur for the wing during STS-107. The filtered responses shown in Figure 7.4-17 demonstrate the response of wing's bending and torsion modes did decay after aerodynamic disturbance, which confirms that the wing was far from flutter instability.

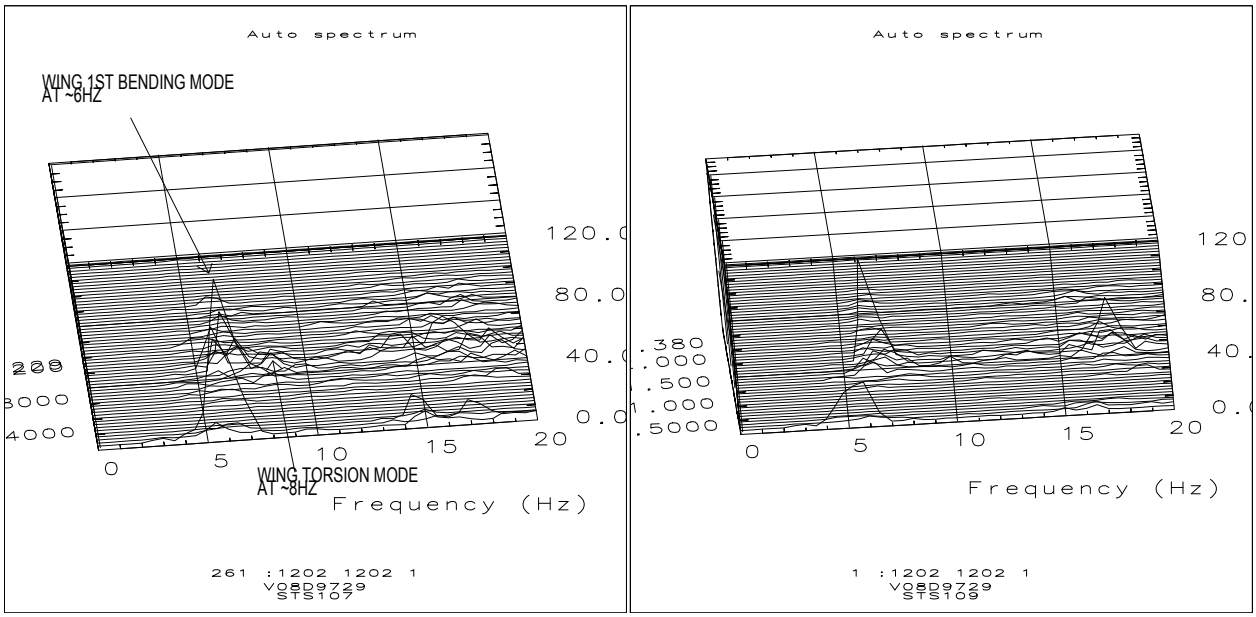

Figure 7.4-16 Wing Modes during STS-107 and STS-109

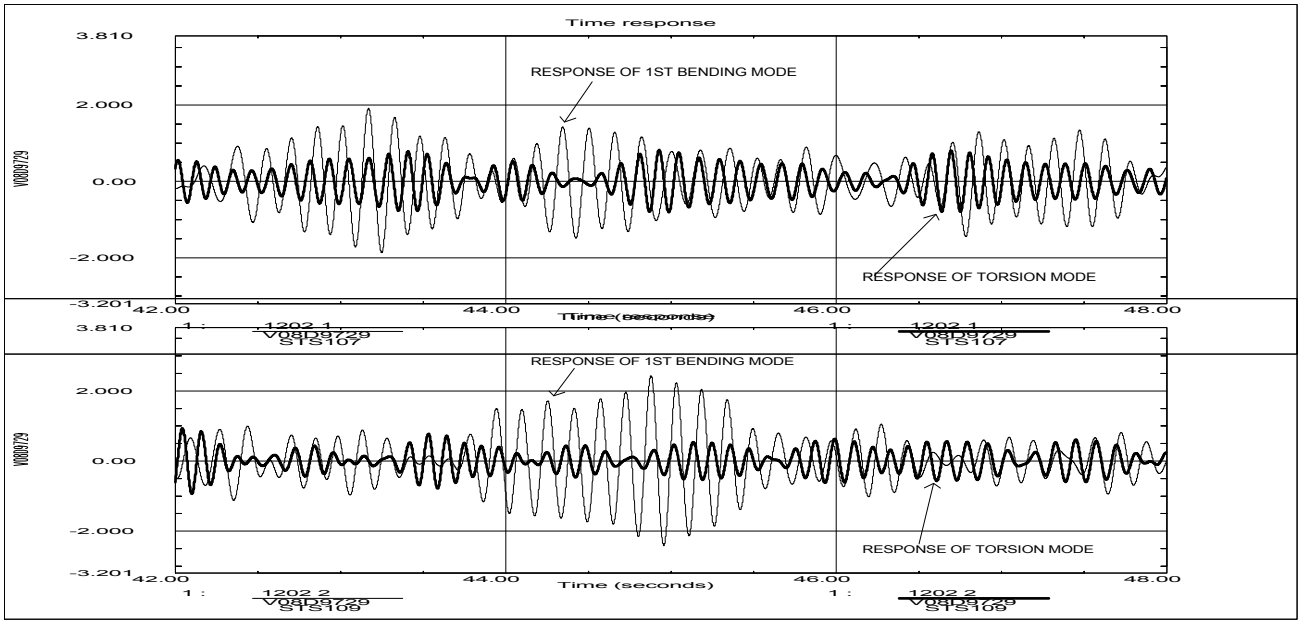

Figure 7.4-17 Filtered Response of Left Outboard Elevon (STS-107 and STS-109)

7.4.1.3 Strain Gage Response

The ascent strain gage data revealed the responses were very similar to STS-109. A comparison of typical gage response is shown in Figure 7.4-18. To compare the dynamic contents of the measurement, a 2-50 Hz band pass filter was applied to isolate the dynamic components. Plots shown in Figure 7.4-19 illustrate the response from two flights are very similar. The RMS values of strain shown in Table 7.4-2 also confirm that the overall level of dynamic strain is very comparable.

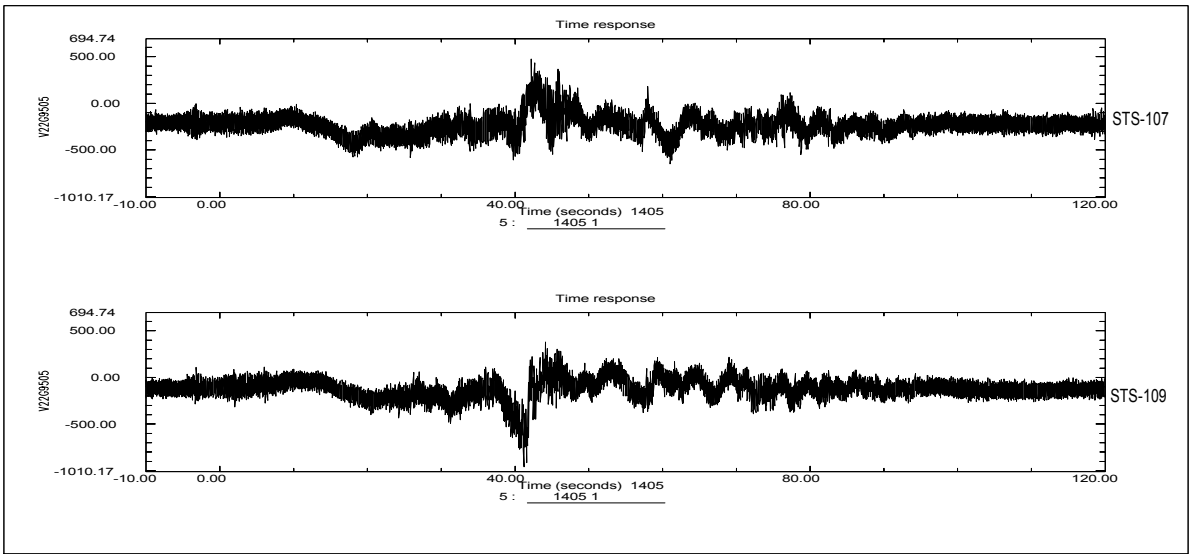

Figure 7.4-18 A Comparison of Strain Gage Response (Tail, Aft Spar Web)

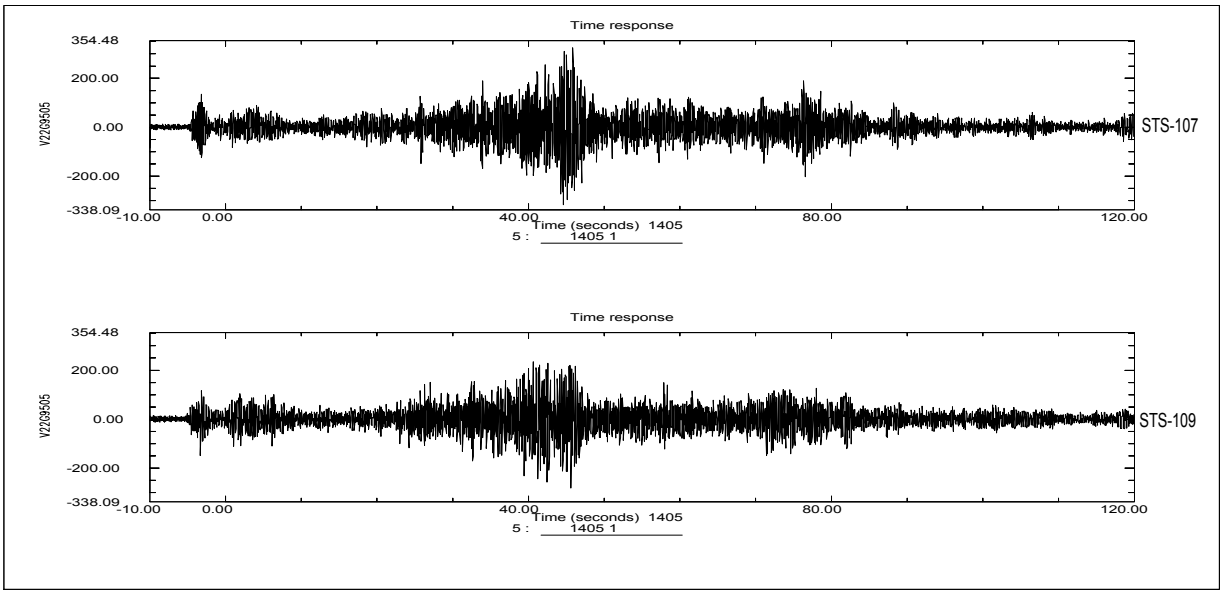

Figure 7.4-19 Dynamic Components of Strain Gage Response (Tail, Aft Spar Web)

Table 7.4-2 A Summary of RMS Values for Strain during Ascent

	T= 0-120 sec		T= 20-80sec.	
	STS107	STS109	STS107	STS109
V22G9501 A(V Fin, Aft Spar Web)	12.8	12.7	16.7	16.3
V22G9502 A(V Fin, Fwd Spar Web)	6.9	6.5	9.0	8.3
V22G9503A(V Fin, Aft Spar Web)	29.0	28.5	36.9	35.5
V22G9504A(V Fin, Fwd Spar Web)	8.9	8.3	11.7	10.9
V22G9505A(V Fin, Aft Spar Web)	45.1	41.5	59.6	53.6
V22G9506A(V Fin, Fwd Spar Web)	12.9	12.5	16.2	15.5
V35G9610A(Aft Fus, OMS Deck)	3.9	4.0	3.8	4.0
V35G9611A(Aft Fus, OMS Deck)	3.2	3.3	3.8	4.0
V35G9612A(Aft Fus, OMS Deck)	1.4	1.5	1.4	1.5
V35G9613A(Aft Fus, OMS Deck)	4.6	4.7	4.6	4.7
V35G9614A(Aft Fus, OMS Deck)	5.1	5.7	5.2	5.9
V35G9615A(Aft Fus, OMS Deck)	4.4	4.6	4.9	5.2
V35G9616A(Aft Fus, OMS Deck)	4.0	4.0	4.7	4.7
V35G9617A(Aft Fus, OMS Deck)	1.8	2.0	2.0	2.2
V35G9618A(Aft Fus, OMS Deck)	3.8	4.1	4.1	4.2
V35G9619A(Aft Fus, OMS Deck)	8.3	8.9	9.7	10.4
V35G9620A(Aft Fus, OMS Deck)	4.1	--	4.1	--
V35G9621A(Aft Fus, OMS Deck)	3.5	--	4.2	--
V35G9622A(Aft Fus, OMS Deck)	1.6	--	1.6	--
V35G9623A(Aft Fus, OMS Deck)	3.9	4.5	4.0	4.6
V35G9624A(Aft Fus, OMS Deck)	6.2	7.0	6.6	7.7
V35G9627A(Aft Fus, OMS Deck)	--	--	--	--
V23G9203A(L. Rud Hinge)	14.3	13.6	19.0	17.5
V23G9204A(L. Rud Hinge)	6.1	6.2	7.1	7.1
V23G9211A(L. Rud Hinge)	4.5	4.5	5.8	5.6
V23G9212A(L. Rud Hinge)	8.9	8.5	11.9	11.1
V23G9215A(L. Rud Hinge)	16.3	16.3	21.7	21.2
V23G9216A(L. Rud Hinge)	18.2	18.9	22.8	23.2
V23G9223A(R. Rud Hinge)	18.7	17.7	24.9	23.3
V23G9224A(R. Rud Hinge)	6.4	6.3	8.3	8.1
V23G9227A(R. Rud Hinge)	13.9	13.1	18.9	17.6
V23G9228A(R. Rud Hinge)	5.2	7.7	6.5	8.8
V23G9235A(R. Rud Hinge)	4.9	4.7	6.1	5.9
V23G9236A(R. Rud Hinge)	9.6	8.7	13.0	11.4
VO8G8041A(Heat Shield)	10.5	10.6	11.8	12.0
VO8G9091A(STN BHS Strut)	37.9	39.5	41.3	43.5

7.4.2 Descent

Although the overall level of acceleration during entry was small compared to ascent, accelerometer data were examined in detail to identify anomalous responses, which might correlate with events during entry. In particular, the left outboard elevon accelerometer (VO8D9729A) was thoroughly studied, since this was the only accelerometer on the left side of the wing. The responses of the accelerometer along with one on the right outboard elevon are shown in Figure 7.4-20. In the figure, responses following three particular events are of interest, thus, are studied in depth: Elevon activation at EI+223 sec., Transient responses at EI+496 and EI+502 sec., and Onset of signal saturation at EI+534 sec. (Note that frequent one-sided spikes are data anomalies and are not valid responses)

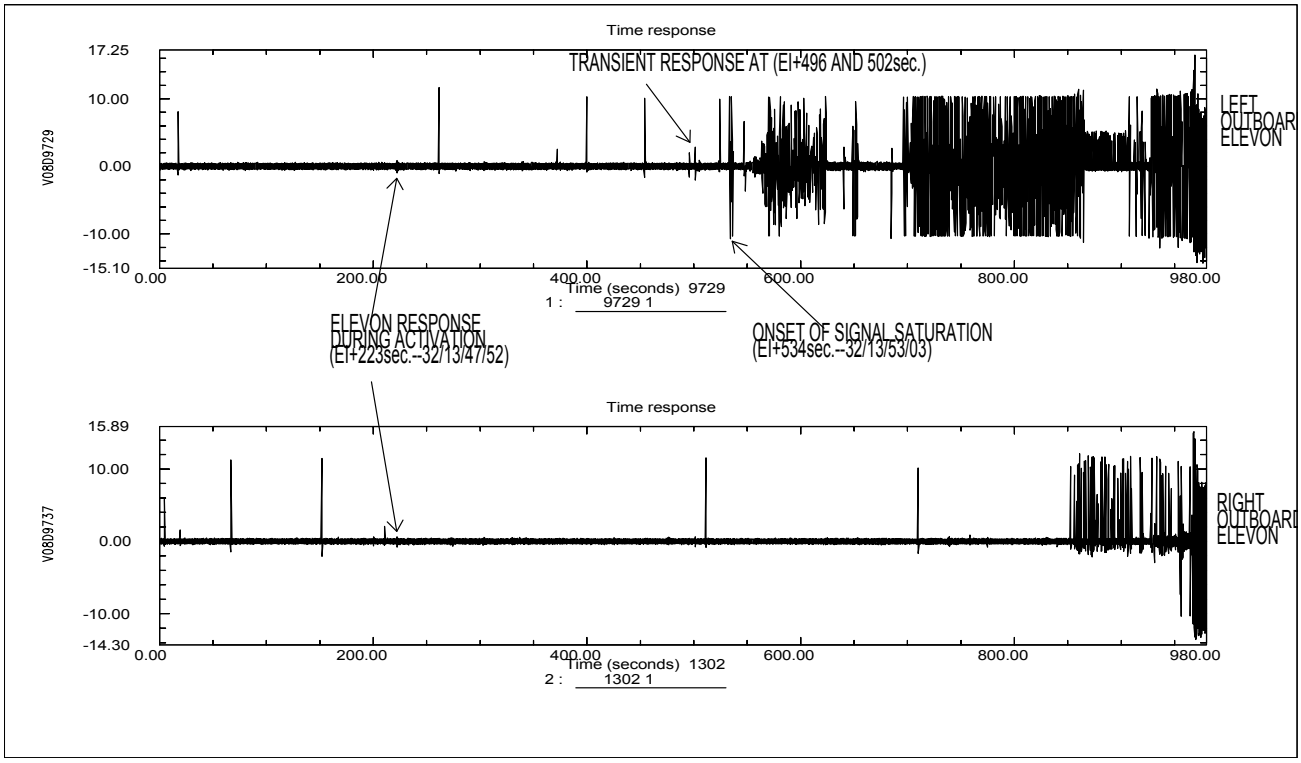

Figure 7.4-20 Left and Right Elevon Response During Entry (STS-107)

The detail plot of elevon response during activation is displayed in Figure 7.4-21. The 6 Hz response of the wing's 1st bending mode is clearly visible on both left and right outboard elevon channels. The presence of this mode verifies a proper operation of both accelerometers.

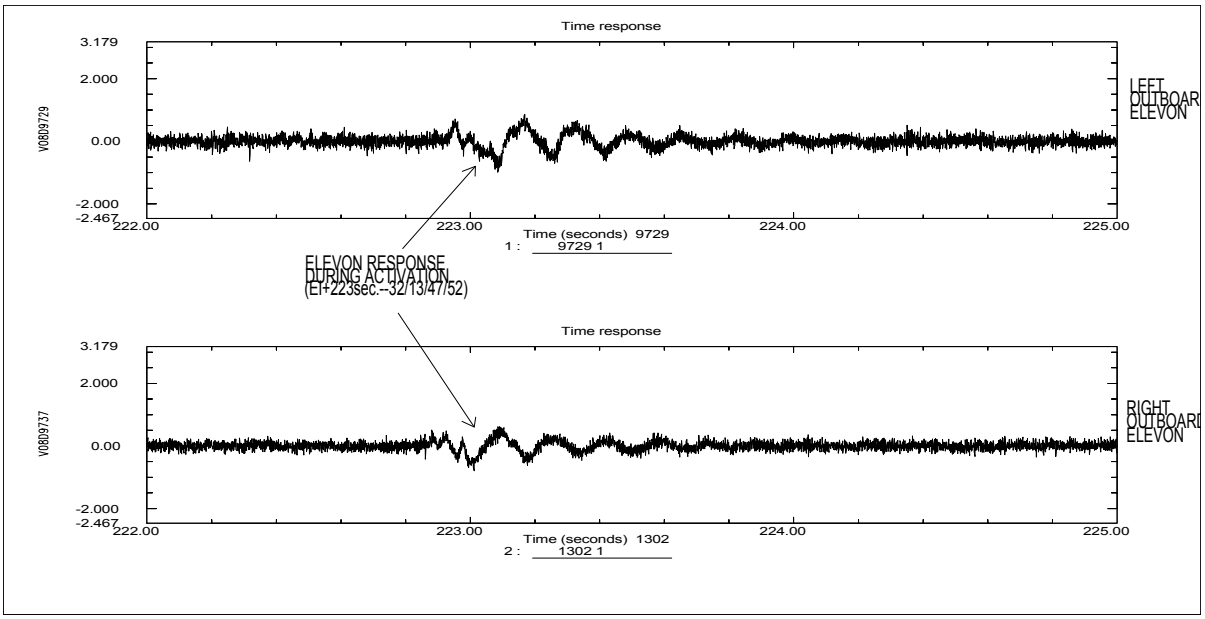

Figure 7.4-21 Elevon Responses during Elevon Activation at EI+223 sec

The second set of events occurred at EI + 496 and 502 seconds, which followed some type of external excitation. The transient response in Figure 7.4-22 was mainly noticeable for the left outboard channel. The PSD's (Figure 7.4-23) of the left outboard elevon channel following these disturbances confirm the existence of wing's 6 Hz bending and other wing/elevon modes. These times coincide with the RCS jet firings, however, similar type of transient response was not observed during other RCS jet firings.

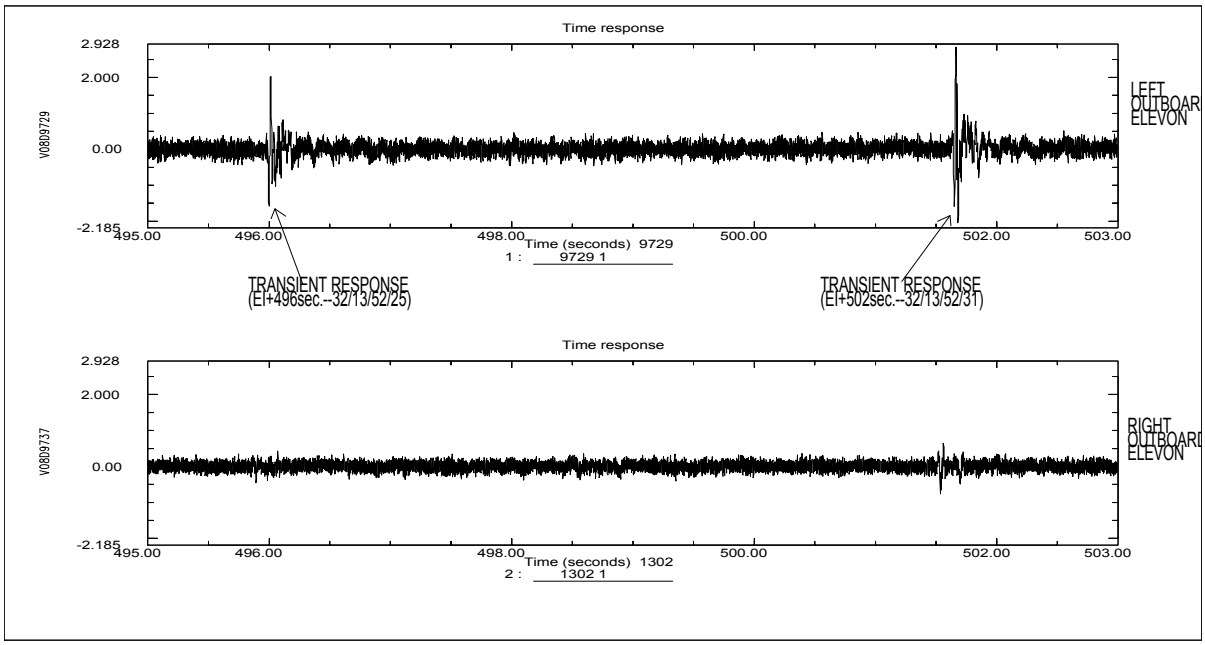

Figure 7.4-22 Transient Responses of Elevons at EI+496 and 502 sec.

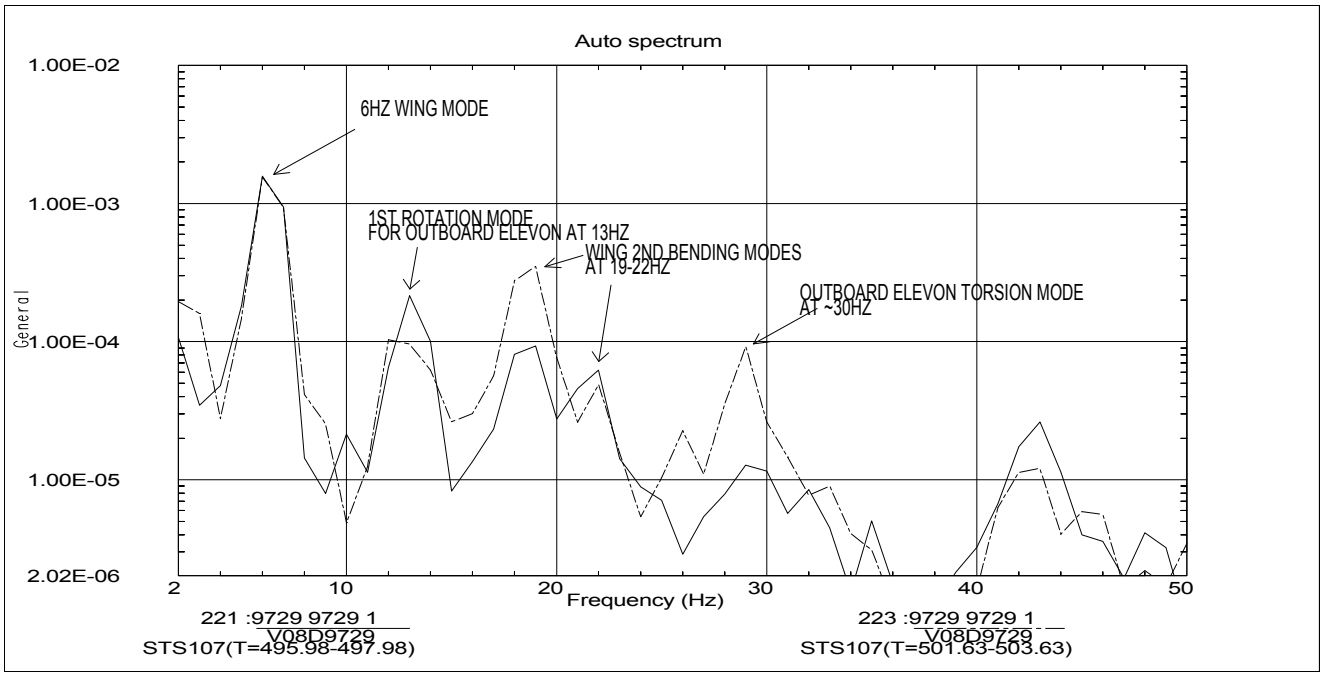

Figure 7.4-23 PSD's of Transient Response at EI+496 and EI+502 sec.

The third event observed at EI+534 indicates an onset of signal saturation for the left outboard channel. The accelerometer reading reached the maximum instrumentation range of 10G (Figure 7.4-24). The displacement computed (Figure 7.4-25) using the acceleration data results in an unrealistic number, which indicates a bad signal. The FFT's computed at various time segments during entry is shown in Figure 7.4-26. The figure illustrates a notable absence of 6 Hz response for the left outboard elevon channel after the onset of signal saturation, while the right outboard data exhibited 6 Hz response beyond EI+534 sec. This finding indicates malfunction of the left outboard channel past this time period.

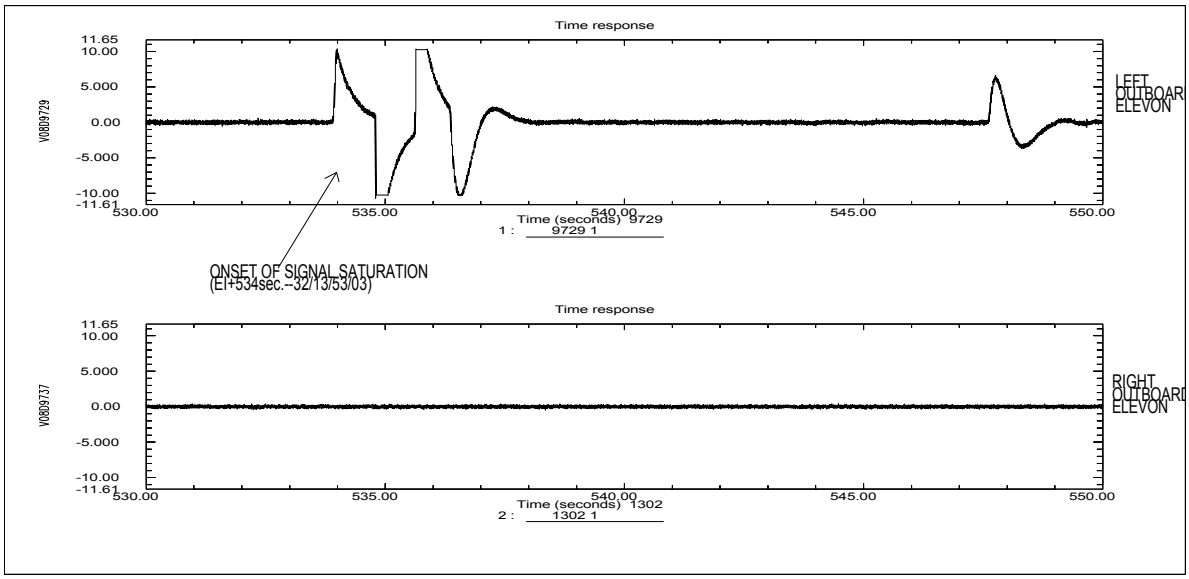

Figure 7.4-24 Onset of Signal Saturation for Left Outboard Elevon at EI+534 sec.

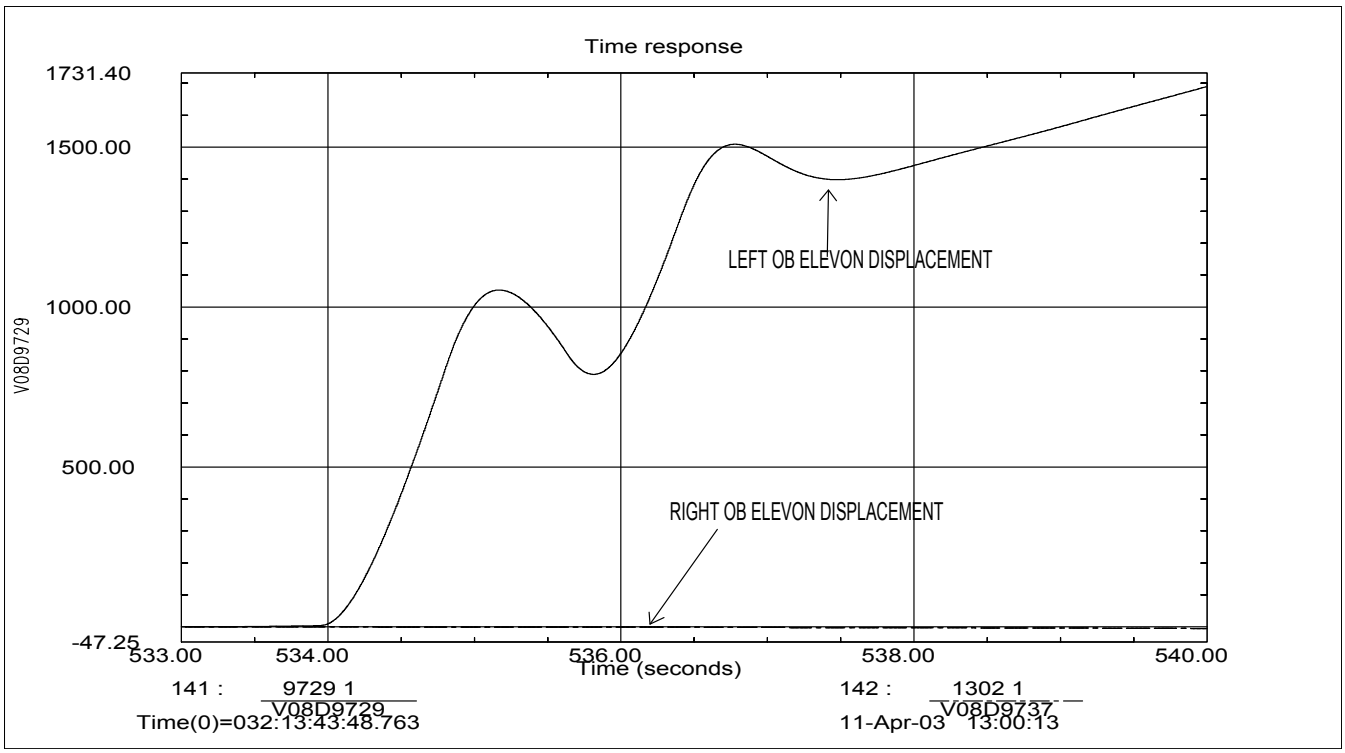

Figure 7.4-25 Displacement of Outboard Elevon Locations

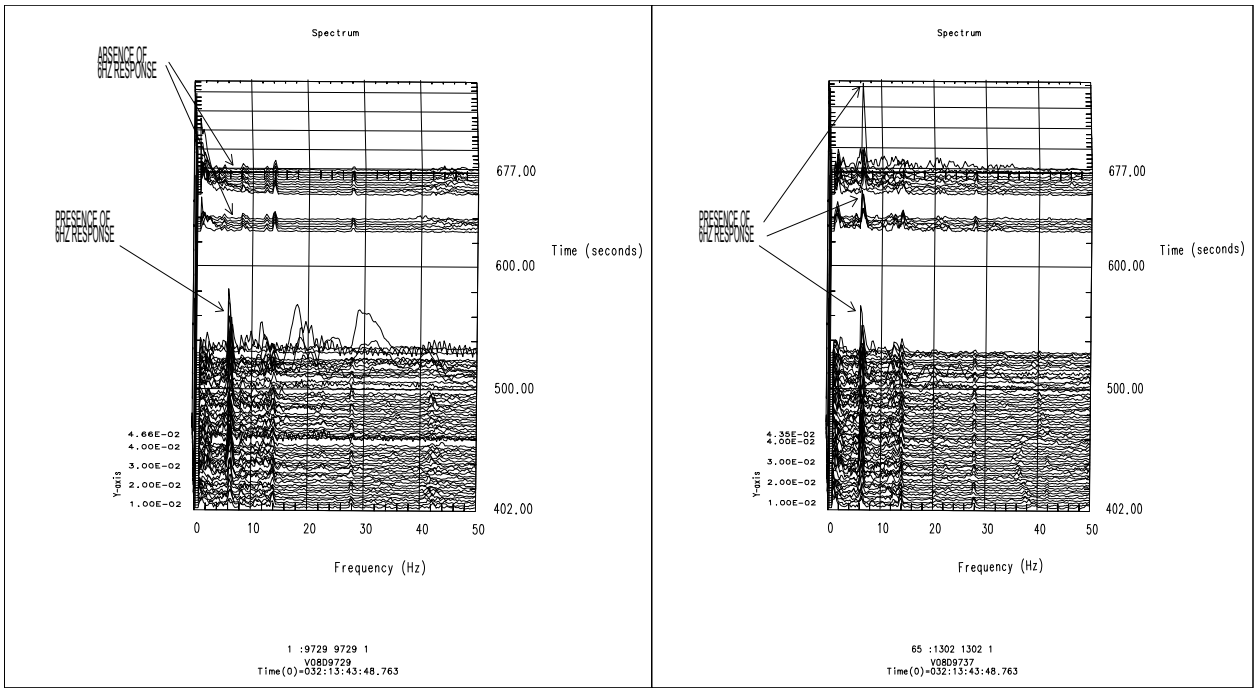

Left Outboard Elevon Right Outboard Elevon

Figure 7.4-26 FFT of Left and Right Outboard Elevon Responses

7.4.2.1 Strain Gage Data Evaluation

Typical strain gage responses are shown in Figure 7.4-27. For the most of entry phase, the strain gage channels are in "snap-shot" mode, where the readings are recorded for one minute and turned off for 4 minutes. Therefore, the only reading during the one minute period (where the strain level is near zero) is valid. In general, frequent one-sided spikes (which are not valid response and should be ignored) were observed during STS-107, which indicate the data quality was not quite as good. Also, extremely low strain level during "on" period makes the accurate assessment of the gage response very difficult. Only qualitative assessments are made. A PSD comparison for typical STS-107 and STS-109 strain data recorded at similar time period is shown in Figure 7.4-28. The figure illustrates the spectral contents are pretty similar. The large amplitude near 20 Hz and 40 Hz for STS-107 is due to the one-sided spikes, thus should be ignored.

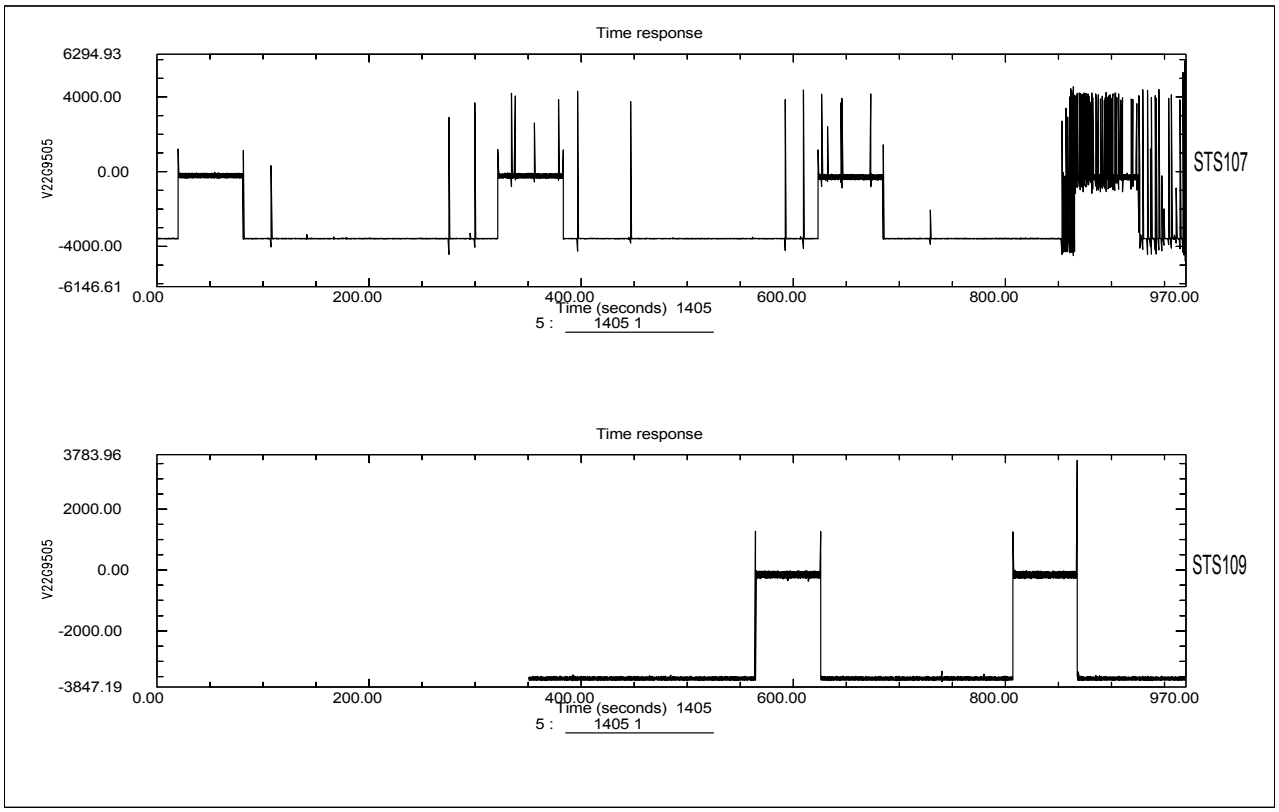

Figure 7.4-27 Strain Gage Response during Entry (Tail Aft Spar Web) STS-107 VS. STS-109

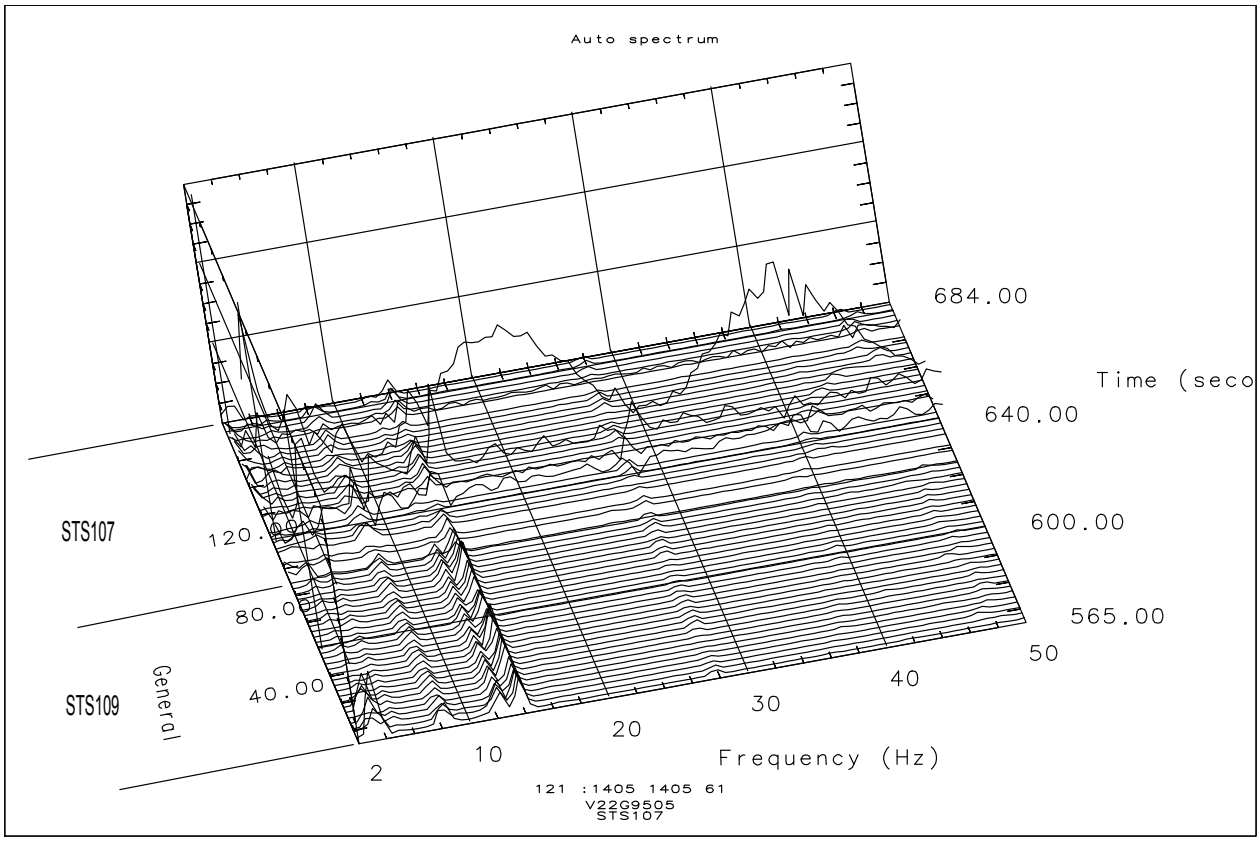

Figure 7.4-28 PSD Comparison of Strain Gage Response During Entry (STS-107 VS. STS-109)

7.4.3 Summary

Accelerometer and high sample rate strain gage responses were evaluated during ascent and entry phases of the STS-107 flight. The magnitude and the frequency contents of the measured acceleration and strain are considered within the family experience based on PSD's and computed RMS values. The excitation of the higher tail modes at 40-42 second period during ascent is similar to what's been experienced during STS-87, thus is considered normal. The distinct peaks observed for the bending and torsion modes of the wing and the tail demonstrate the flutter instability did not occur during ascent. The in-depth study of the left outboard elevon acceleration from flight and analysis using FEM models indicate the peak response observed at ~82 seconds could have come from the debris impact in addition to other aerodynamic disturbances. An absence of additional accelerometers on the left wing make it difficult to determine with certainty. During descent, the accelerometer data revealed the malfunction of the left outboard elevon accelerometer channel starting at EI+534 seconds

7.5 Feasible Wing Deformation Prior to Loss of Signature

7.5.1 Analysis Objective

The objective of the wing deflection analysis can be categorized into three distinct phases:

- Initial - the first analytical purpose was to assess OV-102 for gross left wing failure due to localized weakening of structural members. This analysis was performed during the early stages of the STS-107 accident investigation. Weakened structural members were assumed to occur from localized thermal heating due to damaged tile and RCC panels. This was considered the first approximation in determining the wing response due to various structural failure scenarios.
- Extended - the second analytical purpose was to expand the damage scenarios to include larger areas of the forward and intermediate wing sections. The analysis attempted to quantify the effects of losing major portions of the wing structure, instead of localized failure of structural elements. For this analysis, complete bottom to top cuts were made at critical structural locations around the main landing gear door wheel well, the wing leading edge spar and the honeycomb skin panels on the top and bottom wing surfaces. Structural member loss was assumed to occur from hot gas ingestion into the wing cavity; however, thermal degradation on the non-failed structures was assumed to be negligible.
- Refined - as the investigation continued, the analysis shifted from investigating various damage scenarios to cases that reflected the most probable events occurring during STS-107. The primary purpose of this analytical phase was to support an integrated analysis of the wing deformation with the aerodynamics group. The damage model was refined to represent a thermal breach at RCC panels 8 & 9, with subsequent hot gas flow into the intermediate wing cavity. Hot gas ingestion was assumed to lead to a loss of the intermediate wing tube struts and the upper wing skin panels. Also considered in this case was thermal weakening of the cavity walls, skins and rib caps.

7.5.2 OV-102 Wing Finite Element Model

A NASTRAN, OV-102 finite element model (FEM) was used to perform the analyses. An illustration of this model is shown in Figure 7.5-1. MSC-PATRAN was utilized for pre-processing of the model and post-processing of the results. The NASTRAN FEM was created from the original ASKA FEM and was previously used as part of the Performance Enhancement (PE) certification analyses, circa 1996. Due to the size and complexity of the FEM, only the wing and portions of the aft and mid fuselage were used. The mid-fuselage and the aft fuselage structure are present to allow for redistributing wing root reactions and deflections.

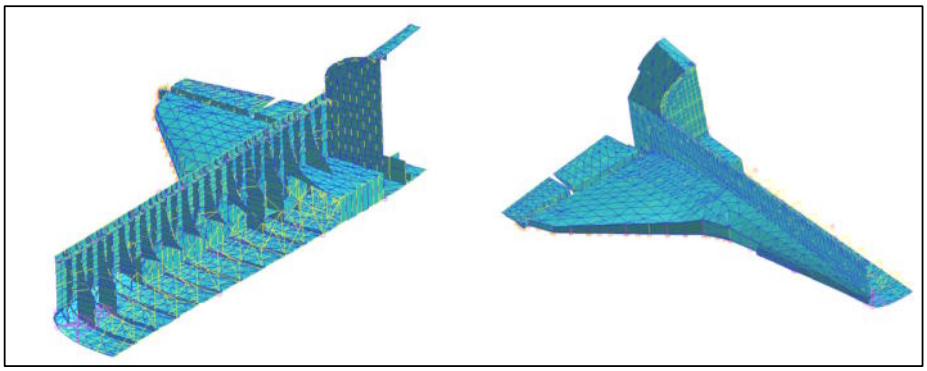

Figure 7.5-1 OV-102 Wing FEM

7.5.3 Load Cases

During the recent contingency abort project, a computational fluid dynamics (CFD) program was used to create a distributed aero pressure database for loads evaluation. This data provided Orbiter aerodynamic loads up to Mach 15. Subsequent to STS-107, and in support of the investigation, the database was expanded beyond Mach 18 in order to determine wing loads similar to those that occurred prior to the breakup. A portion of the Mach 18 expanded database is shown in Table 7.5-1. The dynamic pressure (Qbar) in the table is 70 psf and that angle of attack (Alpha) is 40 °. The load set that most closely resembles STS-107 is for an elevon angle of –2.98 degrees (De). This load set is highlighted in the table.

Table 7.5-1 Wing Loads, M=18

Wt	Xcg	Mach	Qbar	Altitude	Alpha	De	Dbf	Nx	Nz	Indicator		Wing Mx			Wing My			Wing Sz		
										Wing Mx	Wing Sz	Total	Aero	Inertial	Total	Aero	Inertial	Total	Aero	Inertial
234215	1078.3	18	70	207175	40	-11.37	11.30	0.05	0.92	0.267	0.181	4691114	6447031	-1755917	5296937	6648960	-1352023	39307	54275	-14968
234215	1078.3	18	70	207175	40	-10.40	10.60	0.05	0.92	0.253	0.181	4790338	6547683	-1757345	5229462	6582854	-1353391	39870	54851	-14980
234215	1078.3	18	70	207175	40	-9.64	9.90	0.05	0.92	0.243	0.181	4871794	6629995	-1758201	5174314	6528539	-1354225	40336	55324	-14988
234215	1078.3	18	70	207175	40	-9.02	9.20	0.05	0.92	0.233	0.181	4945690	6704639	-1758949	5124006	6478890	-1354883	40761	55755	-14994
234215	1078.3	18	70	207175	40	-8.40	8.50	0.05	0.92	0.223	0.182	5017525	6777221	-1759696	5075182	6430722	-1355540	41173	56174	-15001
234215	1078.3	18	70	207175	40	-7.78	7.80	0.04	0.92	0.214	0.182	5087389	6847831	-1760442	5027778	6383975	-1356196	41574	56581	-15007
234215	1078.3	18	70	207175	40	-7.16	7.10	0.04	0.92	0.205	0.182	5155312	6916500	-1761188	4981776	6338628	-1356853	41962	56976	-15013
234215	1078.3	18	70	207175	40	-6.54	6.40	0.04	0.92	0.196	0.182	5221298	6983232	-1761934	4937171	6294680	-1357509	42339	57359	-15020
234215	1078.3	18	70	207175	40	-5.92	5.70	0.04	0.92	0.187	0.182	5285425	7048106	-1762682	4893914	6252080	-1358166	42705	57731	-15026
234215	1078.3	18	70	207175	40	-5.48	5.00	0.04	0.92	0.181	0.182	5331767	7094767	-1763000	4862904	6221390	-1358486	42970	57999	-15029
234215	1078.3	18	70	207175	40	-5.10	4.30	0.04	0.92	0.176	0.183	5372428	7135619	-1763190	4835843	6194549	-1358706	43203	58233	-15030
234215	1078.3	18	70	207175	40	-4.74	3.60	0.04	0.92	0.171	0.183	5410271	7173639	-1763369	4810722	6169622	-1358900	43419	58451	-15032
234215	1078.3	18	70	207175	40	-4.44	2.90	0.04	0.92	0.166	0.183	5441861	7205389	-1763528	4789779	6148810	-1359031	43600	58633	-15033
234215	1078.3	18	70	207175	40	-4.14	2.20	0.04	0.92	0.162	0.183	5472515	7236202	-1763687	4769510	6128672	-1359163	43775	58810	-15035
234215	1078.3	18	70	207175	40	-3.84	1.50	0.04	0.92	0.158	0.183	5502245	7266091	-1763846	4749910	6109204	-1359294	43945	58981	-15036
234215	1078.3	18	70	207175	40	-3.54	0.80	0.04	0.92	0.157	0.183	5531060	7295065	-1764005	4730971	6090396	-1359426	44109	59146	-15037
234215	1078.3	18	70	207175	40	-3.25	0.10	0.04	0.92	0.157	0.183	5557818	7322008	-1764190	4713405	6072962	-1359557	44261	59300	-15039
234215	**1078.3**	**18**	**70**	**207175**	**40**	**-2.98**	**-0.60**	**0.04**	**0.92**	**0.157**	**0.183**	**5598759**	**7363171**	**-1764412**	**4685453**	**6045141**	**-1359688**	**44500**	**59540**	**-15041**
234215	1078.3	18	70	207175	40	-2.71	-1.30	0.04	0.92	0.157	0.183	5643147	7407781	-1764634	4655014	6014834	-1359820	44760	59802	-15043

A certification load case at Mach 18 does not exist for the Orbiter since structural significant loading does not occur during this portion of the descent phase. At the time of PE, descent load cases used for analyzing the Orbiter only extended to Mach 1.5. After STS-107, it was decided that creating a Mach 18 load case was not feasible due to the time constraint; therefore, it was decided that a currently existing load case would be used. Determining the applicable case was based upon two criteria: that the environment needed to be supersonic and that the wing shears and moments between the two load cases were of similar magnitude. A steady pitch terminal area energy management (TAEM) load case was selected. The aerodynamic loads for the selected case, TA2130, are shown in Table 7.5-2. Note that the wing moment values are approximately three times the aerodynamic values seen during STS-107. Root shear values are roughly 2 times the STS-107 conditions. Results, such as deflections and stresses, from this case need to be divided by 2 to approximate the STS-107 conditions just prior to vehicle break-up. It should be noted that the wing is designed to withstand root moments (Mx) up to a limit value of 32 million in-lbs, with a factor of safety of 1.4 above this load; the maximum loads for STS-107 entry were below 20% of the ultimate capability of an intact wing.

Table 7.5-2 Analytical Load Case

Report Condition	Mach	Description	Q (psf)	S/B (deg)	B/F (deg)	Elv (deg)	a (deg)	NZ (g's)	Mx	My	Sz
TA2130	**1.50**	**STEADY PITCH**	**375**	**55**	**16.57**	**-14.32**	**8.28**	**1.21**	**14,732,017**	**12,493,593**	**94,399**

7.5.4 Analytical Procedure

7.5.4.1 Damage Simulation

In order to simulate damage to the Orbiter wing, the modulus of elasticity for each damaged FEM element was reduced. This removed the stiffness of the elements, thus degrading the load carrying capability of the structural members. During the initial analysis phase, the modulus was reduced to 10% of nominal value for failed members. Reducing the stiffness by an order of magnitude was appropriate since the purpose was to gain an understanding of load distribution through the wing due to localized damage. The extended analytical phase; however, used a modulus of elasticity reduced to 1% of nominal value. This was done in order to help ensure that the damaged FEM elements were having no effect on the results. During the refined analytical phase, wing structures that were being heated, but not failed, were also reduced in stiffness. Wing honeycomb skin panels were reduced to 50% of nominal modulus value. This simulated de-bonded inner face-sheets. Other primary structural members, such as ribs, spars and skin panels away from the damage, but still exposed to thermal extremes were reduced to 30 % of modulus.

7.5.4.2 Screening Criteria

After running and obtaining results for the damage cases, a generalized screening process was used to find structures where load redistribution showed a significant increase. The screening was necessary to post-process large amounts of data in a reasonable amount of time and to provide a consistent methodology for the different analysts working on the project to employ.

The screening process consisted of comparing the stresses, loads and displacement for an undamaged element to a damaged element. A ratio of damaged to undamaged results was developed for each element and node within the wing. The definition of the load ratio is shown below:

$$R_{load} = \frac{\text{Damaged}}{\text{Undamaged}}$$

A large ratio does not necessarily equate to a significant change. A relatively small change could easily result in a large load ratio if the magnitudes of the data were small. As an example, a deflection changing from 0.001 inch to 0.002 inch would represent a 100% increase; however, due to the low magnitude, the increase would not represent a significant shift. Similarly, certain stress and load levels, depending on the magnitude, could be rationalized to be inconsequential. Table 7.5-3 shows the screening criteria that were established to reduce the amount of post-processed data.

Table 7.5-3 FEM Result Screening Criteria

FEM Entity	Data Type	Screening Criteria		Comment
		Load	Ratio	
Nodal	Displacement	--	> |15%|	--
Element	Stress	> 5000 psi	> |1.4|	Element types: CROD, CTRIA, CTRIA, CQUAD, CSHEAR
Element	Force	> 500 lbf	> |1.4|	Element types: CROD

7.5.4.3 Sub-Structuring

Wing elements and nodes were “sub-structured” into groups for comparative purposes. By organizing the structure into manageable groups, quicker conclusions could be drawn as to load re-distribution and deflections of the wing. Table 7.5-4 shows the sub-structure identification names associated with the associated portions of the model.

Table 7.5-4 Sub-Structured Identification

Location	Data Type	Sub-Structure ID
Leading Edge	Displacement	global_disp_LE
Leading Edge	Stress, Force	global_elem_LE
Fuselage to Wing Interface	Force	global_elem_IF
Global Wing Beams	Stress, Force	global_elem_Beams
Web Elements Inboard of Y_O198	Stress	global_webs_quad4 global_webs_tria3
Global Wing Nodes	Displacement	global_disp_WG

The first two sub-structured groups in Table 7.5-4 are for the wing leading edge (WLE) spar. Refer to Figure 7.5-2 and Figure 7.5-3 for the locations of these elements and nodes. The groups expand from panel 6, just forward of the Xo1040 spar, to the Xo1307 spar. The WLE was sub-structured separately from the rest of the wing due to the significance of the WLE in this investigation.

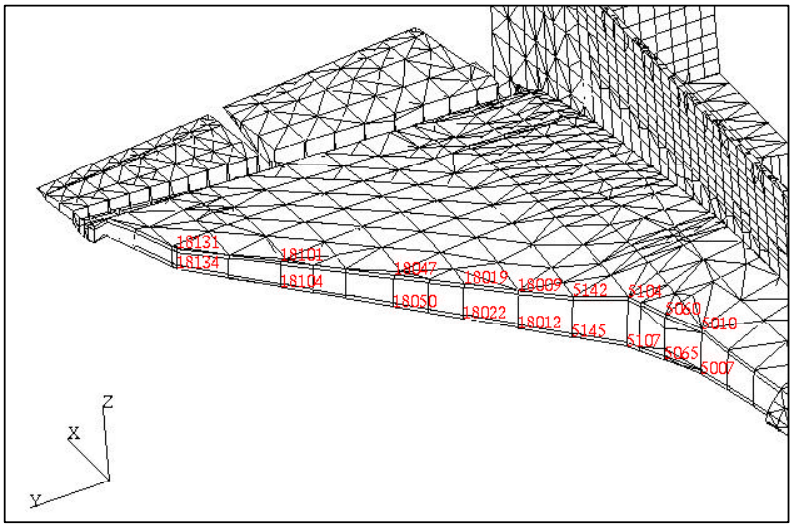

Figure 7.5-2 WLE Nodes

Only selected nodes along and the top and bottom of the WLE were sub-structured. Nodes were selected in order to provide an overall view of deflections along the WLE; therefore, a smaller sampling was appropriate. Similarly, only the WLE webs were selected for this sub-structured group. This was done in order to obtain an overall idea of the WLE load distribution as opposed to the rest of the wing.

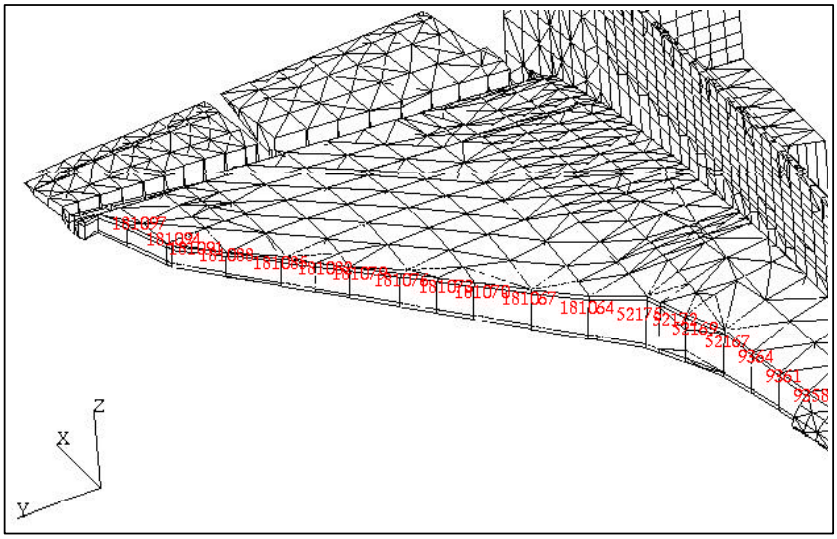

Figure 7.5-3 WLE Panel Elements

The wing torque box attaches to the wing carry thru (WCT) structure at locations Xo1191, Xo1249, Xo1307 and Xo1365. Additional bolts are located along the upper skin contour between the major spar attachments. The upper wing-to-WCT are loaded in tension and the lower wing-to-WCT is made through shear splices. Beam elements representing the wing interface bolt locations were sub-structured into a separate group. Figure 7.5-4 shows these elements and the location relative to the vehicle.

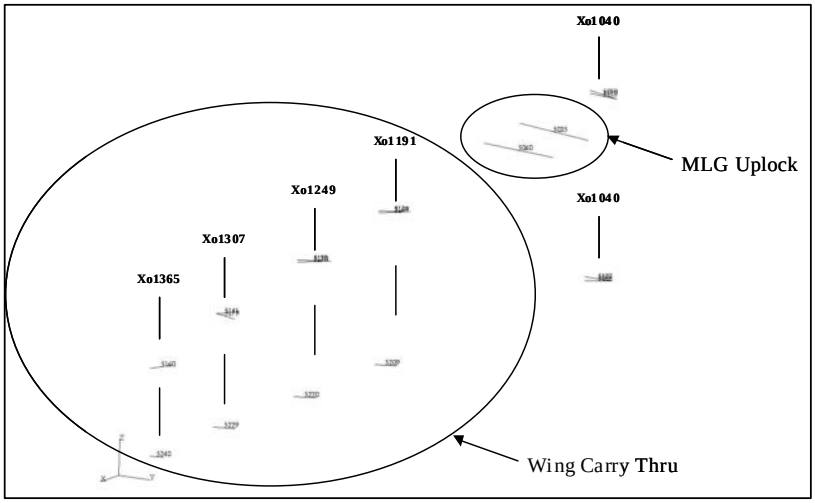

Figure 7.5-4 Wing-to-Fuselage Interface Elements

Due to criticality of the wing beam elements, most all were sub-structured for post-processing. These elements, shown if Figure 7.5-5, spanned the entire wing and included the glove area. Some areas, such as the main landing gear door hinges, were not included since damage would not produce a large effect to the wing.

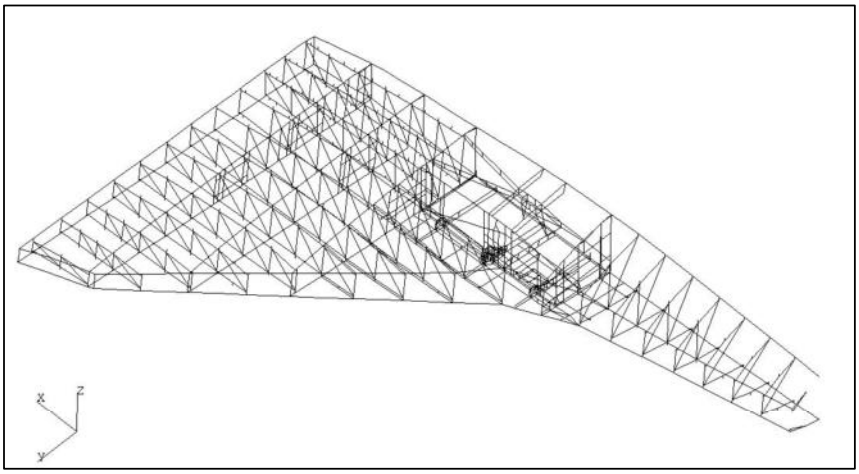

Figure 7.5-5 Wing Beam Elements

The wing model consists of a large amount of web elements. Early on in the analysis, it was decided that the beam elements provided good coverage for load distribution for the overall wing. This included load distribution through skin panels and spar webs. Therefore, to help limit the amount of elements data for post-processing, only the webs inboard of Yo198 would be sub-structured as being of particular interest relative to outboard rib webs. This group is shown in Figure 7.5-6. The X-station locations of the web elements spanned from Xo1010 to Xo1307.

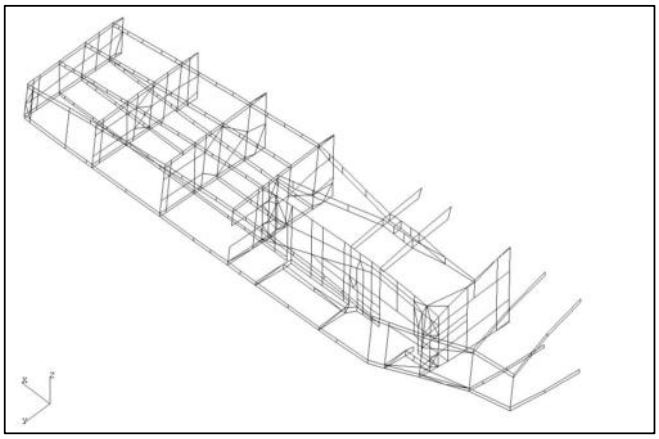

Figure 7.5-6 Inboard Wing Web Elements

As with the wing beam elements, all wing nodes were sub-structured. An illustration is provided in Figure 7.5-7. These groups of nodes were used to obtain an understanding of wing deflections based upon the various damage cases.

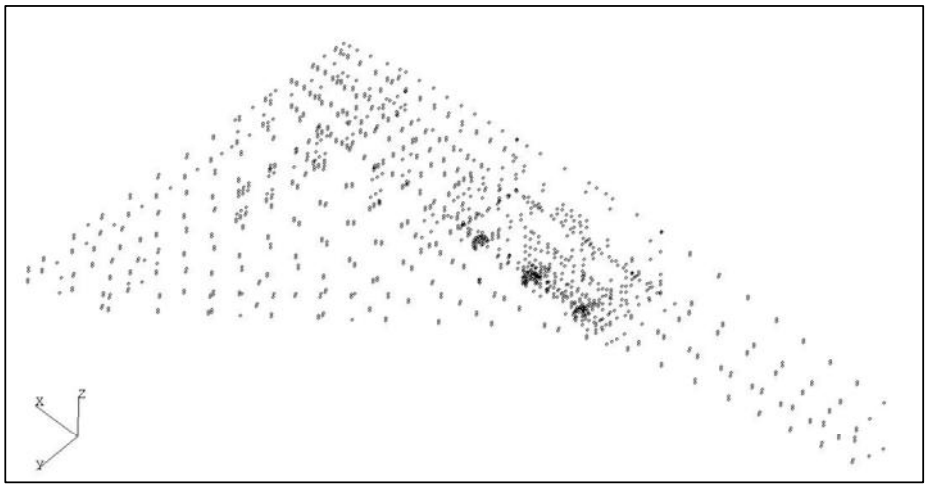

Figure 7.5-7 Wing Nodes

7.5.4.4 Post-Processing Tools

Two separate in-house Excel utilities were used for post-processing the analysis data. One utility reads the NASTRAN data output files for each damage case and creates separate files that categorizes results based upon the sub-structured elements. The second utility compares the results from each sub-structured data file to the undamaged results. Each utility was written in Visual Basic and provide a consistent and quick method for screening the sub-structured element by the criteria shown in Table 7.5-3.

7.5.5 Analysis Results

7.5.5.1 Initial (Small) Damage Analysis

The initial phase of the wing analysis attempted to assess the impact of localized skin, spar and rib damage to an overall effect on the wing. The analysis was performed for thermally weakened structure in locations deemed to be structurally significant. The screening criteria provided in Table 7.5-3 were used to determine wing areas where stresses, forces and displacements showed a significant increase in deflection and load.

The locations studied, along with the corresponding case files, are shown in Table 7.5-5. Most of the damaged areas are located in the intermediate wing with some WLE locations forward of the Xo1040 spar.

Table 7.5-5 Damage Locations, Initial Damage Failure Analysis

Case File	Location Studied
dam1191_1	Xo1191 lower spar cap and bottom skin aft of MLG well, aft, outboard corner
damle_1	MLG fwd hinge fitting, adjacent bottom skin and leading edge lower cap
damle_2	MLG fwd hinge fitting, adjacent bottom skin and leading edge lower cap and web to upper cap
damtube_1	Removed fwd diagonal truss tube from Yw198 rib (Elem 5812)
damtube_2	Removed fwd vertical truss tube from Yw198 rib (Elem 5561)
dis1191L	Disconnected Xo1191 spar cap and attached elements from mid-fuselage
dis1249L	Disconnected Xo1249 spar cap and attached elements from mid-fuselage
dis1307L	Disconnected Xo1307 spar cap and attached elements from mid-fuselage
dis1365L	Disconnected Xo1365 spar cap and attached elements from mid-fuselage
yo167_01	Yo167 rib lower spar cap at Xo1040 bulkhead
yo167_02	Yo167 rib lower spar cap at near door hinge point 1
yo167_03	Yo167 rib lower spar cap at near door hinge point 3
yo167_04	Yo167 rib lower spar cap at Xo1191bulkhead
yo167_05	Yo167 rib lower spar cap at near door hinge point 2
x1040y167-Damage1	Intersection Xo1040 spar and Yo167 rib at the lower wing surface

Table 7.5-6 lists the results for the initial damage failure analysis. As can be seen, the relative stress/load ratios show reasonable increases in element forces, stresses and displacements. The maximum load increases occurred for case damle_2. Wing beam elements showed a maximum increase 3.06 for case damle_2; however, the magnitude of the beam force was lower than the certified design load. The maximum wing-to-fuselage interface forces show a maximum increase of 8%. Based upon the capability of the interface bolts, an 8% increase is not considered significant. Maximum displacement was on the order of 39%. This was from a damaged element and was not considered realistic.

Table 7.5-6 Damage Locations, Initial Damage Failure Analysis

Case File	Maximum Load Ratio Results			
	Beam Force	Displ	LE Stress	IF Force
dam1191_1	1.54	1.03	1.02	1.08
damle_1	1.68	1.20	1.03	1.04
damle_2	3.06	1.39	1.16	1.08
damtube_1	2.29	1.08	1.07	1.02
damtube_2	1.72	1.03	1.02	1.02
dis1191L	2.00	1.17	1.05	1.06
dis1249L	2.00	1.17	1.01	1.02
dis1307L	2.90	1.23	1.00	1.03
dis1365L	1.06	1.06	1.00	1.01
yo167_01	1.58	1.01	1.00	1.00
yo167_02	2.18	1.01	1.00	1.01
yo167_03	1.41	1.01	1.00	1.01
yo167_04	--	1.01	1.00	1.01
yo167_05	1.92	1.01	1.00	1.00
x1040y167-Damage1	1.76	1.05	1.00	1.01

For the six separate locations along the Yo167 bottom rib cap, surrounding skins and web were checked for the effects of thermal degradation. Five of the damage locations were assessed along the Yo167 rib, lower cap and skins. For these cases, only the rib caps and skins were damaged. A sixth case with damaged Yo167 rib web elements was then considered. This case assumes impingement of hot gases onto the web and is indicative of burn through at Yo167 lower rib skins. Based upon the results, it was determined that localized failures of these locations are not sufficient to induced an overall wing structural failure. One element for all six damage locations violated screening criteria. As shown in Table 7.5-6, this element had a 2.18 load ratio. Element still maintains positive margin of safety based upon comparison to the certification database.

The conclusion from the analysis of small damage regions was that only the local areas were significantly affected. These would not produce a general wing failure, nor would they cause the local failure to propagate to a wider area.

7.5.5.2 Expanded Damage Analysis

The expanded damage analysis was performed to create more severe damage scenarios and to assess the wing response to a complete loss of load path due to damage in major structural areas. Seven damaged locations, shown in Figure 7.5-8, were examined during this phase of the analysis. The first two cases were centered about the WLE spar panels, just forward and aft of the Xo1040 spar. Cases 3 through 5 concentrated on the wheel well. In these areas, structure was assumed to be completely lost from the bottom wing surface to the top wing surface. Case 6 was created to see the effects of losing bottom surface honeycomb skin panels. Case 7 was the first attempt at specifically recreating the probable damage scenario experienced during STS-107. Case 7 was eventually modified to create the refined damage FEM.

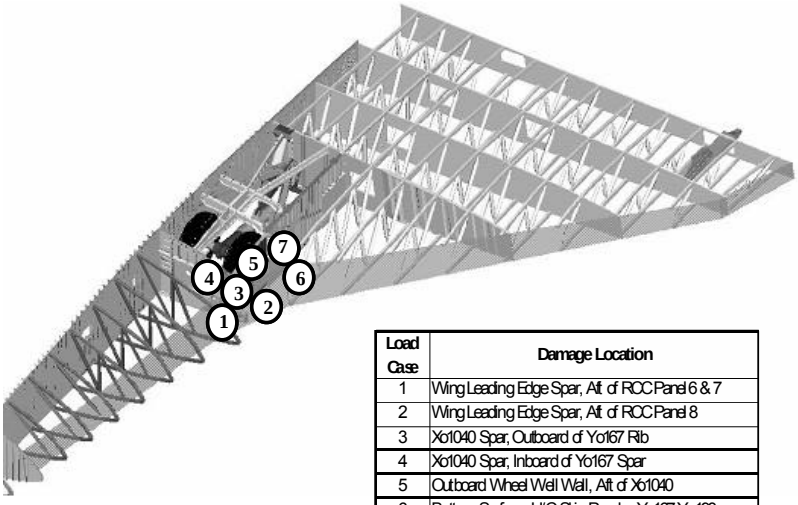

Load Case	Damage Location
1	Wing Leading Edge Spar, Aft of RCC Panel 6 & 7
2	Wing Leading Edge Spar, Aft of RCC Panel 8
3	Xo1040 Spar, Outboard of Yo167 Rib
4	Xo1040 Spar, Inboard of Yo167 Spar
5	Outboard Wheel Well Wall, Aft of Xo1040
6	Bottom Surface, H/C Skin Panels, Yo167-Yo198
7	- Upper Surface, H/C Skin Panel, Yo167-Yo198 - First Diagonal and Vertical Struts on Yo198 Frame

Figure 7.5-8 Damage Locations, Expanded Analysis

The total number of criteria violations for various data types, as described in Section 7.5.4.2, is shown in Table 7.5-7. From this table it can be noted that no significant fuselage interface violations occurred. This suggests that the amount of applied damage was not significant enough to cause the wing to detach from the main body. The total number of displacement criteria violations increases from the initial damage case, suggesting larger overall wing deflections. The stress violations also increase from the initial case. Some of these stress violations are significant, but a review of the certification analysis suggests that the parts still maintain a positive margin of safety. Overall, these results suggest a large amount of load redistribution does occur; however, wing failure from re-distribution is unlikely.

Table 7.5-7 Expanded Damage Analysis, Criteria Violations per Case

Damage Case	Stress	Displacement	Fuselage I/F Forces
1	135	26	0
2	94	11	0
3	94	0	0
4	61	0	0
5	20	0	0
6	131	21	0
7	142	0	0

7.5.5.2.1 Wing Displacements

Table 7.5-8 lists the total wing deflection criteria violations. Of the seven cases, cases 1, 2 and 6 showed displacement ratios greater than ±15%. The other cases displayed no criteria violations for deflections. (Note that for the expanded analysis, the deflection criterion was changed from a ±5% increase from damaged-to-undamaged condition, to a ±15% increase.) The maximum delta deflection was 0.24 inches, occurring for Case 2. A review of these violations suggests nothing significant from a structural strength standpoint.

Table 7.5-8 Wing Nodal Deflection Violations per Case

Damage Case	Criterial Violations		Wing Ratios		LE Ratios	
	Total Wing	LE Only	Max	Min	Max	Min
1	26	4	1.23	0.79	1.22	1.20
2	9	8	1.22	1.16	1.22	1.20
3	0	0	0	0	0	0
4	0	0	0	0	0	0
5	0	0	0	0	0	0
6	21	0	1.31	0.79	0	0
7	0	0	0	0	0	0

Note that these results contain ratios that are lower than the initial damage case results shown in Table 7.5-6. This is due to damaged elements being included in the initial analysis results. For the expanded case, localized damage effects were screened out.

Illustrations of the case 1, 2 and 6 displacement violation nodes are shown in Figure 7.5-9. For case 1, the violations are located in the glove area and near the WLE spar. This is consistent with a loss of load path between glove area and Xo1040 spar. The change in magnitude from undamaged to damaged are relatively small (0.11 inches), however. For Case 2, displacement violations are located at the WLE, which is consistent where the damage was located. As previously stated, the maximum delta deflection was 0.24 inches. The load path between the Xo1040 bulkhead and glove area has been restored, resulting in no violations in the glove area. For case 6, displacement violations are located at the wing glove area, suggesting that the lower panels help provide structural rigidity to elements of the Xo1040 spar.

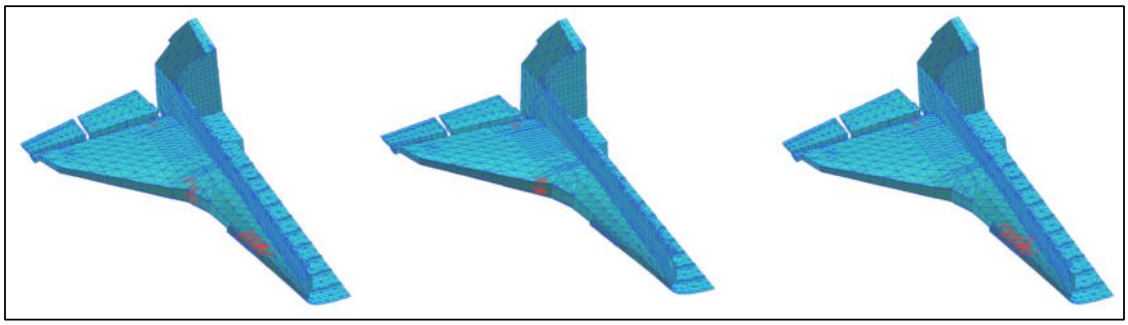

Figure 7.5-9 Node Displacement Violations

7.5.5.2.2 Wing-To-Fuselage Interface

As seen in Table 7.5-9, the results from the wing-to-fuselage comparison show no significant rise in loading from expanded damage conditions. The maximum load increase of 8% occurs for damage case 7. The location is at the X_O1040 upper wing-spar to fuselage interface. The maximum load increase along the lower wing interface is 7%, occurring at the X_O1191 wing-spar to fuselage interface. Note that the wing-carry-thru (WCT) interface reactions remain largely unchanged. This suggests that the main wing structure attaching the wing to the fuselage is not being compromised. The largest change for the lower wing interface is 7% at the X_O1191 lower spar interface.

Table 7.5-9 Wing-to-Fuselage Reaction Data

I/F Location	ELEM ID	Node ID	X_o	Y_o	Z_o	Case01	Case02	Case03	Case04	Case 05	Case06	Case 07	
Upper Wing	5070	5021	1040	105	342	1.04	1.00	1.01	1.02	1.00	0.97	1.00	
	5122	5023	1040	105	341	1.01	1.03	1.00	0.99	1.00	0.97	1.08	Max
	5035	5123	1090	105	339	0.97	0.97	0.95	0.95	0.99	1.00	0.97	
	5060	5194	1116	105	336	0.97	0.97	0.96	0.97	1.00	0.99	0.97	
	5124	5269	1191	105	325	0.99	0.99	0.99	1.00	1.00	0.97	1.00	Wing Carry Thru Locations
	5169	5054	1191	105	324	1.01	1.01	1.00	1.00	1.00	1.01	1.00	
	5133	5360	1249	105	317	1.02	1.01	1.01	1.01	1.00	1.03	1.00	
	5170	5059	1249	105	317	1.00	1.00	1.00	1.00	1.00	1.00	1.00	
	5141	5435	1307	105	308	0.99	0.99	0.99	1.00	1.00	0.97	1.00	
	5179	5435	1307	105	308	1.01	1.01	1.00	1.00	1.00	1.01	1.00	
	5160	5626	1365	112	300	1.02	1.02	1.01	1.01	1.00	1.04	1.00	
Lower Wing	5088	5018	1040	105	272	0.86	0.86	0.81	0.77	0.97	0.65	0.99	
	5123	5029	1040	105	273	0.85	0.85	0.80	0.77	0.97	0.60	0.99	
	5209	5265	1191	105	269	1.06	1.04	1.03	1.03	1.01	1.07	1.01	Wing Carry Thru Locations
	5220	5362	1249	105	267	1.01	1.01	1.00	1.01	1.00	1.01	1.00	
	5229	5437	1307	105	266	1.00	1.00	1.00	1.00	1.00	1.00	1.00	
	5240	5624	1365	112	267	0.98	0.98	1.00	0.99	1.00	0.99	1.00	

7.5.5.2.3 Stress & Force Results

Stress and force violations are summarized in Table 7.5-10. The most significant increases occur with cases 1, 6 and 7. Generally, the criteria violations are concentrated around the areas that have been damaged, with little impact to wing-to-fuselage interface, torque box or glove area.

Table 7.5-10 Stress and Force Violations

Damage Case	Element Type				Total Violations
	CTRIA3	CSHEAR	CROD	CQUAD4	
1	11	6	98	20	135
2	3	4	68	19	94
3	13	4	59	18	94
4	8	3	42	8	61
5	4	1	14	1	20
6	29	4	73	25	131
7	14	8	99	21	142

The stress violation dispersions illustrate load re-distributions within the wing. Dispersions for each of the cases are shown in Figure 7.5-10. Note that cases 2 & 7 show the widest area of dispersion. Case 2 load ratios are highly concentrated around the damaged WLE spar web, with some ratios scattered aft. Suggesting that there is not much load transfer moving toward the inboard wing structure. Case 7 also has high ratios around the damage area, but shows loads being distributed toward the wing-to-fuselage interface. Cases 4 & 5 show the least amount of dispersion, suggesting that the loads being routed around the wheel well is being more evenly distributed than with cases 2 & 7. Highly concentrated load

redistribution is observed for case 1, 3, & 6 around the area of damage. However, the dispersion does not move inward or outward.

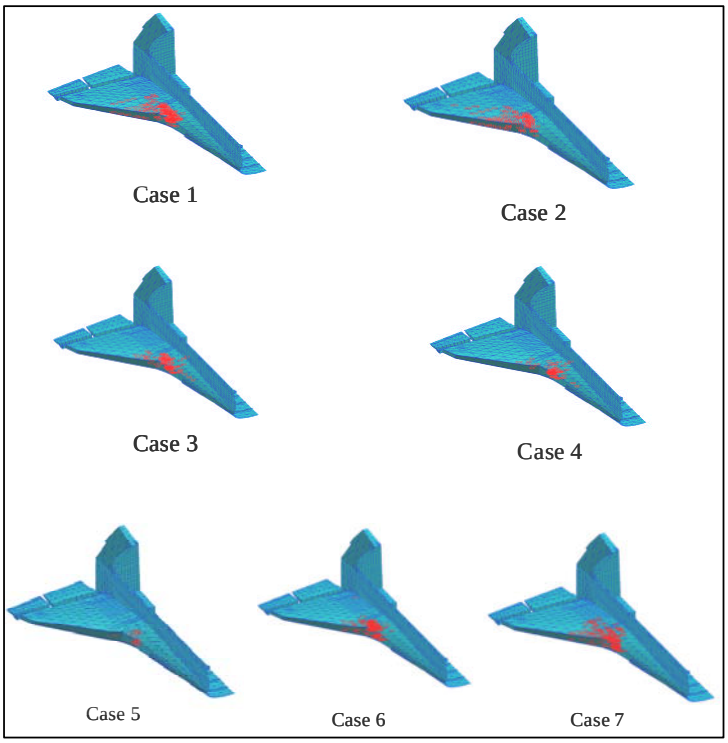

Figure 7.5-10 Stress/Force Violation Dispersions per Case

Table 7.5-11 shows the critical elements for each load case. The results show that, although load redistribution increases significantly with the expanded damage cases, the magnitudes were well within certification limits. The critical element for case 1, element 5515, was the closest to the certification load. This element is located in the Yo167 rib, near the main landing gear door forward hinge. The increase results from the damage WLE spar transferring the loads to the Xo1040 spar and Yo167 rib. The highest load shown in Table 7.5-11 is at element 5116, case 3. This element represents a beam in the Xo1040 spar. The load increase is to be expected since the element is close to the damaged area. Element 9053 represents a wing glove truss tube strut, located at the aft end of the glove at station Xo1010. Case 3 is the most critical for this element. This is due to the load path from the Xo1040 spar being lost and distributing an increased load forward.

Table 7.5-11 Critical Elements

Damage Case	Data	Type	Comp	ID	Damaged	Undamaged	Maximum Cert Load
1	Element Force	Crod	N (lb)	5515	820	51	967
2	Element Stress	Crod	Sx (psi)	5614	3542	204	10839
3	Element Stress	Crod	Sx (psi)	9053	-6774	-3853	-9886
4	Element Stress	Crod	Sx (psi)	5116	29731	11181	42877
5	Element Stress	Crod	Sx (psi)	5121	-3884	-1105	-10291
6	Element Stress	Ctria3	Sxy1 (psi)	51942	2699	1454	14111
7	Element Stress	Crod	Sx (psi)	5344	-4659	-1937	-14848

7.5.5.3 Refined Wing Stress Analysis

Structural analysis of a significantly damaged wing was requested to investigate potential sources of wing deformation. Correlation between the analytical results and the STS-107 measured aerodynamic data was the primary purpose of the analysis. Results were delivered to Aerodynamics group to study changes in aero coefficients seen during STS-107 descent.

The study was primarily focused on damage to the intermediate wing section. An attempt was made to model damage as closely as possible to the most probable failure scenario on STS-107, i.e., WLE spar breech at RCC panels 8 & 9. Three types of damage were applied to the FEM for this analysis. The first damage type was at areas where hot gas impingement was assumed to fail the structure. Susceptible structures were all the rib struts in the intermediate wing, the WLE spar behind RCC panels 8 & 9 and the top honeycomb panels just outboard of the wheel well wall. The modulus in these areas was set to 1% of their normal value. The second type of damage was concentrated on the upper and lower intermediate wing panels. The assumption was that the skin panels were affected by hot gas ingestion into the cavity, but not failed. The stiffness for these structures was reduced by a factor of two. The final type of damage was at the intermediate wing rib spars, Yo167 rib and the Xo1191 spar. Hot gas ingestion was assumed to lower the modulus of these locations by 30%. Refer to Figure 7.5-11 for the damage areas and modulus reduction values.

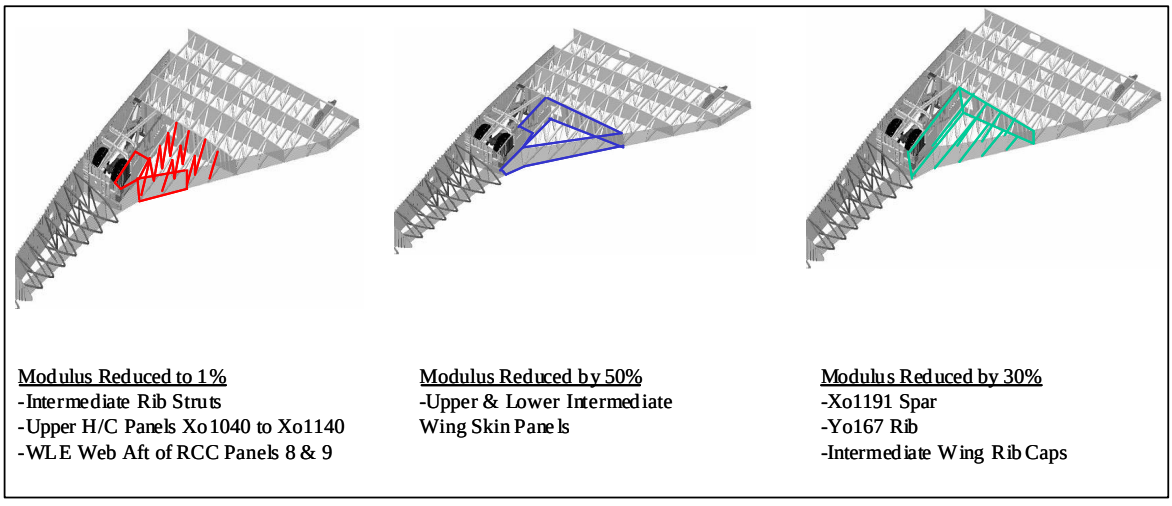

Figure 7.5-11 Refined Wing Damage Case

This linear FEM analysis was performed to show overall wing deformation, while hand calculations were done for local, non-linear effects on the lower wing skin. The FEM results show small deflections even with severe damage to the intermediate wing. The maximum delta deflection was 0.78 inch (Z), while the wing tip deflection increases to 0.25 inch. The wing tip deflection is nominally 1.1 inch. Maximum deflection results for the undamaged and damaged cases, as well as the difference between the two cases, are provided in Table 7.5-12.

Table 7.5-12 Refined Wing Damage, FEM Deflection Results

Condition	X (in)	Y (in)	Z (in)	RSS
Damaged Wing	0.1541 -0.1176	0.2298 -0.1334	1.3603 -0.0783	1.38817 0.19432
Undamaged Wing	0.0768 -0.1222	0.0681 -0.1236	1.0999 -0.0895	1.1047 0.19551
Delta Deflection	0.0774 -0.0195	0.2546 -0.1174	0.7822 -0.2561	-- --

Figure 7.5-12 shows the deflection of the wing with the refined damage. Significant distortion occurs around the intermediate wing just aft of RCC panels 8 & 9. Beyond this region, the wing deflections increase towards the wing tip. No significant deflections occur inboard of RCC panels 8 & 9. This is due to a denigrated load path from the outboard wing to the inboard wing.

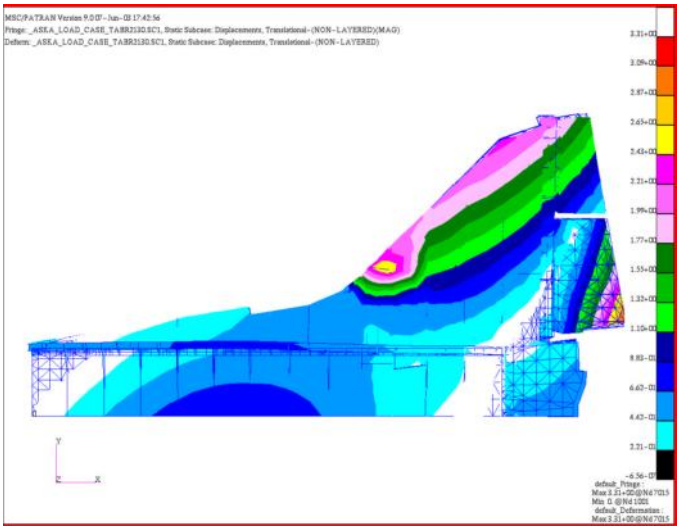

Figure 7.5-12 Refined Wing Damage, FEM Deformation Plot

Wind tunnel testing indicated that deflections of up to five inches are required to emulate the aerodynamic profile experienced during STS-107. These results show that the aerodynamic load at Mach 18 was not able to achieve overall wing deflections of this level, even with severe damage.

Hand analyses were performed to determine the maximum deflections that could occur on the lower wing skin panels. Three components were considered to cause the deflections. The first was a differential pressure across the panels. The difference in the free stream flow and the heated intermediate wing compartment was calculated to be 0.25 psi. This delta pressure was based on a pressure coefficient (Cp) of 1.0 and a dynamic pressure of 70 psf. The external pressure was approximately 0.5 psi with an

internal pressure of 0.25 psi, post breach. Potential loss of rib capability was considered as part of the analysis. As the loss of a rib can effectively double the width of the analysis panel, this can have a significant effect on the deflections calculated. For example, deflection increases as the fourth power of panel width based on this uniform pressure loading. To account for the partial effectivity of the rib cap, after the rib struts are lost, a factor (Leff Factor in Table 7.5-14) was assumed to produce an effectively shorter panel. The loss of the Yo198 rib is somewhat less effective based on the presence of the MLG door hinge backup structure found between panels 4,5, and 6. The effect of the loss of the rib between panel 8 and 9 is also less, because the rib is relatively short.

Two thermal scenarios were considered in addition to the pressure deflection: a thermal gradient across the honeycomb panel face sheets and a de-bonding of the inner face sheet. The deflection due to thermal gradient is a function of temperature differential from the inner to outer face sheet. This deflection increases as square of the panel width. The loss of the inner face sheet assumes a new stable configuration occurring when the tile gaps (.045 inch design; 0.050 inch assumed) are closed. Once the de-bonding occurs and the stable configuration has been reached, it was assumed that the outer face sheet acts as a membrane. This deflection is also a function of the square of panel width. The de-bond deflection is additive with delta pressure, but not thermal gradient deflection.

The hand analyses show that larger deflections are possible if a face sheet de-bond occurs. Note that this local, non-linear deflection scenario was not modeled in the FEM. The hand analysis results are shown in Table 7.5-13 and Table 7.5-14, with the wing panel layout shown in Figure 7.5-13. The results indicate that deflections are still relatively small without the loss of any ribs. Expanding the analysis to include damaged ribs, however, indicates that deflections of up to 5” are possible with the loss of three ribs and debond of the inner facesheet.

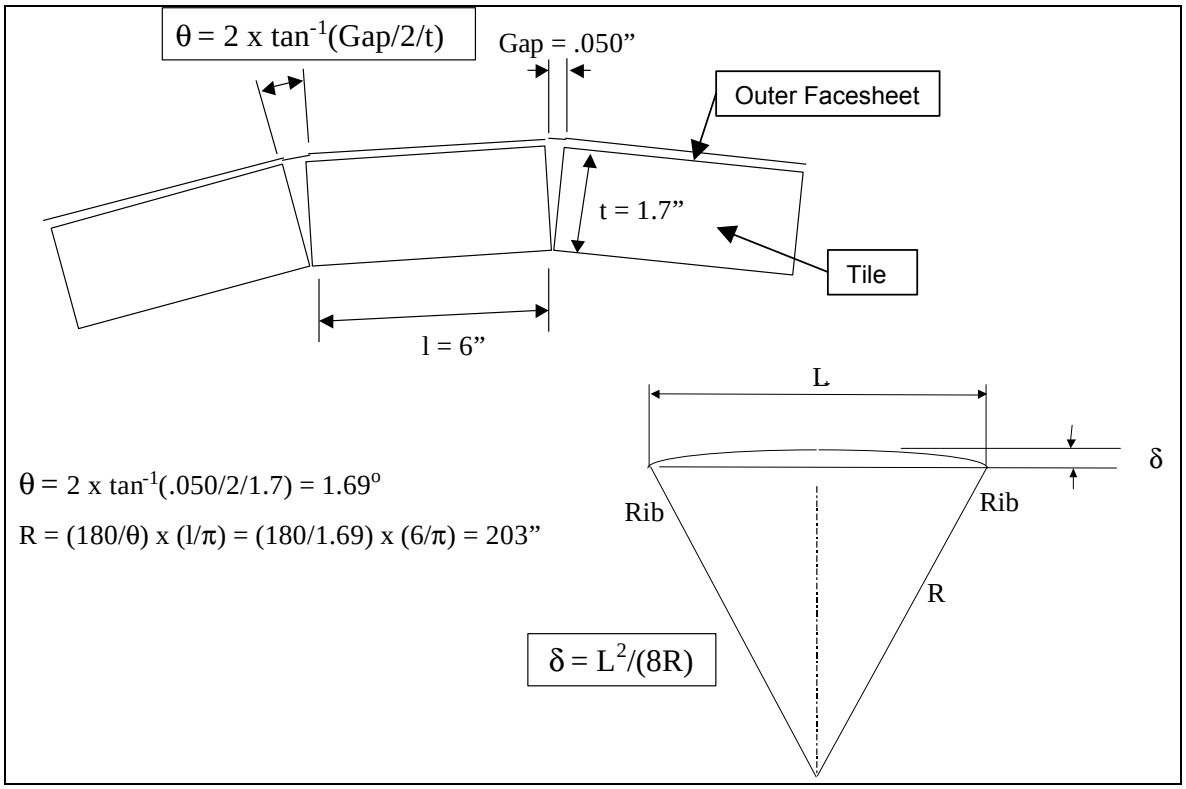

Figure 7.5-13 Calculations for Outer Facesheet and Tile Deflection

Table 7.5-13 Refined Wing Damage, Panel Deflection Results

Single Panel (Ribs Intact)									
Panel ID	Length	Leff Factor	Leff	Deflection for DP	Tile Gap	Deflection	Total Deflection	Yinbd	Youtbd
4	31	1	31	0.015	0.05	0.61	0.63	167	198
5	31	1	31	0.022	0.05	0.61	0.63	167	198
6	31	1	31	0.017	0.05	0.61	0.63	167	198
7	28	1	28	0.027	0.05	0.50	0.53	198	225
8	28	1	28	0.035	0.05	0.50	0.54	225	254
9	28	1	28	0.035	0.05	0.50	0.54	254	282

Table 7.5-14 Refined Wing Damage, Multi-Panel Deflection Results

Multiple Panel										
Panel ID	Length	Leff Factor	Leff	Deflection	Tile Gap	Deflection	Total Defl	Yinbd	Youtbd	Condition
4,5,6,7	59	0.8	47	0.13	0.05	1.42	1.56	167	225	1 rib lost
7,8	56	0.9	50	0.31	0.05	1.62	1.93	198	254	1 rib lost
4,5,6,7,8	87	0.7	61	0.67	0.05	2.37	3.04	167	254	2 ribs lost
4,5,6,7,8,9	115	0.65	75	1.52	0.05	3.56	5.09	167	254	3 ribs lost

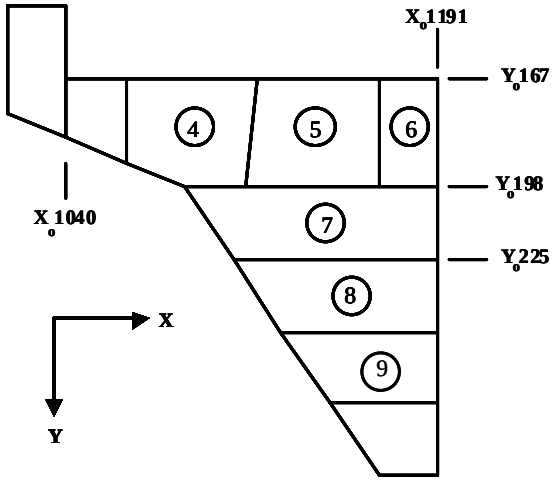

Figure 7.5-14 Lower Wing Panel Layout

7.5.6 Conclusions

Three distinct phases of analysis were performed on the OV-102 wing in order to help determine the most probable cause of the vehicle breakup. The “initial” analysis phase was performed to assess gross wing failure possibilities due to localized weakening of wing structural members. Results from this analysis showed that, although localized load increases do occur, the possibility of a gross wing failure or further damage propagation due to localized damage is highly remote. The “extended” analytical phase expanded the damage to larger areas of the forward and intermediate wing sections. These analyses attempted to quantify the effects of losing major portions of the intermediate wing structure. For this analysis, complete bottom to top “cuts” were made at critical structural locations around the main landing gear door wheel well, the wing leading edge spar and the honeycomb skin panels on the top and bottom wing surfaces. Results showed significant load redistribution throughout the wing; however, no structural members were shown to fail. The “refined” phase changed the investigative focus to a damage case that reflected the probable scenario occurring prior to the breakup. This analysis was initiated at the request of the Orbiter Aerodynamics groups in order to support an integrated analysis of the wing deformation. A combination of FEM analyses and hand analyses were used for this phase. The FEM results showed a change in overall wing panel deflections of approximately ¾”. However, hand analyses were able to show up to 5” inch deflections of the wing lower surface with de-bonded inner wing skin facesheets and loss of the intermediate wing ribs outboard of Yo167.

7.6 Stress Appendix

Appendix for Section 7.2

Table 7.6-1 FEM Summary Table of Results

		Temperatures									Results		
Case	Description	Default	Spar Web	Upper Skin	Lower Skin	Upper Spar Cap	Lower Spar Cap	Obd/Aft Upper Skin	Other (see notes)		Stress	Microstrain	Notes
4A	Calibration Case	70	70	70	70	70	70	70	-	Upper Cap (5073)	0	0	
										Lower Cap (5090)	0	0	
4B	Equal heating of spar web, upper and lower skins	70	180	180	180	70	70	70	-	Upper Cap (5073)	3749	354	
										Lower Cap (5090)	4445	419	
4C	Heating of only outboard, aft upper skin	70	70	70	70	70	70	400	-	Upper Cap (5073)	6668	629	
										Lower Cap (5090)	451	43	Nodes 73, 84, 95, 104, 103, 116, 141, 129
4D	Heat spar web, upper & lower skins, and outboard aft upper skin	70	180	180	180	70	70	400	-	Upper Cap (5073)	10416	983	
										Lower Cap (5090)	4896	462	
4E	Unequal heating of spar web, upper and lower skins	70	110	180	180	70	70	70	-	Upper Cap (5073)	3025	285	
										Lower Cap (5090)	2935	277	
4F	Heat lower skin near spar only	70	70	70	180	70	70	70	-	Upper Cap (5073)	-171	-16	
										Lower Cap (5090)	2210	208	
4G	Heat WLE nodes near panels 8/9	70	70	70	70	70	70	70	400	Upper Cap (5073)	-276	-26	
										Lower Cap (5090)	-602	-57	Nodes at y226 to 400°F
4H	Heating of only outboard, aft lower skin	70	70	70	70	70	70	70	400	Upper Cap (5073)	-377	-36	
										Lower Cap (5090)	119	11	Outboard, aft lower skin
4I	Heat spar web nodes only	70	110	70	70	70	70	70	-	Upper Cap (5073)	413	39	
										Lower Cap (5090)	863	81	Compare to 4E
4J	Heat sections of y167 Rib	70	70	70	70	70	70	70	200	Upper Cap (5073)	1	0	
										Lower Cap (5090)	5	0	167 Rib Web Nodes to 200°F
4K	Heating of only outboard, aft upper skin (see 4C)	70	70	70	70	70	70	200	-	Upper Cap (5073)	2627	248	
										Lower Cap (5090)	178	17	Compare to 4C
4L	Heating of only upper spar cap nodes	70	70	70	70	150	70	70	-	Upper Cap (5073)	-5474	-516	
										Lower Cap (5090)	-343	-32	
4M	Heating of only aft upper skin (wheel well)	70	70	70	70	70	70	70	200	Upper Cap (5073)	1273	120	Heating of aft upper skin in MLGD compartment
										Lower Cap (5090)	-108	-10	
4N	Heating of only aft upper skin (wheel well)	70	70	70	70	70	70	70	200	Upper Cap (5073)	3951	373	
										Lower Cap (5090)	-184	-17	4M plus nodes 73,95,103,116,129
M1	Mechanical load case TABR 2130 No Damage	-	-	-	-	-	-	-	-	Upper Cap (5073)	-1472	-139	
										Lower Cap (5090)	5868	554	
M2	Mechanical load case TABR 2130 Removed outboard aft upper skin	-	-	-	-	-	-	-	-	Upper Cap (5073)	-1432	-135	
										Lower Cap (5090)	5802	547	
A1	Combined heating	70	110	110	110	110	70	145	-	Upper Cap (5073)	141	13	
										Lower Cap (5090)	1549	146	
A2	Combined heating II	70	145	145	145	145	75	-	190	Upper Cap (5073)	-116	-11	Lose outboard aft upper skin (set to 70) Heat nodes 73,95,103,116,129 only
										Lower Cap (5090)	2388	225	
A3	Combined heating III	70	175	175	175	175	80	-	215	Upper Cap (5073)	777	73	
										Lower Cap (5090)	3082	291	Heat aft upper skin (wheel well) to 215
A4	Combined heating IV	70	175	175	175	175	90	-	260	Upper Cap (5073)	2122	200	
										Lower Cap (5090)	2513	237	Heat aft upper skin (wheel well) to 260

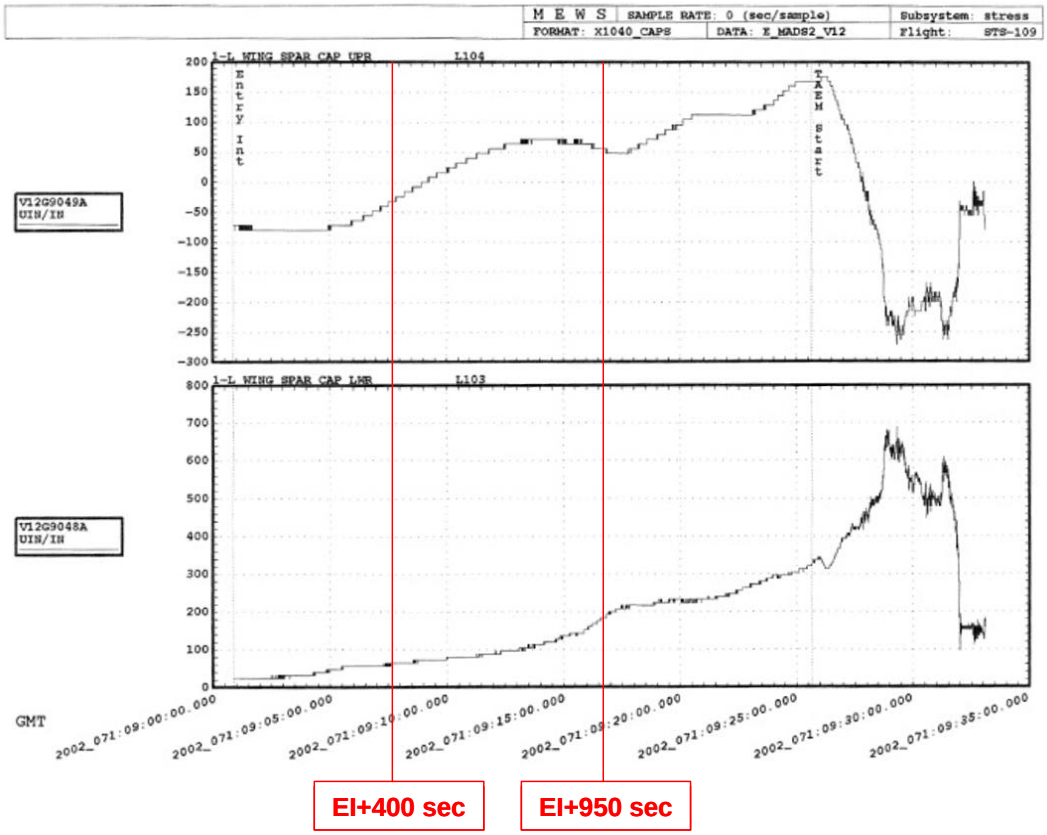

Figure 7.6-1 STS-109 Nominal Entry Strains

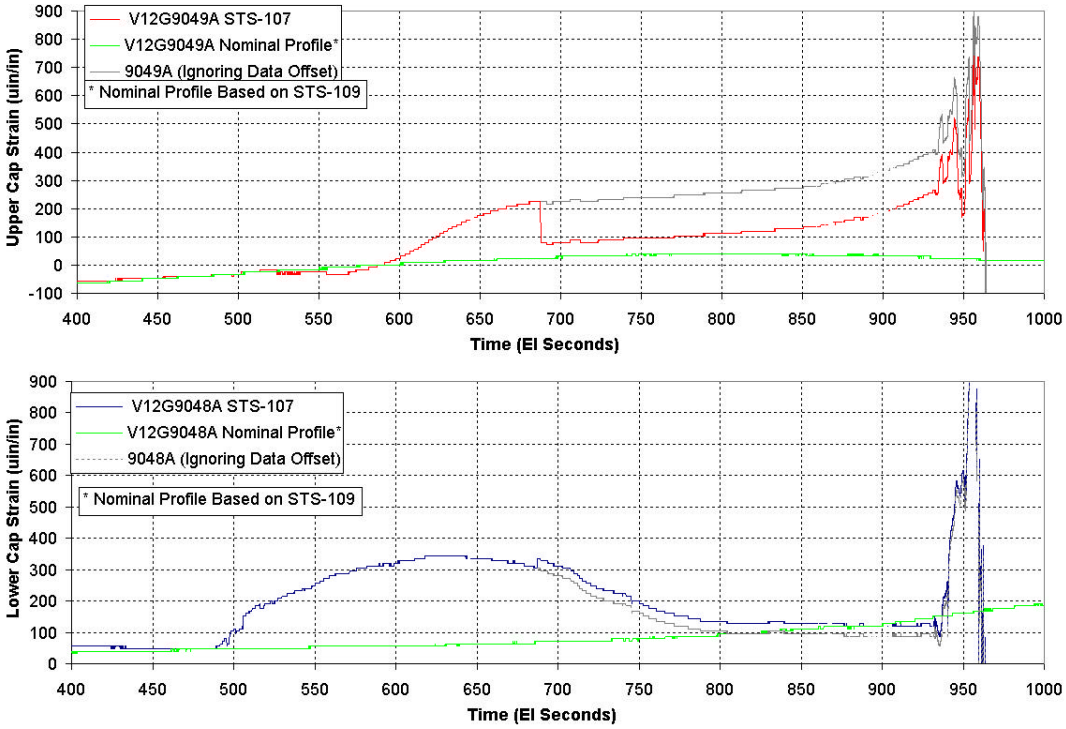

Figure 7.6-2 STS-107 Full Data Reconstruction

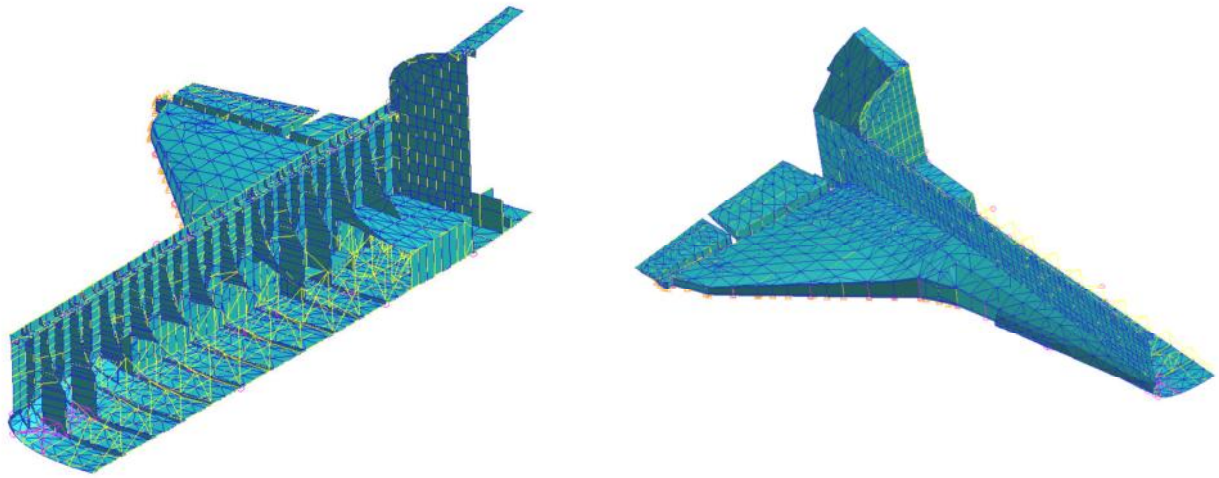

Figure 7.6-3 Complete FEM Model Illustration

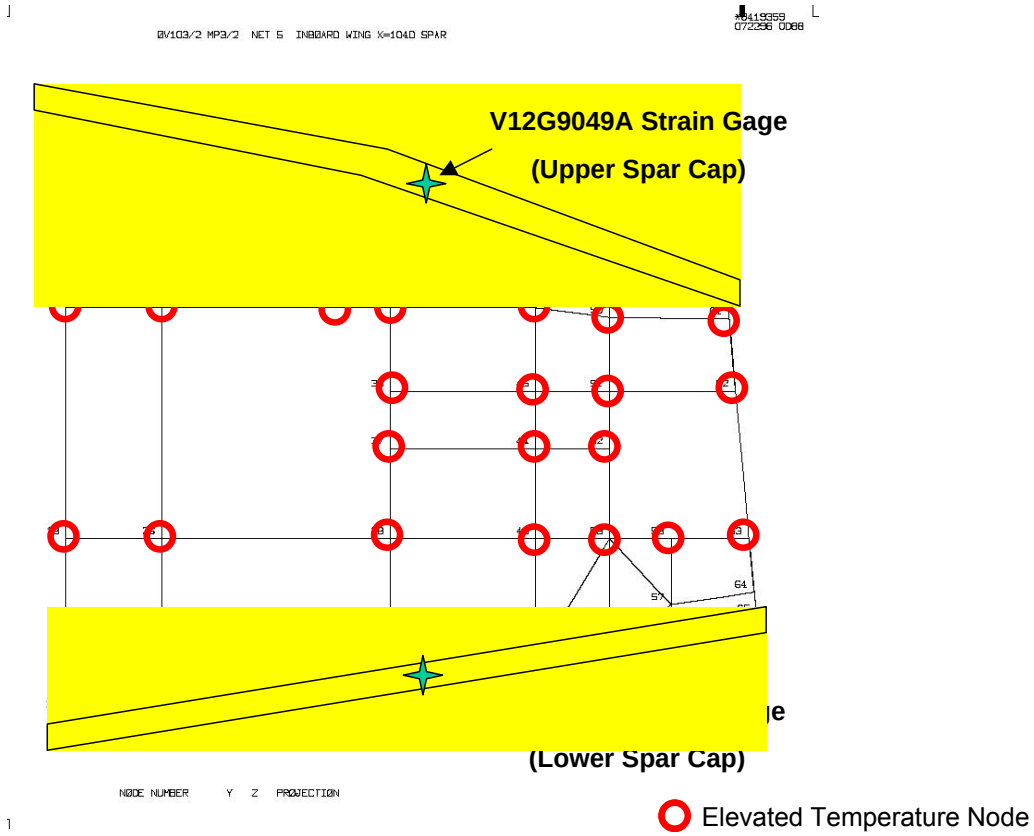

Figure 7.6-4 FEM Illustration, Xo1040 Spar Nodes

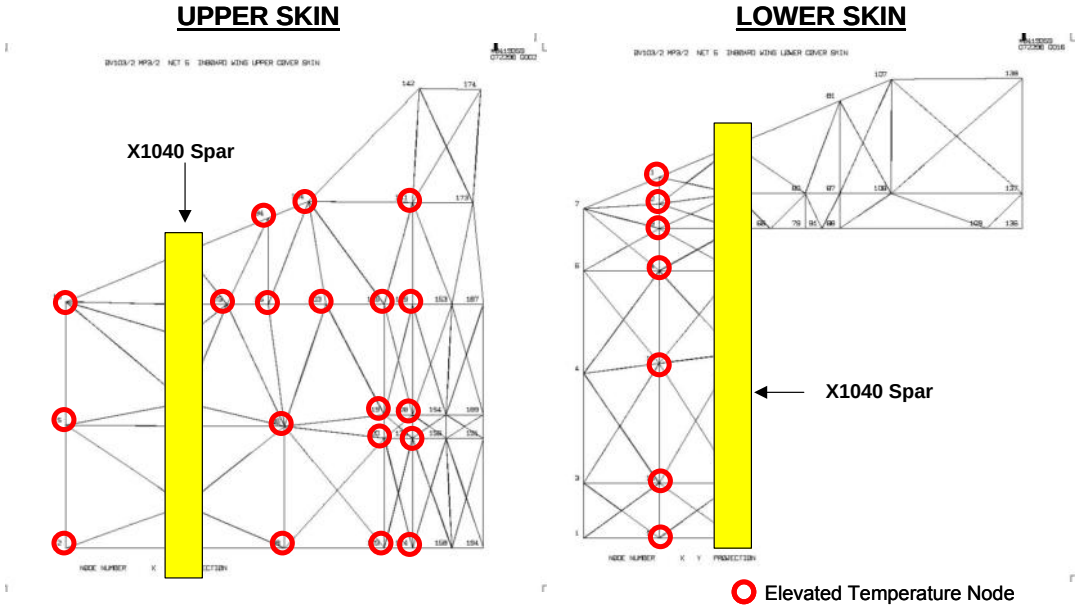

Figure 7.6-5 FEM Illustration, Nearby Skin Nodes

Appendix for Section 7.3

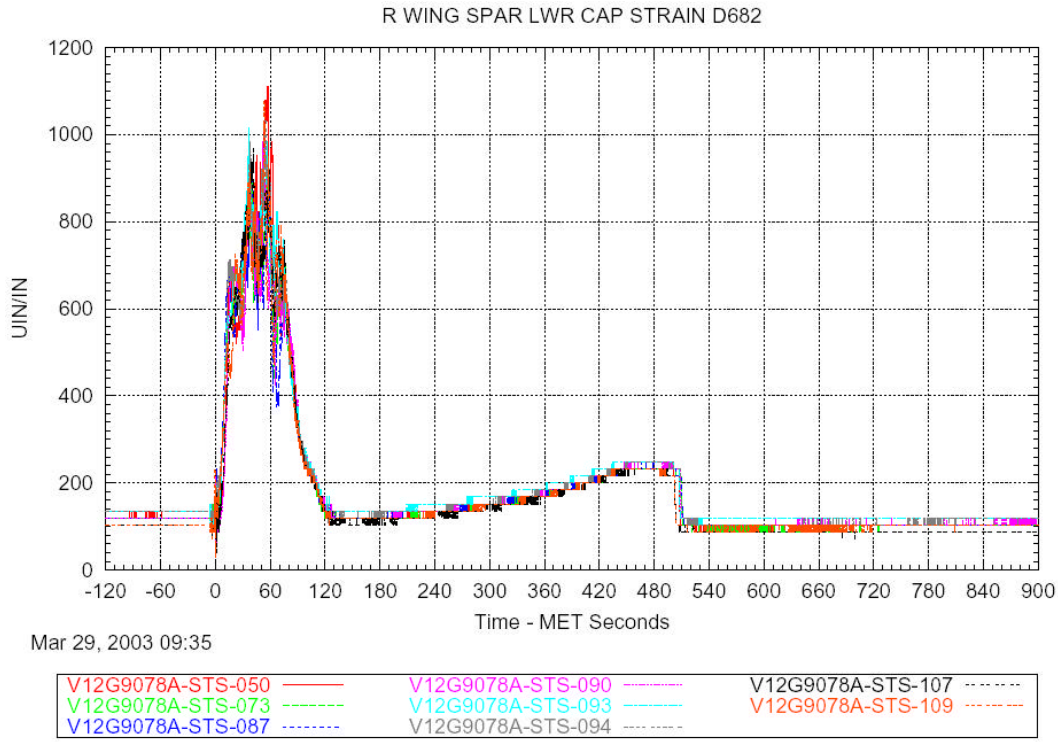

Figure 7.6-6 Typical Ascent Response

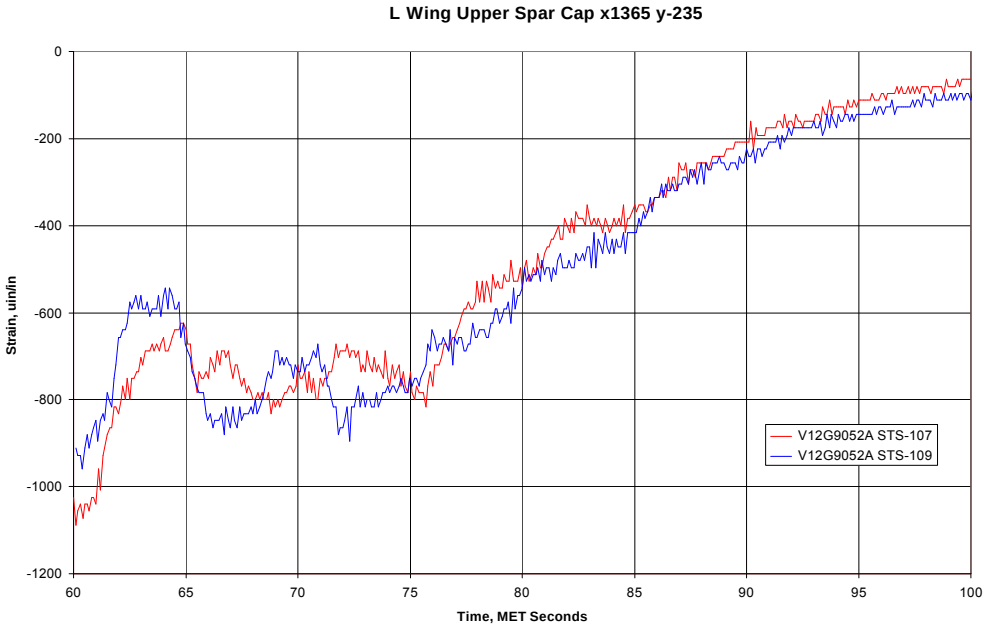

Figure 7.6-7 Interesting Signature Near Suspect Debris Impact Event

642

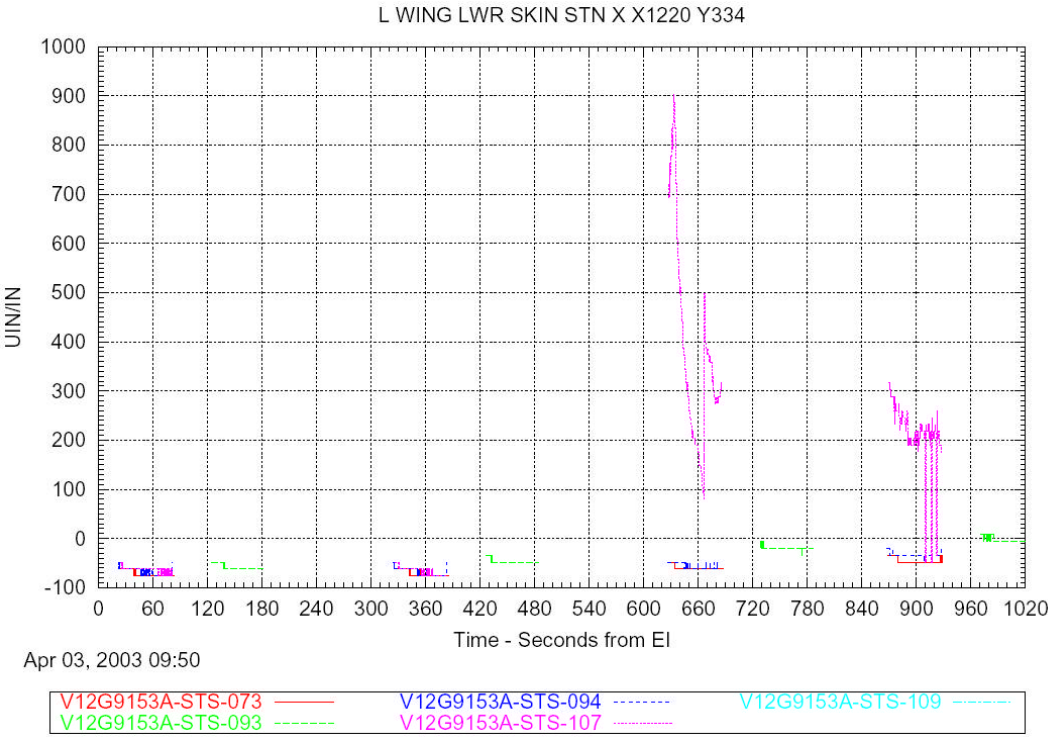

Figure 7.6-8 Typical PCM3 Entry Response

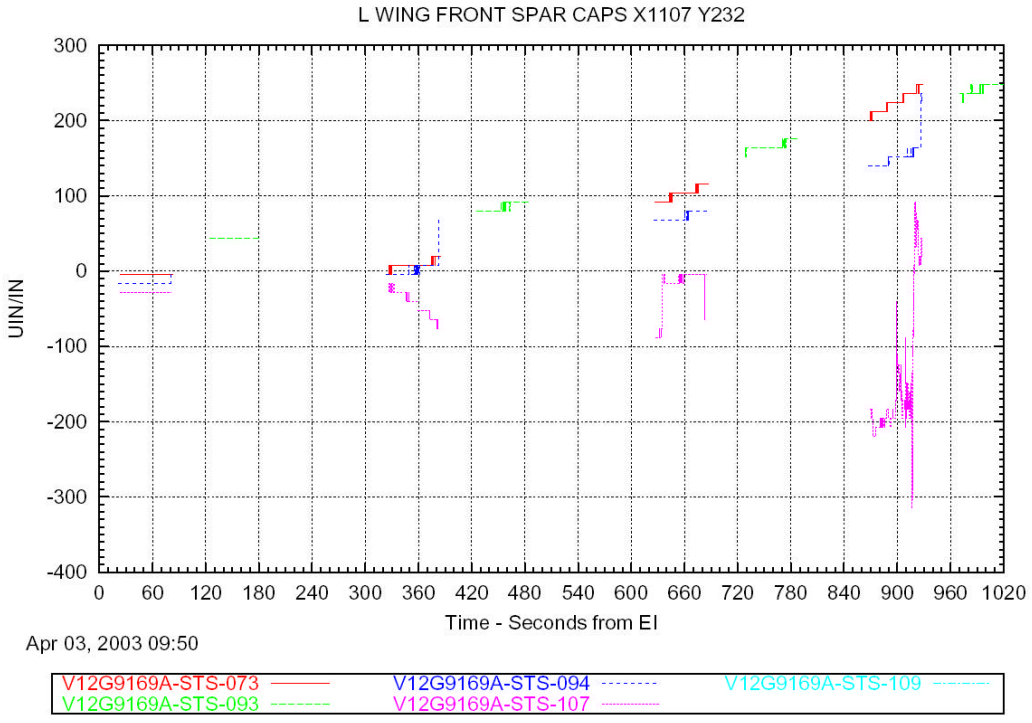

Figure 7.6-9 PCM3 Entry Response With Suspected Off-Nominal Trend

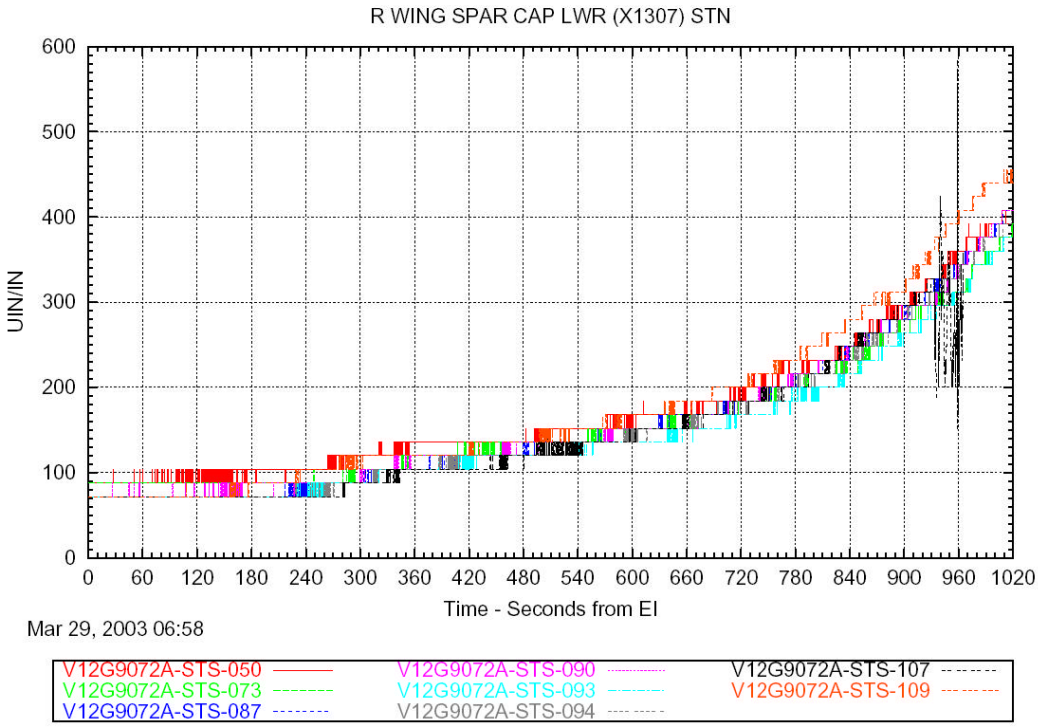

Figure 7.6-10 Typical, Nominal Right Wing Entry Response

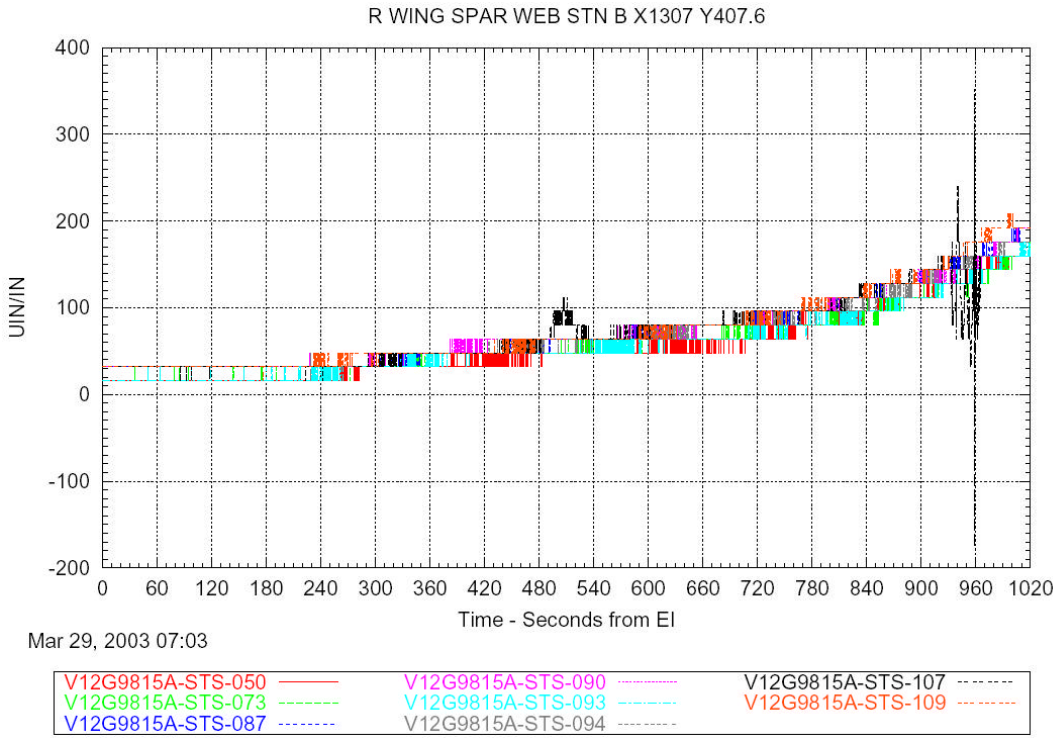

Figure 7.6-11 Right Wing Entry Brief Off-Nominal Response With Subsequent Return to Nominal

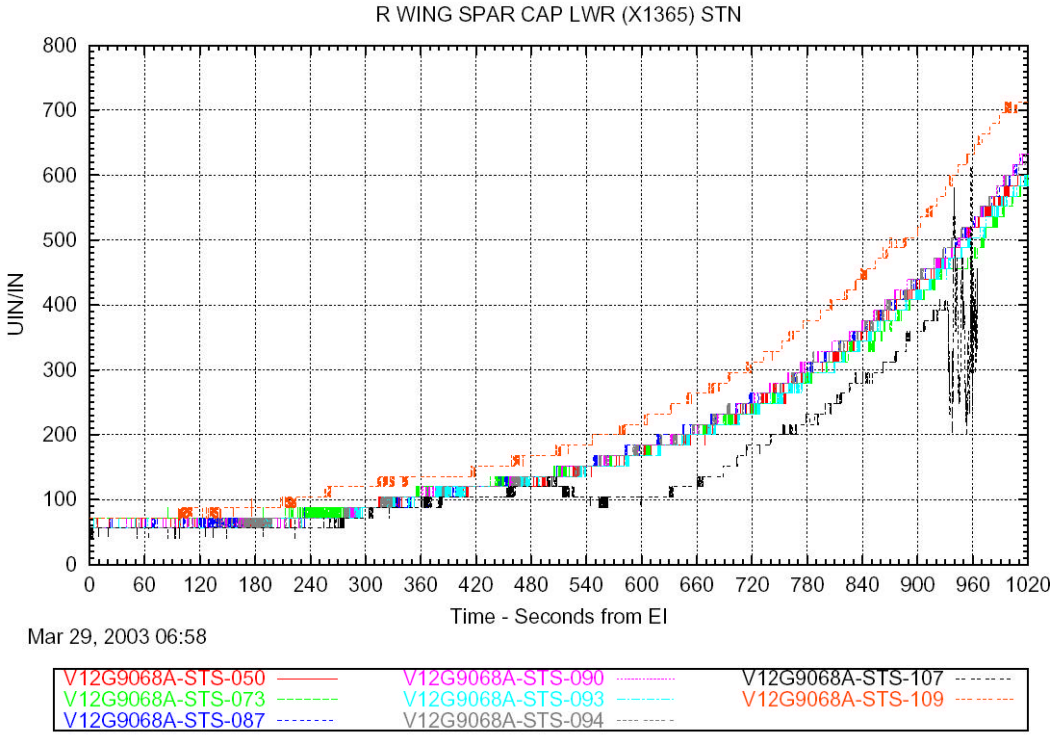

Figure 7.6-12 Right Wing Entry Off-Nominal Response With Subsequent Data Offset

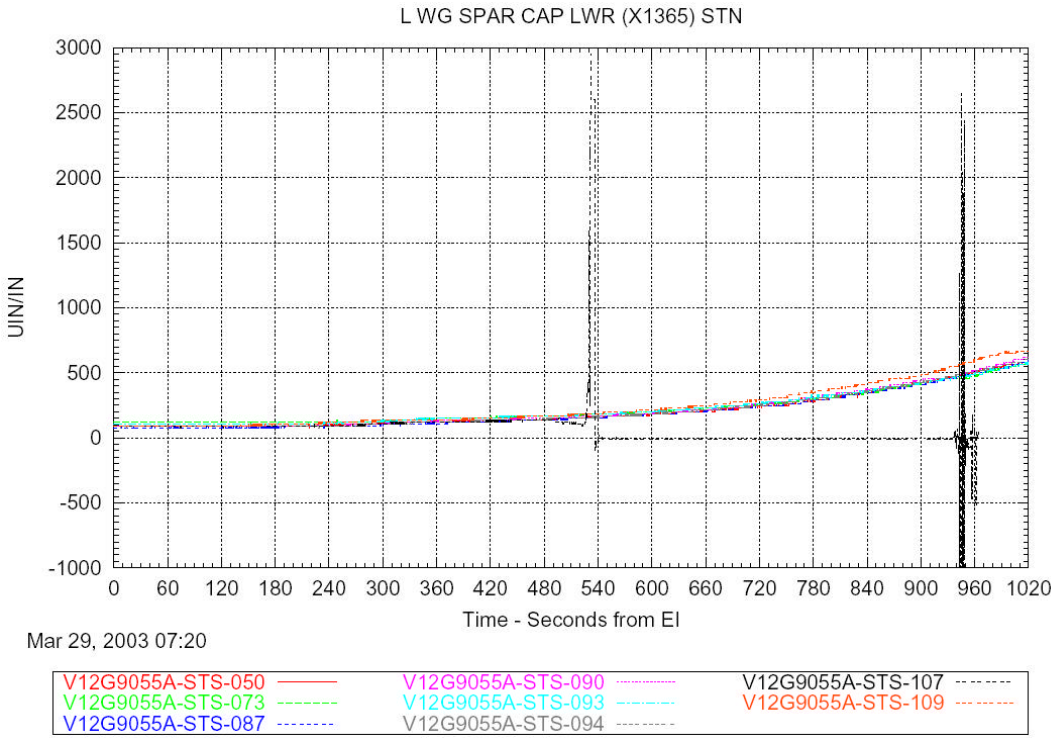

Figure 7.6-13 Typical Left Wing Entry Gage Failure

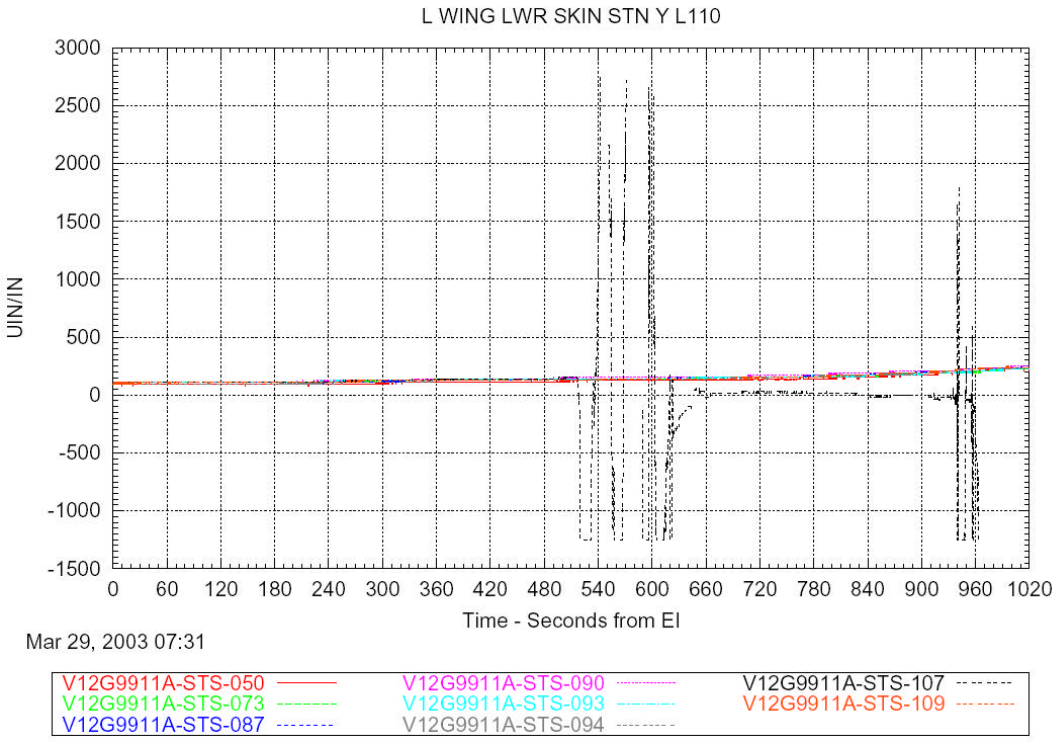

Figure 7.6-14 Left Wing Entry Gage Failure With Multiple Off-Scale Oscillations

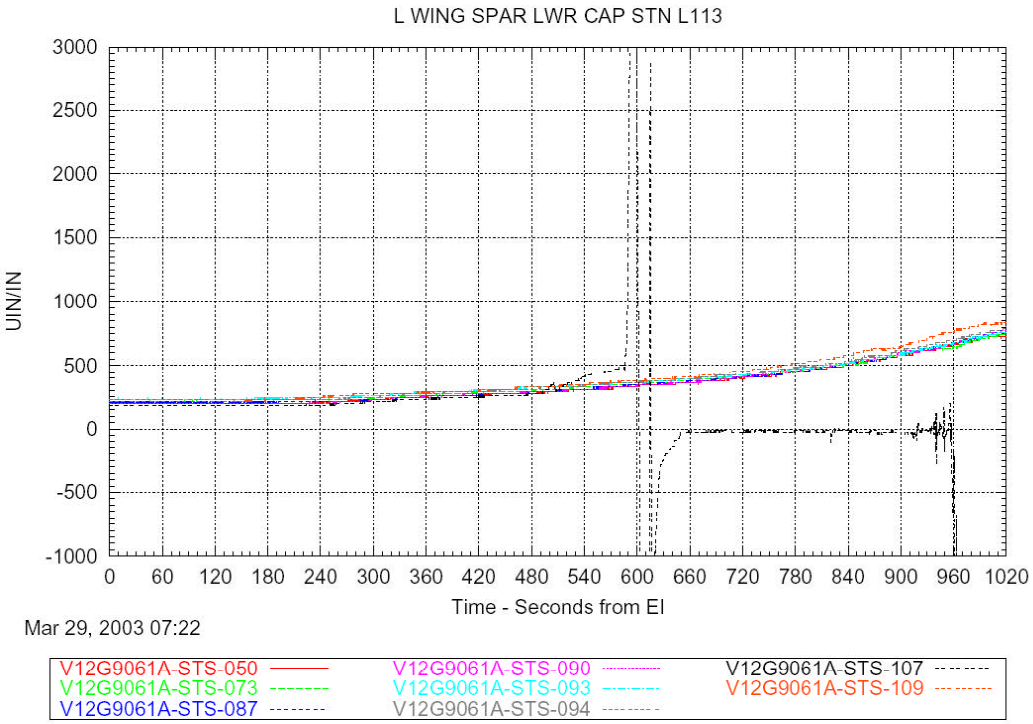

Figure 7.6-15 Left Wing Entry Gage Failure With Preceding Off-Nominal Inflection

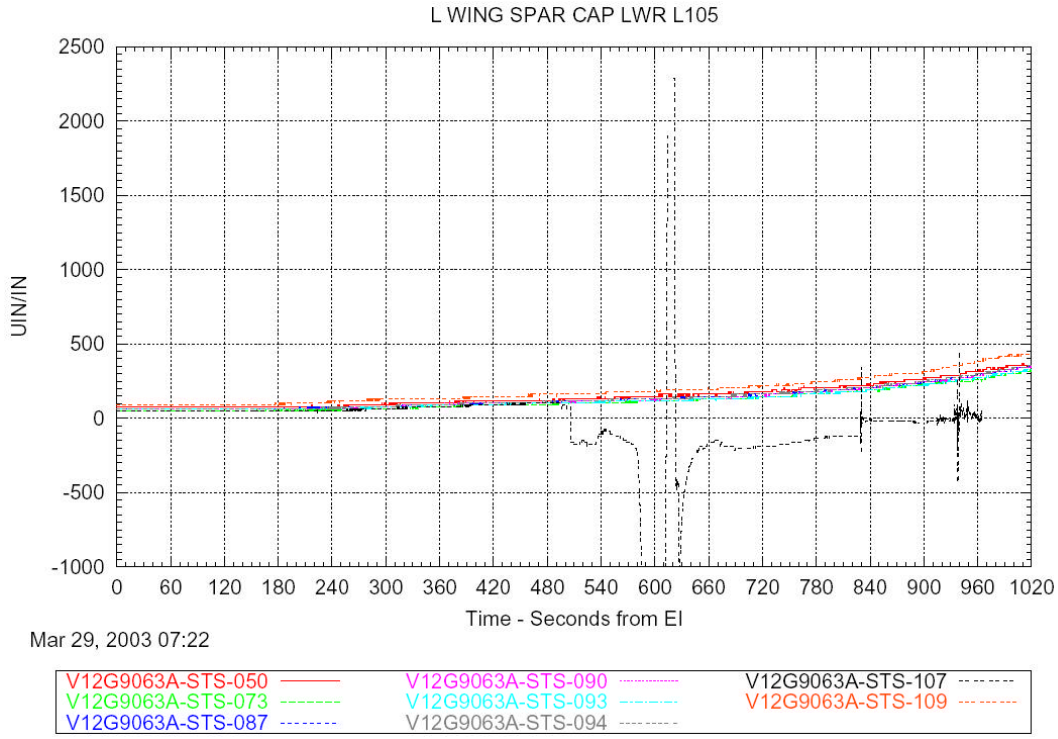

Figure 7.6-16 Left Wing Entry Gage Failure With Subsequent Nonzero Response

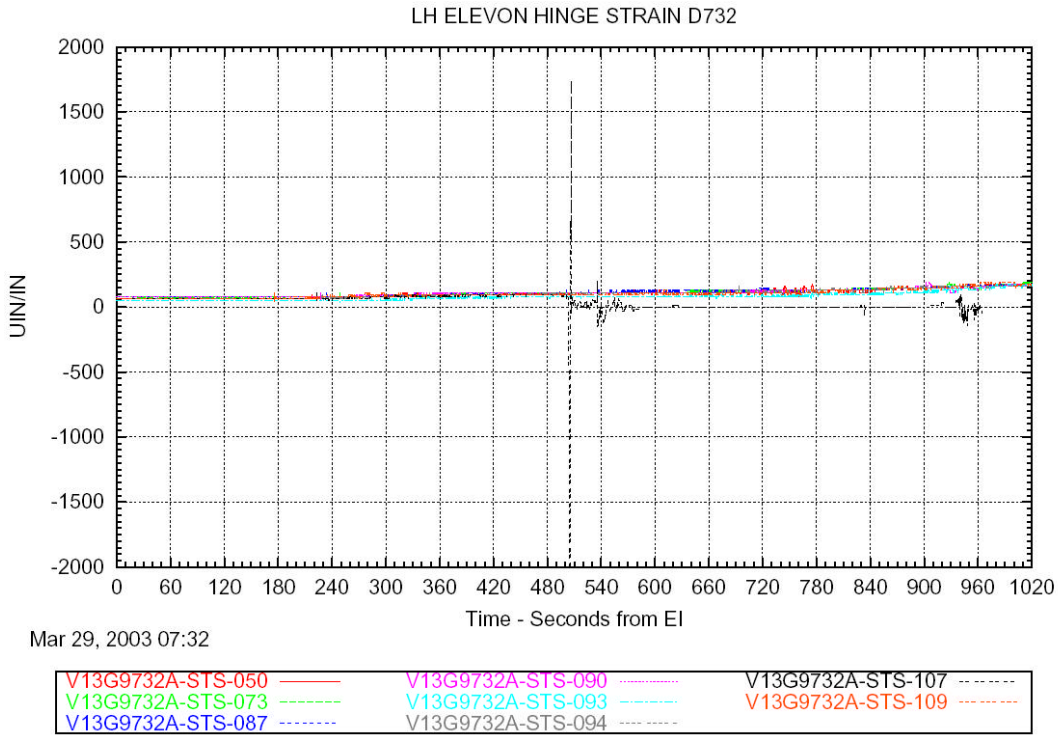

Figure 7.6-17 Typical Left Wing Elevon Entry Gage Failure

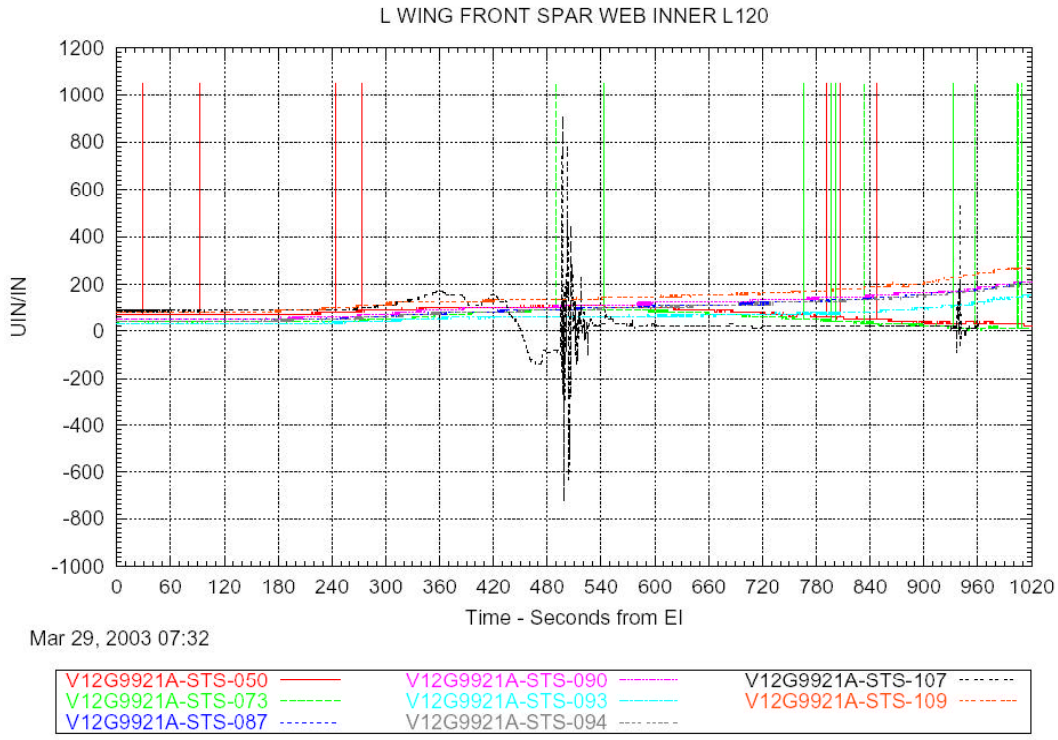

Figure 7.6-18 V12G9921A Entry Response

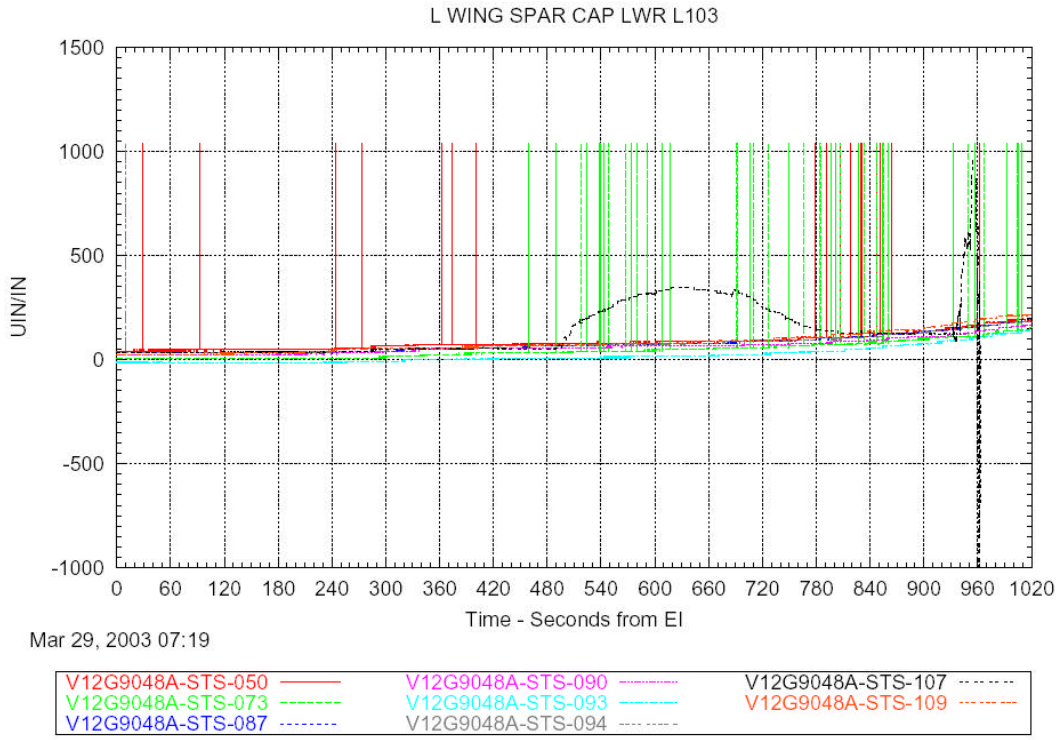

Figure 7.6-19 V12G9048A Entry Response

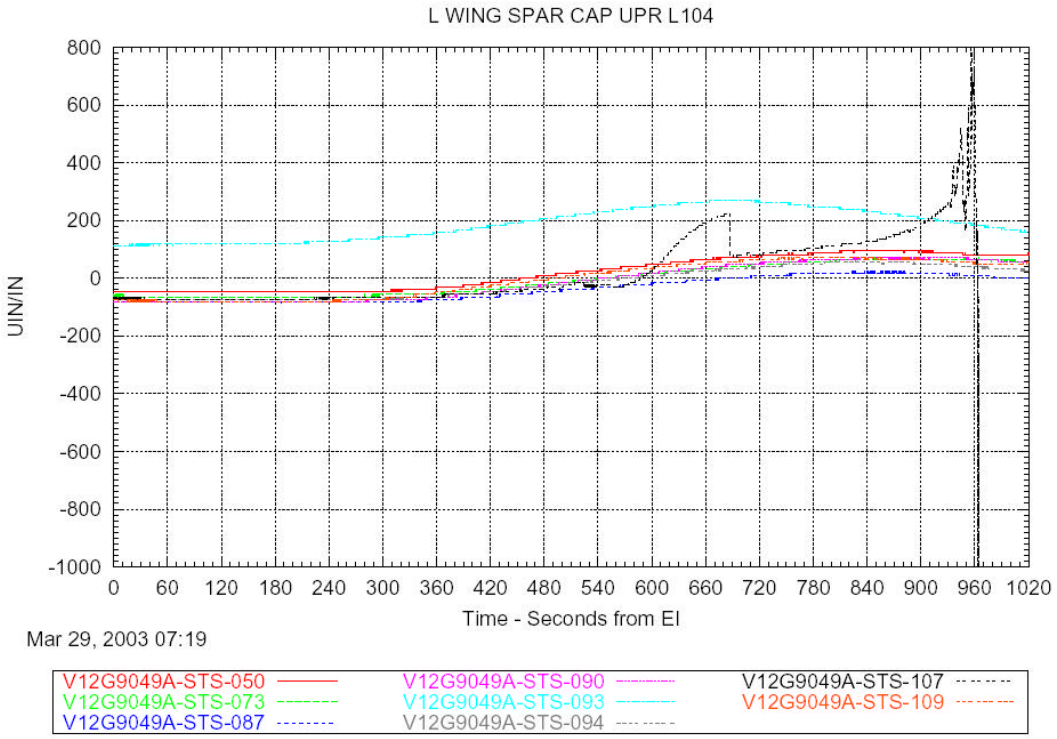

Figure 7.6-20 V12G9049A Entry Response

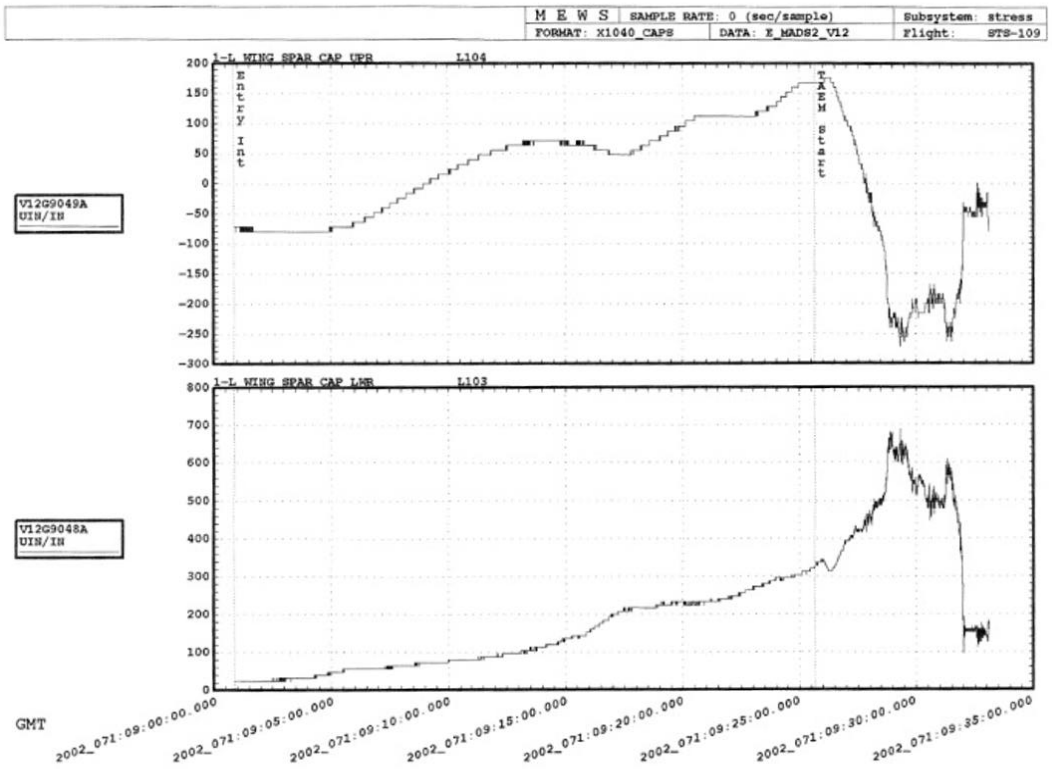

Figure 7.6-21 Xo1040 Spar Caps Nominal Entry (STS-109)

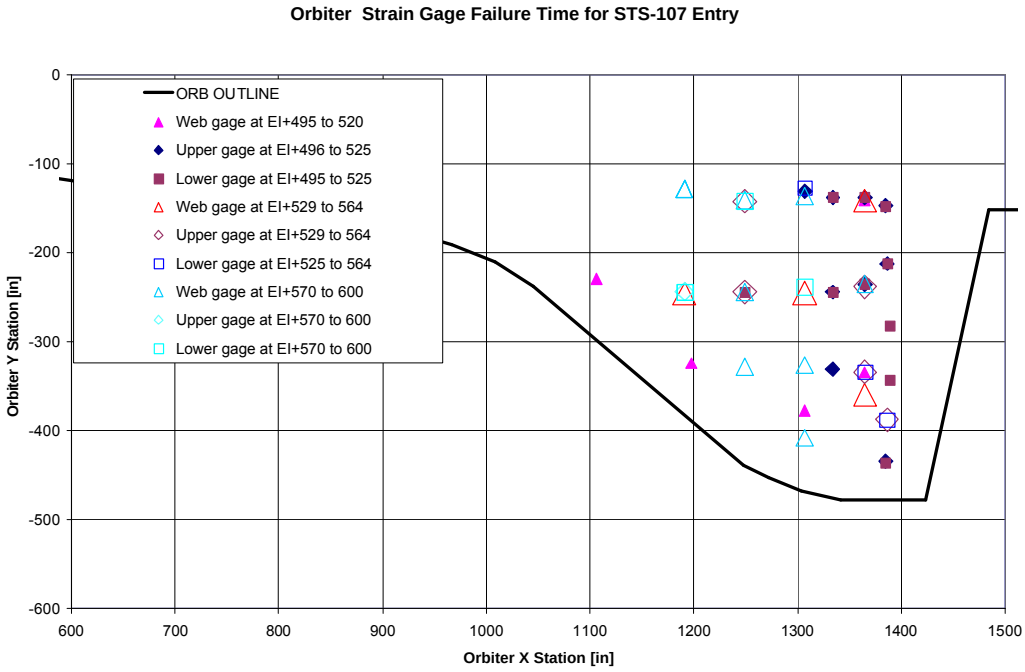

Figure 7.6-22 Left Wing Strain Gage Failure Times

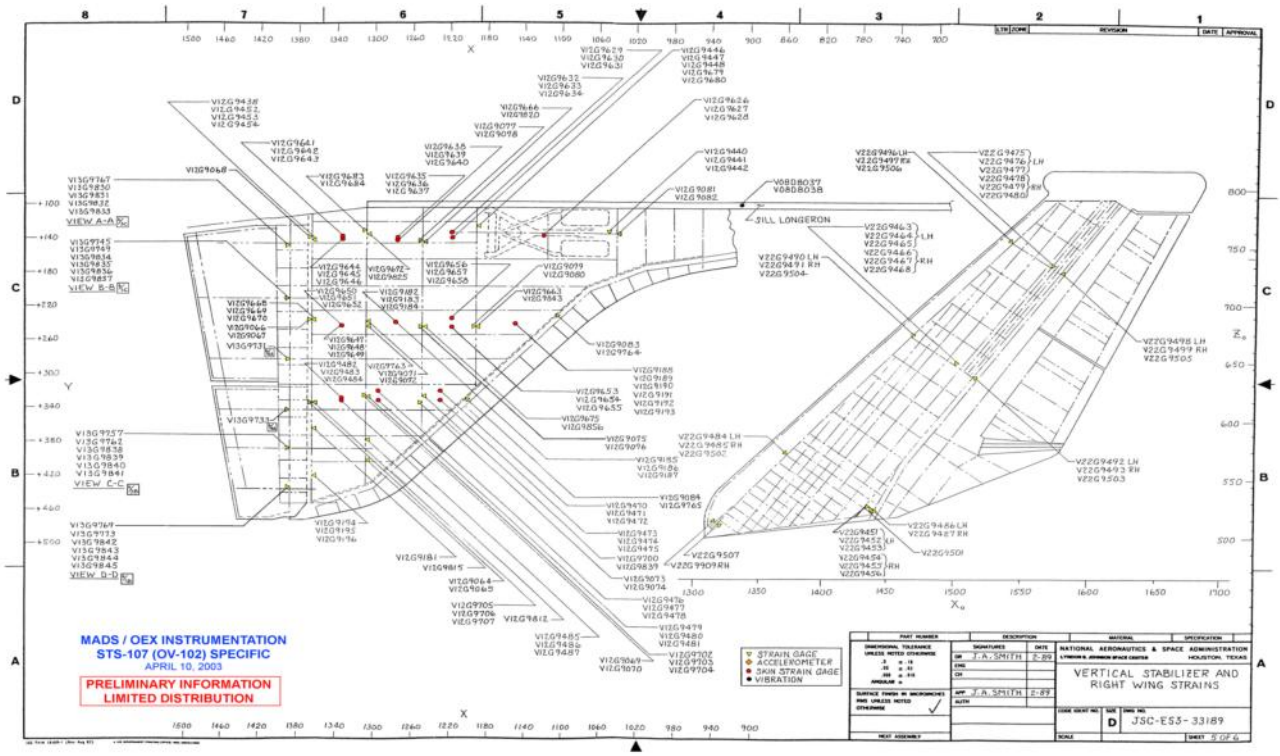

Figure 7.6-23 Right Wing Strain Gage Locations

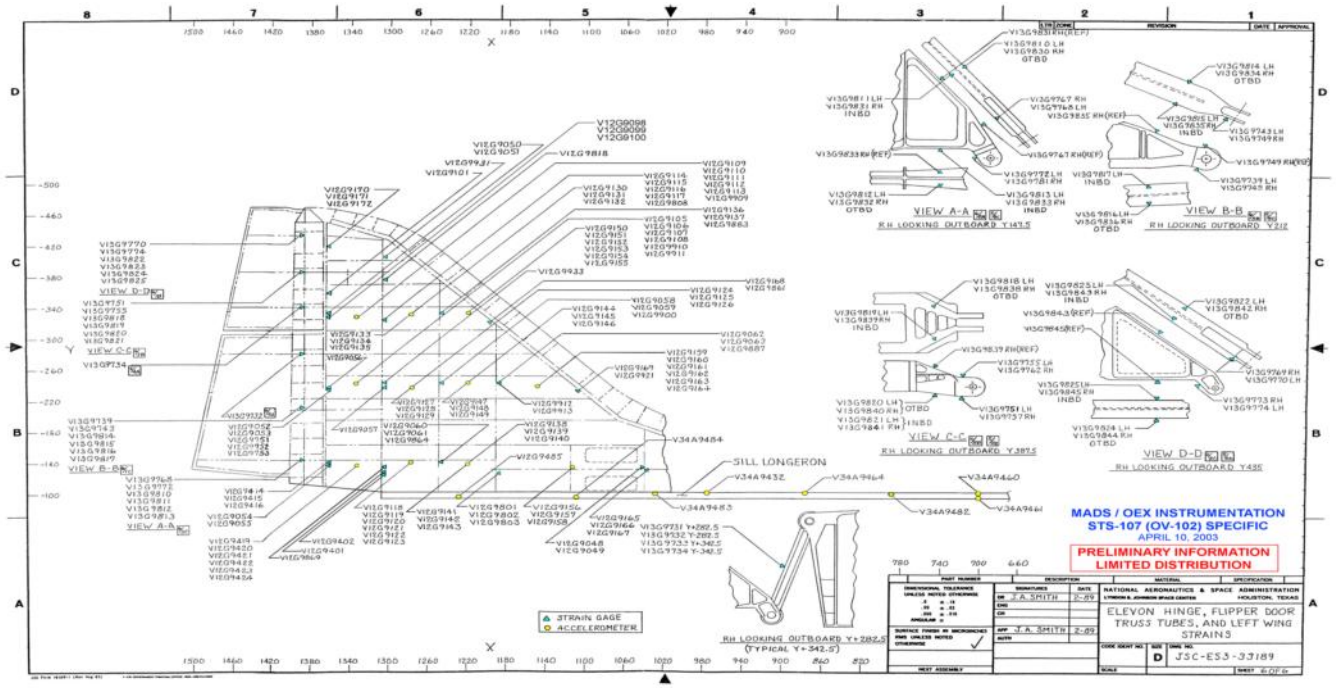

Figure 7.6-24 Left Wing Strain Gage Locations

7.7 Reference – MADS PCM Installation Drawings

Installation drawings for MADS PCM strain gages are as follows:

M072-754119
M072-754120
M072-755107
M072-756106
MC621-0004
V070-784102
V070-786117
VR70-754001

The appropriate drawing for a given strain gage installation may be determined from reference to document number JSC 23560, “OV-102 Modular Auxiliary Data System Measurement Locations”. All relevant installation drawings are included for reference in the data CD that accompanies this report.

8 CONCLUSIONS

The Aerodynamic/Aerothermodynamic/Thermal/Structures Team has completed analyses to support the Columbia Accident Investigation. The completion of this activity has resulted in the formulation of a most probable initial damage and damage progression scenario that can be used with results of other teams to identify the root cause of the Columbia accident.

The culmination of multiple analyses and tests suggest the following entry damage scenario:

Entry Interface to spar burn through:

Columbia began entry with damage to the wing leading edge reinforced-carbon-carbon (RCC) most likely in panels 7 or 8.

Hot gas was ingested into the cavity behind the RCC panels from the beginning of the entry profile. Internal aerothermodynamic and venting analyses show that the flow of hot gas into the RCC cavity was vectored outboard down the RCC cavity and up and aft toward the top of the wing leading edge spar. The hot gas impinged on the RCC panel rib and spanner beam insulation resulting in very high localized heating.

The panel 9 spar strain gage registered the first off-nominal indications at approximately 270 seconds from EI. Stress analysis shows that the panel 9 spar strain gage readings are consistent with shear strain associated with a temperature gradient that developed as the top of the spar is heated by the ingestion of hot gas.

Panel 9 clevis temperature began an off-nominal temperature increase at approximately 290 seconds from EI due to heating from conduction through the insulation and heating from convection due to sneak flow between the insulation and the clevis. Thermal analysis suggests that this response is consistent with flow entering an aperture with an area consistent with a ten inch diameter hole.

CFD analysis and wind tunnel test results modeling increased flow out of thermally degraded/expanded vents located at the top of the RCC cavity suggest that disturbed flow on the leeside of the vehicle can displace the strake and canopy vortices and temporarily reduce localized heating to the left sidewall and left OMS pod.

The damage magnitude is consistent with negligible aerodynamic increments experienced during this period.

Spar burn through to off-nominal increase in sidewall and OMS pod temperatures:

Spar burn through occurred by approximately 487 seconds from EI. This time is supported by:

Wing Spar Strain analysis	-> 420 - 470 sec
1040 Spar Strain analysis	-> 488 sec
Leading Edge Spar wire harness failure	-> 487 sec
Bit flip in wheel well measurement	-> 488 sec
Panel 8/9 thermal analysis	-> 490 sec

Analyses of spar burn through times suggest that the initial damage was consistent with a breach in the lower portion of RCC panel 8 with an area consistent with a six to ten inch diameter hole.

CFD analysis suggests that the transverse momentum of the flow of hot gas entering the RCC cavity is redirected as the flow impinges on RCC ribs and spanner beam hardware and insulation. As a result, the local pressure is increased and the plume entering the intermediate wing is directed normal from the spar toward the main landing gear compartment wall.

Thermal analysis of plume heating on wire bundles and the wheel well wall supports the location of the breach on the panel 8 spar.

Thermal analysis of measured temperature profiles for components in the wheel well show that convective heating is required to produce the measured results. This is consistent with the modeled burn through of the main landing gear compartment wall at approximately EI+601 seconds.

Increased heating of the left sidewall and OMS pod can be explained by redirection of the wing leading edge windward flow to the leeside through either a severely damaged and/or missing upper RCC carrier panel(s), severely damaged or missing full RCC panel (e.g. panel 9), or damaged upper wing just aft of the wing leading edge. Test and analyses of these damage conditions yields aerodynamic increments consistent with flight extracted aero between EI+500 to EI+600 seconds.

Evaluation of final aerodynamic increments:

Damage in the left wing cavity continued to progress until loss of signal. This damage resulted in a significant depression forming on the lower surface of the left wing due to burn though of intermediate wing truss tubes and compromised structural strength associated with heating internal to the wing. The depression in the lower wing resulted in external flow patterns that effectively increased the lift and drag on the left wing resulting in the large positive rolling moment and large negative yawing moment just prior to loss of signal.

As a final comment on the damaged configuration test and analysis results, it must be pointed out again that the nature of this analysis and the conclusions to be drawn from them should be limited to a proper engineering perspective. The test and analysis conducted for the investigation were performed on representative geometries. The representative geometries that have been assessed were chosen in a very dynamic investigation environment as engineers interpreted the latest results from wind tunnel testing, CFD analysis, flight measurement evaluation, recovered hardware forensics, etc. The fact that these geometries were chosen for investigation purposes should not be misconstrued as exactly reproducing the damaged configuration encountered in flight. These representative damaged configurations, however, do provide an insight into the nature and level of damage necessary to result in the loss of Columbia and her STS-107 crew.

9 CREDITS

The authors wish to recognize the outstanding efforts of the many personnel that directly or indirectly supported the AATS team. Numerous personnel from various organizations provided data, products or services in support of AATS team activities. Personnel supporting the accident investigation primarily through the AATS team are listed in Appendix B of this report. Many others, however, provided support through other teams and therefore are not individually credited here. The following teams are recognized for providing essential support to the AATS team:

Timeline Team
Vehicle Data Mapping Team
Integrated Entry Environments Team
Hardware Forensics Team
Scenario Team

In addition, many AATS team members did not author parts of this final report even though they were key contributors on the team, mostly due to reassignment to other activities later in the investigation. These individuals provide invaluable expertise, especially during the initial phase of the investigation. These team members are listed below:

Aerodynamics
Gary Bourland, NASA Johnson Space Center
James Brown, NASA Ames Research Center
Joe Gamble, NASA Johnson Space Center
Jim Greathouse, NASA Johnson Space Center
Gerald LeBeau, NASA Johnson Space Center
Chris Madsen, NASA Johnson Space Center
Charles Miller, NASA Langley Research Center
Phil Stuart, NASA Johnson Space Center

Aerothermodynamics
Ed Alexander, Boeing Houston
Maria Barnwell, Boeing Houston
Basil Hassan Ph. D., Sandia National Laboratories
Ron Merski, Ph. D., NASA Langley Research Center
Charles Miller, NASA Langley Research Center
Habib Sharifzadeh, Boeing Huntington Beach
Carl Peterson, Sandia National Laboratories
Richard Wheless, NASA Langley Research Center

Thermal
Stan Bouslog, Lockheed
Kevin Bowcutt, Boeing Huntington Beach
Doug Cline, Boeing Houston
Dianna Coronado, Boeing Houston
Don Curry, NASA Johnson Space Center
Fred Ghayasi, Boeing Huntington Beach
Andy Hong, NASA Johnson Space Center
John Kowal, NASA Johnson Space Center
Ronald K. Lewis, NASA Johnson Space Center
Jim Milhoan, Lockheed
Don Picetti, Boeing Huntington Beach
Steve Rickman, NASA Johnson Space Center
Dave Russell, Boeing Houston
Habib Sharifzadeh, Boeing Huntington Beach
John Sharp, NASA Marshall Space Flight Center
Lung-Chen Wong, Boeing Houston

Stress
Tony Chi, Boeing Huntington Beach
Scott Foust, Boeing Huntington Beach
Bill Novak, Boeing Huntington Beach
Dave Okino, Boeing Huntington Beach
Steve Scotti, NASA Langley Research Center

10 Acknowledgements

The work presented in this document is but a small demonstration of the total efforts of more than one hundred dedicated engineers and scientists across the country in support of the aerodynamic, aerothermodynamic, thermal, and structural analysis portion of this investigation. Those efforts are not only applicable to understanding Columbia's fate, but will also be used to improve future human space flight vehicle designs. Regardless of how outstanding our efforts, they merely shadow the tragic loss of Columbia and her crew. We dedicate these efforts and the immediate sacrifices of our families and loved ones since the morning of February 1, 2003, to Columbia, her crew, and the lifelong sacrifices of the crew's families and loved ones.

We would also like to recognize the devotion to space flight on the part of the Orbiter program engineers and flight controllers, as well as the dedication of the Space Shuttle and Orbiter program managers. The extreme energies put forth by the manned space flight community during this investigation must be acknowledged, for without their incredible insight, experience and focused drive, the understanding of Columbia's final flight would not have been possible within the allotted time frame. The passion exhibited by this team is the same unyielding dedication that keeps us moving forward, pursuing the vision of manned space flight.

Finally, we dedicate these results, the methods developed and the understanding acquired, to the future of manned space flight and all future crews. By pushing our limitations with each ensuing flight, we utilize the wisdom of the many sacrifices of the past in conjunction with our curiosity, to learn more and continue to follow the better path in mankind's quest for the stars.

References

1. NSTS-37376 Data Review and Timeline Reconstruction Team Final Report in support of the Columbia Accident Investigation

2. NSTS-37382 Integrated Entry Environment (IEE) Team Final Report in support of the Columbia Accident Investigation

3. NSTS-37383 Vehicle Data Mapping Final Report in support of the Columbia Accident Investigation

4. NSTS-37385 Hardware Forensics Team Final Report in support of Columbia Accident Investigation

5. NSTS-37386 Materials and Processes Failure Analysis Team Final Report in support of Columbia Accident Investigation

6. NSTS-37397 Vehicle Reconstruction Team Final Report in support of the Columbia Accident Investigation

7. NSTS-60502 Columbia Working Scenario Final Report

APPENDICES

Appendix A - Acronyms and Abbreviations

AATS	**Aerodynamic/Aerothermodynamic/Thermal/Structures**
ABLT	**Asymmetric Boundary Layer Transition**
ADTA	**Air Data Transducer Assembly**
aero	**Aerodynamic**
AFB	**Air Force Base**
Al	**Aluminum**
APU	**Auxiliary Power Unit**
ARC	**Ames Research Center**
ASA	**Reacting Flow Environments (Branch)**
BC	**Boundary Condition**
BFS	**Backup Flight System**
BHB	**Boeing Huntington Beach**
BL	**Boundary Layer**
BP	**Body Point**
B-RKDN	**Boeing Rocketdyne**
BTU	**British Thermal Unit**
CAD	**Computer-Aided Design**
CAIB	**Columbia Accident Investigation Board**
CART3D	**Cartesian Three Dimensional**
CF4	**Carbon Tetra-Flouride**
CFD	**Computational Fluid Dynamics**
CG	**Center of Gravity**
Comm	**Communication**
DAC	**DSCM Analysis Code**
DAO	**Data Assimilation Office**
DSMC	**Direct Simulation Monte Carlo**
EI	**Entry Interface**
ENV	**Environment**
EOM	**End of Mission**
FC	**Flight Control**
FCS	**Flight Control System**
FEM	**Finite Element Model**
FFT	**Fast Fourier Tranform**
FRSI	**Flexible Reusable Surface Insulation**
ft	**Feet**
FWD	**Forward**
GMT	**Greenwich Mean Time**
GN&C	**Guidance, Navigation and Control**
GNC	**Guidance, Navigation and Control**
GPS	**Global Positioning Satellite**
GRAM	**Global Reference Atmosphere Model**
GSFC	**Goddard Space Flight Center**
Hyd	**Hydraulic**
IEE	**Integrated Entry Environment**
IML	**Inner Mold Line**
IMU	**Inertial Measurement Unit**
INBD	**Inboard**
IR	**Infrared**
JSC	**Johnson Space Center**
Kn	**Knudsen Number**
KSC	**Kennedy Space Center**
LaRC	**Langley Research Center**
LE	**Leading Edge**
LESS	**Leading Edge Subsystem**

LG	**Landing Gear**
LH	**Left Hand**
LHIB	**Left hand Inboard**
LMG	**Left Main Gear**
LMSC	**Lockheed Management Sevices Company**
Ln	**Line**
LOS	**Loss of Signal**
LT	**Left**
M	**Mach**
MADS	**Measurement Acquisition Data System**
MEDS	**Multifunction Electronic Display Subsystem**
MET	**Mission Elapsed Time**
MLG	**Main Landing Gear**
MLGD	**Main Landing Gear Door**
MMOD	**Micro Meteoroid Orbital Debris**
MPH	**Miles per hour**
MPS	**Main Propulsion System**
MSFC	**Marshall Space Flight Center**
MSID	**Measurement Stimulus Identification**
NAIT	**NASA Accident Investigation Team**
NASA	**National Aeronautics and Space Administration**
NAV	**Navigation**
NLG	**Nose Landing Gear**
NSTS	**National Space Transportation System**
OADB	**Operational Aerodynamic Data Book**
OARE	**Orbital Acceleration Research Experiment**
OB	**Outboard**
ODRC	**Orbiter Data Reduction Complex**
OEX	**Orbiter Experimentation**
OFT	**Operational Flight Test**
OI	**Operational Instrumentation**
OML	**Outer Mold Line**
OMS	**Orbital Maneuvering System**
OSH	**Off Scale High**
OSL	**Off Scale Low**
OUTBD	**Outboard**
OVE	**Orbiter Vehicle Engineering**
OVEWG	**Orbiter Vehicle Engineering Working Group**
PCM	**Pulse Code Modulation**
PCM	**Pulse Code Modulation**
PDSS	**PRACA Data Support System**
PIC	**Pyro Initiator Controller**
PRACA	**Problem Resolution And Corrective Action**
Press	**Pressure**
PRSD	**Power Reactant Storage and Distribution**
PRT	**Prevention / Resolution Team**
PSD	**Power Spectral Density**
psf	**Pounds per square foot**
RCC	**Reinforced Carbon-Carbon**
RCG	**Reaction Cured Glass**
RCS	**Reaction Control System**
RMS	**Root mean square**
RTD	**Resistant Temperature Devise**
RTV	**Room Temperature Vulcanizing**
SABER	**Sounding of the Atmosphere using Broadband Emission Radiometry**
sec	**second**
SES	**Shuttle Engineering Simulator**
SGS	**Simple Geometric Shapes**
SiC	**Silicon Carbide**

SILTS	**Shuttle Infrared Leeside Temperature Sensing**
SLA	**Stereolithography**
SNL	**Sandia National Laboratories**
SOFI	**Spray On Foam Insulation**
SPR	**Suspect Problem Report**
SR&QA	**Safety, Reliability & Quality Assurance**
SSVEO	**Space Shuttle Vehicle Engineering Office**
STS	**Shuttle Transportation System**
Surf	**Surface**
Sw	**Switch**
Sys	**System**
TAEM	**Terminal Area Energy Management**
TAS	**True Air Speed**
TC	**Thermocouple**
Temp	**Temperature**
TEOS	**Tetraethyl Orthosilicate**
TIM	**Technical Interchange Meeting**
TIMED	**Thermosphere Ionosphere Mesosphere Energetics and Dynamics**
TMM	**Thermal Math Model**
TPS	**Thermal Protection System**
Unlk	**Unlock**
Uplk	**Uplock**
USA	**Unified Solution Algorithm**
USA	**United Space Alliance**
VGM	**Volume Grid Manipulator**
Vlv	**Valve**
VT	**Vertical Tail**
WBS	**Work Breakdown Structure**
WCT	**Wing Carry Through**
WLE	**Wing Leading Edge**
WSTF	**White Sands Test Facility**
WT	**Wind Tunnel**
WTT	**Wind Tunnel Test**

Appendix B - Team Member List & Biographies

Team Lead Biographies

Pam Madera
Ms. Madera has twenty years of experience in the Space Shuttle Program. Her current position is Subsystem Area Manager for Orbiter Vehicle and Systems Analysis for United Space Alliance in support of the NASA JSC Orbiter Vehicle Engineering Office. She provides oversight of analysis activities associated with the flight readiness, mission support as well as design changes.

Steven Labbe – Aerodynamics Team
Mr. Steven G. Labbe is a 1984 graduate of the University of Cincinnati with a Bachelor of Science Degree in Aerospace Engineering. He has been employed by NASA since 1981, beginning as a cooperative education student at the Lewis (now Glenn) Research Center. He transferred to the Johnson Space Center as a coop and accepted a full-time position in 1984. He currently serves as the Chief of the Applied Aeroscience and Computational Fluid Dynamics Branch. Previous positions at NASA include: Aeroscience Branch Engineer responsible for the development and analysis of Shuttle aerodynamic characteristics; Professional Development Program (PDP) participation via rotational assignment at NASA Ames Research Center in the Applied CFD Analysis Branch; Space Shuttle Ascent Aerodynamic Sub System Manager; Aeroscience Branch Aerodynamics Group Leader; X-38 Project, Aeroscience and Flight Mechanics, Division Chief Engineer/Flight Dynamics Team Lead; X-38 Aerodynamics Lead; and Deputy Chief, Applied Aeroscience & CFD Branch.

Joe Caram – Aerothermodynamics Team
Mr. Caram is an aerospace engineer employed at NASA Johnson Space Center since 1989 working in the Aeroscience and Flight Mechanics Division of the Engineering Directorate. He received his Bachelor of Science and Masters of Science degrees from Texas A&M University in 1986 and 1989, respectively. Until recently he was serving as chief engineer for the feasibility studies of the Orbital Space Plane on Expendable Launch Vehicles (08/02 – 01/03) and X-38 Project EG Division Chief Engineer / Flight Dynamics Lead (03/96 – 07/03). Previous positions at NASA include: Aeroscience Branch engineer responsible for development and analysis of aerothermodynamic environments of various configurations including the Space Shuttle Orbiter. In that position Mr. Caram was responsible for developing math models of the shock-shock interaction heating to the wing leading edge of the Orbiter (9/89 – 3/91) and lead a team investigating Orbiter early/asymmetric hypersonic boundary layer transition (6/92 – 12/95). Other activities during the 1991 to 1995 time frame included being aerothermodynamics team lead in support of advanced projects such as Assured Crew Return Vehicle, First Lunar Outpost, Single Launch Core Station, and Liquid FlyBack Booster. Mr. Caram is an Associate Fellow of AIAA and author or co-author of 20 publications including AIAA conference papers and journal articles, NASA TM's and Symposia.

Charles Campbell – External Aerothermodyanamic Environment Sub-team Lead
Chuck Campbell has been a member of the Applied Aeroscience and CFD Branch at NASA Johnson Space Center since 1990 and has had extensive experience in the application of CFD and wind tunnel testing to manned spacecraft design. Significant activities he has been involved with include the Orbiter Boundary Layer Transition Working Group in the mid-1990's, and hypersonic aerodynamic and aerothermodynamic design for the X-38 Crew Return Vehicle. He holds an Bachelor of Science from the University of Minnesota (1990) in Aerospace Engineering and Mechanics, and a Master of Science from the University of Houston (1998) in Mechanical Engineering.

Team Lead Biographies, Concluded

Steve Fitzgerald – Internal Aerothermodyanamic Environment Sub-team Lead
Steve Fitzgerald joined the Applied Aeroscience and CFD Branch of the Johnson Space Center as a cooperative education student in 1984. Since that time, he has worked a wide range of fluid dynamic fields ranging from numerical simulation of arcjet flows and re-entry flows to rarefied gas dynamics and on-orbit plume impingement flows. As the JSC plume lead, he was a principal author of the Orbiter plume impingement enviromnents and served as a principal investigator for two space flight experiments. In his role as X-38/Crew Return Vehicle aerothermal lead, he oversaw the development of the complete aerothermal database for the X-38, integrating CFD efforts from three separate agencies, and hypersonic wind tunnel testing results from both U.S. and European facilities. Steve holds Bachelors (1986) and Masters (1988) degrees from Texas A&M University in Aerospace Engineering. He presently serves as deputy chief for the GN&C Design and Analysis Branch.

Chris Madden – Thermal Team Lead
Mr. Christopher B. Madden is a 1987 graduate of the University of Texas at Austin with a Bachelor of Science Degree in Aerospace, Aeronautical and Astronautics. He completed his Master of Mechanical Engineering at the University of Houston in 1993. He has been employed by NASA/Johnson Space Center since 1984 where he began as a cooperative student in the Thermal Analysis Section. Mr. Madden is currently serving as the Deputy Chief of the Thermal Design Branch. His previous duties included performing thermal analysis of reentry spacecraft thermal protection systems including the Space Shuttle and other advanced spacecraft; investigation of Space Shuttle thermal anomalies; design and planning of arc-jet tests in support of thermal protection system design and analysis; conducting simulations of orbital debris reentry, and lead engineer for the X-38 structures team including the composite aeroshell and thermal protection system.

Mike Dunham – Stress Team Lead
Mike Dunham is currently is the Boeing Subsystem Manager for Orbiter Stress, Loads and Dynamics. He has worked on Shuttle Orbiter program for 21 years and has a Masters in Civil Engineering Structures from the University of Missouri-Columbia.

Aerodynamics Sub-Team

NASA Johnson Space Center

Rick Barton
Jerry Borrer
Gary Bourland
Kevin Dries
Joe Gamble
Reynaldo Gomez
Jim Greathouse
Mark Hammerschmidt
Steve Labbe
Gerald LeBeau
Randy Lillard
Forrest Lumpkin
Ricardo Machin
Chris Madsen
Fred Martin
Phil Robinson
Steven Robinson
Josh Schneider
Melanie Siloski
Phil Stuart
Tuan Truong
Darby Vicker

Ames Research Center

James Brown
Carol Carroll
David Kinney
James Reuther

Langley Research Center

Karen Bibb
Maria Bobskill
Greg Brauckmann
Pete Gnoffo
Bill Scallion
Charles Miller
Ramadas Prabhu
Bill Woods

Boeing - Houston

Olman Carvajal
Brandon Reddell
Georgi Ushev

Aerodynamics Sub-Team, Concluded

Boeing - Huntington Beach

Rick Burrows
Sergio Carrion
Ron Pelley
Karuna Rajagopal
Harry Sexton
Jeff Stone

Aerothermodynamics Sub-Team

NASA Johnson Space Center

Jerry Borrer
Katie Boyles
Chuck Campbell
Joe Caram
Steve Derry
Kevin Dries
Steve Fitzgerald
Gerald LeBeau
Chien Li, Ph. D.
Forrest Lumpkin, Ph. D.
Randy Lillard
Carl Scott, Ph. D.

NASA Johnson Space Center – White Sands Facility

Harold Beeson, Ph. D
Tim Gallus
Miguel Maes
Mike Shoffstall
Joel Stoltzfus
Bruce Wilson, Ph. D

Langley Research Center

Steve Alter
Kim Bey, Ph. D
Maria Bobskill, Ph. D
Kamran Daryabeigi
Joel Everhart, Ph. D
Chris Glass, Ph. D
Pete Gnoffo, Ph. D
Frank Greene
Harris Hamilton
Tom Horvath
William Kleb
Ron Merski, Ph. D
Charles Miller
Bob Nowak, Ph. D
Ricky Thompson
Bill Wood, Ph. D
William Wood??
Richard Wheless
Kay Wurster
Vince Zoby

Aerothermodynamics Sub-Team, Continued

Ames Research Center

James Brown, Ph. D
Dean Kontinos, Ph. D
Ryan McDaniel
Joe Olejniczak, Ph. D
James Reuther, Ph. D

Marshall Space Flight Center

Herb Bush
Mark Cousins
W. Dahm
Will Downs
Tim Karigan
Ken Kittredge
Al Mayers
David McDaniels
Stu Nelson
Richard Norman
Maurice Prendergast
Joe Ruf
Greg Schunk
John Sharp
Jim Sieja
Mickey White
Joe Wilson

Boeing - Houston

Ed Alexander
Maria Barnwell
Dennis Chao
Mark Fields
Ignacio Norman
K.C. Wang
Lung Wong

Boeing - Huntington Beach

Kevin Bowcutt, Ph. D
Michelle Chaffey
Dan Dominik
Fred Ghahyasi
Suk Kim, Ph. D.
Gerry Kinder
Todd Magee
Kurian K. Mani, Ph. D
Charles R. Olling , Ph. D
Don Picetti
Karuna Rajagopal, Ph. D
Leonel Serrano
Habbib Sharifzedah

Aerothermodynamics Sub-Team, Concluded

Boeing - Rocketdyne

Shashi Aithal
Edward Ascoli
Cliff Bampton
Steve Barson
Pai Chang
Willard Clever
Adon Delgado Jr.
John Fasheh
Scott Halloran
Yann-Fu Hsu
Zhining Liu
Michael Jacques
Dale Ota
S, V. Ramakrishnan
Touraj Sahely
Mark Stewart
Wallace Weider
Kaye Yun

Sandia National Laboratories

Tom Bickel, Ph. D
Michail Gallis, Ph. D
Basil Hassan, Ph. D
Roy Hogan, Ph. D
Dave Kuntz, Ph. D.
William Oberkamphf, Ph. D.
Jeff Payne
Carl Peterson, Ph. D
Ed Piekos, Ph. D.
Don Potter
Art Ratzel, Ph. D
Chris Roy, Ph. D.

AFRL

Susan Arnold
Peter Erbland
Roger Kimmel
James Miller
Richard Neumann

Lockheed Martin

Stan Bouslog
Jose Dobarco-Otero
Tom Paul
Bill Rochelle
Ries Smith

Thermal Sub-Team

NASA Johnson Space Center

Michael Baine
Stan Bouslog
Charlie Camarda
Chuck Campbell
Joe Caram
Joyce Carpenter
Harry Chang
Eric Christiansen
Don Curry
Horatio De La Fuente
Steven Del Papa
Steve Derry
Bonnie Dunbar
Steve Fitzgerald
Mike Fowler
Vadim Gandelsman
Andrew Hong
Eric Hurlbert
Justin Kerr
John Kowal
Gerald LeBeau
Ronald K. Lewis
Stan Love
Chris Madden
Robert Maraia
Tom Modlin
Dan Newswander
Tom Paul
Steve Rickman
Rodney Rocha
Alvaro Rodriguez
Stephanie Wilson

NASA Johnson Space Center – White Sands Facility

Joel Stoltzfus

Langley Research Center

Brian Hollis
Stephen Scotti

Ames Research Center

Scott Lawrence

Thermal Sub-Team, Continued

Marshall Space Flight Center
Joe Ruf
Greg Schunk
John Sharp

Boeing - Houston

Ed Alexander
Maria Barnwell
Shannon Belknap
John Blake
Scott Christensen
Doug Cline
Dennis Chao
Diana Coronado
Tim Davies
Stan Kennedy
Mohammed Nasrullah
Than Nguyen
David Norman
Ignacio Norman
Alfred Olaleye
Renee Rabke
Dave Russell
Steven Tidwell
John Tran
K.C. Wang
Lung-Chen Wong
Michael Zhang

Boeing - Huntington Beach

Kevin Bowcutt
Michelle Chaffey
Dan Dominik
Faustino Garcia
Fred Ghahyasi
Gerry Kinder
Kurian K. Mani
Charles R. Olling
Don Picetti
Karuna Rajagopal
Habbib Sharifzedah

Cimarron

James Smith

Thermal Sub-Team, Concluded

Boeing – Kennedy Space Center

Dan Bell

Boeing - Rocketdyne
Steve Barson
Scott Halloran

Sandia National Laboratories

Tom Bickel
Michail Gallis
Basil Hassan
Roy Hogan
David Kuntz
Jeff Payne
Carl Peterson
Ed Piekos
Don Potter
Art Ratzel

SAIC (Science Application International Corporation)
Omar Hatamleh
Mohamed Ishmael

AFRL
Peter Erbland
Roger Kimmel

Lockheed Martin
Stan Bouslog
Bill Rochelle
Jim Milhoan
Matthew Vogel

United Space Alliance
Pam Madera

Structures Sub-Team

NASA Johnson Space Center

Trevor Kott
Julie Kramer
Tom Modlin
Deneen Taylor

Langley Research Center

Max Blosser
Lynn Bowman
Roger Chen
Kamran Daryabeigi
Christapher Lang
Stephen Scotti

Boeing - Houston

Jason Adair
Bob Clark
Mike Dunham
Danny Le
Aaron Leinmiller
Gus (Constantine) Michalopolous
Darwin Moon
Paul Parker
Shawn Sorenson

Boeing - Huntington Beach

Tony Chi
Gary Collier
Ken Fiorelli
Scott Foust
Judy Goldish
George Hartnett
Mahesh Jain
Mike Koharchick
Jerry Lai
John McKinney
Bill Novak
Dave Okino
Charles Park
Al Richardson
Lou Swayne
Ed Tong
Jerry Warren